Electrochemical and Spectrochemical Studies of Biological Redox Components

Karl M. Kadish, EDITOR

University of Houston

Based on a symposium
sponsored by the ACS Division
of Analytical Chemistry
at the 181st Meeting of the
American Chemical Society,
Atlanta, Georgia,
March 30–April 2, 1981.

ADVANCES IN CHEMISTRY SERIES **201**

AMERICAN CHEMICAL SOCIETY
WASHINGTON, D. C. 1982

Electrochemical and spectrochemical studies of

Library of Congress Cataloging in Publication Data

Electrochemical and spectrochemical studies of biological redox components.
(Advances in chemistry series, ISSN 0065–2393; 201)
Includes bibliographies and index.

1. Bioelectrochemistry—Congresses. 2. Oxidation–reduction reaction—Congresses. 3. Spectrum analysis—Congresses.
I. Kadish, Karl M., 1945– . II. American Chemical Society. Division of Analytical Chemistry. III. Series.

QD1.A355 201 540s [574.19'2] 82–11487
[QP517.B53]
ISBN 0–8412–0661–9 ADCSEJ 1–748
1982

Advances in Chemistry Series

M. Joan Comstock, *Series Editor*

FOREWORD

ADVANCES IN CHEMISTRY SERIES was founded in 1949 by the American Chemical Society as an outlet for symposia and collections of data in special areas of topical interest that could not be accommodated in the Society's journals. It provides a medium for symposia that would otherwise be fragmented, their papers distributed among several journals or not published at all. Papers are reviewed critically according to ACS editorial standards and receive the careful attention and processing characteristic of ACS publications. Volumes in the ADVANCES IN CHEMISTRY SERIES maintain the integrity of the symposia on which they are based; however, verbatim reproductions of previously published papers are not accepted. Papers may include reports of research as well as reviews since symposia may embrace both types of presentation.

ABOUT THE EDITOR

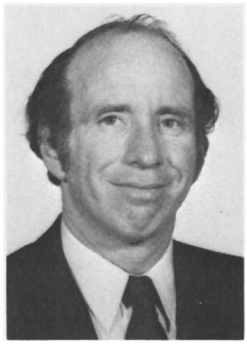

KARL M. KADISH is professor of Chemistry at the University of Houston. He received his B.S. degree from the University of Michigan in 1967 and his Ph.D. from Pennsylvania State University in 1970. He was a postdoctoral fellow at the University of New Orleans in 1970/71 and a chargé de recherche at the Universitè de Paris VI in 1971/72. Before joining the University of Houston in 1976 he was on the faculty of California State University, Fullerton. In 1981 he was a Visiting Professor of Chemistry at the Universitè Louis Pasteur, Strasbourg, France. Dr. Kadish's research interests include porphyrin chemistry, electrochemistry of biologically important compounds, redox reactions of transition metal complexes, and spectroelectrochemistry.

PREFACE

DURING RECENT YEARS, the study of biological redox components has intensified and broadened to include a large number of researchers outside the traditional biochemistry areas. Papers on biological redox components now regularly appear in such diverse journals as *Analytical Chemistry, Biochemistry, Inorganic Chemistry, Journal of the Electrochemical Society, Journal of Electroanalytical Chemistry,* and *Bioelectrochemistry and Bioenergetics,* as well as the more broad-based *Journal of the American Chemical Society.* The Society of Bioelectrochemistry, which consists of chemists, biochemists, and physiologists, was founded in 1980, and a Gordon Research Conference was started the same year in the area of bioelectrochemistry. In addition, numerous symposia are now regularly held in Europe and in the United States on topics described as bioelectrochemistry, biological electrochemistry, bioanalytical chemistry, bioinorganic chemistry, inorganic biochemistry, and biomimetic chemistry.

The main purpose of the symposium on which this volume is based was to bring together both technique and problem-oriented people from many of the above areas. It was hoped that the symposium would stimulate an exchange of ideas by bringing together investigators from diverse backgrounds who were working on closely related topics. Thus, analytical, inorganic, physical, and organic chemists, as well as biochemists were included as speakers.

This volume contains 29 chapters and covers such topics as electron transfer in porphyrins, heme proteins, cytochrome oxidase, and copper proteins. Model systems for the primary photochemical events of photosynthesis, the electrochemistry of reduced pterin cofactors, and the electrochemistry of molecular oxygen and superoxide are also covered. In addition, novel aspects of electron transfer kinetic theory, thin layer spectroelectrochemistry, NMR spectroscopy, magnetic circular dichroism and surface enhanced Raman spectroscopy are presented in the context of biological redox reactions. The presentations include reviews as well as reports of original research.

All of the authors in this collection are leading experts from academic and government research laboratories. Two papers are from Canadian laboratories, four are from European laboratories, and one is from a Japanese laboratory. The varied backgrounds of the authors and

the balanced range of topics make this volume useful to both students and active researchers in the field.

A grant from the Petroleum Research Fund and financial support from the Analytical Chemistry Division of the American Chemical Society provided travel funds, which made participation in the conference possible for six speakers from Europe and Japan. I also owe thanks to the authors who were extremely prompt in meeting the many deadlines I imposed upon them.

KARL M. KADISH
University of Houston
Houston, Texas 77004

July 2, 1982

Studies of Biological Redox Systems by Thin-Layer Electrochemical Techniques

WILLIAM R. HEINEMAN, C. WILLIAM ANDERSON,[1]
H. BRIAN HALSALL, MARILYN M. HURST,[2] JAY M. JOHNSON,[3]
GEORGE P. KREISHMAN, BARBARA J. NORRIS,[4]
MICHAEL J. SIMONE, and CHIH-HO SU[5]

University of Cincinnati, Department of Chemistry, Cincinnati, OH 45221

Thin-layer electrochemical techniques were developed for measuring E°′ *and* n*-values of biological redox systems. A spectropotentiostatic method combines optical measurements of the biocomponent with potential control of a thin solution layer. Coupling of the biocomponent to the electrode potential is achieved by chemical modification of the electrode or by addition of a mediator–titrant. The temperature dependence of* E°′ *is determined easily. This condition is exemplified by cytochrome c for which measurements were sufficiently precise to resolve a nonlinear behavior in the* E°′ *temperature dependence. Biocomponents with no observable optical properties can be studied by thin-layer pulse coulometry and thin-layer staircase coulometry. In these techniques,* E°′ *and* n *are determined by measuring charge as a function of potential. The activity of galactose oxidase was measured while simultaneously controlling its oxidation state. The oxidation state is controlled by a gold electrode (coupled with ferricyanide as a mediator–titrant) in a thin-layer cell with a peroxide electrode inserted in one side. The relative activity of the enzyme is monitored by measuring peroxide production from the enzyme-catalyzed reaction of substrate.*

[1] Current address: Duke University, Department of Chemistry, Durham, NC 27706
[2] Current address: University of North Carolina at Greensboro, Department of Chemistry, Greensboro, NC 27412
[3] Current address: Yellow Springs Instrument Co., Yellow Springs, OH 45387
[4] Current address: Abbott Laboratories, North Chicago, IL 60064
[5] Current address: University of Houston, Department of Chemistry, Houston, TX 77004

0065-2393/82/0201-0001$06.25/0

Investigating the redox characteristics of biological redox systems is important for understanding biological processes such as oxidative phosphorylation and photosynthesis (*1*, *2*). The measurement of formal reduction potentials ($E°'$) and electron transfer stoichiometries (n-values) is a significant aspect of these investigations. Many biological species such as cytochromes (*3*, *4*) and ferredoxins (*5*) undergo heterogeneous electron transfer very slowly or irreversibly. Such behavior is usually attributable to severe adsorption of the biocomponent or to insulation of the redox center from the electrode by the surrounding protein structure. These biological species are difficult to study by conventional electrochemical methods such as cyclic voltammetry.

Spectroelectrochemical techniques based on mediator–titrants (*6*) have been developed and effectively used to measure the $E°'$ and n-values for biological systems that exhibit irreversible electrochemical behavior. The indirect coulometric titration method was applied to the study of cytochrome c (*7*), cytochrome c oxidase (*8–12*), intact mitochondria, and submitochondrial particles (*13*). Soluble spinach ferredoxin also was studied by this technique (*14*). Methods based on the thin-layer electrode were applied to the study of cytochrome c (*3*, *15*), myoglobin (*15*), and galactose oxidase (*16*). These thin-layer electrochemical techniques are described and discussed in this chapter.

Thin-Layer Cells

A thin-layer electrochemical cell confines a thin solution layer adjacent to one or more electrodes (*17*). The thickness of this layer is typically less than 0.3 mm. Complete electrolysis of electroactive species occurs rapidly as a result of the short diffusional path within the thin solution layer. This feature enables rapid conversion of redox couple oxidation states throughout the thin layer by appropriate potential control of the working electrode. The electrochemical techniques described here are all based on this feature of rapid electrolysis.

An optically transparent thin-layer electrode (OTTLE) confines a thin layer of solution adjacent to an electrode that is transparent to light (*18*). This arrangement enables spectral and electrochemical measurements to be made simultaneously on the thin solution layer by an optical beam passing through both solution and electrode.

An easily constructed OTTLE is the gold minigrid sandwiched between two microscope slides with Teflon tape spacers, as shown in Figure 1 (*3*). Solution is drawn from the reservoir cup into the thin layer by suction at the top of the cell. The thin solution layer is typically 0.2–0.3 mm thick, a compromise value that gives maximum optical path length while retaining the thin-layer feature of rapid electrolysis. In such a cell only about 40 μL is electrolyzed in the volume

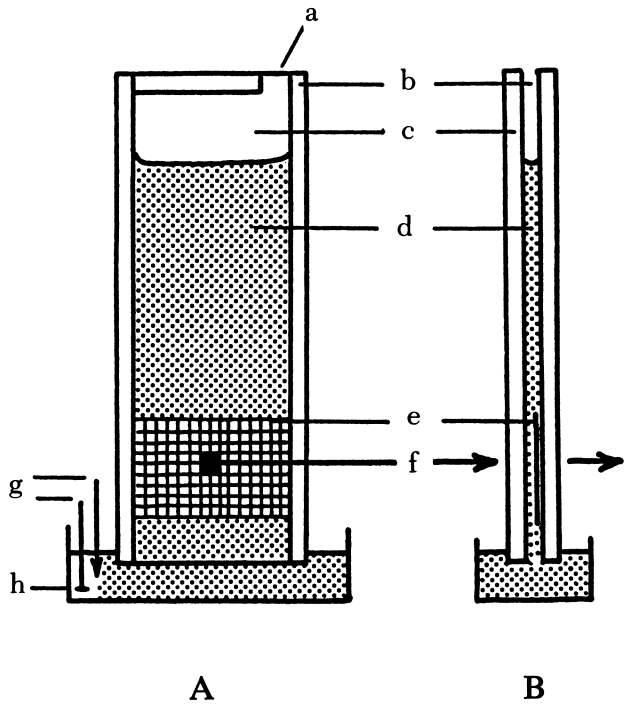

Figure 1. Front (A) and side (B) views of OTTLE (3). Key: a, point of suction application to change solution; b, Teflon tape spacers; c, microscope slides (1 × 3 in.); d, solution between microscopic slides; e, transparent gold minigrid electrode; f, optical path of spectrophotometer; g, reference and auxiliary electrodes; h, cup containing solution. (Reproduced from Ref. 3. Copyright 1975, American Chemical Society.)

defined by the area of the minigrid, although a few milliliters are required to use the cell. Oxygen can be excluded, when necessary, by placing the cell in a plastic box fitted with optical windows and filled with inert gas (*19*). Sample deoxygenation and transfer techniques were developed. The extensive use of this cell is attributable to its simplicity and ease of fabrication.

The transparent electrode used most often in the OTTLE is gold minigrid (*3*, *18*), with either 100 wires/in. (80% transparent) or 500 wires/in. (60% transparent). Mercury can be deposited on the gold minigrid to extend the negative potential range (*20*). Other transparent electrodes such as platinum mesh (*21*), tin oxide (*6*), and reticulated vitreous carbon also were used (*22*).

Several OTTLE cells were developed for use with biological systems where anaerobicity and small total volume are important. The cell shown in Figure 2 requires less than 100 μL to fill (*23*). It is easily

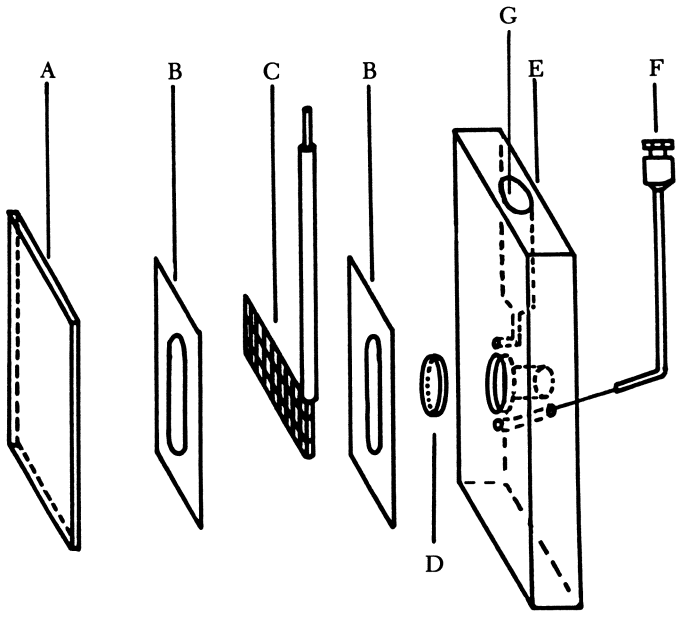

Figure 2. Small-volume OTTLE (23). Key: A, quartz cover plate; B, Teflon spacers; C, gold minigrid; D, quartz disk; E, plastic body; F, inlet syringe; G, overflow reservoir for reference and auxiliary electrode. (Reproduced, with permission, from Ref. 23. Copyright 1979, Academic Press.)

machined from a Lucite block. The machined block facilitates the introduction of solution between the quartz cover plate and the disk that defines the thin layer. Cells of this type were used extensively in our studies of cytochrome c. A cell of similar design was used in conjunction with liquid chromatography (*24*).

An OTTLE that is particularly useful for low temperature measurements was reported (*25*). A circulating, long-optical-path, spectroelectrochemical thin-layer cell (CLOSET) that retains the fast electrolysis feature of the thin-layer cell, but has a 1-cm optical path, was described (*26, 27*).

A semipermeable thin-layer cell that enables control of the oxidation state of a redox enzyme while simultaneously monitoring the product of substrate reaction is shown in Figure 3. This cell was used to study galactose oxidase [vide infra (*16*)].

Spectropotentiostatic Technique

A spectropotentiostatic technique was developed for determining formal reduction potentials, $E^{\circ\prime}$, and electron stoichiometries, n-values, of redox couples (3). The basis of this technique is control of the ratio $[O]/[R]$ of the redox couple in the thin solution layer by the potential applied to the cell. The redox couple is incrementally converted from one oxidation state to the other by a series of applied potentials (E_{appl}) for which each corresponding value of $[O]/[R]$ is determined from spectra. Each potential is maintained until electrolysis ceases so that the equilibrium value of $[O]/[R]$ is established as defined by the Nernst equation. For biological systems that undergo slow-electron transfer with the electrode, a mediator–titrant can be added to convey electrons between electrode and biocomponent, that is, couple the solution potential to the electrode potential. Reduction/oxidation of the biocomponent is thus indirect through the mediator–titrant as shown in Scheme I for a reduction.

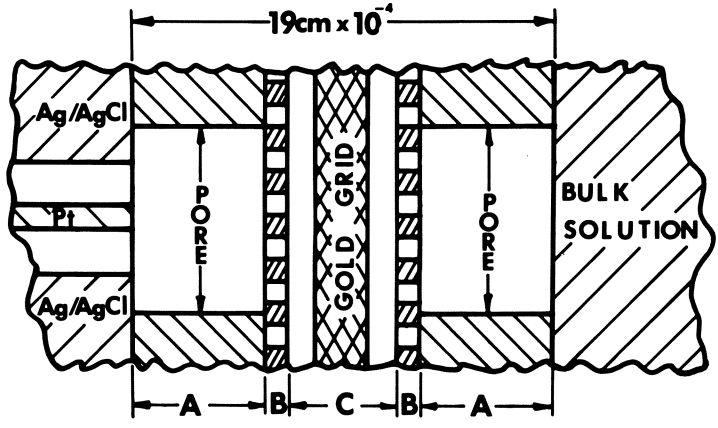

Figure 3. Microscopic cross section of semipermeable thin-layer cell. A, 5-μm thick porous polycarbonate support material for cellulose acetate membrane with pores nominally 12 μm in diameter and a pore density of 1×10^5 pores/cm². B, cellulose acetate membrane that is approximately 1 μm thick and contains pores approximately 6 Å in diameter. C, thin layer ($\sim 4 \times 10^{-4}$ cm thick) containing a 500-lpi gold minigrid electrode (~ 2.5 μm thick). One of the Ag/AgCl electrodes behind the thin-layer cell is used as the reference electrode for the gold minigrid electrode. The other Ag/AgCl and the Pt electrode are used to measure H_2O_2 amperometrically. Dimensions of the electrodes and the pores are not to scale.

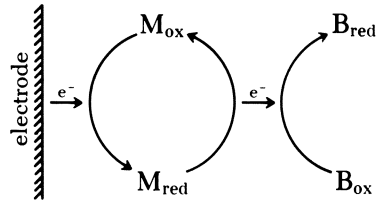

Scheme I

The applicable Nernst equation for mediator–titrant and biocomponent is

$$E_{appl} = E^{\circ\prime}_m + \frac{RT}{n_m F} \log \frac{[O_m]}{[R_m]} = E^{\circ\prime}_b + \frac{RT}{n_b F} \log \frac{[O_b]}{[R_b]} \qquad (1)$$

where m and b refer to the mediator–titrant and the biocomponent, respectively; and $E^{\circ\prime}$ and n are determined from a Nernst plot of the values for E_{appl} and the corresponding values of $[O]/[R]$, as determined from the spectra recorded for each potential.

The spectropotentiostatic technique was used extensively with cytochrome c (*3*, *23*, *28–30*). The cyclic voltammogram in Figure 4 illustrates the extent of irreversibility for cytochrome c at a gold minigrid in an OTTLE. The addition of 2,6-dichlorophenolindophenol (DCIP) as a mediator–titrant enhances the rate of reduction/oxidation of cytochrome c by the following indirect process at the electrode:

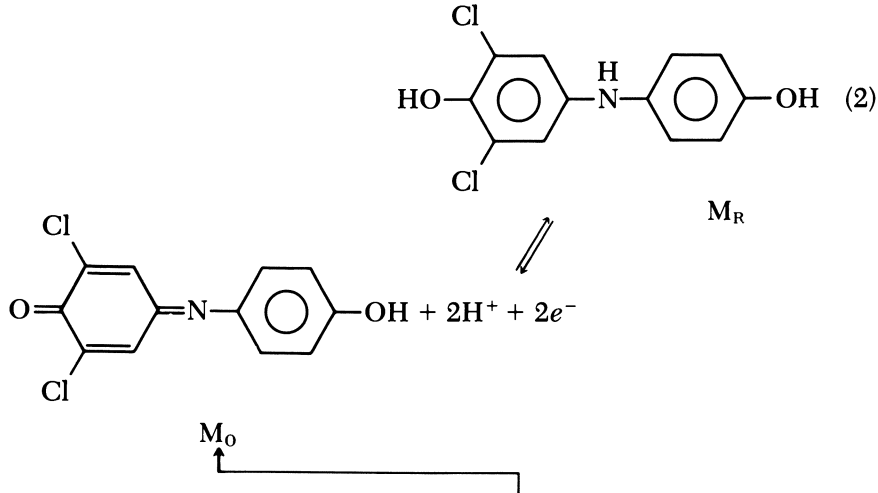

(2)

and in the solution: M_R + 2 cyt c(ox) ⇄ M_O + 2 cyt c(red) (3)

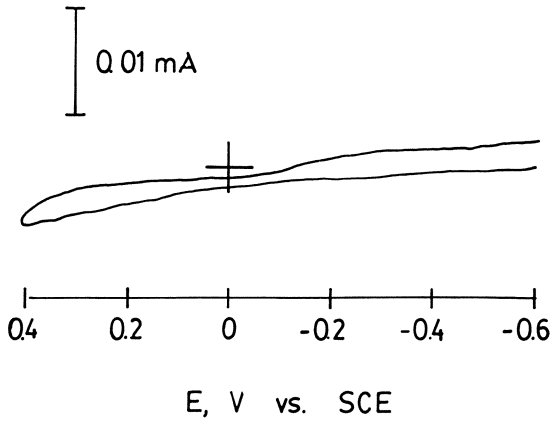

Figure 4. Thin-layer cyclic voltammogram of 0.5 mM cytochrome c in 0.1 M NaCl, pH 7.0 phosphate buffer. Scan rate 1 mV/s. Initial scan, positive from −0.6 V.

Spectra for cytochrome c (with the mediator–titrant added) for a series of applied potentials are shown in Figure 5. The cytochrome is fully oxidized at 300 mV and fully reduced at −600 mV vs. SCE. Spectra were recorded under conditions of equilibrium, that is, current had dropped to a negligible level and spectral changes had ceased. About 10 min is required to achieve equilibrium after a potential change, although this time is dependent on the mediator–titrant concentration and the OTTLE design. Typical Nernst plots for cytochrome c at various temperatures are shown in Figure 6. Values of $E^{\circ\prime} = 262 \pm 1$ mV vs. SHE and $n = 1.00$ are obtained from the intercept and the slope, respectively, at 25°C (*3*). Thus, very precise values of $E^{\circ\prime}$ can be obtained for a biological redox system that essentially is electrochemically irreversible at a gold electrode.

The spectropotentiostatic technique, in conjunction with the OTTLE, facilitates the acquisition of thermodynamic parameters dealing with the temperature dependence of $E^{\circ\prime}$ of a biocomponent (*28,29*). The temperature of the OTTLE is easily controlled by clamping a cell of the type shown in Figure 2 between two water circulating thermal blocks. Nernst plots for cytochrome c at different temperatures are shown in Figure 6. The reduction potential of horse heart cytochrome c, in various sodium halide solutions in H_2O and D_2O, was measured over the temperature range of 25 to 50°C (*28–30*). All samples in D_2O and samples in H_2O not containing chloride ion give a linear temperature dependence. In aqueous chloride solutions, the temperature de-

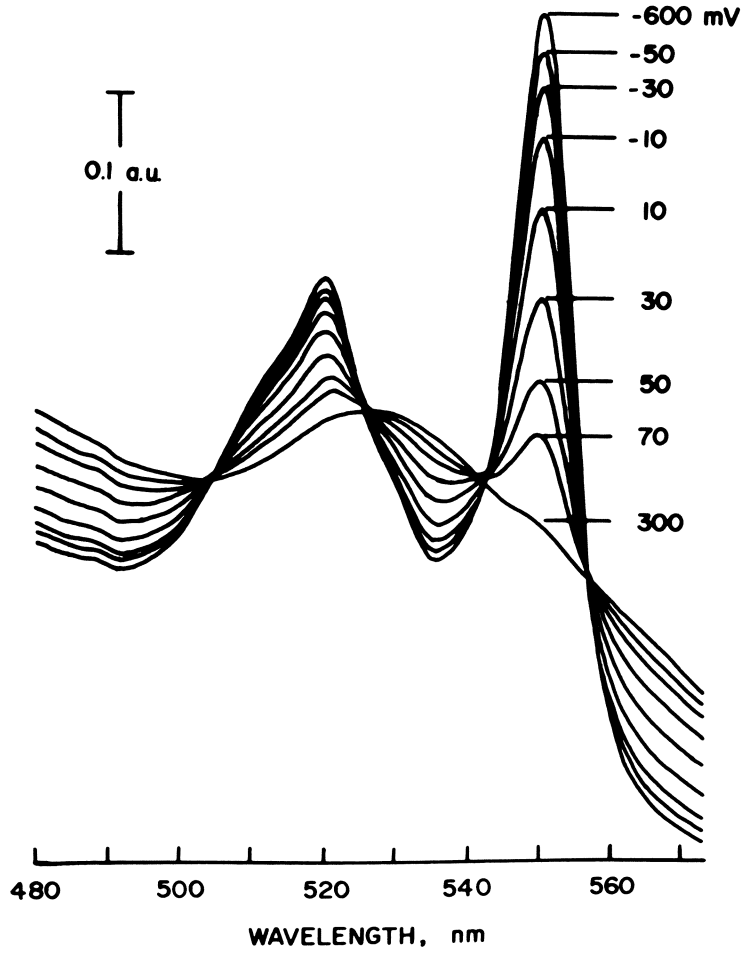

Figure 5. Spectra of 0.5 mM cytochrome c with 0.1 mM DCIP (mediator–titrant) in 0.5 M phosphate buffer, pH 7.0, for a series of applied potentials, vs. SCE (23). (Reproduced, with permission, from Ref. 23. Copyright 1979, Academic Press.)

pendence is nonlinear with an apparent intersection point at 42°C, as shown in Figure 7. This nonlinear behavior was interpreted in terms of a structural change in the bulk water at 42°C for Cl^-–H_2O solutions. In this case the good precision of the spectropotentiostatic technique is essential in defining the nonlinear behavior.

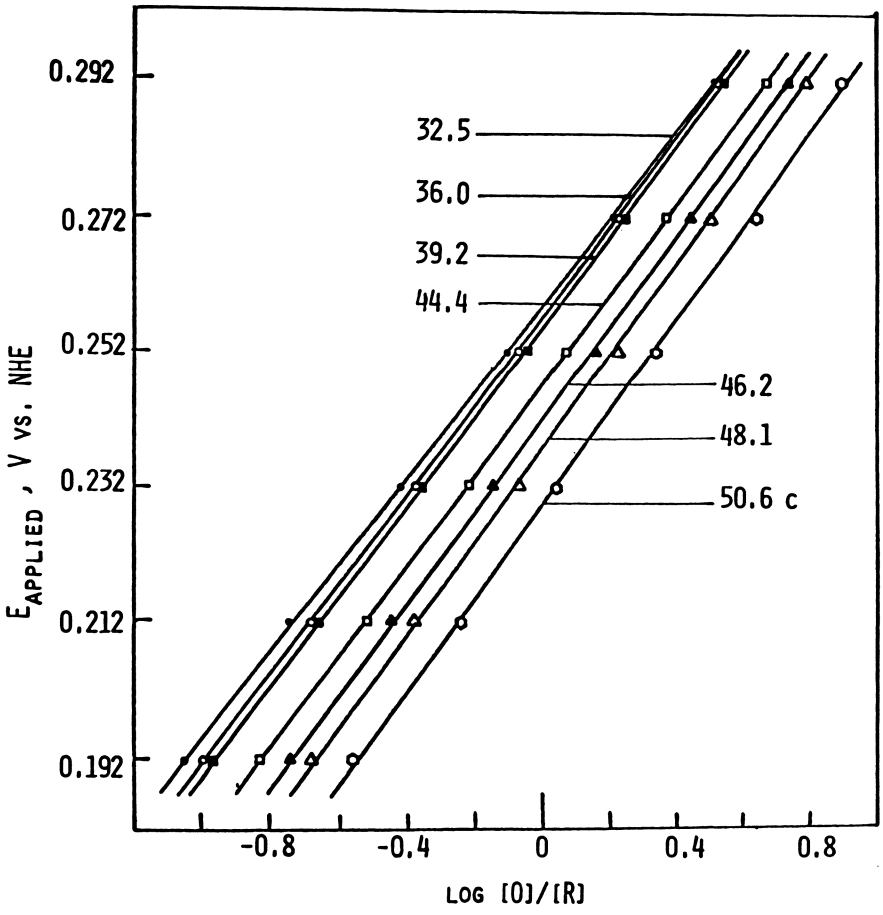

Figure 6. Nernst plots for 0.1 mM cytochrome c, 0.1 mM DCIP (mediator–titrant), pH 7.0, 0.1 M phosphate buffer, and 0.1 M NaCl at varying temperatures, °C. [O]/[R] obtained at 550 nm from spectra recorded in OTTLE of the type in Figure 2 (15). *(Reproduced, with permission, from Ref. 15. Copyright 1979, Elsevier Sequoia.)*

Spectropotentiostatic measurements have been made on several other biocomponents. Spectra of myoglobin with phenazine methosulfate as the mediator–titrant gave a Nernst plot with $E^{\circ\prime}$ = 46.4 mV vs. SHE and n = 0.95 (*15*). Measurements were made at various temperatures on the copper blue proteins azurin, plastocyanin, and stellacyanin with appropriate mediator–titrants (*31*). Vitamin B_{12} has been investigated by OTTLE methods (*21, 32–36*). In this case, no mediator–titrants were necessary, although the electrode reaction for the cobalt(III)/cobalt(II) couple was very slow (*36*). Photosynthetic electron transport components proved amenable to investigation by OTTLE techniques (*25*).

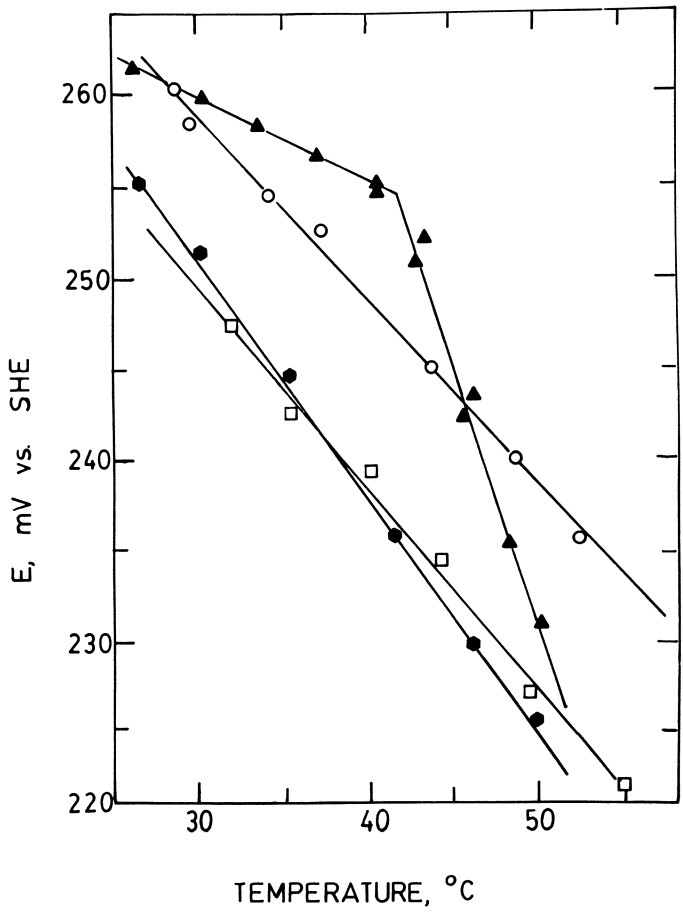

Figure 7. Temperature dependence of E°′ *for horse heart cytochrome c in 0.10* M *sodium halide solutions in* H_2O. *Solutions contain 0.10* M *sodium phosphate buffer, pH 7.0, and 0.1 m*M *DCIP* (29). *Key:* ○, Fl^-; ▲, Cl^-; ⬢, Br^-; *and* □, I^-. *(Reproduced, with permission, from Ref.* 29. *Copyright 1978, Elsevier Sequoia.)*

Although it was originally developed for the study of biological redox components (3), the OTTLE spectropotentiostatic technique is equally useful for the study of inorganic metal complexes (37) and organic compounds (*38*).

The advantage of the OTTLE spectropotentiostatic technique is the ease with which the redox state can be controlled in the thin solution layer. Reversible redox systems can be cycled repetitively

between oxidation states. A disadvantage is the short optical path of the OTTLE, necessitating the use of higher concentrations of the biocomponent. Signal averaging techniques and multiple passes of the optical beam through the OTTLE can minimize this problem.

Mediator–Titrants. Control of the solution potential by reduction/oxidation of the biocomponent via a mediator–titrant (*6*) is crucial for obtaining values of $E^{\circ\prime}$ for some biological systems (*39*). For example, hours rather than minutes are required to electrolyze cytochrome c in the OTTLE in the absence of a mediator–titrant (*3*). Requirements for an optimum mediator–titrant for use in the OTTLE are rapid, reversible heterogeneous electron exchange with the electrode and homogeneous electron transfer with the biocomponent, stability in both oxidation states, absence of spectral properties that interfere with optically monitoring the biocomponent, and absence of binding with the biocomponent causing a shift in $E^{\circ\prime}$ of the biocomponent. The potential range over which a mediator–titrant will control solution potential was measured for numerous compounds (*39*). A typical mediator–titrant will control the solution potential over a range of $E^{\circ\prime} \pm 50$ mV. A large potential range can be covered by mixing mediator–titrants with $E^{\circ\prime}$ values that span the desired range (*39*).

An alternative approach to the use of mediator–titrants for coupling the electrode to the biocomponent is chemical modification of the electrode. Although relatively new, this approach already has shown promising results for cytochrome c (*40*), myoglobin (*41*), and ferredoxin (*5*).

Spectroscopic Techniques. UV–visible absorption spectroscopy was the main optical technique used in conjunction with OTTLE studies of biological systems (*3*). Light-induced absorption changes, fluorescence yield changes, and circular dichroism also were measured with the OTTLE in studies of photosynthetic electron transport components (*25*).

The fluorescence emission spectrum of tryptophan-59 in cytochrome c recently was measured for the oxidized and reduced forms (Figure 8) (*42*). Because fluorescence usually is sensitive to small environmental changes of the fluorophor, small conformational changes in the protein can be detected. The fluorescence intensity of the tryptophan of cytochrome c is attenuated greatly by two factors: (1) efficient energy transfer to the heme and (2) quenching by other cytochrome c molecules in solution. Taking these two factors into account, the observed ratio of fluorescence intensities for the two forms can be explained if one assumes a movement of the tryptophan toward the heme of 0.7 ± 0.3 Å on reduction. Because the two forms of the cytochrome c were generated in situ in the OTTLE, this analysis could be carried out utilizing uncorrected spectra. In addition, the lower detec-

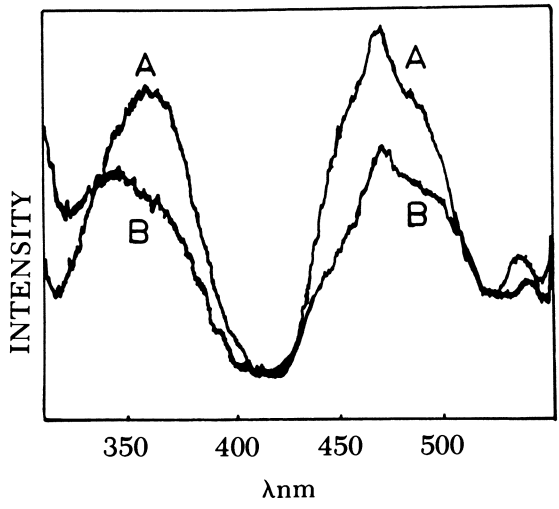

Figure 8. Thin-layer fluorescence emission spectra of tryptophan-59 in cytochrome c. A, Reduced state, E_{appl} = −600 mV vs. SCE; B, oxidized state, E_{appl} = 200 mV vs. SCE. 288-nm excitation. Conditions: 1.0 mM cytochrome c, 0.05 mM DCIP, and 0.5 M NaCl in 0.1 M phosphate buffer, pH 7.0. (Reproduced, with permission, from Ref. 42. Copyright 1982, Academic Press.)

tion limit of fluorescence enables measurements to be made on much lower concentrations of cytochrome c than is possible with UV–visible absorption spectroscopy.

Thin-Layer Pulse and Staircase Coulometry

Two thin-layer electrochemical techniques were developed for measuring $E^{\circ\prime}$ and n of biocomponents with such weak spectral changes that the spectropotentiostatic technique is impractical (*43*). The two techniques do not require the measurement of optical changes in either the biocomponent or the mediator–titrant. They are based on the charge response to potential pulse or potential staircase excitation signals. Both techniques can be used with the OTTLEs shown in Figures 1 and 2.

Thin-Layer Pulse Coulometry. In thin-layer pulse coulometry, the electrode potential is stepped from a single initial potential, at which the redox component(s) is entirely in one oxidation state, to a series of potentials that convert an increasing fraction of the redox component(s) into another oxidation state. The excitation waveform is shown in Figure 9A. For each potential, the ratio of the concentrations of oxidized to reduced forms, $[O]/[R]$, of the redox species in the thin

solution layer adjusts by electrolysis to the value required by the Nernst equation (for a reversible system). The thin-layer electrode enables the equilibrium $[O]/[R]$ value corresponding to each potential step to be obtained from the charge required for electrolysis of the thin solution layer. The range of the series of potentials to which the electrode is stepped is selected to span the $E°'$ of the redox component so that charges are obtained for the extremes of complete oxidation and reduction as well as for intermediate values of $[O]/[R]$. A plot of the charge for each potential step vs. the potential to which the electrode is stepped gives a Q–E plot that resembles the traditional polarogram. The $E°'$ and n-values are obtained from the intercept and slope, respectively, of a Nernst plot in the form of Equation 4.

$$E_{\text{appl}} = E^{\circ\prime}_{O,R} + \frac{RT}{nF} \log \frac{Q_T - Q}{Q} \tag{4}$$

where Q_T is the total charge required to convert all of O to R.

To obtain the $E°'$ and n for a nonelectroactive biocomponent, a Q–E plot is first obtained for a mediator–titrant with an $E°'$ in close proximity to the redox potential of the biological species. Such a plot for the mediator–titrant DCIP is shown by Curve A in Figure 10. The biocomponent is then added to the solution and a second Q–E plot is obtained. The resulting plot for the addition of cytochrome c is shown by Curve B in Figure 10. In this case, Q contains the charge required to electrolyze both the mediator–titrant (direct electron exchange with the electrode) and the biocomponent (indirect electron exchange by

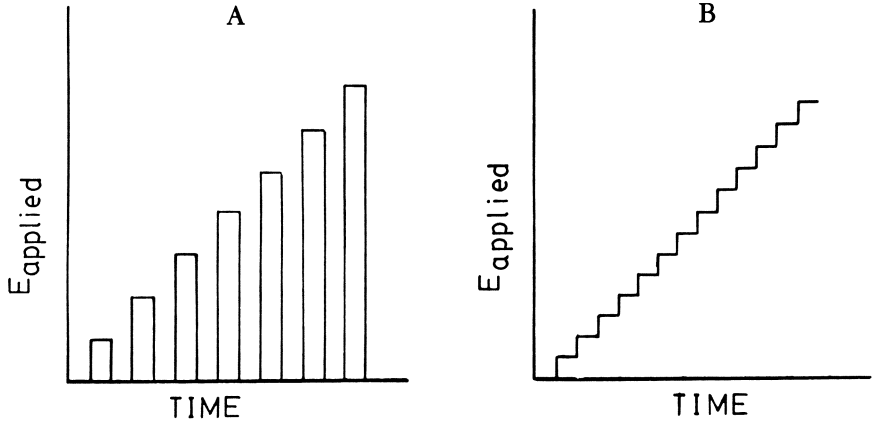

Figure 9. Potential excitation signals for A, thin-layer pulse coulometry and B, thin-layer staircase coulometry. (Reproduced from Ref. 43. Copyright 1981, American Chemical Society.)

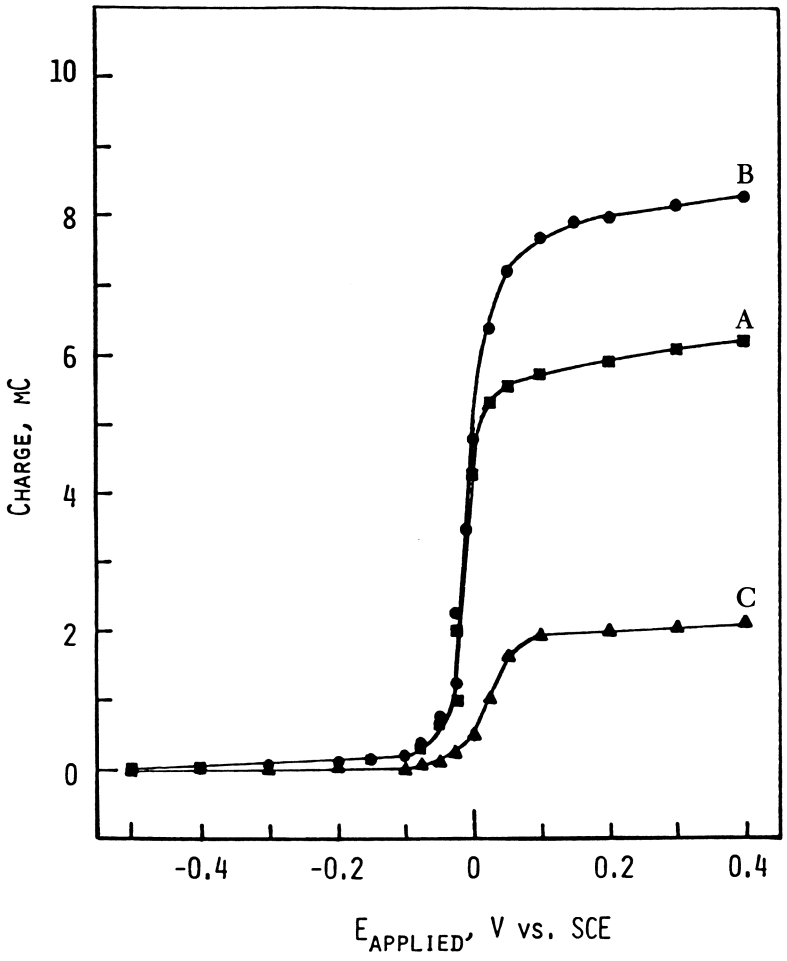

Figure 10. Charge–potential curves for thin-layer pulse coulometry. Conditions: A, 0.8 mM DCIP; B, 0.55 mM cytochrome c and 0.8 mM DCIP; and C, component of B which is due to cytochrome c as obtained by the difference in B and A. All solutions contain 0.2 M NaCl, pH 7.0 phosphate buffer. $E_{initial} = -0.6$ *V. (Reproduced from Ref. 43. Copyright 1981, American Chemical Society.)*

homogeneous reaction with the mediator–titrant) to the appropriate value of $[O]/[R]$ as dictated by the individual Nernst equations. The Q–E plot for the biocomponent is obtained indirectly from the difference of the above two Q–E plots, Curve C in Figure 10. The Nernst plot of Curve C for cytochrome c is linear. Calculated values of $E^{\circ\prime}$ and n for cytochrome c are 14 mV vs. SCE and 1.00, respectively.

Thin-Layer Staircase Coulometry. In this technique, the electrode potential is scanned from an initial potential (at which the redox species is completely in one oxidation state) to a final potential (at which the redox species in the thin layer was converted completely to another oxidation state) by means of a staircase waveform as shown in Figure 9B. Each step is sufficiently long to allow the new value of $[O]/[R]$ to be established throughout the thin layer of solution. The current accompanying each potential change in the staircase is integrated to give the value of Q required to establish the new equilibrium value of $[O]/[R]$. The values of Q are plotted as a function of the respective potentials to which the electrode is stepped. The resulting Q–E curve is peak-shaped, analogous to a differential pulse voltammogram. The $E^{\circ\prime}$ and n-values are obtained from the peak potential and the midpoint peak width, $\Delta E_{1/2}$, respectively. Calculations show that $\Delta E_{1/2}$ should be as follows for a reversible system: $n = 1$, 90 mV; $n = 2$, 45 mV; and $n = 3$, 30 mV.

Measurement of $E^{\circ\prime}$ and n for a biocomponent such as cytochrome c is accomplished by an indirect procedure analogous to that described above for the pulse method. A staircase voltammogram for the mediator–titrant DCIP alone is shown by Curve A in Figure 11. Curve B is the voltammogram for a solution containing a concentration of DCIP identical to that for Curve A plus cytochrome c. Subtraction of Curve A from B gives Curve C, which is the Q–E plot for cytochrome c. The peak potential for this voltammogram is 18 mV vs. SCE. This potential agrees well with the value determined by the pulse technique. The $\Delta E_{1/2}$ value of 86 mV is in good agreement with the expected value of 90 mV for a one-electron system.

Measurement of Enzyme Activity as a Function of Solution Potential

The activity of metalloprotein enzymes such as galactose oxidase depends on the oxidation state of the metal that is incorporated into the protein structure (*44–47*). Galactose oxidase is an enzyme that is quite nonspecific, catalyzing the production of hydrogen peroxide from a variety of substrates including galactose, glycerin, dihydroxyacetone, and glyceraldehyde (*48*, *49*). The oxidation of galactose by oxygen catalyzed by galactose oxidase is representative of these reactions (*50*).

$$\text{galactose} + O_2 \xrightarrow[\text{oxidase}]{\text{galactose}} H_2O_2 + \text{galactohexodialdose} \qquad (5)$$

A convenient method for monitoring activity is measurement of hydrogen peroxide production. Galactose oxidase contains a single cop-

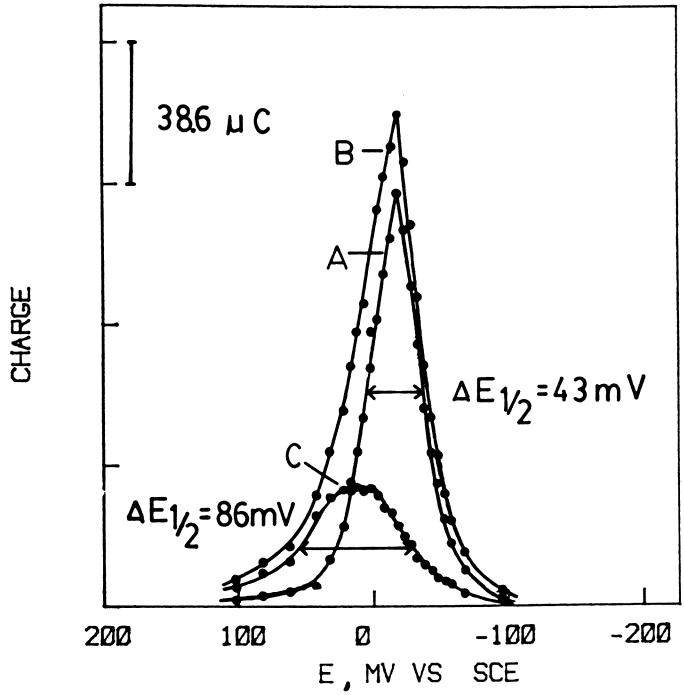

Figure 11. Charge–potential curves for thin-layer staircase coulometry. Conditions: A, 0.25 mM DCIP; B, 0.25 mM cytochrome c and 0.25 mM DCIP; and C, cytochrome c component of B obtained by subtracting A from B. Step height = 5 mV; scan direction, positive. All solutions contain 0.2 M NaCl in pH 7.0 phosphate buffer. (Reproduced from Ref. 43. Copyright 1981, American Chemical Society.)

per ion. The enzyme is inactive in the reduced state, Cu^{1+}, and active in the oxidized state (*45*, *50*, *51*).

The enzyme activity for galactose oxidase as a function of the oxidation state of the copper ion can be measured with a semipermeable thin-layer electrochemical cell that incorporates two working electrodes. One electrode controls the redox state of the enzyme by coupling through a mediator–titrant. The second electrode measures amperometrically the concentration of hydrogen peroxide resulting from the enzyme-catalyzed reaction (*52*). In one configuration the thin-layer electrochemical cell consisted of a gold minigrid electrode sandwiched between two cellulose acetate membranes. A cross section of the cell is shown schematically in Figure 3. The cellulose acetate membrane (attached to a polycarbonate support membrane) is permselective based on size. Thus, the cell has the usual characteristics of a thin-layer cell in that total electrolysis can be achieved rapidly by the gold grid as long as the species being electrolyzed is too large

(>200 mol. wt.) to diffuse out of the cellulose acetate membrane on the time scale of the experiment. Yet, materials that are small enough to pass rapidly through the membrane can be introduced into the thin layer from the adjacent bulk solution. A platinum electrode is positioned against one of the membranes. Because the membrane is permeable to H_2O_2, Reaction 5 can be monitored by measuring the current flowing at this platinum electrode when it is maintained at a potential sufficiently positive to reoxidize H_2O_2 to O_2 (*52*). Thus, by measuring the steady state hydrogen peroxide production by means of the platinum electrode behind one semipermeable membrane, the relative steady state activity of galactose oxidase in the thin layer can be determined in the presence of any particular substrate that is introduced into the bulk solution and allowed to equilibrate across the outer cellulose acetate membrane.

The thin-layer property of the cell is exemplified by the cyclic voltammogram in Figure 12A for buffered 4×10^{-3} *M* ferricyanide and galactose oxidase. As the potential of the gold minigrid is scanned from 0 V vs. Ag/AgCl to 0.4 V, the anodic current peak indicates oxidation of ferrocyanide to ferricyanide. Scan reversal results in a cathodic peak due to reduction back to ferrocyanide. Because the ferrocyanide–ferricyanide couple is trapped within the cellulose acetate membrane, the cyclic voltammogram exhibits typical thin-layer behavior of negligible peak separation and peak widths at a half-height of approximately 90 mV (*17*).

Because the ferricyanide–ferrocyanide couple functions as a mediator–titrant to couple the electrode potential to the galactose oxidase redox state, a positive potential scan converts the galactose oxidase into its oxidized form which catalyzes substrate reaction with O_2. The reaction produces H_2O_2 which is detected by anodic current flowing at the platinum electrode. This current at the platinum electrode (held at +0.7 V vs. Ag/AgCl) as a function of the potential of the gold minigrid is shown by the voltammogram in Figure 12B. The onset of a limiting current at ca. 0.3 V vs. Ag/AgCl is indicative of complete galactose oxidase conversion to the oxidized form. This current is at steady state because the outer membrane is permeable to the glycerin substrate. The approximate reversibility is indicated by the reverse scan behavior.

This configuration (Figure 3) is useful for determining whether or not there is an activity dependence on solution potential. However, the relative permeability of the outer cellulose acetate membrane to substrate is so low that diffusion of substrate across the outer membrane is rate limiting. This situation causes the apparent dependence of activity upon solution potential to be distorted to an extent dependent on the diffusion coefficient of the substrate, the concentration of enzyme behind the membrane, and the rate of the enzyme reaction (*16*).

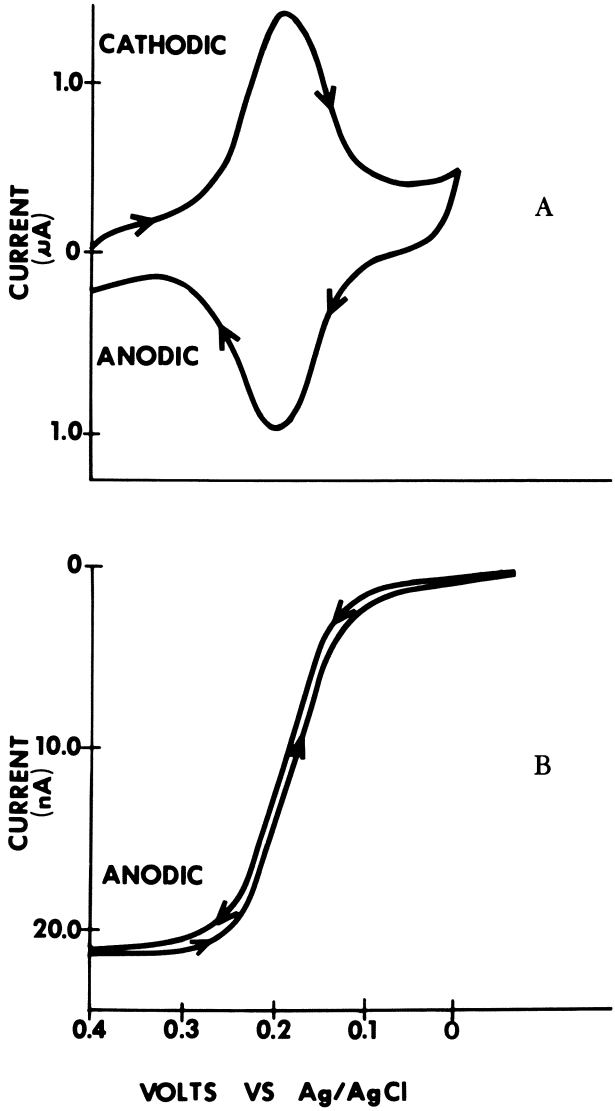

Figure 12. Activity–potential profile for the galactose oxidase-catalyzed oxidation of glycerin. The thin layer contained 4×10^{-3} *M ferricyanide and also galactose oxidase. The bulk solution was a pH 7.3, 0.07* M *phosphate buffer also* 4×10^{-3} M *in ferricyanide and 0.5* M *in potassium chloride. A, Thin-layer cyclic voltammogram for the oxidation/reduction of ferrocyanide–ferricyanide at the gold grid. Scan rate = 2 mV/s. B, Plot of* H_2O_2 *current measured amperometrically as the gold grid electrode was scanned at 2 mV/s. The scan began after glycerin was introduced into the stirred bulk solution at a final concentration of about* 5×10^{-3} M *and a steady state* H_2O_2 *current had been achieved at the Pt electrode.*

For accurate determination of the dependence of activity on solution potential for galactose oxidase, a second cell configuration must be studied (*16*). In this configuration a more permeable outside membrane (0.03-μm pore size polycarbonate) is used so that diffusion of substrate is not as limited as in the first configuration. However, the permeability of this membrane to mediator–titrant must still be low enough to maintain control of the solution potential within the enzyme layer. Also, because the pores in the outer membrane are large enough for the enzyme to escape, the enzyme must be polymerized behind the membrane. For galactose oxidase, polymerization with glutaraldehyde does not affect significantly the dependence of activity on solution potential. Finally, even in this configuration, diffusion of substrate across the outside membrane does become rate limiting as the concentration of enzyme behind the membrane is increased. The point at which diffusion becomes rate limiting depends primarily on how rapidly the substrate is turned over by the enzyme. With galactose oxidase the rates of turnover are so diverse for the various substrates that at high enzyme concentrations the apparent dependence of activity on solution potential can be extremely different for the various substrates. Thus, low enough enzyme concentration must be chosen so that the rate of the enzyme reaction becomes rate limiting. Under these conditions the dependence of activity upon solution potential can be determined (*16*).

The voltammogram in Figure 12B is a unique measurement of relative enzyme activity as a function of solution potential, distorted to some degree because diffusion of substrate into the enzyme layer is rate limiting. The shape of the wave is determined by diffusion of substrate from the stirred bulk solution through the stagnant thin-layer region, the fraction of galactose oxidase that is in the enzymatically active oxidation state (controlled by the gold minigrid), the kinetics of the substrate–enzyme reaction, and the subsequent diffusion of H_2O_2 to the platinum electrode. As previously explained, the distortion caused by the fact that substrate diffusion across the outer membrane is rate limiting can be eliminated under the appropriate conditions. This technique constitutes a novel and simple means of determining the dependence of activity upon solution potential for hydrogen peroxide-producing enzyme–substrate reactions.

Conclusion

Thin-layer electrochemical cells enable precise, rapid control of solution redox potential with simultaneous acquisition of spectra on microliter volumes of solution. The cells provide a versatile means of determining formal reduction potentials, electron stoichiometries, and

spectra of biological redox components. They also are applicable to the measurement of enzyme activity as a function of solution potential.

Acknowledgments

This research was supported in part by the National Science Foundation.

Literature Cited

1. Bishop, N. I. *Annu. Rev. Biochem.* **1971,** *40,* 197–226.
2. Wilson, D. F.; Dutton, P. L.; Erecinska, M.; Lindsay, J. G.; Sato, N. *Acc. Chem. Res.* **1972,** *5,* 234–241.
3. Heineman, W. R.; Norris, B. J.; Goelz, J. F. *Anal. Chem.* **1975,** *47,* 79–84.
4. Betso, S. R.; Klapper, M. H.; Anderson, L. B. *J. Am. Chem. Soc.* **1972,** *94,* 8197–8204.
5. Landrum, H. L.; Salmon, R. T.; Hawkridge, F. M. *J. Am. Chem. Soc.* **1977,** *99,* 3154–3158.
6. Szentrimay, R.; Yeh, P.; Kuwana, T. In "Electrochemical Studies of Biological Systems," Sawyer, D. T., Ed.; ACS SYMPOSIUM SERIES, No. 38, ACS: Washington, D.C., 1977; Chapter 9.
7. Hawkridge, F. M.; Kuwana, T. *Anal. Chem.* **1973,** *45,* 1021–1027.
8. Heineman, W. R.; Kuwana, T.; Hartzell, C. R. *Biochem. Biophys. Res. Commun.* **1972,** *49,* 1–8.
9. Heineman, W. R.; Kuwana, T.; Hartzell, C. R. *Biochem. Biophys. Res. Commun.* **1973,** *50,* 892–900.
10. Mackey, L. N.; Kuwana, T.; Hartzell, C. R. *FEBS Lett.* **1973,** *36,* 326–329.
11. Fujihira, M.; Kuwana, T.; Hartzell, C. R. *Biochem. Biophys. Res. Commun.* **1974,** *61,* 538–543.
12. Anderson, J. L.; Kuwana, T.; Hartzell, C. R. *Biochemistry,* **1976,** *15,* 3847–3855.
13. Szentrimay, R.; Kuwana, T. *Anal. Chem.* **1978,** *50,* 1879–1883.
14. Rickard, L. H.; Landrum, H. L.; Hawkridge, F. M. *Bioelectrochem. Bioenerg.* **1978,** *5,* 686–696.
15. Heineman, W. R.; Meckstroth, M. L.; Norris, B. J.; Su, C.-H. *Bioelectrochem. Bioenerg.* **1979,** *6,* 577–585.
16. Johnson, J. M.; Halsall, H. B.; Heineman, W. R., unpublished data.
17. Hubbard, A. T.; Anson, F. C. In "Electroanalytical Chemistry"; Bard, A. J., Ed.; Dekker: New York, 1970; Vol. 4, Chapter 2.
18. Murray, R. W.; Heineman, W. R.; O'Dom, G. W. *Anal. Chem.* **1967,** *39,* 1666–1668.
19. Su, C.-H., Ph.D. Dissertation, University of Cincinnati, Cincinnati, Ohio, 1981.
20. Meyer, M. L.; DeAngelis, T. P.; Heineman, W. R. *Anal. Chem.* **1977,** *49,* 602–606.
21. Lexa, D.; Saveant, J. A.; Zickler, J. *J. Am. Chem. Soc.* **1977,** *99,* 2786–2790.
22. Norvell, V. E.; Mamantov, G. *Anal. Chem.* **1977,** *49,* 1470–1472.
23. Anderson, C. W.; Halsall, H. B.; Heineman, W. R. *Anal. Biochem.* **1979,** *93,* 366–372.
24. Pinkerton, T. C.; Hajizadeh, K.; Deutsch, E.; Heineman, W. R. *Anal. Chem.* **1980,** *52,* 1542–1544.
25. Hawkridge, F. M.; Ke, B. *Anal. Biochem.* **1977,** *78,* 76–85.
26. Anderson, J. L. *Anal. Chem.* **1979,** *51,* 2312–2315.
27. Anderson, J. L.; Kincaid, J. R. *App. Spectrosc.* **1978,** *32,* 356–362.
28. Anderson, C. W.; Halsall, H. B.; Heineman, W. R.; Kreishman, G. P. *Biochem. Biophys. Res. Commun.* **1977,** *76,* 339–344.

29. Kreishman, G. P.; Anderson, C. W.; Su, C.-H.; Halsall, H. B.; Heineman, W. R. *Bioelectrochem. Bioenerg.* **1978,** *5,* 196–203.
30. Kreishman, G. P.; Su, C.-H.; Anderson, C. W.; Halsall, H. B.; Heineman, W. R. In "Bioelectrochemistry: Ions, Surfaces, Membranes;" Blank, M., Ed.; ACS ADVANCES IN CHEMISTRY SERIES, No. 188, ACS: Washington, D.C., 1980; Chapter 11.
31. Sailasuta, N.; Anson, F. C.; Gray, H. B. *J. Am. Chem. Soc.* **1980,** *101,* 455–458.
32. Kenyhercz, T. M.; DeAngelis, T. P.; Norris, B. J.; Heineman, W. R.; Mark, Jr., H. B. *J. Am. Chem. Soc.* **1976,** *98,* 2469–2477.
33. Kenyhercz, T. M.; Mark, Jr., H. B. *J. Electrochem. Soc.* **1976,** *123,* 1656–1662.
34. Kenyhercz, T. M.; Yacynych, A. M.; Mark, Jr., H. B. *Anal. Lett.* **1976,** *9,* 203–215.
35. Mark, Jr., H. B.; Kenyhercz, T. M.; Kissinger, P. T. in "Electrochemical Studies of Biological Systems;" Sawyer, D. T., Ed.; ACS SYMPOSIUM SERIES, No. 38, ACS: Washington, D.C., 1977; Chapter 1.
36. Itabashi, E.; Mark, Jr., H. B. *Rev. Polarog.* **1977,** *23,* 98.
37. Rohrbach, D. F.; Heineman, W. R.; Deutsch, E. *Inorg. Chem.* **1979,** *18,* 2536–2542.
38. DeAngelis, T. P.; Heineman, W. R. *J. Chem. Ed.* **1976,** *53,* 594–597.
39. Meckstroth, M. L.; Norris, B. J.; Heineman, W. R. *Bioelectrochem. Bioenerg.* **1981,** *8,* 63–70.
40. Eddowes, J. M.; Hill, H. A. O. *J. Am. Chem. Soc.* **1979,** *101,* 4461–4464.
41. Stargardt, J. F.; Hawkridge, F. M.; Landrum, H. L. *Anal. Chem.* **1978,** *50,* 930–932.
42. Simone, M.; Kreishman, G. P.; Heineman, W. R. *J. Coll. Interfac. Sci.*, in press.
43. Su, C.-H.; Heineman, W. R. *Anal. Chem.* **1981,** *53,* 594–598.
44. Santhanum, K. S. U.; Jespersen, J.; Bard, A. J. *J. Am. Chem. Soc.* **1977,** *99,* 274–276.
45. Dyrkacz, G. R.; Libby, R. D.; Hamilton, G. A. *J. Am. Chem. Soc.* **1976,** *98,* 626–628.
46. Stankovich, M. I., Ph.D. Dissertation, University of Texas at Austin, Austin, Texas, 1975.
47. Tanford, C. *J. Am. Chem. Soc.* **1952,** *74,* 6036.
48. Hamilton, G. A.; DeJersey, J.; Adolf, P. K. In "Oxidases and Related Redox Systems"; King, T. E.; Mason, H. S.; Morrison, M., Eds.; Wiley: New York, 1965; Vol. 1, p. 103.
49. Tressel, P., State University of New York at Buffalo, personal communication, 1979.
50. Bereman, R. D.; Ettinger, M. J.; Kosman, D. J.; Kurland, R. J. in "Bioinorganic Chemistry-II" Raymond, K. N., Ed.; ACS ADVANCES IN CHEMISTRY SERIES, No. 162, ACS: Washington, D.C., 1970; pp. 263–280.
51. Hamilton, G. A.; Adolf, P. K.; de Jersey, J.; DuBois, G. C.; Dyrkacz, G. R.; Libby, R. D. *J. Am. Chem. Soc.* **1978,** *100,* 1899–1912.
52. Taylor, P. J.; Knetec, E.; Johnson, J. M. *Anal. Chem.* **1977,** *49,* 789–794.

RECEIVED for review June 2, 1981. Accepted October 13, 1981.

Spectroelectrochemical Determination of Heterogeneous Electron Transfer Kinetic Parameters

ERIC E. BANCROFT and HENRY N. BLOUNT[1]

University of Delaware, Center for Catalytic Science and Technology, Brown Chemical Laboratory, Newark, DE 19711

FRED M. HAWKRIDGE[1]

Virginia Commonwealth University, Department of Chemistry, Richmond, VA 23284

Four spectroelectrochemical approaches to the determination of heterogeneous electron transfer kinetic parameters are described. These include single potential step chronoabsorptometry for the characterization of irreversible heterogeneous electron transfer kinetics, single potential step chronoabsorptometry for the characterization of quasi-reversible heterogeneous electron transfer kinetics, asymmetric double potential step chronoabsorptometry for the characterization of both irreversible and quasi-reversible heterogeneous electron transfer kinetics, and derivative cyclic voltabsorptometry for the characterization of both irreversible and quasi-reversible electron transfer kinetics. The validity of these techniques is established for the irreversible oxidation of ferrocyanide at tin oxide optically transparent electrodes in pH 7.00 solution and for the quasi-reversible oxidation of ferrocyanide at platinum optically transparent electrodes in the same medium. The applicability of these techniques to the determination of the potential dependence of the heterogeneous electron transfer rate constants for both the reduction of horse heart ferricytochrome c and its subsequent reoxidation is demonstrated.

[1] To whom correspondence should be addressed.

0065-2393/82/0201-0023$07.75

The coupling of optical spectroscopic probes with electrochemical perturbations of optically transparent electrodes (OTEs) has given rise to fruitful hybrid methodologies for the assessment of electrochemical properties of biological molecules (*1*). The majority of these investigations have addressed the determination of the formal redox potentials and *n*-values of biological redox molecules (BRMs) through the use of electrochemical mediator titrants (MTs) (*2*). Both optically transparent thin-layer electrochemical (OTTLE) cells, as well as somewhat larger "small volume" cells, have been successfully used in these studies (*3*, *4*).

New OTE systems that facilitate direct electron transfer between the electrode per se and BRMs without a solution-resident MT permit spectroelectrochemical kinetic characterizations of *heterogeneous* electron transfer reactions of these species (*5–10*). Such characterizations are essential to an understanding of the mechanistic aspects of the in vivo reactions of BRMs that function physiologically as interfacial electron transfer agents [e.g., the cytochrome c/cytochrome c oxidase system (*11*)].

For those OTEs that either inherently or by virtue of surface modification exhibit appreciable rates of direct electron transfer with BRMs, single potential step spectroelectrochemistry (chronoabsorptometry) has recently been applied to the determination of the characteristic heterogeneous electron transfer kinetic parameters for these systems (*8–10*). Although useful, this approach has been restricted (vide infra) to the examination of unidirectional electron transfer processes of systems that exhibit a very low degree of electrochemical reversibility. Spectroelectrochemical techniques have now been developed for the determination of the kinetic parameters characteristic of both the forward and back heterogeneous electron transfer processes for systems exhibiting any degree of reversibility.

A heterogeneous electron transfer system may be represented as

$$O + ne^- \underset{k_{b,h}}{\overset{k_{f,h}}{\rightleftharpoons}} R \qquad (1)$$

where $k_{f,h}$ and $k_{b,h}$ are the heterogeneous electron transfer rate constants for the forward (O to R) and back (R to O) processes, respectively. Both of these rate constants can be expressed in terms of

1. The formal heterogeneous electron transfer rate constant ($k^{\circ\prime}_{s,h}$), which is that value of either $k_{f,h}$ or $k_{b,h}$ at the formal potential of the system ($E^{\circ\prime}_{O/R}$).
2. The transfer coefficient of the electron transfer process (α).
3. The number of electrons involved in the rate determining step in the electron transfer process (n_a).

4. The overpotential (η) to which the system is subjected ($\eta = E - E^{\circ\prime}_{O/R}$, where E is the potential of the electrode at which the electron transfer process is taking place).

In Butler–Volmer formalism, $k_{f,h}$ and $k_{b,h}$ are expressed as

$$k_{f,h} = k^{\circ\prime}_{s,h} \exp\left[- \frac{\alpha n_a F}{RT} (E - E^{\circ\prime}_{O/R}) \right] \quad (2)$$

and

$$k_{b,h} = k^{\circ\prime}_{s,h} \exp\left[\frac{(1 - \alpha) n_a F}{RT} (E - E^{\circ\prime}_{O/R}) \right] \quad (3)$$

The perceived degree of electrochemical reversibility of the heterogeneous charge transfer process is a manifestation of the magnitude of $k^{\circ\prime}_{s,h}$ and the time scale of the observation of the system. If the heterogeneous electron transfer kinetics of a system are sufficiently slow (small $k^{\circ\prime}_{s,h}$) that application of negative overpotentials (favoring the forward reaction, Equation 2) results in a flux of material that is dependent on $k_{f,h}$ but is independent of $k_{b,h}$, then this sytem can be said to be electrochemically irreversible on the time scale of the experiment. The determination of $k_{f,h}$ as a function of η from either electrochemical or spectroelectrochemical measurements is straightforward and gives rise to the evaluation of $k^{\circ\prime}_{s,h}$ and α. However, if the heterogeneous electron transfer kinetics of a system are more facile (moderate $k^{\circ\prime}_{s,h}$), then application of negative overpotentials can result in a flux of material that is impacted by both $k_{f,h}$ and $k_{b,h}$. Such systems are said to exhibit quasi-reversible behavior on the time scale of the experiment. The evaluation of heterogeneous electron transfer kinetic parameters from electrochemical or spectroelectrochemical characterizations of these quasi-reversible systems is somewhat more complex than for irreversible systems, but can be more informative in that kinetic information regarding the back reaction is also obtained. To date, heterogeneous electron transfer kinetics have been reported for three biological molecules. Myoglobin exhibits irreversible electron transfer kinetic behavior at viologen-modified gold electrodes ($k^{\circ\prime}_{s,h} \simeq 10^{-9}$ to 10^{-11} cm/s). In contrast, cytochrome c behaves in a quasi-reversible manner at semiconductor and modified gold surfaces ($k^{\circ\prime}_{s,h} \simeq 10^{-4}$ to 10^{-5} cm/s). Soluble spinach ferridoxin also exhibits quasi-reversible behavior at viologen-modified gold electrodes ($k^{\circ\prime}_{s,h} \simeq 10^{-5}$ cm/s).

For both reversible and irreversible systems, knowledge of the kinetic parameters characteristic of the back reaction is essential to an understanding of the mechanisms of heterogeneous electron transfer. In the context of Equation 1, kinetic characterization of the back reaction could be readily realized by simply carrying out electrochemical or spectroelectrochemical experiments with solutions containing R

rather than O as implied in the foregoing discussion. Although true in principle, this approach may not be attractive either because of experimental constraints or because of sample integrity. Thus, experimental strategies that simultaneously afford kinetic information regarding both forward and reverse heterogeneous electron transfer reactions are highly desirable.

The utility of spectroelectrochemical techniques in the study of electron transfer processes has been amply demonstrated (*12–15*). Two major advantages of spectroelectrochemistry compared to purely electrochemical methods for the determination of heterogeneous electron transfer kinetic parameters are the molecular specificity of the optical measurement and freedom from errors associated with charge transfer processes, both faradaic and nonfaradaic, other than the redox reaction of interest. Biological sample preparations often contain unknown impurities as a consequence of isolation and purification procedures, and such impurities are far more likely to adversely impact an electrochemical measurement than the corresponding spectroelectrochemical one.

Single Potential Step Chronoabsorptometry: Irreversible Systems

The experimental heterogeneous electron transfer system can be represented by Equation 1. Assume that the sample is present in the oxidized form and that the optical absorbance of R, the product of the electron transfer reaction, will be monitored without interference from the precursor, O.

For the charge transfer process given by Equation 1, application of a potential step of sufficient magnitude to cause the forward reaction to proceed at a rate governed by $k_{f,h}$ gives rise (*15*) to the time-dependent absorbance $A_R(\lambda,t)$ of the electrode reaction product:

$$A_R(\lambda,t) = \frac{\epsilon_R(\lambda)\, C_O^\circ D_O}{k_{f,h}} \left[\frac{2k_{f,h}t^{1/2}}{\pi^{1/2}D_O^{1/2}} + \exp\left(\frac{k_{f,h}^2 t}{D_O}\right) \operatorname{erfc}\left(\frac{k_{f,h}t^{1/2}}{D_O^{1/2}}\right) - 1 \right] \quad (4)$$

where C_O° and D_O are the bulk concentration and diffusion coefficient, respectively, of the precursor and ϵ_R is the molar absorptivity of the product. If the magnitude of the potential step applied to the OTE is sufficiently large to cause the forward reaction in Equation 1 to proceed at a diffusion-controlled rate, then the time-dependent optical absorbance of the electrode reaction product, A_R^D, is given by (*16*)

$$A_R^D(\lambda,t) = \frac{2}{\pi^{1/2}}\, \epsilon_R(\lambda) D_O^{1/2} C_O^\circ t^{1/2} \quad (5)$$

The ratio of the kinetically controlled absorbance (Equation 4) to the diffusion-controlled absorbance (Equation 5) affords the normalized absorbance, A_N:

$$A_N(\lambda,t) = 1 + \frac{\pi^{1/2}}{2\zeta}[\exp(\zeta^2)\mathrm{erfc}(\zeta) - 1] \quad (6)$$

where

$$\zeta = \frac{k_{f,h}t^{1/2}}{D_O{}^{1/2}} \quad (7)$$

The normalized absorbance of the electrode reaction product depends on the dimensionless kinetic parameters $k_{f,h}t^{1/2}/D_O{}^{1/2}$ as shown in Figure 1, and this working curve provides a convenient means of determining $k_{f,h}$ (*15*).

The utility of this approach has been experimentally demonstrated with a model system, the oxidation of ferrocyanide in pH 7.00 solution at tin oxide OTEs, and the results obtained were in excellent agreement with those reported using purely electrochemical tech-

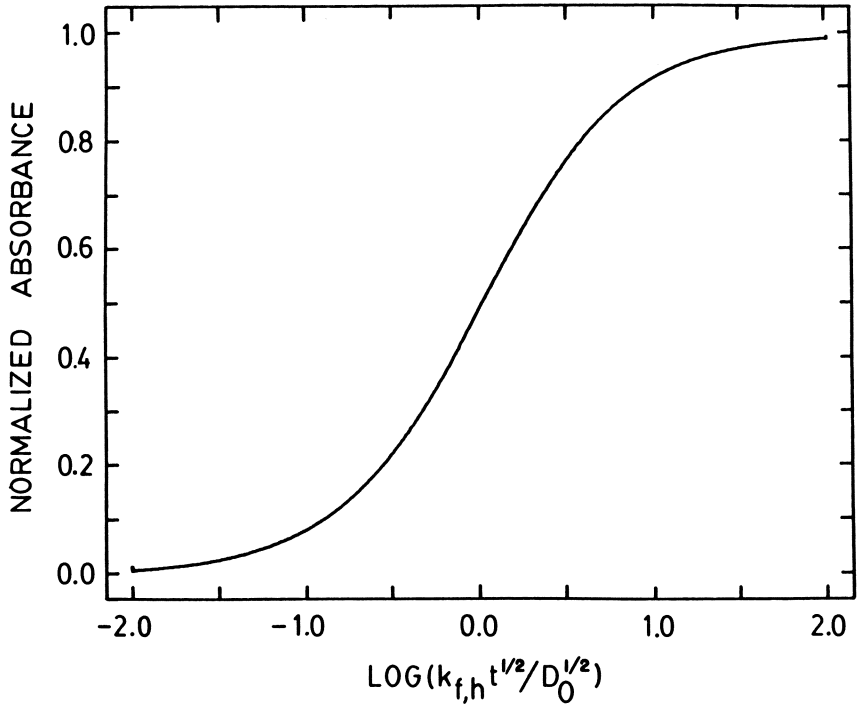

Figure 1. Working curve for spectroelectrochemical determination of heterogeneous electron transfer rate constants for irreversible reactions (15).

niques (*15*). The chronoabsorptometric method has been successfully applied to the determination of $k^{o\prime}_{s,h}$ and α for the reduction of myoglobin at viologen-modified gold minigrid OTEs (*8*).

The validity of this approach to the determination of heterogeneous electron transfer kinetic parameters is predicated on the irreversibility of the charge transfer process (*15*). Use of the working curve shown in Figure 1 for the analysis of data derived from quasi-reversible systems can result in significant errors in the calculated heterogeneous rate constants and, in turn, can lead to false conclusions regarding $k^{o\prime}_{s,h}$ and α (vide infra).

Single Potential Step Chronoabsorptometry: Quasi-Reversible Systems

If the electron transfer kinetics of the reaction given in Equation 1 are sufficiently facile such that application of a potential step perturbation which favors the forward process results in a flux of material that depends on *both* $k_{f,h}$ and $k_{b,h}$, then the time-dependent absorbance of the electrode reaction product is given by (*17*)

$$A_R(\lambda,t) = \frac{\epsilon_R(\lambda)C^\circ_O k_{f,h}}{\left(\frac{k_{f,h}}{D_O^{1/2}} + \frac{k_{b,h}}{D_R^{1/2}}\right)^2}\left[2\left(\frac{k_{f,h}}{D_O^{1/2}} + \frac{k_{b,h}}{D_R^{1/2}}\right)\frac{t^{1/2}}{\pi^{1/2}} + \exp\left(\left(\frac{k_{f,h}}{D_O^{1/2}} + \frac{k_{b,h}}{D_R^{1/2}}\right)^2 t\right)\mathrm{erfc}\left(\left(\frac{k_{f,h}}{D_O^{1/2}} + \frac{k_{b,h}}{D_R^{1/2}}\right)t^{1/2}\right) - 1\right] \quad (8)$$

In concert with the diffusion-controlled absorbance given in Equation 5, the normalized absorbance for this quasi-reversible case, $A_R(\lambda,t)/A^D_R(\lambda,t)$, is given by

$$A_N(\lambda,t) = \frac{\zeta\pi^{1/2}}{2\xi^2}\left[\frac{2\xi}{\pi^{1/2}} + \exp(\xi^2)\mathrm{erfc}(\xi) - 1\right] \quad (9)$$

where ζ is defined by Equation 7 and

$$\xi = \left[\frac{k_{f,h}}{D_O^{1/2}} + \frac{k_{b,h}}{D_R^{1/2}}\right]t^{1/2} \quad (10)$$

Because Equation 9 embodies both ζ and ξ, this form does not readily lend itself to the expression of a working curve where $k_{f,h}$ and $k_{b,h}$ can be evaluated from an experimentally determined normalized absorbance. Formation of the ratio

$$\frac{\xi}{\zeta} = 1 + \left[\frac{k_{b,h}D_O^{1/2}}{k_{f,h}D_R^{1/2}}\right] \quad (11)$$

and substitution of Equations 2 and 3 into Equation 10 affords

$$\xi = \zeta[1 + (D_O^{1/2}/D_R^{1/2})\exp\{n_aF(E - E^{o\prime}_{O/R})/RT\}] \quad (12)$$

In view of the relationship between ξ and ζ given in Equation 12, the normalized absorbance for the quasi-reversible process (Equation 9) can be expressed as a function of ζ and gives rise to a unique working curve for each value of the overpotential employed. Figure 2 shows a family of such working curves constructed for $n_a = 1$ and overpotentials that range from values anodic of the $E^{\circ\prime}$ of the system ($\eta > 0$) to values sufficiently cathodic of the $E^{\circ\prime}$ ($\eta < 0$) that the system is caused to behave in an irreversible fashion (i.e., the back reaction becomes negligible). The quasi-reversible working curve for $\eta \leq -160$ mV is indistinguishable from the irreversible case (Figure 1).

A convenient experimental test for this predicted chronoabsorptometric behavior of quasi-reversible systems is provided by the oxidation of ferrocyanide to ferricyanide at a platinum optically transparent electrode in pH 7.00 phosphate buffer. The cyclic voltammetry of this quasi-reversible system is shown in Figure 3. Acquisition of chronoabsorptometric data following steps to overpotential values ranging from $\eta = +78$ to -26 mV (*see* Figure 3) gave rise to the

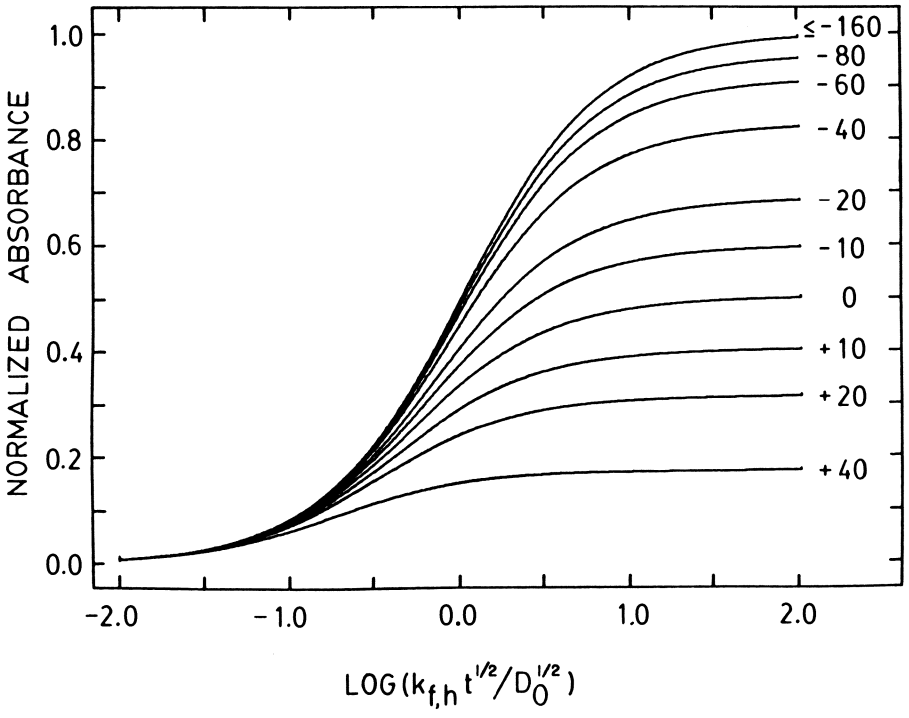

Figure 2. Working curves for spectroelectrochemical determination of heterogeneous electron transfer rate constants for quasi-reversible reactions. Numerical values correspond to $n_a\eta$ where η is expressed in mV (17).

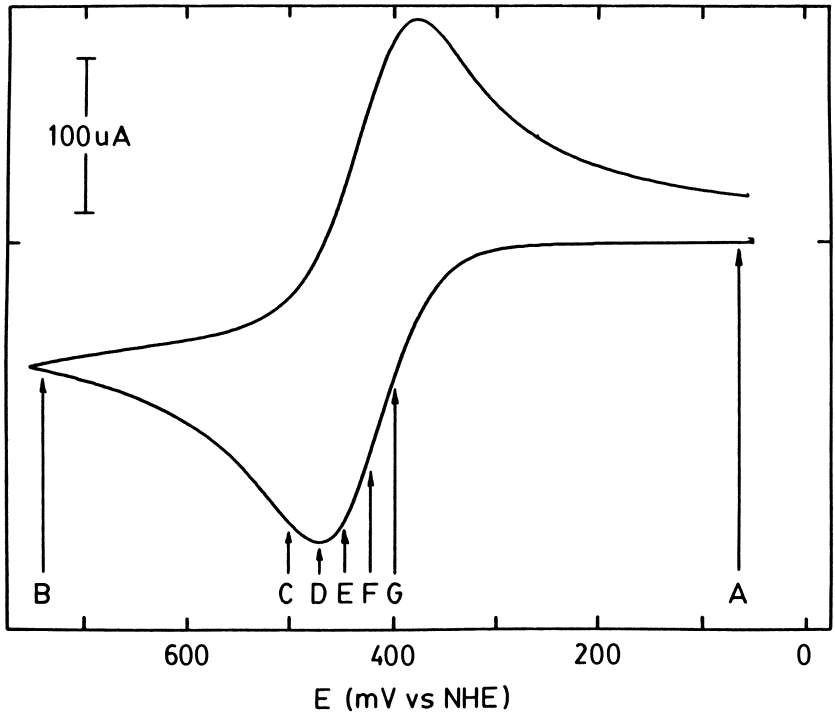

Figure 3. Cyclic voltammetry of 4.71 mM $K_4Fe(CN)_6$ in pH 7.00 phosphate buffer at a platinum OTE. Area = 0.30 cm^2, sweep rate = 50 mV/s. For single potential step experiments, initial potential A = 66 mV, diffusion step limit B = 740 mV, kinetic step limits: C = 502 mV, D = 472 mV, E = 447 mV, F = 421 mV, and G = 398 mV (17).

absorbance–time transients shown in Figure 4. Note that in this experimental system, the precursor is the reduced form of the couple and the "forward" step for the oxidation of ferrocyanide corresponds to $k_{b,h}$ in Equation 1. The absorbance transients shown in Figure 4 were normalized to the diffusion-controlled case (Trace B, Figure 4) and were analyzed using both the irreversible model and the quasi-reversible model. For data analysis by the irreversible model, the working curve shown in Figure 1 was used; for analysis of the data according to the quasi-reversible model, working curves analogous to those shown in Figure 2 were used, but were constructed for the experimental overpotentials employed. The results of these analyses are shown in Table I. The solid circles shown in Figure 4 are the theoretical absorbance values calculated from Equations 8 and 12 together with the values of η employed in the experiments. According to simple electron transfer theory (Equations 2 and 3), log ($k_{b,h}$) should vary linearly with overpotential. As shown in Figure 5, the heterogeneous electron transfer rate

constant for the oxidation of ferrocyanide, evaluated according to the quasi-reversible model, exhibits the expected behavior, whereas the one evaluated according to the irreversible model does not. For the irreversible data treatment, there is both a displacement of the rate constants to lower values and a pronounced downward curvature in the log ($k_{b,h}$) vs. η plot. Attempts to fit these data derived from the

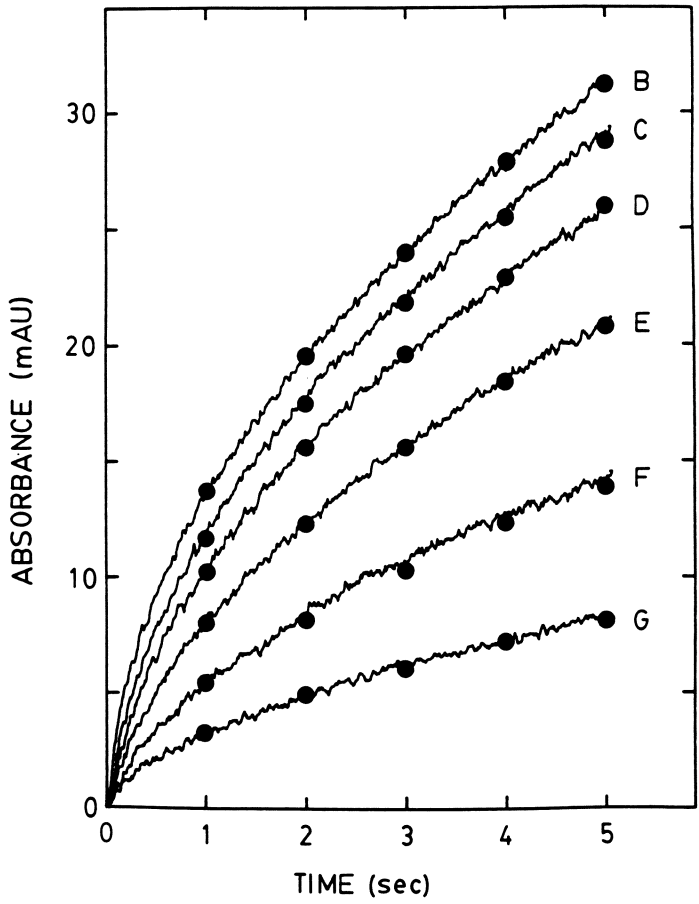

Figure 4. Absorbance–time behavior for single potential step oxidation of 4.71 mM ferrocyanide at a platinum OTE in pH 7.00 solution. Solid lines are experimental transients; solid circles are theoretical responses calculated from Equation 8. Curve B: $\eta = 316$ mV, theoretical response calculated from Equation 5. Curve C: $\eta = 78$ mV, $k_{f,h} = 7.92 \times 10^{-4}$ cm/s, $k_{b,h} = 1.59 \times 10^{-2}$ cm/s; Curve D: $\eta = 48$ mV, $k_{f,h} = 1.44 \times 10^{-3}$ cm/s, $k_{b,h} = 9.34 \times 10^{-3}$ cm/s; Curve E: $\eta = 23$ mV, $k_{f,h} = 2.42 \times 10^{-3}$ cm/s, $k_{b,h} = 5.92 = 10^{-3}$ cm/s; Curve F: $\eta = -3$ mV, $k_{f,h} = 4.14 \times 10^{-3}$ cm/s, $k_{b,h} = 3.68 \times 10^{-3}$ cm/s; Curve G: $\eta = -26$ mV, $k_{f,h} = 6.66 \times 10^{-3}$ cm/s, $k_{b,h} = 2.42 \times 10^{-3}$ cm/s (17).

Published on June 1, 1982 on http://pubs.acs.org | doi: 10.1021/ba-1982-0201.ch002

Table I. Heterogeneous Electron Transfer Rate Constants for the Single Potential Step Oxidation of Ferrocyanide at Platinum Evaluated by Irreversible and Quasi-Reversible Models

	$k_{b,h}{}^a(cm/s) \times 10^3$									
	$\eta^b = -26$ mV		$\eta = -3$ mV		$\eta = 23$ mV		$\eta = 48$ mV		$\eta = 78$ mV	
Time, s[c]	*Irrev.*[d]	*Quasi.*[e]	*Irrev.*	*Quasi.*	*Irrev.*	*Quasi.*	*Irrev.*	*Quasi.*	*Irrev.*	*Quasi.*
0.50	0.961	2.20	1.91	3.90	3.83	5.60	6.71	8.76	11.5	14.2
1.00	0.825	2.20	1.63	4.07	3.32	5.92	6.36	8.26	11.6	14.7
1.50	0.699	2.23	1.39	3.66	3.03	5.73	5.78	9.27	11.9	15.6
2.00	0.637	2.70	1.31	4.09	2.87	6.14	5.80	9.27	11.6	16.1
2.50	0.581	2.52	1.21	4.27	2.67	6.02	5.67	9.41	10.5	15.0
3.00	0.511	2.56	1.12	3.93	2.51	5.96	5.30	9.53	10.7	15.8
3.50	0.482	2.31	1.07	4.17	2.43	6.30	5.13	9.21	10.6	16.0
4.00	0.459	2.39	1.01	4.14	2.28	5.90	4.92	9.42	9.98	16.1
4.50	0.436	2.35	0.940	3.68	2.21	6.19	4.78	9.53	9.98	16.2
5.00	0.419	2.34	0.927	3.87	2.16	6.33	4.62	9.62	9.44	15.5
Mean	0.601	2.38	1.25	3.97	2.73	6.01	5.51	9.23	10.8	15.5
SD	(±0.180)	(±0.16)	(±0.32)	(±0.22)	(±0.54)	(±0.24)	(±0.68)	(±0.42)	(±0.8)	(±0.7)

Note: $[K_4Fe(CN)_6]$ = 4.71 m*M* in pH 7.00 phosphate buffer (0.07 *M*). Data taken from Ref. *17*.

[a] According to Equation 1.

[b] $\eta = E_{step} + E_{ref} - E^{o\prime}$; $E^{o\prime}$ for $Fe(CN)_6^{3-}/Fe(CN)_6^{4-}$ = 424 mV vs. NHE (*18*).

[c] Following onset of potential step.

[d] Equation 6.

[e] Equation 9.

Source: Reproduced from Ref. 17. Copyright 1981, American Chemical Society.

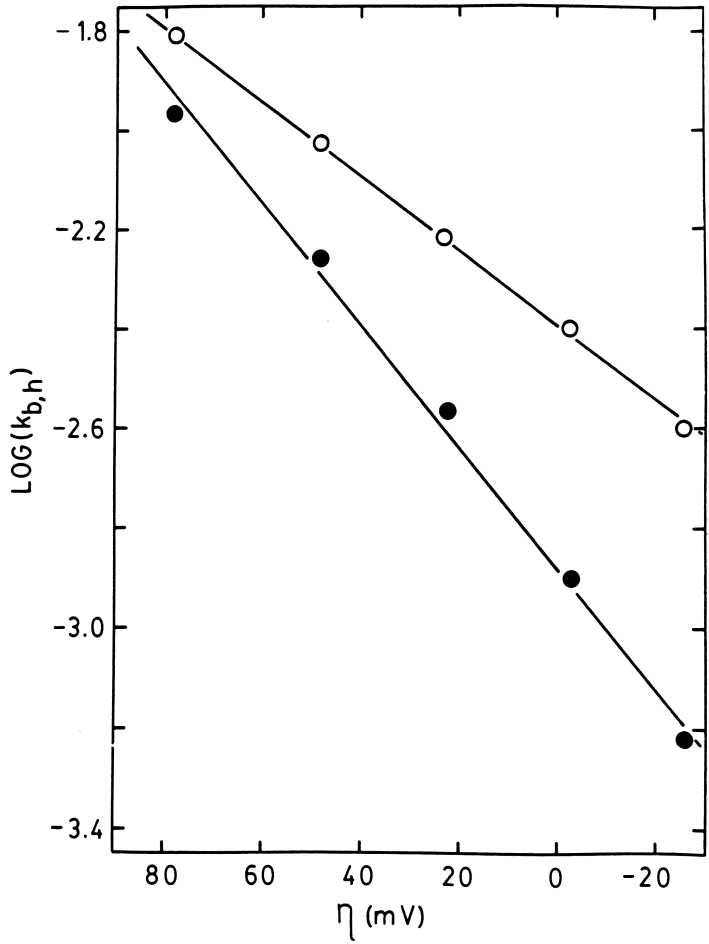

Figure 5. Dependence of log ($k_{b,h}$) *evaluated according to irreversible model* (●, $k^{o'}_{s,h} = 1.35 \times 10^{-3}$ *cm/s*, $(1 - \alpha) = 0.722$) *and quasi-reversible model* (○, $k^{o'}_{s,h} = 3.89 \times 10^{-3}$ *cm/s*, $(1 - \alpha) = 0.469$) *on overpotential* (17).

irreversible model to the behavior predicted by Equation 3 lead to an erroneously low value of $k^{o'}_{s,h}$ and an erroneously high value of $(1 - \alpha)$; hence, the value of α determined from these data would be correspondingly lower than the correct one. Consideration of the apparent nonlinear dependence of log $k_{b,h}$ on η could also lead to the conclusion that the transfer coefficient is potential dependent.

Examination of Figure 2 reveals that at small values of the kinetic argument $k_{f,h}\, t^{1/2}/D_O{}^{1/2}$, all working curves coalesce to the same value of normalized absorbance. At larger values of $k_{f,h}\, t^{1/2}/D_O{}^{1/2}$, analysis of quasi-reversible data according to the irreversible model leads to er-

rors in the calculated value of $k_{f,h}$. This error increases with increasing values of $k_{f,h}\ t^{1/2}/D_O{}^{1/2}$ and less robust (more anodic) overpotentials for the system as represented by Equation 1. Table II provides insight into the magnitude of the errors in the kinetic parameter ($k_{f,h}\ t^{1/2}/D_O{}^{1/2}$) arising from analysis of quasi-reversible data according to the irreversible model. Summarized here are those maximum values of $k_{f,h}\ t^{1/2}/D_O{}^{1/2}$ which, if determined using the working curve for the irreversible model rather than the appropriate working curve for the quasi-reversible model, result in the specified relative error in the corresponding rate constant. As n_a increases, these $k_{f,h}\ t^{1/2}/D_O{}^{1/2}$ values become proportionately less stringent for $\eta < 0$, but proportionately more stringent for $\eta > 0$.

Whenever normalized parameters are utilized in kinetic analysis, attention must be given to the uncertainty in the calculated rate constant relative to the uncertainty in the measured parameter. The nonlinear dependences of the normalized absorbance on log ($k_{f,h}t^{1/2}/D_0{}^{1/2}$) shown in Figures 1 and 2 lead to the conclusion that for a given overpotential, the time domain of the chronoabsorptometric experiment should be chosen such that the normalized absorbance values used for kinetic analysis fall on the rising portion of the working curve where $d(A_N)/d(\log (k_{f,h}t^{1/2}/DO^{1/2}))$ is greatest. Although highly desirable, it is not always experimentally convenient to conduct experiments in this manner. Data may have to be acquired that afford normalized absor-

Table II. Threshold Values of $k_{f,h}t^{1/2}/D_O{}^{1/2}$ That Result in Specified Relative Error in $k_{f,h}$ if Back Reaction is Neglected

	$(k_{f,h}t^{1/2}/D_O{}^{1/2})_{max} \times 10$				
$\eta(mV)$	$RE^a = 1\%$	$RE = 2\%$	$RE = 5\%$	$RE = 10\%$	$RE = 20\%$
40	0.0576	0.0793	0.152	0.308	0.678
20	0.0866	0.134	0.321	0.664	1.46
10	0.115	0.188	0.470	0.966	2.14
0	0.152	0.278	0.689	1.43	3.11
−10	0.206	0.391	1.01	2.09	4.52
−20	0.298	0.585	1.48	3.04	6.54
−40	0.633	1.26	3.14	6.36	13.4
−60	1.36	2.68	6.56	13.0	27.2
−80	2.88	5.62	13.4	26.4	55.5
−100	6.02	11.5	27.1	53.7	115
−120	12.3	23.2	55.1	111	242
−140	24.9	47.2	111	235	520

[a] Relative error in $k_{f,h}$.

Source: Reproduced from Ref. 17. Copyright 1981, American Chemical Society.

bance values, which fall either near the foot of the working curve or near the upper plateau. For a given uncertainty in the experimentally derived normalized absorbance, the corresponding error in the calculated kinetic parameter is greater in these regions where $d(A_N)/d(\log(k_{f,h}\, t^{1/2}/D_O^{1/2}))$ is less. Figure 6 shows the relative error in the calculated heterogeneous rate constant $k_{f,h}$ resulting from an uncertainty of ±0.001 in the experimentally derived normalized absorbance as a function of normalized absorbance. As would be expected, those working curves for the quasi-reversible model that correspond to more positive overpotentials give rise to greater errors in the calculated rate

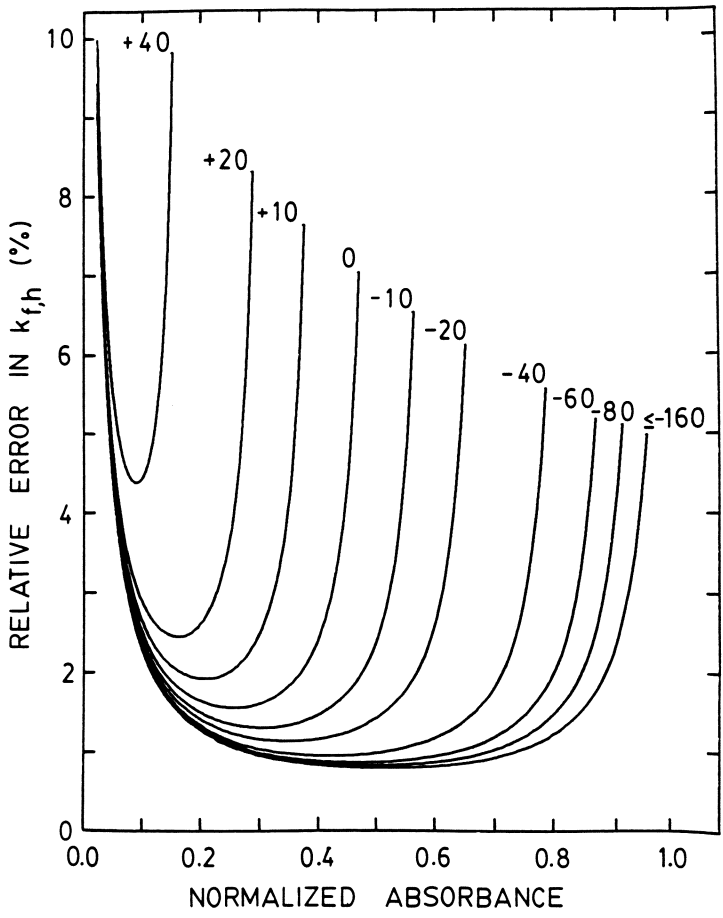

Figure 6. Dependence of relative error in $k_{f,h}$ *arising from an uncertainty of ±0.001 in the normalized absorbance on normalized absorbance. Numerical values are those for* $n_a\eta$ *shown in Figure 2* (17).

constant for a specified uncertainty in the measured normalized absorbance. If $n_a = 2$, then the relative error curve for $\eta = -10$ mV is identical to that calculated for $\eta = -20$ mV in the $n_a = 1$ case. In like manner, the curve corresponding to $\eta = -20$ mV for $n_a = 2$ is the same as that for $\eta = -40$ mV when $n_a = 1$. The same relationship holds for positive overpotentials as well.

Asymmetric Double Potential Step Chronoabsorptometry: Irreversible and Quasi-Reversible Systems

Although the analysis of single potential step chronoabsorptometric data according to a quasi-reversible model takes the back reaction into account, it does not provide an independent measure of $k_{b,h}$ and $(1 - \alpha)$ (Equations 1–3). As noted, the kinetic parameters characteristic of the back reaction represented in Equation 1 could be ascertained by carrying out single potential step chronoabsorptometric experiments starting with the reduced form of the system. An example of this technique was just presented for ferrocyanide. With BRMs, however, the reduced forms of many samples react with oxygen or are available only in their oxidized forms. In principle, the sample could be converted to its reduced form by controlled potential electrolysis prior to the execution of potential step chronoabsorptometric experiments, but this conversion is often experimentally undesirable for several reasons. First, the oxidized form of the couple may not exhibit an accessible optical absorption with which its formation can be monitored during oxidative potential steps. If a *decrease* in the optical absorbance of the precursor has to be monitored, the small decrease in absorbance corresponding to disappearance of the precursor will result in a poor signal-to-noise ratio. Second, inefficient stirring in small volume cells can cause exhaustive prior electrolysis to require an unduly long time. Third, exhaustive electrolysis dictates that an isolated auxiliary electrode be employed. This experimental arrangement may be inconvenient, and the products of the auxiliary electrode reaction may compromise the integrity of the sample. Also, the effects of long-term electrolysis on the behavior of surface-modified electrodes commonly employed in heterogeneous kinetic characterizations of BRMs are not yet known. Thus, an experimental protocol that provides independent kinetic information regarding the back reaction when the precursor is already in that redox form is highly desirable.

One experimental approach that satisfies these requirements involves the use of asymmetric double potential step perturbation of the OTE. Initially, the potential is stepped to a value that causes the forward reaction in Equation 1 to proceed at a diffusion-controlled rate. After some time, τ, the potential is stepped back to a less extreme

value, which causes a portion of the reduced form of the couple produced during the initial step to be converted back to the oxidized form. If at τ the electrode potential is stepped back to sufficiently positive values such that the back reaction proceeds at a diffusion-controlled rate, then $A_R(\lambda,t > \tau)$ is a linear function of $[t^{1/2} - (t - \tau)^{1/2}]$ (*16*). At present, no tractable analytical solution exists which describes the temporal dependence of $A_R(\lambda,t > \tau)$ for back step potentials less than that required for the diffusion-controlled reoxidation of *R* (*14*, *19*, *20*). Consequently, the heterogeneous rate constant for the back reaction ($k_{b,h}$ in Equation 1) is determined for the experimental system under study by digital simulation of $A_R(\lambda,t)$ and adjustment of the simulation $k_{b,h}$ value until satisfactory agreement between simulation and experiment is obtained. As $k_{b,h}$ is varied to attain agreement between simulation and experiment, $k_{f,h}$ necessarily must vary also. The ratio of these two rate constants is fixed by the overpotential and n_a:

$$k_{b,h}/k_{f,h} = \exp\{n_a F(E - E^{\circ\prime}_{O/R})/RT\} \quad (13)$$

The viability of this method of determining the heterogeneous kinetic parameters for the back reaction in quasi-reversible systems has been established using the ferricyanide–ferrocyanide couple at platinum OTEs in pH 7.00 solution. Recalling that this redox couple is initially in the reduced form, determination of the $k_{f,h}$ values for this test system is tantamount to determination of the $k_{b,h}$ values were this system initially in the oxidized form in the context of the foregoing discussion and Equation 1.

The sequence of potential steps employed in these experiments is shown in Figure 7. Initially, the potential of the OTE is stepped from A to B where the oxidation of ferrocyanide proceeds at a diffusion-controlled rate. After a 5-s interval, the potential is stepped back to the values indicated by C through H for a series of experiments. The resulting time-dependent absorbance of ferricyanide observed during this series of potential step sequences is shown in Figure 8. Overlaid on these transients are the best-fit simulated values of the absorbance. The values of $k_{f,h}$ used in these simulations are summarized in Table III. The dependence of log ($k_{f,h}$) on overpotential for the reduction of ferricyanide is shown in Figure 9, together with the dependence of log($k_{b,h}$) on overpotential for the oxidation of ferrocyanide. These $k_{b,h}$ values are those determined from the single potential step chronoabsorptometric measurements described earlier. The value of $k^{\circ\prime}_{s,h}$ determined from $k_{b,h}$ values (single potential step measurements), 3.89 ($\pm$0.09) $\times$ 10^{-3} cm/s, is in excellent agreement with that determined from $k_{f,h}$ values (asymmetric double potential step measurements),

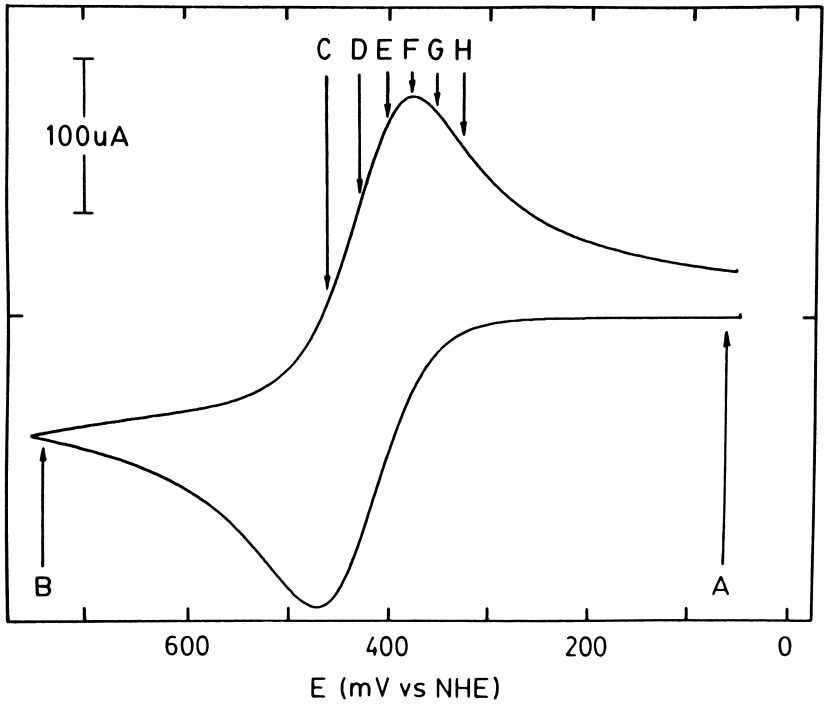

Figure 7. Cyclic voltammetry of 4.71 mM $K_4Fe(CN)_6$ showing asymmetric double potential step sequence. Initial potential and reverse diffusion step limit A = 66 mV, forward diffusion step limit B = 740 mV, kinetic reverse step limits: C = 463 mV, D = 428 mV, E = 403 mV, F = 377 mV, G = 353 mV, and H = 326 mV. Experimental conditions for cyclic voltammetry are given in Figure 3.

Table III. Heterogeneous Electron Transfer Rate Constants for the Asymmetric Double Potential Step Reduction of Ferricyanide at Platinum

$\eta^a(mV)$	$k_{f,h}^{b,c}(cm/s) \times 10^3$
39	1.79 (±0.06)[d]
4	3.73 (±0.21)
−21	6.71 (±0.48)
−47	11.5 (±1.2)
−71	17.5 (±0.8)
−98	30.9 (±1.8)

Note: Oxidative (initial) potential step to η = 326 mV for τ = 5.00 s; $[K_4Fe(CN)_6]$ = 4.71 m*M* in pH 7.00 phosphate buffer (0.07 *M*).

[a] Reductive (reverse) potential steps; $\eta = E_{step} + E_{ref} - E^{o\prime}$; data acquired for 5.00 s following step reversal.

[b] According to Equation 1.

[c] From digital simulation data fits; values shown are means of four determinations.

[d] Parentheses contain one standard deviation.

4.11 (±0.17) × 10^{-3} cm/s. Quite good agreement is also found between the values of α, 0.534 (±0.022), derived from asymmetric double step measurements and $(1 - \alpha)$, 0.469 (±0.011), determined from the single step experiments. Simulation studies have shown that the asymmetric double potential step absorbance–time responses are more sensitive to changes in α than to changes in $k^{o'}_{s,h}$ when back step potentials in the

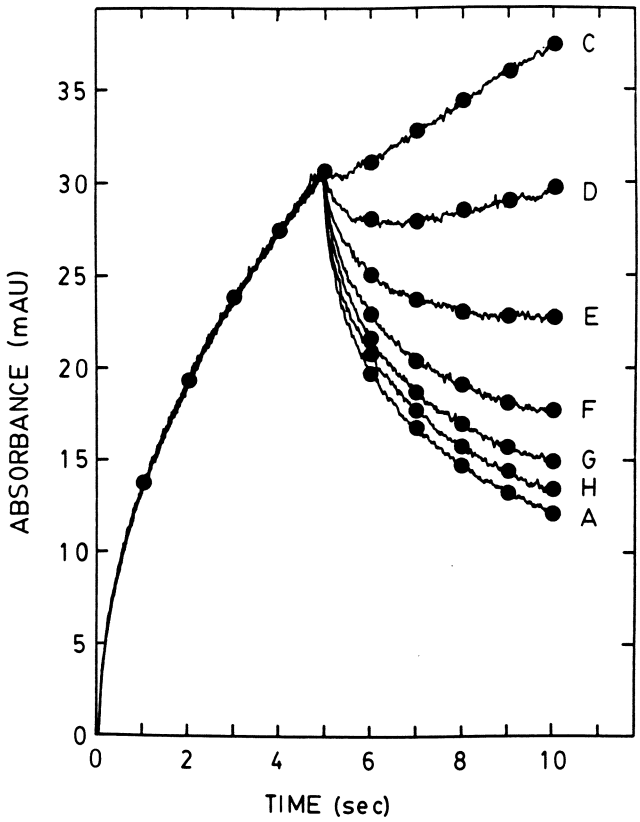

Figure 8. Absorbance–time behavior for asymmetric double potential step oxidation of 4.71 mM ferrocyanide and subsequent reduction of ferricyanide at a platinum OTE in pH 7.00 solution. Solid lines are experimental transients; solid circles are best fit values from digital simulation. Forward step: $\eta = 326$ *mV,* $k_{f,h} = 5.66 \times 10^{-6}$ *cm/s,* $k_{b,h} = 1.25$ *cm/s. For reverse steps, Curve C:* $\eta = 39$ *mV,* $k_{f,h} = 1.79 \times 10^{-3}$ *cm/s,* $k_{b,h} = 8.17 \times 10^{-3}$ *cm/s; Curve D:* $\eta = 4$ *mV,* $k_{f,h} = 3.73 \times 10^{-3}$ *cm/s,* $k_{b,h} = 4.36 \times 10^{-3}$ *cm/s; Curve E:* $\eta = -21$ *mV,* $k_{f,h} = 6.71 \times 10^{-3}$ *cm/s,* $k_{b,h} = 2.96 \times 10^{-3}$ *cm/s; Curve F:* $\eta = -47$ *mV,* $k_{f,h} = 1.15 \times 10^{-2}$ *cm/s,* $k_{b,h} = 1.85 \times 10^{-3}$ *cm/s; Curve G:* $\eta = -71$ *mV,* $k_{f,h} = 1.75 \times 10^{-2}$ *cm/s,* $k_{b,h} = 1.10 \times 10^{-3}$ *cm/s; Curve H:* $\eta = -98$ *mV,* $k_{f,h} = 3.09 \times 10^{-2}$ *cm/s,* $k_{b,h} = 6.81 \times 10^{-4}$ *cm/s; Curve A:* $\eta = -358$ mV, $k_{f,h} = 2.63$ *cm/s,* $k_{b,h} = 5.75 \times 10^{-6}$ *cm/s.*

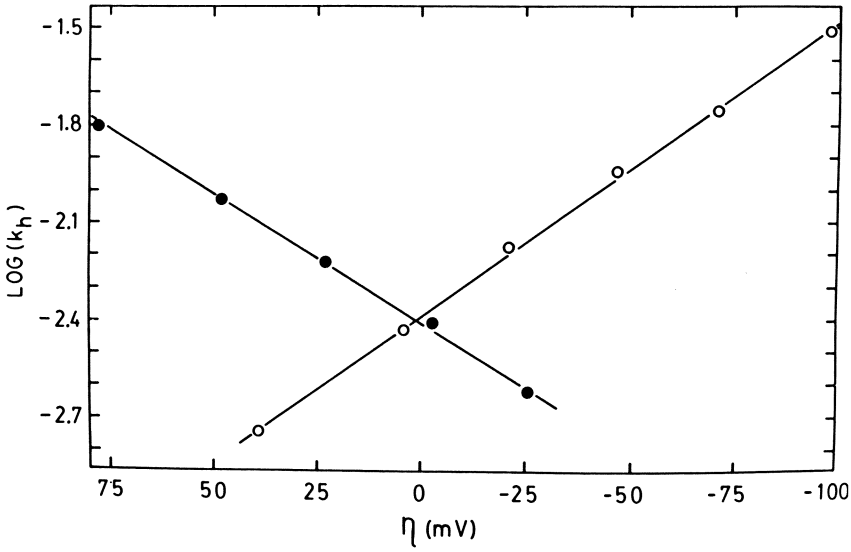

Figure 9. Dependence of log ($k_{f,h}$) *from asymmetric double potential step chronoabsorptometric measurements (* ○, $k^{\circ\prime}_{s,h} = 4.11 \times 10^{-3}$ *cm/s,* $\alpha = 0.534$*) and log* ($k_{b,h}$) *from single potential step chronoabsorptometric measurements [*●, $k^{\circ\prime}_{s,h} = 3.89 \times 10^{-3}$ *cm/s,* $(1 - \alpha) = 0.469$*] on overpotential for ferrocyanide system at a platinum OTE. Coefficients of correlation;* $k_{f,h}$ *data,* R = 0.9993; $k_{b,h}$ *data,* R = 0.9986.

vicinity of the $E^{\circ\prime}$ are employed, and are more sensitive to changes in $k^{\circ\prime}_{s,h}$ than to changes in α when back step potentials well-removed from the $E^{\circ\prime}$ are used.

Derivative Cyclic Voltabsorptometry

Linear potential sweep perturbation of an OTE in conjunction with optical monitoring of the electrode reaction product gives rise (*21*) to an experimental tool that offers unique advantages for the characterization of heterogeneous electron transfer reactions. In this technique, the absorbance (A_R) of the electrode reaction product (R, Equation 1), which is the optical analog of the total charge passed, is differentiated with respect to the linearly varying electrode potential. This derivative optical signal (dA_R/dE) is displayed as a function of sweep potential as shown in Figure 10. The resulting dA_R/dE vs. E waveform is morphologically identical to the cyclic voltammetric response of the redox couple. For reversible systems, the peak amplitude of the derivative optical response is given by

$$(dA_R/dE)_p = \beta\, n^{1/2}\, \epsilon_R(\lambda)\, D_O^{1/2}\, C_O^{\circ}\, \nu^{-1/2} \qquad (14)$$

where $\beta = -0.0881\ \mathrm{mV}^{-1/2}$, C_O° is in moles per liter, and the sweep rate,

ν, is in millivolts per second. Equation 14, an optical analog of the Randles–Sevcik equation, exhibits two striking features. First, the amplitude of the derivative voltabsorptometric peak, unlike the monitored signals in other transient spectroelectrochemical methods, depends on the n-value of the system. Second, the derivative voltabsorptometric signal is *inversely* dependent on the rate of potential sweep. Hence derivative cyclic voltabsorptometry (DCVA) is a technique that is analogous to, and at the same time a complement of,

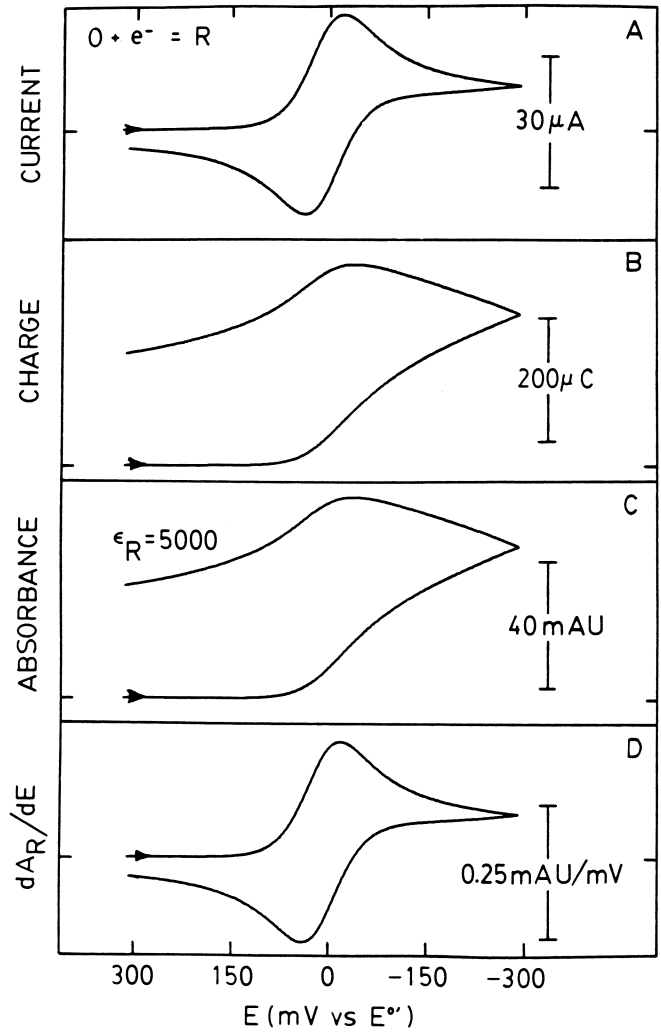

Figure 10. Simulated current (A), charge (B), absorbance (C), and dA_R/dE *(D) responses for reversible monoelectronic reduction of* O. *Scan rate = 25 mV/s, area = 0.25 cm², $\epsilon_R = 5.0 \times 10^3$ M^{-1} cm^{-1}, $D_O = D_R = 6.0 \times 10^{-6}$ cm^2/s, $C_O^\circ = 1.0$ mM.*

cyclic voltammetry. The advantages derived from the use of optical monitoring of electrode reactions, together with the inverse dependence of the derivative optical signal on sweep rate, strongly suggest the application of DCVA to the characterization of heterogeneous electron transfer reactions of BRMs. Hence, when the rates of heterogeneous electron transfer of irreversible and quasi-reversible systems dictate that slow rates of potential sweep be employed for their kinetic characterizations, the DCVA technique becomes particularly advantageous relative to its purely electrochemical counterpart (cyclic voltammetry), whose sensitivity decreases with decreasing sweep rate.

The oxidation of ferrocyanide at platinum OTEs is a convenient system with which the application of the DCVA technique to quasi-reversible systems can be demonstrated. Moreover, the kinetic results obtained by this experimental method can be directly compared with those determined by single potential step and asymmetric double potential step techniques. Figure 11 shows the DCVA responses for this system at sweep rates of 23.3, 47.5, and 95 mV/s. Overlaid on these

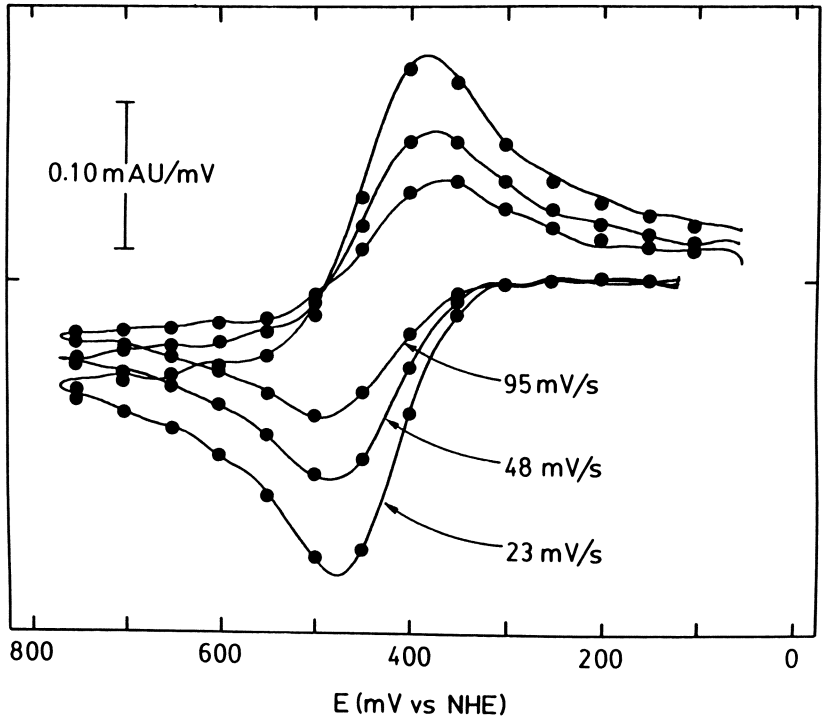

Figure 11. Derivative cyclic voltabsorptograms for 4.71 mM $K_4Fe(CN)_6$ at a platinum OTE in pH 7.00 solution. Solid lines are experimental responses, solid circles are digitally simulated responses. Values of $k^{\circ\prime}_{s,h}$ and α employed in the simulation are given in Table IV.

derivative voltabsorptomograms are simulated responses generated using the parameters listed in Table IV. The agreement between simulation and experiment shown in Figure 11 is quite good. Also, the values of $k^{o\prime}_{s,h}$ and α that are characteristic of the DCVA responses of this system are in excellent agreement with those determined by single potential step and asymmetric double potential step techniques (cf., Tables I, III, and IV).

Applications to Biological Molecules

The single potential step chronoabsorptometric technique has recently been employed to determine the heterogeneous electron transfer kinetic parameters of three different biological molecules: myoglobin (*8*, *10*), horse heart cytochrome c (*10*), and soluble spinach ferredoxin (*9*). The salient features of these investigations are summarized in Table V. In every case, the chronoabsorptometric data were analyzed according to the irreversible model described previously. The error associated with the use of this model for the kinetic analyses of these systems is most pronounced at low overpotentials, long times of observation, and large values of $k^{o\prime}_{s,h}$. For the systems shown in Table V, the use of the irreversible model introduced less than 1% error in the evaluated rate constants for myoglobin and cytochrome c (cf., Table II). For the ferredoxin system, the maximum error in $k_{f,h}$ arising from use of the irreversible model for kinetic analysis is approximately 20% at observation times of 60 s for $\eta = -16$ mV and decreases to approximately 6% at 60 s for $\eta = -101$ mV. Because the values of $k_{f,h}$ at low overpotentials are actually larger than those reported (*9*), $k^{o\prime}_{s,h}$ is somewhat larger than the reported value and α is correspondingly smaller.

Table IV. Heterogeneous Electron Transfer Kinetic Parameters for Ferrocyanide System at Platinum OTE Evaluated by Derivative Cyclic Voltabsorptometry

$\nu(mV/s)$	$k^{o\prime a}_{s,h}(cm/s) \times 10^3$	α^a	$\Delta E^b_p(mV)$
23.3	4.3	0.53	94
47.5	4.0	0.52	102
95.0	4.2	0.56	125
Mean	4.2 ($\pm$0.2)[c]	0.54 ($\pm$0.02)[c]	

Note: $[K_4Fe(CN)_6]$ = 4.71 m*M* in pH 7.00 phosphate buffer (Titrisol, Merck) containing 0.10 *M* NaCl.

[a] From digital simulation of DCVA responses shown in Figure 11. Simulation parameters are: $[K_4Fe(CN)_6]$ = 4.71 m*M*, $D_R = 6.50 \times 10^{-6}$ cm^2/s (*22*), $D_O = 7.65 \times 10^{-6}$ cm^2/s (*22*), ϵ_O(420 nm) = 1020 M^{-1} cm^{-1} (*21*), $E^{o\prime}$ = 424 mV vs. NHE (*18*), ν = 23.3, 47.5, and 95.0 mV/s.

[b] $\Delta E_p = E_{p(a)} - E_{p(c)}$.

[c] Standard deviation.

Published on June 1, 1982 on http://pubs.acs.org | doi: 10.1021/ba-1982-0201.ch002

Table V. Heterogeneous Electron Transfer Kinetic Parameters of Biomolecules Determined by Single Potential Step Chronoabsorptometry

Biomolecule[a]	*OTE*[b]	*Solution Conditions*	*Observation Aperture(s)*[c]	*Range of η(mV)*[d]	$k^{o'}_{s,h}$(*cm/s*)	*α*	*Reference*
Myoglobin	methyl viologen-modified gold minigrid	pH 7.00 phosphate buffer[e], 0.10 *M* NaCl	25–50	−396/−516	3.9×10^{-11}	0.88	8
Cytochrome c	methyl viologen-modified gold minigrid	pH 7.00 phosphate buffer (0.07 *M*), NaCl (0.10 *M*)	25–50	−70/−397	1.3×10^{-5}	0.27	10
Cytochrome c	Fluoride-doped tin oxide	pH 7.00 phosphate buffer (0.07 *M*), NaCl (0.10 *M*)	5–18	−178/−528	6.8×10^{-6}	0.32	10
Cytochrome c	Tin-doped indium oxide	pH 7.00 phosphate buffer (0.07 *M*), NaCl (0.10 *M*)	5–18	−8/−127	3.1×10^{-5}	0.50	10
Ferredoxin	methyl viologen-modified gold minigrid	pH 7.50 tris buffer[f] (0.15 *M*), NaCl (0.20 *M*)	30–60	−16/−101	6.5×10^{-5}	0.60	9

Note: For reductive potential steps; data analysis by irreversible model.
[a] Concentrations are [Mb] = 20–50 μM; [Cyt c] = 40–103 μM; [Fd] = 78–124 μM.
[b] Details of surface modification given in references.
[c] For kinetic analyses.
[d] Maximum/minimum values employed for kinetic analysis.
[e] Titrisol (Merck).
[f] Trizma (Sigma).

The asymmetric double potential step chronoabsorptometric technique has been applied to the determination of the kinetics of the back reaction of cytochrome c

$$\text{cyt c (III)} + e^- \underset{k_{b,h}}{\overset{k_{f,h}}{\rightleftharpoons}} \text{cyt c (II)} \qquad (15)$$

at tin oxide OTEs. Values of $k_{b,h}$ determined at various back (oxidative) step overpotentials are summarized in Table VI together with those values of $k_{f,h}$ at various forward (reductive) overpotentials that were determined by the single potential step method. The dependences of $\log(k_{f,h})$ and $\log(k_{b,h})$ on η are shown in Figure 12. Although the reductive and oxidative kinetic data are internally self-consistent, extrapolation of these respective sets of data affords quite different values of $k^{o\prime}_{s,h}$ and α. Whereas the reductive potential step experiments give rise to values of $k^{o\prime}_{s,h} = 4.37\ (\pm 0.20) \times 10^{-6}$ cm/s and $\alpha = 0.268\ (\pm 0.008)$, the asymmetric double potential step experiments indicate that for the oxidation of ferrocytochrome c the formal heterogeneous rate constant is much larger [$k^{o\prime}_{s,h} = 2.63\ (\pm 0.18) \times 10^{-5}$ cm/s] and the transfer coefficient also is significantly larger [$(1 - \alpha) = 0.101\ (\pm 0.009)$].

To establish the validity of these results, the ferricytochrome c system was exhaustively converted to the reduced form (ferrocytochrome c) by controlled potential electrolysis and then oxidative single

Table VI. Heterogeneous Electron Transfer Rate Constants for the Reduction of Ferricytochrome c and the Oxidation of Ferrocytochrome c at Tin Oxide OTEs

Reduction		*Oxidation*	
$\eta^a(mV)$	$k^b_{f,h}(cm/s) \times 10^4$	$\eta(mV)$	$k^c_{b,h}(cm/s) \times 10^4$
−228	0.418	172	0.478
−278	0.791	272	0.783
−328	1.31	472	2.15
−378	2.36	572	2.19
−428	3.98	672	3.60
−478	8.30		
−528	9.33		
−628	26.4		

Note: [Cyt c] = 94 μM, pH 7.00 phosphate buffer (0.07 M), NaCl (0.10 M).

[a] $E^{o\prime}$ = 260 mV vs. NHE (23).

[b] Evaluation by either irreversible or quasi-reversible single potential step model gives same result at these values of η; average relative deviation for duplicate measurements is ca. 8%; kinetic analysis time domain is 1.5–18 s.

[c] Analysis by digital simulation of asymmetric double potential step response; τ = 18 s; kinetic analysis time domain is 19.5–36 s; average relative deviation for duplicate experiments is ca. 15%.

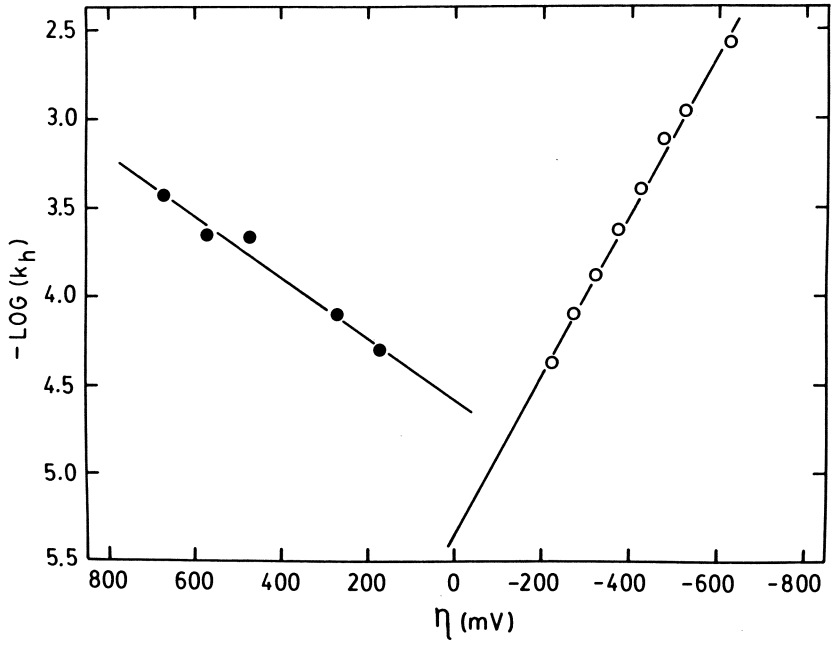

Figure 12. Dependence of log ($k_{f,h}$) *from single potential step chronoabsorptometric measurements (* ○, $k^{o'}_{s,h} = 4.37 \times 10^{-6}$ *cm/s,* $\alpha = 0.268$*) and log* ($k_{b,h}$) *from asymmetric double potential step chronoabsorptometric measurements [*●, $k^{o'}_{s,h} = 2.63 \times 10^{-5}$ *cm/s,* $(1 - \alpha) = 0.101$*] on overpotential for cytochrome c system at a tin oxide OTE. Coefficients of correlation:* $k_{f,h}$ *data,* R = 0.9976; $k_{b,h}$ *data,* R = 0.9846.

potential step chronoabsorptometric experiments were performed to provide an independent measure of $k^{o'}_{s,h}$ and α for this reverse reaction. The results of these experiments are summarized in Table VII and confirm that indeed the phenomenon seen in Figure 12 is also noted by the single potential step chronoabsorptometric technique at both tin oxide and methyl viologen-modified gold OTEs. Further confirmation of this grossly different heterogeneous electron transfer kinetic behavior of the two redox forms of cytochrome c in this medium is afforded by the DCVA response shown in Figure 13. The simulated response (solid circles) for $k^{o'}_{s,h} = 2.2 \times 10^{-6}$ cm/s and $\alpha = 0.31$ is in good agreement with the experimentally observed reductive behavior (solid line). On potential sweep reversal, however, the experimental response does not reflect the behavior expected for the oxidation of ferrocytochrome c if these values of $k^{o'}_{s,h}$ and α remain valid. The oxidative dA_R/dE signal should rise more sharply if indeed $(1 - \alpha)$ is $(1 - 0.31) = 0.69$. That the signal does not follow the expected behavior is indicative of a much smaller value of $(1 - \alpha)$, hence a much larger

Published on June 1, 1982 on http://pubs.acs.org | doi: 10.1021/ba-1982-0201.ch002

Table VII. Heterogeneous Electron Transfer Kinetic Parameters for Cytochrome c System

[Cyt c], μM	*Electrode*	*Reaction*[a]	*Technique*[b]	$k^{o'}_{s,h}$ *(cm/s)*	*α*	*Reference*
77	methyl viologen-modified gold minigrid	III + e^- = II	SPS/CA	1.0 (±0.2)[c] = 10^{-5}	0.24 (±0.03)[c]	10
77	methyl viologen-modified gold minigrid	II = III + e^-	SPS/CA (PR)	5.8 (±0.6) × 10^{-6}	0.74 (±0.02)	24
103	tin oxide	III + e^- = II	SPS/CA	6.8 (±0.8) × 10^{-6}	0.32 (±0.01)	10
103	tin oxide	III + e^- = II	SPS/CA	6.3 (±0.7) × 10^{-6}	0.28 (±0.02)	24
103	tin oxide	II = III + e^-	SPS/CA (PR)	4.9 (±0.7) × 10^{-5}	0.95 (±0.01)	24
94	tin oxide	III + e^- = II	SPS/CA	4.4 (±0.2) × 10^{-6}	0.27 (±0.01)	25
94	tin oxide	II = III + e^-	ADPS/CA	2.6 (±0.2) × 10^{-5}	0.90 (±0.01)	25

Note: Solution at pH 7.00 (0.07 *M* phosphate buffer), containing 0.10 *M* NaCl.

[a] III + e^- = II indicates reduction of ferricytochrome c; II = III + e^- indicates oxidation of ferrocytochrome c.

[b] SPS/CA: single potential step chronoabsorptometry; PR: prior reduction by exhaustive controlled-potential electrolysis; ADPS/CA: asymmetric double potential step chronoabsorptometry.

[c] Standard deviation.

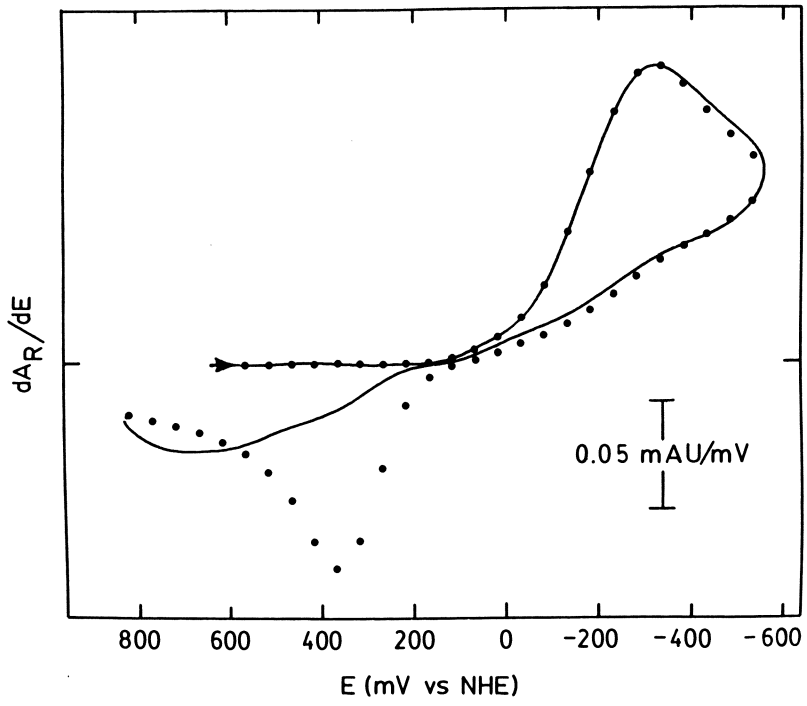

Figure 13. Derivative cyclic voltabsorptogram for 89 μM ferricytochrome c at a tin oxide OTE in pH 7.00 phosphate buffer (0.07 M) containing 0.10 M NaCl (solid line). Sweep rate = 4.0 mV/s, absorbance of ferrocytochrome c monitored at 416 nm ($\Delta\epsilon_{416}$ = 5.7 × 10⁴ M^{-1} cm^{-1}) (26). Solid circles are for simulated response using $k^{\circ\prime}_{s,h}$ = 2.2 × 10^{-6} cm/s, α = 0.31, $D_O = D_R$ = 1.10 × 10^{-6} cm^2/s (27). (Reproduced, with permission, from Ref. 27. Copyright 1981, Academic Press.)

value of α as is observed in the oxidative potential step experiments (Table VII). Whether this behavior is a manifestation of interactions between the biomolecule and some solution component(s) or the electrode and some solution component(s) has not been definitively established at this time (*24*).

In summary, the four techniques described can be expected to become increasingly important kinetic probes as new electrode systems are developed that facilitate direct electron transfer between the electrode and biological molecules.

Acknowledgments

This work was supported in part by the University of Delaware Institute of Neuroscience (NIH Biomedical VII), the North Atlantic

Treaty Organization, the National Science Foundation (PCM79-12348), and the National Institutes of Health (GM27208-02). The experimental expertise of E. F. Bowden, C. D. Crawley, and J. S. Sidwell is gratefully acknowledged.

Literature Cited

1. Sawyer, D. T. "Electrochemical Studies of Biological Systems"; ACS SYMPOSIUM SERIES, No. 38, ACS: Washington, D.C., 1977.
2. Wilson, G. S. In "Methods in Enzymology"; Fleischer, S.; Packer, L., Eds.; Academic: New York, 1978; Vol. 54, p. 396.
3. Heineman, W. R. *Anal. Chem.* **1978,** *50* 390A.
4. McCreery, R. L. *CRC Crit. Revs. Anal. Chem.* **1978,** *7,* 89.
5. Yeh, P.; Kuwana, T. *Chem. Lett.* **1977,** 1145.
6. Landrum, H. L.; Salmon, R. T.; Hawkridge, F. M. *J. Am. Chem. Soc.* **1977,** *99,* 3154.
7. Stargardt, J. F.; Hawkridge, F. M.; Landrum, H. L. *Anal. Chem.* **1978,** *50,* 930.
8. Bowden, E. F.; Hawkridge, F. M.; Blount, H. N. *Bioelectrochem. Bioenerg.* **1980,** *7,* 447.
9. Crawley, C. D.; Hawkridge, F. M. *Biochem. Biophys. Res. Commun.* **1981,** *99,* 516.
10. Bowden, E. F.; Wang, M.; Hawkridge, F. M. *J. Electrochem. Soc.* **1980,** *127,* 131C.
11. Ferguson-Miller, S.; Brautigan, D. L.; Margoliash, E. In "The Porphyrins"; Dolphin, D., Ed.; Academic: New York, 1979; Vol. 7, pp. 149–240.
12. Kuwana, T.; Heineman, W. R. *Acct. Chem. Res.* **1976,** *9,* 241.
13. Kuwana, T. *Ber. Bunsenges. Phys. Chem.* **1973,** *77,* 858.
14. Bard, A. J.; Faulkner, L. R. "Electrochemical Methods"; Wiley: New York, 1980, p. 183.
15. Albertson, D. E.; Blount, H. N.; Hawkridge, F. M. *Anal. Chem.* **1979,** *51,* 556.
16. Winograd, N.; Blount, H. N.; Kuwana, T. *J. Phys. Chem.* **1969,** *73,* 3456.
17. Bancroft, E. E.; Blount, H. N.; Hawkridge, F. M. *Anal. Chem.* **1981,** *53,* 1862.
18. Hawkridge, F. M.; Kuwana, T. *Anal. Chem.* **1973,** *45,* 1021.
19. Corrigan, D. A.; Evans, D. H. *J. Electroanal. Chem.* **1980,** *106,* 287.
20. Kimmerle, F. M.; Chevalet, J. *J. Electroanal. Chem.* **1969,** *21,* 237.
21. Bancroft, E. E.; Sidwell, J. S.; Blount, H. N. *Anal. Chem.* **1981,** *53,* 1390.
22. von Stackelberg, M.; Pilgram, M.; Toome, V. *Z. Elektrochem.* **1953,** *57,* 342.
23. Cusanovich, M. A. In "Bioorganic Chemistry"; E. E. van Tamelen, Ed.; Academic: New York, 1978, Vol. 4, p. 118.
24. Chapter 7 in this book.
25. Bancroft, E. E.; Blount, H. N.; Hawkridge, F. M., unpublished data.
26. Van Buuren, K. J. H.; Van Gelder, B. F.; Wilting, J.; Braams, R. *Biochim. Biophys. Acta* **1974,** *333,* 421.
27. Bancroft, E. E.; Blount, H. N.; Hawkridge, F. M. *Biochem. Biophys. Res. Commun.* **1981,** *101,* 1331.

RECEIVED for review June 2, 1981. Accepted November 23, 1981.

Spectroelectrochemical Determination of the Temperature Dependence of Reduction Potentials

Tris(1,10-phenanthroline) Complexes of Iron and Cobalt with c-Type Cytochromes

VERNON T. TANIGUCHI, WALTHER R. ELLIS, JR., VINCE CAMMARATA, JOHN WEBB,[1] FRED C. ANSON, and HARRY B. GRAY

California Institute of Technology, Arthur Amos Noyes Laboratory, Pasadena, CA 91125

Recent advances in applying thin-layer spectroelectrochemical methods to determine formal reduction potentials (E°) *and electron stoichiometries* (n-*values) of metalloproteins have been extended to the study of the temperature dependences of the* E°-*values of c-type cytochromes. Isothermal and nonisothermal electrochemical cells are described briefly and the conventions used to assign electron transfer reaction entropies,* ΔS°_{rc}, *to redox half-cell reactions are discussed. Calibration of the nonisothermal behavior of the spectroelectrochemical cells is performed using Fe(1,10-phenanthroline)*$_3^{3+/2+}$ *and Co(1,10-phenanthroline)*$_3^{3+/2+}$, *two redox couples for which both isothermal and nonisothermal results are available. A detailed study of the temperature dependence of the formal reduction potential of horse heart cytochrome c yields the following thermodynamic parameters:* ΔH°, -14.5 *kcal/mol;* ΔS°, -28.5 *eu; and* ΔS°_{rc}, -12.9 *eu. Preliminary* ΔS°_{rc} *values for several other c-type cytochromes are as follows: tuna cytochrome c,* -10.3 *eu;* Rhodospirillum rubrum *cytochrome* c_2, -9.6 *eu;* Pseudomonas aeruginosa *cytochrome* c_{551}, -16.2 eu; Rhodospirillum rubrum *cytochrome c',* $+0.5$ *eu; and* Rhodopseudomonas palustris *cytochrome c',* -6.0 *eu.*

[1] Current address: Murdoch University, School of Mathematical and Physical Sciences, Murdoch, Perth, W.A. 6150, Australia.

0065-2393/82/0201-0051$06.00/0

Elucidation of the thermodynamics of metalloprotein electron transfer reactions (*1–15*) is a matter of fundamental importance in biochemistry (*16*). The enthalpies and entropies of metalloprotein electron transfer reactions are influenced by changes in protein conformation and solvation as well as other structural and medium effects (*2–11, 13–15*). Such effects are involved (*16, 17*) in the mechanisms of metalloprotein binding and electron transfer to membrane-bound complexes. This chapter describes experiments that use spectroelectrochemical methods to determine metalloprotein electron transfer enthalpies and entropies.

Variable Temperature Electrochemical Cells

Thermodynamic parameters for metalloprotein electron transfer reactions have been obtained from measurements of the temperature dependences of the equilibrium constants for reactions of metalloprotein redox couples with inorganic complexes (*1–3, 6–8, 9, 14*), from calorimetric measurements (*4, 5, 9, 14*), and from indirect calculations (*9, 12, 14*). Recent experiments show (*18–22*) that spectroelectrochemical methods employing thin-layer electrolysis cells (*23–25*) with optically transparent electrode materials (*26*) enable the rapid and accurate determination of metalloprotein reduction potentials ($E°$). The relative ease with which such $E°$ values can be obtained [as compared to the more commonly employed chemical (*1–9, 12, 14*) and potentiometric (*27–30*) procedures] makes the study of the temperature dependences of metalloprotein $E°$ values a much more tractable problem.

However, unlike the classical equilibrium, kinetic, and calorimetric experiments, studies of the temperature dependences of properties of electrochemical cells involve certain added complications. In addition to the redox half-reaction of interest, one must deal experimentally with at least one other half-cell reaction to complete the electrochemical cell. A suitable reference electrode half-cell is usually employed and, as a result, properties of the reference electrode half-reaction also can contribute to the observed temperature dependent properties of the complete cell reaction. An arrangement commonly employed is described by the following cell

$$\underbrace{\mathrm{Hg}|\mathrm{Hg_2Cl_2(sat.)},\ \mathrm{KCl(sat.)}\|\mathrm{KCl(sat.)}\|M^{m+},\ M^{(m-n)+}|M'}_{T(\text{varied})}$$

in which a saturated calomel electrode (SCE) is used as the reference half-cell, M^{m+} and $M^{(m-n)+}$ represent the oxidized and reduced halves of the redox couple of interest, and M' represents the working electrode material. Such so-called "isothermal" cell arrangements, in

which the temperature of the entire electrochemical cell is varied, were used in most of the early redox thermodynamic studies (*31–38*) on inorganic complexes in aqueous solution.

The temperature dependence of the overall cell potential in such isothermal cell experiments provides ground-state enthalpy ($\Delta H°$) and entropy ($\Delta S°$) changes for the complete cell reaction (*33–35, 37*)

$$M^{m+} + (n/2) \cdot H_2 = M^{(m-n)+} + n \cdot H^+ \quad (1)$$

which now is referenced to the standard hydrogen gas electrode (NHE), using the following expression for the temperature dependence of the SCE (*35, 39*)

$$E°_{SCE}(T) = 0.2444 - 0.00066(T - 25) \quad (2)$$

where T is temperature in degrees Centigrade ($20° < T < 35°$) and $E°_{SCE}(T)$ is the potential in volts of the SCE (vs. NHE) at temperature T.

For the net entropy change for the complete cell reaction

$$\Delta S° = (S°_{red} - S°_{ox}) + (n \cdot S°_{H^+} - n/2 \cdot S°_{H_2}) \quad (3)$$

where the $S°$ terms represent partial molal entropies, the entropy difference due to the redox half-cell of interest can be separated from that due to the reference electrode half-cell by third-law considerations (*40*). The partial molal entropy of dihydrogen, H_2, is 31.2 eu (*41*). Whereas some precedent exists for an "absolute" entropy scale with $S°_{H^+}$ approximately equal to −5.5 eu (*35, 37, 42, 43*), most of the current literature on aqueous inorganic complexes (*31–37*) and metalloprotein redox couples (*2–4, 6, 7, 9, 14, 15*) employs the so-called "practical" scale (*37, 41, 44*), which assigns a value of zero to $S°_{H^+}$. Adhering to the practical entropy scale convention, rearrangement of Equation 3 indicates that for a one-electron redox process ($n = 1$)

$$S°_{red} - S°_{ox} = \Delta S° + 15.6 \text{ eu} \quad (4)$$

Thus, the difference in partial molal entropies between the reduced and oxidized halves of a one-electron redox couple [often called the "reaction entropy", $\Delta S°_{rc}$ (*43, 45*)] is equal to the net entropy change for the complete cell reaction, $\Delta S°$, plus 15.6 eu in an isothermal cell experiment.

Although isothermal electrochemical cells are straightforward on a conceptual and thermodynamic basis, certain practical considerations make them unsuitable for routine use in extensive investigations. The difficulties encountered relate to the amount of time required for several of the common reference electrodes to reach true temperature

equilibrium. The attainment of thermal phase equilibria (e.g., solid vs. liquid) often is necessary in certain reference electrodes [SCE and Ag(Ag Cl)]. In the early isothermal cell experiments (*33–35, 37*) separate SCEs were prepared and equilibrated to different temperatures for at least 2 days before use.

A cell arrangement of the type

$$\underbrace{\mathrm{Hg|Hg_2Cl_2(sat.),\ KCl(sat.)||KCl(sat.)}}_{T_1(\text{fixed})}\ \underbrace{|\mathrm{KCl(sat.)||}M^{m+}, M^{(m-n)+}|M'}_{T_2(\text{varied})}$$

can be utilized effectively to circumvent the problems associated with isothermal electrochemical cells (*45*). In such a nonisothermal cell arrangement, only the temperature of the redox half-cell of interest is varied. The temperature of the reference electrode half-cell is maintained at some fixed, constant temperature. As described previously (*45*), if the temperature coefficients of certain thermal junction potentials can be made either negligible or constant relative to the overall temperature coefficient of the nonisothermal cell ($dE°/dT$), reaction entropies for redox couples can be determined directly from nonisothermal cell measurements

$$\Delta S°_{rc} = S°_{red} - S°_{ox} = nF(dE°/dT) \tag{5}$$

where F is the Faraday constant and n is the number of electrons transferred. Such $\Delta S°_{rc}$ values are absolute with respect to those determined from isothermal experiments only when it can be demonstrated that the various thermal junction potentials do not contribute significantly to the temperature coefficient of the nonisothermal cell potential. Such considerations do not, however, affect the relative values of the nonisothermal $\Delta S°_{rc}$, because the thermal junction potentials are the same in each case.

To study the thermodynamics of metalloprotein electron transfer reactions, we employed spectroelectrochemical methods using thin-layer electrolysis cells and optically transparent electrodes (OTEs) to which the nonisothermal electrochemical cell configuration was adapted.

Experimental

Materials. Horse heart cytochrome c (type VI), from Sigma Chemical Co., was purified on a CM-cellulose column according to published procedures (*46*) prior to use. Ruthenium(III) mediator–titrant: $[Ru(NH_3)_5py](ClO_4)_3$ was prepared as described previously (*47*). The sodium salt (indicator grade) of 2,6-dichloroindophenol (Aldrich Chemical Co.) was used with-

out further purification. Ionic strength 0.1 *M*, pH 7.0 sodium phosphate buffer (1.97×10^{-2} *M* $NaH_2PO_4 \cdot H_2O$, 2.68×10^{-2} *M* Na_2HPO_4) was prepared from analytical grade reagents. All protein and buffer solutions were prepared using deionized water purified by a Barnstead NANOpure water purifier.

Gold electroformed mesh (minigrid, 60% transmittance) was used as the working electrode material in the thin-layer cells (Buckbee–Mears Co.). Teflon tape spacer (Dilectric Corp.) was 0.1 mm thick. Epoxi-Patch epoxy (Dexter Corp.) was used to seal the working thin-layer cell compartment. Rosin Solder Cream soft solder, Archer brand from Radio Shack, was used to make the external electrical contact to the minigrid electrode. Optical windows were of high quality quartz (0.15-cm thickness, transparency to 170 nm).

Apparatus. Anaerobic optically transparent thin-layer electrolysis (OTTLE) cells were similar in design to cells already described (*21*). The working OTTLE cell compartment (2×2 cm) was supported in a Lucite or Kel-F (Teflon) cell body ($1.2 \times 2.5 \times 7.0$ cm) in the manner described in Reference *21*. Optical path lengths varied from 0.1 to 0.4 mm (with Teflon tape spacers), with two opposing minigrids used in the thicker cells. Electrical contact to the minigrid was through an 18-gauge copper wire soldered to a portion of the minigrid left exterior to the thin cell (*21*). Working OTTLE cell compartments were sealed permanently and attached to the cell bodies using epoxy cement. Cell bodies were designed to allow the working cell compartments to be rebuilt simply by cutting away the epoxy sealant with a sharp scalpel.

Two T 7/25 inner tapers were machined lengthwise into the cell bodies and connected to the thin-layer cavity through two 2×7 mm filling ports. Our nonisothermal salt bridge consisted of a 5 mm $\times$ 25 cm Pyrex tube filled with deoxygenated saturated potassium chloride solution. The bottom end was terminated in a T 7/25 outer ground glass joint with a platinum junction and a Sargent–Welch calomel reference electrode (miniature, platinum junction, #S–30080–17) resided at the top. A platinum wire auxiliary electrode was sealed into a tube of soft glass with a T 5/20 outer ground glass joint. This apparatus was supported in a compartment consisting of a T 5/20 inner ground glass joint on top of a T 7/25 outer ground glass joint terminated by a (fine) porous glass frit. This compartment contained deoxygenated supporting electrolyte and served to isolate the auxiliary electrode from the protein solution.

Methods. Protein solutions were deoxygenated prior to use by gentle vacuum/argon cycling on a vacuum/purified argon double manifold. Protein solutions were loaded into the OTTLE cells under anaerobic conditions using either rubber septum caps and syringe techniques or within a Vacuum Atmospheres Co. HE–43–2 Dri-Lab plus HE–493 Dri-Train inert atmosphere box. The reference and auxiliary electrode apparatus was sealed into the appropriate OTTLE cell body compartments with Apiezon H grease. The fully loaded OTTLE cells had a dead solution volume of about 0.7 mL. The actual volumes of the thin-layer cavities varied from about 30 to 90 μL.

Formal reduction potentials at different temperatures for the metalloproteins were determined using the OTTLE cells in a nonisothermal electrochemical cell configuration. Potentials were applied across the thin-layer cells with a Princeton Applied Research Model 174A polarographic analyzer and were measured accurately with a Keithly 177 microvolt DMM digital multimeter. Cell temperatures were varied using a specially constructed variable temperature cell holder and constant temperature water bath and mea-

sured directly with an Omega Engineering, Inc. precision micro thermocouple (plus Fluke 2175A Digital Thermometer, ±0.2°) situated in the protein solution in close proximity to the thin-layer cavity. The SCE reference electrode was separated from the thermostated cell by the nonisothermal salt bridge and maintained at ambient room temperature. All UV–visible spectra were obtained with a Cary 219 recording spectrophotometer.

Formal reduction potentials were determined by sequentially applying a series of potentials, E(applied), across the thin-layer cell. Each potential was maintained until electrolysis ceased so that the equilibrium value of the ratio of concentrations of oxidized to reduced forms of all redox couples in solution, $[O]/[R]$, was established as defined by the Nernst equation. Complete electrolysis occurred rapidly as a result of the short diffusional path length created by the thin solution layer. A "small molecule," electrochemically reversible redox couple (mediator–titrant) with an $E°$ close to that of the metalloprotein was included to facilitate electron transfer between the metalloprotein redox couple and the working electrode (*48*, *49*). Redox couples were converted in increments from one oxidation state to the other by the series of applied potentials, for which each value of $[O]/[R]$ was determined from the corresponding overlay spectra. Formal reduction potentials and n-values were determined from plots of E(applied) vs. log $[O]/[R]$. At least seven data points were included in each Nernst plot.

Calibration of the Nonisothermal OTTLE Cells

An earlier publication (*15*) described the empirical approach used to calibrate our nonisothermal electrochemical cells. The redox thermodynamics of the $Fe(phen)_3^{3+/2+}$ and $Co(phen)_3^{3+/2+}$ couples (where phen represents 1,10-phenanthroline) were determined using our apparatus and the results were compared with published values from isothermal and nonisothermal experiments.

Figures 1 and 2 illustrate results that are typical of the data obtained for the $Fe(phen)_3^{3+/2+}$ and $Co(phen)_3^{3+/2+}$ couples, respectively, using thin-layer spectroelectrochemistry. The results obtained when such experiments are performed as a function of temperature are presented in Tables I and II and illustrated in Figures 3 and 4. The temperature coefficients of the nonisothermal cell potentials, $dE°/dT$, were determined from the slope of a linear least squares fit to the $E°$ vs. temperature data. Because we were testing a nonisothermal cell arrangement, reaction entropies ($\Delta S°_{rc}$) were calculated directly from Equation 5. Complete cell entropies adjusted to the NHE scale ($\Delta S°$) were determined from Equation 4. Standard free-energy changes for the complete cell reaction were calculated from the $E°$ values (V vs. NHE) at 25°C and the standard enthalpy changes ($\Delta H°$) were determined from the corresponding $\Delta G°$ and $\Delta S°$ values.

Table III summarizes our entropy results (*15*) for the $Fe(phen)_3^{3+/2+}$ and $Co(phen)_3^{3+/2+}$ couples along with published values from isothermal and nonisothermal experiments. Excellent agreement is obtained for the entropies for $Fe(phen)_3^{3+/2+}$ from the nonisothermal

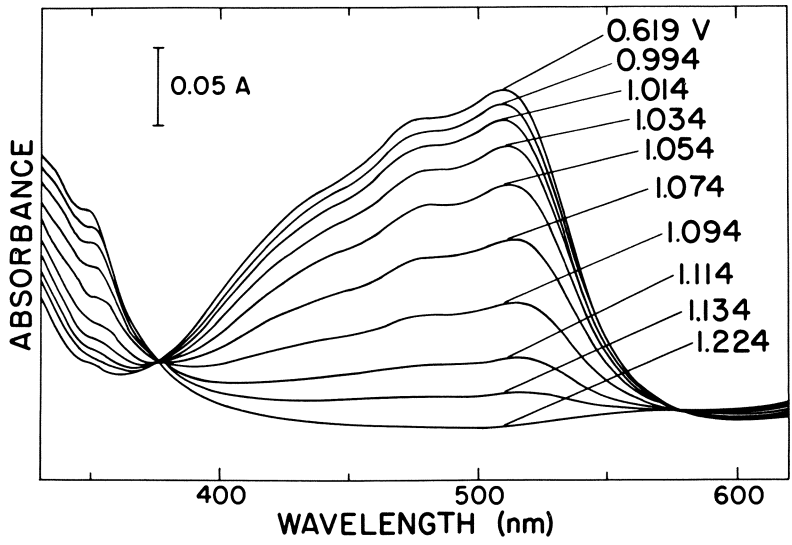

Figure 1a. Thin-layer spectroelectrochemistry of $Fe(phen)_3^{3+/2+}$ (sulfate salt), 0.4 mM, pH 2.33 (HNO_3); ionic strength, 0.1 M ($NaNO_3$), 14.4°C. Overlay spectra at different values of the applied potential, E_{appl}, in V vs. NHE.

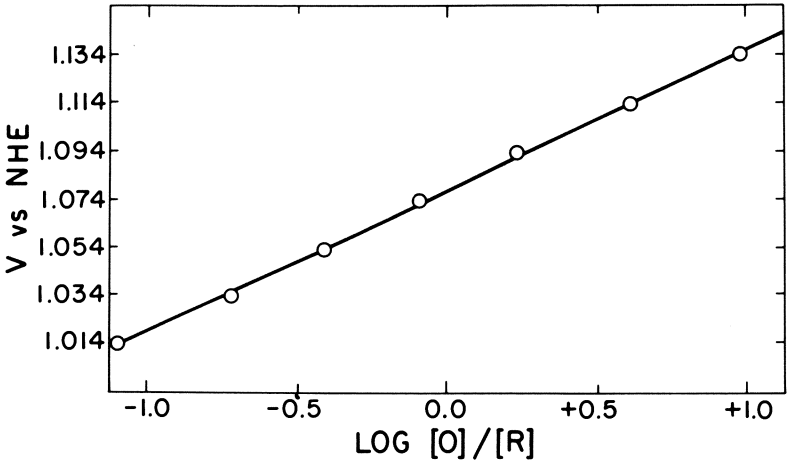

Figure 1b. Nernst plot of the data in Figure 1a.

OTTLE experiments and the isothermal potentiometric experiments that were performed under identical conditions of pH and ionic strength. Furthermore, the entropies for both $Fe(phen)_3^{3+/2+}$ and $Co(phen)_3^{3+/2+}$ from nonisothermal OTTLE and cyclic voltammetry experiments and isothermal potentiometric experiments are all in satis-

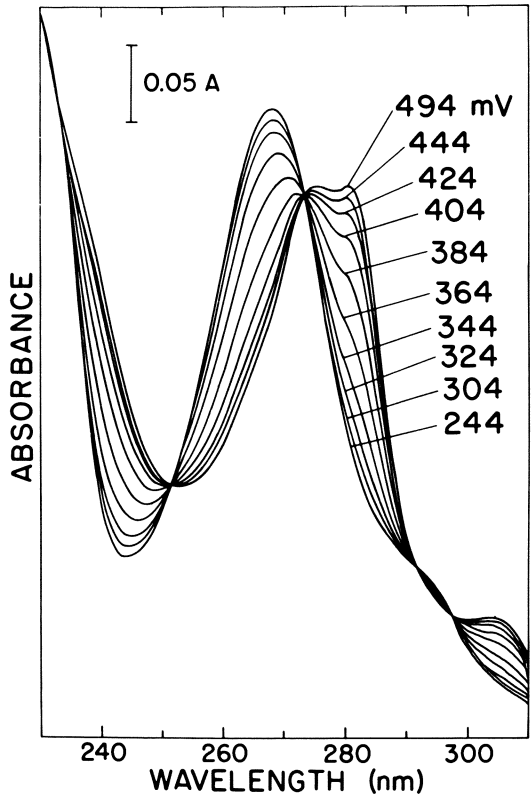

Figure 2a. Thin-layer spectroelectrochemistry of $Co(phen)_3^{3+/2+}$ (perchlorate salt), 0.2 mM; ionic strength, 0.1 M, pH 7 sodium phosphate buffer, 22.2°C. Overlay spectra at different values of E_{appl}, in mV vs. NHE.

factory agreement, particularly if reasonable allowances are made for the differences in experimental conditions.

The agreement between the ΔS°_{rc} values determined from isothermal and nonisothermal experiments indicates that the temperature coefficients of the various thermal junction potentials in our nonisothermal OTTLE cells do not contribute significantly to the observed temperature coefficient of the overall cell potential. Therefore, Equation 5 can be used to determine ΔS°_{rc} directly for redox couples that are suitable for study with our nonisothermal OTTLE cells. Results for the corresponding reduction potentials, free energies, and enthalpies are given in Table IV.

Redox Thermodynamics for Horse Heart Cytochrome c

The thin-layer spectroelectrochemical results obtained for horse heart cytochrome c are displayed in Figure 5. Any desired ratio of

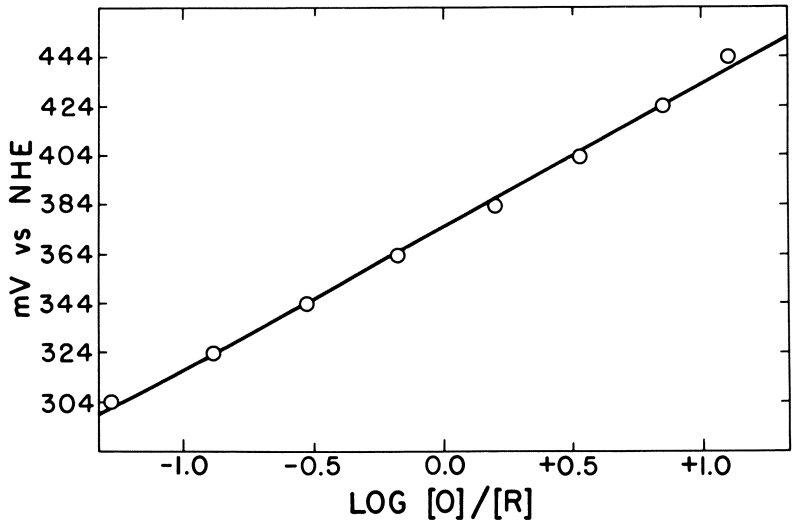

Figure 2b. Nernst plot of the data in Figure 2a.

Table I. Temperature Dependence of the Formal Reduction Potential, $E°$, for $Fe(phen)_3^{3+/2+}$ Using Nonisothermal Thin-Layer Spectroelectrochemistry

T[a] (°C)	E°[b] (*V vs. NHE*)	RT/F[c] (*mV*)	r^{2}[d]
5.2	1.077	55	0.998
9.8	1.078	58	0.999
11.2	1.074	58	0.998
14.4	1.078	59	0.999
15.1	1.075	61	0.999
15.7	1.074	59	0.998
20.9	1.072	60	0.999

Note: $Fe(phen)_3^{3+/2+}$ (sulfate salt), 0.4 m*M*, pH 2.33 (HNO_3); ionic strength, 0.1 *M* ($NaNO_3$).
[a] ±0.2°.
[b] ±0.002 V.
[c] Experimental Nernst slope at temperature *T*.
[d] Linear correlation coefficient.

oxidized to reduced protein, $[O]/[R]$, was established easily and maintained merely by adjusting the overall solution potential via the potentiostat. Electrolysis to equilibrium was accelerated by the addition of suitable redox mediators. Both $Ru(NH_3)_5py^{3+/2+}$ (where py represents pyridine) and 2,6-dichloroindophenol were used to ascertain the independence of the protein $E°$ values on the particular mediator–titrant employed. A region of the cytochrome c absorption spectrum in which the mediators showed negligible absorption in both reduced and oxidized states was monitored.

Table II. Temperature Dependence of the Formal Reduction Potential, $E°$, for $Co(phen)_3^{3+/2+}$ Using Nonisothermal Thin-Layer Spectroelectrochemistry

T[a] (°C)	E°[b] (mV vs. NHE)	RT/F[c] (mV)	r^{2}[d]
8.8	361	56	1.000
9.6	365	55	0.999
13.3	368	57	0.999
13.5	368	58	0.998
16.9	372	56	0.999
18.6	374	54	0.999
18.9	368	56	1.000
22.2	374	57	1.000
25.3	377	57	0.999
28.0	378	64	1.000

Note: $Co(phen)_3^{3+/2+}$ (perchlorate salt), 0.2 mM; ionic strength, 0.1 M, pH 7 sodium phosphate buffer.

[a] ±0.2°.

[b] ±2 mV.

[c] Experimental Nernst slope at temperature T.

[d] Linear correlation coefficient.

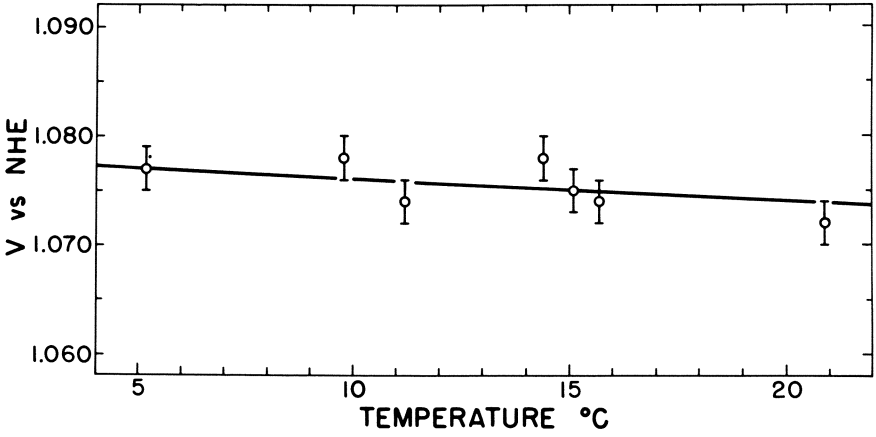

Figure 3. Temperature dependence of E° *for* $Fe(phen)_3^{3+/2+}$ *using nonisothermal thin-layer spectroelectrochemistry where* E° *(25°) = 1.073 V (NHE) and the slope* $= -1.90 \times 10^{-4}$ *V/°C.*

Horse heart cytochrome c exhibited reversible, one-electron Nernstian behavior in these experiments. Electrolysis to equilibrium occurred significantly faster when chromatographically pure (*46*) Sigma type VI horse heart cytochrome c was employed (cf. the upper right inset in Figure 5). In addition, the experimentally determined

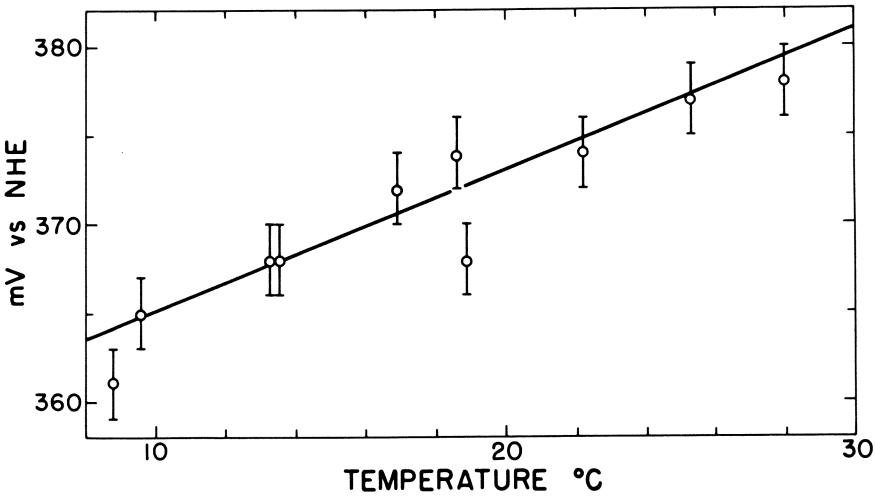

Figure 4. Temperature dependence of E° *for* $Co(phen)_3^{3+/2+}$ *using nonisothermal thin-layer spectroelectrochemistry where* E° *(25°) = 377 mV (NHE) and the slope* $= +7.92 \times 10^{-4}$ *V/°C.*

thermodynamic parameters (discussed later) were slightly different from those obtained for the nonpurified Sigma type VI protein (*15*).

Results for the temperature dependence of the cytochrome c formal reduction potential are presented in Table V and illustrated in Figure 6 [$E°$ (25°C) = 260 ± 2 mV (NHE) and $dE°/dT = -5.61 \pm 0.5 \times 10^{-4}$ V/°C for the given pH and supporting electrolyte conditions]. Thermodynamic parameters are as follows: $\Delta S°$, −28.5 ± 1.2 eu; $\Delta S°_{rc}$, −12.9 ± 1.2 eu; $\Delta G°$, −6.00 ± 0.05 kcal/mol; and $\Delta H°$, −14.5 ± 0.4 kcal/mol. These values are in excellent agreement with published parameters (*6*, *7*) for horse heart cytochrome c (pH 7, μ = 0.1 *M*): $\Delta S°$, −28 ± 5 eu; $\Delta S°_{rc}$, −13 ± 5 eu; $\Delta G°$, −6.0 kcal/mol; and $\Delta H°$, −14.5 ± 1.5 kcal/mol.

Reaction Entropies for Other Cytochromes c

The temperature dependences of the formal reduction potentials of several other c-type cytochromes were studied (*51*). Even at this early stage in our work, certain interesting comparisons can be made. All the cytochromes exhibit either essentially zero or slightly negative electron transfer reaction entropies. These $\Delta S°_{rc}$ values do not correlate with the overall charge on the protein (cf. Table VI), as found with simple inorganic complexes of iron [e.g., consider the following $\Delta S°_{rc}$ values: $Fe(CN)_6^{3-/4-}$, −49 eu (*35*); $Fe(H_2O)_6^{3+/2+}$, +43 eu (*45*)]. Indeed, evidence (*7*) indicates that the reaction entropies reflect rather small

Published on June 1, 1982 on http://pubs.acs.org | doi: 10.1021/ba-1982-0201.ch003

Table III. Values of $\Delta S°$ and $\Delta S°_{rc}$ ($= S°_{red} - S°_{ox}$) for the $Fe(phen)_3^{3+/2+}$ and $Co(phen)_3^{3+/2+}$ Redox Couples

Couple	$\Delta S°$ *(eu)*	$\Delta S°_{rc}$ *(eu)*	*Electrolyte*	*Method*	*Reference*
$Fe(phen)_3^{3+/2+}$	-20.8 ± 2	-5.2 ± 2	4.5×10^{-3} *M* HNO_3 $\mu = 0.1$ *M* ($NaNO_3$)	isothermal potentiometric Pt electrode	*34*
	-12.6 ± 2	3 ± 2	0.05 *M* KCl +25 m*M* phen	nonisothermal cyclic voltammetry Pt electrode	*45*
	-20.0 ± 2	-4.4 ± 2[a]	4.5×10^{-3} *M* HNO_3 $\mu = 0.1$ *M* ($NaNO_3$)	nonisothermal OTTLE Au electrode	[b]
$Co(phen)_3^{3+/2+}$	-3.6	12	$\mu = 0.01$ *M*	isothermal potentiometric Pt electrode	*50*
	6.4 ± 4	22 ± 3	0.05 *M* KCl + 25 m*M* phen	nonisothermal cyclic voltammetry Pt electrode	*45*
	2.7 ± 3	18.3 ± 3[c]	phosphate buffer $\mu = 0.1$ *M* pH 7.0	nonisothermal OTTLE Au electrode	[b]

[a] From $E°$ vs. temperature data collected in the range 5–16°C.
[b] This work.
[c] From $E°$ vs. temperature data collected in the range 7–30°C.

Published on June 1, 1982 on http://pubs.acs.org | doi: 10.1021/ba-1982-0201.ch003

Table IV. Additional Thermodynamic Parameters for the $Fe(phen)_3^{3+/2+}$ and $Co(phen)_3^{3+/2+}$ Redox Couples

Couple	E° *(25°C) (V vs. NHE)*	ΔG° *(kcal/mol)*	ΔH° *(kcal/mol)*	*Method*	*Reference*
$Fe(phen)_3^{3+/2+}$	1.099	−25.3 ± 0.1	−31.5 ± 0.5	isothermal potentiometric Pt electrode	*34*
	1.114	−25.7	−29.3	nonisothermal cyclic voltammetry Pt electrode	*45*
	1.073[a] (±0.002)	−24.7 ± 0.1	−30.8 ± 1.3	nonisothermal OTTLE Au electrode	[b]
$Co(phen)_3^{3+/2+}$	0.399	−9.2	−10.3	isothermal potentiometric Pt electrode	*50*
	0.387	−8.9	−9.2	nonisothermal cyclic voltammetry Pt electrode	*45*
	0.377 (±0.002)	−8.7 ± 0.1	−9.5 ± 0.3	nonisothermal OTTLE Au electrode	[b]

Note: Supporting electrolytes are the same as those given in Table III.
[a] The value for $E°$ at 25°C was extrapolated from the experimentally determined $dE°/dT$.
[b] This work.

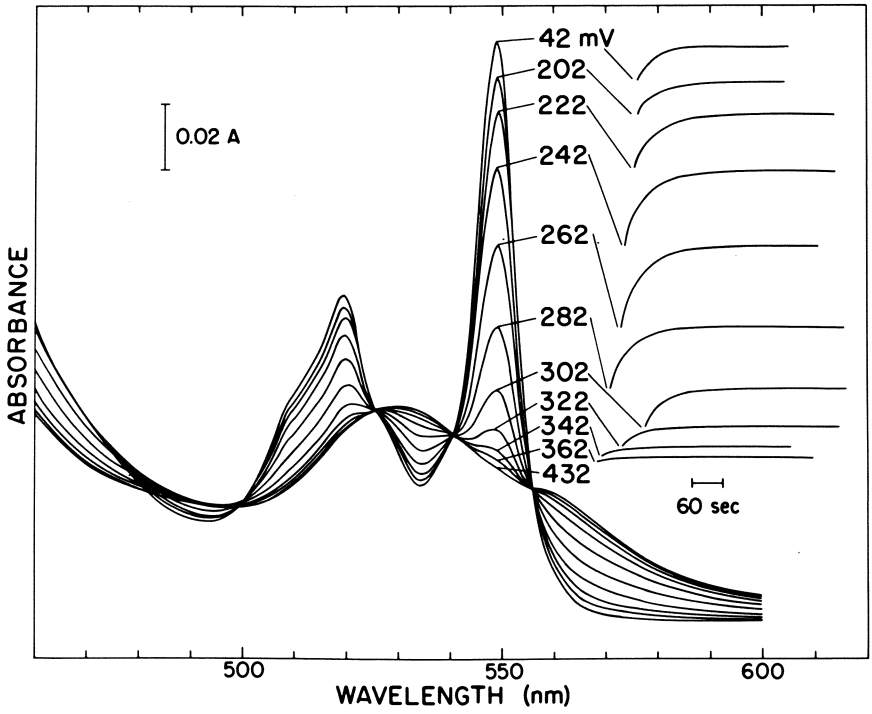

Figure 5a. Thin-layer spectroelectrochemistry of horse heart cytochrome c, 0.13 mM; ionic strength, 0.1 M, pH 7 sodium phosphate buffer, 25.0°C; [$Ru(NH_3)_5py(ClO_4)_3$], 0.65 mM. Overlay spectra and absorbance changes at 550 nm as a function of time at different values of the applied potential, E_{appl}, in mV vs. NHE.

changes in protein structure in the vicinity of the heme c sites. One possibility is that these small structural changes are related to the degree of exposure of the heme c group to water molecules, because the c′ proteins, whose sites are exposed to a degree, exhibit more positive $\Delta S°_{rc}$-values. We associate solvent exposure with less tightening of the protein framework structure on reduction; in other words, less protein conformational change is needed to accommodate the insertion of an electron if the heme c group in question can interact with water molecules.

Such a simple interpretation cannot account for all redox metalloprotein reaction entropies. Proteins with relatively exposed heme c groups exhibit more negative $\Delta S°_{rc}$-values than can be accommodated satisfactorily by our crude model (e.g., cytochrome c_{551} from *Pseudomonas aeruginosa*). More research will be required before the thermodynamics of single redox center metalloprotein electron transfer reactions can be understood in a quantitative sense.

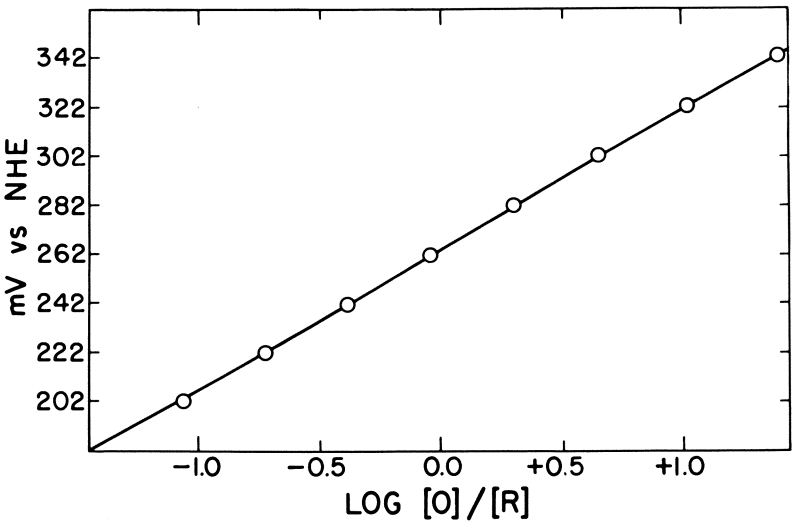

Figure 5b. Nernst plot of the data in Figure 5a.

Table V. Temperature Dependence of the Formal Reduction Potential, $E°$, for Horse Heart Cytochrome c Using Nonisothermal Thin-Layer Spectroelectrochemistry

T[a] (°C)	E°[b] (*mV vs. NHE*)	RT/F[c] (*mV*)	r²[d]
8.6	269	56	1.000
9.2	270	56	1.000
15.5	267	57	1.000
16.8[e]	265	58	0.999
19.8	262	56	1.000
20.2	263	58	1.000
24.4	262	59	1.000
29.8	257	60	0.999
30.6	258	59	1.000
35.2	254	61	1.000
39.4	253	59	0.999

Note: Cytochrome c, 0.13 m*M*; ionic strength, 0.1 *M*, pH 7 sodium phosphate buffer; $[Ru(NH_3)_5py](ClO_4)_3$, 0.65 m*M*.

[a] ±0.2°.

[b] ±2 mV.

[c] Experimental Nernst slope at temperature *T*.

[d] Linear correlation coefficient.

[e] Redox mediator 2,6-dichloroindophenol, 0.03 m*M*.

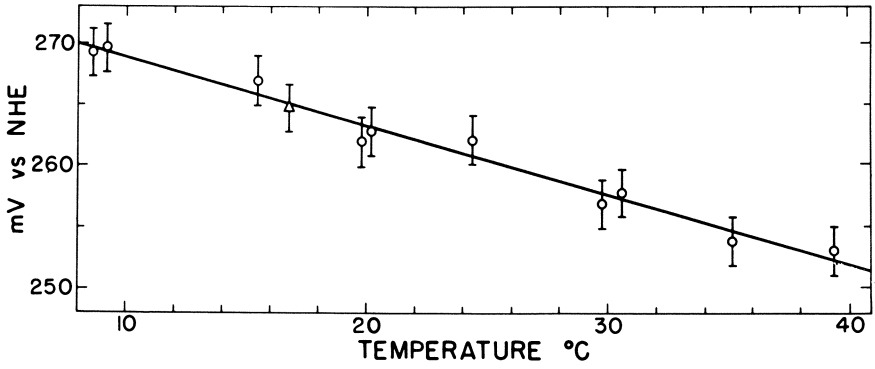

Figure 6. Temperature dependence of E° *for horse heart cytochrome c using nonisothermal thin-layer spectroelectrochemistry where* E° *(25°C) = 260 mV (NHE) and the slope = −5.61 = 10^{-4} V/°C. Key:* ○, $Ru(NH_3)_5py^{3+/2+}$; *and* △, *2,6-dichloroindophenol.*

Table VI. A Comparison of ΔS°_{rc}-Values for c-Type Cytochromes (Ionic Strength 0.1 *M*, pH 7) with the Corresponding Protein Isoelectric pH Values

Protein	$\Delta S^\circ_{rc}(eu)$	*pI*[a]
Cytochrome c′ (*Rhodospirillum rubrum*)	+0.5	5.6 (52)
Cytochrome c′ (*Rhodopseudomonas palustris*)	−6.0	9.4 (53)
Cytochrome c_2 (*R. rubrum*)	−9.6	6.2 (52)
Cytochrome c (tuna)	−10.3	10.04 (54)
Cytochrome c (horse)	−14.9	10.05 (54)
Cytochrome c_{551} (*Pseudomonas aeruginosa*)	−16.2	4.7 (55)

[a] References for the protein isoelectric pH values are given in parentheses.

Acknowledgments

The authors thank T. Takano for the tuna cytochrome c samples and for many helpful discussions. Also we thank R. G. Bartsch, M. D. Kamen, T. E. Meyer, and S. A. Schichman for providing samples of the bacterial cytochromes. Part of the research was performed during the period when J. Webb was a visiting Fulbright Fellow at California Institute of Technology.

The spectroelectrochemical studies of cytochromes were supported by National Science Foundation Grant CHE80–24863. This is Contribution No. 6463 from the Arthur Amos Noyes Laboratory.

Literature Cited

1. Ball, E. G. *Biochem. Z.* **1938,** *295,* 262.
2. Hanania, G. I. H., Ph.D. Thesis, Cambridge, England, 1953.
3. George, P.; Hanania, G. I. H.; Eaton, W. A. In "Hemes and Hemoproteins"; Chance, B.; Estabrook, R. W.; Yonetani, T., Eds.; Academic: New York, 1966; pp. 267–271.
4. George, P.; Eaton, W. A.; Trachtman, M. *Fed. Proc.* **1968,** *27,* 526.
5. Watt, G. D.; Sturtevant, J. M. *Biochemistry* **1969,** *8,* 4567.
6. Margalit, R.; Schejter, A. *FEBS Lett.* **1970,** *6,* 278.
7. Margalit, R.; Schejter, A. *Eur. J. Biochem.* **1973,** *32,* 492.
8. Jacks, C. A.; Bennett, L. E.; Raymond, W. N.; Lovenberg, W. *Proc. Natl. Acad. Sci. U.S.A.* **1974,** *71,* 1118.
9. Goldberg, M.; Pecht, I. *Biochemistry* **1976,** *15,* 4197.
10. Anderson, C. W.; Halsall, H. B.; Heineman, W. R.; Kreishman, G. P. *Biochem. Biophys. Res. Commun.* **1977,** *76,* 339.
11. Kreishman, G. P.; Su, C.-H.; Anderson, C. W.; Halsall, H. B.; Heineman, W. R. In "Bioelectrochemistry: Ions, Surfaces, Membranes,"; Blank, M., Ed.; ACS ADVANCES IN CHEMISTRY SERIES, No. 188; ACS: Washington, D.C., 1980; pp. 169–185.
12. Wherland, S.; Pecht, I. *Biochemistry* **1978,** *17,* 2585.
13. Sailasuta, N.; Anson, F. C.; Gray, H. B. *J. Am. Chem. Soc.* **1979,** *101,* 455.
14. Goldberg, M., Ph.D. Thesis, Weizmann Institute of Science, Rehovot, Israel, 1979.
15. Taniguchi, V. T.; Sailasuta-Scott, N.; Anson, F. C.; Gray, H. B. *Pure Appl. Chem.* **1980,** *52,* 2275.
16. Walz, D. *Biochim. Biophys. Acta* **1979,** *505,* 279.
17. Margalit, R.; Schejter, A. *Eur. J. Biochem.* **1973,** *32,* 500.
18. Heineman, W. R.; Norris, B. J.; Goelz, J. F. *Anal. Chem.* **1975,** *47,* 79.
19. Norris, B. J.; Meckstroth, M. L.; Heineman, W. R. *Anal. Chem.* **1976,** *48,* 630.
20. Hawkridge, F. M.; Ke, B. *Anal. Biochem.* **1977,** *78,* 76.
21. Anderson, C. W.; Halsall, H. B.; Heineman, W. R. *Anal. Biochem.* **1979,** *93,* 366.
22. Heineman, W. R.; Meckstroth, M. L.; Norris, B. J.; Su, C. *Bioelectrochem. Bioenerg.* **1979,** *6,* 577.
23. Reilley, C. N. *Rev. Pure Appl. Chem.* **1968,** *18,* 137.
24. Hubbard, A. T.; Anson, F. C. In "Electroanalytical Chemistry"; Bard, A. J., Ed.; Dekker: New York, 1970; Vol. 4, pp. 129–214.
25. Hubbard, A. T. *Crit. Rev. Anal. Chem.* **1973,** *3,* 201.
26. Bard, A. J.; Faulkner, L. R. In "Electrochemical Methods–Fundamentals and Applications"; Wiley: New York, 1980; p. 578.
27. Rodkey, F. L.; Ball, E. G. *J. Biol. Chem.* **1950,** *182,* 17.
28. Henderson, R. W.; Rawlinson, W. A. *Biochem. J.* **1956,** *62,* 21.
29. Dutton, P. L.; Wilson, D. F.; Lee, C.-P. *Biochemistry* **1970,** *9,* 5077.
30. Myer, Y. P.; Saturno, A. F.; Verma, B. C.; Pande, A. *J. Biol. Chem.* **1979,** *254,* 11202.
31. George, P.; Hanania, G. I. H.; Irvine, D. H. *J. Chem. Phys.* **1954,** *22,* 1616.
32. George, P.; Hanania, G. I. H.; Irvine, D. H. *Recl. Trav. Chim. Pays-Bas* **1956,** *75,* 759.
33. George, P.; Hanania, G. I. H.; Irvine, D. H. *J. Chem. Soc.* **1957,** 3048.
34. George, P.; Hanania, G. I. H.; Irvine, D. H. *J. Chem. Soc.* **1959,** 2548.
35. Lin, J.; Breck, W. G. *Can. J. Chem.* **1965,** *43,* 766.
36. Eaton, W. A.; George, P.; Hanania, G. I. H. *J. Phys. Chem.* **1967,** *71,* 2016.
37. Hanania, G. I. H.; Irvine, D. H.; Eaton, W. A.; George, P. *J. Phys. Chem.* **1967,** *71,* 2022.
38. Lavallee, D. K.; Lavallee, C.; Sullivan, J. C.; Deutsch, E. *Inorg. Chem.* **1973,** *12,* 570.
39. Ives, D. J. G.; Janz, G. J. In "Reference Electrodes"; Academic: New York, 1961; p. 161.

40. Pitzer, K. S.; Brewer, L. In "Thermodynamics"; 2nd ed.; McGraw–Hill: New York, 1961; Chap. 32.
41. Latimer, W. M. In "Oxidation Potentials"; 2nd ed.; Prentice–Hall: New York, 1952; p. 30.
42. Gurney, R. W. In "Ionic Processes in Solution"; McGraw–Hill: New York, 1953; Chap. 10.
43. Yee, E. L.; Weaver, M. J. *Inorg. Chem.* **1980,** *19,* 1077.
44. Latimer, W. M.; Pitzer, K. S.; Smith, W. V. *J. Am. Chem. Soc.* **1938,** *60,* 1831.
45. Yee, E. L.; Cave, R. J.; Guyer, K. L.; Tyma, P. D.; Weaver, M. J. *J. Am. Chem. Soc.* **1979,** *101,* 1131.
46. Brautigan, D. L.; Ferguson-Miller, S.; Margoliash, E. In "Methods in Enzymology"; Colowick, S. P.; Kaplan, N. O., Eds.; Academic: New York, 1978; Vol. 53; pp. 128–164.
47. Cummins, D.; Gray, H. B. *J. Am. Chem. Soc.* **1977,** *99,* 5158.
48. Szentrimay, R.; Yeh, P.; Kuwana, T. In "Electrochemical Studies of Biological Systems"; Sawyer, D. T., Ed.; ACS SYMPOSIUM SERIES, No. 38, ACS: Washington, D.C., 1977; pp. 143–169.
49. Prince, R. C.; Linkletter, S. J. G.; Dutton, P. L. *Biochim. Biophys. Acta* **1981,** *635,* 132.
50. Chou, M.; Creutz, C.; Sutin, N. *J. Am. Chem. Soc.* **1977,** *99,* 5616.
51. Taniguchi, V. T.; Ellis, W. R., Jr.; Cammarata, V.; Webb, J.; Anson, F. C.; Gray, H. B., unpublished data.
52. Bartsch, R. G.; Kakuno, T.; Horio, T.; Kamen, M. D. *J. Biol. Chem.* **1971,** *246,* 4489.
53. Bartsch, R. G. In "Methods in Enzymology"; Part A; Colwick, S. P.; Kaplan, N. O.; Eds.; Academic: New York, 1971; Vol. 23, p. 346.
54. Barlow, G. H.; Margoliash, E. *J. Biol. Chem.* **1966,** *241,* 1473.
55. Horio, T.; Higashi, T.; Sasagawa, M.; Kusai, K.; Nakai, M.; Okunuki, K. *Biochem. J.* **1960,** *77,* 194.

RECEIVED for review June 17, 1981. Accepted January 7, 1982.

Surface Enhanced Raman Spectroscopy

A New Technique for Studying Interfacial Phenomena

RONALD L. BIRKE, JOHN R. LOMBARDI, and LUIS A. SANCHEZ

City University of New York, City College, Department of Chemistry, New York, NY 10031

The technique of surface enhanced Raman spectroscopy (SERS) is reviewed with emphasis on the electrochemical environment. The experimental setup and factors that optimize the Raman scattering intensity are discussed. Such factors include the range of metal substrates and adsorbate molecules that show the effect and the external experimental parameters affecting the intensity. These parameters are laser frequency, angle of incidence of the laser beam, electrode potential, and pretreatment of the electrode. Theoretical models of the enhancement are outlined and recent work is discussed.

Surface enhanced Raman spectroscopy (SERS) is a new spectroscopic technique that allows one to obtain vibrational spectra of molecules adsorbed on metal substrates under in situ conditions. SERS was first studied at a silver working electrode of an electrochemical cell, and it is ideal for obtaining spectral information at a metal electrode/electrolyte interface, although its applications extend far beyond the electrochemical environment. Our main concern, however, will be with SERS at electrode interfaces.

The measurement of Raman scattering from the electrode interface at a given electrode potential, together with measurement of current at such an electrode, has the possibility of identifying completely the nature of the electrochemical process, a goal long sought by electrochemists. Other methods for obtaining similar in situ spectral in-

0065-2393/82/0201-0069$10.75/0

formation at an electrode/electrolyte interface, such as internal (or external) reflectance spectroelectrochemistry and elipsometry, are not as specific or as sensitive as SERS. This great sensitivity of the "giant Raman effect," as SERS also has been called, results from an unexpectedly large inelastic scattering cross section. A general agreement of the causes of the SERS phenomenon has not been achieved, but enough is known to indicate that the method is a powerful laser Raman analytical tool. It is especially useful for molecules that contain coordinating atoms such as nitrogens with lone pairs, and for this reason it is a particularly good method for spectroelectrochemical studies of biologically important molecules.

This chapter reviews methods for obtaining SERS, experimental observations made concerning the phenomenon, experimental parameters that directly affect the SERS intensity, theoretical explanations of the phenomenon, and applications of the SERS technique. An earlier detailed review article (*1*) contains references through 1978. A critical review of the theories of SERS, covering literature up to mid-1979, has appeared in print (*2*). A more recent review (*3*) concentrates on two of the latest theoretical mechanisms for SERS. The present article contains references through the beginning of 1981.

The first report of the Raman spectroscopy (RS) of molecules adsorbed at a metal electrode under in situ electrochemical conditions was published in 1973 (*4*). A laser Raman spectrum of a thick layer of mercurous halides formed from mercury plated on platinum was obtained. The Raman spectrum of pyridine adsorbed on a silver electrode under potentiostatic control in potassium chloride electrolyte medium was reported in 1974 (*5*). This study opened up a new field of scientific inquiry, which has grown rapidly in the last several years. The intensity of the Raman spectrum of pyridine was enhanced (*6, 7*) by at least five to six orders of magnitude over what could be expected from the scattering cross section of the isolated molecule. This enhanced scattering intensity allows the observation of a surface Raman spectrum of a monolayer of adsorbed species. It is impossible to obtain a spectrum from a laser beam passing through the same number of molecules in a volume element of the bulk media. The explanation of this surface enhancement is now under intense study by theoretical and experimental chemists and physicists throughout the world.

The Electrochemical SERS Experiment

To achieve SERS under potentiostated electrochemical conditions in a three-electrode cell, the working electrode (Ag or another metal that shows the effect) is exposed to a beam of laser light and the scattered light is collected with a spectrometer. One possible collection

configuration is a 90° angle collection geometry, as shown in Figure 1a. The sum of the angle of incidence, ϕ_i, and the angle of observation, ϕ_s, is a constant 90°, and the angle of incidence is varied by rotating the electrode, which is on a *X–Y–Z* micropositioner. If the specular reflected beam is allowed to enter the monochromator, the laser gas emission lines must first be removed. This configuration is a conventional one, and it is convenient to use with commercially available Raman instruments, like the SPEX Ramalog 1401, where the laser beam enters the cell from the bottom side. It has the disadvantage that the angle of incidence or observation can not be varied easily.

Another collection configuration is the back scattering geometry, as shown in Figure 1b. In this geometry the position of the laser beam can be rotated more easily to change independently the angle of incidence, ϕ_i. In either collection geometry the electrode can be a relatively thick metal wire inserted in an insulating sheath, a metal film deposited on a conducting surface, or a metal foil. The laser beam is focused to a spot or a line on the electrode surface that is usually smaller than the electrode surface area. The spot focusing mode appears easier to align than the line focusing mode.

A simply constructed electrochemical cell for SERS is shown in Figure 2. Both the bottom, for the 90° collection geometry, and one side of the cell are made with an optically flat quartz window. The working electrode potential is controlled with respect to a Luggin capillary reference electrode by a potentiostat that provides current through the counter electrode. Well-defined SERS spectra can be obtained with 0.05 *M* SERS-active species in 0.1 *M* aqueous potassium chloride supporting electrolyte. The nature and concentration of the anion of the supporting electrolyte effects the SERS intensity, as will be discussed later. The cell also should have provisions for degassing and drainage of the solution. Other types of cells, such as a gasket-type cell where the electrode can be positioned as close to the front window as possible without distorting the diffusion layer (*1*) and a rotating disk cell with a similar provision (*8*), also were used.

The most intense Raman signal is found for a silver electrode when it is subjected to an oxidation/reduction cycle that forms silver chloride on anodization and reforms silver on cathodization. The initial experiments of Fleischmann et al. (*5*), using pyridine as a Raman active species at silver, involved the repeated cycling of the electrode for long periods (15 min) to roughen the electrode surface. These authors initially believed that the oxidation/reduction cycling increased significantly the surface area of the electrode so that the well-defined spectrum of pyridine could be obtained. The Raman signal showed that the ring-breathing modes of pyridine, 1004 and 1036 cm^{-1} in aqueous solution, were shifted on the silver electrode to 1008 and 1037

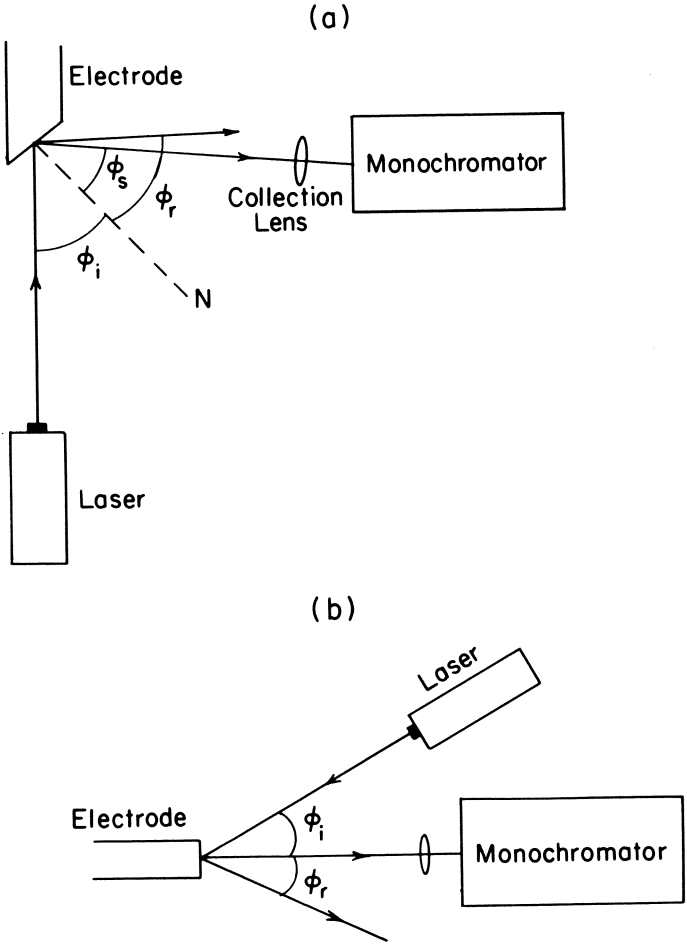

Figure 1. Scattering collection geometries. a, 90° mode; b, back scattering mode.

cm^{-1}, and that a new, highly potential-dependent band at 1025 cm^{-1} appeared at 0.00 V vs. the saturated calomel electrode (SCE) and decreased with potential, finally disappearing between −0.80 and −1.00 V vs. SCE (*5*). When these measurements were repeated (*6*) with a highly (alumina) polished silver electrode using a double potential step pretreatment of −0.60 to +.20 V vs. SCE (allowing 25.00 mC/cm^2 to flow through to the Ag electrode) and returning −0.60 V, very intense Raman spectra of pyridine were observed that were even larger (30–100-fold) than those observed by the roughening procedure of

Fleischmann et al. (5). A similar observation was made (7) using a single triangular sweep to pretreat the electrode. Estimates of the surface area increase in the Fleischmann experiment are approximately tenfold, so that an area effect could not explain the observed intensity even with the highly roughened surfaces. Calculations based on the number of molecules in a monolayer of coverage with end-on adsorption with respect to number of molecules in a volume element encountered by the laser beam in solution indicated that the enhancement factor of the electrode surface on the Raman scattering cross section of an isolated molecule is 10^5–10^6 (*6*, *7*, *9*). This observation of an anomalously intense Raman scattering led to the name "Surface Enhanced Raman Scattering" (SERS).

A complete block diagram for the spectroelectrochemical apparatus sufficient to obtain SERS with a conventional photon counting apparatus and a computer interface, as used in our laboratory, is illustrated in Figure 3. Typical laser power at the electrode is 100 mW and the spectral bandpass is 2–5 cm^{-1}. Data files of 500 24-bit double precision data words (points) can be stored in the PDP–8/E and sent to the DEC–10 for permanent storage on the disk with a file name structure. Eight storage buffers are available in the PDP–8/E and mathematical manipulation such as smoothing, integration, and subtraction of one 500-point spectrum from another can be accomplished in the minicomputer. A complete spectrum of 3000 double-precision points also can be recorded continuously using six buffers and kept as one file on the DEC–10.

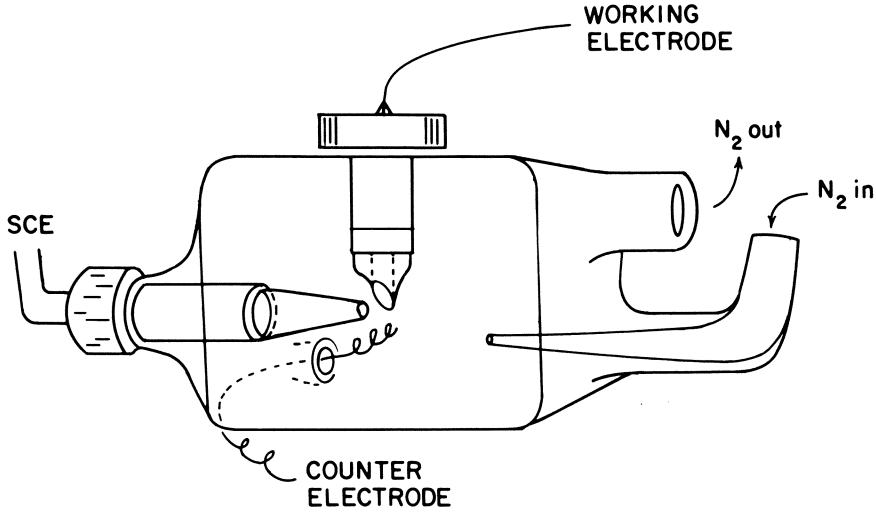

Figure 2. Simple electrochemical cell for SERS.

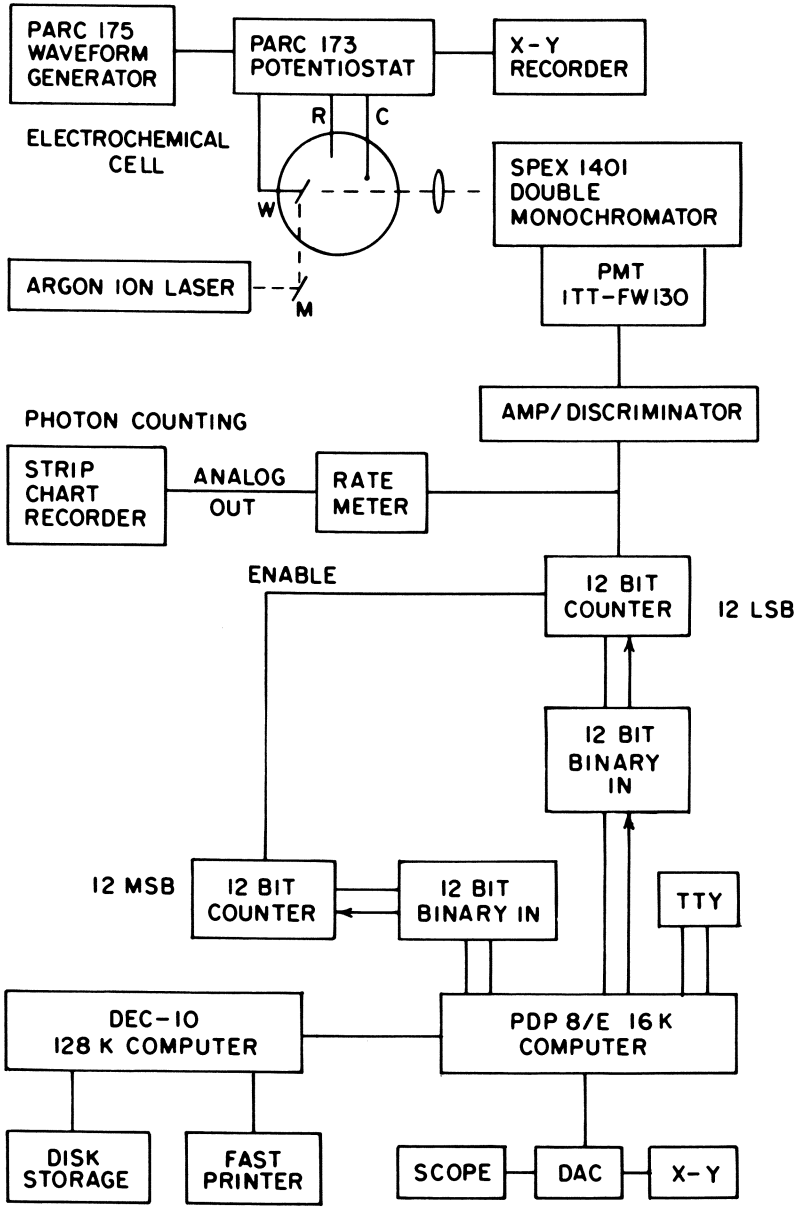

Figure 3. Block diagram of a complete computer interfaced spectro-electrochemical system for recording SERS.

A typical stripchart recorded spectrum of 0.05 *M* piperidine in 0.1 *M* potassium chloride at a silver electrode (using the Spex Ramalog instrument) is shown in Figure 4. Spectra obtained using the computer interface are shown in a later figure.

A second type of spectroelectrochemical instrumentation, using an optical multichannel analyzer (OMA) that allows rapid data acquisition, also was used to obtain SERS spectra (*10*). The particular instrument used in this study had a SIT vidicon camera at the focal plane of the spectrometer and a long-wavelength-pass interference filter at the entrance slit of the spectrometer to reduce background scatter due to the laser radiation (*10*). We built a similar system using an intensified reticon diode array detector. An OMA system allows a complete spectrum of 500 to 2000 points to be obtained in milliseconds, and is ideal for the study of transient SERS phenomena. Figure 5 shows the Raman intensity vs. wavenumber spectra as a function of time during an electrode potential sweep for 0.01 *M* KCN in 0.1 *M* K_2SO_4 at a silver electrode (*11*). The scan rate is 50 mV/s. The rise and fall of various bands are attributed to the formation of different species at the electrode surface (*11*).

Experimental Characteristics of SERS

Metal Substrates and Interfacial Systems that Can be Used to Obtain SERS. In addition to the many studies at a silver/electrolyte interface using 488- or 514.5-nm laser excitation in an electrochemical cell (*11–23*), SERS also has been seen with a copper electrode (*24–29*) and with a gold electrode (*25, 26*). The first observation of SERS on copper was very weak (*24*) but later it was found that, for both the copper and gold electrode, laser excitation in the red is necessary to achieve enhancement (*25–29*). SERS was reported recently using 488- and 514.5-nm excitation on a mercury electrode (*30, 31*); however, it is now doubtful whether this observation is a true SERS phenomenon (vide infra). Raman scattering reported at a platinum electrode (*14, 32–34*) primarily appear to result from resonance Raman scattering.

Other interfacial systems besides the electrochemical one can be used to observe SERS. SERS was observed at a metal/gas interface (*35*), at metal/ultra high vacuum (UHV) interfaces (*36–42*), at solid/solid interfaces (tunnel-junction configurations) (*43–45*), at metal island film/liquid interfaces (*46*), at metal grating/thin-film interfaces (*47, 48*), at silver and gold metal sol/liquid interfaces (*49–51*), and on metal precipitates of silver (*52*) in contact with aqueous solution. The metal/gas or UHV interfaces just referred to were studied with silver, gold, and copper substrates. A SERS effect also was observed for nickel supported on silica in an atmosphere of carbon monoxide and hydrogen (*53*).

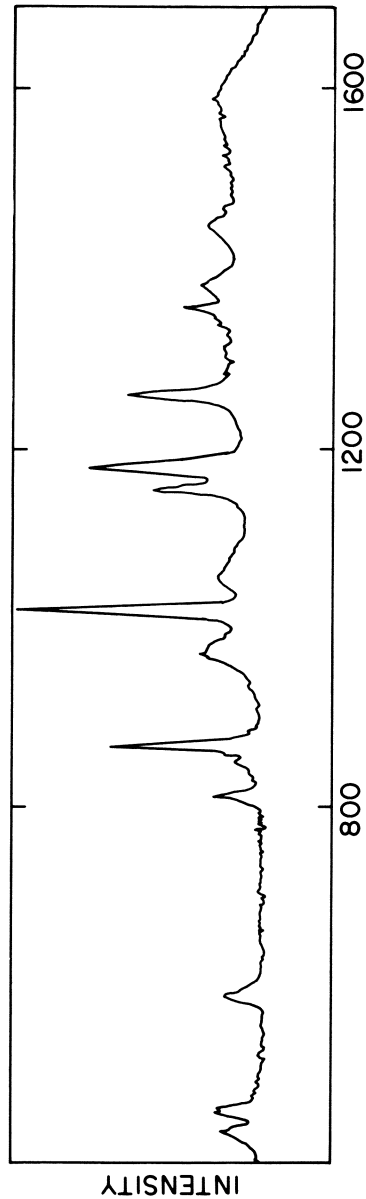

Figure 4. Spectrum of 0.05 M piperidine in 0.10 M KCl observed from a Ag electrode after double potential step pretreatment consisting of −0.6 to +0.2 V (held for 2 s) and back to −0.6 V, all vs. SCE. Full-scale sensitivity was 10^4 counts/s, scan rate was 50 cm^{-1}/min, and a 0.5-s time constant was used with rate meter photon counting. A 514.5-nm laser excitation was used. The effective bandpass was 2 cm^{-1}.

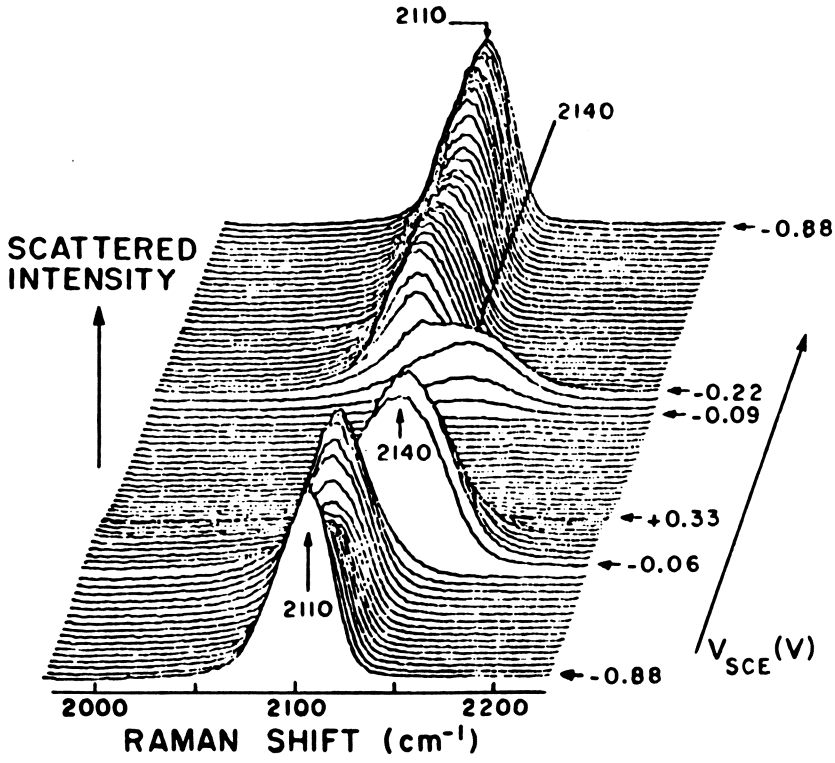

Figure 5. Raman intensity as a function of wavenumber and potential during a second oxidation–reduction sweep for 0.1 M K_2SO_4 and 0.01 M KCN at a Ag electrode as recorded with an optical multichannel analyzer system. The sweep rate was 50 mV/s. (Reproduced, with permission, from Ref. 11. Copyright 1980, North-Holland Publishing Co.)

Studies at tunnel junctions with an Al/aluminum oxide/adsorbate/metal configuration (*44*, *45*) showed SERS with silver and copper, but definitely not with lead and tin. However, lead sulfate and lead dioxide layers deposited on a lead foil showed Raman scattering (*54*). Studies at a silver–palladium alloy showed SERS only at low percentages of palladium (less than 5%) (*55*). Evidence indicates that SERS is found definitely for the Group Ib coinage metals and possibly for nickel, which borders on this group, although nickel has not been studied in an electrochemical environment where SERS can be demonstrated unambiguously. The wide range of the metal/adsorbate interface contacted by either an electrolyte, gas, vacuum, or solid phase makes the SERS technique the most general method existing for the in situ study of interfacial phenomenon.

Effect of Surface Pretreatment—Roughness. The largest SERS signals were observed on silver electrodes subjected to a single double potential step or triangular sweep with an anodic potential limit of

+0.20 to +0.30 V vs. SCE. Above a maximum of 30 mC/cm^2, the signal intensity reaches a plateau and then decreases beyond 50 mC/cm^2 (*1*, *6*, *9*). Similar results (*15*) on single crystal electrodes, silver (100) and silver (111), show that the relative intensity of the 1006-cm^{-1} pyridine line increases with the number of monolayers of silver produced in the pretreatment step, eventually leveling out above 10 monolayers on the silver (100) face (*12*).

Silver electrodes that were not anodized with a pretreatment step also show some enhancement. Van Duyne and co-workers (*1*, *27*) found that a polished silver or copper electrode, without electrochemical pretreatment, gives an enhancement factor of 10^4 with pyridine at −0.6 V vs. SCE. This enhancement on silver reportedly decayed below background when the electrode potential was shifted to 0.0 V vs. SCE (*1*). Silver electrodes highly polished mechanically with 0.3- to 0.05-μm diameter particles of an aluminum slurry showed, under examination by scanning electron microscopy (SEM), a flat surface indicating that the surface roughness was less than the resolution (250 Å) of the particular scanning electron microscopy (SEM) technique used (*56*). Raman signals from these surfaces with pyridine and $K_2Pt(CN)_4$ exhibited an enhancement factor of 10^4. Depending on the Raman spectrometer, the enhancement must be at least 100–1000 to observe SERS. The conclusion is that an oxidation/reduction cycle is not a prerequisite to observe SERS and that roughness on a scale larger than 250 to 500 Å only contributes a factor of at most 100 to the enhancement mechanism (*56*).

Scanning electron microscopy has been used to examine SERS metal substrates in a number of investigations. On a silver electrode, after pretreatment by an oxidation/reduction cycle, nodular deposits were noted (*57–59*). Some SEM micrographs showed dendritic growth with nodule heights and lateral spacings of several thousand angstroms (*57*); others showed metallic bumps of several hundred angstroms (*58*). These nodules were similar to the spherical particles seen with sols (*49*). When small amounts of charge were passed on a silver (111) electrode in a single cycle pretreatment, surface plasmon excitation with electroreflectance measurements was not observed (*18*, *58*). These latter results indicated that when small amounts of charge are passed there is no surface roughness on a scale of 100–1000 Å; however, SERS is observed.

There apparently are several scales of roughness to consider. One scale "macroroughness" observable with SEM has particle sizes from 250 to several thousand angstrom units, another scale "microroughness" has particles sizes from 50 to 250 Å, and a third scale "atomic-scale microroughness," not seen by SEM, is on the order of atomic dimensions. The chemical nature of the electrode surface also has

been analyzed by Auger electron spectroscopy (AES), which shows a remarkably clean surface (*1*, *56*, *57*) for the pretreated electrode.

The enhancement factor for mechanically roughened electrodes at the metal/air interface is at least two orders of magnitude less than that of the electrochemically pretreated metal/electrolyte interface (*35*). Studies using scanning electron microscopy show that large Raman scattering (RS) enhancements are seen from surfaces with roughness due to nodules of ca. 1000 Å in diameter for Ag surfaces in ultra high vacuum (UHV) systems, whereas for smooth surfaces the scattering is below the sensitivity threshold of the Raman spectrometer (*38*). Increases in the density of the nodules at nearly constant monolayer coverage of cyanide showed large intensity increases (*59*). These results (*38*, *59*) contradict previously discussed experiments (*56*) and may indicate a difference in mechanism between the electrochemical and UHV SERS phenomenon.

The results of Rowe et al. (*38*) for roughened silver surfaces (ca. 1000-Å particles) in ultra high vacuum systems show an interesting dependence of RS intensity on surface coverage. The 991-cm^{-1} peak of pyridine grows in a linear manner with coverage, as measured by sticking coefficients with an AES technique. These experiments indicate that molecules beyond a monolayer show SERS and that the enhancement extends at least 35 Å away from the surface. These results were used to support a long range (electromagnetic) enhancement model; however, they contradict earlier studies of Smardzewski et al. (*37*), who concluded that only molecules in the first monolayer give SERS. The Smardzewski et al. results were based on the observation that the SERS spectrum of a layer of deuterated pyridine (py-d_5) covering a monolayer of nondeuterated pyridine (py-h_5) on silver gives bands only from nondeuterated pyridine. Recent experiments of Zwemer, Shank, and Rowe (*42*) show peaks for both deuterated and nondeuterated pyridine when two monolayers of py-d_5 are deposited on one monolayer of py-h_5 at silver. The researchers suggest (*42*) that the pyr-h_5 layer discussed in Smardzewski's studies was very thick, making it impossible to observe py-d_5 peaks. Another indication that long range effects are taking place in UHV studies are spacer experiments (*60*) in which the Raman-active molecule is separated from a rough silver film by a polymer layer and enhancements of RS are seen at separations as large as 100 Å.

Enhancement at 35–100 Å away from the interface is inconsistent with electrode potential modulated experiments at a silver electrode–solution interface, which indicates that only molecules in the diffuse double layer (ca. 10 Å with 0.1 *M* KCl) give rise to SERS (*1*). Recent UHV experiments lend support to the idea that only molecules in the first few monolayers give strong SERS. Eesley (*40*) used the change in

silver surface work function to determine coverage of pyridine in a UHV system and found the RS intensity levels off for three different vibrations after 2–3 Langmuirs (L). A similar result for pyridine in a UHV system was found (*41*) using silver island films and a quartz crystal microbalance to measure coverage. Pockrand and Otto (*61*) studied pyridine adsorbed on silver films at temperatures around 130 K with an exposure range of 0.03 to 10^2 L. At exposures less than 1 L, the 1006-cm^{-1} band is quite intense and reaches saturation at about 2 L. After exposures of about 100 L the 994-cm^{-1} band appears and grows with additional coverage, indicating a thick condensed pyridine layer. The investigators conclude (*61*) that an explanation of SERS on the basis of electromagnetic resonances is unlikely.

Experiments to probe the role of surface roughness in SERS were designed using silver evaporated films under UHV conditions. Wood and Klein (39) showed that when a silver film, which gives SERS for CO adsorbed at 120 K, was annealed overnight at room temperature and then recooled and reexposed to CO under the same condition, the Raman signal of CO was dramatically reduced by a factor of 500 and the background was reduced by a factor of 20. In fact, the Raman signal of CO was lost in the noise of the spectrometer (*see* Figure 6). The researchers argue that room temperature annealing destroys the en-

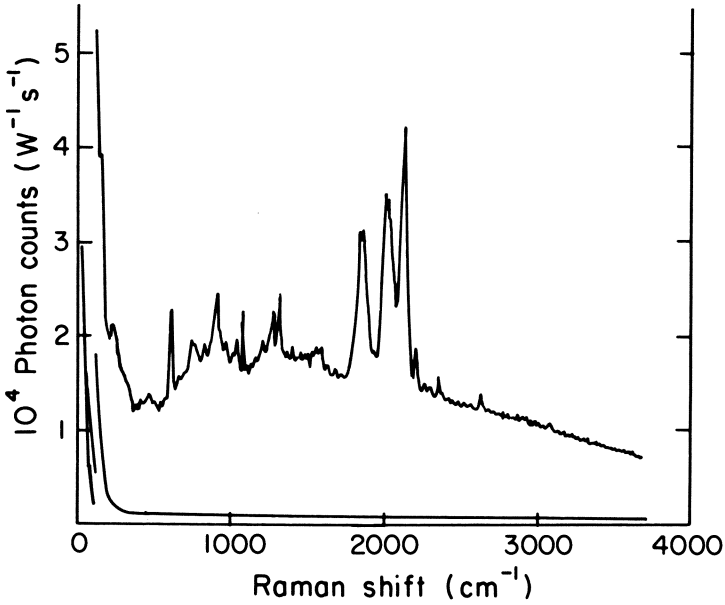

Figure 6. SERS spectrum of CO adsorbed on Ag. The upper curve is for 10^5 L exposure of CO on Ag at 120 K. The lower curve is the spectrum of the same film after annealing at room temperature and then reexposure to 10^5 L of CO at 120 K. (Reproduced, with permission, from Ref. 39. Copyright 1980, Pergamon Press, Ltd.)

hancement properties of the silver films, meaning that enhancement requires surface roughness (*39*). Pockrand and Otto conducted a similar experiment with adsorbed pyridine on silver film in UHV (*3*, *62*). Variation of the temperature from 120 to around 230 K, back to 120 K with exposure to pyridine, and then to room temperature shows that the Raman signal of the 1006-cm^{-1} line of pyridine reaches a maximum at 220 K, returns to its previous value when 120 K is reached the second time, then remains flat until around 220 K, where the signal falls to a very low count when warmed to room temperature. Interpretation of the results of the temperature cycle indicate that the SERS temperature dependence reflects the density and efficiency of atomic scale active sites that are annealed in the 200 K region (*62*). Furthermore, by comparison with the Rayleigh and Raman intensity variations as a function of temperature, the investigators conclude that the decay of bumps of size 50–1,000 Å is an unlikely reason for the changes in SERS intensity. Except for the interpretation of Pockrand and Otto (*62*), the conclusions with respect to surface roughness for the other UHV studies cited (*38*, *39*, *42*) seem inconsistent with the observations concerning surface roughness of Schultz et al. (*56*), where under electrochemical conditions 10^4 enhancement is found without "macroroughness"

Effect of Laser Excitation Frequency and Power. Various groups also investigated the dependency of the SERS signal on excitation frequency (*6*, *7*, *13*, *18*, *39*, *48*, *61*, *63*). The results of these studies showed that the frequency dependence was a strong function of the surface state and the vibrational mode observed. However, some of these investigations indicated that on silver the signal increased twentyfold when the laser excitation shifted from blue to red (*13*, *18*, *39*, *48*). Figure 7 shows the relative Raman intensity of the 1008-cm^{-1} band of pyridine on a silver electrode as a function of the wavelength of the exciting laser light for three different investigations (*13*, *18*, *48*). The dashed line shows the relative reflectance curve with units (which decrease) on the right. The minimum of the $\Delta R/R$ curve corresponds to the maximum of the excitation curve in the 700- to 800-nm region.

High intensity SERS has been seen on copper (*25–29*) and gold (*25*, *39*) only with laser excitation in the red region of the visible spectrum—647.1-nm Kr^+ laser line (*25*) and 645-nm dye laser line (*27*). When a 568-nm line was used for excitation, the SERS effect was not observed (*25*). A plot of the logarithm of experimental enhancement factor vs. excitation energy on silver and copper (*27*) showed fair agreement with the logarithm of the theoretical enhancement factor vs. excitation energy based on an image dipole enhancement mechanism. However other theoretical treatments that contain the composite dielectric function of the metal surface and electrolyte would show a similar excitation wavelength dependence.

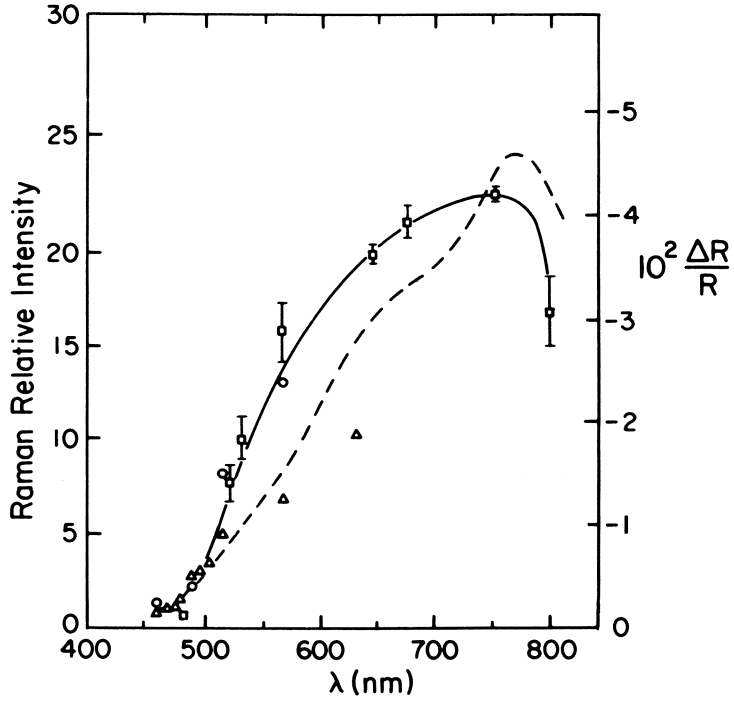

Figure 7. Relative Raman intensity as a function of exciting laser frequency for the 1008-cm^{-1} Raman band of pyridine on a Ag electrode. Key: — —, Δ R/R curve after Pettinger et al.; △, from J. Creighton et al. (13); and ○, from B. Pettinger et al. (18); □, from A. Girlando et al. (48). (Reproduced, with permission, from Ref. 48. Copyright 1980, North-Holland Publishing Co.)

Of particular interest is the investigation of pyridine scattering from silver and gold aqueous sol particle (*49*). The SERS excitation profiles of the 1010- and 1038-cm^{-1} bands have maxima that fall at the same place as the longer wavelength red extinction (adsorption and scattering) maximum of the pyridine adsorbed on the silver sol. Also, the SERS maximum shifts to longer wavelengths as the particle size increases. Transmission electron microscopy showed the sol particles to be in the range of 10–500 Å in diameter.

An explanation of the SERS from sols consistent with these facts is that the vibrations of the adsorbed pyridine molecules are modulating the polarizability of the metal particles, which thus scatter the light with a Raman component of Mie scattering (*49*). The similarity of the extinction curve and the Raman excitation profiles are interpreted as proving the involvement of collective resonant excitation of dipolar and higher multipolar plasma modes of the conduction electrons (*49*).

All measurements of Raman peak intensity made as a function of laser power show a linear dependence up to ca. 200 mW. A nonlinear dependence would suggest a multiphoton process. One must avoid very high laser power because interfacial damage may occur.

The Effect of the Angle of Incidence of Exciting Light and Measurement of the Depolarization Ratio. In addition to a frequency resonance, SERS shows angular resonances. The plot of the intensity vs. the angle of incidence showed a sharp peak for silver (58) and also for copper and gold (25) with a half-width of about 10°. For silver, copper, and gold the angle of incidence was around 60° for peak intensity (25, 58). Figure 8 shows the intensity vs. the angle of incidence plot with a resonance around 60°. (The peak at 45° is caused by laser light reflected directly into the entrance slit of the spectrometer.) These experiments emphasize that the Raman intensity will depend on both excitation frequency and angle of incidence, as well as electrode pretreatment. The angular resonances for silver, gold, and copper were

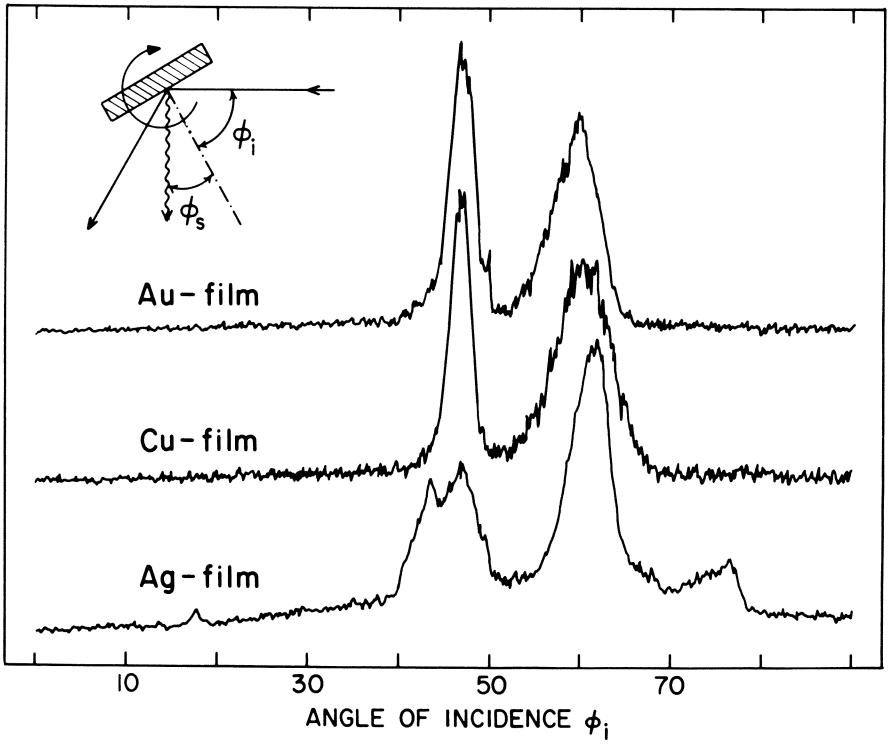

Figure 8. Raman intensity vs. angle of incidence for Au, Ag, and Cu electrodes for 0.05 M pyridine in 0.1 M NaCl at ca. 1012–1015 cm^{-1}. (Reproduced, with permission, from Ref. 26. Copyright 1980, North-Holland Publishing Co.)

considered as additional evidence for SERS by surface plasmon excitation (25). An enhancement of the Raman signal as a function of the angle of incidence of the exciting laser beam also was found with a thin coating of polystyrene on a silver holographic grating (*47*). In this case, *p*-polarized light (electric vector parallel to the plane of incidence) shows the angular dependence although *s*-polarized light (electric vector perpendicular to the plane of incidence) does not show it, which parallels the behavior of the respective reflectivities. These results are interpreted in terms of the excitation of the plasmon surface polaritons by coupling through the vector grating.

A surface plasmon may be thought of as a quasi-particle associated with the collective vibrational wave motion of free conduction electrons in the metal surface space (similar to the relationship between photons and electromagnetic waves). The surface plasmon is a longitudinal excitation (the wave vector and electric field vector are parallel). The optical photon is a transverse electromagnetic wave in which the wave vector and electric field vectors are orthogonal. For photon–surface plasmon coupling to occur, both energy (frequency) and momentum (wave vector) must be conserved, that is, in the latter case the wave vector of the laser light must equal the vector sum of the wave vectors of the scattered light and the scattering quasi-particle. This quasi-particle, or quantum of the coupled surface plasmon–photon field is called the plasmon surface polariton (PSP). For proper momentum matching in the excitation of the PSP, theory requires surface microroughness and also an angular dependence of the Raman signal. The use of diffraction gratings as surface substrates shows that the SERS signal can be increased by the excitation of PSP resonances of molecules adsorbed at the surface (*43, 47, 48, 64*). In addition, these resonances can be seen by using attenuated total reflection configurations (*65, 66*).

Polarization studies on roughened metal electrodes always have shown high values of the depolarization ratio, ρ. These bands are said to be depolarized. For *p*-polarized laser light $\rho = I_\perp/I_\parallel$, where $I_\perp$ is the intensity of the scattered radiation polarized perpendicular to the scattering plane and $I_\parallel$ is the intensity of scattered radiation polarized parallel to the scattering plane. Values of ρ are about zero for symmetrical vibrations in solution, whereas $\rho = 0.60$ to 0.75 for all SERS bands, indicating depolarization of the scattered radiation in SERS. This observation is characteristic of SERS bands.

Effect of Electrode Potential at Silver Electrodes. One of the features of SERS from electrode surfaces is that the spectra show wave number shifts from both the neat and solution normal Raman spectra. These shifts, and the fact that some bands are potential dependent, are probably the best criteria for proving that the spectrum observed, indeed, is surface enhanced. A study of the relative Raman intensity as a

function of electrode potential (*1*, *6*) of six totally symmetric vibrational modes of pyridine was carried out on silver by remaining on the band peak and scanning the potential from 0.0 to −1.00 V vs. SCE at about 1.0 V/s. To avoid changes in peak wave number as a function of potential, the spectral bandpass of the spectrometer was widened to 20 cm^{-1}. The bell-shaped curves obtained by averaging several sweeps showed that different vibrational modes peaked at different potentials (*6*). The most intense mode, the ring-breathing vibration at 1006 cm^{-1}, peaked at ca. −0.6 V vs. SCE and three other modes peaked around −0.8 V SCE. The point of zero charge (PZC) of silver in aqueous potassium chloride is around −0.7 V vs. SCE (*67*, *68*). If these curves were following the adsorption–desorption curve of pyridine on silver, all of the modes probably would show the same maximum around the PZC.

We have conducted similar experiments without averaging for 0.05 *M* piperidine in 0.1 *M* potassium chloride on silver. The results (Figure 9) (*69*) for four bands, assigned to the $-CH_2$ rock at 1017 and 1053 cm^{-1}, the $-CH_2$ twist at 1182 cm^{-1}, and the surface peak at 222 cm^{-1}, show that these curves have about the same maximum at ca. −0.5 V vs. SCE. Other bands, due to the CH stretch in the 2700 to 3000 cm^{-1} region, show an intensity maximum around −0.8 V vs. SCE. These curves (Figure 10) (*69*) were recorded with the computer interface of Figure 3.

Other studies of the effect of potential on band intensities show that the relative intensities of the two ring-breathing modes of pyridine on silver (1008 and 1037 cm^{-1}) show a reversal of intensity as the electrode is made more negative (*70*, *71*). At −0.2 V, the band at 1037 cm^{-1} is more intense than the band at 1008 cm^{-1}; at −0.35 V, the two bands are nearly equal; and at −0.6 V vs. SCE, the band at 1008 cm^{-1} is more intense. Comparison of these results with similar ratios on sols were used to estimate the surface potential on the sols (*51*).

The conclusion from these potential-dependent studies is that, at this stage of the development of SERS, SERS intensities vs. electrode potential cannot be used to obtain (with any accuracy) the effect of the electrode potential on the adsorption of the Raman active species because other factors influence the intensity vs. voltage curve.

An extremely potential dependent and rather broad SERS band is seen with a variety of molecules in the 100 to 250-cm^{-1} region that does not appear in the solution Raman spectra. The source of this band is a matter of controversy (a more complete discussion is given later), but generally it is agreed that the band is due to a surface vibration between the metal and a species adsorbed on the metal. We observed (*72*) that the peak wave number of the band shifts to lower wave numbers as the electrode potential becomes more negative. In fact, the frequency of the band is proportional to the square root of the elec-

trode potential. Because the frequency of a band for a simple harmonic oscillator is proportional to the square root of the force constant, we derived a relationship that gives a direct proportionality between the frequency and the square root of the rational electrode potential, $E - E_{pzc}$ (72). This derivation was based on the effect on the force constant of a change in the compact double-layer electric field felt by the oscillating bond as the potential is changed. The origin of the electric field change was attributed to the discreteness of the charge

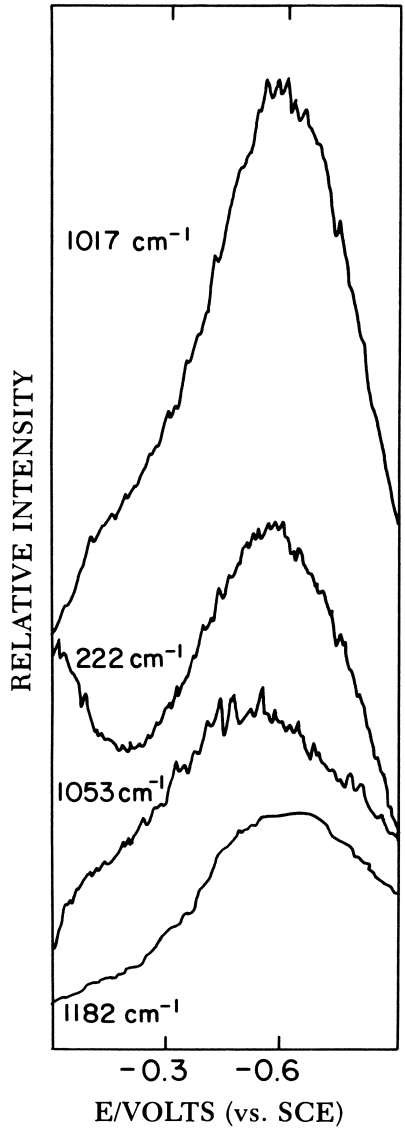

Figure 9. Raman intensity vs. electrode potential at a Ag electrode for 0.05 M piperidine in 0.50 M KCl for several vibrational bands. Other conditions given in Figure 4 with the exception of the bandpass, which was 10 cm⁻¹.

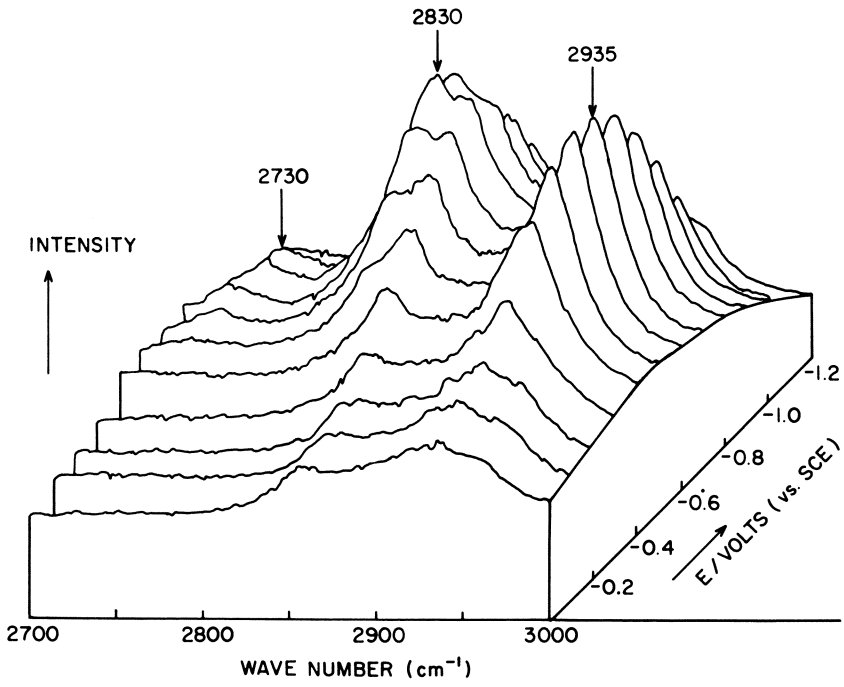

Figure 10. Raman intensity vs. wavenumber vs. electrode potential at a Ag electrode for 0.05 M piperidine in 0.10 M KCl for several CH stretching vibrational bands. Some pretreatment as in Figure 4. Full-scale sensitivity was 9 × 10³ counts/s, scan rate was 50 cm⁻¹/min and sample period 1.2 s was used with the digital counter. A 488-nm laser excitation was used.

effect of specifically adsorbed chloride ions. Calculations agree fairly well with the observed behavior (*72*). However, other factors, such as the intrinsic effect of potential (electrode charge) on the force constant, also should be taken into account in a more complete analysis of this effect. In general, one would predict a weakening of the surface band as the potential is moved in a negative direction.

Effect of Electrode Potential at Mercury Electrodes. In a previous report (*31*) of SERS at a mercury electrode formed by adhering a thick layer of mercury on platinum, we based part of our evidence of the existence of SERS at mercury on the fact that there was a potential dependence of what appeared to be a symmetric ring-breathing mode of pyridine at 1010 cm^{-1}. This dependence had an unusual shape in that the Raman intensity was level from 0.0 to −0.6 V vs. SCE and then rose to a plateau at −0.9 V vs. SCE (Figure 3) (*31*). Additional experiments showed that this behavior is caused by surface impurities formed when the mercury film electrode is first placed in the solution of the electrochemical cell. If the Hg/Pt electrode is first potentiostated at potentials more negative than −0.9 V vs. SCE, the rise in

intensity around −0.6 V is not found. Figure 11 shows the potential dependence of the intensity after potentiostating a solution of 0.05 *M* pyridine in 0.1 *M* potassium chloride at −1.0 V vs. SCE. The 1010-cm^{-1} band was observed as the Hg/Pt electrode was cycled at 5 mV/s from −0.3 to −2.1 V, from −2.1 to +0.6 V, and back to −0.3 V all vs. SCE. The intensity gradually drops off as the potential reaches the hydrogen evolution region, −1.6 V, and returns again to the same level when rescanned in a positive direction. At 0.15 V vs. SCE, there is a sharp cutoff in the Raman signal as the potential is scanned in the positive direction. This potential corresponds to the potential at which mercurous chloride is formed on the electrode (*31*). On the reverse scan toward negative potentials, the Raman signal sharply rises to its previous value.

The sharp cutoff intensity vs. potential curve does not correspond to coverage vs. potential curves for pyridine obtained by electrochemical techniques (*73*) or to other SERS intensity vs. potentials curves on silver. Subsequent polarization studies showed that the signals observed were totally polarized, which is not characteristic of SERS but is to be expected for light reflected from the electrode surface due to the emission lines of the argon ion laser. Unexplained lines in the reported spectrum of pyridine (*31*) proved to be reflected emission lines, as did other lines that fortuitously occurred at pyridine vibrational frequencies. Previous studies on silver with the same configuration did not show these reflected lines because silver, after an oxidation–reduction cycle, is not a reflective surface. When the reflected light was eliminated, we did not observe a SERS signal for pyridine on mercury. The earlier report of SERS from pyridine on mercury (*30*) did not show peaks that were shifted from either neat or aqueous pyridine, which would be expected for SERS lines. Thus, it is doubtful that mercury is an adequate substrate for SERS.

Effect of the Concentration of Raman Active Species and the Concentration and Nature of Supporting Anions. Studies of absolute intensities as a function of concentration are difficult with SERS because the electrode surface has a pronounced effect on the intensities and it cannot be reproduced from experiment to experiment. Thus, very few studies have been made of SERS intensity as a function of concentration. Jeanmaire and Van Duyne (*6*) found that the SERS intensity grows as a function of bulk pyridine concentration reaching saturation at around 50 m*M*. These results do not agree with a previously measured adsorption isotherm (*74*), where saturation occurred at much lower concentrations. The difference is attributed to increased packing in the SERS experiment when the molecules at high concentrations are thought to adsorb with their molecular plane perpendicular to the electrode surface, as opposed to a parallel orientation at lower concentrations (*1*).

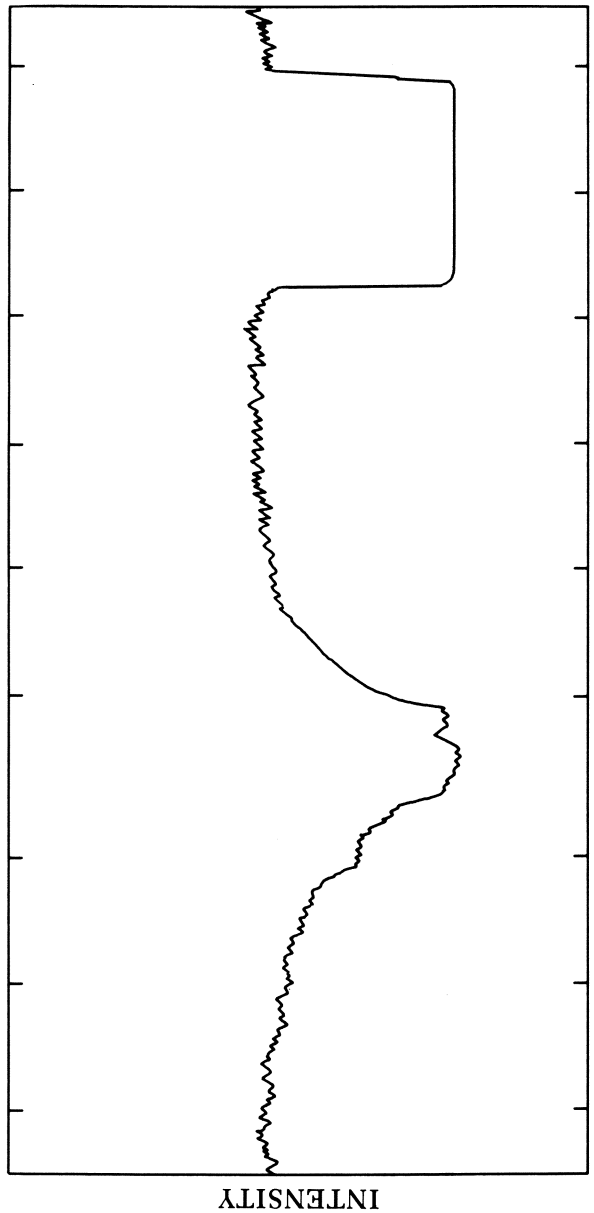

Figure 11. Intensity vs. electrode potential at a Hg electrode for 0.05 pyridine in 0.1 M KCl for the 1010-cm^{-1} mode. The Hg was adhered to a Pt electrode surface. A 514.5-Å excitation was used.

A radiochemical method was used to measure the amount of pyridine adsorbed on a silver electrode under conditions similar to SERS experiments—in 50 m*M* pyridine and 0.1 *M* potassium chloride (*75*). The amount of adsorbed pyridine was measured as a function of charged passed in the pretreatment step. The investigators (*75*) found 10 monolayers of pyridine, or 8×10^{15} molecules/cm^2, after passing an amount of charge similar to the SERS experiment. Thus, they concluded that multilayer adsorption was taking place. However, radioisotope experiments with adsorbed CN^- on silver showed that under SERS conditions only a monolayer of CN^- was adsorbed (*59, 76*).

SERS intensity also was affected by anion concentrations. A plot of relative intensity vs. Cl^- concentration showed a maximum intensity at a 2:1 ratio of Cl^- to pyridine concentration (*6*). Coadsorption of pyridine and Cl^- leads to pyridine adsorption being dependent on Cl^- adsorption (*1*). The effect of other anions on pyridine SERS intensity only has been studied in a preliminary way (*1, 6*). At a ratio of 2:1, anion to pyridine, the order of the intensity of the 1006 cm^{-1} peak was $I^- >> Br^- = Cl^- > SCN^- > HPO_4^= > SO_4^= > ClO_4^-$. Clearly more work on the effect of anion concentration and type and other solution conditions is needed to obtain a better picture of their effect on SERS spectra. Investigations of the effect of halide ions on water scattering (*70, 77*) are discussed later.

Background Continuum in SERS. A background continuum has been observed in SERS (*21, 35, 78, 79*). This continuum extends from the Rayleigh tail to about 4200 cm^{-1}. The oxidation–reduction pretreatment cycle increases the background intensity as well as the molecular peaks. We also observed that there is a potential dependence of the background signal, which follows that of the 1006-cm^{-1} peak of pyridine (*21*). This background was attributed to luminescence caused by a radiative recombination process produced by photoionization (*21*). Picosecond Raman gain experiments on the continuum near 2000 cm^{-1} showed that it is not a Raman effect but is most likely due to a luminescence (*80*). Other explanations of the continuum include surface roughness induced scattering by electron-hole pair excitations in the metal (*78*), and that part of the continuum is a superposition of numerous weak SERS lines (*81*).

On silver there is a pronounced rise in the background between 1300 and 1600 cm^{-1}, which contains lines at 1350 and 1550 cm^{-1} not attributable to an added Raman active molecule. The features in this region were originally attributed to adsorbed $CO_3^=$ (*35*), and also a carboxy species formed from a surface reaction involving CO_2 (*82*). Recently, these bands have been correlated with graphitic carbon overlayers on the silver surface (*63, 83, 84*). The Raman scattering is so

strong the even submonolayer amounts give observable Raman signals (*63*). Similar features have not been observed from SERS on other metals (Cu, Au), and therefore, the enhancement mechanism can not be based on an effect due to these layers.

Molecules and Ions that Show SERS. NEUTRAL MOLECULES. Of the chemical species that show SERS, the most intensely studied have been the nitrogen heterocycles and the aliphatic and aromatic amines. Among these compounds, SERS has been seen at a silver electrode with pyridine (*1, 4, 6*), 2-, 3-, and 4-methylpyridines (*23*), 2-, 3-, and 4-cyanopyridines (*19*), piperidine (herein) and (*6, 70*), aniline, (*1*), pyridine-d_5 (*1*), 4-acetylpyridine (*1, 6, 85*), *N*-methylimidazole (*1*), quinoline (*48*), isoquinoline (*48, 86*), pyrimidine (*10*), 2,4,6-trimethylpyridine (*1*), 2,4-dicyanopyridine (*1*) 2,6-dimethylpyridine (*87*), *N,N*-dimethylcyanamide (*1*), pyrazine (*10, 22*), *p*-nitrosodimethylaniline (*14*), and pyridine-*N*-oxide (*85*). The fact that piperidine gives a strong SERS signal was used to support the hypothesis of bonding to the silver electrode via the nitrogen atom in an end-on configuration (*1*). Because piperidine does not contain π-electrons, it can not interact through π-bonding in the flat configuration. Pyrazine is interesting in that it has a center of symmetry, and therefore, should have mutually exclusive IR and Raman modes. However, both Raman and IR active modes are observed with SERS (*10, 22*), indicating a lowering of molecular symmetry (*22*) from D_{3h} to probably C_{2v}, which is further proof of the close contact of the molecule to the surface.

Both Raman and IR modes also were observed with SERS on films of ethylene condensed on vapor-deposited silver on an aluminum surface (*88*) under vacuum conditions. Lines occur in the spectrum that were attributed to two sources, one a surface layer next to the silver and the other a thick layer of solid C_2H_4. Selection rules for the C_{2v} symmetry derived from an image-dipole theory apparently were not obeyed (*22, 88*). The SERS spectrum of propylene on the vapor-deposited silver also was observed (*88*).

The original study of Fleischmann et al. (*4*) showed in situ spectra of surface layers of mercurous chloride, mercurous bromide, and mercuric oxide on a mercury electrode; however, there probably was a thick multilayer formation in this study. Electrogenerated layers of Ag_2O and photoelectrochemically generated AgO have also been studied at a silver electrode (*89*).

CYANIDE AND THIOCYANATE ANIONS. Numerous anionic ligands have exhibited SERS. Various studies of the simple anions like cyanide (CN^-) (*10, 11, 20, 35, 70, 76*) and thiocyanate (SCN^-) (*12, 70, 90, 92*) have been undertaken. We should also point out that CO, which is not an ion but is isoelectronic with CN^-, has been studied

under UHV conditions (*36*, *91*). In the CN^- case, spectral data were interpreted in terms of various $AgCN_n^{-(n-1)}$ species at the silver surface. A species made up of three CN^- ions bonded to a Ag^+ adion [$Ag(CN)_3^{2-}$] with C_{3v} surface symmetry at −1.0 V vs. SCE was proposed (*76*). This assignment was made by comparison with the solution Raman band of $Ag(CN)_3^=$. A study (*70*) of the entire SERS spectrum found that it resembles the Raman spectrum of solid $KAg(CN)_2$, and a $Ag(CN)_2$-like unit with C_2 site symmetry was assigned as the surface species. Vibrational modes in SERS are shifted consistently to lower wave numbers with respect to the solid or solution complexes. This behavior is rationalized as due to the difference between the silver surface atoms, which are most likely only partially charged, and the fully charged ions of the complexes (*70*). In the potential region −0.9 to −1.3 V, the CN stretching frequency shifts to lower values as the electrode is made more negative, a trend also found with nitrogen-containing compounds (*72*). Time resolved spectral peaks were assigned (*11*) to the formation of solution-like complexes of $Ag(CN)_4^{3-}$ and $Ag(CN)_3^{2-}$ (2110 cm^{-1}), $Ag(CN)_2^-$ (2140 cm^{-1}), and AgCN (2110 cm^{-1}), which appear at different voltages (*see* Figure 5).

For SCN^- on silver, the earliest study (*12*) on highly roughened silver electrodes showed a potential-dependent weak band that corresponds to the CN stretch. Reexamination of the system (*92*) showed a band at 0.0 V that was assigned to a AgSCN-like surface layer. Between −0.5 and −1.0 V vs. SCE the band shifts from 2120 to 2070 cm^{-1}. This shifting band is assigned to a species with two SCN^- for each surface silver atom based on the spectra of solid $NH_4Ag(SCN)_2$. At −1.0 V, the band at 2070 cm^{-1} is weak and is assigned to free SCN^-. SERS at a silver electrode in 0.1 *M* KCl and in 0.05 *M* KSCN at −0.2 V showed (*70*) a strong band at 2118 cm^{-1} and bands at 440, 230, and 180 cm^{-1}. The surface species were assigned (*70*) to a $Ag(SCN)_2^-$ unit and even though Cl^- was present, only SCN^- apparently was adsorbed. Allen and Van Duyne (*90*) also studied this system using 0.05 *M* NaSCN in 0.95 *M* NaCl or $NaClO_4$ with a single double step electrode pretreatment. They propose that Ag–S coordination predominates but that some Ag–N bonding also takes place. Thus, at the PZC both types of bonding occur, but by changing the potential and thus the charge on silver, the orientation of SCN^- can be inverted. The investigators also argue that the 2100-cm^{-1} feature arises from one SCN^- interaction with silver and not two, as concluded by Gold and Buck (*92*) and Pemble (*70*). In the absence of Cl^-, addition of Cd^{2+} profoundly affects the spectrum and Allen and Van Duyne find evidence for Cd^{2+} interaction with the surface via a bridging SCN^- group (*90*). Although the interpretations of SERS spectra for CN^- and SCN^- by various groups are somewhat different, the molecular information on surface bonding that can be obtained by SERS clearly is unavailable by any other tech-

nique. Unambiguous interpretation of surface species will have to wait until an explanation of the SERS phenomenon, which is consistent with all experimental observations, is achieved.

HALIDE IONS AND PYRIDINE PLUS HALIDE IONS. Various studies also have been made of halide ions using SERS (*51, 70, 77, 90*). On silver sols (*51*), bands for adsorbed halides have been assigned as I^- (112 cm^{-1}), Br^- (163 cm^{-1}), and Cl^-(235 cm^{-1}). On silver electrodes, halide bands have been identified as due to I^- (115 cm^{-1}/90 cm^{-1}), Br^- (162 cm^{-1}/143 cm^{-1}), and Cl^- (240 cm^{-1}) (*77*). Evidence of coadsorption of water and halide ions from the changes in the Raman bands of water in the presence and absence of halide ions also was found (*76*). In addition, very low lying bands, attributed to vibrational modes of a surface pseudo lattice of halides, are found that shift with a change in halide ion type—Cl^- (8.5 cm^{-1}), Br^- (7 cm^{-1}), and I^- (6 cm^{-1}). The 240-cm^{-1} band for Cl^- grows as a function of chloride ion concentration, leveling off in the region of 1.0 *M* activity where the coverage is reported to reach 0.8. The source of Raman scattering is attributed to a specifically adsorbed chloride ion or a surface $AgCl_2^-$ species. More work is needed to establish that the Raman signal seen in these experiments is linearly proportional to the surface coverage of a halide species, that is, that the scattering cross section is independent of coverage.

Dornhaus and Chang (*93*) observe line shifts for the low lying band (100–200 cm^{-1}) with pyridine in the presence of Cl^-, Br^-, and I^-. Similar results were seen by Pemble (*70*). The former authors also report that the frequency of the band shifts with potential (*93*). Dornhaus and Chang (*94*) and Pettinger and Wetzel (*81*) attributed the 240-cm^{-1} peak of pyridine in the presence of Cl^- to the symmetrical Cl–Ag–Cl stretch. The chloride ions and the pyridine are coadsorbed, and are pictured as bound to the same adatom of Ag, forming a N–$AgCl_n$, n = 1, 2, . . group (*81*). In the absence of pyridine, the SERS spectrum of Cl^- in H_2O on roughened silver electrodes at −0.2 V vs. SCE shows H_2O bands at 3498 cm^{-1} for the symmetrical OH stretch and at 1610 cm^{-1} for the symmetrical OH bending vibration (*77*). Because these lines are not observed when chloride is replaced by sulfate or propanoate, they are attributed to coadsorbed H_2O and Cl^- structures at the silver electrode surface (*77*).

The type of surface species giving rise to the band around 239 cm^{-1} for pyridine in KCl solution at a silver electrode has been a matter of continued controversy. This band was first assigned as the Ag–N stretching mode for pyridine in KCl (*13*). Later the 239-cm^{-1} band was attributed to residual silver chloride and a line at 216 cm^{-1} was assigned as the Ag–N vibrational mode (*1*). Other researchers see a line at 227 cm^{-1} at pH = 1.2, where the pyridine nitrogen would be protonated, and also see the line disappear in Br^- solution and assign this

line to Cl_2^- (*95*); still others attribute the line to Ag–Cl^- scattering (*57*). Based on the potential dependence of the band intensity, an unspecified species containing both pyridine and Cl^-, possibly PyH^+Cl^-, tentatively was proposed, which desorbs as the potential is made more negative (*71*). This behavior also would fit previously reported models (*81*, *93*) where $AgPyCl_2^{2-}$ is the species. When the surface species desorbs pyridine, hydrogen bonding to water is proposed to take its place (*71*).

We reported that for solutions of biological bases and amino acids in 0.2 *M* KCl, the band in the 240-cm^{-1} region has considerable intensity on the electrode at the expense of other Raman lines, and that its maximum shifts to lower wave numbers as the electrode potential moves from −0.1 to ca. −0.8 V vs. SCE (*72*). To substantiate the assignment of the band in the 200–240-cm^{-1} region to a Ag–N stretch, we examined the SERS spectrum of pyridine on silver sols in the absence of chloride. A very prominent band at 239 cm^{-1} already was reported (in this system), which does not appear in the solution spectrum, but it was not mentioned whether any Cl^- was present (*49*). In the absence of Cl^- on the Ag sols, a very well-defined band at 239 cm^{-1} is found, which is taken as definite proof of the possibility of a Ag–N stretching vibration (*96*). Because pyridine in the absence of Cl^- (*96*), and Cl^- in the absence of pyridine (*51*), and the two together apparently give the same spectral band, it is difficult to assign unambiguously this surface band. The shift of this band for several different molecules fits the change in reduced mass of a single silver atom–molecule band. This correlation was made with eleven nitrogen-containing molecules for the Ag–N stretch, and for formate, acetate, and pyridine-*N*-oxide where a Ag–O stretch is postulated (*96*).

The shift in the band in the 200-cm^{-1} region with both the type of halide and the type of molecular Raman active species is evidence of a halide–silver–adsorbate complex at the surface. The most reasonable type of complex apparently consists of an adatom of silver with coadsorbed halide and molecular adsorbate bound to it. We also looked at the line shape of the surface band and found that it best fits a Gaussian distribution, indicating inhomogeneous line broadening (*86*).

OTHER ANIONIC SPECIES. Other anions that give well-resolved SERS spectra also have been studied. These include the simple anion, azide (N_3^-) (*97*), and more complicated anions like citrate (*98*), ethylenediaminetetraacetate (EDTA) (*99*), and $PtCN_4^{2-}$ (*56*), all at a silver electrode. For azide, the scattering species is a thin layer of AgN_3 (*97*). Hexacyanoruthenate, $RuCN_6^{4-}$, (*100*) and MoO_4^- (*101*) were studied at both silver and copper electrodes.

NONPOLAR MOLECULES. The list of nitrogen-containing organic compounds, and anionic ligands previously cited as giving SERS spectra, is indicative of the large variety of polar species that can be

studied with SERS at a metal/electrolyte interface. Two reports cite relatively nonpolar molecules as giving a SERS spectra (*30, 50*). SERS was reported (*30*) for benzene and cyclohexane deposited on mercury from the gas phase as well as for pyridine but not for methanol, and weaker enhancement for carbon tetrachloride. Another study (*50*) reported enhanced Raman spectra of benzene, deuterobenzene, acetonitrile, pyridine, *N,N*-dimethylaniline, and crystal violet on silver sols. Thus far, SERS of molecules without coordinating atoms have not been seen in an electrochemical experiment.

MOLECULES THAT SHOW SURFACE ENHANCED RESONANCE RAMAN SCATTERING AND APPLICATIONS TO THE STUDY OF ELECTRODE PROCESSES. Crystal violet is a dye that exhibits resonance Raman scattering (RRS) in solution. At the electrode surface both RRS and SERS could be obtained from adsorbed crystal violet and methyl violet, and the enhancement was multiplicative, or 10^{11} to 10^{12} (*6*). Such enhancement factors may be overestimated. Recent studies (*102*) of dyes excited to an electronic transition show that the Raman intensity from the dye adsorbed on silver metal island films deposited on silica is only about 200 times that of the dye adsorbed on the pure silica substrate. Thus, the enhancement factor on the silver metal islands in this case is only ca. 2×10^8. Other studies showed that adsorbed species that exhibit RRS in solution can be studied at electrodes, for example, *p*-nitrosodimethylaniline on a platinum electrode (*14*) and the dye, Rose Bengal, on a zinc oxide semiconductor electrode (*103*).

A recent study of diphenylthiocarbazone (dithizone) anion and its redox forms was made at a silver electrode in aqueous alkaline solution (*104*) using a spinning electrode cell (*8*). The Raman signal for the dithizone anion and oxidation products show what appears to be both RRS and SERS. The existence on the electrode of adsorbed dithizone anion and the predominant oxidation product, the disulfide, is confirmed by a comparison of SERS spectra with authentic samples of the species. This investigation is one of the first to use SERS to study products of an electrode reaction.

Another experimental study of an electrode reaction was achieved using SERS. For the electrochemical reduction of 4-cyanopyridine on silver, a change in mechanism as a function of potential was demonstrated (*105*). With a neutral pH electrolyte at potentials around −0.6 V vs. SCE, evidence is given for two follow-up chemical reactions, one producing 4-aminomethylpyridine and the other CN^- and pyridine. The evidence also indicated that the latter mechanism predominates at −1.0 V vs. SCE, as established by the rise of the CN^- peak at this potential.

The two examples of the use of SERS to investigate the mechanism of electrode processes at silver is a good indication that the method will provide the type of molecular information needed to

study such problems. Many applications of SERS to the study of electrode processes will certainly be forthcoming.

SERS Studies of Biologically Important Molecules

The possibility of using SERS for the study of molecules adsorbed on electrodes from very low solution concentrations, where both surface and resonant Raman occur from the adsorbed molecules, is very promising and should be useful especially for biologically important molecules. One very interesting study is that of the bile pigment biliverdine (aetiobiliveridine-IV-8) and a partial structure of the compound, dimethylpyrromethenone with a silver sol solution (*106*). Resonance Raman spectra are difficult to obtain for these compounds because the fluorescences completely obscure the Raman bands. However, well-defined SERS spectra can be obtained on the silver sols at 2×10^{-7} *M* biliverdine and 5×10^{-7} *M* pyrromethenone. This phenomenon is attributed to the reduction of fluorescence by the very low concentrations needed to achieve the SERS spectra. It has been thought that fluorescence also would be enhanced at the surface but these results show that Raman enhancement is much larger than fluorescence, which may be quenched by the electrode.

Another demonstration of the utility of SERS for studying biological molecules is the study (*107*) where SERS spectra of cytochrome c and myoglobin could be observed on silver electrodes at a concentration below 1×10^{-6} *M*. At −0.6 V vs. SCE, the spectrum of cytochrome c shows that the heme iron is in the low spin iron (II) oxidation state. This result suggests that the solution species, which is iron(III), is reduced at the electrode. At −0.2 V vs. SCE, the SERS spectrum shows low spin iron(III) cytochrome c. The vibrational bands of the adsorbed species are within 6 cm^{-1} of the solution species, which is evidence that extensive denaturation does not take place. Myoglobin appears to undergo similar reduction at −0.6 V and reoxidation at −0.2 V, but the evidence is not as certain as in the cytochrome c case because of a shift in SERS of the oxidation state marker bands from their solution values. The authors conclude (*107*) that adsorbed species are being observed and that the underlying enhancement mechanism has a basis similar to SERS with small molecules.

SERS spectra of 10^{-5} *M* cobalt tetrasulfonated phthalocyanine adsorbed on a silver electrode were recorded as a function of potential and the effect of different laser excitation energies was studied (*108*). A rotating cell was used to minimize local heating effects in the absorbing solution. Possible configurations of adsorbed monomers and oxygen bonded dimers at the electrode surface were given, but it is not possible to distinguish between the models on the basis of the SERS data.

Finally, we will discuss SERS studies of some biologically important molecules that do not absorb in the visible region and thus do not show RRS, but which can be seen with SERS. SERS spectra of 2×10^{-3} *M* adenine, adenosine, and adenosine 5′-monophosphate adsorbed at a silver electrode in 0.1 *M* KCl, 10^{-3} *M* PO_3^{-2}, and 10^{-4} *M* EDTA adjusted to pH 8 were reported (*109*). These species and other adenine nucleotides also were investigated in an associate study (*110*). During an earlier investigation (*72*), we obtained the SERS spectra of adenine, guanine, and inosine. The guanine SERS spectra actually was found in a 1 : 1 methanol : H_2O mixture, which is one of the few cases where mixed solvents were used to obtain SERS. At a higher percentage of methanol to H_2O, it was not possible to observe the SERS spectrum. Details of these spectra were not reported and Table I shows a comparison of relative intensity (the strongest band set to 100) at a given wave number for the solution and SERS spectrum of adenine. The SERS spectrum was obtained for 0.1 *M* adenine in 0.2 *M* potassium chloride, and 0.5 *M* sodium hydroxide solution. The SERS spectrum at −0.6 V vs. SCE, as already reported (*109*), is many times more intense than the solution spectrum. The most intense bands of

Table I. Observed Frequencies and Relative Intensities of Adenine (6-Aminopurine) for the Solution and Surface Enhanced Raman Spectra

Adenine Normal		*Surface (−0.6 V)*	
(cm^{-1})	*Intensity*	*(cm^{-1})*	*Intensity*
		165	49
		220	24
300	11		
535	11		
		605	12
627	11	630	12
722	100	730	100
960	22		
1135	11	1170	24
		1215	12
1250	56	1255	12(B)
		1275	75(B)
1315	11	1320	49
1330	100		
1365	22	1414	26(B)
1453	22		
1543	22		
		1545	37(B)
		1600	24(B)
1650	11		

the solution spectrum, 722 and 1330 cm^{-1}, can be assigned as skeleton vibrations of the adenine ring (*109*). The band around 730 cm^{-1} in the SERS spectra is the ring-breathing vibration and is the strongest one in the spectrum (*see* Table I). This assignment also is found for adenosine and adenosine 5′-monophosphate (5′-AMP). New surface peaks appear at 165 and 220 cm^{-1} in our adenine SERS spectrum although several weaker peaks in the normal Raman spectrum are not observed on the surface at all. These results show that we are observing the spectrum of surface adenine. Koglin and coworkers (*109, 110*) concluded on the basis of a very strong peak around 245 cm^{-1} in the 5′-AMP and adenosine 5′-triphosphate (5′-ATP) spectra, that the phosphate group and the adenine ring of the nucleotide were interacting with the surface. Inorganic phosphate does not show a band in the 200-cm^{-1} region and coadsorption of Cl^- and adsorbate to give a band around 240 cm^{-1} is very likely. Thus, the conclusion that the 245-cm^{-1} band is due to surface phosphate must be regarded as tentative.

The Nature of a SERS Active Chemical Species

The necessity of a chemical bonding interaction between the metal substrate and the adsorbate has been postulated as a prerequisite of SERS in several investigations. Furtak and co-workers (*111, 112*) observed a SERS spectrum of pyridine on gold at 514.5-nm laser excitation only after depositing 1.3 monolayers of silver. They conclude that the coulombic interactions of the surface are gold-like and that the silver is necessary as a bridge for the excited electronic states of gold to communicate with those of pyridine (*111*). Our work with acridine shows a SERS spectrum on silver, whereas anthracene, which is identical to acridine except for the replacement of a nitrogen by a carbon atom, does not exhibit SERS (*113*). This result demonstrates the necessity in SERS of sites in the molecule that can coordinate chemically to the surface. Another indication of the sensitivity of SERS to the surface coordination of the adsorbate are the experiments (*46, 114*) with 4-pyridine carboxylic acid (isonicotinic acid) and benzoic acid in a silver island film-glass sandwich. When the carboxylate end of the benzoic acid was chemisorbed on the silver island film, the molecule gave SERS; however, when the carboxylate was chemisorbed on the glass substrate, and not on the silver film side of the sandwich, no SERS appeared. The 4-pyridine carboxylic acid with two coordinating sites gave SERS in either configuration (*46*). Similar results were reported (*45*). Apparently, what is necessary in SERS is a particular type of adsorption bond that produces "a chemical bond with the metal of moderate strength" (*112*). This bond allows electronic coupling between the surface and adsorbate.

Summary of SERS Characteristics

In order to explain the source of the surface enhancement, a theoretical model must account for a large number of experimental observations. Several mechanisms most likely will be necessary to incorporate all of the experimental findings. A summary of SERS characteristics that must be accounted for by a theoretical model that deals with the phenomenon are listed:

1. Silver, copper, gold, and probably nickel show the effect, with the largest enhancements occurring on silver.
2. A wide range of molecules and ions give a SERS signal. All of these species investigated at a metal/electrolyte interface have the possibility of some type of coordination to the metal surface.
3. Enhancement factors of 10^5–10^6 are found at electrodes for species that do not give resonance Raman scattering in solution.
4. Species that show resonance Raman scattering in solution show a combined enhancement factor of 10^8–10^{10} on the surface.
5. Roughening by chemical, mechanical, or electrochemical means produces increased enhancement, but roughening is not an absolute prerequisite for observing SERS.
6. A background continuum is found with SERS that has the same intensity vs. potential characteristics as SERS and appears to be a luminescent process.
7. SERS vibrational modes are depolarized.
8. The angle of incidence of the exciting light has an effect on SERS intensity.
9. SERS intensity can be enhanced by excitation of plasmon surface polaritons (PSPs).
10. The effect of laser excitation frequency on SERS intensity departs from the frequency to the fourth-power dependence found in normal Raman scattering, and is dependent on the optical properties of the metal substrate.
11. The effect of electrode potential on the SERS intensity in many cases depends on the vibrational mode examined.

Theoretical Models of SERS

Many theoretical models have been proposed to explain SERS. Among these models are the effect of the high field in the inner Helmholtz layer at a metal–electrolyte interface, (*1*, *9*), the image–dipole enhancement mechanism, (*115–119*), coupling to surface plasmons

through roughness to give a resonance Raman effect (*120–122*), electroreflectance models (*35, 123, 124*), charge transfer enhancement models (*78, 125*), single particle excitations giving rise to a resonance Raman effect, (*20, 78, 126–128*), atomic scale roughness-induced electronic Raman scattering (*76, 123, 129, 130*), electromagnetic effects at the resonance site such as the lightning rod effect (*131*), the influence of local dipolar surface plasmons (*132*), electromagnetic effect for general geometries (*133*), electromagnetic theory of an electrical dipole on the surface of a spherical metal particle (*134*), Mie scattering on adsorbent bound sols (*49*), excitation of transverse collective electron resonances (*135, 136*), surface-induced resonant Raman scattering derived from a classical model (*137–139*), and fundamental treatments of local fields (*140–142*). Many of the models have similar features. Some of the theoretical models were discussed in an excellent review (*2*).

It is not our purpose to discuss the details of each of the various theories in this chapter. Those theories that appeared in the literature prior to mid-1979 already were discussed critically (*2*). Rather, we will try to describe some of the more recent theories and to indicate their correspondence to experimental results. Of the earlier theoretical mechanisms, the effect of the high static Helmholtz double-layer field, and to some extent the electroreflectance models, received little additional attention. The image–dipole theory, however, received further consideration, and so we will comment on this model as it is related to some of the more recent experimental and theoretical results.

The simplest image–dipole model assumes the surface to behave as a perfect mirror, postulating that the enhancement is due to an oscillating point dipole plus its image. This model predicts the correct order of magnitude of the enhancement at atomic distances where the classical image theory should break down—ca. 2 Å. This theory also predicts that there should be strong scattering from vibrational modes with dipolar components perpendicular to the electrode and no scattering from those parallel to the surface. Experiments with 2-, 3-, and 4-cyanopyridines (*19*) and 2-, 3-, and 4-methylpyridines (*23*) can be correlated with the cosine squared of the angle between the normal to the electrode and the direction of the substituent bond in agreement with the above prediction. However, SERS also was found for vibrational components parallel to the electrode, which is inconsistent with the image dipole theory (*23*).

The image–dipole theory also predicts that molecules with no permanent dipole moment should have considerably weaker enhancements than those with a permanent moment. However, enhancements for nonpolar pyrazine are the same order of magnitude as for pyridine (*22*).

There are also theoretical difficulties with a simple point image dipole theory. First, it is based on a multipolar expansion of the molecular charge distribution in which higher multipoles are ignored. This results in a polarizability expression with a singularity when the molecule approaches the surface closer than some critical distance. It is this singularity that apparently is responsible for the giant enhancement, 10^5–10^6. However, at such short distances the higher multipoles cannot be discarded, and when included, the singularity no longer is obtained. More detailed quantum mechanical SCF Hartree calculations show that the polarizability gives only a slight enhancement at this critical distance (*143*). A treatment (*142*) of the image fields at a flat surface, which takes into account finite molecular size and the nonlocal response of the metal, is a much better model for the real metal/molecule electromagnetic interaction. An order of magnitude calculation gives an enhancement factor of 10^3 for a spherical molecule. The most recent view of the image dipole model is that it may account for part of the enhancement and thus should be combined with other models to give the total enhancement effect (*56*, *142*).

As illustrated in the list of theories previously given, electromagnetic theories in which local scattering fields are enhanced have received much recent attention. These theories were stimulated by the observation of the necessity of roughness in metal/ultra high vacuum experiments (*38*). One of the most complete expositions of electromagnetic effects is the theory of Gersten and Nitzan (*132*). This theory of a surface modeled as a hemispheroid protruding from a flat conducing plane with an adsorbed molecule along its major symmetry axis shows that metals with large negative real components of the dielectric function and small imaginary components will have large polarizabilities and thus high efficiency for the SERS effect (*132*). This is the condition for exciting the dipolar surface plasmon and explains why copper and gold are only seen with red laser light. The results of similar electromagnetic theories of Kerker et al. (*134*), where the surface structures are modeled as spheres, and McCall et al. (*133*) are qualitatively the same as the theory of Gersten and Nitzan (*132*). The enhancement ratios with the latter electromagnetic theory are of the order of magnitude found experimentally and are dependent strongly on the shape and size of the metal protrusion, which would explain the effect of the pretreatment of the surface. The effect of the angle of incidence on the intensity, molecular dipole orientation effects, and to some extent the high depolarization ratio found experimentally also could correlate with this type of theory (*132*). This theory also explained peaks found around 8 cm^{-1} from the Rayleigh line in the SERS spectrum (*144–146*) in terms of an acoustical vibrational mode of the metal protrusion. Finally, the broad background radiation, which ap-

pears to be a luminescence and probably not a Raman effect as concluded from picosecond Raman gain spectroscopy (*80*), can be attributed to the decay of the excited dipolar surface plasmons.

One of the major difficulties with the surface plasmon theory is the lack of reference to the role of individual molecules and the nature of their interaction with the surface. In principle, any molecule physisorbed to the surface should show the effect. However, molecules vary widely in their enhancement at a metal/electrolyte interface. Pyridine, quinoline, and acridine show a strong enhancement on a silver electrode, but benzene, naphthalene, and anthracene do not. A survey of molecules with strong enhancement indicate the probable need for a lone pair of electrons, which can in some way strongly overlap with metal orbitals. This need indicates that at least a weak chemisorption is needed for the effect. A model was proposed (*122*) that considers modulation by the molecular vibrations of the tunneling induced metallic surface charge as well as the field enhancement. Tunneling is related to the barrier to electron transfer between molecule and metal, that is, a weak chemical bond. Surface plasmons are presumed to be resonantly excited through surface roughness. The enhancement ratio is a very sensitive function of the barrier height, but more weakly dependent on the distance between the molecule and the surface.

The adatom hypothesis, another plausible theory, explains the background continuum and SERS as roughness-induced Raman scattering due to atomic scale roughness (*3*, *76*, *123*, *130*, *147*). In this model, the adsorbate is pictured as bound to metallic adatoms and this atomic scale microroughness leads to breakdown of momentum conservation (*76*). Although the Raman gain experiments (*80*) show the background to be luminescent, this theory also may explain the continuum if one assumes that radiative excitation and recombination of excited electron-hole pairs gives a "hot" luminescent (*148*) background continuum, and that resonant Raman scattering is taking place due to electron-hole pair excitation and electron–adsorbate interactions. Strong depolarization of both the continuum and SERS is predicted by this model, as observed experimentally. The experiments previously discussed, which indicate that SERS is confined to molecules in the surface monolayer, support this model; however, the effect of the metal dielectric function supports an electromagnetic theory.

Our recent experiments with 2,6-dimethylpyridine (*87*) show that there is no distortion of the methyl vibrations in the SERS spectrum. If the molecule is attached to the surface through a Ag–N bond, then the only way to relieve the steric interactions of the methyl groups and the adjacent silver atoms is by atomic scale roughness, such as an adatom-2,6-dimethylpyridine complex. Furthermore, correlation of the surface complex stretching frequency with an adatom–molecule complex

(*96*) is further evidence for the existence of this species. Other evidence of the role of the adatom–complex comes from RS intensity vs. potential profile studies. If the potential is scanned in a negative direction beyond ca. −1.2 V vs. SCE and then back in a positive direction, the scattering intensity does not track itself on the reverse scan (*6, 21, 149*). The interpretation of this phenomenon is that at the most negative potentials the desorption of the ligands occurs, especially halides, from the silver adatom–ligand complex, which allows the adatoms to be incorporated into the metal lattice destroying the complexes (*149*). Addition of a silver salt at a potential on the reverse scan after RS quenching has occurred shows a regrowth of the SERS signal, which is believed to be caused by redeposition of silver producing new adatoms and surface complexes. This phenomenon may support an adatom scattering mechanism or an electromagnetic field enhancement theory. In support of the latter case, pretreatment oxidation–reduction cycle still is necessary to achieve the original enhancement, and the role of the adatom complex may only be necessary to bind the Raman active species on sites at the apex of sharp surface protrusions where the field (lightning rod) effect is most efficient (*131*).

A complete theory of the SERS effect has not yet been achieved. Apparently, more than one enhancement mechanism is taking place so the earlier attempts to explain the total enhancement by one mechanism eventually will be replaced by a model that includes several mechanisms. It is highly probable that, in addition to an image effect, both macroroughness electromagnetic field enhancement and microroughness-induced electronic coupling enhancement will have to be considered in such a model. Initial attempts were made along these lines (*122, 128*), but a complete, generally accepted theory will require more experimental and theoretical developments.

Acknowledgments

The authors thank the National Science Foundation (CHE-7911159) and the PSC-BHE Research Award Program of the City University of New York for financial assistance. We would also like to thank K. Arya, R. P. Buck, M. Kerker, J. I. Gersten, A. Otto, B. Pettinger, M. R. Philpott, M. E. Pemble, and R. P. Van Duyne for sending preprints of their work before publication and J. I. Gersten and D. A. Weitz for discussions of their work. Finally, we thank D. L. Akins for his comments concerning this review.

Literature Cited

1. Van Duyne, R. P. "Chemical and Biochemistry Applications of Lasers"; Moore, C. B., Ed.; Academic: New York, 1979; Vol. 4, Ch. 5.

2. Furtak, T. E.; Reyes, J. *Sur. Sci.* **1980,** *93,* 382.
3. Otto, A. *Proc. 6th Solid-Vacuum Interface Conf., Delft.* 1980, to be published.
4. Fleischmann, M.; Hendra, P. J.; McQuillan, A. J. *J. Chem. Soc., Chem. Commun.* **1973,** 80.
5. Fleischmann, M.; Hendra, P. J.; McQuillan, A. J. *Chem. Phys. Lett.* **1974,** *26,* 163.
6. Jeanmaire, D. L.; Van Duyne, R. P.; *J. Electroanal. Chem.* **1977,** *84,* 1.
7. Albrecht, M. G.; Creighton, J. A. *J. Am. Chem. Soc.* **1977,** *99,* 5215.
8. Pemberton, J. E.; Buck, R. P. *Appl. Spectrosc.* **1981,** *35,* 571.
9. Van Duyne, R. P. *J. Phys. (Paris)* **1977,** *38,* C5-239.
10. Dornhaus, R.; Long, M. B.; Benner, R. E.; Chang, R. K. *Surf. Sci.* **1980,** *93,* 240.
11. Benner, R. E.; Dornhaus, R.; Chang, R. K.; Laube, B. L. *Surf. Sci.* **1980,** *101,* 341.
12. Cooney, R. P.; Reid, E. S.; Fleischmann, M.; Hendra, P. J. *J. Chem. Soc., Faraday Trans. 1* **1977,** *173,* 1691.
13. Creighton, J. A.; Albrecht, M. G.; Hester, R. E.; Mathew, J. A. D. *Chem. Phys. Lett.* **1978,** *55,* 55.
14. Hagen, G.; Glavaski, B. S.; Yeager, E. *J. Electroanal. Chem.* **1978,** *88,* 269.
15. Pettinger, B.; Wenning, U. *Chem. Phys. Lett.* **1978,** *56,* 253.
16. Albrecht, M. G.; Evans, J. F.; Creighton, J. A. *Surf. Sci.* **1978,** *75,* L777.
17. Albrecht, M. G.; Creighton, J. A. *Electrochim. Acta* **1978,** *23,* 1103.
18. Pettinger, B.; Wenning, U.; Kolb, D. M. *Ber. Bunsenges. Phys. Chem.* **1978,** *832,* 1326.
19. Allen, C. S.; Van Duyne, R. P. *Chem. Phys. Lett.* **1979,** *63,* 455.
20. Furtak, T. E. *Solid State Commun.* **1978,** *28,* 903.
21. Birke, R. L.; Lombardi, J. R.; Gersten, J. I. *Phys. Rev. Lett.* **1979,** *43,* 71.
22. Erdheim, G. R.; Birke, R. L.; Lombardi, J. R. *Chem. Phys. Lett.* **1980,** *69,* 495.
23. Bunding, K. A.; Lombardi, J. R.; Birke, R. L. *Chem. Phys.* **1980,** *49,* 153.
24. Paul, R. L.; McQuillan, A. J.; Hendra, P. J.; Fleischmann, M. *J. Electroanal. Chem.* **1975,** *66,* 248.
25. Wenning, U.; Pettinger, B.; Wetzel, H. *Chem. Phys. Lett.* **1980,** *70,* 49.
26. Pettinger, B.; Wenning, U.; Wetzel, H. *Surf. Sci.* **1980,** *101,* 409.
27. Allen, C. S.; Schatz, G. C.; Van Duyne, R. P. *Chem. Phys. Lett.* **1980,** *75,* 201.
28. Temperini, M. L. A.; Chagas, H. C.; Sala, O. *Chem. Phys. Lett.* **1981,** *79,* 75.
29. Marinyuk, V. V.; Lazorenko-Manevich, R. M.; Kolotyrkin, Ya. M. *J. Electroanal. Chem.* **1980,** *110,* 111.
30. Naaman, R.; Buelow, S. J.; Cheschnovsky, O.; Herschbach, D. R. *J. Phys. Chem.* **1980,** *84,* 2692.
31. Sanchez, L.; Birke, R. L.; Lombardi, J. R. *Chem. Phys. Lett.* **1981,** *79,* 219.
32. Cooney, R. P.; Reid, E. S.; Hendra, P. J.; Fleischmann, M. *J. Am. Chem. Soc.* **1977,** 2002.
33. Heitbaum, J.; *Z. Phys. Chem.* **1977,** *105,* 351.
34. Hendra, P. J.; Fleischmann, M.; Cooney, R. P. *J. Chem. Soc., Chem. Commun.* **1977,** *7,* 235.
35. Otto, A. *Surf. Sci.* **1978,** *75,* L392.
36. Wood, T. H.; Klein, M. V. *J. Vac. Sci. Technol.* **1979,** *16,* 459.
37. Smardzewski, R. K.; Colton, R. J.; Murday, J. S. *Chem. Phys. Lett.* **1979,** *68,* 53.
38. Rowe, J. E.; Shank, C. V.; Zwemer, D. A.; Murray, C. A. *Phys. Rev. Lett.* **1980,** *44,* 1770.
39. Wood, T. H.; Klein, M. V. *Solid State Commun.* **1980,** *35,* 263.
40. Eesley, G. L. *Phys. Rev. Lett.* **1981,** *81A,* 193.

41. Seki, H.; Philpott, M. R. *J. Chem. Phys.* **1980,** *73,* 5376.
42. Zwemer, D. A.; Shank, C. V.; Rowe, J. E. *Chem. Phys. Lett.* **1980,** *73,* 201.
43. Tsang, J. C.; Kirtley, J. R.; Bradley, J. A. *Phys. Rev. Lett.* **1979,** *43,* 772.
44. Tsang, J. C.; Kirtley, J. R. *Proc. U.S.-USSR Symp. "Inelastic Light Scattering in Solids"*; J. L. Birman; H. Z. Cummins; K. K. Rebane, Eds.; Plenum: New York, 1979.
45. Tsang, J. C.; Kirtley, J. R. *Solid State Commun.* **1979,** *30,* 617.
46. Burstein, E.; Chen, C. Y.; Lundquist, S. *Proc. U.S.-USSR Symp. "Inelastic Light Scattering in Solids"*; by J. L. Birman, H. Z. Cummins, K. K. Rebane, Eds.; Plenum: New York; 1979; p. 479.
47. Girlando, A.; Philpott, M. R.; Heitmann, D.; Swalen, J. D.; Santo, R. *J. Chem. Phys.* **1980,** *72,* 5187.
48. Girlando, A.; Gordon II, J. G.; Heitmann, D.; Philpott, M. R.; Seki, H.; Swalen, J. D. *Surf. Sci.* **1980,** *101,* 417.
49. Creighton, J. A.; Blatchford, C. G.; Albrecht, M. G. *J. Chem. Soc. Faraday Trans. 2* **1979,** *75,* 790.
50. Lippitsch, M. E. *Chem. Phys. Lett.* **1980,** *74,* 125.
51. Wetzel, H.; Gerischer, H. *Chem. Phys. Lett.* **1980,** *76,* 460.
52. McQuillan, A. J.; Pope, C. G. *Chem. Phys. Lett.* **1980,** *71,* 349.
53. Krasser, W. *Int. Conf. on Raman Spectroscopy, Ottawa, Canada,* 1980, p. 420.
54. Varma, R.; Melendres, C. A.; Yao, N. P. *J. Electrochem. Soc.* **1980,** *127,* 1416.
55. Furtak, T. E.; Kester, J. *Phys. Rev. Lett.* **1980,** *45,* 1652.
56. Schultz, S.; Janik-Czachor, M.; Van Duyne, R. P. *Surf. Sci.* **1981,** *104,* 419.
57. Evans, J. P.; Albrecht, M. G.; Ullevig, D. E.; Hexter, R. M. *J. Electroanal. Chem.* **1980,** *106,* 209.
58. Pettinger, B.; Wenning, U.; Wetzel, H. *Chem. Phys. Lett.* **1979,** *67,* 192.
59. Bergman, J. G.; Heritage, J. P.; Pinczuk, A.; Worlock, J. M.; McFee, J. H. *Chem. Phys. Lett.* **1979,** *68,* 412.
60. Murray, C. A.; Allara, D. L.; Rhinewine *Phys. Rev. Lett.* **1981,** *46,* 57.
61. Pockrand, I.; Otto, A. *Solid State Commun.* **1980,** *35,* 861.
62. Pockrand, I.; Otto, A. *Solid State Commun.*, in press.
63. Tsang, J. C.; Demuth, J. E.; Sanda, P. N.; Kirtley, J. R. *Chem. Phys. Lett.* **1980,** *76,* 54.
64. Sanda, P. N.; Warlaumont, J. M.; Demuth, J. E.; Tsang, J. C.; Christmann, K.; Bradley, J. A. *Phys. Rev. Lett.* **1980,** *45,* 1519.
65. Pettinger, B.; Tadjeddine, A.; Kolb, D. M. *Chem. Phys. Lett.* **1980,** *66,* 544.
66. Dornhaus, R.; Benner, R. E.; Cheng, R. K.; Chabay, I. *Surf. Sci.* **1980,** *101,* 367.
67. Frumkin, A. N. *J. Electroanal. Chem.* **1973,** *46,* 161.
68. Paik, W. K.; Genshaw, M. A.; Bockris, J. O. M. *J. Phys. Chem.* **1970,** *74,* 4266.
69. Sinowitz, N.; Dentkis, G.; Sanchez, L. A.; Lombardi, J. R.; Birke, R. L. unpublished data.
70. Pemble, M. E. Ph. D. Thesis, Univ. of Southampton, Southampton, England, 1980.
71. Atkinson, G. F.; Guzonas, D. A.; Irish, D. E. *Chem. Phys. Lett.* **1980,** *75,* 557.
72. Venkatesan, S.; Erdheim, G.; Lombardi, J. R.; Birke, R. L. *Surf. Sci.* **1980,** *101,* 387.
73. Damaskin, B. B. *Electrochim. Acta* **1964,** *9,* 231.
74. Barradas, R. G.; Conway, B. E. *J. Electroanal. Chem.* **1963,** *6,* 314.
75. Blondeau, G.; Froment, M.; Zerbino, J.; Jaffrazic-Renault, N.; Revel, G. *J. Electroanal. Chem.* **1979,** *105,* 409.
76. Billmann, J.; Kovacs, G.; Otto, A. *Surf. Sci.* **1980,** *92,* 153.

77. Fleischman, M.; Hendra, P. J.; Hill, I. R.; Pemble, M. E. *J. Electroanal. Chem.* **1981**, *117*, 243.
78. Burstein, E.; Chen, Y. J.; Chen. C. Y.; Lindquist, S.; Tossatti, E. *Solid State Commun.* **1979**, *29*, 567.
79. Furtak, T. E.; Reyes-Corona, J. *Surf. Sci.* **1980**, *93*, 351.
80. Heritage, J. P.; Bergman, J. G.; Pinczuk, A.; Worlock, J. M. *Chem. Phys. Lett.* **1979**, *67*, 229.
81. Pettinger, B.; Wetzel, H. *Chem. Phys. Lett.* **1981**, *78*, 398.
82. Hendra, P. J.; Fleischmann, M.; McQuillan, A. J. *J. Electroanal. Chem.* **1975**, *65*, 933.
83. Mahoney, M. R.; Howard, M. W.; Cooney, R. P. *Chem. Phys. Lett.* **1980**, *71*, 59.
84. Cooney, R. P.; Mahoney, M. R.; Howard, M. W. *Chem. Phys. Lett.* **1980**, *76*, 448.
85. Bunding, K. A. Ph. D. Thesis, City University of New York, New York, 1980.
86. Lombardi, J. R.; Birke, R. L. *Surf. Sci.* **1980**, *95*, L259.
87. Bunding, K.; Birke, R. L.; Lombardi, J. R. *Chem. Phys.* **1980**, *54*, 115.
88. Moskovits, M.; Dilella, D. P. *Chem. Phys. Lett.* **1980**, *73*, 500.
89. Kotz, R.; Yeager, E. *J. Electroanal. Chem.* **1980**, *111*, 105.
90. Allen, C. S.; Van Duyne, R. P., to be published in *J. Am. Chem. Soc.*
91. Dilella, D.; Gohin, D. P.; Lipson, R.; McBreen, P.; Moskovits, M. *J. Chem. Phys.* **1980**, *73*, 4282.
92. Gold, A. S.; Buck, R. P. *J. Raman Spec.* **1979**, *8*, 323.
93. Dornhaus, R.; Chang, R. K. *Solid State Commun.* **1980**, *34*, 811.
94. Dornhaus, R.; Chang, R. K., to be published in *Surf. Sci.*
95. Regis, A.; Corset, J. *Chem. Phys. Lett.* **1980**, *70*, 305.
96. Lombardi, J. R.; Shields Knight, E. A.; Birke, R. L. *Chem. Phys. Lett.* **1981**, *79*, 214.
97. Kunz, R. E.; Gordon II, J. G.; Philpott, M. R.; Girlando, A. *J. Electroanal. Chem.*, **1980**, *112*, 391.
98. Kerker, M.; Siiman, O.; Bumm, L. A.; Wang, D-S. *Appl. Opt.* **1980**, *19*, 3253.
99. Wetzel, H.; Pettinger, B.; Wenning, U. *Chem. Phys. Lett.* **1980**, *75*, 173.
100. Allen, C. S.; Van Duyne, R. P. *J. Am. Chem. Soc.* **1981**, *103*, 7497.
101. Allen, C. S.; Van Duyne, R. P., to be published in *Surf. Sci.*
102. Weitz, D. A., private communication, 1981.
103. Yamada, Y.; Amamiya, T.; Tsubomara, H. *Chem. Phys. Lett.* **1979**, *56*, 591.
104. Pemberton, J. E.; Buck, R. P. *J. Phys. Chem.* **1981**, *85*, 248.
105. Allen, C. S.; Van Duyne, R. P., to be published in *J. Electroanal. Chem.*
106. Lippitsch, M. E. *Chem. Phys. Lett.* **1981**, *79*, 2.
107. Cotton, T. M.; Schultz, S. G.; Van Duyne, R. P. *J. Am. Chem. Soc.* **1981**, *102*, 7960.
108. Kotz, R.; Yeager, E. *J. Electroanal. Chem.* **1980**, *113*, 113.
109. Koglin, E.; Sequaris, J. M.; Valenta, P. *J. Mol. Struc.* **1980**, *60*, 421.
110. Ervin, K. M.; Koglin, E.; Seguaris, J. M.; Valenta, P.; Nurenberg, H. W. *J. Electroanal. Chem.* **1980**, *114*, 179.
111. Loo, B. H.; Furtak, T. E. *Chem. Phys. Lett.* **1980**, *71*, 68.
112. Furtak, T. E.; Trott, G.; Loo, B. H. *Surf. Sci.* **1980**, *101*, 374.
113. Bernard, I.; Lombardi, J. R.; Birke, R. L., unpublished data.
114. Chen, C. Y.; Burnstein, E. *Bull. Am. Phys. Soc.* **1978**, *24*, 341.
115. King, F. W.; Van Duyne, R. P.; Schatz, G. C. *J. Chem. Phys.* **1978**, *69*, 4472.
116. Shatz, G. C.; Van Duyne, R. P. *Surf. Sci.* **1980**, *101*, 425.
117. Eesley, G. L.; Smith, J. K. *Solid State Commun.* **1979**, *31*, 815.
118. Efrima, S.; Metiu, H. *Chem. Phys. Lett.* **1978**, *60*, 59.
119. Efrima, S.; Metiu, H. *J. Chem. Phys.* **1979**, *70*, 1602.

120. Philpott, M. R. *J. Chem. Phys.* **1975**, *62*, 1812.
121. Hexter, R. M.; Albrecht, M. G. *Spectrochim. Acta, Part A*, **1979**, *35*, 233.
122. Kirtley, J. R.; Jha, S. S.; Tsang, J. C. *Solid State Commun.* **1980**, *30*, 509.
123. Otto, A. *Surf. Sci.* **1980**, *92*, 145.
124. McCall, S. L.; Platzman, P. M. *Bull. Am. Phys. Soc.* **1979**, *24*, 340.
125. Aussenegg, F. R.; Lippitsch, M. E. *Chem. Phys. Lett.* **1978**, *59*, 214.
126. Gersten, J. I.; Birke, R. L.; Lombardi, J. R. *Phys. Rev. Lett.* **1979**, *43*, 147.
127. Fuchs, R. *Bull. Am. Phys. Soc.* **1979**, *24*, 339.
128. Arya, K.; Zeyher, R., *Phys. Rev.* **1981**, *24*, 1852.
129. Chen, C. Y.; Burstein, E. *Bull. Am. Phys. Soc.* **1979**, *24*, 341.
130. Otto, A.; Timper, J.; Billmann, J.; Kovacs, G.; Pockrand, I. *Surf. Sci.* **1980**, *92*, L55.
131. Gersten, J. I. *J. Chem. Phys.* **1980**, *72*, 5779–5780.
132. Gersten, J. I.; Nitzan, A. *J. Chem. Phys.* **1980**, *73*, 3023.
133. McCall, S. L.; Platzman, P. M.; Wolff, P. A. *Phys. Lett.* **1980**, *77A*, 381.
134. Kerker, M.; Wang, D.-S.; Chew, H. *Appl. Optics*, **1980**, *19*, 4159.
135. Moskovits, M. *J. Chem. Phys.* **1978**, *69*, 4159.
136. Moskovits, M. *Solid State Comm.* **1979**, *32*, 59.
137. Efrima, S.; Metiu, H. *J. Chem. Phys.* **1979**, *70*, 2297.
138. Efrima, S.; Metiu, H. *J. Chem. Phys.* **1979**, *70*, 1939.
139. Efrima, S.; Metiu, H. *Surf. Sci.* **1980**, *92*, 417.
140. Lee, T. K.; Birman, J. L. *Phys. Rev.* **1980**, *B22*, 5953, 5961.
141. Weber, W. H.; Ford, G. W. *Phys. Rev. Lett.* **1980**, *44*, 1774.
142. Ford, G. W.; Weber, W. H. *Surf. Sci.*, **1981**, *109*, 451.
143. Hilton, P. R.; Oxtoby, D. W. *J. Chem. Phys.* **1980**, *72*, 6346.
144. Genack, A. Z.; Weitz, D. A.; Gramila, T. J. *Surf. Sci.* **1980**, *101*, 381.
145. Weitz, D. A.; Gramila, T. J.; Genack, A. Z.; Gersten, J. I. *Phys. Rev. Lett.* **1980**, *45*, 355.
146. Gersten, J. I.; Weitz, D. A.; Gramila, T. J.; Genack, A. Z. *Phys. Rev. Lett.* **1980**, *22*, 4562.
147. Otto, A.; Timper, J.; Billmann, J.; Pockrand, I. *Phys. Rev. Lett.* **1980**, *45*, 46.
148. Timper, J.; Billmann, J.; Otto, A.; Pockrand, I. *Surf. Sci.* **1980**, *101*, 348.
149. Wetzel, H. A.; Gerischer, H.; Pettinger, B. *Chem. Phys. Lett.* **1981**, *80*, 392.

RECEIVED for review June 2, 1981. Accepted December 14, 1981.

Control of Redox Potentials in Mononuclear and Dinuclear Copper Cryptates

J. P. GISSELBRECHT and M. GROSS

Université Louis Pasteur, Laboratoire d'Electrochimie et de Chimie Physique du Corps Solide, Equipe de Recherches Associée au CNRS (n° 468), Institut Le Bel, 67000 Strasbourg, France

The electrochemical behavior of mononuclear and dinuclear macrocyclic copper complexes was studied on solid electrodes in water and in organic media, and the factors controlling the redox properties of the complexes were identified. In mononuclear complexes, the formal redox potential of the copper(II)/copper(I) system ranged from −0.10 to +0.49 V vs. SCE in water. This potential was shifted to more positive values by introducing thioether groups in the macrocycle and by increasing the size of the N*-substituents. In dinuclear copper complexes, symmetrical cryptates exhibited a single, reversible dielectronic interconversion between the dicopper(II) and the dicopper(I) cryptate. On the other hand, one nonsymmetrical cryptate exhibited two successive and distinct monoelectronic reduction steps, as a consequence of the large difference between the two coordination sites in the ligand. Incremental stabilization of copper(I) relative to copper(II) was observed with changes in chemical composition of the ligand and coordination geometry of the copper ions for all dinuclear macrocyclic copper complexes studied.*

In recent years, strong efforts were directed toward the understanding and reproducibility of experimental data dealing with the physicochemical properties of copper in copper proteins and enzymes through appropriate synthetic coordinating ligands (*1*, 2).

Of special relevance in this context are the spectral and redox properties of the copper(II)/copper(I) system in natural molecules, which are characterized by reversible electron transfers having formal

0065-2593/82/0201-0109$08.25/0

potentials ranging from +0.2 to +0.8 V vs. NHE. Electrochemical results on synthetic models (*3–6*) gave clear-cut evidence that appropriate design of ligands coordinated to copper may have marked effects on the redox potential of the copper(II)/copper(I) couple and on the spectral properties of the cupric complex. Synthetic mononuclear chelates were described (*6*) whose redox properties (one-electron reversible transfer at markedly positive potentials) and spectral characteristics (intense band around 600 nm) mimic those of blue mononuclear copper proteins (type 1 copper).

Recently (*7*), experimental reproducibility of the spectral and redox properties of type 3 copper[1] were achieved in a model, although low-molecular weight copper complexes, which reproduce separately some properties of type 3 copper, were previously reported (*8–18*). In this chapter we present a systematic study of the effects of typical macrocyclic ligand characteristics on the redox behavior of the copper(II)/copper(I) couple, in mononuclear and in dinuclear chelates. Monocyclic, bicyclic, and tricyclic ligands were used; their typical properties were presented elsewhere (*19*).

Experimental

All measurements were carried out at 25°C using platinum, glassy carbon, or gold electrodes. Unless otherwise noted, all reported measurements were taken using platinum electrodes. With some complexes the current–voltage curves were distorted on platinum due to adsorption effects and in these cases either gold or glassy carbon electrodes were utilized. These electrodes showed less surface effects, and thus better defined current–voltage curves could be observed. No differences in potentials were observed between the three types of electrode material. These three electrodes were also used as rotating disk electrodes (RDE) with rotation rates from 250 to 5000 rev/min. The measurements were performed with an electrochemical device consisting of a potentiostat (SOLEA Tacussel PRT 20 X), a voltage pilot unit (SOLEA Tacussel GSTP 2), a current–potential converter (SOLEA Tacussel ADTP 1), and a potentiometric *XY*-recorder (IFELEC IF 3802). This device also was used for cyclic voltammetric measurements at scan rates up to 1 V/s.; for higher scan rates, the signal was stored in a two-channel transient recorder (BRYANS 512 A), and afterwards plotted on the *XY*-potentiometric recorder. Potentiostatic coulometry provided the amount of Faradays exchanged per mole of cryptate. Throughout the measurements, a calomel electrode was used as reference electrode, in a saturated aqueous solution of potassium chloride (SCE). This electrode was connected electrically to the studied solution by a bridge filled with the solvent plus the background electrolyte used in the cell.

Experiments were performed in propylene carbonate (PC) containing 0.1 *M* tetraethylammonium perchlorate (TEAP), dimethyl sulfoxide (DMSO) containing 0.1 *M* TEAP, in 0.1 *M* KCl aqueous solutions for those complexes that were soluble in water.

[1] These characteristics of type 3 copper are (a) Cu(II)/Cu(I) formal redox potential about 0.4 to 0.5 V vs. NHE, (b) reversible two-electron transfer, (c) very large antiferromagnetic coupling constant and lack of EPR signal in both the oxidized and reduced states of the complex, (d) electronic absorption band near 330 nm.

We investigated eleven mononuclear complexes with Ligands **1a–5** and seven dinuclear complexes with Ligands **6–12.** The syntheses of these complexes was reported previously (*16, 20, 21*).

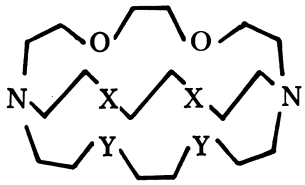

1a: X = Y = O

1b: X = O; Y = S

1c: X = Y = S

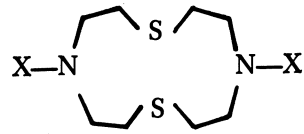

2a: X = H

2b: X = CH_3

2c: X = $CH_2C_6H_5$

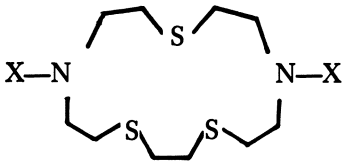

3a: X = H

3b: X = CH_3

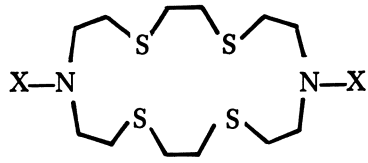

4a: X = H

4b: X = CH_3

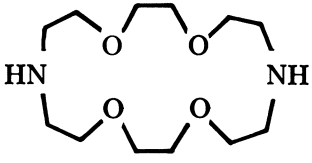

5

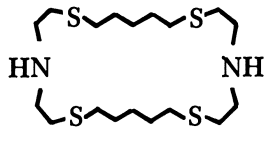

6

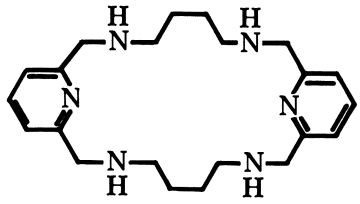

7

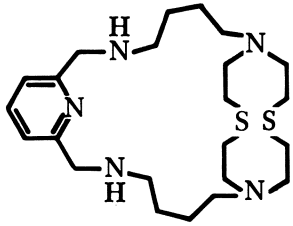

8

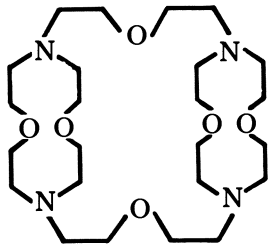

9

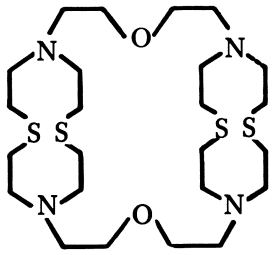

10

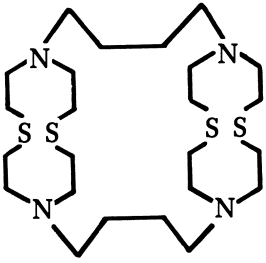

11

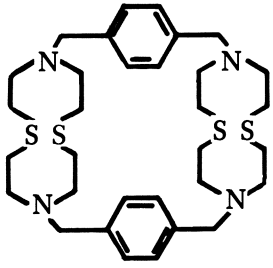

12

Mononuclear Copper Chelates

Physicochemical data on the copper(II) complexes with **1a–5** have been very scarce. Several stability constants were measured[2,3] and indicate a high stability of the oxidized form in solution. Also, structural analysis of the cupric complex with **5** revealed that copper(II) is octahedrally coordinated with four out of the six bonds belonging to the macrocycle **5** (*24*, *25*), whereas an approximately tetragonal pyramid is observed in the cupric complex with **2** from the known structure (*17*) of the corresponding dinuclear complex with **10**, which contains two subunits of macrocycle **2**.

Results

Redox measurements on the copper complexes with **1a–5** (Table I) revealed that all of the copper(II) complexes—except for those with **1a** and **5**—were reduced at a RDE in two single, one-electron steps. The first step was the reversible reduction from a copper(II) to a copper(I) complex; the second step, at more negative potentials, was the reduction from a copper(I) complex to nonvalent copper and free unaltered ligand in solution. Figure 1 is given as an example documenting the two one-electron transfer reduction mechanism for the cupric complex with **3a** and also illustrates the important difference between the potentials of the two reduction steps. Figure 2, for the same complex, shows clearly the reversibility of the cupric–cuprous system. The obtaining of a nonvalent copper after the second step was ascertained by a copper deposit on the platinum RDE. The second step [Cu(I) → Cu(0)] may be observed only in solvents that have a large cathodic electroactivity range, such as PC. In contrast, in PC the copper(II) complexes with **1a** and **5** were reduced to nonvalent copper and free ligand in a single two-electron step [with **1a**, Cu(II) reduces to Cu(0) at −1.7 V vs. SCE, and with **5** at −0.95 V vs. SCE].

Stationary Voltammetry. For those cupric complexes reduced in two distinct one-electron steps (Table I), the stationary voltammetry curves at a RDE indicated that the Cu(II) → Cu(I) reduction is diffusion controlled. This analysis is based on both the proportionality between the cathodic limiting current (I_{lim}) and the analytical concentration of the complex as well as from Levich's (*26*) linear plot of $1/I_{lim} = f(1/\omega^{1/2})$. Logarithmic analysis [$\log (I/I_{lim} - I) = f(E)$] of the Cu(II) → Cu(I) cathodic curves (Tables II and III) corresponded to reversible or quasi-reversible processes. Because the studied solutions did not con-

[2] Log *K* [Cu(II)–L] in H_2O + 0.1 *M* TEAP 25°C with ligands **1a** (6.81) and **5** (6.18) (*22*).

[3] Log *K* [Cu(II)–L] in H_2O + 0.1 *M* TEAP 25°C with ligands **2a** (8.44), **2b** (12.75), **3a** (13.04) (*23*).

Table I. Redox Measurements on Mononuclear Copper Complexes

Ligand	*log* $K_{(Cu(II)-L)}$[a]	*Reduction steps*
1a,	6.81[b]	one, di-*e*
1b		two, mono-*e*
1c		two, mono-*e*
2a, 2b, 2c	8.44[c]	
	12.75[c]	two, mono-*e*
3a, 3b	13.04[c]	two, mono-*e*
4a, 4b	—	two, mono-*e*
5	6.18[b]	one, di-*e*

[a] Copper complexation with ligand L is represented by Cu–L. Experiments were performed in water plus 0.1 *M* TEAP at 25°C.

[b] Log *K* [Cu(II)–L] in H_2O + 0.1 *M* TEAP 25°C with ligands **1a** (6.81) and **5** (6.18) (22).

[c] Log *K* [Cu(II)–L] in H_2O + 0.1 *M* TEAP 25°C with ligands **2a** (8.44), **2b** (12.75), and **3a** (13.04) (23).

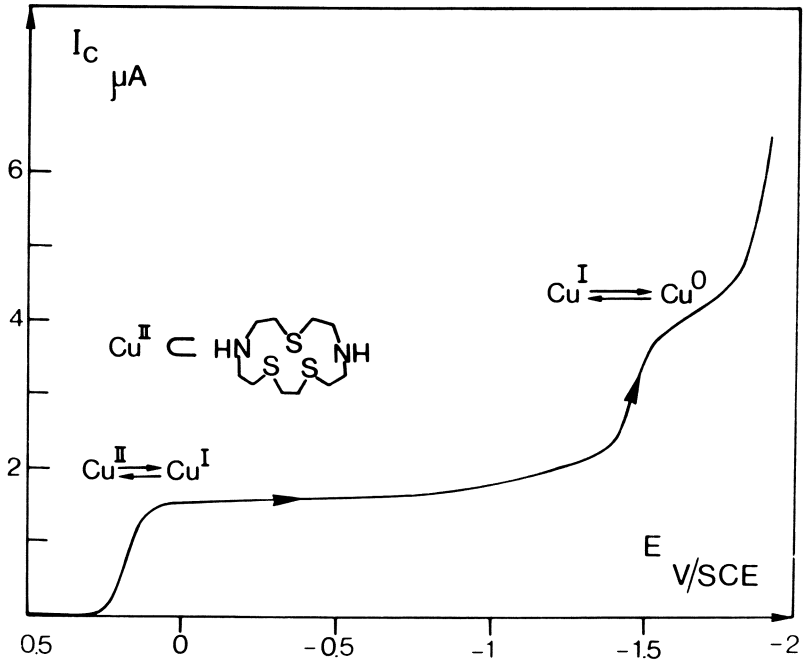

Figure 1. The monoelectronic reduction waves of the Cu(II) complex with 3a: in PC + 0.1 M *TEAP, on a platinum RDE (2000 rev/min), [Cu(II)] = 1.9 · 10⁻⁴* M.

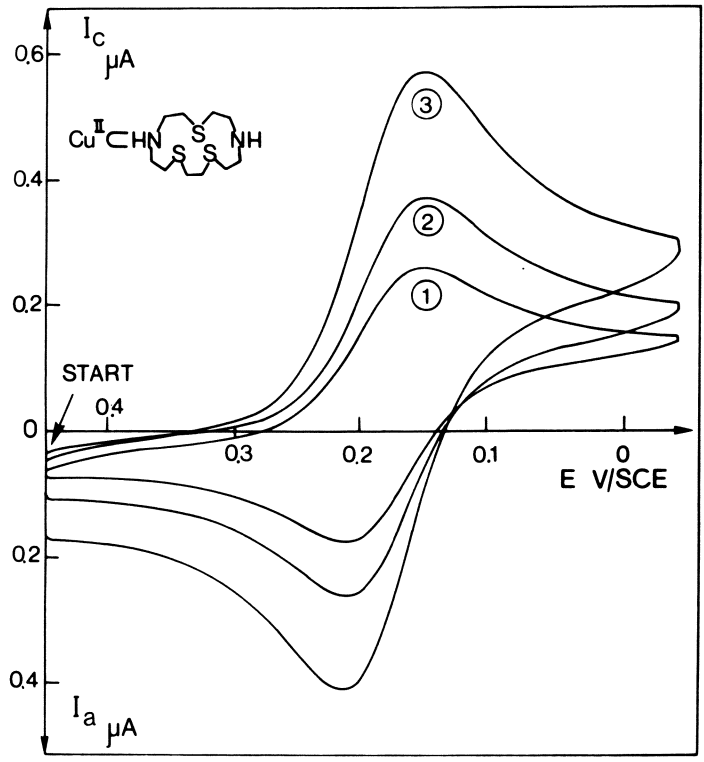

Figure 2. Cyclic voltammogram of the first reduction step [Cu(II) → Cu(I)] in Cu(II)–3a (c = 1.9 · 10⁻⁴ M). Electrode: Pt Solution: PC + 0.1 M TEAP. Scan rates: 1, 10 mV/s; 2, 20 mV/s; 3, 50 mV/s.

tain free ligand in excess [all solutions were prepared from crystallized copper(II) complexes of stoichiometry 1 : 1], the observed linearity of the plots [log $(I/I_{lim} - I) = f(E)$] confirmed that the number of ligands coordinated to copper remained constant throughout the reduction (27). Thus, the reduction product of copper(II) is always a copper(I) complex of identical stoichiometry. On the other hand, further reduction of the complex from copper(I) to copper(0) may be carried out only at rather negative potential, indicative of the high stability of the copper(I) complex generated by the first reduction step.

Cyclic Voltammetry. Measurements on the first reduction step [Cu(II) → Cu(I)] provide clear-cut information on the reversibility of the electrode processes (Tables II and III). Some complexes are reduced reversibly as indicated by an invariant and close to 58-mV peak separation ΔE_p ($\Delta E_p = E_{p_a} - E_{p_c}$) at low scan rates ($v < 0.1$ V/s). For other complexes, only quasi-reversible reduction occurs, which is also

Published on June 1, 1982 on http://pubs.acs.org | doi: 10.1021/ba-1982-0201.ch005

Table II. Redox Characteristics of the Cu(II)/Cu(I) Couple Complexed in Ligands 1 to 4, in H_2O + 0.1 *M* KCl

	RDE			*Cyclic Voltammetry*		
Ligand	$E_{1/2}$ *Cu(II)/Cu(I)* *(V vs. SCE)*	*Slope (mV)* [E *vs.* *log* $(I/I_d - I)$]	$E_{1/2}$ *Cu(I)/Cu(0)* *(V vs. SCE)*	$\Delta E_p = E_p^{an} - E_p^{cath}$ *(mV)*	E°′ Cu(II)/Cu(I) (V vs. SCE)	E°′ *Cu(II)/Cu(I)* *(V vs. NHE)*
2a	−0.10	61	−0.67	70	−0.10	+0.14
2b	−0.02	58	—	70	−0.025	+0.22
2c	~+0.14	—	—	—	—	~+0.38
3b	+0.14	56	—	70	+0.145	+0.38
4a	−0.10	66	—	66	−0.10	+0.14
4b	+0.28 (composite)	90	—	100	+0.31	+0.55
1b	~+0.18	—	−0.50	—	—	~+0.42
1c	+0.49 (composite)	65	—	65	+0.49	+0.73

Note: RDE experiments and cyclic voltammograms were carried out on Pt.

Published on June 1, 1982 on http://pubs.acs.org | doi: 10.1021/ba-1982-0201.ch005

Table III. Redox Characteristics of the Cu(II)/Cu(I) Couple Complexed in Ligands 1 to 4 in PC + 0.1 *M* TEAP

	RDE			*Cyclic Voltammetry*		
Ligand	$E_{1/2}$ *Cu(II)/Cu(I) (V vs. SCE)*	*Slope (mV) [E vs. log (I/I$_d$ − I)]*	$E_{1/2}$ *Cu(I)/Cu(0) (V vs. SCE)*	$\Delta E_p = E_p^{an} - E_p^{cath}$ *(mV)*	$E^{\circ\prime}$ Cu(II)/ *Cu(I) (V vs. SCE)*	$E^{\circ\prime}$ *Cu(II)/ Cu(I) (V vs. NHE)*[a]
2a	+0.13	65	—	70	+0.14	+0.25
2b	+0.22	60	−1.15	60	+0.23	+0.34
2c	+0.30	64	−1.45	66	+0.31	+0.42
3a	+0.17	60	−1.46	66	+0.18	+0.29
3b	+0.31	60	—	60	+0.32	+0.43
4a	+0.024	72	—	60	+0.04	+0.15
4b	+0.44 (composite)	83	−1.25	70	+0.44	+0.55
1b	+0.35	65	−1.47	60	+0.35	+0.46
1c	+0.65 (composite)	75	—	80	+0.65	+0.76

[a] Corrected for liquid junction potential.

seen from stationary curves on the RDE [Tables II and III, complexes with Ligand **4b** in water and Ligands **4b** and **1c** in PC]. The $E^{\circ\prime}$ values given in Tables II and III were calculated from E_{p_a} and E_{p_c} [$(E_{p_a} + E_{p_c})/2$] and are almost identical to the $E_{1/2}$ obtained at a RDE. This calculation also was used for the reduction steps that were almost reversible [Tables II and III, Ligands **4b** and **1c**].

For all of the complexes studied (except for Cu(II) in **2c** and **1b** in aqueous solutions) the heterogeneous rate constants were estimated at the formal potential $E^{\circ\prime}$ Cu(II)/Cu(I) (*28*); all calculated k values ranged from 10^{-3} to 10^{-2} cm/s and no significant effect was detected from the nitrogen substituents nor from the solvents (H_2O or PC).

Peculiar Behavior Observed for Some Cryptates. REDUCTION OF COPPER(II) IN COMPOUNDS **2c, 4b,** AND **1c** IN WATER. In water, the complex of copper(II) with **2c** does not show any wave by stationary voltammetry on a RDE. Instead, the voltammetric curves are peak shaped, which may be ascribed to a passivating film generated at the electrode surface during the reduction process. Therefore, the given reduction potential (+0.14 V vs. SCE) is only approximate. Further anodic polarization of the electrode at +0.25 V vs. SCE eliminates the film. On the other hand, for solutions of 1 : 1 cupric complexes with **4b** and **1c,** mixed anodic–cathodic waves are observed for **4b** and entirely anodic waves for **1c,** thus indicating that a significant (with **4b**) or quantitative (with **1c**) spontaneous homogeneous redox reaction occurs, which converts a copper(II) complex to copper(I) complex in these solutions.

REDUCTION OF COPPER(II) IN COMPOUNDS **4a, 4b,** AND **1c** IN PC. In PC, results were obtained for the reduction of copper(II) complexes with **4b** and **1c** [which is spontaneously reduced chemically to Cu(I) complexes, *see* following section] that were very similar to those just reported for the same complexes in water. For copper(II) complexes with **4a** and **4b** (Table III), stationary voltammograms on RDE, appeared less reversible than cyclic voltammograms. This drawn-out character of the stationary curves may likely be ascribed to a slow chemical process occurring in the solution of complexes involving **4b** and **4a**; on the shorter time scale of cyclic voltammetry, these processes may be prevented from interfering with the electron transfer kinetics.

Thus, when cryptated in **1c** or **4b,** divalent copper is spontaneously reduced to the monovalent complex in water as well as in PC. Also, after correction for the liquid junction potential between PC and H_2O (*29*):

$$E_{SCE} \text{ in PC} + 0.1\ M \text{ TEAP} - E_{SCE} \text{ in } H_2O + 0.1\ M \text{ KCl} = 0.13 \text{ V}$$

and for the potential of the SCE referred to the NHE (0.242 V), cupric complexes whose half-wave reduction potentials are more cathodic than +0.50 V vs. NHE remain stable in both solvents, whereas cupric complexes whose potentials are more anodic than +0.50 V vs. NHE are reduced spontaneously through homogeneous redox processes, partially [Cu(II)–**4b**] or quantitatively [Cu(II)–**1c**]. Such behavior implies that the reductant involved exhibits a standard redox potential close to, and not much more anodic than, +0.50 V vs. NHE.

Discussion

Relative Stability of Copper(II) and Copper(I) in Complexes. When copper(II) is complexed by ligands containing only nitrogen and oxygen heteroatoms (Ligands **1a** and **5**), reduction of copper(II) occurs in a single two-electron transfer step. In other complexes where copper is coordinated to sulfur heteroatoms, the standard redox potential of copper(II)/copper(I) shifts with the relative stability of copper(II) and copper(I) that are complexed by the same ligands. Depending on this relative stability, the resulting potential is expected to be more cathodic or more anodic than the standard redox potential of the uncomplexed copper(II)/copper(I) system, according to the known relationship (*30*, *31*) (at 25°C):

$$[E_{1/2}\mathrm{Cu(II)/Cu(I)}]_{\mathrm{complexed}} = [E_{1/2}\mathrm{Cu(II)/Cu(I)}]_{\mathrm{uncomplexed}} - 0.059 \log_{10} \frac{K_{\mathrm{ox}}}{K_{\mathrm{red}}} \quad (1)$$

where K_{ox} and K_{red} are the stability constants of the cupric and cuprous complexes, respectively. Several $E_{1/2}$Cu(II)/Cu(I) were determined[4] for the complexes in Tables II and III. Most half-wave potentials of the complexed copper(II)/copper(I) species are more positive than the standard potential of uncomplexed copper(II)/copper(I). The value used in Equation 1, in the absence of complexation, was the standard redox potential of copper(II)/copper(I) in water. This potential was initially given as +0.153 V vs. NHE (*32*). Later data gave a range of about +0.16 to +0.17 V vs. NHE (*33*–*35*). However, the questionable element in the data leading to $E°$ = +0.153 V vs. NHE for the aqueous copper(II)/copper(I) couple was the hydration free energy of copper(I), whereas reliable data were available for divalent

[4] [*E Cu(II)/Cu(I)*]$_{1/2}$/NHE have been calculated, for the studied complexes, from experimental [*E* Cu(II)/Cu(I)]$_{1/2}$/SCE through the following relationship: [*E* Cu(II)/Cu(I)]$_{1/2}$ complex/NHE = [*E* Cu(II)/Cu(I)]$_{1/2}$ complex/SCE + *E* SCE/NHE − E_j where E_j = 0 in water, and +0.13 (*29*) in PC.

copper [$E°$Cu(II)/Cu(0) in water = +0.34 V vs. NHE] (*32*). Recent findings (*36*) confirmed both the reliability of $[Cu(II)/Cu(0)]_{aq}$ data ($E°$ = +0.34 V vs. NHE) and the questionability of $[Cu(II)/Cu(I)]_{aq}$ potential (+0.153 V vs. NHE). However, from the dissociation constant of cuprous ions (*37*) experimentally obtained in water at 25°C, and with the assumption, based on these arguments, that $E°[Cu(II)/Cu(0)]_{aq}$ = +0.34 V vs. NHE is indeed correct, $E°[Cu(I)/Cu(0)]_{aq}$ may be calculated equal to +0.52 V vs. NHE. The resulting $E°$ calculated for Cu(II)/Cu(I) using these values for Cu(I)/Cu(0) and Cu(II)/Cu(0) is then $E°[Cu(II)/Cu(I)]_{aq}$ = +0.16 V vs. NHE. This value, based on reliable experimental data, is quite close to the value reported in 1952 (*32*).

Thus, as $E°[Cu(II)/Cu(I)]_{aq}$ = +0.16 V vs. NHE, it may be concluded from Equation 1 and Tables II and III that most of the copper(I) complexes are more stable than the copper(II) complexes with the ligands used.

For complexes of Ligands **2a** and **2b** with copper(II) the logarithms of the stability constants are known in water[3] and the corresponding values can be calculated for copper(I) from the electrochemical half-wave potentials: log K_{stab} = 8.1 with **2a** [Cu(I)–**2a**] and log K_{stab} = 13.8 with **2b** [Cu(I)–**2b**]. Such high stability of copper(I) complexes is quite uncommon in water. This high stability is consistent with the rather negative potential ($E_{1/2}$ = −0.67 V vs. SCE) observed for the reduction of [Cu(I)–**2a**] in water.

Common Effect of Ligand Size and of the Number of Sulfur Heteroatoms on the Redox Potential of Copper(II)/Copper(I) in the Macrocycles. To characterize this effect, macrocyclic ligands of different size were used with identical substituents on the nitrogens. The redox behavior of copper(II) complexes was examined in water and in propylene carbonate for the twelve-, fifteen-, and eighteen-membered monocyclic ligands. In the first series of these macrocyclic ligands, the substituent on the nitrogens was hydrogen and in the second series it was methyl (Table IV).

As a general trend in either series, the formal redox potential for the couple Cu(II)/Cu(I) shifts anodically with increasing size of the macrocycle and with increasing number of sulfur heteroatoms. One exception is observed for **4a**. These results were qualitatively expected from the known effect of the number of sulfur donor atoms in a monocyclic ligand, because previous experiments (*6*) revealed that coordinating copper to sulfur strongly stabilizes monovalent copper more than divalent copper. Furthermore, these results revealed that solvent effects are much more important on small cycles than on large cycles.

Effect of Nitrogen Substituents on the Redox Potential of Copper(II)/Copper(I). In this study, three groups of complexes were compared (Table V). In a given group, ligands differ from each other only by the nature of the substituent on the nitrogen. Potentials shown in Table V show that, for a given macrocycle, the formal redox potential of Cu(II)/Cu(I) is anodically shifted as the substituent on the nitrogen becomes more bulky and exhibits better electron donor properties. However, the latter characteristics cannot account for the observed shift, because increasing electron donor effect would induce cathodic shifts of the potential (*38–40*), whereas an anodic shift is observed

Table IV. Effect of Ligand Size and Number of Sulfur Heteroatoms on the Redox Potential of Cu(II)/Cu(I) in Macrocycles 2, 3, and 4

Ligand	E°′ *Cu(II)/Cu(I)* (H_2O) *(V vs. SCE)*	E°′ *Cu(II)/Cu(I) (PC) (V vs. SCE)*[a]
2a	−0.10	+0.01
3a	—	+0.05
4a	−0.10	−0.09
2b	−0.025	+0.10
3b	+0.14	+0.19
4b	+0.31	+0.30

[a] Corrected for liquid junction potential

Table V. Effect of Nitrogen Substituents on the Redox Potential of the Complexed Cu(II)/Cu(I) Couple

Ligand	E°′ *Cu(II)/Cu(I)*[a] *(V vs. SCE)*	E°′ *Cu(II)/Cu(I)*[b] *(V vs. SCE)*
2a	−0.10 (0.5)[c]	+0.13 (25)
2b	−0.02 (11)[d]	+0.22 (8×10^2)
2c	+0.14 (5.7×10^3)	+0.30 (1.8×10^4)
3a	—	+0.17 (115)
3b	+0.14 (5.7×10^3)	+0.31 (2.7×10^4)
4a	−0.10 (0.5)	+0.024 (0.4)
4b	+0.31 (4.4×10^6)	+0.44 (4.5×10^6)

Note: Values in parentheses are the ratio of the stability constant of Cu(I) in L to the stability constant of Cu(II) in L.

[a] In H_2O + 0.1 *M* KCl.

[b] In PC + 0.1 *M* TEAP.

[c] As log K_{stab} for Cu(II)L is 8.44, it may be calculated that log K_{stab} for Cu(I)L is 8.1.

[d] Same comment: log K_{stab} for Cu(II)L is 12.75, thus log K_{stab} for Cu(I)L is 13.8.

here. The trend observed with these complexes is reminiscent of that observed for other complexes (5), where an anodic shift of the potential paralleled the change of nitrogen substituents from hydrogen to butyl. This shift was rationalized (5) in terms of ligand steric constraints due to substituents that favored nonplanar copper(I) complexes. Similar arguments may be developed to account for the present results. Also, the visible spectra of copper(II) complexes reveal, for a given macrocycle, a red shift of the *d–d* band when the nitrogen substituents change from hydrogen to methyl and a further shift upon changing to benzyl (Table VI). Such a shift is indicative of conformational changes in the macrocycle (*41–43*) corresponding to a closer tetrahedral coordination of copper(II) in the presence of the benzyl group than in the presence of hydrogen.

Number of Sulfur Heteroatoms in the Macrocycle and the Standard Potential of Copper(II)/Copper(I). MONOCYCLIC LIGANDS **2** TO **5.** Cupric complexes of these ligands exhibit redox properties that depend critically on the ligand chemical composition. Thus, in PC + 0.1 *M* TEAP the copper(II) complex with **5** undergoes a two-electron irreversible reduction at $E_{1/2} = -0.95$ V vs. SCE, whereas in the same solvent the cupric complex with **4a** is reversibly reduced from copper(II) to copper(I) at $+0.03 \pm 0.01$ V vs. SCE. As documented in Tables II–IV, the presence of sulfur heteroatoms in the macrocyclic ligands clearly stabilizes monovalent copper with respect to divalent copper. This result is consistent with Pearson's hard and soft acid and base (HSAB) principle (*44*): among the six heteroatoms in the ligand **4a** that may coordinate to copper(I) (soft acid), the four sulfur atoms are soft bases. In contrast, the macrocycle **5** consists of four oxygens (hard bases) and two nitrogens that are intermediate bases. Crystallographic analysis of the copper(II) complex with **5** revealed (*24*) that divalent copper (intermediate acid) is coordinated to the two nitrogens and to two oxygens, as expected from the preferred coordination of copper(II) to nitrogen predicted by HSAB theory. Based on the

Table VI. Spectral and Redox Shifts from Nitrogen Substituents in PC + 0.1 *M* TEAP

Ligand	*Cu(II)* d–d *(nm)*	$\sigma \rightarrow Cu$ *(nm)*	$\sigma \rightarrow Cu$ *(nm)*	E°′ *Cu(II)/Cu(I) (V vs. SCE)*[a]
2a	595	370	310	+0.01
2b	600	375	325	+0.10
2c	620	375	325	+0.18
4a	610	385	310	−0.09
4b	670	415	340	+0.31

[a] Corrected for liquid junction potential.

same arguments of Pearson, it may be expected that monovalent copper would coordinate in **5** only with the two nitrogens, thus leading to unstable linear geometry (*45*) in this macrocycle **5.**

BICYCLIC LIGANDS **1a, 1b,** AND **1c.** As observed with monocyclic ligands, sulfur heteroatoms markedly stabilize monovalent vs. divalent copper, and this effect increases with the number of sulfurs in the cycle. The effect is clearly observable from **1b** to **1c** (Tables II and III)—redox potential difference of 0.3 V—and it may be ascribed to the macrobicyclic structure of the ligand.

Dinuclear Copper Cryptates

In this series of complexes (**6–12**), all ligands exhibit two distinct coordination sites that are able to accommodate copper(II) and copper(I). In this respect, three salient characteristics of the ligands should be noted:

1. In Ligands **6** and **7**, each coordination site is tridentate, the coordinating Lewis bases being two sulfur and one nitrogen in **6**, and three nitrogens in **7.**
2. Ligand **8** exhibits the special feature of having two very different coordination sites, one site being quite similar to that in ligand **7**, the other site being much like the site observed in the mononuclear chelates of the twelve-membered Ligands **2a–2c** and also similar to those of Ligand **10.**
3. In the macrotricyclic series **9** to **12,** the oxygen heteroatoms in the twelve-membered monocycles are substituted by sulfur from **9** to **10, 11** and **12.** Also, using two identical monocyclic subunits, the chemical composition of the side-branch linking the two monocycles was changed in **10–12.**

None of the dinuclear complexes, except Ligand **6,** exhibited significant Cu–Cu coupling, as consistently verified experimentally (*18*) and expected theoretically (*46*). The redox behavior of the copper(II)/copper(I) couple in these ligands is expected to provide significant insight into the parameters allowing control of the thermodynamics of the electron transfers from dinuclear copper(II) to dinuclear copper(I) moieties.

Results

The redox characteristics of the dinuclear copper chelates with Ligands **6–12** are given in Table VII.

Dinuclear Copper Complex with 6. The ESR-silent (*47*) crystallized complex of **6** with two $Cu(N_3)_2$ groups is only very slightly solu-

Published on June 1, 1982 on http://pubs.acs.org | doi: 10.1021/ba-1982-0201.ch005

Table VII. Redox Characteristics of Dinuclear Copper Chelates (Stoichiometry: Two Coppers/One Ligand)

				Cu(II)/Cu(I)				*Cu(I)/Cu(0)*		
Ligand	*Color*	*Solvent*	*Electrode*	*Number of reduction steps*	n *(F/mol)*	$E_{1/2}$ *(V vs. SCE)*	*slope [log (I/I_d − I)]*	*Number of reduction steps*	$E_{1/2}$ *(V vs. SCE)*	n *(F/mole)*
							mV/u log			
6	yellow-brown	DMSO	Pt	1	2	+0.10	90	1	−0.70	2
7	light blue	PC	Hg	1	2	−0.20	73	1	−0.65	2
8	green	PC	Hg	2	1/1	+0.31	—		−0.61	1/1
						−0.17		2	−1.0	
9	light blue	PC	Pt	1	2	+0.28	revers.	1	−0.75	2
10	violet	H_2O	Pt	1	2	+0.20	57			
		PC	Pt	1	2	+0.27	80	1	−1.50	2
11	green	H_2O	Au	1	2	+0.08	62			
		PC	C_{vitr}	1	2	+0.22	82			
12	brown	H_2O	Au	1	2	+0.29	89			
		PC	Au	1	2	+0.48	63			

ble in several organic solvents, but it dissolves reasonably, although slowly, in DMSO resulting in a yellow-brown solution (*47*) [absorption bands at 280 nm (ϵ = 6000 M^{-1} cm^{-1}), 398 (ϵ = 3750), 738 (ϵ = 2250)]. This solution is not thermodynamically stable and the color turns to green-brown after 24 h, then to green after 48 h, corresponding to the decomplexation of one of the two complexed copper(II) atoms, as expected from the higher stability of the mononuclear copper(II) complex than that of the dinuclear copper(II) species (*48*)[5]. However, considering the time scale of the redox experiments, this partial decomplexation may be neglected if fresh solutions of the dinuclear copper(II) complex are used in the electrochemical measurements, as in this study.

Using fresh solutions of the complex $Cu(N_3)_2$–**6**, redox studies revealed (*7*) three reactions on platinum in the electroactivity range of DMSO + 0.1 *M* TEAP (+1.2 to −1.9 V vs. SCE).

1. The first signal was an oxidation at $E_{1/2}$ = +0.88 V vs. SCE, corresponding to the oxidation of azides N_3^- released in solution after dissolution of the initial complex. Subsequent analyses demonstrated that this oxidation involved two out of the four azides initially included in each dinuclear copper(II) complex.
2. A second signal, at $E_{1/2}$ = +0.10 V vs. SCE, corresponds to the reversible (*7*) dielectronic reduction from [Cu(II), Cu(II)] to [Cu(I), Cu(I)], which actually results from the merging of two monoelectronic subsequent steps, respectively

   [Cu(II), Cu(II)]/[Cu(II), Cu(I)] ($E^{\circ\prime}$ = +0.12 V vs. SCE)

   and

   [Cu(II), Cu(I)]/[Cu(I), Cu(I)] ($E^{\circ\prime}$ = +0.06 V vs. SCE)

3. The last step ($E_{1/2}$ = −0.70 V vs. SCE) is dielectronic and corresponds to the reduction of [Cu(I), Cu(I)] to free, unaltered Ligand **6** and to uncomplexed Cu(0).

Dinuclear Complex of $Cu(ClO_4)_2$ with 7. In propylene carbonate (+0.1 *M* TEAP) dc polarograms on a Dropping Mercury Electrode (DME) revealed two reduction waves at $E_{1/2}$ = −0.20 ± 0.01 V vs. SCE (logarithmic slope = 73 mV/log) and at $E_{1/2}$ = −0.65 ± 0.01 V vs. SCE (logarithmic slope = 90 mV/log) (Figure 3). The unequal heights of the two reduction waves result from a slight adsorption wave merged with

[5] $(CuL)^{2+}$: log β = 9.84. $(Cu_2L)^{4+}$: log β = 12.88.

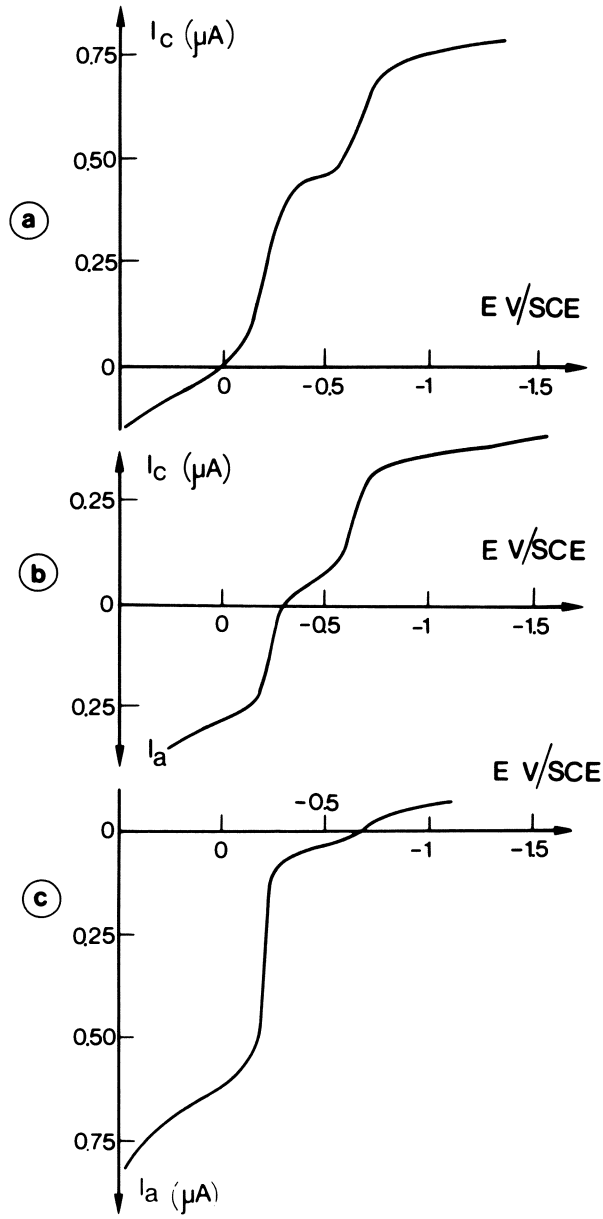

Figure 3. dc Polarograms of a dinuclear Cu(II) complex with 7 (anion: ClO_4^-). Solvent: PC + 0.1 M TEAP. Key: a, reduction of the dinuclear complex $[Cu(II)]_2$-7; b, polarogram recorded after exhaustive coulometry at −0.400 V vs. SCE; and c, polarogram recorded after exhaustive coulometry at −0.900 V vs. SCE.

the first reduction step. Potentiostatic coulometry of this first wave gives 2F/mol, the color of the solution turning from light blue to yellow.

After exhaustive coulometry performed on the first reduction step, the recorded polarogram shows (Figure 3b) one oxidation wave at $E_{1/2} = -0.22 \pm 0.1$ V vs. SCE and, as expected, the remaining unaltered second reduction wave at $E_{1/2} = -0.65$ V vs. SCE. Exhaustive coulometry on this second wave at −0.9 V vs. SCE indicates 1.9 F/mol, whereas the solution becomes colorless. Polarograms recorded after this second coulometry exhibit only the oxidation wave at −0.20 V vs. SCE (Figure 3c), which was also observed in solutions containing only the free Ligand **7**. The oxidation at −0.20 V vs. SCE was authenticated as the ligand-assisted oxidation of the mercury electrode, which was studied already (*49*) with nitrogen-containing macrocyclic ligands. Thus, the first reduction step of the complex corresponds to the dielectronic reduction of [Cu(II), Cu(II)]–**7** to [Cu(I), Cu(I)]–**7**, and the second step leads, through the reduction of both Cu(I) atoms, to uncomplexed nonvalent copper and free, unaltered Ligand **7**. The first step (two-electron reduction) may be reversed, and cycled many times by successive cathodic and anodic exhaustive coulometries.

Dinuclear Complex of $Cu(ClO_4)_2$ with 8. Polarograms on mercury revealed four discrete reduction steps in PC + 0.1 *M* TEAP. However, the $E_{1/2}$ and the geometry of these four waves were such that they prevented any straightforward analysis of the four steps. Therefore, the reduction potentials were obtained with a precision of ±0.01 V by differential pulse polarography (Figure 4) and gave, respectively, values of +0.31, −0.17, −0.61, and −1.00 V vs. SCE. The current of the last step (at −1.00 V vs. SCE) was much smaller than that of the three others. Owing to the poor resolution of the waves, the lack of detailed information led us to assign the waves by a comparison of their potentials with those of analogous binuclear symmetrical complexes (with **7** and **10**) and also, with those of mononuclear corresponding chelates with Ligands **2**.

The first reduction, at $E_p = +0.31$ V vs. SCE, is monoelectronic and was observed at identical peak potentials on glassy carbon or on mercury electrodes. This finding indicates that this step does not involve chemical reaction of the electrode material. As the mononuclear cupric complex with twelve-membered Ligand **2c** was shown (Table III) to be reduced to the cuprous complex at +0.30 V vs. SCE in this solvent (PC), the present step at +0.31 V vs. SCE may be ascribed to the reduction of copper(II) to copper(I) in the twelve-membered monocyclic subunit of **8**, where four Lewis bases (two sulfurs and two nitrogens) are available to coordinate the copper.

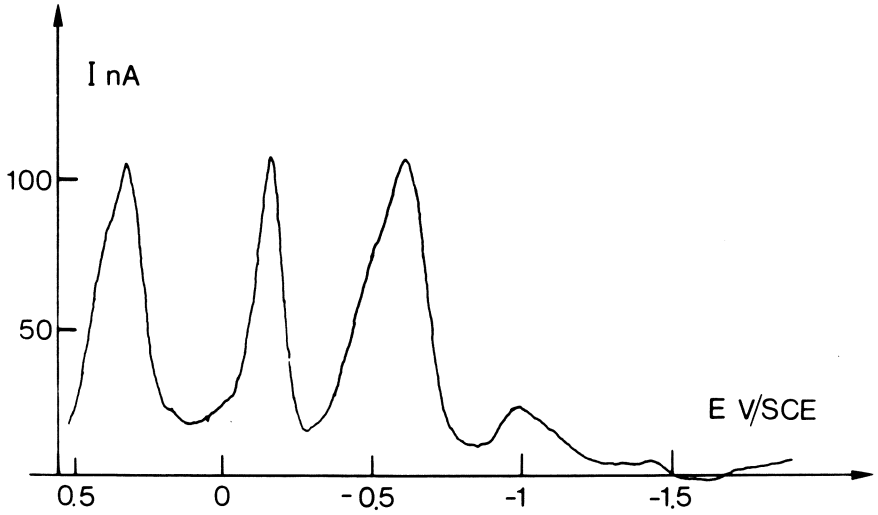

Figure 4. Differential pulse polarogram of dinuclear Cu(II) complex with asymmetrical Ligand **8**. *Electrode: Hg, Medium: PC + 0.1 M TEAP.*

The second reduction is also monoelectronic and is observed at a potential (E_p = −0.17 V vs. SCE) close to that ($E_{1/2}$ = −0.20 V vs. SCE) corresponding to the reduction of the two coppers in symmetrical Ligand **7**. Therefore, this reaction may be ascribed to the reduction of copper(II) [to Cu(I)], which is coordinated to the tridentate site involving three nitrogens in dissymmetrical Ligand **8**.

Using similar arguments just mentioned, the third redox process (E_p = −0.61 V vs. SCE) is attributed to the reduction of one Cu(I) to Cu(0) in the tridentate site of **8**, involving a similar conformation as in **7**.

The fourth step (E_p = −1.00 V vs. SCE) would be expected to correspond to the reduction of Cu(I) to Cu(0) in the twelve-membered cycle involving two nitrogens and two sulfurs. However, the small amplitude of the signal as compared with those of the first three remains unexplained. One possibility is that a chemical reaction follows electron transfer, for instance, partial dissociation of the mononuclear cuprous complex generated after the first three one-electron reductions.

Thus, the dinuclear complex of copper(II) with **8** exhibits remarkable redox properties; as a result of the marked differences in the two coordination sites, the redox potentials of Cu(II)/Cu(I) as well as of Cu(I)/Cu(0) couples are significantly shifted. In addition, the reduction potentials corresponding to Cu(II) → Cu(I) remain almost unchanged in a given coordination site, as indicated by a comparison of the values

obtained in **8** with the values given for symmetrical Ligands **7** or **10** or Ligand **2c** in Table III (Figure 5). These results indicate that an appropriate control of the coordination sites around the coppers in polynuclear complexes may be used as an efficient tool to design polynuclear complexes in which cascade-like polyelectron processes may be tuned and operated efficiently.

Reduction of the Dinuclear Complex of $Cu(ClO_4)_2$ with 9. In PC, this copper(II) complex is reduced in two dielectronic steps at $E^{\circ\prime}$ = +0.25 V vs. SCE {[Cu(II), Cu(II)] to [Cu(I), Cu(I)]} and at $E^{\circ\prime}$ = −0.75 V vs. SCE {[Cu(I), Cu(I)] to nonvalent uncomplexed copper and free Ligand **9**}.

Cyclic voltammograms indicate that the first cathodic step {[Cu(II), Cu(II)] to [Cu(I), Cu(I)]} is reversible (peak potentials independent of scan rate up to 0.1 V/s). From a previously described method (*50*), $\Delta E^{\circ\prime}$ = 60 mV was calculated as the difference between the formal potentials ($E_1^{\circ\prime}$ and $E_2^{\circ\prime}$) corresponding, respectively, to the first and the second electron transfer. On the same time scale of the electrochemical methods, both $E_1^{\circ\prime}$ and $E_2^{\circ\prime}$ are merged in the single two-electron step at +0.25 V vs. SCE. Thus, $E_1^{\circ\prime}$ = +0.28 V vs. SCE and $E_2^{\circ\prime}$ = +0.22 V vs. SCE. Also, the dinuclear cuprous complex with **9**, when electrogenerated by exhaustive reduction corresponding to the first reduction step, is unstable and undergoes slow chemical degradation in the solution.

Dinuclear Complexes of Copper(II) with 10, 11, and 12 in Aqueous 0.1 *M* KCl. In the electroactivity range corresponding to this solvent on a rotating disk electrode (from +1.2 to −0.9 V vs. SCE) a unique two-electron reduction wave is observed for these dinuclear copper(II) complexes.

The observed wave corresponds to the reduction from [Cu(II), Cu(II)] to [Cu(I), Cu(I)], as confirmed by electronic absorption and ESR spectra recorded in the solution before and after exhaustive reduction at 2 F/mol (*15*).

With the dinuclear cupric complexes of **10** and **11**, the limiting cathodic currents are diffusion controlled, as indicated from the plot $1/I_{lim}$ vs. $1/\omega^{1/2}$ (linear through origin) (*26*). Cyclic voltammograms of these two complexes are indicative of a reversible redox process at the electrode, at low scan rates (<100 m/s), with a difference ΔE_p between the anodic and cathodic peak potentials being 65 mV (with **10**) and 80 mV (with **11**). At higher scan rates, analysis of the voltammograms was obscured for **11** by a chemical reaction subsequent to the electron transfer, whereas, in the complex with **10**, the excellent stability of the initial reactant and of the reduced product allowed complete analysis of the voltammograms. In the complex with **10**, the difference between the formal potentials of the two one-electron steps corresponding to

Published on June 1, 1982 on http://pubs.acs.org | doi: 10.1021/ba-1982-0201.ch005

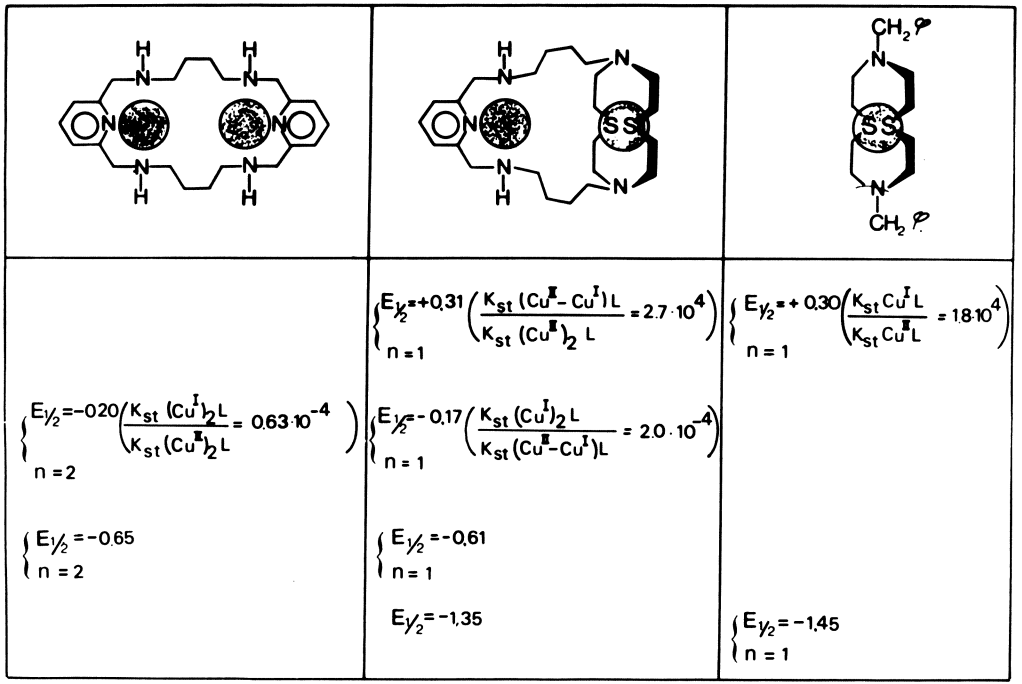

Figure 5. Comparison of the reduction potentials of the dinuclear Cu(II) complex with disymmetrical Ligand 8 (medium: PC + 0.1 M TEAP). All $E_{1/2}$ in volts vs. SCE. Values in parentheses are the ratio of the stability constants of, respectively, the reduced to the oxidized conjugated form; ○ is Cu(II) or Cu(I).

the two-electron redox process was calculated according to known procedures (*50*) and was (*15*) equal to $\Delta E^\circ = 30 \pm 5$ mV, which is quite close to the value 35.6 mV corresponding to the reduction of two independent redox centers (*51*, *52*).

As for the dinuclear cupric complex with **12**, redox measurements show that it undergoes, in part, a spontaneous chemical reduction to [Cu(I), Cu(I)] in solution. For instance, stationary voltammograms on a gold RDE remained characterized by a constant $E_{1/2}$ at +0.29 V vs. SCE, although the entire wave shifted with time along the current axis from the cathodic toward the anodic side, resulting finally in a mixed anodic–cathodic wave. The anodic limiting current was diffusion controlled, whereas the cathodic limiting current involved a chemical step in addition to the electron transfer. This chemical step becomes undetectable when the redox process is studied in PC + 0.1 *M* TEAP, as documented later.

Dinuclear Complexes of Copper(II) with 10, 11, and 12, in PC + 0.1 *M* TEAP. When studied on solid electrodes in PC where inhibiting processes are absent, all three complexes exhibit qualitatively analogous behavior. The conversion of [Cu(II), Cu(II)] to [Cu(I), Cu(I)] is detectable as a single two-electron wave on the rotating disk electrode. The limiting cathodic current was checked as being diffusion controlled, and spectroscopic evidence was obtained (absorption and ESR spectra) that the two electrons transferred to [Cu(II), Cu(II)] indeed generate [Cu(I), Cu(I)].

The characteristics of the redox couple [Cu(II), Cu(II)]/[Cu(I), Cu(I)] are given in Table VII.

In cyclic voltammetry, the anodic and cathodic peak currents are equal at all scan rates. However, as the reduction was quasi-reversible in all three complexes, ΔE_p increases with the scan rate and, as a consequence, $\Delta E'^\circ$ (*50*) between the two successive one-electron transfers could not be calculated. However, as ΔE_p is less than 100 mV at low scan rates, $\Delta E'^\circ$ still can be estimated to be less than 60 mV.

Discussion

The results obtained on the redox behavior of dinuclear copper chelates (Table VII) provide general trends on the structure–redox reactivity relationship in the studied complexes.

The data collected clearly demonstrate that all of the ligands studied stabilize copper(I) vs. copper(II), and that the copper(I) stabilization increases with the number of sulfur heteroatoms. This conclusion is consistent with previous observations on other ligands (*5*, *6*). In any of these dinuclear complexes, stabilization of copper(I) is documented by the anodic shift of the $E_{1/2}$ corresponding to Cu(II)/Cu(I) (in the

strictest sense this shift illustrates the stabilization of Cu(I) relative to Cu(II), in the ligand) and also by the cathodic shift of $E_{1/2}$ corresponding to Cu(I)/Cu(0), in the ligand. In this respect, the results observed for the reduction of dinuclear cupric complexes in **9** lead to the following observations:

1. $E_{1/2}$ [Cu(II), Cu(II)] → [Cu(I), Cu(I)] in **9** is very close to the $E_{1/2}$ measured in the homologous Ligand **10** (although **10** involves sulfurs and **9** does not).
2. $E_{1/2}$ [Cu(I), Cu(I)] → 2 Cu(0) is much more negative in **10** (−1.50 V vs. SCE) than in **9** (−0.75 V vs. SCE).

The first observation is a clear indication that the ratio of the stability constants of the cuprous to the cupric dinuclear complexes is almost identical in Ligands **9** and **10.** However, the second observation indicates that the cuprous complex with **10** is much more stable than with **9.** This result is fully consistent with our observation that the Cu(I) dinuclear complex in **9** is chemically unstable, as mentioned. The complex with **9** is the first reported in which reversible, dielectronic interconversion of [Cu(II), Cu(II)]/[Cu(I), Cu(I)] occurs at very positive potentials (about +0.5 V vs. NHE) in the presence of only nitrogen and oxygen as Lewis base heteroatoms (5). Furthermore, replacement of the oxygen heteroatoms by sulfur (**9–10**) basically stabilizes copper(I). However, the ability of a given dinuclear copper complex to act as a two-electron acceptor/donor at positive potentials depends primarily on the relative stability of copper(II) and copper(I) in the macrocyclic ligand. The redox behavior of such complexes with **9** and **10** shows that the relative stability of copper(I) compared to copper(II) in each complex depends critically on the coordination geometry much more than on the presence of oxygen or sulfur in the cycle.

In terms of selectively shifting the redox potential of a given couple [here Cu(II)/Cu(I)], results obtained with the dinuclear cupric/cuprous complexes in **7, 8,** and **10** (Table VII) provide further unambiguous evidence that controlling the coordination stereochemistry is tantamount to controlling the redox potential of Cu(II)/Cu(I), as both of the redox sites are noninteracting in the complexes.

In addition, the dinuclear complex with **8** illustrates that the excellent selectivity operating on the redox potentials through the coordination geometry provides a basis for the rational synthesis of mixed-valence complexes of predictable stability (Figure 5).

As an example documenting this conclusion, the coproportionation constant K_{copr} of the complex with asymmetrical Ligand **8,** whose equation is:

$$[Cu(II), Cu(II)]\text{–}\mathbf{8} + [Cu(I), Cu(I)]\text{–}\mathbf{8} \rightarrow 2[Cu(II), Cu(I)]\text{–}\mathbf{8}$$

was calculated as equal to 1.3×10^8 at 25°C in PC + 0.1 *M* TEAP (assuming $E_{1/2} = E°$, and the redox reactions being reversible).

These conclusions on dinuclear copper complexes may be extended to other dimetallic homonuclear and heteronuclear complexes; work is in progress on this point (*53*).

Finally, the symmetrical dinuclear complexes of copper with Ligands **10, 11,** and **12** were used to clarify the effect of the side chains linking the two monocyclic subunits to the Cu(II)/Cu(I) redox potentials. As spectral results revealed that the two coppers in a given complex do not interact significantly (*18*), each complex may be considered as the duplication of two mononuclear subunits of identical structure and redox potential, each subunit involving one copper coordinated to a monocycle bearing one-half lateral chain on each nitrogen. The results on mononuclear chelates revealed that bulky substituents on nitrogens induce anodic shifts of the Cu(II)/Cu(I) potential, thus stabilizing copper(I) with respect to copper(II), and, as already observed in other mononuclear complexes (*5*), this effect may be ascribed to an increased distortion of the coordination sphere—from planar to tetrahedral-distorted—as the size of the nitrogen substituents increases. Probably, then, in the dinuclear complexes with **10, 11,** and **12,** the same qualitative arguments hold. However, at variance with mononuclear chelates, in ligands like **10, 11,** and **12,** other conformational elements come into play, so that the whole flexibility of the ligand, rather than just the flexibility of the side chains, may be considered as a crucial parameter in the preferential stabilization of a given form, ox or red. However, the less flexible the lateral chain (flexibility decreasing from **11** to **10,** and to **12**), the more copper(I) is stabilized toward copper(II), probably due to correlative increasing distortion of each two monocycles (two nitrogens, two sulfurs). Quantitative correlation in the series is prevented by the interaction of copper with oxygen in the complex with **10** (*17*). *See* Figure 6.

On the other hand, of all the dinuclear complexes, the complex with **6,** 2[Cu(II)$(N_3)_2$]–**6,** is unique in being able to simultaneously replicate the redox properties (reversible two-electron acceptor/donor at rather positive potential) and the magnetic characteristics (ESR silent) of type 3 copper pairs in copper enzymes (*7*).

The redox and spectral properties of the dinuclear copper complex with **6** are much akin to those reported on triketonate dicopper complexes (*14, 15*), with the additional feature that the standard redox potential of the complex with **6** is positive and is close to those reported for type 3 copper proteins[1], at variance with other models (*14, 15*).

In addition, the results obtained on dinuclear copper complexes other than those with ligand **6** provide the answer to a question (*14*), as

Published on June 1, 1982 on http://pubs.acs.org | doi: 10.1021/ba-1982-0201.ch005

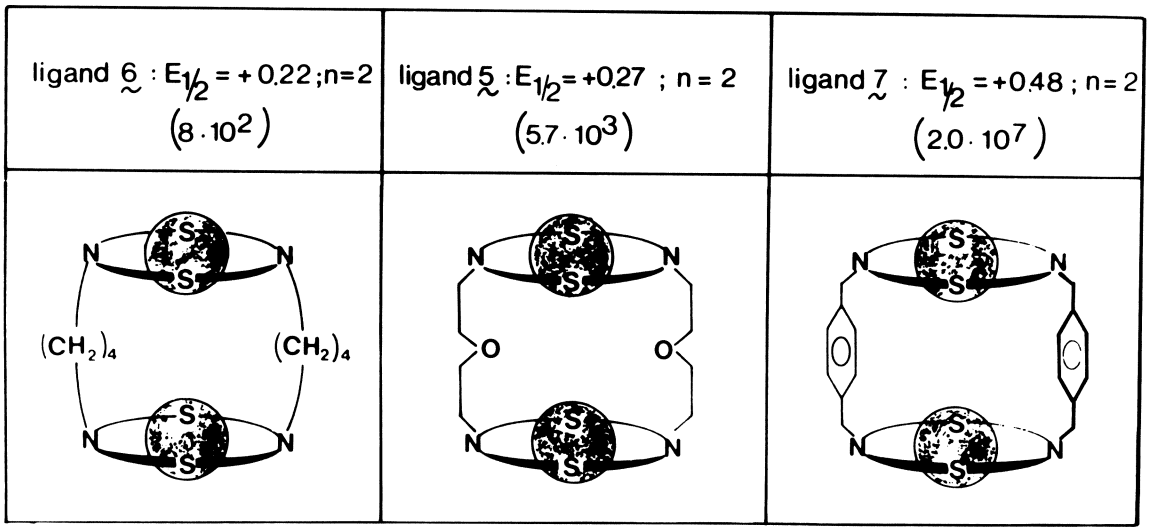

Figure 6. Effect of the side chain on the redox potential [Cu(II), Cu(II)]/[Cu(I), Cu(I)] and on the relative stability of cuprous to cupric dinuclear complexes with Ligands **10**, **11**, *and* **12**. *All* $E_{1/2}$ *are in Table II. Values of* $\{K_{stab}$ *of* $[Cu(I)]_2L/K_{stab}$ *of* $[Cu(II)]_2L\}$ *are* 5.7×10^3, 8×10^2, *and* 2.0×10^7 *for* **10**, **11**, *and* **12**, *respectively. Medium: PC + 0.1 M TEAP.*

they demonstrate clearly that the two adjacent coppers(II) in a complex do not need to be strongly interacting to allow a reversible, two-electron cathodic transfer, as already discussed in a previous paper devoted to the dinuclear complex with **10** (*15*).

Conclusion

First, the mononuclear complexes studied revealed that the formal redox potential of Cu(II)/Cu(I) is anodically shifted, that is, copper(I) stabilized vs. copper(II), by increasing the number of sulfur atoms in the macrocyclic ligands. This trend is verified for a given ligand structure (for instance from **1a** to **1c**, from **5** to **4a**) and also when thioether groups are increasingly introduced into the macrocyclic ligand, for example, from **2** to 3 and **4**. Oxygen heteroatoms in a ligand are unfavorable to the conversion of copper(II) to copper(I) in these mononuclear complexes. These results are consistent with, and to some extent predictable from previous observations on other complexes (*5*, *6*) as well as from HSAB considerations (*44*). Second, the formal redox potential of Cu(II)/Cu(I) also is shifted anodically when steric strains are exerted on the complexing macrocycle such that conformational changes occur that alter the preferred coordination of copper(II). Such changes may very well result from the substitution of bulky groups (like methyl or benzyl) for hydrogen on the nitrogens.

With dinuclear cryptates, the results obtained are consistent with the conclusions drawn from the results on mononuclear cryptates, and they provide additional information:

- The Cu(II)/Cu(I) potential depends almost always on the coordinating site, so that two identical sites induce a single two-electron transfer, whereas nonidentical sites (*see* Ligand **8**) induce two distinct, one-electron steps.
- Specific effects of the bicyclic structure of the ligand are observable, as for instance with Ligand **9** where $E°$ Cu(II)/Cu(I) is quite similar to the potential observed in the presence of thioethers (Ligands **10**, **11**, and **12**), and is at variance with the results in corresponding mononuclear cryptates (Ligands **4** and **5**).
- The occurrence of a reversible, two-electron transfer is independent of the coordination of bridging units between the two coppers (*see* complex with **6** and **10**).

Thus, unambiguous information is now made available on the ligand design required to form stable copper(II) and copper(I) complexes whose redox properties mimic satisfactorily those of copper proteins.

More generally, the above results on the redox properties of mononuclear and dinuclear copper complexes provide rational ele-

ments in understanding the control of redox potentials in natural multielectron metalloorganic redox mediators.

Until now wide efforts had been directed to the control of redox potentials of models. Convincing evidence exists that such control may indeed be achieved efficiently through appropriate substitutions in the ligand(s) and/or coordination changes on the metal ion. Typically, the redox potential of a given couple in such systems may be shifted by an interval as large as 1 V (*54*). However, in many circumstances the shift of the redox potentials through such means is rather questionable in living systems.

The results presented in this chapter provide reasonable clues to the possibility of achieving the control of redox potentials mainly through the conformation of the ligand surrounding the redox active metal, in addition to the effects on the potentials of the chemical composition of the ligand.

Acknowledgments

We are indebted to S. Sullivan, B. Dietrich, A. Alberts (Laboratoire de Chimie Organique Physique) and J. M. Lehn (Université Louis Pasteur, Strasbourg) for the syntheses of the ligands.

Literature Cited

1. Gray, H. B. In "Bioinorganic Chemistry," Dessy, R.; Dillard, J.; Taylor, L., Eds.; ACS ADVANCES IN CHEMISTRY SERIES, No. 100, ACS: Washington, D.C., 1971; p. 365.
2. Fee, J. A. *Struct. Bonding* **1975,** *23,* 1–60.
3. James, B. R.; Williams, J. P. *J. Chem. Soc.* **1961,** 2007.
4. Hawkins, C. J.; Perrin, D. D. *J. Chem. Soc.* **1962,** 1351.
5. Patterson, G. S.; Holm, R. H. *Bioinorg. Chem.* **1975,** *4,* 257.
6. Dockal, E. R.; Jones, T. E.; Sokol, W. F.; Engerer, R. J.; Rorabacher, D. B.; Ochrymowycz, L. A. *J. Am. Chem. Soc.* **1976,** *98,* 4322.
7. Louis, R.; Agnus, Y.; Weiss, R.; Gisselbrecht, J. P.; Gross, M. *Nouv. J. de Chimie,* **1981,** 5 (2), 71.
8. Harris, C. M.; Hoskins, B. F.; Martin, R. L. *J. Chem. Soc.* **1959,** 3728.
9. Majumbar, A. K.; Saka, S. C. *J. Indian Chem. Soc.* **1973,** *50,* 697.
10. Corbett, M.; Hoskins, B. F.; McLeod, N. J.; O'Day, B. P. *Acta Crystallogr., Sect. A* **1972,** *28,* 576.
11. Gupta, S.; Kalia, K. C.; Chatravorty, A. *Inorg. Chem.* **1971,** *10,* 1534.
12. de Courcy, J. S.; Waters, T. N.; Curtis, N. F. *J. Chem. Soc., Chem. Comm.* **1977,** 572.
13. Fenton, D. E.; Schroeder, R. R.; Lintvedt, R. L. *J. Am. Chem. Soc.* **1978,** *100,* 1931.
14. Fenton, D. E.; Lintvedt, R. L. *J. Am. Chem. Soc.* **1978,** *100,* 6367.
15. Gisselbrecht, J. P.; Gross, M.; Alberts, A. H.; Lehn, J. M. *Inorg. Chem.* **1980,** *19,* 1386.
16. Alberts, A. H.; Annunziata, R.; Lehn, J. M. *J. Am. Chem. Soc.* **1977,** *99,* 8502.
17. Louis, R.; Agnus, Y.; Weiss, R. *J. Am. Chem. Soc.* **1978,** *100,* 3604.

18. Kahn, O.; Morgenstern-Badaray, I.; Audière, J. P.; Lehn, J. M.; Sullivan, S. *J. Am. Chem. Soc.* **1980,** *102,* 5935.
19. Lehn, J. M. *Struct. and Bonding* **1973,** *16,* 1.
20. Dietrich, B.; Lehn, J. M.; Sauvage, J. P. *Tetrahedron Lett.* **1969,** *34,* 2885.
21. Dietrich, B.; Lehn, J. M.; Sauvage, J. P. Chem. Commun. **1970,** 1055.
22. Arnaud-Neu, F.; Spiess, B.; Schwing-Weill, M. J. *Helv. Chim. Acta* **1977,** *60,* 263.
23. Sullivan, S.; Lehn, J. M., personal communication.
24. Herceg, M.; Weiss, R. *Inorg. Nucl. Chem. Lett.* **1970,** *6,* 435.
25. Herceg, M.; Weiss, R. *Acta Crystallogr., Sect. B* **1973,** *29,* 542.
26. Levich, V. G. "Physicochemical Hydrodynamics"; Prentice–Hall: New York, 1962.
27. Butler, C. G.; Kaye, R. C. *J. Electroanal. Chem.* **1964,** *8,* 463.
28. Nicholson, R. S. *Anal. Chem.* **1965,** *37,* 1351.
29. Diggle, J. W.; Parker, A. J. *Aust. J. Chem.* **1974,** *27,* 1617.
30. Kolthoff, I. M.; Lingane, J. J. "Polarography"; Wiley: New York, 1952; p. 217.
31. Heyrovsky, J.; Kuta, J. "Principles of Polarography"; Academic: New York, 1966; p. 157.
32. Latimer, W. "Oxidation Potentials"; Prentice–Hall: New York, 1952.
33. Kolthoff, I. M.; Coetzee, J. F. *J. Am. Chem. Soc.* **1957,** *79,* 1852.
34. Yves, D. G. J.; Janz, G. J. "Reference Electrodes"; Academic: New York, 1961; p. 333.
35. Dobos, D. "Electrochemical Data"; Am. Elsevier: New York, 1975; p. 248.
36. Khomutov, N. E. *Russ. J. Phys. Chem.* **1962,** *36,* 1095; **1964,** *38,* 681; **1966,** *40,* 315.
37. Tindall, G. W.; Bruckenstein, S. *Anal. Chem.* **1968,** *40,* 1402.
38. Bossu, F. P.; Chellappa, K. L.; Margerum, D. W. *J. Am. Chem. Soc.* **1977,** *99,* 2195.
39. Grimshaw, J.; Hamilton, R. *J. Electroanal. Chem.* **1980,** *106,* 339.
40. Addison, A. W.; Stenhouse, J. H. *Inorg. Chem.* **1978,** *17,* 2161.
41. Bjerrum, J.; Ballhausen, C. J.; Jorgensen, C. K. *Acta Chem. Scand.* **1954,** *8,* 1245.
42. Furlani, C.; Morpurgo, G. *Theor. Chim. Acta* **1963,** *1,* 102.
43. Sacconi, L.; Giampolini, M. *J. Chem. Soc.* **1964,** 276.
44. Pearson, R. G. *J. Chem. Educ.* **1968,** *45,* 581, 643.
45. Cotton, F. A.; Wilkinson, G. "Advanced Inorganic Chemistry," 3rd ed.; Wiley: New York, 1972; p. 904.
46. Mehrotra, P. K.; Hoffmann, R. *Inorg. Chem.* **1978,** *17,* 239.
47. Agnus, Y.; Louis, R.; Weiss, R. *J. Am. Chem. Soc.* **1979,** *101,* 3381.
48. Arnaud-Neu, F.; Schwing-Weill, M. J., unpublished data.
49. Peter, F.; Gross, M.; Pospisil, L.; Kuta, J. *J. Electroanal. Chem.* **1978,** *90,* 239.
50. Myers, R. L.; Shain, I. *Anal. Chem.* **1969,** *41,* 980.
51. Ammar, F.; Savéant, J. M. *J. Electroanal. Chem.* **1973,** *47,* 215.
52. Flanagan, J. B.; Margel, S.; Bard, A. J.; Anson, F. *J. Am. Chem. Soc.* **1978,** *100,* 4248.
53. Gisselbrecht, J. P.; Gross, M., unpublished data.
54. Giraudeau, A.; Callot, H. J.; Jordan, J.; Ezahr, I.; Gross, M. *J. Am. Chem. Soc.* **1979,** *101,* 3857.

RECEIVED for review June 30, 1981. Accepted November 30, 1981.

The Synthesis, Electrochemistry, and Reactivity of Binuclear Copper(I) Complexes as Mimics of Protein Active Sites

ROBERT R. GAGNÉ, ROBERT P. KREH,[1] and JOHN DODGE

California Institute of Technology, Division of Chemistry and Chemical Engineering, Pasadena, CA 91125

Several binuclear cuprous complexes were synthesized as potential models for binuclear copper protein sites. Appropriate modifications of the polydentate ligand systems resulted in a wide range of reduction potentials. In this manner, utilizing only nitrogen and oxygen ligands, high reduction potentials comparable to those of the protein binuclear sites were achieved. The new binuclear copper(I) complexes appear to be only tricoordinated in solution but in some instances demonstrate significant copper(I)–copper(I) interactions in the solid state. The CO and O_2 reactivities of these compounds also were explored.

An understanding of the interactions between dioxygen and transition metal sites in proteins is valuable from a pedagogical standpoint as well as for possible practical applications to electron transfer catalysis [e.g., the reduction of dioxygen to water in fuel cells (*1*)]. For copper proteins, a binuclear active site is utilized for a direct interaction with molecular oxygen. These proteins include hemocyanin, which is responsible for reversible oxygenation in the blue blood of various mollusks and arthropods (*2*); tyrosinase, which catalyzes the oxidation of substrates by dioxygen in a variety of organisms (*3, 4*); and laccase, which catalyzes the reduction of dioxygen to water and is found in Asian lacquer trees and white rot fungi (*5, 6*).

[1] Current address: University of Georgia, Department of Chemistry, Athens, GA 30602

0065-2393/82/0201-0139$06.00/0

Several interesting features in these copper proteins were noted and investigated:

1. Although the exact number and geometry of the ligands bound to the copper centers is unknown, nitrogenous ligands (histidine, in particular) were implicated (*7*). A peroxide moiety bridging the two cupric ions in oxyhemocyanin and oxytyrosinase was popularized (*8–11*).
2. In the oxidized forms, all three binuclear cupric sites are strongly antiferromagnetically coupled (*12, 13*).
3. The tyrosinase and laccase binuclear sites exhibit two-electron reductions at potentials that are rather high (≥0.36 V vs. NHE) for the proposed all nitrogen–oxygen copper coordination (*13–16*).

These properties and the dioxygen binding of these copper sites have been addressed by direct study of the proteins and investigations of appropriate model compounds. Some success was attained in mimicking the binuclear copper active sites in terms of ligand environments, redox properties, magnetic interactions, and dioxygen binding (*17–28*). To help elucidate the relationships between ligand environments, redox potentials, and dioxygen reactivity we investigated the chemistry of a series of binuclear copper(I) complexes. To clearly define and preserve the coordination sphere around each copper, polydentate ligands were employed (*29–32*). We approximated the proposed protein ligand environment as closely as possible, and thus, only nitrogen and oxygen donors were used.

The first series of binuclear copper compounds to be discussed were generated by modifications on the macrocyclic ligand system in Compound **1.**

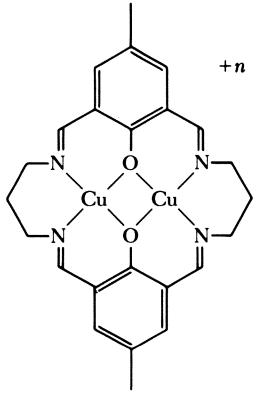

1

The second system employs the potentially binucleating ligand *N,N,N',N'*-tetrakis(2-pyridylmethyl)ethylendiamine (TPEN).

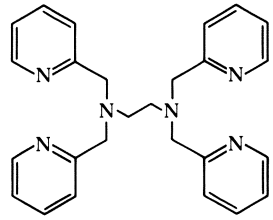

TPEN

Through variation of the polydentate ligands, unusual copper(I) coordination environments were found, and a wide range of reduction potentials were realized.

Binuclear Systems Derived from 2-Hydroxy-5-Methylisophthalaldehyde

Our initial work on binuclear systems focused on Compound **1**, synthesized previously (*31–33*). This binuclear complex exhibits a two-step reduction at −0.52 and −0.91 V vs. NHE. These very negative potentials indicate the destabilization of copper(I) relative to copper(II), which most likely results from the square-planar arrangement of "hard" oxygen and nitrogen ligands. [Structural and electronic factors influencing copper reduction potentials were documented (*34*).]

To stabilize copper(I) and thereby raise the reduction potentials toward the high values found for tyrosinase and laccase, binucleating ligands that contain somewhat "softer" aromatic nitrogen ligands in a more flexible framework (to allow a tetrahedral geometry around each copper) were designed. This approach led to the synthesis of Complexes **2–4**, shown in Scheme I along with visible absorption and magnetic data (*35*). [During the course of this work, complexes similar to **3** and **4** were reported by others (*36*)]. In all three copper(II) complexes, both copper atoms are presumably bound to an aromatic nitrogen. This bonding was demonstrated by an x-ray structural determination of Compound **4** (*37*). (*See* Table I for compound numbers and structures.) Each copper(II) is actually pentacoordinated; one copper atom is bound to the oxygen of a water molecule and the other copper is bound to the oxygen of the hydroxy bridge of an adjacent molecule.

The electrochemistry of these nonmacrocyclic complexes, **2–4**, is irreversible as shown in Figure 1 for Compound **2**, in dimethylformamide (DMF). This irreversibility may be a result of the relatively

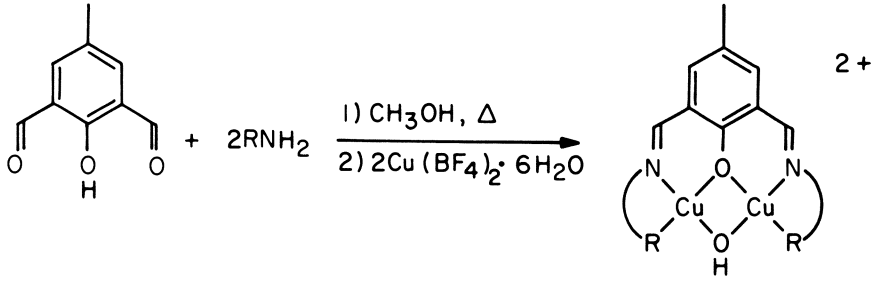

	R	λ (ε)	μ_{eff}/Cu
2	$-CH_2-$ 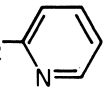	630(160)	1.4
3	$-CH_2CH_2-$ 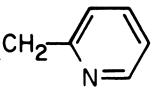	645(120)	1.2
4	$-CH_2CH_2-$ 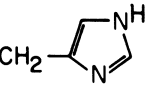	630(100)	0.96

*Scheme I. Preparation of binuclear copper(II)–copper(II) complexes (**34**). Spectra were recorded in methanol solution at 25°C. Magnetic susceptibilities are given in B.M., measured at 25°C, and corrected for diamagnetism, but not for TIP.*

labile hydroxy bridge, which is a poor ligand for copper(I). The introduction of pyrazole did produce reversible electrochemical behavior, also shown in Figure 1. Similar results were observed for Compound **3**, but Compound **4** gave irreversible electrochemistry even with added pyrazole.

Controlled potential electrolysis (CPE) at −0.35 and −0.70 V of Compound **2**, plus an equivalent amount of pyrazole, indicated that each wave corresponds to a one-electron process. No attempt was made to isolate a mixed-valent species; but the binuclear cuprous complex, Compound **5**, was synthesized by CPE at −0.70 V (n = 2.0) of an acetonitrile solution containing Compound **2** and an equivalent amount of pyrazole (35).

Compound **5** also was synthesized directly from cuprous starting materials. Similar reactions with 2-aminomethylpyridine or 2-(2′-aminoethyl)pyridine as sidearms and with pyrazole and 3,5-dimethylpyrazole as bridging ligands gave Complexes **6–8**. (*see* Table

Published on June 1, 1982 on http://pubs.acs.org | doi: 10.1021/ba-1982-0201.ch006

Table I. Binuclear Copper Complexes and Reduction Potentials

$$Cu(II)Cu(II)L^{+3} + e^- \overset{E_1^f}{\rightleftharpoons} Cu(II)Cu(I)L^{+}$$

$$Cu(II)Cu(I)L^{+2} + e^- \overset{E_2^f}{\rightleftharpoons} Cu(I)Cu(I)L$$

Compound Number	*Sidearm* (R)	*Bridge* (X)	E_1^f [a]	E_2^f [a]	n [b]
1	—	—	−0.52	−0.91	2.0 [c]
2	2-(pyridyl)methyl	hydroxide	[d]	[d]	[d]
3	2-(2′-pyridyl)ethyl	hydroxide	[d]	[d]	[d]
4	2-(4′-imidazoyl)ethyl	hydroxide	[d]	[d]	[d]
5	2-(pyridyl)methyl	pyrazolate	−0.211	−0.452	2.0
6	2-(pyridyl)methyl	3,5-dimethyl-pyrazolate	−0.190	−0.374	—
7	2-(2′-pyridyl)ethyl	pyrazolate	−0.110	−0.344	2.0
8	2-(2′-pyridyl)ethyl	3,5-dimethyl-pyrazolate	−0.113	−0.267	2.0
9	phenylmethyl	pyrazolate	0.146	−0.081	—
10	phenylmethyl	3,5-dimethyl-pyrazolate	0.206	0.005	—
11	2-phenylethyl	pyrazolate	0.128	−0.078	—
12	2-phenylethyl	3,5-dimethyl-pyrazolate	0.205	0.009	—
13	1-propyl	pyrazolate	0.146	−0.076	—
14	2-propyl	pyrazolate	0.193	0.001	1.9
15	*t*-butyl	pyrazolate	0.240	0.053	2.0
16	*t*-butyl	3,5-dimethyl-pyrazolate	0.239	0.080	—
17	phenyl	pyrazolate	0.144	−0.032	—
18	*p*-(dimethylamino)-phenyl	pyrazolate	0.146	−0.048	—
19	*p*-acetylphenyl	pyrazolate	0.152	0.008	—

Note: These values were measured by differential pulse polarography in DMF using a platinum indicating electrode.

[a] Potentials are given in V vs. NHE. Potentials were measured vs. ferrocene as an internal redox couple, then corrected to vs. NHE using a value of 0.40 V for ferrocene vs. NHE (*24*, *38*, *39*).

[b] These values for n were determined by CPE at a potential 200 mV more positive than E_1^f.

[c] This value was determined by CPE at −1.16 V (*31*, *32*).

[d] Irreversible electrochemistry.

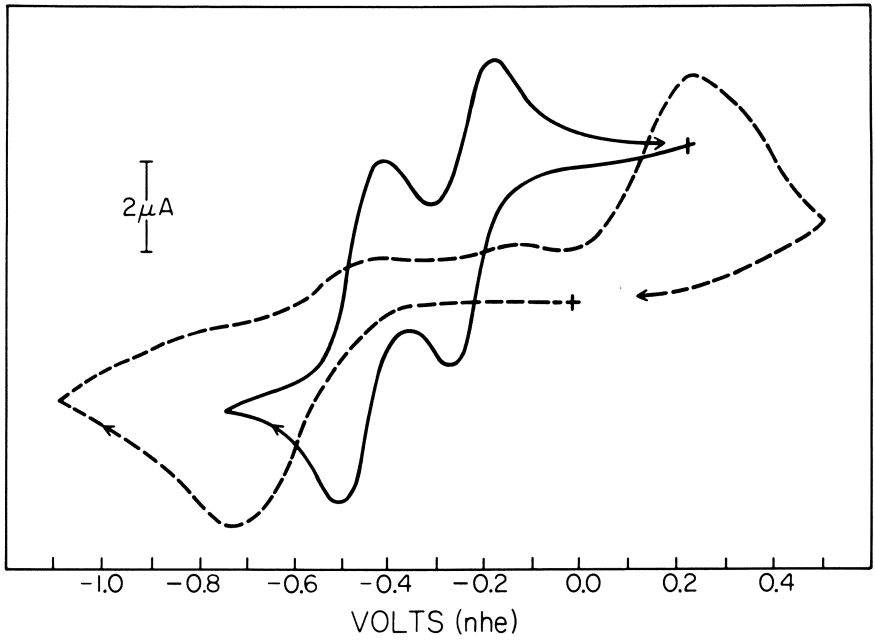

Figure 1. Cyclic voltammograms of DMF solutions of Compound **2** *(----), and Compound* **2** *containing one equivalent of pyrazole (—). Both voltammograms were observed with a platinum electrode, using 0.1 M TBAP as the electrolyte at a scan rate of 200 mV/s. (Reproduced from Ref. 35. Copyright 1979, American Chemical Society.)*

I and Scheme II.) The coordination environment around each copper(I) of these complexes was expected to be a tetrahedral arrangement of one oxygen and three nitrogen ligands. A crystallographic analysis of Compound **7**, did not yield the expected structure, however.

Crystallographic Analysis of Compound 7

The actual structure of **7** is depicted in Figure 2 along with pertinent bond distances (*35*). The pyridine nitrogen atoms are not coordinated and each copper is bound to three ligand atoms in what is almost a T-geometry, with the largest angles being between the imine and pyrazolate nitrogens. The copper–nitrogen bonds are shorter than most distances that were reported for copper(I) complexes with nitrogen ligands (*22*, *23*, *40–43*). The average lengths are 1.88 Å for the copper–pyrazole nitrogen bonds and 1.90 Å for the copper–imine nitrogen bonds. The copper–oxygen distances are substantially longer, averaging 2.09 Å. These bond lengths, along with the very large

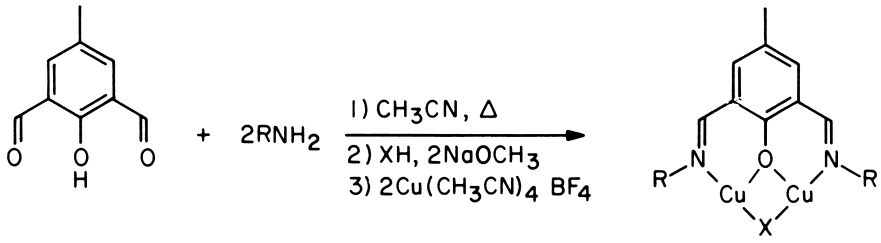

Scheme II.

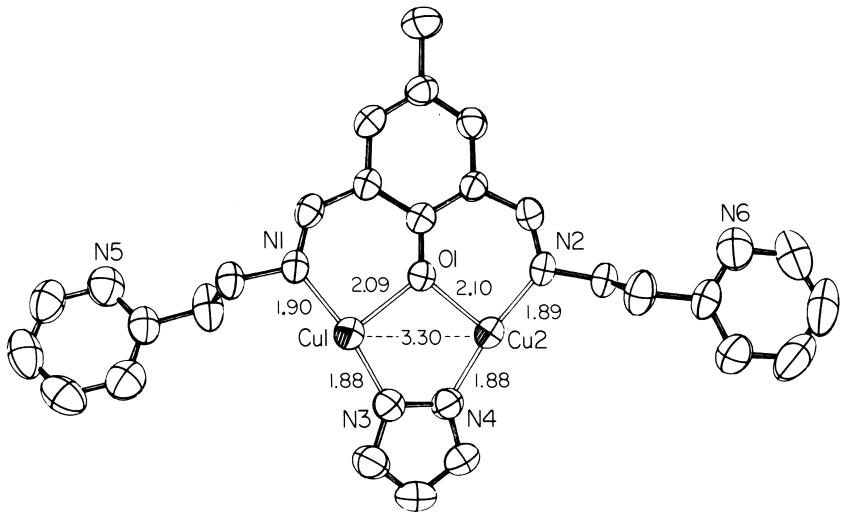

Figure 2. Molecular structure of Compound 7, including labels for noncarbon atoms and selected bond lengths (35). Bond angles: N1-Cu1-N3, 167.6°; O1-Cu1-N1, 91.7°; O1-Cu1-N3, 97.1°; N2-Cu2-N4, 170.7°; O1-Cu2-N2, 91.5°; and O1-Cu2-N4, 96.8°.

N–Cu–N bond angles (ca. 170°) may suggest some degree of dicoordinated character, which may be especially favorable for copper(I) interactions with these nitrogenous ligands.

The intramolecular copper–copper distance, 3.304 Å, is long enough to make any direct interaction unlikely. However, an intermolecular interaction apparently does occur between copper atoms. The molecules line up in an infinite array such that relatively close contact (2.968 Å) exists between copper atoms of adjacent molecules (Figure 3). The overlapping ligand atoms of neighboring molecules also come close to one another. The mean plane containing the phenoxide oxygen, the imine nitrogen, and the three carbons con-

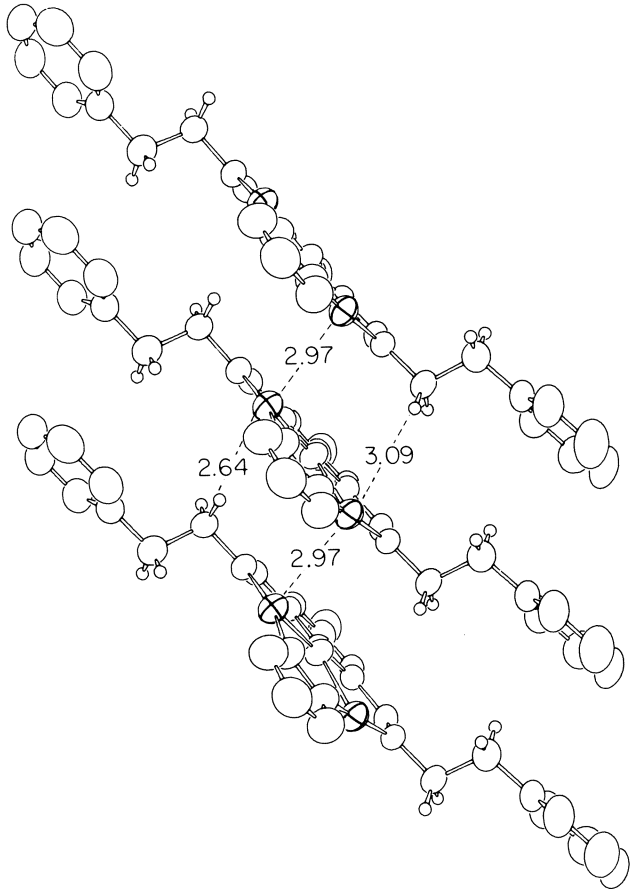

Figure 3. Crystal packing of Compound **7**, *showing a section of an infinite stack of molecules that forms in the solid state. The three molecules are corresponding ones from three different unit cells, translated along the* b *axis (which lies in the vertical direction in the orientation of this figure). All copper atoms lie in the same plane, parallel to the page. The pyrazolate groups are directed out of the page, toward the reader. The shortest copper–copper distance, 2.97 Å, occurs between atoms in neighboring molecules, connected by dashed lines in the figure. The closest intermolecular Cu–H contacts also are shown (*35*).*

necting these atoms is situated at an average distance of 3.20 Å away from the corresponding plane directly below in the neighboring molecule. This distance is somewhat shorter than the separation usually observed between stacked π-delocalized molecules (*44–46*).

Thus, an intermolecular copper–copper bond and/or an interaction between the delocalized π-systems of adjacent molecules appears

to be favored in the solid state. Copper(I)–copper(I) interactions with metal separations as short as 2.45 Å are known, but all previously characterized species with proposed copper(I)–copper(I) interactions have at least one bridging ligand between the two interacting copper atoms (*47–49*). The structures of the analogous species, **5–8,** are probably similar to this structure found for Compound **7.**

Synthesis and Solution Structures of Compounds 9–19

The structure of Compound **7** suggested the synthesis of a series of compounds that had no donor atoms on the sidearms (R), that is, Complexes **9–19,** Table I. These compounds were synthesized analogously to the synthesis of Compounds **5–8** (Scheme II). All cuprous compounds were fully characterized by elemental analysis, IR and NMR spectroscopy, and mass spectroscopy on selected compounds (*35*). These compounds also proved to be crystalline solids, stable in the absence of dioxygen. Because the polydentate ligand systems employed provide only tricoordination for each copper, these compounds are presumed to be tricoordinated in solution.

All compounds that have nonbulky sidearms are brown in the solid state, this color being due, in part, to a 600-nm band observed in the solid state nujol mull spectrum (Curve A in Figure 4). This band is not present in the spectrum of the complex with *t*-butyl sidearms, Compound **15,** which is red in the solid state as well as in solution (Curve C, in Figure 4). This 600-nm absorption also is absent in the spectra of Compounds **14** and **16.** The 600-nm band may be attributed to an intermolecular interaction that may be inhibited by the presence of large *t*-butyl sidearms. This interaction appears to be only a solid state phenomenon, because the 600-nm band was not found in solution spectra (e.g., Curve B, Figure 4), even in very concentrated solutions.

The solution structure of Compound **7** appears to be similar to that found in the solid state with the absence of the intermolecular copper–copper interaction. The pyridine nitrogens do not appear to be bound in benzene solution, because the NMR signal for the proton on the carbon adjacent to the pyridine nitrogen of Compound **7** occurs at the same position, within experimental error, as the corresponding proton from 2-(2′-aminoethyl)pyridine (i.e., 8.44 ± 0.02 ppm δ from TMS). In fact, all compounds that contain pyridine on the sidearms exhibit this resonance at the same position, within experimental error (i.e., 8.42 ± 0.04 ppm δ from TMS). The resonance of this proton would be expected to shift downfield on binding to a copper(I) ion. (We observed this effect for the ligand *N,N,N′,N′*-tetrakis(2-pyridylmethyl)-ethylenediamine (TPEN), where binding of copper(I) to the pyridine nitrogens causes a downfield shift of 0.13 ppm for the ring proton

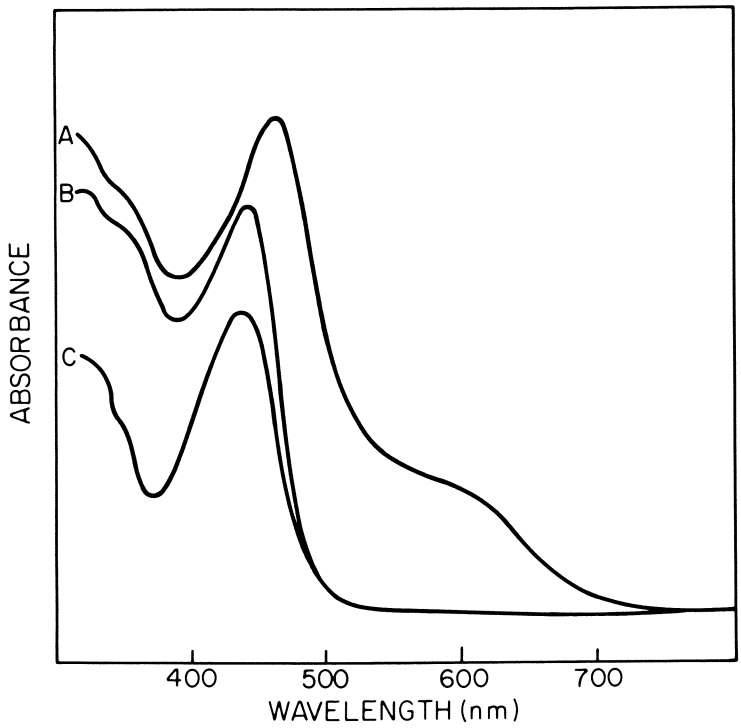

Figure 4. Electronic absorption spectra. Key: A, Compound 11 in the solid state; B, Compound 11 in a hexane solution; and C, Compound 15 in the solid state. (Reproduced from Ref. 35. Copyright 1979 American Chemical Society.)

nearest nitrogen (*50*). Downfield shifts of 0.4–0.7 ppm were observed for the proton in the 2-position of an imidazole ring on binding copper(I) (*51*). Furthermore, sharp resonances were observed for the pyrazole protons of these compounds (e.g., a doublet at 7.87 ppm and a triplet at 6.43 ppm for Compound **14**). This observation indicates that there is no equilibrium between bound and unbound pyrazole; hence, the pyrazolate bridge must be totally bound to the copper(I) ions or totally dissociated in benzene solutions (unlikely, at best).

Electrochemical Analysis for the Series 5–19

All binuclear copper(I) compounds presented in Table I exhibited cyclic voltammetry similar to the solid line in Figure 1, but a wide range of reduction potentials were observed (*35*). Several trends can be observed from Table I. In the following discussion, the formal potentials for the second reduction, (E_2^f), Equation 1, will be used since these processes were more reversible and slightly more systematic

$$Cu(II)Cu(I)L^+ + e^- \overset{E_1^f}{\rightleftharpoons} Cu(I)Cu(I)L \quad (1)$$

than the E_1^f potentials. The general trends, however, are the same with both processes.

The first point of interest is the effect of possible binding sites (i.e., pyridine) in the sidearms. The following series of potentials (E_2^f) was observed: Compound **11**, (−0.078 V) ≈ Compound **9**, (−0.081 V) ≫ Compound **7**, (−0.344 V) > Compound **5**, (−0.452 V). This finding indicates that the complexes containing the pyridine rings provide a more favorable environment for copper(II) relative to copper(I) when compared to their benzene ring analogues. Because the pyridine nitrogens do not appear to be bound to the copper(I) ions (in solution or in the solid state), the effect of these pyridine rings must be largely on the oxidized copper(II) sites. Hence, the pyridines apparently bind to the copper ions on oxidation, Compound **20**, and dissociate from copper(I) on reduction, Compound **7**, (Scheme III). In the similar cupric complex, **4**, the imidazole nitrogens were shown to be coordinated in the solid state x-ray structure (*37*). Most likely, sidearm pyridine nitrogens would also coordinate to copper(II). The dependence of the cyclic voltammogram on scan rate (as a result of the process in Scheme III) was not investigated. Compounds **5–19** also indicate that the methylpyridine sidearm provides a better environment for copper(II) than does the ethylpyridine sidearm. This condition may be a result of the geometry of the sidearms and their relative ability to bind to the copper(II) centers.

The introduction of methyl substituents on the pyrazolate bridges causes an increase in the reduction potential (E_2^f) as follows: Compound **6**, (−0.374 V) > Compound **5**, (−0.452 V) and Compound **10**, (+0.005 V) > Compound **9**, (−0.081 V). An inductive effect of the methyl groups would stabilize copper(II) relative to copper(I), but the reverse trend is actually observed. The steric bulk of the methyl groups

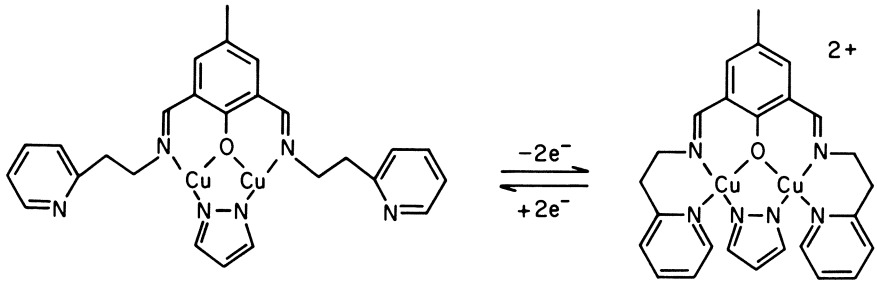

7 **20**

Scheme III.

may be responsible for the relative destabilization of copper(II). These methyl groups may inhibit the binding of both pyridine (from the sidearms) and dimethylformamide (solvent) to the oxidized copper(II) ions by partially blocking the fourth, square-planar binding site around each copper(II). Furthermore, shielding the copper centers from the solvent molecules with hydrophobic groups (such as these methyls) may not allow the polar DMF molecules to efficiently solvate the charged copper(II) species. Relative stabilization of copper(I) also results from more bulky sidearms, as reflected in the following series (E_2^f): Compound **15,** (+0.053 V) > Compound **14,** (+0.001 V) > Compound **13,** (−0.076 V).

Finally, an electronic effect on E_2^f is observed in the series of compounds that have phenyl rings bonded directly to the imine nitrogens: Compound **19,** (+0.008 V) > Compound **17,** (−0.032 V) > Compound **18,** (−0.048 V). Here, the electron-withdrawing carbonyl substituent results in relative copper(I) stabilization, while the electron-donating dimethylamine substituent results in relative Cu(II) stabilization. Similar effects of remote substituents were reported recently for a series of mononuclear copper(II) complexes (*24*).

The oxidation/reduction of these compounds in two one-electron steps was the expected behavior for two interacting metal centers (*31*, *32*). This sequential behavior was observed for the series of binuclear complexes, **21,** recently investigated (*52*). Stepwise oxidation/reduction was also found for many ruthenium(II) dimers, in which closer proximity and greater interactions between the ruthenium centers correlates with a greater separation of the two redox processes (and larger comproportionation constants) (*53–56*). [A reversible two-electron reduction was observed for well-separated cupric ions (*27*),

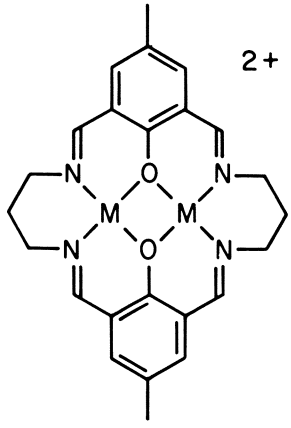

M = Mn, Fe, Co, Ni, Cu

21

and a curious exception to the stepwise electrochemistry exhibited by strongly interacting metals is reported for a series of binuclear triketonato copper(II) complexes (*25*).]

Binuclear Systems Derived from N,N,N',N'-Tetrakis(2-pyridylmethyl)ethylenediamine (TPEN)

The apparent preference of cuprous ions for lower coordination numbers (i.e., two, three, and four) (*35*, *47–49*, *57*) suggested the possibility of the hexadentate ligand, TPEN, performing as a bridging ligand between two copper(I) ions. Indeed, a binuclear cuprous complex, **22**, employing the TPEN ligand was synthesized as shown in Scheme IV (*50*). The structure of Compound **22**, was somewhat surprising and is shown in Figure 5 along with pertinent bond lengths and angles. Rather than the expected tricoordination or tetracoordination (including BF_4 as a ligand), each copper appears to bind only two nitrogen ligands at close distances (~1.9 Å), with a third, weak Cu–N interaction (2.30 Å). Furthermore, the two strongly bound nitrogen ligands, on a given copper, originate from pyridine rings on opposite ends of the ethylenediamine bridge. Apparently, the molecule adopts this conformation to maximize the copper–copper interaction (2.78 Å). The structures presented herein for Compounds **7** (Figure 2) and **22** (Figure 5) indicate a preference of copper(I) for a somewhat linear arrangement of two nitrogen ligands. [Coordination of this type was observed in other binuclear and mononuclear copper(I) complexes (*58–60*).] However, in both of the present cases the third ligand (i.e., phenolate oxygen or tertiary nitrogen) is rather "hard" and hence unfavorable for copper(I). Therefore, the observed coordination of these compounds may largely reflect preference for relatively "soft" ligands. Both systems (**7** and **22**) apparently foster a direct copper–copper interaction. [There is a theoretical basis for an attraction between copper(I) ions (*49*)].

Compound **22**, undergoes an extensive ligand rearrangement in the presence of carbon monoxide to form the dicarbonyl, **23** (Scheme IV) (*50*). The crystal structure of this complex revealed a pseudotetrahedral geometry as shown in Figure 6. Each copper is bound to three nitrogen ligands, with two short Cu–N distances of ca. 2.04 Å (between copper and the pyridine nitrogens) and one long Cu–N distance of ca. 2.17 Å (between copper and the tertiary amine nitrogen). Although the shorter Cu–N bond lengths are within the range expected for Cu(I)–N bonds (*29*, *30*, *47–49*, *61–63*), the Cu(I)–N (tertiary amine) distance is long, possibly indicating a lower affinity between the cuprous ion and the "hard" tertiary amine ligand. The Cu–C bond lengths average 1.80

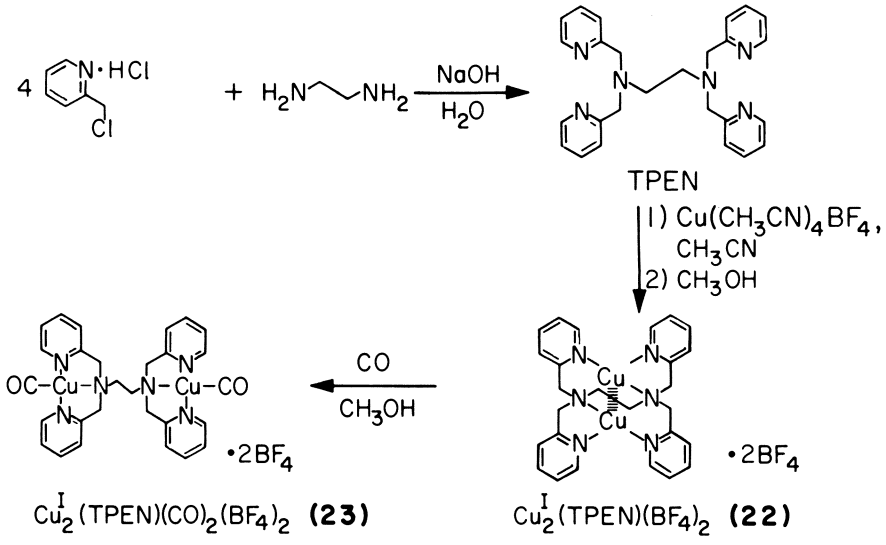

Scheme IV.

Å, and the C–O bond lengths average 1.11 Å with a Cu–C–O angle of 176°. These values are in agreement with other previously reported tetracoordinated and pentacoordinated copper(I) carbonyls (*30*, *61–63*).

Carbon Monoxide and Dioxygen Reactivity

In the TPEN system (i.e., **22** and **23**) the coordination environment about copper depends on the presence or absence of a potential fourth ligand (CO). In contrast, the series of Complexes **5–19** showed no tendency to bind CO or pyridine as a fourth ligand. The reason for this difference is not clear because molecular models indicate that Complexes **5–19** could form a pseudotetrahedral geometry with the addition of a fourth ligand. Thus, a special stabilization apparently occurs for cuprous ions in Complexes **5–19** such that significant energy would be lost on the binding of a fourth ligand (*60*).

To further complicate the issue of carbon monoxide binding to copper(I), a number of square-planar, tetracoordinated cuprous complexes (including **1**, $n = 1$) bind CO as a fifth ligand (*29–32*, *40*, *41*). Obviously, the geometry and type of ligands around copper(I) affect its CO binding ability. The nature of these effects, however, remains obscure. [Hemocyanin will bind only one molecule of carbon monoxide per binuclear copper(I) site (*64*).]

All copper(I) compounds reported herein react irreversibly with oxygen in solution. Compounds **5–19** form green or brown products from orange dimethylformamide solutions and Compounds **21** and **22** form blue products from colorless acetonitrile solutions. These autoxidation products were not characterized.

Conclusions

Stable binuclear copper(I) complexes were prepared using polydentate ligands. The structures reported in this chapter, as well as

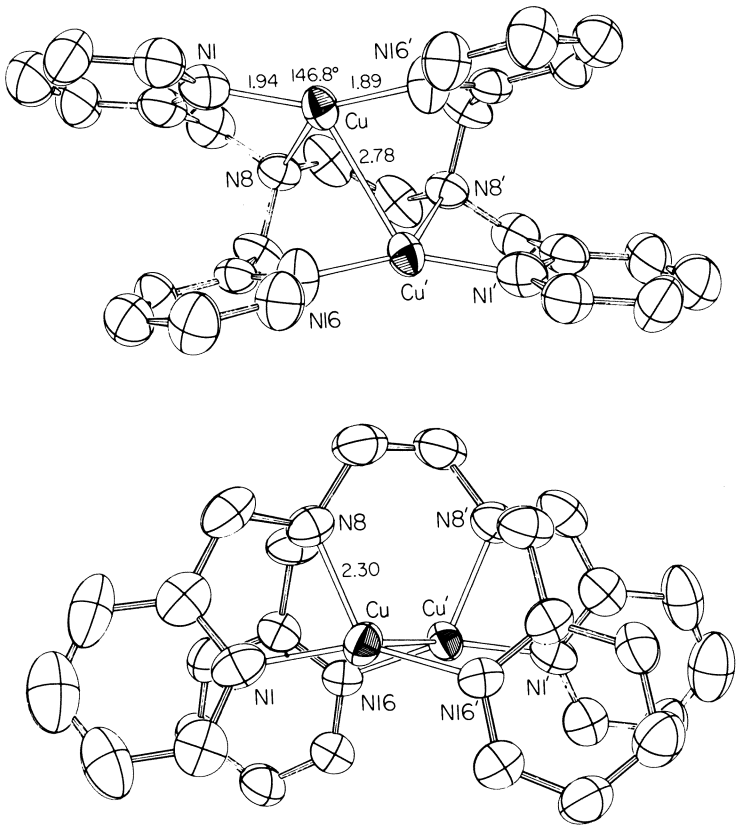

Figure 5. ORTEP diagrams of $Cu_2(TPEN)^{2+}$, including selected bond lengths and angles (50). The dication lies on a twofold rotation axis, perpendicular to the page in the upper drawing and parallel to the page in the lower one.

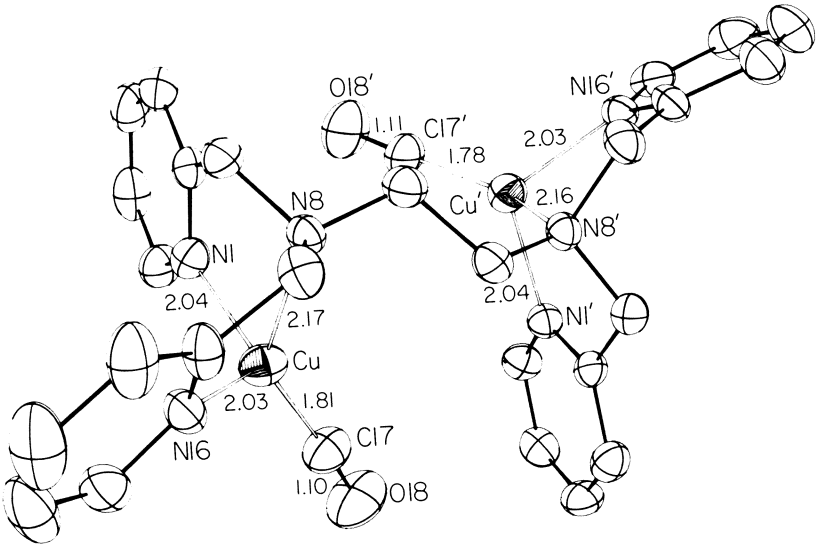

Figure 6. ORTEP drawing of $Cu_2(TPEN)(CO)_2^{2+}$, including selected bond lengths (50). This molecule, unlike $Cu_2(TPEN)^{2+}$, does not have exact twofold symmetry.

the structures found for other cuprous systems, demonstrate that a wide variety of coordination environments can be assumed by copper(I) ions. The number and geometry of ligands preferred by copper(I) are extremely sensitive to minor ligand alterations. These effects are not well-defined, and, as a result, one must exercise caution in the prediction of structures for cuprous compounds.

With the exception of Compounds **2–4, 21,** and **22,** which exhibited irreversible electrochemistry, all binuclear copper complexes exhibit two one-electron redox processes at well-defined potentials. By systematic variations in the bridging (X) and sidearm (R) groups (*see* Scheme II and Table I), a wide range of reduction potentials was realized. The highest reduction potentials were observed for Complex **16** in which the copper(I) centers are somewhat buried within the hydrophobic substituents. With reduction potentials of $E_1^f = 0.239$ V and $E_2^f = 0.080$ V, the ligand environment in **16** represents a substantial improvement over the original square-planar, tetracoordinated ligand environment provided by the starting model, **1.** These high reduction potentials are comparable to those of the protein binuclear sites (*13–16*); hence, it is not unreasonable to believe that these proteins utilize only nitrogen and/or oxygen ligands around each copper. Indeed, dicoordination and/or tricoordination can be considered for the reduced form of the binuclear sites.

The oxidation/reduction of these compounds in well-separated, one-electron steps contrasts with the available electrochemical information on the binuclear protein sites. Although no electrochemical data are available on hemocyanin, for both laccase and tyrosinase a single potential was associated with the overall two-electron reduction of the binuclear copper site (*13–16*, *65*). Correlations between the electrochemical behavior of the new compounds, **5–19**, and of the proteins are difficult because of solvation effects, the different techniques employed, possible nonequilibria in the proteins, and other reasons (*65*, *66*). Nonetheless, the electrochemical behavior reported for the new compounds suggests that the two-electron reduction of laccase and of tyrosinase is not a simple reduction of two equivalent copper ions that strongly interact through bridging ligands.

Acknowledgments

We greatly appreciate assistance given by Richard E. Marsh and Michael McCool, and financial support from the National Institutes of Health.

Literature Cited

1. Bockris, J.; Srinivasan, S. "Fuel Cells: Their Electrochemistry"; McGraw-Hill: New York, 1969.
2. Contie, R. In "Inorganic Biochemistry"; Eichhorn, G. I., Ed.; Am. Elsevier: New York, 1973; p. 344.
3. Mason, H. S. *Annu. Rev. Biochem.* **1965,** *35*, 595–634.
4. Vanneste, W. H.; Zuberbühler, A. In "Molecular Mechanisms of Oxygen Activation"; Hayaishi, O., Ed.; Academic: New York, 1974; p. 371.
5. Fee, J. A. Struct. Bonding **1975,** *23*, 1–60.
6. Vänngård, T. I. In "Biological Applications of Electron Spin Resonance"; Swartz, H. M.; Bolton, J. R.; Borg, D. C., Eds.; Wiley: New York, 1972; p. 411.
7. Wurzbach, J. A.; Grunthaner, P. J.; Dooley, D. M.; Gray, H. B., Grunthaner, F. J.; Gay, R. R.; Solomon, E. I. *J. Am. Chem. Soc.* **1977,** *99*, 1257–1258.
8. Freedman, T. B.; Loehr, J. S.; Loehr, T. M. *J. Am. Chem. Soc.* **1976,** *98*, 2809–2815.
9. Eickman, N. C.; Himmelwright, R. S.; Solomon, E. I. *Proc. Natl. Acad. Sci. U.S.A.* **1979,** *76*, 2094–2098.
10. Brown, J. M.; Powers, L.; Kincaid, B.; Larrabee, J. A.; Spiro, T. G. *J. Am. Chem. Soc.* **1980,** *102*, 4210–4216.
11. Larrabee, J. A.; Spiro, T. G. *J. Am. Chem. Soc.* **1979,** *102*, 4217–4223.
12. Solomon, E. I.; Dooley, D. M.; Wang, R.; Gray, H. B.; Cerdonia, M.; Mogno, T.; Romani, G. L. *J. Am. Chem. Soc.* **1976,** *98*, 1029–1031.
13. Makino, N.; McMahill, P.; Mason, H. S.; Moss, T. H. *J. Biol. Chem.* **1974,** *249*, 6062–6066.
14. Reinhammar, B. R. M.; Vänngård, T. I. *Eur. J. Biochem.* **1971,** *18*, 463–468.
15. Reinhammar, B. R. M. *Biochim. Biophys. Acta* **1972,** *275*, 245–259.

16. Farver, O.; Goldberg, M.; Lancet, A.; Pecht, I. *Biochem. Biophys. Res. Commun.* **1976,** *73,* 494–500.
17. Amundsen, A. R.; Whelan, J.; Bosnich, B. *J. Am. Chem. Soc.* **1977,** *99,* 6730–6739.
18. Simmons, M. G.; Wilson, L. J. *Chem. Commun.* **1978,** 634–636.
19. Bulkowski, J. E.; Burk, P. L.; Ludmann, M. F.; Osborn, J. A. *Chem. Commun.* 1977, 498–499.
20. Lehn, J. M.; Pine, S. H.; Watanabe, E.; Willark, A. K. *J. Am. Chem. Soc.* **1977,** *99,* 6766–6768.
21. Alberts, A. H.; Annunziata, R.; Lehn, J. M. *J. Am. Chem. Soc.* **1977,** *99,* 8502–8504.
22. Arcus, C. S.; Wilkinson, J. L.; Mealli, C.; Marks, T. J.; Ibers, J. A. *J. Am. Chem. Soc.* **1974,** *96,* 7464–7565.
23. Mealli, C.; Arcus, C. S.; Wilkinson, J. L.; Marks, T. J.; Ibers, J. A. *J. Am. Chem. Soc.* **1976,** *98,* 711–718.
24. Yokoi, H.; Addison, A. W. *Inorg. Chem.* **1977,** *16,* 1341–1349.
25. Fenton, D. E.; Lintvedt, R. L. *J. Am. Chem. Soc.* **1978,** *100,* 6367–6375.
26. Gagné, R. R.; Gall, R. S.; Lisensky, G. C.; Marsh, R. E.; Speltz, L. M. *Inorg. Chem.* **1979,** *18,* 771–781.
27. Louis, R.; Agnus, Y.; Weiss, R.; Gisselbrecht, J. P.; Gross, M. *Nouveau J. de Chemie* **1981,** *5(2),* 71–73.
28. Gisselbrecht, J. P.; Gross, M.; Alberts, A. H.; Lehn, J. M. *Inorg. Chem.* **1980,** *19,* 1386.
29. Gagné, R. R. *J. Am. Chem. Soc.* **1976,** *98,* 6709–6710.
30. Gagné, R. R.; Allison, J. L.; Gall, R. S.; Koval, C. A. *J. Am. Chem. Soc.* **1977,** *99,* 7170–7178.
31. Gagné, R. R.; Koval, C. A.; Smith, T. J. *J. Am. Chem. Soc.* **1977,** *99,* 8367–8368.
32. Gagné, R. R.; Koval, C. A.; Smith, T. J.; Cimolino, M. C. *J. Am. Chem. Soc.* **1979,** *101,* 4571–4580.
33. Pilkington, N. H.; Robson, R. *Aust. J. Chem.* **1970,** *23,* 225–236.
34. Patterson, G. S.; Holm, R. H. *Bioinorg. Chem.* **1975,** *4,* 257–275.
35. Gagné, R. R.; Kreh, R. P.; Dodge, J. A. *J. Am. Chem. Soc.* **1979,** *101,* 6917–6927.
36. Gryzbowski, J. J.; Merrell, P. H.; Urbach, F. L. *Inorg. Chem.* **1978,** *17,* 3078–3082.
37. Gagné, R. R.; McCool, M. W.; Marsh, R. E. *Acta Crystallogr., Sect. B* **1980,** *b36,* 2420.
38. Bauer, D.; Breant, M. In "Electroanalytical Chemistry"; Bard, A. J.; Ed.; Dekker: New York, 1975; Vol. 8, pp. 282–344.
39. Gagné, R. R.; Koval, C. A.; Lisensky, G. C. *Inorg. Chem.* **1980,** *19,* 2854–2855.
40. Gagné, R. R.; Allison, J. L.; Lisensky, G. C. *Inorg. Chem.* **1978,** *17,* 3563–3571.
41. Gagné, R. R.; Allison, J. L.; Ingle, D. M. *Inorg. Chem.* **1979,** *18,* 2767–2774.
42. Lewin, A. H.; Michl, R. J.; Gani, P.; Lepore, U. *Chem. Commun.* **1972,** 661–662.
43. Brown, I. D.; Dunitz, J. D. *Acta Crystallogr.* **1961,** *14,* 480–485.
44. Cotton, F. A.; Wilkinson, G. "Advanced Inorganic Chemistry"; Wiley: New York, 1972; p. 288.
45. Moustakali-Mavirdis, I.; Hadjoudis, E.; Mavridis, A. *Acta Crystallogr., Sect. B* **1978,** *b34,* 3709–3715.
46. Herbstein, F. H. In "Perspectives in Structural Chemistry"; Dunitz, J. D.; Ibers, J. A., Eds.; Wiley: New York, 1972; Vol. 4, p. 166.
47. Camus, A.; Marsich, N.; Nardin, G.; Randaccio, L. *Inorg. Chim. Acta* **1977,** *23,* 131–144.
48. Jardine, F. *Adv. Inorg. Chem. Radiochem.* **1975,** *17,* 115–163.

49. Mehrotra, P. K.; Hoffmann, R. *Inorg. Chem.* **1978,** *17,* 2187–2189.
50. Gagné, R. R.; Kreh, R. P.; Dodge, J. A.; Marsh, R. E.; McCool, M. *Inorg. Chem.* **1982,** *21,* 254–261.
51. Suguira, Y. *Inorg. Chem.* **1978,** *17,* 2177–2182.
52. Spiro, C. L., Ph.D. Dissertation, California Institute of Technology, Pasadena, CA, 1981.
53. Creutz, C.; Taube, H. *J. Am. Chem. Soc.* **1969,** *91,* 3988–3989.
54. Creutz, C.; Taube, H. *J. Am. Chem. Soc.* **1973,** *95,* 1086–1094.
55. Weaver, T. R.; Meyer, T. J.; Adeyemi, S. A.; Brown, G. M.; Eckberg, R. P.; Hatfield, W. E.; Johnson, E. C.; Murray, R. W.; Untereker, D. *J. Am. Chem. Soc.* **1975,** *97,* 3039–3048.
56. Callahan, R. W.; Keene, T. R.; Meyer, T. J.; Salmon, D. J. *J. Am. Chem. Soc.* **1977,** *99,* 1064–1073.
57. Ellen, P.; Bradley, D.; Hursthouse, M.; Meek, D. *Coord. Chem. Rev.* **1977,** *24,* 1–95.
58. O'Connor, J. E.; Janusonis, G. A.; Corey, E. R. *J. Chem. Soc. Chem. Commun.* **1968,** 445–446.
59. Brown, I. D.; Dunitz, J. D. *Acta Crystallogr.* **1961,** *14,* 480–485.
60. James, B. R.; Williams, R. J. P. *J. Chem. Soc.* **1961,** 2007–2019.
61. Bruce, M. I.; Ostazewski, A. P. *J. Chem. Soc., Dalton Trans.* **1973,** 2433–2436.
62. Churchill, M. R.; DeBoer, B. G.; Rotella, F. J.; Abu Salah, O. M.; Bruce, M. I. *Inorg. Chem.* **1975,** *14,* 2051–2056.
63. Pasquali, M.; Floriani, C.; Gaetani-Manfredotti, A. *Inorg. Chem.* **1980,** *19,* 1191–1197.
64. Fager, L. Y.; Alben, J. O. *Biochemistry* **1972,** *11,* 4786–4792.
65. Farver, O.; Goldberg, M.; Wherland, S.; Pecht, I. *Proc. Natl. Acad. Sci. U.S.A.* **1978,** *75,* 5245–5249.
66. Hill, C. L.; Renaud, J.; Holm, R. H.; Mortenson, L. E. *J. Am. Chem. Soc.* **1977,** *99,* 2549–2557.

RECEIVED for review June 2, 1981. ACCEPTED March 15, 1982.

The Heterogeneous Electron Transfer Properties of Cytochrome c

EDMOND F. BOWDEN and FRED M. HAWKRIDGE[1]

Virginia Commonwealth University, Department of Chemistry, Richmond, VA 23284

HENRY N. BLOUNT[1]

The University of Delaware, Brown Chemical Laboratory, Newark, DE 19711

The heterogeneous electron transfer kinetic parameters of horse heart cytochrome c were evaluated at pH 7.0. This work was directed at determining the formal heterogeneous electron transfer rate constant, $k^{o'}_{s,h}$, *and the electrochemical transfer coefficient,* α, *at three different electrode surfaces: gold electrodes electrochemically modified with methyl viologen, fluoride-doped tin oxide optically transparent electrodes (OTEs), and tin-doped indium oxide OTEs. Kinetic parameters of cytochrome c were evaluated using samples in the totally oxidized and in the totally reduced forms. Kinetic effects arising from anion binding to cytochrome c were investigated for phosphate and chloride in the presence of the nonbinding buffer tris(hydroxymethyl)aminomethane–cacodylic acid. The kinetic parameters were determined using single potential step chronoabsorptometry at all three electrodes and using rotating disk electrode voltammetry at the methyl viologen-modified gold disk electrode.*

The thermodynamics and homogeneous electron transfer kinetics of cytochrome c have been studied widely. Extensive reviews point to the important questions that remain unanswered regarding the mechanism by which electrons are transferred by cytochrome c in mammalian oxidative phosphorylation (*1–8*). The pathway by which

[1] To whom correspondence should be addressed.

0065-2393/82/0201-0159$06.00/0

cytochrome c accepts electrons from the membrane-bound cytochrome c reductase and then donates electrons to cytochrome c oxidase, which is also membrane bound, remains a point of controversy. The impetus for studying the energetics and kinetics of cytochrome c electron transfer reactions derives primarily from the need to understand its electron transfer mechanism(s).

Several mechanisms have been proposed for cytochrome c (*1–6*), all based on indirect evidence. An electron hopping mechanism involving transfer of an electron through various aromatic residues in the protein fabric was proposed (*8*). This mechanism was subsequently abandoned because of its failure to account for structural and energetic factors (*9*). The involvement of a π-cation radical intermediate was also proposed (*10*) but was not experimentally verified. Electron tunneling was proposed for bacterial cytochromes (*11–13*) and this mechanism also may be operative in mammalian cytochrome c. Possibly the most widely accepted mechanism involves electron transfer at the exposed heme edge of cytochrome c. This mechanism was first proposed for cytochrome c (*14*) and later for *Rhodospirillum rubrum* c_2, a photosynthetic cytochrome (*15*). This outer sphere mechanism was widely tested through use of exogenous and endogenous redox reactants and through studies of the effect of solution pH, ionic strength, and ion binding on the homogeneous electron transfer kinetics of cytochrome c (*1–5*). Support for the heme edge electron transfer mechanism was provided by these homogeneous electron transfer kinetic studies. However, the mechanism by which cytochrome c transfers electrons physiologically remains to be established.

The determination of the electron transfer kinetics of direct heterogeneous reactions between cytochrome c and several electrode surfaces was the objective of this study. The reason for pursuing this type of measurement is that cytochrome c physiologically transfers electrons at membrane interfaces. Hence, the physiological electron transfer reactions of cytochrome c may proceed via a mechanism that contains elements of a simple heterogeneous electron transfer model. This work utilized newly developed and previously reported electrode surfaces and methods.

Direct Electrochemical Studies of Cytochrome c

Cytochrome c has been studied extensively by direct voltammetric methods at mercury electrodes (*16–24*). Strong adsorption of cytochrome c on the mercury surface during reduction has been widely reported. The adsorbed layer has been variously described as forming a flattened layer with pores where reduction of diffusing cytochrome c occurs (*23*), a layer at which a self-exchange reaction occurs between the reduced adsorbed molecules and those diffusing to the electrode

(*20*), and an adsorbed layer of denatured cytochrome c (*24*). Cytochrome c also has been studied directly at gold minigrid electrodes (*25*), indium oxide thin-film optically transparent electrodes (OTEs) (*26*), and at gold electrodes on which 4,4′-bipyridine was adsorbed (*27–31*).

Formal heterogeneous electron transfer kinetic parameters for the reduction of cytochrome c have been reported (*24*, *29*). Based on linear sweep voltammetry, the formal heterogeneous electron transfer rate constant ($k^{o\prime}_{s,h}$) and the electrochemical transfer coefficient (α) for the reduction of cytochrome c at mercury were estimated to be 10^{-10} to 10^{-11} cm/s and ca. 0.5, respectively (*24*). At the 4,4′-bipyridine/gold electrode surface, ac impedance methods were used to determine that $k^{o\prime}_{s,h} = 1.6 \times 10^{-2}$ cm/s, with no value given for the electrochemical transfer coefficient (*29*).

Single Potential Step Chronoabsorptometry

The method of single potential step chronoabsorptometry (SPS/CA) permits the determination of heterogeneous electron transfer kinetic parameters for optically absorbing species at OTEs (*32*). The principal advantages of this method compared to other electrochemical methods are its insensitivity to charge consuming processes other than the reaction of interest and the molecular specificity provided by the optical probe. A detailed description of the application of this method, which neglects the effect of the back reaction (irreversible processes), as well as the more recent application of a method that accounts for the back reaction (quasi-reversible processes) was presented (*33*).

The need for the SPS/CA method directly followed the reports of the electroactivity of gold minigrid electrodes, which were electrochemically modified with methyl viologen, toward the direct reduction and oxidation of ferredoxin (*34*) and myoglobin (*35*). The application of the SPS/CA method to the determination of the heterogeneous electron transfer kinetic parameters was reported for the reduction of myoglobin (*36*) and ferredoxin (*37*) at this electrode surface. Recent work extended the application of SPS/CA to cytochrome c, which was studied at the modified gold minigrid surface and at fluoride-doped tin oxide and tin-doped indium oxide OTEs (*38*). The effects of pH and ionic strength on the heterogeneous reductive electron transfer parameters for myoglobin were also described (*38*).

In the present work, SPS/CA was used to evaluate the effects of ion binding to cytochrome c on heterogeneous electron transfer kinetic parameters at fluoride-doped tin oxide OTEs. In addition, initial results from oxidative SPS/CA measurements for cytochrome c were obtained at the modified gold minigrid surface and at the fluoride-

doped tin oxide OTE surface. These latter experiments were performed to directly measure the rate constants for the back reaction (oxidation) to determine the agreement of the heterogeneous electron transfer reactions of cytochrome c with the simple electron transfer theory used in kinetic analyses.

Experimental

Apparatus. The electrochemical and optical instrumentation was described previously (*36, 38*). The spectroelectrochemical cells were based on a previously reported design and had an optical pathlength of ca. 1 mm (*39*). Rotating disk voltammetry was performed with a Pine Instrument Company Model ASR-2 rotator.

The gold minigrid electrodes were 200 lines per inch, 67% transmittant and 0.1 mil nominal thickness from Buckbee–Mears Co. The gold rotating disk electrode, 7.5-mm diameter, was Model DD20 from Pine Instrument Co. Tin-doped indium oxide and fluoride-doped tin oxide OTEs were ca. 20 ohms/square from PPG Industries.

Chemicals. Methyl viologen (K & K Laboratories) was recrystallized three times from methanol. The phosphate buffer was prepared from Titrisol, pH 7.0 (E. Merck Co.) or from reagent grade salts. Cacodylic acid and tris(hydroxymethyl)aminomethane, reagent grade, were obtained from Sigma Chemical Co. The cacodylic acid was recrystallized twice from ethanol. All other chemicals were reagent grade and solutions were prepared in glass distilled water.

Procedures. Gold electrodes were modified with methyl viologen as previously described (*36*). The semiconductor OTEs were cleaned by successively subjecting them to 5 min of ultrasonic agitation in Alconox, ethanol, and distilled water (twice) after a previously described procedure (*40*).

SPS/CA measurements were performed at 550 or 416 nm and $\Delta\epsilon$ values of 21,100 (*41*) and 57,000 $M^{-1}cm^{-1}$ (*42*), respectively, were used in all calculations. The diffusion coefficient used in all calculations was 1.1×10^{-6} cm^2/s (*28*). This value was experimentally verified (± 0.05) from the slope of plots of absorbance vs. $t^{1/2}$ for 22 diffusion-controlled SPS/CA transients at a fluoride-doped tin oxide OTE. The formal potential for cytochrome c, which was used to determine overpotential step values, was 0.260 V vs. NHE (*2*). All experiments were performed at 25 ± 2°C.

Reduction and Oxidation of Cytochrome c at Various Electrodes

Table I summarizes the electron transfer kinetic behavior seen for horse heart cytochrome c at the three electrode surfaces reported here. These results were all obtained with solutions containing 0.07 *M* phosphate and 0.10 *M* NaCl, pH 7.0, using SPS/CA. Rate parameters obtained from previous reductive potential step experiments with ferricytochrome c (Entries 1, 4, 6) (*38*) are shown in Figure 1. Entry 3 data for cytochrome c reduction at tin oxide resulted from a recent experiment that duplicated the conditions for Entry 4. The consistency between these two sets of data obtained 6 months apart is quite good.

Published on June 1, 1982 on http://pubs.acs.org | doi: 10.1021/ba-1982-0201.ch007

Table I. Heterogeneous Electron Transfer Kinetic Parameters for Cytochrome c at Various OTEs

Entry	[*Cyt c*], μM[a]	*log* $k^{o'}_{s,h}$, *cm/s*	α	*Electrode*	*Potential steps*
1	77.3	−4.99(±0.12)[b]	0.24(±0.03)	MGM[c]	reductive[d,e]
2	77.3	−5.24(±0.05)	0.74(±0.02)[f]	MGM	oxidative
3	101	−5.20(±0.08)	0.28(±0.02)	SnO_2[g]	reductive
4	103	−5.17(±0.05)	0.32(±0.01)	SnO_2	reductive[e]
5	103	−4.31(±0.07)	0.95(±0.01)[f]	SnO_2	oxidative
6	43.0	−4.51(±0.05)	0.50(±0.04)	In_2O_3[h]	reductive[e]

[a] All solutions contained 0.07 *M* phosphate buffer, pH 7.0 and 0.1 *M* NaCl.
[b] Parentheses contain one standard deviation.
[c] Methyl viologen-modified gold minigrid electrode.
[d] Reductive SPS/CA performed on oxidized sample of cytochrome c.
[e] From Ref. 38.
[f] Oxidative SPS/CA performed on reduced sample of cytochrome c, value is from (1 − α).
[g] Fluoride-doped tin oxide OTE.
[h] Tin-doped indium oxide OTE.

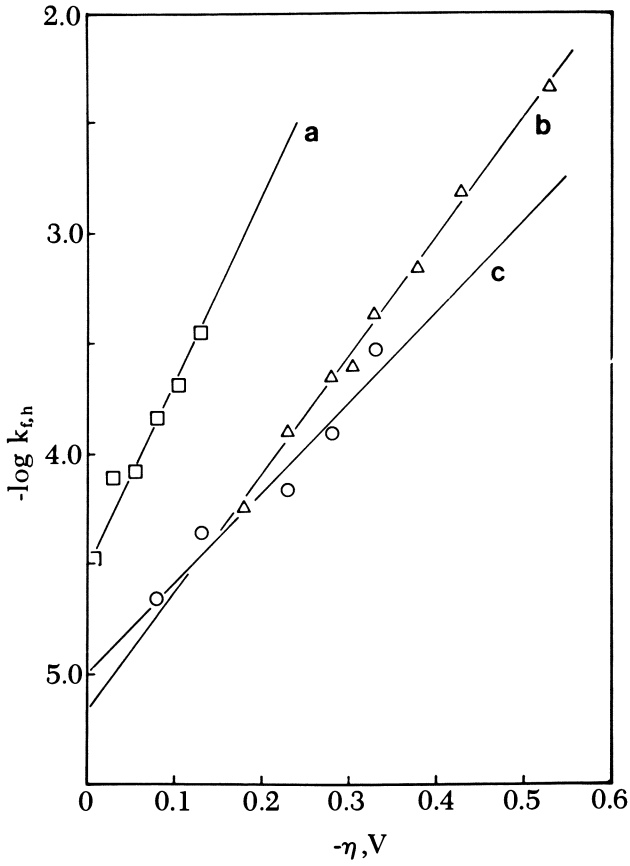

Figure 1. Log $k_{f,h}$ vs. overpotential for the reduction of cytochrome c. Letter designation/electrode material/entry correspondence in Table I: a, tin-doped indium oxide, Entry 6; b, fluoride-doped tin oxide, Entry 5; c, methyl viologen-modified minigrid, Entry 1.

As noted previously (38), the sameness of the reductive kinetic results, when compared to those obtained at the 4,4'-bipyridine/gold electrodes (29) and at mercury (24), argues for the existence of a similar protein/solution interface at these three electrode surfaces. The presence of an adsorbed protein layer at these electrode surfaces is a likely possibility but is not established.

Oxidative SPS/CA experiments were performed in a manner identical to the reductive experiments except that positive overpotential steps were applied to the electrodes exposed to bulk ferrocytochrome c. Analysis of absorbance–time data yields, for each overpotential, a

$k_{b,h}$ (assuming that $k_{f,h}$ corresponds to reduction). A linear plot of log $k_{b,h}$ vs. overpotential (η) affords $k^{\circ\prime}_{s,h}$ from the intercept and $(1 - \alpha)$ from the slope. According to Butler–Volmer formalism (*43*), a simple heterogeneous electron transfer reaction (with only one physical pathway for both oxidation and reduction) should yield the same value of $k^{\circ\prime}_{s,h}$, independent of whether the measured reaction is a reduction or an oxidation. Furthermore, the values of the transfer coefficient obtained from the separate reductive and oxidative experiments should agree. In the experiments of Table I, these criteria are not met for the fluoride-doped tin oxide OTE (Entries 3 and 4 compared to 5) or the methyl viologen-modified gold minigrid electrode (compare Entries 1 and 2). For the former electrode, the transfer coefficients differ by ca. 0.65, and the $k^{\circ\prime}_{s,h}$ values differ by nearly an order of magnitude in the oxidation and reduction experiments. Similar disparities also exist for the latter electrode, but to a lesser degree. Reasons for this discrepancy may involve ion binding to cytochrome c, a pathway dependence on the reaction direction, and semiconductor surface effects. Work is in progress to determine the reason(s) for these discrepancies.

The heterogeneous electron transfer kinetic parameters for the reduction of cytochrome c were also investigated at a methyl viologen-modified rotating gold disk electrode (RDE) to compare the results of this steady state technique with the results obtained by the SPS/CA transient technique. The gold RDE was first polished successively with 1-, 0.3-, and 0.1-μm alumina slurries followed by an ultrasonic distilled water rinse. The gold RDE was then modified following the procedure described for gold minigrids (*36*). Standard RDE kinetic analysis (*43*) of data obtained for a deoxygenated solution of 166 μM cytochrome c, 0.07 M phosphate buffer, and 0.10 M NaCl, pH 7.0, yielded values for log $k^{\circ\prime}_{s,h}$ of -5.24 (± 0.22) and α of 0.21 (± 0.03). These preliminary results demonstrate that RDE voltammetry at the methyl viologen-modified gold disk electrode can be utilized to measure the heterogeneous electron transfer kinetics of cytochrome c. This result is in agreement with the results of the SPS/CA transient technique (*38*).

Anion Effects on the Heterogeneous Electron Transfer Kinetics of Cytochrome c

Specific cation and anion binding to one or both redox forms of cytochrome c is a well-established phenomenon (*44*, *45*). Changes in homogeneous electron transfer rates between cytochrome c and soluble redox partners also have been observed and attributed to ion binding (*2*, *46*, *47*). This section describes evidence which shows that

specific anion effects, presumably resulting from binding to cytochrome c, can influence heterogeneous electron transfer rates in a measurable and reproducible fashion.

For these experiments, cytochrome c was dissolved in pH 7.0 tris(hydroxymethyl)aminomethane (0.09 *M*)/cacodylic acid (0.10 *M*) buffer (Buffer A) of calculated ionic strength equal to 0.08 *M*. This buffer system is considered to be nonbinding with respect to cytochrome c (*46*, *48*). Evaluation of reductive electron transfer kinetic parameters was then performed at fluoride-doped tin oxide OTEs both in the presence and absence of added salts. First the results with buffer alone will be presented in some detail followed by results obtained in the presence of chloride and phosphate.

Figure 2 shows typical absorbance–time transients for the reduction of cytochrome c in Buffer A for a number of overpotential steps.

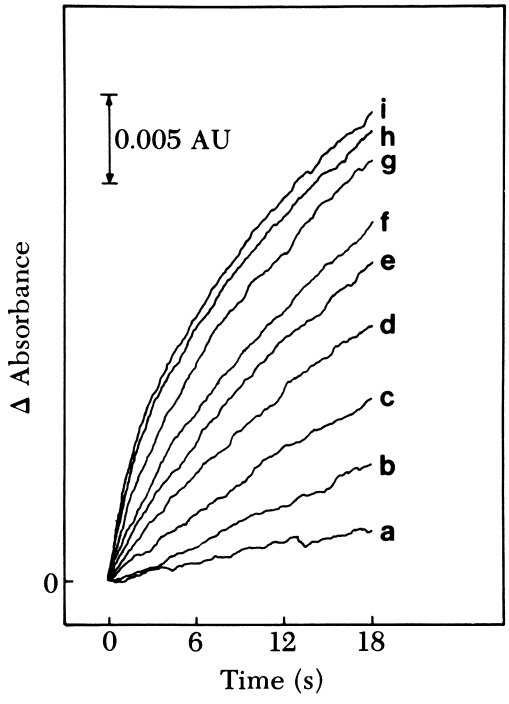

Figure 2. Typical SPS/CA absorbance–time transients for the reduction of cytochrome c. Solution contained 97.6 μM cytochrome c, and Buffer A, pH 7.0 (ionic strength = 0.08 M) at a fluoride-doped tin oxide OTE from Table III, Entry 1. Trace/overpotential in mV/transient number in experimental sequence: a, −78, #10; b, −128, #6; c, −178, #20; d, −228, #14; e, −278, #18; f, −328, #4; g, −428, #1; h, −628, #5; and i, −728, #8.

The reproducibility was very good and no measurable loss in response was seen during the random acquisition of more than thirty SPS/CA transients. Table II shows the $k_{f,h}$ values calculated for transients a through g of Figure 2. Excellent fit to the SPS/CA theory for irreversible electron transfer is indicated by the small standard deviations. This assertion is further corroborated in Figure 3, which presents the kinetic working curve along with data from transients b, c, d, f, and g. Only these data are shown for clarity. For each transient, experimental normalized absorbance is plotted for five observations (t = 6, 9, 12, 15, and 18 s) vs. log $[(k_{f,h}t^{1/2})/D^{1/2}]$ using the average $k_{f,h}$ values from Table II. If experiment fits theory, all five points for each transient should fall on the working curve and this is indeed the case. Values obtained for t = 3 s were not included in any of the $k^{o\prime}_{s,h}$ and α determinations, because their fit to the working curve was not good in some cases. This deviation is probably a result of the greater relative error inherent in measuring the absorbance–time response at short times.

For the reduction of cytochrome c at fluoride-doped tin oxide OTEs in pH 7.0 Buffer A, averaging the results in Entries 1 and 2 of Table III yields log $k^{o\prime}_{s,h} = -4.75$ and $\alpha = 0.32$. Entries 3 and 4 of the same table indicate that the effect of 10 mM phosphate ($[H_2PO_4^-]/[HPO_4^{2-}] \simeq 0.7$) in this same system is to decrease log $k^{o\prime}_{s,h}$ by ca. 0.4 and α by ca. 0.07. In the electrochemical sense, cytochrome c reduction at tin oxide is more irreversible in the presence of phosphate. Experimentally, this fact is evidenced by a significant reduction in the magnitudes of the absorbance–time transients shown in Figure 2 upon addition of phosphate. That this observed difference is significant is shown by the error limits and the experimental reproducibility indicated in Entries 1–4 of Table III. One experiment performed with 10 mM NaCl added to the Buffer A showed a slight decrease in reversibility as evidenced by a smaller transfer coefficient (*see* Entry 5). However, compared with the phosphate effect, this result is not striking and repetitive experiments will be necessary to establish the validity of this difference. The kinetic results presented in Table III are graphed in Figure 4.

The results just presented indicate that specific ion binding can significantly influence heterogeneous electron transfer rates of cytochrome c. Using values for ion binding constants previously reported (*44*), a 10-mM concentration of phosphate or chloride is sufficient to bind essentially all of the cytochrome c molecules at 100 μM concentration. Evidently, two anions bind to each cytochrome c (*49*). The results presented in Table III and Figure 4 support the view that phosphate and chloride bind at different sites on cytochrome c (*50*) and suggest the involvement of this molecular feature in the reduction of this metalloprotein at tin oxide OTEs.

Table II. Heterogeneous Electron Transfer Rate Constants for the Reduction of Cytochrome c at a Fluoride-Doped Tin Oxide OTE

η, mV	$k_{f,h}$, cm/s[a]
− 78	$3.10(\pm 0.20) \times 10^{-5}$
−128	$7.49(\pm 0.07) \times 10^{-5}$
−178	$1.51(\pm 0.02) \times 10^{-4}$
−228	$2.68(\pm 0.03) \times 10^{-4}$
−278	$4.53(\pm 0.07) \times 10^{-4}$
−328	$6.21(\pm 0.02) \times 10^{-4}$
−428	$1.28(\pm 0.05) \times 10^{-3}$

[a] Rate constants are mean values of five observations taken at equal increments over the 6- to 18-s time domain. Parentheses contain one standard deviation.
Note: Solution conditions are given in Figure 2.

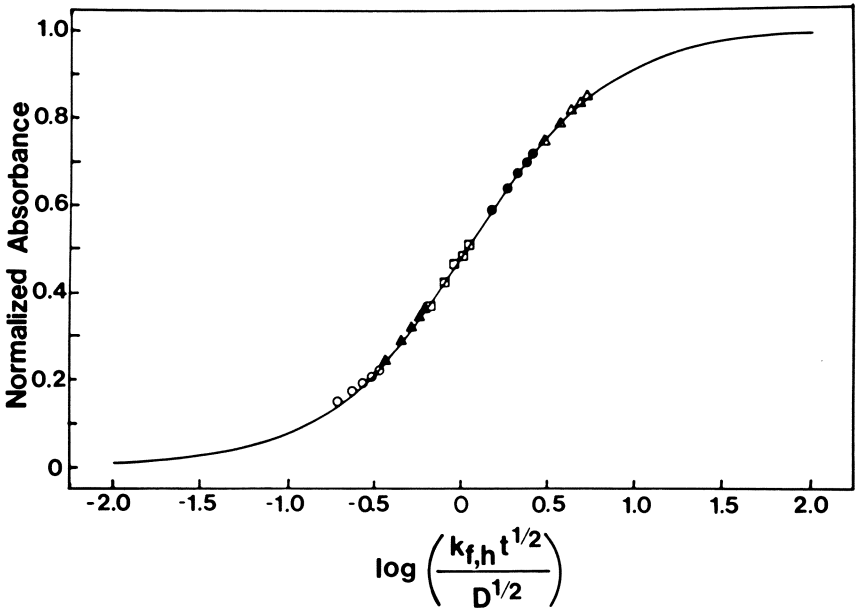

Figure 3. Normalized absorbance vs. log $[(k_{f,h}t^{1/2})/D^{1/2}]$ *working curve with typical data for the reduction of cytochrome c at a fluoride-doped tin oxide OTE. Data shown correspond to appropriate transients in Figure 2 and were calculated using the* $k_{f,h}$ *values from Table II. Key:* ○, $\eta = -128$ *mV;* ▲, $\eta = -178$ *mV;* □, $\eta = -228$ *mV;* ●, $\eta = -328$ *mV; and* △, $\eta = -428$ *mV.*

Table III. Anion Effects on the Heterogeneous Electron Transfer Kinetic Parameters for Cytochrome c

Entry	*log* $k^{\circ\prime}_{s,h}$, *cm/s*	α	*Electrolyte*
1	−4.79(±0.05)[a]	0.30(±0.01)	Buffer A
2	−4.71(±0.01)	0.34(±0.01)	Buffer A
3	−5.13(±0.05)	0.24(±0.01)	Buffer A + 10 m*M* phosphate
4	−5.14(±0.02)	0.26(±0.01)	Buffer A + 10 m*M* phosphate
5	−4.78(±0.03)	0.28(±0.01)	Buffer A + 10 m*M* NaCl

Note: SPS/CA at SnO_2 OTEs, 96 to 98 μM cytochrome c, all solutions at pH 7.0, and all experiments are reductive.

[a] Parentheses contain one standard deviation.

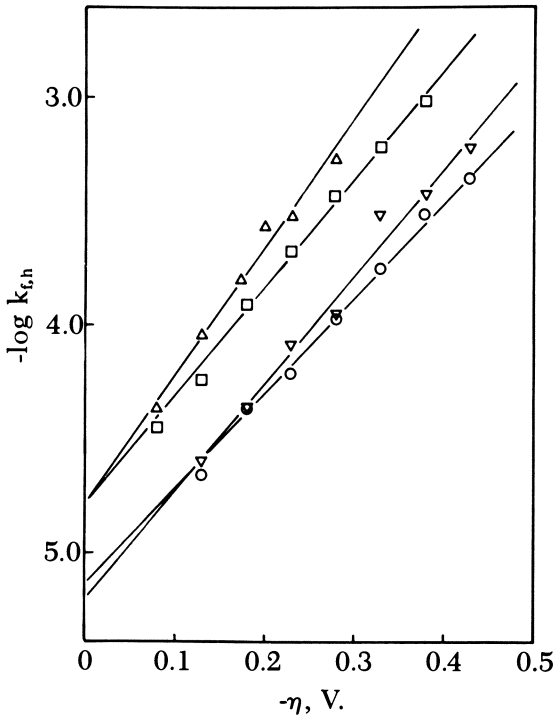

Figure 4. Anion effect on the SPS/CA reduction kinetics of cytochrome c at fluoride-doped tin oxide OTEs. Key: △, Buffer A, pH 7.0 (Entry 1 of Table III); □, Buffer A + 10 mM NaCl (Entry 5 of Table III); ○, Buffer A + 10 mM phosphate (Entry 3 of Table III); and ▽, 0.07 M phosphate, 0.10 M NaCl, pH 7.0 (Entry 3 of Table I).

The results and conclusions just presented are the first reported evidence for specific ion effects on heterogeneous electron transfer kinetics for a biological redox molecule. Although the effect is thought to arise from binding to cytochrome c molecules, the anions may possibly be exerting an important effect on the oxide semiconductor surface. Additional experiments, including variation of anion concentration, will be required to assess these potential causes. A final point that requires clarification concerns the phosphate effect. At pH 7.0, both $H_2PO_4^-$ and HPO_4^{2-} are present at significant concentrations and it is not clear whether there is a difference in their ion binding behavior. Additional experiments performed over a pH range of ca. 6–8 should resolve this question.

Acknowledgments

The support of the National Science Foundation (PCM79-12348), the National Institutes of Health (GM27208-02), and the University of Delaware Institute of Neuroscience (NIH Biomedical VII) is gratefully acknowledged. The assistance of Charlene D. Crawley and Eric E. Bancroft in some aspects of this work is gratefully acknowledged.

Literature Cited

1. Sutin, N. In "Bioinorganic Chemistry–II," Raymond, K. N., Ed.; ACS ADVANCES IN CHEMISTRY SERIES, No. 162, ACS: Washington, D.C.; 1977; pp. 156–172.
2. Cusanovich, M. A. In "Bioorganic Chemistry"; E. E. van Tamelen, Ed.; Academic: New York, 1978; Vol. 4, pp. 117–145.
3. Ferguson-Miller, S.; Brautigan, D. L.; Margoliash, E. In "The Porphyrins"; D. Dolphin, Ed.; Academic: New York, 1979; Vol. 7, pp. 149–240.
4. Timkovich, R., Ibid., pp. 241–294.
5. Wherland, S.; Gray, H. B. In "Biological Aspects of Inorganic Chemistry"; A. W. Addison et al., Eds.; Wiley: New York, 1977; pp. 289–368.
6. Williams, R. J. P.; Moore, G. R.; Wright, P. E., Ibid., pp. 369–401.
7. Walz, D. *Biochim. Biophys. Acta* **1979,** *505,* 279–353.
8. Dickerson, R. E.; Takano, T.; Kallai, O. B.; Samson, L. In "Structure and Function of Oxidation Reduction Enzymes"; A. A. Keison; A. Ehrenberg, Eds.; Pergamon: Oxford, England, 1972; p. 69.
9. Dickerson, R. E.; Timkovich, R. In "The Enzymes"; P. D. Boyer, Ed.; Academic: New York, 1975; Vol. 11, Part A, pp. 397–547.
10. Dolphin, D.; Felton, R. H. *Acc. Chem. Res.* **1974,** *7,* 26.
11. DeVault, D.; Chance, B. *Biophys. J.* **1966,** *6,* 825.
12. Hopfield, J. J. *Proc. Nat. Acad. Sci. U.S.A.* **1974,** *71,* 3640.
13. Salemme, F. R. *J. Mol. Biol.* **1976,** *102,* 563.
14. Castro, C. E.; David, H. F. *J. Am. Chem. Soc.* **1969,** *91,* 5405.
15. Salemme, F. R.; Kraut, J.; Kamen, M. C. *J. Biol. Chem.* **1973,** *248,* 7701.
16. Griggio, L.; Pinamonti, S. *Atti. Ist. Veneto Sci. Lett. Arti.* **1965–1966,** *124,* 15.
17. Betso, S. R.; Klapper, M. H.; Anderson, L. B. *J. Am. Chem. Soc.* **1972,** *94,* 8197.

18. Scheller, F.; Jänchen, M.; Lampe, J.; Prümke, H. J.; Blanck, J.; Palecek, E. *Biochim. Biophys. Acta* **1975,** *412,* 157.
19. Scheller, F.; Prümke, H. J. *Stud. Biophys.* **1976,** *60,* 137.
20. Scheller, F. *Bioelectrochem. Bioenerg.* **1977,** *4,* 490.
21. Kuznetsov, B. A.; Mestechkina, N. M.; Shumakovich, G. P. *Bioelectrochem. Bioenerg.* **1977,** *4,* 1.
22. Haladjian, J.; Bianco, P.; Serre, P. A. *J. Electroanal. Chem.* **1980,** *106,* 397.
23. Kuznetsov, B. A.; Shumakovich, G. P.; Mestechkina, N. M. *Bioelectrochem. Bioenerg.* **1977,** *4,* 512.
24. Haladjian, J.; Bianco, P.; Serre, P. A. *Bioelectrochem. Bioenerg.* **1979,** *6,* 555.
25. Heineman, W. R.; Norris, B. J.; Goelz, J. F. *Anal. Chem.* **1975,** *47,* 79.
26. Yeh, P.; Kuwana, T. *Chem. Lett.* **1977,** 1145.
27. Eddowes, M. J.; Hill, H. A. O. *J. Chem. Soc., Chem. Commun.* **1977,** 771.
28. Eddowes, M. J.; Hill, H. A. O. *J. Am. Chem. Soc.* **1979,** *101,* 4461.
29. Eddowes, M. J.; Hill, H. A. O.; Uosaki, K. *J. Am. Chem. Soc.* **1979,** *101,* 7113.
30. Cass, A. E. C.; Eddowes, M. J.; Hill, H. A. O.; Uosaki, K.; Hammond, R. C.; Higgins, I. J.; Plotkin, E. *Nature* **1980,** *285,* 673.
31. Eddowes, M. J.; Hill, H. A. O.; Uosaki, K. *Bioelectrochem. Bioenerg.* **1980,** *7,* 527.
32. Albertson, D. E.; Blount, H. N.; Hawkridge, F. M. *Anal. Chem.* **1979,** *51,* 556.
33. Bancroft, E. E.; Blount, H. N.; Hawkridge, F. M., *Anal. Chem.* **1981,** *53,* 1862.
34. Landrum, H. L.; Salmon, R. T.; Hawkridge, F. M. *J. Am. Chem. Soc.* **1977,** *99,* 3154.
35. Stargardt, J. F.; Hawkridge, F. M.; Landrum, H. L. *Anal. Chem.* **1978,** *50,* 930.
36. Bowden, E. F.; Hawkridge, F. M.; Blount, H. N. *Bioelectrochem. Bioenerg.* **1980,** *7,* 447.
37. Crawley, C. D.; Hawkridge, F. M. *Biochem. Biophys. Res. Commun.* **1981,** *99,* 516.
38. Bowden, E. F.; Wang, M.; Hawkridge, F. M. *J. Electrochem. Soc.* **1980,** *127,* 131C.
39. Shu, F. R.; Wilson, G. S. *Anal. Chem.* **1976,** *48,* 1676.
40. Armstrong, N. R.; Lin, A. W. C.; Fujihira, M.; Kuwana, T. *Anal. Chem.* **1976,** *48,* 741.
41. Van Gelder, B. F.; Slater, E. C. *Biochim. Biophys. Acta* **1962,** *58,* 593.
42. Van Buuren, K. J. H.; Van Gelder, B. F.; Wilting, J.; Braams, R. *Biochim. Biophys. Acta* **1974,** *333,* 421.
43. Bard, A. J.; Faulkner, L. R. "Electrochemical Methods"; Wiley: New York, 1980.
44. Nicholls, P. *Biochim. Biophys. Acta* **1974,** *346,* 261.
45. Osheroff, N.; Koppenol, W. H.; Margoliash, E. In "Frontiers of Biological Energetics"; P. L. Dutton; J. S. Leigh; A. Scarpa, Eds.; Academic: New York, 1978; Vol. 1, p. 439.
46. Cusanovich, M. A.; Miller, W. G. *Bioelectrochem. Bioenerg.* **1974,** *1,* 448.
47. Cummins, D.; Gray, H. B. *J. Am. Chem. Soc.* **1977,** *99,* 5158.
48. Barlow, G. H.; Margoliash, E. *J. Biol. Chem.* **1966,** *241,* 1473.
49. Margalit, R.; Schejter, A. *Eur. J. Biochem.* **1973,** *32,* 500.
50. Osheroff, N.; Borden, D.; Koppenol, W. H.; Margoliash, E. *J. Biol. Chem.* **1980,** *255,* 1689.

RECEIVED for review June 2, 1981. ACCEPTED November 4, 1981.

Binding as a Prerequisite for Rapid Electron Transfer Reactions of Metalloproteins

M. J. EDDOWES and H. A. O. HILL

Inorganic Chemistry Laboratory, South Parks Road, Oxford, OX1 3QR, England

The electrochemistry of cytochrome c at a surface-modified gold electrode is described. Cyclic voltammetry and ac impedance studies show that the protein undergoes a rapid quasi-reversible electron transfer reaction, with $k_s^\circ = 1.5 \times 10^{-4}$ *m/s. Rotating disk electrode studies show that the protein binds to the electrode prior to electron transfer. The electrochemistry of cytochrome c, cytochrome* c_3*, and ferredoxin at the mercury electrode, on which these proteins adsorb, is also discussed. A general mechanism, involving binding of the protein to the electrode prior to electron transfer, and hence, analogous to that observed in the physiological redox reactions of cytochrome c, is proposed to account for the observed electron transfer reactions of metalloproteins at electrodes. Such binding is, most likely, a prerequisite for rapid electron transfer in the reactions of metalloproteins.*

The electron transfer reactions of cytochrome c, a low-molecular weight, soluble, heme protein component of the mitochondrial respiratory chain, were the subject of intense biochemical and physicochemical studies to determine how the protein achieves the observed ease of electron transfer and still maintains the degree of specificity and control necessary for its efficient function. Kinetic studies (*1–5*) indicated that cytochrome c forms a complex with its physiological redox partners prior to electron transfer, and various equilibrium studies (*6–10*) confirmed the existence of such protein–protein complexes. The lysine residues of cytochrome c were shown (*11–14*) by chemical modification and other studies to be important to its physiological redox reactions, consistent with (*15*) their distri-

0065-2393/82/0201-0173$07.25/0

bution on the surface of the protein. Detailed and specific chemical modification studies (*16–25*) have since defined the binding domain on cytochrome c (which interacts with its physiological redox partners, cytochrome c reductase, cytochrome c peroxidase, and cytochrome c oxidase) to be around the exposed heme edge of cytochrome c and have confirmed the importance of particular lysine residues in this interaction.

The electron transfer reactions between small molecule redox reagents and cytochrome c also were investigated, and binding between the reactants was observed. For example, the redox reaction between cytochrome c and the ferro–ferricyanide couple was studied (*26–29*) using a variety of techniques, and apparently the reaction proceeds via a tightly bound precursor complex, the formation of which precedes the electron transfer event itself. A similar reaction sequence also was indicated by kinetic studies of the redox reactions between small molecule redox couples and other metalloproteins, such as the blue-copper proteins (*30–33*) and the ferredoxins (*34–36*).

Conventional electrochemical methods, which might be considered the most direct method for the study of redox species, enjoyed limited success in their application to the study of cytochrome c and redox proteins in general. Despite the facility of electron transfer between physiological redox-partner proteins, rapid, direct electron transfer between electrodes and metalloproteins in solution has been reported infrequently. Where rapid electron transfer is observed, adsorption of the protein at the electrode surface generally occurs. For example, at the mercury electrode, well-defined polarographic waves were observed for the reduction of cytochrome c (*37–41*), cytochrome c_3 (*42, 43*), and ferredoxin (*44*); in each case adsorption effects were clearly indicated. In addition, we showed (*45–49*) that at a surface-modified gold electrode, where well-defined voltammetric waves are observed for the reduction and oxidation of cytochrome c, rapid and reversible binding of the protein to the electrode occurs. This binding, which is an essential feature of the electrode process, may be analogous to that between cytochrome c and its physiological redox partners in that it appears to depend (*47*) on the lysine residues of the cytochrome c.

A suitable binding interaction would apparently be of major importance in determining the kinetics of the electron transfer reactions of redox proteins. We here review the current experimental data concerning the electron transfer reactions of metalloproteins at electrodes. In particular we consider the involvement of adsorption phenomena in such reactions and their relation to complex formation in other redox reactions of metalloproteins. The role of binding in the rate enhancement, control, and specificity of physiological redox processes is also discussed.

Electrochemistry of Cytochrome c at a Modified Gold Electrode

Cyclic Voltammetry Studies. As reported (*46*), the dc and ac cyclic voltammograms of horse heart cytochrome c at a gold electrode in the presence of 4,4′-bipyridyl (Figure 1) show that a quasi-reversible, one-electron process occurs, with a half-wave potential, $E_{1/2}$ = +0.25 V vs. (NHE). This electrode process is attributable to the reduction and oxidation of the heme iron prosthetic group of cytochrome c. Controlled potential reduction and oxidation, followed spectrophotometrically, confirm that the electrode process involves the heme iron. The electrode reaction also was studied (*47*, *48*) using ac impedance methods, which show that the reaction is rapid with a standard electrochemical rate constant, $k_s^\circ = 1.5 \times 10^{-4}$ m/s.

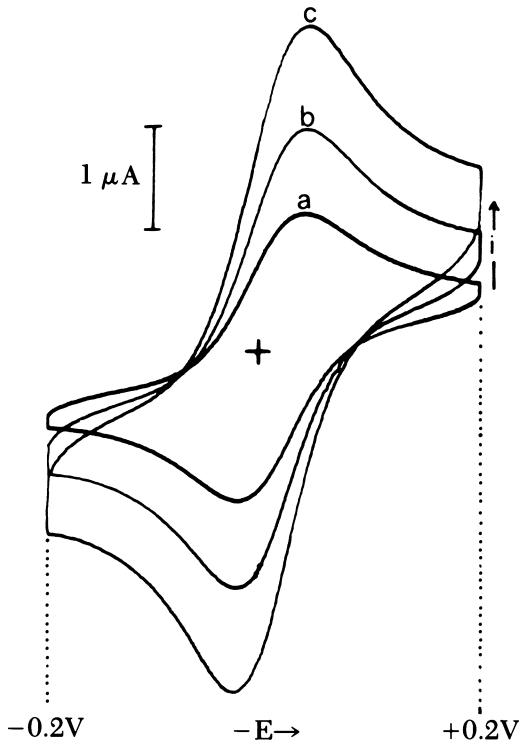

Figure 1. Cyclic voltammetry (dc) of horse heart ferricytochrome c (5 mg/mL) in 0.1 M $NaClO_4$, 0.02 M phosphate buffer at pH 7, in the presence of 10^{-2} M 4,4′-bipyridyl in the potential range +0.20 to −0.20 V vs. SCE, at sweep rates a, 20 mV/s; b, 50 mV/s; and c, 100 mV/s. The scan rate independent separation of forward and reverse peaks of 60 mV indicates that, under these conditions, the reaction is essentially diffusion controlled. (Reproduced from Ref. 46. Copyright 1979, American Chemical Society.)

The reaction is not observed in the absence of 4,4′-bipyridyl, but 4,4′-bipyridyl alone is not electroactive in the potential region where the voltammetric waves are observed and therefore cannot be acting as a conventional mediator in this case. Furthermore, the observed voltammetry indicates that the electrode process involves direct electron transfer between the electrode and the protein. 4,4′-Bipyridyl appears to act (*46*, *48*, *50*) by adsorbing on the gold electrode surface, thereby modifying it, and thus providing a suitable interface at which the electrode reaction of cytochrome c may take place.

The electrode reaction of cytochrome c at the modified gold electrode shows (*47*) some striking similarities to its reaction with its physiological redox partners in that both are inhibited (*11–14*) by chemical modification of the cytochrome c lysine residues and by the competitive inhibitor, poly-L-lysine (Figure 2). These results suggest the possibility of an interaction between cytochrome c and the modified electrode surface analogous to that between cytochrome c and its physiological partners and, as such, indicate that cytochrome c binds to the electrode prior to electron transfer.

Rotating Disk Electrode Studies. By analogy with its physiological redox reactions, a similar multi-step mechanism is outlined in Scheme I for the electrode reaction of cytochrome c in which it binds to the electrode surface before the electron transfer event itself occurs. This mechanism was investigated (*49*) using the rotating disk technique.

$A_\infty \underset{k_D}{\overset{k_D}{\rightleftharpoons}} A_0$	transport in solution
$A_0 \underset{\Gamma_L k_{des}}{\overset{k_{ads}}{\rightleftharpoons}} A_{ads}$	adsorption and desorption of reactant
$A_{ads} \underset{\Gamma_L k_{-e}}{\overset{\Gamma_L k_e}{\rightleftharpoons}} B_{ads} + e$	electron transfer
$B_{ads} \underset{k_{ads}}{\overset{\Gamma_L k_{des}}{\rightleftharpoons}} B_0$	desorption and adsorption of product
$B_0 \underset{k_D}{\overset{k_D}{\rightleftharpoons}} B_\infty$	transport in solution

Scheme I

Scheme I represents the reaction $A \rightleftharpoons B + e$ where A is ferrocytochrome c, B is ferricytochrome c, and Γ_L/mol m^{-2} is the number of adsorption sites per unit area on the modified electrode. The various rate constants describe the rates of the following processes: the rate constant k_D/m s^{-1} is the mass transport rate constant for a rotating disk electrode, describing the transport of material from the bulk of the solution to the electrode, and is given by the Levich equation (*51*)

$$k_D = 1.55\ D^{2/3}\nu^{-1/6}W^{1/2} = BW^{1/2} \quad (1)$$

where W is the rotation speed in Hertz. The rate constant k_{ads} describes the rates of adsorption of both the reduced and oxidized forms of cytochrome c and has the usual dimensions of the electrochemical rate constant. The rate constants k_e and k_{-e} are the potential-dependent rate constants for the forward and backward electron transfer reactions be-

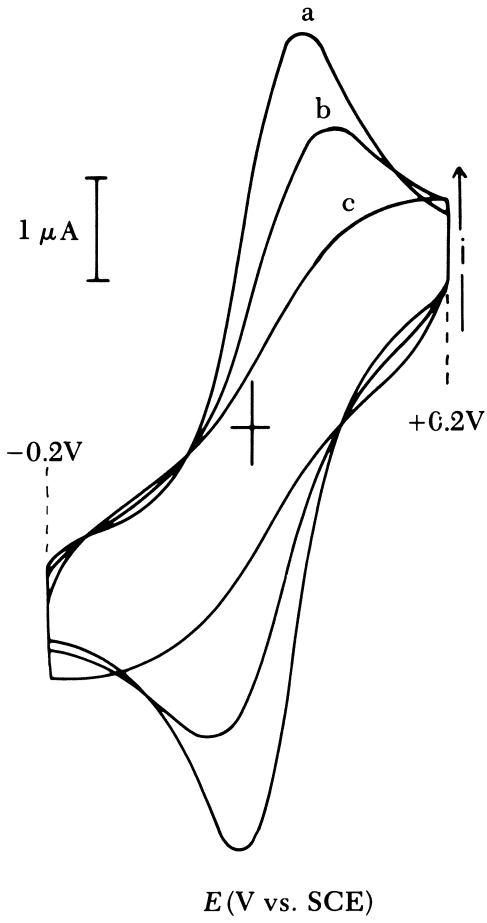

Figure 2. Cyclic voltammograms (dc) of horse heart ferricytochrome c (5 mg/mL) in 0.1 M $NaClO_4$, 0.02 M phosphate buffer at pH 7 in the presence of 1,2-bis(4-pyridyl)ethylene in the potential range +0.2 V to −0.2 V vs. SCE with poly-L-lysine at a, 0; b, 1; and c, 1.5 mg/mL. The dc potential scan rate was 100 mV/s. The increasing irreversibility with increasing poly-L-lysine concentration illustrates its inhibitory effect due to blockage of adsorption sites on the electrode surface. (Reproduced from Ref. 47. Copyright 1979, American Chemical Society.)

tween adsorbed species and the electrode in units of reciprocal seconds, and are given by

$$k_e = k_e^\circ \exp\left[\frac{\alpha nF}{RT}(E - E^\circ)\right] \tag{2a}$$

for the anodic process and

$$k_{-e} = k_e^\circ \exp\left[-\frac{\beta nF}{RT}(E - E^\circ)\right] \tag{2b}$$

for the cathodic process, where k_e° is the standard first-order electron transfer rate constant between adsorbed species and the electrode at the standard electrode potential of the system, E°. The coefficients α and β are the normal anodic and cathodic charge transfer coefficients. The rate constant k_{des} describes the rates of desorption of the reduced and oxidized forms of cytochrome c and is also in units of reciprocal seconds.

Equations that describe the dependence of current on potential and rotation speed for the proposed reaction scheme at the rotating disk electrode are derived by consideration of the following equations for the flux, j in mols per square meter per second, of A to B:

$$\left.\begin{aligned} j &= k_D(a_\infty - a_0) && \text{(transport of reactant)} \\ &= k_{ads}(1 - \theta_a - \theta_b)a_0 - \Gamma_L k_{des}\theta_a && \text{(net adsorption of reactant)} \\ &= \Gamma_L k_e \theta_a - \Gamma_L k_{-e}\theta_b && \text{(electron transfer)} \\ &= \Gamma_L k_{des}\theta_b - k_{ads}(1 - \theta_a - \theta_b)b_0 && \text{(net desorption of product)} \\ &= k_D(b_0 - b_\infty) && \text{(transport of product)} \end{aligned}\right\} \tag{3}$$

where θ_a and θ_b are the fraction of sites occupied by A and B, respectively. Elimination of θ_a, θ_b, a_0, and b_0 by equating these flux equations gives the general result:

$$\begin{aligned} j^{-1}k_{ads}k_{des}\Gamma_L(k_e a_\infty - k_{-e}b_\infty) = {} & k_D^{-1}k_{ads}k_{des}\Gamma_L(k_e + k_{-e}) \\ & + (k_{des}\Gamma_L + k_{ads}a_\infty + k_{ads}b_\infty)(k_e + k_{-e} + k_{des}) \end{aligned} \tag{4}$$

When the electrode is sufficiently positive, k_e will be so large and k_{-e} so correspondingly small that terms containing k_e will dominate and the limiting current, i_L, will be observed. The limiting current is described, for oxidation, by Equation 5, the appropriate form of the Koutecky–Levich equation (52) for Scheme I:

$$i_L^{-1} = (FAa_\infty)^{-1}\left[\frac{1}{k_D} + \frac{1}{k_{ads}} + \frac{a_\infty}{\Gamma_L k_{des}} + \frac{b_\infty}{\Gamma_L k_{des}}\right] \tag{5}$$

This expression, together with Equation 1, predicts that plots of i_L^{-1} against $W^{-1/2}$ should be linear with a gradient, representing the transport term, proportional to the reciprocal reactant concentration, a_∞^{-1}.

The intercept, I, corresponding to the rate of the surface step in the electrode reaction, is given, for oxidation, by

$$I = (FA)^{-1}\left[\frac{1}{k_{ads}a_\infty} + \frac{1}{\Gamma_L k_{des}} + \frac{b_\infty}{a_\infty \Gamma_L k_{des}}\right] \quad (6)$$

In this expression the terms in the square bracket represent the rate-limiting processes at the electrode surface. The first and second terms describe the adsorption and desorption of reactant and product respectively, and the third term describes the competition of the reactant, A, and the product, B, for adsorption sites, that is, product inhibition. Equation 6 predicts that, in the absence of product in bulk solution ($b_\infty = 0$), I should vary linearly with the reciprocal of the concentration of the reactant (a_∞^{-1}) and that the corresponding plots should have a slope proportional to k_{ads}^{-1} and an intercept proportional to k_{des}^{-1}. Furthermore, it predicts that the reaction should be inhibited by addition of the product to the bulk solution, such that, for a constant value of reactant concentration, a_∞, I varies linearly with product concentration, b_∞.

An equation describing the current–voltage curve may be obtained from the general expression, Equation 4; for oxidation in the case where product is absent from the bulk solution ($b_\infty = 0$) it is given by

$$\frac{i_L - i}{i} = \exp\left[\frac{nF}{RT}(E - E^\circ)\right] + \left(\frac{k_{des}}{k_e^\circ}\right)\exp\left[-\alpha\frac{nF}{RT}(E - E^\circ)\right]\left(1 - \frac{i_L}{i_{Lev}}\right) \quad (7)$$

where i_L is the observed limiting current and i_{Lev} ($=k_D a_\infty$) is the theoretical diffusion-limited current predicted by the Levich equation. The apparent standard electrochemical rate constant, k_s°, may also be derived from Equation 4 and is given by

$$k_s^\circ = \frac{k_{ads}k_{des}\Gamma_L k_e^\circ}{[k_{des}\Gamma_L + k_{ads}(a_\infty + b_\infty)](2k_e^\circ + k_{des})} \quad (8)$$

This expression shows that k_s° is not only a function of the individual rate constants k_{ads}, k_{des}, and k_e° but is also dependent upon concentration, such that the apparent rate constant will decrease as the concentration increases.

Current–voltage curves for the reduction of ferricytochrome c and the oxidation of ferrocytochrome c obtained at a rotating gold disk electrode with 4,4′-bipyridyl in solution (Figure 3) are close to the reversible limit, showing that, at this concentration, the overall charge transfer process at the surface is fast. Values for the half-wave potential

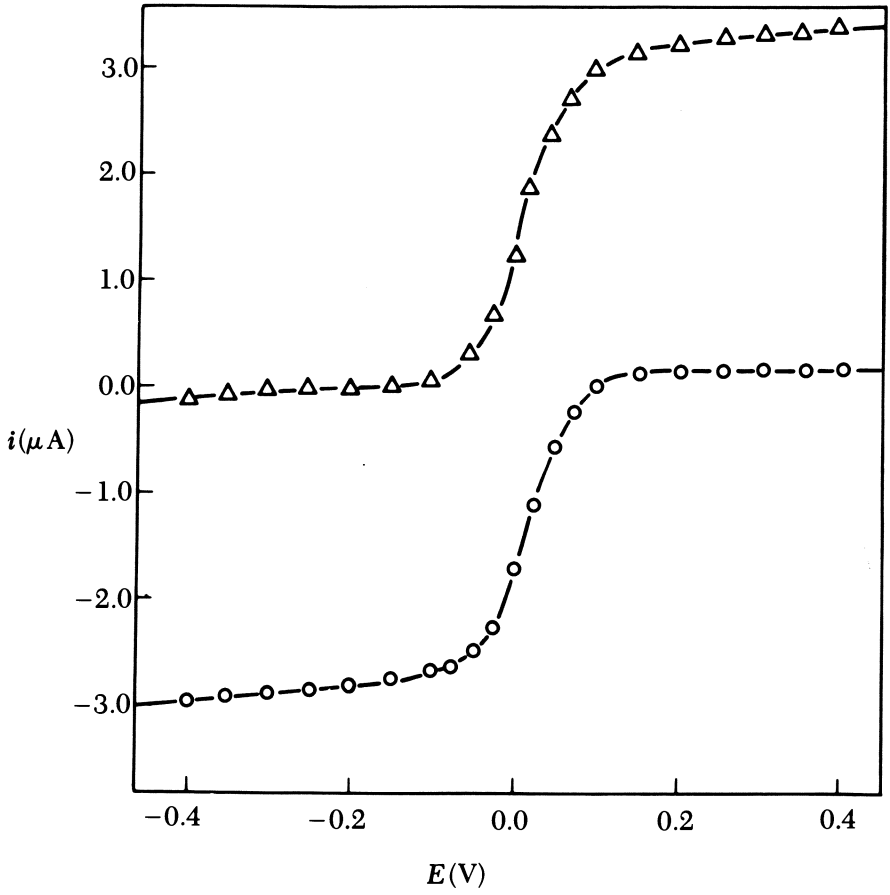

Figure 3. Typical current–voltage curves for the oxidation (△) and reduction (○) of cytochrome c at a rotating gold disk electrode modified with 4,4'-bipyridyl. Rotation speed, W = 25 Hz. (Reproduced from Ref. 49. Copyright 1981, American Chemical Society.)

are in good agreement with previously obtained (*45*, *46*) values. The rotation speed dependence of the limiting current, i_L, for both the oxidation and reduction reactions of cytochrome c, does not obey the Levich equation (*51*) in which i_L varies linearly with $W^{1/2}$, showing that the limiting current is not determined by transport alone and therefore, that there must be some other potential-independent rate-limiting step in the overall process. Koutecky–Levich plots for the reduction of ferricytochrome c (Figure 4) and oxidation of ferrocytochrome c are linear and the slopes of these plots provide a value for the diffusion coefficient, $D = 1.1 \times 10^{-10}$ m²/s, in good agreement with previously determined values (*53*, *54*). The rate of the surface step, represented

by the reciprocal of the intercept, I, of the Koutecky–Levich plots, shows a dependence on reactant concentration (Figure 5) as predicted for Scheme I by Equation 6 and also shows the predicted inhibition by added product (Figures 6 and 7). The observed kinetics are consistent with the proposed reaction mechanism, and from the slopes and intercepts of these plots, values for k_{ads} and k_{des} are obtained.

Further studies (*49*) using the ac rotating ring–disk technique (55) confirm the involvement of the adsorption step in the electrode reac-

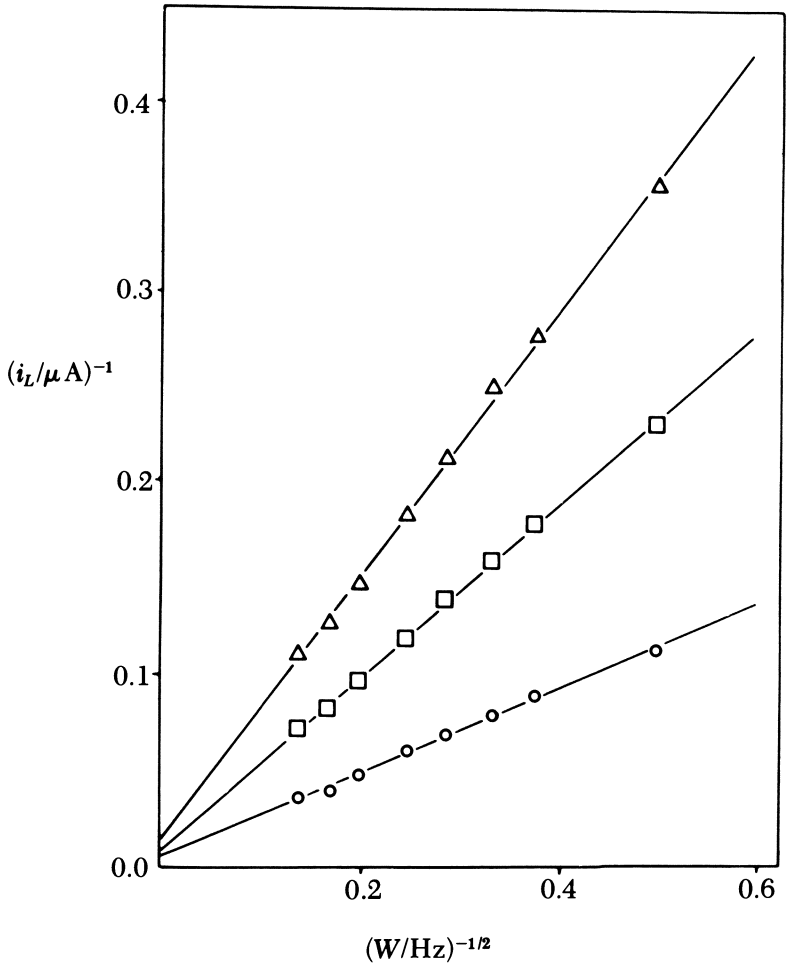

Figure 4. Typical Koutecky–Levich plots, according to Equation 5, of the limiting current, i_L, for the reduction of ferricytochrome against the square root of rotation speed, $W^{1/2}$. Key (ferricytochrome c concentration): △, 26; □, 48; and ○, 101 μM. The slope of these plots represent the reciprocal transport rate and the intercept represents the reciprocal overall rate of the surface step.

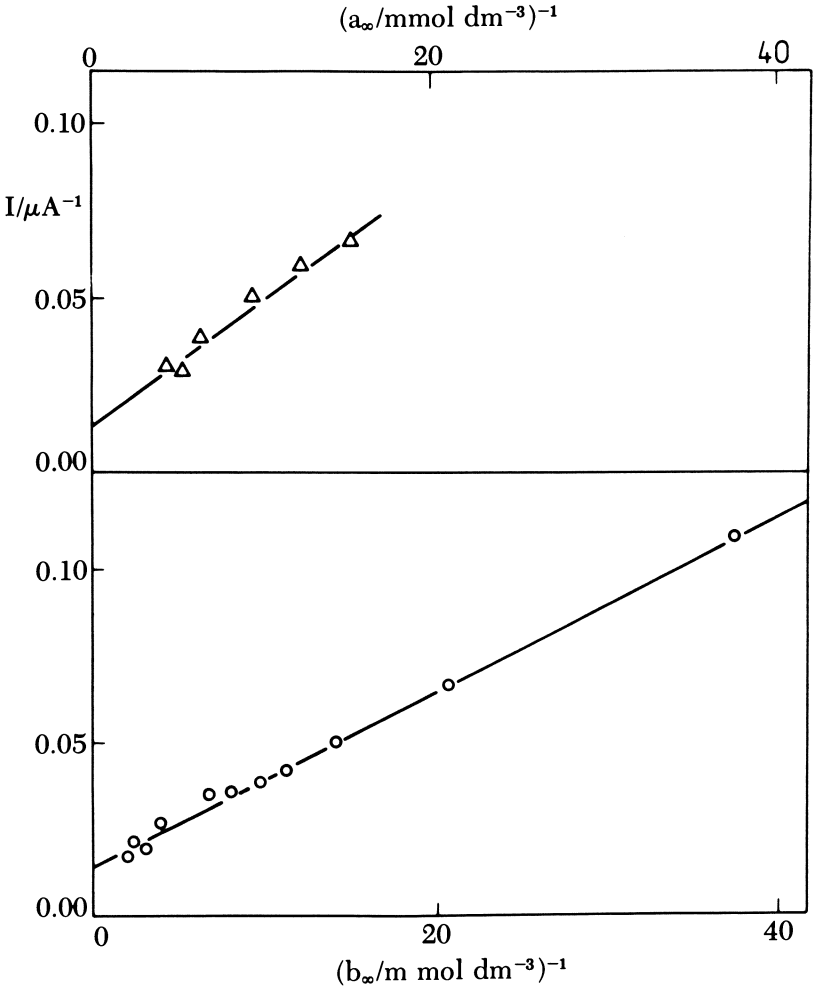

Figure 5. Variation of the intercept, I, of the Koutecky–Levich plots with reactant concentration according to Equation 6 for oxidation (top) and reduction (bottom) of cytochrome c. From the slopes and intercepts of these plots values for k_{ads} and k_{des} were obtained. (Reproduced from Ref. 49. Copyright 1981, American Chemical Society.)

tion and provide a value for the adsorption equilibrium constant, $K = 2 \times 10^4 M^{-1}$, which is in good agreement with that determined from the rotating disk kinetics ($K = k_{ads}/k_{des}$), and gives a value for the limiting surface coverage, Γ_L, consistent with monolayer formation. Detailed analysis (*49*) of the current–voltage curve (Figure 3), according to Equation 7, provides a value for the first-order electron transfer rate

constant, k_e°, consistent with the value for the standard electrochemical rate constant, k_s°, determined (*47*, *48*) from ac impedance experiments. The values of the various rate constants are as follows: $k_{ads} = 3 \times 10^{-4}$ m/s, $k_{des} = 50\ s^{-1}$, $k_e^\circ = 50\ s^{-1}$, and $\Gamma_L = 1.2 \times 10^{-6}$ mol/m^2.

These studies clearly demonstrate the involvement of a rapid reversible binding step in the electrode reaction of cytochrome c, as outlined in Scheme I. The importance of this binding step in achieving rapid electron transfer is discussed later.

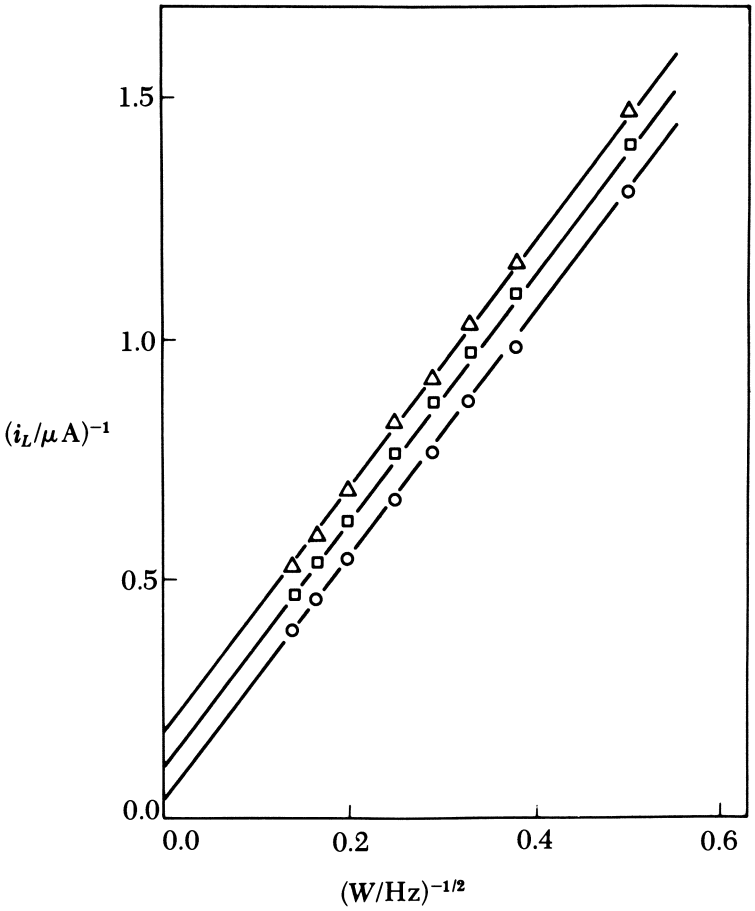

Figure 6. Typical Koutecky–Levich plots for the oxidation of ferrocytochrome c (86 μM), in the presence of different concentrations of ferricytochrome c: ○, 0; □, 105; and △, 225 μM. The increase in the intercept (representing the reciprocal rate of the surface step) with increasing product concentration illustrates its inhibitory effect as predicted by Equation 6. (Reproduced from Ref. 49. Copyright 1981, American Chemical Society.)

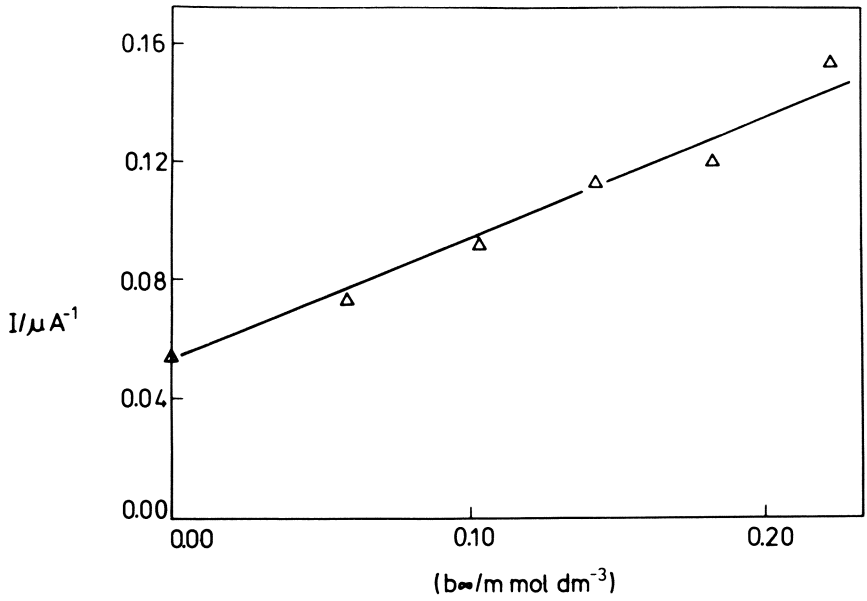

Figure 7. Variation of the intercept, I, of the Koutecky–Levich plots with product concentration at constant reactant concentration for the oxidation of ferrocytochrome c (86 μM) (as shown in Figure 6) (49).

The Electrochemistry of Cytochrome c at the Mercury Electrode

Although the electron transfer reaction of cytochrome c at the mercury electrode has been studied for many years, the first detailed polarographic study (37) demonstrated that well-defined polarographic waves were attributable to the reduction of the heme iron prosthetic group. At low protein concentrations the behavior is essentially reversible, but becomes increasingly irreversible with increasing protein concentration (Table I). This apparent self-inhibition of the electrode process was attributed to protein adsorption at the electrode surface. The limiting current shows a linear dependence on protein concentration (Table I), indicating diffusion control, but the apparent diffusion coefficient, determined from this dependence, is significantly lower than that measured by hydrodynamic methods.

Betso et al. (37) proposed two mechanisms to explain the retarded mass-transport rate. First, that cytochrome c, in order to reach the electrode and be reduced, must diffuse through an adsorbed protein layer, presumably at a slower rate than in free solution. The observed limiting current then will reflect the overall diffusional transport rate through both media and not simply that through aqueous solution. Second, they suggested that, if the reaction proceeds via electron ex-

change between the electrode and adsorbed protein, with subsequent electron exchange between adsorbed protein and freely diffusing cytochrome c, and if the electron transfer occurs via the exposed heme edge only, then rotational diffusion of the adsorbed species, carrying charge from the electrode to cytochrome c in solution, may be the slow step in the mass transport process. They also proposed that a retarded rate of electron transfer through an adsorbed protein layer to freely diffusing cytochrome c may account for the irreversibility in the observed polarograms and that the increasing irreversibility with increasing protein concentration is consistent with a concomitant increase in protein coverage of the electrode. The study clearly demonstrates that, despite adsorption phenomena, the electrode process results in the conversion of freely diffusing ferricytochrome c to freely diffusing ferrocytochrome c and, therefore, the electron transfer mechanism must involve either electron transfer through the adsorbed protein layer or exchange between adsorbed product and free solution reactant species.

These original experimental findings were confirmed (*38*) and further studies (*39*, *40*) employed differential capacitance and radiochemical measurements to investigate the adsorption behavior of the protein. The form of the adsorption isotherm indicates a simple equilibrium between adsorbed and solution species with a binding constant, $K \sim 4 \times 10^5 M^{-1}$. We derive this value from the reported data

Table I. Concentration Dependence of Polarographic Behavior of Cytochrome c in Tris–Cacodylate, pH 6.05

Protein Concentration, (M)	$E_{1/2}$ (V)	$i_d/conc$ (A/mM)
17.7	+0.005	0.85
20.3	+0.005	0.69
26.2	−0.005	1.07
35.5	−0.005	1.24
40.1	−0.009	1.07
41.0	−0.005	1.11
63.7	−0.065	0.99
67.0	−0.030	1.02
83.7	−0.070	1.22
104.7	−0.095	1.10
129.4	−0.100	1.19
130.9	−0.130	1.10
163.6	−0.155	1.19
204.5	−0.160	0.97

Source: Reproduced from Ref. 37. Copyright 1972, American Chemical Society.

(*38–40*), assuming, for simplicity, a Langmuir adsorption isotherm. However, Scheller prefers (*41*) a mechanism similar to one originally proposed, in which an irreversibly adsorbed layer of protein retards the rate of electron transfer between the electrode and the freely diffusing protein. Nevertheless, exchange between adsorbed and solution species was observed (*39*) and the possibility of a dual mechanism, involving both electron transfer through the adsorbed layer to protein in solution and exchange between reduced adsorbed and oxidized solution species, was considered.

Any mechanism proposed for the reduction of cytochrome c at the mercury electrode must attempt to account for the following experimental observations:

1. The observed polarograms are essentially reversible at low cytochrome concentrations.
2. The observed polarograms become increasingly irreversible as the protein concentration is increased.
3. The diffusion coefficient determined from the limiting current is anomalously low.
4. The protein adsorbs at the electrode surface.

The mechanisms originally proposed by Betso et al. and further developed by Scheller et al. might qualitatively account for each of these experimental observations independently, but a single mechanism cannot readily account for each observation simultaneously. For example, the mechanism proposed to account for the low mass transport rate must do so throughout the concentration range investigated, and this presumes that the electrode surface is fully covered by an adsorbed layer of protein over this entire concentration range. Conversely, the mechanism proposed to explain the transition from reversible to irreversible behavior as the protein concentration increases presupposes that the surface coverage is concentration-dependent. This mechanism requires that at low protein concentrations the surface coverage is low, so that electron transfer is not impeded by an adsorbed layer of protein. Consequently, rapid electron transfer may occur at a predominantly unblocked surface, resulting in the observed, essentially reversible, behavior. On the other hand, at high concentrations the surface coverage must be high so that electron transfer occurs predominantly through the adsorbed layer at a retarded rate, resulting in irreversibility in the observed polarograms. Furthermore, any mechanism that assumes irreversible adsorption appears to be inconsistent with the nature of the adsorption isotherm. Therefore, the mechanisms so far proposed to explain the electrochemical behavior of cytochrome c at the mercury electrode apparently cannot adequately account for all of the experimental observations.

The polarographic behavior of cytochrome c exhibits the same general features that we described for the behavior of cytochrome c at the modified gold electrode. That is, in both cases adsorption of the protein at the electrode surface occurs and self-inhibition effects are observed. In addition, the prevalence of reaction mechanisms involving the formation of tightly bound complexes in the homogeneous solution redox reactions of cytochrome c suggest that such a mechanism may also be applicable to the reaction at the mercury electrode. We therefore considered the possibility that the electron transfer reaction of cytochrome c at the mercury electrode follows the reaction mechanism, outlined in Scheme I, that we showed to be operative at the modified gold electrode.

The diffusional transport problem for the dropping mercury electrode is, qualitatively, the same as that for the rotating disk electrode. As in the case of the rotating disk, the transport flux, j, to the dropping mercury electrode may be written (56) as follows:

$$j = k_D (c_\infty - c_0)$$

where

$$k_D = (36\pi)^{1/3} \left(\frac{m'}{\rho}\right)^{2/3} \left(\frac{7}{3} D\right)^{1/2} t^{1/6} \tag{9}$$

where m' is the mercury flow rate in kg/s, ρ is the density of mercury, and t is the lifetime of the drop. The theory developed for Scheme I may be applied to the results obtained at the dropping mercury electrode. However, unlike the rotating disk electrode, the dropping mercury electrode does not truly represent a steady state and, in applying the equations developed for Scheme I, we neglect the possibility of any time dependence of the protein adsorption at the dropping mercury electrode during the life of the drop. In addition, the simple theory takes no account of the possibility of any potential dependence of protein adsorption that may lead to deviations from the predicted quantitative behavior. Nevertheless, in the absence of a more complete, and necessarily more complex, theory for the dropping mercury electrode itself, the theory for the rotating disk electrode forms a useful basis for the qualitative description of the current–voltage curves observed at the dropping mercury electrode.

As expressed by Equation 5, the limiting current for an electrode process that follows the mechanism in Scheme I is controlled by the adsorption kinetics as well as the diffusional transport rate, and hence, will be lower than that predicted on the basis of pure diffusion control. For cases where this reaction scheme is operative, a diffusion coefficient calculated from the limiting current, assuming it to be simply

diffusion limited, will be lower than the true value. Scheme I can account for the low values of the limiting current (*see* Table I), originally determined (37), and the anomalously low diffusion coefficient, $D = 0.5 \times 10^{-10}$m^2/s, determined from them.

As described by Equation 8, the rate constant, k_s°, for an electron transfer reaction that follows the reaction mechanism in Scheme I is a function of the three rate constants that describe the overall rate of electron transfer, k_{ads}, k_{des}, and k_e°, and also the concentration of the reactant; Equation 8 shows that the apparent k_s° value will decrease with increasing concentration. The form of the current–voltage curve, and in particular, its dependence on concentration, may be found by considering Equation 7. The first term on the right side represents the Nernstian response expected for a reversible system, and the second term represents deviations from this response due to the kinetics of the electrode process. Substituting $i = i_{L/2}$ into Equation 7 yields an expression for the half-wave potential, which, for the reduction, is given by

$$\exp\left[\frac{nF}{RT}(E_{1/2} - E^\circ)\right] + \frac{k_{des}}{k_e^\circ}\left(1 - \frac{i_L}{i_{Lev}}\right)\exp\left[\frac{\beta nF}{RT}(E_{1/2} - E^\circ)\right] = 1 \quad (10)$$

This expression shows that, because, according to Equation 5, i_L/i_{Lev} gets progressively smaller as the concentration is increased, $\exp[nF/RT(E_{1/2} - E^\circ)]$ will progressively decrease from its reversible limit of 1: that is, the measured $E_{1/2}$ for reduction will exhibit an increasing negative shift from E° as the protein concentration is increased, as is indeed observed (37) (*see* Table I).

The reaction mechanism outlined in Scheme I accounts, qualitatively, for the major features of the observed polarograms. In addition, the observed adsorption isotherm is that expected for such a reaction scheme. Therefore, the electron transfer reaction of cytochrome c at the mercury electrode follows a reaction sequence in which the electron transfer event is preceded by adsorption of the protein at the electrode surface. The protein probably binds directly to the mercury surface. On the other hand, the proposal that an irreversibly adsorbed layer of protein is formed at the electrode cannot be discounted. Initial formation of an irreversibly adsorbed layer to form a surface to which the native protein can bind in the manner proposed could also account for the observed polarograms. However, because the observed polarography can be explained in terms of Scheme I without involvement of an irreversibly adsorbed layer of protein, such a proposal,

which originally sought to explain the experimental current–voltage relationships, is essentially redundant. In addition, such behavior is inconsistent with the observed adsorption isotherm, and it is unlikely that rapid electron transfer would be exhibited through even a monolayer of protein, the order of 30 Å thick. Whatever the nature of the electrode surface, we conclude that the reaction mechanism is that given in Scheme I and the adsorption step is crucial in the overall reaction mechanism.

In addition to the polarographic studies, the reversible electrode reaction of cytochrome c at a tin-doped indium oxide electrode was reported (*57*). The observed cyclic voltammetry indicates a simple, diffusion-controlled reversible process, but the apparent diffusion current determined from the peak current is anomalously low, as in the polarographic studies. These results show that the process is not purely diffusion controlled and that an additional rate-limiting process, other than electron transfer, is present in the overall reaction mechanism. Therefore, this potential independent rate-limiting step may be a rapid adsorption–desorption step and, as in the case of the electron transfer reaction of cytochrome c at the other electrodes just described, the reaction at the indium oxide electrode follows the reaction mechanism outlined in Scheme I. Possibly an interaction between the acidic oxide surface and the basic lysine residues of the protein is responsible for the proposed binding.

Other Electrochemical Studies of Metalloproteins

In addition to the studies of mitochondrial cytochrome c, the multiheme c-type cytochrome from the *Desulfovibrio* sulfate-reducing bacteria, cytochrome c_3, also was the subject (*42*, *43*, *58*) of electrochemical investigation. Preliminary studies (*58*) showed that cytochrome c_3 gives well-defined dc and ac cyclic voltammograms at the modified gold electrode; and hence, that it takes part in a rapid and apparently diffusion-controlled electron transfer reaction at this electrode.

Cytochrome c_3 also was studied (*42*, *43*) at the mercury electrode where again well-defined voltammetric waves are observed in cyclic voltammetry, normal pulse, and differential pulse polarography. In this case adsorption of the protein at the mercury surface was clearly indicated by the observation that mercury drops formed in a solution of cytochrome c_3 do not readily coalesce, and later by differential capacitance measurements. No conclusions were drawn concerning the mechanism of these reactions from the current–voltage data, other than that any kinetic steps involved must be relatively rapid compared

with the diffusion rate. However, because rapid electron transfer is observed in conjunction with considerable adsorption of the protein on the mercury electrode, the mechanism may involve rapid adsorption and desorption steps like those observed with cytochrome c at the modified gold electrode.

Ferredoxins were studied (*44*, *59–65*) at the mercury electrode. Although the electrochemistry appears (*59*) to be complicated by decomposition at the electrode surface, a more recent study (*44*) indicates that reduction of the iron–sulfur prosthetic group may be achieved in alkaline solution with pH > 8. Again, adsorption of the protein at the electrode is evident, supporting our suggestion that binding between the protein and the electrode is a crucial factor in the electron transfer reactions of metalloproteins.

Discussion

The role of the adsorption step in determining the kinetics of the overall electron transfer reaction of cytochrome c at an electrode may now be considered. Using transition-state theory, the free-energy profile for the electron transfer reaction of cytochrome c at the modified electrode at its standard electrode potential was constructed (*49*). The free energies of activation of the three steps in the reaction may be calculated using the transition-state theory expression, $k = \exp - \Delta G^{\ddagger}/RT$. For the adsorption step the frequency factor, $Z = 10^2$ m/s is used, which is the collision frequency used in the Marcus treatment (*66*), but for the first-order electron transfer and desorption steps the usual first order frequency factor, kT/h is used. The following values for the free energies of activation are obtained: adsorption, $\Delta G^{\ddagger} = 31$ kJ/mol; and desorption and electron transfer, $\Delta G^{\ddagger} = 63$ kJ/mol. The free-energy profile is shown in Figure 8.

The most important feature of this free-energy profile is that the binding energy is large, and as such is responsible for considerable rate enhancement of the overall rate of the electrode reaction. The overall rate is determined, not only by the probability of electron transfer between the electrode and species at the surface, but also by the probability of finding the species at the surface. The binding energy can therefore influence the overall rate by determining the distribution of species at the surface. For example, if the binding energy of the protein to the surface was zero, the equilibrium constant for binding would be given by the ratio of the frequency factors for adsorption and desorption, $K_0 = k_{ads}/k_{des} = 2 \times 10^{-11}$ m, where $\Delta G^{\ddagger}_{ads} = \Delta G^{\ddagger}_{des}$. Using this value for the binding constant and the measured first-order electron transfer rate constant for species at the surface of the modified electrode, the standard electrochemical rate constant, $k_s = K_0 k_e^{\circ} = 10^{-9}$

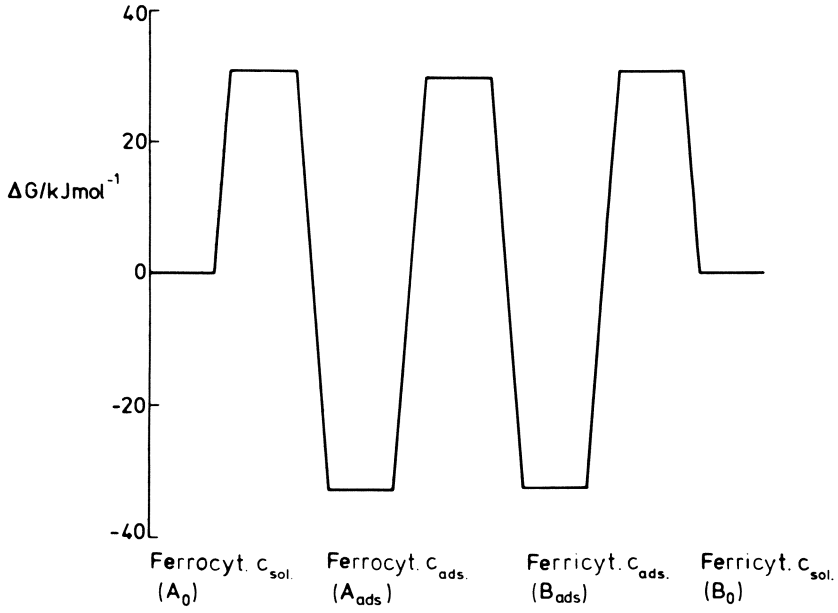

Figure 8. The free-energy profile for the reduction and oxidation of cytochrome c at a gold electrode, modified with 4,4'-bipyridyl, held at a potential, E = E°. *(Reproduced from Ref.* 49. *Copyright 1981, American Chemical Society.)*

m/s was calculated for the case where there is zero-binding energy. This value compares with the measured rate at the modified electrode, where the binding energy is large, k_s = 1.5 m/s.

The binding of the protein to the surface is clearly of great importance in the enhancement of the overall rate of the electrode reaction at the modified electrode and may explain why the reaction is very slow (*67*) at the unmodified electrode, where favorable binding interaction may not be possible. Furthermore, the requirement for such a binding interaction may be general and so may account for the fact that rapid-electron exchange between electrodes and proteins is not observed, except where adsorption phenomena also are encountered.

Rate enhancement, according to this model, is a simple consequence of the binding energy that holds the reactants together and stabilizes the intermediate precursor complex, thereby overcoming the large activation energy for electron transfer itself and increasing the overall rate above that expected for a simple collisional process. Catalysis of this nature is a familiar concept in enzyme catalysis (*68–70*) and electrocatalysis (*71*). On the other hand, classical electron transfer theory, according to the Marcus formulation (*66*), introduces a work term, representing the work necessary to bring the reactants to-

gether, to account for differences in the interaction between pairs of reactants and this work term may be equated with the binding energy in our model. The electrostatic contributions to this work term are particularly important factors in the Marcus theory analysis of electron transfer reactions between metalloproteins and small molecule redox reagents (*72*, *73*).

However, strong binding alone may not necessarily lead to rate enhancement, and the adsorption and desorption rates must be fast for rapid exchange between adsorbed product and solution reactant species. The adsorption and desorption rate constants determined from the rotating disk kinetics showed that these rates are indeed rapid at the modified gold electrode.

Having discussed the electron transfer reaction of cytochrome c at an electrode, it will be instructive to consider its physiological redox reactions and the possible requirements for its efficient function in the mitochondrial respiratory chain. Three possible requirements may be identified: (1) that cytochrome c reacts rapidly with its physiological redox partners, (2) that it should not react with redox species other than its physiological redox partners, and (3) that the rate of electron transfer be controlled to meet the required respiratory rate. As briefly discussed, binding between cytochrome c and its physiological redox partners is of crucial importance in these electron transfer reactions and a strong correlation is found (*25*, *74*) between the measured physiological activity of a variety of cytochromes c and the strength of binding in their complexes with the oxidase. The binding energy apparently is an important factor in the control of the overall electron transfer rate. Furthermore, the strength of binding is dependent on the concentration of anions in solution (*74*). In particular ADP, ATP, and phosphate affect the oxidase reaction and respiratory control may be achieved in this fashion (*74*). Therefore, the required rapidity, specificity, and control in the physiological redox reactions of cytochrome c can be achieved by suitable binding interactions.

The lysine residues of cytochrome c are important in determining its reactivity with its physiological redox partners. Chemical modifications that replace the positive charge of the lysine ϵ-amino group with a neutral or negatively charged group inhibit the physiological redox reactions of cytochrome c (*11*, *13*, *14*). The involvement of the positively charged lysine residues is further illustrated (*11*, *12*, *14*) by the competitive inhibition shown by basic proteins and the synthetic polypeptide, poly-L-lysine. The x-ray structure (*75*) also supports (*15*) the suggestion that the lysine residues, which are highly conserved and form a ring around the exposed heme edge, are an important feature of the protein. Comparative kinetic studies (*74*, *76*, *77*) of the

oxidase activity of a wide variety of c-type cytochromes with varying amino acid sequences further indicate the importance of the lysine residues in determining the reactivity of the protein. Following the observation (*16*) that modification of lysine 13 alone dramatically decreases the activity of cytochrome c, many detailed and specific chemical modification studies were made (*17–25*) to define the surface domain of cytochrome c involved in its physiological binding. These studies confirmed the involvement of those lysine residues in the vicinity of the exposed heme edge. Cytochrome c apparently binds in an orientation that not only brings the heme group as a whole close to its physiological redox partner, but also brings the exposed heme edge adjacent to it. This preferred orientation (*78*) might facilitate the electron transfer reaction by minimizing the distance between redox centers in the protein complex and allowing electron transfer via the exposed heme edge rather than through the polypeptide fabric of the protein.

In view of the nature of the physiological redox reactions of cytochrome c just outlined, the electron transfer reactions of cytochrome c will probably be slow, except where a favorable binding interaction provides considerable rate enhancement, with the possible further requirement that this binding be in a preferred orientation. Furthermore, this binding interaction may be a physiological necessity, because it provides rapidity in the required reaction pathway and allows for specificity and possibly control. This conclusion clearly has serious implications for the study of the electrochemistry of metalloproteins at electrodes because it implies that rapid electron transfer between metalloproteins and electrodes might be achieved only in cases where adsorption, analogous to binding in the physiological case, occurs. This suggestion is supported by the experimental studies of cytochrome c and other proteins at a variety of electrodes, as discussed.

As demonstrated (*47–49*) at the modified electrode, the electron transfer reaction of cytochrome c shows some striking analogies with its physiological redox reactions. Not only does the electrode reaction include an analogous binding step, but this binding apparently involves the cytochrome c lysine residues. That is, both chemical modification of the lysine residues and the competitive inhibitor, poly-L-lysine, inhibit the electrode reaction (*47, 48*). Previous work (*47–49*) suggested that the binding interaction observed in the electrode reaction is similar to that in the physiological case and involves the lysine residues in the vicinity of the exposed heme edge. The ϵ-amino groups of these lysine residues may hydrogen bond to the exposed pyridyl nitrogen of the adsorbed 4,4′-bipyridyl layer and bind the cytochrome with the exposed heme edge adjacent to the electrode surface, thereby

facilitating the electron-transfer reaction. Although the transition-state theory analysis of the rate enhancement due to binding just discussed does not take into account the possibility of such a preferred orientation of the protein at the surface, if, as indicated (*47*, *48*), cytochrome c does bind in a preferred orientation at the modified gold electrode, then this may be a further important feature of this electrode surface. Therefore, not only is rapid and reversible binding at the electrode essential, but this binding must be in the correct orientation.

Although the nature of the adsorption of cytochrome c, cytochrome c_3, and ferredoxin at mercury is less well-defined, the experimental observations that rapid electron transfer occurs in these cases, along with adsorption of the protein at the surface, further support our proposal that a favorable binding interaction between the protein and the electrode is a prerequisite for rapid electron transfer.

Conclusions

Studies of the electron transfer reactions of cytochrome c at a modified gold electrode and at the dropping mercury electrode indicate that binding of the protein to the electrode surface is a prerequisite for the achievement of rapid, direct electron transfer between electrodes and cytochrome c in solution. This binding is essential to overcome the large activation energy for electron transfer. However, binding alone does not necessarily lead to rapid electron transfer. In addition, it may be essential that the adsorption and desorption rates be fast in order that rapid exchange between adsorbed and solution species can occur, and that cytochrome c bind in a preferred orientation that brings the heme group close to the electrode surface, to enable rapid electron transfer between the bound protein and the electrode.

With the development of other suitable electrode surfaces that enable a protein to bind rapidly and reversibly to the electrode, it should prove possible to achieve rapid electron transfer between electrodes and other redox proteins which, hitherto, was not possible at conventional electrode surfaces. The development of such electrodes should enable the use of electrochemical methods for the study of redox proteins and should also enable the use (*79–81*) of enzymes as electrocatalysts.

Acknowledgments

The authors thank W. J. Albery, A. E. G. Cass, and A. R. Hillman for useful discussion. Support from the Science and Engineering Research Council, the National Research Development Corporation, and Johnson Matthey Ltd. is gratefully acknowledged.

Literature Cited

1. Nicholls, P. *Biochim. Biophys. Acta* **1974,** *346,* 261–310.
2. Smith, L.; Conrad, H. *Arch. Biochem. Biophys.* **1956,** *63,* 403–413.
3. Minnaert, K. *Biochim. Biophys. Acta* **1961,** *50,* 23–34.
4. Yonetani, T.; Ray, G. S. *J. Biol. Chem.* **1966,** *241,* 700–706.
5. Nicholls, P.; Mochan, E. *Biochem. J.* **1971,** *121,* 55–67.
6. Orii, Y.; Sekuzu, I.; Okunuki, K. *J. Biochem. (Tokyo)* **1962,** *51,* 204–215.
7. Nicholls, P.; Mochan, E. *Biochem. J.* **1971,** *121,* 69–82.
8. Gupta, R. K.; Yonetani, T. *Biochim. Biophys. Acta* **1973,** 502–508.
9. Kaminsky, L. S.; Chiang, Y.-L.; Yu, C. A.; King, T. E. *Biochem. Biophys. Res. Commun.* **1974,** *59,* 688–692.
10. Chiang, Y.-L.; Kaminsky, L. S.; King, T. E. *J. Biol. Chem.* **1976,** *251,* 29–36.
11. Takemori, S.; Wada, K.; Ando, K.; Hosokawa, M.; Sekuzu, Z.; Okunuki, K. *J. Biochem. (Tokyo)* **1962,** *52,* 28–37.
12. Davies, H. C.; Smith, L.; Wasserman, A. R. *Biochim. Biophys. Acta* **1964,** *85,* 238–246.
13. Fanger, M. W.; Harbury, H. A. *Biochemistry* **1965,** *4,* 2541–2545.
14. Mochan, E. *Biochim. Biophys. Acta* **1970,** *216,* 80–95.
15. Salemme, F. R.; Kraut, J.; Kamen, M. D. *J. Biol. Chem.* **1973,** *248,* 7701–7716.
16. Wada, K.; Okunuki, K. *J. Biochem. (Tokyo)* **1969,** *66,* 249–262.
17. Staudenmayer, N.; Ng, S.; Smith, M. B.; Millet, F. *Biochemistry* **1977,** *16,* 600–604.
18. Smith, H. T.; Staudenmayer, N.; Millet, F. *Biochemistry* **1977,** *16,* 4971–4974.
19. Ahmed, A. J.; Smith, H. T.; Smith, M. B.; Millet, F. S. *Biochemistry* **1978,** *17,* 2479–2483.
20. Pettigrew, G. *FEBS Lett.* **1978,** *86,* 14–16.
21. Rieder, R.; Bosshard, H. R. *FEBS Lett.* **1978,** *92,* 223–226.
22. Ferguson-Miller, S.; Brautigan, D. L.; Margoliash, E. *J. Biol. Chem.* **1978,** *253,* 149–159.
23. Rieder, R.; Bosshard, H. R. *J. Biol. Chem.* **1978,** *253,* 6045–6053.
24. Kang, C. H.; Brautigan, D. L.; Osheroff, N.; Margoliash, E. *J. Biol. Chem.* **1978,** *253,* 6502–6510.
25. Osheroff, N.; Brautigan, D. L.; Margoliash, E. *J. Biol. Chem.* **1980,** *255,* 8245–8251.
26. Stellwagen, E.; Shulman, R. G. *J. Mol. Biol.* **1973,** *80,* 559–573.
27. Stellwagen, E.; Cass, R. D. *J. Biol. Chem.* **1975,** *250,* 2095–2098.
28. Miller, W. G.; Cusanovich, M. A. *Biophys. Struct. Mech.* **1975,** *1,* 97–111.
29. McCray, J. A.; Kihara, T. *Biochim. Biophys. Acta* **1979,** *548,* 417–426.
30. Goldberg, M.; Pecht, I. *Biochemistry* **1976,** *15,* 4197–4208.
31. Segal, M. G.; Sykes, A. G. *J. Am. Chem. Soc.* **1978,** *100,* 4585–4592.
32. Lappin, A. G.; Segal, M. G.; Weatherburn, D. C.; Sykes, A. G. *J. Am. Chem. Soc.* **1979,** *101,* 2297–2301.
33. Lappin, A. G.; Segal, M. G.; Weatherburn, D. C.; Henderson, R. A.; Sykes, A. G. *J. Am. Chem. Soc.* **1979,** *101,* 2302–2306.
34. Armstrong, F. A.; Sykes, A. G. *J. Am. Chem. Soc.* **1978,** *101,* 7710–7715.
35. Armstrong, F. A.; Henderson, R. A.; Sykes, A. G. *J. Am. Chem. Soc.* **1979,** *101,* 6912–6917.
36. Armstrong, F. A.; Henderson, R. A.; Sykes, A. G. *J. Am. Chem. Soc.* **1980,** *102,* 6545–6551.
37. Betso, S. R.; Klapper, M. H.; Anderson, L. B. *J. Am. Chem. Soc.* **1972,** *94,* 8197–8204.
38. Scheller, F.; Janchen, M.; Lampe, J.; Prumke, H.-J.; Blanck, J.; Palecek, E. *Biochim. Biophys. Acta* **1976,** *412,* 157–167.

39. Scheller, F.; Prumke, H.-J.; Schmidt, H. E. *J. Electroanal. Chem.* **1976,** *70,* 219–227.
40. Scheller, F.; Prumke, H.-J.; Schmidt, H. E.; Mohr, P. *Bioelectrochem. Bioenerg.* **1976,** *3,* 328–337.
41. Scheller, F.; Prumke, H.-J. *Stud. Biophys.* **1976,** *60,* 137–142.
42. Niki, K.; Yagi, T.; Inokuchi, H.; Kimura, K. *J. Electrochem. Soc.* **1977,** *124,* 1889–1891.
43. Niki, K.; Yagi, T.; Inokuchi, H.; Kimura, K. *J. Am. Chem. Soc.* **1979,** *101,* 3335–3340.
44. Kakutani, T.; Toriyama, K.; Ikeda, T.; Senda, M. *Bull. Chem. Soc. Jpn.* **1980,** *53,* 947–950.
45. Eddowes, M. J.; Hill, H. A. O. *J. Chem. Soc., Chem. Commun.* **1977,** 721–722.
46. Eddowes, M. J.; Hill, H. A. O. *J. Am. Chem. Soc.* **1979,** *101,* 4461–4464.
47. Eddowes, M. J.; Hill, H. A. O.; Uosaki, K. *J. Am. Chem. Soc.,* **1979,** *101,* 7113–7114.
48. Eddowes, M. J.; Hill, H. A. O.; Uosaki, K. *Bioelectrochem. Bioenerg.* **1980,** *7,* 527–537.
49. Albery, W. J.; Eddowes, M. J.; Hill, H. A. O.; Hillman, A. R. *J. Am. Chem. Soc.,* **1981,** *103,* 3904.
50. Hill, H. A. O.; Uosaki, K. *J. Electroanal. Chem.* **1981,** *122,* 321.
51. Levich, V. G. "Physicochemical Hydrodynamics"; Prentice Hall: Engelwood Cliffs, NJ, 1962.
52. Koutecky, J.; Levich, V. G. *Zh. Fiz. Khim.* **1958,** *32,* 1565–1575.
53. Theorell, H. *Biochem. Z.* **1936,** *285,* 207–218.
54. Ehrenberg, A. *Acta Chem. Scand.* **1957,** *11,* 1257–1270.
55. Albery, W. J.; Hillman, A. R. *J. Chem. Soc., Faraday Trans. 1,* **1979,** *75,* 1623–1634.
56. Albery, W. J. "Electrode Kinetics"; Clarendon: Oxford, England, 1975.
57. Yeh, P.; Kuwana, T. *Chem. Lett.* **1977,** 1145–1148.
58. Eddowes, M. J.; Elzanowska, H.; Hill, H. A. O. *Biochem. Soc. Trans.* **1979,** *9,* 735–737.
59. Ikeda, T.; Toriyama, K.; Senda, M. *Bull. Chem. Soc. Jpn.* **1979,** *52,* 1937–1943.
60. Wietzmann, P. D. J.; Kennedy, I. R.; Caldwell, R. A. *FEBS Lett.* **1971,** *17,* 241–244.
61. Dalton, H.; Zubieta, J. *Biochim. Biophys. Acta* **1973,** *322,* 133–140.
62. Chien, Y. W. *J. Pharm. Sci.,* **1976,** *65,* 1471–1476.
63. Kiselev, B. A.; Kazakova, A. A.; Evstigneev, V. B.; Gins, V. K.; Mukhin, E. N. *Biofizika* **1976,** *21,* 35–39.
64. Hill, C. L.; Renaud, J.; Holm, R. H.; Mortenson, L. E. *J. Am. Chem. Soc.* **1977,** *99,* 2549–2557.
65. Bianco, P.; Haladjian, J. *Biochem. Biophys. Res. Commun.* **1977,** *78,* 323–327.
66. Marcus, R. A. *J. Phys. Chem.* **1963,** *67,* 853–857.
67. Heineman, W. R.; Norris, B. J.; Goelz, J. P. *Anal. Chem.* **1975,** *47,* 79–84.
68. Jencks, W. P. "Catalysis in Chemistry and Enzymology"; McGraw-Hill: New York, 1969.
69. Jencks, W. P. *Mol. Biol. Biochem. Biophys.* **1980,** *32,* 3–25.
70. Albery, W. J.; Knowles, J. R. *Biochemistry* **1976,** *15,* 5631–5640.
71. Appleby, A. J. *Mod. Aspects Electrochem.* **1974,** *9,* 369–478.
72. Sutin, N. In "Bioinorganic Chemistry—II," Raymond, K. N., Ed.; ACS ADVANCES IN CHEMISTRY SERIES, No. 162, ACS: Washington, D.C., 1977, 156–172.
73. Wherland, S.; Gray, H. B. In "Biological Aspects of Inorganic Chemistry"; Addison, A. W.; Cullen, W. R.; Dolphin, D.; James, B. R. Eds.; Wiley: New York, 1977; pp. 289–368.

74. Ferguson-Miller, S.; Brautigan, D. L.; Margoliash, E. *J. Biol. Chem.* **1976,** *251,* 1104–1115.
75. Mandel, N.; Mandel, G.; Trus, B. L.; Rosenberg, J.; Carlson, G.; Dickerson, R. E. *J. Biol. Chem.* **1977,** *252,* 4619–4636.
76. Kamen, M. D.; Errede, B. *Biochemistry* **1978,** *17,* 1015–1027.
77. Dethmers, J. K.; Ferguson-Miller, S.; Margoliash, E. *J. Biol. Chem.* **1979,** *255,* 11973–11981.
78. Salemme, F. R. *Annu. Rev. Biochem.* **1977,** *46,* 299–329.
79. Higgins, I. J.; Hammond, R. C.; Plotkin, E.; Hill, H. A. O.; Uosaki, K.; Eddowes, M. J.; Cass, A. E. G. In "Hydrocarbons in Biotechnology"; Harrison, D. E. F.; Higgins, I. J.; Watkinson, R. Eds.; Inst. Petro.: London, 1980; pp. 181–193.
80. Scheller, F.; Renneberg, R.; Schwarze, W.; Strnad, G.; Pommerening, K.; Prumke, H.-J.; Mohr, P. *Acta Biol. Med. Ger.* **1979,** *38,* 503–509.
81. Tarasevich, M. R. *Bioelectrochem. Bioenerg.* **1979,** *6,* 587–597.

RECEIVED for review June 2, 1981. ACCEPTED October 7, 1981.

Electrochemical Studies of Cytochrome c_3 of *Desulfovibrio vulgaris*

KATSUMI NIKI—Yokohama National University, Department of Electrochemistry, Hodogaya-ku, Yokohama 240, Japan

TATSUHIKO YAGI—Shizuoka University, Department of Chemistry, Shizuoka 422, Japan

HIROO INOKUCHI—Institute for Molecular Science, Okazaki 444, Japan

The isolation, purification, biological function, and structure (including tertiary structure) of cytochrome c_3 from Desulfovibrio vulgaris *are briefly discussed. The electrochemical reaction rate of the adsorbed cytochrome c_3 film on a mercury electrode is very rapid and it becomes electrochemically inactive once the film is reduced. However, the inactive film does not hinder the electrode reaction of cytochrome c_3 from the bulk of the solution. Potentiometric, polarographic, and cyclic voltammetric results reveal that the electrode reaction is reversible and diffusion controlled. The formal potential of the ferricytochrome/ferrocytochrome couple is −0.528 V (−0.287 V vs. NHE). The electrode reaction rate constant is 0.7 cm/s. From the simulation of the deferential pulse polarographic data, the best fit values of the individual standard potentials were obtained as −0.467, −0.519, −0.539, and −0.580 V. Cytochrome c_3, adsorbed on a mercury electrode, catalyzes the reduction of dioxygen to water, and the highest catalytic activity is attained when one-half of the electrode surface is covered by cytochrome c_3.*

Cytochrome c_3 is an electron carrier protein present in the strictly anaerobic dissimilatory sulfate-reducing bacteria, *Desulfovibrio*. Different kinds of cytochrome c_3 were discovered from different

0065-2393/82/0201-0199$06.00/0

species of sulfate-reducing bacteria in genus *Desulfovibrio* (*1, 2*), and now cytochrome c_3 is a marker protein in taxonomy of the sulfate-reducing bacteria distinguishing *Desulfovibrio* from *Desulfotomaculum* (*3*). Cytochrome c_3 is described as "low potential low spin cytochrome with some thioether binding side chain of heme as in mitochondrial cytochrome c . . . It exists in multiheme form as a monomer . . ." (*4*). Cytochrome c_3 isolated from *Desulfovibrio vulgaris* Miyazaki is similar to mammalian cytochrome c in molecular weight and in absorption spectrum. However, it contains four hemes in a single polypeptide chain and has a very negative redox potential. This chapter is concerned with the biochemical and physicochemical aspects of cytochrome c_3 of *Desulfovibrio vulgaris* Miyazaki and its unusual electrochemical behavior.

Biochemical Aspects

Isolation and Purification of Cytochrome c_3. Cytochrome c_3 is a major cytochrome component present in the soluble fraction of the cell-free extract of *Desulfovibrio* (*5, 6*). It is a basic protein with an isoelectric point near or over 10 (*1, 2, 7–10*), except for that from *D. gigas* whose isoelectric point is 4.5 (*11*). Passage of the soluble fraction of *D. vulgaris* through a column of Amberlite CG-50 (NH_4^+-form) and subsequent elution by 0.1 *M* NH_3 from the column separate cytochrome c_3 and some basic proteins from most of the other proteinaceous substances. Purification by gel-filtration chromatography with a Sephadex G-50 (fine) column followed by rechromatography with an Amberlite CG-50 (NH_4^+) yields a pure cytochrome c_3 preparation with a purity index of 3.0, which is defined as the ratio of the absorbance at 552 mm (alpha peak) in the ferro-form to that at 280 mm in the ferri-form (*2, 8*).

Spectral Properties. The absorption spectra of cytochrome c_3 are similar to c-type cytochromes. The spectrum of the ferri-form can be recorded from the visible to the UV region. However, that of the ferro-form in the UV region cannot be readily recorded because of the intense absorption of $Na_2S_2O_4$ used in routine methods to reduce cytochromes. The whole spectrum of the ferro-form can be taken when cytochrome c_3 is reduced by the catalytic action of a trace of purified hydrogenase (EC 1.12.2.1) under the hydrogen atmosphere (*2*). The spectral characteristics of cytochrome c_3 extracted from *D. vulgaris* are shown in Table I.

One spectral characteristic of cytochrome c_3 that was overlooked is the positioning of isosbestic points on both sides of the γ-peak of the ferro-form, that is, 412 and 432 nm (*2, 12*) (Table I). The distance between these two isosbestic points is only 20 nm in the case of cyto-

Table I. Spectral Data for Cytochrome c_3 from *Desulfovibrio vulgaris*

Peak positions in the ferri-form (nm): 530, 410(γ), and 350(δ)
Peak positions in the ferro-form (nm): 552(α), 524(β), 419(γ), 323(δ), and 280(protein)
Isosbestic points (nm): 560, 542, 532, 508, 432, 412, 343, and 254
Millimolar absorptivity at 552 nm in the ferro-form: 110 $mM^{-1} \cdot cm^{-1}$
Absorbance ratios:

- ferro-α/ferri-280 = 3.0
- ferro-β/ferro-α = 0.52
- ferro-γ/ferro-α = 6.3
- ferri-γ/ferro-α = 4.0
- ferro-δ/ferro-α = 1.05
- ferri-δ/ferro-α = 0.77

chrome c_3, whereas typically in those of other c-type cytochromes having one heme, the corresponding isosbestic points are 406 and 431 nm, with the distance between them being 25 nm (the γ-peak of the eucaryotic cytochrome c is blue-shifted by 6 nm from that of *Desulfovibrio* cytochromes, and so are the isosbestic points). We observed repeatedly that when cytochrome c_3 lost its biological function as an electron carrier for *Desulfovibrio* hydrogenase by any method, the isosbestic point shifted from 432 to 437 nm. The narrowing of the γ-peak of cytochrome c_3 might be a reflection of its intramolecular heme–heme interaction in its tetraheme structure.

Biochemical Function. Since its discovery in strict anaerobes, cytochrome c_3 has been assumed to be an electron mediator in the bacterial electron transfer system. Cytochrome c_3 enhanced the rate of hydrogen uptake by the cell-free extract of *D. vulgaris* Hildenborough in the presence of thiosulfate or tetrathionate, but not in the presence of sulfite (*1*). The addition of cytochrome c_3 resulted (*7*) in a recovery of the formic hydrogenase activity of the cell-free extract from which cytochrome c_3 was removed by passing through an Amberlite CG 50 (NH_4^+) column (*13*). This cytochrome was involved in the reduction of hydroxylamine and elementary sulfur (*13*), sulfite (*14*), and adenosine phosphosulfate (*15*) in a hydrogen atmosphere. These observations were in accord with the idea that the bacterial hydrogenase system might be directly linked to cytochrome c_3, which possesses the same electron carrier function as ferredoxin in the clostridial hydrogenase (EC 1.18.3.1) system (*16*). Direct proof that *Desulfovibrio* hydrogenase reduces cytochrome c_3 was reported (*17*, *18*). Hydrogen is produced by partially purified *Desulfovibrio* hydrogenase from an electron donor, $Na_2S_2O_4$, only in the presence of cytochrome c_3, and not in the presence of ferredoxin. Cytochrome c_3 is a direct electron carrier for the hydrogenase preparation from bacteria in genus *Desulfovibrio*,

that is: the hydrogenases from *D. vulgaris* Miyazaki (*17–21*), *D. vulgaris* Hildenborough, (*22*), and *D. gigas* (*23*).

The production of hydrogen from formate (formic hydrogenlyase reaction) is catalyzed by the enzyme system of hydrogenase and formate dehydrogenase [formate:ferricytochrome c-553 oxidoreductase (*24*)] in the presence of two electron carrier proteins, cytochrome c_3 and cytochrome c-553. The sulfite reduction is catalyzed by an enzyme system of hydrogenase and sulfite reductase in the presence of two electron carriers, cytochrome c_3 and flavodoxin (*25*). Hydrogen production from pyruvate by the phosphoroclastic enzyme system requires the cooperation of cytochrome c_3 and ferredoxin for *D. vulgaris* (*26*), and cytochrome c_3 and flavodoxin for *D. gigas* (*27*). The oxidation of lactate is catalyzed by an enzyme, D-lactate dehydrogenase (D-lactate:ferricytochrome c-553 oxidoreductase) (*28*), and the reduction of adenylylsulfate is reported to be linked to cytochrome c_3 (*15*). These results indicate that cytochrome c_3 plays an important role in the electron transfer system. It is not proved whether the $NAD(P)^+/NAD(P)H$ system participates in the electron transfer system in *D. vulgaris*.

Structure. The primary structures of several cytochrome c_3 molecules purified from different species of *Desulfovibrio* were elucidated. These include the cytochromes from *D. vulgaris* Miyazaki (*29*), *D. vulgaris* Hildenborough (*30, 31*), *D. gigas* (*32*), *D. desulfuricans* (*33*), *D. desulfuricans* Norway (*34*), and *D. salexigens* (*35*). These sequences are given in Table II. It is shown that cytochrome c_3 Miyazaki contains 107 amino acid residues and its molecular weight is 13,995. These sequences display rather poor homology. Although there are eight cysteine residues in these sequences in conformity to their tetraheme structures, the heme-attaching sites are not identical. The cytochromes from both *D. vulgaris* and *D. gigas* contain two Cys-x-y-Cys-His sequences and two Cys-a-b-c-d-Cys-His sequences, whereas the other cytochromes contain three Cys-x-y-Cys-His sequences and only one Cys-a-b-c-d-Cys-His sequence. Because these heme-attaching sites must have different conformations, the cytochromes from *D. vulgaris* and *D. desulfuricans* naturally do not share a common precipitation antigenic determinant as judged by an immunodiffusion test (*36*).

Cytochrome c_3 from *D. gigas* is an acidic protein with pI = 4.5, whereas most other cytochromes c_3 are basic proteins with pI over 10. Two kinds of proteins having completely different ionic properties have the identical biological function in different but closely related microorganisms. The tertiary structure of cytochrome c_3 from both *D. desulfuricans* Norway (*34*) and *D. vulgaris* Miyazaki (*37*) was elucidated. The crystal structure of *D. vulgaris* Miyazaki belongs to the orthorhombic system (space group $P\ 2_12_12_1$), with the cell unit of a =

Published on June 1, 1982 on http://pubs.acs.org | doi: 10.1021/ba-1982-0201.ch009

Table II. Comparison of the Amino Acid Sequences of Cytochromes c_3 from Species of *Desulfovibrio*

Species[a]	*Amino Acid Sequence*[b]
1	A P K A P A D G L K M D K T K Q P
2	A P K A P A D G L K M E A T K Q P
3	V D V P A D G A K I D F I A G G E K N L
4	A D A P G D D Y V I S A P E G M K A K P K G D K P G A L Q K T
5	V D A P A D M V I K A P A G A K V T K A P
6	V D A P G D M V L K A P A G A K M T K A P
1	V V F N H S T H K A V K C G D C H H P V N G K E N Y Q K C A T A G
2	V V F N H S T H· K S V K C G D C H H P V N G K E D Y R K C G T A G
3	V V F N H S T H K D V K C B B C H H Z P G B K Q Y A G C T T D G
4	V P F P H T K H A T V E C V Q C H H X X A D G G A V K K C T T S G
5	V A F S H K G H A S M D C K T C H H K W D G A G A I Q P C Q A S G
6	V D F S H K G H A A L D C T K C H H K W D G K A E V K K C S A E G
1	C H D N M D K K D K S A K G Y Y H A M H D K G T K F K S
2	C H D S M D K K D K S A K G Y Y H V M H D K N T K F K S
3	C H N I L D K A D K S V N S W Y K V V H D A K G G A K P T
4	C H D S L E F R D K A N A K D I K L V E S A F H T Q
5	C H A N T E S K K G D D S F Y M A F H E R K S E K S
6[c]	C H V (B T S) K (K G K K S T P K) F Y S A F H S K S D I S
1	C V G C H L E T A G A D A A K K K E L T G C K G S K C H S
2	C V G C H V E V A G A D A A K K K D L T G C K K S K C H E
3	C I S C H K D K A G D D K E L K K K L T G C K G S A C H P S
4	C I D C H A L K K K D K K P T G P T A C G K C H T T N
5	C V G C H K S M K K G P T K C T E C H P K N
6	C V G C H K A L K K A T G P T K C G D C H P K K K

[a] Species are as follows: 1, *D. vulgaris* Miyazaki; 2, *D. vulgaris* Hildenborough; 3, *D. gigas;* 4, *D. desulfuricans* Norway; 5, *D. desulfuricans;* and 6, *D. salexigens.*

[b] Amino acids are as follows: A, alanine; B, aspartic acid or asparagine; C, cysteine; D, aspartic acid; E, glutamic acid; F, phenylalanine; G, glycine; H, histidine; I, isoleucine; K, lysine; L, leucine; M, methionine; N, asparagine; P, proline; Q, glutamine; R, arginine; S, serine; T, threonine; V, valine; W, tryptophan; X, unknown; Y, tyrosine; and Z, glutamic acid or glutamine.

[c] Sequences in parentheses are estimated.

52.8, b = 68.1, and c = 34.9 Å. The shape of the cytochrome c_3 molecule is an ellipsoid with overall dimensions of 33 × 34 × 39 Å. The iron-to-iron distances ranged from 11.3 to 18.1 Å, and the angles between porphyrin rings are shown in Table III. Each heme is linked to two cysteine residues through thioether bonds as for cytochrome c. The fifth and sixth ligands of each iron atom are nitrogen of imidazole in the histidyl residue. Each heme is exposed to a different environment and, consequently, is expected to have a different redox potential.

Electrochemical Aspects

Adsorption of Cytochrome c_3 on Mercury Electrode. The adsorption behavior of cytochrome c_3 at the electrode surface is important in the elucidation of not only electrochemical redox reactions but also biological functions of cytochrome c_3 as an electron carrier in the respiratory chain.

The differential capacitance–time curves of the dropping mercury electrode in cytochrome c_3 solutions revealed that the adsorption of the heme protein on the mercury electrode is irreversible and diffusion controlled. That is, the amount of the adsorbed heme protein can be evaluated by using Koryta's equation (*38*):

$$\Gamma = 0.736\, C_p(D_p t)^{1/2}$$

where C_p is the concentration of protein (mol/cm^3), D_p is the diffusion coefficient of protein (cm^2/s), and t is the time elapsed from the birth of the mercury drop (s). The surface coverage defined as $\theta = \Gamma/\Gamma_{max}$ was evaluated from the concentration dependence of the differential capacitance at the dropping mercury electrode, where Γ is the surface concentration of cytochrome c_3 and Γ_{max} the maximum surface concentration (*39*). The maximum surface concentration, Γ_{max}, was calculated from the concentration at θ = 1 by using Koryta's equation. The maximum concentration obtained was 0.92 × 10^{-11} mol/cm^2 at −0.90 V [all electrode potentials in this chapter are referred to a saturated calomel electrode (SCE) at 25°C], which agrees with the result obtained by the potential step chronocoulometric method (*40*). Accordingly, the area

Table III. Heme–Heme Distances (upper right in Angstrom units) and Heme–Heme Angles (lower left in degrees) (*37*)

Heme	*1*	*2*	*3*	*4*
1	—	16.3	18.1	12.8
2	71	—	12.4	16.2
3	22	89	—	11.3
4	80	64	82	—

occupied by the adsorbed cytochrome c_3 molecule is 1800 Å^2, which is 1.35 times greater than the projected area of the cytochrome c_3 molecule in the crystal. The extent of the deformation (or unfolding) of the cytochrome c_3 molecule at the mercury electrode is considered to be small. On the other hand, the spreading of the cytochrome c molecule at the electrode surface is 1.8 times greater, that of the ribonuclease molecule is 2.2–2.9 times, and that of the lysozyme molecule is 1.3–2.0 times greater (*41*).

Electrochemical Properties of Adsorbed Cytochrome c_3. A fresh mercury drop (hanging mercury drop electrode, HMDE) was equilibrated for about 1 min in cytochrome c_3 solution ($10^{-5} \sim 10^{-4}$ *M*). After the mercury drop was rinsed thoroughly by phosphate buffer solution, the HMDE was transferred into the deaerated 0.03 *M* phosphate buffer solution without cytochrome c_3 and then cyclic voltammograms of the adsorbed cytochrome c_3 were recorded. The reduction peak of ferricytochrome c_3 was observed only on the first scan at −0.5 V as shown in Figure 1 (*40*). No reoxidation peak of ferrocytochrome c_3 was detected on the reverse scan, and no peak was observed on further repetition of the scanning. The electrochemically inactive adsorbed layer of cytochrome c_3 was stable and was not reoxidizable by exposure to the oxygen atmosphere. The same electrochemical behavior was reported as was for the cyclic voltammetry of the adsorbed monolayer of cytochrome c on the mercury electrode (*42*).

The potential step chronocoulometric technique (43) was employed to investigate the reduction of the adsorbed cytochrome c_3 on the mercury electrode (*40*). After the complete saturation of the dropping mercury electrode by ferricytochrome c_3, the electrode potential was stepped from −0.3 to −0.7 V. The number of electrons involved in the reduction of the adsorbed ferricytochrome c_3 was four and its reaction was almost instantaneous. The reduction of ferricytochrome c_3 in the bulk of the solution was confirmed to be diffusion controlled. On the other hand, the reoxidation of the adsorbed ferrocytochrome c_3, which was reduced electrochemically at the electrode, was not observed. The chemically generated ferrocytochrome c_3 was also electrochemically inactive when it was adsorbed on the mercury electrode. The adsorbed ferricytochrome film was stable and no appreciable desorption was observed after 30 min in the phosphate buffer solution. The adsorbed ferrocytochrome c_3 was confirmed to be stable by monitoring the differential capacitance of the electrode throughout the reduction and oxidation processes of the adsorbed cytochrome c_3 film.

The electron exchange between the electrode and cytochrome c_3 in the bulk of the solution (discussed later in this chapter) is not restricted by the monolayer of cytochrome c_3 at the electrode surface. In addition, the amount of the adsorbed cytochrome on the mercury elec-

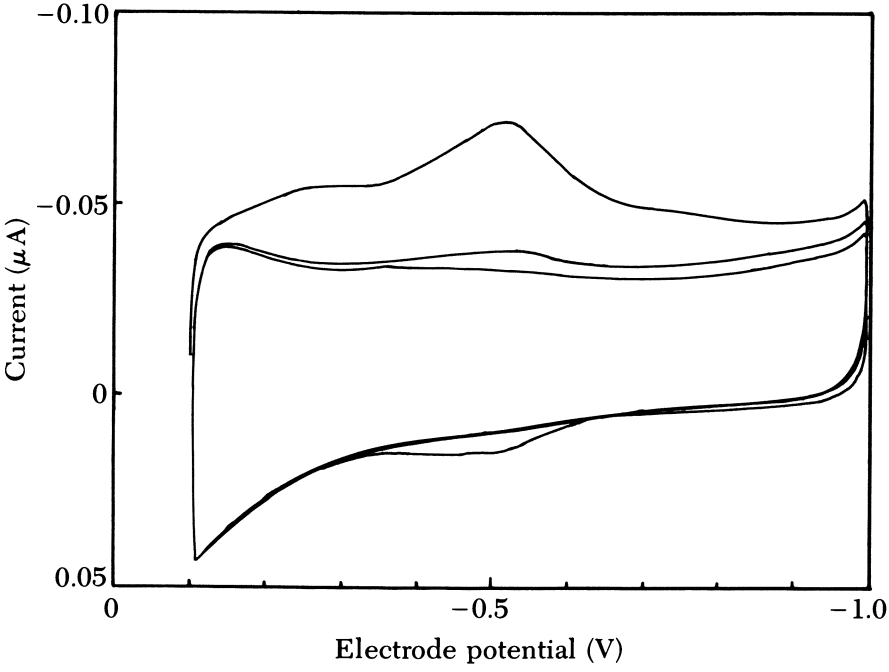

Figure 1. Cyclic voltammogram of the adsorbed cytochrome c_3 (monolayer) on hanging mercury drop electrode in 0.03 M phosphate buffer solution at pH 7.0. Scan rate, 100 mV/s; A = 0.0143 cm² (40).

trode surface is so small (1 microcoulomb/cm²) and the electrochemical reaction rate constant is so large that the experimental errors caused by the adsorbed species in cyclic voltammetry and pulse polarography are insignificant (*40*).

Potentiometric Studies. The potentiometric measurements were carried out in 0.03 *M* phosphate buffer solution at pH 7.0 with a slow dropping mercury electrode (drop time ~30 s) as an indicator electrode. The ratio of the ferri-form to the ferro-form is varied by the enzymatic reduction of the ferri-form with a controlled amount of hydrogen in the presence of a small amount of hydrogenase (hydrogen: ferricytochrome c_3 oxidoreductase, EC 1.12.2.1.). The plot of log (C_O/C_R) vs. electrode potential produces a straight line with a Nernst slope of 93 mV as shown in Figure 2. The apparent number of electrons involved in the overall electrode reaction

$$\text{ferricytochrome } c_3 + 4e \rightleftharpoons \text{ferrocytochrome } c_3$$

is calculated to be 0.64. The apparent formal potential, which is the

mean redox potential of the four individual hemes in the molecule, is −0.528 ±0.001 V (−0.287 V vs. NHE) (*44*). The deviation from the linear plot at the C_O/C_R ratio less than 0.5 predicts a multistep reduction of cytochrome c_3.

Pulse Polarographic Studies. Cytochrome c_3 produces a single well-defined reduction wave with a small preceding wave at the dropping mercury electrode, as shown in Figure 3. The half-wave potential is −0.527 V, which is equal to the apparent formal potential in potentiometry, and the logarithmic plot is a straight line with an inverse slope of 0.085 mV, from which the number of electrons involved in the electrode reaction is estimated to be 0.70 (*44*).

The polarogram obtained by a scan-reversal pulse polarography depends markedly on the reversibility of the electrode reaction (*45*). In the cytochrome c_3 solution the ratio of the limiting currents for cathodic and anodic scans is unity and the half-wave potential on the cathodic scan is equal to that on the reverse scan. These results provide strong evidence for the reversible electrode reaction of cytochrome c_3 on the mercury electrode. Our galvanostatic double pulse measurements revealed that the apparent electrode reaction rate constant of the ferricytochrome c_3/ferrocytochrome c_3 system is 0.7 cm/s. The diffusion coefficients of ferricytochrome c_3 and ferrocytochrome c_3 calculated from the pulse polarographic data were 0.94×10^{-6}

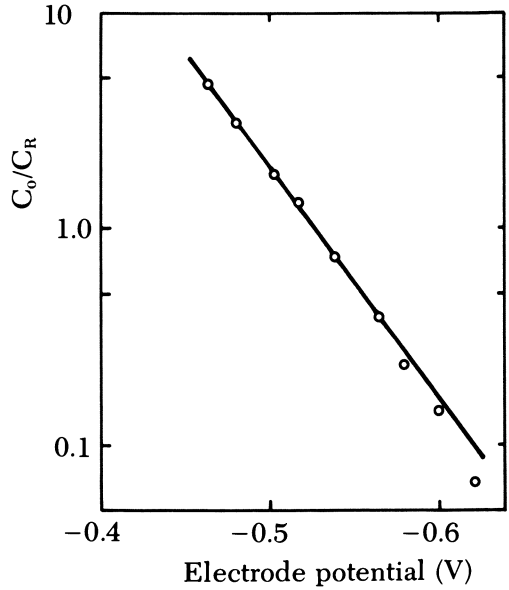

Figure 2. Equilibrium potentials of the ferricytochrome/ferrocytochrome c_3 in 0.03 M phosphate buffer solution at pH 7.0 (44).

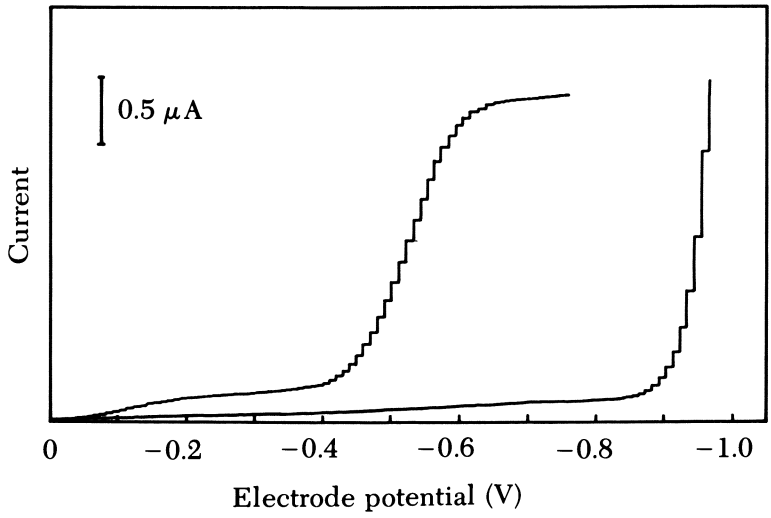

Figure 3. Normal pulse polarograms of the reduction of ferricytochrome c_3 and of the base solution (0.03 M phosphate buffer). Cytochrome c_3 concentration, 1.24×10^{-4} M; m = 2.82 mg/drop; sampling time, 50 ms (44).

cm^2/s. This value is in agreement with that of horse heart ferricytochrome c determined by a hydrodynamic technique (*46*).

Cyclic Voltammetric Studies. The cyclic voltammogram of cytochrome c_3 is distorted and broader than expected from the four-electron reaction (*47*). The same is true in c_3-type cytochromes from *D. vulgaris* Hildenborough and *D. desulfuricans* Norway (*48*). The peak potentials of these cytochromes are independent of both the scan rate and the concentration of cytochrome c_3 within the investigated range. The peak current varies linearly with the square root of the scan rate and the ratio of the cathodic to anodic peak current is almost unity.

The cathodic peak current is only 1/2.5 of the peak current expected from a reversible four-electron process. The cathodic and anodic peak potentials are −0.55 and −0.46 V, respectively. The number of electrons involved in the electrode process is calculated to be 0.61 from the peak-to-peak separation (*47*). In the case of cytochrome c_3 from *D. vulgaris* Hildenborough the cathodic and anodic peak potentials are −0.62 and −0.51 V, respectively (*48*). On the other hand, cytochrome c_3 from *D. desulfuricans* Norway shows two cathodic peaks at −0.45 and −0.63 V and the anodic peak at −0.54 V (*48*). The cathodic peak at −0.2 V observed in both cases is probably due to the reduction of a contaminated oxygen. The electrode process of cytochrome c_3 from *D. vulgaris* Hildenborough at −0.56 V is likely to correspond to the redox reaction of ferricytochrome c_3/ferrocyto-

chrome c_3 of Miyazaki because of the similarity in the primary structure between cytochrome c_3 from *D. vulgaris* Miyazaki and that from *D. vulgaris* Hildenborough (the degree of homology between these cytochromes c_3 is 87%) as shown in Table II. However, cytochrome c_3 from *D. desulfuricans* Norway has the least homology to our cytochrome c_3 (the degree of homology is only 28%), and the different electrode process of cytochrome c_3 can be expected.

Differential Pulse Polarographic Study. The differential pulse polarogram of ferricytochrome c_3 is well-defined, as shown in Figure 4. The polarogram is slightly distorted from the symmetry with the peak potential of −0.522 V, from which the half-wave potential of a reversible system in normal pulse polarography is calculated to be −0.527 V. However, the peak height is smaller than that expected from a reversible four-electron reaction and the half-peak width is also broader than that expected. The half-wave potentials of *D. vulgaris* Hildenborough cytochrome c_3 are estimated to be −0.49 V (ill-defined) and −0.58 V (main wave) from the differential pulse polarography, and those of *D. desulfuricans* Norway are estimated in the same way to be −0.40 V (well-defined) and −0.58 V (main wave) (*49*).

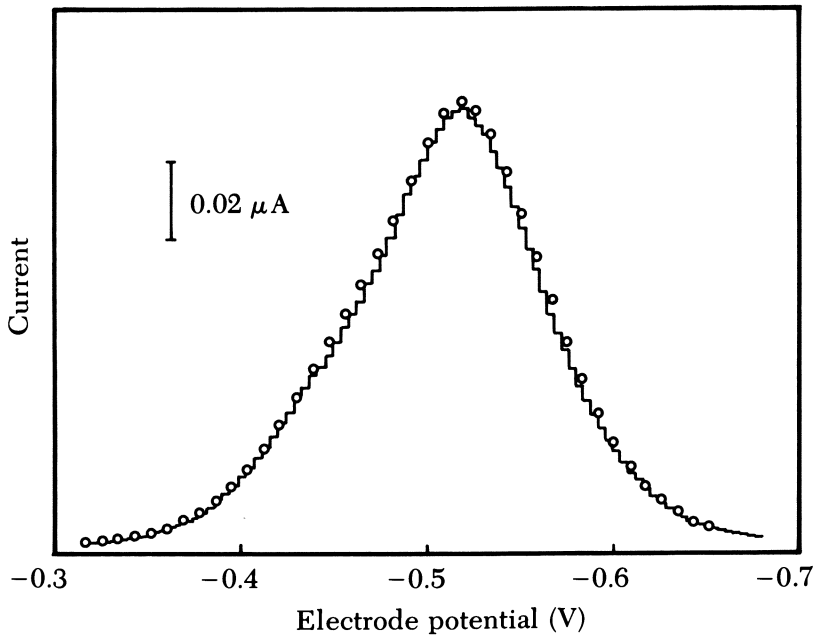

Figure 4. Differential pulse polarogram for the reduction of ferricytochrome c_3 (1.24×10^{-4} M) in 0.03 M phosphate buffer solution (—) and best fit differential pulse polarography simulation (○) (57). m = 1.99 mg/drop; sampling time, 70 ms; modulation amplitude, 10 mV.

Elucidation of the Redox Potential of Hemes in Cytochrome c_3. The redox states of cytochrome c_3 from *D. vulgaris* Hildenborough were studied extensively by ESR (*50–52*), Mössbauer spectroscopy (*53*), NMR (*54, 55*), and ESR coupled with potentiometry (*56*). In the course of the reoxidation of ferrocytochrome c_3 with oxygen, a stable intermediate at a half-reoxidized state was observed in the ESR measurements (*50, 51*). The redox cycling by chemical reduction and reoxidation with oxygen revealed that the individual hemes were reoxidized at different rates indicating dissimilar hemes at 8.5 K (*52*). McDonald et al. (*54*) reported that three different oxidation states appear to develop in the reoxidation of ferrocytochrome c_3; I, one ferri-heme and three ferro-hemes; II, two ferri-hemes and two ferro-hemes; and III, fully oxidized hemes. On the other hand, Dobson et al. (*55*) observed that the reduction of ferricytochrome c_3 with dithionite proceeds in two two-electron steps. The reduction of cytochrome c_3 was predicted to proceed in four one-electron steps with unequally spaced standard potentials (the spacings are −26, −9, and −5 mV) (*56*). The formal potential is estimated to be −0.56 V.

Our investigation showed that cytochrome c_3 from *D. vulgaris* Miyazaki contains four heme groups and the voltammetric data indicate that these four redox centers are characterized by four separate but closely spaced redox potentials, with each center exhibiting reversible electron transfer on a mercury electrode. We developed theoretical responses for the reduction of molecules containing four similar but nonequivalent redox sites for cyclic voltammogram and differential pulse polarogram (*57*).

Definition of the four individual standard potentials is given by the following scheme where C_O is the fully oxidized and C_4 the fully reduced cytochrome:

$$C_O \underset{E_1^\circ}{\overset{e}{\rightleftharpoons}} C_1 \underset{E_2^\circ}{\overset{e}{\rightleftharpoons}} C_2 \underset{E_3^\circ}{\overset{e}{\rightleftharpoons}} C_3 \underset{E_4^\circ}{\overset{e}{\rightleftharpoons}} C_4$$

and by the expression:

$$E = E_i^\circ - (RT/F)\ln(C_i/C_{i+1})$$

The individual standard potentials are macroscopic rather than microscopic parameters. Thus, C_1 does not signify reduction of a particular heme group but is simply the equilibrium distribution of all molecules that have one reduced site and three oxidized sites, namely, a collection of the species $R_1O_2O_3O_4$, $O_1R_2O_3O_4$, $O_1O_2R_3O_4$, and $O_1O_2O_3R_4$. The theoretical voltammetric responses were generated by digital simulation with techniques developed previously (*58*).

Cyclic Voltammetry (CV). For the CV simulations, semi-infinite, linear diffusion to a plane electrode was employed. A number of simulations for equally spaced E_i° values were performed, and the values of the difference between anodic and cathodic peak potentials, ΔE_p, and the cathodic peak current function, $\sqrt{\pi}\,\chi\,(at)$ are given in Figures 5 and 6 as functions of the spacing between the standard potentials, $\Delta E^\circ = E_{i+1}^\circ - E_i^\circ$. The current function is defined (59) by $i/FAD^{1/2}C^*(Fv/RT)^{1/2}$ where i is the current, A is the electrode area, D is the diffusion coefficient of the reactant, C* is the bulk concentration of the reactant, v is the scan rate, and the other symbols have their normal meaning. Positive values of the spacing correspond to the reaction that becomes easier as reduction proceeds and in the limit of very positive spacing, ΔE_p approaches 14.2 mV, which corresponds to the reversible four-electron reaction. Similarly, the cathodic peak current function approaches the theoretical value of 3.57 (59). From a comparison of the present results with the values in Figures 5 and 6, the spacing of the standard potentials is estimated to be −35 mV provided that the standard potentials are equally spaced.

Differential Pulse Polarography (DPP). The simulations were based on semi-infinite linear diffusion to the expanding plane model for the dropping mercury electrode (58). The best fit simulation with the experimental results was obtained from the analysis of DPP data

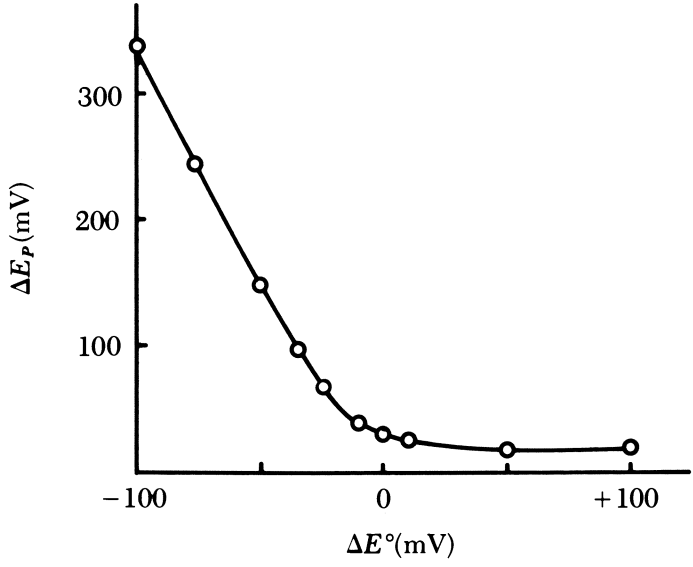

Figure 5. Dependence of peak potential separation on ΔE° *for equally spaced standard potential (* 57*).*

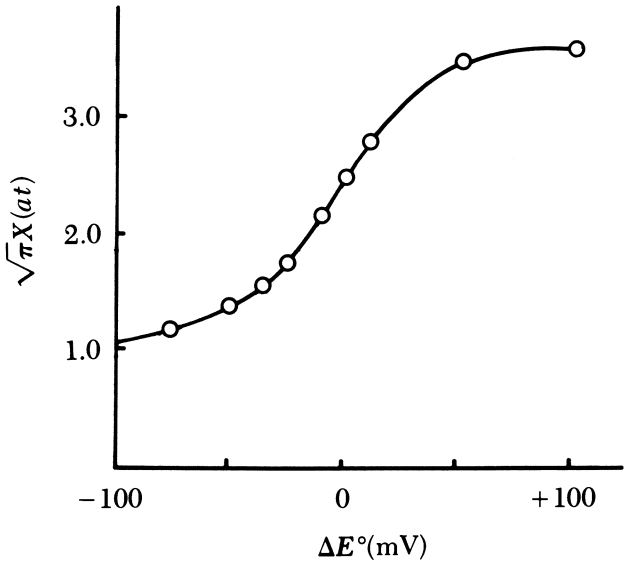

Figure 6. Dependence of cathodic peak current function on $\Delta E°$ *for equally spaced standard potential* (57).

because DPP is more sensitive to small variations in the standard potentials than is CV and the background signal is less of a problem for DPP than for CV. The best fit values for the individual potentials for DPP and CV are $E°_1 = -0.467$, $E°_2 = -0.519$, $E°_3 = -0.539$, and $E°_4 = -0.580$ V.

Figures 4 and 7 compare the best fit simulation with the experimental results. A good agreement with the experiments was obtained for both DPP and CV. The asymmetry in the splitting of the standard potentials was effected in the DPP data as a leading shoulder on the polarogram. No hint of this asymmetry was observed in the CV simulation.

Several conclusions about the properties of cytochrome c_3 from *D. vulgaris* Miyazaki may be drawn from these results. Certainly the centers may not be described as equivalent, noninteracting redox sites. The model we favor is the one where the heme centers are chemically different and are weakly interacting. The intrinsic ease of reduction of each center differs from the others and perhaps is also affected by the oxidation states of adjacent centers.

The Effect of Foreign Proteins on the Electrode Reaction of Cytochrome c_3. The limiting current for the reduction of cytochrome c_3 at the dropping mercury electrode is suppressed by the addition of cytochrome c. However, both the half-wave potential of pulse polaro-

gram and the peak potential of differential pulse polarogram are not affected. The relation between the fraction of cytochrome c_3 on the fully covered electrode surface by both cytochrome c_3 and cytochrome c and the degree of suppression of the limiting current for the reduction of ferricytochrome c_3 (in arbitrary unit) is shown in Figure 8. The limiting current is not proportional to the concentration but deviates from the linear relation. This result indicates that only the sites occupied by cytochrome c_3 act as active centers for the electron transfer between the electrode and ferricytochrome c_3 from the bulk of the solution. The limiting current for the reduction of cytochrome c_3 is not affected by the addition of ribonuclease as is seen for the reduction of cytochrome c with ribonuclease (*60*). On the other hand, the shift of the half-wave potential is observed. That is, the electrode reaction becomes irreversible.

The Catalytic Reduction of Molecular Oxygen by Cytochrome c_3. The reduction of molecular oxygen in phosphate buffer solution at pH 7.0 proceeds in two steps on the mercury electrode. The first wave corresponds to the reduction of oxygen to hydrogen peroxide and the

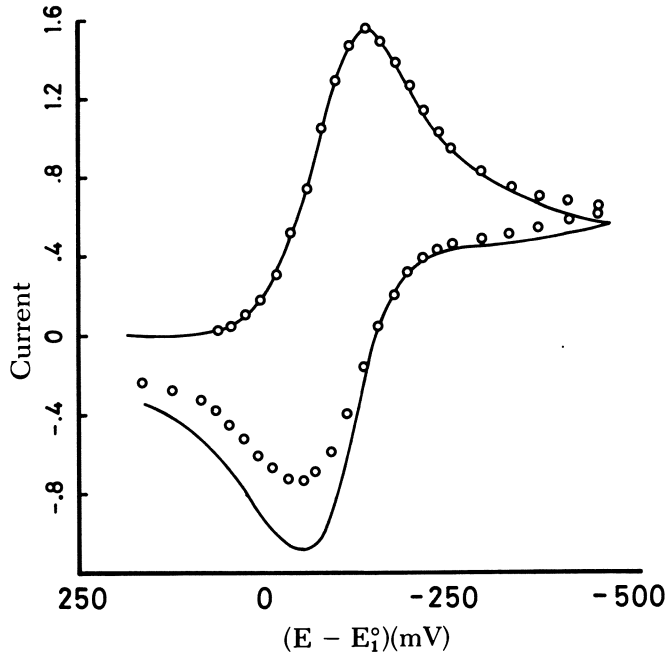

Figure 7. Comparison of experimental CV data (○) (47) to the best fit simulation (—). The data were obtained by correcting the experimental values for background and then normalizing the cathodic peak to the same scale as the simulated results. Scan rate, 0.2 V/s (57).

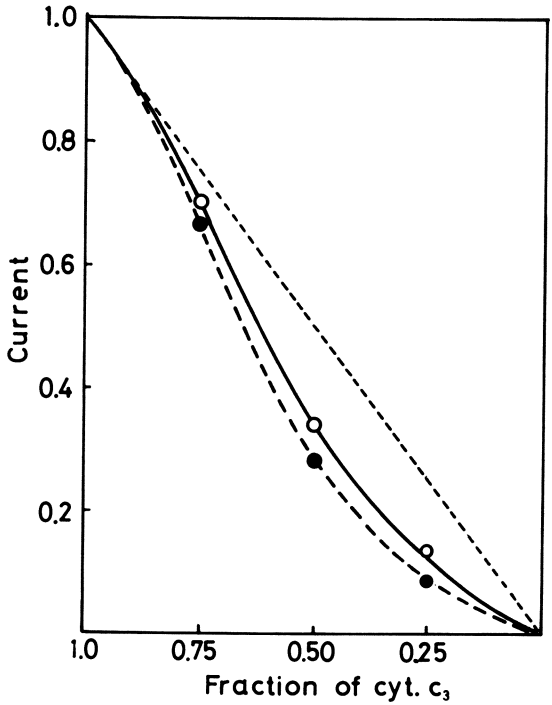

Figure 8. Effect of cytochrome c on the polarographic limiting current for the reduction of ferricytochrome c_3 in 0.03 M phosphate buffer solution. Total concentration of heme proteins was 1.12×10^{-4} M.

second wave to a further reduction of hydrogen peroxide to water. The first wave height increases by the addition of ferricytochrome c_3. Finally, the second wave merges into the first wave when the surface coverage of the mercury electrode by cytochrome c_3 is about 46%. With a further increase in the surface coverage of the electrode by cytochrome c_3, the first wave height tends to decrease and reaches a constant value (*61*). The second wave height from the baseline remains constant throughout the experiments. Probably, coreduction of dioxygen via two-electron and four-electron pathways takes place simultaneously in the potential region of the first wave. The fraction of the direct four-electron reduction of dioxygen to water in the first wave region with respect to the surface coverage of the dropping mercury electrode by cytochrome c_3 is shown in Figure 9.

The effect of cytochrome c, which is electrocatalytically inactive, on the reduction of oxygen was studied in 4×10^{-6} *M* cytochrome c_3 solution, in which nearly 100% of oxygen is reduced directly to water. The surface coverage of the electrode by cytochrome c_3 in this solution

was estimated to be 46% with the dropping mercury electrode of drop time 2 s. The addition of cytochrome c to this solution caused the decrease in the fraction of the four-electron reduction as shown in Table IV. In the mixed solutions of 5.6×10^{-5} *M* cytochrome c_3 and 5.6×10^{-5} *M* cytochrome c, the fraction of the four-electron reduction of dioxygen became very small. The polarogram for the reduction of dioxygen in this solution, after the correction for the reduction current of these heme proteins, was nearly identical to that obtained in the heme protein-free solution.

Dioxygen most likely is activated in the cavities between cytochrome c_3 molecules at the electrode surface because the highest yield of the four-electron reduction of dioxygen is attained when half of the mercury electrode surface is covered by cytochrome c_3. This assumption is also supported by the results that show the addition of electrocatalytically inactive proteins such as cytochrome c, which reduces the number of cavities for activating dioxygen on the electrode, markedly suppresses the fraction of the four-electron reduction of oxygen as seen in Table IV. In the present case, the cooperation of hemes in the molecule as proposed previously (*62*, *63*) with face-to-face porphyrin is very unlikely because of the compact arrangement of the cytochrome c_3 molecule. The electrons may be released cooperatively from the metal centers in the adjacent adsorbed cytochrome c_3 molecules to

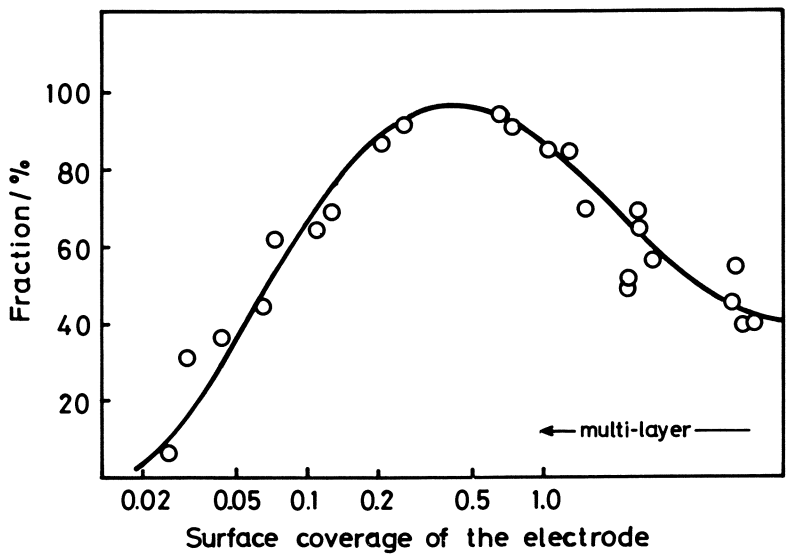

Figure 9. Fraction of the four-electron reduction of oxygen on dropping mercury electrode with respect to the surface coverage of cytochrome c_3 in 0.03 M *phosphate buffer solution at pH 7.0.*

Table IV. Effect of Cytochrome c Concentration on the Fraction of the Four-Electron Reduction of Oxygen

Concentration of cytochromes c[a]	*Surface coverage*		*Fraction of four-electron reduction*
	$\theta_{cyt.c_3}$	$\theta_{cyt.c}$	
—	0.46	—	1.00
2×10^{-6}	0.46	0.27	0.78
4×10^{-6}	0.46	0.54	0.45
8×10^{-6}	0.15	0.85	0.28
2×10^{-5}	0.07	0.93	0.18

[a] The concentration of cytochrome c_3 was 4×10^{-6} *M* in all cases.

dioxygen in the cavity on the electrode with a submonolayer of cytochrome c_3, because the hemes in cytochrome c_3 are exposed on the surface of the molecule.

The reduction of dioxygen to hydrogen peroxide through a dense adsorbed cytochrome layer on the electrode probably proceeds either directly at the electrode or indirectly through a metal center in the cytochrome molecule. This reaction mechanism may be similar to the catalytic reduction of dioxygen by many monometallic macrocyclic complexes. The two-electron reduction of dioxygen to hydrogen peroxide is always dominant, probably because these catalysts have a single metal center.

The catalytic disproportionation mechanism of hydrogen peroxide at the electrode surface may be denied by the fact that the fraction of the four-electron reduction of oxygen is much lower at the electrode fully covered by cytochrome c_3 than at a half-covered electrode. The temperature dependence of the fraction of the four-electrode reduction of oxygen was insignificant. This result also suggests that the disproportionation mechanism is improbable.

Acknowledgments

The authors are grateful to Haruo Mizota and Shin-ichi-ro Imabayashi, Yokohama National University, for their helpful assistance in research. This work was supported by a Grant-in-Aid for Special Project Research Nos. 511312 and 56112009 from the Ministry of Education, Science, and Culture.

Literature Cited

1. Postgate, J. R. *J. Gen. Microbiol.* **1956,** *14,* 545.
2. Yagi, T.; Maruyama, K. *Biochem. Biophys. Acta* **1971,** *243,* 214.
3. Postgate, J. R.; Campbell, L. L. *Bacteriol. Rev.* **1966,** *30,* 732.

4. Int. Union of Biochem. "Enzyme Nomenclature, Recommendations (1978) of the Nomenclature Committee of the Int. Union of Biochem.;" Academic: New York, 1979; p. 599.
5. Postgate, J. R. *Biochem. J.* **1954,** *56,* xi; *58,* ix.
6. Ishimoto, M.; Koyama, J.; Nagai, Y. *Bull. Chem. Soc. Jpn.* **1954,** *27,* 565.
7. Ishimoto, M.; Koyama, J.; Yagi, T.; Shiraki, M. *J. Biochem.* **1957,** *44,* 413.
8. Horio, T.; Kamen, M. D. *Biochim. Biophys. Acta* **1961,** *48,* 266.
9. Drucker, H.; Trousil, E. B.; Campbell, L. L.; Barlow, G. H.; Margoliash, E. *Biochemistry* **1970,** *9,* 1515.
10. Drucker, H.; Trousil, E. B.; Campbell, L. L. *Biochemistry* **1970,** *9,* 3395.
11. Le Gall, J.; Mazza, G.; Dragoni, N. *Biochim. Biophys. Acta* **1965,** *99,* 385.
12. Tsuji, K.; Yagi, T. *Arch. Microbiol.* **1980,** *125,* 35.
13. Ishimoto, M.; Yagi, T.; Shiraki, M. *J. Biochem.* **1957,** *44,* 707.
14. Ishimoto, M.; Yagi, T. *J. Biochem.* **1961,** *49,* 103.
15. Ishimoto, M.; Fujimoto, D. *J. Biochem.* **1961,** *50,* 299.
16. Mortenson, L. E.; Valentine, R. C.; Carnahan, J. E. *Biochem. Biophys. Res. Commun.* **1962,** *7,* 448.
17. Tamiya, N.; Yamaguchi, Y.; Honya, M.; Yagi, T. *Biochem. Biophys. Res. Commun.* **1966,** *22,* 43.
18. Yagi, T.; Honya, M.; Tamiya, N. *Biochim. Biophys. Acta* **1968,** *153,* 699.
19. Yagi, T. *J. Biochem.* **1970,** *68,* 549.
20. Yagi, T.; Kimura, K.; Daidoji, H.; Sakai, F.; Tamura, S.: Inokuchi, H. *J. Biochem.* **1976,** *79,* 661.
21. Yagi, T.; Endo, A.; Tsuji, K. "Hydrogenases: Their Catalytic Activity, Structure and Function;" Schlegel, H. G.; Schneider, K., Eds.; E. Goltze: Göttingen, 1978; pp. 107–124.
22. Haschke, R. H.; Campbell, L. L. *J. Bacteriol.* **1970,** *105,* 249.
23. Bell, G. R.; Lee, J.-P.; Peck, H. D., Jr; Le Gall, J. *Biochimie,* **1978,** *60,* 315.
24. Yagi, T. *Biochim. Biophys. Acta* **1979,** *548,* 96.
25. Irie, K.; Kobayashi, K.; Kobayashi, M.; Ishimoto, M. *J. Biochem.* **1973,** *73,* 353.
26. Akagi, J. M.; Adams, S. *J. Biol. Chem.* **1967,** *242,* 2478.
27. Hatchikian, E. C.; Le Gall, J. *Ann. Inst. Pasteur* **1970,** *118,* 288.
28. Ogata, M.; Arihara, K.; Yagi, T. *J. Biochem.* **1981,** *89,* 1423.
29. Shinkai, W.; Hase, T.; Yagi, T.; Matsubara, H. *J. Biochem.* **1980,** *87,* 1747.
30. Ambler, R. P. *Biochem. J.* **1968,** *109,* 47–48P.
31. Trousil, E. B.; Campbell, L. L., *J. Biol. Chem.* **1974,** *249,* 386.
32. Ambler, R. P.; Bruschi, M.; Le Gall, J. *FEBS Lett.* **1969,** *5,* 115.
33. Ambler, R. P.; Bruschi, M.; Le Gall, J. *FEBS Lett.* **1971,** *18,* 347.
34. Haser, R.; Pierrot, M.; Frey, M.; Payan, F.; Astier, J. P.; Bruschi, M.; Le Gall, J. *Nature* **1979,** *282,* 806.
35. Ambler, R. P. *FEBS Lett.* **1971,** *18,* 351.
36. Drucker, H.; Campbell, L. L. *J. Bacteriol.* **1969,** *100,* 358.
37. Higuchi, Y.; Bando, S.; Kusunoki, M.; Matsu-ura, Y.; Yasuoka, N.; Kakudo, M.; Yamanaka, T.; Yagi, T.; Inokuchi, H. *J. Biochem.* **1981,** *89,* 1659.
38. Koryta, J. *Collect. Czech. Chem. Commun.* **1953,** *18,* 206.
39. Frumkin, A. N. *Z. Phys.* **1926,** *35,* 792.
40. Niki, K.; Imabayashi, S., unpublished data.
41. Scheller, F.; Janchen, M.; Prumke, H.-J. *Biopolymers* **1975,** *14,* 1553.
42. Haladjian, J.; Bianco, P.; Serre, P. A. *J. Electroanal. Chem.* **1979,** *104,* 555.
43. Christie, J. H.; Lauer, G.; Osteryoung, R. A. *J. Electroanal. Chem.* **1964,** *7,* 60.
44. Niki, K.; Yagi, T.; Inokuchi, H.; Kimura, K. *J. Am. Chem. Soc.* **1979,** *101,* 3335.
45. Oldham, K. B.; Parry, E. P. *Anal. Chem.* **1970,** *42,* 229.
46. Ehrenberg, A. *Acta Chem. Scand.* **1957,** *11,* 1257.
47. Niki, K.; Yagi, T.; Inokuchi, H.; Kimura, K. *J. Electrochem. Soc.* **1977,** *124,* 1889.

48. Bianco, P.; Faugue, G.; Haladjian, J. *J. Electroanal. Chem.* **1979,** *104,* 385.
49. Bianco, P.; Haladjian, J. *Biochim. Biophys. Acta* **1979,** *545,* 86.
50. DerVartanian, D. V.; Le Gall, J. *Biochim. Biophys. Acta* **1971,** *243,* 53.
51. DerVartanian, D. V. *J. Magn. Reson.* **1973,** *10,* 170.
52. Le Gall, J.; Bruschi-Heriaud, M.; DerVartanian, D. V. *Biochim. Biophys. Acta* **1971,** *234,* 499.
53. Ono, K.; Kimura, K.; Yagi, T.; Inokuchi, H. *J. Chem. Phys.* **1975,** *63,* 1640.
54. MacDonald, S. S.; Phillips, W. D.; Le Gall, J. *Biochemistry* **1974,** *13,* 1952.
55. Dobson, C. M.; Hoyle, N. J.; Geraldes, C. F.; Wright, P. E.; Williams, R. J. P.; Bruschi, M.; Le Gall, J. *Nature* **1974,** *249,* 425.
56. DerVartanian, D. V.; Xavier, A. V.; Le Gall, *J. Biochimie* **1978,** *60,* 321.
57. Sokol, W. F.; Evans, D. H.; Niki, K.; Yagi, T. *J. Electroanal. Chem.* **1980,** *108,* 107.
58. Feldberg, S. W. In "Electroanalytical Chemistry;" Bard, A. J., Ed.; Dekker: New York, 1969; Vol. 3, pp. 199–296.
59. Nicholson, R. S.; Shain, I. *Anal. Chem.* **1964,** *36,* 706.
60. Kuznetsov, B. A.; Shumakovich, G. P.; Mestechkina, N. M. *Bioelectrochem. Bioenerg.* **1977,** *4,* 512.
61. Niki, K.; Takizawa, Y.; Kumagai, H.; Fujiwara, R.; Yagi, T.; Inokuchi, H. *Biochim. Biophys. Acta* **1981,** *636,* 136.
62. Collman, J. P.; Marrocco, M.; Denisevichi, P.; Koval, C.; Anson, F. C. *J. Electroanal. Chem.* **1979,** *101,* 117.
63. Collman, J. P.; Denisevichi, P.; Konai, T.; Marrocco, M.; Koval, C.; Anson, F. C. *J. Am. Chem. Soc.* **1980,** *102,* 6027.

RECEIVED for review June 2, 1981. ACCEPTED October 8, 1981.

Electrode Reactions of Protein Prosthetic Groups

F. SCHELLER and G. STRNAD

Central Institute of Molecular Biology, Academy of Science of the German Democratic Republic, 1115 Berlin-Buch, German Democratic Republic

The exchange rate of the adsorbed molecules and the degree of structural changes determine the character of the electrode process. Additionally, the ability of the first adsorption layer to transfer electrons to molecules of the bulk phase, that is, the rate of the intermolecular electron transfer between the layers, is responsible for deviations from a reversible polylayer electrode process: decrease of limiting current, overvoltage, and suppression of reoxidation. The electrode process seems to be more similar to the mechanism in biological electron transfer chains than to the random collision processes following an outer or inner sphere mechanism.

The fast oxidation of reducing organic substances like NADH, glucose, uric acid, and different drugs is an important precondition for the function of living systems. These redox reactions are catalyzed both by single enzymes and by electron transfer chains (*1*). On the other hand, at metal electrodes these oxidation processes require a high anodic overvoltage and may be masked by the background discharge. Thus, the combination of enzymatic substrate oxidation with the transfer of the reducing equivalents to the electrode promises an improvement in the rate and specificity of the electrode processes that are applied in bio-fuel cells, enzyme reactors, and sensors.

The key problem in the use of enzymes in accelerating electrode processes is the optimization of the electron transfer between the enzyme active site and the electrode. In principle, two different approaches may be offered (Figure 1):

1. Low molecular redox systems called mediators are suited to transfer electrons between the enzyme and the electrode. This principle frequently was used with glu-

0065-2393/82/0201-0219$06.00/0

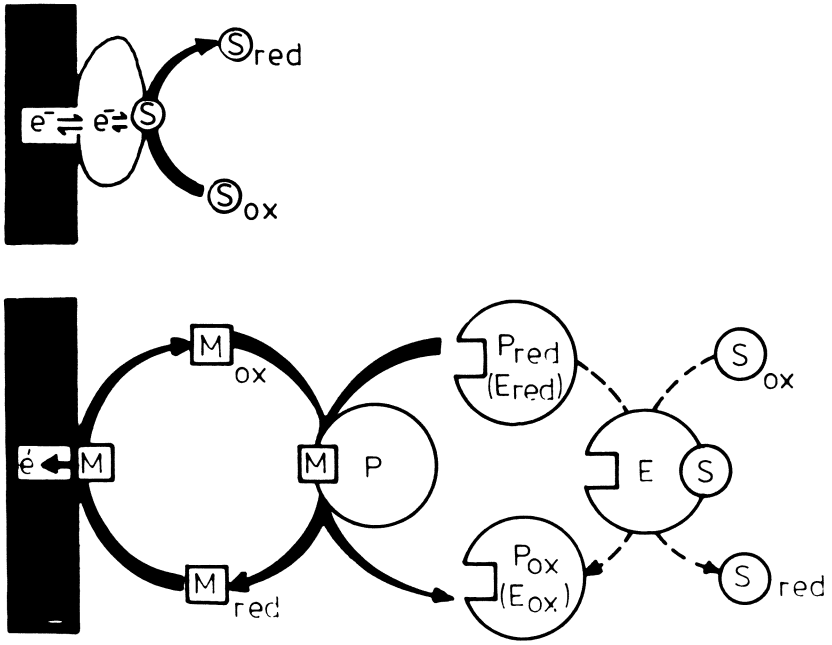

Figure 1. Principles of the electron transport from the enzyme active site to the electrode.

cose oxidation catalyzed by glucose oxidase in enzyme electrodes (*2*, *3*) and fuel cells (*3*, *4*).

2. The feasibility of direct electron transfer from the enzyme active site to the electrode also was established with several proteins (*5a–5c*). Heterogeneous electron transfer is attracting increasing attention in biotechnology (*6*).

In this chapter the present state of protein electrochemistry will be illustrated using data from the literature and results obtained with the flavoprotein glucose oxidase. The mechanism of the electron transfer between proteins and electrodes will be discussed on the basis of correlations between the conductivity of protein films and the character of the respective electrode process.

Results and Models of the Electrode Process

Although the protein-free prosthetic groups, for example, flavin (*7*) and hemin (*8*), show a diffusion-controlled electron exchange with the electrode, the high molecular weight and the surface activity of the proteins may cause drastic changes in their electrochemical behavior. With biopolymers, structural factors must also be taken into account,

such as the accessibility of the reducible groups and structural changes on adsorption.

With proteins the electrode-active part and the adsorbing tails are united in one molecule, so the rate of adsorption exchange directly determines the nature of the electrode process.

Rapid Adsorption Exchange

A rapid exchange of the adsorbed molecules by particles in the bulk of the solution was found only with several peptides (*9*). The limiting current increased with the concentration of the solution, without reaching a saturation value.

Irreversible Adsorption of First Layer

As demonstrated by adsorption studies with radioactively labeled proteins (*10*) and the "film transfer method" (*11*), the molecules adsorbed immediately at the electrode exchange very slowly. At higher concentrations additional protein molecules accumulated at the electrode by the formation of polylayers (*12*).

The electrode process is a heterogeneous reaction where the rate is increased in one direction and decreased in the opposite direction by the applied electric field. The electric field at the electrode/electrolyte interphase extends over a distance of 5–8 Å at the ionic strength used. Provided that the protein adsorption does not drastically change the potential distribution, the electrode reaction can be accelerated by the applied electrode potential only up to the first layer. Therefore a polylayer electrode process requires electron transfer through the adsorption layer.

The irreversible protein adsorption at electrodes is equivalent to a chemical modification of the electrode surface. Therefore, the electrode processes may exhibit a character analogous to chemically modified electrodes possessing a polymer layer that contains reversible redox centers (*13*, *14*). The conductivity of this layer is based on the electron transfer between redox centers, which would involve the jumping of electrons from one group to another ("hop mechanism"). With proteins, metal complexes are the overwhelming majority of such electron transfer centers; flavins, quinone, and thiol groups are also suited for electron transfer. These centers provide a path of 10–15 Å through the protein fabric. Figure 2 demonstrates that a parallelism exists between the resistivity of anhydrous protein films (*15*) and the deviations from the reversible polylayer electrode process indicated by the monolayer reduction, decrease of limiting current, i_{lim}, shift of the half-wave potential $E_{1/2}$, or inhibition of the reoxidation.

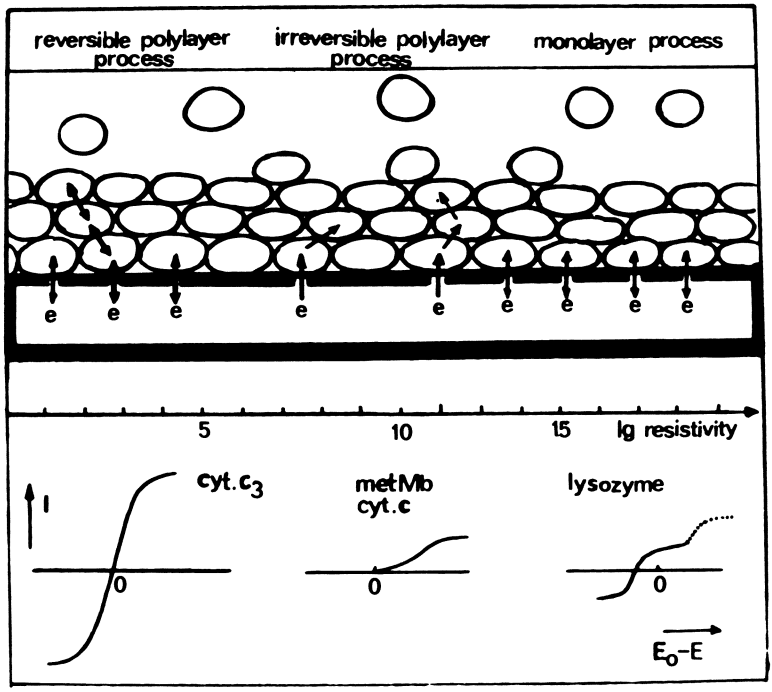

Figure 2. Schematic representation of the relation between the resistivity of anhydrous protein films and the character of the electrode reaction.

Reduction of the First Adsorption Layer

The resistivity, ρ, of films formed by the simple proteins lysozyme or trypsin is so high that no electric current is observed ($\rho > 10^{14}$ $\Omega \cdot$ cm) (*15*). For lysozyme and a number of proteins containing disulfide bridges (*16–20*) or FeS centers (*21–25*), the electrode process is restricted to the first adsorption layer.

The limiting current levels off at the complete saturation of the electrode surface. This phenomenon holds for the polarographically reversible reduction of FeS centers in adrenodoxin (Figure 3). This result demonstrates, in agreement with the high resistivity of the protein film, the inhibition of the electron transfer into the polylayer.

The flavoproteins cholesterol oxidase (*Schizophyllum commune*) and choline oxidase (*Cylindrocarpon didymum*) exhibit similar electrochemical characteristics. Ando et al. (*26*) found an oxidation and a reduction dc wave at the hanging drop mercury electrode (HDME), which was attributed to the covalently bound FAD of the enzyme adsorbed on the electrode surface.

The macroscale electrolysis [in a potential region where only one monolayer is reduced at the dropping mercury electrode (DME) or HDME] leads to the reduction of the proteins with FeS centers or disulfide bridges, respectively (*16*, *22*) in the bulk solution. This result shows that during the electrolysis the protein molecules in the first adsorption layer are exchanged with those in the bulk of the solution. This process is obviously too slow to be detected during the lifetime of the reaction by the DME. Following this mechanism, the enzymatic inactivity of the reduction products of ferredoxin (*11*) and adrenodoxin (*27*) may be explained by the direct interaction of the reacting proteins with the electrode surface, thus leading to irreversible structural changes.

Also, proteins without any pronounced wave in the polarograms may be irreversibly reduced in the first adsorption layer. Contrary to our earlier interpretations (*28*) of the dc polarograms of solubilized fractions of liver cytochrome P-450, the chromatographically purified P-450 LM_2 does not exhibit any polarographic wave. The polarographic wave at the half-wave potential of −580 mV indicates the reduction of cytochrome b_5, a constituent of the solubilized fractions.

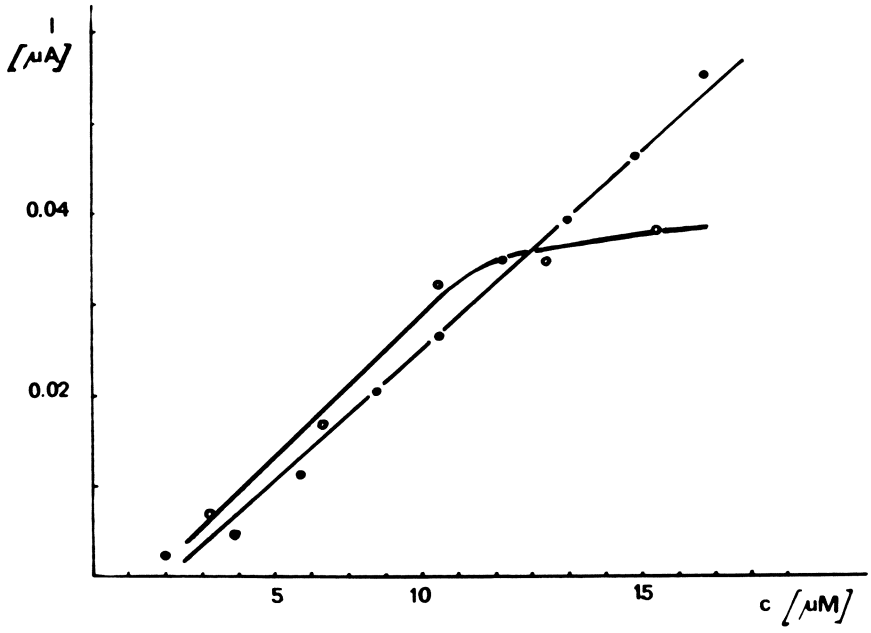

Figure 3. Concentration dependence of the peak current in the differential pulse polarograms with adrenodoxin (○) and trypsin (●). Solutions contain 0.1 M phosphate buffer, pH 7 (background with adrenodoxin), 0.1 M $Na_4B_4O_7$, and 0.1 M KCl, pH 9.2 (background with trypsin). At 1 mV/s where t = 2 *s, and* d = 25 *mV.*

Nevertheless, in the macroscale electrolysis at the potential of −800 mV at the mercury pool electrode, we obtained a product containing native ferrous cytochrome P-450. With a carbon cathode, the inactive but not completely destroyed reduction product, cytochrome P-420, was obtained (*29a*, *29b*). For cytochrome P-450, was calculated an exchange rate per monolayer of ~100 s (*30*), both from the preparative electrolysis and the substrate conversion by the adsorbed protein.

The second adsorption layer is involved in the cathodic reduction of insulin (*16*, *31*). This electron transfer to the second layer requires a higher electric energy than the reduction of the first layer. With trypsin, in analogy with the dc polarographic limiting current (*16*), the peak height in the differential pulse polarograms (Figure 3) shows no saturation at high bulk concentrations. An explanation of this result may be a fast exchange of the second adsorption layer.

Bianco and Haladjian (*21*) found with ferredoxin (*Desulfovibrio gigas*), above the saturation of the electrode, a further increase of the current, whereas the peak potential varies only slightly. Probably, the reduction process extends to several layers.

Reduction of Polylayers

With the heme proteins cytochrome c (*32*, *33*), cytochrome c_3 (*34*, *35*), cytochrome c_7 (*36*), cytochrome b_5 (*29a*), methemoglobin (*37*), and metmyoglobin (*38*), and the flavoprotein glucose oxidase (*39*), the current increases linearly with concentration above the completion of the first adsorption layer. The electron transfer is obviously not restricted to the first layer.

Irreversible Polylayer Reduction

The role of the prosthetic group for the electric resistivity is demonstrated by the fact that the apoprotein itself is an insulator ($\rho > 10^{14}$ $\Omega \cdot$ cm) and the resistivity of monohemoproteins is about 10^9–10^{11} $\Omega \cdot$ cm (*15*). As mentioned, the structure of the proteins drastically influences the electrode process.

At the DME, intact glucose oxidase from *Aspergillus niger* and from *Penicillium notatum* exhibits only a very small peak in the differential pulse polarograms. On the other hand, we established a fast electrode reaction with glucose oxidase samples submitted to a limited proteolysis during purification procedures. In this process a partial degradation of the glucose oxidase takes place and leads to a decrease of the molecular weight. These fragments possess a high specific activity, as was proved by the oxygen consumption method. In the differen-

tial pulse polarograms this glucose oxidase showed a well-shaped peak (39), the summit potential of which corresponded very well to the redox potential $E^{\circ\prime}$ of −305 mV vs. SCE (*40*). Free flavin adenine dinucleotide (FAD) showed an ~100-mV more cathodic peak. The peak (39), the summit potential of which corresponded very well to the the peak potential is independent of the protein concentration.

The enzymatic activity of the adsorbed glucose oxidase fragments was established by the finding that the reduction of the FAD groups by glucose brings about a decrease of the cathodic current (the sum of the background and the glucose oxidase reduction current) by about twice the value of the step height of the oxidized glucose oxidase. This result demonstrates that the deeper curve of Figure 4 reflects the anodic oxidation of the protein $FADH_2$ groups. This oxidation current is increased up to a factor of two with rising glucose concentration. The enzymatic basis of this effect was demonstrated by the ineffectivity of denatured enzyme. The increase in current is based on the regenera-

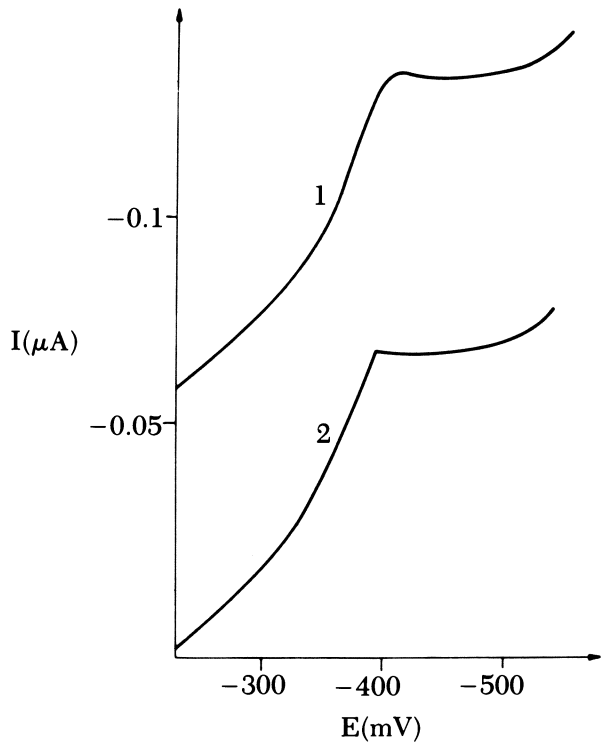

Figure 4. Normal pulse polarograms of glucose oxidase. Solution contains 0.1 M *phosphate buffer, pH 7. At 2 mV/s where* t = *2 s. Curve 1 = 7 μM glucose oxidase and Curve 2 = 7 μM glucose oxidase + 10 μM glucose.*

tion of the reduced glucose oxidase by the substrate glucose. The Brutto reaction represents the anodic oxidation of glucose. In the reaction cycle glucose oxidase acts as a real biocatalyst accelerating the oxidation of its substrate.

The protein structure also depends on the conditions of adsorption (*41*). The electrode reaction of a denatured cytochrome c layer formed by adsorption at low bulk concentration is irreversible. Only in the first scan is the reduction of the ferri-form indicated by a peak in the cyclic voltammograms, although the reoxidation was not observed (*33*). In accordance with this result, the absence of a faradaic peak in the adsorption region of the ac polarograms was established (*42*).

The reduction of the polylayer formed at higher concentrations (*33*) required a lower overvoltage than that of the monolayer of denatured cytochrome c molecules. Because of the small contact area at high surface concentration, native molecules coexist in the first adsorption layer. Most likely, these molecules are reduced more easily and may transfer electrons into the next layers.

The polylayer reduction process with cytochrome c, cytochrome b_5, metmyoglobin, and methemoglobin has the following characteristic features at mercury electrodes:

1. The cathodic reduction gives a current signal in polarograms or cyclic voltammograms, but the anodic oxidation cannot be demonstrated.
2. With monohemo proteins, the limiting current is smaller than that calculated by the Ilkovich equation for the diffusion-controlled electrode process.
3. Both pH and ionic strength influence the current.
4. The addition of the respective reduced protein does not influence the current. An excess of several inert globular proteins, for example, bovine serum albumin with cytochrome c, does not decrease the limiting current (*12*). In contrast, the addition of poly-L-lysine inhibits the electrode process. Therefore, the structure of the first adsorption layer seems to determine the rate of the electrode process.
5. The value of i_{lim} depends linearly on the square root of the mercury column height, as is predicted for a diffusion-controlled electrode process (*32*). This statement is underlined by the finding that the peak current of the cathodic reduction of cytochrome c depends linearly on the square root of the scan rate at the HDME (*33*). In contrast, at the amalgamated gold electrode the peak current grows linearly with increasing scan rate, indicating that the ferricytochrome c is reduced in the adsorbed state (*43*).

6. The half-wave potential is more negative than the formal redox potential. This overvoltage cannot be explained on the basis of the heterogeneous rate constant k_{el} calculated by the Marcus theory using the rate constant k_{11} of the electron self-exchange reaction (*8*, *44*, *45*).
7. The value of $E_{1/2}$ becomes more negative with increasing protein concentration and it depends on pH and ionic strength.

At electrodes these proteins behave similarly to low molecular weight redox systems (e.g., heavy metal ions) on addition of surface active substances, in that they show a decrease of limiting current and shift of the wave position.

In accordance with the inhibition effects found with a low-molecular weight redox system (*46*), the following approaches may be proposed to explain the results (Figure 5):

The decrease of the active electrode surface by the irreversibly adsorbed molecules of the first adsorption layer leads to a partially blocked surface. The limiting current of an electrode reaction occurring at "conducting islands" separated by an average distance r, which corresponds approximately to the thickness of the diffusion layer δ is given by the following relationship (*47*):

$$i_{lim} = \frac{nFDc}{\delta + f(\delta/r)} \tag{1}$$

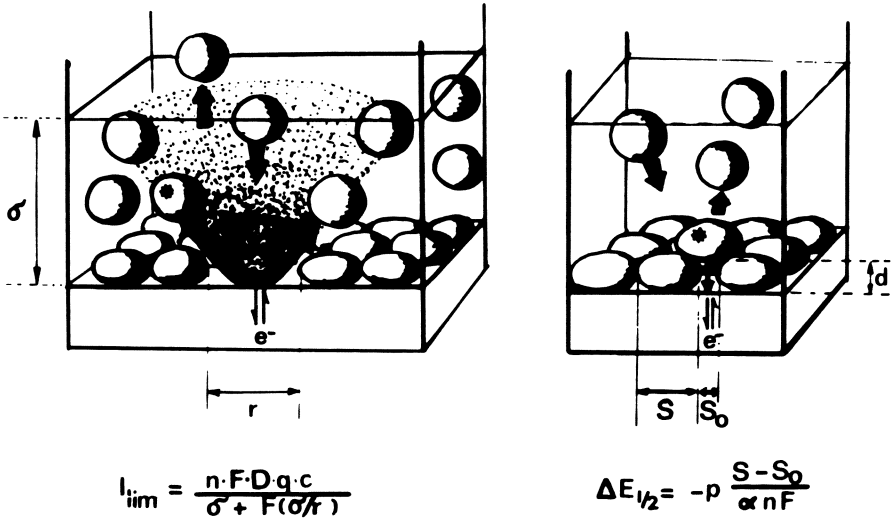

Figure 5. Model of partially blocked electrode surface.

This equation requires a linear concentration dependence of the limiting current with a smaller slope as compared with an uncovered electrode. In contrast to the smaller molecules, the reduction of proteins may proceed only in relatively large sites where the distances between them are greater than the thickness of the diffusion layer.

The linear dependence of the limiting current on the root of the mercury column height also corresponds to this model.

The average distance d of discharging molecules to the electrode will grow with increasing surface pressure, P, and consequently the $E_{1/2}$ is shifted. The work to be done against the pressure is compensated by the increase of the electrical energy (*48a*):

$$E_{1/2} = -P(S - S_0)/\alpha nF \qquad (2)$$

where S = the surface area of a molecule and S_0 = the area of a pore in the adsorption layer.

Because the desorption rate of the second layer is rather low and cannot account for the rate of the electrode process observed, the electrons must travel through the adsorption layer. The control of the electrode process by a slow intermolecular electron transfer would explain the decrease of the limiting current, but it contradicts the diffusion limitation of the protein–electrode reactions. Also, the ineffectiveness of inert proteins (*12*) argues against a control by specific intermolecular electron transfer in the cytochrome c polylayer.

Reversible Multilayer Electrode Process

The multi-heme protein ferrocytochrome c_3 has at 268 K a resistivity of only 57 $\Omega \cdot$ cm (*15*). It was the first heme protein showing a polarographically reversible polylayer oxidation–reduction process (*34*). Recently, Bianco and Haladjian (*36*) established, with the three heme-containing protein cytochrome c_7, the same type of electrochemical behavior. For the ferredoxin of *Clostridium pasteurianum* (*48b*) (four Fe–S centers), a diffusion-controlled reduction at the DME also was obtained.

In the first cycle the reduction of the adsorbed cytochrome c_3 is a very fast electrode process. In contrast, no oxidation peak is observed with adsorbed cytochrome c_3 on the DME. Therefore the adsorbed layer, consisting of ferrous cytochrome c_3, becomes electrochemically inactive in repetitive scans. However, the electron transfer through this inactive electrode coating to molecules of the second layer is a polarographically reversible process. In dilute cytochrome c_3 solution, the reacting molecules of the second layer may be in a fast adsorption exchange. The electrode reaction through a polylayer formed at high

protein concentrations is a rather slow process. Both the anodic and the cathodic peaks in the cyclic voltammograms decrease in repetitive scans (*49*).

With cytochrome c_3, the addition of cytochrome c suppresses the limiting current, but the half-wave potential is not altered (*50*). This result supports the theory that the substitution of cytochrome c_3 molecules by cytochrome c gives rise to the formation of a partially blocked electrode (*see* Equation 1). Thus, from the first layer of cytochrome c_3 a rapid intermolecular electron transfer has to occur so that the mass transport is the slowest step.

Besides the intermolecular electron transfer, the charge injection from the electrode into the first adsorption layer may control the electrode process. The decisive role of this process is underlined by the finding that modification of the electrode surface by means of polymeric methyl viologen (*51*), or covalent grafting with methyl viologen derivatives (*52*), or the adsorption of 4,4′-bipyridyl (*53*, *54a*, *54b*), leads to a quasi-reversible electrode reaction for the multilayers of ferredoxin or cytochrome c. The conducting layers of these compounds possessing a conjugated π-electron system are as likely to prevent the irreversible protein adsorption as to facilitate the electron transfer to the first protein layer.

A significant rate of the electrode reaction of intact glucose oxidase, both from *Penicillium notatum* and from *Aspergillus niger*, was found at the gold minigrid electrode modified by polymeric methyl viologen (*55*). The potential step spectroelectrochemical experiments were performed in a thin-layer cell monitoring the change in absorbance at 460 nm vs. time (Figure 6). On application of a potential of −400 mV vs. SCE, the absorbance decreases continuously reaching, after 10 min, the value of glucose oxidase reduced by glucose. The original absorbance is achieved by anodic oxidation at 200 mV vs. SCE. No change of the total spectrum between 600 and 300 nm was found after three cycles of complete reduction and oxidation of the same glucose oxidase sample. This result shows that the native structure of the enzyme may be retained.

Yeh and Kuwana (*56*) demonstrated a diffusion-controlled, reversible electron transfer from the tin-supplemented indium oxide electrode to cytochrome c. Whereas the position of the anodic and cathodic peak potential corresponded to the redox potential, the diffusion coefficient determined from the peak currents was too small by a factor of about two.

Indirect evidence for a fast electron-exchange between the protein prosthetic group and the electrode was obtained by catalysis of the electrochemical substrate conversion by several enzymes (bioelectro catalysis). The electron-exchange was accelerated by the interac-

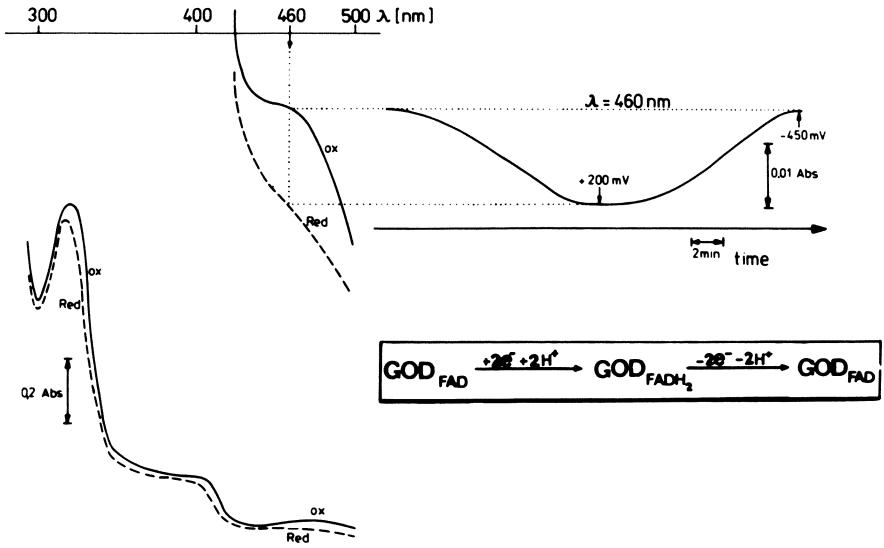

Figure 6. Optically transparent thin-layer electrochemical cell results of glucose oxidase at the methyl viologen-modified gold minigrid electrode. Solutions contain 0.1 M *phosphate buffer, pH 5.8 and 0.1* mM *glucose oxidase from* Penicillium notatum *with a 0.18-mm optical pathlength. The gold minigrid electrode has a 60% optical transparency with 120 wires/in.*

tion of the enzyme with a semiconducting gel (*57–60*) or with organic metals (*61–63*). However, the formation of the reduced protein was not demonstrated directly.

Deviations from the reversible behavior also occur at modified electrodes with proteins that have a slow intermolecular electron-exchange (low k_{11} value).

We studied the effect of modifying a gold electrode by adsorption of 4,4′-bipyridyl on the behavior of intact glucose oxidase. Preliminary results indicated that glucose oxidase is reducible only in the first cycle but not anodically reoxidized at the modified plane gold electrode. Thus, addition of glucose removes the cathodic peak but does not bring about a corresponding oxidation signal. Cytochrome P-450 (*29b*), methemoglobin, and metmyoglobin exhibit at the bipyridyl-modified gold electrode only a reduction peak, but no reoxidation signal was found. As with the mercury electrode, the peak potentials shifted in the cathodic direction.

These results demonstrate that both the modification of the electrode surface and changes of the protein moiety drastically influence the character of the electrode process.

Biological Significance

Electron transfer proteins play a dominant role in the catalysis of electron transport and the coupled energy conversion in the respiratory chain. In contrast to the small molecule electron transfer, the mechanism of intermolecular and intramolecular electron transfer of biological macromolecules in detail (*1*) is not understood fully. This fact is particularly perplexing in light of the extensive research in this area.

One approach to the elucidation of these complex systems was the kinetic study of isolated oxidoreductases with small molecule reagents. The goal of such research is the elucidation of reaction pathways available to the proteins. The second principle was the classical study of intact or partially disrupted preparations of electron transfer chains.

In the last few years increasing attention was paid to the direct electron transfer between the electrode and proteins. The reversible cathodic reduction of several layers obviously requires a rapid transfer of electrons to the first protein layer coupled with a fast intermolecular electron transfer. The second step of this process is more similar to that of the electron transfer in biological redox chains than to the outer sphere collision reactions with low molecular weight partners. Therefore, the heterogeneous electron transfer appears to be the most direct method used to investigate the redox properties of proteins.

This hypothesis is in agreement with results (*64*) that established analogies between the reaction of cytochrome c at the bipyridyl-covered gold electrode and its reaction with cytochrome oxidase. The modification of cytochrome lysine residues or the addition of poly-L-lysine influences both the electrode reaction and the oxidation by the oxidase.

The proposed analogy of the electrode process and protein reactions is the basis of the application of the Marcus theory (*65*). For outer sphere electron transfer, the rate constant of the self-exchange reaction, k_{11}, allows one to draw conclusions on the rate constant, k_{el}, of the electrode process:

$$\left(\frac{k_{11}}{10^3}\right)^{1/2} \geq k_{el} \tag{3}$$

Using the k_{11} value of $10^3 \cdot 1/M \cdot s$ (*66*) for cytochrome c the estimated value of k_{el} predicts a polarographically reversible electrode process. On the other hand, the rate constants of self-exchange with metmyoglobin ($4 \times 10^2 \cdot 1/M \cdot s$) (*67*) and methemoglobin ($3 \times 10^3 \cdot 1/M \cdot s$) (*67*) give a k_{el} for a quasi-reversible and one irreversible electrode reaction, respectively. The electrochemical behavior of the hemoproteins at

modified electrodes exhibited the proposed parallelism to the rate of the homogeneous redox reaction.

Technological Aspects

In biotechnology, the direct electron transfer between the enzyme molecules and the metal electrode offers new prospects because the electrode may substitute both cofactor and electron-transferases.

Pioneering experiments (*68*, *69*) were carried out using glucose oxidase in fuel cells operating on glucose and oxygen. Many carbon electrodes were fabricated and tested where the enzyme was covalently bound to the electrode, embedded in a carbon powder, or entrapped in a polyacrylamide gel–platinum gauze matrix. The low current density was attributed to difficulty in electron transfer between the enzyme and the conducting electrode surface. Also, during covalent grafting of glucose oxidase at the electrode surface no electron exchange with the protein prosthetic group was found (*70–72*). These results are in agreement with the finding (*73*) that no exchange current between the platinum-indicator electrode and the dissolved protein was measurable in the absence of mediators. Nevertheless, reagentless enzyme electrodes, which reuse the cofactor nicotine adenine dinucleotide (NAD), were established by this principle (*74–76*). With glucose oxidase or lactic dehydrogenase, the substrate-dependent regeneration current was used as the measuring signal (*77*, *78*).

On the other hand, the chemical modification of the electrode surface resulted in a considerable acceleration of the electrode reaction. This approach was used in bio-fuel cells using hydrogenase and laccase (*57*, *59*) and in sensors for glucose (*63*) and lactate (*61*) on the basis of glucose oxidase or cytochrome b_2. The same approach may be applied to the indirect electrochemical conversion of substrate to obtain a desired level of product, for example, lactate, in vivo.

In general, cofactor-dependent systems should be devised for the cofactorless electrochemical substrate or energy conversion using the direct protein–electrode reaction.

Conclusions

Both in the mechanism of biological electron transfer chains and in the heterogeneous electron transfer between the active site of proteins and electrodes, many basic problems are unsolved. The development and application of modified electrodes and the derivatization of proteins will contribute considerably to the elucidation of the mechanism of biological redox reactions.

In addition to the theoretical importance of these electrode reactions, the major stimulus for directing the efforts of scientists to this

study is their advantageous applications in biotechnology. The application of enzymes as catalysts of organic electrode reactions attracts increasing attention. Furthermore, the substrate specificity of enzymes offers much promise for designing specific sensors for quantitative analysis.

Literature Cited

1. Moore, G.; Williams, R. *Coord. Chem. Rev.* **1976,** *18,* 125.
2. Schläpfer, P.; Mindt, W.; Racine, P. *Clin. Chim. Acta* **1974,** *57,* 283.
3. Suzuki, S.; Takahashi, F.; Sotoh, J.; Sonobe, N. *Bull. Chem. Soc. Jpn* **1975,** *48,* 3246.
4. Weibel, F.; Doge, C. *Arch. Biochem. Biophys.* **1975,** *169,* 146.

5a. Berg, H. In "Topics in Bioelectrochemistry and Bioenergy"; G. Milazzo, Ed.; Wiley: London, New York, Sydney, Toronto, 1976; 1, p. 39.

5b. Senda, M.; Ikeda, T.; Kakutani, T.; Kano, K.; Kinoshita, H. *Bioelectrochem. Bioenerg.* **1981,** *8,* 151.

5c. Palecek, E. *Bioelectrochem. Bioenerg.* **1981,** *8,* 469.

6. Berezin, I.; Varfolomeev, S. *Appl. Biochem. Bioeng.* **1980,** *2,* 259.
7. Janik, B.; Elving, P. *Chem. Rev.* **1968,** *68,* 295.
8. Kadish, K.; Jordan, J. *J. Electrochem. Soc.* **1978,** *125,* 1250.
9. Miller, I.; Werber, M. *J. Electroanal. Chem.* **1979,** *100,* 103.
10. Scheller, F.; Prümke, H.-J.; Schmidt, H.; Mohr, P. *Bioelectrochem. Bioenerg.* **1976,** *3,* 328.
11. Kuznetsov, B.; Mestechkina, N.; Shumakovich, G. *Bioelectrochem. Bioenerg.* **1977,** *4,* 1.
12. Kuznetsov, B.; Shumakovich, G.; Mestechkina, N. *Bioelectrochem. Bioenerg.* **1977,** *4,* 512.
13. Dobbelhofer, K. *Electrochim. Acta* **1980,** *25,* 871.
14. Shigehara, K.; Oyama, N.; Anson, F. *J. Am. Chem. Soc.* **1981,** *103,* 2552.
15. Nakahara, Y.; Kimura, K.; Inokuchi, H.; Yagi, T. *Chem. Lett.* **1979,** 877.
16. Cecil, R.; Weitzman, P. *Biochem. J.* **1964,** *93,* 1.
17. Stankovich, M.; Bard, A. *J. Electroanal. Chem.* **1977,** *85,* 173.
18. Stankovich, M.; Bard, A. *J. Electroanal. Chem.* **1978,** *86,* 189.
19. Pavlovic, O.; Miller, I. *Exp. Suppl.* **1971,** *18,* 513.
20. Kwee, S.; Lund, N. *Bioelectrochem. Bioenerg.* **1975,** *2,* 231.
21. Bianco, P.; Haladjian, J. *Biochem. Biophys. Res. Commun.* **1977,** *78,* 323.
22. Weitzman, P.; Kennedy, J.; Caldwell, R. *FEBS Lett.* **1971,** *17,* 241.
23. Kiselev, B.; Kazakova, A.; Evstigneev, B.; Gins, B.; Mychin, B. *Biophysics* **1976,** *21,* 35.
24. Kakutani, T.; Torijama, K.; Ikeda, T.; Senda, M. *Bull. Chem. Soc. Jpn* **1980,** *53,* 947.
25. Feinberg, B.; Ying-Kit Lau, *Bioelectrochem. Bioenerg.* **1980,** *7,* 187.
26. Ando, S.; Ikeda, T.; Senda M. *Rev. Polarogr.* **1980,** *26,* 18.
27. Scheller, F.; Strnad, G.; Kühn, M.; Akhrem, A. *Proc. 5th Int. Symp. Bioelectrochem.* Weimar, **1979,** 47.
28. Scheller, F.; Renneberg, R.; Strnad, G.; Pommerening, K.; Mohr, P. *Bioelectrochem. Bioenerg.* **1977,** *4,* 500.

29a. Kuznetsov, B.; Mestechkina, M.; Izotov, M.; Karuzina, I.; Karjakin, A.; Archakov, A. *Biochem. (Russ.)* **1979,** *44,* 1569.

29b. Archakov, A.; Kuznetsov, B.; Izotov, M.; Karuzina, I. *Bull. Acad. Sci. USSR,* **1981,** *258,* 216.

30. Scheller, F.; Renneberg, R.; Schwarze, W.; Strnad, G.; Pommerening, K.; Prümke, H.-J.; Mohr, P. *Acta Biol. Med. Ger.* **1979,** *38,* 503.
31. Berg, H. *Stud. Biophys.* **1979,** *75,* 209.

32. Betso, S.; Klapper, M.; Anderson, L. *J. Am. Chem. Soc.* **1972,** *94,* 8197.
33. Haladjian, J.; Bianco, P.; Serre, P. *Bioelectrochem. Bioenerg.* **1979,** *6,* 555.
34. Niki, K.; Yagi, T.; Inokuchi, H.; Kimura, K. *J. Am. Chem. Soc.* **1979,** *101,* 3335.
35. Bianco, P.; Haladjian, J. *Biochim. Biophys. Acta* **1979,** *545,* 86.
36. Bianco, P.; Haladjian, J. *Bioelectrochem. Bioenerg.* **1981,** *8,* 239.
37. Scheller, F.; Jänchen, M.; Lampe, J.; Prümke, H.-J.; Blanck, J.; Palacek, E. *Biochim. Biophys. Acta* **1975,** *412,* 157.
38. Scheller, F.; Jänchen, M. *Stud. Biophys.* **1974,** *46,* 153.
39. Scheller, F.; Strnad, G.; Neumann, B.; Kühn, M.; Ostrowski, W. *Bioelectrochem. Bioenerg.* **1979,** *6,* 117.
40. Stankovic, M.; Schöpfer, L.; Massey, V. *J. Biol. Chem.* **1978,** *253,* 4871.
41. Scheller, F.; Jänchen, M.; Prümke, H.-J. *Biopolymers* **1975,** *14,* 1553.
42. Scheller, F. *Bioelectrochem. Bioenerg.* **1977,** *4,* 490.
43. Tarasevich, M.; Bogdanovskaya, V. *Bioelectrochem. Bioenerg.* **1976,** *3,* 589.
44. Feinberg, B.; Gross, M.; Kadish, K.; Marano, R.; Pace, S.; Jordan, J. *Bioelectrochem. Bioenerg.* **1974,** *1,* 73.
45. Scheller, F.; Prümke, H.-J. *Stud. Biophys.* **1976,** *60,* 137.
46. Lipkowski, J.; Galus, Z. *J. Electroanal. Chem.* **1975,** *61,* 11.
47. Landsberg, R.; Scheller, F. *Anal. Chem.* **1973,** *45,* 420.
48a. Kuznetsov, B. *Bioelectrochem. Bioenerg.* **1981,** *8,* 681.
48b. Hill, C.; Renaud, J.; Holm, H.; Mortenson, L. *J. Am. Chem. Soc.* **1977,** *99,* 2549.
49. Niki, K., personal communication.
50. Niki, K.; Kumagai, H.; Fugiwara, R.; Yagi, T.; Inokuchi, H. *Biochim. Biophys. Acta* **1981,** *636,* 136.
51. Landrum, H.; Salmon, R.; Hawkridge, F. *J. Am. Chem. Soc.* **1977,** *99,* 3154.
52. Lewis, N.; Wrighton, M. *Science* **1981,** *211,* 944.
53. Eddowes, M.; Hill, H. *J. Am. Chem. Soc.* **1979,** *101,* 4461.
54a. Eddowes, M.; Hill, H.; Uosaki, K. *Bioelectrochem. Bioenerg.* **1980,** *7,* 527.
54b. Albery, W.; Eddowes, M.; Hill, H.; Hillman, A. *J. Am. Chem. Soc.* **1981,** *103,* 3904.
55. Stagard, J.; Scheller, F.; Hawkridge, F., unpublished data.
56. Yeh, P.; Kuwana, T. *Chem. Lett.* **1977,** *10,* 1145.
57. Berezin, J.; Bogdanovskaja, V.; Varfolomeev, S.; Tarasevich, M.; Jaropolov, A. *Dokla. Akad. Nauk. SSSR* **1979,** *240,* 615.
58. Tarasevich, M. *Bioelectrochem. Bioenerg.* **1979,** *6,* 587.
59. Berezin, J.; Varfolomeev, S. *Appl. Biochem. Bioengin.* **1980,** *2,* 259.
60. Varfolomeev, S.; Berezin, J. *J. Mol. Cat.* **1978,** *4,* 387.
61. Kulys, J.; Schbirmizkas, S. *Bull. Acad. Sci. USSR* **1979,** *245,* 137.
62. Kulys, J.; Samalius, S.; Schbirmizkas, G. *FEBS Lett.* **1980,** *114,* 7.
63. Cenas, N.; Kulys, J. *Bioelectrochem. Bioenerg.* **1981,** *8,* 103.
64. Eddowes, M.; Hill, H.; Uosaki, K. *J. Am. Chem. Soc.* **1979,** *101,* 7113.
65. Marcus, R. *J. Chem. Phys.* **1965,** *43,* 679.
66. Gupta, R. *Biochim. Biophys. Acta* **1973,** *292,* 291.
67. Mauk, A.; Gray, H. *Biochem. Biophys. Res. Commun.* **1979,** *86,* 206.
68. Drake, R. *U.S. Government Report,* 1968, PB 177695.
69. Lahoda, E.; Liu, C.; Wingard, L. *Biotechnol. Bioeng.* **1975,** *17,* 413.
70. Shu, F.; Wilson, G. *Anal. Chem.* **1976,** *48,* 1679.
71. Kamin, R.; Wilson, G. *Anal. Chem.* **1980,** *52,* 1198.
72. Bourdillon, C.; Bourgeous, J.; Thomas, D. *J. Am. Chem. Soc.* **1979,** *102,* 4231.
73. Duke, F.; Kust, R.; King, L. *J. Electrochem. Soc.* **1969,** *116,* 32.
74. Scheller, F.; Jänchen, M.; Seyer, I. *DDR-Patentschrift* **1976,** 125560.
75. Blaedel, W.; Jenkins, R. *Anal. Chem.* **1976,** *48,* 1240.

76. Blaedel, W.; Engstrom, R. *Anal. Chem.* **1980,** *52,* 1691.
77. Durliat, H.; Comtat, M. *J. Electroanal. Chem.* **1978,** *89,* 221.
78. Durliat, H.; Comtat, M. *Anal. Chem.* **1980,** *52,* 2109.

RECEIVED for review June 2, 1981. ACCEPTED December 14, 1981.

Mapping of the Energy Levels of Metallophthalocyanines via Electronic Spectroscopy, Electrochemistry, and Photochemistry

A. B. P. LEVER, S. LICOCCIA, K. MAGNELL, P. C. MINOR, and B. S. RAMASWAMY

York University, Department of Chemistry, 4700 Keele Street, Downsview, Ontario, Canada, M3J 1P3

The mapping of the energy levels in metallophthalocyanines is accomplished by a combination of electrochemistry, electronic spectroscopy, and photochemistry. This chapter reviews the electrochemical properties of metallophthalocyanines and includes a large amount of previously unpublished data. The results are rationalized in terms of the nature of the electron transfer, that is, redox at metal or ligand. Well-defined correlations are shown to exist between the ease of oxidation or reduction of the phthalocyanine ligand and the oxidation state, and/or polarizing power, of the metal ion. Solvent and ring substitution effects also are presented and explained. Charge transfer transition energies can be calculated directly from these data, and agreement between experiment and theory is excellent. Finally, the data are used to calculate both the photogenerated excited state redox energies and the thermodynamics of quenching by donors and acceptors.

Phthalocyanine (MPc) complexes have significant importance for many reasons, including their similarity to the biologically important metalloporphyrins, their classical use as dyestuffs, and their developing use as components of various solar energy conversion devices.

0065-2393/82/0201-0237$06.00/0

Of paramount importance in understanding and predicting the physics and chemistry of the metallophthalocyanines is knowledge of the energy levels therein. This knowledge can be gained through study of the electronic spectroscopy (absorption and emission), electrochemistry, photochemistry (and photophysics), and photoelectron spectroscopy of these species. In this chapter we address the first three of these techniques and consider the information obtained from their use.

The lower excited states (up to at least 35,000 cm^{-1}) of a wide range of metallophthalocyanine derivatives can be identified and mapped. These states vary as a function of the environment (solvent, axial coordination, etc.), phthalocyanine ring substituent, nature and size of metal ion, oxidation state, and electronic configuration.

The excited states may be classified as π–π^* and n–π^* transitions, primarily located on the phthalocyanine ring. The ligand (Pc ring) to metal charge transfer (LMCT), metal to ligand charge transfer (MLCT), and d–d transitions primarily occur on the metal atom. These transitions may occur in two spin manifestations. In addition, spin coupling can occur between metal ion ground state wave functions and excited state wave functions of the phthalocyanine ring to yield a range of triplet–multiplets.

The following three sections review progress in the electrochemistry, electronic spectroscopy, and photochemistry of metallophthalocyanines. The data reported for metallophthalocyanines may be compared usefully with the data obtained for the porphyrins discussed in Chapter 13 in this volume.

Electrochemistry

Many reports (*1–18*) discuss the electrochemical properties of the metallophthalocyanines, but only in recent literature have these data coalesced into a useful working body of knowledge.

In general, oxidation and reduction are expected at the metal center and at the phthalocyanine ring. In each case, one or more electron transfer processes may be observed. Indeed, two successive ring oxidations and up to four successive ring reductions may occur. Ring reductions are generally electrochemically reversible, but ring oxidations usually are not (at least on platinum). Generally, no more than two redox processes were characterized at a given metal center.

Identification of the nature of a given redox product usually is based on electronic spectroscopy and, where relevant, electron spin resonance (ESR) spectroscopy (*2, 9, 12*). Generally, it is possible to deduce unequivocally whether a reduction or oxidation occurred at the metal center or phthalocyanine ring. Phthalocyanine anion and

cation radical electronic spectra are quite distinct from those of the $Pc(-2)^1$ species (*12*, *19*), although some confusion may exist when low-oxidation state transition-metal ions, such as iron(I), are involved (*9*).

The higher filled and lower empty energy levels of a typical metallophthalocyanine are illustrated in Figure 1 (*20–23*). The two highest filled orbitals[2] of relevance to our discussion are π-orbitals with a_{1u} [highest occupied molecular orbital (HOMO)] and a_{2u} symmetry, respectively; and the lowest empty ring orbitals are the e_g [lowest unoccupied molecular orbital (LUMO)] and b_{2u} π^*-orbitals. The metal valence orbitals may be buried inside the filled phthalocyanine levels, or filled and/or empty valence orbitals may occur in the HOMO–LUMO gap; in addition, empty metal orbitals may lie at energies comparable to, or above, the LUMO phthalocyanine level.

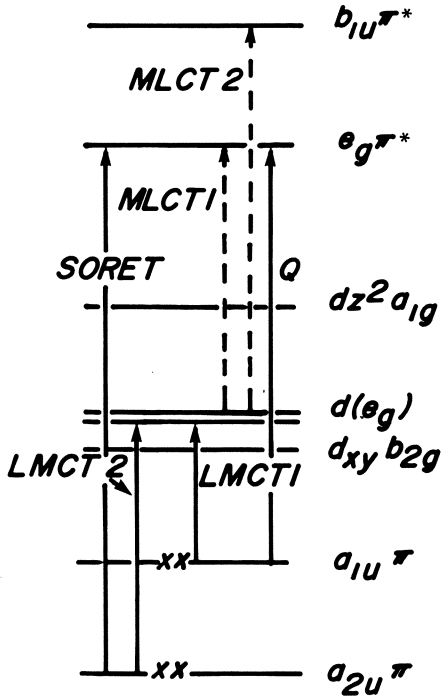

Figure 1. A simplified energy level diagram for a metallophthalocyanine. LMCT and MLCT are ligand to metal, and metal to ligand charge transfer transitions, respectively.

[1] The phthalocyanine nomenclature used here is presented in Ref. *19*.

[2] An energy level of symmetry (*xy*) localized on the peripheral nitrogen atoms is omitted because there is no evidence that it plays a role in the spectroscopy.

Phthalocyanine redox chemistry may be classified conveniently into two sections: main groups and transition groups.

Main Group Phthalocyanine Electrochemistry. Redox chemistry in the main groups is usually quite straightforward; generally the metal atom center is unaffected, and all observable processes occur on the phthalocyanine ring. For main group ions that lie in the phthalocyanine plane, the first ring oxidation (from HOMO) is separated from the first ring reduction (to LUMO) by approximately 1560 mV (Table I), which is the magnitude of the molecular bandgap. This value seems largely unaffected by the nature of the main group metal, although some deviation may occur if the metal is too large to be accommodated by the phthalocyanine center (*14*).

However, the absolute energies of first oxidation or reduction vary considerably, and depend on the size and charge of the metal ion. The ease of oxidation or reduction of the phthalocyanine unit depends on the electric field generated by the central metal ion. Indeed, there is a clear relationship between the polarizing power of the central ion, expressed as (ze/r) and the redox energy. The more polarizing is the ion, the easier it is to reduce the phthalocyanine ring, and the more difficult the ring is to oxidize. A good linear relationship is observed between these quantities (*14*) defined by Equations 1 and 2:

$$\text{oxidation } (ze/r)(E^\circ - 1.410) = -0.012 \quad (1)$$

$$\text{reduction } (ze/r)(E^\circ + 0.145) = -0.012 \quad (2)$$

where the potentials are referenced to the normal hydrogen electrode (NHE) and the radii used originate from Ref. *24*. The lines are essentially parallel. Thse data imply a HOMO–LUMO separation of about 1.56 V, independent of the central main group ion, provided it lies in the plane (*14*). This treatment is discussed later.

The second reduction process appears, on the average, about 420 mV more negative than the first reduction (Table I) but these potentials are more scattered and less directly dependent on the polarizing power of the central ion; nevertheless, metallophthalocyanines with the more polarizing ions are generally more readily reduced to the ring dianion. The third- and fourth-reduction processes occur near −1.7 to −1.8 and −2.0 V (Table I) (*12*) (for both main and transition group ions). These data are displayed in Figure 2. For the first two reduction processes, the ease of reduction follows the sequence:

$$PcH_2 < PcMg(II) < Pc^{2-}\,[Pr_4N]_2 > PcAl(III)X$$

This sequence may be rationalized in terms of increasing negative charge on the phthalocyanine ligand when passing from the covalent

Published on June 1, 1982 on http://pubs.acs.org | doi: 10.1021/ba-1982-0201.ch011

Table I. Main Group Metallophthalocyanine Electrochemistry

Complex	*Solvent*[b]	c^{++}/c^{+}	c^{+}/c	c/c^{-}	$c^{-}/c^{=}$	$c^{=}/c^{3-}$	c^{3-}/c^{4-}	*Reference*
$PcSi(IV)R_2$[a]	DMF			−0.30	−0.895			*14*
PcAl(III)Cl	DMA		1.39	−0.26				*16*
	DMF			−0.29	−0.74	−1.18	−1.74	*12*
	DMF		1.155	−0.415				tw[c], *14*
	DMF		1.18	−0.415	−0.86			*6*
	DMF		1.15	−0.42				*15*
PcGa(III)Cl	DMF		1.105	−0.495	−0.895			tw, *14*
PcIn(III)Cl	DMF		1.070	−0.475	−0.710			*14*
	DMF		1.080	−0.41				*15*
PcMg(II)	DMF		0.94	−0.71				*16*
	DMF			−0.67	−1.15	−1.90	−2.34	*12*
	DMF	1.50	0.89	−0.68	−1.04			tw, *14*
	DMF	1.50	0.85	−0.725				*6*
	DMA			−0.72				*15*
PcCd(II)	DMF		0.78	−0.93				tw, *6*, *14*
PcHg(II)	DMF		0.49	−1.06				*14*
	DMF		0.490	−1.065				tw
PcPb(II)	DMF		0.91	−0.48	−0.770			*9*, *14*, *15*
PcBa(II)	DMF	1.01	0.695	−0.250	−0.840			tw
PcNa(I)	DMF			−0.82				*15*
$Pc^{2-}(PRA)^{+}{}_2$[d]				−1.00	−1.31	−1.71	−1.95	*12*
PcH_2	CLN		1.34					*10*
	DMF		0.865	−0.58				*15*
	DMF			−0.42	−0.82	−1.69	−1.99	*12*
$TbPcH_2$	CHC	1.18	0.865	−0.58	−0.95			*44*
$TsPcH_2$	DMSO		1.14[e]	−0.285	−0.73	−1.57		*11*

Note: Data rounded off to 5 mV. Redox potentials, $E_{1/2}$, vs. NHE.

[a] R = O-*t*-Amyl.

[b] Solvents: DMF, dimethylformamide; DMA, dimethylacetamide; DMSO, dimethyl sulfoxide; CLN, chloronaphthalene; CHC, dichloromethane.

[c] tw, this work.

[d] PRA, *N*-propylammonium cation.

[e] Two-electron oxidation.

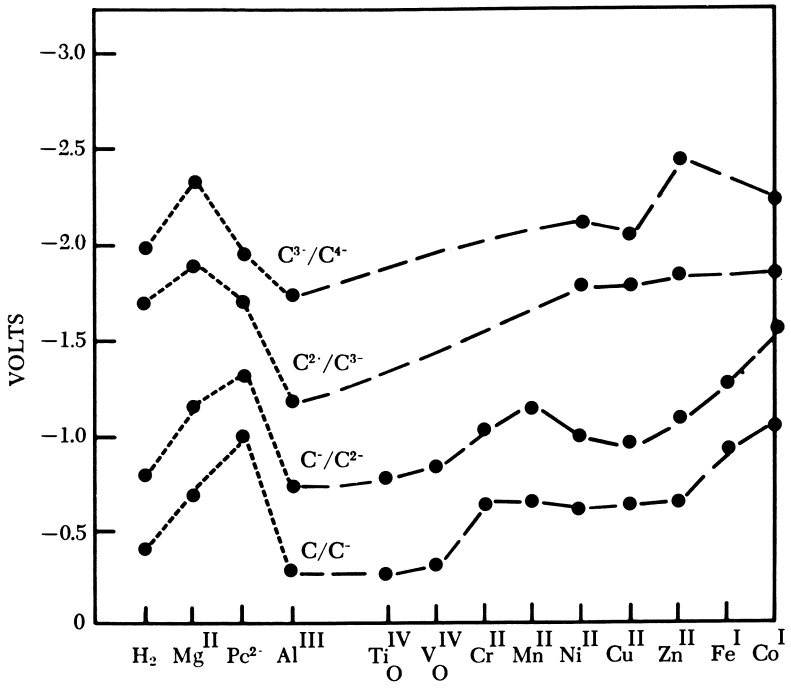

Figure 2. Sketch of the variation in first-, second-, third-, and fourth-ring reduction potentials as a function of metal ion and oxidation state. All data vs. NHE.

NH bond in PcH_2, to a fairly electrostatic interaction with the electropositive magnesium, and finally to a full negative charge with the propylammonium salt. For aluminum(III), the high polarizing power of this ion leads to a more covalent interaction and a reduced negative charge on the phthalocyanine ligand. These potentials monitor the negative charge on the phthalocyanine ligand.

Transition Group Phthalocyanine Electrochemistry. The presence of a transition metal ion appears to perturb the redox processes occurring at the phthalocyanine unit; however, a pattern similar to the main group species can be discerned. In many cases, one or more redox processes may occur at the central ion at potentials lying between ring oxidation and reduction. If the solvent, supporting electrolyte, or an added ligand can bind to the axial sites of the metal ion in one (or more) of its oxidation levels, then the observed redox potential often depends markedly on the choice of solvent, electrolyte, or added ligand.

Table II gives data for transition metal ion phthalocyanines where solvent coordination is not strongly perturbing, that is, in weak donor

Published on June 1, 1982 on http://pubs.acs.org | doi: 10.1021/ba-1982-0201.ch011

Table II. Transition Metal Phthalocyanine Redox Potentials in Weakly Coordinating Solvents vs. NHE

Complex	Electronic Spectrum: Q Band	Electronic Spectrum: Soret	c^{++}/c^{+}	c^{+}/c	c/c^{-}	$c^{-}/c^{=}$	Reference
TbPcTi(IV)O	14.43	28.33		1.09	−0.275	−0.780	tw
TbPcV(IV)O	14.31	29.00		1.18	−0.335	−0.840	tw
TbPcCr(II)	14.82	28.74		0.945	−0.630	−1.115	tw
TsPcCr(III)Na_3	14.37	28.09		0.75?	−0.155	−0.760	tw
TbPcMn(III)OAc	13.97	27.17			0.125	−0.650	tw
PcMn(II)	15.15			0.100	−0.450		*3*
TdPcFe(II)	14.81	27.93		0.84			tw
PcFe(II)				0.615[a]	−0.310[a]	−0.93[a]	*2*
TsPcFe(II)					−0.50	−0.91	*45*
TsPcFe(II)$(CN)_2$					−0.98	−1.32	*45*
PcCo(II)	14.88[b]	28.74[b]		−0.130	−1.160[b]		*10*
PcCo(II)			1.04[a]	0.04[a]			*16*
TsPcCo(II)			1.08[c]	0.64[d]	0.005	−1.05	tw
TbPcCo(II)			1.40[e]	0.88[e]			*16*
PcNi(II)	14.90[b]	28.49[b]		1.29[b]	−0.61[b]	−0.99[b]	*10*
TsPcNi(II)				1.19	−0.465	−0.90	tw, *18*
PcCu(II)	14.75[b]	28.57[b]		1.22[b]	−0.600[b]	−0.94	*10*
TbPcCu(II)					−0.675	−1.10	tw
TsPcCu(II)				1.13	−0.510	−0.90	tw
TsPcCu(II)				1.11[c]	−0.495	−0.875	*11*
PcZn(II)	14.68[b]			0.92[b]	−0.65	−1.09	*9, 10*
PcZn(II)				1.02	−0.56		*16*
PcRu(II)CO(Py)	15.70[f]	29.24[f]		1.15[f]			*13*
PcRu(II)$(Py)_2$	16.10[f]	31.75[f]		1.01[f]			*13*

Note: All data are reported in DMF with TEAP or similar perchlorate supporting electrolyte except those annotated as follows. The letter c represents the complex listed in the left column. Underlined data represent metal oxidation or reduction, otherwise the phthalocyanine is oxidized or reduced. It does not follow therefore that each column represents the same oxidation state for each complex. TbPc, TsPc, and TdPc refer, respectively, to tetra-*t*-butyl-, tetrasulfonyl-, and tetradodecylsulfonamidophthalocyanines.

[a] Dimethylacetamide solution.
[b] Chloronaphthalene solution.
[c] Two-electron oxidation.
[d] Irreversible.
[e] Dichlorobenzene solution.
[f] Dichloromethane solution.

solvents, or involving metals that bind weakly along the axis. These data should be generally interpretable without taking into consideration severe perturbation by solvent effects.

Electronic and ESR spectroscopy demonstrated that the OTi(IV), OV(IV), Ni(II), Cu(II), and Zn(II) species do not undergo redox processes at the metal at potentials between ligand oxidation and reduction. Iron and cobalt, on the other hand, can form M(I), M(II), and M(III) species at these intermediate potentials, that is, oxidation of the phthalocyanine ligand occurred after the metal was oxidized to M(III), and reduction of the phthalocyanine ligand occurred only after reduction of the metal to M(I). Chromium and manganese phthalocyanines form M(II) and M(III) oxidation states (*5–13*).

In parallel with main group phthalocyanine chemistry, the ability to reduce a metallophthalocyanine increases, that is, the potential becomes more positive, as the oxidation state of the central ion increases. This ability can be seen from the data comparisons abstracted from Table II and shown in Tables III, IV, and Figure 2.

Not surprisingly, the potentials are similar to those of main group ions of the same oxidation state and approximate size, although this fact apparently was not recognized clearly in the past. Because the spread in potentials for a given metal oxidation state is remarkably small, and there is a clear enough separation between the ranges for at

Table III. Potentials, vs. NHE, for the First Reduction of the Phthalocyanine Ring as a Function of Central Ion Oxidation State

Complex	*Pc(−2)M(IV)O/ Pc(−3)M(IV)O*	*Pc(−2)M(II)/ Pc(−3)M(II)*	*Pc(−2)M(I)/ Pc(−3)M(I)*
TbPcVO	−0.275		
TbPcTiO	−0.335		
TbPcCr		−0.630	
TsPcCr		−0.760	
TbPcMn		−0.650	
TsPcMn		−0.475	
PcMn		−0.450	
PcFe			−0.930
TsPcFe			−0.840
PcCo			−1.16
TsPcCo			−1.050
PcNi		−0.610	
TbPcCu		−0.635	
PcCu		−0.600	
PcZn		−0.650	

Note: *see* Table II for references to the literature and abbreviations. In general, these potentials show little solvent dependence.

Table IV. Second Reduction Process for Transition Metallophthalocyanines

Complex	*Pc(−3)M(IV)O/ Pc(−4)M(IV)O*	*Pc(−3)M(II)/ Pc(−4)M(II)*	*Pc(−3)M(I)/ Pc(−4)M(I)*	*Ref.*
TbPcTiO	−0.780			tw
TbPcVO	−0.840			tw
TbPcCr(II)		−1.115		tw
PcMn(II)		−1.22		*3*
		−1.26		*12*
TsPcMn(II)		−1.115		tw
TsPcFe(II)			−1.27	tw
PcFe(II)			−1.32	*12*
PcCo(II)			−1.56	*12*
PcNi(II)		−0.99		*12*
TsPcNi(II)		−0.925 (−1.69)		*11*
		−0.89		tw
PcCu(II)		−0.94		*12*
TsPcCu(II)		−0.870 (−1.655)		*11*
TbPcCu(II)		−1.10		tw
PcZn(II)		−1.09 (−1.82, −2.44)		*12*

Note: See Tables I–III for abbreviations. Data in parentheses refer to successive reductions. Redox potentials vs. NHE.

least the first and second reduction, the potentials generally can be used diagnostically to identify the oxidation state of the central transition metal ion.

Most oxidations of the phthalocyanine ring in transition metal phthalocyanines are electrochemically irreversible, obscuring oxidation state trends. Trivalent and tetravalent transition metal phthalocyanines generally oxidize a little above 1.0 V; this trend is also true for the more polarizing divalent ions, nickel(II) and copper(II). Pc(−2)Zn also oxidizes near 1.0 V while the earlier first row transition metal phthalocyanines oxidize at slightly more negative potentials.

Solvent effects on these ligand redox potentials are small. However, solvent effects on metal redox process potentials can be extraordinarily large. Table V gives the ranges for various redox processes as a function of solvent and/or supporting electrolyte. The effect of solvent depends clearly on the electronic configurations of the species involved, and the effect of supporting electrolyte depends on whether there is binding of the anion to either component of the couple.

The iron(II)/iron(I) and cobalt(III)/cobalt(II) couples both involve low spin d^6/d^7 configurations. Strongly binding axial ligands (solvent molecules) destablize the z^2 electron (in d^7) and favor oxidation to the

Table V. Solvent Effects on Transition Metallophthalocyanine

Metal Ion	*Solvent/X⁻* [a]	*c⁺/c*	*c/c⁻*	*c⁻/c⁼*
PcCr(II)[b]	DMF/Py	+0.04/−0.155		
PcMn(II)[c]	DMF/DMSO/Py	0.045/−0.10	−0.45/−0.575	−1.10/−1.28
PcFe(II)[d]	DMF/DMSO/Py	0.90/−0.085	−0.31/−0.845	−0.87/−1.085
TsPcFe(II)[e]	DMSO/KCN		−0.98	−1.31
PcCo(II)[f]	DCB/DMF/DMSO/Py/4-EtPy	0.88/0.24	−0.1/−0.7	−1.11/−1.18

[a] Supporting electrolytes include tetraalkylammonium chlorides, bromides, and perchlorates. Numbers indicate upper and lower boundaries for observed potentials. These data include tetrasulfonated and tetra-*t*-butyl derivatives. Solvents: DMF, dimethylformamide; DMSO, dimethyl sulfoxide; Py, pyridine; DCB, *o*-dichlorobenzene. Redox potentials vs. NHE.
[b] This work.
[c] Ref. 3.
[d] Ref. 2.
[e] Ref. 45.
[f] This work, Ref. 8.

low spin d^6 species. Thus, in both cases the potentials shift negatively with increasing donor strength of the solvent, which follows the order

$$\text{DMA} = \text{DMF} < \text{DMSO} < \text{pyridine} \quad (3)$$

where DMA, DMF, and DMSO represents dimethylamine, dimethylformamide, and dimethyl sulfoxide, respectively.

Indeed, there is a linear correlation of these potentials with Gutmann Donicity Number (25) of the solvent (8). The cobalt(II)/cobalt(I) couple (low spin d^7/d^8) also shifts negatively with increasing donicity of the solvent, probably because axial binding to the square planar d^8 cobalt(I) is weak or nonexistent. The iron(III)/iron(II) couple (low spin d^5/d^6), however, shows the opposite trend shifting positively with increasing donicity of the solvent (8, 9). This fact best can be explained by synergism, where strongly coordinating axial ligands favor back donation by the low spin d^6 ion into phthalocyanine π-acceptor orbitals. Back donation in iron(III) is weaker because of the greater charge on the metal. Table V shows that these solvent effects can be quite dramatic. For example, a solution of iron(II) phthalocyanine in pyridine containing chloride ion is air stable, but a similar solution in DMA or DMF with chloride ion rapidly air oxidizes to iron(III) phthalocyanine (9). Moreover, if cyanide ion is added to a solution of tetrasulfonated iron(II) phthalocyanine, the iron(II) state is stabilized to a remarkable degree (Table V) through axial coordination of cyanide ions. Indeed, unsubstituted iron(II) phthalocyanine is soluble in water if cyanide ions are present (5). Even more remarkable stabilization of iron(II) is seen when imidazole is used as an axial ligand (Table V) (7).

When a series of substituted pyridines were used as solvents (*8*), both the cobalt(III)/cobalt(II) and cobalt(II)/cobalt(I) couples shifted negatively with increasing pK_a of the solvent. This result may be explained in terms of the Drago E and C model (*26*) given that for this series the electrostatic component, E, is changing while the covalent component, C, remains roughly constant, an observation in agreement with similar porphyrin redox data (*27*). An interesting solvent effect is observed when cobalt(II) Pc is oxidized to cobalt(III) Pc. Because the latter species has a very strong propensity to be hexacoordinated with two axially bound solvent molecules, the oxidation potential is clearly solvent dependent. In a noncoordinating solvent such as dichlorobenzene, a hexacoordinated cobalt(III) species cannot be formed. Under these conditions, the Co(III) Pc/Co(II) Pc couple shifts positively to a considerable extent, such that the initial oxidation of the species is to form a cobalt(II) phthalocyanine cation radical (*16*). When pyridine is added to such a solution, a cobalt(III) species apparently is formed.

Preliminary data for chromium(III) phthalocyanines reveal increased stabilization of chromium(II) with strong donor solvents. This effect could be due to stabilization of the low spin d^4 chromium(II) through back donation to the phthalocyanine ring. However, further data are necessary to understand this phenomenon, especially as a similar stabilization of low-spin d^5 manganese(II) phthalocyanine apparently is not evident (Table V). Some data exist concerning the effect of ring substitution on redox energies (*see* Table II), however, significantly less so than in the porphyrin series (*28*). Generally, electron donors favor ring oxidation and disfavor ring reduction. An interesting comparison exists for sulfonic acid substitution where the neutral acid form of TsPcFe(III) reduces at −0.40 V [vs. normal hydrogen electrode (NHE)] while the sodium salt, with four negative charges on the periphery of the molecule, does not reduce until −0.67 V (*5*). The second reduction is similarly, but a little less markedly, effected. For substituents such as chloride, methyl *tert*-butyl, sulfonic acid, carboxylic acid, and others, the shifts in redox energies (except for special cases such as just indicated where the charge on the ring is modified) rarely exceed 100 mV.

Electronic Spectroscopy

Gouterman et al. (*20–23*) first detailed the electronic structure of metallophthalocyanines, showing that the two principal bands (both $^1E_u \leftarrow {}^1A_{1g}$) (for $S = 0$ metal ions) in the visible spectrum of all phthalocyanine (−2) species could be assigned as $\alpha_{1u}(\pi) \rightarrow e_g(\pi^*)$ (Q band near 600 nm) and $a_{2u}(\pi) \rightarrow e_g(\pi^*)$ (Soret band near 350 nm). Unlike the porphyrin system (*28*), the a_{1u} and a_{2u} orbitals are fairly well-separated in energy, and these two transitions do not, therefore,

mix appreciably. Emission data reveal that the spin triplet component of the Q band lies about 5000–5500 cm^{-1} below the spin singlet (*29*). In systems lacking charge transfer absorption, such as most of the main group species, it is this spin triplet that is likely to be photoactive when the phthalocyanine is utilized as a photocatalyst. The ^1Q state (fluorescence) has a lifetime of only a few nanoseconds, while the triplet state lifetime is in the microsecond–millisecond region at liquid nitrogen temperature (*29, 30*). Where paramagnetic ions such as copper(II) are concerned, this lowest state most likely is a triplet–multiplet, lying at roughly the same energy as ^3Q (*28, 31*).

However, the situation can change dramatically when charge transfer transitions are present. Such transitions occur whenever metal d-levels lie at energies inside the HOMO–LUMO bandgap of the phthalocyanine (or close to, but above the LUMO energy). Such transitions were discussed in depth (*31*) and only a summary of these data is provided here.

With moderately oxidizing ions such as manganese(III) and chromium(III), charge transfer absorption from both the phthalocyanine a_{1u} and a_{2u} orbitals into $e_g(d)$ orbitals on the metal is allowed electronically and observed readily, the former transition lying in the near IR region (Figure 1, Table VI).

Consider the charge transfer transition:

$$Pc(-2)(a_{1u})^2Cr(III)d^3 \rightarrow Pc(-1)(a_{1u})Cr(II)d^4$$

labeled LMCT1 in Figure 1. This reaction may be construed as the sum of two redox processes, viz:

$$Pc(-2)(a_{1u})^2Cr(III)d^3 + e^- \rightleftharpoons Pc(-2)(a_{1u})^2Cr(II)d^4 \quad (4)$$

$$Pc(-2)(a_{1u})^2Cr(II)d^4 \rightleftharpoons Pc(-1)(a_{1u})Cr(II)d^4 + e^- \quad (5)$$

whose potentials[3] [−0.40 and −(+0.70)V] can be summed to yield a transition energy of 1.10 eV, that is, a predicted charge transfer energy of 8870 cm^{-1}, in satisfactory agreement with an observed transition at 7900 cm^{-1}. Both chromium(III) and manganese(III) exhibit charge transfer bands in the near IR region, although for manganese(II) and chromium(II) species these LMCT bands are blue-shifted to approximately 11,000 cm^{-1}. A treatment similar to the one indicated in Equations 3–5 allows prediction of the energies of these charge transfer transitions generally to within an accuracy of about 1000 cm^{-1} (Table VI).

[3] Estimated potential is given in Ref. *31*.

Table VI. Observed and Calculated Charge Transfer Data (DMF)

Complex	*Observed Energy* (cm^{-1})	*Calculated Energy* (cm^{-1})	*Assignment*[a]
TsPcCr(II)	11,780	11,935	LMCT1
	?	13,710	MLCT2
	25,510	24,925	LMCT2
TsPcCr(III)	7,900	8,870	LMCT1
	20,080	22,590	LMCT2
	?	23,710	MLCT2
PcMn(II)	10,910	10,970	LMCT1
	?	15,725	MLCT2
	26,300	26,180	LMCT2
TbPcMn(III)	7,630	6,535	LMCT1
	20,120	19,740	LMCT2
	?	22,100	MLCT2

[a] The charge transfer transitions concerned are $a_{1u} \rightarrow e_g(d)$ LMCT1; $a_{2u} \rightarrow e_g(d)$ LMCT2 and $e_g(d) \rightarrow b_{1u}(\pi^*)$ MLCT2 (*31*). The counterion for chromium(III) is a sulfonic acid residue, and for manganese(III) it is acetate.

Further proof of the assignment is obtained by location of a second charge transfer band (LMCT2), arising from a_{2u} to $e_g(d)$ (Figure 1), lying between the *Q* and Soret bands. Most significantly, the energy separation between these two charge transfer bands is almost exactly equal to the energy separation between the *Q* and Soret bands (*31*)[3]. Virtually all the anticipated LMCT bands in the first-row transition metal phthalocyanines can be assigned and calculated by this simple procedure. MLCT band energies also can be calculated, but appear to be too weak to be observed. The energies of orbitally forbidden LMCT transitions also can be derived by this technique, allowing the presumed detection of states that cannot be observed directly by electronic spectroscopy (*see* Table VI).

Surprisingly, such a simple relationship between electronic absorption bands and redox potential energies is successful. Evidently, the entropy differences between the various components of the couple are very small. Moreover, the LMCT transitions appear to be (0–0) in vibrational character, eliminating another possible source of disagreement between calculated redox energy and observed data (*31*). Precedent for such agreement between charge transfer energies and sums of redox potentials exists (*32*, *33*). Because these LMCT transitions frequently lie at energies below the *Q* band, they (or higher spin versions) are likely to be photochemically active. However, lifetime data are not yet available.

Hence, a combination of electronic absorption spectroscopy and

electrochemical measurement can map the energy levels of a metallophthalocyanine with considerable accuracy, and provide a measure of the redox potentials of the various excited states, information of considerable value in understanding photochemical behavior. Although few heavy transition metal ion phthalocyanines have been investigated to date, their behavior is not expected to vary greatly from the details presented in this chapter (provided the metals lie inside the phthalocyanine macrocycle ring). In general, their *d*-levels will be buried below the phthalocyanine HOMO level and redox processes at the metal are not expected.

Photochemistry

A range of main group, first row, and later transition metal ions were screened recently for their ability to generate reduced methyl viologen (MV^+) when irradiated (into the *Q* band) in the presence of methyl viologen (MV^{2+}) and a donor such as triethanolamine (*34*). Species containing Mg, TiO, Cr(II), Fe(II), Zn(II), Rh(III), and Ru(II) generated reduced methyl viologen, albeit in small yield (<.01%). Other metal ions, specifically VO, Cr(III), Mn(III), Fe(III), Co(II), Ni(II), and Cu(II) did not generate reduced methyl viologen under similar conditions.

Ions with low lying (near IR) LMCT bands clearly were photochemically inactive because much of the excitation energy was lost by intersystem crossing from the *Q* band to the low lying LMCT band.

Several mechanisms are possible by which reduced methyl viologen (MV) might be produced. Specifically, reductive quenching of the excited state of the photocatalyst (c*) by the donor, yielding c^-, could result in formation of MV^+ by reaction of MV^{2+} with c^- in a following thermal reaction. Alternatively, c* could be quenched oxidatively by MV^{2+} yielding MV^+ directly, together with c^+, which could then return to the ground state c by a thermal reaction with the donor.

Detailed kinetic studies, not yet undertaken, are necessary to deduce unequivocally which mechanism is occurring.

Given the ground state redox data discussed in the section on electrochemistry, together with the electronic absorption data given in the section on electronic spectroscopy, the redox potentials of the excited states, c*, can be derived (*35–37*). Thus, if E_{en} (in electron volts) is the equilibrated excited state energy of the lowest, photochemically active, excited state of the photocatalyst, then the redox potentials involving c* are:

$$c^+/c^* = c^+/c - E_{en} \quad (6)$$

$$c^*/c^- = c^-/c + E_{en} \quad (7)$$

These equations should be fairly accurate provided that the entropy differences between ground and excited states are small, as apparently is the case.

The thermodynamic driving forces for the various excited state and ground state reactions just discussed may be calculated from these data. The results obtained from this calculation enable (*34*) the complexes to be divided readily into two sets, one in which the thermodynamics of one or more processes make most unfavorable the production of reduced methyl viologen and one set in which the thermodynamics are less unfavorable or even slightly favorable. Experimentally, the inactive metallophthalocyanines clearly belong to the former set, and the active species to the latter set. However, the thermodynamics for the formation of reduced methyl viologen were not strongly favorable for any case yet studied, explaining, in part, why the yields were not high for these species.

Kinetic phenomena, that is, suppression of otherwise thermodynamically favorable back reactions, play a dominant role in determining which catalysts are suitable and which are not. It is equally clear from this investigation (*34*) that studies such as those shown in the "electrochemistry" and "electronic spectroscopy" sections can provide a sound basis for understanding photocatalytic behavior, and can influence the design of future catalysts. Growing interest in the use of metallophthalocyanines in solar energy conversion attests to the potential value of such catalysts (*2*, *15*, *34*, *38–43*). Such data are also of significant value in understanding biological photoredox behavior, especially events occurring during photosynthesis.

Acknowledgments

This research is part of a joint project with A. J. Bard (University of Texas at Austin) supported by the Office of Naval Research (Washington). We are also indebted to the Natural Sciences and Engineering Research Council (Ottawa) for financial support.

Literature Cited

1. Lever, A. B. P.; Wilshire, J. P. *Can. J. Chem.* **1976**, *54*, 2514.
2. Lever, A. B. P.; Wilshire, J. P. *Inorg. Chem.* **1978**, *17*, 1145.
3. Lever, A. B. P.; Minor, P. C.; Wilshire, J. P. *Inorg. Chem.* **1981**, *20*, 2550.
4. Gavrilov, V. I.; Tomilova, L. G.; Shelepin, I. V.; Luk'yanets, E. A. *Elektrokhimiya*, **1979**, *15*, 1058.
5. Lever, A. B. P. *Adv. Inorg. Chem. Radiochem.* **1965**, *7*, 27.
6. Lexa, D.; Reix, M. *J. Chim. Phys.* **1974**, *71*, 510, 517.
7. Kadish, K. M.; Bottomley, L. A.; Cheng, J. S. *J. Am. Chem. Soc.* **1978**, *100*, 2731.
8. Lever, A. B. P.; Minor, P. C. *Adv. Mol. Relax. Inter. Proc.* **1980**, *18*, 115.
9. Shephard, V. R. Jr.; Armstrong, N. R. *J. Phys. Chem.* **1979**, *83*, 1268.

10. Wolberg, A.; Manassen, J. *J. Am. Chem. Soc.* **1970,** *92,* 2982.
11. Rollman, L. D.; Iwamoto, R. T. *J. Am. Chem. Soc.* **1968,** *90,* 1455.
12. Clack, D. W.; Hush, N. S.; Woolsey, I. S. *Inorg. Chim. Acta* **1976,** *19,* 129.
13. Dolphin, D.; James, B. R.; Murray, A. J.; Thornback, J. R. *Can. J. Chem.* **1980,** *58,* 1125.
14. Lever, A. B. P.; Minor, P. C. *Inorg. Chem.* **1981,** *20,* 4015.
15. Loutfy, R. O.; Cheng, Y. C. *J. Phys. Chem.* **1980,** *74,* 2902.
16. Giraudeau, A.; Fan, F-R. F.; Bard, A. J. *J. Am. Chem. Soc.* **1980,** *102,* 5137.
17. Fanning, J. C.; Park, G. B.; James, C. G.; Heatley, W. R., Jr. *J. Inorg. Nucl. Chem.* **1980,** *42,* 343.
18. Beck, F. *Ber. Bunsenges. Phys. Chem.* **1973,** *77,* 35.
19. Myers, J. F.; Rayner-Canham, G. W.; Lever, A. B. P. *Inorg. Chem.* **1975,** *14,* 461.
20. McHugh, A. J.; Gouterman, M.; Weiss, C., Jr. *Theor. Chim. Acta* **1972,** *24,* 346.
21. Edwards, A. M.; Gouterman, M. *J. Mol. Spectrosc.* **1970,** *33,* 292.
22. Schaffer, A. M.; Gouterman, M. *Theor. Chim. Acta* **1972,** *25,* 62; **1973,** *30,* 9.
23. Gouterman, M. In "The Porphyrins"; Dolphin, D.; Ed. 1977; Vol. III.
24. Shannon, R. D.; Prewitt, C. T. *Acta Crystallogr., Sect. B,* **1969,** *25,* 925.
25. Gutmann, V. "The Donor Acceptor Approach to Molecular Interactions"; Plenum: New York; 1978.
26. Drago, R. S. *Struct. and Bond.* **1973,** *15,* 13.
27. Kadish, K. M.; Bottomley, L. A. *Inorg. Chem.* **1980,** *19,* 832.
28. Davis, D. G. In "The Porphyrins"; Dolphin, D.; Ed. 1978; Vol. V, p. 127; Felton, R. H. ibid p. 53.
29. Vincett, P. S.; Voigt, E. M.; Rieckhoff, K. E. *J. Chem. Phys.* **1971,** *55,* 4131.
30. Yoshino, K.; Kaneto, K.; Inuishi, Y. *J. Phys. Soc. Jpn.* **1973,** *35,* 120.
31. Lever, A. B. P.; Licoccia, S.; Minor, P. C.; Ramaswamy, B. S.; Pickens, S. R.; Magnell, K. *J. Am. Chem. Soc.* **1981,** *103,* 6800.
32. Dainton, F. S.; James, D. G. L. *J. Chim. Phys.* **1951,** *48,* C18.
33. Barnes, J. C.; Day, P. *J. Chem. Soc.* **1964,** 3886.
34. Lever, A. B. P.; Licoccia, S.; Ramaswamy, B. S.; Kandil, A.; Stynes, D. V. *Inorg. Chim. Acta* **1981,** *51,* 169.
35. Meyer, T. J. *Isr. J. Chem.* **1976,** *15,* 200.
36. Whitten, D. G. *Accts. Chem. Res.* **1980,** *13,* 83.
37. Weller, A., *Revs. Pure Appl. Chem.* **1968,** *16,* 115.
38. Jaeger, C. D.; Fan, F-R.; Bard, A. J. *J. Am. Chem. Soc.* **1980,** *102,* 2592.
39. Loutfy, R. O.; Sharp, J. H. *J. Appl. Electrochem.* **1977,** *7,* 315.
40. Fan, F-R.; Faulkner, L. R. *J. Am. Chem. Soc.* **1979,** *101,* 4779.
41. Darwent, J. R. *Chem. Commun.* **1980,** 805.
42. Harriman, A.; Richoux, M. C. *J. Photochem.* **1980,** *14,* 253.
43. Tanno, T.; Wohrle, D.; Kaneko, M.; Yamada, A. *Ber. Bunsenges. Phys. Chem.* **1980,** *84,* 1032.
44. Loutfy, R. O., personal communication, 1981.
45. Li, C.; Chin, D. *Anal. Lett.* **1975,** *8,* 291.

RECEIVED for review April 17, 1981. ACCEPTED November 12, 1981.

Electrochemical and Spectroscopic Studies of Iron and Cobalt Porphodimethenes

A Mononuclear Hydroxoiron(III) Tetrapyrrole Complex

ANDREAS BOTULINSKI, JOHANN WALTER BUCHLER[1], and KIONG LAM LAY—Institut für Anorganische Chemie, Technische Hochschule Darmstadt, D-6100 Darmstadt, Federal Republic of Germany

JÜRGEN ENSLING—Institut für Anorganische und Analytische Chemie, Universität Mainz, D-6500 Mainz, Federal Republic of Germany

HANS TWILFER—Abteilung Physiologische Chemie, Technische Hochschule Aachen, D-5100 Aachen, Federal Republic of Germany

JOCHEN BILLECKE, HEIKO LEUKEN, and BERNHARD TONN Institut für Anorganische Chemie, Technische Hochschule Aachen, D-5100 Aachen, Federal Republic of Germany

Iron porphodimethenes (α,γ-dihydroporphyrins) represent a special class of sterically and electronically modified hemes in which both axial coordination sites show impaired accessibility, especially α,γ-*di*-tert-*butyloctaethylporphodimethene. This feature allows the isolation of the first definitely identified mononuclear hydroxoiron(III) complex of a porphinoid ligand system, hydroxo[*α,γ-*di*-*tert*-*butyl*-α,γ-dihydrooctaethylporphinato]iron(III). The hemin-like coordination group is characterized by* $\mu_{eff} = 5.7$ *B.M.,* $\nu_{OH} = 3661\ cm^{-1}$, $g_{\perp} = 5.84$, $g_{\parallel} = 2.00$, $\delta = 0.314$ *mm/s (metallic Fe, 1.5 K), and* $\Delta E_Q = 0.56$ *mm/s in magnetic measurements and IR, ESR, and Mössbauer spectra. Instead of OH, a variety of other axial ligands can be bound by the di-*tert*-butylporphodimethene, for example, F, Cl, NO, N_3, NCS, OCN, and OMe. Notable exceptions are cyanide and carbon*

[1] Author to whom correspondence should be addressed.

0065-2393/82/0201-0253$07.50

*monoxide. The corresponding cobalt di-*tert*-butylporphodimethene shows a strongly diminished affinity toward dioxygen, although cyclic voltammetry indicates an easier metal oxidation in porphodimethenes than in porphyrins.*

During investigations to elucidate the influence of the central metal on the hydrogenation of metalloporphyrins, various oxygen-sensitive metal porphodimethenes (α,γ-dihydroporphyrins) were studied (*1*, *2*, *3*). Air stable α,γ-dimethyl-α,γ-dihydrooctaethylporphyrin complexes, for example, the hemin $Fe(OEPMe_2)Cl$ (**1Aa**, Table I) (*4*), or $Co(OEPMe_2)$ (**1Bb**) (*5*) were obtained in a systematic study that revealed the special electronic and steric modification of the porphodimethene core. Proton NMR investigations (*2*, *6*) and x-ray crystallography (*7*, *8*, *9*) demonstrated the *syn–axial–exo* configuration of the two methyl groups, which were introduced by a reductive methylation (*10*), and the more firmly bound axial ligand X, for example, in $Ni(OEPMe_2)$ (**1Cb**) (*7*), $TiO(OEPMe_2)$ (**1Dc**) (*8*), and $Os(OEPMe_2)CO \cdot Py$ (**1Ed**) (*9*).

The *syn–axial–exo* configuration may also be described as a roof-like folded porphodimethene with both R and X in "chimney positions" (*3*). This configuration is sketched for a general iron porphodimethene $Fe(OEPR_2)XL$ (**A**) in Figure 1, I. Both axial coordination sites are impeded: X by the two alkyl groups, R and L by the folding of the macrocycle. The latter effect leads to a somewhat prolonged axial Os–N bond in **1Ed** (*9*), whereas the former results in a retardation of the acidolysis of the μ-oxo complex **1Ae** as compared with the known μ-oxobisiron(III) porphyrins (*4*).

Basic hydrolysis of hemins produces μ-oxo complexes in all known cases from porphyrins (*11*), even from sterically hindered porphyrins, for example, the "picket fence" heme (*12*). Hydrolysis is immediately followed by condensation. This reaction is exemplified by iron porphodimethenes as follows (R = CH_3, C_2H_5, n-C_3H_7, i-C_3H_7):

$$\underset{\textbf{Aa}}{2\ Fe(OEPR_2)Cl} \underset{\text{acidolysis}}{\overset{\text{condensation}}{\overset{H_2O/OH^-}{\underset{2\ HCl}{\rightleftharpoons}}}} \underset{\textbf{Ae}}{[Fe(OEPR_2)]_2O} \qquad (1)$$

Thus, a linear extension of R does not strongly increase the steric hindrance of X (Figure 1, I), and the resulting μ-oxo complexes probably have configuration II (Figure 1); models show that a μ-oxo bridge cannot be formed under the roof (*4*).

Use of *tert*-butyl as the alkyl group (R) in iron porphodimethenes was noted previously (*13*, *14*). The present paper describes the spectroscopic characterization of the exclusively mononuclear α,γ-di-*tert*-

Table I. Structure and Numbering of Metal Dialkyloctaethylporphodimethenes

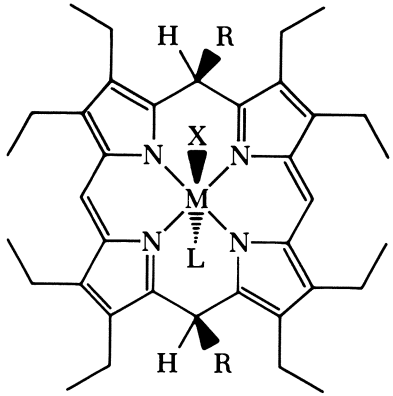

Number	*R (alkyl group)*
1	CH_3
2	$C(CH_3)_3$

Capital Letter	*M (metal)*
A	Fe
B	Co
C	Ni
D	Ti
E	Os

Lowercase Letter[a]	*X*	*L*	*Lowercase Letter*	*X*	*L*
a	Cl	—	**n**	O_2	—
b	—	—	**o**	Py	O_2
c	O	—	**p**	F	—
d	CO	Py[b]	**q**	OAc[c]	—
e	O/2[d]	—	**r**	OCN	—
f	—	OH	**s**	NCS	—
g	OCH_3	—	**t**	OPhpBut[e]	—
h	OC_6H_5	—	**u**	CN	—
i	N_3	—	**v**	CN	CN
j	NO	—	**w**	1-Meim[f]	—
k	NO	Py	**x**	1-Meim	1-Meim
l	Py	—	**y**	Br	Br
m	Py	Py	**z**	Pip[g]	Pip

[a] In text, lowercase letters followed by prime (′) indicate that X and L are reversed.
[b] pyridine
[c] acetate
[d] μ-oxo complex
[e] *p-t*-butylphenoxide
[f] 1-methylimidazole
[g] piperidine

butyloctaethylporphodimethenatoiron(III) complexes, Fe(OEPBut$_2$)-XL **2Aa, 2Af–2Aj, 2Ap,** and **2Ar–2At** (*see* Table I). For these complexes, in Reaction 1, hydrolysis stops at the stage of the hydroxide, Fe(OEPBut$_2$)OH (**2Af**). Some electrochemical data and spectral properties of other iron porphodimethenes, Fe(OEPMe$_2$)XL, and cobalt porphodimethenes [Co(OEPR$_2$), **1Bb** and **2Bb**] are also presented in this chapter.

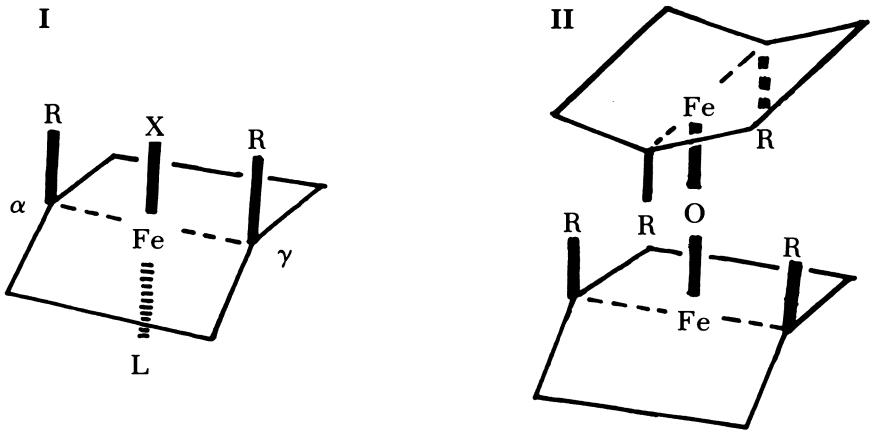

Figure 1. Presumed steric features of a mononuclear iron porphodimethene, Fe(OEPMe$_2$)XL, ***I****, and the μ-oxobis[porphodimethenatoiron (III)] system, [Fe(OEPMe$_2$)]$_2$ O,* ***II****. The porphodimethene core is approximated by a rectangle folded about the α,γ-line ("roof-like folding", R,X in "chimney positions").*

The hydroxide Fe(OEPBut$_2$)OH (**2Af**) is the first fully characterized mononuclear hydroxoiron(III) complex of a porphinoid ligand system, for which spectral data were communicated previously (*14*). In more recent reports on iron porphyrins with steric hindrance on both sides of the molecular plane, isolated hydroxyl groups were identified only by IR spectroscopy (*15, 16*).

A thorough description of the instrumental analysis of metal porphodimethenes can be found in several scientific theses (*5, 17–22*).

Experimental

Preparation of Iron Porphodimethenes. Iron porphodimethenes were synthesized according to previously published procedures (*4*) from the corresponding α,γ-dialkyloctaethylporphodimethenes and iron pentacarbonyl (*10, 17, 18*). The hemins Fe(OEPR$_2$)X (where X = OCH_3, OC_6H_5, N_3, F, Cl, Br, OAc, OCN, NCS, and OPhpBut) were obtained by acidolysis of the μ-oxo complex **1Ae** (Reaction 1) or esterification of the hydroxide **2Af** and were crystallized without chromatography in the presence of excess X^-.

Preparation of Hydroxo[α,γ-di-*tert*-butyl-α,γ-dihydrooctaethylporphinato]iron(III), Fe(OEPBut$_2$)OH (2Af) (*13, 14*). A 576-mg (1.12-mmol) sample of α,γ-di-*tert*-butyl-α,γ-dihydrooctaethylporphyrin [H$_2$(OEPBut$_2$), obtained from zinc octaethylporphyrin by reductive alkylation (*6,10*) with $C(CH_3)_3I$ and demetalation] was refluxed 4 h with 300 mg (1.17 mmol) of I_2 and 3 mL (21 mmol) of $Fe(CO)_5$ in 80 mL of toluene under nitrogen. After cooling and filtration, the solution was taken to dryness in vacuo and the residue was chromatographed on alumina (grade III, neutral, 40 × 3 cm) with toluene. The first brownish fraction contained unreacted porphodimethene and some unidentified iron complexes. The second red fraction yielded the

product **2Af** after elution with toluene–acetone (9:1), evaporation of the solvent, crystallization from cyclohexane, and drying at 45°C/10^{-3} mm. Compound **2Af**, a powder, reacts with alcohols, concentrated acetone, and traces of acids (e.g., hydrochloric acid from decomposition of methylene chloride) to give the corresponding hemins. Yield: 394 mg (48.8%). Analysis of $C_{44}H_{63}N_4FeO$ (719.9 g/mol): calculated, C, 73.41; H, 8.82; N, 7.78; O, 2.23; Fe, 7.76%; found, C, 73.71; H, 9.00; N, 7.62; O, 2.35; Fe, 7.15 (combustion residue) %.

Preparation of Cobalt Porphodimethenes 1Bb and 2Bb. The porphodimethene, $H_2(OEPR_2)$ (0.5 mmol), was refluxed under nitrogen with $Co_2(CO)_8$ (1.4 mmol) and I_2 (0.2 mmol) in toluene for 1 h. The solution was taken to dryness in vacuo; the residue was chromatographed on alumina (grade III, neutral) and eluted with cyclohexane–toluene (9:1) under nitrogen. The first, yellow–brown fraction yielded $Co(OEPR_2)$ [**1Bb:** 221 mg, 67% (*5*), **2Bb:** 261 mg, 69% (*13*, *21*)] as black–brown crystals after evaporation to dryness, recrystallization from cyclohexane, and drying at 45°C/10^{-3}mm. Analysis of **1Bb**, $C_{38}H_{50}N_4Co$ (621.78 g/mol): calculated, C, 73.41; H, 8.10; N, 9.01; O, 0.00%; found. C, 73.31; H, 7.92; N, 9.13; O, 0.24%. Analysis of **2Bb**, $C_{44}H_{62}N_4Co$ (705.94 g/mol): calculated, C, 74.86; H, 8.85; N, 7.94%; found, C, 74.73; H, 8.90; N, 8.05%.

Preparation of Liganded Cobalt Porphodimethenes. The cobaltichrome salts $[Co(OEPMe_2)L_2]PF_6$, L = Py, 1-Meim, piperidine (**1Bm, 1Bx, 1Bz** as cations, Table I) were obtained by treatment of solutions of **1Bb** with excess L, air, and NH_4PF_6 in $CHCl_3$–CH_3OH (*5*). The corresponding octaethylporphyrin derivatives, $[Co(OEP)L_2]PF_6$, were prepared similarly (*13*, *14*).

Preparation of Hemichrome Salts. The octaethylhemichrome salts $[Fe(OEP)L_2]PF_6$ (L = Py, 3-chloropyridine,1-Meim) and the corresponding porphodimethene hemichrome salts, $[Fe(OEPMe_2)L_2]PF_6$ (L = Py,1-Meim) were obtained from the chlorohemins by boiling with excess L and NH_4PF_6 in methylene chloride and crystallizing (*19*, *20*, *23*).

Instrumental Analysis. Optical spectra were recorded with a Unicam SP800B spectrophotometer, IR spectra with a Perkin-Elmer 621 instrument (KBr pellets), EPR spectra with a Bruker B-ER 420 spectrometer (toluene glass), and proton NMR spectra with a Bruker WH-90 pulse Fourier transform spectrometer (pulse width ~1μs, 100 to 1000 scans, internal lock with $CDCl_3$ as solvent).

The Mössbauer spectrometer was equipped with a ^{57}Co–Rh source (20 mCi) at 295 K, an electromechanical vibrator, a 90% Kr–10% CO_2 proportional counter, and a 400-channel analyzer (*24*, *25*). Isomer shifts (δ) refer to metallic iron. The values of δ and the quadrupole splitting, ΔE_Q, were obtained by a least-squares fit of the measured spectra to Lorentzian line shapes. The absorber samples contained ^{57}Fe in natural abundance and were enclosed in airtight perspex holders containing 0.2 mg of ^{57}Fe/cm^2.

Magnetic measurements of solid **2Af** were performed with a Faraday balance as described elsewhere (*26*).

Cyclic voltammograms were run with Princeton Applied Research equipment: a potentiostat 173 and universal programmer 175, a Philips XY recorder PM 8125, and a Beckman platinum button electrode.

Electrochemistry and Optical Spectra

The cyclic voltammograms of some octaethylhemichrome salts and the corresponding porphodimethene hemichrome salts were re-

corded previously (*20*). Some results are compared in Figure 2 and Table II. The hemichrome salts show reversible Fe(II)–Fe(III) steps only in the presence of excess axial ligand L; otherwise the hemichrome dissociates in solution (*27*, *28*). The cobaltichrome salts derived from octaethylporphyrin and α,γ-dimethyloctaethylporphodimethene also were studied (Table II) (*5*). The Co(II)–Co(III) step is irreversible in a moderate excess of axial base L; a rather large negative shift of the peak potential for reduction, E_p (red), indicates destabilization of the reduced form and a preference for pentacoordination in Co(II) tetrapyrroles. Irreversible behavior is frequently found with cobalt porphyrins (*29*). Generally, the metal ion is more easily oxidized in porphodimethenes than in the porphyrin system, apparently because of the smaller central N_4 hole in the porphodimethene core (*7*). The axial ligand dependence shows the usual trend as elaborated with osmium porphyrins earlier (*30*), that is, the imidazole system shifts the metal(II–III) step to highly negative values.

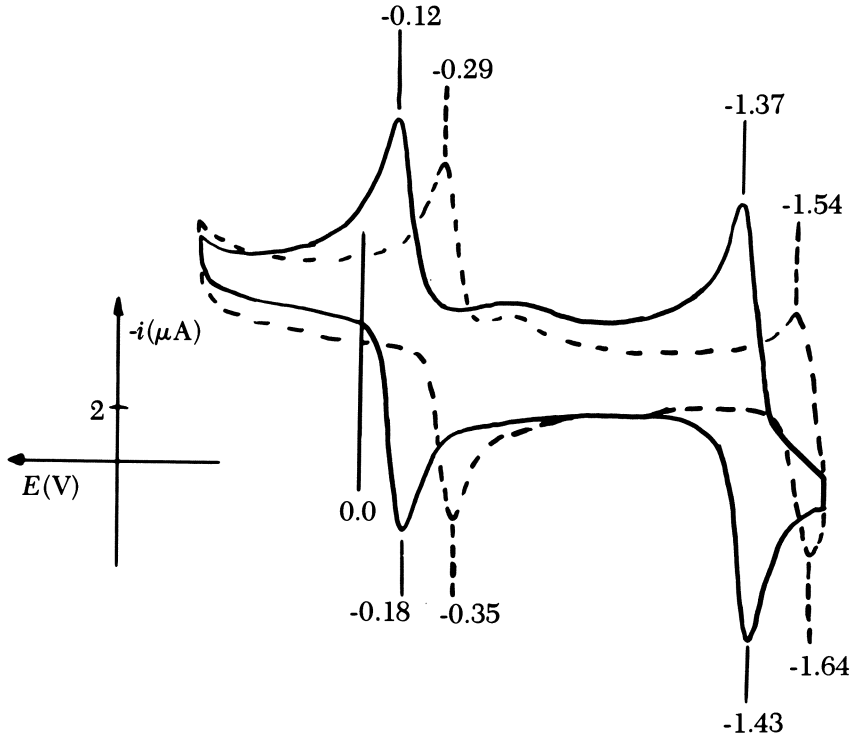

*Figure 2. Cyclic voltammograms of the dipyridine octaethylhemichrome salt, [Fe(OEP)Py₂]PF₆ (—), and the corresponding porphodimethene derivative, [Fe(OEPMe₂)Py₂]PF₆ (**1Am**) (---) (see Table II).*

Table II. Comparison of Metal (II/III) Oxidation–Reduction Potentials of Bisligand Octaethylporphyrin and Decaalkylporphodimethene Complexes

L in Hemichrome Salts[a]	*[Fe(OEP)L₂]PF₆*			*[Fe(OEPMe₂)L₂]PF₆*		
	$E_p(ox)$	$E_p(red)$	$E_{1/2}$	$E_p(ox)$	$E_p(red)$	$E_{1/2}$
3-Chloro-pyridine	−0.03	−0.41	—	−0.16	−0.22	(−0.19?)
Pyridine	−0.12	−0.18	−0.15	−0.29	−0.35	−0.32
1-Methyl-imidazole	−0.38	−0.44	−0.41	−0.47	−0.55	−0.51

L in Cobaltichrome Salts[b]	*[Co(OEP)L₂]PF₆*		*[(Co(OEPMe₂)L₂]PF₆*	
	$E_p(ox)$	$E_p(red)$	$E_p(ox)$	$E_p(red)$
Pyridine	0.22	−0.51	0.19	−0.61
Piperidine	not measured		0.27	−0.64
1-Methyl-imidazole	0.03	−0.81	0.23	−0.96

[a] $[Fe(OEP)L_2]PF_6$ vs. $[Fe(OEPMe_2)L_2]PF_6$
[b] $[Co(OEP)L_2]PF_6$ vs. $[Co(OEPMe_2)L_2]PF_6$
Note: Taken in acetonitrile with ~10% L added; $E[V]$ vs. Hg_2Cl_2/NaCl electrode, tetrabutylammonium hexafluorophosphate as supporting electrolyte; $E_p(ox)$ = peak potential of anodic scan; $E_p(red)$ = peak potential of cathodic scan; scan rate = 0.1 V/s.

The optical spectra of the porphodimethene hemins (Figure 3, Table III) show three bands that are sometimes not well-resolved. A hypsochromic shift occurs with the band at the shortest wavelength as the π donor strength of the axial ligand X increases. With Fe(II) complexes [e.g., the nitrosyl complexes **1Aj** (*4*) and **2Aj**] the spectra only show one uncharacteristic band. Hence, axial ligation phenomena, for example, dioxygen binding, are difficult to investigate. The greater ease of metal oxidation expressed in the electrochemical results should favor irreversible oxidation. Therefore, instead of trying reversible oxygenation, we studied the steric hindrance introduced by the *tert*-butyl groups in the hemin **2Aa.**

A Mononuclear Hydroxoiron(III) Porphodimethene

As stated in the introduction, the di-*tert*-butylporphodimethenatoiron(III) system (Figure 1, I) is sterically hindered above and below the roof-like, folded tetrapyrrole system. This steric hindrance is further illustrated in Figure 4, which shows the hydroxoiron(III) porphodimethene, $Fe(OEPBut_2)OH$ (**2Af**), in two possible configu-

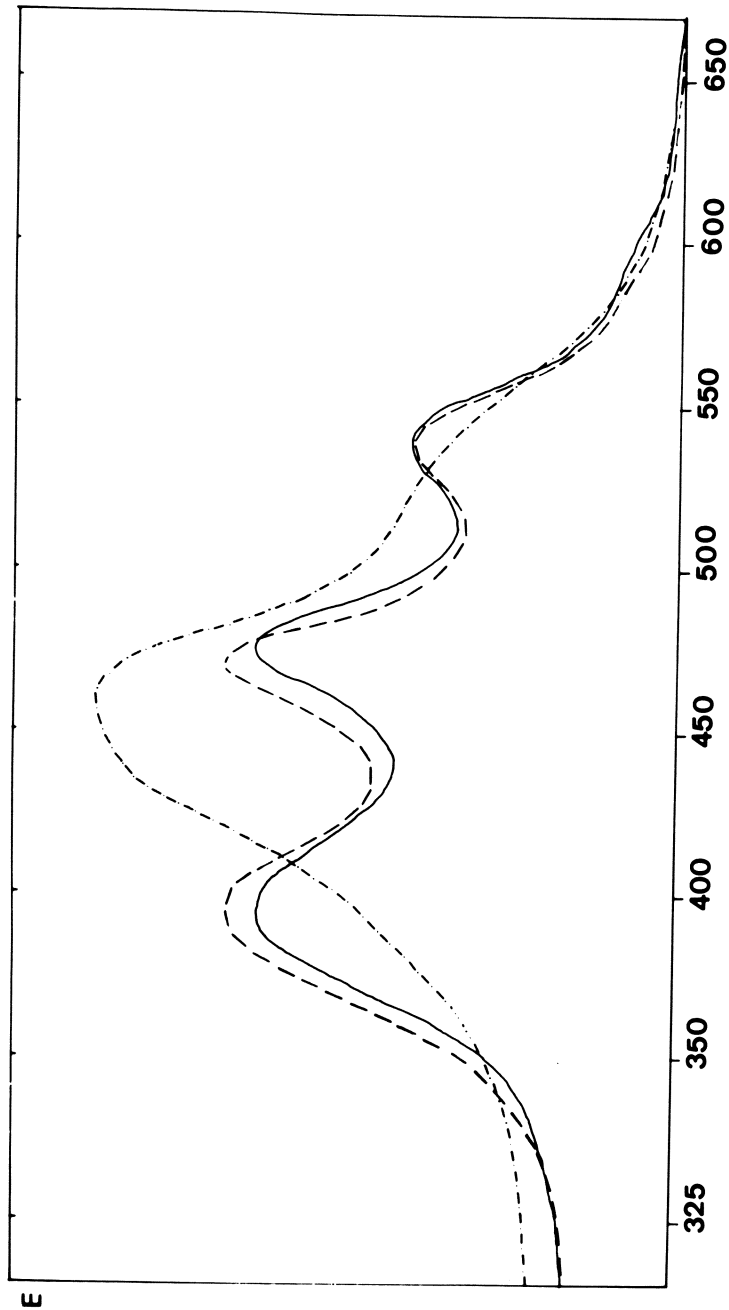

Figure 3. Qualitative optical absorption spectra of **2Af** (—), **2Ag′** (---), *and* **2Aj′** (– · – · –).

rations, the *syn–axial* form III, and the *anti–axial* form IV. Form IV is formed from any hemin Fe(OEPBut$_2$)X instead of a μ-oxobis-iron(III) complex on exhaustive alkaline hydrolysis according to Reaction 1.

The *syn–axial–exo* configuration is analogous to the proved structure of the compound TiO(OEPMe$_2$) (**1Dc**) and is further supported by the close relationship of the TiO, FeCl, and FeOR coordination groups in metalloporphyrin stereochemistry (*31*). However, an x-ray structure determination of a dimethylacetamide solvate, Fe(OEPBut$_2$)OH · DMA, showed that the *anti–axial* configuration IV is correct (*see* Note added later).

The elemental analysis of **2Af** clearly excluded a μ-oxo complex by the high oxygen value. The presence of a hydroxyl group is positively indicated by a sharp ν_{OH} at 3630 cm^{-1} in the IR spectrum, part of which is shown in Figure 5. Figure 5 also shows the corresponding spectral regions of the metallooctaethylporphyrins, Al(OEP)OH (*32*), Si(OEP)(OH)$_2$ (*33*), and Sn(OEP)(OH)$_2$ (*33*) in which the hydroxyl groups are isolated and therefore have a rather high hydroxyl valence frequency above 3600 cm^{-1}.

Another proof of the mononuclear character of **2Af** is its magnetic moment, μ_{eff} = 5.7 B.M., measured in the solid state between 70 and 293 K. The somewhat reduced value (as compared with the expected 5.9 B.M.) is explained by a quantum mechanical admixture of 16% of the $^4A_1$ spin state to the basic 84% of the $^6A_1$ spin state (*34*). μ-Oxo complexes show antiferromagnetic behavior (*26*) not at all found with **2Af.** Further evidence for the mononuclear state of **2Af** is the ESR, Mössbauer, and proton NMR spectra.

Two typical chemical reactions (*11*) of hemes or hemins (the formation of carbonyl hemes or dicyanohemichrome anions) proceed according to Reaction 2 with Fe(II) porphodimethenes (*5*) or Reaction 3

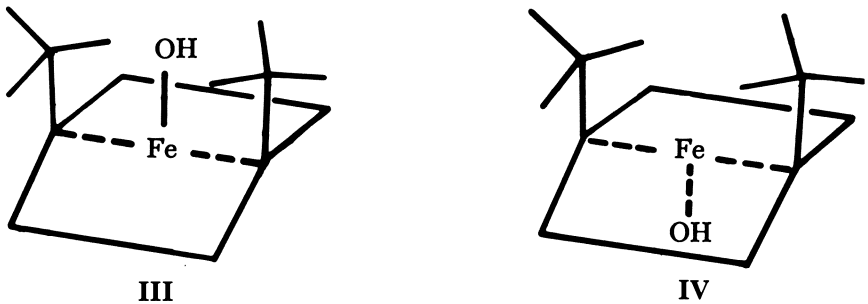

Figure 4. Syn-axial (exo) *or* anti-axial (endo) *configurations (III or IV) of* **2Af** *(see "Note added later").*

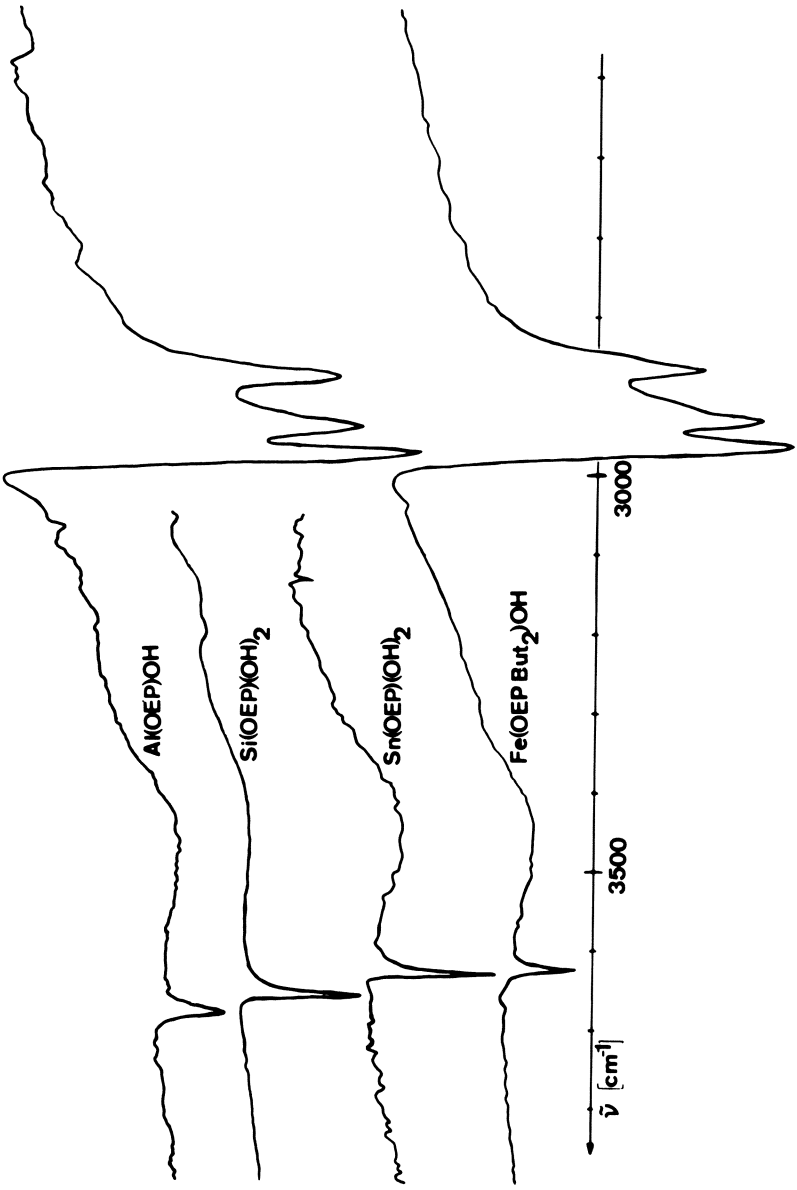

Figure 5. IR spectra of the octaethylporphyrin complexes Al(OEP)OH, Si(OEP)(OH)$_2$, Sn(OEP)(OH)$_2$, and the porphodimethene complex, Fe(OEPBut$_2$)OH in the ν_{OH}/ν_{CH} region.

with Fe(III) porphodimethenes (*17*) for R = CH_3, but not at all (*13*, *14*, *18*) for R = $C(CH_3)_3$.

$$\underset{\textbf{1Am (not 2Am)}}{Fe(OEPR_2)Py_2} + CO \rightarrow \underset{\textbf{1Ad}}{Fe(OEPR_2)CO \cdot Py} + Py \quad (2)$$

$$\underset{\textbf{1Aa (not 2Aa')}}{Fe(OEPR_2)Cl} + 2\,CN^{\ominus} \rightarrow \underset{\textbf{1Av}}{[Fe(OEPR_2)(CN)_2]^{\ominus}} + Cl^{\ominus} \quad (3)$$

In the di-*tert*-butyl series, not even a monocyanide is seen. A possible explanation for this may be the following: Reactions 2 and 3 were run in the presence of pyridine, which by analogy to the proved configuration of **2Af** probably preferentially occupies the position L under the roof. Therefore, carbon monoxide or cyanide can only enter the hemochrome or the hemichrome cation from the strongly hindered position X, if at all.

Many observations in the di-*tert*-butylporphodimethene series can be understood if one assumes that hexacoordinated species $Fe(OEPBut_2)XL$ are not formed at all, and that all pentacoordinated species have the configurations $Fe(OEPBut_2)L$ or $Co(OEPBut_2)L$. Pentacoordinated compounds within the dimethylporphodimethene series, for example, $Fe(OEPMe_2)NO$, $Co(OEPMe_2)NO$, or the hemins $Fe(OEPMe_2)X$ listed in Table III probably have the configurations **1Aj, 1Bj,** or **1Ap** etc. Corresponding species within the di-*tert*-butylporphodimethene series should have the opposite configurations, such as, **2Aj'**, **2Bj'**, or **2Ag'** to **2Aj'** shown in Table III. However, these configurations remain to be checked by selected crystal structure determinations.

The cobalt complexes, $Co(OEPBut_2)Py$ or $Co(OEPBut_2)$(1-Meim) (**2Bl'** or **2Bw'**), cannot be oxidized by air to give the cobaltichrome cations **2Bm** or **2Bx** in the presence of excess Py or Meim. Neither the neutral diligand species, **2Bm** and **2Bx**, nor the dioxygen complex, **2Bo'**, can be formed; the oxidation is thus impeded. Application of stronger oxidants removes the *tert*-butyl groups, and cobalt octaethylporphyrins are obtained.

Electron Spin Resonance Spectra

Table IV summarizes the results of an electron spin resonance study of iron porphodimethenes (*21*, *35*, *36*). Rhombic symmetry is indicated for nearly all complexes with kinked axial ligand systems, that is, the latter are preferentially oriented above one of the bonds between the central iron atom and a nitrogen atom of the porphodimethene ligand. The only exceptions are the phenoxide, **2Ah'**, and the hydroxide, **2Af** (*see* Figure 6, upper right). Lack of rhombicity

Table III. Electronic Absorption Spectra of Iron and Cobalt Porphodimethenes M(OEPR$_2$)X

Compound[a]	λ_{max}: *Absorption maxima (log ε in brackets)*	*Solvent*[b]
1Ap	383 (4.51 sh[c]), 426 (4.53), 441 (4.51 sh), 531 (3.99)	
1Ar	401 (4.50), 447 (4.38 sh), 600 (3.47 sh)	
1Ai	407 (4.57), 451 (4.40 sh), 603 (3.53 sh)	
1As	406 (4.57), 446 (4.43 sh), 628 (3.51 sh)	
2Af′	394 (4.46), 473 (4.46), 536 (3.27)	benzene
2Ag′	396 (4.46), 473 (4.47), 541 (4.17)	1% CH_3OH added
2At′	400 (4.49), 477 (4.48), 561 (4.09)	
2Ap′	400 (4.45), 475 (4.40), 563 (3.97)	
2Ar′	402 (4.59), 459 (4.41 sh), 598 (3.72 sh)	
2As′	409 (4.60), 467 (4.31 sh), 589 (3.66 sh)	
2Ai′	410 (4.57), 465 (4.40 sh), 593 (3.74 sh)	
2Aa′	410 (4.65), 471 (4.41 sh), 623 (3.60 sh)	
2Aj′	446 (4.51), 529 (4.19 sh)	
1Bb	420 (4.60 sh), 456 (4.67), 498 (4.44 sh)	
2Bb	425 (4.43 sh), 461 (4.62), 502 (4.34 sh)	toluene

[a] See Table I for numbering system.
[b] The solvent was CH_2Cl_2 unless otherwise stated.
[c] Shoulder.
Note: Spectra of compounds **1Aa, 1Ae, 1Ag, 1Ah, 1Aj, 1Aq** were published previously (*4*).

is explained by a special orientation of the phenoxide group below the roof along the α,γ-line in **2Ah′** and by the mobility of the hydroxyl proton in **2Af.**

Therefore, a diagnostic feature of the isolated hydroxyl group is the axial ESR spectrum otherwise observed with axially symmetrical species like the chlorohemins **1Aa** and **2Aa′**. The methoxide **2Ag′** is electronically closely related to the hydroxide **2Af** (*see* Figure 11), but shows the largest rhombicity observed with the hemins (*see* Figure 6, upper left). Rhombicities of the corresponding octaethylporphyrins, Fe(OEP)OMe or Fe(OEP)OPh, are somewhat smaller than those of **1Ag** or **1Ah** and amount to 4.07 or 2.78%, respectively (*21*).

The ESR spectrum of Fe(OEPBut$_2$)NO **2Aj′** (*see* Figure 6, lower left) is closely related to the ESR spectrum of the monomeric nitrosyl hemoglobin I of *Chironomus thumni thumni* (*37*), especially when the latter is treated with sodium dodecyl sulfate (*38*). Like the latter modified hemoglobin, **2Aj′** does not accept a second axial ligand. The spectrum is not altered in the presence of a large excess of pyridine. The sterically unhindered Fe(OEPMe$_2$)NO **1Aj** has a spectrum similar

Published on June 1, 1982 on http://pubs.acs.org | doi: 10.1021/ba-1982-0201.ch012

Table IV. *g*-Values of Iron Porphodimethenes

Compound[a]	g_{xx}	$g_{\perp}$	g_{yy}	$g_{zz}(g_{\parallel})$	R[b]
1Aa		5,91		1,99	0
1Ag[c]	6,39		5,56	1,99	5,19
1Ah	6,27		5,70	1,99	3,56
2Aa′		5,83		2,00	0
2Ag′	6,26		5,67	1,99	5,56
2Ah′		5,70		2,00	0
2Af		5,84		2,00	0
2Ai	6,19		5,64	2,00	3,44[d]
1Aj	2,091		2,027	2,009	a(^{14}NO) = 1,61[e]
1Ak[f]	2,082		1,974	2,005	a(^{14}NO) = 2,12; a(^{14}NPy) = 0,706
2Aj′	2,091		2,058	2,011	a(^{14}NO) = 1,65
2Ak[f]	Compound is not formed—spectrum of 2Aj′ observed.				

[a] See Table I.
[b] Rhombicity, R = $[(g_{xx} - g_{yy})/16] \cdot 100[\%]$.
[c] 3% Methanol added.
[d] Taken at 3,6 K.
[e] Nitrogen hyperfine coupling constant [mT].
[f] Taken in pyridine/toluene (1 : 9)
Note: Bruker B-ER 420, X-band, 77 K, frozen solvent toluene (if not otherwise stated).

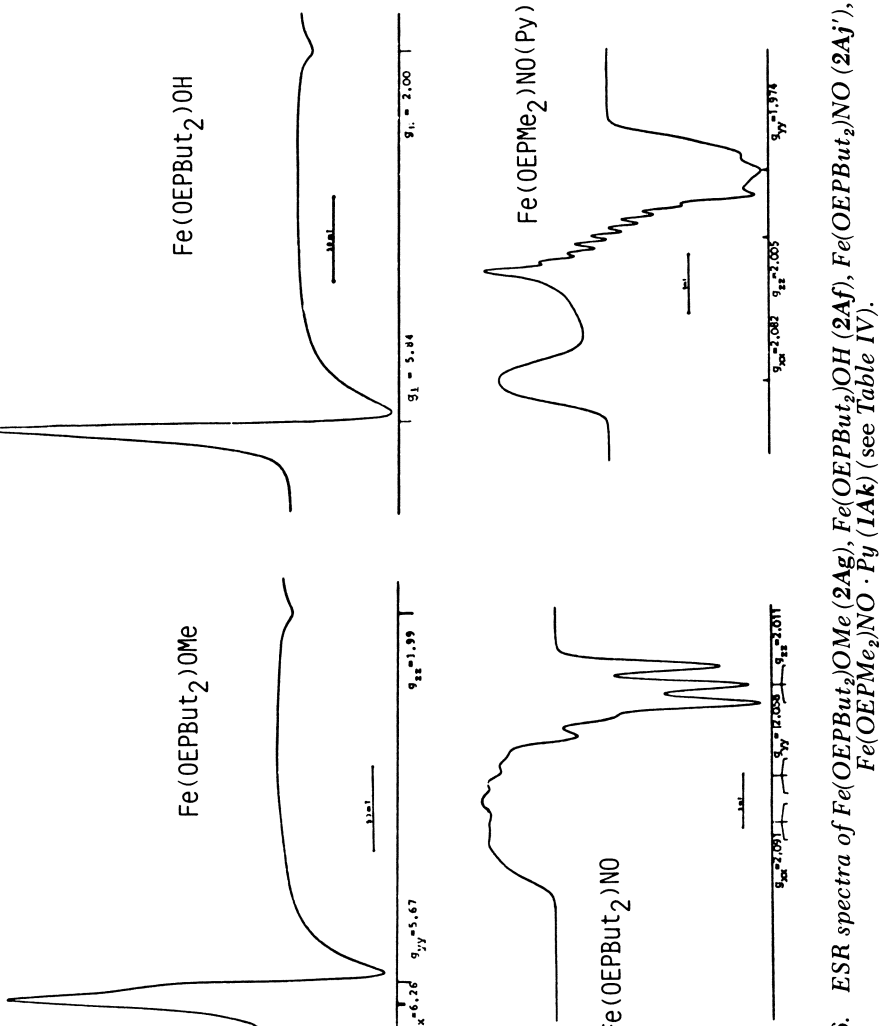

*Figure 6. ESR spectra of Fe(OEPBut$_2$)OMe (**2Ag**), Fe(OEPBut$_2$)OH (**2Af**), Fe(OEPBut$_2$)NO (**2Aj'**), and Fe(OEPMe$_2$)NO · Py (**1Ak**) (see Table IV).*

to **2Aj'** with a better resolution of the axial ^{14}N hyperfine splitting. On addition of pyridine, the spectrum changes to the one shown in the lower right of Figure 6, which is clearly assigned to Fe(OEP-Me_2)NO · Py **1Ak.** The spectrum is similar to that of the tetraphenylporphyrin derivative, Fe(TPP)NO · Pip (*39*), but is much better resolved.

Several researchers investigated the reversible oxygenation of cobalt porphyrins and other cobalt chelates by ESR analyses of the species involved (*40–42*). We were curious to see whether the cobalt porphodimethenes would undergo the same reactions. This is clearly the case for the α,γ-dimethyl derivative, as shown in Table V and Figure 7, which corresponds to Reactions 4, 5, and 6, established at −40°C and analyzed by ESR spectra:

$$\underset{\textbf{1Bb}}{Co(OEPMe_2)} \underset{(5)}{\overset{Py}{\rightleftharpoons}} \underset{\textbf{1Bl}}{Co(OEPMe_2)Py}$$

$$\begin{array}{ccc} & (4)\ O_2 \uparrow\downarrow -40°C & (6)\ O_2 \uparrow\downarrow -40°C \\ \underset{\textbf{1Bn}}{Co(OEPMe_2)O_2} & & \underset{\textbf{1Bo}}{Co(OEPMe_2)Py \cdot O_2} \end{array}$$

The ESR parameters of **1Bn** correspond to the cobalt octaethylporphyrin system (*41*). The ESR spectra of $Co(OEPMe_2)Py$ and $Co(OEPMe_2)Py \cdot O_2$ are very similar in shape to the published features of the analogous cobalt complexes of the diacetylacetoneethyleneimine system, Co(acacen)Py and Co(acacen)Py · O_2 (*42*), but are better resolved.

Reaction 5 proceeds with $Co(OEPBut_2)$ (**2Bb**), but Reaction 4 occurs only to a very minor extent, and Reaction 6 was not observed (*see* Table V). This result is another example of a blockade of the second coordination site after the first one is occupied in the di-*tert*-butylporphodimethene series (*see* the nitrosyl **2Aj'**).

Mössbauer Spectroscopy

Mössbauer spectra of iron porphyrins have attracted much attention (*43–46*), and spectra shown in Figures 8 and 9 were measured and discussed in detail (*21*). The discrimination: mononuclear hydroxo complex–binuclear μ-oxo complex will be elaborated here. The assignment of these configurations from the isomer shifts δ and the quadrupole splittings ΔE_Q is not possible if one compares the new values listed in Table VI for the hydroxo complex, $Fe(OEPBut_2)OH$ (**2Af**), and the μ-oxo complexes, $[Fe(OEPMe_2)]_2O$ (**1Ae**) and $[Fe(ODM)]_2O$. The

Published on June 1, 1982 on http://pubs.acs.org | doi: 10.1021/ba-1982-0201.ch012

Table V. g-Values of Cobalt Porphodimethenes

Compound[a]	g_{xx}	$g_{\perp}$	g_{yy}	$g_{zz}(g_{\parallel})$	a_{xx}	$a_{\perp}$	a_{yy}	$a_{zz}(a_{\parallel})$	$a(^{14}NPy)$[b]
1Bb		2,559		2,015		11,54		13,11	
1Bl[c]	2,455		2,357	2,011	—		3,78	10,14	1,40
1Bn[d]	?		?[e]	2,096	?		?[e]	2,80	
1Bo[d]	?		?[e]	2,093	?		?[e]	2,02	
2Bb		2,496		2,019		7,94		13,03	
2Bl′[c]	2,447		2,335	2,014	—		3,47	10,40	1,02
2Bn′[d]	Only a small fraction of **2Bn** formed[f]								
2Bo′[d]	No dioxygen adduct formed from **2Bl′**, not even at −70°C								

[a] See Table I.
[b] Hyperfine coupling constants [mT].
[c] Taken in pyridine/toluene (1:9).
[d] Prepared by admitting O_2 to solutions of **1Bb, 2Bb, 1Bl** or **2Bl** at −40°C.
[e] Hyperfine structure not resolved.
[f] Spectrum not interpretable.
Note: Conditions were as given in Table IV.

Published on June 1, 1982 on http://pubs.acs.org | doi: 10.1021/ba-1982-0201.ch012

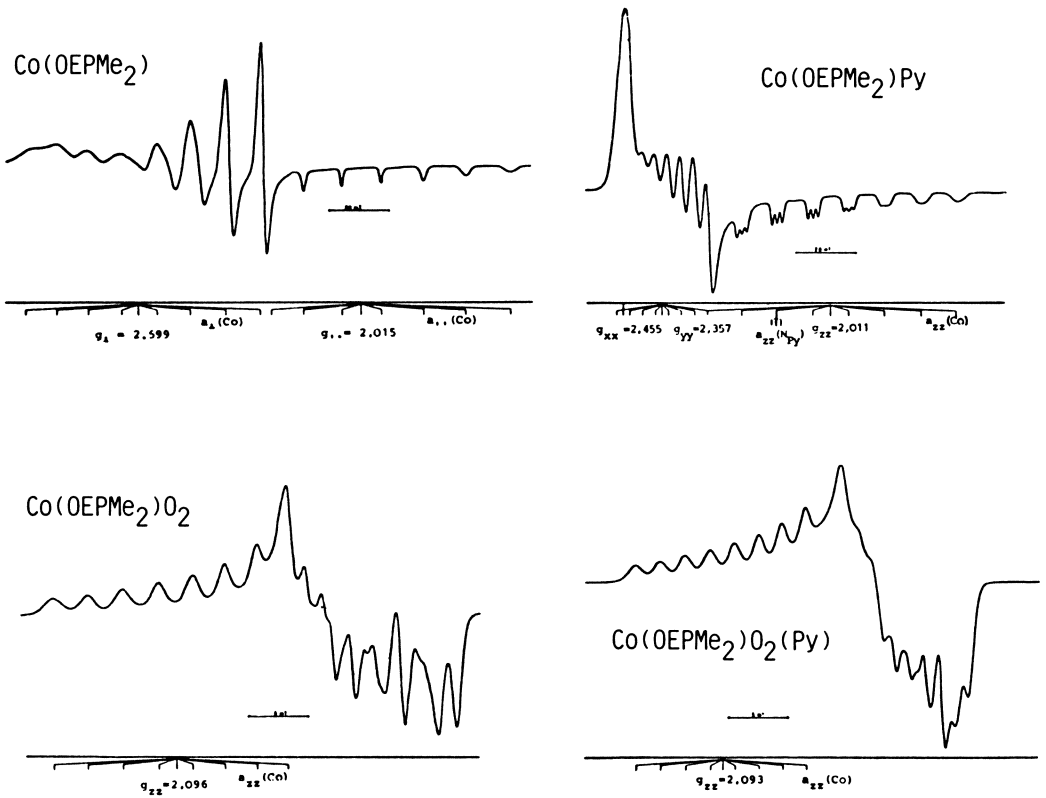

*Figure 7. ESR spectra of Co(OEPMe$_2$) (**1Bb**), Co(OEPMe$_2$)Py (**1Bl**), Co(OEPMe$_2$)O$_2$ (**1Bn**), and Co(OEPMe$_2$)PyO$_2$ (**1Bo**) (see Table V).*

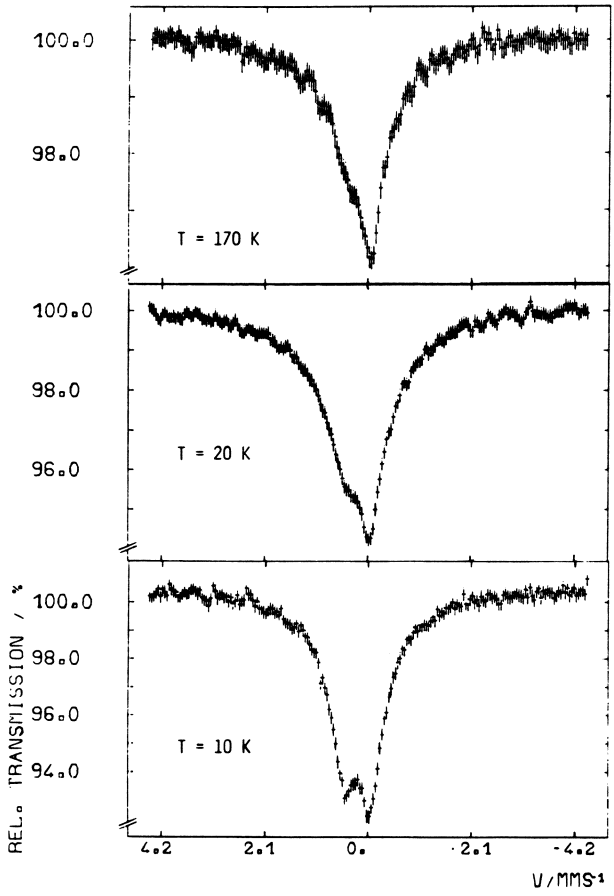

*Figure 8. Mössbauer spectra of the hydroxoiron(III) complex, Fe(OEPBut$_2$)OH (**2Af**), at various temperatures.* Continued on next page.

latter porphyrin derivative is the formal α,γ-dehydrogenation product of **1Ae**, μ-oxobis[α,γ-dimethyloctaethylporphinatoiron(III)] (*17*). Review of the literature for the octaethylporphyrin complexes, Fe(OEP)Cl, Fe(OEP)OMe, and [Fe(OEP)]$_2$O (*45*, *46*) does not provide supporting data.

The different temperature dependence of the hemins and μ-oxo complexes leads to a clear distinction. An asymmetric broadening of the doublet at temperatures rising above a few K is a typical feature of hemins (*43*, *44*), and just this effect is seen for Fe(OEPBut$_2$)OH (Figure 8). On the other hand, μ-oxo complexes do not show such an asymmetric magnetic broadening below room temperature, as do [Fe(OEPMe$_2$)]$_2$O and [Fe(ODM)]$_2$O (Figure 9).

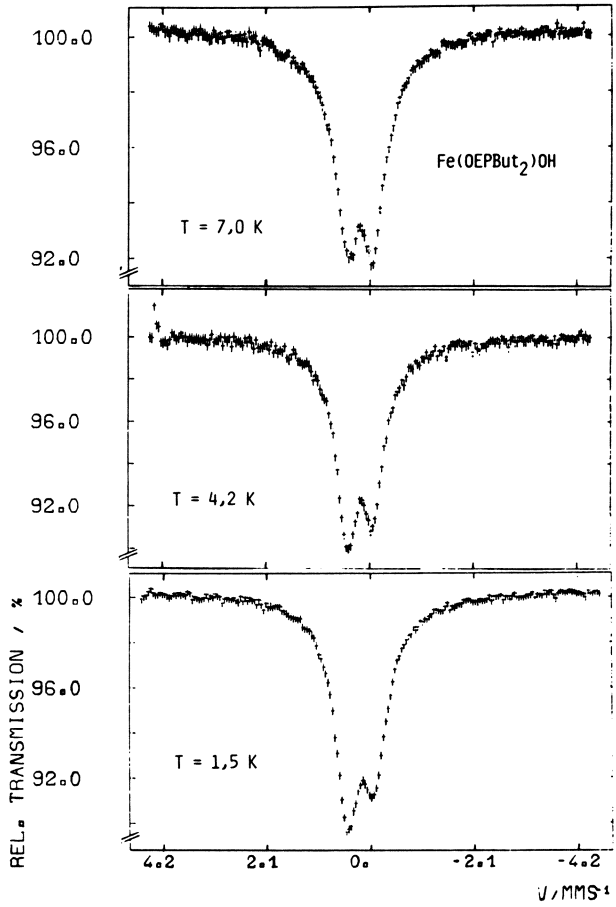

Figure 8. Continued. *Mössbauer spectra of the hydroxoiron(III) complex, Fe(OEPBut$_2$)OH (**2Af**), at various temperatures.*

Nuclear Magnetic Resonance Spectra

The proton NMR spectra of the α,γ-dimethyloctaethylporphodimethene hemins, Fe(OEPMe$_2$)X (where X = OMe, F, N_3, OAc, OCN, Cl, NCS, and Br; Series **1**) and of the α,γ-di-*tert*-butyloctaethylporphodimethene hemins, Fe(OEPBut$_2$)X (where X = OMe, OH, OPhpBut, F, NCS, N_3, Cl, OCN, and Br; Series **2**) were measured (*18*). The purpose of the previous work (*18*) was to find correlations between the configurations of Series **1** and **2**. A *syn–axial–exo* configuration for the hemins of Series **1** is reasonable because of their structural relation to TiO(OEPMe$_2$) (**1Dc**) (*8*). The results of the crystal structure determination of Fe(OEPBut$_2$)OH (**2Af**) indicated that all hemins of Series **2** have the *anti–axial* configuration.

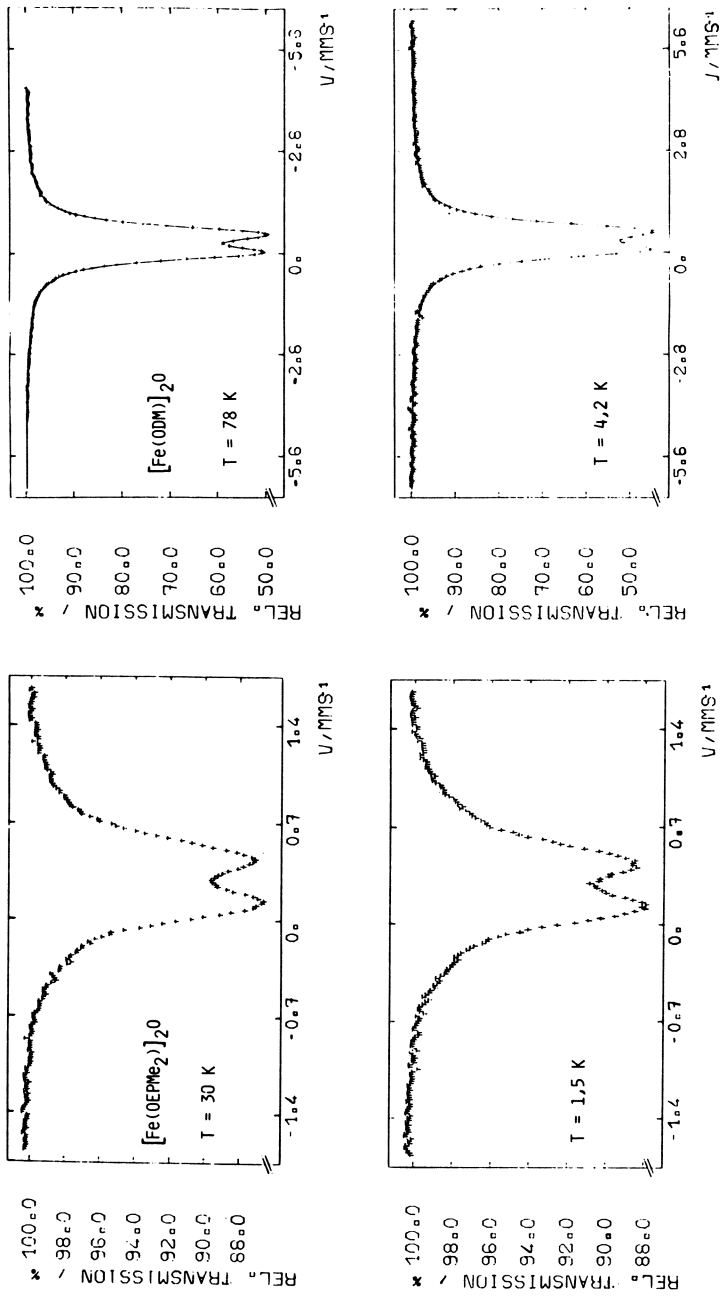

Figure 9. Mössbauer spectra of μ-oxobis[α,γ-dimethyl-α,γ-dihydrooctaethylporphinatoiron(III)], [Fe(OEPMe$_2$)]$_2$O, IAe, and μ-oxobis[α,γ-dimethyloctaethylporphinatoiron(III)], [Fe(ODM)]$_2$O, at various temperatures.

Table VI. Mössbauer Parameters of the Mononuclear Hydroxo Complex 2Af and the μ-Oxo Complexes 1Ae and [Fe(ODM)]$_2$O

T [*K*]	δ (*mm/s*)	ΔE_Q (*mm/s*)
	Compound **2Af**	
170	0.304 ± 0.1	0.54 ± 0.02
80	0.314	0.54
30	0.294	0.52
20	0.304	0.53
10	0.314	0.53
7.0	0.304	0.54
4.2	0.304	0.53
1.5	0.314	0.56
	Compound **1Ae**	
30	0.284 ± 0.01	0.57 ± 0.01
10	0.284	0.57
4.2	0.284	0.58
1.5	0.284	0.58
	[Fe(ODM)]$_2$O	
78	0.388 ± 0.005	0.523 ± 0.005
4.2	0.453	0.529

Note: δ = 0, metallic iron.

The proton NMR spectra of Fe(OEPMe$_2$)NCS (**1As**) and Fe(OEPBut$_2$)OH (**2Af**) are displayed in Figure 10. The high field region, $0 < \delta < 10$ ppm, cannot be fully interpreted. Integration of the spectra suggested that the first two humps between 1 and 2 ppm represent part of the methyl or *tert*-butyl groups with diastereotopic protons. Another part is probably buried under the hump at ~6 ppm, which represents the 24 methyl protons of the peripheral ethyl groups. Some very broad, flat signals at 17 and 32 ppm in the spectrum of the thiocyanate **1As** could be due to the α,γ- or β,δ-protons; the β,δ-protons, however, should be expected at much higher field strength (*47*).

Four signals of equal intensity between 25 and 80 ppm in the low-field region are characteristic for all porphodimethenes and are reliably assigned to the 16 methylene protons of the peripheral ethyl groups. Octaethyl hemin, Fe(OEP)Cl (*47*), has two diastereotopic (and anisochronous) methylene protons (C_{4v} symmetry), and Fe(OEPR$_2$)X (C_{2v} symmetry), therefore, must have four diastereotopic methylene protons. In Fe(OEP)Cl the separation is only ~3 ppm, and in the porphodimethene it could be as large as 50 ppm if the extreme set of signals belongs together. Thus an assignment of the signals to specific positions of the pyrrole rings cannot be made. (An initial proton NMR investigation of iron porphodimethenes (*48*) came to a slightly differ-

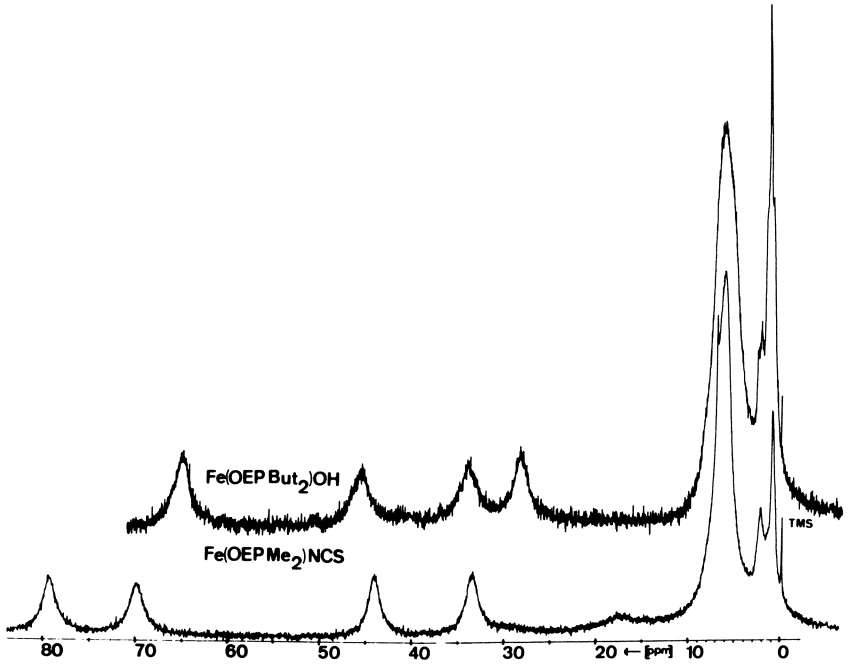

Figure 10. Proton NMR spectra of iron(III) complexes Fe(OEPBut$_2$)-OH, **2Af** *(upper trace) and Fe(OEPMe$_2$)NCS,* **1As** *(lower trace).*

ent conclusion.) These four signals are very susceptible to any variation of the axial ligand and the associated change in spin density transfer from the metal to the porphodimethene core because of their large variation in chemical shift.

The dependence of the chemical shifts of the methylene proton signals of the axial ligands within Series **1** and **2** is schematically represented in Figure 11. Both series demonstrate a progressive spread-out of the four signals as the basicity of the anion X decreases. The hydroxide ion is in a close position to the methoxide. The sequence of anions is not the same in both series; some replacements occur, especially with the pseudohalides, OCN^- and NCS^-. Series **2** has a smaller spread and looks somewhat more irregular than Series **1**.

These differences do not seem major and cannot be used to make any configurational assignment. They may be due to a different and variable angle of folding of the two pyrromethene halves in Series **1** and **2**; in addition, a variable saddle-like deformation should also be considered. Finally, these differences could be due to the suspected opposite configurations of the two series. The folding angle between the normals of the pyrromethene halves in **1Cb, 1Dc** and **1Ed** lies

between 38 and 52°, and the normals of the pyrrole rings of each pyrromethene half may form angles between 1 and 23° (*7, 8, 9*). Such variations certainly affect the transfer of spin density from the metal to the periphery when they occur in iron(III) porphodimethenes, and are more likely found with the more sterically hindered Series **2.**

Note added later: After submission of this chapter, an x-ray structure determination of a dimethylacetamide solvate of the hydroxoiron(III) porphodimethene, $Fe(OEPBut_2)OH \cdot DMA$, was performed by W. R. Scheidt and coworkers (*49*). The compound has the *anti–axial* configuration IV (*see* Figure 4). This surprising result necessitates further structure determinations of pentacoordinated $Fe(OEPMe_2)X$, $Co(OEPMe_2)X$, and $Co(OEPBut_2)X$ systems to determine which axial positions are preferentially occupied. If the configurations of all these systems were known, the reactivity differences of the α,γ-dimethyl and the α,γ-di-*tert*-butyl series would be more easily explained.

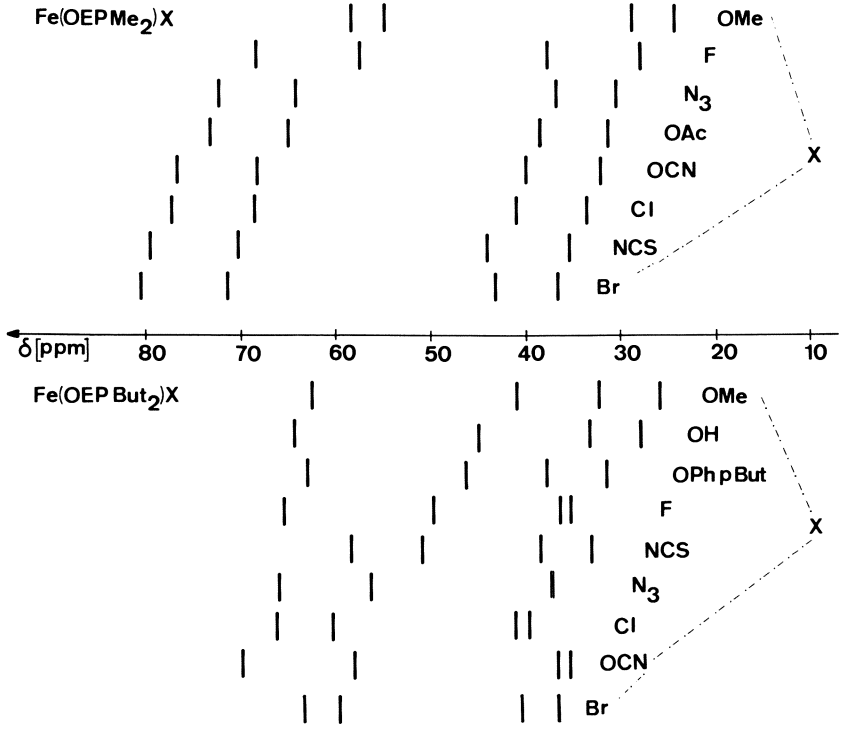

Figure 11. Comparison of the chemical shifts, δ[ppm], of the four low-field proton NMR signals (see Figure 10) for the porphodimethene hemin series $Fe(OEPMe_2)X$ and $Fe(OEPBut_2)X$ for a variation of X (X = anion as indicated).

Acknowledgments

The authors thank K. Gersonde (Aachen), J. Grobe (Darmstadt), and P. Gütlich (Mainz) for the use of their ESR, NMR, and Mössbauer equipment and H. A. O. Hill (Oxford) for initial help with NMR spectra. Financial support of the Deutsche Forschungsgemeinschaft, the Fonds der Chemischen Industrie, and the Vereinigung von Freunden der Technischen Hochschule Darmstadt is gratefully acknowledged. We thank W. R. Scheidt for illuminating discussions and for the determination of the crystal and molecular structure of the hydroxoiron(III) porphodimethene.

Literature Cited

1. Buchler, J. W.; Schneehage, H. H. *Angew. Chem.* **1969,** *81,* 912; *Int. Ed. Engl.* **1969,** *8,* 893.
2. Buchler, J. W.; Schneehage, H. H. *Tetrahedron Lett.* **1972,** 3803.
3. Buchler, J. W.; Puppe, L.; Rohbock, K.; Schneehage, H. H. *Ann. N. Y. Acad. Sci.* **1973,** *206,* 116.
4. Buchler, J. W.; Lay, K. L. Z. *Naturforsch.* **1975,** *30b,* 385.
5. Tonn, B., Ph.D. Dissertation, Technische Hochschule Aachen, 1979.
6. Buchler, J. W.; Puppe, L. *Liebigs Ann. Chem.* **1974,** 1046.
7. Dwyer, P. N.; Buchler, J. W.; Scheidt, W. R. *J. Am. Chem. Soc.* **1974,** *96,* 2789.
8. Dwyer, P. N.; Puppe, L.; Buchler, J. W.; Scheidt, W. R. *Inorg. Chem.* **1975,** *14,* 1782.
9. Buchler, J. W.; Lay, K. L.; Smith, P. D.; Scheidt, W. R.; Rupprecht, G. A.; Kenny, J. A. *J. Organomet. Chem.* **1976,** *110,* 109.
10. Buchler, J. W.; Puppe, L. *Liebigs Ann. Chem.* **1970,** *740,* 142.
11. Buchler, J. W. In "The Porphyrins"; Dolphin, D., Ed.; Academic: New York, 1978; Vol. 1, pp. 389–483.
12. Collman, J. P.; Gagne, R. R.; Reed, C. A.; Halbert, T. R.; Lang, G.; Robinson, W. T. *J. Am. Chem. Soc.* **1975,** *97,* 1427.
13. Buchler, J. W.; Lay, K. L., unpublished data.
14. Buchler, J. W. *Angew. Chem.* **1978,** *90,* 425; *Angew. Chem., Int. Ed. Engl.* **1978,** *17,* 407.
15. Cense, J.-M.; Le Quan, R. M. *Tetrahedron Lett.* **1979,** 3725–3728.
16. Groves, J. T.; Haushalter, R. C.; Nakamura, M.; Nemo, T. E.; Evans, B. J. *J. Am. Chem. Soc.* **1981,** *103,* 2884–2885.
17. Lay, K. L., Ph.D. Dissertation, Technische Hochschule Aachen, 1975.
18. Botulinski, A. Diplomarbeit, Technische Hochschule Darmstadt, 1981.
19. Tonn, M. Diplomarbeit, Technische Hochschule Aachen, 1975.
20. Tonn, B. Diplomarbeit, Technische Hochschule Aachen, 1976.
21. Billecke, J., Ph.D. Dissertation, Technische Hochschule Aachen, 1980.
22. Puppe, L., Ph.D. Dissertation, Technische Hochschule Aachen, 1972.
23. Hill, H. A. O.; Skyte, P. D.; Buchler, J. W.; Lueken, H.; Tonn, M.; Gregson, A. K.; Pellizer, G. *J. Chem. Soc., Chem. Commun.* **1979,** 151.
24. Gütlich, P.; Link, R.; Trautwein, A. "Mössbauer Spectroscopy and Transition Metal Chemistry"; Springer: Berlin, 1978.
25. Ensling, J., Ph.D. Thesis, Technische Hochschule Darmstadt, 1970.
26. Lueken, H.; Buchler, J. W.; Lay, K. L. Z. *Naturforsch.* **1976,** *31b,* 1596.
27. Truxillo, L. A.; Davis, D. G. *Anal. Chem.* **1975,** *47,* 2260.
28. Constant, L. A.; Davis, D. G. *J. Electroanal. Chem.* **1976,** *74,* 85.

29. Fuhrhop, J. H.; Kadish, K. M.; Davis, D. G. *J. Am. Chem. Soc.* **1973,** *95,* 5140.
30. Buchler, J. W.; Kokisch, W.; Smith, P. D. *Struct. Bonding (Berlin)* **1978,** *34,* 80–134.
31. Scheidt, W. R. In "The Porphyrins"; Dolphin, D., Ed.; Academic: New York, 1978; Vol. 3, pp. 463–511.
32. Inhoffen, H. H.; Buchler, J. W. *Tetrahedron Lett.* **1968,** 2057.
33. Buchler, J. W.; Puppe, L., unpublished data.
34. Lueken, H., unpublished data.
35. Billecke, J.; Buchler, J. W.; Lay, K. L.; Twilfer, H. *Biophys. Struct. Mech.* **1980,** *6(Suppl.),* 26.
36. Ibid., 27.
37. Overkamp, M.; Twilfer, H.; Gersonde, K. *Z. Naturforsch.* **1976,** *31c,* 524.
38. Twilfer, H., Ph.D. Dissertation, Technische Hochschule Aachen, 1979.
39. Wayland, B. B.; Olson, L. W. *J. Am. Chem. Soc.* **1974,** *96,* 6037.
40. Walker, F. A. *J. Am. Chem. Soc.* **1970,** *92,* 4235.
41. Walker, F. A. *J. Magn. Res.* **1974,** *15,* 201.
42. Jones, R. D.; Summerville, D. A.; Basolo, F. *Chem. Rev.* **1979,** *79,* 139–179.
43. Hambright, P.; Bearden, A. J. In "Porphyrins and Metalloporphyrins"; Smith, K. M., Ed.; Elsevier: Amsterdam, 1975; pp. 539–553.
44. Sams, J. R.; Tsin, T. B. In "The Porphyrins"; Dolphin, D., Ed.; Academic: New York, 1979; Vol. 4, pp. 425–478.
45. Dolphin, D. H.; Sams, J. S.; Tsin, T. B.; Wong, K. L. *J. Am. Chem. Soc.* **1978,** *100,* 1711.
46. Tang, S. C.; Koch, S.; Papaefthymiou, G. C.; Foner, S.; Frankel, R. B.; Ibers, J. A.; Holm, R. H. *J. Am. Chem. Soc.* **1976,** *98,* 2414.
47. La Mar, G. N.; Walker (Jensen), F. A. In "The Porphyrins"; Dolphin, D., Ed.; Academic: New York, 1979; pp. 61–157.
48. Skyte, P. D., Ph.D. Dissertation, University of Oxford, 1978.
49. Scheidt, W. R., personal communication; Buchler, J. W.; Lay, K. L.; Lee, Y. J.; Scheidt, W. R. *Angew. Chem. Suppl.* **1982,** in press.

RECEIVED for review June 2, 1981. ACCEPTED August 17, 1981

Redox Tuning of Iron Porphyrins

LAWRENCE A. BOTTOMLEY

Florida State University, Department of Chemistry, Tallahassee, FL 32306

LARRY OLSON[1] and KARL M. KADISH

University of Houston, Department of Chemistry, Houston, TX 77004

A detailed description of the most important factors that influence synthetic iron porphyrin electron transfer reactions at electrodes is reported. Quantitative relationships that describe (1) the standard potential in terms of the porphyrin ring structure; (2) axial coordination of the central metal ion by nitrogenous bases, monovalent counterions, and diatomic ligands; and (3) the solvent in which the electron transfer is studied are presented. Combinations of these factors can be utilized to plan the synthesis of the appropriate iron porphyrin that will possess the desired standard potential (E°), the desired number of electrons in the redox reaction, as well as the desired ultimate reaction site (whether metal centered or porphyrin ring centered).

The electron transfer properties of hundreds of metalloporphyrins have been reported (*1–5*). Porphyrins with dozens of conjugated ring structures containing over thirty different central metal ions have been probed electrochemically to determine the redox behavior of the parent compound and its oxidized or reduced forms. Central metal ion valence of the parent complexes varied between +4 and +1, depending on the specific metal and the surrounding porphyrin ring structure. Electrooxidation or reduction can yield either a change in the valence of the central metal ion or a metalloporphyrin with an increased or decreased number of π-electrons on the porphyrin ring. The ultimate product formed at the electrode depends on the specific metal ion, the porphyrin ring structure, and the medium in which the electrode reaction is investigated.

[1] On leave of absence from Grand Canyon College, Phoenix, AZ 85017

0065-2393/82/0201-0279$09.25/0

This chapter provides a detailed description of the most important factors that influence synthetic iron porphyrin redox reactions. From the biomimetic point of view, a fundamental understanding of model compound reactivity is essential for a complete description of the electron transfer reactions that exist in vivo. Focusing on the structurally related porphyrins **I–III**, we will demonstrate systematically how to tune model compound reactivity to obtain a desired standard potential ($E°$), a desired number(s) of electrons transferred in the reaction sequence, or a desired ultimate product (e.g., change in the valence of the central metal or generation of a π-cation or π-anion radical). Such tuning can be accomplished by a systematic variation of one or more of the following: porphyrin ring structure; axial coordination of the central metal ion by nitrogenous bases, monovalent counterions and/or diatomic ligands; and the specific solvent in which the electron transfer reaction is carried out. Whenever possible, we will quantify the influence of each factor on the redox parameters studied.

In substituted metalloporphyrins **I–III**, (*m*, *p*-R)TPP denotes *meta*- or *para*-substituents on the phenyl rings of 5,10,15,20-tetraphenylporphyrin; (*meso*-R)OEP denotes substituents on the 5-position of 2,3,7,8,12,13,17,18-octaethylporphyrin; (R)TPPM denotes a substituent placed on the 3-, 8-, 13-, or 18-position of 5,10,15,20-tetraphenylporphyrin; and M denotes a transition metal or hydrogen covalently bound to the four core nitrogens.

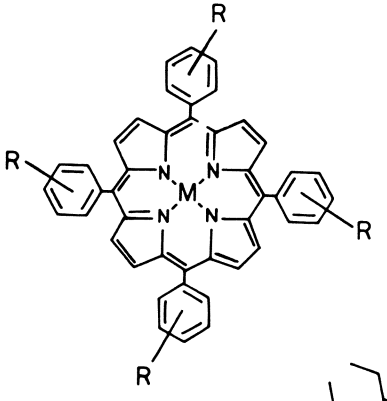

[(*p*,*m*-R)TPPM] **I**

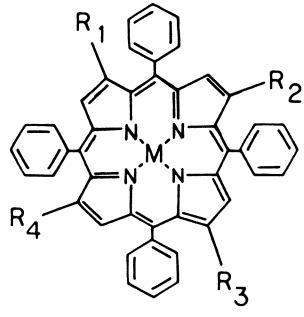

[(R)TPPM] **III**

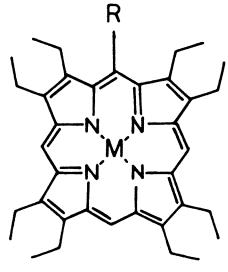

[(*meso*-R)OEPM] **II**

Effect of Porphyrin Structure

The degree and mode of transmission of electron density from various points on the porphyrin ring through the σ- and π-orbitals of the four nitrogens to the central metal has interested researchers investigating the physical properties and chemical reactivity of metalloporphyrins (*1*, *6–11*). Because of the conjugated nature of the porphyrin ring systems, electron-donating or electron-withdrawing groups on the periphery of the molecule significantly modify the basicity of the porphyrin nitrogens. This effect is manifested by a systematic change in a number of physical properties of metalloporphyrins including their redox behavior. In this regard, the central themes of this section will be first, to analyze the extent to which porphyrin ring structure determines the redox potential and, second, to demonstrate the design of a synthetic porphyrin with appropriate redox properties, for example, a metalloporphyrin that possesses a desired $E°$ for central metal ion oxidation and a second desired $E°$ for electrogeneration of the porphyrin π-anion radical. Such a prediction requires a fundamental understanding of the impact that each particular porphyrin substituent has on the redox potential for each type of electron transfer a metalloporphyrin can undergo.

Earlier work on substituent effects of porphyrin redox processes involved comparisons of the differences in potential between the metal-centered reactions for iron complexes of natural porphyrins and those reactions of the synthetic porphyrins, 2,3,7,8,12,13,17,18-octaethylporphinatoiron chloride (OEPFeCl) and 5,10,15,20-tetraphenylporphinatoiron chloride (TPPFeCl). For a series of naturally occurring porphyrins in aqueous media containing pyridine, the most positive reduction potential was found for iron protoporphyrin IX, while iron mesoporphyrin or iron coproporphyrin gave the most negative potential. However, the differences in $E°$ were less than 100 mV (*1*). For example, in aqueous media buffered at pH 9.6, potentials of +0.015 and −0.063 V were measured for the iron(III)/iron(II) couple of the pyridine complexes of iron protoporphyrin IX and iron mesoporphyrin, respectively. [All potentials are referenced to the saturated calomel electrode (SCE).] Similarly, potentials of −0.183 and −0.247 V were measured for the same couple with cyanide complexes of iron protoporphyrin IX and iron coproporphyrin, respectively. In the nonaqueous solvent dimethyl sulfoxide, Mc_2SO, similar differences in potential were measured (*12*) for the hydroxide complexes of a series of naturally occurring porphyrins.

To compare quantitatively the effect of substituents between naturally occurring and synthetic iron complexes, half-wave potentials for a series of iron porphyrins were measured (*13*) in dimethylformamide (DMF), under the same experimental conditions (*see* Table I).

Table I. Half-Wave Potentials for Reduction of Ferric Porphyrins in DMF

Complex[a]	*Fe(III)/ Fe(II)*	*Fe(II)/ Fe(I)*	*Fe(I)/Fe(I) radical*	*Reference*
$(CN)_4$TPPFeCl	−0.12	−0.26	−0.73	*27*
TPPFeCl	−0.18	−1.03	−1.65	*26, 27, 86*
ProtoFeCl	−0.27	−1.19	−1.68	*12, 13, 52*
DeuteroFeCl	−0.30	−1.20	−1.79	*13, 51*
EtioFeCl	−0.34	−1.25	−1.91	*13*
OEPFeCl	−0.34	−1.24	−1.90	*13*

Note: Potentials are referenced to the SCE, uncorrected for liquid junction potentials.

[a] For complex names, see Structures **I–III** and accompanying description in text. Other abbreviations are protoFeCl for protoporphyrin IX iron chloride and deutero-FeCl for deuteroporphyrin iron chloride.

The most positive potential was obtained for the reactions of TPPFeCl, and the most negative potential was obtained for the reactions of OEPFeCl or etioporphinatoiron chloride (EtioFeCl). This result was true for all three electroreductions of each complex. Because absolute porphyrin ring basicities were not known for the complexes investigated, an arbitrary scale of ring basicity was constructed from potential data. Using the potentials obtained for the reduction of the iron(I) form of each complex in Table I, except 5,10,15,20-tetra(*p*-cyanophenyl)porphinatoiron chloride [(CN_4)TPPFeCl], to the π-anion radical, a plot was constructed with an arbitrary slope of 1.0. This plot permitted the assignment of an ad hoc porphyrin basicity. Using this basicity, slopes of 0.88 and 0.53 were obtained for the iron(II)/iron(I) and iron(III)/iron(II) couples, respectively. These data showed that the effect of substituents on the porphyrin ring increased with increasing negative charge and is about 160–180% greater for reactions involving the π-system than for reactions involving the Fe(III) $\rightleftharpoons$ Fe(II) reactions.

The problem of quantitatively correlating the half-wave potential ($E_{1/2}$) values of many naturally occurring porphyrins with their basicity was solved recently (*14, 15*). Reduction potentials for over seventy-five pyrrole-substituted free base porphyrins were measured under identical conditions. Whenever possible, porphyrin basicities were determined empirically. In all cases, the porphyrins that are more difficult to reduce also have higher pK_3 values (defined as the negative log of the equilibrium constant for the following reaction):

$$(\text{porphyrin})\ H_2 + H^+ \rightleftharpoons (\text{porphyrin})\ H_3^+ \qquad (1)$$

Figure 1 depicts the excellent linear relationship obtained between pK_3 and $E_{1/2}$ for a series of 3,8-disubstituted deuteroporphyrin methyl esters. The pK_3 or $E_{1/2}$ values for any new porphyrins of this type can be predicted by the following model:

$$pK_3 = -5.9(E_{1/2}) - 5.2 \quad (2)$$

Chronologically, however, the impact of minor changes in porphyrin structure on $E_{1/2}$ were elucidated using symmetrically substituted synthetic metalloporphyrin complexes. Porphyrin molecules containing a specific electron-donating or electron-withdrawing substituent were synthesized systematically. Half-wave potential values then were determined for the redox reactions of interest and compared with those determined for the unsubstituted porphyrin.

The effect of porphyrin ring substituents on the physicochemical properties of metalloporphyrins can be quantitated readily by the use of the Hammett–Taft linear free-energy relationship (*16*):

$$\Delta \log K = \log \frac{K_{(R)}}{K_{(H)}} = \sigma\rho \quad (3)$$

In this equation, K is either an equilibrium or rate constant; σ, the

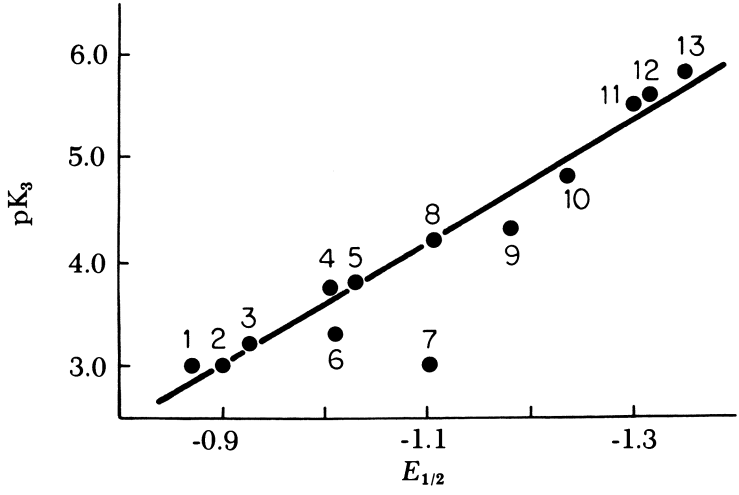

Figure 1. Correlation between pK_3 and $E_{1/2}$ *for electroreduction of 3,8-disubstituted deuteroporphyrin dimethyl esters in DMF. Substituents: 1,* CO_2CH_3; *2, CHO; 3, H,*NO_2; *4,* $CHCH_2$,*CHO; 5, H,CHO; 6,* $COCH_3$; *7, Br; 8, H,*CO_2CH_3; *9, CHNOH; 10,* $CHCH_2$; *11, H; 12,* $(CH_2)_2CO_2CH_3$; *and 13,* CH_2CH_3. *Adapted from results presented in Refs. 14, 15, and 40.*

Hammett substituent constant, is a measure of the electron-donating or electron-withdrawing characteristics of the particular substituent R; and ρ, the linear free-energy reaction parameter, measures the sensitivity of the reaction under study to the effect of substituents. Equation 3 can be applied to electrochemical data by substitution of the following relationships

$$\Delta G^\circ = -nFE^\circ = -RT \ln K \tag{4}$$

$$E_{1/2} \simeq E^\circ = \frac{RT}{nF} \ln K = 2.303 \frac{RT}{nF} \log K \tag{5}$$

yielding Equation 6

$$\Delta E_{1/2} = E_{1/2(R)} - E_{1/2(H)} = \sigma \rho_{EMF} \tag{6}$$

where EMF represents the electromotive force. The sensitivity of the redox potential to the porphyrin ring substituent can be compared with reaction sensitivities as measured by other physicochemical properties or parameters via Equation 7

$$n\rho_{EMF} = 0.0591\ \rho \tag{7}$$

where n equals the number of electrons transferred in the redox reaction assuming both ρ and ρ_{EMF} are determined at 25°C. Standard values of σ for a large number of aryl and alkyl substituents have been compiled and tabulated (*16–21*). These tables show that different values of σ for a particular substituent are available. Selection of the appropriate value depends on the degree of inductive, resonance, and steric interaction of the substituent with the molecular reaction site.

The validity of Equations 3 and 6, in general, has been demonstrated for thousands of organic and inorganic compounds. However, for metalloporphyrin electrode reactions, linear free-energy relationships involving half-wave potentials were published in the mid 1970's. The electrode reactions of *meta*- and *para*-phenyl-substituted tetraphenylporphyrins of the general formula (*p*-R)TPPM and (*m*-R)TPPM (**I**) were studied (*22–26*). Electrode reactions of tetraphenylporphyrins where the substituent was placed directly on the porphyrin ring have been described (*27–30*). Syntheses of pyrrole-substituted porphyrins have been described (*31, 32*). Electron-withdrawing substituents, whether attached directly to the porphyrin ring or on the phenyl group, produced easier reductions and more difficult oxidations.

Initial studies of the four electrode reactions of (*p*-R)TPPH$_2$ in a variety of nonaqueous solvents yielded linear free-energy relation-

ships (23). Values of ρ for the electrogeneration of the π-anion radical, $[(p\text{-R})\text{TPPH}_2]^-$, decreased from 73 mV in CH_2Cl_2 to 53 mV in dimethyl sulfoxide (DMSO). Studies (*24*, *25*) of substituent effects involving metalloporphyrin complexes where the central metal ion was Co, Mn, Ni, Fe, VO, Cu, and Zn showed that the magnitude of ρ was specific for the type of electron transfer. An average ρ-value of 70 ± 10 mV was obtained for oxidation of the porphyrin ring to yield a π-cation radical or dication. Average ρ-values of 60 ± 10 mV were reported for the first porphyrin ring reduction to yield the π-anion radical and 70 ± 10 mV for the second porphyrin ring reduction to yield the dianion of a series of first row transition metal complexes of (*p*-R)TPPM. Comparable ρ-values were measured for (*p*-R)TPPCo (*33*) and for (*p*-R)TPPRu(Co)(pyridine) (*34*).

Placement of a given substituent directly onto the porphyrin ring results in a much larger shift in potential compared to that observed for the phenyl-substituted complexes. For porphyrin complexes of the general formula (R)TPPH_2, $E_{1/2}$ for generation of the porphyrin π-anion shifted linearly with substituent, yielding a ρ-value of 280 mV. When contrasted with phenyl-substituted porphyrin complexes where four substituents on the same molecule accounted for a ρ-value of between 53 and 73 mV, depending on solvent, a fourfold to fivefold increase in substituent sensitivity was obtained just by moving the substituent onto the porphyrin, four bonds closer to the core nitrogens. This effect is demonstrated further by comparison of substituent sensitivities for oxidation to form π-cation radicals (*see* Figure 2). Pyrrole ring-substituted porphyrins gave a ρ-value of 170 mV when $E_{1/2}$ was plotted versus σ_p. The ρ-value obtained for a series of *meso*-substituted octaethylporphyrins of the general formula (*meso*-R)OEPH_2, was 510 mV, eight times larger than the corresponding value obtained for the phenyl-substituted complexes (*3*).

Sequential substitution of R directly onto the porphyrin ring resulted in somewhat unexpected results (*28*, *29*). Half-wave potentials for reduction of $(\text{CN})_n\text{TPPH}_2$ varied linearly, shifting anodically by 250 mV per cyano group. When the bromo group was substituted sequentially onto the ring instead of the cyano group, half-wave potentials varied nonlinearly with n. The nonadditivity of bromine substitution was attributed (*27*) to steric interactions between bromines and the phenyl rings in *peri* positions. This steric interaction results in an increase in the activation barrier for phenyl ring rotation, reducing any resonance contribution from the phenyl groups to the conjugated porphyrin ring system. Another manifestation of the bromine–phenyl ring steric interaction is the generation of a structural deformation, especially with respect to the planarity of the pyrrole and *meso*-carbon atoms. In either case, the effects of steric hindrance

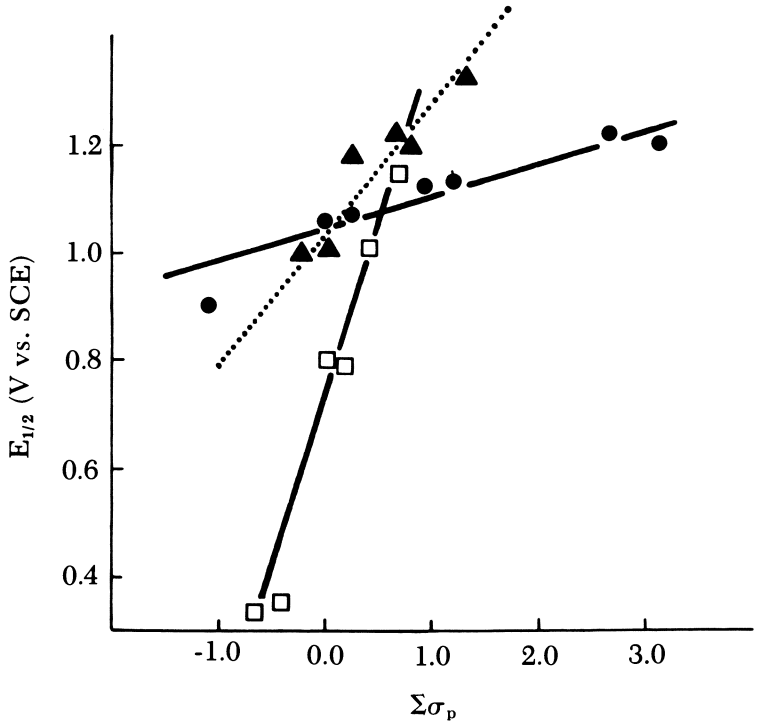

Figure 2. Comparison of linear free-energy relationships for electro-oxidation of substituted free base porphyrins. Key: △, (R)TPPH$_2$; □, (meso-R)OEPH$_2$; and ●, (p-R)TPPH$_2$. Adapted from Refs. 3, 25, and 28.

tend to increase with increasing number of bromine atoms, gradually offsetting the inductive effects of the electron-withdrawing substituent.

Half-wave potentials for oxidation of (CN)$_n$TPPH$_2$ were related curvilinearly to n (28). In fact, the potential difference between the first and second oxidation waves decreased from 270 mV, when the porphyrin was unsubstituted, to 180 mV for monosubstitution, to 0 mV for the tetrasubstituted complex.

The influence of the porphyrin substituent is not limited to redox reactions involving the porphyrin π-system. For a series of transition metal complexes of the form (p-R)TPPM, ρ for the electrode reaction M(III) $\rightleftharpoons$ M(II) apparently depended (25) on the number of d-electrons of the central metal. As the number of d-electrons decreased from d^8 (Ni) to d^5 (Fe) to d^4 (Mn), ρ increased from 18 to 38 to 54 mV, respectively, when determined in CH_2Cl_2. However, decreasing the number of d-electrons on the same metal does not yield a corresponding increase in ρ. This fact is readily shown from the results

presented in Table II. For (*p*-R)TPPCo, as the number of *d*-electrons is reduced, ρ-values also decrease when $E_{1/2}$ is measured in either Me_2SO or butyronitrile (PrCN). In benzonitrile, ρ appears to be independent of the number of *d*-electrons. For (*p*-R)TPPFeCl, ρ decreases with decreasing number of *d*-electrons when the $E_{1/2}$ measurement is made in CH_2Cl_2, DMF, and DMSO. In dimethylacetamide (DMA), ρ appears independent of the number of *d*-electrons. Finally, in butyronitrile, two values of ρ are observed for the d^6 to d^5 transition. This observation suggests the lack of any clear-cut trend between ρ and the number of central metal ion *d*-electrons. One explanation given is that ρ is much more sensitive to the overall charge on the molecule than to the numbers of *d*-electrons. The overall charge on positively charged metalloporphyrin complexes ranged (*26*) from +1 to −1. Alternatively, the lack of any observed dependence of ρ on numbers of *d*-electrons in the (*p*-R)TPPCo and (*p*-R)TPPFe studies and the marked dependence of ρ on the particular solvent used suggests that a change in the central metal ion coordination tends to offset the impact of phenyl ring substituents on the observed $E_{1/2}$ values. This latter explanation is supported by the strong dependence of $E_{1/2}$ for both TPPCo and TPPFe on solvent donicity (vide infra).

One of the most surprising results emerging from the studies of metalloporphyrin substituent effects is the occurrence of unpredictable changes in the mechanism, or route of electron transfer. For most of the systems investigated, metal-centered reactions were well-separated in potential from ligand-centered electron transfers. Although ρ-values for metal-centered reactions were typically one-half the magnitude of the ρ-values measured for ligand-centered electron transfers, reaction site crossovers were observed only for (*p*-R)TPPNi.

Table II. The Dependence of ρ on the Number of *d*-Electrons of the Central Metal for Several Complexes of the Form (*p*-R)TPPM

Central Metal	*Solvent*	*Oxidation Process*[a] $d^8 \rightleftharpoons d^7$	$d^7 \rightleftharpoons d^6$	$d^6 \rightleftharpoons d^5$
Co	DMSO	38	18	—
	butyronitrile	41	34	—
	benzonitrile	44	44	—
Fe	CH_2Cl_2	—	68	38
	butyronitrile	—	24	0.0, 51[b]
	DMF	—	37	30
	DMSO	—	35	25
	DMA	—	20	20

[a] ρ-values are listed in millivolts.
[b] *See* Ref. 26 for details.

The potential difference between the first and second oxidation processes decreased (*22*) with increased substituent electron-withdrawing strength (150 mV for R = OCH_3; 100 mV for R = H; and 0 mV for R = Cl, $COOCH_3$, and NO_2 when measured in CH_2Cl_2/0.1 *M* tetrabutylammonium perchlorate (TBAP). Previous experiments (*35*) showed that electrooxidation of TPPNi in benzonitrile initially produced a nickel(III) species, $[TPPNi(III)]^+$, which, with time, interconverted to a radical species $[TPPNi(II)]^{+\cdot}$ For most metalloporphyrins, the potential separation between the first and second oxidation processes is 290 ± 50 mV for ring-centered electron transfers. Potential separations much less than this value are observed when one of the processes involves a change in the central metal valence. Therefore, the potential separations observed for (*p*-R)TPPNi seemed to indicate that the first oxidation process was ring centered. Electron-withdrawing groups placed on the phenyl rings stabilized the nickel(II) to such a level that the metal-centered oxidation overlapped the cation radical generating process.

EPR data showed (*36*) that for TPPNi in CH_2Cl_2, both electron transfers were ring centered. However, on cooling, an internal interconversion from $[TPP^+]Ni(II)$ to $[TPPNi(III)]^+$ occurs. The potentials for both oxidation processes also were supporting electrolyte dependent ($\Delta E_{1/2}$ = 100 mV for TBAP and 320 mV for $TBAPF_6$). Interconversion from a cation radical to the metal-centered species had been suggested previously for lead porphyrins (*37*). Thus, even though the electronic configuration of a metalloporphyrin can be determined, the route of electron transfer is still a subject of speculation. The variation in oxidation potential differences for nickel porphyrins with changes in substituent, solvent, and supporting electrolyte suggests that the interconversion phenomenon must depend on a number of closely balanced, interactive factors.

Variation of the number of electrons transferred by changes in porphyrin substituent has not been limited to (*p*-R)TPPNi where R was the electron-withdrawing functional groups Cl, $COOCH_3$, and NO_2. Bielectronic reductions have been observed for porphyrins containing from one to four *N*-methyl-4-pyridinium groups (*15*). The pyrrole-substituted complex $(CN)_4TPPH_2$ is doubly oxidized at 1.43 V in CH_2Cl_2 (*28*). An identical bielectronic oxidation process was observed (*38*) for $[p\text{-}(CH_3CH_2)_2N]TPPH_2$ at 0.40 V. Remarkably, metal insertion into the latter complex resolves the bielectronic process into two, well-resolved, one-electron transfers. With $(CN)_4TPPH_2$, electron-withdrawing substituents on the porphyrin periphery produce the same mechanistic change as $[p\text{-}(CH_2CH_3)_2N]$, an electron-donating substituent. Clearly, different highest occupied molecular orbital (HOMO) values are involved and the need for molecular orbital calculations to resolve this anomaly seems apparent.

Effect of Axial Ligation

Dynamic coordination of metalloporphyrins has been a very active field of study (*39–41*). The profound impact that changes in the porphyrin coordination sphere have on the measured redox potentials has been well-documented (*3–5, 42*). The forthcoming discussion does not attempt to provide yet another review of this area. Instead, the emphasis is placed on how to make use of the known coordination chemistry of metalloporphyrins in the design of new molecules that will possess a desired redox potential(s). For clarity, we divided the discussion into four artificial categories: axial coordination by counterions, by solvent molecules, by substituted pyridines, and by diatomic molecules. Emphasis is placed on the reactions of iron porphyrins with the inclusions of cobalt, manganese, and chromium porphyrin reactivities for comparison.

Counterion Effects. Surprisingly, elucidation of the potential dependence on the iron(III) porphyrin counterion was determined only recently, despite the ease with which such molecules can be prepared. Treatment of any hematin dimer with the dilute acid HX, in excess, quantitatively yields monomeric material with X axially coordinated to the iron center (*43*).

Bottomley and Kadish (*44*) recently completed a systematic study of the influence of counterion on the observed $E_{1/2}$. In noncoordinating, nonaqueous solvents, the first reduction of TPPFeX [Fe(III) → Fe(II)] becomes much more difficult (shifts cathodically by up to 720 mV) as the counterion varies from the weakly coordinating ClO_4^- anion to the tightly bound F^- anion. This behavior indicates the preferential stabilization of the iron(III) species over the iron(II) form. The iron(III) porphyrin–counterion binding strength increases in the order $ClO_4^- < Br^- < N_3^- < F^-$ and this order is reflected in the half-wave potentials. In these instances, the iron–counterion bond can be described best as highly covalent in character. For comparison, Figure 3 depicts half-wave potentials for electroreduction of TPPFeX and TPPMnX in CH_2Cl_2. Manganese(III) is stabilized preferentially (*45*) over manganese(II), but by only 180 mV as the counterion is varied between ClO_4^- and the tightly coordinated N_3^-. Over the same range of counterions, iron(III) reduction potentials vary by 510 mV. Clearly, the metal(III) reduction can be tuned, but the potential range over which this effect is operative depends greatly on the nature of the central metal.

The characterization of the formal central metal ion valence produced by oxidation of synthetic iron(III) porphyrin monomers has been a point of controversy. Both TPPFeCl and OEPFeCl were oxidized (*46, 47*) in CH_2Cl_2 at a platinum button. From the measured magnetic susceptibilities and the observed visible spectra, the first

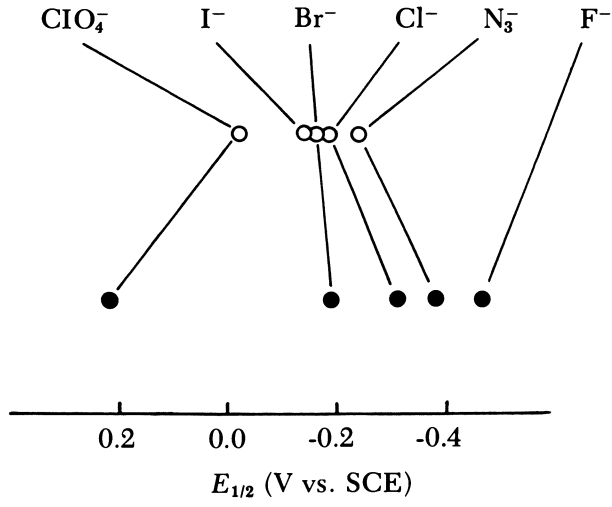

Figure 3. Plot of half-wave potentials for electroreduction of TPPFeX (●) and TPPMnX (○) in CH_2Cl_2 containing 0.1 M TBAP.

electrooxidation process was assigned as metal-centered, formally producing an iron(IV) species. Oxidation of $TPPFeClO_4$, TPPFeBr, and TPPFeCl in CH_2Cl_2 all occurred (*33*) at approximately the same potential (1.08 ± 0.3 V). Recent measurements (*48*) on twelve different TPPFeX complexes confirmed these results. The TPPFeX oxidation potential did not vary with changes in X when $E_{1/2}$ was measured in CH_2Cl_2 (*44*, *49*). Similar results were obtained in six different nonaqueous solvents. These data are summarized in Table III and call into question the iron(IV) assignment. The strong dependence of the iron(III) reduction potential, and the independence of the iron(III) oxidation potential, on the type of counterion strongly suggests that the site of oxidation is ring centered. Because redox potentials alone are insufficient to differentiate between the assignment, a reinvestigation of this system was needed. This task indicated (*50*) that, for TPPFeX at least, oxidation indeed yields an iron(III) radical.

Solvent Effects. Half-wave potentials for the reduction of a number of TPPFeX complexes at a platinum electrode were reported (*51*). When $X = Cl^-$, OAc^-, and SCN^-, the potentials observed in DMF were −0.20, −0.20, and +0.04 V, respectively. Potentials of −0.34, −0.21, and +0.14 V were reported (*33*) for reduction of TPPFeX in CH_2Cl_2, where $X = Cl^-$, Br^-, and ClO_4^-. When $X = Cl^-$, TPPFeX was reduced at −0.09 V in DMSO (*12*). Based on these initial studies, it was concluded that coordinating solvents shifted the

Published on June 1, 1982 on http://pubs.acs.org | doi: 10.1021/ba-1982-0201.ch013

Table III. Half-Wave Potentials[a] for Oxidation of TPPFeX in Selected Solvents

	Solvent				
Counterion	CH_2Cl_2[a]	$EtCl_2$[b]	C_6H_5CN[b]	$PrCN$[b]	$(CH_3)_2CO$[b]
BF_4^-	1.10[c]	—	—	—	—
ClO_4^-	1.09, 1.11[b]	1.13	1.13	1.24	1.17
I^-	1.09	—	—	—	—
NO_3^-	1.10	—	—	—	—
SO_4^{2-}	1.11	—	—	—	—
Br^-	1.10, 1.18[b]	1.17	1.14	1.14	1.17
Cl^-	1.11, 1.14[b]	1.17	1.16	1.16	1.17
NCS^-	1.10	—	—	—	—
OPh^-	1.08	—	—	—	—
$p\text{-}CH_3C_6H_4SO_3^-$	1.11	—	—	—	—
HSO_4^-	1.09	—	—	—	—
N_3^-	1.08, 1.18[b]	1.12	1.13	1.15	1.16
F^-	1.09, 1.15[b]	1.15	1.13	1.10	—

Note: Except where noted, values are taken, uncorrected for liquid junction potentials, from Ref. *48*.
[a] Potentials are referenced to the SCE.
[b] Values are taken, uncorrected for liquid junction potentials, from Ref. *44*.
[c] Value is taken, uncorrected for liquid junction potentials, from Ref. *87*.

iron(III) reduction potential in a positive (anodic) direction, whereas strongly coordinating anions shifted the potential in a negative (cathodic) direction. Later studies (*26, 44, 49, 52–54*) concentrated on the reduction of (*p*-R)TPPFeCl in various solvents. The unsubstituted complex was reduced (*26*) at −0.11, −0.11, and −0.15 V in DMSO, DMA, and DMF, respectively. In very weakly coordinating solvents such as CH_2Cl_2 or butyronitrile, the half-wave potentials shifted to −0.29 and −0.32 V. These results seemed to confirm the earlier postulate that coordinating solvents shifted half-wave potentials in a positive direction. In this instance, solvent coordination to the iron(II) center was presumed responsible for the direction of the potential shift resulting in preferential stabilization of the iron(II) form over iron(III).

Recent studies (*44, 49, 54*) clearly demonstrated the interacting effects of axially bound solvent molecules and axially coordinated monovalent anions and their influence on the iron(III) redox potential. This interaction was elucidated with a systematic variation of five different anions bound to OEPFeX and TPPFeX and measurement of their respective redox reactions in twelve different nonaqueous solvents.

Table IV lists the potentials observed for reduction of TPPFeX in nonaqueous media. In all but two solvents, the potential shifts in a negative direction as the strength of the iron–counterion bond increases. However, the magnitude of the potential shift is solvent dependent. The potential difference ($\Delta E_{1/2}$) between reduction of TPPFeF and $TPPFeClO_4$ is 720 mV in CH_2Cl_2, 580 mV in PrCN, 450 mV in DMF, and 0.0 V in DMSO and pyridine. This behavior is a function of the inherent ability of the solvent to coordinate to the iron(II) center (the reduction product) and the solvent's ability to displace the counterion from the iron(III) center. These phenomena are operative simultaneously. For example, in DMF the reduced iron(II) species is coordinated weakly by one solvent molecule. One would expect a small positive potential shift as a result. However, DMF also is able to displace ClO_4^- from the iron(III) center ($\beta_2 = 9 \times 10^4 M^{-2}$) (*44*), shifting the reduction potential of this species in a negative potential direction. The net result is a decrease in $\Delta E_{1/2}$ (as compared to CH_2Cl_2) and reflects a change in the structure of both the reactant and product. In DMF, $\Delta E_{1/2}$ between the starting species, when X = F^- and ClO_4^-, is actually the potential difference between reduction of TPPFeF and $TPPFe(DMF)_2^+ClO_4^-$ to the common product TPPFe(DMF). In depth evaluations have been worked out for each solvent (*44, 49, 54*).

The solvent dependence on $E_{1/2}$ for a given X also is not as straightforward as implied from earlier studies. Figure 4 is a plot of the reduction potential of TPPFeX vs. the Gutmann donor number (*55*) for each

Published on June 1, 1982 on http://pubs.acs.org | doi: 10.1021/ba-1982-0201.ch013

Table IV. Half-Wave Potentials for the Electroreduction of TPPFeX at a Pt Electrode in Selected Solvents

Solvent	*Gutmann Donor Number*[a]	*Counterion, X*						
		ClO_4^-	Br^-	SCN^-	Cl^-	OAc^-	N_3^-	F^-
$EtCl_2$	0.0	0.24	−0.19	—	−0.31	—	−0.38	−0.47
CH_2Cl_2	0.0	0.22	−0.21	—	−0.29	—	−0.42	−0.50
CH_3NO_2	2.7	0.10	—[b]	—	—[b]	—	—[b]	—[b]
ϕ-CN	11.9	0.20	−0.18	—	−0.34	—	−0.39	−0.57
CH_3CN	14.1	0.11	—[b]	—	—[b]	—	—[b]	—[b]
PrCN	16.6	0.13	−0.15	—	−0.27	—	−0.33	−0.45
$(CH_3)_2CO$	17.0	0.09	−0.16	—	−0.28	—	−0.34	−0.43
THF	20.0	0.17	−0.24	—	−0.34	—	−0.38	−0.47
DMF	26.6	−0.05	−0.05	0.04[c]	−0.18	−0.20[c]	−0.25	−0.40
DMA	27.8	−0.04	−0.05	—	−0.15	—	−0.24	−0.36
DMSO	29.8	−0.09	−0.09	—	−0.10	—	—[d]	−0.09(−0.40)[e]
Py	33.1	0.15	0.17	—	0.16(−0.25)[e]	—	0.15(−0.28)[e]	0.16(−0.46)[e]

Note: All solvents were 0.1 *M* in tetrabutylammonium perchlorate. Potentials are uncorrected for liquid potentials and are referenced against the SCE. Unless noted, these data are taken from Refs. *44* and *49*.

[a] Taken from Ref. *89*.

[b] Complex was insoluble in solvent system.

[c] Taken from Ref. *51*.

[d] Two different electrode processes were overlapped (*44*).

[e] Second reduction process (*44*).

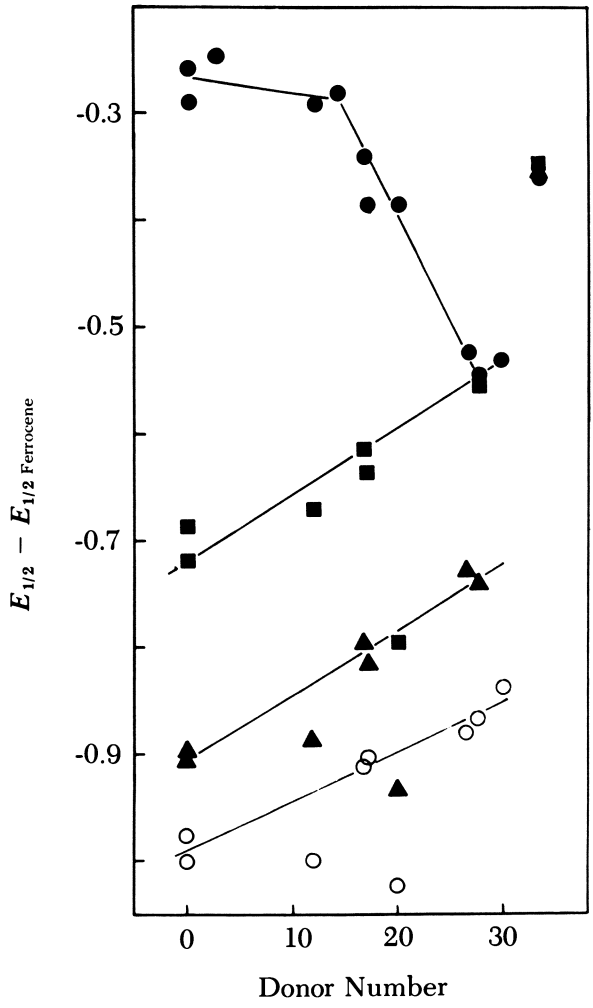

Figure 4. Half-wave potential dependence on the solvent donicity for TPPFeX. Key: ●, X = ClO_4; ■, X = Br^-; ▲, X = N_3^-; and ○, X = F^-. (Reproduced from Ref. 44. Copyright 1981, American Chemical Society.)

solvent for X = ClO_4^-, Br^-, N_3^-, or F^-. To eliminate differences in liquid junction potential contributions (*56, 57*) (l.j.p.) arising between one solvent and another, the potentials were referenced against the measured value of the ferrocene/ferrocinium ion couple (*58, 59*) in each solvent. The results obtained, and the differences between complexes where X = ClO_4^- and X = Br^-, N_3^-, or F^-, lucidly demonstrate the interacting effects of solvent and counterion on the electrode reactions of iron(III) and iron(II) porphyrins.

In solvents of donicity up to ~15, the potential for reduction of $TPPFeClO_4$ (Figure 4) remained essentially constant. This finding suggests that in these solvents, ClO_4^- is bound to the iron(III) center and that there is either weak or no direct interaction between the solvent and the iron. Independent NMR experiments (*60*) confirmed that ClO_4^- is axially coordinated in CH_2Cl_2. As the solvent donicity increases from 15, the iron(III)/iron(II) potential shifts negatively with increased donor number. Pyridine is an exception to this trend, with an observed potential 250 mV more positive than would be predicted.

In marked contrast to the effect of solvent on $TPPFeClO_4$ reduction, potentials of TPPFeX reduction (where X = Br^-, Cl^-, N_3^-, and F^-) are shifted in a positive potential direction by coordinating solvents. As is depicted in Figure 4 for X = Br^-, N_3^-, and F^-, the most negative potentials occurred in nonbonding solvents [tetrahydrofuran (THF) excepted] and the most positive redox potential was observed in pyridine. The magnitude and direction of the potential shift with solvent indicate a strong stabilization of iron(II) relative to iron(III). Stability constant measurements of TPPFe and TPPFeCl confirm this observation. The value of $\log \beta_2$ for axial ligand binding to iron(II) in CH_2Cl_2 is 7.45 (*61*) to 7.8 (*62*) for pyridine and 0.53 for DMF (*61*). In contrast, TPPFeCl binds pyridine weakly and DMF does not bind pyridine at all.

The lack of fit by pyridine to the trends observed for all of the complexes investigated may be an inherent property of the metal–donor atom interaction or it may result from a change in coordination sphere that is different in pyridine from all of the other solvents investigated. It is not due to errors in liquid junction potential correction because deviations from the predicted potential also are observed for the reaction TPP Co(III) $\rightleftharpoons$ TPP Co(II). In the latter case, the potential observed in pyridine is greater than 350 mV more negative than would be predicted from an $E_{1/2}$ vs. donor number plot. The deviation of potential in THF for X = Br^-, Cl^-, N_3^-, and F^-, but not for ClO_4^-, also has been discussed. Such deviations from linearity indicate possible differences in chemistry for a given compound and suggest further experiments regarding its characterization.

The interdependence of type of solvent and counterion on the iron porphyrin redox potentials depends also on the basicity of the porphyrin ring. This effect readily is seen from a comparison of the redox potentials of OEPFeX and TPPFeX as a function of solvent (*see* Table V). In CH_2Cl_2, the increase in the preferential stabilization of iron(III) by variation in X for OEPFeX parallels that observed for TPPFeX. The reduction of OEPFeF is 730 mV more cathodic than the reduction of $OEPFeClO_4$, which compares favorably with a potential difference of 720 mV observed for TPPFeX. The absolute difference of potential

Published on June 1, 1982 on http://pubs.acs.org | doi: 10.1021/ba-1982-0201.ch013

Table V. Comparison of Half-Wave Potentials for the Fe(III) to Fe(II) Reduction of OEPFeX and TPPFeX in Selected Solvents

		Counterion				
Solvent[a]	*Complex*	ClO_4^-	Br^-	Cl^-	N_3^-	F^-
CH_2Cl_2	$TPPFe^+$	0.22	−0.21	−0.29	−0.42	−0.50
	$OEPFe^+$	0.10	−0.34	−0.42	−0.52	−0.63
	$\Delta E_{1/2}$[b]	0.12	0.12	0.13	0.10	0.13
DMF	$TPPFe^+$	−0.05	−0.05	−0.18	−0.25	−0.40
	$OEPFe^+$	−0.18	−0.22	−0.34	−0.45	−0.64
	$\Delta E_{1/2}$[b]	0.13	0.17	0.16	0.20	0.24
Py	$TPPFe^+$	0.15	0.17	0.16(−0.25)[c]	0.15(−0.28)[c]	0.16(−0.46)[c]
	$OEPFe^+$	−0.04	−0.03	−0.03	−0.03(−0.52)[c]	−0.04(−0.57)[c]
	$\Delta E_{1/2}$[b]	0.19	0.20	0.19	0.18	0.20

Note: Taken from Ref. *88*.

[a] All solvents were 0.1 *M* in tetrabutylammonium perchlorate. Potentials are uncorrected for liquid junction potentials and are referenced against the SCE.

[b] $\Delta E_{1/2} = E_{1/2(TPPFeX)} - E_{1/2(OEPFeX)}$.

[c] $E_{p,c}$ (cathodic peak potential) of second cathodic process (*44*).

between TPPFeX and OEPFeX for a given counterion is a constant 0.12 ± 0.01 V in this solvent.

In pyridine, solvent molecules displace the counterion, yielding hexacoordinated iron(III) reactants and iron(II) products at the electrode. Identical potentials are observed for all counterions for a given porphyrin moiety. The absolute potential difference between $TPPFe(py)_2^+ X^-$ and $OEPFe(py)_2^+ X^-$ for a given X is a constant 0.19± 0.01 V. In CH_2Cl_2, all species of OEPFeX or TPPFeX have pentacoordinated iron centers. In pyridine, all species of $OEPFe(py)_2^+ X^-$ and $TPPFe(py)_2^+ X^-$ have hexacoordinated, in-plane iron centers. Because OEP is a more basic porphyrin moiety, the increased electron density at the core nitrogens would be expected to result in more difficult reductions than for TPP. Also, nitrogen σ-orbital overlap with iron *d*-orbitals is substantially higher with in-plane iron centers as compared to their out-of-plane counterparts. Therefore, an enhancement of the effect of porphyrin ring basicity on the redox potential would be expected for metal-centered electron transfers with an in-plane iron compared to an out-of-plane iron center. The absolute potential differences (0.12 V in CH_2Cl_2 and 0.19 V in pyridine) apparently bear this out.

In the weakly coordinating solvent DMF, the potential shift of OEPFeF with respect to $OEPFeClO_4$ is 460 mV, 110 mV larger than observed for the TPPFeX counterparts. A diminished log β_2 for addition of two DMF molecules to $OEPFeClO_4$ could account easily for the potential differences observed between the two porphyrin moieties. In contrast to the trends observed in CH_2Cl_2 and pyridine, the absolute potential differences ($\Delta E_{1/2}$) between TPPFeX and OEPFeX for a given counterion depend on X and ranges from 0.13 to 0.24 V. At this time, it is not clear if the variability in $\Delta E_{1/2}$ is due to changes in metal spin state, changes in axial ligation, or changes in the iron–porphyrin plane distance. However, these results clearly demonstrate that the effects of counterion, solvent, and porphyrin structure must be considered collectively when designing a new molecule with desired redox potentials.

Nitrogenous Base Effects. The type and degree of axial ligation have a dramatic effect on the redox potential of iron porphyrins (*3–5, 42, 44, 49, 54, 62, 63*). The nature and magnitude of this effect also depend on the porphyrin ring structure, the solvent system, the valence and spin states of the iron center, and on the presence or absence of any coordinating anions. Historically, two approaches have been used to study the dependence of $E_{1/2}$ on metalloporphyrin complexation. First, a desired adduct is isolated and then $E_{1/2}$ is determined for this species under a set of rigidly controlled experimental conditions. Care must be taken to ensure that the species being oxidized or re-

duced at the electrode is the adduct and not a new species generated by reaction of the electrolyte medium and the solute. This method only permits the determination of $E_{1/2}$ and the electron transfer reversibility. An alternative approach is to generate the desired adduct in situ. A selected metalloporphyrin reagent is transformed into the desired adduct via a set of continuously varying experimental conditions (e.g., increasing the concentration of the ligand). Shifts in the redox potential over the range of experimental conditions permit the determination of reaction stoichiometries for all species encountered. In addition, formation constants often can be computed directly from the potential data. This second approach, although much more complicated than the first method, allows the investigator to determine the chemistry of the metalloporphyrin in the absence of an electron transfer. Numerous equations relating complex stabilities to potential data have been derived (*64*). The Lingane solution, however, is the equation most often used in the metalloporphyrin area and is outlined as follows.

For the generalized metalloporphyrin electron transfer

$$[\mathrm{PM}]^{m+} + ne \rightleftharpoons [\mathrm{PM}]^{(m-n)} \tag{8}$$

complexation reactions often are observed for the oxidized species, the reduced species, or both. Changes in axial coordination concomitant with electron transfer can be evaluated from potential shifts as the ligand concentration is varied. Anodic or cathodic shifts in potential from that observed for the uncomplexed species depend on the stoichiometry of the oxidized and/or reduced complex, the concentration of free ligand in solution, and the magnitudes of the formation constants of the oxidized and/or reduced complex(es). Where the oxidized species forms a complex when the reduced form does not, the magnitude of the potential shift can be predicted by

$$\Delta E_{1/2} = (E_{1/2})_c - (E_{1/2})_s = -\frac{0.059}{n} \log \beta_{ox} - \frac{0.059}{n} (p) \log [\mathrm{L}] \tag{9}$$

at 25°C where $(E_{1/2})_c$ and $(E_{1/2})_s$ are the half-wave potentials of the complexed and uncomplexed oxidized species, respectively; β_{ox} is the formation constant of the oxidized complex; [L] is the free concentration of the complexing ligand; p is the number of ligands bound to the oxidized species; and n is the number of electrons transferred in the diffusion-controlled reaction, ox + $ne \rightleftarrows$ red.

Similarly, when the reduced form reacts with ligand and the oxidized form does not, a more easily reducible species results. The magnitude of the potential shifts in this case are predicted by

$$\Delta E_{1/2} = \frac{0.059}{n} \log \beta_{red} + \frac{0.059}{n} (q) \log [L] \quad (10)$$

at 25°C where β_{red} is the formation constant of the complex and q equals the number of ligands that are coordinated in the complex. Finally, where both species at the electrode are complexed, the potential shifts are predicted by

$$\Delta E_{1/2} = - \frac{0.059}{n} \log \left(\frac{\beta_{ox}}{\beta_{red}} \right) - \frac{0.059}{n} (p - q) \log [L] \quad (11)$$

Investigations of ligand binding to the highly air-sensitive iron(II) porphyrins can be performed readily by employment of electrochemical methodologies. The iron(II) species may be generated at the electrode and its coordination chemistry may be explored with the only necessary precaution being maintenance of a deoxygenated solution. When iron(I) porphyrins do not bind axial ligands (*51*, *65*), product stoichiometry and the adduct formation constant can be determined readily from potential shifts as defined in Equation 9. Determination of the ligand binding characteristics of iron(III) porphyrins with electrochemical methodologies are generally slightly more complicated. Most ligands that coordinate to iron(III) also coordinate to iron(II), but in many instances the stoichiometry depends on the ligand concentration. When large differences in formation constants for iron(III) and iron(II) exist, Equations 9 and 10 may be utilized over a limited range of ligand concentrations. In the most extreme case, determination of the binding properties of iron(III) electrochemically necessitates a prior study of the reactivity of the corresponding iron(II) species with the ligand under study (*see* Equation 11).

Iron porphyrins form both monoaxial and diaxial adducts with nitrogenous bases. In most instances, the formation constant for addition of the first axial ligand is one to two orders of magnitude less than for addition of the second axial ligand (*66*). The observation of only diadduct formation manifests this condition. However, monoadducts have been observed in some instances, especially with sterically hindered ligands (such as 2-methylimidazole). Adduct formation with this type of ligand causes both the iron(III) and iron(II) centers to be pulled up to 0.5 Å out of the porphyrin plane (*67*). Ironically, the label "sterically hindered" applies only to the iron(II) adduct where only pentacoordinated complexes have been observed. Both pentacoordinated and hexacoordinated complexes are observed for iron(III), but with decreased formation constants as compared to their unhindered counterparts.

Modern electrochemical techniques to measure the relative sta-

bility constants and half-wave potentials for iron(III)/iron(II) containing axially complexed nitrogenous bases in nonaqueous media were first used (*51*) in 1974. In this study, TPPFeX and the iron(III) complex of deuteroporphyrin IX dimethyl ester were utilized as the starting porphyrin. Di(ligand) adducts were formed with either simple imidazole (Im) addition or by preparation of a heme peptide containing di-*l*-histidine. The results depended on the counterion. When OAc^- or Cl^- were the counterions, complexation by imidazole to both iron(III) and iron(II) produced an anodic shift of the standard potential from that of PFeX (P = porphinato) by approximately 80 to 120 mV. When X = SCN^-, however, the potential was shifted in a cathodic direction by approximately 100 mV from the starting potential. This shift, which was not explained at the time, is now better understood in terms of the counterion effect for PFeX potentials. Potentials for reduction of $PFe(L)_2^+ X^-$ will be relatively constant for a given value of X and those for PFeX can vary by up to 720 mV. The direction of the shift for X = Cl^- and OAc^- indicates a greater stability for iron(II) than for iron(III), and the potential shift for X = SCN^- indicates an opposite relative stability. The value of $\log \beta_2$ for TPP $Fe(Im)_2$ virtually is independent of counterion ($\log \beta_2 = 7.1 \pm 0.3$ in DMF). Because the iron(III) complexation reaction involves halide displacement,

$$PFeX + 2\,L \rightleftharpoons P\,Fe(L)_2^+\,X^- \qquad (12)$$

$\log \beta_2$ for this species will vary as a function of both X and the binding strength of the ligand.

Changes in axial ligation with an aim toward modification of redox behavior can be accomplished in a straightforward fashion once the binding strength of all coordinating species in solution is known. The relationship between ligand binding strength and $E_{1/2}$ was best shown in a recent paper (*62*). Current–voltage curves were obtained for axial adducts of TPPFe with eleven substituted pyridines ranging in pK_a from 0.67 to 9.71. For all of the ligands, the potentials of the iron(III) reduction and the iron(II) reduction were related linearly to the pK_a of the ligand. For solutions of TPPFe containing 1.0 *M* ligand, the most positive reduction potential occurred for $TPPFe(L)_2$ where L = 3,5-dichloropyridine ($E_{1/2}$ = 1.38 V, $\log \beta_2 = 5.5$) and the most negative potential occurred for L = 4-picoline ($E_{1/2} = -1.55$ V, $\log \beta_2 = 8.3$). The most positive iron(III) reduction potential occurred for $TPPFe(L)_2^+$ where L = 3,5-dichloropyridine ($E_{1/2}$ = 0.31 V, $\log \beta_2 = 3.4$) and the most negative potential occurred for L = 4-(dimethylamino)pyridine ($E_{1/2} = -0.17$ V, $\log \beta_2 = 16.3$). Thus, by variation of the substituted pyridine axially bound to the iron center the reduction was tuned over a 480-mV range for iron(III) and greater

than 170 mV for iron(II). Similar potential shifts were obtained (*62*, *68*) for OEPFe, but the potentials for a given pyridine adduct were shifted as a result of porphyrin basicity effects.

Diatomic Ligand Effects. Axial ligands that possess π-acceptor properties have received comparatively limited attention from electrochemists even though carbonyl (*68–70*), nitrosyl (*71–75*), cyanide (*1*), dioxygen (*76–78*), and thiocarbonyl (*79*, *80*) complexes have been studied intensively spectroscopically. This neglect is surprising because the only requisite for the study of the redox chemistry of iron porphyrins in the presence of gaseous diatomics is the changing of the composition of the atmosphere above the solution. The ability of these π-acceptor ligands to alter dramatically the energies of metal *d*-orbitals can result in oxidation–reduction reactions quite different from corresponding halide or nitrogenous base complexes. A notable example of this ligand effect was the observation (*81*, *82*) that coordination of carbon monoxide can change the site of oxidation from metal centered in the dipyridine complex of ruthenium(II) tetraphenylporphyrin to a ring-centered oxidation in the carbonyl complex. The following discussion presents an overview of those factors that affect oxidation–reduction potentials and electron transfer mechanisms in π-acceptor complexes of metalloporphyrins and the implication for redox tuning in iron systems.

Nitrosyl (NO) complexes of iron(II) porphyrins are among the best characterized and most stable of the diatomic adducts. Both TPPFeNO and OEPFeNO are low spin $S = \frac{1}{2}$ systems that are pentacoordinated in CH_2Cl_2. Reversible one-electron oxidations and reductions are observed in cyclic voltammetry with approximately the same potential differences between the OEP and TPP rings as found in other derivatives (*83*, *84*). Stabilization of the +2 oxidation state by nitric oxide is evident from comparison with iron(III)/iron(II) potentials for halide or dipyridine complexes (Table VI). This property is reflected in the relative inertness toward air oxidation of the nitrosyl. Nitric oxide and thiocarbonyl complexes have the most positive oxidation potentials of any reported ferrous porphyrins.

Iron carbonyl (CO) complexes are oxidized irreversibly whether hexacoordinated as in EtioFe(CO)(Im) and OEPFe(CO)(py) or pentacoordinated as in TPPFeCO. The $[FeCO]^+$ unit is thus considerably more labile than $[FeNO]^+$ and even weakly coordinating anions such as ClO_4^- can displace CO. At −37°C and scan rates of 10 V/s, however, reversible oxidation–reduction waves are seen and the equilibrium between the mono- and dicarbonyl can be detected (*84*, *85*).

Although axial coordination of one of the diatomic π-acceptor ligands shifts the iron (II)/iron(III) oxidation anodically from 500 to 1270 mV, no parallel trends are apparent for reduction of the diatomic

Table VI. Half-Wave Potentials for Oxidation and Reduction of Several Ferrous Porphyrin Complexes with Diatomic Molecules, in Dichloromethane

Complex	*Diatomic Ligand*	*Trans-Ligand*	$E_{1/2(ox)}$	$E_{1/2(red)}$
TPPFe	NO	—	0.74[a,b]	−0.93[b]
	CO	—	0.60[b,c]	−1.22[b]
	NO	py	0.54[a,c]	−0.98[b]
	CO	py	0.50[a,d]	—
	CO	Im	0.38[a,c]	—
OEPFe	NO	—	0.60[b,d]	−1.10[b]
	CS	—	0.73[d]	—
	NO	py	0.57[c,d]	—
	CO	py	0.43[c,d]	—
	CS	py	0.58[d]	—
	CS	N-MeIm	0.52[d]	—
	CS	pip	0.58[c,d]	—
EtioFe	CO	Im	0.32[c,e]	—

Note: All potentials vs. SCE.
[a] Taken from Ref. 3.
[b] Taken from Refs. 83 and 84.
[c] Irreversible reduction. The value presented in the anodic peak potential, $E_{p,a}$.
[d] Taken from Ref. 79.
[e] Taken from Ref. 82.

complexes. In the carbonyl adduct, the iron(II)/iron(I) potential is shifted cathodically by 160 mV from uncomplexed TPPFe(II), reflecting a stabilization of iron(II) over iron(I). In the nitrosyl adduct, however, reduction occurs at −0.93 vs. −1.07 V for TPPFe(II) and −1.52 V for $TPPFe(py)_2$. The relative ease of reduction indicates that not only is iron(II) stabilized by coordination to NO, but that what is at least formally an iron(I) state is stabilized to an even greater extent. This behavior is highly unusual because iron(I) porphyrins normally do not coordinate axial ligands. This observation is not too surprising, however, because other d^7-ions [such as Co(II)] bind nitric oxide extremely well. Further efforts to isolate and characterize the $[FeNO]^-$ and $[FeCO]^-$ species are now in progress.

The odd electron in TPPFeNO is known from electron spin resonance (ESR) to occupy a bonding orbital with both Fed_{z^2} and σ_N character (*71*). Occupation of this orbital requires a bent Fe–N–O fragment to remove the degeneracy of the ligand π^*-orbitals and provide an orbital suitable for overlap with the d_{z^2}. The Fe–N–O bond angle is approximately 140° in several crystal structures of iron(II) nitrosyls (*73*, *74*).

Reduction of TPPFeNO should place a second electron in this σ-bonding orbital, which will be delocalized substantially onto the

ligand. Evidence from cyclic voltammetry is consistent with this view in that nitric oxide remains bound to the metal and $[FeNO]^-$ is stabilized relative to TPPFe(I). Oxidation of TPPFeNO removes the single unpaired bonding electron to give spin-paired $[FeNO]^+$, which is isoelectronic with Fe(II)CO. Both of these complexes are labile and require a positive pressure of NO or CO to ensure coordination in solution.

The considerably greater stability of diatomic molecule adducts of second and third row transition metals is due to enhanced π-backbonding. M(II)/M(III) potentials for ruthenium and osmium nitrosyl porphyrins are about +1.0 V and the oxidized products even can be chromatographed and recrystallized in air (79). Cyclic voltammetry of ruthenium and osmium carbonyl porphyrins yields reversible, one-electron oxidations, unlike their iron counterparts. Thiocarbonyl adducts of Fe, Ru, and osmium porphyrins are oxidized reversibly at a platinum electrode, manifesting the increased σ-donor, π-acceptor properties of CS compared with CO.

The use of electrochemical means to generate new oxidation states of diatomic molecule complexes of metalloporphyrins can provide valuable insights into structure–bonding relationships. A series such as $[FeNO]^+$, FeNO, and $[FeNO]^-$ porphyrins is uniquely suited to probing the metal–ligand oxidation states that lie between those of the porphyrin ring.

Tuning of $E_{1/2}$

Previous attempts at developing quantitative relationships between a given factor and the observed $E_{1/2}$ have been somewhat successful, as just detailed. The redox potential of a new iron porphyrin can be predicted with a reasonable degree of accuracy using these relationships, if and only if the experimental conditions originally used in developing the model are maintained rigorously. This constraint has limited use of these relationships because often the new compound cannot be studied under the prescribed conditions (e.g., due to insolubility or instability). A second limitation is that most relationships developed heretofore were highly specific. Redox potential predictions for new molecules were inaccurate because the complex did not belong to the limited class governed by the model. Finally, the models were constructed based on the assumption that their influence on $E_{1/2}$ was unrelated to all other factors. The previous discussion clearly demonstrates the fallacy of this approach.

Models that would incorporate the influences of all significant factors and their interactions on the observed potential would be highly desirable. We have undertaken the construction of such models. Our initial goal is to develop a quantitative description of the influence

of axial ligation, solvent coordination, and porphyrin ring structure on ferrous porphyrins. This choice is based in part on the biological implications of electron transfer reactions involving iron(II) porphyrins and in part on the wealth of information presently available on its redox chemistry.

A previous study (62) reported a linear relationship between the pK_a of the nitrogen donor atom for several substituted pyridines axially ligated to TPPFe(II) and the reduction potential observed in CH_2Cl_2 which was 1.0 *M* in ligand. The linear least-squares best-fit equation was

$$E_{1/2} = 0.0260(pK_a) - 1.38 \quad (13)$$

Additionally, formation constants for addition of two such ligands were computed and also were related linearly to pK_a

$$\log \beta_2 = 0.440(pK_a) + 5.40 \quad (14)$$

Insertion of the latter relationship and $(E_{1/2})_s$ into Equation 9 yields

$$(E_{1/2}) = -0.0260(pK_a) - 0.118 \log C_L - 1.38 \quad (15)$$

This expression quantitatively describes the potential range over which the reduction of $TPPFe(L)_2$ can be tuned simply by varying the type of substituted pyridine and its concentration. The constraints on this equation are first, that the ligand used must be a nonsterically hindered substituted pyridine (as well as piperidine or aniline) with limited π-donor or acceptor ability; second, that the ligand concentration range must be between 3×10^{-3} and 3.0×10^{0} *M*. Figure 5 depicts these relationships with the "tunable region" contained inside the dotted portion. Accessible potentials lie between −1.06 [the potential of the uncomplexed TPPFe(II)] and −1.63 V [the reduction of the Fe(I) species to the radical]. This plot shows the large number of ligand-type and concentration combinations that might be used to obtain an iron porphyrin with a desired iron(II) reduction potential.

For example, suppose an iron(II) porphyrin complex that has a reduction potential of −1.40 V is desired. The isopotential line segment labeled −1.40 in Figure 5 relates all possible ligand pK_a values and bulk ligand concentrations that will produce an iron(II) complex electroreducible in CH_2Cl_2 at a platinum electrode at −1.40 V. This condition can be achieved by making a 1.0 m*M* TPPFe solution 0.632 *M* in 3-bromopyridine ($pK_a = 2.84$), 0.102 *M* in pyridine ($pK_a = 5.28$), or 0.011 *M* in 4-(dimethylamino)pyridine ($pK_a = 9.71$).

Expansion of this model to include the influence of changes in porphyrin ring basicity on the observed reduction potential is accom-

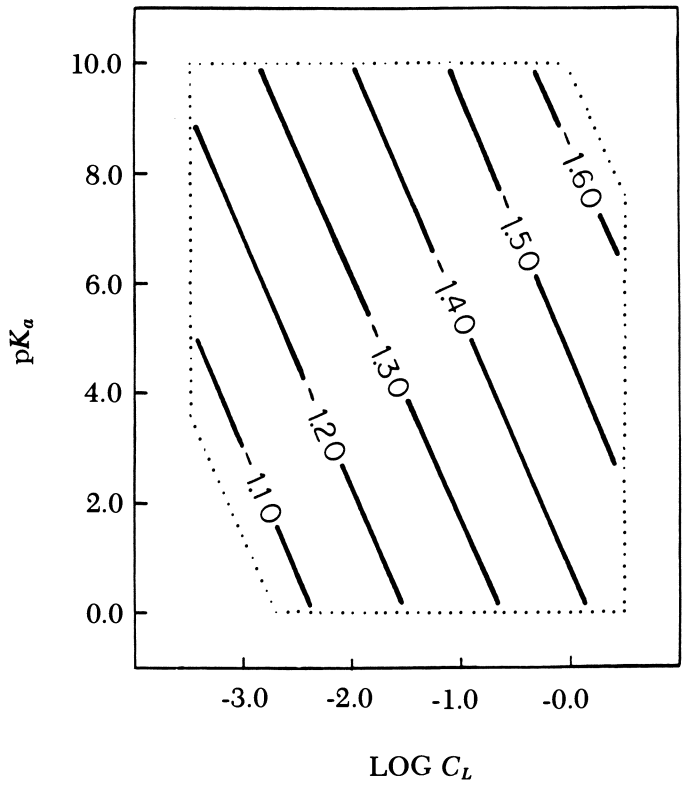

Figure 5. Plot depicting the tunable potential range for electroreduction of TPPFe(L)$_2$ in CH_2Cl_2 as a function of the type of substituted pyridine as measured by its pK_a *value and its bulk concentration. Numbered line segments correspond to* pK_a, *log* C_L *combinations, which result in the indicated potential.*

plished in a straightforward fashion. Previous studies on porphyrin substituent effects showed that the following equation can be used to predict the potential of (*p*-R)TPPFe reduction in CH_2Cl_2:

$$E_{1/2_R} = 0.068(4\sigma) + E_{1/2_H} \quad (16)$$

Incorporation of this relationship into the model yields

$$E_{1/2_{R,C}} = 0.068(4\sigma) - 0.0260(pK_a) - 0.118 \log C_L - 1.38 \quad (17)$$

where $E_{1/2_{R,C}}$ denotes the half-wave potential for reduction of the axially complexed, phenyl ring substituted TPPFe(II) complex. The constraints imposed on this model are identical to those previously encountered and assume that changes in porphyrin basicity impacts

$E_{1/2}$ and the formation of axial adducts equally. Figures 6 and 7 depict two representations of Equation 17. In Figure 6, the tunable region is shown over which the potential for reduction of (p-R)TPPFe(py)$_2$ can be varied by appropriate selection of phenyl ring substituent and bulk pyridine concentration. Figure 7 depicts the tunable region over which the potential for reduction of (p-R)TPPFe(L)$_2$ can be varied at a ligand concentration of 1.0 M by appropriate selection of phenyl ring substituent and type of ligand.

Summary

The results presented in this chapter show that half-wave potentials for TPPFeX reduction depend on the nature of the counterion, the porphyrin ring structure, the presence of coordinating ligands, and the donicity of the solvent. The type of counterion associated with iron(III) and iron(II) is the most predominant factor governing the type of elec-

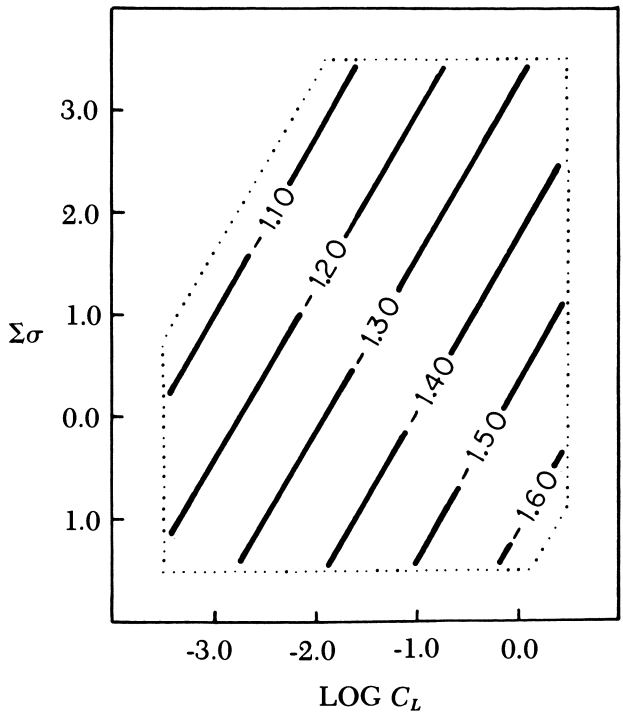

Figure 6. Plot depicting the tunable potential range for electroreduction of (p-R)TPPFe(py)$_2$ in CH_2Cl_2 as a function of the phenyl ring substituent, R (as measured by the Hammett σ-value) and the bulk concentration of pyridine. Numbered line segments correspond to the substituent constant (σ), log C_L combinations, which result in the indicated potentials.

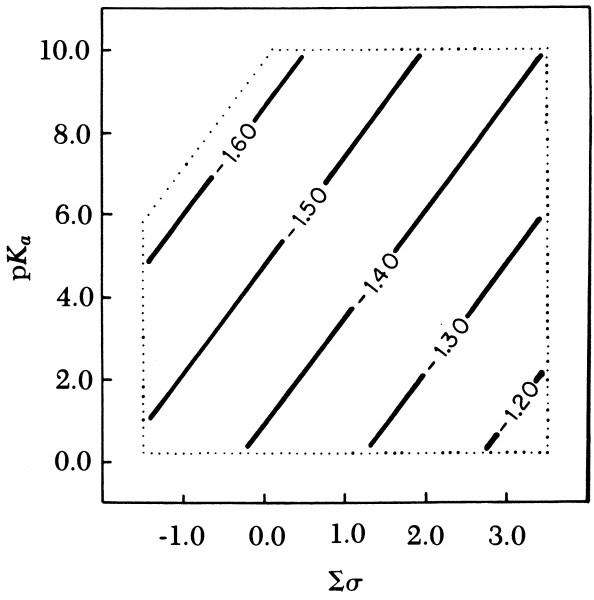

Figure 7. Plot of the tunable potential range for electroreduction of (p-R)TPPFe(L)$_2$ in CH_2Cl_2 as a function of the type of substituted pyridine (as measured by its pK$_a$) and the phenyl ring substituent (as measured by the Hammett σ-value) at a bulk ligand concentration of 1.0 M. Numbered line segments correspond to the ligand pK$_a$, substituent constant combinations, which result in the indicated potentials.

tron transfer mechanism observed for electroreduction of iron porphyrins (*44*). In a nonbonding solvent, the redox potential of the iron(III)/iron(II) couple can be tuned over a 720-mV potential range by appropriate selection of the iron(III) counterion. This range, as well as the stoichiometry of both the electrode reactant and product, can be modified by changing the solvent in which the redox reactions are carried out. Complexation by anions or nitrogenous bases produces a 1400-mV tunable potential range by modification of the electrode reactant and product.

For a complete understanding of the influence of each factor, the electrode mechanism must be defined clearly in each solvent. A general redox mechanism, which shows all observed counterion and solvent association to iron(III) and iron(II), is depicted in Figure 8 where L denotes either a nitrogenous base or solvent molecule. In solvents of donor number less than 12, the electrode reactant is TPPFeX, which may be reduced to either $[TPPFeX]^-$ or TPPFe depending on the nature of X. In solvents with donor number between 12 and 29, the product is $[TPPFeX]^-$, TPPFeL, or $[TPPFeX(L)]^-$. These products

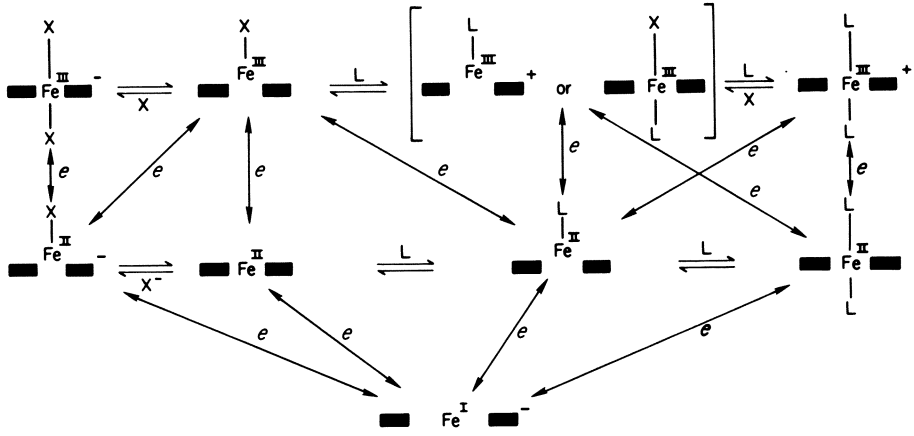

Figure 8. Schematic of electron transfer pathways for electroreduction of Fe(III) porphyrin.

may be transient intermediates depending on the nature of X and can convert to TPPFe(L) as the ultimate product. In solvents with a donor number greater than 29 (such as py) disolvent adducts as well as the mixed ligand adducts are formed for both the reactant and product. In DMSO, when the counterion is F^-, the electrode reactant is $[TPPFeX_2]^-$. This species can be reduced to $[TPPFeX]^-$ and ultimately to $[TPPFe]^-$. In the presence of nitrogenous bases, anion and solvent molecules may be displaced yielding monoadducts and diadducts for both iron(II) and iron(III). In all cases (except perhaps NO), electroreduction of ferrous porphyrins yielded the tetracoordinated iron(I) anion. More specific details are described elsewhere (*44*, *49*).

Ultimately, we seek to characterize, predict, and control synthetic metalloporphyrin reactivity. The successful redox tuning of iron(II) porphyrin potentials encourages us to pursue expansion of our model to include additional redox factors. Current efforts are being directed toward modeling the reactions of ferric porphyrins as well as other first-row transition metalloporphyrins.

Acknowledgments

The authors thank the National Institutes of Health (Grant GM 2517-02) and the National Science Foundation (Grants SPI-8013117 and CHE-7921536) for support of this work.

Literature Cited

1. Falk, J. E. "Porphyrins and Metalloporphyrins"; Elsevier: Amsterdam, C, Neth., 1964.

2. Clark, W. H. "Oxidation–Reduction Potentials of Organic Systems"; Williams & Wilkins: Baltimore, MD., 1960.
3. Fuhrhop, J. H. In "Porphyrins and Metalloporphyrins"; Smith, K. M., Ed.; Elsevier: New York, 1975.
4. Felton, R. H. In "The Porphyrins"; Dolphin, D., Ed.; Academic: New York, 1978; Vol. 5, Ch. 3.
5. Davis, D. G. In "The Porphyrins", Dolphin, D., Ed.; Academic: New York, 1978; Vol. 5, Ch. 4.
6. Caughey, W. S.; Fujimoto, W. Y.; Johnson, B. P. *Biochemistry* **1966,** *5,* 3830.
7. McLees, B. D.; Caughey, W. S. *Biochemistry* **1968,** *7,* 642.
8. Caughey, W. S.; Deal, R. M.; McLees, B. D.; Alben, J. O. *J. Am. Chem. Soc.* **1962,** *84,* 1735.
9. Meot-Ner, M.; Adler, A. D. *J. Am. Chem. Soc.* **1972,** *94,* 4763.
10. Meot-Ner, M.; Adler, A. D. *J. Am. Chem. Soc.* **1975,** *97,* 5107.
11. Walker, F. A.; Hui, E.; Walker, J. M. *J. Am. Chem. Soc.* **1975,** *97,* 2390.
12. Kadish, K. M.; Davis, D. G. *Ann. N.Y. Acad. Sci.* **1973,** *206,* 495.
13. Kadish, K. M.; Larson, G. *Bioinorg. Chem.* **1977,** *7,* 95.
14. Williams, R. F. X.; Hambright, P. *Bioinorg. Chem.* **1978,** *9,* 537.
15. Worthington, P.; Hambright, P.; Williams, R. F. X.; Feldman, M. R. *Inorg. Nucl. Chem. Lett.* **1980,** *16,* 441.
16. Leffler, J. E.; Grunwald, E. "Rates and Equilibria of Organic Reactions"; Wiley: New York, 1963; p. 172–9.
17. Taft, R. W., Jr. In "Steric Effects in Organic Chemistry"; M. S. Newman, Ed.; Wiley: New York, 1956.
18. Jaffe, H. H. *Chem. Rev.* **1953,** *53,* 191.
19. Zuman, P. "Substituent Effects in Organic Polarography"; Plenum: New York, 1967.
20. Hammett, C. P. "Physical Organic Chemistry," 2nd ed.; McGraw–Hill: New York, 1970.
21. Brown, H. C.; Okamota, Y. *J. Am. Chem. Soc.* **1958,** *80,* 4979.
22. Kadish, K. M.; Morrison, M. M. *Inorg. Chem.* **1976,** *15,* 980.
23. Kadish, K. M.; Morrison, M. M. *J. Am. Chem. Soc.* **1976,** *98,* 3326.
24. Kadish, K. M.; Morrison, M. M. *Bioinorg. Chem.* **1977,** *7,* 107.
25. Kadish, K. M.; Morrison, M. M. *Bioelectrochem. Bioenerg.* **1977,** *3,* 480.
26. Kadish, K. M.; Morrison, M. M.; Constant, L. A.; Dickens, L.; Davis, D. G. *J. Am. Chem. Soc.* **1976,** *98,* 8387.
27. Giraudeau, A.; Callot, H. J.; Jordan, J.; Ezhar, I.; Gross, M. *J. Am. Chem. Soc.* **1979,** *101,* 3857.
28. Giraudeau, A.; Callot, H. J.; Gross, M. *Inorg. Chem.* **1979,** *18,* 201.
29. Giraudeau, A.; Ezhar, I.; Gross, M.; Callot, H. J.; Jordan, J. *Bioelectrochem. Bioenerg.* **1976,** *3,* 519.
30. Callot, H. J.; Giraudeau, A.; Gross, M. *J. Chem. Soc., Perkin Trans. 2* **1975,** *12,* 1321.
31. Callot, H. J. *Tetrahedron Lett.* **1973,** 4987.
32. Callot, H. J. *Bull. Soc. Chim. Fr.* **1974,** 1492.
33. Wolberg, A. *Isr. J. Chem.* **1974,** *12,* 1031.
34. Rillema, D. P.; Nagle, J. K.; Barringer, L. F., Jr.; Meyer, T. J. *J. Am. Chem. Soc.* **1981,** *103,* 56.
35. Wolberg, A.; Manassen, J. *Inorg. Chem.* **1970,** *9,* 2365.
36. Johnson, E. C.; Niem, T.; Dolphin, D. *Can. J. Chem.* **1978,** *56,* 1381.
37. Ferguson, J. A.; Meyer, T. J.; Whitten, D. G. *Inorg. Chem.* **1972,** *11,* 2767.
38. Malinsky, T.; Chang, D.; Bottomley, L. A.; Kadish, K. M., submitted for publication in *Inorg. Chem.*
39. Tsutsui, M.; Taylor, G. A. In "Porphyrins and Metalloporphyrins," Smith, K. M., Ed.; Elsevier: Amsterdam, C, Neth., 1975, Ch. 7.
40. Hambright, P., In "Porphyrins and Metalloporphyrins," Smith, K. M., Ed.; Elsevier, Amsterdam, C, Neth., 1975, Ch. 6.

41. Scheidt, W. R. In "The Porphyrins", Dolphin, D., Ed.; Academic: New York, 1979; Vol. 3, Ch. 10.
42. Buchler, J. W.; Kokisch, W.; Smith, P. D. In "Structure and Bonding", Dunitz, J. D. Ed.; Springer (New York): New York, 1978, Vol. 34.
43. Dolphin, D.; Sams, J. R.; Tsin, T. B. *Inorg. Chem.* **1977,** *16,* 711.
44. Bottomley, L. A.; Kadish, K. M. *Inorg. Chem.* **1981,** *20,* 1348.
45. Kelly, S. L.; Kadish, K. M., unpublished data.
46. Felton, R. H.; Owen, G. S.; Dolphin, D.; Forman, A.; Borg, D. C.; Fajer, J. *Ann. N.Y. Acad. Sci.* **1973,** *206,* 504.
47. Felton, R. H.; Owen, G. S.; Dolphin, D.; Fajer, J. *J. Am. Chem. Soc.* **1971,** *93,* 6332.
48. Phillippi, M. A.; Shimomura, E. T.; Goff, H. M. *Inorg. Chem.* **1981,** *20,* 1322.
49. Bottomley, L. A.; Rhodes, R. K.; Kadish, K. M., presented at the *Proceedings of the Symposium on Interaction Between Iron and Proteins in Oxygen and Electron Transport,* Airlie, VA, April, 1980.
50. Chapter 15 in this book.
51. Lexa, D.; Momenteau, M.; Mispelter, J. *Biochim. Biophys. Acta* **1974,** *338,* 151.
52. Constant, L. A.; Davis, D. G. *Anal. Chem.* **1975,** *47,* 2253.
53. Constant, L. A.; Davis, D. G. *J. Electroanal. Chem.* **1976,** *74,* 85.
54. Kadish, K. M.; Beroiz, D.; Bottomley, L. A. *Inorg. Chem.* **1978,** *17,* 1124.
55. Gutmann, V. "The Donor–Acceptor Approach to Molecular Interactions"; Plenum: New York, 1978.
56. Popovych, O. In "Treatise on Analytical Chemistry," 2nd ed.; Kolthoff, I. M.; Elving, P. J., Eds.; Wiley: New York, 1978; Vol. 1, pp. 711–71.
57. Popovych, O. *CRC Crit. Rev. Anal. Chem.* **1970,** *1,* 73.
58. Bauer, D.; Breant, M. *J. Electroanal. Chem.* **1976,** *8,* 282.
59. Gagne, R. R.; Koval, C. A.; Lisensky, G. C. *Inorg. Chem.* **1980,** *19,* 2854.
60. Goff, H.; Shimomura, E. *J. Am. Chem. Soc.* **1980,** *102,* 31.
61. Brault, D.; Rougee, M. *Biochemistry* **1974,** *13,* 4591.
62. Kadish, K. M.; Bottomley, L. A. *Inorg. Chem.* **1980,** *19,* 832.
63. Buchler, J. W. *Angew. Chem. Int. Ed. Engl.* **1978,** *17,* 407.
64. Crow, D. R. "Polarography of Metal Complexes"; Academic: London, 1969.
65. Cohen, I. A.; Ostfeld, D.; Lichtenstein, B. *J. Am. Chem. Soc.* **1972,** *94,* 4522.
66. Walker, F. A.; Lo, M.-W.; Ree, M. T. *J. Am. Chem. Soc.* **1976,** *98,* 5542.
67. Scheidt, W. R. *Acc. Chem. Res.* **1977,** *10,* 339.
68. Bottomley, L. A.; Kadish, K. M., unpublished data.
69. Wayland, B. B.; Mehne, L. F.; Swartz, J. *J. Am. Chem. Soc.* **1978,** *100,* 2379.
70. Traylor, T. G. *Acc. Chem. Res.* **1981,** *14,* 102.
71. Wayland, B. B.; Olson, L. W. *J. Am. Chem. Soc.* **1974,** *96,* 6037.
72. Scheidt, W. R.; Hoard, J. C. *J. Am. Chem. Soc.* **1973,** *95,* 8281.
73. Scheidt, W. R.; Frisse, M. E., *J. Am. Chem. Soc.* **1975,** *97,* 17.
74. Scheidt, W. R.; Hatano, K.; Rupprecht, G. A.; Piciulo, P. L. *Inorg. Chem.* **1979,** *18,* 292.
75. Stong, J. D.; Burke, J. M.; Daly, P.; Wright, P.; Spiro, T. G. *J. Am. Chem. Soc.* **1980,** *102,* 5815.
76. Collman, J. P. *Acc. Chem. Res.* **1977,** *10,* 265.
77. Collman, J. P.; Gagne, R. R.; Reed, C. A.; Halbert, T. R.; Lang, G.; Robinson, W. T. *J. Am. Chem. Soc.* **1975,** *97,* 1427.
78. Jones, R. D.; Summerville, D. A.; Basolo, F. *Chem. Rev.* **1979,** *79,* 139.
79. Buchler, J. W.; Kokisch, W.; Smith, P. D., Tonn, B. *Z. Naturforsch.* **1978,** *33b,* 1371.
80. Mansuy, D.; Battioni, J. P.; Chottard, J. C. *J. Am. Chem. Soc.* **1978,** *100,* 4311.

81. Brown, G. M.; Hopf, F. R.; Ferguson, J. A.; Meyer, T. J.; Whitten, D. G. *J. Am. Chem. Soc.* **1973,** *95,* 5939.
82. Brown, G. M.; Hopf, F. R.; Meyer, T. J.; Whitten, D. G. *J. Am. Chem. Soc.* **1975,** *97,* 5385.
83. Olson, K. W.; Schaeper, D.; Lancon, D.; Kadish, K. M. *J. Am. Chem. Soc.* **1982,** *104,* 2042.
84. Kadish, K. M.; Olson, L. W.; Lancon, D.; Su, D. H.; Schaeper, D., presented at the *181st Nat. Meet. Am. Chem. Soc., Atlanta, GA, March,* **1981.**
85. Kadish, K. M.; Olson, L. W.; Schaeper, D., submitted for publication.
86. Lexa, D.; Momenteau, M.; Mispelter, J. *Bioelectrochem. Bioenerg.* **1974,** *1,* 108.
87. Cohen, I. A.; Lavallee, D. K.; Kopelove, A. B. *Inorg. Chem.* **1980,** *19,* 1098.
88. Kadish, K. M.; Bottomley, L. A.; Kelly, S.; Schaeper, D.; Shiue, L. R. *Bioelectrochem. Bioenerg.* **1981,** *8,* 213.
89. Sawyer, D. T. and Roberts, Jr. J. L. "Experimental Electrochemistry for Chemists"; Wiley: New York, 1974; p. 174.

RECEIVED for review August 13, 1981. ACCEPTED November 23, 1981.

Electrochemistry of Protoporphyrin IX Compared to Synthetic Models

KAREY L. HOLLAND[1] and JOSEPH JORDAN

Pennsylvania State University, Department of Chemistry, University Park, PA 16802

Normal pulse polarography and cyclic voltammetry of the free base protoporphyrin IX (PP) yielded well-defined reduction waves in aqueous solutions in the presence of tetramethylammonium hydroxide. Electroreduction occurred in three discrete steps, which were each coulometrically identified as two-electron transfers. Each step was characterized as an EC'-type mechanism, with proton transfer as the rate-determining reaction. All reduction sites on PP were methine bridges yielding, successively, phlorin, porphomethene, and porphyrinogen structures. Remarkably, these products are entirely analogous to the electroreduction products of porphyrin c and differ significantly from the chlorin-type products obtained from Collman's picket fence porphyrin. The picket fence porphyrin is a vital component of a synthetic myoglobin model, but undergoes electroreduction at different acceptor sites, viz., at pyrrolic double bonds.

The electron transfer kinetics of cytochrome c are remarkably fast: the rate constant of cellular respiration is on the order of 10^7 to 10^9 L/mol · s (*1*) and the rate of the cross reaction

$$\text{ferrocytochrome c} + Fe(CN)_6^{3-} = \text{ferricytochrome c} + Fe(CN)_6^{4-} \quad (1)$$

is comparable ($k = 10^7$ L/mol · s) (*2*, *3*). On the other hand, the analogous reaction of hemoglobin:

$$\text{hemoglobin} + Fe(CN)_6^{3-} = \text{methemoglobin} + Fe(CN)_6^{4-} \quad (2)$$

[1] Current address: International Business Machines, Inc., General Technology Division, Essex Junction, VT 05452

0065-2393/82/0201-0313$06.00/0

is three orders of magnitude slower (*4*). The view is widespread that the electron transfer, which converts the central iron atom from the divalent to the trivalent (formal) oxidation state via Reactions 1 and 2, occurs through the plane of the equatorial porphyrin ligands of the prosthetic groups (*5*). In this context, the electrooxidation–reduction properties of porphyrins are of obvious relevance. In a previous study (*6*, *7*), we reported that the electroreduction of porphyrin c proceeded via an EC′ mechanism involving a two-electron transfer followed by protonation. The product was a phlorin, **I**, that is, the reductive attack occurred at a methine bridge. At more negative potentials, the same electroreductive pattern recurred implicating successive methine bridges yielding, in turn, a porphomethene, **II**, and a porphyrinogen, **III**. This type of behavior, that is, electroreductive attack at methine bridge positions, is common to numerous porphyrins (*8–12*) and was inferred (*9*), by analogy, for protoporphyrin IX (the prosthetic group of hemoglobin and myoglobin). On the other hand, in chemical reductions of porphyrins (*13*) the initial electron acceptor site is a pyrrole double bond (rather than a methine bridge), and the product is a chlorin, **IV**, (rather than a phlorin). Remarkably, recent studies (*12*, *14*) revealed that Collman's picket fence porphyrin (*15*) [tetra(α,α,α,α-*o*-

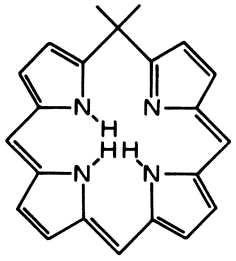

I (phlorin)

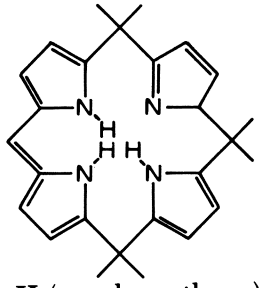

II (porphomethene)

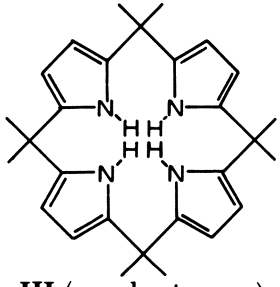

III (porporphyrinogen)

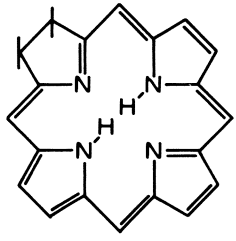

IV (chlorin)

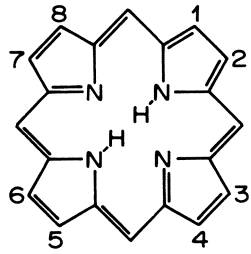

porphin

protoporphyrin: 1,3,5,8 CH_3; 2,4 $CH{=}CH_2$; 6,7 CH_2CH_2COOH

porphyrin c: 1,3,5,8 CH_3; 2,4 $CH(CH_3)SCH_2CH(NH_2)COOH$; 6,7 CH_2CH_2COOH

hematoporphyrin: 1,3,5,8 CH_3; 2,4 CH_2CH_2OH; 6,7 CH_2CH_2COOH

picket fence porphyrin: tetra($\alpha,\alpha,\alpha,\alpha$-*o*-pivalamidophenyl)porphin

pivalamidophenyl)porphin], which is the equatorial ligand of iron in a synthetic myoglobin model, was exceptional in that it yielded a chlorin by electroreduction (via an ECE mechanism described elsewhere). This unexpected finding suggests that the electroreduction of protoporphyrin may proceed by a mechanism analogous to that of the picket fence porphyrin (yielding a chlorin). Alternatively, protoporphyrin may produce a phlorin in a manner similar to the typical behavior of most other porphyrins. Surprisingly, no definitive voltammetric investigation of the protoporphyrin free base has been reported in aqueous solution to date, although the aqueous protoporphyrin diacid was the subject of one paper (*16*). The kinetics and mechanisms of electroreduction of the aqueous protoporphyrin free base, as revealed through polarography, cyclic voltammetry, and coulometry, are reported and discussed in this chapter.

Experimental

General. All potentials reported in this chapter were referred to the aqueous saturated calomel reference electrode, whose potential is +0.2412 V vs. the normal hydrogen electrode (NHE) at 25°C. The sign convention of the International Union of Pure and Applied Chemistry (IUPAC) is used throughout, that is, the more anodic (oxidizing) a potential, the more positive the assignment. All current values reported were corrected for residual current. Uncompensated IR drops were negligible under the experimental conditions. Numerical assignments for electrochemical rate parameters are "apparent values," that is, they were not corrected for double layer effects (even though these may have been appreciable due to specific adsorption). Precision is expressed as the standard deviation of the mean $[s/(n)^{1/2}]$.

Chemicals. Protoporphyrin IX disodium salt, obtained from ICN Biochemical, was converted to the free acid by ether extraction (*17*) and crystallized by solvent evaporation. Purity was ascertained by spectrophotometry and by elemental analysis (Schwartzkopf Analytical). Tetramethylammonium hydroxide (TMAH) (1 *M*) was purchased from Southwestern Analytical Chemicals, Inc. All water was deionized and triply distilled.

Instrumentation. The reference half-cell was an aqueous saturated calomel electrode (SCE). The working electrode used for pulse polarography was a conventional dropping mercury electrode (DME), equipped with a drop knocker Model 172 [supplied by EG&G Princeton Applied Research Corp. (PAR)]. A stirred mercury pool was employed for coulometry and a Kemula's hanging drop mercury electrode (HDME) (Metrohm Model BM5–03, distributed by Brinkmann Instruments Inc.) was employed for cyclic voltammetry. Auxiliary electrodes were mercury pools for polarography and cyclic voltammetry and platinum gauze for coulometry. Cyclic voltammetry and polarography were performed in a 15-ml water-jacketed cell; water circulating through the water jacket was thermostated at (25.0 ± 0.1)°C. Normal pulse polarography (drop time, 0.5 s; pulse width, 57 ms; current sampling time, 17 ms, mercury flow rate, 2.3 mg/s) was performed on PAR Models 170 and 174 Electrochemical Systems. The PAR Model 170 also was utilized for cyclic voltammetry, and data acquisition at high scan rates was expedited by a minicomputer. Coulometric experiments were carried out on both the PAR Model 170 and a Wenking potentiostat (supplied by Brinkmann Instruments, Inc.) in combination with a PAR Model 379 coulometer and a PAR 175 universal programmer. Visible spectra were obtained on a Cary Model 118 (Varian Associates) as well as a Hewlett–Packard Model 8450A Spectrophotometer (Hewlett–Packard Co.).

Results

Protoporphyrin IX (PP) is an amphoteric molecule, soluble only in acidic media (as the dication) or basic media (where the propionate groups are not protonated). To study the electroreduction of the protoporphyrin free base in an aqueous environment, a strong alkali (0.5 *M* TMAH) was employed as the supporting electrolyte. The stability of PP in aqueous TMAH was ascertained spectrophotometrically: PP was stable for at least 20 days.

Polarography. Conventional polarography (using drop times of 2–4 s) of PP revealed three reduction waves, only the most positive (anodic) being well-defined. On the other hand, normal pulse polarography using drops knocked off at $t = 0.5$ s, produced three well-defined waves, presumably because adsorption was minimized. The waves are shown in Figure 1 and are designated as Waves *X*, *Y*, and *Z*.

The limiting currents of Waves *X*, *Y*, and *Z* were proportional to concentration in the range of 10^{-4} to 10^{-2} M PP and i_d/C (where i_d is the diffusion limited current and C is the bulk concentration) was approximately 1.5 μA/mmol/L. Studies of the limiting currents as a function of mercury column height (h, appropriately corrected for back

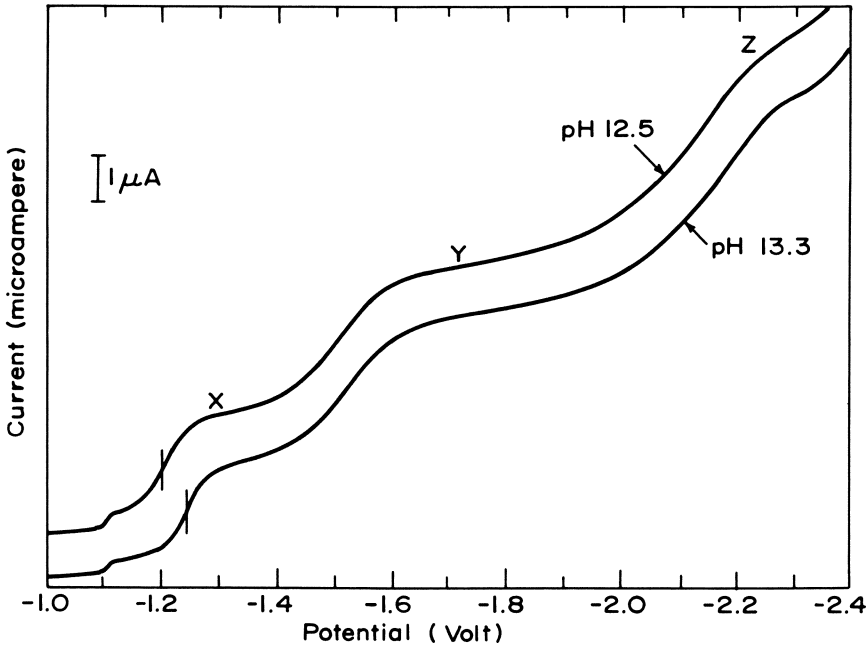

Figure 1. Normal pulse polarograms of 9.1 × 10^{-4} M protoporphyrin. Supporting electrolytes: pH 13.3, 0.5 M aqueous TMAH; pH 12.4, mixture of TMAH + TMACl. Curves shifted arbitrarily along ordinate axis.

pressure) substantiated diffusion as the predominant control mechanism. A slight effect of adsorption was apparent: the slope of the log–log plot of i_d vs. h was 0.55, which compared to 0.50 for pure diffusion control. To assess whether Nernstian reversibility prevailed and to estimate the number of Faradays transferred per mole of PP (i.e., the n-value), the normal pulse polarograms were subjected to conventional wave analysis. Log $[i/(i_d - i)]$ was plotted vs. potential in accordance with the equation

$$E = E_{1/2} - \frac{2.3RT}{nF} \log\left[\frac{i}{i_d - i}\right] \tag{3}$$

The relevant plots for Waves X and Y are shown in Figure 2, where

$$S(\text{slope}) = \frac{dE}{d \log[i/(i_d - i)]}$$

(Analysis of the analytical geometry of Wave Z was not attempted due to its proximity to the solution decomposition potential.) As is apparent from Figure 2, the wave analysis plot of Wave X was not linear:

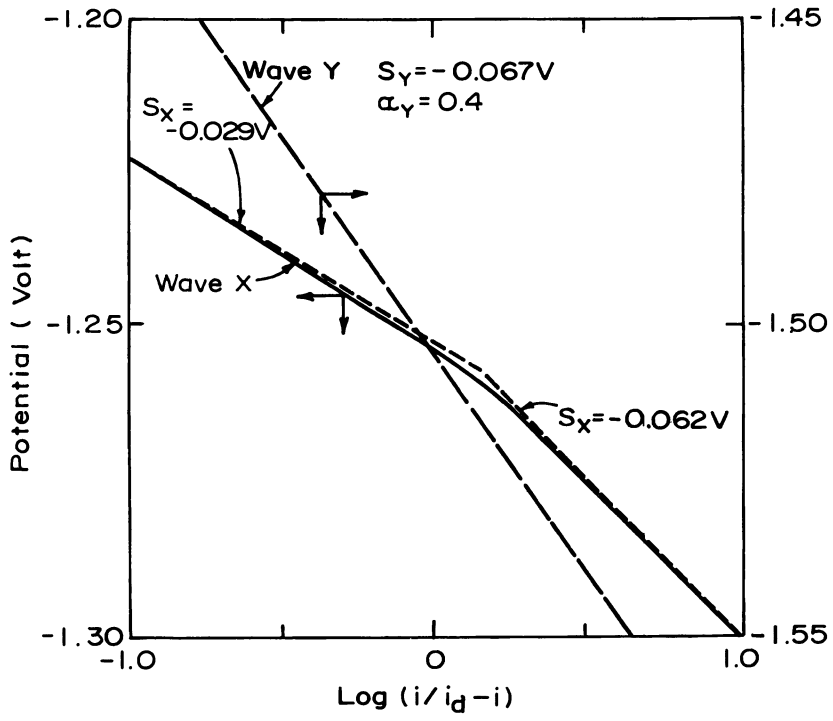

Figure 2. Wave analysis plots. Waves X *and* Y *identified in Figure 1.*

the initial slope was 0.029 V and the final slope was larger, which is consistent with a so-called quasi-reversible electroreduction where $n_X = 2$. The wave analysis plot of Wave Y was rectilinear with a slope of 0.067 V, which is consistent with a totally irreversible two-electron transfer and $\alpha = 0.4$.

Using $n = 2$, the diffusion coefficient, D_0, of PP was computed from the appropriate normal pulse polarographic limiting current equation (*18*).

$$i_d = 4.6 \times 10^4 nCD_0^{1/2} m^{2/3} t_m^{1/6} \beta^{-1/3}(1 + \beta/3) \text{ where } \beta = \frac{t_m}{t_p + t_m} \quad (4)$$

where i_d is the diffusion limited current in microamperes; C is the millimolar bulk concentration; m is the flow rate of mercury; t_m is the time elapsed between the start of the potential pulse application and the start of current sampling; t_p is the time of growth of the mercury drop before the pulse is applied; and D_0, t, and m are expressed in cgs units. A value of $D_0 = (1.3 \pm 0.1) \times 10^{-6}$ cm^2/s was obtained. This value was in good agreement with $D_0 = 1.4 \times 10^{-6}$ cm^2/s estimated

from a conventional polarogram of the first wave of PP using the classical Ilkovic Equation.

Coulometry and Spectroscopy. To verify conclusively the number of electrons involved in the electroreduction reactions, which account for Waves *X* and *Y*, coulometry was performed at controlled potentials corresponding to the plateau region of each wave. The findings are summarized in Table I. It easily is deduced from the data in the table that $n_X = n_Y = 2$, which is consistent with the results of the wave analysis plots. We also assign $n_Z = 2$, because $i_{d,X}$, $i_{d,Y}$, and $i_{d,Z}$ were equal in any given solution. The spectra of the reduction products, which correspond to Waves *X*, *Y* and *Z*, are shown in Figure 3. A comparison with authentic spectra of analogous compounds (*19*) (i.e., of other porphyrins, corresponding phlorins, porphomethenes, and porphyrinogens), obtained in aqueous solution at pH > 9, makes it apparent that the reduction product of Wave *X* had a phlorin structure. The ratio, *R*, in the Soret band region between the extinction coefficient of the phlorin and the parent porphyrin is of particular interest, as illustrated:

	Wavelength of Phlorin Peak (nm)	*R (at Wavelength of First Column)*
Figure 3	400	0.25
Reference *19*	440	0.25

The exact position of the phlorin peaks is a function of pH, solvent, and other things (*8*, *19*). However, in any given solvent the dramatic decrease of the Soret band (fourfold, $R = 0.25$!) is indicative of reduction having occurred at a methine bridge. A peak at longer wavelength,

Table I. Coulometric Data

Potential[a]	*Micromoles PP*[b]	Q (*coulombs*)	n (*F/mol*)
Wave *X*, −1.35 V	1.19	2.16×10^{-2}	1.88
	4.22	8.59×10^{-2}	2.11
	2.31	4.46×10^{-2}	2.00
	5.05	9.90×10^{-2}	2.04
	8.60	1.75×10^{-2}	2.10
		Average $n_X = 2.0 \pm 0.1$	
Wave *Y*, −1.6 V	10.0	37.1×10^{-2}	3.80
	5.0	20.1×10^{-2}	4.16
	5.0	19.2×10^{-2}	3.98
		Average $(n_X + n_Y) = 4.0 \pm 0.2$	

[a] Selected to correspond to diffusion current plateau.
[b] In 5 mL of solution.

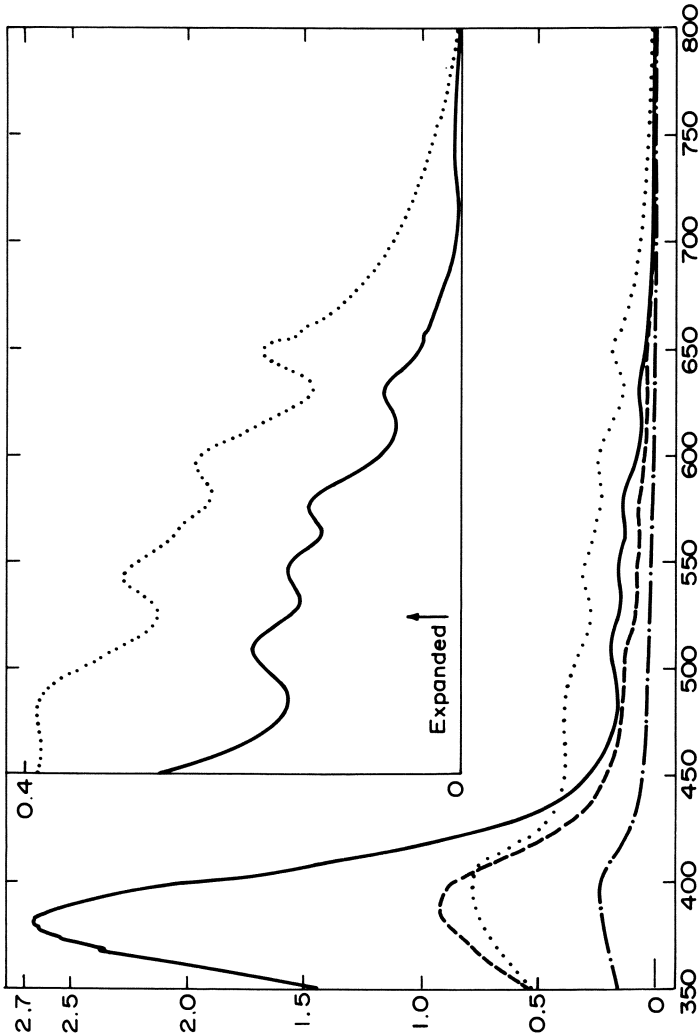

Figure 3. Spectra of protoporphyrin (—) and its electroreduction products. Protophlorin (· · ·), protoporphomethene (---), and protoporphyrinogen (– · –) produced by controlled potential electrolysis.

likewise dependent on solvent and pH, also substantiates the formation of a phlorin (viz., Figure 3: 648 nm; Ref. 19: 645 nm). The spectra of the products corresponding to Waves Y and Z were characteristic of porphomethene and porphyrinogen structures, respectively.

Cyclic Voltammetry. The kinetics and mechanisms of electroreduction of the free base protoporphyrin in aqueous TMAH were investigated by cyclic voltammetry at scan rates varying between 0.02 and 500 V/s. Cyclic voltammograms, with a switching potential, E_λ, of -1.9 V, yielded three cathodic peaks (illustrated in Figure 4): Peaks X_c and Y_c (corresponding to Waves X and Y of Figure 1) and an adsorption prepeak. At scan rates less than 0.2 V/s, no anodic peaks were observed. However, at scan rates faster than 0.2 V/s, two anodic peaks, X_a and Y_a', appeared. Figure 4 shows that Peaks X_c and X_a are genuine redox counterparts, separated by 0.03 V. On the other hand, Peaks Y_c and Y_a' are separated by almost 1 V. Related peak pairs are examined in detail below.

PEAKS X_c AND X_a. The more negative (cathodic) of the two anodic peaks, Peak X_a, was identified as the direct counterpart of Peak X_c because it was observed even when E_λ was -1.4 V (i.e., 0.1 V more positive than Peak Y_c). The diagnostic criteria of Shain and coworkers (*20, 21*) were applied to Peaks X_c and X_a (using $E_\lambda = -1.4$ V) to elucidate the reduction mechanisms. Relevant plots are shown in Figure 5. The plot of the ratio between anodic and cathodic peak currents vs. scan rate (top curve in Figure 5) substantiated (*20*) that the electroreduction mechanism was EC'. The relationship of the current function ($i_{p,c}/v^{1/2}$) to scan rate is revealed in the bottom curve of Figure 5. The rapid increase in the current function at scan rates greater than 2 v/s was caused by weak adsorption effects (*21*) and rendered the diagnostic plot inconclusive. These adsorption effects also account for the poorly defined classical polarograms mentioned earlier.

To determine the rate of the C' (irreversible chemical) reaction, the ratio of anodic to cathodic peak currents ($i_{p,a}/i_{p,c}$) was plotted, as shown in Figure 6, as a function of the length of time, τ, required to scan from $E_{1/2}$ to E_λ; τ is inversely proportional to the scan rate. The ratio $i_{p,a}/i_{p,c}$ is a function of log $k_f\tau$, where k_f is the forward rate constant of reaction C'. The rate constant k_f was calculated (using the data in Figure 6) by a known method (*20*). The data obtained are listed in Table II, yielding

$$k_f = (1.3 \pm 0.1)\ \text{s}^{-1} \tag{5}$$

assuming pseudo-first-order kinetics.

At scan rates larger than 0.5 V/s, the potential separation, ΔE, between Peaks X_c and X_a can be measured, and ΔE is plotted vs. scan

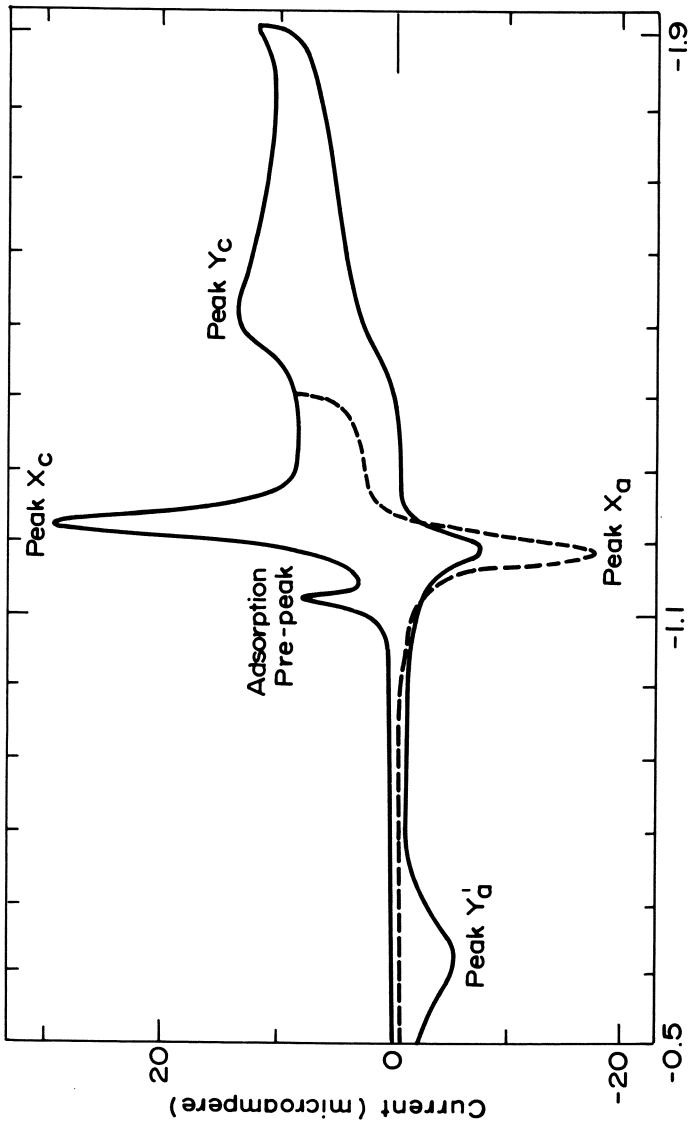

Figure 4. Cyclic voltammograms of 10^{-3} M protoporphyrin in 0.5 M aqueous TMAH. Scan rate: 5 V/s. Solid curve: switching potential, $E_\lambda = -1.9$ V; dashed curve, $E_\lambda = -1.4$ V.

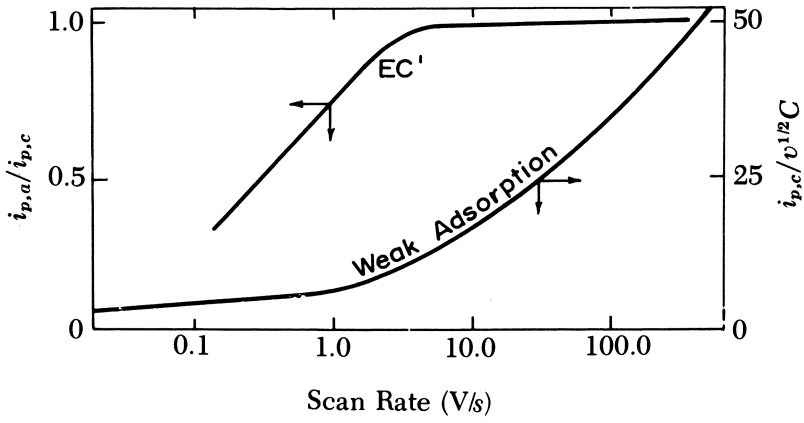

Figure 5. Experimental diagnostic plots (20) for Peaks X_c *and* X_a *(identified in Figure 4) based on cyclic voltammograms of* 10^{-3} M *protoporphyrin in 0.5* M *TMAH. Switching potential: −1.4 V. Mechanisms identified as in Refs. 20 and 21.*

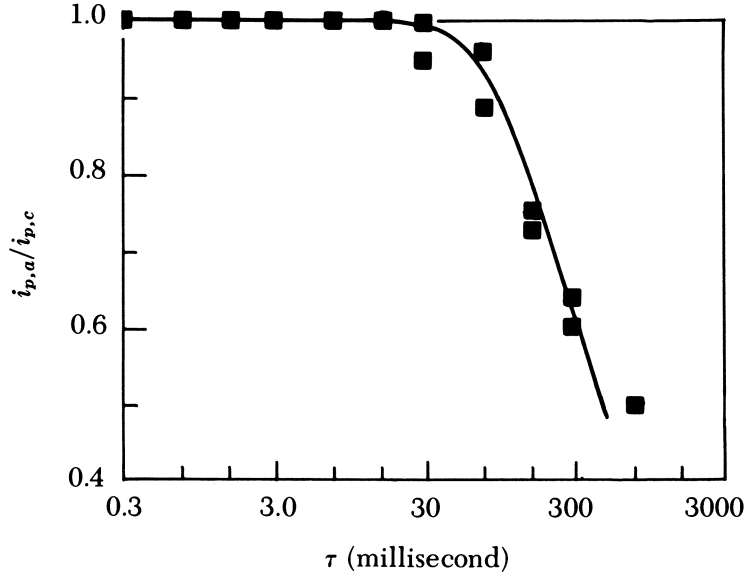

Figure 6. Experimentally determined ratio of anodic and cathodic peak currents of peaks X_c *and* X_a *plotted vs. the time,* τ*, required to scan from* $E_{1/2}$ *to* E_λ*. Plot based on Ref. 20.*

Table II. Evaluation of the Rate Constant for the C′ Component in the EC′ Sequence of Peaks X_c and X_a

v (V/s)	τ (s)	$i_{p,a}/i_{p,c}$	$k_f\tau$	k_f (s^{-1})
0.5	0.430	0.625	0.55	1.3
1.0	0.215	0.769	0.29	1.3
2.0	0.083	0.909	0.11	1.3
5.0	0.043	0.952	0.059	1.2
			Average =	1.3 ± 0.1

Note: Calculations based on Ref. *21* and data plotted in Figure 6, where the variable τ is defined.

rate in Figure 7. At scan rates between 0.5 and 20 V/s the potential separation between Peaks X_c and X_a was 0.028 V, consistent with a diffusion-controlled two-electron transfer process. At scan rates greater than 20 V/s, the peak potential separation increased due to control by electron transfer kinetics, as documented in Figure 7. From the relevant data, the standard electrochemical rate constant of the corresponding two-electron transfer process was calculated using the method developed by Nicholson (*22*). Results are shown in Table III, yielding an assignment of $k_s = 3 \times 10^{-2}$ cm/s effective at $E = -1.248$ V. On the other hand, a plot of the cathodic peak potential vs. scan rate allows calculation of the transfer coefficient, α, because theory requires

$$\frac{\Delta E_{p,c}}{\Delta \log_{10} v} = \frac{2.3RT}{2\alpha n_a F} = \frac{0.030}{\alpha n_a} \text{ at } 25°C \tag{6}$$

The corresponding empirical slope of 0.031 is uniquely consistent with $n_a = 2$ and $\alpha = 0.5$. To verify further these assignments, αn_a was calculated by application of the relationship between the peak potential, $E_{p,c}$, and the potential at half-peak current, $E_{p/2}$,

$$E_{p,c} - E_{p/2} = 0.0477\ (\alpha n_a)^{-1} \tag{7}$$

for a totally irreversible system. At high scan rates (200 V/s), Peak X_c approaches totally irreversible behavior. Under these conditions ($E_{p,c} - E_{p/2}$) was found to be 0.050, which is in agreement with $n_a = 2$ and $\alpha = 0.5$. The possibilities that a chemical step might be interposed between two-electron transfers, or that a disproportionation mechanism might be involved, were explored carefully at scan rates up to 500 V/s. Appropriate diagnostic criteria (*20*, *22*) failed to reveal any ECE 1 or ECE 2 mechanisms.

PEAKS Y_c AND Y_a'. No oxidation peak corresponding directly to Peak Y_c ever was observed at any scan rate. However, an oxidation

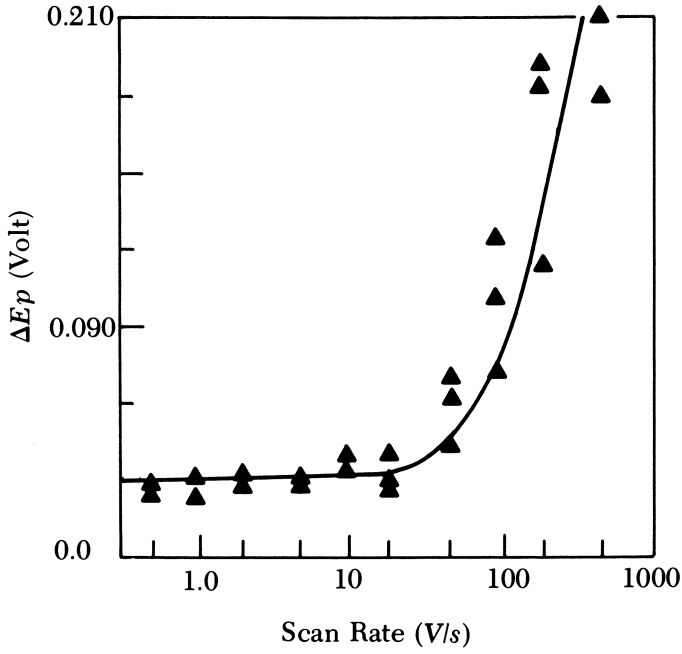

Figure 7. Experimentally determined potential separation, ΔE_p, between Peaks X_c and X_a as a function of scan rate.

peak, Y_a', appeared at −0.6 V (*see* Figure 4), that is, approximately 1 V more positive than Peak Y_c, and was observed only when E_λ was negative (cathodic) of Peak Y_c. The presence of Peak Y_a' implies that the electrode reaction, which occurred at Peak Y_c, had an EC′ mechanism. The appropriate diagnostic criteria (*20*) were applied to Peak Y_c and the results shown in Figure 8 substantiated that the mechanism was indeed EC′. However, the change in the current function ($i_{p,c}/v^{1/2}C$) was appreciably larger (viz., approximately −30%) than the theoretically predicted −10%. This discrepancy is accounted for by adsorption. The opposite nature of the effect compared to Figure 5 (where the current function increased rather than decreased) is due to the adsorbate being a product in Figure 5 vs. a reactant in Figure 8.

pH EFFECT. As is apparent from Figure 1, normal pulse polarographic waves of PP shifted negatively (cathodically) with increasing basicity. Similar shifts were observed by cyclic voltammetry of Peak X_c at scan rates where diffusion control prevailed. Quantitatively, the shifts were consistent with an assignment of

$$\frac{p_X}{n_X} = 0.5 \text{ for } p_X = 1 \qquad (8)$$

Table III. Rate Constant for the Two-Electron Transfer Step of the E Component in the EC′ Sequence of Peaks X_c and X_a

v (*V/s*)	n · ΔE_p[a] (*V*)	ψ[b]	k_s[c] (*cm/s*)
20	0.058		
50	0.136	0.275	0.030
100	0.202	0.121	0.020
200	0.228	0.10	0.026
		Average = 0.025 ± 0.005	

[a] *See* Figure 7.
[b] Function tabulated in Ref. 22.
[c] Effective at −1.248 V.

where $n_X = 2$ and p_X denotes the number of electrons and protons involved in the C′ step of the EC′ sequence of Wave *X*. As expected, dE_p/dpH decreased significantly at faster scan rates, as the follow-up reaction (C′) was gradually "shut out" by the decreasing "time-window."

Discussion

The experimental findings in strongly basic aqueous solutions are accounted for by the reaction sequence outlined in Scheme I. In the shorthand designations seen in Scheme I [e.g., P(0) for protoporphyrin], the parenthetic numerals (23) refer to an arbitrary oxidation state scale where the porphyrin molecule is assigned a formal oxidation number of zero.

The most positive (anodic) reduction wave of protoporphyrin (Wave *X* in Figure 1 and Scheme I) implies a two-electron transfer, viz.,

$$P(0) + 2e = [P(-II)]^{2-} \quad (9)$$

The two-electron transfer was not resolved into successive one-electron transfer steps by cyclic voltammetry even at potential scan rates as high as 500 V/s. The peak separation ($\Delta E = 0.028$ V) was consistent with a Nernst reversible two-electron transfer in a range of scan rates between 0.50 and 20 V/s. The value of ΔE increased at scan rates faster than 50 V/s, yielding the rate constant $k_s = 3 \times 10^{-2}$ cm/s. The spectrum of the two-electron reduction product, P(−II), was characteristic of a phlorin structure (*see* Structure **I**). The phlorin dianion is obviously amenable to protonation via Reaction 10.

$$[P(-II)]^{2-} + HOH = [P(-II)H]^{-} + OH^{-} \quad (10)$$

Effects of Reaction 10 were indeed observed and are described as follows.

1. Cyclic voltammograms of protoporphyrin in aqueous base (Figure 4) revealed that Wave *X* involved an EC′ mechanism, that is, a two-electron transfer step (Reaction 9) succeeded by a slow chemical reaction for which the protonation process (Reaction 10) is the obvious choice under the experimental conditions. The possibility that the free radical anion $[P^{\cdot}(-I)]^{-}$, rather than the phlorin dianion, was the proton acceptor was discounted, because the experimental evidence indicated conclusively that a single-stage two-electron transfer process preceded the irreversible chemical reaction. State-of-the-art experiments ruled out any intervening ECE 1 or ECE 2 (disproportionation) mechanisms. Reaction 10 would account satisfactorily for the findings in the top curve of Figure 5, which show that current ratios for anodic to cathodic peaks varied with scan rate. At very slow scan speeds, no anodic peak was observed at all by cyclic

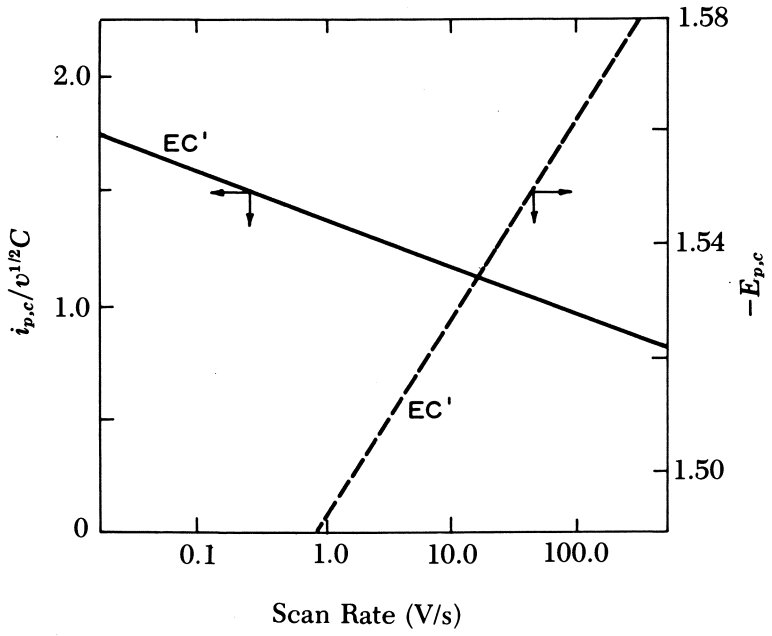

Figure 8. Experimental diagnostic plots for Peak Y_c *(identified in Figure 4) based on cyclic voltammograms of* 10^{-3} M *protoporphyrin in 0.5* M *TMAH. Switching potential:* -1.9 *V. Mechanism identified as in Ref.* 20.

voltammetry due to the protonation (Reaction 10), which scavenged $[P(-II)]^{2-}$ before potentials sufficiently positive (anodic) to reoxidize $[P(-II)]^{2-}$ were attained. However, at faster scan speeds a well-defined anodic peak was observed with $|i_{p,a}| = |i_{p,c}|$ and $\Delta E_p = 0.028$ V. Accordingly, we postulate that the half-life of 0.5 s inferred from Figure 6 pertains to the phlorin dianion, $[P(-II)]^{2-}$.

2. Decreasing basicity increased the ease of electroreduction of P(0), as was evidenced by a positive (anodic) shift of the polarographic half-wave potential and of the peak potential observed at the hanging drop mercury electrode.

The experimental findings for the second polarographic reduction step (corresponding to Wave Y in Figure 1) indicate that it proceeded by an EC′ mechanism, analogous to that of the first reduction step, yielding the overall reaction

$$[P(-II)H]^- + 2e + 2H^+ = [P(-IV)H_3]^- \quad (11)$$

where the P(−IV) moiety has a porphomethene structure. The assignment of the two H^+ (rather than one) in Equation 11 is predicated on considerations of plausible Brönsted base strengths of the anions $[P(-IV)H_2]^{2-}$ and $[P(-IV)H_3]^-$.

For Wave Z, we postulate a two-electron–two-proton transfer, which is analogous to Reaction 11, viz.,

$$[P(-IV)H_3]^- + 2e + 2H^+ = [P(-VI)H_5]^- \quad (12)$$

where the product has a porphyrinogen structure.

This work represents the first known successful study of the electrochemistry of the protoporphyrin free base in aqueous solutions. The study was feasible, because pulsed voltammetric techniques minimized adsorption that interfered with conventional dc polarography. Nevertheless, adsorption did produce some anomalous current functions in Figures 5 and 8 and may have affected the rate constant assignments reported in Table III. Although this possibility does not alter the central conclusions of this chapter (presented in Scheme I), it may be desirable to use double potential step chronocoulometry for verifying the numerical values in Table III. Our most salient finding is the involvement of three discrete, two-electron reduction steps. Two of these steps were characterized conclusively as two-electron transfers by coulometry. The only reported electrochemical investigation of PP in aqueous solution (*16*) was carried out in the presence of 0.1 *M* HCl, where the electroreducible species was undoubtedly the protoporphyrin dication (rather than the porphyrin free base). The find-

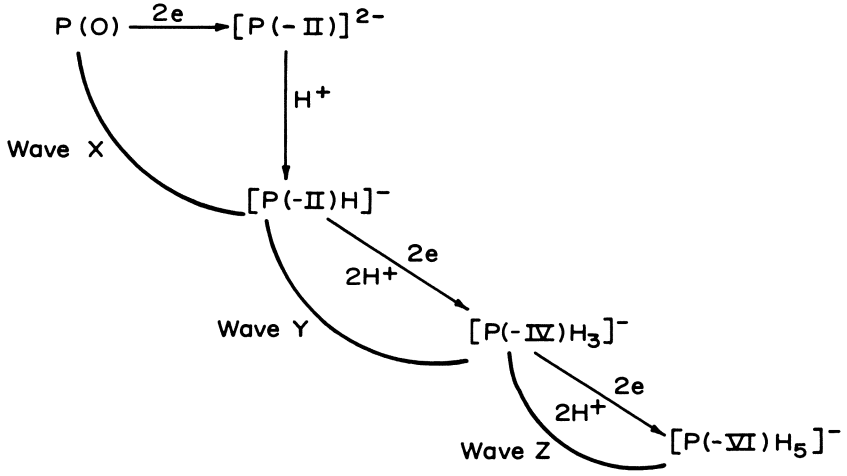

Scheme I. Proposed electroreduction mechanisms for free-base protoporphyrin in aqueous TMAH. Key: P(0), protoporphyrin; P(−II), protophlorin; P(−IV), protoporphomethene; P(−VI), protoporphyrinogen.

ings of that investigation (summarized in Table IV) agree with our results in as much as two two-electron transfers (corresponding to the first two reduction waves) were substantiated. In the study of the dication (*16*), the third wave was obscured by a catalytic hydrogen wave. The half-wave potentials of the dication (*see* Table IV) were considerably more positive than the corresponding half-wave potentials of the free-base porphyrin in strong alkali (this work), which is consistent with trends reported earlier (*6*, *8*, *16*, *23*).

The electrochemistry of protoporphyrin in dimethylformamide (DMF) has been documented in two studies of electroreduction (*9*, *24*) and one study of electrooxidation (*25*). Sequences of n-values (number of Faradays per mole) reported for electroreduction were 1, 1, and 4 and 1, 1 based solely on voltammetric measurements. Coulometric verification of these assignments has not been reported. Our work in DMF yielded surprisingly variable n-values, which fluctuated from $n = 1$ to $n = 2$ for Waves *X* and *Y*. The polarography of protoporphyrin in DMF requires further study because results are critically dependent on an unknown variable (possibly a trace impurity that affects the relevant kinetics and mechanisms).

For oxygen carrying systems, the oxygen transport and storage capabilities of hemoglobin and myoglobin conceivably may be related to the electroreduction mechanisms that occur in protoporphyrin. The recently reported (*11*, *12*, *14*) unique electroreduction behavior of Collman's picket fence porphyrin (leading to a chlorin) was indeed radically different from the electroreduction mechanisms of porphyrin c

Table IV. Comparison With Data Reported in the Literature for Protoporphyrin IX in Acidic and Basic Aqueous Solutions

	n		$E_{1/2}$[b]	
Wave[a]	*In 0.5 M TMAH*[c]	*In 0.1 M HCl*[d]	*In 0.5 M TMAH*[c]	*In 0.1 M HCl*[d]
X	2	2	−1.25	−0.47
Y	2	2	−1.49	−0.70
Z[e]	2	—[f,g]	−2.17	−0.93[g]

[a] Waves identified as in Figure 1.
[b] Vs. SCE.
[c] Supporting electrolyte, TMAH; electroreducible moiety, protoporphyrin free base (this work).
[d] Electroreactive moiety: protoporphyrin dication (*16*).
[e] Wave Z identified as protoporphyrin reduction in TMAH only.
[f] Not reported.
[g] Wave assigned to hydrogen evolution.

Table V. Electroreduction and Oxygen Binding Characteristics

		Electroreduction Mechanism[b]		
(1) *Moiety*	(2) *O_2 Carrying Capability*[a]	(3) *Type*	(4) *Reaction Sequence*	(5) *Product*
Protoporphyrin IX	+	EC′	I. Two-electron transfer II. Protonation	phlorin
Picket fence porphyrin	+	ECEC	I. Electron transfer II. Conformational change III. Electron transfer IV. Protonation	chlorin
Porphyrin c	—	EC′	I. Two-electron transfer II. Protonation	phlorin
Hematoporphyrin IX	?[c]	ECE	I. Electron transfer II. Protonation III. Electron transfer	phlorin

[a] Of related hemoproteins or model compounds.
[b] Of first two-electron transfer step.
[c] Hematoporphyrin IX is not a component of any natural hemoprotein, nor has it been incorporated in any synthetic hemoprotein model.

(*6, 7, 11, 12*) and of hematoporphyrin (*11, 12, 23*), both of which yield phlorins. These findings are summarized in Table V, Columns 3, 4, and 5. The oxygen carrying capabilities of corresponding hemoproteins are listed for comparison (Column 2). As evident from Table V, no obvious correlation exists between the electroreduction mechanisms of the porphyrin and the oxygen binding characteristics of the related hemoprotein or model compound.

Acknowledgment

This work was supported by the Solar Energy Research Institute (SERI) under Subcontract XP–9–8002–10 with The Pennsylvania State University.

Literature Cited

1. Chance, B.; Williams, G. R. *Adv. Enzymol.* **1956,** *17,* 65.
2. Brandt, K. G.; Parks, P. C.; Czerlinski, G. H.; Hess, C. P. *J. Biol. Chem.* **1966,** *241,* 4180.
3. Sutin, N.; Christman, D. R. *J. Am. Chem. Soc.* **1961,** *86,* 1773.
4. Antonini, E.; Brunori, M.; Wyman, J. *Biochem.* **1965,** *114,* 545.
5. Feinberg, B. A.; Gross, M.; Kadish, K. M.; Marano, R. S.; Pace, S. J.; Jordan, J. *Bioelectrochem. and Bioenerg.* **1974,** *1,* 73.
6. Ting, C. C. Y.; Jordan, J.; Gross, M. In "Electrochemical Studies of Biological Systems," Sawyer, D. T., Ed.; ACS SYMPOSIUM SERIES, No. 38, ACS: Washington, D.C., 1977; p. 26.
7. Ting, C. C. Y., Ph. D. Thesis, Pennsylvania State University, University Park, PA, 1978.
8. Peychal-Heiling, G.; Wilson, G. S. *Anal. Chem.* **1971,** *43,* 545, 550.
9. Mairanovskii, V. G.; Mamaev, V. M.; Ponomarev, G. V.; Marinova, R. I.; Evstigneeva, R. P. *Zh. Obshch. Khim.* **1974,** *44,* 2508; *J. Gen. Chem. USSR (Engl. Trans.)* **1974,** *44,* 2468.
10. Callot, H. J.; Giraudeau, A.; Gross, M. *J. Chem. Soc., Perkin Trans.* 2, **1975,** 1321.
11. Jordan, J.; Bump, C. M. *Extended Abstracts,* Electrochem. Soc., May 1980, 80–81, 1146.
12. Jordan, J. *Proceedings,* Heyrovsky Memorial Congress on Polarography, 1980, I, 157.
13. Whitlock, H. W., Jr.; Hanauer, R.; Oester, M. Y.; Bower, B. K. *J. Am. Chem. Soc.* **1969,** *91,* 7485.
14. Bump, C. M., Ph. D. Thesis, Pennsylvania State University, University Park, PA, 1979.
15. Collman, J. P.; Gagne, R. R.; Reed, C. A.; Halbert, T. R.; Lang, G.; Robinson, W. T. *J. Am. Chem. Soc.* **1975,** *97,* 1427.
16. Ricci, A.; Pinamonti, S.; Bellavita, V. *Ric. Sci.* **1960,** *30,* 2497.
17. Fuhrhop, J.-H.; Smith, K. M. "Porphyrins and Metalloporphyrins"; Am. Elsevier: New York, 1975; p. 830.
18. Bond, A. M. "Modern Polarographic Methods in Analytical Chemistry"; Dekker: New York, 1980; p. 244.
19. Mauzerall, D. *J. Am. Chem. Soc.* **1962,** *84,* 2437.
20. Nicholson, R. S.; Shain, I. *Anal. Chem.,* **1964,** *36,* 706.
21. Wopschall, R. H.; Shain, I. *Anal. Chem.,* **1967,** *39,* 1514.

22. Nicholson, R. S. *Anal. Chem.*, **1965,** *37*, 1351.
23. Spendel, V. A. Ph. D. Thesis, Pennsylvania State University, University Park, PA, 1978.
24. Williams, R. F. X.; Hambright, P. *Bioinorg. Chem.*, **1978,** *9*, 537.
25. Stanienda, A.; Biebl, G. Z. *Phys. Chem. N.F.*, **1967,** *52*, 254.

RECEIVED for review June 2, 1981. ACCEPTED November 24, 1981.

Iron(I) and Iron(IV) Porphyrins

CHRISTOPHER A. REED

University of Southern California, Chemistry Department, Los Angeles, CA 90007

Critical review of the literature on iron(I) and iron(IV) porphyrins reveals many ambiguities in the assigned spin and oxidation states. The question of whether a redox reaction has occurred at the iron atom or at the porphyrin ring in highly reduced or highly oxidized complexes is not semantic and can usually be decided collectively from UV–VIS spectroscopy, Mössbauer spectroscopy, and structural parameters derived from x-ray crystallography. The low spin iron(I) state has considerable validity in iron porphyrin complexes that are reduced below the iron(II) level. Complexes that are oxidized above the iron(III) level give rise to either iron(IV) porphyrins or, more often, iron(III) radical cations. The site of redox is largely dictated by the nature of the axial ligation. Highly reduced and highly oxidized iron porphyrin complexes provide a basis for understanding intermediates in the reactions of cytochrome P-450 and the peroxidases.

Iron porphyrin complexes have been studied intensively in their commonly occurring oxidation states, iron(II) and iron(III). All possible spin states are known and from x-ray crystal structure determinations a consistent and reliably predictive relationship between spin state and structure has evolved (*1*). Along with various magnetic criteria, both Mössbauer spectra (2) and proton NMR spectra (3) are notably diagnostic of spin and oxidation states. The systematics are sufficiently well-established such that most properties of iron(II) and iron(III) porphyrin complexes are understood and can be predicted with a good degree of metrical accuracy and confidence.

On the other hand, comparable definitive characterization of highly reduced or highly oxidized iron porphyrins is lacking. The literature contains many inconsistencies on iron(I) porphyrins and many

0065-2393/82/0201-0333$07.00/0

ambiguities in the characterization of so-called iron(IV) porphyrins. This situation should be clarified because such porphyrins may have considerable relevance to understanding the redox mechanisms by which the hemoproteins peroxidase, catalase, and cytochrome P-450 carry out their chemistry. Often, the characterization of an iron porphyrin complex cannot be considered definitive until its x-ray crystal structure has been determined and a fairly complete battery of spectroscopic probes has been applied. Early solution work on UV–VIS spectroscopy, electrochemistry, and magnetic measurements has turned out to be less than adequate. Improved syntheses and a more extensive use of Mössbauer and NMR spectroscopy and x-ray crystal structure determination has recently allowed the resolution of many ambiguities.

Iron(I) Porphyrins

Reduction of an iron porphyrin complex below the iron(II) oxidation state was first reported in 1971 (*4*). Spectroscopic properties of a red complex presumed to be $[Fe(TPP)]^-$ were determined. This complex was prepared by sodium amalgam reduction of the μ-oxo iron(III) complex $Fe_2(TPP)_2O$ in tetrahydrofuran (THF) solution (TPP = tetraphenylporphyrinate). A distinctive low temperature EPR spectrum with $g_\perp = 2.30$ and $g_\parallel = 1.93$ was observed. Such anisotropy is consistent with a single, metal-localized unpaired electron and by comparison with d^7-cobalt(II) porphyrin complexes, a low spin iron(I) formulation was assigned. However, an iron(II) porphyrin radical anion formulation, where an $S = 1$ iron is strongly spin-coupled to the $S = \frac{1}{2}$ radical giving an overall $S = \frac{1}{2}$ state, would be equally consistent with the EPR spectrum. But, the magnetic moment, determined at higher temperatures, was considerably in excess of that expected for an $S = \frac{1}{2}$ iron(I) center. This finding led to the proposal that the spin state changed to an $S = \frac{3}{2}$ state on thawing of the frozen tetrahydrofuran solution. Spin state–structure relationships in iron porphyrins suggest that such a high spin iron(I) species is very unlikely because unrealistic core expansion or out-of-plane iron displacement [greater than for high-spin iron(II)] would be required (*1*). Moreover, the VIS spectral maxima at 540 and 605 nm reported for $[Fe(TPP)]^-$ (*4*) are uncomfortably close to those of the red iron(II) complex $Fe(TPP)(THF)_2$ (539 and 610 nm), which is an $S = 2$ high spin complex (*5*). Most likely the reported magnetic moment ($\mu = 5.2$ BM) is due not to $[Fe(TPP)]^-$ but to a mixture containing mostly high spin iron(II). Because iron(II) porphyrins are EPR silent and the EPR technique was not applied quantitatively, only small amounts of authentic $[Fe(TPP)]^-$ would be necessary to match the observations.

A subsequent electrochemical study of $[Fe(TPP)]^-$ and related iron porphyrins (*6*) strengthened the low spin assignment in frozen solution, and further EPR studies were conducted. $[Fe(TPP)]^-$ may be devoid of axial ligation, even in the presence of good donors such as imidazole or pyridine. The slight solvent dependence of the EPR spectrum was interpreted in terms of a $(d_{z^2})^1$ configuration by comparison to cobalt(II) porphyrins. Both the $(d_{z^2})^1$ configuration and the overall negative charge provide a rationale for the lack of axial coordination but the ground state is by no means certain. A $(d_{xz})^1$ configuration is equally viable.

A third study (*7*) reported a synthetic route that, for the first time, allowed isolation of a crystalline sodium salt, Na[Fe(TPP)].

$$Na^+ \text{ naphthalide}^{\cdot -} + Fe(II)(TPP) \xrightarrow{THF} Na[Fe(TPP)] + \text{naphthalene}$$

Aerobic sensitivity created difficulties in obtaining elemental analyses, but atom ratios were satisfactory for Na[Fe(TPP)], except for carbon. This result occurred probably because THF solvation was not taken into account. Unexplained, however, was the high magnetic moment (μ = 5.0 BM). Although such a value is similar to that obtained in the original solution work, it is again inconsistent with a low spin $S = \frac{1}{2}$ iron(I) complex. The likely origin of this high magnetic moment is aerobic uptake of oxygen by $[Fe(TPP)]^-$ to form the high spin iron(III) species $[Fe(O_2)(TPP)]^-$.

When the synthesis and characterization are carried out under scrupulously anaerobic conditions, purple crystals of formulation $[Na(THF)_3][Fe(TPP)]$ are produced (*8*). [*Anal.* Calculated for $C_{56}H_{52}O_3N_4FeNa$: C, 74.08; H, 5.77; N, 6.17. Found: C, 74.34; H, 5.94; N, 6.06. Quantitative GLC analysis for THF: calculated: 23.8%. Found: 25.4%] This isolated product had a room-temperature magnetic moment of 2.3 BM, which is much closer to that expected of an $S = \frac{1}{2}$ system. The complex reacts immediately with oxygen in the solid state with a concomitant increase in magnetic moment, approaching 5.9 BM (*8*).

The early synthetic study (*7*) also reported that $[Fe(TPP)]^-$ binds carbon monoxide to give an unusual "hyper" type UV–VIS spectrum related to cytochrome P-450. This observation is at odds with the earlier reported inability of $[Fe(TPP)]^-$ to bind axial ligands. Repeating this experiment (*8*) indicated that CO has no effect on the UV–VIS spectrum of $[Fe(TPP)]^-$ in THF (392 Soret,424 Soret,512,576sh, 605sh, and 674 nm) and that the spectrum reported for the proposed CO adduct (455 nm Soret) can be accounted for either by the presence of the dianion $[Fe(TPP)]^{2-}$ (358 and 448 nm Soret) or by the presence of an apparently different form of $[Fe(TPP)]^-$, the so-called form A (457 nm Soret).

Thus, alternative explanations can be given for all the anomalous properties reported for so-called iron(I) porphyrins. Because the spin state of an iron porphyrin is always reflected in its structure (*1*), we decided to determine the x-ray crystal structure of $[Fe(TPP)]^-$ to check for consistency with the spin and axial ligation states deduced. Crystals suitable for x-ray were obtained from a pyridine–THF solution of Na[Fe(TPP)] in the presence of dibenzo-18-crown-6 (*8*). The product has the formulation $[Na(crown)(THF)_2][Fe(TPP)] \cdot THF$. Pyridine ligation was absent, despite its use as cosolvent. The anion is tetracoordinated and planar with an average Fe–N distance of 1.988 (1) Å (*9*). This distance is entirely consistent with the lack of $d_{x^2-y^2}$ occupation in the low spin state. It is slightly longer than that of the intermediate-spin iron(II) complex Fe(TPP) (1.97 Å) as expected from valency charge considerations. It is slightly shorter than those of low spin hexacoordinated iron(II) complexes (~2.00 Å) and is far removed from those of high spin iron(II) complexes (~2.08 Å).

Finally, the Mössbauer spectrum of crystalline $[Na(THF)_3][Fe(TPP)]$ was determined and the isomer shift (δ) relative to metallic iron is 0.65 mm/s (*10*). This value is very high for an iron porphyrin and is quite consistent with the high electron density at the nucleus of iron in the formally univalent oxidation state. Table I lists some representative examples that illustrate the usual trend of increasing δ with decreasing oxidation state. However, the apparently straightforward trend in δ is deceptive. Exceptions can easily be found. In the absence of magnetic field investigations (which do not help in diamagnetic compounds) a simple trend in isomer shift should be accepted with caution. Similarly, the quadrupole shift may defy a simple explanation. In the present case the large value (ΔEq = 2.23 mm/s) is consistent with the large charge asymmetry expected of this tetragonal ion.

Iron (I) porphyrins might appear to be well-behaved systems with all properties consistent with an $S = \frac{1}{2}$ d^7 system. On close inspection, however, two properties are somewhat out of line with the iron(I) porphyrin formulation and are more consistent with an iron(II) porphyrin radical anion formulation, $[Fe(TPP \cdot)]^-$. First, the UV–VIS spectrum is quite like that of a porphyrin radical anion having broad, low intensity Soret maxima and broad maxima in the α,β-region compared with, for example, Fe(TPP) in THF (*see* Figure 1). Apart from such broadening, red-shifted Soret bands also are considered diagnostic of porphyrin radical anions (*19*). However, the major Soret bands of Fe(TPP) and of $[Fe(TPP)]^-$ are essentially the same wavelength in THF. Second, inspection of the bond lengths and angles of the porphinato core in $[Fe(TPP)]^-$ show trends that may be consistent with occupation of the porphyrin lowest unoccupied molecular orbital

Published on June 1, 1982 on http://pubs.acs.org | doi: 10.1021/ba-1982-0201.ch015

Table I. Trend in Mössbauer Parameters (mm/s at 4.2 K) with Oxidation State of Iron

Compound	*Oxidation State*	*Iron Spin State*	*Overall Spin State*	δ (*rel. Fe*)	ΔEq	*Reference*
$[Fe(TPP)]^-$	I[a]	$S = \frac{1}{2}$	$S = \frac{1}{2}$	0.65	2.23	*10*
$[Fe(TPP)]^{2-}$	I[a]	low	$S = 0$	0.48	1.29	*10*
Fe(TPP)	II	$S = 1$	$S = 1$	0.52	1.51	*11*
$Fe(TPP)(pip)_2$	II	$S = 0$	$S = 0$	0.51	1.44	*11*
FeX(TPP)	III	$S = \frac{5}{2}$	$S = \frac{5}{2}$	0.41–0.47	0.46–0.70	*12*
$[FeCl(TPP\cdot)]^+$	III	$S = \frac{5}{2}$	$S = 2$	0.41	0.56	*13*
FeO(TPP)(1-MeIm)	IV	$S = 1$	$S = 1$	0.11	1.24	*14*
Compd ES of CCP	IV	$S = 1$	$S = 1, S = \frac{1}{2}$[b]	0.05	1.55	*15*
Compd II of HRP	IV	$S = 1$	$S = 1$	0.03	1.61	*16*
$FeO(TMP\cdot)Cl$	IV	$S = 1$	$S = 1, S = \frac{1}{2}$[c]	0.05	1.49	*17*
Compd I of HRP	IV	$S = 1$	$S = 1, S = \frac{1}{2}$[c]	0.08	1.25	*18*

[a] Probably in resonance with Fe(II). *See* text.
[b] The $S = \frac{1}{2}$ radical is protein located and does not interact significantly with the $S = 1$ iron atom.
[c] Weakly interacting.

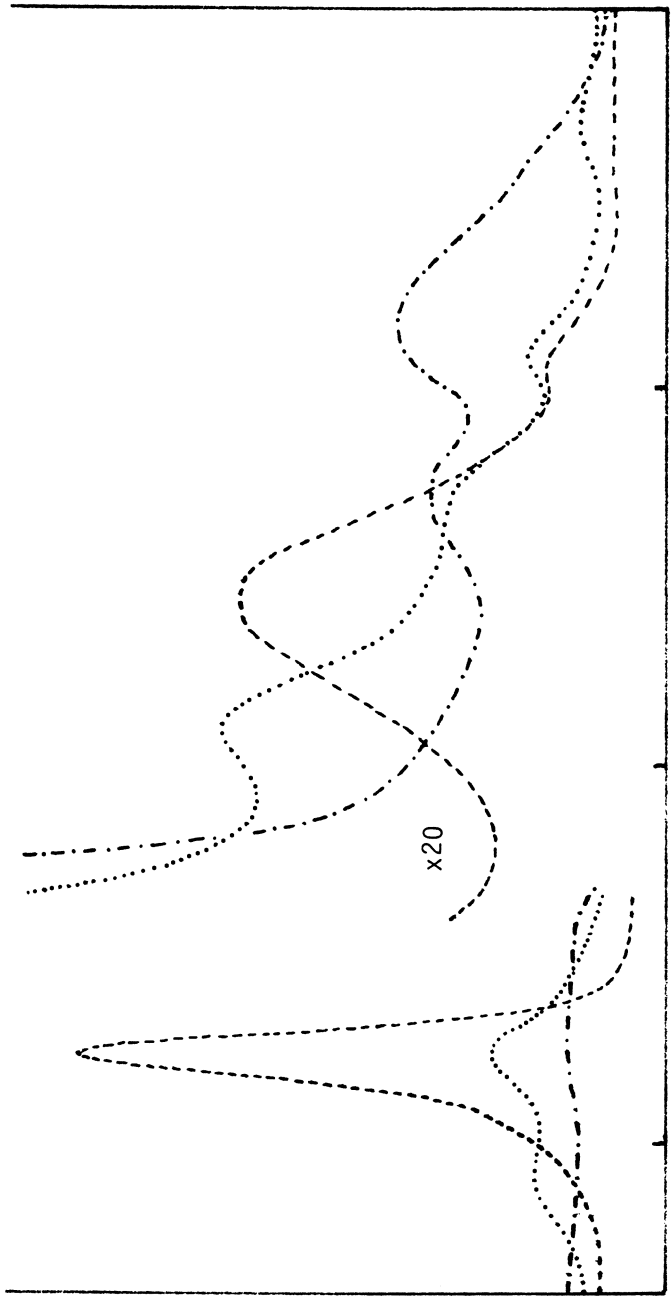

Figure 1. UV–VIS spectra of Fe(II)(TPP), Na[Fe(TPP)] and Na_2[Fe(TPP)] in THF solution (8). Key: ---, Fe(TPP); · · ·, [Fe(TPP)]$^-$; and - · -, [Fe(TPP)]$^{2-}$

(LUMO). In Figure 2 three structures are compared: $Fe(TPP)(THT)_2$ as a typical low spin iron(II) porphyrin of well-defined valency (*20*); $[Fe(TPP)]^-$ as its sodium crown–THF-solvated salt (*9*); and $[Fe(TPP)]^{2-}$, the further reduced species that quite unambiguously has porphyrin radical anion character (discussed later) (*9*). The bond distances are listed in order for these three compounds in the upper right quadrant of Figure 2 and the labeling scheme is in the upper left quadrant. The lengthening of the C_b–C_b and C_a–N bonds and the shortening of the C_a–C_b bond in $[Fe(TPP)]^-$ relative to those of a normal planar porphyrin are consistent with some population of the porphyrin LUMO, an e_g orbital that is antibonding with respect to C_b–C_b and C_a–N and bonding with respect to C_a–C_b (*21*). More x-ray structures of unambiguous radical anion complexes are needed to clarify the full effects of LUMO population.

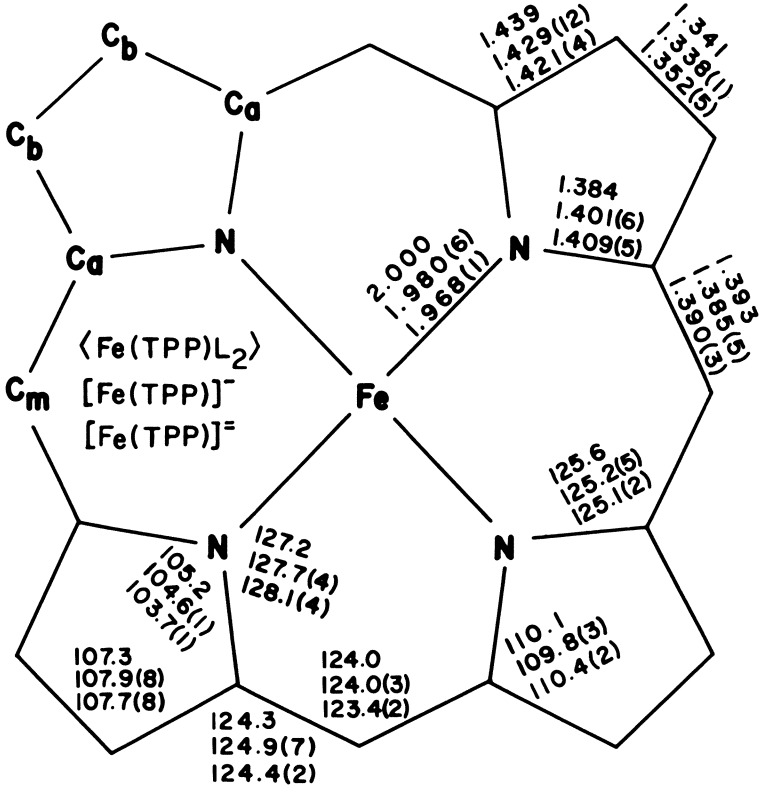

Figure 2. Porphyrin core dimensions for $Fe(TPP)(THT)_2$, $[Fe(TPP)]^-$, and $[Na(THF)_3]_2[Fe(TPP)]$ (9). Each group of digits gives the dimensions for these three species in their respective order.

The conclusion is that some contribution of a spin-coupled iron(II) porphyrin radical anion formulation to the iron(I) porphyrin formulation may be necessary to rationalize fully the properties of $[Fe(TPP)]^-$. Resonance forms can be written with iron(I) as the major contributor:

$$[Fe(I)(TPP)]^- \leftrightarrow [Fe(II)(TPP \cdot)]^-$$

Such resonance suggests that in the formalized iron(I) contributor the unpaired electron must reside in an orbital of the same symmetry as the porphyrin LUMO. Because the porphyrin LUMO has e_g symmetry, the singly occupied iron(I) orbital must be d_{xz} or d_{yz}.

This observation is in conflict with the $(d_{z^2})^1$ configuration suggested by EPR results, which compared iron(I) to the isoelectronic Co(II)(TPP) (*6*). This issue remains to be resolved, but the $(d_{xz})^1$ spin configuration for iron(I) would be more in keeping with the $(d_{xz},d_{yz})^2$ configuration of Fe(II)(TPP) where the d_{z^2} orbital is lower in energy than d_{xz},d_{yz}.

In summary, the low spin iron(I) formulation for $[Fe(TPP)]^-$ is an adequate assignment for most properties, but some resonance contribution from a spin-coupled iron(II) radical formulation is needed to rationalize the broadness of the UV–VIS spectrum and the subtle differences in core bond lengths between $[Fe(TPP)]^-$ and a normal iron porphyrin. For the first time, a single, discrete valency is inadequate for describing a metalloporphyrin complex. Typically, a porphyrin can be considered a "hard," innocent ligand and the issue of assigning oxidation states is not semantic. For example, both valence isomers of an oxidized nickel porphyrin were observed. The metal oxidized $[Ni(III)(TPP)]^+$ can be converted to the ring oxidized $[Ni(II)(TPP \cdot)]^+$ simply by making minor alterations in the solvation environment of the complex (*22*), suggesting that both Ni and TPP maintain discrete valencies in a chemical equilibrium:

$$[Ni(III)(TPP)]^+ \rightleftharpoons [Ni(II)(TPP \cdot)]^+$$

Whether a true equilibrium exists has not been investigated. However, this interpretation is to be contrasted with the resonance between valency hybrids just suggested for iron(I). If resonance contributors are needed with radical anion structures but not for radical cation structures, a rationale may lie in orbital overlap symmetries. Although the e_g LUMOs of a porphyrin have the correct symmetry for overlap with the (d_{xz},d_{yz}) metal orbitals, neither the a_{2u} nor the a_{1u} HOMOs (highest

occupied molecular orbitals) have the correct symmetry for overlap with any of the metal *d*-orbitals. However, lack of overlap does not rule out spin coupling in radical cations.

Choice of an integral valency depends on the particular physical property that forms the basis of the assignment. The foregoing analysis demonstrates that Mössbauer spectroscopy can be a good probe of the iron oxidation state, UV–VIS spectroscopy may be the best probe of the oxidation level of the porphyrin, and a consistency check with an x-ray crystal structure is highly desirable. Magnetic criteria are frequently ambiguous. Electrochemical criteria for distinguishing ring redox from metal redox include the ~2.25-V difference in potential between the first ring oxidation and the first ring reduction (*23*). This criterion is not particularly helpful for iron porphyrins. Another electrochemical criterion for identifying the site of redox involves comparing the reduction potentials for M(TPP) (M = metal) complexes with those of the tetracyano-substituted tetraphenylporphyrin complexes M(TPP–CN_4) (*24*). Differences of 1.0 ± 0.1 V indicate ring redox, whereas metal centered redox usually has much smaller differences. For the iron(III–II) reduction the difference is only 0.05 V but for the next reduction, the difference is 0.8 V. This result supports the iron(I) assignment but also indicates that the iron(I–II) potential is close to the TPP–TPP^- potential.

One puzzling feature of the electrochemical production of iron(I) porphyrins remains. Both electrochemical studies (*6*, *25*) report two forms of $[Fe(TPP)]^-$, labeled A and B. They are distinguished by UV–VIS spectra and form B corresponds to the synthetically accessible species (390 and 424 nm Soret) already discussed. Form A is produced when reduction is carried out at a more negative potential. In light of the chemistry now established for $[Fe(TPP)]^-$, it is not clear how two noninterconvertible forms could exist. The involvement of hydroxide was discussed (*25*) but the reduction level of A (362 and 457 nm Soret) was not unambiguously determined. The air sensitivity of these highly reduced species makes this work experimentally very demanding, but more studies are needed to assign a formula and structure to the so-called form A of $[Fe(TPP)]^-$.

Utility of Iron(I) Porphyrins: A New Type of Dioxygen Adduct

Iron(I) porphyrins do not appear to be biologically important because the very negative iron(I–II) redox potential is inaccessible with typical biological reducing agents. However, the one-electron reduction of the oxygen adduct derived from ferrous cytochrome P-450

[formally an Fe(III) superoxo complex (*26*)] is the key step that initiates monooxygenase chemistry:

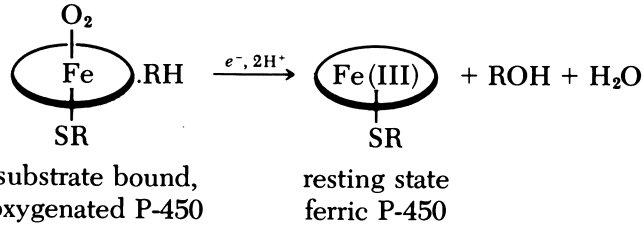

In the presence of organic substrate (RH) and a source of protons, the one-electron reduced oxygen adduct reacts rapidly, without isolable intermediates, to give oxygenated substrate (ROH) and H_2O (*27*). Conceptually, the one-electron reduction of an oxygen adduct is the same as adding O_2 to an iron(I) porphyrin. It is also conceptually the same as adding superoxide to an iron(II) porphyrin (*28*).

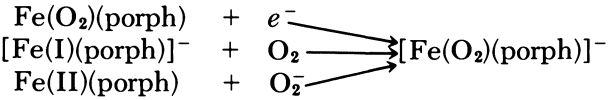

Ignoring the effect of axial ligation, the reaction of iron(I) porphyrin with oxygen should yield a new type of reduced oxygen complex, possibly related to the key reduction step in the cytochrome P-450 cycle.

Treatment of $[Fe(TPP)]^-$ with dry oxygen in THF solution at low temperatures or as a solid at room temperature produces $[Fe(O_2)(TPP)]^-$ as its sodium salt (*8*). It is spectroscopically identical to the species produced by treatment of Fe(TPP) with superoxide ion (*28*, *29*). It is characterized by UV–VIS spectroscopy (433, 564, and 607 nm in THF), EPR spectroscopy (g = 8, 4.22, 1.98 in frozen DMSO), Mössbauer spectroscopy [δ = 0.57 mm/s, ΔEq = 1.0 mm/s at 4.2 K in the solid state (*10*)], and vibrational spectroscopy of the octaethylporphyrinate (OEP) analogue [νO–O = 806 cm^{-1} (*28*)]. The effects of temperature and applied magnetic field on the Mössbauer spectrum are readily interpretable in terms of a high-spin $S = \frac{5}{2}$ iron(III) state (*10*). Taken all together these data suggest a peroxo iron(III) formulation for $[Fe(O_2)(TPP)]^-$ with triangular dihapto coordination like $Ti(O_2)(OEP)$ (*30*):

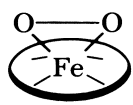

Although $[Fe(III)(O_2)(TPP)]^-$ lacks the axial thiolate coordination of cytochrome P-450, this work suggests that a peroxo intermediate could form at the dioxygen adduct reduction step in the P-450 catalytic cycle, possibly with transitory axial-ligand dissociation. More work is needed to validate such speculation, however.

Thus, although iron(I) porphyrins themselves are unlikely intermediates in hemoprotein biochemistry, their reaction chemistry may lead to useful model compounds.

Further Reduced Iron Porphyrins

Electrochemical production of a species that is two-electron reduced below iron(II) was identified by UV–VIS spectroscopy (*6*, *25*) (*see* Figure 1) and assigned the formula $[Fe(TPP)]^{2-}$. This green species is presumably the same as that seen as the final product of Na(Hg) reduction of $Fe_2(TPP)_2O$ (*4*), and on the basis of the broad maxima and the red-shifted Soret band was formulated as a radical anion of iron(I), $[Fe(I)(TPP\cdot)]^{2-}$. A synthesis for this dianion was developed by treating FeCl(TPP) with three equivalents of sodium anthracenide in THF solution (*8*). Dark green crystals of the disodium salt were isolated and analyzed for $[Na(THF)_3]_2[Fe(TPP)]$ [*Anal.* Calculated for $C_{68}H_{76}O_6N_4FeNa_2$: C,71.19; H,6,68; N,4.88. Found: C,71.42; H,6.78; N,5.08.] This species is extremely air sensitive, decomposing aerobically to $[Fe(TPP)]_2O$. It is diamagnetic and shows no EPR signal when pure. As usual, magnetic data do not allow one to distinguish between three possible, but not exclusive, formulations: (1) an iron(0) d^8-porphyrin, $[Fe(0)(TPP)]^{2-}$, (2) a spin-coupled $S = \frac{1}{2}$ iron(I) porphyrin radical anion, $[Fe(I)(TPP\cdot)]^{2-}$, and (3) a spin-coupled $S = 1$ iron(II) porphyrin diradical dianion, $[Fe(II)(TPP{:})]^{2-}$. As mentioned earlier, the green color and UV–VIS spectral features are consistent with radical anion character of the porphyrin ring (*see* Figure 1) suggesting that the iron(I) and/or the iron(II) formulations are most suitable. However, Mössbauer spectroscopy and an x-ray crystal structure were desirable to make a firmer assignment.

The x-ray crystal structure of $[Na(THF)_3]_2[Fe(TPP)]$ was determined (*9*) and reveals the 2 : 1 ion-paired structure illustrated in Figure 3. The average Fe–N distance is 1.968 (2) Å, which is consistent with a low spin state. In Figure 2 the ring bond lengths are compared with those of an iron(II) low spin porphyrin and with $[Fe(TPP)]^-$. Again, the lengthening of C_b–C_b and C_a–N and the shortening of C_a–C_b suggests population of the porphyrin LUMO, more so than with $[Fe(TPP)]^-$. The structural results therefore support the iron(I) radical formulation but do not readily distinguish it from the iron(II) diradical formulation.

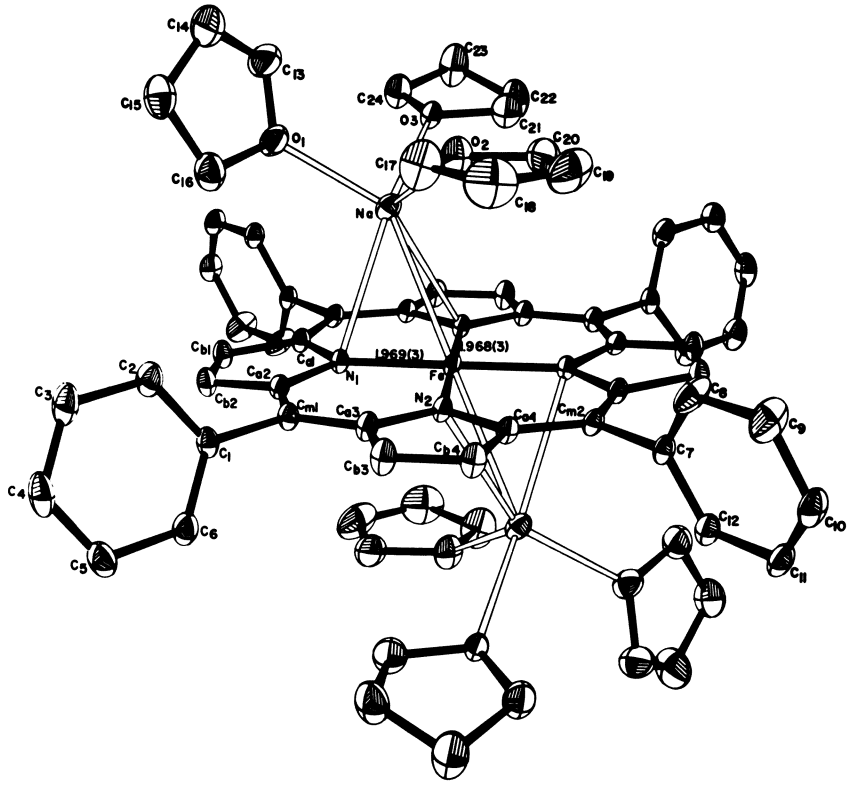

Figure 3. The crystal structure of [Na(THF)$_3$]$_2$[Fe(TPP)] (9).

The somewhat surprising result comes from the Mössbauer spectrum. The isomer shift of [Na(THF)$_3$]$_2$[Fe(TPP)] is 0.48 mm/s (*10*), which is comparable with iron(II) porphyrins not iron(I) (*see* Table I). A value similar to iron(I) or even higher might have been expected but not lower. Two possible explanations for this result are (1) the ion-pairing with sodium via the porphinato nitrogen atoms may decrease the *s*-electron density seen by the iron nucleus, making the dianion appear to be more oxidized than the monoanion [Fe(TPP)]$^-$ (δ = 0.65 mm/s) and (2) an unexpectedly large contribution could come from the iron(II) diradical structure to the formulation. In fact, all the data on [Fe(TPP)]$^{2-}$ can be rationalized by the spin-coupled iron(II) diradical formulation. However, an unexplained fact is that the two-electron reduction of iron(II) retains largely iron(II) character while the one-electron reduction gives largely iron(I) character. Thus, a resonance hybrid of iron(I) and iron(II) is favored.

$$[Fe(I)(TPP\cdot)]^{2-} \leftrightarrow [Fe(II)(TPP:)]^{2-}$$

Considered individually, both of these contributors must be completely spin-coupled because these formulations are in resonance, not in equilibrium, and the complex is diamagnetic. Metathesis with alkylammonium salts to remove the sodium ion-pairing is being attempted to resolve the ambiguity in the Mössbauer interpretation (*8*).

[FeCl(TPP)]⁺: Iron(IV) Porphyrin or Iron(III) Radical Cation?

In the first report (*31*) of an iron porphyrin oxidized above the iron(III) level, Fe(OAc)(TPP) was electrochemically oxidized to a species written $[Fe(TPP)]^{2+}$, and on the basis of its UV–VIS spectrum (broad, blue-shifted, moderately low intensity Soret at 396 nm and broad α,β-region) assigned an iron(III) radical cation formulation, $[Fe(III)(TPP\cdot)]^{2+}$. A magnetic moment of 2.71 BM was interpreted as an overall $S = 1$ system having a low spin $S = \frac{1}{2}$ iron(III) and an $S = \frac{1}{2}$ porphyrin radical with no spin-coupling. In view of subsequent measurements on the very closely related $S = 2$ chloride complex $[FeCl(TPP)]^+$, this magnetic susceptibility measurement most likely was in error. Wet solvents probably gave rise to $[Fe(TPP)]_2O$ and its oxidation products. These antiferromagnetically coupled systems have low magnetic moments and the published UV–VIS spectra are consistent with their presence as major components.

Solutions of $[FeCl(TPP)]^+$ were prepared by electrochemical methods (*32*, *33*). The complex was assigned a high spin iron(IV) formulation based on the $S = 2$ spin state, UV–VIS and proton NMR spectroscopy, and molecular orbital calculations. The closely related [Fe(*p*-methoxyTPP)Cl]⁺ shows similar spectroscopic properties to the analogous protoporphyrin IX dimethyl ester complex (*34*). However, none of these data unambiguously distinguish between the alternate formulations of $[FeCl(TPP)]^+$ as (1) a high spin iron(IV) porphyrin or (2) a high spin iron(III) radical cation where the $S = \frac{5}{2}$ iron is spin-coupled to the $S = \frac{1}{2}$ porphyrin radical to give an overall $S = 2$ state (*19*).

In keeping with the views that Mössbauer spectroscopy is one of the best criteria of oxidation and spin states of the iron and that a synthetic method that allowed isolation of $[FeCl(TPP)]^+$ for x-ray analysis was desirable to resolve this problem, this system was reinvestigated (*13*). A convenient synthetic method was developed by using the hexachloroantimonate salts of organic radicals ($R\cdot^+$) as clean, one-electron oxidants of known potential.

$$FeCl(TPP) + R\cdot^+SbCl_6^- \xrightarrow{CH_2Cl_2} [FeCl(TPP)][SbCl_6] + R$$

In many respects these reagents represent the synthetic equivalent of controlled potential electrochemistry. The product [FeCl(TPP)][$SbCl_6$] is isolable as black crystals and has a UV–VIS spectrum in dichloromethane identical to that reported for $[FeCl(TPP)]^+$ produced electrochemically. The magnetic moment (μ = 5.1 BM) is indicative of four unpaired electrons and Curie–Weiss law behavior (5–300 K) shows it to be a well-behaved $S = 2$ system. This magnetic moment also rules out the unlikely formulation of $[FeCl(TPP)]^+$ as an uncoupled porphyrin radical cation of intermediate spin iron(III) because some coupling of adjacent $S = \frac{3}{2}$ and $S = \frac{1}{2}$ systems would be expected at 5 K. Notably, the Mössbauer spectrum of [FeCl(TPP)][$SbCl_6$] is very much like high spin iron(III), not only in terms of the isomer shift and quadrupole splitting (*see* Table I), but also in the asymmetry of the doublet as a function of temperature (*13*). This evidence is particularly compelling for a high spin iron(III) radical formulation. All the spectroscopic data previously used to support the alternate iron(IV) assignment (*32*, *33*) can be reinterpreted. The UV–VIS spectrum of $[FeCl(TPP)]^+$ has most of the characteristics of a radical cation including a broad α,β-region and a Soret band (396 nm) that is broadened, blue-shifted, and lowered in intensity compared to FeCl(TPP) (*see* Figure 4). These characteristics were probably overlooked at first because the radical characteristics are not as dramatic as in an ideal case such as $[Zn(TPP\cdot)]^+$ where metal and ligand orbital energies are presumably well-separated. The proton NMR spectrum has the β-pyrrole protons markedly shifted downfield (−63.8 ppm) in a manner reminiscent of high spin iron(III) [−79 ppm in FeCl(TPP)] (*3*). The value of −69 ppm originally reported (*32*) probably arose from signal averaging from a mixture of $[FeCl(TPP)]^+$ and FeCl(TPP). This large downfield shift is probably due to spin density in the $d_{x^2-y^2}$ orbital and it is notably unlike that of the high spin d^4-complex MnCl(TPP) [+20 ppm (*3*)], which has $d_{x^2-y^2}$ unoccupied. Because MnCl(TPP) is isoelectronic with high spin iron(IV), it is probably a good NMR model. The chemical shifts of the phenyl protons are analyzed in more detail elsewhere (*34*). The single occupation of the porphyrin HOMO in $TPP\cdot^+$ might be expected to shift various ring vibrational modes. Interestingly, [FeCl(TPP)][$SbCl_6$] has a strong band at 1290 cm^{-1} in the IR spectrum that does not appear in FeCl(TPP). This band does not arise from the anion and is seen in other TPP radical cation species (*35*). This band appears to be a uniquely diagnostic criterion of radical cations of TPP.

The final arbiter of this formulation question will be the x-ray crystal structure because a high spin iron(III) atom in $[FeCl(TPP)]^+$ should have coordination group parameters entirely different from an iron(IV) atom. With $d_{x^2-y^2}$ occupied, high spin iron(III), if pentacoor-

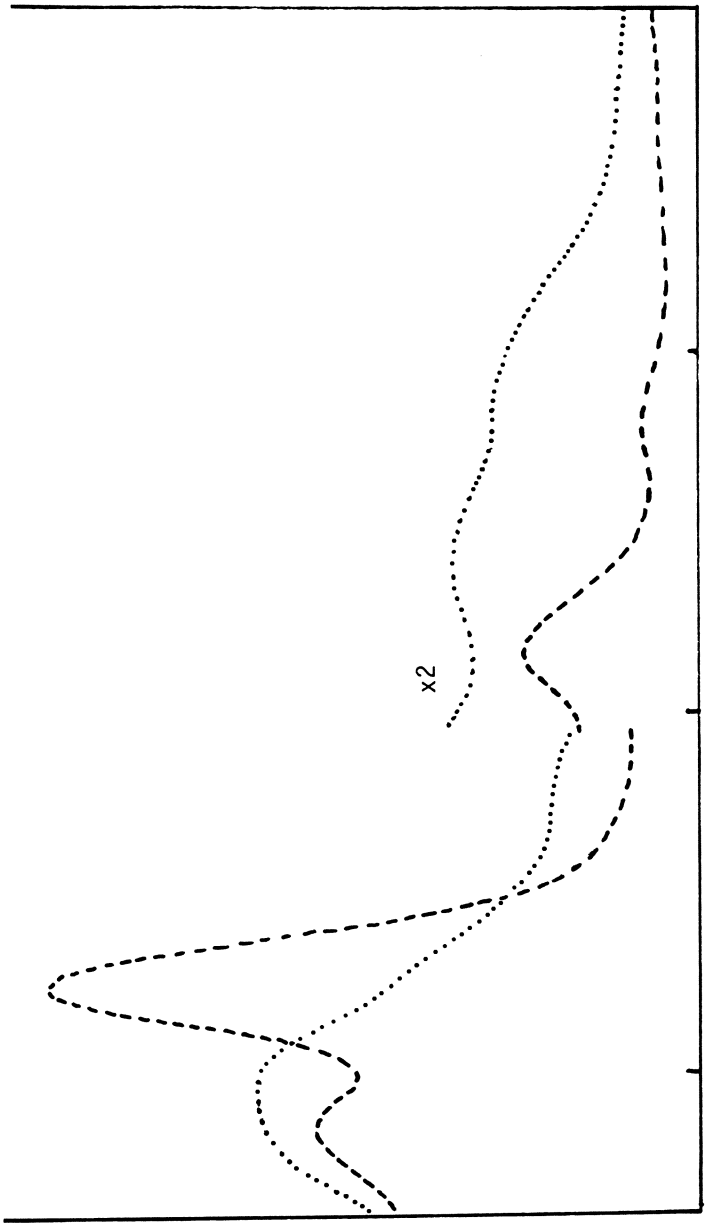

Figure 4. UV–VIS spectra of Fe(III)Cl(TPP) (---) and [Fe(III)Cl(TPP)][$SbCl_6$] (· · ·) in dichloromethane (35). These essentially are identical to those of Ref. 33.

dinated should have long Fe–N distances (~2.05 Å) and should be displaced considerably (~0.5 Å) from the porphyrin plane. On the other hand, high spin iron(IV), having $d_{x^2-y^2}$ unoccupied, is expected to show short Fe–N distances (≲2.00 Å) and coordination group parameters similar to, but slightly contracted from, MnCl(TPP).

The electrochemical criteria for distinguishing metal oxidation from ring oxidation are at best ambiguous and at worst misleading for iron. The 2.25 ± 0.15-V difference between the first ring oxidation and first ring reduction of most octaethylporphyrinate (OEP) complexes leads to ambiguity in Fe(OEP)(OH) (*23*). For Fe(TPP) derivatives the $[Fe(I)(TPP)]^-/[Fe(III)Cl(TPP\cdot)]^+$ difference is ~2.1 V and the $[Fe(TPP)]^{2-}/Fe(III)Cl(TPP\cdot)]^+$ ring difference is ~2.7 V. Clearly, the 2.25-V criterion is not applicable in this case. The difference between the first and second ring oxidations is frequently 0.29 ± 0.05 V, suggesting another criterion for assigning redox steps (*19*). In etioporphyrin I iron(III) chloride and tetra-*p*-tolylporphyrin iron(III) chloride differences of 0.54 and 0.43 V, respectively, were used to substantiate the iron(IV) assignment (*33*). In view of the conclusion that $[FeCl(TPP)]^+$ is not iron(IV) and the likelihood that the etioporphyrin I and tolylporphyrin analogues are likewise not iron(IV), this electrochemical criterion is apparently not always reliable. Of substantially more reliability is the criterion of insensitivity of ring oxidation to axial ligation change (*36*). This study lends support to the ring oxidation of FeCl(TPP). Thus, although in favorable cases electrochemical criteria can support the assignment of a site of redox, they should not be relied on in cases where metal redox potentials may be close to ring potentials.

In summary, the weight of evidence is heavily against an iron(IV) formulation for $[FeCl(TPP)]^+$ and because an x-ray single-crystal study is in progress (*37*) and extended x-ray absorption fine structure (EXAFS) measurements are being made (*38*), the final resolution of this question can be anticipated in the near future. Mössbauer spectroscopy has proved to be a decisive probe for the oxidation state of iron. Furthermore, although UV–VIS spectroscopy remains a useful probe of the oxidation level of the porphyrin, it is not always clearcut. Spectral patterns that identify porphyrin radicals (*19, 39*) tend to portray ideal cases. For iron, where the *d*-orbital energies are close to those of the porphyrin HOMO or LUMO, less predictable spectra arise. Possibly NMR and IR criteria will eventually prove to be of greater utility than UV–VIS in identifying radical character in a porphyrin.

Some comment must be made on the nature of the intramolecular antiferromagnetic coupling between a paramagnetic metal center and a porphyrin radical cation. The overall $S = 2$ character of $[Fe(III)Cl(TPP\cdot)]^+$ indicates that coupling is very large. This finding

is in marked contrast with Compound I of horseradish peroxidase where a very small coupling ($-J \simeq 2$ cm^{-1}) between the $S = 1$ iron(IV) and the porphyrin radical is observed (*18*). Similarly, the $[Cu(II)(P\cdot)]^+$ species apparently has negligible coupling, giving rise to two unpaired electrons (*31*, *40*). One report, however, found diamagnetism (*39*). Clearly, there are too few unambiguous data to reveal any systematic trends. Because antiferromagnetic interactions are generally difficult to rationalize, it is of little use to speculate on why coupling is strong in $[Fe(III)Cl(TPP\cdot)]^+$ but not in other complexes. Population of all the *d*-orbitals in high spin d^5-iron(III) certainly maximizes the opportunity for coupling.

Oxidized μ-Oxo Ferric Dimers

The two-electron electrochemical oxidation of $[Fe(TPP)]_2O$ occurs in discrete steps separated by ~0.3 V (*33*). This situation has allowed study of both the one-electron oxidized "mixed-valence" compound, $[Fe_2(TPP)_2O]^+$ and the two-electron oxidized product, $[Fe_2(TPP)_2O]^{2+}$. The $Fe_2(OEP)_2O$ complex apparently behaves in a very similar manner.

The singly oxidized species $[Fe_2(TPP)_2O]^+$ was characterized both in solution and in the solid state (*33*, *34*). The UV–VIS spectrum is not compellingly radical cation-like but is suggestive of one (*see* Figure 5). It shows a reduced intensity Soret band and a broadened α,β-region but no blue-shifting of the Soret. The low magnetic moment ($\mu = 2.9$ at 40°C) was tentatively interpreted as a mixture of $S = \frac{1}{2}$ and $S = \frac{3}{2}$ states in equilibrium (*33*) but is more likely to arise from antiferromagnetic coupling. The ESR spectrum ($g = 2.059$, 1.993) is consistent with metal-localized unpaired spin (*33*), but it does not rule out a porphyrin radical because its spin would almost certainly be coupled to the iron as in $[FeCl(TPP\cdot)]^+$. The proton NMR assignments have been put on a firm basis (*34*) and temperature dependence studies support the presence of antiferromagnetism. The best evidence for a porphyrin radical formulation comes from the appearance of the diagnostic 1280-cm^{-1} IR band (*35*). A report of a synthetic method of isolating $[Fe_2(TPP)_2O]^+$ as a BF_4^- or PF_6^- salt and the determination of magnetic, Mössbauer, EPR, and IR characteristics (*41*) should probably be entirely discounted because the presence of fluoro-bridged dimers provides a more acceptable rationale for the observations (*42*). Compared to $[FeCl(TPP\cdot)]^+$, the presence of an oxo ligand should improve the accessibility of iron(IV) but the weight of evidence is toward a radical cation formulation for $[Fe_2(TPP)_2O]^+$ rather than a mixed-valence iron(III)–(IV) species. The determination of its Mössbauer spectrum and x-ray crystal structure should lead to a confident assignment.

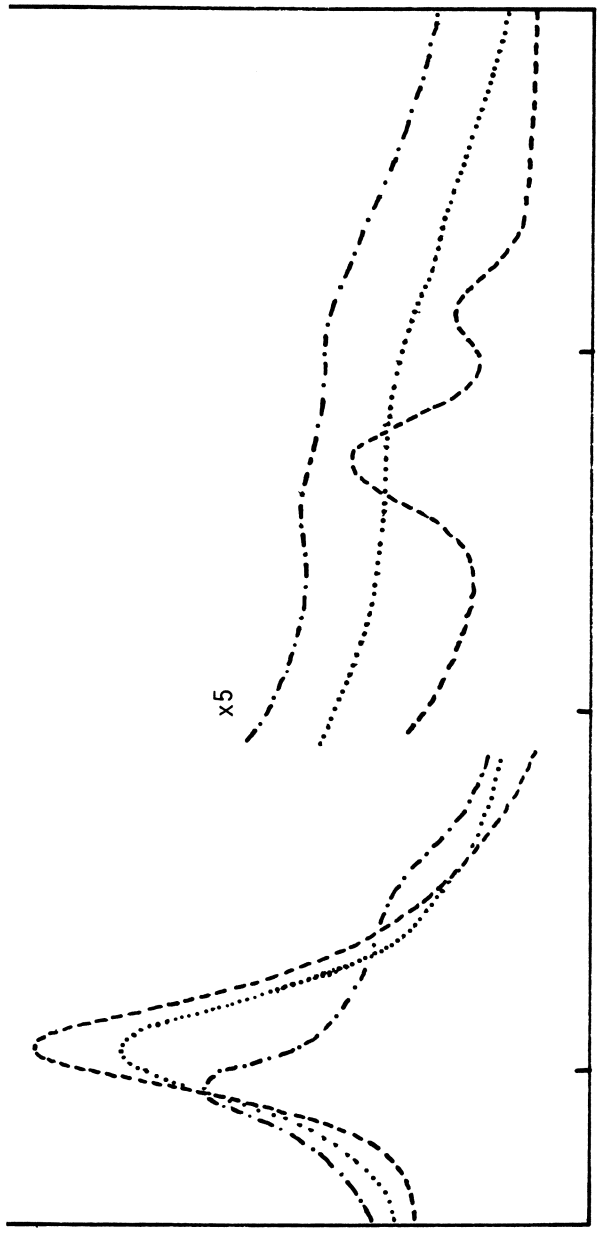

Figure 5. UV–VIS spectra of $Fe_2(TPP)_2O$ (---), $[Fe_2(TPP)_2O]^+SbCl_6^-$ (· · ·), and $[Fe_2(TPP)_2O]^{2+}$ $2SbCl_6^-$ (- · -) in dichloromethane (35). These essentially are identical to those of Ref. 33.

A comparison may be drawn between $[Fe_2(TPP)_2O]^+$ and the isoelectronic nitride $Fe_2(TPP)_2N$ (*43*). This species, however, defies straightforward formulation despite extensive study of its physical properties. Magnetic criteria such as susceptibility measurements and ESR spectroscopy clearly show that the dimer is an overall $S = \frac{1}{2}$ system with the unpaired electron localized on the FeNFe moiety (*43*, *44*). All experiments show the two iron atoms to be identical so that an averaged valence formalism is required (*43*). Because the UV–VIS spectrum shows no porphyrin radical cation characteristics, the metals can be assigned an averaged iron(III)–(IV) valency. The compound is a so-called Class II mixed-valence compound and can be viewed as having an iron(III $\frac{1}{2}$) valency, represented by equal contribution from two resonance forms:

$$Fe(III)—N{=}Fe(IV) \leftrightarrow Fe(IV){=}N—Fe(III)^{\cdot}$$

The unanswered question is that of the spin state(s). The Mössbauer spectra were interpreted as indicative of high spin (*43*); the x-ray crystal structure is more in accord with an average of low spin iron(III) and high spin iron(IV) (*44*); the XPS spectra require a low spin assignment (*45*), and the resonance Raman suggest a high spin state (*46*). So, unlike all of the monomeric iron porphyrins discussed previously, the assignment of spin states to iron in $Fe_2(TPP)_2N$ appears to be at best, permanently ambiguous and at worst, one of those nuisance questions of inorganic chemistry.

In a somewhat related manner, the ambiguous assignment of oxidation and spin states in carbene complexes of the type $Fe(CR_2)$(porph) points to the noninnocent behavior of a carbene ligand (*47*):

$$Fe(IV){=}CR_2 \leftrightarrow Fe(II) \leftarrow{:}CR_2$$

Some iron(IV) character can be invoked to rationalize the similarity of the UV–VIS spectra of vinylidene complexes with Compound II of peroxidases (*48*).

In addition to the singly oxidized μ-oxo dimer there is also the doubly oxidized species $[Fe_2(TPP)_2O]^{2+}$ and its OEP analogue. First produced electrochemically (*32*), the diperchlorate salt now has been isolated (*34*). The bishexachlorantimonate salt can also be synthesized using $R \cdot {}^+SbCl_6^-$ reagents (*35*). The visible spectrum of $[Fe_2(TPP)_2O]^{2+}$ is rather like a cation radical having a broadened blue-shifted Soret band at 396 nm and a broadened α,β-region (*see* Figure 5). This spectrum suggests an iron(III) radical formulation but is by no means conclusive without Mössbauer and structural corrobora-

tion. Strong antiferromagnetic coupling via the oxo bridge is suggested by an analysis of the proton NMR spectrum (*34*). The appearance of a strong 1290-cm^{-1} band in the IR spectrum of $[Fe_2(TPP)_2O][SbCl_6]_2$ is diagnostic of porphyrin radical formulation (*35*), and others (*34*) favor such an assignment over the iron(IV) formulation previously assigned (*33*).

Monomeric Iron(IV) Porphyrins

The solution characterization of what is apparently the first authentic iron(IV) porphyrin was reported recently (*49*). μ-Peroxo iron(III) dimers can be cleaved homolytically with ligands (L) such as 1-methylimidazole (1-MeIm), pyridine, or piperidine to yield oxo iron(IV) porphyrins [FeO(porph)L]:

$$\text{(porph)Fe–O–O–Fe(porph)} + 2\ \text{1-MeIm} \xrightarrow[\text{toluene}]{-90°C} 2\ \text{FeO(porph)L}$$

The reaction must be carried out at low temperatures under scrupulously aprotic conditions, and the product is unstable in solution above −30°C. The UV–VIS spectrum of FeO(TmTP)(1-MeIm) (TmTP = tetra-*m*-tolylporphinato) is typically metalloporphyrin-like and shows no cation radical character. The magnetic susceptibility is 2.9 BM at −40°C, and the Curie law behavior of the porphyrin shifts in the proton NMR spectrum suggests a well-behaved monomeric $S = 1$ system. These data support an intermediate spin iron(IV) formulation and the close similarity of the susceptibility and electronic spectra to those of Compound II of peroxidases is very gratifying.

The central importance of this complex to iron(IV) porphyrin chemistry and its relevance to peroxidase chemistry make definitive structural characterization a paramount objective. The thermal instability of FeO(TPP)(1-MeIm) means this characterization will not be easy, but in the absence of an x-ray structure, Mössbauer spectroscopy can provide additional characterization. Spectra were obtained for FeO(TPP)(1-MeIm) (*14*) and they give strong support to the iron(IV) assignment. The isomer shift (δ) is 0.11 mm/s at 4.2 K and the quadrupole splitting is 1.24 mm/s. Such a low isomer shift reflects a high oxidation state, and δ progresses from a high of 0.65 in the iron(I) porphyrin to a low of 0.03 in iron(IV) hemoproteins (Table I). The temperature and applied magnetic field dependencies of Fe(O)(TPP)(1-MeIm) are in accord with an $S = 1$ state and closely mimic the spectra of Compound E.S. of cytochrome c peroxidase (CCP) (*14*, *15*).

The comparison of Fe(IV)O(TPP)(1-MeIm) and $[Fe(III)Cl(TPP\cdot)]^+$ demonstrates how the site of redox is dictated by the axial

ligand. The ferryl moiety (Fe=O) provides the only axial ligation capable of stabilizing iron(IV) in mononuclear species. The nitrido moiety (FeNFe) also seems to show this capacity in dimers. The unique ability of oxo ligands to stabilize high oxidation states of transition metals is well-known and only fluoride, hydroxide, and alkoxide axial ligation remain as untested but viable alternatives in the search for other iron(IV) porphyrin complexes. The circumstantial evidence for oxo ligation in iron(IV) hemoproteins is now quite strong, although hydroxo ligation cannot be ruled out.

Further Oxidized Iron Porphyrins

Iron porphyrins that are two-electron oxidized above iron(III) have been referred to as iron(V) porphyrins purely as a formalism of convenience. Apparently, however, the one-electron oxidation products of $S = 1$ iron(IV) porphyrins are actually iron(IV) radical cations. Synthetically, they were approached by reaction of iodosobenzene or peracid reagents with iron(III) porphyrins.

A green intermediate of possible composition FeO(OEP)Cl was reported in the interaction of Fe(OEP)Cl with iodosylxylene (*50*). Some UV–VIS spectral similarity with Compound I of catalase (Cat I) lends support to the assignment of an iron(IV) radical cation. Such spectral similarity is not, however, much closer to Cat I than an oxidized carbene complex is to HRP I (*48*). Clearly, structural assignments based upon modest spectral similarity should be made with considerable caution. A magnetic moment of 4.8 BM was reported and a high spin iron(IV) assignment suggested. This report is inconsistent with expectations based on HRP I and leaves some doubt about the identity of this complex. The high-spin state of iron(IV), if it exists, remains to be established in a definitively characterized porphyrin complex.

A more definitive characterization of the product of iron(III) porphyrins with "oxygen atom" reagents was published (*17*). Treatment of FeCl(TMP) (TMP = tetramesitylporphyrinate) with *m*-chloroperoxybenzoic acid gives a green intermediate, which can be studied spectroscopically at lowered temperatures. Its Mössbauer spectrum (*see* Table I) is similar to the $S = 1$ iron(IV) species Fe(O)(TPP)(1-MeIm). Its magnetic moment of 4.2 BM is slightly larger than expected for an $S = \frac{3}{2}$ system but is consistent with an essentially noncoupled $S = 1$ iron(IV) and a porphyrin radical cation. The proton NMR spectrum shows pyrrole shifts (−27 ppm) typical of a radical cation, which, together with the distinctly radical cation-like UV–VIS spectrum leads to the assignment of an iron(IV) radical cation formulation:

$$\text{Fe(III)Cl(TMP)} + \text{RCOOOH} \rightarrow \text{Fe(IV)O(TMP}\cdot)\text{Cl} + \text{RCOOH}$$

The product's UV–VIS spectrum somewhat resembles that of Compound I of HRP, which is also green and is widely accepted to be an iron(IV) radical cation (*18*, *51*). Although oxo axial ligation is proposed in both Fe(O)(TMP)Cl and HRP I, the conjugate acid, namely hydroxide, cannot be ruled out. Also, the presence or absence of other axial ligation such as chloride or solvent (methanol) is unknown.

Chemically related to this green complex is a red complex that can be generated either by treatment of the green complex with base (OH^-) or by treatment of FeCl(TMP) with iodosobenzene (*17*). Its true nature is quite puzzling. Its Mössbauer spectrum ($\delta = -0.03$ ppm, $\Delta E = 2.13$ mm/s) suggests of either iron(IV) or iron(V) but its magnetic moment (2.9 BM) is indicative of a Curie law behaved overall $S = 1$ system. No strong EPR signals are noted, but the proton NMR has the β-pyrrole resonance in the downfield position ($\delta - 33.5$ ppm) usually associated with a radical cation.

Work on these highly oxidized iron porphyrin complexes is very demanding experimentally. The much needed information on their structures and the resolution of uncertainties in their properties is greatly hampered by their high reactivity toward hydrocarbons. The integrity of the ferryl ligation remains to be established, at least by IR spectroscopy, and closer models for HRP I and Cat I need to be sought.

Finally, Fe(IV)(O)(P·)X species do not show much evidence for spin-coupling between the $S = 1$ metal and $S = \frac{1}{2}$ ring. This finding is in contrast to $[Fe(III)Cl(TPP\cdot)]^+$ where coupling is complete. For HRP I the coupling constant has been estimated from Mössbauer and EPR spectroscopy to be $-J \sim 2$ cm^{-1} (*18*) whereas in $[FeCl(TPP\cdot)]^+$ $|-J|$ must be $\gg 200$ cm^{-1}. Almost nothing is understood about the mechanism(s) and magnitude of antiferromagnetic coupling in metalloporphyrin radical species.

In summary, authentic iron(IV) porphyrins are accessible when an oxo ligand is present. Complexes of the type Fe(IV)O(TPP)L are good models for Compound II of HRP and compounds of the type Fe(IV)O(TMP·)Cl are satisfactory models for Compound I. Their reactivity is currently receiving considerable attention (*27*, *52*) and is leading to a long awaited insight into the chemical mechanisms by which the peroxidases and the cytochromes P-450 function.

Acknowledgments

Much of the present understanding of the iron porphyrins discussed in this review has arisen from collaborative studies with W. Robert Scheidt (University of Notre Dame), George Lang (Pennsylvania State University), and Jean-Claude Marchon (Centre Etudes

Nucleaires de Grenoble). I particularly thank them, their students, and my students who are cited in the references. I also thank John T. Groves and Harold Goff for discussion of results prior to publication.

I sincerely hope that the authors whose work I reinterpret will grant me the liberty of critical scientific enquiry and the license of alternative interpretation.

Literature Cited

1. Scheidt, W. R.; Reed, C. A. *Chem. Rev.*, **1981**, *81*, 543–555.
2. Sams, J. R.; Tsin, T. B. In "The Porphyrins"; Dolphin, D., Ed.; Academic: New York, **1979**; Vol. 4, 425–478.
3. La Mar, G. N.; Walker, F. A. In "The Porphyrins"; Dolphin, D., Ed.; Academic: New York, **1979**; Vol. 4, pp. 61–157.
4. Cohen, I. A.; Ostfeld, D.; Lichtenstein, B. *J. Am. Chem. Soc.* **1972**, *94*, 4522–4525.
5. Reed, C. A.; Mashiko, T.; Scheidt, W. R.; Spartalian, K.; Lang, G. *J. Am. Chem. Soc.* **1980**, *102*, 2302–2306.
6. Lexa, D.; Momenteau, M.; Mispelter, J. *Biochim. Biophys. Acta* **1974**, *338*, 151–163.
7. Collman, J. P.; Sorrell, T. N.; Dawson, J. H.; Trudel, J. R.; Bunnenburg, E.; Djerassi, C. *Proc. Nat. Acad. Sci. U.S.A.* **1976**, *73*, 6–10.
8. Mashiko, T.; Reed, C. A., unpublished data.
9. Haller, K. J.; Scheidt, W. R.; Reed, C. A., unpublished data.
10. Lang, G.; Reed, C. A., unpublished data.
11. Collman, J. P.; Hoard, J. L.; Kim, N.; Lang, G.; Reed, C. A. *J. Am. Chem. Soc.* **1975**, *97*, 2676–2681.
12. Maricondi, C.; Straub, D. K.; Epstein, L. M. *J. Am. Chem. Soc.* **1972**, *94*, 4157–4159.
13. Gans, P.; Marchon, J.-C.; Reed, C. A.; Regnard, J.-R. *Nouv. J. Chimie* **1981**, *5*, 203–204.
14. Simonneaux, G.; Scholz, W. R.; Lang, G.; Reed, C. A., *Biochim. Biophys. Acta* **1982**, *715*.
15. Lang, G.; Spartalian, K., Yonetaini, T. *Biochim. Biophys. Acta* **1976**, *451*, 250–258.
16. Schulz, C.; Chiang, R.; Debrunner, P. G. *J. Phys.* **1979**, *40*, C2–534–536.
17. Groves, J. T.; Haushalter, R. C.; Nakamura, M.; Nemo, T. E.; Evans, B. J. *J. Am. Chem. Soc.* **1981**, *103*, 2884–2886.
18. Schulz, C. E.; Devany, P. W.; Winkler, H.; Debrunner, P. G.; Doan, N.; Chiang, R.; Rutter, R.; Hager, L. P. *FEBS Lett.* **1979**, *103*, 102–105.
19. Fuhrhop, J.-H. *Struct. Bonding* **1974**, *18*, 1–67.
20. Mashiko, T.; Reed, C. A.; Haller, K. J.; Kastner, M. E.; Scheidt, W. R. *J. Am. Chem. Soc.* **1981**, *103*, 5758–5767.
21. Gouterman, M. *J. Mol. Spectrosc.* **1961**, *6*, 138–163.
22. Dolphin, D.; Niem, T.; Felton, R. H.; Fujita, I. *J. Am. Chem. Soc.* **1975**, *97*, 5288–5290.
23. Furhop, J. H.; Kadish, K. M.; Davis, G. D. *J. Am. Chem. Soc.* **1973**, *95*, 5140–5147.
24. Giraudeau, A.; Callot, H. J.; Jordan, J.; Ezhar, I.; Gross, M. *J. Am. Chem. Soc.* **1979**, *101*, 3857–3862.
25. Kadish, K. M.; Larson, G.; Lexa, D.; Momenteau, M. *J. Am. Chem. Soc.* **1975**, *97*, 282–288.
26. Reed, C. A.; Cheung, S. K. *Proc. Nat. Acad. Sci. U.S.A.* **1977**, *74*, 1780–1784.
27. Groves, J. T. *Adv. in Inorg. Biochem.* **1979**, *1*, 119–145.

28. McCandlish, E.; Miksztal, A. R.; Nappa, M.; Sprenger, A. Q.; Valentine, J. S.; Stong, J. D.; Spiro, T. G. *J. Am. Chem. Soc.* **1980,** *102,* 4268–4271.
29. Afanas'er, I. B.; Prigoda, S. V.; Khenkin, A. M.; Shteinman, A. A. *Dokl. Akad. Nauk. SSSR, Engl.* **1977,** *236,* 902–905.
30. Guilard, R.; Latour, J.-M.; Lecomte, C.; Marchon, J.-C.; Protas, J.; Ripoll, D. *Inorg. Chem.* **1978,** *17,* 1228–1237.
31. Wolberg, A.; Manassen, J. *J. Am. Chem. Soc.* **1970,** *92,* 2982–2991.
32. Felton, R. H.; Owen, G. S.; Dolphin, D.; Fajer, J. *J. Am. Chem. Soc.* **1971,** *93,* 6332–6334.
33. Felton, R. H.; Owen, G. S.; Dolphin, D.; Forman, A.; Borg, D. C.; Fajer, J. *Ann. N.Y. Acad. Sci.* **1973,** *206,* 504–515.
34. Phillippi, M. A.; Goff, H. M. *J. Am. Chem. Soc.* **1979,** *101,* 7641–7643.
35. Shimomura, E. T.; Phillippi, M. A.; Goff, H. M.; Scholz, W. F.; Simonneaux, G.; Reed, C. A. *J. Am. Chem. Soc.* **1981,** *103,* 6778–6780.
36. Phillippi, M. A.; Shimomura, E. T.; Goff, H. *Inorg. Chem.* **1981,** *20,* 1322–1325.
37. Marchon, J. C., personal communication.
38. Hahn, J.; Hodgson, K. O.; Reed, C. A., unpublished data.
39. Dolphin, D.; Muljiani, Z.; Rousseau, K.; Borg, D. C.; Fajer, J.; Felton, R. H. *Ann. N.Y. Acad. Sci.* **1973,** *206,* 177–200.
40. Mengersen, C.; Subramanian, J.; Fuhrhop, J.-H. *Mol. Phys.* **1976,** *32,* 893–897.
41. Wollman, R. G.; Hendrickson, D. N. *Inorg. Chem.* **1977,** *16,* 723–733.
42. Cohen, I. A.; Lavallee, D. K.; Kopelove, A. B. *Inorg. Chem.* **1980,** *19,* 1098–1100.
43. Summerville, D. A.; Cohen, I. A. *J. Am. Chem. Soc.* **1976,** *98,* 1747–1752.
44. Scheidt, W. R.; Summerville, D. A.; Cohen, I. A. *J. Am. Chem. Soc.* **1976,** *98,* 6623–6628.
45. Kadish, K. M.; Bottomley, L. A.; Brace, J. G.; Winograd, N. *J. Am. Chem. Soc.* **1980,** *102,* 4341–4344.
46. Schick, G. A.; Bocian, D. F. *J. Am. Chem. Soc.* **1980,** *102,* 7982–7984.
47. Mansuy, D.; Chottard, J.-C.; Lange, M.; Battioni, J.-P. *J. Mol. Cat.* **1980,** *7,* 215–226.
48. Mansuy, D.; Lange, M.; Chottard, J.-C. *J. Am. Chem. Soc.* **1979,** *101,* 6437–6439.
49. Chin, D.-H.; Balch, A. L.; La Mar, G. N. *J. Am. Chem. Soc.* **1980,** *102,* 1446–1448.
50. Chang, C. K.; Kuo, M.-S. *J. Am. Chem. Soc.* **1979,** *101,* 3413–3415.
51. Dolphin, D.; Forman, A.; Borg, D. C.; Fajer, J.; Felton, R. H. *Proc. Nat. Acad. Sci. U.S.A.* **1971,** *68,* 614–618.
52. Chin, D.-H.; La Mar, G. N.; Balch, A. L. *J. Am. Chem. Soc.* **1980,** *102,* 5945–5947.

RECEIVED for review June 2, 1981. ACCEPTED September 14, 1981.

Magnetic Resonance of Oxidized Metalloporphyrins

HAROLD M. GOFF[1], MARTIN A. PHILLIPPI, ARDEN D. BOERSMA, and ANDREW P. HANSEN

University of Iowa, Department of Chemistry, Iowa City, IA 52242

Iron(III) porphyrin anion complexes undergo reversible one-electron oxidation at platinum electrodes in apolar media. In favorable cases, oxidized products have been isolated from supporting electrolyte in analytically pure form. Although earlier reports favored electron abstraction from a metal-centered molecular orbital to yield an iron(IV) species, the results cited here for weak-field anion complexes of iron(III) tetraphenylporphyrins(TPP) favor predominant porphyrin-centered oxidation. This result is demonstrated by the fact that NMR hyperfine coupling constants for phenyl protons of TPPFe(Cl)(ClO_4) are equivalent to those determined by ESR of known π-radical species. Mössbauer results are also consistent with little perturbation of charge at the iron center on oxidation. Unique IR bands observed for both oxidized $TPPFe^{2+}$ species and $TPPZn^{+}$ π-cation radicals may serve to distinguish the site of oxidation. Analogous results are reported for oxidized manganese porphyrins. Low spin diimidazole adducts of oxidized iron porphyrins are spectroscopically observed at low temperature. Porphyrin radical character is also apparent in these derivatives. The chemistry of electrochemically oxidized metalloporphyrins and other reported iron(IV) species is reviewed in the context of known hemoprotein oxidation reactions.

Reversible one- or two-electron oxidation of the iron(III) porphyrin prosthetic group occurs during the catalytic cycle of peroxidases

[1] Author to whom correspondence should be addressed.

0065-2393/82/0201-0357$06.00/0

and catalase (*1–3*). Such oxidation is also postulated for redox processes of other hemoproteins. The best characterized oxidation sequences are those for horseradish peroxidase (HRP), for which hydrogen peroxide or organic peroxides presumably abstract two electrons from the heme group to give Compound I:

$$PFe(III)^+ + H_2O_2 \rightarrow \cdot PFe(IV){=}O^+ + H_2O$$
$$\mathbf{I}$$

One-electron substrate reduction yields Compound II:

$$\cdot PFe(IV){=}O^+ + S \rightarrow PFe(IV){=}O + \cdot S^+$$
$$\mathbf{II}$$

Iron(IV) porphyrin π-cation radical formulations for Compound I of HRP and catalase were suggested previously (*4*). Current support for this unusual redox structure is based on electronic, ESR, and Mössbauer spectral measurements. Thus, the electronic spectrum of HRP Compound I exhibits a broad Soret band with diminished intensity, and broad, nondistinctive visible region bands like those observed for π-cation radical metalloporphyrins. Detection of a very broad $g = 2$ ESR signal for Compound I also supports a π-cation radical state (*5*). The strongest evidence favoring metal-centered oxidation in both Compounds I and II is found in Mössbauer isomer shift values of very near 0.0 mm/s (*5–7*).

Oxidation of aromatic or sulfur-based amino acid residues appears to occur for cytochrome c peroxidase (CCP) (*8*). Two-electron oxidation of CCP yields a species spectrally equivalent to HRP Compound II, but exhibiting a sharp ESR signal and ENDOR resonances interpreted as involving a methionine redox site (*9*). Based on NMR results, some researchers (*10–12*) suggested an analogous formulation for HRP Compound I in which an amino acid residue is oxidized and the iron(IV) porphyrin is in the high spin state. Large isotropic NMR shifts may be explained by the widely accepted iron(IV) porphyrin π-cation radical electronic structure (*13, 14*). Additional comment on this point is made (vide infra) with respect to our results for oxidized model compounds. Even more convincing arguments for the iron(IV) π-cation radical formulation for HRP Compound I are found in ENDOR spectra, which reveal radical coupling with ring methyl–methylene protons and pyrrole nitrogen atoms (*15*).

High oxidation state intermediates were also postulated for cytochrome P-450 (*16, 17*) and cytochrome oxidase (*18*). The net reaction for a portion of the cytochrome P-450 cycle can be summarized by:

$$PFe(II) + O_2 + e^- + 2\ H^+ \rightarrow \cdot PFe(IV){=}O + H_2O$$

The Compound I analog was not identified, but its presence is implicated through generation from the iron(III) state by hydrogen peroxide and by similar substrate reactions of cytochrome P-450 and peroxidases. An iron(IV) porphyrin state was also postulated as a means of explaining the "silent" ESR component of oxidized cytochrome oxidase (*18*). However, more recent findings provide no support for a highly oxidized heme during the cytochrome oxidase cycle.

Systematic generation and physical examination of oxidized iron porphyrin intermediates in isolated iron porphyrins might be parallel in significance to the demonstrably productive oxygen binding studies of iron porphyrin model compounds (*19*, *20*). In this regard the chemistry of isolated iron(IV) porphyrin compounds is critically reviewed, with emphasis on recent results from this laboratory for both oxidized iron and manganese porphyrin complexes. The following high oxidation state species and reactions will be considered: (1) iron porphyrin μ-nitrido dimeric complexes, (2) carbene and vinylidene complexes, (3) iodosylbenzene oxidations, (4) μ-peroxo iron porphyrin reactions, (5) other chemical oxidations, and (6) electrochemically oxidized metalloporphyrin compounds, to include those extensively studied by this research group.

Iron Porphyrin–μ-Nitrido Dimeric Complexes

In a xylene reflux, nitrogen was eliminated from the azide complex, $TPPFeN_3$, to yield the μ-nitrido dimer, TPPFe–N–FeTPP (*21*). An x-ray structure determination confirmed the formulation (*22*). Assigning the bridging nitrogen atom a −3 charge puts formal charges of +3 and +4, or an average of +3.5, on the iron centers. Iron atoms are equivalent on the Mössbauer time scale and increased charge on iron centers is reflected in an isomer shift value of +0.10 mm/s (vs. 0.29 mm/s for TPPFe–O–FeTPP) (*21*).

The μ-nitrido dimer is oxidized chemically or electrochemically (+0.17 V, SCE) to yield the monocation dimer (*23*). The product is formally an iron(IV)–iron(IV) species. Solution characterization by proton NMR reveals that, unlike the odd-spin parent dimer, the oxidized complex exhibits little paramagnetic character, presumably as a consequence of strong coupling through the μ-nitrido bridge. This finding is evident in linewidth and shift differences for spectra in Figures 1a and 1c. Addition of pyridine to TPPFe–N–FeTPP (Figure 1b) yields no spectral changes other than appearance of free pyridine resonances. In contrast, addition of pyridine to the oxidized dimer (Figure 1d) induces changes in porphyrin resonances, and pyridine resonances (not shown) are shifted upfield by porphyrin ring currents. Both monopyridine and dipyridine ligation are detected, and pyridine exchange is rapid on the NMR time scale at ambient temperature. The

higher oxidation state iron center seemingly exhibits a higher binding affinity for nitrogenous bases than does that of the parent, neutral dimer.

Carbene and Vinylidene Complexes

Combination of iron porphyrins and chlorinated hydrocarbons in the presence of a strong reducing agent yields isolable iron porphyrin–carbene complexes (*24–27*). Aromatic substituents may further stabilize the adduct in the form of a vinylidene complex (*25*):

$$\text{TPPFe(II)} + \text{Cl}_3\text{CCHAr}_2 \xrightarrow[-2\ \text{Cl}^-]{\text{Fe}^\circ} \xrightarrow{-\text{HCl}} \text{TPPFeC}{=}\text{CAr}_2$$

This product is quite remarkably air-stable, but may be oxidized by agents such as ferric chloride or cupric chloride. Based on spectral similarity of the oxidized vinylidene complex and the spectrum of HRP Compound I, the following predominant resonance form was originally invoked (*26, 27*):

$$\text{TPPFe(IV)}{=}\text{C}{=}\text{CAr}_2$$

Although the magnetic moment (μ_{eff} = 3.7 B.M.) is consistent with such a formulation, the unusual ESR g = 4.4 value suggests the intermediate spin, S = 3/2, state of iron(III) porphyrins (*28–30*). This information and analogous reactions of carbenes (generated from diazoalkenes) with cobalt (*31–33*) and nickel (*34*) porphyrins suggested an iron–carbon–pyrrole nitrogen-bridged adduct of the type shown in Figure 2 (*35*). Simultaneous x-ray crystallographic work and NMR solution measurements demonstrated the validity of this bridged structure (*36, 37*). Hence, the unusual spectroscopic properties of oxidized vinylidene–iron porphyrin complexes result from porphyrin modification reactions rather than from oxidation to an iron(IV) state. Recent iterative Hückel calculations for unoxidized vinylidene complexes are inconsistent with iron(IV) character (*3*).

Iodosylbenzene Oxidations

Iodosylbenzene (*38–42*) [or 2-iodoso-*m*-xylene (*43*)] was an effective oxidizing agent for conversion of alkanes to alcohols and alkenes to epoxides in the presence of metalloporphyrin catalyst. A 50% conversion of cyclohexane to cyclohexyl alcohol was possible based on the iodosylbenzene consumed, using TPPMnCl (*40*). Similar results were reported in Reference *41* as was the formation of significant cyclohexyl chloride or other cyclohexyl adducts of the original manganese(III) anionic ligand. These results are particularly noteworthy in view of the need for mild-condition CH bond activation catalysts, and in terms of

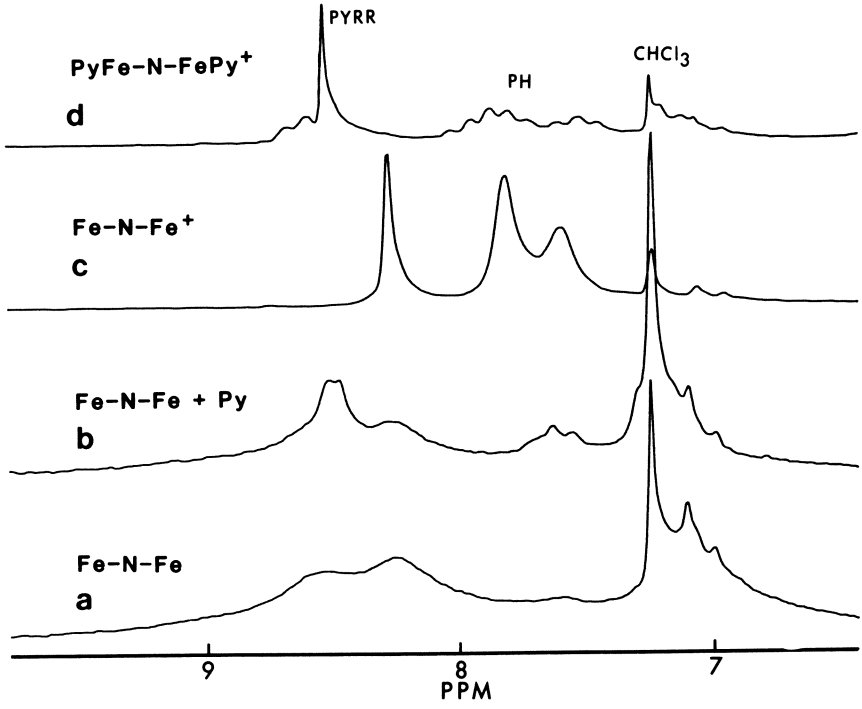

Figure 1. Proton NMR spectra of TPPFe-N-FeTPP species, $CDCl_3$ solvent, 26°C, 5 m M dimer, referenced to TMS.

partial simulation of the monooxygenase action of cytochrome P-450. The postulated active oxidant in these reactions is the metal–oxo complex, which can be described with the same resonance structure as that of HRP Compound I:

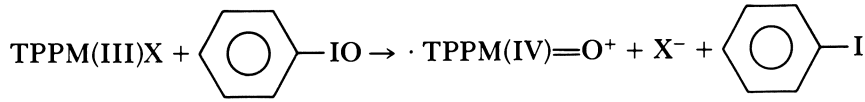

Spectroscopic observations at reduced temperature (*43*) or within seconds of mixing TPPFeCl (*44*) and iodosylbenzene reveal absorption bands resembling those of HRP Compound I. The corresponding manganese compound was generated and partially characterized at low temperature (*40–42*). A manganese(V) assignment based on the μ_{eff} value of 2.9 B.M. (*40*) must be considered as a formalism rather than a description of the electronic structure. Enhanced stability of the analogous oxidized TPPCrX complex permitted isolation and room temperature characterization (39). A chromium(V) oxidation state was

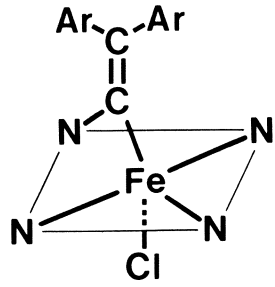

Figure 2. Alternate structure for the oxidized iron porphyrin vinylidene complex.

inferred from the 2.05-B.M. magnetic moment value. IR measurements demonstrated the presence of a Cr=O linkage associated with a 1026-cm^{-1} band. Generation of the oxidized chromium complex was also possible using *m*-chloroperoxybenzoic acid or sodium hypochlorite.

The oxidized iron porphyrin species generated in situ was further characterized using iodosylbenzene or *m*-chloroperoxybenzoic acid as oxidizing agents (*45*). Reaction of iron(III) tetramesitylporphyrin chloride (TMPFeCl) with two-electron equivalents of oxidizing agent yields solution species adequately stable at low temperatures for examination by NMR, visible–UV, and Mössbauer spectroscopy. Chemical properties of oxidized products depend on the oxidizing agent (Table I). Oxidation by *m*-chloroperoxybenzoic acid produces gross changes in the proton NMR spectrum of TMPFeCl. The far downfield pyrrole proton NMR signal of the parent compound can be contrasted with a signal upfield from TMS in the oxidized form. This pattern is consistent with electron abstraction from the $d_{x^2-y^2}$ orbital. The surprisingly large mesityl proton NMR shifts are best explained by significant unpaired spin density at the methine-carbon atom of a π-cation radical iron porphyrin. Iodosylbenzene oxidation yields a similar upfield pyrrole proton resonance, but the mesityl proton signals are virtually unshifted from diamagnetic positions. This latter observation does not rule out radical character, however, as the a_{1u} radical type exhibits little spin density at the methine-carbon atom (*3*). An analogy is found in oxidized manganese porphyrins (vide infra), which are classified as π-cation radicals, but which show no significant phenyl proton NMR shifts. Magnetic moment values and visible spectra (color) for the two compounds generated by iodosylbenzene or *m*-chloroperoxybenzoic acid oxidation differ significantly (Table I). That these differences are due to spin and/or ligation state rather than oxidation state is demonstrated by interconversion of the two species through addition of acid or base (*45*). Very low Mössbauer isomer shift values confirm the high oxidation state of the iron atom. Further characterization of these species should serve to better define the reaction chemistry of oxidized iron porphyrins.

Table I. Properties of Oxidized Iron Porphyrins

Property	*Iron Tetramesityl-porphyrin Chloride*[a]		*Iron Tetra-m-tolyl-porphyrin Chloride*[b]	*Iron Tetraphenylporphyrin Chloride*	
Oxidizing agent	ArCOOOH	ArIO	O_2 (+1-Me Imidazole)	Electrochem.[c] (ClO_4^- salt)	$R^+SbCl_6^-$[d] ($SbCl_6^-$ salt)
Electrons transferred	2	2	1	1	1
Proton NMR (temp.)[e]	(−77°C)	(−73°C)	(−73°C)	(26°C)	(29°C)
pyrrole-H	−27 ppm	−33.5	pyrrole-H 5	66	66
o-methyl	24, 26	2.4	*o*-H 9	37.6, 34.4	39
m-H	68	7.6	*m*-H 8	−12.4	−15.1
p-methyl	11.1	2.8	*p*-H 8 *m*-methyl 3	29.5	31
Visible–UV	406, 645 nm (green)	(red)	~420, ~560, ~585	397, 530, 600, 820	387, 533, 615, 750
Magnetic moment	4.2 B.M.	2.9	2.9	5.5[f]	5.1
Mössbauer					
I.S.[g]	0.05 mm/s	−0.03	0.11[h]	0.45	0.40
Q.S.	1.49 mm/s	2.13	1.24[h]	1.27	0.55
Reactivity toward olefins	more reactive	less reactive	not determined	not determined	

[a] Ref. 45.
[b] Ref. 48.
[c] Ref. 57.
[d] Ref. 53.
[e] Referenced to TMS, downfield shifts are given a positive sign.
[f] For TPP(*p*-OCH_3)Fe(Cl)(ClO_4).
[g] Referenced to iron metal.
[h] Ref. 50.

μ-Peroxo Iron Porphyrin Reactions

A μ-peroxo dimeric iron(III) porphyrin species was generated at low temperatures through dioxygen attack on iron(II) porphyrins (*46*, *47*):

$$2\text{PFe(II)} + \text{O}_2 \xrightarrow{-80^\circ\text{C}} \text{PFe(III)–O–O–Fe(III)P}$$

Antiferromagnetic coupling through the peroxo bridge is significant, with $2J = -265$ K. Upon warming to room temperature the iron(III) μ-oxo dimer is formed:

$$2\,\text{PFe(III)–O–O–Fe(III)P} \xrightarrow{25^\circ\text{C}} 2\,\text{PFe(III)–O–Fe(III)P} + \text{O}_2$$

Addition of two equivalents of nitrogenous base to the μ-peroxo dimer at low temperature generates a new spectroscopic species (*48*):

$$\text{PFe(III)–O–O–Fe(III)P} + 2\,\text{B} \rightarrow 2\,\text{BPFeO or BPFe–O–O–FePB}$$

The unique proton NMR spectrum of this base adduct is shown in Figure 3 and various properties are described in Table I. Curie law behavior of proton NMR shift values implies that antiferromagnetic coupling through a bridging ligand would have to be very small; hence, the monomeric structure is favored. Such a structure is isoelectronic with HRP Compound II, BPFe(IV)=O. With a magnetic moment of 2.9 B.M. per iron atom the species must be in the low spin state. Rapid reaction with iron(II) porphyrins and oxygen transfer reaction with triphenylphosphine (*49*) to yield the oxide further support the monomeric formulation. The paramagnetic NMR shifts for this compound are very small, and may be contrasted with considerably larger values for *m*-chloroperoxybenzoic acid and iodosylbenzene oxidation products. Relatively small paramagnetic shifts are observed, however, for HRP Compound II (*11–14*), and are rationalized by theoretical treatments that place sizable unpaired spin density on the axial oxygen ligand (*3*). Mössbauer spectral studies (*50*) further support an iron(IV), $S = 1$, configuration for the 1-methylimidazole adduct generated from the μ-peroxo species.

Other Chemical Oxidations

Although halogens and halogen derivatives are adequate oxidants for various divalent metalloporphyrins (*51*, *52*), only recently has an oxidizing agent of general utility been reported for iron(III) and other trivalent porphyrins (*53*). The stable phenoxathiin cation radical, as the $SbCl_6^-$ salt, provides adequate redox potential for single-electron oxidation of all common iron(III) porphyrins. Further details of the preparation and characterization of oxidized iron porphyrins are pro-

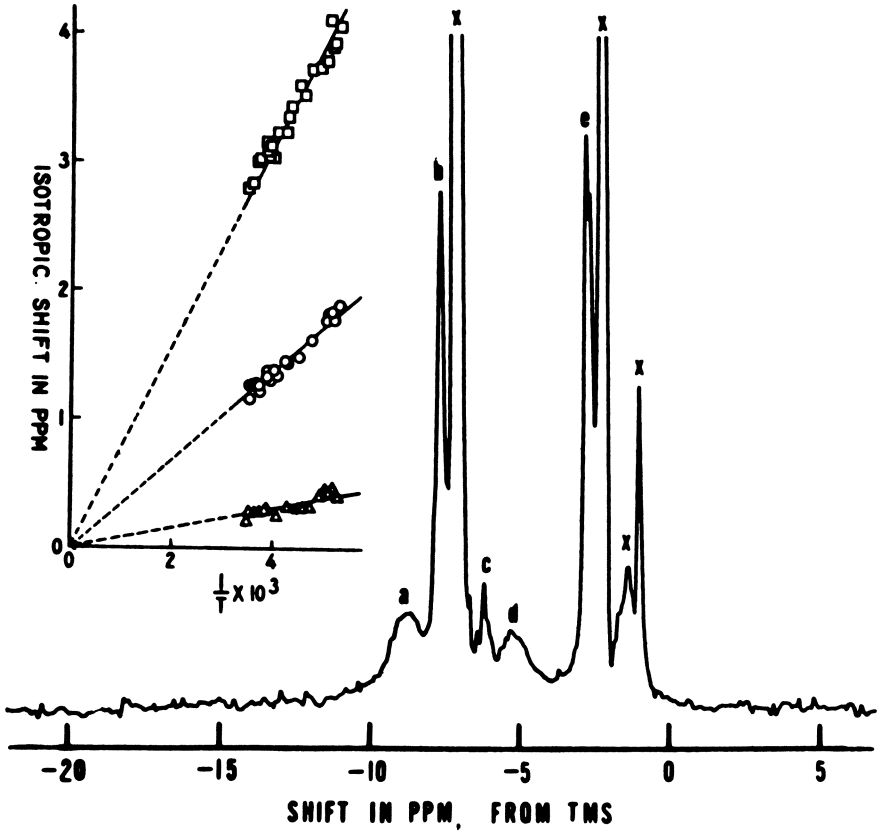

Figure 3. Proton NMR spectrum of TPP(m-CH_3)Fe–O–O–FeTPP(m-CH_3) with excess 1-methylimidazole in toluene-d_8 at 200 K. Key: a = o-phenyl-H, b = m- and p-phenyl-H, c = uncoordinated 1-methylimidazole, d = pyrrole-H, and e = m-methyl-H. (Reproduced from Ref. 48. Copyright 1980, American Chemical Society.)

vided elsewhere (*50*). The chemical oxidant generates oxidized iron porphyrins with electronic structures equivalent to those prepared by electrochemical oxidation (vide infra). Although the reagent has been used to a limited extent, zinc porphyrin oxidations occur with the cation radical perchlorate of dibenzodioxin (*54*).

In special cases two additional chemical oxidants are of value. Electrochemically oxidized iron porphyrins were utilized as chemical oxidants for iron porphyrins (*55*) or other metalloporphyrins (*52*) with lower oxidation potential. The doubly oxidized $[(TPPFe)_2O](ClO_4)_2$ species is especially useful in this regard (*55*). An additional chemical oxidant system is viable for metalloporphyrins with lower oxidation potentials ($\lesssim$1.0 V, SCE). Thus, one equivalent of iodine (in

chloroform) added to a methylene chloride solution of the metalloporphyrin, followed by a suitable silver salt ($AgClO_4$ or $AgCF_3SO_3$ in acetone, or $AgNO_3$ in acetonitrile) oxidizes the metalloporphyrin. This method was used for zinc porphyrins (*54*, *56*), and more recently for various iron porphyrin derivatives (*23*, *57*).

A report of air oxidation of μ-oxo iron(III) porphyrin dimers in the presence of strong Lewis acids (BF_3, $Et_2O \cdot BF_3$, HBF_4, and HPF_6) (*58*) was refuted by subsequent electrochemical measurements (*59*).

Electrochemical Oxidations

Literature Results. Wolberg and Manassen found that electrochemical oxidation of various metalloporphyrins yielded species adequately stable for in situ spectroscopic examination (*60*). In particular, one-electron oxidation of TPPFe(III)X gave a product with a broadened Soret band, no detectable ESR signals, and a solution magnetic moment of 2.7 B.M. Based on these observations, the oxidized product was formulated as an iron(III) porphyrin π-cation radical species. Benzonitrile was employed as a preparative electrolytic solvent, unlike subsequent studies where methylene chloride was utilized. This solvent difference and the possibility of other competing reactions may explain differences in magnetic moment values obtained by other workers.

Similar preparative scale electrochemical oxidations employed tetrapropylammonium perchlorate as a supporting electrolyte in methylene chloride solvent (*61*, *62*). Iron(III) octaethylporphyrin was examined along with TPPFeCl and the μ-oxo dimer forms of both synthetic iron(III) porphyrins. The singly oxidized species, $(TPPFe)_2OClO_4$, was isolated following evaporation of solvent and a hot water wash to remove supporting electrolyte salts. Reversibility of oxidations was confirmed via both electrochemical and iodide ion reduction to the parent iron(III) species. The singly oxidized μ-oxo dimers exhibited an ESR signal near $g = 2$, and a reduced magnetic moment of 2.9 B.M. (40°C) as a consequence of Fe–Fe antiferromagnetic coupling. A solution magnetic moment of 5.1 B.M. was obtained for $TPPFeCl^+$. Based largely on NMR spectral measurements, the oxidized derivatives were formulated as iron(IV) compounds. This interpretation followed from the relatively small (4–7 ppm) isotropic shifts for phenyl protons of $TPPFeCl^+$ and $(TPPFe)_2O^+$.

Recent Results for Oxidized Iron Porphyrins. Chemical and electrochemical oxidation of high spin iron(III) porphyrins was evaluated in detail in this laboratory. To stabilize the oxidized state, various anionic ligands were synthetically incorporated in place of usual chloride ligands. The complete list includes X = F^-, Cl^-, Br^-, I^-,

ClO_4^-, SO_4^{2-}, NO_3^-, N_3^-, NCS^-, OPh^-, OAc^-, p-$CH_3C_6H_4SO_3^-$, HSO_4^-, and $CF_3SO_3^-$ (*63*). Quite surprisingly, the first oxidation potential for the TPPFeX complexes was invariant at 1.10 ± 0.02 V (SCE, 0.1 *M* Bu_4NClO_4, CH_2Cl_2). This observation is consistent with (but does not prove that) electron abstraction is from a porphyrin-based rather than a metal-centered molecular orbital.

Oxidation potentials are diminished and stability of the oxidized product is considerably enhanced via incorporation of electron-releasing substituents in the porphyrin structure. The oxidized iron p-methoxytetraphenylporphyrin derivatives are more readily isolated and show more favorable stability with respect to autoreduction. Modification of the synthetic procedures in References *61* and *62* permitted isolation of oxidized compounds of analytical purity in favorable cases (*57*). Oxidized iron tetraphenylporphyrin, octaethylporphyrin, etioporphyrin, and natural-derivative porphyrin compounds were prepared in both the monomeric and μ-oxo dimeric forms. Isolable two-electron oxidized μ-oxo dimer compounds were readily generated. Characterization of one such species is demonstrated in Figure 4, through NMR monitoring of a titration of $(TPPFe)_2O$ into a solution of $(TPPFe)_2O^{2+}$ (*55*). Upon addition of one equivalent of $(TPPFe)_2O$, the spectrum for the singly oxidized complex (which may be prepared directly) is obtained. Continual addition of $(TPPFe)_2O$ yields spectra approaching that of the parent $(TPPFe)_2O$. Such measurements demonstrate both rapid intramolecular and intermolecular electron transfer, as well as the reversibility of electrochemical oxidations. Peak assignments are also facilitated by sequential spectral observation.

Proton NMR spectra are likewise obtained for oxidized monomeric complexes, and spectral assignments are listed in Table I (*53*, *57*). Large phenyl proton isotropic shifts differ from those reported earlier (*61*, *62*), perhaps as a consequence of electron exchange with considerable amounts of reduced material. A strong case can be made for π-cation radical character of the oxidized iron porphyrin based on the alternation in direction and magnitude of phenyl proton shifts. Thus, the ESR coupling constant of 0.32 Gauss for the phenyl protons of $TPPZnClO_4$ π-cation radical (*64*) may be translated as an NMR isotropic shift of 23 ppm, or as observed chemical shift values of 31 ppm downfield or −15 ppm upfield from TMS. Correspondence of these values expected for a porphyrin radical and those measured for $TPPFe(Cl)(ClO_4)$ is compelling evidence for the iron(III) π-cation radical nature of oxidized iron porphyrin complexes containing weak-field anionic ligands. The same conclusion is reached for the chemically oxidized TPPFeCl species (*53*).

Of the two possible porphyrin radical states (*3*), the $TPPFe(Cl)(ClO_4)$ complex must be representative of the a_{2u} type. This radical

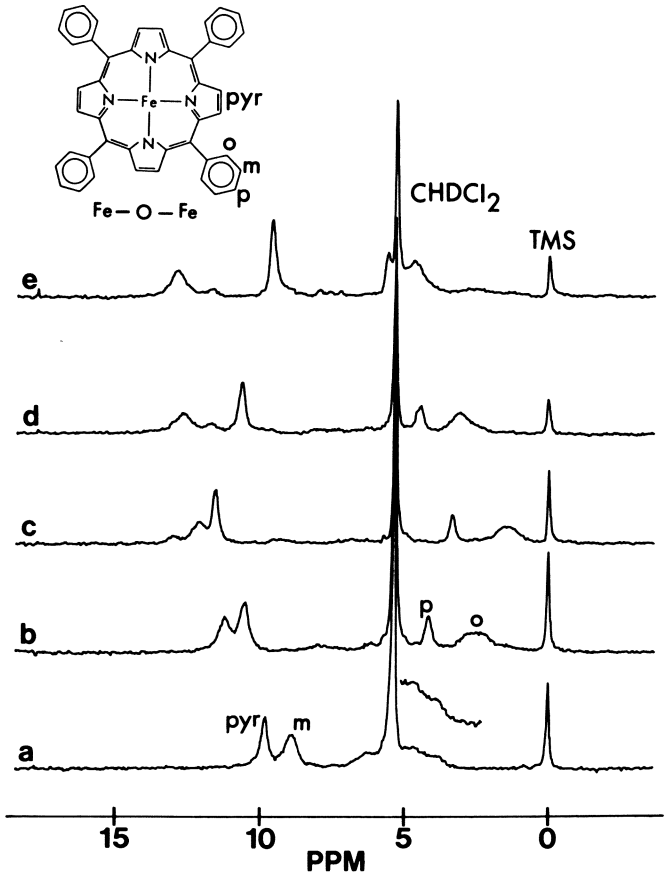

Figure 4. Proton NMR titration of [(TPPFe)$_2$O](ClO$_4$)$_2$ by (TPPFe)$_2$O; oxidized dimer originally 5 mM in 0.5 mL of CD$_2$Cl$_2$, 26°C. Moles of (TPPFe)$_2$O added (×10^6): a, 0.0; b, 1.05; c, 2.50; d, 3.91; and e, 5.00. (Reproduced from Ref. 55. Copyright 1979, American Chemical Society.)

type is expected to exhibit large unpaired radical spin density at methine carbon positions. The OEPFe(Cl)(ClO$_4$) derivative, on the other hand, is better described as an a_{1u} radical type. Although calculations predict no unpaired spin density at methine carbon atoms for this radical, ESR measurements reveal a methine proton coupling constant of 1.48 Gauss for OEPMgClO$_4$ (3). A shift of the OEPFeCl methine proton NMR signal from −54 to −18 ppm upon oxidation (57) is not rationalized by the 1.48-Gauss coupling constant of known a_{1u} radicals. However, a direct correspondence is not necessarily expected, because the methine proton experiences a large and variable spin density transfer from the iron center (65). A high spin configuration

is indicated by solution magnetic moments of 5.5 B.M. for both TPP(p-OCH_3)Fe(Cl)(ClO_4) and OEPFe(Cl)(ClO_4) (*57*).

Mössbauer results for both chemically and electrochemically oxidized chloro complexes also show little perturbation of charge at the iron center as compared with parent species (Table I). Isomer shift values of 0.4 mm/s for parent iron porphyrin chloro complexes are changed by no more than 0.05 mm/s upon oxidation (*53*, *57*), in contrast to the appearance of very low isomer shift values for monomeric complexes presumably containing an oxo ligand.

IR spectroscopy also provides a diagnostic tool for detecting porphyrin π-cation radical character (*66*). For known zinc and cobalt TPP radical complexes an intense new band appears in the 1280-cm^{-1} region. This band is also present in both oxidized monomeric and dimeric TPPFe species, as well as in oxidized TPPMnCl complexes discussed later. Likewise, oxidation of OEP complexes of iron(III), cobalt(III), and zinc(II) is associated with the appearance of a diagnostic band in the 1550-cm^{-1} region.

Various reactions of oxidized iron porphyrins were investigated (*67*). For example, stoichiometric acid cleavage of the oxidized μ-oxo dimers yields expected (oxidized) monomeric derivatives. Addition of nitrogenous bases at room temperature reduces the iron porphyrin. At −50°C, on the other hand, NMR spectral monitoring of imidazole addition to oxidized monomeric iron porphyrins demonstrates diligation of the imidazole group as a preferred equilibrium condition. A large upfield and downfield spread of phenyl proton signals is consistent with a low spin iron(III) π-cation radical formulation, as described for the high spin iron(III) porphyrin radicals. A solution magnetic moment value of 2.8 B.M. supports a low spin $S = 1$ (or $S = \frac{1}{2} + S = \frac{1}{2}$) configuration. π-Cation radical character is strongly indicated by the spread of TPPFe phenyl proton signals, but no significant antiferromagnetic coupling between radical and iron(III) is apparent. This situation is analogous to that of HRP Compound I for which antiferromagnetic coupling between iron(IV) and radical spins is very small. A porphyrin ring methyl signal at 133 ppm (222 K) for the diimidazole complex of oxidized iron etioporphyrin (*67*) explains the large ring methyl shifts of HRP Compound I as being due to radical spin delocalization rather than the suggested high spin iron(IV) formulation (*10–12*).

Oxidized Manganese Porphyrins. Aside from the iodosylbenzene-oxidized species discussed previously, manganese(IV) porphyrins have been prepared in basic aqueous solution through the action of hydrogen peroxide or sodium hypochlorite (*68–73*). The dioxygen-manganese(II) adduct has been formulated as a peroxomanganese(IV) complex (*74–76*). We performed preparative-scale electrochemical oxidation reactions for manganese(III) porphyrins as de-

scribed for iron porphyrins. Similar oxidation potentials and solubilities permit analogous oxidation and isolation procedures. Oxidations were typically performed using a platinum working electrode in methylene chloride solution containing 1.0 mg of manganese porphyrin/mL and 0.1 *M* in tetrapropylammonium perchlorate supporting electrolyte. The counterelectrode and reference electrode were separated from bulk solution by fine glass frits. The current flow was allowed to drop to 1% of the original value at which time the electrolysis was stopped. Oxidation was monitored by UV–visible spectral measurements, as shown in Figure 5. The oxidized material may be reversibly reduced by tetrabutylammonium iodide salt (a large excess must be avoided or the manganese(III) iodide complex is formed).

Oxidation potentials measured by cyclic voltammetry approximate those for corresponding iron(III) porphyrins (1.1 V vs. SCE for TPPMnCl). Cyclic voltammetric scans of the oxidized products were equivalent to those for the initial complex, thus indicating no irrever-

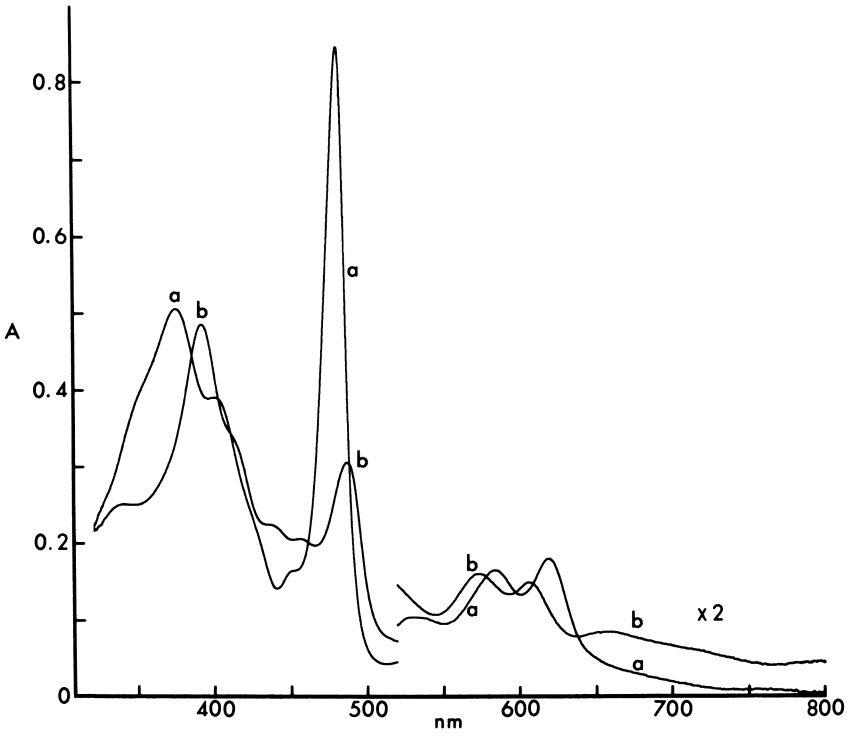

Figure 5. Electronic spectra of manganese porphyrins, CH_2Cl_2, approx. 9×10^{-5} M. Key: a, TPPMnCl, reduced product of material in spectrum b and b, TPPMn(Cl)(ClO_4).

sible modification of the porphyrin ring. Isolation of oxidized product was accomplished by first evaporating the methylene chloride solution, with slow addition of benzene. Tetrapropylammonium perchlorate is insoluble in benzene and was separated by filtration. The benzene solution containing oxidized manganese porphyrin was then subjected to slow rotary evaporation with addition of heptane. The solid product may be separated by filtration and vacuum dried at room temperature. Oxidized compounds prepared in this manner include TPPMn(Cl)(ClO_4), TPP(p-OCH_3)Mn(Cl)(ClO_4), and OEPMn(Cl)(ClO_4).

Proton NMR spectra for manganese(III) porphyrins were reported previously (77). The spectrum for TPPMnCl is found in Figure 6a.

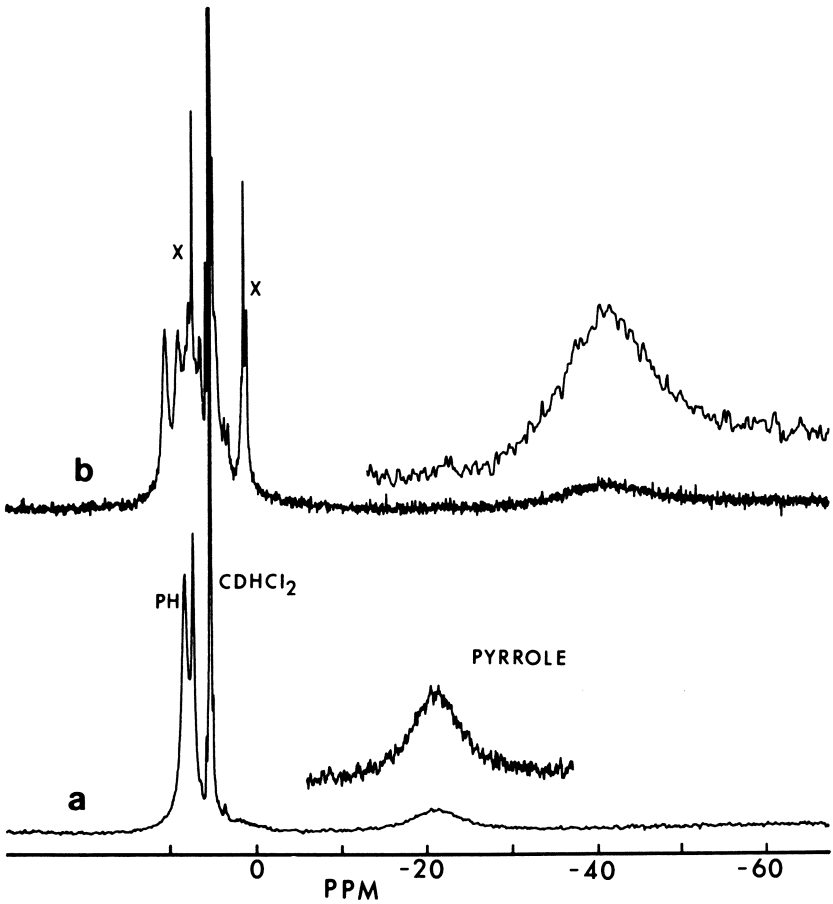

Figure 6. Proton NMR spectra of manganese porphyrins, CD_2Cl_2 solvent, 29°C, TMS reference. Key: a, TPPMnCl and b, TPPMn(Cl)-(ClO_4); X = salt and benzene impurities.

This species is isoelectronic with an iron(IV) porphyrin, but the pyrrole proton resonance is far upfield rather than downfield as is oxidized TPPFe(Cl)(ClO_4). This observation further supports the π-cation radical formulation for oxidized iron porphyrins. A proton NMR spectrum for TPPMn(Cl)(ClO_4) is shown in Figure 6b. No gross spectral changes are noted upon oxidation, and the large splitting of phenyl signals does not occur. The major spectral change is found in broadening and upfield shift of the pyrrole proton resonance. Chemical shift values for OEPMn(Cl)(ClO_4) are as follows (with those for OEPMnCl listed in parentheses): methine, 70 PPM (52); CH_2, 16.3 (22.8); and CH_3, 2.7 (2.6).

Electron spin resonance spectra are observed for the odd-spin, oxidized manganese complexes, as may be seen in Figure 7. A broad $g = 2.0$ feature is common to all species, with linewidths ranging from 300 Gauss for OEPMn(Cl)(ClO_4) to 500 Gauss for TPP(p-OCH_3)-Mn(Cl)(ClO_4). A weaker $g = 3.0$ component is apparent for OEPMn-(Cl)(ClO_4). Variable appearance of this second signal and different linewidths may reflect different magnitudes and mechanisms for radical–manganese spin–spin interactions among diverse porphyrin structural types. These spectra differ from those of known or suggested manganese(IV) compounds (*73–75, 78*) in exhibiting much broader absorptions lacking any hyperfine structure. The best explanation is based on the manganese(III) π-cation radical formulation. The $g = 2$ signal is most likely derived from the radical, with considerable electronic relaxation from the paramagnetic metal center. The magnetic moment value of 4.7 B.M. for TPPMn(Cl)(ClO_4) is invariant with temperature (−50° to 29°C), indicating that any antiferromagnetic behavior is either very strong or very weak. The manganese must be high spin, but the magnetic moment value is not otherwise particularly elucidating in terms of possible "spin-only" formulations.

Assignment of the manganese(III) π-cation radical electronic structure is consistent with the broadening and intensity loss of Soret bands, and a general increase in intensity in the long wavelength spectral region. Absence of large isotropic phenyl proton NMR shifts is indicative of little unpaired spin density at the methine position, and is readily explained by assuming that an a_{1u} type radical is formed. Oxidized manganese porphyrins are isoelectronic with HRP Compound I, but admittedly differ in spin state.

Conclusion

A variety of physical evidence demonstrates the radical character of electrochemically oxidized iron and manganese porphyrins. This formulation must be qualified, however, by noting that these species

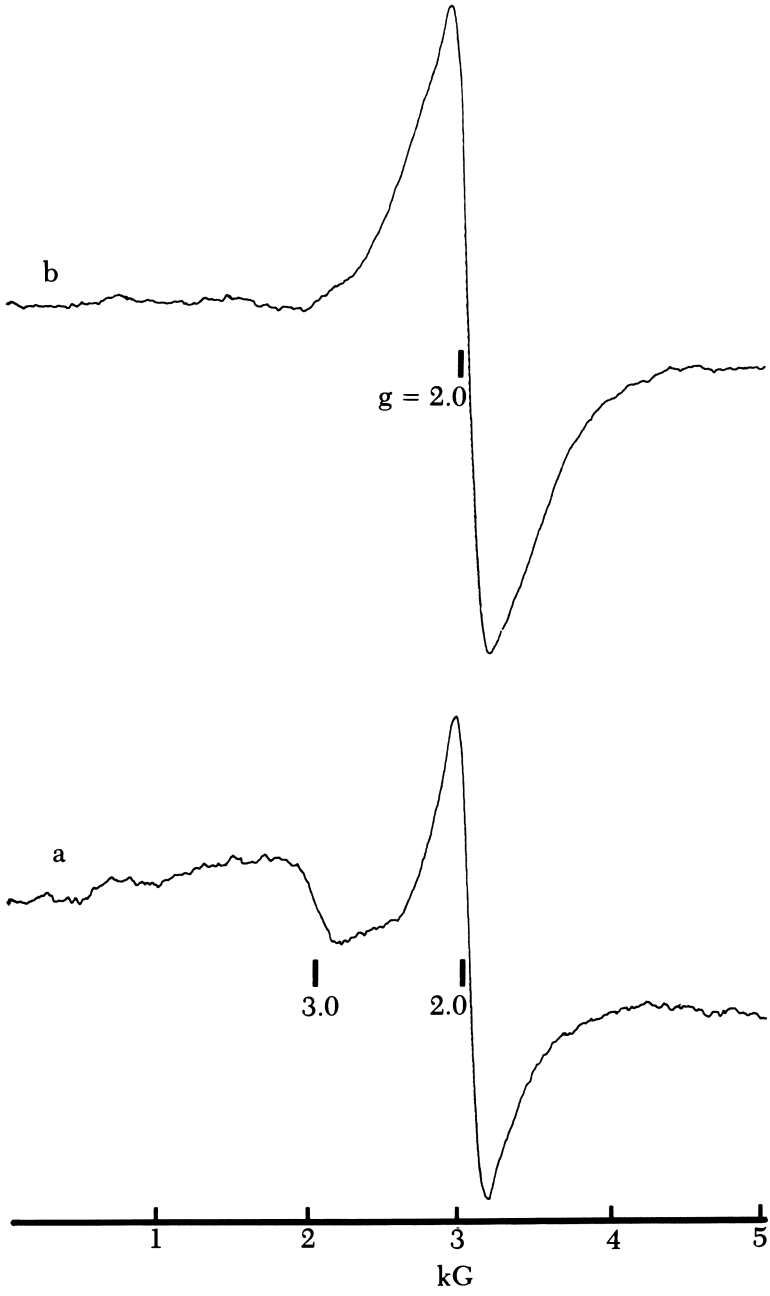

Figure 7. ESR spectra of oxidized manganese porphyrins, 2 mM in 1:1 methylene chloride–toluene, 77 K, 50–5050 Gauss sweep. Key: a, OEPMn(Cl)(ClO_4) and b, TPP(p-OCH_3)Mn(Cl)(ClO_4).

are associated with only weak-field anionic ligands. The well-recognized role of oxo ligands in stabilizing high oxidation state metal ions seems to apply for the oxidized metalloporphyrins generated by iodosylbenzene oxidation or μ-peroxo dimer cleavage reactions. The role of a *trans*-imidazole or similar strong-field ligand in dictating and/or stabilizing metal-centered oxidation remains to be elucidated.

Acknowledgments

Support from NSF Grant CHE 79-10305 and NIH Grant GM 28831-01 is gratefully acknowledged. We thank R. E. Coffman of this Department for assistance with ESR determinations, and D. N. Hendrickson of the University of Illinois for providing Mössbauer measurements.

Literature Cited

1. Hewson, W. D.; Hager, L. P. In "The Porphyrins;" Dolphin, D., Ed.; Academic: New York, 1979; Vol. 7, pp. 295–332.
2. Dunford, H. B.; Stillman, J. S. *Coord. Chem. Rev.* **1976,** *19,* 187.
3. Hanson, L. K.; Chang, C. K.; Davis, M. S.; Fajer, J. *J. Am. Chem. Soc.* **1981,** *103,* 663.
4. Dolphin, D.; Forman, A.; Borg, D. C.; Fajer, J.; Felton, R. H. *Proc. Natl Acad. Sci. USA* **1971,** *68,* 614.
5. Schulz, C. E.; Devaney, P. W.; Winkler, H.; Debrunner, P. G.; Doan, N.; Chiang, R.; Rutter, R.; Hager, L. P. *FEBS Lett.* **1979,** *103,* 102.
6. Harami, T.; Maeda, Y.; Morita, Y.; Trautwein, A.; Gonser, U. *J. Chem. Phys.* **1977,** *67,* 1164.
7. Moss, T. H.; Ehrenberg, A.; Bearden, A. J. *Biochemistry* **1969,** *8,* 4159.
8. Yonetani, T.; Schleyer, H.; Ehrenberg, A. *J. Biol. Chem.* **1966,** *241,* 3240.
9. Hoffman, B. M.; Roberts, J. E.; Brown, T. G.; Kang, C. H.; Margoliash, E. *Proc. Natl. Acad. Sci. USA* **1979,** *76,* 6132.
10. Morishima, I.; Ogawa, S. *J. Am. Chem. Soc.* **1978,** *100,* 7125.
11. Morishima, I.; Ogawa, S. *Biochem. Biophys. Res. Commun.* **1978,** *83,* 946.
12. Morishima, I.; Ogawa, S. *Biochemistry* **1978,** *17,* 4384.
13. La Mar, G. N.; de Ropp, J. S. *J. Am. Chem. Soc.* **1980,** *102,* 395.
14. La Mar, G. N.; de Ropp, J. S.; Smith, K. M.; Langry, K. C. *J. Biol. Chem.* **1981,** *256,* 237.
15. Roberts, J. E.; Hoffman, B. M.; Rutter, R.; Hager, L. P. *J. Biol. Chem.* **1981,** *256,* 2118.
16. Chang, C. K.; Dolphin, D. In "Bioorganic Chemistry;" Van Tamelen, E. E., Ed.; Academic: New York, 1978; Vol. 4, pp. 37–80.
17. Moore, G. R.; Williams, R. J. P. *Coord. Chem. Rev.* **1976,** *18,* 125.
18. Seiter, C. H. A.; Angelos, S. G. *Proc. Natl. Acad. Sci. USA* **1980,** *77,* 1806.
19. Traylor, T. G.; Chang, C. K.; Geibel, J.; Berzinis, A.; Mincey, T.; Cannon, J. *J. Am. Chem. Soc.* **1979,** *101,* 6716.
20. Reed, C. A. In "Metal Ions in Biological Systems;" Sigel, H., Ed.; Dekker: New York, 1978; Vol. 7, pp. 277–310.
21. Summerville, D. A.; Cohen, I. A. *J. Am. Chem. Soc.* **1976,** *98,* 1747.
22. Scheidt, W. R.; Summerville, D. A.; Cohen, I. A. *J. Am. Chem. Soc.* **1976,** *98,* 6623.
23. Kadish, K. M.; Rhodes, R. K.; Bottomley, L. A.; Goff, H. M. *Inorg. Chem.* **1981,** *20,* 3195.
24. Mansuy, D. *Pure Appl. Chem.* **1980,** *52,* 681.

25. Mansuy, D.; Lange, M.; Chottard, J.-C. *J. Am. Chem. Soc.* **1978,** *100,* 3213.
26. Mansuy, D.; Lange, M.; Chottard, J.-C. *J. Am. Chem. Soc.* **1979,** *101,* 6437.
27. Mansuy, D.; Chottard, J.-C.; Lange, M.; Battioni, J. P. *J. Mol. Catalysis* **1980,** *7,* 215.
28. Maltempo, M. M. *J. Chem. Phys.* **1974,** *61,* 2540.
29. Reed, C. A.; Mashiko, T.; Bentley, S. P.; Kastner, M. E.; Scheidt, W. R.; Spartalian, K.; Lang, G. *J. Am. Chem. Soc.* **1979,** *101,* 2948.
30. Goff, H.; Shimomura, E. *J. Am. Chem. Soc.* **1980,** *102,* 31.
31. Johnson, A. W.; Ward, D.; Batten, P.; Hamilton, A. L.; Shelton, G.; Elson, C. M. *J. Chem. Soc., Perkin Trans. I* **1975,** 2076.
32. Johnson, A. W.; Ward, D. *J. Chem. Soc., Perkin Trans. I* **1977,** 720.
33. Batten, P.; Hamilton, A. L.; Johnson, A. W.; Mahendran, M.; Ward, D.; King, T. J. *J. Chem. Soc., Perkin Trans. I* **1977,** 1623.
34. Callot, H. J.; Tschamber, T.; Chevrier, B.; Weiss, R. *Angew. Chem., Int. Ed. Engl.* **1975,** *14,* 567.
35. Goff, H. M.; Phillippi, M. A. *Inorg. Nucl. Chem. Lett.* **1981,** *17,* 239.
36. Chevrier, B.; Weiss, R.; Lange, M.; Chottard, J.-C.; Mansuy, D. *J. Am. Chem. Soc.* **1981,** *103,* 2899.
37. Latos-Grazynski, L.; Cheng, R.-J.; La Mar, G. N.; Balch, A. L. *J. Am. Chem. Soc.* **1981,** *103,* 4270.
38. Groves, J. T.; Nemo, T. E.; Myers, R. S. *J. Am. Chem. Soc.* **1979,** *101,* 1032.
39. Groves, J. T.; Kruper, W. J. *J. Am. Chem. Soc.* **1979,** *101,* 7613.
40. Groves, J. T.; Kruper, W. J.; Haushalter, R. C. *J. Am. Chem. Soc.* **1980,** *102,* 6375.
41. Hill, C. L.; Schardt, B. C. *J. Am. Chem. Soc.* **1980,** *102,* 6374.
42. Willner, I.; Otvos, J. W.; Calvin, M. *J. Chem. Soc., Chem. Commun.* **1980,** 964.
43. Chang, C. K.; Kuo, M.-S. *J. Am. Chem. Soc.* **1979,** *101,* 3413.
44. Groves, J. T.; Kruper, W. J.; Nemo, T. E.; Myers, R. S. *J. Mol. Catalysis* **1980,** *7,* 169.
45. Groves, J. T.; Haushalter, R. C.; Nakamura, M.; Nemo, T. E.; Evans, B. J. *J. Am. Chem. Soc.* **1981,** *103,* 2884.
46. Chin, D.-H.; La Mar, G. N.; Balch, A. L. *J. Am. Chem. Soc.* **1980,** *102,* 4344.
47. Chin, D.-H.; Del Gaudio, J.; La Mar, G. N.; Balch, A. L. *J. Am. Chem. Soc.* **1977,** *99,* 5486.
48. Chin, D.-H.; Balch, A. L.; La Mar, G. N. *J. Am. Chem. Soc.* **1980,** *102,* 1446.
49. Chin, D.-H.; La Mar, G. N.; Balch, A. L. *J. Am. Chem. Soc.* **1980,** *102,* 5945.
50. Reed, C. A., Chapter 15 in this book.
51. Fajer, J.; Borg, D. C.; Forman, A.; Felton, R. H.; Vegh, L.; Dolphin, D. *Ann. N.Y. Acad. Sci.* **1973,** *206,* 349.
52. Fajer, J.; Borg, D. C.; Forman, A.; Adler, A. D.; Varadi, V. *J. Am. Chem. Soc.* **1974,** *96,* 1238.
53. Gans, P.; Marchon, J.-C.; Reed, C. A.; Regnard, J.-R. *Nouv. J. Chimie* **1981,** *5,* 203.
54. Shine, H. J.; Padilla, A. G.; Wu, S.-M. *J. Org. Chem.* **1979,** *44,* 4069.
55. Phillippi, M. A.; Goff, H. M. *J. Am. Chem. Soc.* **1979,** *101,* 7641.
56. Barnett, G. H.; Smith, K. M. *J. Chem. Soc., Chem. Commun.* **1974,** 772.
57. Phillippi, M. A.; Goff, H. M., submitted for publication.
58. Wollman, R. G.; Hendrickson, D. N. *Inorg. Chem.* **1977,** *16,* 723.
59. Cohen, I. A.; Lavallee, D. K.; Kopelove, A. B. *Inorg. Chem.* **1980,** *19,* 1098.
60. Wolberg, A.; Manassen, J. *J. Am. Chem. Soc.* **1970,** *92,* 2982.
61. Felton, R. H.; Owen, G. S.; Dolphin, D.; Fajer, J. *J. Am. Chem. Soc.* **1971,** *93,* 6332.
62. Felton, R. H.; Owen, G. S.; Dolphin, D.; Forman, A.; Borg, D. C.; Fajer, J. *Ann. N.Y. Acad. Sci.* **1973,** *206,* 504.

63. Phillippi, M. A.; Shimomura, E. T.; Goff, H. M. *Inorg. Chem.* **1981,** *20,* 1322.
64. Fajer, J.; Borg, D. C.; Forman, A.; Dolphin, D.; Felton, R. H. *J. Am. Chem. Soc.* **1970,** *92,* 3451.
65. Budd, D. L.; La Mar, G. N.; Langry, K. C.; Smith, K. M.; Nayyir-Mazhir, R. *J. Am. Chem. Soc.* **1979,** *101,* 6091.
66. Shimomura, E. T.; Phillippi, M. A.; Goff, H. M.; Scholz, W. F.; Reed, C. A., *J. Am. Chem. Soc.* **1981,** *103,* 6778.
67. Phillippi, M. A.; Goff, H. M., submitted for publication.
68. Loach, P. A.; Calvin, M. *Biochemistry* **1963,** *2,* 361.
69. Tabushi, I.; Kojo, S. *Tetrahedron Lett.* **1974,** 1577.
70. Tabushi, I.; Kojo, S. *Tetrahedron Lett.* **1975,** 305.
71. Tabushi, I.; Koga, N. *Tetrahedron Lett.* **1978,** 5017.
72. Tabushi, I.; Koga, N. *J. Am. Chem. Soc.* **1979,** *101,* 6456.
73. Boucher, L. J. *Coord. Chem. Rev.* **1972,** *7,* 289.
74. Weschler, C. J.; Hoffman, B. M.; Basolo, F. *J. Am. Chem. Soc.* **1975,** *97,* 5278.
75. Hoffman, B. M.; Szymanski, T.; Brown, T. G.; Basolo, F. *J. Am. Chem. Soc.* **1978,** *100,* 7253.
76. Hanson, L. K.; Hoffman, B. M. *J. Am. Chem. Soc.* **1980,** *102,* 4602.
77. La Mar, G. N.; Walker, F. A. *J. Am. Chem. Soc.* **1975,** *97,* 5103.
78. Richens, D. T.; Sawyer, D. T. *J. Am. Chem. Soc.* **1979,** *101,* 3681.

RECEIVED for review June 2, 1981. ACCEPTED August 11, 1981.

Models of the Cytochromes b

The Effect of Unsymmetrically Placed Phenyl Substituents on the Redox Potentials of a Series of Iron Tetraphenylporphyrins and Their Bis(*N*-methylimidazole) Complexes

F. ANN WALKER[1], JUDITH A. BARRY, VIRGINIA L. BALKE, GREGORY A. McDERMOTT, MICHAEL Z. WU, and PETER F. LINDE

San Francisco State University, Department of Chemistry, San Francisco, CA 94132.

A series of unsymmetrical (m- *or* p-*phenyl-substituted) tetraphenylporphyrin complexes of iron(III),* $FeClTPP(X)_x(Y)_y$ *(x + y = 4), were synthesized, and the redox potentials of these compounds and their bis(*N*-methylimidazole) complexes were measured by cyclic voltammetry. The redox potentials of the low spin iron(III)/iron(II) couple correlate roughly with the sum of the Hammett σ-constants of the substituents, although the cathodic peak potentials of the high spin iron(III)/iron(II) reduction do not. The electrochemical results are compared with those obtained from ESR spectroscopy, NMR spectroscopy, and equilibrium constants for axial ligand addition. A unified explanation of the results from all of these techniques is presented. The effect of unsymmetrical substitution on the π-orbital(s) of the porphyrin that interact with the relevant* d-*orbital(s) of the metal is discussed, and the reasons that this effect is transferred to the iron center for high spin, but not for low spin, iron(III) and iron(II) are given.*

Cytochromes b are low-potential heme proteins that appear to be present in all energy-transducing membranes (*1–4*). To be classified as a b cytochrome, the protein must contain extractable pro-

NOTE: This is Part 6 of a series.

[1]Recipient, NIH Research Career Development Award, 1976–81.

0065-2393/82/0201-0377$11.00/0

toheme (*1*, *4*). That is, unlike cytochromes c, b cytochromes contain noncovalently bound heme. The reduced forms of purified cytochromes b have their α-bands between 558 and 565 nm and are unaffected by addition of CO or CN^- (*1*, *3*, *4*). Because they are usually tightly bound to membranes, their isolation and purification has been difficult. Nevertheless, the water-soluble half of proteolyzed microsomal cytochrome b_5 from calf liver has been crystallized and its three-dimensional molecular structure determined by x-ray crystallography (*4–6*). The structure shows that protoheme is held in a cleft near the surface of the protein by coordination of an imidazole nitrogen of each of two histidine (HIS) side chains of the protein (HIS 39 and 63) to the axial positions of the iron (*4*, *5*). The orientation of the heme was re-evaluated (*6*) and found to be consistent with that predicted from NMR studies (*7*). Not only the physical properties, but also the amino acid sequences of such diverse heme proteins as bakers' yeast flavocytochrome b_2, liver sulfite oxidase, and bovine erythrocyte cytochrome b_5 are very similar to that of microsomal b_5 (*8–13*). These observations suggested that all of these heme proteins belong to a "novel protein superfamily", which involves the same coordination sphere for iron and similar molecular surface areas involved in the recognition of cytochrome c and the reductases of each protein; thus, the b-type cytochromes in such diverse organisms as higher animals and yeast have a common evolutionary ancestor (*13*).

The similarity in the spectral properties of the cytochromes b of various species in Table I (*14–26*) suggests that the coordination sphere for iron consists of the four nitrogens of protoporphyrin IX and two imidazole nitrogens of histidine residues. However, the redox potential of the iron(III)/iron(II) couple varies so greatly, over a range of 450 mV for all cytochromes b listed in Table I and at least 32 mV for the best characterized members of this group (b_2 and b_5), but the coordination sphere of iron remains the same. Possibly "the protein" causes the redox potentials of the identical reaction center to differ. The mechanism by which each protein confers on its heme center a unique redox potential and/or other unique physical properties is unclear. Some ways that have been suggested include: (1) changing the ligand field of the ligated histidines through hydrogen-bonding of the imidazole N–H to other protein residues (*27*); (2) pressing hydrophobic protein residues against certain parts of the heme and thereby altering the π-electron distribution in the heme (*28*, *29*); and (3) aligning the ligated histidine imidazole planes in unique orientations with respect to the unsymmetrical protoporphyrin ring (**I**) and with respect to each other (*30*, *31*). The model studies described herein are designed to test the second possibility: that by altering the electron distribution in the heme, the redox potentials of the iron(III)/iron(II) couple may be altered.

Published on June 1, 1982 on http://pubs.acs.org | doi: 10.1021/ba-1982-0201.ch017

Table I. Redox Potentials of Selected Cytochromes b

Cyto-chrome	*Source*	E *part*[a] *(mV)*	*Method of Solubilization*	$E_{m,7}$[b] *(mV)*	*Reference*
b	beef heart	73			*14*
b ($b\text{-}562_1$)	*Rhodospirillum rubrum*	+18 (n = 2)			*15*
($b\text{-}562_2$)		−160			
b_2	bakers' yeast	−12	trypsin digestion	−40	*16*
b_5	calf liver microsomes	20	trypsin digestion	20	*17*
b_5	rabbit liver microsomes		detergent	20 (pH 7.20)	*18*
	rabbit liver microsomes		trypsin digestion	18 (pH 7.29)	*18*
b_5	endoplasmic reticulum of calf liver	10	detergent	0	*19*
	endoplasmic reticulum of calf liver	10	trypsin digestion	130	*19*
b_5	human erythrocytes		(soluble)	−2	*18*
b_6	chloroplasts	5 (n = 2)			*20*
b-555	larvae of housefly		(soluble)	11	*21*
b-558	*Nostoc muscorum*	345			*22*
b-559	chloroplasts	383, 77 (2 : 1)			*23*
b-560	*Chromatium*	−5 ($E_{m,8}$)			*24*
b-561 (b_k)	pigeon heart mitochondria	40			*25*
b-562	beef heart mitochondria	154			*26*
b-565 (b_t)	pigeon heart mitochondria	−30			*27*

[a] Redox potential of the particulate (membrane-bound) protein vs. NHE.
[b] Midpoint potential of the solubilized protein at pH 7.0, unless otherwise specified. Reference = NHE.

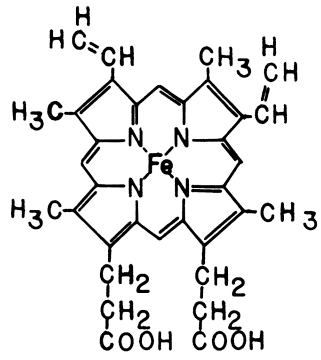

Structure I. Iron protoporphyrin IX, the naturally occurring heme of the cytochromes b.

meso-Tetraphenylporphyrins (**II**) are a totally synthetic family of molecules, which allow the systematic and quantitative study of the physical and chemical properties of the heme nucleus. One of the useful features of *meso*-tetraphenylporphyrins for the present study is that the phenyl rings are constrained so as to be out of the plane of the porphyrin ring most of the time (*32*) because of steric interference between the β-pyrrole and *o*-phenyl protons. [The barrier to rotation of the phenyl rings in ruthenium(III), indium(III), and titanium(IV) tetraphenylporphyrins is ca. 11–17 Kcal/mol (*33*)]. Thus, the transfer of electronic effects—from the many possible substituents, R, which might be introduced onto the phenyl rings to the porphyrin ring—is largely, if not entirely, inductive, at least in metal-coordinated tetraphenylporphyrins (*27*, *34–41*). [The electronic spectral shifts of metal-free tetraphenylporphyrins (TPPs) and their dications apparently are unique among the linear-free-energy relationships of tetraphenylporphyrins in that they indicate the presence of a large resonance electronic effect of substituents on the phenyl rings (*42*)]. We recently reported (*41*) that the NMR spectra of a series of six metal-free porphyrins, $H_2TPP(p\text{-}Cl)_x(p\text{-}NEt_2)_y$ ($x + y = 4$; $x = 0 - 4$), and several of their zinc(II) complexes show essentially no evidence of π-electron delocalization (π-conjugation): for example, the ring current was unaltered beyond the pair of β-pyrrole protons, H_a, closest to the unique phenyl in the H_2- or $ZnTPP(p\text{-}Cl)_3(p\text{-}NEt_2)_1$ isomer, (**III**, X = *p*-Cl, Y = *p*-NEt_2). Therefore, such unsymmetrical placement of substituents, as in **III**, should provide a means of altering the electron density in one specific region of the porphyrin ring, a *meso*-position, as might be done within a protein by the close proximity of some side chain to the heme π-electron system.

NMR studies (*43*) of the low spin iron(III) complexes of a series of compounds of type **III** and related structures clearly showed that the

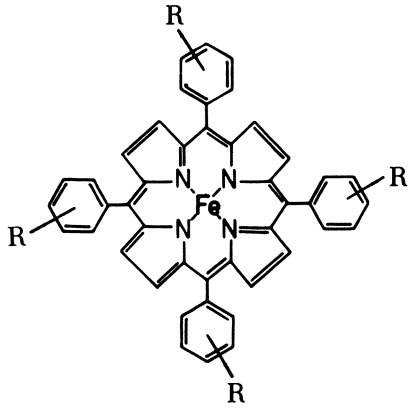

Structure II. Synthetic, symmetrically tetra-substituted tetraphenylporphyrin complexes of iron.

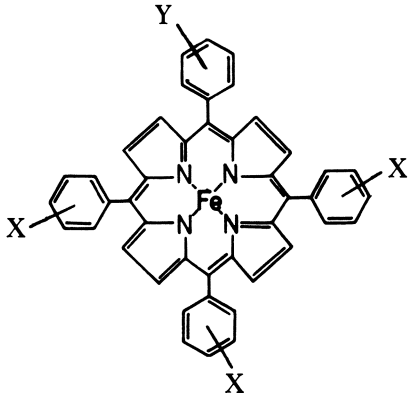

Structure III. Unsymmetrically substituted tetraphenylporphyrin complexes prepared for this study.

π-orbital into which the unpaired electron is delocalized is influenced profoundly by the inductive transfer of electron density to, or from, a unique substituent on one of the phenyl rings. The more different the unique substituent is from the other three, as measured by the difference in the familiar Hammett σ-constants (*44*) ($\Delta\sigma = \sigma_Y - \sigma_X$), the more different the isotropic shift of the β-pyrrole protons nearest that phenyl is from the shift of its immediate neighbors (*43*).

In contrast to our NMR results, ESR studies of the same low spin iron(III) complexes indicate (*45*) that the magnetic anisotropy of iron is not affected by unsymmetrical phenyl substitution such as in **III**, but rather depends on the total electronic effect of all substituents, as measured by the sum of the Hammett σ-constants ($\Sigma\sigma$).

The present study was undertaken to determine whether, and if so, how the redox potentials of iron porphyrins are altered by unsym-

metrical substitution on the phenyl rings. Previous studies of the effect of substituents on the redox potentials of both metal- and ring-centered redox reactions have shown that $E_{1/2}$ varies linearly with $\Sigma\sigma$ for symmetrically substituted TPPs (*36–40*). Our purpose was thus to see whether the redox potentials of unsymmetrically substituted iron TPPs correlate with those of the symmetrical derivatives, or whether consistent deviations from the expected linear correlation of $E_{1/2}$ with $\Sigma\sigma$ exist.

To eliminate from consideration at this time the effect of hydrogen-bonding of the imidazole N–H to other molecules in the solution, thus potentially altering the redox potentials as in possibility 1 mentioned earlier, *N*-methylimidazole was chosen as the axial ligand in this study. To allow these *N*-methylimidazole ligands to rotate freely so as not to have preferred axial ligand plane alignments as in possibility 3 just mentioned, we concentrated mainly on *m*- and *p*-phenyl-substituted derivatives of Structure **III.**

As part of this study, we evaluated the equilibrium constants for the addition of one and two *N*-methylimidazole molecules to iron(III) and iron(II) in dimethylformamide (DMF), which is potentially capable of solvating the axial positions of iron, and in dichloromethane, which is not. The purpose of this part of our investigation was to provide information on the concentration of *N*-methylimidazole necessary to fully complex both iron(III) and iron(II) porphyrins in order to guide us in measuring the redox potentials of the cytochrome b active site models, as well as to demonstrate the utility and facility of cyclic voltammetric techniques in measuring equilibrium constants for ligand addition to electroactive metals.

Experimental

Symmetrical tetraphenylporphyrins were prepared according to the method of Adler et al. (*46*), and were purified by gravity column chromatography on silica gel (Baker chromatographic grade). Unsymmetrical tetraphenylporphyrins were prepared by a modification of this method, in which half of the mole quantity of aldehyde required for the synthesis was provided by one *o*-, *m*-, or *p*-substituted benzaldehyde and half by a different benzaldehyde. This procedure led to an approximately statistical (1:4:2:4:4:1) distribution of isomers, which usually (except for those prepared from *p*-diethylamino or any nitrobenzaldehyde) crystallized from propionic acid. All product mixtures were analyzed by thin-layer chromatography (TLC) (Eastman Chromagram, silica gel) to determine what solvent system would allow separation of the isomers. Often the best solvent mixture was 70% benzene–30% petroleum ether. Only when one of the types of phenyl substituents was a polar group (-OCH_3, -NEt_2, -CN, or -NO_2) could the separation be effected, and even then, only for the *p*-Cl, *p*-NEt_2 combination was it possible to separate the *cis*- and *trans*-isomers of the 2 X, 2 Y formula (*41*). Small amounts of the isomers could be separated by high performance liquid chromatography

(HPLC), but because of low solubility, quantity separations were done on large gravity flow columns (3 cm × 1.5 m). Many fractions were collected and checked by TLC before combining the fractions containing one pure isomer. The identity of the purified compounds was established by NMR spectroscopy, particularly by observing the resonance pattern of the pyrrole protons at about 8.8–9.0 ppm downfield from tetramethylsilane (TMS) (*41*).

Iron and zinc were inserted into the porphyrin ring by the method of Adler et al. (*47*) with the following modification: after refluxing the porphyrin and metal salt in DMF until the reaction was complete, determined by electronic absorption spectroscopy, the solution was cooled to room temperature. An equal volume of dichloromethane was added and the mixture was then poured through approximately 500 mL H_2O in a separatory funnel and the CH_2Cl_2 layer immediately drawn off without shaking. The CH_2Cl_2 layer was then reintroduced to 500 mL of pure H_2O in the separatory funnel, shaken, and separated. This procedure was repeated three additional times to remove all DMF. The dichloromethane solution was evaporated to dryness, the sample redissolved in a small quantity of CH_2Cl_2, poured onto a dry silica gel column (1.5 cm × 25 cm), and eluted with 10% methanol–90% CH_2Cl_2 in the case of iron, or pure benzene in the case of zinc. The metalloporphyrin fraction was evaporated to dryness. Iron-containing samples were treated further by redissolving them in CH_2Cl_2 and bubbling gaseous HCl through them to reconvert any μ-oxo dimer back to the chloroiron monomer form. The samples then were evaporated again to dryness.

N-Methylimidazole and triethylamine (Aldrich) were purified by conventional distillation, and 2-methylimidazole (Aldrich) was recrystallized from benzene before use. Tetrabutylammonium perchlorate (TBAP) (Southwestern Analytical) was recrystallized from boiling absolute methanol and dried in vacuo over P_2O_5. For electrochemical studies, spectrograde dichloromethane (Fisher) was used without further purification, and DMF (MCB spectrograde) was distilled at reduced pressure over P_2O_5 before use.

Solutions for electrochemical investigations were approximately 10^{-3} *M* in metalloporphyrin and 10^{-1} *M* in electrolyte (TBAP). Aliquots of 15 to 30 mL of the resulting solution were placed in the water-jacketed electrochemical cell (Princeton Applied Research) maintained at 21 ± 1°C and deaerated prior to the voltammetric run by purging with nitrogen gas (Air Products), which was deoxygenated thoroughly by means of a Matheson 6404 nitrogen filter and presaturated with CH_2Cl_2 or DMF. The temperature was controlled to ±0.5°C during each run.

Cyclic voltammetry studies were carried out using a three-electrode system with a PAR Model 173 potentiostat/galvanostat, a PAR Model 175 universal programmer, and a Hewlett–Packard Model 7040 x–y recorder. The working electrode was constructed out of a short length of platinum wire soldered to copper wire, sealed in soft glass, and fired into a button. Platinum foil sealed in lead glass served as the counter electrode. Platinum electrodes routinely were cleaned by dipping them in alcoholic KOH followed by distilled water, then concentrated HNO_3 followed by distilled water, then acetone, and finally CH_2Cl_2. A commercial saturated calomel electrode (SCE) was used as reference electrode. It was connected to an aqueous saturated KCl solution, which was separated from the metalloporphyrin solution by a fine glass frit made of unfired Vycor (PAR).

Half-wave potentials (for reversible waves) or peak potentials (for irreversible waves) for the iron(II)/iron(I) and iron(III)/iron(II) reactions of tetraphenylporphinatoiron chloride (TPPFeCl) were measured in the absence of

ligand and as a function of the *N*-methylimidazole concentration over the range 1×10^{-4} to 1×10^{-1} *M* in DMF and CH_2Cl_2. The symmetrical and unsymmetrical phenyl-substituted derivatives of TPPFeCl in dichloromethane solution were scanned over the potential range +2.2 to −1.5 V in the absence of added ligand and then in the presence of 5×10^{-3} and 1×10^{-1} *M* *N*-methylimidazole (*N*-MeIm). The iron(III)/iron(II) peak was expanded and scanned slowly (20 or 50 mV/min) to obtain cathodic and anodic peak potentials unaffected by the kinetics of ligand exchange.

For zinc(II) porphyrins, half-wave potentials for the $ZnP^+ = ZnP$ and $ZnP^{2+} = ZnP^{+\cdot}$ reactions were measured in CH_2Cl_2, and the $ZnP = ZnP^-$ and $ZnP^{-\cdot} = ZnP^{2-}$ reactions were measured in DMF.

Results

Typical scans of $(m\text{-F})_4$TPPFeCl in CH_2Cl_2 in the absence of *N*-MeIm and as a function of [*N*-MeIm] are shown in Figure 1. The iron(III)/iron(II) reaction is not reversible, and the anodic peak is somewhat misshapen in the absence of *N*-MeIm. This fact was reported previously (*48*), and is due in large part to the fact that Cl^-, although bound to iron(II) during the time scale of its production by reduction of iron(III), diffuses away before iron(II) is re-oxidized in the reverse scan, and thus the cathodic and anodic sweeps represent the redox of different species of iron(II) (*49*).

The $E_{1/2}$ values for the iron(III)/iron(II) and iron(II)/iron(I) couples of TPPFeCl were measured as a function of [*N*-MeIm] over the concentration range 1×10^{-4}–1×10^{-1} *M* in DMF and CH_2Cl_2 solutions. Plots of the values of $E_{1/2}$ for the two couples as a function of log [*N*-MeIm] are presented in Figure 2a and b, respectively. These plots were analyzed according to the method outlined by Kadish et al. (*39*) to yield the equilibrium constants for addition of one and two *N*-methylimidazole ligands to both TPPFe(III)Cl and TPPFe(II). The equilibrium constants for the two possible steps of ligand addition to each of these complexes are defined by the reactions below:

$$\text{TPPFe(II)} + N\text{-MeIm} \overset{\beta_1^{II}}{\rightleftharpoons} \text{TPPFe(II)}(N\text{-MeIm}) \quad (1)$$

$$\text{TPPFe(II)} + 2\ N\text{-MeIm} \overset{\beta_2^{II}}{\rightleftharpoons} \text{TPPFe(II)}(N\text{-MeIm})_2 \quad (2)$$

$$\text{TPPFe(III)Cl} + N\text{-MeIm} \overset{\beta_1^{III}}{\rightleftharpoons} \text{TPPFe(III)}(N\text{-MeIm})\text{Cl} \quad (3)$$

$$\text{TPPFe(III)Cl} + 2\ N\text{-MeIm} \overset{\beta_2^{III}}{\rightleftharpoons} \text{TPPFe(III)}(N\text{-MeIm})_2^+\text{Cl}^- \quad (4)$$

Obtaining all four constants depends on the fact that TPPFe(I) does not bind *N*-methylimidazole. Thus, the relationship

$$(E_{1/2})_c = (E_{1/2})_s - \frac{0.059}{n} \log \frac{\beta_p^{ox}}{\beta_q^{red}} - \frac{0.059}{n} \log [L]^{p-q} \quad (5)$$

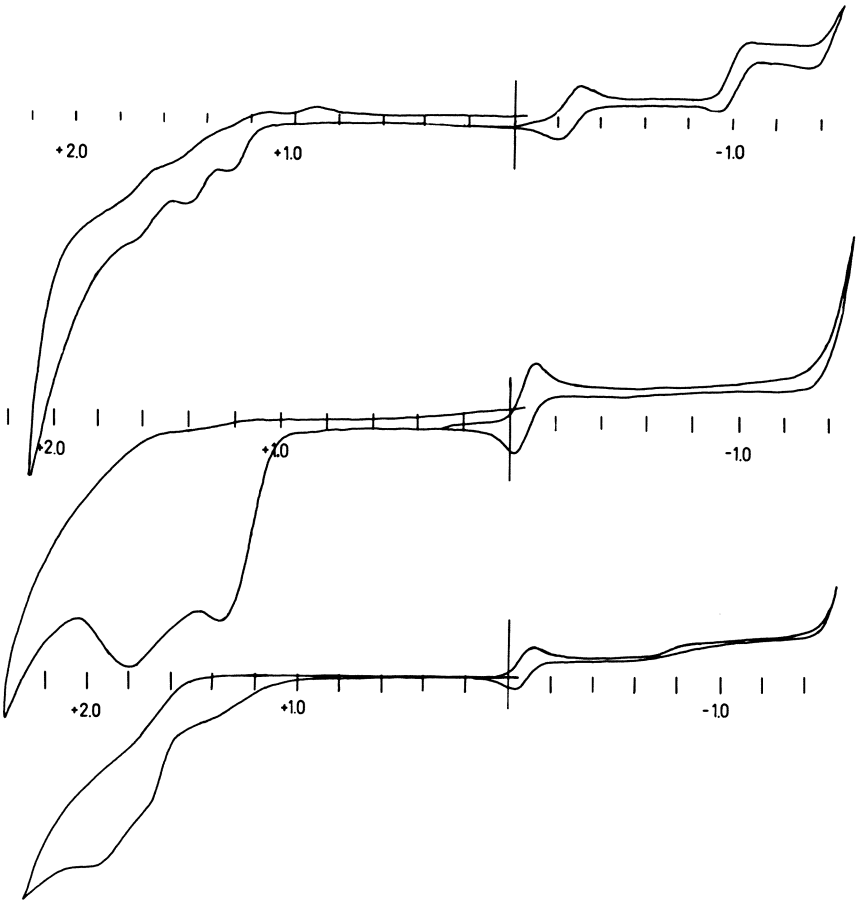

Figure 1. Cyclic voltammograms of 1.0 × 10^{-3} M (m-F)$_4$ TPPFeCl in CH_2Cl_2 with 0.1 M TBAP. Top: without added ligand; center: with 5 × 10^{-3} M N-MeIm; and bottom: with 1 × 10^{-1} M N-MeIm. Scan rate: 50 mV/min. Scale: volts vs. SCE.

(in which $(E_{1/2})_c$ and $(E_{1/2})_s$ are the half-wave potentials of the complexed and uncomplexed oxidized species, respectively, β_p^{ox} and β_q^{red} are the formation constants of the oxidized and reduced complexes, [L] is the concentration of free ligand at equilibrium, p and q are the number of ligands bound to the oxidized and reduced species, respectively, and n is the number of electrons transferred in the diffusion-controlled reaction ox + $n\ e^- \rightleftharpoons$ red) reduces to

$$(E_{1/2})_c = (E_{1/2})_s - 0.059 \log \beta_p^{II} - 0.059 \log [L]^p \quad (6)$$

for the iron(II)/iron(I) wave. Thus, in DMF, β_1^{II} and β_2^{II} [for addition of one and overall addition of two axial ligands to iron(II)] in principle

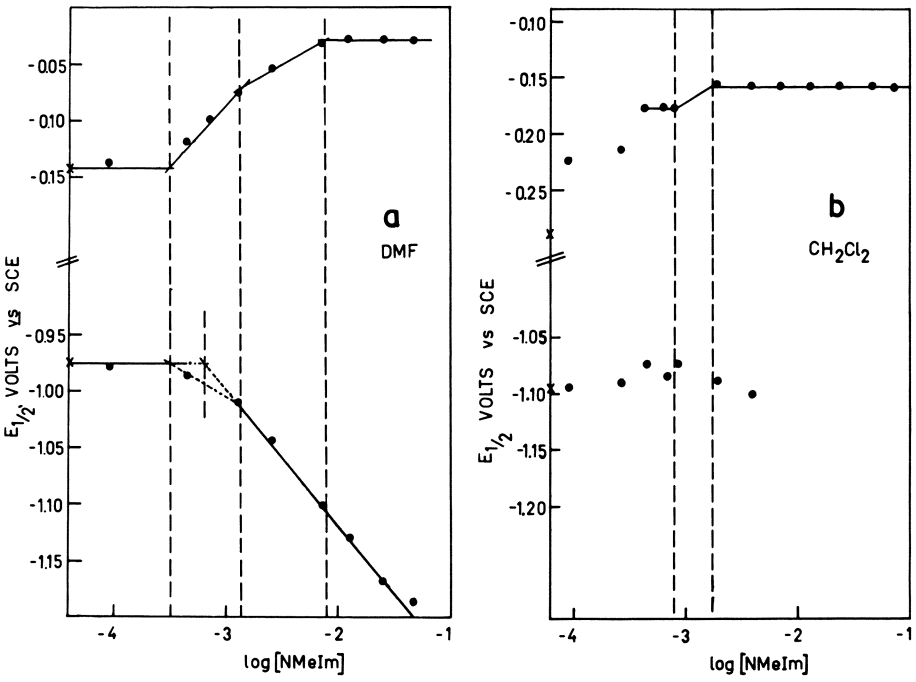

Figure 2. Plots of $E_{1/2}$ for the Fe(III)/Fe(II) (top) and Fe(II)/Fe(I) (bottom) couples of TPPFeCl as a function of a log [N-MeIm]$_{eq}$: a, in DMF and b, in CH_2Cl_2. The dotted lines in Part a demonstrate an ambiguity in the interpretation of the low N-MeIm concentration region: the Fe(II)/Fe(I) wave suggests formation of TPPFe(N-MeIm), while in the same concentration region the Fe(III)/Fe(II) wave suggests that Fe(II) has two N-MeIm ligands. The value listed in Table II is that calculated from the Fe(II)/Fe(I) wave. The vertical dashed lines mark off ligand concentration regions in which the predominant reactions are those shown in Schemes I and II.

may be calculated directly from the data of Figure 2 for the iron(II)/iron(I) couple, and β_1^{III} and β_2^{III} may be calculated by combining the data for the iron(III)/iron(II) and iron(II)/iron(I) couples. The concentration of free ligand must be obtained by an iterative process, because a portion of total ligand added is used to complex the major redox-active species present, in this case iron(III). Estimates of β_1^{III} and β_2^{III} from an initial plot of $E_{1/2}$ vs. log [*N*-MeIm]$_0$ are thus used to calculate log [*N*-MeIm]$_{eq}$ used in plotting Figure 2. The resulting β_1 and β_2 values in DMF are given in Table II, and the reactions involved in Figure 2a are summarized in Scheme I.

In CH_2Cl_2 (Figure 2b), the situation is less clearcut than in DMF (Figure 2a), apparently because the electrode reactions are slower. The cathodic peak of the iron(III)/iron(II) couple is misshapen at low

Published on June 1, 1982 on http://pubs.acs.org | doi: 10.1021/ba-1982-0201.ch017

Table II. Equilibrium Constants for Addition of Imidazoles to TPPFeCl in Two Solvents: Comparison of Electrochemical and Spectral Determinations

Ligand	*Method*	β_1^{II}	β_2^{II}	β_1^{III}	β_2^{III}
		Solvent = DMF			
N-MeIm	cyclic voltammetry[a]	$(3.6 \pm 1.2) \times 10^3$[b]	$(2.1 \pm 0.1) \times 10^6$	$(2.5 \pm 0.8) \times 10^2$	$(2.4 \pm 0.5) \times 10^4$
	electronic absorption spectroscopy[a] (*27*)	—	—	126	6.11×10^4
2-MeIm	cyclic voltammetry[a]	$(3.9 \pm 1.2) \times 10^3$	—	$(3.5 \pm 1.5) \times 10^2$	$(3.0 \pm 0.5) \times 10^3$
		Solvent = CH_2Cl_2			
N-MeIm	cyclic voltammetry[c]	$(2.2 \pm 1.0) \times 10^3$[d]	$(1.7 \pm 0.7) \times 10^6$[d]	27 ± 10[d]	(1.0×10^4)
	electronic absorption spectroscopy[a] (*27*)	—	—	88	1.0×10^4
	indirect measurement of electronic absorption spectrum (from stopped-flow photometry) (*53*, *54*)	—	—	3	1×10^4

[a] $T = 25 \pm 0.5$°C.
[b] *See* caption to Figure 2.
[c] $T = 21 \pm 1.0$°C.
[d] Derived values based on $\beta_2^{III} = 1.0 \times 10^4$.

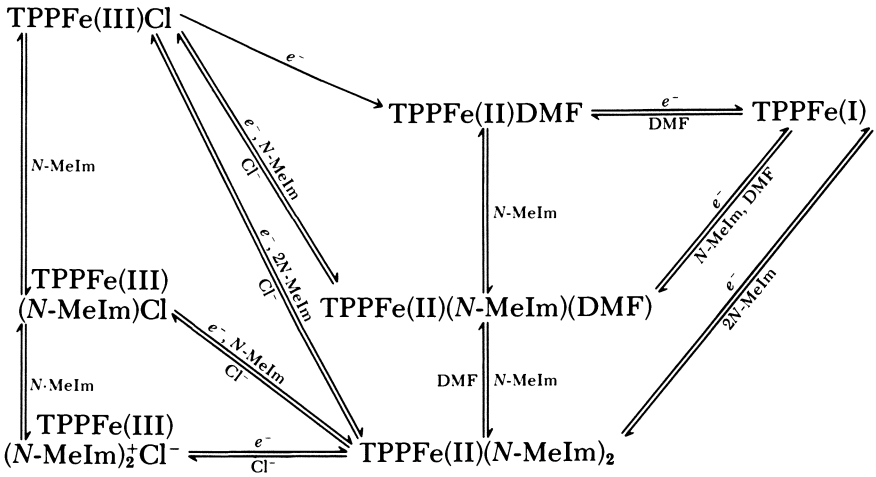

Scheme I

($< 4 \times 10^{-4}$ *M*) *N*-MeIm concentration; the $E_{1/2}$ of the iron(II)/iron(I) couple does not shift significantly with change in [*N*-MeIm], but the waves decrease in amplitude until they can no longer be observed above $[N\text{-MeIm}]_0 = 5 \times 10^{-3}$ *M*. We attribute the iron(III)/iron(II) cathodic peak behavior to slow gain of ligand by iron(II) following reduction of TPPFeCl; and the iron(II)/iron(I) wave behavior is attributed to slow loss of ligand(s) by iron(I) following reduction of Fe(II)(*N*-MeIm) or Fe(II)(*N*-MeIm)$_2$ followed by slow gain of ligand(s) on reoxidation of iron(I). [The disappearance of the iron(II)/iron(I) peak for tetracoordinated TPPFe on addition of *N*-MeIm must be accompanied by the appearance of new peaks at the appropriate potentials for redox of the mono- and bis(*N*-MeIm) complexes, but these are apparently so cathodically shifted that they are obscured by the redox of the solvent.] Despite the lack of β_1^{II} and β_2^{II} information obtained from the iron(II)/iron(I) wave and the irreversible behavior of the iron(III)/iron(II) peak at low ligand concentrations, considerable information is still available concerning the ligand equilibria of iron(III) and iron(II) in CH_2Cl_2: (1) from $[N\text{-MeIm}]_0$ of $\sim 6.3 \times 10^{-4}$ to 1.1×10^{-3} *M*, both iron(III) and iron(II) have the same number of axial ligands bound, presumably one, based on the behavior at higher [*N*-MeIm]$_0$; (2) between the $[N\text{-MeIm}]_0 = 1.1 \times 10^{-3}$ and 2.5×10^{-3} *M*, iron(II) has one more axial ligand than iron(III); and (3) above 2.5×10^{-3} *M N*-MeIm, both iron(III) and iron(II) again have the same number of axial ligands. The derived values of β_2^{II} and β_1^{III}, based on the value of β_2^{III} measured by visible spectroscopy, are listed in Table II, and the reactions involved in Figure 2b are summarized in Scheme II.

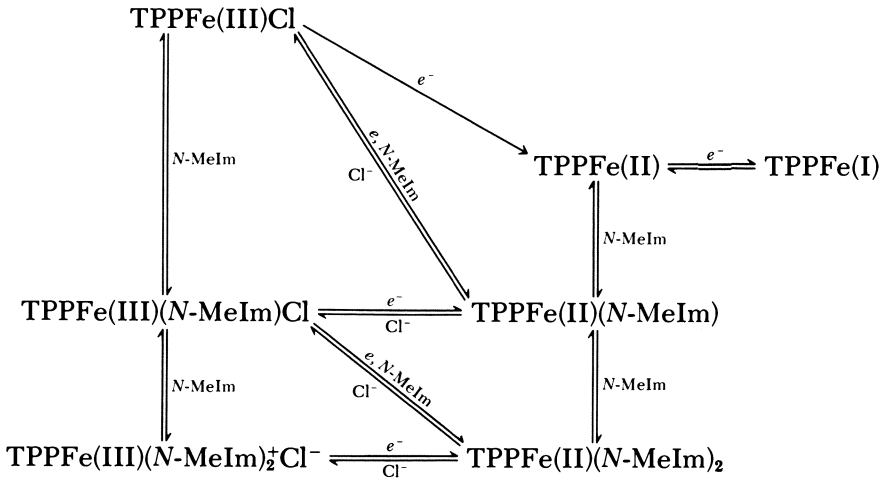

Scheme II

On the basis of the data of Figure 2b and Table II, the peak potentials and $E_{1/2}$ values derived therefrom, in volts, for all accessible redox reactions within the range of solvent stability provided by CH_2Cl_2 were measured for the symmetrical and unsymmetrical phenyl-substituted derivatives of TPPFeCl in the absence of added ligand and in the presence of sufficient *N*-MeIm to fully complex both iron(III) and iron(II) (usually 1.0×10^{-1} *M*). Typical scans are illustrated in Figure 1 by tetra(*m*-fluoro)tetraphenylporphinatoiron chloride [(*m*-F)$_4$TPPFeCl] in the absence of added ligand and in the presence of 5×10^{-3} *M* and finally 1×10^{-1} *M* *N*-MeIm. The absence of well-defined cathodic peaks in the positive potential range is characteristic of many of the compounds; and thus, these waves were not analyzed further. The iron(III)/iron(II) redox wave for all compounds, with and without *N*-methylimidazole, was expanded by reducing the potential range to encompass only that reaction in order to facilitate greater accuracy in the measurement of peak potentials. The peak potentials and $E_{1/2}$ values derived therefrom for the iron(III)/iron(II) couple are presented in Table III for the redox reaction in the presence and absence of *N*-methylimidazole, along with the sum of the Hammett σ-constants of the substituents on the tetraphenylporphyrin ligand. The $E_{1/2}$ values of the bis(*N*-methylimidazole) complexes of Table III are plotted in Figure 3, and the cathodic peak potentials of the non-imidazole-complexed forms of the compounds of Table III are plotted in Figure 4 vs. the sum of the Hammett σ-constants of the substituents. Because of the method of preparation of the chloroiron form of these

Published on June 1, 1982 on http://pubs.acs.org | doi: 10.1021/ba-1982-0201.ch017

Table III. Cathodic Peak Potentials for Reduction of High Spin Iron(III), and Half-Wave Potentials for Low Spin Iron(III)/Iron(II) Redox in Dichloromethane

TPP Substituent(s)[a]	$\Sigma\sigma^b$	$\Delta\sigma^b$	*Without* N-*MeIm* E_p^c (*V*)	*With* N-*MeIm* 5×10^{-3} M $E_{1/2}$ (*V*)	*With* N-*MeIm* 1×10^{-1} M $E_{1/2}$ (*V*)
4*p*-NEt_2H^+	3.280[c]	0	−0.260		
1*p*-Cl, 3*p*-NEt_2H^+	2.687[c]	−0.593	−0.250		
1*m*-F, 3*m*-NO_2	2.467	−0.373	−0.300	−0.003	+0.001
1*p*-H, 3*p*-NO_2	2.334	−0.778	−0.289	−0.026	−0.027
4*m*-CN	2.240	0	−0.259	+0.002	+0.011
trans-2*p*-Cl, 2*p*-NEt_2H^+	2.094[c]	(0.593)[d]	−0.332		
cis-2*p*-Cl, 2*p*-NEt_2H^+	2.094[c]	(0.593)[d]	−0.150		
1*m*-CH_3, 3*m*-NO_2	2.061	−0.779	−0.318	−0.030	−0.036
1*m*-NO_2, 3*m*-F	1.721	+0.373		−0.064	−0.057
1*p*-NEt_2H^+, 3*p*-Cl	1.501[c]	+0.593	−0.250		
4*m*-Cl	1.492	0	−0.316	−0.076	−0.076
4*m*-F	1.348	0	−0.311	−0.078	−0.073
4*p*-Cl	0.908	0	−0.319	−0.094	−0.082
1*p*-NH_3^+	0.82[c]	+0.82	−0.346		
1*p*-NO_2	0.778	+0.778	−0.305	−0.101	−0.103
1*m*-NO_2	0.710	+0.710	−0.236	−0.114	
1*m*-NO_2, 3*m*-CH_3	0.503	+0.779	−0.328	−0.120	−0.124
4*m*-OCH_3	0.460	0	−0.360	−0.150	−0.146
1*p*-NO_2, *p*-CH_3	0.268	+0.948	−0.340	−0.129	−0.114
1*m*-$NHCOCH_3$	0.21	+0.21	−0.454	−0.186	−0.174
1*m*-OCH_3	0.115	+0.115	−0.341	−0.152	

Published on June 1, 1982 on http://pubs.acs.org | doi: 10.1021/ba-1982-0201.ch017

4H	0.000	0	−0.383	−0.161	−0.158
1*p*-$NHCOCH_3$	0.00	0	−0.413	−0.218	
1*p*-OCH_3, 3*p*-F	−0.082	−0.330	−0.421	−0.136	
1*p*-CN, 3*p*-OCH_3	−0.144	+0.928	−0.344	−0.140	
1*p*-NEt_2, 3*p*-Cl	−0.149[e]	−1.057	−0.370	−0.144	
1*p*-OCH_3	−0.268	−0.268	−0.454	−0.168	
4*m*-CH_3	−0.276	0		−0.171	
1*p*-NH_2	−0.66	−0.66		−0.164	
4*p*-CH_3	−0.680	0	−0.399	−0.175	−0.178
1*p*-F, 3*p*-OCH_3	−0.742	+0.330		−0.172	
4*p*-OCH_3	−1.072	0	−0.454	−0.204	−0.200
trans-2*p*-Cl, 2*p*-NEt_2	−1.206[e]	(1.057)[d]	−0.517	−0.175	
cis-2*p*-Cl, 2*p*-NEt_2	−1.206[e]	(1.057)[d]	−0.358	−0.192	
1*p*-Cl, 3*p*-NEt_2	−2.263[e]	+1.057	−0.419	−0.194	−0.212
4*p*-NEt_2	−3.32[e]	0	−0.587	−0.273	−0.260
1*o*-$NHCOCH_3$	+0.7[f]	+0.7[f]	−0.401	−0.110	
1*o*-$NHCOCH_2CH_2C_6H_5$	+0.8[f]	+0.8[f]	−0.332	−0.100	
1*o*-$NHCO_2CH_3$	+0.75[f]	+0.75[f]	−0.310	−0.104	
1*o*-$NHCO_2CH_2CH_2Im$	−0.2[f]	−0.2[f]	−0.217	−0.148	
1*o*-NO_2	+0.4[f]	+0.4[f]	−0.317	−0.126	
1*o*-OCH_3	−0.4[f]	−0.4[f]	−0.332	−0.162	
1*o*-NH_2	−0.2[f]	−0.2[f]	−0.45	−0.148	

Note: T = 21 ± 1°C; Potentials, in V, vs. SCE. $E_{1/2}$ (Ferrocinium ⇌ Ferrocene) = +0.465 V; ΔE_p = 83 mV.
[a] The numbering system used here indicates 1–4 phenyls substituted on the *o*-, *m*-, or *p*-position.
[b] σ-Constants taken from Ref. *44*.
[c] σ-Constant for protonated amines assumed equal to that for $-N(CH_3)_3^+$ (+0.88) (*44*).
[d] Because these compounds are not of the 3X, 1Y type, the calculation of $\Delta\sigma$ is not comparable.
[e] σ-Constant for $-NEt_2$ assumed equal to that for $-NMe_2$ (−0.83) (*44*).
[f] σ-Constants of *ortho*-substituents are not known. Values listed are derived from Figure 4 (*see* text).

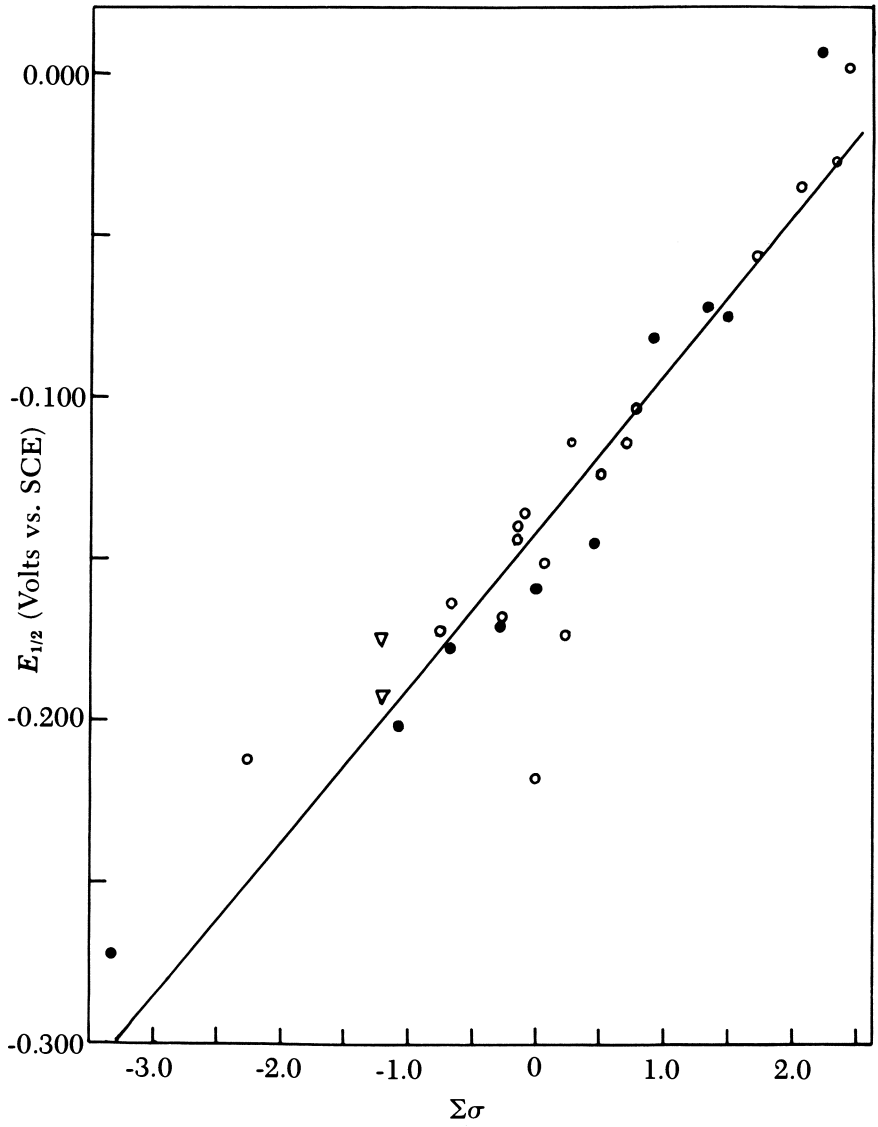

Figure 3. Plot of $E_{1/2}$ *for the LS Fe(III)/Fe(II) redox reaction vs. the sum of the Hammett sigma constants (44) of the phenyl substituents of symmetrical tetra-substituted (●) and unsymmetrical 3X, 1Y (○) derivatives of TPPFe(*N*-MeIm)*$_2$ $^+Cl^-$. *Also included are the* cis- *and* trans-*isomers of (*p*-Cl)*$_2$*(*p*-*NEt*$_2$*)*$_2$ *TPPFe(*N*-MeIm)*$_2$ $^+Cl^-$ *(▽). Data taken from Table III. The slope,* ρ, = +0.048 V.

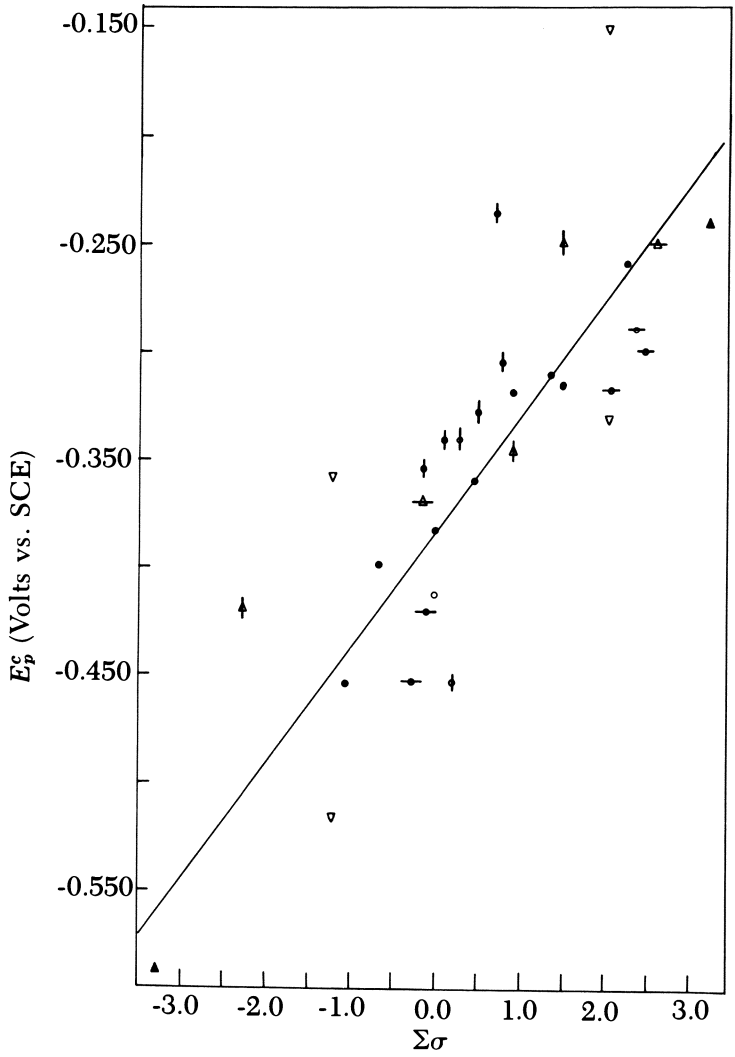

Figure 4. Plot of the cathodic peak potentials for HS Fe(III) reduction vs. the sum of the Hammett sigma constants (44) *of the phenyl substituents of symmetrical tetra-substituted (● or ▲) and unsymmetrical 3 X, 1 Y (○ or △) derivatives of TPPFeCl. Key: △, ▲, estimated peak potentials of protonated and unprotonated forms of amino- or diethylamino-containing derivatives; ▽, data for the* cis- *and* trans-*isomers of protonated and unprotonated forms of (*p-Cl)$_2$(p-NEt$_2$)*TPPFeCl; ⏃, ⊖, ⏃, ⏃, the sign of* $\Delta\sigma$ ($\sigma_Y - \sigma_X$) *of the unsymmetrical compounds (+ and −, respectively). Data taken from Table III. The slope,* ρ, = +0.052 V.

compounds (i.e., treatment with gaseous HCl), the $-NH_2$ and $-NEt_2$ substituted derivatives contained protonated amino groups when initially placed in CH_2Cl_2 solution. Such samples gave complex iron(III)/iron(II) waves (Figure 5). Attempts to simplify the wave shapes and to obtain the redox potentials of the deprotonated amino forms by addition of a small amount of triethylamine failed to produce reversible iron(III)/iron(II) waves. However, the complex wave of Figure 5 could be decomposed into two limiting waves, whose cathodic peak potentials were consistent with those expected from the sum of the Hammett σ-constants of the totally protonated and totally deprotonated forms (Figure 4).

Redox potentials for porphyrin ring oxidation and reduction of symmetrical and unsymmetrical TPPZn(II) complexes are presented in Table IV, and the results are plotted vs. the sum of the Hammett σ constants in Figure 6.

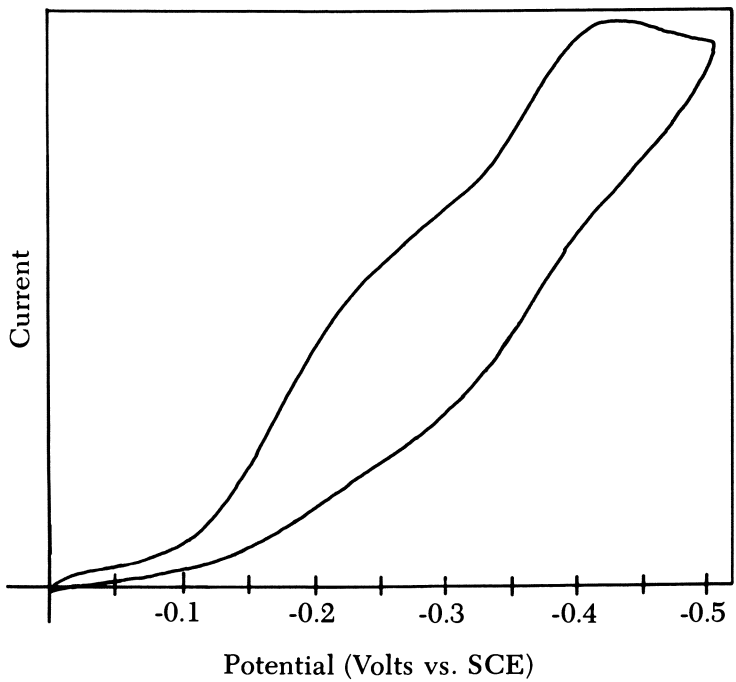

Figure 5. Scan of the Fe(III)/Fe(II) peak of (p-Cl)$_1$(p-NEt_2)$_3$*TPPFeCl and its protonated diethylamino derivatives. The two peaks observed are attributed to the triprotonated* (E_p^c = *−0.419 V) and unprotonated* (E_p^c = *−0.260 V) forms. Scan rate, 50 mV/min; [Fe porphyrin] = 1 ×* 10^{-3} M; *[TBAP] = 0.1* M.

Published on June 1, 1982 on http://pubs.acs.org | doi: 10.1021/ba-1982-0201.ch017

Table IV. Half-Wave Potentials for Ring Oxidation and Reduction of Symmetrical and Unsymmetrical Zinc Tetraphenylporphyrins

			$E_{1/2}$ (V vs. SCE)			
TPP Substituents(s)	$\Sigma\sigma$	$\Delta\sigma$	$ZnP^{2+} = ZnP^{+\cdot}$ *(in CH_2Cl_2)*	$ZnP^{+\cdot} = ZnP$ *(in CH_2Cl_2)*	$ZnP = ZnP^{-}$ *(in DMF)*	$ZnP^{-} = ZnP^{2-}$ *(in DMF)*
1*p*-H, 3*p*-NO_2	+2.334	−0.778	+1.21	+0.910	−1.065	−1.34
1*p*-OCH_3, 3*p*-CN	+1.712	−0.928	+1.151	+0.872	~−.93	~−1.38
4*p*-Cl	+0.904	0	+1.13	+0.830	−1.22	−1.66
1*p*-NO_2, 3*p*-H	+0.778	+0.778	—	—	−1.05	−1.56
1*p*-OCH_3, 3*p*-Cl	+0.413	−0.495	+1.17	+0.846	−1.25	—
1*p*-NO_2, 3*p*-CH_3	+0.268	+0.948	+1.11	+0.781	−0.90	−1.27
4H	0.000	0	+1.10	+0.768	−1.30	−1.70
1*p*-CN, 3*p*-OCH_3	−0.144	+.928	+1.050	+0.743	−1.353	~−1.54
1*p*-NEt_2, 3*p*-Cl	−0.15	−1.06	—[a]	—[a]	−1.28	—
4*m*-CH_3	−0.276	0	+1.08	+0.744	−1.31	−1.72
4*p*-CH_3	−0.680	0	+1.07	+0.706	−1.326	−1.73
1*p*-H, 3*p*-OCH_3	−0.804	+.268	+1.10	+0.805	−1.10	−1.32
4*p*-OCH_3	−1.072	0	+1.004	+0.673	−1.369	−1.77
2*p*-NEt_2, 2*p*-Cl *trans*	−1.19	|1.06|	—[a]	—[a]	−1.275	−1.70
2*p*-NEt_2, 2*p*-Cl *cis*	−1.19	|1.06|	—[a]	—[a]	−1.33	−1.72
1*p*-Cl, 3*p*-NEt_2	−2.26	+1.06	—[a]	—[a]	−1.38	—

[a] Peaks not reversible.

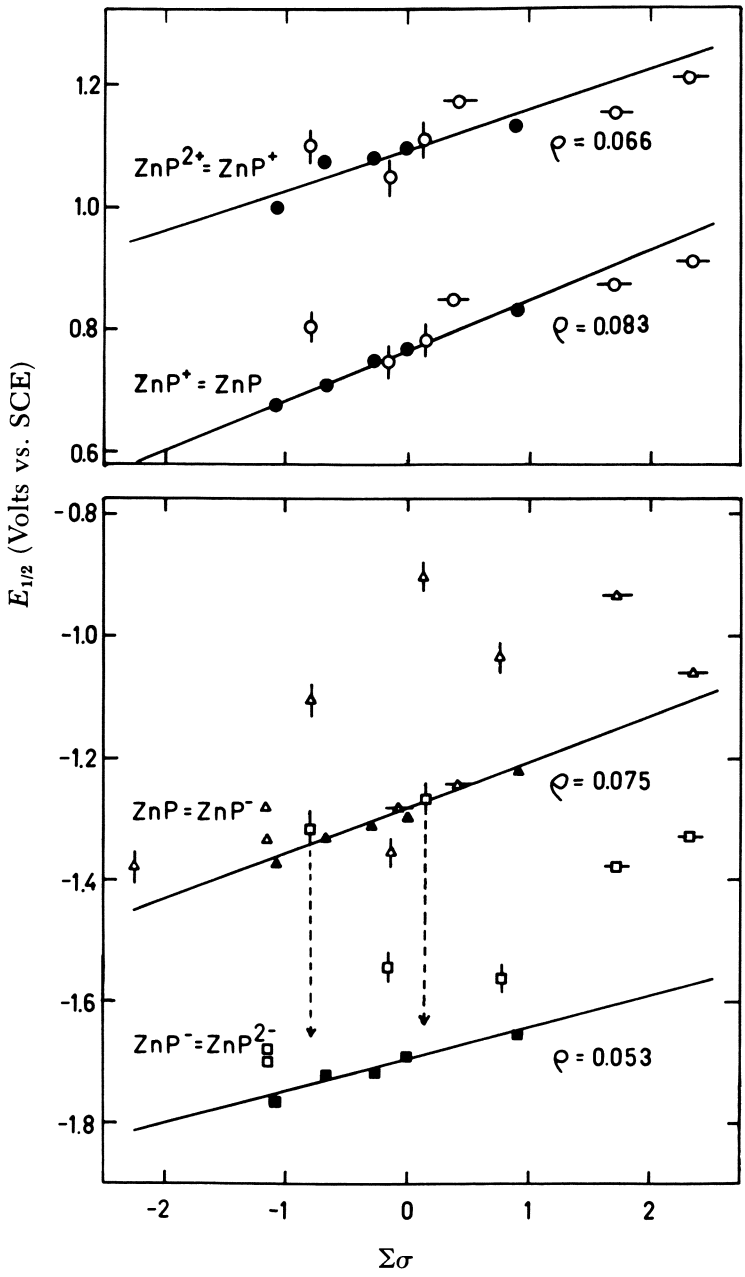

Figure 6. Plot of $E_{1/2}$ *for porphyrin ring oxidation and reduction of symmetrical (●) and unsymmetrical (○) derivatives of TPPZn(II) vs. the sum of the Hammett sigma constants* (44). *The slopes, ρ, are given in the figure.*

Discussion

Measurement of Equilibrium Constants for Complexation of *N*-Methylimidazole with Iron(III) and Iron(II) Tetraphenylporphyrins. Cyclic voltammetry provides an excellent means of measuring equilibrium constants of complex formation between transition metals and ligands when the rate of ligand exchange is rapid enough to yield quasi-reversible redox waves, particularly when the interest is in a metal in an unstable or highly reactive oxidation state. Kadish and coworkers have used this method to evaluate the stepwise and overall equilibrium constants for addition of pyridines to iron(II) (*39*, *50*), cobalt(II) and cobalt(III) (*39*, *50*), and manganese(II) and manganese(III) (*50*, *51*) porphyrins as a function of the electronic effects of symmetrically placed substituents on the porphyrin ring and the basicity of the pyridine. The highly dioxygen-sensitive iron(II) porphyrins provide excellent examples of the ease of measurement of β_1^{II} and β_2^{II} (or the stepwise K_2^{II}) by cyclic voltammetry: a series of fifteen data points may be obtained in several hours by adding aliquots of ligand to the air-stable iron(III) solution in the reaction cell and purging with nitrogen each time before scanning the iron(III)/iron(II) and iron(II)/iron(I) peaks to produce a plot such as in Figure 2a or b. In comparison, to obtain the same final information by visible spectroscopic studies of iron(II) porphyrin solutions would require first, the preparation of a spectroscopically pure and reproducible [i.e., free of μ-oxo dimer of iron(III) porphyrin] sample of the iron(II) porphyrin; second, the preparation of solutions containing a constant concentration of iron(II) porphyrin and varying amounts of ligand in a rigorously oxygen-free dry box or high vacuum line; third, successful transfer of these samples to the UV–visible spectrophotometer; and fourth, the observation of time-independent spectra. Such procedures are tedious and time consuming and seldom lead to trustworthy results.

To test the agreement between equilibrium constants obtained from cyclic voltammetry and visible spectroscopy, we measured β_1^{III} and β_2^{III} for *N*-methylimidazole addition to TPPFeCl in DMF by combination of the data provided by the iron(III)/iron(II) and iron(II)/iron(I) waves as outlined in the section entitled "Results"; and we compared the results with those obtained from spectroscopic studies (*27*, *51*), as shown in Table II. The value of β_2^{III} for *N*-methylimidazole complex formation is about a factor of 2.4 smaller, and the value of β_1^{III} a factor of two larger, by electrochemical than by spectroscopic evaluation. However, the difference in β_2^{III} is a relatively small factor when one considers the size of the constant; the difference in β_1^{III} values is probably meaningless, because a number of assumptions exist in the estimation of β_1^{III} from visible spectroscopic measurements, and the

reported estimates were considered accurate to only a factor of two (27). Furthermore, the conditions under which the measurements were made are somewhat different: the iron porphyrin was five times as concentrated in the electrochemical studies, but this factor is probably not important based on our previous studies of the dependence of β_2^{III} on $[TPPFeCl]_0$ (27). Of greater importance is the fact that the solution also contained 10^{-1} M TBAP, not present in the solutions of the electronic spectral studies. If the factor of about a 2.4 reduction in β_2^{III} is real, then there may well be a Debye–Hückel relationship between activity and concentration, particularly of the ion-paired product $TPPFe(N\text{-}MeIm)_2^+Cl^-$ in DMF. (This hypothesis has not yet been tested.) Nevertheless, the results in DMF suggest that the relative sizes of constants for a series of related reactions measured by cyclic voltammetry are reliable. A comparison of the estimated β_1^{II} for addition of one N-methylimidazole and one 2-methylimidazole ligand to TPPFe(II) in DMF showed that the constants are almost identical. Despite this fact, TPPFe(N-MeIm) readily adds a second N-MeIm ligand (52), whereas TPPFe(2-MeIm) does not add a second 2-MeIm ligand (52). This behavior is all the more curious when one notes (Table II) that TPPFe(III) forms a stable bis(2-MeIm) complex (27). The reasons for this unique behavior of 2-MeIm on iron(II) have not been explained adequately to date, and we have no new insights to offer.

The probable complexation of DMF to iron(II) and its possible complexation to iron(III) were seen to be potentially complicating features of our interpretation of the equilibrium constants for ligand addition and our desired investigation of the dependence of redox potential on the nature and distribution of phenyl substituents on the unsymmetrical TPPs. Thus, we investigated the N-methylimidazole concentration dependence of $E_{1/2}$ for the iron(III)/iron(II) and iron(II)/iron(I) peaks, Figures 1, 2b in CH_2Cl_2. Unfortunately, the iron(II)/iron(I) peak involves such slow ligand exchange that no information could be obtained directly from that redox reaction concerning the size of β_1^{II} or β_2^{II}. The iron(III)/iron(II) peak, however, enabled us to calculate that $\log \frac{\beta_2^{III}}{\beta_2^{II}} = -2.24$, $\log \frac{\beta_1^{III}}{\beta_1^{II}} = -1.90$, and that $\log \frac{\beta_1^{III}}{\beta_2^{II}} = -4.58$. Taking the value of β_2^{III} in CH_2Cl_2 determined from spectroscopic measurements gives the results shown in Table II. Again, as in DMF, there is acceptable agreement in the value of β_1^{III} determined by the two methods, considering the inadequacies in the assumptions made in estimating β_1^{III} by visible spectroscopy (27). Neither our electrochemical result nor that obtained from visible spectroscopy (27) are in acceptable agreement with the value of

β_1^{III} estimated from indirect measurement of the electron absorption spectrum of the mono-*N*-MeIm complex of TPPFeCl using stopped-flow photometry (*53*, *54*) (Table II). The large difference in the β_1^{III} values possibly is due to the fact that the mono-*N*-MeIm complex can exist in two possible forms: the hexacoordinated TPPFeCl(*N*-MeIm) and the pentacoordinated ion pair TPPFe(*N*-MeIm)$^+$Cl. The time scale of the stopped-flow photometric measurement (*53*, *54*) may be fast enough to catch the mono-*N*-MeIm complex before Cl^- has dissociated. Several lines of unpublished evidence obtained in this laboratory, including ESR and NMR spectra of monoimidazole iron(III) porphyrin complexes, suggested that the major form of these complexes in CH_2Cl_2 and $CHCl_3$ is the pentacoordinated ion pair. The time scales of both visible spectroscopy and cyclic voltammetry (at the slow scan rates employed in this study) are such that the mono-*N*-MeIm complex should be in its thermodynamically stable ratio of pentacoordinated and hexacoordinated forms. Comparison of these data to those of Sweigert et al. (*53*, *54*) suggests that the ratio of hexacoordinated to pentacoordinated forms present at equilibrium in CH_2Cl_2 may be of the order of 10 : 1.

A comparison of the data for *N*-MeIm addition to TPPFe(III) and TPPFe(II) shows that in going from the less polar [ϵ = 9 (*55*), E_T = 41.1 (*56*)] CH_2Cl_2 to the more polar DMF [ϵ = 37 (*55*), E_T = 43.8 (*56*)], β_1^{II} and β_2^{II} do not change significantly, yet β_2^{III} increases by about a factor of 2.4 and β_1^{III} by a factor of about 5.6. This result suggests that the chloride ion is dissociated more completely from iron(III) in the mono-*N*-methylimidazole complex in DMF than in CH_2Cl_2.

For purposes of the following section, the important conclusion to be drawn from the data of Figure 2b and Table II is that above [*N*-MeIm]$_0$ = 2.5 × 10^{-3} *M* both iron(III) and iron(II) have two *N*-methylimidazole ligands bound, and the $E_{1/2}$ of the iron(III)/iron(II) couple is independent of [*N*-MeIm]. Thus, to be certain that the *N*-MeIm complexes of the FeTPPs with very electron-withdrawing substituents are measured in this limit, we measured the $E_{1/2}$ values discussed in the following section in the presence of not only 5 × 10^{-3} *M*, but also 10^{-1} *M* *N*-MeIm.

The Dependence of the Iron(III)/Iron(II) Redox Potential on the Electron-Donating or Electron-Withdrawing Nature of Substituents in Symmetrical and Unsymmetrical Tetraphenylporphyrin Complexes.

IN THE PRESENCE OF EXCESS *N*-METHYLIMIDAZOLE: CYTOCHROME B MODELS. When bound to two *N*-methylimidazoles, iron(III) and iron(II) porphyrins are both low spin (*52*, *57*) (one and zero unpaired electrons, respectively). Thus, the electron transfer between these two oxidation states in their low spin (LS) forms [LS $d^5 \rightleftharpoons$ LS d^6, with electron configurations $(d_{xy})^2(d_{xz,yz})^3 \rightleftharpoons$

$(d_{xy})^2(d_{xz,yz})^4$], should be exceedingly facile and should lead to reversible waves with $E_p^a - E_p^c$ theoretically equal to 57 mV at room temperature (58). Above 8.7×10^{-3} *M* *N*-MeIm in DMF, $E_p^a - E_p^c = 57 \pm 2$ mV; yet in CH_2Cl_2 above 2.5×10^{-3} *M* *N*-MeIm, $E_p^a - E_p^c$ was 77 ± 2 mV at a 20-mV/min scan rate, and was independent of ligand concentration above these points in each solvent. Although the value obtained in CH_2Cl_2 is larger than the theoretical prediction (58), it is actually less than the $E_p^a - E_p^c$ observed for ferrocene in the same solvent (Table III, footnote *a*), suggesting that solvent-dependent electrode effects lead to the larger-than-theoretical separation. Because the species involved in this redox reaction are identical in DMF and CH_2Cl_2, the LS iron(III) $\rightleftharpoons$ LS iron(II) redox reaction is considered reversible. This reversibility is necessary if the present compounds are to be acceptable models of the cytochromes b, because the same axial ligands and metal spin states are involved in those iron(III)/iron(II) (electron transfer) redox reactions.

No relationship was found between $E_{1/2}$ and the difference in σ-constants between unlike substituents for the low spin iron forms (Table III). Hence the $E_{1/2}$ values, in volts, of the compounds from Table III, were plotted vs. the sum of the Hammett σ-constants of the substituents present on the phenyl rings (Figure 3) to see whether any evidence exists for anomalous behavior of unsymmetrically substituted tetraphenylporphyrins as compared to symmetrically substituted ones. As Figure 3 shows, the $E_{1/2}$ dependences of both symmetrical and unsymmetrical compounds fall on the same line with relatively little scatter. The slope of this line, ρ, is 0.048 V, which is similar to the value found (discussed later) for the high spin iron complexes. The largest deviations are shown by the $E_{1/2}$ values of mono(*p*-$NHCOCH_3$)TPPFe(*N*-MeIm)$_2^{+,0}$, mono(*m*-$NHCOCH_3$)TPPFe(*N*-MeIm)$_2^{+,0}$, tetra(*m*-CN)TPPFe(*N*-MeIm)$_2^{+,0}$, and (*m*-NO_2)$_3$(*m*-F)TPPFe(*N*-MeIm)$_2^{+,0}$. The first two $E_{1/2}$ values appear to be exceptions to the general linear relationships found in this study in terms of not only their electrochemical, but also their NMR behavior (*43*) (discussed later). Their behavior suggests that the *N*-bound *meta*- and *para*-amide groups have very different apparent σ-constants in the tetraphenylporphyrin system (ca. -0.5 and -1.5, respectively) than those listed in Table III, and this possibility is presently under further investigation. The last two $E_{1/2}$ values appear anomalous for another reason: from NMR signal intensities and linewidths of the (*m*-tetracyano)tetraphenylporphinatoiron bis(*N*-methylimidazole) cation[(*m*-CN)$_4$TPPFe(*N*-MeIm)$_2^+$] and tri(*m*-nitro)-*m*-fluorotetraphenylporphinatoiron bis(*N*-methylimidazole) cation[(*m*-NO_2)$_3$(*m*-F)TPPFe(*N*-MeIm)$_2^+$] peaks, we suspect that there is a low spin ($S = \frac{1}{2}$) $\rightleftharpoons$ intermediate spin ($S = \frac{3}{2}$) or high spin ($S = \frac{5}{2}$) equilibrium involved in these complexes that contain extreme

electron-withdrawing substituents; and that this equilibrium may affect the iron(III)/iron(II) redox potential.

The fact that the $E_{1/2}$ values of both symmetrical and unsymmetrical TPPFe(*N*-MeIm)$_2^{+,0}$ complexes correlate with the sum of the Hammett σ-constants of the substituents indicates that the *e*-symmetry *d*-orbitals of iron(III) into which the electron goes on reduction, d_{xz} and d_{yz}, appear degenerate in these low spin iron porphyrins, even though NMR studies suggest that the *e*-symmetry orbitals of the porphyrin ring into which the unpaired electron density of low spin iron(III) is delocalized are not degenerate (*43*). This result will be discussed further, and possible explanations will be given.

The linear correlation between $E_{1/2}$ and $\Sigma\sigma$ for low spin iron porphyrins shown in Figure 3 can be used to assign σ-constants to mono-*ortho*-substituted FeTPP complexes if it is assumed that potential restriction of rotation of one *N*-MeIm ligand by the *ortho*-substituent does not affect $E_{1/2}$. The σ-values derived from Figure 3 are listed in the final section of Table III. The apparent σ-values of the *o*-$NHCO_2CH_3$ and *o*-$NHCO_2CH_2Im$ groups are very different. This indicates that restriction of rotation of an axial imidazole does affect $E_{1/2}$. Thus the $E_{1/2}$ values, as well as the NMR contact shift patterns (*59*), of mono-*ortho*-substituted TPPFe(*N*-MeIm)$_2^+$ complexes are determined by a combination of substituent effect and hindered ligand rotation.

IN THE ABSENCE OF ADDED LIGAND. Bottomley and Kadish recently showed (*48*) that, in the nonbonding solvents dichloromethane and dichloroethane, the following electron transfer sequence is involved for TPPFeX (X = F, N_3, Cl, Br, . . . ClO_4):

$$\begin{array}{ccc} \text{TPPFeX} & \overset{e^-}{\rightleftharpoons} & \text{TPPFeX}^- \\ \uparrow\downarrow \text{X}^- & & \uparrow\downarrow \text{X}^- \\ \text{TPPFeClO}_4 & \underset{\text{ClO}_4^-}{\overset{e^-}{\rightleftharpoons}} & \text{TPPFe} \end{array} \qquad \begin{array}{l} \text{(7a)} \\ \\ \text{(7b)} \end{array}$$

In the limit of slow sweep rate, for X = Cl, the cathodic wave represents Reaction 7a and the anodic wave represents a combination of Reactions 7a and 7b. Iron(III) is known to be high spin (five unpaired electrons) (*31*) when bound to chloride, and intermediate spin (three unpaired electrons) when bound to perchlorate (*60*). The two iron(II) species probably also have different spin states: tetracoordinated iron(II) porphyrins are of intermediate spin state (two unpaired electrons) (*61*) and $TPPFeX^-$ probably is high spin (four unpaired electrons), as are other pentacoordinated iron(II) porphyrins (*52*, *62*). Because the cathodic peak was well formed for all of the compounds

studied, and because it represents the formation of a single species on electron transfer, we looked for correlations between the cathodic peak potentials of the iron(III)/iron(II) reduction and the Hammett σ-constants of the substituents of our symmetrical and unsymmetrical iron porphyrins. Although the cathodic peak potential does not, of itself, represent a true thermodynamic quantity, it is a measure of the relative stability of the high spin states of iron(III) and iron(II). The cathodic peak potentials of the high spin compounds from Table III were plotted vs. the sum of the Hammett σ-constants of the substituents present on the phenyl rings (Figure 4). Figure 4 shows that the values of E_p^c of symmetrical tetraphenylporphyrin complexes of high spin iron(III)/iron(II) follow a fairly linear relationship with the sum of the Hammett σ-constants of the substituents. We find that ρ = 0.052 V, somewhat larger than the value reported for the linear-free-energy relationship of $E_{1/2}$ of the mixed high spin–intermediate spin iron(III)/iron(II) couple, (ρ = 0.038) (*63*). However, a major contribution to the difference in ρ is probably due to the difference in the σ-values used, especially for *m*-CN, in this work and Reference *63*.

Unsymmetrical tetraphenylporphyrin complexes deviate from the linear correlation found for symmetrical iron TPPs, with those unsymmetrical complexes having three electron-donating groups and one electron-withdrawing group ($\Delta\sigma$ positive, by our definition) generally lying above the line and those having three electron-withdrawing groups and one electron-donating group ($\Delta\sigma$ negative) lying below the line. Notable exceptions to this rule are again the mono-*p*-$NHCOCH_3$ ($\Delta\sigma$ = 0) and the mono-*m*-$NHCOCH_3$ ($\Delta\sigma$ = +0.210) derivatives, both of which would again appear to be "normal" if the σ-constants of the *meta*- and *para*-*N*-bound amides were quite negative (−2.0 and −1.0, respectively, in this case).

Porphyrin Ring Oxidation and Reduction: Electrochemistry of Symmetrical and Unsymmetrical Zinc(II) Porphyrins. In Table IV are summarized the $E_{1/2}$ values, in volts, for the two possible steps of ring oxidation, measured in CH_2Cl_2, and the two possible steps of ring reduction, measured in DMF, for a series of symmetrical and unsymmetrical derivatives of ZnTPP. In all cases the waves behaved reversibly, and no evidence of formation of phlorins or isoporphyrins (*64*) was detected from cyclic voltammograms. The resulting $E_{1/2}$ values are plotted vs. $\Sigma\sigma$ in Figure 6.

The redox potentials of all four ring reductions of symmetrical ZnTPPs clearly varies linearly with $\Sigma\sigma$, as reported previously (*37*), such that electron-withdrawing groups shift $E_{1/2}$ to more positive potentials for all reduction reactions. The sensitivity of each redox reaction to substituents (i.e., the ρ-values listed in Figure 6) differ somewhat from those reported previously (*37*). We find that the one-

electron ring oxidation and reduction reactions are considerably more sensitive to the electronic properties of substituents than are the formation of the dication or dianion.

Unsymmetrically substituted ZnTPP complexes have fairly normal (based on their linear-free-energy correlation) oxidation potentials, but generally have more positive reduction potentials, than their $\Sigma\sigma$-value would have predicted—never more negative values of $E_{1/2}$ than predicted—irrespective of whether one substituent is electron withdrawing and three electron donating, or the reverse. The same situation applies to reduction potentials of the 2*p*-Cl, 2*p*-NEt_2 isomers. Thus, it generally is easier to reduce an unsymmetrical ZnTPP derivative than it is to reduce its symmetrical counterpart with the same $\Sigma\sigma$-value. On the other hand, the ease of ring oxidation is essentially independent of whether the ZnTPP is symmetrically or unsymmetrically substituted. These results are totally compatible with the nature of the π-orbitals involved in ring reduction vs. ring oxidation: for ring reduction, electrons are added to the lowest unoccupied molecular orbital (LUMO) E_g orbitals (*64*, *65*) called the $4e(\pi)$ orbitals by Longuet–Higgins and Pople (*65*). These orbitals have large electron probabilities at opposite *meso*-positions, and differ by 90° in the orientation of their nodal planes (*66*) (Figure 7). The anion radical of the supposedly symmetrical Zn(etio II)$^-$ (where etio represents etioporphyrin) exhibits (*67*) an absorption spectrum consistent with only one component of the ^2E_g ground state (one of the two orbitals of Figure 7) contributing to the first electronic transition; thus, even symmetrically substituted zinc(II) porphyrin anion radicals have a distorted geometry, which removes the degeneracy of the $4e(\pi)$ orbitals on the time scale of the electronic excitation. For the unsymmetrically substituted ZnTPPs, the degeneracy of the $4e(\pi)$ orbitals is expected to be permanently removed, thus placing one of the two orbitals of Figure 7 at lower energy than it would have been in the symmetrically substituted ZnTPP analog (and the other at higher energy). Addition of an electron to the lower energy orbital thus should occur at less negative potential than expected for a symmetrically substituted ZnTPP.

In contrast, it has been shown (*68*) that, in ring oxidation of ZnTPP to the cation radical in the presence of ClO_4^-, the electron is removed from the a_{2u} orbital. Because this orbital is nondegenerate (*66*), unsymmetrical substitution cannot cause choice of one orbital over another. Therefore, in ring oxidation, unlike ring reduction, unsymmetrically substituted ZnTPPs behave no differently than their symmetrically substituted counterparts.

Comparison of Electrochemical Results with ESR Data for Low Spin Iron(III) Porphyrins. The *g*-values of the rhombic low spin iron(III) complexes of the symmetrically and unsymmetrically substi-

tuted tetraphenylporphyrin complexes studied varied linearly with the sum of the Hammett σ-constants of the substituents (*45*). Perhaps the most useful way to show this relationship graphically is to plot the tetragonal and rhombic magnetic anisotropy terms, $g_1^2 - \frac{1}{2}(g_2^2 + g_3^2)$ and $g_2^2 - g_3^2$, respectively, against the sum of the σ-constants, as shown in Figure 8. Thus, both the tetragonal and rhombic magnetic anisotropies of low spin iron(III) decrease with increasing electron-withdrawing character of the porphyrin ring, irrespective of whether substituents are placed symmetrically or unsymmetrically (*45*). Comparing Figures 4 and 8, we see that ESR data for low spin iron(III) porphyrins, as well as redox potentials for the low spin iron(III)/iron(II) couple, correlate with the sum of the σ-constants of the substituents.

Comparison of Electrochemical Results with NMR Data for Low Spin Iron(III) Complexes. We have recently discussed the NMR spectra of unsymmetrically substituted tetraphenylporphyrin complexes of low spin iron(III) (*43*). The combination contact- and dipolar-shifted pyrrole proton resonances appear as a pattern of peaks (Figure 9) whose relative intensities and positions are totally consistent with the pattern of unsymmetrical substitution, in light of the fact (*43*) that the unpaired electron is known to be delocalized into the (filled) 3*e* (π) porphyrin orbitals (Figure 10) by ligand-to-metal π

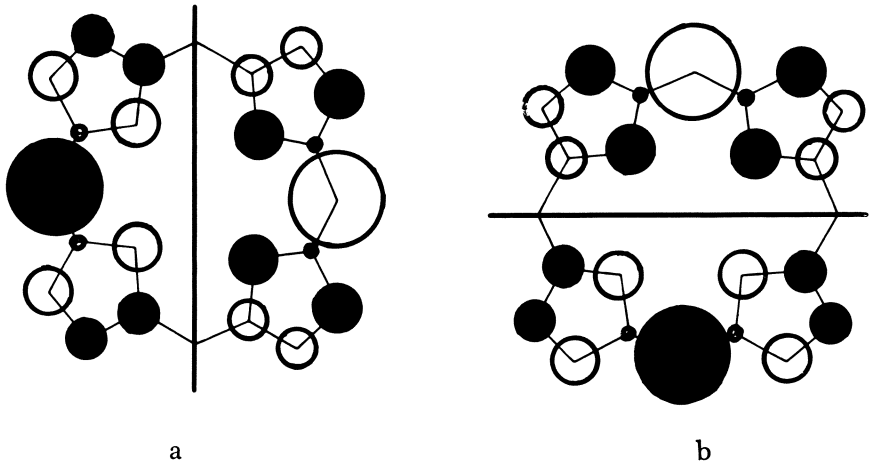

Figure 7. Electron density distribution in the porphyrin 4e(π) orbitals (65), *which are the LUMOs of ZnTPPs. The sizes of the circles depict the relative sizes of the squares of the atomic orbital mixing coefficients,* c_i^2, *for each atom, and thus represent the relative electron density expected at that position. The 4e(π) orbitals shown in a and b are linear combinations of those shown in Ref.* 63; *the linear combinations are appropriate for* meso-*substituted porphyrins.*

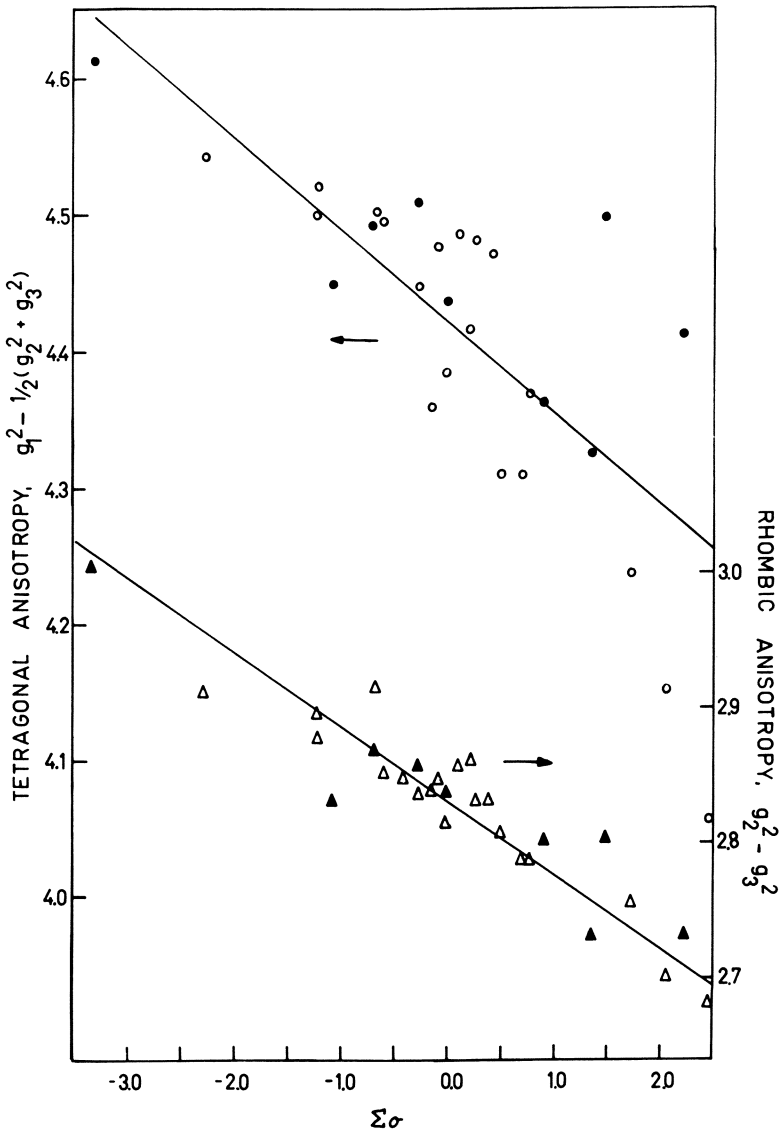

Figure 8. ESR data for low spin derivatives of TPPFe(N-MeIm)$_2^+$Cl$^-$ plotted as the tetragonal magnetic anisotropy term $g_1^2 - \frac{1}{2}(g_2^2 - g_3^2)$ (left axis, circles) and the rhombic magnetic anisotropy term $g_2^2 = g_3^2$ (right axis, triangles) vs. the sum of the Hammett sigma constants (44) of the substituents. ● and ▲ represent symmetrical complexes; ○ and △ represent unsymmetrically substituted complexes. Data taken from Ref. 45. The slopes, $\rho_{tet} = -0.066$ and $\rho_{rhom} = -0.052$ (where tet and rhom represent tetragonal and rhombic, respectively).

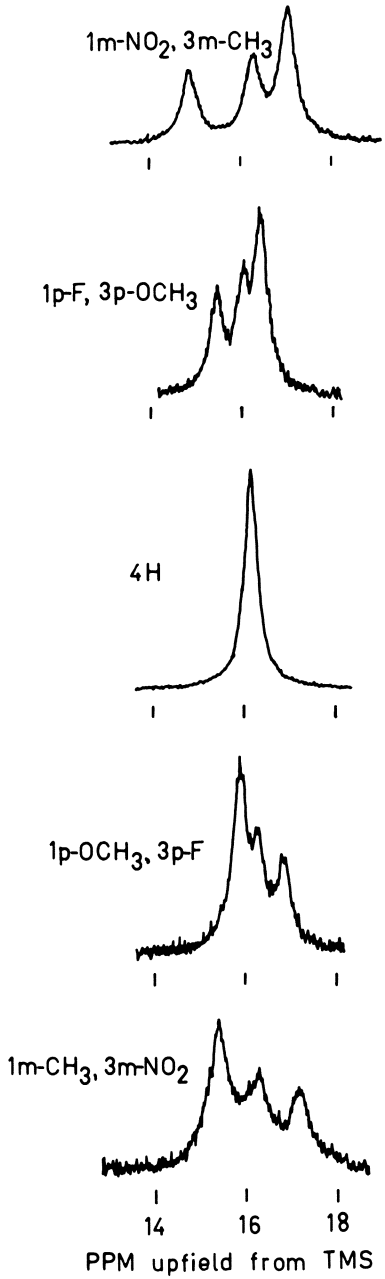

Figure 9. NMR spectra of the pyrrole-H region of four unsymmetrically (3X, 1Y) and one symmetrically substituted derivatives of TPPFe(N-MeIm)$_2^+$, arranged from top to bottom in order of decreasing difference in $\Delta\sigma$ ($\sigma_Y - \sigma_X$).

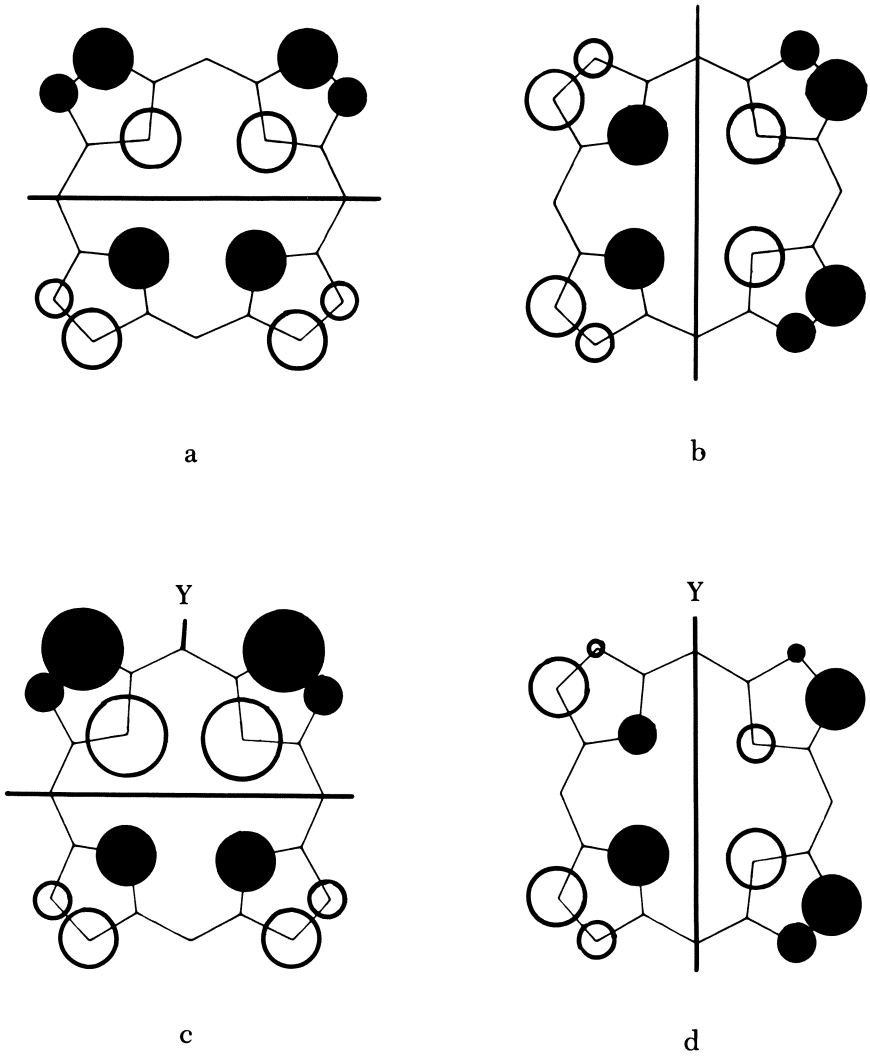

Figure 10. a and b: Symmetry and electron density distribution in the two degenerate $3e(\pi)$ *orbitals of porphine and symmetrical* meso-*tetraphenylporphyrins* (60, 61)*; c: the modified electron density distribution in that* $3e(\pi)$ *orbital of unsymmetrical (3X, 1Y) TPPs into which unpaired electron density is delocalized by* $L \rightarrow M$ π *backbonding when Y is more electron donating than X; d: the modified electron density distribution in that* $3e(\pi)$ *orbital utilized when Y is more electron withdrawing than X.*

back-bonding (57). Thus, the presence of one electron-donating group, with three electron-withdrawing groups on the four phenyl rings increases the total electron density at the unique *meso*-position. This increased electron density is felt as far away as the closest β-pyrrole positions. Increased electron density at the closest β-pyrrole positions encourages the choice of the $3e(\pi)$ orbital, which has large electron density at those particular pyrrole positions, as the one into which the unpaired electron will be delocalized. That is, introduction of one electron-donating substituent on one phenyl ring splits the degeneracy of the $3e(\pi)$ orbitals, so that the orbital having large electron density at those pyrrole positions closest to the unique phenyl is shifted to higher energy; and its former partner is shifted to lower energy. Ligand-to-metal π back-bonding occurs with the higher energy of the two now nondegenerate $3e(\pi)$ orbitals (Figure 10c), so that the pyrrole positions closest to the electron-donating phenyl group will have a particularly large unpaired electron density. This condition leads to a larger contact shift at these pyrrole positions, and thus the pyrrole proton peak furthest upfield from tetramethylsilane (TMS) is due to the protons at the pyrrole positions closest to the unique phenyl. Based on the pattern of electron distribution in the $3e(\pi)$ orbitals (Figure 10c), the next most upfield pyrrole peak can be assigned to the pyrrole protons furthest away from the unique phenyl, and the most downfield pyrrole peak (twice as intense as each of the others) to the remaining four pyrrole protons. The reverse situation occurs when the unsymmetrical molecule contains three electron-donating groups and one electron-withdrawing group (Figure 10d). Thus, the separation between highest-field and lowest-field pyrrole peaks (Figure 9), as expected, increases as the difference in electron-donating and electron-withdrawing character of the two types of substituents increases; and the pattern of peak intensities reverses from 2:1:1 when Y is more electron withdrawing than X to 1:1:2 when X is more electron withdrawing than Y (Figure 9) (*43*). This fact may be quantified by plotting the separation between the peak of intensity 2 and the most distant peak of intensity 1 ($\Delta\delta$) against the difference in the Hammett σ-constants for the two types of substituents ($\Delta\sigma$), as shown in Figure 11 (*43*). A similar plot of $\Delta\delta$ vs. the sum of the Hammett σ-constants of the substituents does not produce a linear correlation. Thus, the NMR peak separations of the pyrrole protons of low spin iron(III) porphyrins correlate with $\Delta\sigma$, and the redox potentials of the low spin iron(III)/iron(II) couple correlate with $\Delta\sigma$.

Comparison of Electrochemical Results with the Equilibrium Constants for Axial Ligation of Symmetrical and Unsymmetrical Iron(III) and Zinc(II) Porphyrins. We recently measured the equilib-

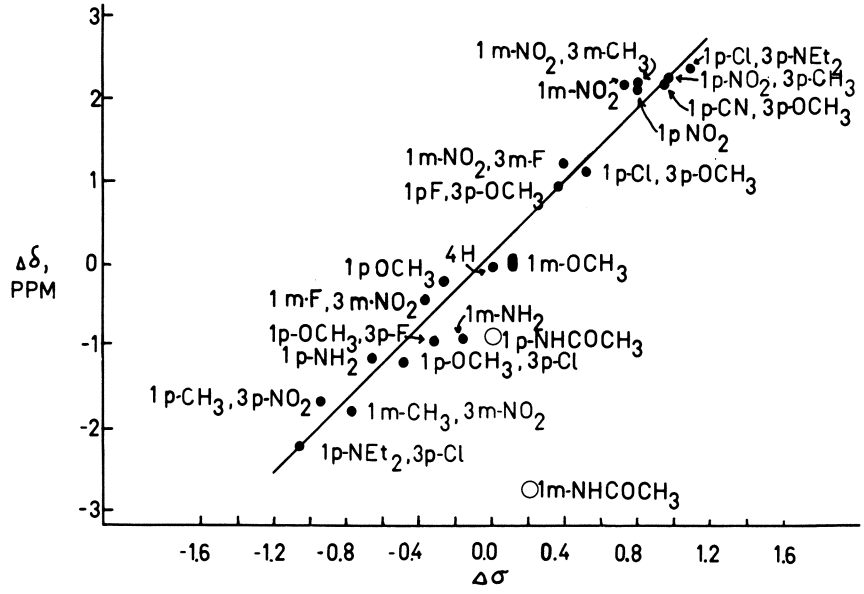

Figure 11. Plot of the separation ($\Delta\sigma$) between the pyrrole peak of area 1 vs. the difference ($\sigma_Y - \sigma_X$) in Hammett sigma constants (45). *Taken from Ref.* 43.

rium constants β_1^{III} and β_2^{III} for addition of *N*-methylimidazole to the series of six compounds, $(p\text{-}NEt_2)_x(p\text{-}Cl)_y$TPPFeCl ($x + y = 4; x = 0 - 4$), in chloroform (*69*) and β_1^{Zn} for addition of 3-picoline to $(p\text{-}NEt_2)_x(p\text{-}Cl)_y$TPPZn in toluene (*70*) by electronic absorption spectroscopy, and the results were compared to already existing data (*27*, *34*) for other symmetrical tetraphenylporphyrins of these two metals. The relationship between log β_2^{III} or log β_1^{Zn} and the sum of the Hammett σ-constants of the substituents is shown in Figure 12a and b, respectively. The mixed chloro-, diethylamino-substituted complexes of iron(III) deviate significantly from the linear correlation observed for all tetra-substituted TPPFeCl derivatives studied so far, although the mixed substituent isomers of ZnTPP lie on the same line as the tetra-substituted compounds. Zinc(II) has a filled $3d$ shell and iron(III) has a $3d^5$ configuration and goes from the symmetrical $(d_{xy})^1(d_{xz,yz})^2(d_{z^2})^1(d_{x^2-y^2})^1$ high spin electron configuration to the unsymmetrical $(d_{xy})^2(d_{xz,yz})^3$ low spin configuration on complexation of two *N*-MeIm ligands. Because the mixed-substituent isomers form less stable complexes with *N*-MeIm than predicted from the behavior of the tetra-substituted compounds, it would appear that by imposing a plane of symmetry on the porphyrin ring one makes it more difficult for *N*-MeIm to bind, whether the pattern of substituents is that of one

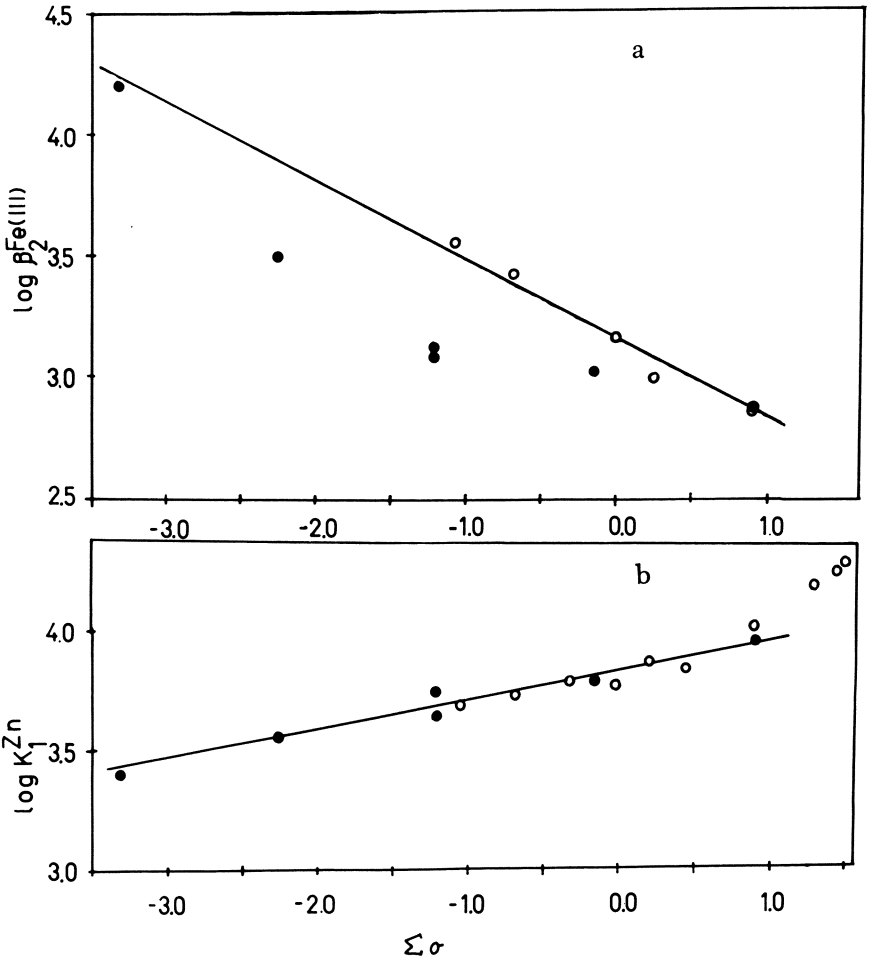

Figure 12. Plot of a: log β_2^{III} (Equation 4) for bis(N-MeIm) complex formation of (1-Cl)$_x$(p-NEt$_2$)$_y$TPP-FeCl (x + y = 4, x = 0 − 4) (●), and b: log β_1^{Zn} for mono-3-picoline complex formation of (p-Cl)$_x$(p-NEt$_2$)$_y$TPPZn (●) vs. the sum of the Hammett sigma constants (44). Data taken from Refs. 69 and 70, respectively. Open circles in a and b are published data [(27) and (34), respectively] for the same reactions of other symmetrically substituted TPPs.

electron-donating and three electron-withdrawing, one electron-withdrawing and three-electron donating, or two of each in the two possible geometries. Thus, the dependence of log β_2^{III} for unsymmetrical iron TPPs is neither on $\Sigma\sigma$ as found for $E_{1/2}$ or g-value anisotropy, nor on $\Delta\sigma$ as found for the NMR peak separations of the pyrrole protons (*69*); whereas the dependence of log K_1^{Zn} is on $\Sigma\sigma$ for symmetrical and unsymmetrical TPPs alike (*70*).

A Unified Approach to the Linear-Free-Energy Relationships Found in this Study: Electrochemistry, ESR, NMR, and Thermodynamics of Ligand Addition

LOW SPIN IRON PORPHYRINS—MODELS OF THE CYTOCHROMES b. The $E_{1/2}$ values and magnetic anisotropies for low spin iron porphyrins correlate with $\Sigma\sigma$, yet NMR peak separations of unsymmetrically substituted low spin TPPFe(III) derivatives correlate with $\Delta\sigma$, and the values of log β_2^{III} for *N*-methylimidazole addition to iron porphyrins do not correlate with either. As the explanation already given for the behavior of ring oxidation and reduction potentials of ZnTPPs suggests, the reason for these results must involve the symmetry of, and electron distribution in, the orbital(s) involved in each of these latter phenomena: the $d_{xz,yz}$ set on iron and the $3e(\pi)$ pair on the porphyrin. NMR spectroscopy probes the unpaired electron density distribution in the $3e(\pi)$ porphyrin orbitals; we find that on lowering the symmetry of the porphyrin ring, the degeneracy of this pair is split. The other three types of measurement probe most directly the iron center, and suggest that the porphyrin ring is sensitive to unsymmetrical substitution, but apparently iron is not. However, this conclusion may not be entirely true, because the symmetry of electron distribution imposed on the π system of the porphyrin by unsymmetrical *meso*-substitution does not match the symmetry of the d_{xz} or d_{yz} orbitals of iron, nor their linear combinations, with which the porphyrin π-system interacts. That is, adjacent rather than opposite porphyrin nitrogens have enhanced electron density (Figure 10); and thus, there is no differentiation in the energy of the d_{xz} and d_{yz} orbitals. Therefore, $E_{1/2}$ for the iron(III)/iron(II) couple and the magnetic anisotropy of low spin iron(III) complexes cannot distinguish between the symmetrical and unsymmetrical substitution pattern on the *meso*-phenyl rings, and log β_2^{III} detects only that unsymmetrically substituted complexes provide poorer interaction between the π-systems of the axial ligands, iron(III), and the porphyrin than do the symmetrically substituted complexes. Thus, we must conclude that unsymmetrical substitution at the *meso*-positions, although excellent for determining quantitatively the nature and orbital symmetry of unpaired electron delocalization onto the porphyrin ring, cannot, for symmetry reasons, allow us to probe the effect of unsymmetrical substitution on the energies of the iron d_{xz} and d_{yz} orbitals and thus, on $E_{1/2}$ and magnetic anisotropy. Conversely, unsymmetrical β-pyrrole substitution should allow us to probe the latter factors but produce much more complex and possibly uninterpretable NMR spectra, because in monopyrrole-substituted porphyrins, all seven remaining pyrrole-H are inequivalent, and in the "a, c" dipyrrole-substituted TPP derivatives of Giraudeau et al. (*71*), there are three types of pyrrole-H.

HIGH SPIN IRON PORPHYRINS—ADDITIONAL INFORMATION ON ORBITAL EFFECTS. In some ways, high spin iron porphyrins yielded the types of electrochemical results that one might naively expect to obtain from the low spin cytochrome b models. That is, the cathodic peak potentials for the iron(III)/iron(II) reduction of unsymmetrically substituted derivatives of TPPFeCl show deviations from the linear correlation obtained for the symmetrically substituted derivatives (Figure 5). Those containing one electron-withdrawing and three electron-donating substituents generally are easier to reduce, and those containing one electron-donating and three electron-withdrawing substituents generally are more difficult to reduce than the symmetrical molecules. To understand why this effect occurs without such deviations for the low spin cytochrome b models, one must recall that on reduction of the electronically symmetrical high spin (HS) iron(III) complexes to HS iron(II), the electron enters the d_{xy} orbital. Although none of the porphyrin π-orbitals has proper symmetry to overlap with d_{xy}, this orbital still may be modified by the σ inductive effect of unsymmetrically placed substituents. Figure 13a shows the electron density distribution and nodal properties of d_{xy} and the expected modification of the electron density distribution when one electron-donating (Figure 13b) or one electron-withdrawing (Figure 13c) *meso*-substituent is introduced into the molecule. The result in the former case (Figure 13b) is that three lobes of d_{xy} become smaller while one becomes larger. We hypothesize that this modification makes it more difficult for the entering electron to find its way, causing E_p^c to be more negative than expected for a symmetrical compound of the same electronic effect (as measured by $\Sigma\sigma$). Conversely, in the latter case (Figure 13c), three lobes of d_{xy} become larger while one becomes smaller, which, hypothetically, makes it easier for the entering electron to find its way, thus causing E_p^c to be less negative than expected for a symmetrical compound of the same $\Sigma\sigma$.

The fact that unsymmetrical substitution does affect E_p^c for the iron(III)/iron(II) reduction of high spin iron, in view of the nature of the orbital into which the electron enters (d_{xy}), lends credence to the suggestion just made that unsymmetrical pyrrole substitution will affect $E_{1/2}$ for the iron(III)/iron(II) redox couple of low spin iron porphyrins by removing the degeneracy of the d_{xz} and d_{yz} orbitals into which the unpaired electron enters.

Summary and Perspectives on the Relationship Between the Results of this Study and the Behavior of the Cytochromes b. The effect of unsymmetrical *meso*-substitution on the redox potentials of our low spin iron cytochrome b models and their high spin precursors may be explained in terms of the symmetry and electron density distribution of the porphyrin π-orbital(s), whose symmetry matches that of the

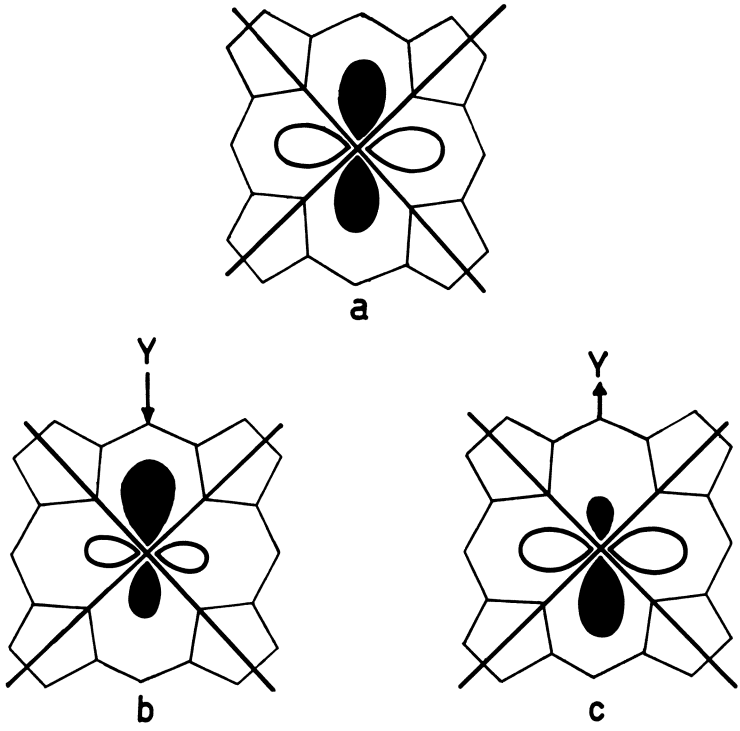

Figure 13. a, Electron density distribution in the d_{xy} *orbital of iron into which the electron goes on reduction of high spin Fe(III) to high spin Fe(II); b, the modified electron density distribution when Y is more electron donating than X; and c, when Y is more electron withdrawing than X.*

d-orbital(s) into which the electron goes on reduction of iron(III) to iron(II). For the low spin forms of iron(III) and iron(II), unsymmetrical *meso*-substitution does not remove the degeneracy of d_{xz} and d_{yz}; and thus, the redox potentials of the low spin complexes of unsymmetrical *meso*-substituted tetraphenylporphyrins are no different from those of their fourfold-symmetrical analogs of equal electronic effect ($\Sigma\sigma$). However, as a result of the understanding of orbital symmetry and electron density effects gained in this study, we predict that unsymmetrically pyrrole-substituted low spin iron porphyrins should show deviations from the linear correlation of $E_{1/2}$ for the iron(III)/iron(II) coupled with $\Sigma\sigma$ due to the nondegeneracy of d_{xz} and d_{yz}.

With regard to the possibility raised in the introduction (possibility 2) that the pressure of different hydrophobic groups against the hemes of the various cytochromes b changes the π-electron density distribution in the heme and thus changes the redox potential of the

iron(III)/iron(II) couple from one protein to another (Table I), we now conclude that hydrophobic groups located above or below *meso*-positions of the heme can have no effect on the redox potentials; rather, only those groups located above or below two opposite (but not two adjacent) pyrrole rings may affect, in principle, the redox potentials. Whether differences in such interactions actually exist for the cytochromes b of Table I remains for protein crystallographers to determine.

Acknowledgments

The financial support of NSF (CHE–79–18217), NIH RCDA (5 KO4 GM 00227), and R01 AM 31038 is gratefully acknowledged.

Literature Cited

1. Kamen, M. D.; Horio, T. *Ann. Rev. Biochem.* **1970,** *39,* 673.
2. Knaff, D. B. *Coord. Chem. Rev.* **1978,** *26,* 47.
3. Cramer, W. A.; Whitmarsh, J.; Horton, P. In "The Porphyrins"; Dolphin, D., Ed.; Academic: New York, 1979; Vol. 7, p. 71.
4. Mathews, F. S.; Czerwinski, E. W.; Argos, P. In "The Porphyrins"; Dolphin, D., Ed.; Academic: New York, 1979; Vol. 7, p. 108.
5. Mathews, F. S.; Argos, P.; Levine, M. *Cold Spring Harbor Symp. Quant. Biol.* **1971,** *36,* 387.
6. Mathews, F. S. *Biochim. Biophys. Acta* **1980,** *622,* 375.
7. Keller, R. M.; Wuthrich, K. *Biochim. Biophys. Acta* **1980,** *621,* 204.
8. Keller, R. M.; Groudinsky, O.; Wuthrich, K. *Biochim. Biophys. Acta* **1973,** *328,* 233.
9. Guiard, B.; Lederer, F. *Biochim. Biophys. Acta* **1978,** *536,* 88.
10. Kessler, D. L.; Rajagopalan, K. V. *J. Biol. Chem.* **1972,** *247,* 6566.
11. Guiard, B.; Lederer, F. *Eur. J. Biochem.* **1977,** *74,* 181.
12. Douglas, R. H.; Hultquist, D. E. *Proc. Natl. Acad. Sci. U.S.A.,* **1978,** *75,* 3118.
13. Guiard, B.; Lederer, F. *J. Mol. Biol.* **1979,** *135,* 639.
14. Urban, P. F.; Klingenberg, M. *Eur. J. Biochem.* **1969,** *9,* 519.
15. Kakuno, T.; Bartsch, R. G.; Nishikawa, K.; Horio, T. *J. Biochem (Tokyo)* **1971,** *70,* 79.
16. Labeyrie, F.; Groudinsky, O.; Jacquot-Armand, Y.; Naslin, L. *Biochim. Biophys. Acta* **1966,** *128,* 492.
17. Weber, H.; Weiss, W.; Staudinger, H. *Hoppe-Seyler's Z., Physiol. Chem.* **1971,** *352,* 109.
18. Abe, K.; Sugita, Y. *Eur. J. Biochem.* **1979,** *101,* 423.
19. Iyanagi, T. *Biochemistry* **1977,** *16,* 2725.
20. Böhme, H.; Cramer, W. A. *Biochim. Biophys. Acta* **1973,** *325,* 275.
21. Ohnishi, K. *J. Biochem. (Tokyo)* **1966,** *39,* 9.
22. Knaff, O. B. *Biochim. Biophys. Acta* **1973,** *325,* 284.
23. Horton, P.; Croze, E. *Biochim. Biophys. Acta* **1977,** *462,* 86.
24. Knaff, D. B.; Buchanan, B. B. *Biochim. Biophys. Acta* **1974,** *376,* 549.
25. Dutton, P. L.; Erecinska, M.; Sato, N.; Mukai, Y.; Pring, M.; Wilson, D. F. *Biochim. Biophys. Acta* **1972,** *267,* 15.
26. Berden, J. A.; Opperdoes, F. R. *Biochim. Biophys. Acta* **1972,** *267,* 7.
27. Walker, F. A.; Lo, M. W.; Ree, M. T. *J. Am. Chem. Soc.* **1976,** *98,* 5552.
28. LaMar, G. N.; Viscio, D. B.; Smith, K. M.; Caughey, W. S.; Smith, M. L. *J. Am. Chem. Soc.* **1978,** *100,* 8085.

29. LaMar, G. N.; Budd, D. L.; Viscio, D. B.; Smith, K. M.; Langry, K. C. *Proc. Natl. Acad. Sci. U.S.A* **1978,** *75,* 5755.
30. Shulman, R. G.; Glarum, S. H.; Karplus, M. *J. Mol. Biol.* **1971,** *57,* 93.
31. LaMar, G. N.; Walker, F. A., In "The Porphyrins"; Dolphin, D., Ed.; Academic: New York, 1979; Vol. 4, p. 61.
32. Meyer, E. F.; Cullen, D. L. In "The Porphyrins"; Dolphin, D., Ed.; Academic: New York, 1979; Vol. 3, p. 513.
33. Eaton, S. S.; Eaton, G. R. *J. Am. Chem. Soc.* **1977,** *99,* 6594.
34. Vogel, G. C.; Beckmann, B. A. *Inorg. Chem.* **1976,** *15,* 483.
35. Walker, F. A.; Hui, E.; Walker, J. M. *J. Am. Chem. Soc.* **1975,** *97,* 2390.
36. Walker, F. A.; Beroiz, D.; Kadish, K. M. *J. Am. Chem. Soc.* **1976,** *98,* 3484.
37. Kadish, K. M.; Morrison, M. M. *Bioinorg. Chem.* **1977,** *7,* 107.
38. Kadish, K. M.; Bottomley, L. A. *J. Am. Chem. Soc.* **1977,** *99,* 2380.
39. Kadish, K. M.; Bottomley, L. A.; Beroiz, D. *Inorg. Chem.* **1978,** *17,* 1124.
40. Rillema, D. P.; Nagle, J. K.; Barringer, L. F.; Meyer, T. J. *J. Am. Chem. Soc.* **1981,** *103,* 56.
41. Walker, F. A.; Balke, V. L.; McDermott, G. A. *Inorg. Chem.,* in press.
42. Meot-Ner, M.; Adler, A. D. *J. Am. Chem. Soc.* **1975,** *97,* 5107.
43. Walker, F. A.; Balke, V. L.; McDermott, G. A. *J. Am. Chem. Soc.* **1982,** *104* 1569.
44. Leffler, J. E.; Grunwald, E. "Rates and Equilibria of Organic Reactions"; Wiley: New York, 1963; p. 173.
45. Walker, F. A.; Reis, D.; Balke, V. L., unpublished data.
46. Adler, A. D.; Longo, F. R.; Finarelli, J. D.; Goldmacher, J.; Assour, J.; Korsakoff, L. *J. Org. Chem.* **1967,** *32,* 476.
47. Adler, A. D.; Longo, F. R.; Kampas, F.; Kim, J. *J. Inorg. Nucl. Chem.* **1970,** *32,* 2443.
48. Bottomley, L. A.; Kadish, K. M. *Inorg. Chem.* **1981,** *20,* 1348.
49. Dr. L. A. Bottomley has found (personal communication) that in noncoordinating solvents the Fe(III)/Fe(II) redox reaction is very sensitive to the concentration of dissolved oxygen and that scrupulous deoxygenation of the solvent is required before it is possible to observe an anodic peak.
50. Kadish, K. M.; Thompson, L. K.; Beroiz, D.; Bottomley, L. A. In "Electrochemical Studies of Biological Systems"; Sawyer, D. T., Ed.; ACS SYMPOSIUM SERIES No. 38, ACS: Washington, D.C., 1977; p. 51.
51. Kadish, K. M.; Kelly, S. *Inorg. Chem.* **1979,** *18,* 2968.
52. Collman, J. P.; Gagne, R. R.; Reed, C. A.; Halbert, T. R.; Lang, G.; Robinson, W. T. *J. Am. Chem. Soc.* **1975,** *97,* 1427.
53. Burdige, D.; Sweigart, D. A. *Inorg. Chim. Acta* **1979,** *28,* L131.
54. Fiske, W. W.; Sweigart, D. A., *Inorg. Chim. Acta* **1979,** *36,* L429.
55. "Handbook of Chemistry and Physics," 50th ed., Chemical Rubber Co.: Cleveland, OH, 1969.
56. Reichardt, C. *Angew. Chem.* **1965,** *4,* 29.
57. LaMar, G. N.; Walker, F. A., *J. Am. Chem. Soc.* **1973,** *95,* 1782.
58. Nicholson, R. S.; Shain, I. *Anal. Chem.* **1964,** *36,* 706.
59. Walker, F. A. *J. Am. Chem. Soc.* **1980,** *102,* 3254.
60. Goff, H.; Shimomura, E. *J. Am. Chem. Soc.* **1980,** *102,* 31.
61. Goff, H.; LaMar, G. N.; Reed, C. A. *J. Am. Chem. Soc.* **1977,** *99,* 3641.
62. Goff, H.; LaMar, G. N. *J. Am. Chem. Soc.* **1977,** *99,* 6599.
63. Kadish, K. M.; Morrison, M. M.; Constant, L. A.; Dickens, L.; Davis, D. G. *J. Am. Chem. Soc.* **1976,** *98,* 8387.
64. Felton, R. H., In "The Porphyrins"; Dolphin, D., Ed.; Academic: New York, 1979; Vol. 5, pp. 53–125.
65. Longuet-Higgins, H. C.; Pople, J. *Proc. Phys. Soc., London, Sect. A* **1955,** *68,* 591.
66. Longuet-Higgins, H. C.; Rector, C. W.; Platt, J. R. *J. Chem. Phys.* **1950,** *18,* 1174.
67. Maslou, V. G. *Opt. Spectrosc.* **1976,** *40,* 275.

68. Fajer, J.; Borg, D. C.; Forman, A.; Dolphin, D.; Felton, R. H. *J. Am. Chem. Soc.* **1970**, *92*, 3451.
69. Balke, V. L.; Walker, F. A., unpublished data.
70. McDermott, G. A.; Walker, F. A., unpublished data.
71. Giraudeau, A.; Callot, H. J.; Jordan, J.; Ezhar, I.; Gross, M. M. *J. Am. Chem. Soc.* **1979**, *101*, 3857.

RECEIVED for review June 2, 1981. ACCEPTED January 4, 1982.

Electrochemistry of Aliphatic Thioethers as Models for Biological Electron Transfer

BRIAN R. COLEMAN, RICHARD S. GLASS, WILLIAM N. SETZER, USHA DEVI G. PRABHU, and GEORGE S. WILSON[1]

University of Arizona, Department of Chemistry, Tucson, AZ 85721

The electrochemical oxidation of a series of aliphatic thioethers was examined in aprotic medium (acetonitrile). The resulting electron transfer process, typically involving two electrons, is significantly facilitated by suitably disposed electron-rich neighboring groups. These moieties aid in stabilizing the positive charge created on the sulfur as a result of electron loss. The nature of this interaction was examined by x-ray studies of selected parent compounds and stable cyclic intermediates, and through models where intramolecular interactions are geometrically precluded. Good correlation was observed between voltammetric peak potentials and ionization potentials determined by UV photoelectron spectroscopy for systems where neighboring-group participation is possible. On the other hand, noninteracting systems show no apparent correlation. The importance of molecular conformation is discussed in light of biological examples.

The redox chemistry of aliphatic sulfides, as exemplified by the side chain of methionine, is poorly understood, in contrast to biological redox reactions involving thiols and disulfides. *S*-Adenosylmethionine is a key biological methylating agent and methionine is involved in the production of coenzyme A derivatives (*1*). This essential amino acid also serves as an axial iron ligand in the heme moiety of a number of

[1] Author to whom correspondence should be addressed.

0065-2393/82/0201-0417$07.25/0

c-type cytochromes, and in the active site of several blue copper proteins. The role of methionine in defining the redox potential of cytochrome c was considered in detail elsewhere (*2*).

The purpose of the present work is to consider the chemical and biochemical evidence in support of the direct involvement of electron-deficient sulfides, typically radical cations and dications, in biological electron transfer. Because these intermediates are generally unstable, it is necessary to employ transient techniques, particularly electrochemical and spectroscopic, to evaluate their properties.

Chemistry of Electron-Deficient Sulfur

Some important reactions involving electron-deficient sulfides are summarized in Table I. Indeed, aliphatic sulfur cation radicals are so reactive that the "simple" cation radical (*A*) can be observed directly in only one situation: where the presence of bulky groups such as in di-*tert*-butyl sulfide (*7*) hinders further sulfur reactions, and thus loss of an α-proton is not possible. Typically, the formation of a paramagnetic dimer is strongly favored as indicated in Reaction 7, and this species was often confused with the cation radical itself (*4*). In general, sulfur-centered cation radicals will have limited stability unless the positive charge on the sulfur can be delocalized by interaction with an electron-rich moiety.

We previously suggested (*16*) that the ordinarily difficult oxidation of aliphatic sulfides may be facilitated by interaction of the resulting electron-deficient sulfur with suitably disposed neighboring groups. This situation is shown in Reaction 2 in which X may be a nucleophile such as an amino, amido, carboxylate, or hydroxyl group. X also could be the π-electron system of an aromatic amino acid side chain, a flavin, or a porphyrin ring. Interactions of the former type were shown to have significant influence on the course of sulfur oxidation (*8*) and will be discussed in this chapter. A special case of neighboring-group participation is given in Reactions 3 and 4, and is typified by the mesocyclic dithioethers in Table II.

Although stable aromatic sulfur cation radicals are well-known (*25*), the observation of a cation radical of **5** by Musker (*11*) was somewhat unexpected. Subsequent observations of a cation radical of **6** and isolable dications for **5–7** as well as the detection of a number of acyclic dithioethers also were surprising. This work was recently reviewed (*13*). The remarkable stability of these electron-deficient sulfides was attributed to a transannular interaction between the two sulfurs resulting in the formation of a sulfuranyl radical with a two-center, three-electron bond (Reaction 3). Bonding schemes in such species were extensively considered (*12*). The spectroscopic and kinetic properties of these cation radicals were studied by pulse radiolysis

Published on June 1, 1982 on http://pubs.acs.org | doi: 10.1021/ba-1982-0201.ch018

Table I. Reactions of Electron-Deficient Aliphatic Sulfides

Cation Radical Formation	*Reference*	*Reaction*
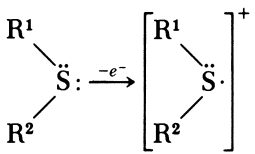 **A**	3–7	1
Intramolecular Interactions (Neighboring-Group Participation)		
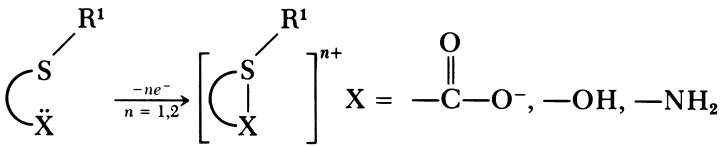	8	2
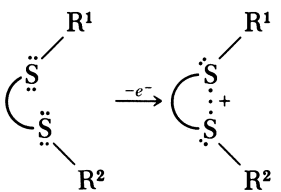 **B**	9–13	3

Continued on next page.

Published on June 1, 1982 on http://pubs.acs.org | doi: 10.1021/ba-1982-0201.ch018

Table I. (*Continued*)

Intramolecular Interactions (Continued)	*Reference*	*Reaction*
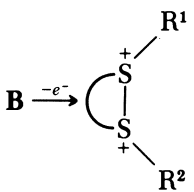 **C**	9, 10, 13, 14	4
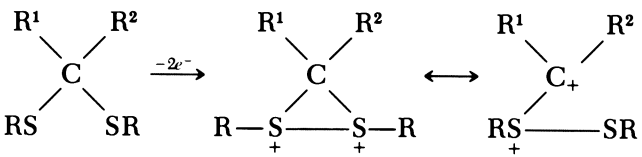 **D**	15	5
D + 2 Nu^- → RSSR + $R^1 R^2 CNu_2$	15	6
Dimer–Adduct Formation		
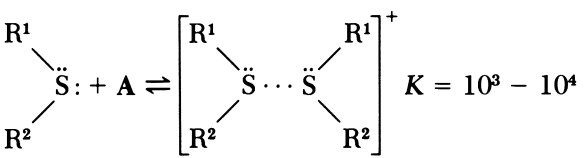 **E**	3–6	7

Published on June 1, 1982 on http://pubs.acs.org | doi: 10.1021/ba-1982-0201.ch018

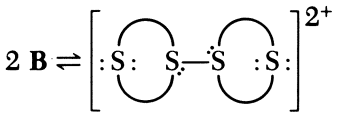

F

$K \approx 10^3$ | 9, 10, 14 | 8

Reaction with Nucleophiles

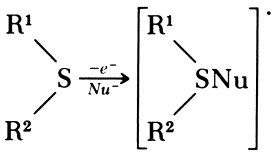

16 | 9

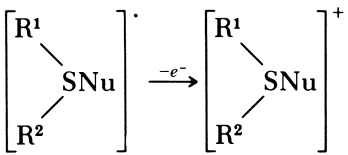

16 | 10

α-Proton Elimination

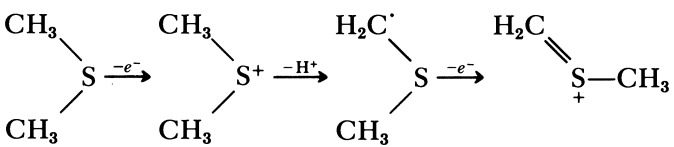

4, 17, 18 | 11

Continued on next page.

Published on June 1, 1982 on http://pubs.acs.org | doi: 10.1021/ba-1982-0201.ch018

Table I. (*Continued*)

Reactions with Medium	*Reference*	*Reaction*
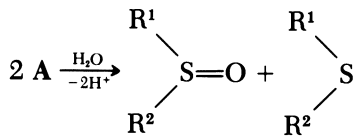	15, 19	12
Fragmentation		
	20	13
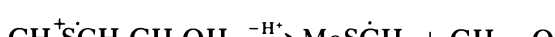		
Electron Transfer		
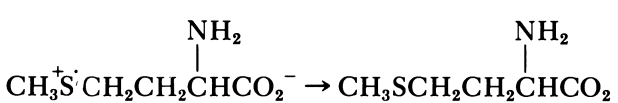	18	14
Specific Reactions of Methionine		
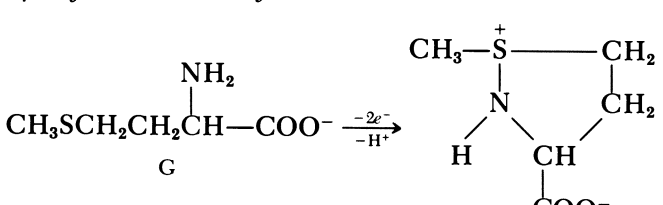	21–23	15

Published on June 1, 1982 on http://pubs.acs.org | doi: 10.1021/ba-1982-0201.ch018

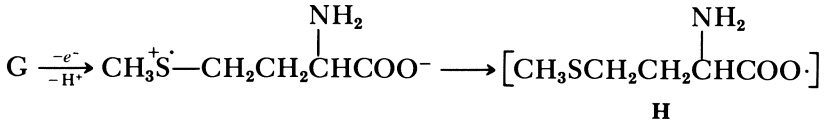

18 16

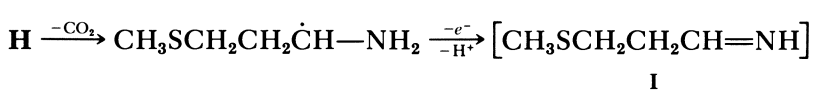

18, 20 17

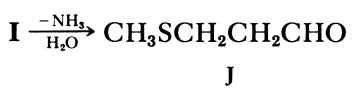

20 18

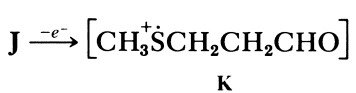

20 19

20 20

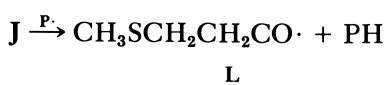

24 21

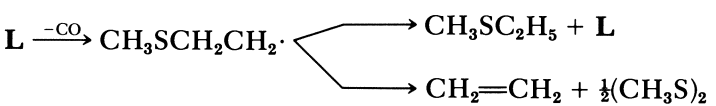

24 22

Published on June 1, 1982 on http://pubs.acs.org | doi: 10.1021/ba-1982-0201.ch018

Table II. Electrochemical and Spectroscopic Properties of Some Aliphatic Thioethers

Compound Number and Name	*Structure*	E_p[a]	*Peak*[b] *Max*	*IP*[c]
1 1,3-Dithiacyclohexane	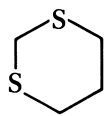	1.14	20080	8.55[s] 8.97
2 1,4-Dithiacyclohexane	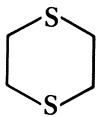	1.25	20410	8.56[s] 9.03
3 1,4-Dithiacycloheptane (DTCH)	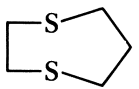	0.84	20410	8.68
4 1,4-Dithiacyclooctane (unDTCO)	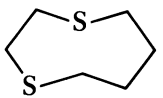	0.81	19380	8.55
5 1,5-Dithiacyclooctane (DTCO)	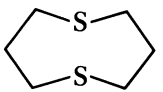	0.343	19160	8.30[s] 8.72
6 1,5-Dithiacyclononane (DTCN)	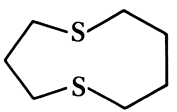	0.424	19080	8.36

Published on June 1, 1982 on http://pubs.acs.org | doi: 10.1021/ba-1982-0201.ch018

7	1,6-Dithiacyclodecane (DTCD)	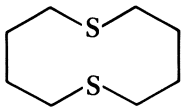	0.424	18940	8.38
8	7,8-Benzo-1,5-dithiacyclononane	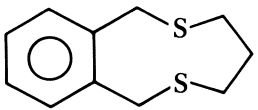	0.48	19760	8.36
9	Thiacyclopentane		1.13	19380	8.44
10	Thiacyclohexane	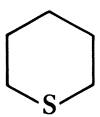	1.32	19490	8.44
11	Thiacyclooctane	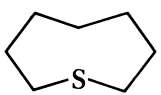	1.15	19050	8.36
12	9-Thiabicyclo[3.3.1]nonane	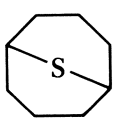	1.17	18080	8.16
13	2,5-Dithiahexane	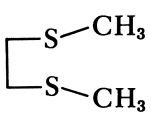	0.97	20580	8.62[a] 8.87

Continued on next page.

Published on June 1, 1982 on http://pubs.acs.org | doi: 10.1021/ba-1982-0201.ch018

Table II. (*Continued*)

Compound Number and Name	*Structure*	E_p[a]	*Peak*[b] *Max*	*IP*[c]
14 2,6-Dithiaheptane	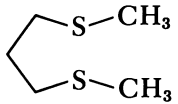	0.66	19880	8.50[s] 8.77
15 2,7-Dithiaoctane	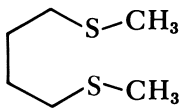	0.67	19920	8.48
16 Di-*tert*-butyl sulfide	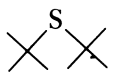	1.06	17990	8.20
17 6-*endo*-Methylthiobicyclo[2·2·1]heptane-2-*endo*-carboxylic acid	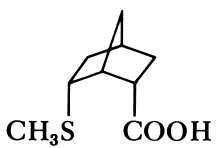	1.20 0.65[d]	19610	8.37
18 6-*endo*-Methylthiobicyclo[2·2·1]heptane-2-*exo*-carboxylic acid	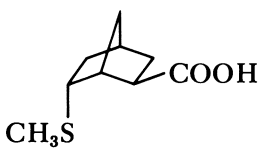	1.28	19800	8.55

Published on June 1, 1982 on http://pubs.acs.org | doi: 10.1021/ba-1982-0201.ch018

19	6-*endo*-Isopropylthiobicyclo[2·2·1]heptane-2-*endo*-carboxylic acid	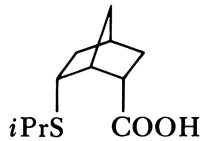	1.30 0.65[d]	18320	8.22
20	6-*endo*-Methylthiobicyclo[2·2·1]heptane-2-*endo*-methanol	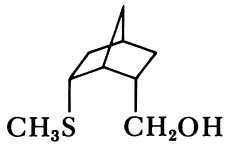	0.56	19190	8.23
21	6-*endo*-Methylthiobicyclo[2·2·1]heptane-2-*exo*-methanol	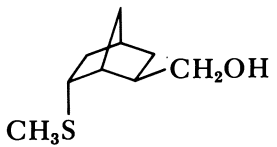	1.20	19230	8.34
22	Methyl 6-*endo*-methylthiobicyclo[2·2·1]heptane-2-*endo*-carboxylate	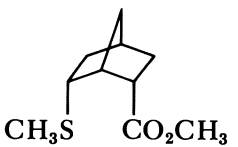	1.21	19880	8.29
23	Methyl 6-*endo*-methylthiobicyclo[2·2·1]heptane-2-*exo*-carboxylate	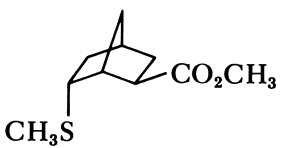	1.29	19760	8.40

Continued on next page.

Published on June 1, 1982 on http://pubs.acs.org | doi: 10.1021/ba-1982-0201.ch018

Table II. (*Continued*)

Compound Number and Name	*Structure*	E_p[a]	*Peak*[b] *Max*	*IP*[c]
24 *O*-Ethyl *N*-[6-*endo*-methylthio-2-*endo*-bicyclo[2·2·1]-heptyl]carbamate		0.98	NR[f]	8.50
25 *O*-Ethyl *N*-[6-*endo*-methylthio-2-*exo*-bicyclo[2·2·1]-heptyl]carbamate		1.20	19840[e]	8.29
26 2-*endo*-Methylthiomethylene, 6-*endo*-methylthiobicyclo-[2·2·1]heptane	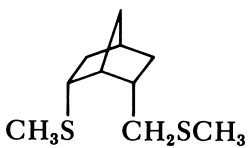	0.63	19230	8.35
27 2-*exo*-Methylthiomethylene, 6-*endo*-methylthiobicyclo-[2·2·1]heptane	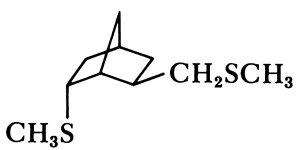	1.21 1.36	19460	8.36

Published on June 1, 1982 on http://pubs.acs.org | doi: 10.1021/ba-1982-0201.ch018

28	*S*-Methyl 6-*endo*-methylthiobicyclo[2·2·1]heptane-2-*endo*-thiocarboxylate	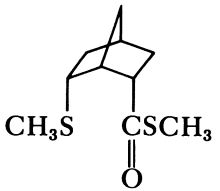	1.12	19460	8.20
29	5-Methyl 6-*endo*-methylthiobicyclo[2·2·1]heptane-2-*exo*-thiocarboxylate	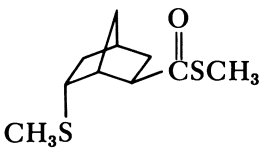	1.42	19840	8.36
30	2-*endo*, 6-*endo*-Bis(methylthio)3-*exo*, 5-*exo*-dichloro-[2·2·1]heptane	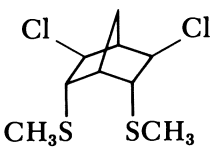	0.75	20490	8.40[s] 8.68

[a] Peak potential at Pt electrode, in acetonitrile, 0.1 *M* $AgNO_3$/Ag electrode, 0.1-V/s scan rate.
[b] TCNE charge transfer complex (cm^{-1}).
[c] Photoelectron spectroscopy S_{3P} (eV).
[d] Base added.
[e] Multiple peaks, lowest energy shown.
[f] Not resolved.
[s] Peak split.

and recently reviewed (*26*). The visible absorption is possibly due to a $\sigma \rightarrow \sigma^*$ transition. The energy for this transition depends upon the degree of p-orbital overlap between the two interacting sulfur atoms. Furthermore, both chemical and electrochemical evidence suggests the existence of a diamagnetic dimer (Reaction 8).

In the absence of stabilizing groups, reactions that may occur include α-proton elimination (Reaction 11), bond cleavage (Reactions 5 and 6), or reaction with the solvent medium (Reaction 12). Reaction of sulfur cation radicals and dications (9, 10) was used to effect phosphorylation of ADP in the presence of orthophosphate (*16*).

The oxidation of methionine and methionine derivatives was also examined. Chemical and electrochemical oxidation result in a stable product: dehydromethionine (Reaction 15). The structure of this compound was confirmed by x-ray crystallography (*23*). Under conditions where radicals are generated, for example, pulse radiolysis or photolysis, reactions are suggested to lead to deamination and decarboxylation (Reactions 17 and 18). Paramagnetic dimers (**E** in Reaction 7) are also apparently involved.

Suitable models for thioether redox reactions in biological systems must take into account the bioenergetics of sulfur oxidation, the products that should form, and the environment in which methionine and other thioethers are likely to be found.

Redox Biochemistry of Thioethers

An important biological redox reaction of thioethers involves formation of the sulfoxide by sulfide oxidation. The resulting product is then significantly more soluble in water and this process, carried out by cytochrome P-450 monooxygenases, is essential to drug metabolism and pesticide detoxification by mammals (*27*, *28*). Recently (*29*) it was shown that the logarithm of the maximum rate of sulfoxidations (log V_{max}) of a series of thioanisole derivatives (ArSMe) by a reconstituted cytochrome P-450 complex isolated from rabbit hepatic microsomes correlates well with peak potentials determined by cyclic voltammetry in acetonitrile and also with Hammett σ^+ values. The formation of the corresponding sulfur cation radicals was suggested as the rate-determining step. Sulfur cation radicals were also suggested in the biosynthesis of ethylene. Ethylene plays an important role in the fruit-ripening process in plants. Although the exact mechanism for the conversion of methionine into ethylene is the subject of debate (*24*), several reaction paths have been suggested as shown in Table I (Reactions 16-22).

Hoffmann et al. (*30*) suggested that the enzymatically active paramagnetic intermediate in the reaction of yeast cytochrome c peroxidase with hydrogen peroxide contains an iron(IV) heme ($S = 1$)

and a methionyl sulfur-based free radical ($S = \frac{1}{2}$), the latter exhibiting unusual stability. A sulfur-centered radical intermediate was postulated, based on EPR and ENDOR measurements, analogous to model compounds such as **E**, $(R_2SSR_2)^{+\cdot}$ (*26*), or the nitrogen analog $(R_2SNR_3)^{+\cdot}$ (*31*). Studies of the x-ray photoelectron spectroscopy of cytochrome c (*32*) suggest partial positive charge on the Met-80 sulfur, although no formal involvement of this sulfur in the redox reactions is known.

The interaction of sulfur atoms with aromatic systems in biomolecules is suggested by a study (*33*) of the crystal structures of eight small globular proteins. The side chains of sulfur-containing amino acids (cysteine and methionine) were close to, and alternate with, the side chains of aromatic amino acids such as histidine, phenylalanine, tryptophan, and tyrosine. Interaction with the π-electron systems of flavins and porphyrins was also suggested. Because many molecules in which such interactions are found are involved in redox reactions, the $s-\pi$ chains were suggested as conduits for electrons. Neighboring groups other than aromatic moieties, such as hydroxyl, carboxyl, amino, amido, guanidino, or sulfur-containing moieties, are other possibilities.

Intramolecular interactions of model compounds, like their biological counterparts, often proceed at elevated rates (*34*). This unusual behavior cannot be attributed merely to high local concentrations. Considerable loss of translational entropy occurs in the transition state and, if the reacting atoms are held in proper orientation, an additional entropic advantage is gained as well. Thus, the suitable disposition of neighboring groups may have the dual advantage of rendering the oxidation more facile while also limiting side reactions. This disposition is particularly important in situations where the thioether may be playing a catalytic role. Therefore, details of the energetics of sulfur electron loss and the characteristics of oxidation intermediates are of interest here.

Aliphatic Thioether Electrochemistry

The oxidation of aliphatic thioethers in aprotic medium (acetonitrile) generally leads to the formation of sulfonium ions, sulfoxides, and various condensed species (*17*, *25*). The first step is usually a two-electron irreversible process occurring at a potential greater than 1.0 V vs. a Ag/Ag^+ (0.1 *M*) reference electrode (approximately 1.3 V vs. SCE). Several presumed reaction paths are given in Table I (Reactions 5, 11, and 12). Sulfur-based cation radicals were formed during oxidation of some aryl sulfides (*35–38*).

To test the hypothesis that neighboring-group participation might facilitate sulfur oxidation, norbornane derivatives of Series A and B were prepared (*8*):

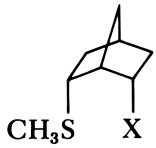

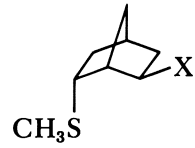

Series A		*Series B*	
17	X = COOH	**18**	X = COOH
17′	X = COO^-	**18′**	X = COO^-
20	X = CH_2OH	**21**	X = CH_2OH
22	X = CO_2CH_3	**23**	X = CO_2CH_3
24	X = $NHCO_2Et$	**25**	X = $NHCO_2Et$
26	X = CH_2SCH_3	**27**	X = CH_2SCH_3
28	X = $COSCH_3$	**29**	X = $COSCH_3$
30	X = SCH_3 (3-*exo*,5-*exo*-dichloro)		

The electrochemical oxidation of Series A and B compounds was studied by cyclic voltammetry in acetonitrile with platinum as the indicating electrode and a Ag/0.1 *M* Ag^+ reference electrode. In Series A the geometry of the norbornane ring results in the *endo*-substituents being well-positioned for neighboring-group participation. The crystal and molecular structures of some of these derivatives were determined by x-ray diffraction (*39, 40*) and the distance between the neighboring group and the sulfur was frequently less than the sum of the van der Waals radii. For **17**, the interaction causes a contra-twist of the norbornane skeleton. Series B, with *exo*-substituents, illustrates the effect of groups that are positioned so that intramolecular interactions are not possible.

Compounds **17** and **18** initially give comparable peak potentials (E_p) corresponding to an irreversible two-electron oxidation, but when the free acids are converted to the corresponding carboxylates (**17′**, **18′**), the *endo*-derivative exhibits a shift of over 600 mV, resulting in a more facile oxidation. By contrast, E_p for **18** and **18′** are the same (*8*). In addition to **17′**, three compounds within the norbornane series exhibit large negative potential shifts: **20, 26** and **30,** undoubtedly related to neighboring-group interaction. The existence of a cyclic intermediate during the electrochemical oxidation of **17′** and **20** was established (*8*). The anodic oxidation of **17′** (Scheme I) leads to the formation of an intermediate acyloxysulfonium salt that can react with water to yield two diastereomeric acid sulfoxides (*41*). Because the yield of the sulfoxide products obtained by controlled potential electrolysis is greater than 90%, the possibility of significant side reactions, such as the Pummerer rearrangement (*42*) or a Kolbe-type oxidative decarboxylation (*43*), can be specifically ruled out. If the electrochemical oxidation

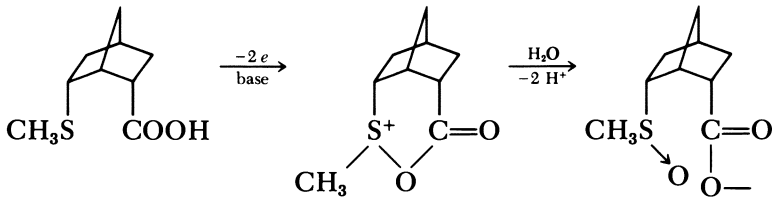

Scheme I

is carried out in the presence of $H_2{}^{18}O$, significant incorporation of ^{18}O into both the carboxylate and sulfoxide moieties is observed. Incorporation of labeled oxygen at the sulfur center is more extensive (60 : 40), as expected. Electrochemical oxidation, moreover, shows some stereoselectivity (70 : 30 ratio of the diastereomers). Chemical oxidation of **20** yields a reasonably stable alkoxysulfonium salt whose x-ray structure was determined (*44*). The x-ray structure of **17** supports the notion of strong interaction of the neighboring group with the sulfur even before the initiation of the electron transfer process.

The electrochemistry of the mesocyclic dithioethers (**3, 5–7**) was examined in detail. For **5,** reversible electron transfer was observed at potentials more than 0.8 V lower than that corresponding to its monothioether analog (**11**). This observation strongly supports the influence of the transannular interaction previously noted. Detailed analysis of the current–voltage curves (*9, 10*) reveals two closely spaced, one-electron transfer steps in which the second electron transfer is about 20 mV easier than the first. An explanation for this somewhat surprising behavior becomes apparent on consideration of the electronic structure of the cation radical. Asmus et al. (*19*) suggested that the odd electron is in an antibonding orbital (σ^*). Removal of this electron on formation of the dication is an energetically favorable situation in spite of the increase in charge that results because of the increase in bonding between the two sulfur atoms. A dimer is also formed in a reversible process (*see* Reaction 8). Under the conditions of these experiments, no contribution from the paramagnetic dimer (Reaction 7) was observed (*10*).

Correlation of Electrochemical and Spectroscopic Data

The correlation of electrochemical data (ease of electron loss or gain) with orbital energy levels, HOMO and LUMO, respectively, has long been of interest. Most studies involved reversible electron transfer of homologous series (typically aromatic hydrocarbons) where solvation energies can be assumed to be essentially constant (*45, 46*). We have examined more than 40 aliphatic thioethers at a platinum elec-

trode in acetonitrile and, in general, they exhibit irreversible two-electron oxidation. Although correlations of Hammett σ values and half-wave potentials of irreversible processes are well-known (*47*), correlations of spectroscopic data are uncommon (*48*). This situation is due to the fact that irreversible electron transfer generally obscures the desired thermodynamic information (*49*).

Nevertheless, the possibility of electrochemical generation and characterization of reactive intermediates remains attractive, and significant progress was made in correlating quantum mechanical, kinetic (*50*), and spectroscopic results (*51*, *52*).

Vertical ionization potentials obtained from UV photoelectron spectroscopic (pes) measurements are characteristic of electron loss on a time scale that does not permit molecular rearrangement (*53*). For molecules having localized and nonbonding electrons, molecular rearrangement is minimal so that the vertical and adiabatic ionization potentials are usually quite comparable. Thus, the sulfur lone pair orbitals will correspond to the highest occupied molecular orbitals (HOMO). By contrast, the electrochemical process not only permits molecular rearrangements but may also include solvation effects.

Table II gives the vertical ionization potentials (IP_{pes}) for a series of aliphatic sulfur compounds along with peak potentials (E_p) obtained under uniform conditions. These results are plotted in Figures 1A and 1B. The plot for the mesocyclic and acyclic thioethers exhibits a larger intercept than that for the norbornane derivatives, undoubtedly due to the well-known inductive effect of alkyl substitution (*54–58*), which results in a lowering of the ionization potential. In this case the norbornane derivatives are more highly substituted, resulting in an average lowering of the ionization potential by 0.16 eV. This result is in reasonable agreement with the observed shift from thiacyclohexane (8.45 eV) to diisopropyl sulfide (8.26 eV) (*55*) of 0.19 eV.

Some compounds do not fall on the line. All such compounds having peak potentials in the region of 1.0–1.4 V vs. Ag/0.1 *M* Ag^+ reference electrode (1.3–1.7 V vs. SCE) are identified with an "isolated" aliphatic sulfur in a molecule where neighboring-group participation is not possible nor likely. Although the ionization potentials vary over 0.4 eV, the E_p values fall within a very narrow range. There is no obvious correlation of E_p and *IP* for this group.

For electrochemically irreversible systems, the E_p of the resulting cyclic voltammetric curve is given by

$$E_p = f(E^{\circ\prime}, k_s, \alpha, n, D, k_1, \nu)$$

where $E^{\circ\prime}$ is the formal potential (related to the reference electrode), k_s the heterogeneous electron transfer rate constant, α is the electron

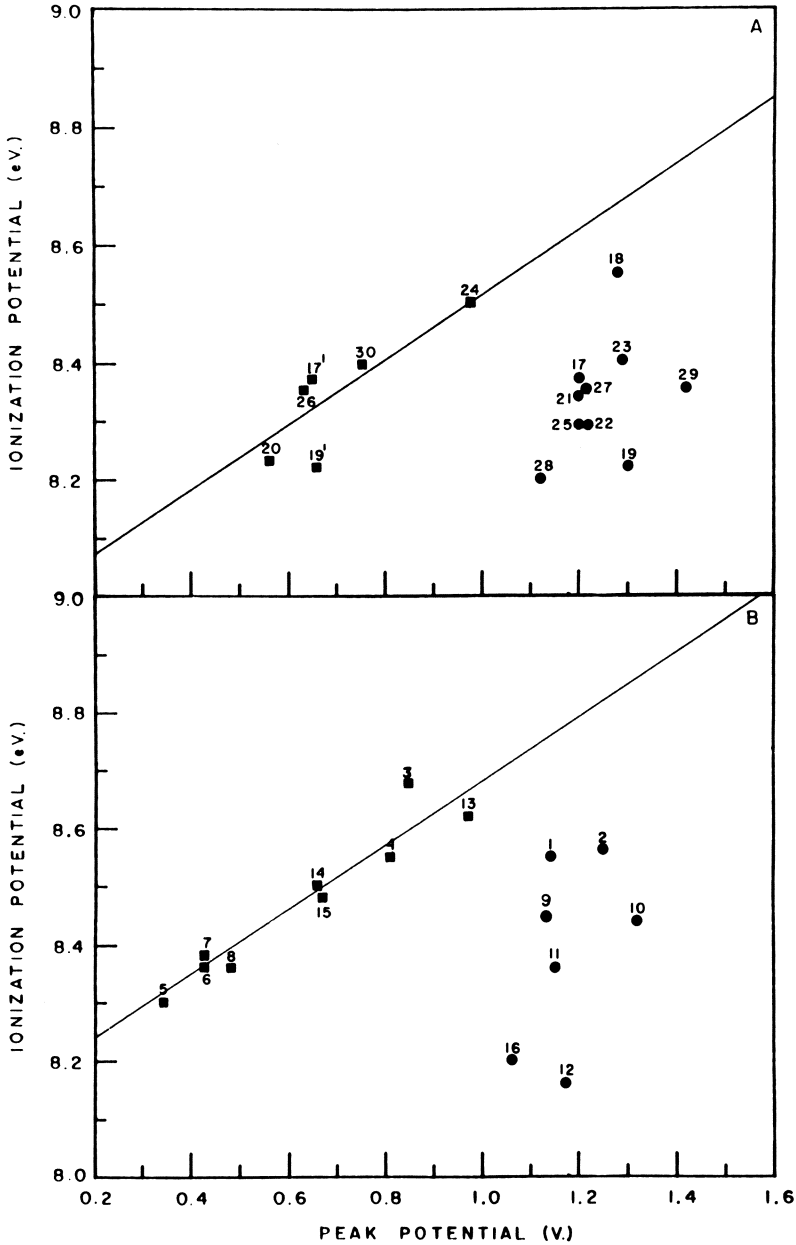

Figure 1. Correlation of peak potential (E_p) *from cyclic voltammetry with vertical ionization potentials from photoelectron spectroscopy. Key: A, norbornane derivatives; B, mesocyclic and acyclic thioethers;* ■, *neighboring group present; and* ●, *neighboring group not present.*

transfer coefficient, n is the number of electrons, D is the diffusion coefficient, k_1 is the rate constant for an irreversible chemical reaction following electron transfer, and ν is the rate of potential scan. The rate-determining step may be controlled by diffusion, heterogeneous electron transfer, the following chemical reaction, or a mixed process (59). The correlation of Figure 1B is particularly remarkable because the interacting systems include cases ranging from quasi-reversible (10^{-2} cm/sec) (*10*) to irreversible electron transfer. Possibly the neighboring group can effectively solvate the sulfur before electron transfer, minimizing the necessity for solvent reorganization during the electron transfer step, thus leading to outer sphere electron transfer. By contrast, extensive reorganization would be required in the noninteracting or isolated systems, resulting in slow electron transfer. The peak potentials for this latter group are essentially independent of the type of electrode employed (platinum, glassy carbon, gold), suggesting that the problem is intrinsic to the electron transfer itself. This question is presently under more detailed investigation.

Good correlation was shown (52) between photoelectron spectroscopically determined ionization potentials and E_p for the irreversible oxidation of a series of homoleptic alkyl metals. Electron transfer was the rate-determining step and E_p was related to the activation free energy for outer sphere electron transfer. These conditions may also be true for the interacting systems even though the overall process is not always irreversible. In contrast to the work in Reference 52, where alkyl substituents have a rather strong influence on the ionization potential, we observed a change of only 0.5 eV as the substituents were varied from methyl to *tert*-butyl. This result is consistent with the fact that the HOMO for the sulfur compounds is a nonbonding orbital and therefore is less sensitive to C–S bond perturbation.

The electron donor properties of organosulfur atoms were the subject of numerous studies (*60–64*). The ionization potential may be calculated for weak charge transfer complexes by spectroscopic measurement of the charge transfer transition according to the second-order perturbation treatment of Mulliken:

$$h\nu_{CT} = IP_D - E_A - \frac{e^2}{R_{DA}} + P \qquad (1)$$

where IP_D corresponds to the ionization potential of the donor (a thioether in this case), E_A is the electron affinity of the acceptor (tetracyanoethylene [TCNE]), R_{DA}, in the coulombic term, corresponds to the mean separation of the donor and acceptor, and P is a second-order perturbation term taking resonance interactions into account (*65, 66*). For simple systems the last three terms of Equation 1 are assumed to remain constant giving the relationship

$$h\nu_{CT} = mIP_D + \text{constant} \quad (2)$$

where $m = 1$. Table II and Figure 2 show the results of these measurements. If the wavelength maximum for the charge transfer complex ($h\nu_{CT}$) is expressed in electron volts, then the slope calculated from Equation 2 would be 0.84. Some significant deviations from the line are generally *endo*-norbornane derivatives in which R_{DA} probably has increased due to steric hindrance. The wavelength maximum for the charge transfer complex appears to be solvent independent because measurements in chloroform give values similar to those in methylene chloride.

Conformational Analysis of Thioethers

The close proximity of neighboring groups of several compounds in Table II was well-established by single crystal x-ray crystallog-

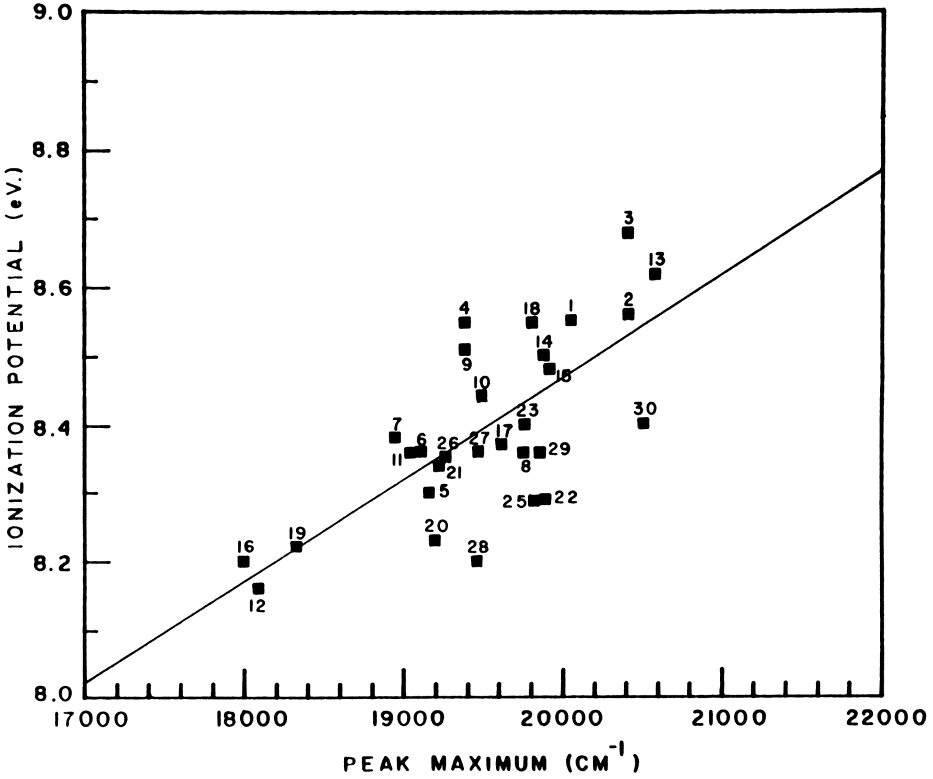

Figure 2. Correlation of vertical ionization potentials with ionization potentials determined by charge transfer spectroscopy in CH_2Cl_2. Tetracyanoethylene (TCNE) was used as electron acceptor.

raphy. It is nevertheless of interest to know to what extent this behavior is reflected in the electron transfer process. We applied force field (MMI) (*67*) CNDO/2 and MINDO/3 (*68*) calculations to the conformational analysis of mesocyclic dithioethers (*69*) whose x-ray structures were previously determined (*70*). This work confirmed the suggestion (*19*) that the orbital geometry and not the S–S distance per se determines the extent of the S–S interaction in the ground state. The pes measurements show splittings resulting from S–S interactions and, as Table III indicates, there is no simple correlation between these values and the S–S distance. The orbital geometry is shown in Figures 3 and 4 and, although **5** indeed has the shortest S–S distance, the favorable orbital overlap accounts for the observed splittings. Our semiempirical MINDO/3 SCF molecular orbital calculations with full geometric optimization show that oxidation to the cation radical and dication does not require major changes in geometry except for a significant eventual shortening of the S–S distance by more than 1 Å. The antibonding orbital has a strong destabilizing influence on the rather weak three-electron bond, whose energy was estimated at 40–120 kJ/mol (*19*). Thus, the unusual electrochemical behavior of **5** is due to a transannular interaction that is strong enough to stabilize the positive charge on the sulfur but weak enough to permit reversible electron transfer.

Table III. Structural Aspects of Mesocyclic Polythioethers

Compounds	*S–S Distance (x-ray)* (Å)	*S–S Splitting*[a] (eV)
3	3.58	0.01
5	3.44[b]	0.43
6	4.11	0.10
7	4.86	0.15

[a] Determined from photoelectron spectroscopy.
[b] From Ref. *71*.

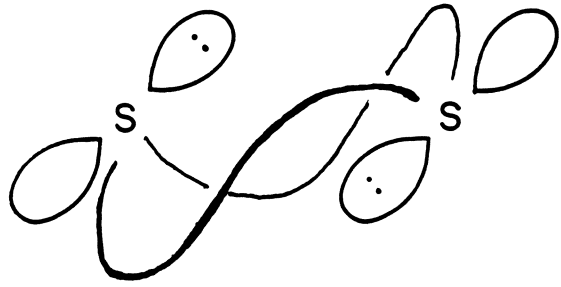

Figure 3. Schematic drawings showing the orientation of the sulfur atoms in Compounds **3**, **6**, *and* **7**.

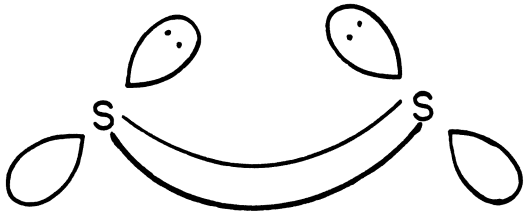

Figure 4. Schematic drawing of sulfur atom orientation in Compound 5.

Thioether redox chemistry in biological systems may involve the rather strict conformational requirements exhibited by the model systems studied. Successful resolution of these questions must await the more detailed spectroscopic examination of intermediates now in progress.

Acknowledgments

This work was supported in part by a grant from the National Institutes of Health (HL-15104).

Literature Cited

1. Lehninger, A. L. "Biochemistry;" 2nd ed.; Worth: New York, 1977, p. 714.
2. Wilgus, H.; Ranweiler, J. S.; Wilson, G. S.; Stellwagen, E. *J. Biol. Chem.* **1978,** *253,* 3265.
3. Gilbert, B. C.; Hodgeman, D. K. C.; Norman, R. O. C. *J. Chem. Soc., Perkin Trans. II* **1973,** 1748.
4. Peterson, R. L.; Nelson, D. J.; Symons, M. C. R. *J. Chem. Soc., Perkin Trans. II* **1978,** 225.
5. Bonafačic, M.; Mockel, H.; Bahnemann, D.; Asmus, K.-D. *J. Chem. Soc., Perkin Trans. II* **1975,** 657.
6. Asmus, K.-D. In "Fast Processes in Radiation Chemistry and Biology;" G. E. Adams; E. M. Fielden; B. D. Michael, Eds.; Wiley: New York, 1973; pp. 40–49.
7. Asmus, K.-D., Bahnemann, D.; Bonifačic, M.; Gillis, H. A. *Faraday Discuss. Chem. Soc.* **1977,** *63,* 213.
8. Glass, R. S.; Duchek, J. R.; Klug, J. T.; Wilson, G. S. *J. Am. Chem. Soc.* **1977,** *99,* 7349.
9. Wilson, G. S.; Swanson, D. D.; Klug, J. T.; Glass, R. S.; Ryan, M. D.; Musker, W. K. *J. Am. Chem. Soc.* **1979,** *101,* 1040.
10. Ryan, M. D.; Swanson, D. D.; Glass, R. S.; Wilson, G. S. *J. Phys. Chem.,* **1981,** *85,* 1069.
11. Musker, W. K.; Wolford, T. L. *J. Am. Chem. Soc.* **1976,** *98,* 3055.
12. Perkins, C. W.; Martin, J. C.; Ardnengo, A. J.; Lau, W.; Alegria, A.; Kochi, J. K. *J. Am. Chem. Soc.* **1980,** *102,* 7753.
13. Musker, W. K. *Acc. Chem. Res.* **1980,** *13,* 200.
14. Musker, W. K.; Wolford, T. L.; Roush, P. B. *J. Am. Chem. Soc.* **1978,** *100,* 6416.
15. Gourcy, J.-G.; Jeminet, G. J.; Simonet, J. *J. Chem. Soc., Chem. Commun.* **1974,** 634.

16. Glass, R. S.; Williams, E. B., Jr.; Wilson, G. S. *Biochemistry* **1974,** *13,* 2800.
17. Cottrell, P. T.; Mann, C. K. *J. Electrochem. Soc.* **1969,** *116,* 1499.
18. Hiller, K. O.; Göbl, M.; Masloch, B.; Asmus, K.-D. *Assoc. Rad. Res.,* in press.
19. Asmus, K.-D.; Bahnemann, D.; Fischer, Ch.-H.; Veltwisch, D. *J. Am. Chem. Soc.* **1979,** *101,* 5322.
20. Yang, S. F.; Ku, H. S.; Pratt, H. K. *J. Biol. Chem.* **1967,** *242,* 5274.
21. Lavine, T. *J. Biol. Chem.* **1943,** *151,* 281.
22. Mann, S. Z. *Anal. Chem.* **1960,** *173,* 112.
23. Glass, R. S.; Duckek, J. R. *J. Am. Chem. Soc.* **1976,** *98,* 965.
24. Pryor, W. A.; Tang, R. H. *Biochem. Biophys. Res. Commun.* **1978,** *81,* 498.
25. Chamber, J. Q. In "Encyclopedia of Electrochemistry of the Elements" (Organic Section); Bard, A. J.; Lund, H., Eds.; Dekker: New York, 1978; Vol. 12, p. 329 ff.
26. Asmus, K.-D. *Acc. Chem. Res.* **1979,** *12,* 436.
27. Estabrook, R. W.; Werringloer, J. In "The Induction of Drug Metabolism;" R. W. Estabrook; E. Lindenlaub, Eds.; Schatlaner: Stuttgart, 1979; p. 187.
28. Ullrich, V. Ed. "Microsomes and Drug Oxidation;" Pergamon: New York, 1977.
29. Watanabe, Y.; Iyanagi, T.; Oae, S. *Tetrahedron Lett.* **1980,** *21,* 3685.
30. Hoffmann, B. M.; Roberts, J. E.; Brown, T. C.; Kang, C. H.; Margoliash, E. *Proc. Nat'l. Acad. Sci. U.S.A.* **1979,** *76,* 6132.
31. Musker, W. K.; Hirschon, A. S.; Doi, J. T. *J. Am. Chem. Soc.* **1978,** *100,* 7754.
32. Isaacson, Y. A.; Majuk, Z.; Brisk, M. A.; Gellender, M. E.; Baker, A. D. *J. Am. Chem. Soc.* **1975,** *97,* 6603.
33. Morgan, R. S.; Tatsch, C. E.; Gushard, R. H.; McAdon, J. M.; Warme, P. K. *Int. J. Pept. Protein Res.* **1978,** *11,* 209.
34. Bruice, T. C. *Annu. Rev. Biochem.* **1976,** *45,* 331.
35. Zweig, A.; Lehnsen, J. E. *J. Am. Chem. Soc.* **1965,** *87,* 2647.
36. Gilmore, J. R.; Mellor, J. M. *Tetrahedron Lett.* **1971,** 3977.
37. Torii, S.; Uneyama, K. *Tetrahedron Lett.* **1972,** 4513.
38. Magno, F.; Bontempelli, G. J. *Electroanal. Chem.* **1972,** *36,* 389.
39. Glass, R. S.; Wilson, G. S.; Setzer, W. N. *J. Am. Chem. Soc.* **1980,** *102,* 5068.
40. Glass, R. S.; Duchek, J. R.; Gopala Prabhu, U. D.; Wilson, G. S. *J. Org. Chem.* **1980,** *45,* 3640.
41. Coleman, B. R.; Wilson, G. S., unpublished data, 1981.
42. Block, E. "Reactions of Organosulfur Compounds;" Academic: New York, 1978; pp. 154 ff.
43. Eberson, L.; Nyberg, K. In "Encyclopedia of Electrochemistry of the Elements;" Bard, A. J.; Lund, H., Eds.; Dekker: New York, 1978; Vol. 12, pp. 273 ff.
44. Setzer, W. N.; Glass, R. S., unpublished data, 1981.
45. Pysh, E. S.; Yang, N. C. *J. Am. Chem. Soc.* **1963,** *85,* 2125.
46. Peover, M. E. J. *Electroanal. Chem.* **1967,** *2,* 1.
47. Zuman, P. "Substituent Effects in Organic Polarography;" Plenum: New York, 1967.
48. Miller, L. L.; Nordblom, G. D.; Mayeda, E. A. *J. Org. Chem.* **1972,** *37,* 916.
49. Savéant, J. M. *Acc. Chem. Res.* **1980,** *13,* 323.
50. Fukuzumi, S.; Wong, C. L.; Kochi, J. K. *J. Am. Chem. Soc.* **1980,** *102,* 2928.
51. Gassman, P. G.; Mullins, M. J.; Richtsmeier, S.; Dixon, D. A. *J. Am. Chem. Soc.* **1979,** *101,* 5793.
52. Klingler, R. J.; Kochi, J. K. *J. Am. Chem. Soc.* **1980,** *102,* 4790.
53. Nelson, S. F.; Peacock, V.; Weisman, G. R. *J. Am. Chem. Soc.* **1976,** *98,* 5269.
54. Cocksey, B. J.; Eland, J. H. D.; Danby, C. J. *J. Chem. Soc. B* **1971,** 790.

55. Kobayashi, M.; Gleiter, R.; Coffen, D. L.; Bock, H.; Schulz, W.; Stein, U. *Tetrahedron* **1977,** *33,* 433.
56. Wagner, G.; Bock, H. *Chem. Ber.* **1974,** *107,* 1974.
57. Bunzli, J. C.; Frost, D. C.; Weiler, L. *J. Am. Chem. Soc.* **1973,** *95,* 7880.
58. Batich, C.; Heilbronner, E.; Quinn, C. B.; Wiseman, J. R. *Helv. Chem. Acta* **1976,** *59,* 515.
59. Nadjo, L.; Savéant, J. M. *J. Electroanal. Chem.* **1973,** *48,* 113.
60. Moreau, W. M.; Weiss, K. *Nature* **1965,** *208,* 1203.
61. Moreau, W. M.; Weiss, K. *J. Am. Chem. Soc.* **1966,** *88,* 204.
62. Aloisi, G. G.; Pignataro, S. *J. Chem. Soc., Faraday Trans. I* **1973,** *69,* 534.
63. Aloisi, G. G.; Santini, S.; Savelli, G. *J. Chem. Soc., Faraday Trans. I* **1975,** *71,* 2045.
64. Aloisi, G. G.; Santini, S.; Sorriso, S. *J. Chem. Soc. Faraday Trans. I* **1974,** *70,* 1908.
65. Foster, R. "Organic Charge-Transfer Complexes;" Academic: New York, 1969.
66. Fukuzumi, S.; Kochi, J. K. *J. Phys. Chem.* **1980,** *84,* 608.
67. Allinger, N. L.; Tribble, M. T.; Miller, M. A.; Wertz, D. H. *J. Am. Chem. Soc.* **1971,** *93,* 1637.
68. Bingham, R. C.; Dewar, M. J. S.; Lo, D. H. *J. Am. Chem. Soc.* **1975,** *97,* 1285.
69. Setzer, W. N.; Wilson, G. S.; Glass, R. S. *Tetrahedron* **1981,** *37,* 2735.
70. Setzer, W. N.; Coleman, B. R.; Wilson, G. S.; Glass, R. S. *Tetrahedron* **1981,** *37,* 2743.
71. Hope, H.; Nichols, B. G. *Acta Crystallog. Sect. B* **1981,** *B37,* 158.

RECEIVED for review June 2, 1981. ACCEPTED October 5, 1981.

Spectroelectrochemical Examination of the Reactions of Chlorpromazine Cation Radical with Physiological Nucleophiles

J. S. MAYAUSKY, H. Y. CHENG, P. H. SACKETT, and R. L. McCREERY

The Ohio State University, Department of Chemistry, Columbus, OH 43210

Previously, the reactions of cation radicals derived from phenothiazine drugs were examined using conventional spectrophotometry and liquid chromatography. The time scale of the techniques limited the pH range to 5 and below, where the reactions were slow enough to monitor accurately. In the present work, the pH range was extended to 4 to 9 using a reflective spectroelectrochemical technique. Reactions of chlorpromazine cation radical with acetate, phosphate, and citrate buffer were examined as a function of pH and buffer concentration. The observed rate was critically dependent on which buffer species were present and on the degree of protonation for polyprotic buffers. The dianions of phosphate and citrate had rates that were 62 and 330 times faster than the monoanions, all else being equal. This rate difference may be due to the ability of the buffer to simultaneously interact with two radicals, thus promoting charge transfer.

Drugs based on the phenothiazine nucleus, particularly chlorpromazine (CPZ), have become the major class of antipsychotics for the treatment of mental disorders, including schizophrenia. The impact of the existence of these drugs on the treatment of mental illness has been enormous, with the need for institutional care often being eliminated through proper drug therapy. The clinical impor-

0065-2393/82/0201-0443$06.00/0

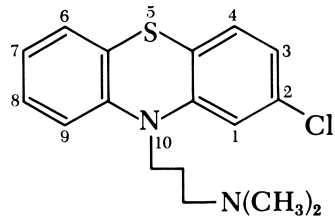

Chlorpromazine

tance of the phenothiazines has spawned a large number of research efforts on their chemistry, pharmacology, analysis, and metabolism. Several reviews of this work have appeared, both in medical and in chemical publications (*1*–*3*).

Of particular relevance to the present discussion are investigations of the cation radical of CPZ and related drugs formed upon the removal of one electron from the ring system. The cation radical and other oxidized forms have been examined in some detail from both biological and strictly chemical standpoints. The interest in the radical stems from three general points. First, CPZ forms a cation radical (*4*, *5*) that is similar to those of polynuclear aromatics (e.g., anthracene and thianthrene), and is therefore an example of a class of widely studied heterocyclic radical ions. The characteristics and reactions of these molecules have been studied in some detail, but questions remain about what factors affect radical behavior. Unlike diphenylanthracene and thianthrene, the 10-substituted phenothiazines form relatively stable radicals in aqueous solutions, but the reasons for this stability are not clear. Second, the cation radical of CPZ is believed to be a key intermediate in the metabolism of the drug (*6*, *7*). Radical ion pathways have been proposed in the formation of two of the three major metabolites, the sulfoxide and ring hydroxylated species, and a radical has been detected by ESR in patients being treated with CPZ (*8*). Third, the CPZ radical ($CPZ^{+\cdot}$) has a variety of effects on biological systems, including enzymes (*9*), DNA (*10*), and membranes (*11*). CPZ^{+} may be responsible for some of the side effects of CPZ treatment, or even for the desired antipsychotic effect (*4*, *6*, *12*). In any case, the radical is very likely to be formed in vivo, and its behavior is likely to be important to the metabolism and activity of the parent drug.

Until 1975, the great majority of work on phenothiazine radical ions was carried out in strong aqueous acids (e.g., 4 *M* H_2SO_4) to stabilize the radical enough to obtain spectroscopic or kinetic data (*13*). Most workers concluded that the decay of CPZ^{+} was second order and resulted from disproportionation of the radical to CPZ and CPZ sulfoxide. However, the kinetics were not straightforward, and the stability of the radical was highly dependent on the solution environ-

ment for reasons that were not clear. An excellent examination of 10-phenylphenothiazine cation radical in acetonitrile and pyridine revealed that the radical did not disproportionate but was attacked directly by available nucleophiles (*14*). This result indicates that the previous work on radical ions of phenothiazine drugs in aqueous solution warrants reexamination.

In addition to work specifically related to phenothiazine drugs, other heterocyclic radical ions have been studied extensively in nonaqueous media. The vast majority indicate that the radical ions react according to Reactions 1–3, where A^+ is the initial radical ion and Z is a nucleophile.

$$A^+ + Z \rightarrow AZ^{+\cdot} \quad (1)$$

$$AZ^{+\cdot} + A^+ \rightarrow AZ^{2+} + A \quad (2)$$

$$AZ^{2+} \rightarrow \text{products} \quad (3)$$

A disproportionation, Reactions 4–6,

$$2A^{+\cdot} \rightarrow A + A^{2+} \quad (4)$$

$$A^{2-} + Z \rightarrow AZ^{2+} \quad (5)$$

$$AZ^{2+} \rightarrow \text{products} \quad (6)$$

would lead to the same overall stoichiometry, but the reactive species for the disproportionation case is a dication rather than a cation radical.

Given this background, our laboratory investigated the kinetics and mechanism of the reactions of phenothiazine radicals in aqueous solution in the pH range 2–7. The radicals were derived from chlorpromazine and other clinically important phenothiazines, and the other solution constituents were restricted to physiologically occurring materials. The objectives of this approach were as follows: (1) determination of the product distribution of cation radical reactions as a function of medium, pH, and radical structure; (2) observation of the rate of radical decay over a wide range of conditions; and (3) establishment of a reaction mechanism for radical decay and clarification of how radical structure or reaction medium affects this mechanism.

Previous reports demonstrated that the products of a phenothiazine cation radical reaction in aqueous solution are highly dependent on both the structure of the radical and on the identity of nucleophiles in the reaction medium. For CPZ^+ in phosphate or carboxylate buffers, 1 mol of radical reacts to form 0.5 mol each of CPZ and chlorpromazine sulfoxide (*15*). If an amine is present in the medium, particularly an amine with a low pK_a, ring hydroxylation occurs and the yield of sulfoxide is substantially below 50% (*16*). If a

piperazine ring is included in the side chain (as in fluphenazine), hydroxylation is observed regardless of the buffer employed (*17*). Finally, substitution at the 2-position does not affect product distribution, nor does demethylation of the CPZ side-chain amine (*18*).

The results permit the conclusion that the radical will either be hydroxylated or form sulfoxide, depending on the presence of nucleophilic, deprotonated amines. In CPZ, the side-chain nitrogen pK_a is high (9.30) and is unlikely to be involved in nucleophilic attack. Therefore, the important nucleophiles are buffer components and only sulfoxide and parent compound are observed as products in phosphate, citrate, or acetate medium. However, when nucleophilic amines are present, either as a buffer component [e.g., *N*-morpholinoethanesulfonic acid (MES), $pK_a = 6.2$] or in the radical's own side chain (e.g., fluphenazine, $pK_1 = 3.9$), hydroxylation is observed (*17*). For an amine to attack the radical and cause hydroxylation its pK_a must be low enough so a sufficient fraction of the amine is deprotonated to compete with other, nonamine nucleophiles. The details of the hydroxylation process are not known, but the sulfoxide and hydroxylated derivatives are two of the three major classes of metabolic products in vivo.

Because the stoichiometry of the reaction of the radical in carboxylate or phosphate buffers was established quantitatively, the kinetics and mechanisms of the decay of several radicals were examined in detail in these media (*15*, *16*, *18*). The overall reaction is given by Equation 7, where CPZO represents CPZ sulfoxide. Synthetic radical perchlorate salt (prepared electrochemically) was dissolved in appropriate solution, and the decay

$$2CPZ^{+\cdot} + H_2O \rightarrow CPZ + CPZO + 2H^+ \quad (7)$$

of $CPZ^{+\cdot}$ was monitored spectrophotometrically at 525 nm. Careful analysis of the decay kinetics confirmed that the reaction was second order, but that it did not involve a disproportionation. The buffer anion acted as a catalyst, with the mechanism being represented by Reactions 8–10, where B^- is buffer anion.

$$CPZ^+ + B^- \overset{K_8}{\rightleftharpoons} (CPZB)\cdot \quad (8)$$

$$(CPZB)\cdot + CPZ^+ \underset{k_{-9}}{\overset{k_9}{\rightleftharpoons}} (CPZB)^+ + CPZ \quad (9)$$

$$H_2O + (CPZB)^+ \xrightarrow{k_{10}} CPZO + HB + H^+ \quad (10)$$

The rate law for this reaction is given by Equation 11[1]

[1] The involvement of water in Reaction 10 dictates that the rate law involve water as a reagent. For the sake of clarity, k_{10} will be assumed to include the water term. So wherever k_{10} appears, it in fact equals $k'_{10}[H_2O]$.

$$\frac{d[CPZ^+]}{dt} = \frac{-2K_8k_9k_{10}[B^-][CPZ^+]^2}{k_{-9}[CPZ] + k_{10}} \quad (11)$$

The original reports should be consulted for the details of this reaction but several important points deserve comment. First, a disproportionation of radical to dication was ruled out for all the systems studied, and the mechanism is consistent with reactions of other radical ions in nonaqueous media (*14*, *19*). Second, the buffer nucleophile greatly accelerates the reaction relative to that in plain water. The half-life of $CPZ^{+\cdot}$ in water at pH 7 (using a pH stat with no buffer) is 4 min (*16*), and the half-life in pH 7 phosphate buffer is approximately 100 ms. Therefore, water is a poor nucleophile for this reaction, and the radical will be attacked by even weaker nucleophiles such as phosphates and carboxylates if they are present. Third, protonation of B^- reduces the free B^- concentration, slowing the rate at lower pH. In the work presented so far, the pH range was limited to the region from 2 to 5, because the rate at higher pH was too fast to monitor by conventional spectrophotometry. The pH dependence results from proton loss in Reaction 8. Because Reaction 8 is in equilibrium, the case where HPO_4^{2-} attacks cannot be distinguished kinetically from the case where $H_2PO_4^-$ attacks with loss of a proton. Fourth, the radical forms a covalent adduct with the nucleophile, which eventually hydrolyzes to regenerate buffer. Thus, the most likely fate of the radical in a physiological environment is attack by biologically occurring nucleophiles, perhaps peptides from receptor sites. Fifth, substitution of CPZ at the 2-position changes the rate in a predictable fashion provided the mechanism is the same (*18*). Electron-withdrawing substituents increase the rate of reaction because the radical becomes more electrophilic.

The main objective of the new results presented in the following section was to extend the kinetic analysis of radical decay to the pH range 2–9. In addition to the greater physiological importance of these results, the factors affecting nucleophile reactivity can be elucidated.

Experimental

The technique used to determine the reaction rate of $CPZ^{+\cdot}$ decay in buffers of near neutral pH was a combination of the approach used by Blount (*20*) and a recently developed reflective spectroelectrochemical technique (*21*). A light beam reflected off a glassy carbon electrode immersed in solution was used to monitor $CPZ^{+\cdot}$ generated at the electrode (λ_{max} = 525 nm). The absorbance vs. time transient occurring after the beginning of electrolysis was recorded in the absence and in the presence of a nucleophile. In all cases where nucleophile was absent, the A vs. $t^{1/2}$ plot was linear, as expected for an uncomplicated diffusion-controlled generation of chromophore.

In the presence of a nucleophile (phosphate, citrate, or acetate) the absorbance was smaller than the uncomplicated case, because the $CPZ^{+\cdot}$ generated at the electrode reacted to form uncolored products (CPZ + CPZO). The ratio of the absorbance with reaction to that without reaction will be referred to as normalized absorbance, A_n. The shape of an A_n vs. time (or log t) plot was characteristic of the rate and mechanism of the reaction between $CPZ^{+\cdot}$ and nucleophile. Comparisons of experimental and theoretical A_n vs. log t plots allowed determination of observed rate constants for $CPZ^{+\cdot}$/nucleophile reactions having time scales in the 10-ms to 10-s range.

When $CPZ^{+\cdot}$ is generated from reduced CPZ at an electrode, the reaction sequence is the same as that in Equations 8–10, except that Reaction 8 is preceded by the one-electron oxidation of CPZ. The decay of $CPZ^{+\cdot}$ after electrogeneration was simulated with well-established finite difference methods, using the fact that the observed quantity is the integral of the $CPZ^{+\cdot}$ concentration throughout the diffusion layer (*20*). When the rate law (Equation 12) is converted to a finite difference form one obtains

$$\frac{\Delta FR_j}{\Delta t} = \frac{-2k_{obs}FR_j^2}{FC_j + X} \tag{12}$$

where FR_j is the fractional radical concentration (relative to bulk CPZ); FC_j is the fractional CPZ concentration (relative to bulk); k_{obs} is the observed rate constant, equal to $K_8K_9k_{10}$ $[B^-]$ where $K_9 = k_9/k_{-9}$; and X equals k_{10}/k_{-9}-$[CPZ]^{bulk}$. Working curves of A_n vs. log $(k_{obs}t)$ were calculated based on Equation 12, with the absorbance being determined from the integrated concentration in all boxes. The value of k_{10}/k_{-9}, and therefore X, was calculated from homogeneous kinetic data obtained at lower pH for all three nucleophiles examined here (*15*, *16*).

In all cases, the absorbance of the reflected beam was monitored at 525 nm after a potential step corresponding to diffusion-controlled generation of $CPZ^{+\cdot}$. The CPZ cation radical was the only solution component that absorbed light at this wavelength. Since CPZ and similar drugs adsorb significantly on solid electrodes, it was necessary to add 50% by volume of methanol to the aqueous buffers to eliminate adsorption. It was verified that the stoichiometry of the reaction was unchanged in this medium. Spectrophotometric examination of the decay kinetics in 50% methanol–H_2O, using the approach described previously (*15*), revealed that the mechanism was qualitatively unchanged from purely aqueous solution. Plots of $1/k_{obs}$ vs. [CPZ] (*15*) revealed that the value k_{10}/k_{-9} in 50% methanol was 2.8×10^{-3} for citrate at pH 2.46, 43×10^{-3} for phosphate at pH 3.14, and 0 for acetate (pH 3.4). These values are somewhat larger than those in water, and will be used in all subsequent calculations. The pK_a values of the buffers employed were determined in 50% methanol by pH titration and were as follows: acetate pK_a, 5.20; phosphate pK_1, 3.30; phosphate pK_2, 7.65; phosphate pK_3, 11.75; citrate pK_1 = 3.70; citrate pK_2, 5.30; citrate pK_3, 6.85. The use of 50% methanol solutions for both the titration and kinetic experiments ensures that species distributions can be accurately calculated from these pK_a values. However, 100% aqueous buffers were used for meter calibrations in this work so that pH and pK_a values are internally consistent but shifted slightly in the absolute sense. In all experiments the ionic strength was adjusted to 0.2 *M* with NaCl. Kinetic runs were conducted at ambient temperature, 23 ± 1°C, with the total buffer concentration at least an order of magnitude greater than the bulk CPZ concentration.

Results

Typical absorbance vs. time transients for the electrogeneration of $CPZ^{+\cdot}$ are shown in Figure 1. In the absence of a nucleophile the curve has the $t^{1/2}$ behavior (Curve 1) expected for a stable electrogenerated chromophore. When phosphate is present, the absorbance is lower due to decay of electrogenerated $CPZ^{+\cdot}$. The decay rate increases with pH as shown in Curves 2–4. Figure 2 compares plots of normalized absorbance vs. log *kt* for several kinetic cases with the experimental points for phosphate buffer. Curve 3 shows the working curve for a first-order reaction, as would be observed if Reaction 8 were rate limiting. Curve 2 is the case for $X = 0$, which corresponds to Reactions 8 and 9 in equilibrium, with Reaction 10 rate limiting. Curve 2 would also be observed for a disproportionation of $CPZ^{+\cdot}$ to CPZ and CPZ^{+2} followed by reaction of CPZ^{+2}. Curve 1 is a plot for $X = 8.3$, the value calculated from the k_{10}/k_{-9} ratio for phosphate determined from conventional spectrophotometric kinetics. The points are experimental results for several pH values in phosphate buffer, which

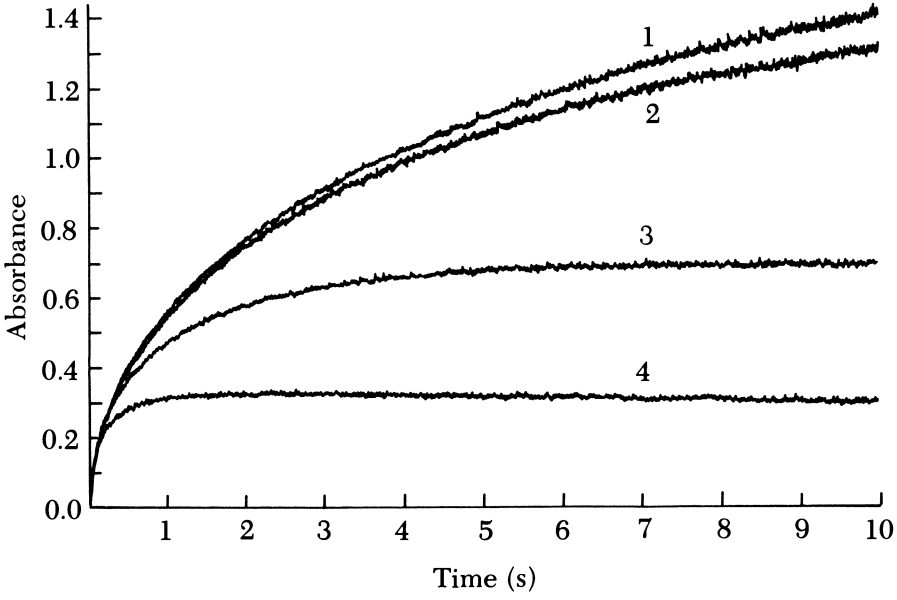

Figure 1. Experimental absorbance vs. time curves (single runs) for 5.0 mM CPZ in 50% MeOH/H_2O solutions. The potential step was from 0 to +0.8 V vs. SCE, the observation wavelength was 525 nm, and the input beam angle was 3.2°. The medium for Curve 1 was 0.2 M NaCl; Curves 2, 3, and 4 were 0.02 F phosphate buffer at pH 3.0, 5.0, and 7.0, respectively.

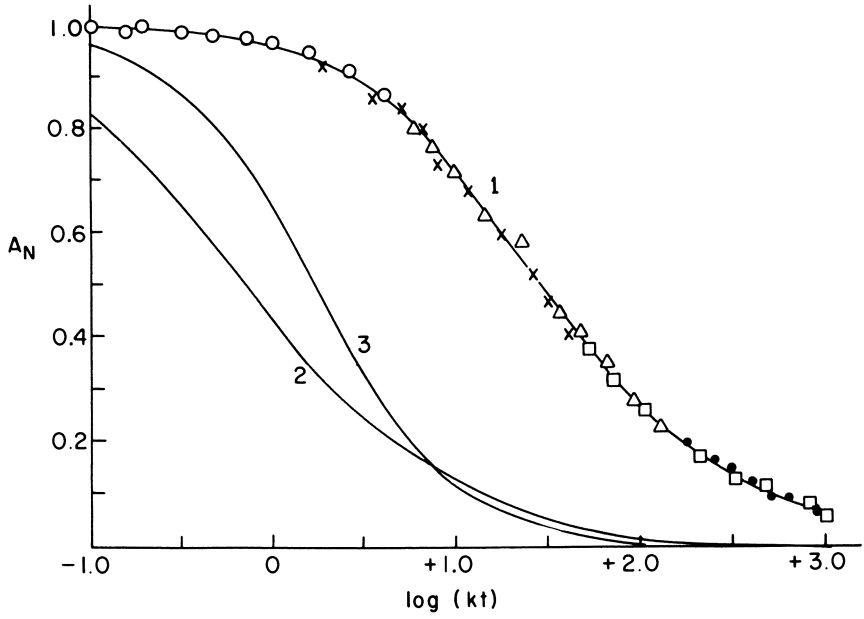

Figure 2. Comparison of theoretical vs. observed normalized absorbance vs. log ($k_{obs}t$). *Curve 1 was calculated from Equation 13 with X = 8.3, and Curve 2 was calculated from the same equation with X = 0. Curve 3 was calculated for a reaction that was first order in* $CPZ^{+\cdot}$. *Points are experimental values in conditions corresponding to the theoretical Curve 1 (0.02 F phosphate buffer, X = 8.3), at various pH values. Key: ○, pH 4.20; X, pH 5.45; △, pH 6.4; □, pH 7.12; and ●, pH 7.41.*

were fit to Curve 1 by adjusting k_{obs}. The bulk CPZ concentration used experimentally was that used to calculate the X value appropriate to Curve 1. Thus, once an experimental A_n vs. t transient is available, k_{obs} may be calculated by comparison with Curve 1, or one like it corresponding to the X value appropriate to the buffer employed.

The procedure illustrated in Figure 2 was used to determine observed rate constants for reactions of $CPZ^{+\cdot}$ with citrate, phosphate, and acetate buffers as a function of pH. For cases where $X \neq 0$ (citrate and phosphate), the value K_8k_9 could be calculated from k_{obs}, X, and the bulk CPZ concentration. For the case where $X = 0$ (acetate) only the overall constant $K_8K_9k_{10}$ could be determined. Values for k_{obs} are listed in Table I for the three nucleophiles examined. Observed rate constants are presented in graphical form in Figure 3 over the pH range 4 to 9. Above pH 9 CPZ will not dissolve significantly and meaningful results were not obtained. Figure 4 shows the dependence of k_{obs} on total buffer concentration at pH 7.

Table I. Observed Spectroelectrochemical Rate Constants for $CPZ^{+\cdot}$ Decay

Acetate (0.2 F)		*Phosphate (0.025 F)*		*Citrate (0.005 F)*	
pH	$k_{obs}(M^{-1}s^{-1})$	*pH*	k_{obs}	*pH*	k_{obs}
3.96	0.029	4.30	0.23	3.61	0.035
4.45	0.076	4.40	0.230	4.05	0.238
5.0	0.197	4.88	0.343	4.50	0.579
5.5	0.337	5.00	0.439	5.05	1.49
6.0	0.425	5.25	0.697	5.53	2.79
6.5	0.495	5.75	1.10	6.00	4.95
7.0	0.562	6.5	5.04	6.40	5.01
7.5	0.510	6.9	17.2	6.60	6.09
		7.0	20.3	6.92	6.24
		7.5	44.9	7.26	6.16
		7.7	67.0	7.80	6.18
		7.75	67.7		
		8.00	75.5		
		8.20	75.7		
		8.70	80.4		
		9.1	80.7		

Discussion

The agreement between theory and experiment shown in Figure 2 indicates that spectroelectrochemical results are consistent with the mechanism of Reactions 8–10. The spectroelectrochemical response can be used to discriminate between first- and second-order reactions, but previous workers demonstrated that the response is not particularly sensitive to less obvious changes in kinetic parameters, such as the rate-determining step. In the present method, however, additional checks besides curve shape are available to establish the validity of the results. Agreement with spectrophotometric data obtained at lower pH values supports the conclusion that the mechanism at pH 7 is the same as that at lower pH values. Thus, the spectroelectrochemical experiment is not being used to determine a mechanism, but to allow measurements in a shorter time domain. The results shown in Figure 2 do not by themselves establish the mechanism, but combined with data from other methods, indicate that the observed rate constants are meaningful numbers reflecting rates of reaction. Additional support for the validity of the spectroelectrochemical results is provided by Figure 4. This figure demonstrates the expected first-order dependence on

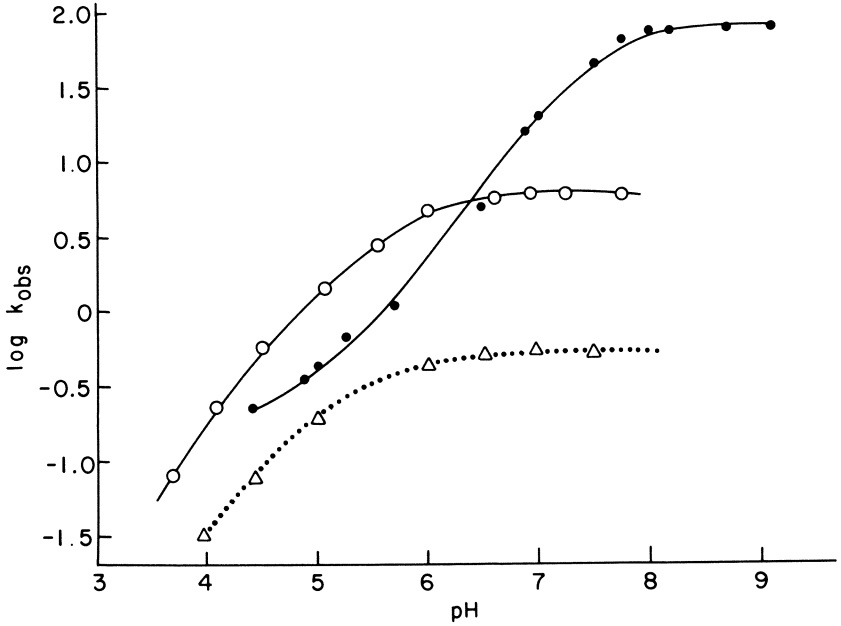

Figure 3. Observed rate constants vs. pH for citrate, phosphate, and acetate buffers (ionic strength = 0.2). Key: ●, 0.025 F phosphate; ○, 0.005 F citrate; and △, 0.2 F acetate.

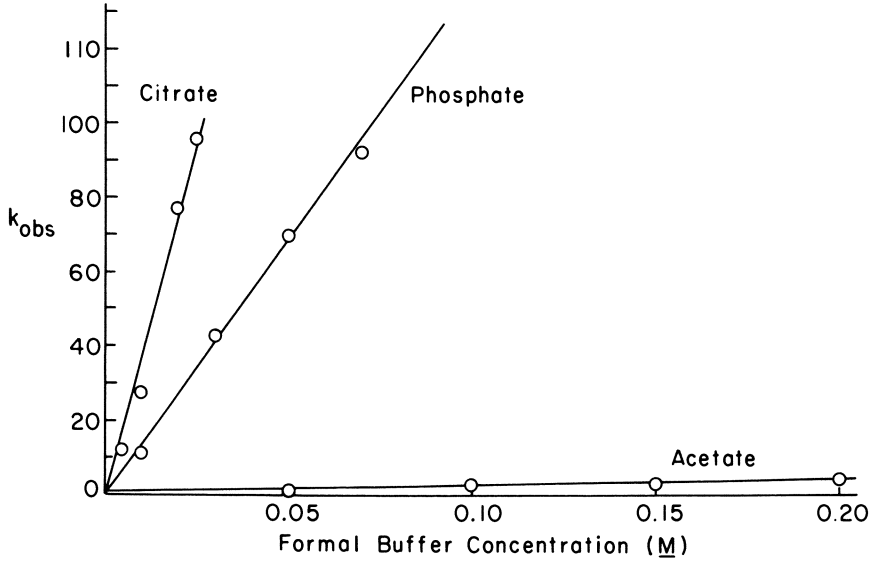

Figure 4. Dependence of observed rate constant on total buffer concentration with pH 7.0. Ionic strength was held constant at 0.2 M.

buffer (nucleophile) concentration and the linearity, at very low total concentration, reflects the catalytic nature of the buffer.

Kinetic results obtained over the wide pH range permit several conclusions about the active form of the nucleophile involved in the reaction. With acetate ion, the log k_{obs} vs. pH plot (Figure 3) shows a break at the pK_a for acetic acid and a pH independent region above this value. When $K_8K_9k_{10}$ is calculated from k_{obs} by dividing by free acetate concentration, the value is constant to 10% over the pH range 4–8. The constant value of $K_8K_9k_{10}$ calculated for this range indicates that the pH effect on k_{obs} is caused solely by changes in free acetate concentration, and that the entire decay can be explained by nucleophilic attack of $CPZ^{+\cdot}$ by acetate ion. Even at pH 7, reactions of other nucleophiles, such as water, hydroxide, or the CPZ side chain, are undetectable compared to the acetate reaction.

Qualitatively similar behavior was observed for phosphate, with the rate above pK_2 being pH independent. In the pH range 8–9, HPO_4^- is clearly the active form of total phosphate and PO_4^{3-} provides no observable contribution. In the pH region 6–7, the observed rate reflects the variation in HPO_4^{2-} concentration with pH, and is consistent with HPO_4^{2-} attack of $CPZ^{+\cdot}$ without proton loss. Below pH 6 the rates are too fast to be accounted for solely by HPO_4^{2-}, so H_2PO_4 must contribute to the rate. The observed rate is therefore governed by

$$k_{obs}C_T = k_{H_2PO_4^-}[H_2PO_4^-] + k_{HPO_4^{2-}}[HPO_4^{2-}] \quad (13)$$

and

$$k_{obs} = \alpha_1 k_{H_2PO_4^-} + \alpha_2 k_{HPO_4^{2-}} \quad (14)$$

where C_T is total phosphate concentration; α_1 and α_2 are fractional concentrations of $H_2PO_4^-$ and HPO_4^{-2}, respectively; $k_{H_2PO_4^-}$ is the value of $K_8K_9k_{10}$ for attack by $H_2PO_4^-$ (without deprotonation); and $k_{HPO_4^{2-}}$ is the value of $K_8K_9k_{10}$ for attack by HPO_4^{2-}. The value of $K_{HPO_4^{-2}}$ was determined from the pH independent region above pH 7, and $K_{H_2PO_4^-}$ was calculated from the rates in the pH region 3–5. For the entire pH range from 3 to 8, Equation 14 was valid to within 15%, indicating that any reactions due to H_3PO_4 or PO_4^{3-} are negligible. The kinetic data for the two phosphate species are included in Table II.

The distinction between a rate for $H_2PO_4^-$ and one for HPO_4^{2-} should be clarified at this point. The case where $H_2PO_4^{2-}$ attacks with proton loss is kinetically indistinguishable from attack by HPO_4^{2-}, be-

Table II. Derived Constants for Various Nucleophilic Species

Nucleophile	K_8k_9	$K_8K_9k_{10}$
CH_3COOH	—	~0
CH_3COO^-	—	2.5
H_3PO_4	~0	~0
$H_2PO_4^-$	2.3×10^3	9.7
HPO_4^{2-}	7.4×10^5	3200
H_3Cit	~0	~0
H_2Cit^-	4.9×10^3	14
$HCit^{2-}$	3.0×10^5	860
Cit^{3-}	4.3×10^5	1200

cause Reaction 8 is in equilibrium. For the sake of clarity, the process will be referred to as attack by HPO_4^{2-}, and its rate constant is $k_{HPO_4^{2-}}$. However, when $H_2PO_4^-$ attacks without proton loss (analogous to the acetate reaction) the appropriate constant is $k_{H_2PO_4^-}$. Therefore, the values of K_8k_9 in Table II for HPO_4^{2-} and $H_2PO_4^-$ represent similar reactions that differ by the additional proton on the phosphate group, which is not lost during Reaction 8.

The pH dependence of the citrate reaction can be analyzed in a similar fashion except that three distinct citrate species contributed to the decay rate. The observed rate is accurately described by Equation 16 where α terms

$$k_{obs} = \alpha_1 k_{H_2Cit^-} + \alpha_2 k_{HCit^{2-}} + \alpha_3 k_{Cit^{3-}} \quad (16)$$

and k terms have meanings analogous to the phosphate case. The entire pH profile can be described by this expression to within 10%, and the values of rate constants for particular species are given in Table II.

The values of derived constants in Table II are direct indications of the overall rates of reaction of individual nucleophilic species after removal of the effects of pH and concentration. Several important observations can be made by comparing the values of $K_8K_9k_{10}$ for the six species examined. First, the monoanionic nucleophiles (CH_3COO^-, $H_2PO_4^-$, and H_2Cit^- have rates that are comparable, varying by only a factor of 5 despite significant changes in structure. Therefore, the large rate difference between citrate and acetate buffers is due to the more highly ionized forms of citrate. Second, removal of a second proton (as in HPO_4^{2-}) greatly accelerates the rate, by a factor of 330 for phosphate and 62 for citrate. Third, removal of the third proton from citrate causes a small increase in rate of about 40%. Finally, the rate increase from singly to doubly ionized phosphate and citrate species is due to the K_8k_9 term, and therefore results from changes in the first two reactions of the three-step process.

Because the rate difference between Cit^{3-} and $HCit^{2-}$ is fairly small, the rate acceleration with deprotonation probably is not simply an electrostatic effect. Removal of protons may aid the oxidation of the adduct, which increases the value of k_9, or the greater negative charge may influence other steps in the mechanism. However, the small difference in rate between Cit^{3-} and $HCit^{2-}$ indicates that the influence of electrostatic charge is minor and unlikely to account for the large difference between the singly and doubly ionized nucleophiles.

A more likely explanation for the rate difference between singly and doubly deprotonated nucleophiles can be provided after considering the intermediate formed by Reaction 8. For HPO_4^{2-} and $HCit^{2-}$, this intermediate possesses a second nucleophilic site. When a second molecule of $CPZ^{+\cdot}$, necessary as an oxidizing agent in Reaction 9, approaches, it can bond to the intermediate through the available site. The proximity of the two radicals can then accelerate the charge transfer of Reaction 9. When the intermediate contains $H_2PO_4^-$ or H_2Cit^-, no free site is available and no facilitation can occur. The Cit^{3-} species provides two extra sites when only one is necessary, resulting in only a modest rate enhancement over that for $HCit^{2-}$.

Another possibility for the rate difference between singly and doubly ionized nucleophiles is variation in k_{10}/k_{-9} with pH. Previous work (*15*) showed this value to be constant with pH in a limited range in the region of pH 2–3. With the wide range of pH employed in the present work, proton loss may occur in Reaction 9, making the ratio k_{10}/k_{-9} (and therefore X) pH dependent. This possibility is presently being investigated with stop–flow techniques.

In conclusion, the kinetics of the decay of chlorpromazine cation radical depend on pH in a fairly complex fashion over the pH range from 3 to 8. Each buffer component has a different rate of reaction with $CPZ^{+\cdot}$, and the variation in overall rate with pH results from changes in the distribution of buffer species. When the nucleophile has two nucleophilic sites, the rate of reaction is greatly enhanced over the case where only one site is available.

Acknowledgments

This work was supported by grants from NIMH (28412) and NSF (CHE-7828068). The authors thank Robert Engelbach for preliminary work on the kinetic simulations.

Literature Cited

1. Bodea, C.; Silbert, I. *Adv. in Heterocycl. Chem.* **1968,** 9, 321.
2. Forrest, I.; Usdin, E. "Psycho Therapeutic Drugs;" Dekker: New York, 1977.
3. Usdin, E.; Eckert, H.; Forrest, I. *Devel. in Neuroscience* **1980,** 7.

4. Piette, L. H.; Bulow, G.; Yamazaki, F. *Biochim. Biophys. Acta* **1964,** *88,* 120.
5. Merkle, F. H.; Discher, C. A. *J. Pharm. Sci.* **1964,** *53,* 620.
6. Forrest, I. S.; Green, D. E. *J. Forensic Sci.* **1972,** *17,* 592.
7. Forrest and Usdin, op. cit. pp. 709–719.
8. Forrest, I. S.; Forrest, F.; Berger, M. *Biochem. Biophys. Acta* **1958,** *29,* 441.
9. Akera, T.; Brody, T. *Biochem. Pharmacol.* **1972,** *21,* 1403.
10. Ohnishi, S.; McConnell, H. *J. Am. Chem. Soc.* **1965,** *87,* 2243.
11. Akera, T.; Kee, C. Y.; Brody, T. *Biochem. Pharm.* **1976,** *25,* 1751.
12. Godey, G. M.; Keyser, H.; Setchell, F. *Nature* (London) **1969,** *223,* 80.
13. Levy, L.; Tozer, T.; Tuck, D.; Loveland, D. *J. Med. Chem.* **1972,** *15,* 989.
14. Evans, J. F.; Lenhard, J. R.; Blount, H. N. *J. Org. Chem.* **1977,** *42,* 983.
15. Cheng, H. Y.; Sackett, P. H.; McCreery, R. L. *J. Am. Chem. Soc.* **1978,** *100,* 962.
16. Cheng, H. Y.; Sackett, P. H.; McCreery, R. L. *J. Med. Chem.* **1978,** *21,* 948.
17. Sackett, P. H.; Mayausky, J. S.; Smith, T. M.; Kalus, S.; McCreery, R. L., *J. Med. Chem.* **1981,** *24,* 1342.
18. Sackett, P. H.; McCreery, R. L. *J. Med. Chem.* **1979,** *22,* 1447.
19. Evans, J. F.; Blount, H. N. *J. Am. Chem. Soc.* **1978,** *100,* 4191.
20. Blount, H. N. *J. Electroanal. Chem.* **1973,** *42,* 271.
21. Skully, J.; McCreery, R. L. *Anal. Chem.* **1980,** *52,* 1885.

RECEIVED for review June 2, 1981. ACCEPTED August 24, 1981.

Electrochemistry of Reduced Pterin Cofactors

GLENN DRYHURST, R. RAGHAVAN, DENIZ EGE-SERPKENCI, and LIONEL G. KARBER

University of Oklahoma, Department of Chemistry, Norman, OK 73019

The redox chemistry of 5,6,7,8-tetrahydropterin (THP) and its 6-methyl and 6,7-dimethyl derivatives has been studied by electrochemical and related methods. The initial electrooxidation of the tetrahydro compounds is an almost reversible 2e–2H$^+$ process giving an unstable quinonoid-dihydropterin, which rearranges in a first-order reaction to give the corresponding 7,8-dihydropterins. The latter species react with water to form an equilibrium mixture of covalently hydrated and non-hydrated 7,8-dihydropterins. The covalently hydrated 7,8-dihydropterins are structurally similar to the tetrahydropterins and are therefore electrooxidized at almost the same potentials. This reaction is also a quasi-reversible 2e–2H$^+$ process giving another unstable quinonoid. The latter compound undergoes a rather fast chemical rearrangement to another intermediate, thought to be an isomeric, but more stable quinonoid. The quinonoids formed from covalently hydrated 7,8-dihydropterin break down to an equimolar mixture of pterin and 7,8-dihydroxanthopterin. The quinonoids formed by oxidation of the hydrated forms of 6-methyl and 6,7-dimethyl-7,8-dihydropterin break down to the corresponding methylated pterins. The non-hydrated forms of the 7,8-dihydropterins are electrooxidized to the corresponding pterins but at more positive potentials.

Tetrahydrobiopterin (**1**) is the natural cofactor for a number of hydroxylase enzymes that utilize molecular oxygen to introduce a

0065-2393/82/0201-0457$08.75/0

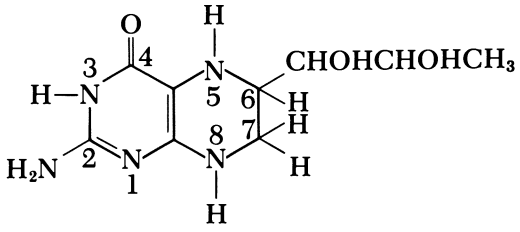

1

hydroxyl group into the aromatic amino acids phenylalanine, tyrosine, and tryptophan (*1–3*). Following his initial studies on the hydroxylation of phenylalanine, Kaufman (*4–6*) proposed Scheme I to explain the enzymic hydroxylation of phenylalanine by oxygen in the presence of phenylalanine hydroxylase and a tetrahydropterin cofactor. Thus, in addition to oxidation of phenylalanine to tyrosine, an oxidation of the cofactor to a quinonoid-dihydro form was proposed. A second enzyme, dihydropteridine reductase, catalyzes reduction of the quinonoid to the tetrahydro level using the reduced form of nicotinamide adenine dinucleotide (NADH) as the reducing agent. In this scheme, there is clearly no obvious functional role for the tetrahydropterin cofactor or a plausible route for activation of oxygen. Numerous theories and suggestions subsequently have been advanced to explain the role of tetrahydrobiopterin and other tetrahydropterin pseudo-cofactors in such hydroxylation reactions (*4–14*). Mechanistic Scheme II proposed by Hamilton (*10*) to explain the hydroxylation of phenylalanine by oxygen in the presence of phenylalanine hydroxylase and tetrahydrobiopterin appears to be one of the more widely accepted. In this mechanism (Scheme II), molecular oxygen is proposed to attack the tetrahydropterin cofactor (**I**, Scheme II) to give a hydroperoxide (**II**, Scheme II). This reaction originally was suggested by Kaufman (*7–9*). The putative hydroperoxide then cleaves across the C(4*a*)–N(5) bond giving a carbonyl oxide (**III**, Scheme II). This "oxene" reagent was thought to be the active hydroxylating agent by transferring an oxygen atom to the substrate S (i.e., aromatic amino acid) with formation of the pyrimidine, **IV** (Scheme II). Cyclization of the pyrimidine gives quinonoid-dihydropterin (**V**, Scheme II), which then is reduced to the corresponding tetrahydropterin by NADH in the presence of dihydropteridine reductase. The fact that 2,5,6-triamino-4-pyrimidone and 5-benzylamino-2,6-diamino-4-pyrimidone also can function as cofactors for phenylalanine hydroxylase and that both compounds are cleaved to an oxidized pyrimidine and an amine (*15*) gives some support for the ring cleavage mechanism (**II** → **III** → **IV**, Scheme II).

Unfortunately, very little experimental evidence supports the

Published on June 1, 1982 on http://pubs.acs.org | doi: 10.1021/ba-1982-0201.ch020

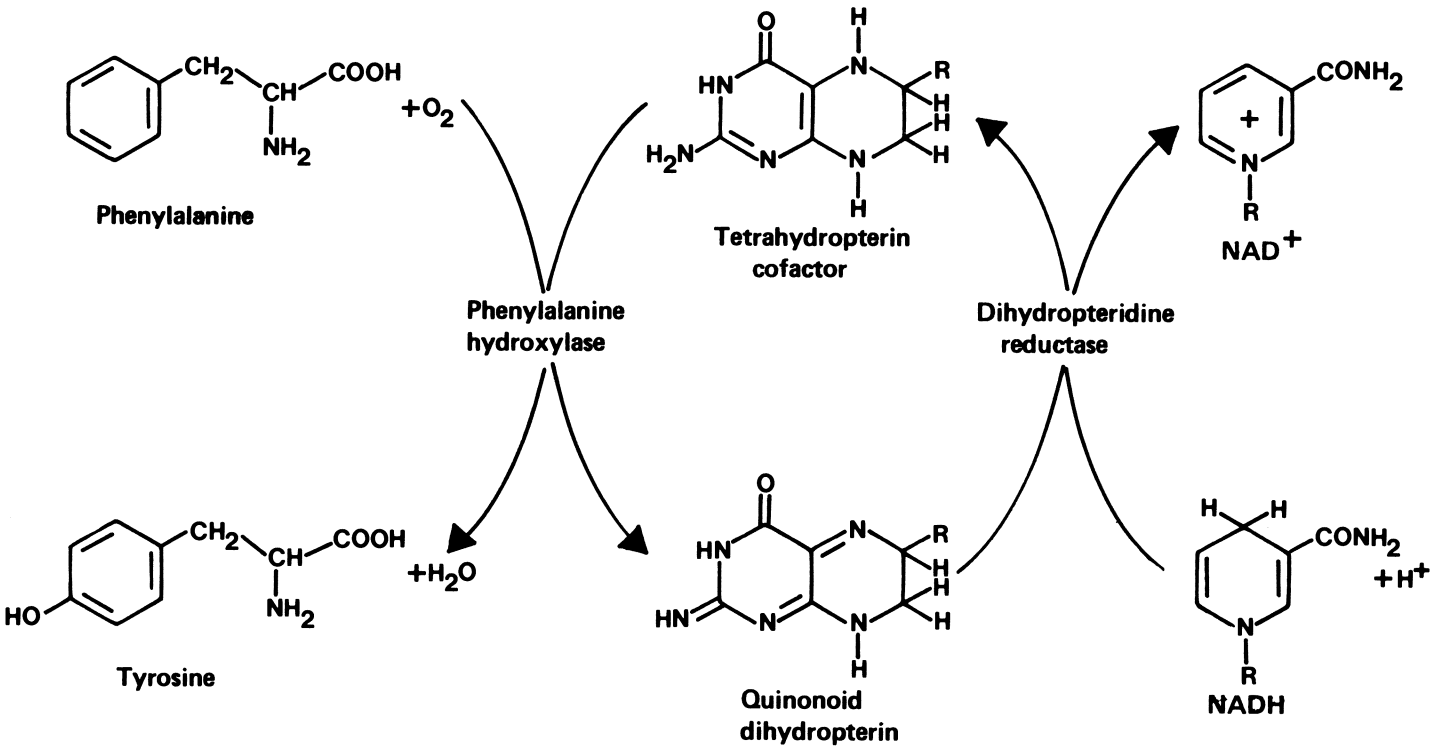

Scheme I

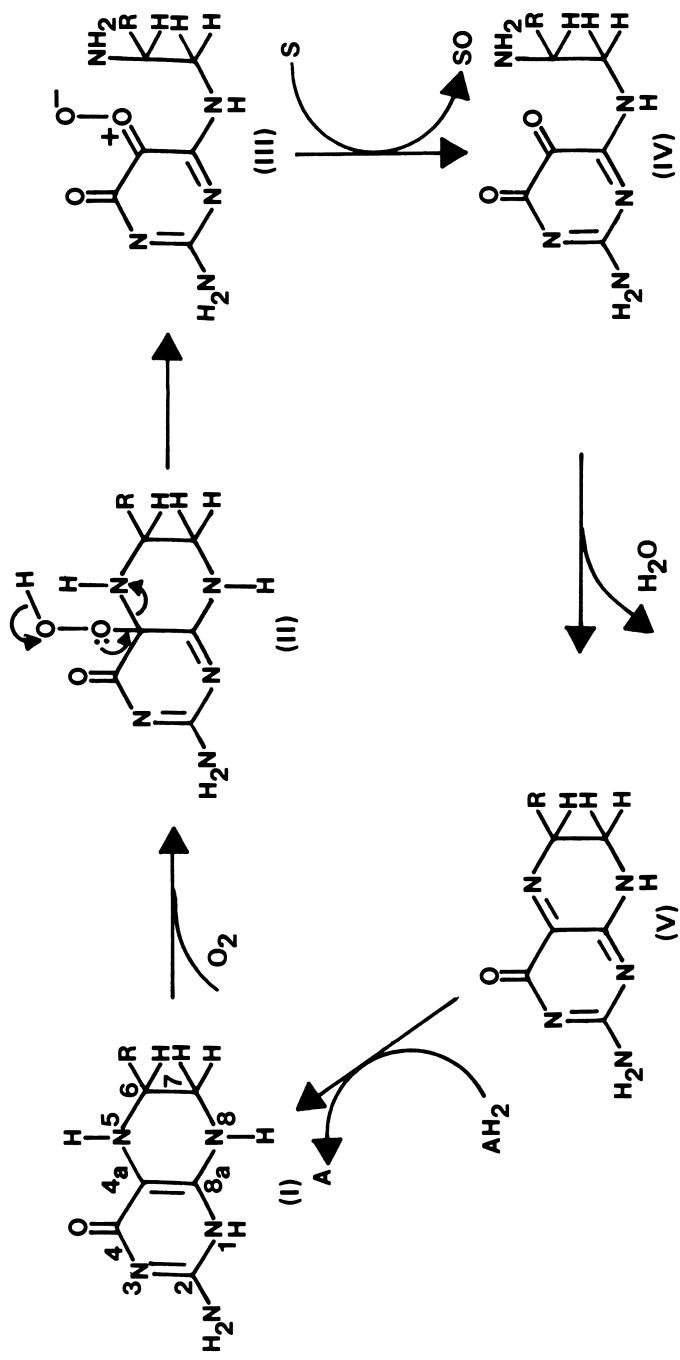

Scheme II

existence of the intermediate species proposed in Scheme II or indeed in the other reaction mechanisms proposed (*4–14*). Kaufman (*7*) detected a transient intermediate (λ_{max} = 250 and 290 nm) during hydroxylation of phenylalanine at pH 8–8.2 in the presence of low concentrations of tetrahydrobiopterin and high hydroxylase concentrations (*7–9*). This intermediate was proposed to be a 4*a*,5-hydrate (**2**).

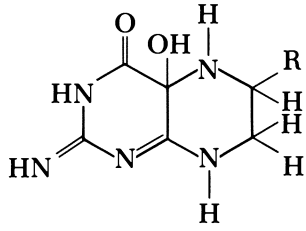

2

However, other mechanisms have not found it necessary to invoke such an intermediate (e.g., Scheme II). Furthermore, the spectrally distinct intermediate noted by Kaufman (*7–9*) apparently can be observed only when tetrahydrobiopterin is the cofactor, not when other pseudo-cofactors are employed.

Loss of amine from pyrimidine cofactors (*15*) is consistent with the ring opening reaction of the pterin cofactors noted in Scheme II. However, no direct evidence supports the existence of a ring-opened intermediate or, in fact, any oxygenated intermediate. Furthermore, fragmentation of pyrimidine cofactors is not proof of a specific activated oxygen reagent such as vinylogous ozone [(*15*) Scheme II].

Mechanisms have been proposed for the autooxidation of tetrahydrobiopterin and tetrahydrofolic acid that involve the intermediacy of radical species rather than hydroperoxides (*11–13*). Radicals also were reported as intermediates in chemical oxidations of tetrahydropterins with H_2O_2 in trifluoroacetic acid (*16*) or iodine in alcohol (*17*).

Quinonoid-dihydropterins have been proposed as the initial, unstable dihydro products of chemical oxidation of tetrahydropterins (*18–21*). Archer and Scrimgeour (*18*), for example, oxidized 6,7-dimethyl-5,6,7,8-tetrahydropterin with ferricyanide and proposed that the corresponding quinonoid-dihydropterin is formed.

Investigators reported (*22*) that 5,6,7,8-tetrahydropterin and its 6-methyl and 6,7-dimethyl derivatives give a single polarographic oxidation wave at the dropping mercury electrode (DME), which is claimed to proceed by an *EE* mechanism, the first step being a one-electron reaction to a cation radical that is oxidized further ($-1e$, $-2H^+$) to quinonoid-dihydropterin. A few cyclic voltammetric exper-

iments at a mercury electrode at pH 9 showed that some tetrahydropterins give quasi-reversible couples and the oxidation peak was presumed to be a $2e$–$2H^+$ reaction to give quinonoid-dihydropterin (*19*). Tetrahydrofolic acid was reported to be oxidized polarographically at pH 6.8 in a $1e$–$1H^+$ reaction to a neutral radical that can either dimerize or undergo additional electrooxidation to quinonoid-dihydrofolic acid, which can rearrange to 7,8-dihydropterin accompanied by side chain cleavage (*23*, *24*).

The available evidence suggests that an unstable quinonoid-dihydropterin intermediate is formed during enzymic, chemical, and electrochemical oxidation of tetrahydropterins. This two-electron deficient compound is unstable and rapidly rearranges to the corresponding 7,8-dihydropterin (*18*).

A careful review of the reported work on the enzymic oxidation of the aromatic amino acids reveals that the role of the tetrahydropterin cofactor is not really understood. Furthermore, a number of clinical and chemical observations cannot be reconciled with any of the proposed mechanistic schemes. For example, recent reports showed that elevated levels of a pterin, believed to be 7,8-dihydroxanthopterin (**3**), were demonstrated in the urine of patients suffering from phenylketonuria[1] (PKU) and with dihydropteridine reductase deficiency (*25*, *26*). Also, autoxidation (*27*) of tetrahydrobiopterin at pH 7.5, and chemical oxidation of tetrahydrofolic acid (*28*) give 7,8-dihydroxanthopterin. The origin of the latter compound cannot be rationalized on the basis of the known chemistry of tetrahydrobiopterin or tetrahydrofolic acid.

Conventional studies of the enzymic hydroxylation reactions that utilize tetrahydropterin cofactors, and chemical and simple polarographic studies of the oxidations of tetrahydropterins have not provided the required understanding of the chemistry of these cofactor species. Mechanistic Schemes I and II showed that in order to understand the roles of reduced pterins in normal and abnormal biological reactions, one must understand the fundamental redox and related chemistry of these compounds. Accordingly, we initiated an investigation into the redox and related chemistry of biologically significant reduced pterins to understand more clearly the biochemical function of these compounds as cofactors in enzymic hydroxylation and other processes. The first step in this investigation was to study the redox chemistry of 5,6,7,8-tetrahydropterin (THP, **4**), 6-methyl-5,6,7,8-tetrahydropterin (6-MTHP, **5**) and 6,7-dimethyl-5,6,7,8-tetrahydropterin (6,7-DMTHP, **6**) using electrochemical and related methodologies. These compounds are all structurally simpler than the natural cofactor

[1] When phenylalanine hydroxylase is missing, or is present in abnormally low levels, phenylalanine cannot be hydroxylated to tyrosine. This condition results in a form of mental retardation.

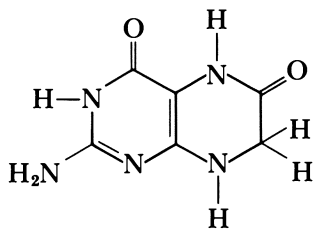

3

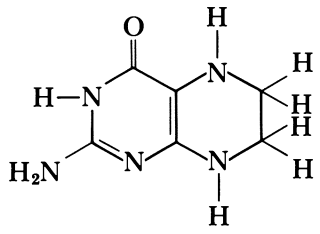

4

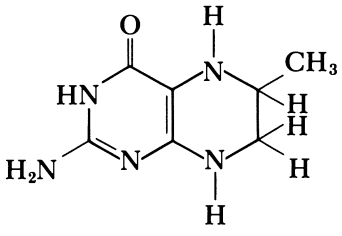

5

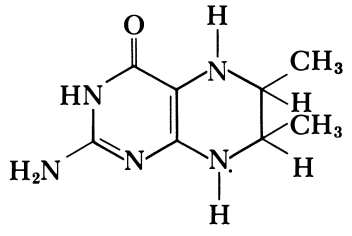

6

tetrahydrobiopterin (**1**), yet all three can function as cofactors[2] for the phenylalanine hydroxylase-catalyzed hydroxylation of phenylalanine (*29*). However, THP leads to formation of only about one-half of the amount of tyrosine formed when tetrahydrobiopterin or the other common pseudo-cofactors are used. This behavior of THP is said to uncouple the enzymic process, that is, to cause formation of H_2O_2 as well as the normal product (*30*).

Experimental

Chemicals. Pterin (2-amino-4-ketopteridine) was obtained from Aldrich. 7,8-Dihydropterin (7,8-DHP) was synthesized using a modification (*31*) of the procedure described elsewhere (*32*). The procedure of Bobst and Viscontini (*33*) was modified slightly (*31*) to prepare THP. The compounds 6-MTHP and 6-methyl-7,8-dihydropterin (6-MDHP) were obtained from Calbiochem. The compound 6,7-DMTHP (monohydrochloride or dihydrochloride) was obtained from Aldrich, and 6,7-dimethyl-7,8-dihydropterin (6,7-DMDHP) was synthesized according to Viscontini (*34*). 6,7-Dimethylpterin (6,7-DMP) was obtained from Sigma, and 7,8-dihydroxanthopterin was prepared by a previously published method (*35*).

Apparatus. Conventional electrochemical equipment was used. Thin-layer spectroelectrochemistry utilized a quartz cell containing an optically transparent reticulated vitreous carbon (RVC) electrode (ca. 0.7-mm thick, 100 pores per inch, Flurocarbon Co.). Atmospheric oxygen was excluded from the thin-layer cell using a modified design of Norris et al. (*36*). Thin-layer spectroelectrochemical experiments utilized Harrick rapid scan spectrometers

[2] They commonly are referred to as pseudo-cofactors.

(Models B and C). All potentials are reported vs. the saturated calomel electrode (SCE) at 25°C. Voltammograms were obtained at a pyrolytic graphite electrode (PGE) having a surface area of about 0.02 cm^2. Unless otherwise stated, experiments were carried out in phosphate buffers having an ionic strength of 0.5 *M*.

Results

The work reported in this chapter is concerned primarily with unsubstituted pterin species, that is, pterin, 7,8-DHP and THP. However, when appropriate, any significant differences between the behavior of the various oxidation states of pterin and the 6-methyl and 6,7-dimethyl derivatives will be noted.

To understand the electrochemistry of THP, one must first understand the behavior of pterin and 7,8-DHP.

Pterin is not oxidized electrochemically at the PGE. However, it does give two well-defined reduction peaks (peaks II_c and III_c, Figure 1A). At least four oxidation peaks (IV_a, D, II_a and III_a, Figure 1A) are observed on the reverse sweep and two new reduction peaks (I_c' and I_c) are observed on the second cathodic sweep. Peaks II_a, III_a, and I_c' will be discussed subsequently under DHP. Peak clipping experiments reveal that oxidation peaks IV_a and D are formed as a result of the reduction peak II_c process (Figure 1B). Peak IV_a increases in height relative to peak II_c with increasing sweep rate. The peak separation between reduction peak II_c and oxidation peak IV_a was 35 ± 10 mV at a sweep rate of 5V/s. This behavior indicates that peaks II_c and IV_a constitute a quasi-reversible redox couple. Scanning through peaks II_c and III_c appears to cause the current for peak D to increase and for quasi-reversible reduction peak I_c to appear (Figure 1C). At low pterin concentrations, oxidation peak D, formed on scanning through peak II_c alone, is small compared to peak II_c; but peak D grows relative to peak II_c with increasing pterin concentration. This result implies that a second-order process is involved in the peak II_c reaction, which generates the species responsible for oxidation peak D.

Attempts to measure coulometric *n*-values on controlled potential reduction of pterin at peak II_c potentials were unsuccessful. Rather large background currents were noted that apparently were related to extensive coating of the electrode surface. The error thus introduced in coulometric measurements was compounded further by the fact that only extremely dilute solutions of pterin could be reduced, owing to its very poor solubility. However, following controlled potential reduction of pterin at peak II_c potentials, the spectrum of the electrolyzed solution (e.g., at pH 7, λ_{max} = 325, 274, and 229 nm) was very similar to that of 7,8-DHP (λ_{max} = 330, 280, and 229 nm). Furthermore, cyclic voltammograms on the electrolyzed solution confirmed the

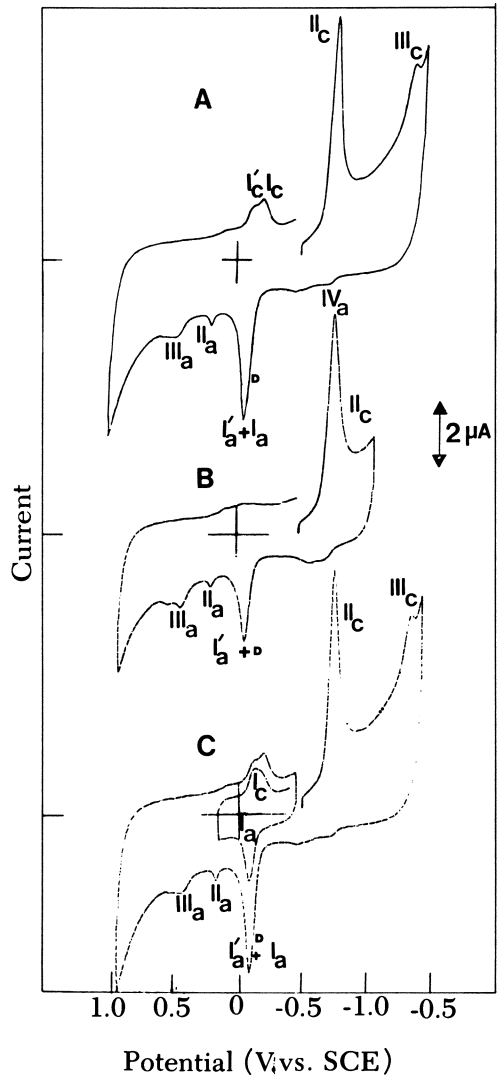

Figure 1. Cyclic voltammograms at the PGE of ca. 0.1 mM pterin in phosphate buffer pH 7.0. Sweep rate: 200 mV/s.

presence of 7,8-DHP, along with small amounts of unreduced pterin, and a species exhibiting an oxidation peak at −0.08 V at pH 7 (i.e., peak D). In several experiments very small oxidation peaks characteristic of 7,8-dihydroxanthopterin (3) also were noted. Isolation and proper characterization of the species formed in the second-order process associated with peak II_c was not possible. However, such a process probably leads to formation of a dimer, in view of the known

tendency of pterins to form such species (*37*, *38*). Combining the information just described with that in the report (*19*) on the electrochemical reduction of 6,7-substituted pterins leads to the conclusion that peak II_c is a $2e$–$2H^+$ reduction of pterin to unstable 5,8-dihydropterin (5,8-DHP, Figure 2). This species is responsible for

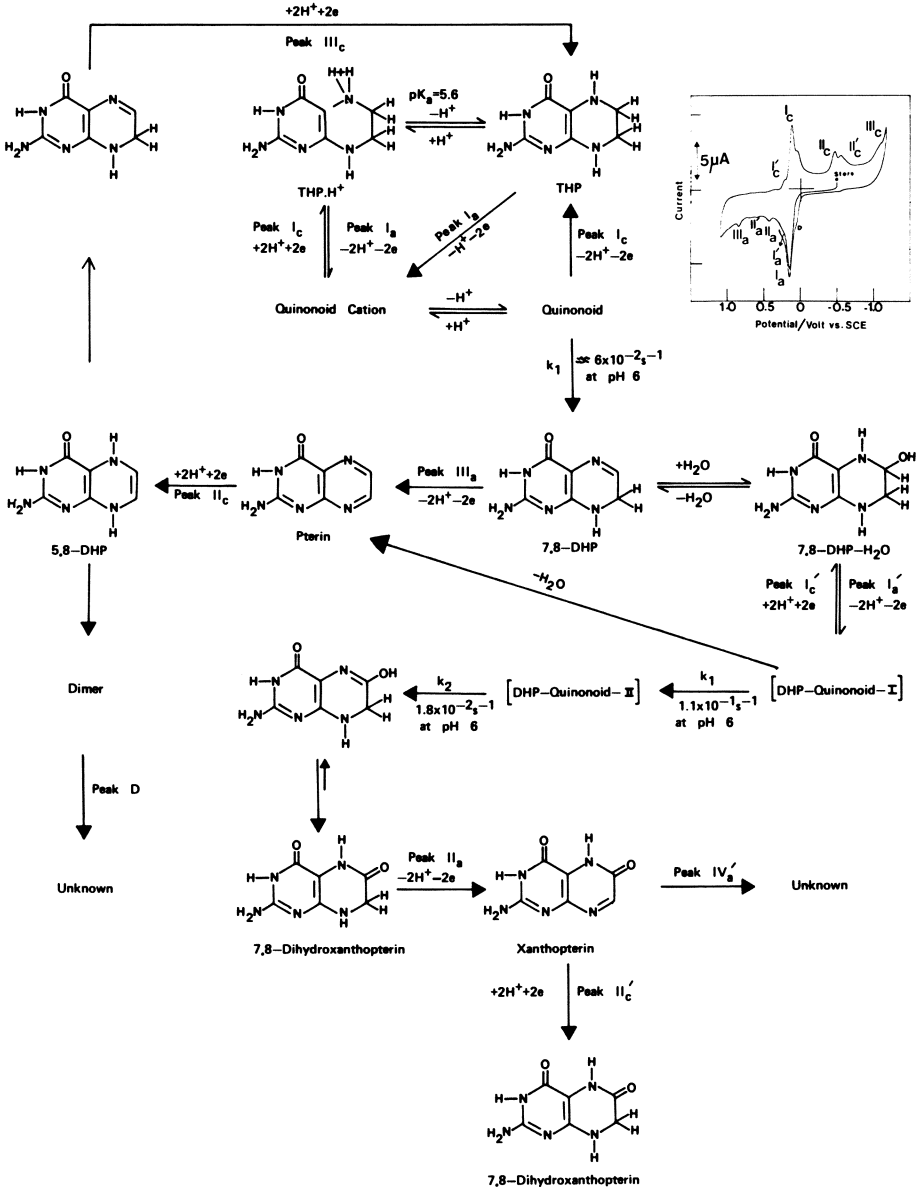

Figure 2. Redox chemistry of pterin, 7,8-DHP, and THP in aqueous solution.

peak IV_a (*see* Figure 1). 5,8-Dihydropterin can rearrange to the more stable 7,8-DHP (Figure 2) or dimerize (or perhaps form some higher molecular aggregate), the dimer species being responsible for oxidation peak D.

6-Methylpterin and 6,7-dimethylpterin gave voltammograms similar to pterin, except that after scanning peak II_c, the dimer oxidation peak D did not appear. Again, however, coulometric experiments on reduction peak II_c did not give meaningful *n*-values.

The electrochemistry of 7,8-DHP is quite complex. Thus, for simplicity, initial discussions will be restricted to the behavior observed at pH 6–7. Linear sweep voltammetry shows that 7,8-DHP exhibits four oxidation peaks at pH 6 (peaks I'_a, II_a, III_a, and IV'_a, Figure 3). At slow sweep rates, peak I'_a is much larger than peak III_a (Figure 3A); but with increasing sweep rate, peak III_a becomes larger than peak I'_a (Figure 3B). Controlled potential coulometry of 7,8-DHP at peak I'_a potentials at pH 6.0 results in the transfer of 2 ± 0.1 electrons per molecule and a precipitate forms in the solution. Voltammetry at positive potentials on the product solution (Figure 4A) revealed that after elimination of peak I'_a, peaks II_a and IV'_a remain, along with some additional very small oxidation peaks and a small reduction peak (IV'_c). This behavior suggests that peaks I'_a and III_a are due to electrooxidation of species that are in some type of equilibrium. Because the heights of peaks II_a and IV'_a are largest at slow sweep rates and are present after controlled potential electrolysis at peak I'_a, they undoubtedly are due to electrooxidation of product generated in the peak I'_a reaction. Voltammetry of the peak I'_a product at negative potentials (Figure 4B) shows the presence of pterin reduction peaks II_c and III_c. The UV spectrum of the peak I'_a oxidation product of 7,8-DHP (λ_{max} = 323, 278, and 228 nm) at pH 6 [λ_{max} = 348 (shoulder), 310, 270, and 220 nm] indicates that a mixture of pterin (λ_{max} = 345, 269, and 230 nm) and another component having a similar spectrum is present. This other component is **3** (λ_{max} = 309, 269, and 220 nm at pH 6). A voltammogram of **3** at pH 6 is presented in Figure 5 that is clearly identical to the product of peak I'_a electrooxidation of 7,8-DHP (Figure 4A). Controlled potential electrooxidation of **3** at peak II_a potentials revealed that the latter peak is a $2e$–$2H^+$ process giving xanthopterin (**7**) in quantitative yield. Utilizing this fact, a coulometric analysis of

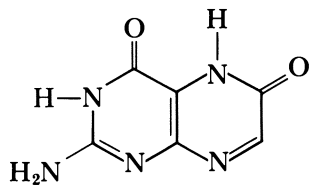

7

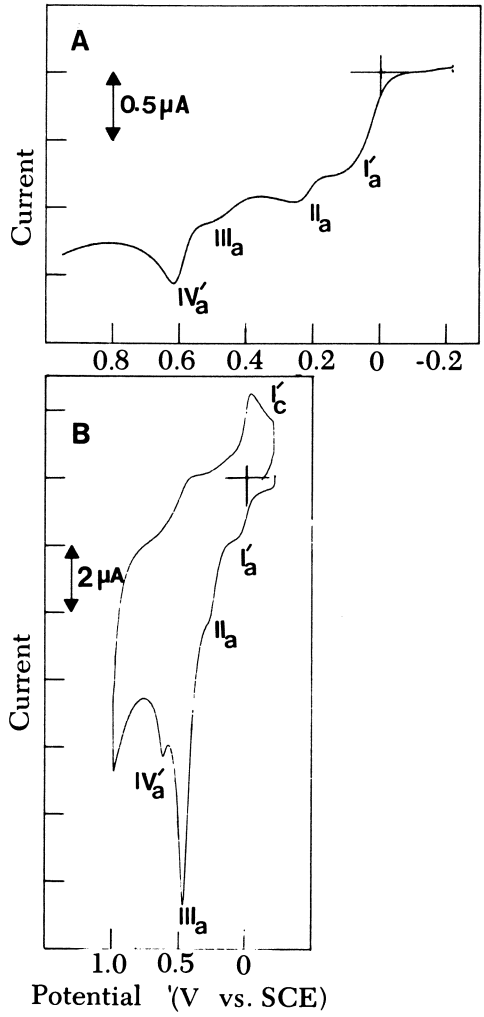

Figure 3. A, Linear sweep (5 mV/s) and B, cyclic (200 mV/s) voltammograms of 0.95 mM 7,8-DHP in phosphate buffer, pH 6.0. Sweeps initiated at −0.2 V toward positive potentials.

the product solution from peak I'_a oxidation of 7,8-DHP was carried out at peak II_a potentials at pH 6, 7, and 8. This analysis revealed that 50 ± 5% of the peak I'_a product is **3**. Thus, the peak I'_a reaction yields a nearly equimolar mixture of pterin (the precipitate formed) and 7,8-dihydroxanthopterin.

For 6-MDHP and 6,7-DMDHP, only two voltammetric oxidation peaks are observed corresponding to peaks I'_a and III_a of 7,8-DHP (*see* Figure 3). Controlled potential coulometry of 6-MDHP and 6,7-

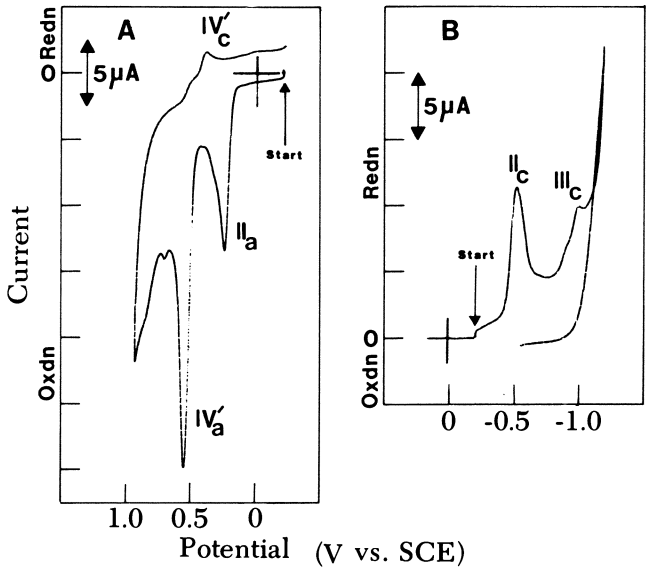

Figure 4. Voltammograms at the PGE of the product mixture obtained after controlled potential electrooxidation of 0.82 mM 7,8-DHP at peak I'_a potentials (0.10 V) in phosphate buffer, pH 6.0. A, Voltammetry at positive potentials and B, voltammetry at negative potentials. Sweep rate: 200 mV/s.

DMDHP at peak I'_a potentials showed it to be a two-electron process with 6-methylpterin and 6,7-dimethylpterin, respectively, being the sole products. Electrolysis at peak I'_a potentials of 6-MDHP and 6,7-DMDHP always resulted in the loss of peak III_a.

The variation of the peak potentials with pH for the voltammetric oxidation peaks of 7,8-DHP, 6-MDHP, and 6,7-DMDHP are shown in Table I. Voltammetry of 7,8-DHP below pH 5.2 revealed that, even under an atmosphere of nitrogen in a deoxygenated solution, the height of peak I'_a slowly decreased and a new oxidation peak grew at more negative potentials. This behavior indicates that 7,8-DHP slowly decomposes to more easily oxidized species. The identity of this species is not known. Because of this effect, detailed studies of the redox chemistry of 7,8-DHP were restricted to pH values above 5.2. Compounds 6-MDHP and 6,7-DMDHP did not show this effect.

Linear sweep and cyclic voltammetry of 7,8-DHP, 6-MDHP, and 6,7-DMDHP revealed that peak I'_a became larger and peak III_a smaller with decreasing pH. Comparison of the cyclic voltammogram of 7,8-DHP at pH 3.4 (Figure 6) with that at pH 6.0 (Figure 3B) illustrates this effect. For 7,8-DHP, peak IV'_a, which is due to electrooxidation of **7** (by comparison with the authentic material) formed in the peak II_a reaction is masked by background current. The new peak

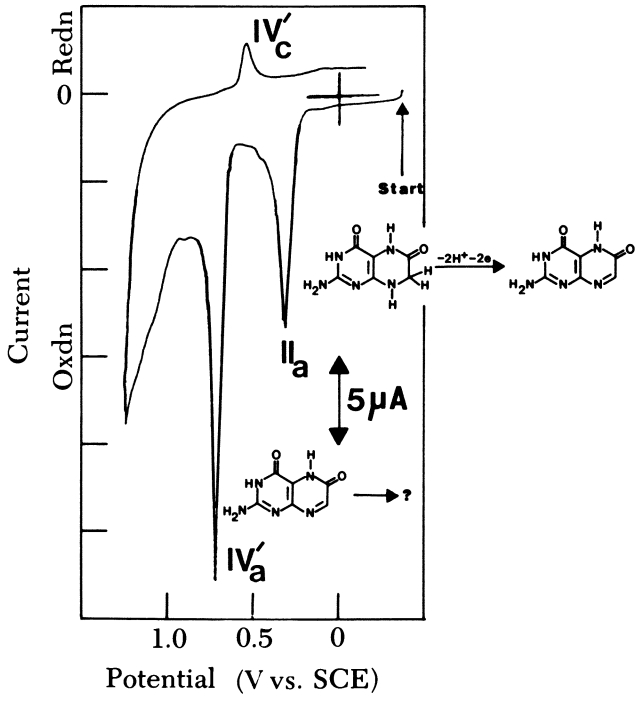

Figure 5. Voltammogram at the PGE of 0.5 mM 7,8-dihydroxanthopterin in phosphate buffer, pH 6.0. Sweep rate: 200 mV/s.

(peak II'_a, Figure 6) that appears at low pH probably is due to a protonated species (*see* later discussion).

Cyclic voltammograms of 7,8-DHP (Figures 3B and 6), 6-MDHP, and 6,7-DMDHP reveal that oxidation peak I'_a gives rise to a product responsible for quasi-reversible peak I'_c. The height of the latter peak grows relative to peak I'_a with increasing sweep rate, indicating that the peak I'_a process gives rise to a reducible, but unstable, product. If the first sweep at a clean PGE is toward negative potentials, then all 7,8-dihydropterins give only reduction peak III_c (Figure 7A). However, on the reverse sweep a large reversible redox couple (peaks I_a and I_c) appears. These peaks occur at very slightly different potentials to peaks I'_a and I'_c and are in fact characteristic of the 5,6,7,8-tetrahydropterins. Peak III_c of the 7,8-dihydropterins is therefore due to a $2e$–$2H^+$ electroreduction to the corresponding 5,6,7,8-tetrahydropterin.

After scanning the four oxidation peaks of 7,8-DHP, not only are peaks I'_c and III_c observed on the reverse cycle (Figure 7B) but also two overlapping reduction peaks (peaks II_c and II'_c) are observed. Peak clipping experiments reveal that the species responsible for peak II_c

(i.e., pterin) is formed in both the peak I'_a and peak III_a oxidations, and the species responsible for peak II'_c is formed in the peak II_a process. Peak II_a, as noted previously, is due to oxidation of **3** to **7**. Experiments with authentic **7** reveal that it gives rise to reduction peak II'_c, and showed that the peak II'_c process is a $2e$–$2H^+$ reduction to give **3**. The 6-methyl and 6,7-dimethyl substituted dihydropterins do not give peaks II_a, IV'_a, and II'_c.

Cyclic voltammetry of the 7,8-dihydropterins clearly indicates that the peak I'_a electrooxidation yields an unstable product that is responsible for peak I'_c. For 7,8-DHP, this product decomposes to a mixture of pterin and **3**; for 6-MDHP and 6,7-DMDHP, the peak I'_a product decomposes to the corresponding pterin. The nature of these decomposition reactions was investigated by thin-layer spectroelectrochemistry. Some representative results obtained at pH 7 for 7,8-DHP are presented in Figure 8. Curve 1 in Figure 8A is the spectrum of 7,8-DHP (λ_{max} = 330, 280, and 230 nm). Initiation of the peak I'_a electrooxidation causes the bands at 280 and 230 nm to decrease and the band at 330 nm to increase and to shift to about 320 nm. After about a 100-s electrolysis, the spectrum shown in Curve 2 of Figure 8A was

Table I. Peak Potential vs. pH Relationships for the Voltammetric Oxidation Peaks of 7,8-Dihydropterins Observed at the PGE

Peak	*pH Range*[a]	E_p/V *vs. SCE*[b]
	7,8-DHP[c]	
I'_a	2–10	0.330–0.042
II_a	2–10	0.510–0.044
III_a	2–10	0.805–0.045
IV'_a	5.2–8[d]	0.880–0.042
	6-MDHP[e,f]	
I'_a	2–6	0.400–0.045
III_a	2–11	0.740–0.049
	6,7-DMDHP[f,g]	
I'_a	2–5	0.48–0.054
III_a	2–5	0.86–0.076
	5–9.3	0.66–0.023
	9.3–11.6	1.35–0.092

[a] All data obtained in phosphate buffers having an ionic strength of 0.5 *M*.
[b] Obtained at a sweep rate of 5 mV/s.
[c] 7,8-Dihydropterin.
[d] Below pH 5.2, peak IV'_a is masked by the background discharge current; and above pH 8, it merges with the decaying portion of peak III_a.
[e] 6-Methyl-7,8-dihydropterin.
[f] Additional peaks at more positive potentials due to the electrooxidation of the pterin derivative(s) are observed.
[g] 6,7-Dimethyl-7,8-dihydropterin.

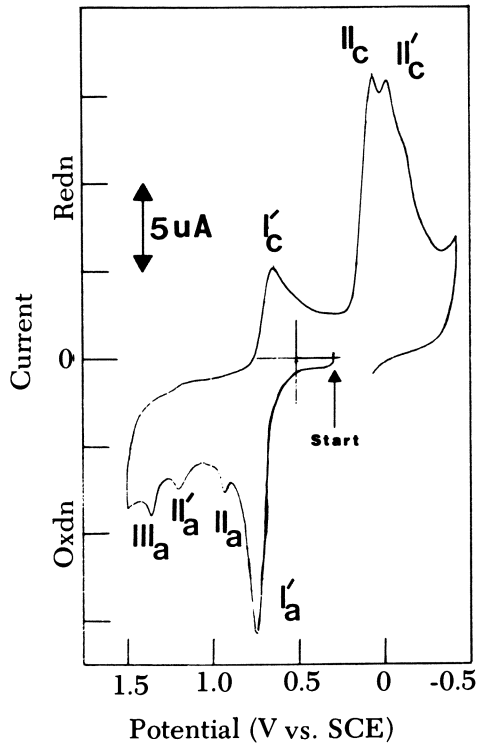

Figure 6. Cyclic voltammogram at the PGE of 0.95 mM 7,8-DHP in phosphate buffer pH 3.4. Sweep rate: 200 mV/s.

observed. Termination of the electrolysis at this point shows the spectrum of an intermediate (λ_{max} = 320, 280, and 228 nm). With time, the spectral changes between Curves 3 and 4 in Figure 8B take place, that is, the two short wavelength bands grow and shift to slightly shorter wavelengths (λ_{max} = 276 and 226 nm) and the long wavelength band decreases very slightly. Curve 4 in Figure 8B is the spectrum of the end product and is that expected for a mixture of pterin (λ_{max} = 336, 267, and 227 nm), **3** (λ_{max} = 309, 274, and 220 nm), and a small amount of unoxidized 7,8-DHP. Similar behavior was noted on electrooxidation of 6-MDHP and 6,7-DMDHP at peak I'_a potentials, except that the product spectrum was identical to the spectrum of the corresponding pterin species. The kinetics of the conversion of the intermediate species to the end products was studied by monitoring absorbance vs. time (*A* vs. *t*) changes of the type shown in Figure 8B but at fixed wavelengths. A typical *A* vs. *t* plot is shown in Figure 9. At 225 nm, initiation of the electrooxidation causes the absorbance to decrease. After terminating the electrolysis, the absorbance continues to de-

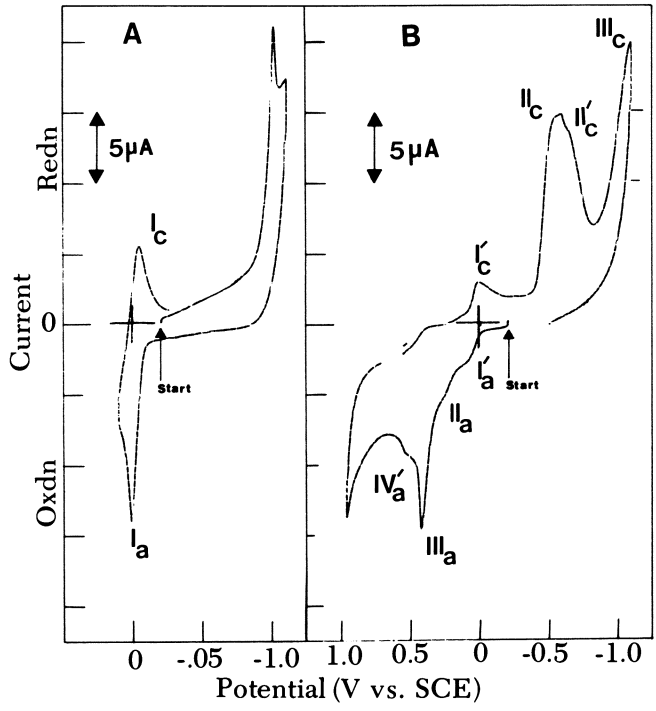

Figure 7. Cyclic voltammograms at the PGE of 0.82 mM 7,8-DHP in phosphate buffer pH 6.0. Sweep rate: 200 mV/s. Initial sweep A, toward negative potentials and B, toward positive potentials.

crease for 10–20 s and then increases. This behavior suggests that two intermediate species are formed: one that decays with a decrease in absorbance to another species, which subsequently decays with an increase of absorbance. The simplest kinetic scheme for such a process is shown in Equation 1.

$$\text{7,8-DHP} \xrightarrow{-2e-2H^+} [\text{intermediate}]_1 \xrightarrow{k_1} [\text{intermediate}]_2 \quad (1)$$
$$\downarrow k_2$$
$$\text{product}$$

A vs. t results were fitted by a nonlinear-least-squares program (*39*) to calculate k_1 and k_2[3], which are first-order rate constants (results shown in Table II). For the electrooxidation of 7,8-DHP at peak I'_a potentials, two products are formed, pterin and **3**. Thus, the mechanism must be more complex for this compound than that shown in Equation 1. Two

[3] Our computational program utilizes an optimizing routine written by E. Enwall incorporating an algorithm of D. W. Marquardt (*39*).

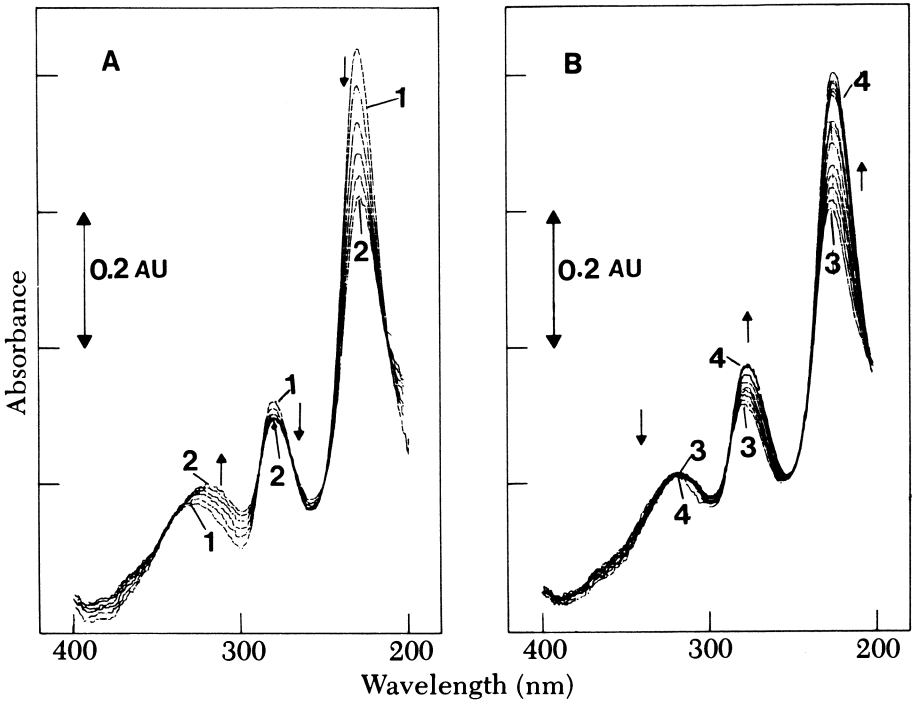

Figure 8. Spectra of 0.46 mM 7,8-DHP in phosphate buffer, pH 7.0, electrolyzing in a thin-layer cell containing an optically transparent RVC electrode. A: Curve 1 is the spectrum of 7,8-DHP; Curve 2 is the spectrum observed after electrolysis for 100 s at Peak I'_a (0.10 V). B: Curve 3 is the spectrum when the electrolysis is terminated; Curve 4 is the spectrum after decay of the intermediate species. Each sweep has a duration of 18.9 s with virtually no time interval between repetitive sweeps.

possible alternative routes are shown in Equations 2a and b. Unfortunately, analysis of A vs. t data does not determine which of these schemes is applicable. However, because both products are formed in almost equal yields, in Equation 2a, k_1 must be almost equal to k_3; yet in Equation 2b, k_2 must equal k_3.

$$\text{7,8-DHP} \xrightarrow{-2H^+,-2e} [\text{intermediate}]_1 \xrightarrow{k_1} [\text{intermediate}]_2 \xrightarrow{k_2} (\text{product})_2 \quad \text{(a)}$$
$$\downarrow k_3$$
$$(\text{product})_1$$

$$\text{7,8-DHP} \xrightarrow{-2H^+,-2e} [\text{intermediate}]_1 \xrightarrow{k_1} [\text{intermediate}]_2 \quad \text{(2)}$$
$$\nearrow k_2 \quad \text{(product)}_1$$
$$\searrow k_3 \quad \text{(product)}_2 \quad \text{(b)}$$

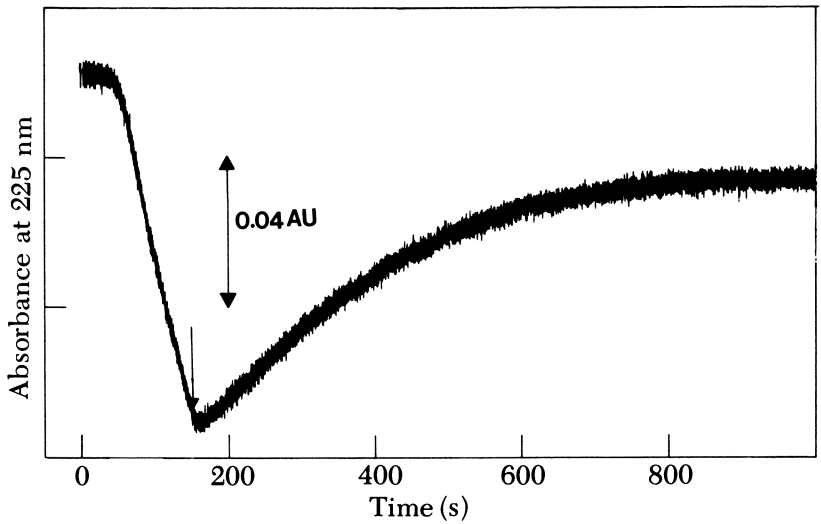

Figure 9. Absorbance vs. time curve observed during, and after, electrooxidation of 0.5 mM 7,8-DHP in phosphate buffer, pH 6.0, at peak I'_a in a thin-layer cell containing a RVC electrode. The arrow indicates when the electrolysis was terminated.

Table II. First-Order Rate Constants Observed for Decay of Intermediates Generated on Electrooxidation of 7,8-Dihydropterins at Peak I'_a Potentials in a Thin-Layer Cell[a]

pH[b]	λ/*nm*[c]	$k_1 \times 10^2/s^{-1}$[d]	$k_2 \times 10^2/s^{-1}$[d]
		7,8-DHP[e]	
5.20	225	7.5 ± 0.5	3.0 ± 0.5
6.00	225	11 ± 5	1.8 ± 0.5
7.00	225	1.0 ± 0.2[f]	
7.95	228	1.0 ± 0.2[f]	
		6,7-DMDHP[g]	
3.0	254	51 ± 0.2	2.9 ± 1.0
4.6	263	55 ± 3	7.0 ± 2.5
5.6	262	33 ± 5	5.4 ± 2.5
6.8	262	36 ± 27	3.7 ± 0.4
7.3	266	106 ± 29	9 ± 3

[a] Containing an optically transparent RVC electrode.
[b] Phosphate buffers having an ionic strength of 0.5 *M*.
[c] Wavelength employed to monitor *A* vs. *t* curve.
[d] *k* Values obtained by fitting *A* vs. *t* data with a nonlinear least-squares program (39).
[e] 7,8-Dihydropterin.
[f] k_1 and k_2 were indistinguishable.
[g] 6,7-Dimethyl-7,8-dihydropterin.

Controlled potential electrooxidation of 7,8-DHP at peak III_a between pH 7 and 9 involved the transfer of 2.5 ± 0.1 electrons per molecule. Voltammetric and spectrophotometric analysis of the product indicated a mixture consisting of 78 ± 6% pterin and 21 ± 6% of **7**. Electrolysis of 6-MDHP and 6,7-DMDHP at peak III_a at pH 2–5 gave *n*-values of 1.9 ± 0.2, with the corresponding pterin as the product.

From these data, we concluded that the redox chemistry of the 7,8-dihydropterins may be rationalized only if the compound exists in aqueous solution in an equilibrium involving a covalently hydrated (7,8-DHP–H_2O, Equation 3) and nonhydrated (7,8-DHP, Equation 3)

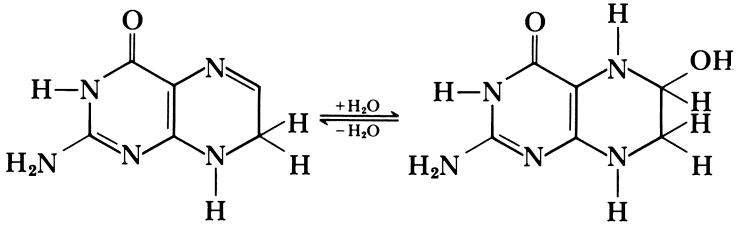

(3)

7,8-DHP **7,8-DHP–H_2O**

forms. Thus peak I'_a is, overall, a $2e$–$2H^+$ quasi-reversible oxidation of the hydrated species to give an unstable quinonoid species. Five tautomeric structures are possible for such a quinonoid (**8–12**). The

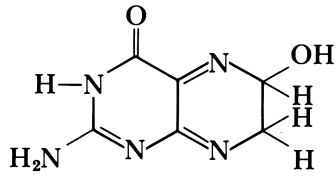

8

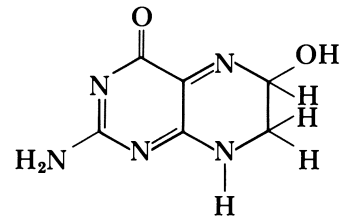

9

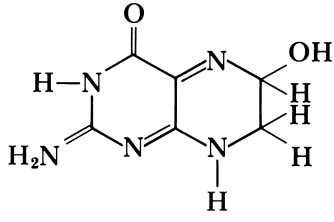

10

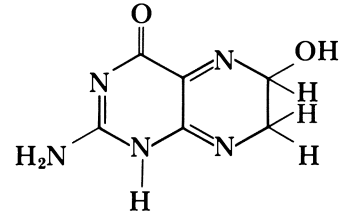

11

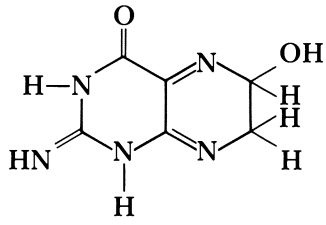

12

actual structure for the primary peak I'_a quinonoid product, which is responsible for peak I'_c in cyclic voltammetry, is not known. For peak I'_a of 7,8-DHP, the kinetic results support the view that the primary quinonoid product (DHP–quinonoid-I, Figure 2) undergoes a first-order rearrangement to a second, more stable, intermediate, which we suspect is one of the other three quinonoid species (DHP-quinonoid-II, Figure 2). These intermediates decompose to give pterin and 7,8-dihydroxanthopterin, as shown in Figure 2. As noted earlier, peak II_a of 7,8-DHP is due to $2e$–$2H^+$ electrooxidation of the latter species to xanthopterin, which in turn is oxidized further in the peak IV'_a process.

For the peak I'_a process of 6-MDHP and 6,7-DMDHP, it is not possible to form 7,8-dihydroxanthopterin; and hence, following the conversion of quinonoid-I to quinonoid-II, a simple dehydration reaction to the corresponding pterin must occur.

Oxidation peak III_a is a $2e$–$2H^+$ irreversible oxidation of the nonhydrated 7,8-dihydropterin species to give pterin, as shown in Figure 2.

In the cyclic voltammetry of 7,8-DHP, **7** is formed in the peak II_a reaction; and hence, peak II'_c appears on the reverse cycle (Figure 7B). Peak II'_a, which appears only at low pH, probably is due to electrooxidation of a protonated form of 7,8-DHP–H_2O.

Linear sweep voltammetry of THP, 6-MTHP, and 6,7-DMTHP at the PGE indicated that at least three pH-dependent oxidation peaks are formed (Table III). For 6-MTHP and 6,7-DMTHP, peak IV_a (Table III) results from electrochemical oxidation of 6-methylpterin and 6,7-dimethylpterin (by comparison with the authentic material), respectively, and will not be discussed further. Peak I_a is always the largest peak at slow sweep rates followed, at more positive potentials, by poorly defined peaks II_a and III_a (Figure 10A). At sweep rates $\geq$ 100 mV/s for THP, for example, the decay of the peak I_a current follows the time course expected for a simple, diffusion-controlled reaction (Figure 10B). However, at slower sweep rates, the rate of current decay is significantly lower than might be expected for an uncomplicated diffusion-controlled reaction (Figure 10A). This behavior suggests that as a result of the peak I_a reaction, a species is rather slowly generated

Table III. Peak Potential vs. pH Relationships for the Voltammetric Oxidation Peaks of 5,6,7,8-Tetrahydropterins

Peak	*pH Range*[a]	E_p/V *vs. SCE*[b]
	THP[c]	
I_a	3–5.6	0.404–0.073
I_a	5.6–10.8	0.180–0.033
II_a	3–10.0	0.510–0.040
III_a	3–10.8	0.980–0.058
	6-MTHP[d]	
I_a	2–11	0.320–0.056
II_a	2–5	0.420–0.055
III_a	3–11	0.730–0.051
IV_a	3–11	1.62–0.064
	6,7-DMTHP[e]	
I_a	2–11	0.309–0.053
II_a	2–4.1	0.442–0.055
III_a	2–4.1	0.847–0.078
III_a	4.1–10.6	0.630–0.021
IV_a	2–11	1.51–0.052

[a] Phosphate buffers having an ionic strength of 0.5 *M*.
[b] Measured at a sweep rate of 5 mV/s.
[c] 5,6,7,8-Tetrahydropterin.
[d] 6-Methyl-5,6,7,8-tetrahydropterin.
[e] 6,7-Dimethyl-5,6,7,8-tetrahydropterin.

that undergoes further electrooxidation at peak I_a potentials. Hence, the decay of peak I_a, particularly at slow sweep rates, is retarded by electrooxidation of the new species. With THP, sweep rate studies (0.2–50 V/s) show that the peak current function ($i_p/ACv^{1/2}$) for peak I_a is 1620 ± 130 μA cm^{-2} m*M* V$^{-1/2}$s$^{1/2}$, which is close to the value expected for a reversible, two-electron electrode reaction (1700 μA cm^{-2} m*M* V$^{-1/2}$s$^{1/2}$). The latter value was calculated using a value for the diffusion coefficient of THP of 5×10^{-6} cm^2/s.

Cyclic voltammograms of THP (Figure 11) reveal that peak I_a is well defined at a sweep rate of 200 mV/s, yet the other oxidation peaks are rather small. Similar behavior was noted for 6-MTHP and 6,7-DMTHP (Figure 12). The behavior of THP is, however, the most complex and therefore has been studied in greatest detail at this time.

Having scanned the various oxidation peaks of THP, at least four reduction peaks are observed on the reverse cycle (I_c, II_c, II_c', III_c, and sometimes I_c', Figure 11). None of these peaks is observed unless the oxidation peaks are first scanned. Reduction peak I_c forms an almost reversible couple with oxidation peak I_a. At relatively low pH values (e.g., <pH 4.3 for THP, <pH ca. 5 for 6-MTHP, and <pH 4 for 6,7-

DMTHP), an additional couple (peaks I'_a and I'_c, Figures 11A and 12A) appears on the first cycle. With THP, oxidation peak D appears on the second cycle.

Peak I_c decreases relative to peak I_a with decreasing sweep rate for all tetrahydropterins, indicating that the primary peak I_a product is unstable and undergoes a chemical follow-up reaction.

Controlled potential coulometric oxidation of THP at peak III_a potentials at pH 7 indicated that four (3.8 ± 0.2) electrons per molecule are transferred. Voltammetry and spectral analysis of the product revealed that THP is converted almost quantitatively (>90%) to pterin. Compounds 6-MTHP and 6,7-DMTHP exhibited almost identical behavior. Coulometry on the rising portion of peak I_a for all tetrahydropterins studied indicated that 2 ± 0.3 electrons per molecule were transferred. Voltammetry and UV spectroscopy of the product revealed

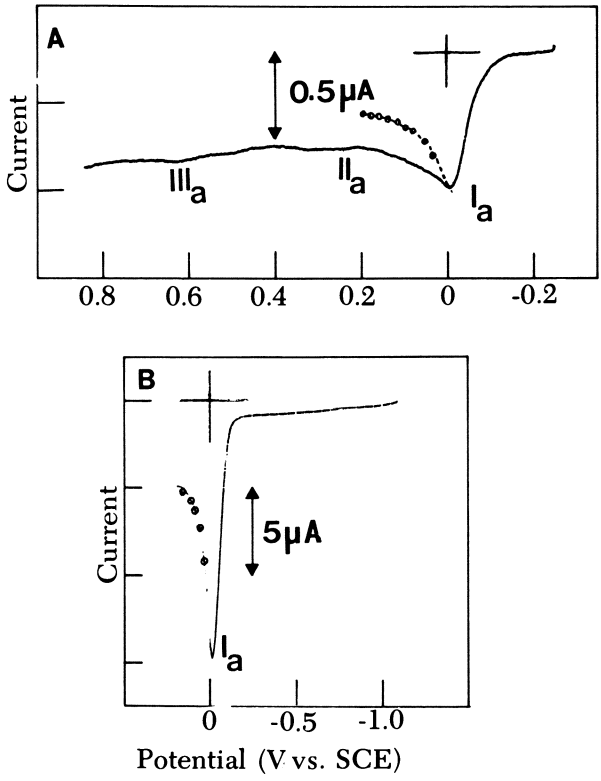

Figure 10. Voltammograms at the PGE of 0.53 mM THP in phosphate buffer, pH 5.85, at sweep rates of A, 5 mV/s and B, 200 mV/s. Points show i–t decay calculated from the Cottrell equation.

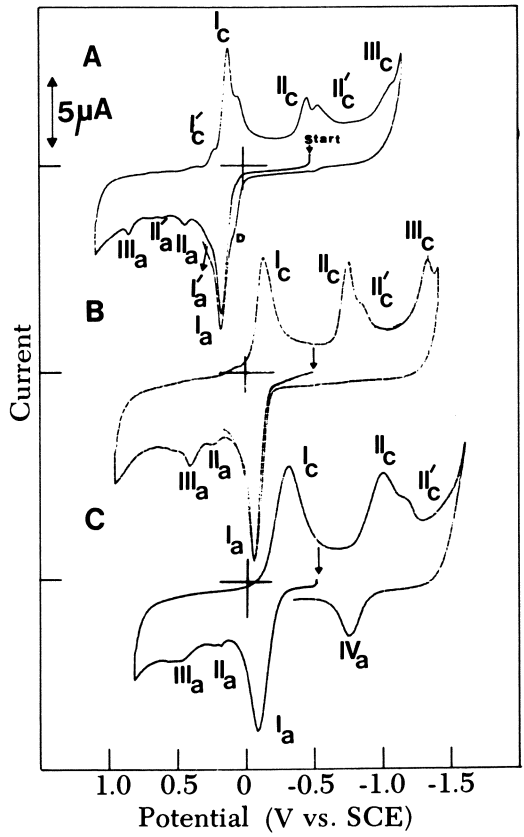

Figure 11. Cyclic voltammograms at the PGE of 0.54 mM THP in phosphate buffers at pH 3.4 (A), 7.05 (B), and 9.98 (C). Sweep rate: 200 mV/s.

that the corresponding 7,8-dihydropterin was formed. However, electrooxidation at, or slightly positive, of peak I_a potentials at around pH 3 resulted in formation of a mixture of pterin and 3. The other two tetrahydropterins gave the corresponding pterins.

Because cyclic voltammetry of all tetrahydropterins (Figures 11 and 12) indicated that the peak I_a reaction gives an unstable intermediate, thin-layer spectroelectrochemical experiments were carried out.

Figure 13A shows the spectrum of THP at pH 7 (λ_{max} = 300 and 220 nm) in a thin-layer cell. Curve 1 in Figure 13B is the spectrum obtained a few seconds after initiating the electrolysis, and Curve 2 is the spectrum about 55 s later. Thus, on electrolysis, the THP band at 220 nm decreases and shifts to longer wavelengths, and the band at 300 nm shifts to shorter wavelengths. After scanning Curve 2 (Figure 13B), the electrolysis was terminated and the spectral changes

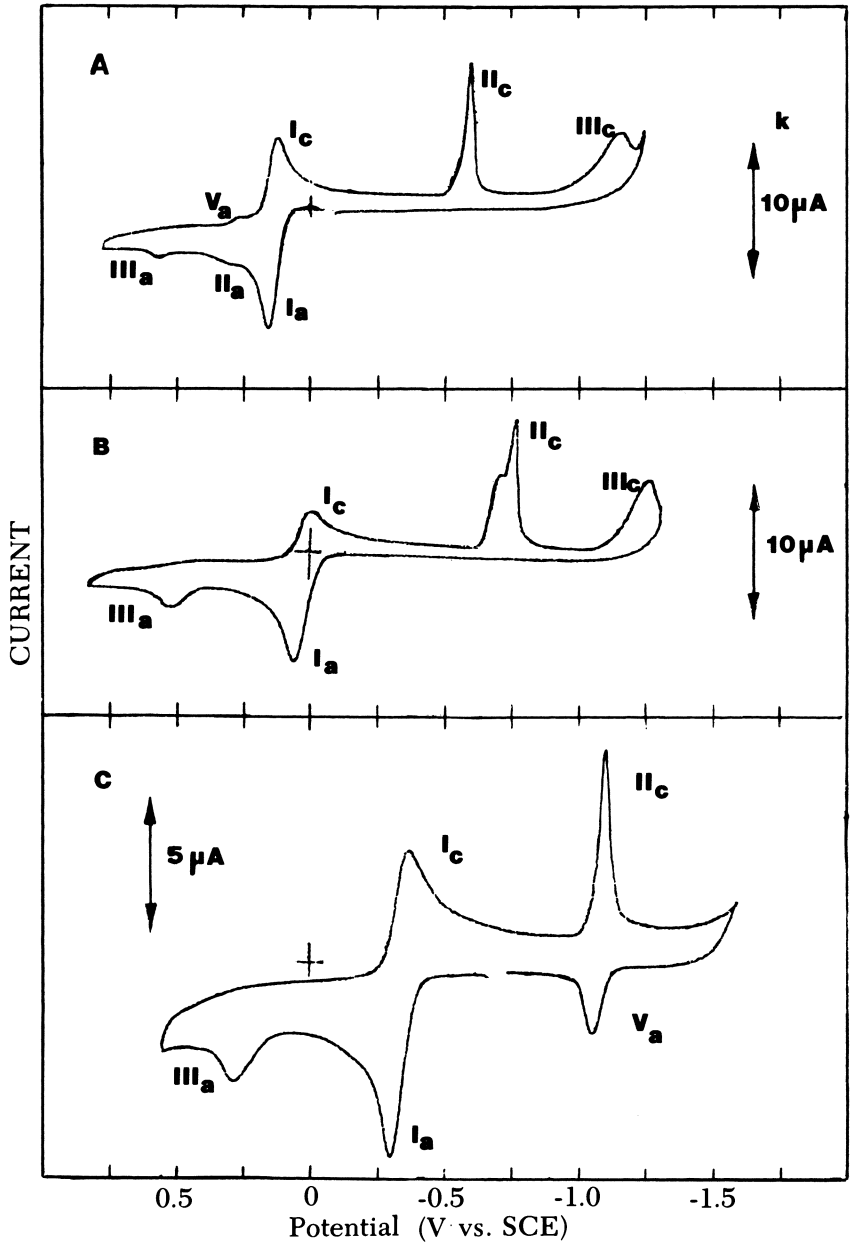

Figure 12. Cyclic voltammograms at the PGE of 1.1 mM 6,7-DMTHP in phosphate buffers at pH 3.1 (A), 5.0 (B), and 11.0 (C). Sweep rate: 50 mV/s.

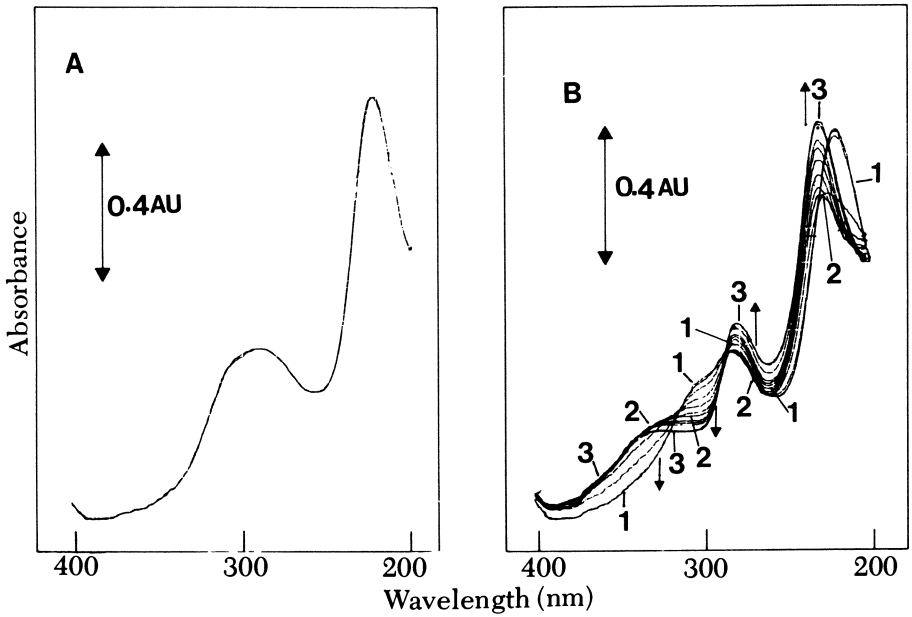

Figure 13. Spectra of 0.6 mM THP in phosphate buffer, pH 7, electrolyzing on the rising portion of peak I_a in a thin-layer cell containing a RVC electrode. A: spectrum of THP. B: Curve 1 is the spectrum a few seconds after initiation of the electrolysis; Curve 2 is the spectrum after 55 s electrolysis; Curve 3 is the spectrum after complete decay of the intermediate and corresponds to 7,8-DHP. In B, each scan was 18.8 s, with no significant interval between scans.

shown between Curves 2 and 3 were observed. Thus, the peaks at 230 and 281 nm grow while the absorbance around 330 nm decreases. The arrows in Figure 13B point in the direction of the latter absorbance changes. Curve 3 is the spectrum of the final product (λ_{max} = 332, 281, and 232 nm), which is close to that expected for 7,8-DHP. Clearly, an unstable intermediate is formed that spontaneously decomposes into 7,8-DHP. The kinetics of this transformation were studied by monitoring either the decay of the UV absorbance of the intermediate or the increase in product absorbance with time. At all pH values studied, this process was first order. Similar behavior was observed on electrochemical oxidation of 6-MTHP and 6,7-DMTHP. Values of the observed rate constants are presented in Table IV. The experimental rate constant was independent of concentration for initial THP concentrations ranging from 0.3 to 3 m*M*. Table IV shows that a bell-shaped relationship between k_{obs} and pH occurs for all three tetrahydropterins, with k_{obs} being maximal at pH 5.6–6.0. The latter fact suggests that $H_2PO_4^-$ catalyzes the chemical follow-up reaction. Indeed, experi-

Table IV. Observed First-Order Rate Constants for the Chemical Reaction of the Intermediate Species Generated on Electrochemical Oxidation of Tetrahydropterins at Peak I_a

pH[a]	$k_{obs} \times 10^2/s^{-1}$[b]
	THP[c]
3.1	2.5
4.1	2.7
5.1	4.3
5.6	5.5
5.9	5.5
6.4	2.9
7.0	1.8
8.4	0.7
	6-MTHP[d]
1.98	1.1
3.10	1.2
3.96	1.7
4.58	1.5
5.60	3.5
6.02	2.9
6.95	1.2
8.05	0.3
9.30	0.3
9.85	0.2
	6,7-DMTHP[e]
2.0	1.4
3.1	2.3
4.0	2.9
4.6	3.0
5.6	4.3
6.0	4.8
6.8	2.0
7.0	1.8
8.0	0.7
9.3	0.5

Note: Electrolysis carried out in a thin-layer cell containing an optically transparent RVC electrode.

[a] Phosphate buffers having an ionic strength of 0.5 *M*.

[b] Mean of at least three replicate determinations.

[c] 5,6,7,8-Tetrahydropterin.

[d] 6-Methyl-5,6,7,8-tetrahydropterin.

[e] 6,7-Dimethyl-5,6,7,8-tetrahydropterin.

ments reveal that for $H_2PO_4^-$ concentrations ranging from 0.04 to 0.4 *M* in pH 5.45 solutions maintained at a constant ionic strength of 2.0 *M* with $NaClO_4$, the value of k_{obs} measured following oxidation of THP increases systematically from 0.69×10^{-2} to 3.5×10^{-2} s^{-1}.

Based on these results, we concluded that peak I_a of the tetrahydropterins is an almost reversible $2e$–$2H^+$ oxidation to give an intermediate quinonoid–dihydropterin (Figure 2). There are five possible structures for such a quinonoid (**13–17**), but insufficient informa-

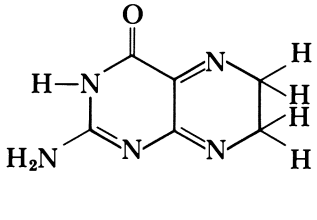

13

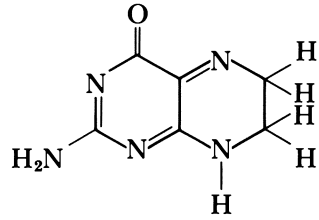

14

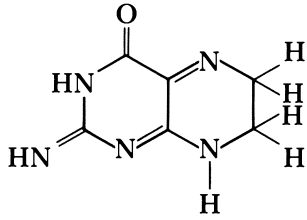

15

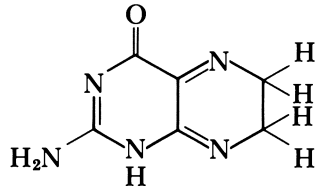

16

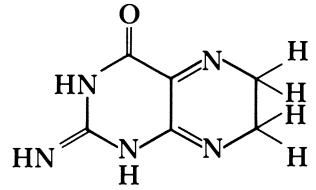

17

tion is available to decide which of these species is preferred. However, the quinonoid intermediate rearranges in a first-order reaction to give the corresponding 7,8-dihydropterin (Figure 2). This compound then partially hydrates to give 7,8-DHP–H_2O, which is oxidized in the peak I_a' process. The latter reaction occurs at potentials very close to peak I_a and accounts for the unusual current decay of voltammetric peak I_a at slow sweep rates (*see* Figure 10A). The chemistry associated with the remainder of the peaks observed on linear and cyclic sweep

voltammetry of THP (I'_a, II_a, II'_a, III_a, IV'_a, I'_c, I_c, II_c, II'_c, III_c, IV_a, and D) and discussed previously are summarized in Figure 2. Peaks II_a, IV'_a, and II'_c are observed only with THP because only for this compound can **3** be formed. Compound **3**, which is responsible for peak II_a, gives **7**, which in turn is oxidized in the peak IV'_a process and reduced at peak II'_c.

Conclusions

The electrochemical and related studies just reported indicate that the redox chemistry of THP, in particular, is quite complex. The initial, quasi-reversible peak I_a process of the tetrahydropterins studied gives an unstable quinonoid of uncertain structure. This two electron-deficient structure then rearranges to the corresponding 7,8-dihydropterin. These investigations of THP, 6-MTHP, and 6,7-DMTHP give no evidence for an initial one-electron reaction giving a radical intermediate, as proposed by others (*22*) on the basis of polarographic studies at a DME.

In conclusion, the 7,8-dihydropterin finally formed as the end product of the peak I_a reaction reacts with water to form an equilibrium mixture of covalently hydrated and nonhydrated species. This hydration reaction clearly is favored in acid solution but for 7,8-DHP, the voltammetric peak corresponding to oxidation of 7,8-DHP–H_2O (peak I'_a) may be observed at pH 7, indicating that the latter species exists to an appreciable extent at around physiological pH. The hydrated forms of the 7,8-dihydropterins are structurally very similar to the tetrahydro compounds (e.g., compare 7,8-DHP–H_2O and THP in Figure 2) and therefore, not surprisingly, are electrooxidized at nearly the same potential as the tetrahydro compounds. This oxidation is also a quasi-reversible $2e$–$2H^+$ reaction giving another unstable quinonoid. The latter putative intermediate undergoes a fast chemical reaction to give a second intermediate, thought to be an isomeric, but more stable, quinonoid. The quinonoids formed from the covalently hydrated forms of 6-MDHP and 6,7-DMDHP rearrange to give the corresponding methylated pterins. However, the quinonoid intermediate generated on peak I'_a oxidation of 7,8-DHP–H_2O breaks down to give a mixture of pterin and 7,8-dihydroxanthopterin. As noted earlier, the latter compound has been found in patients suffering from PKU or a dihydropteridine reductase deficiency (*25, 26*). In addition, tetrahydrobiopterin (**1**) and tetrahydrofolic acid are thought to undergo cleavage at the C(6)–C(1′) bond during oxidation (*11, 40, 41*). Such a reaction should result in the formation of 7,8-DHP and 7,8-DHP–H_2O. The electrochemical results reported in this chapter indicate that the almost reversible oxidation potential of the latter species is very similar to that

of THP. Thus, 7,8-DHP–H_2O quite possibly could function as a cofactor in the aromatic amino acid hydroxylation with the formation of DHP-quinonoid-I/DHP-quinonoid-II intermediates (*see* Figure 2). The latter intermediates may not be reducible by dihydropteridine reductase and, in the case of a deficiency of the latter enzyme, could not be reduced. The result would be the formation of 7,8-dihydroxanthopterin. This proposal is only one scheme to account for the appearance of the latter compound in the urine of patients with PKU or dihydropteridine reductase deficiency and must be regarded as speculative at this time. This fact is particularly true because the detailed redox chemistry of tetrahydrobiopterin, tetrahydrofolic acid, and their 7,8-dihydro derivatives is not known. However, as noted previously (*41*), 7,8-dihydrobiopterin might play an important role in many of the reactions of tetrahydrobiopterin.

Acknowledgments

This work was supported by Grant No. GM–25842–03 from the National Institutes of Health. Additional support was provided by the Research Council of the University of Oklahoma.

Literature Cited

1. Kaufman, S. *Trans. N.Y. Acad. Sci.* **1964,** *26,* 977.
2. Brenneman, A. R.; Kaufman, S. *Biochem. Biophys. Res. Commun.* **1964,** *17,* 1964.
3. Lovenberg, W.; Jequier, E.; Sjoerdsma, A. *Science* **1967,** *155,* 217.
4. Kaufman, S. *Proc. Natl. Acad. Sci. U.S.A.* **1963,** *50,* 1085.
5. Kaufman, S. *J. Biol. Chem.* **1959,** *234,* 2677.
6. Kaufman, S. *J. Biol. Chem.* **1964,** *239,* 332.
7. Kaufman, S. In "Chemistry and Biology of Pteridines"; Pfleiderer, W., Ed.; de Gruyter: Berlin, 1975; pp. 291–304.
8. Huang, C.; Max, E. E.; Kaufman, S. *J. Biol. Chem.* **1973,** *248,* 4233.
9. Kaufman, S. *Adv. Exp. Med. Biol.* **1976,** *74,* 91.
10. Hamilton, G. A. In "Progress in Bioorganic Chemistry"; Kaiser, E. T.; Kézdy, F. J., Eds.; Wiley: New York, 1971; Vol. 1, pp. 141–142.
11. Blair, J. A.; Pearson, A. J. *J. Chem. Soc., Perkin Trans. 2* **1974,** 80.
12. Pearson, A. J. *Chem. Ind. (London)* **1974,** 233.
13. Blair, J. A.; Pearson, A. J.; Robb, A. J. *J. Chem. Soc. Perkin Trans. 2* **1975,** 18.
14. Blair, J. A.; Pearson, A. J. *J. Chem. Soc. Perkin Trans. 2* **1975,** 245.
15. Bailey, S. W.; Ayling, J. E. *J. Biol. Chem.* **1980** *225,* 7774.
16. Ehrenberg, A.; Hemmerich, P.; Müller, F.; Okada, T.; Viscontini, M. *Helv. Chim. Acta* **1967,** *50,* 411.
17. Bobst, A. *Proc. Natl. Acad. Sci. U.S.A.* **1971,** *68,* 541.
18. Archer, M. C.; Scrimgeour, K. G. *Can. J. Biochem.* **1970,** *48,* 278.
19. Kwee, S.; Lund, H. *Biochim. Biophys. Acta* **1973,** *297,* 285.
20. Kaufman, S. *J. Biol. Chem.* **1961,** *236,* 804.
21. Vonderschmitt, D. J.; Scrimgeour, K. G. *Biochem. Biophys. Res. Commun.* **1967,** *28,* 302.
22. Archer, M. C.; Scrimgeour, K. G. *Can. J. Biochem.* **1970,** *48,* 526.
23. Kretzschmar, K.; Jaenicke, W. *Z. Naturforsch. Teil B* **1971,** *26,* 225.

24. Kretzschmar, K.; Jaenicke, W. Z. *Naturforsch. Teil B* **1971,** *26,* 999.
25. Watson, B. M.; Armarego, W. L. F.; Schlesinger, P.; Cotton, R. G. H.; Dauks, D. M. In "Chemistry and Biology of Pteridines"; Kisliuk, R. L.; Brown, G. M., Eds.; Elsevier: New York, 1980; p. 159.
26. Watson, B. M.; Schlesinger, P.; Cotton, R. G. H. *Clin. Chim. Acta* **1977,** *78,* 417.
27. Pfleiderer, W. In "Chemistry and Biology of Pteridines"; Kisliuk, R. L.; Brown, G. M., Eds.; Elsevier: New York, 1980; p. 941.
28. Chippel, D.; Scrimgeour, K. G. *Can. J. Biochem.* **1970,** *48,* 999.
29. Ayling, J. E.; Boehm, G. R.; Textor, S. C.; Pirson, R. A. *Biochemistry* **1973,** *12,* 2045.
30. Storm, C. B.; Kaufman, S. *Biochem. Biophys. Res. Commun.* **1968,** *32,* 788.
31. Raghavan, R.; Dryhurst, G., *J. Electroanal. Chem.* **1981,** *129,* 189.
32. Stuart, A.; Wood, H. C. S.; Duncan, D. *J. Chem. Soc. C* **1966,** 285.
33. Bobst, A.; Viscontini, A. *Helv. Chim. Acta* **1966,** *49,* 875.
34. Viscontini, M. *Methods Enzymol.* **1971,** *18B,* 678.
35. Stuart, A.; West, D. W.; Wood, H. C. S. *J. Chem. Soc.* **1964,** 4769.
36. Norris, B. J.; Meckstroth, M. L.; Heineman, W. R. *Anal. Chem.* **1976,** *48,* 630.
37. Pfleiderer, W. In "Chemistry and Biology of Pteridines"; Iwai, K.; Goto, M.; Akino, M.; Iwanami, Y., Eds.; Int. Academic Print.: Tokyo, 1970; p. 7.
38. Rokos, K.; Pfleiderer, W. In "Chemistry and Biology of Pteridines"; Pfleiderer, W., Ed.; de Gruyter: Berlin, 1975; p. 931.
39. Marquardt, D. W. *J. Soc. Ind. App. Math.* **1963,** *2,* 431.
40. Viscontini, M.; Mohlmann, E. *Helv. Chim. Acta* **1959,** *42,* 836.
41. Pfleiderer, W. In "Chemistry and Biology of Pteridines"; Pfleiderer, W., Ed.; de Gruyter: Berlin, 1975; p. 941.

RECEIVED for review June 2, 1981. ACCEPTED October 11, 1981.

Photosynthetic Energy Transduction

Spectral and Redox Characteristics of Chlorophyll Radicals in Vitro and in Vivo

J. FAJER[1], I. FUJITA, M. S. DAVIS, A. FORMAN, and L. K. HANSON

Brookhaven National Laboratory, Department of Energy and Environment, Upton, NY 11973

K. M. SMITH

University of California, Department of Chemistry, Davis, CA 95616

Optical, redox, and paramagnetic resonance results, as well as theoretical calculations, are presented for cation and anion radicals of magnesium tetraphenylchlorin, and serve as guides to the properties of chlorophyll ions. Electrochemical cells designed to generate the radicals are described. The spectral signatures of chlorophyll (and pheophytin) radicals in vitro are compared with those of the primary donors and acceptors of plant photosynthesis to identify the transients observed in vivo. The model studies and the theoretical calculations suggest that the protein environment of the chlorophylls in the reaction center can modulate their properties significantly, and may impose specific orientations as well as hydrogen bonding on the substituent groups of the chromophores.

Plant photosynthesis functions via two photosystems (PS) that cooperatively fix carbon dioxide (PS I) and evolve oxygen (PS II). A combination of optical and paramagnetic resonance spectroscopy recently resulted in a generalized mechanism by which green plants (and algae) transduce an incident photon into the oxidants and reductants that drive the biochemistry of the organisms. The light harvested

[1] Author to whom correspondence should be addressed.

0065-2393/82/0201-0489$07.25/0

by antenna pigments is funneled to a reaction center where a chlorophyll (or chlorophylls), P, is raised to its excited state, P^*, and transfers an electron to a nearby acceptor, A_1 (labeled I in PS II), within a few picoseconds. This primary charge separation is then stabilized by the rapid translocation of the electron to a secondary acceptor, A_2, for an overall reaction (*1–27*):

$$PA_1A_2 \xrightarrow{h\nu} P^*A_1A_2 \rightarrow P^+A_1^-A_2 \rightarrow P^+A_1A_2^-$$

Acceptor A_2 is an iron–sulfur protein in PS I (*13, 27*) and an iron–plastoquinone (Fe–Q) complex in PS II (*25, 26*). The primary donors, P, are believed to be oxidized chlorophylls (Chl), P-700$^+$ in PS I and P-680$^+$ in PS II (*1–10*). Electron spin resonance (ESR) (*6*), electron nuclear double resonance (ENDOR) (*28, 29*), and optical and circular dichroism (*30*) results led to the proposal that P-700 is a dimer (or "special pair") of chlorophylls, although a monomeric enol form of Chl recently was postulated (*31*).

The nature of P-680$^+$ in PS II is considerably more ambiguous: linewidths of ESR signals attributed to P-680$^+$ range from 7 to 9 G (*32–37*) (vs. 7 G for P-700$^+$), resulting in proposals of monomer (*33*), dimer (*34–36*) and even trimer (*32*) configurations. Even more puzzling are the large differences in oxidation potentials of P-700 and P-680. Titrations of P-700 yield a midpoint potential (*1–5*) ranging between +0.4 and +0.5 V against the normal hydrogen electrode, whereas the minimum potential needed to oxidize water to oxygen at the physiological pH sets a lower limit of +0.8 V (*4, 5*) for P-680.

We describe here in vitro magnetic, redox, and optical properties of chlorophyll (Structure I) and magnesium tetraphenylchlorin (MgTPC, Structure II), a model compound, and their π-cation radicals, which illustrate the environmental factors capable of altering the properties of Chl in vivo. The oxidation potentials and ESR characteristics of the chlorins are sensitive functions of solvent and counterion. These changes may be explained by theoretical calculations that predict the existence of a nearly degenerate excited state whose degree of interaction is influenced by the perturbations caused by the axial ligands, that is, the immediate environment of the Chl. Comparison of the optical, redox, and magnetic data of the chlorins in vitro with those attributed to P-680 suggests that many of the properties of P-680 can be rationalized in terms of a Chl monomer ligated by neighboring (protein?) molecules (*38*).

We also review in vitro and in vivo optical and paramagnetic resonance results that have led to the identification of Chl as the primary acceptor, A_1, of PS I (*13, 14, 17, 18, 21, 23*) and of pheophytin (Pheo, a metal-free Chl) as the acceptor, I, of PS II (*17–20, 24, 26*). Here again,

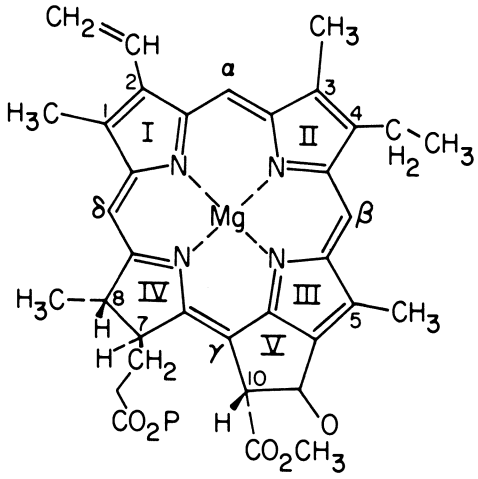

Structure I

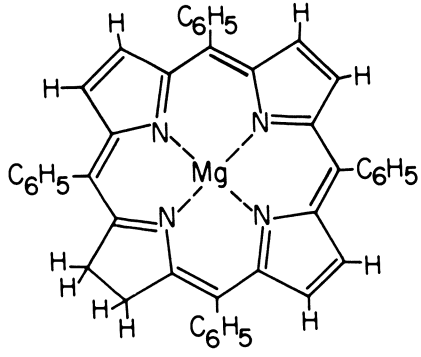

Structure II

model studies and theoretical calculations suggest that the protein environment of the chlorophylls in the reaction center can modulate their properties and may impose specific orientations as well as hydrogen bonding on the substituent groups of the chromophores (*18*, *39a*).

Experimental

The ESR and ENDOR techniques were described previously (*40*). The radicals were generated electrochemically at platinum electrodes in rigorously dried and degassed solvents using tetrapropylammonium or tetrabutylammonium perchlorate as carrier electrolyte. Three electrochemical cell

configurations were used. For cation radicals, which are not sensitive to traces of oxygen, a cell (Figure 1) was constructed to allow simultaneous cyclic voltammetry, controlled potential electrolysis, and optical measurements. The working electrode consisted of a Pt basket with a mesh bottom into which was fitted a tube ending in a fritted glass disk. This tube contained a mesh Pt basket as a counterelectrode. This configuration offered large effective surface areas for both electrodes and allowed the flow of several milliamperes in a solvent of low dielectric constant such as dichloromethane ($\epsilon = 9$) containing 10^{-3} *M* reactant and 0.1 *M* $(C_3H_7)_4NC10_4$ as electrolyte. A thin reference electrode fit directly into the top of the cell. The whole assembly was purged with dry nitrogen or argon and the flow of gas served both to stir the solution and to exclude oxygen and water. The stirred solution moved past the optical cell and allowed spectra to be recorded. (The entire cell assembly readily fit into the sampling compartments of Cary 17 or 219 spectrophotometers, and was small enough to be inserted into an optical dewar within the sampling compartments for low-temperature measurements.) At the end of the electrolysis, cyclic voltammetry could be performed on the product via the two Pt leads, which end in beads, inserted below the working electrode. The reversibility of the reaction could also be checked by regeneration of the parent compound simply by reversing the polarity of the working and counterelectrodes.

For anion radicals, which require rigorous exclusion of water and oxygen, solutions containing the solvent, reactant, and carrier electrolyte were contacted with molecular sieves, Al_2O_3, and degassed on a vacuum line in a side arm of the cell shown in Figure 2. The cell assembly was then sealed off and the solution was poured into the cell. A Pt wire served as quasi-reference electrode. A magnetic stirrer, rotated by an outside magnet mounted on the flexible shaft of a stirring motor, pumped the solution over the working electrode and through an optical cell. For ESR measurements, the assembly shown in Figure 3 was used. Outgassed solutions, prepared as just described, were poured into the cell to cover the electrodes, and enough current was passed through the solution to convert 80–90% of the porphyrin to radical. (A more elaborate version employed a quasi-reference electrode.) After the cell was sealed off from the vacuum line, ESR and ENDOR measurements were obtained in the thin side arm, and the identity of the product was verified spectrophotometrically in the attached optical cell.

Chlorophyll and pheophytin were prepared by standard techniques (*38*). The syntheses of ^{15}N-tetraphenylporphyrin (95% ^{15}N), and of magnesium tetraphenylchlorin were reported (*38*, *41*).

Methyl pyropheophorbide-*a*, deuterated at the 5-, 10-, and δ-positions (pyropheo-d_6, *see* Structure III) was prepared as follows: methyl pheophorbide-*a* (200 mg) was refluxed under nitrogen in 50 mL of dry collidine containing 4 mL of D_2O for 16 h. The solvents were removed under vacuum and the residue was crystallized from methanol–methylene chloride to give 196 mg (93%) of compound, partially deuterated at positions 5 and 10. To exchange the δ-position, this material was heated for 4 h at 110°C in 12 mL of deuteroacetic acid and 3 mL of dioxane, under nitrogen. The solution was diluted with methylene chloride; washed with water, then aqueous sodium bicarbonate; dried over anhydrous sodium sulfate; and evaporated to dryness. After crystallization from methylene chloride–methanol, a 96% recovery of methyl pyropheophorbide-*a* was obtained. NMR spectroscopy indicated that the δ-proton was >75% exchanged, that the 10-methylene was totally exchanged, but that the 5-methyl was only about 50% exchanged (labeled

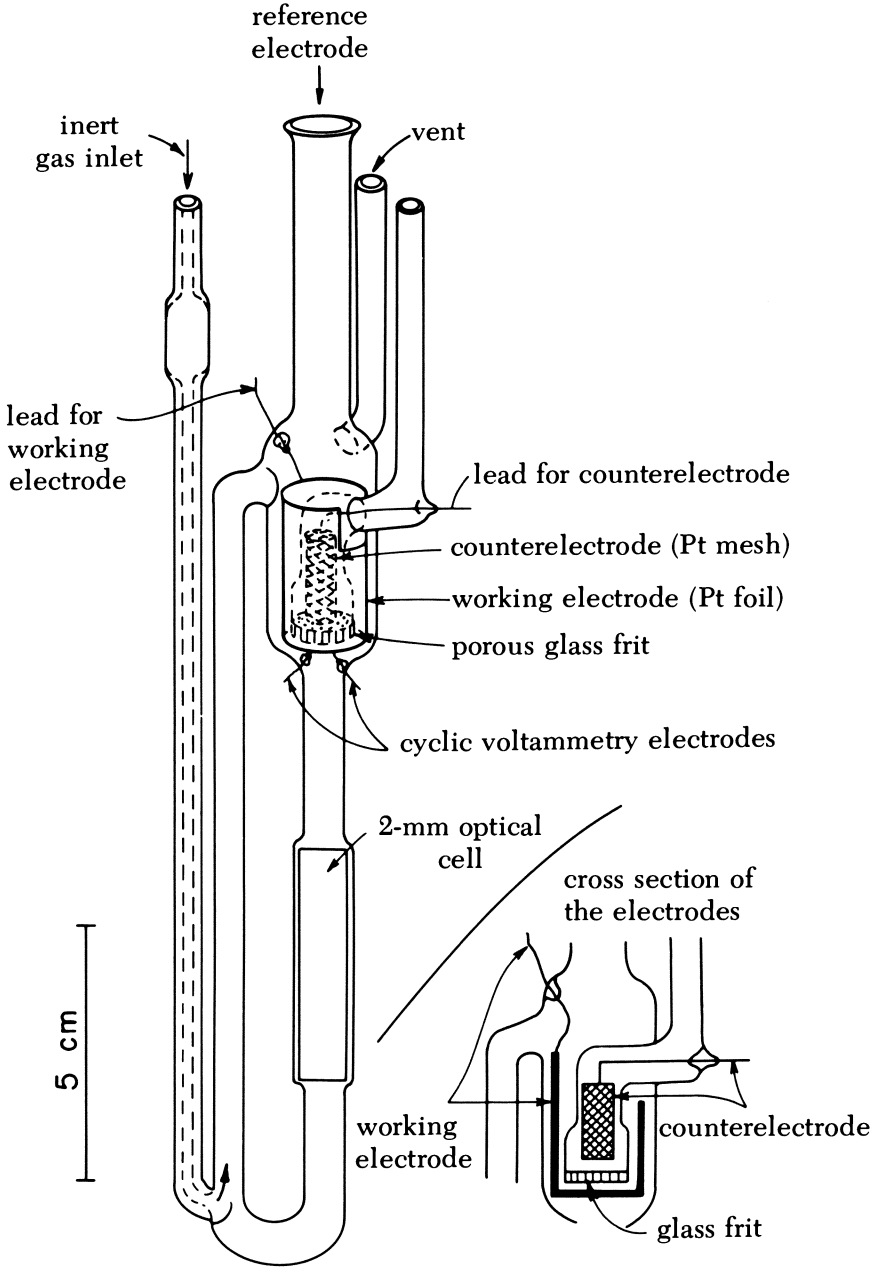

Figure 1. Electrooptical cell for controlled potential electrolysis, cyclic voltammetry, and optical measurements.

pyropheo-d_4 in Figure 9). The partially deuterated material was therefore retreated as follows: 46.5 mg in 20 mL of dry pyridine and 2 mL of D_2O was refluxed for 92 h under nitrogen. After evaporation to dryness, use of toluene as a solvent chaser, and crystallization from methylene chloride–methanol, 39.5 mg (85% recovery) of the required pyropheo-d_6 was obtained. NMR spectroscopy showed that the peak assigned to the 5-methyl was totally absent (i.e., >95% deuteration).

Triton-treated subchloroplast particles enriched in PS I (one PS I reaction center/30 Chl molecules) or in PS II (one PS II reaction center/30–40 Chls) were prepared and the primary acceptors were trapped as described in References *18*, *20*, and *26*.

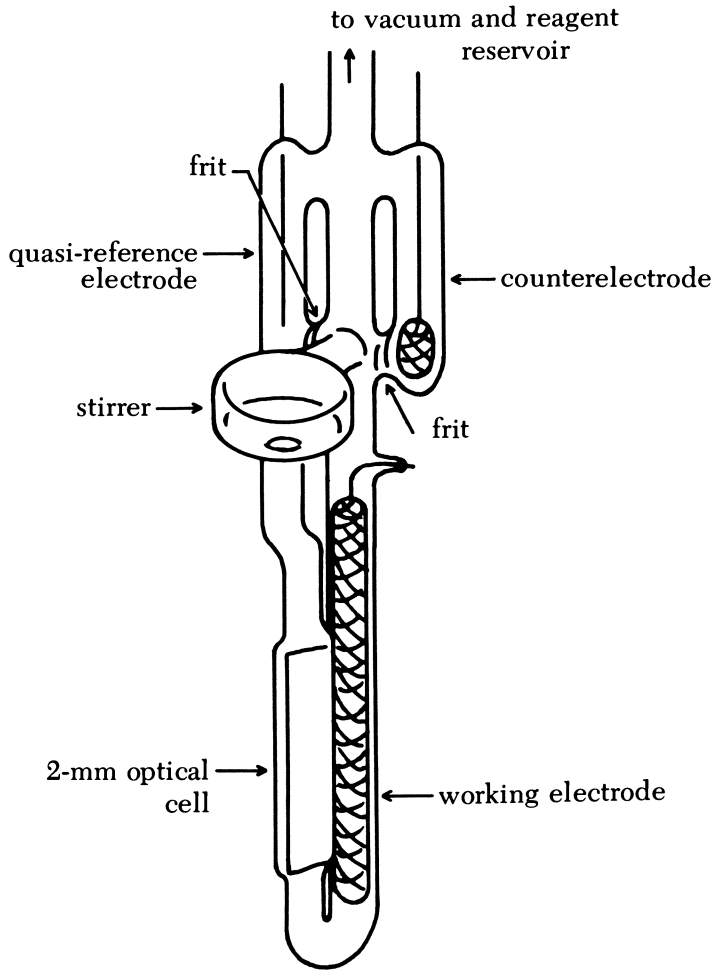

Figure 2. Electrochemical cell for in vacuo electrolysis.

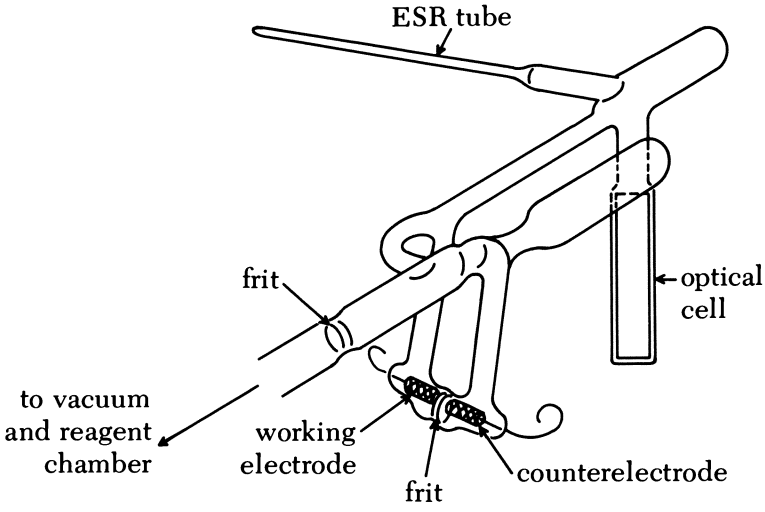

Figure 3. Electrochemical cell for ESR–optical measurements in vacuo.

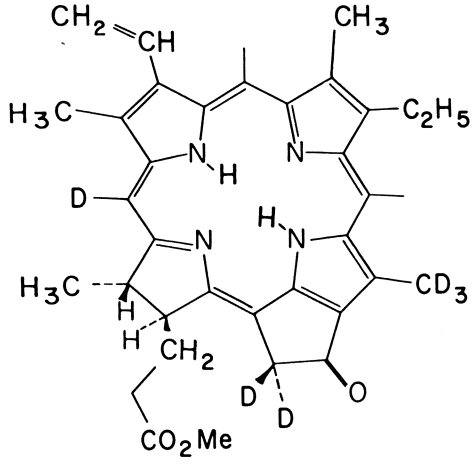

Structure III

Theoretical Calculations

The charge iterative extended Hückel (IEH) program, parameters, and limits of convergence are described in References *41*, *42*, and *43*. The computations for the chlorophyll (and pheophytin) models shown in Table II used coordinates from the x-ray structures of ethyl chlorophyllide-*a* dihydrate (*44*) and methyl pheophorbide-*a* (*45*). The calculations for the pheophytin anions represent the average of two

tautomeric forms in which the two central protons are localized on the nitrogens of rings I and III or rings II and IV.

Results and Discussion

Cation Radicals and the Primary Donor of Photosystem II. The spectral changes caused by the one-electron oxidation of Chl in methylene chloride–tetrahydrofuran mixtures are shown in Figure 4. The bleaching of the major absorption bands and the appearance of new transitions in the red region parallel those found for zinc (*41*) and magnesium (*46*) chlorins. The spectral data suggest therefore that the changes observed are characteristic of the oxidation of the chlorin π-system, and, thus that MgTPC is a reasonable model for Chl. In methylene chloride, the $MgTPC^+$ ClO_4^- cation displays a five-line ESR spectrum (Figure 5a) due to four protons with hyperfine splittings, $a_H = 5.6$ G, as demonstrated by the simulation of Figure 5b. This hyperfine interaction can readily be assigned to the four β-protons of the saturated ring of the chlorin by selective deuteration: substitution

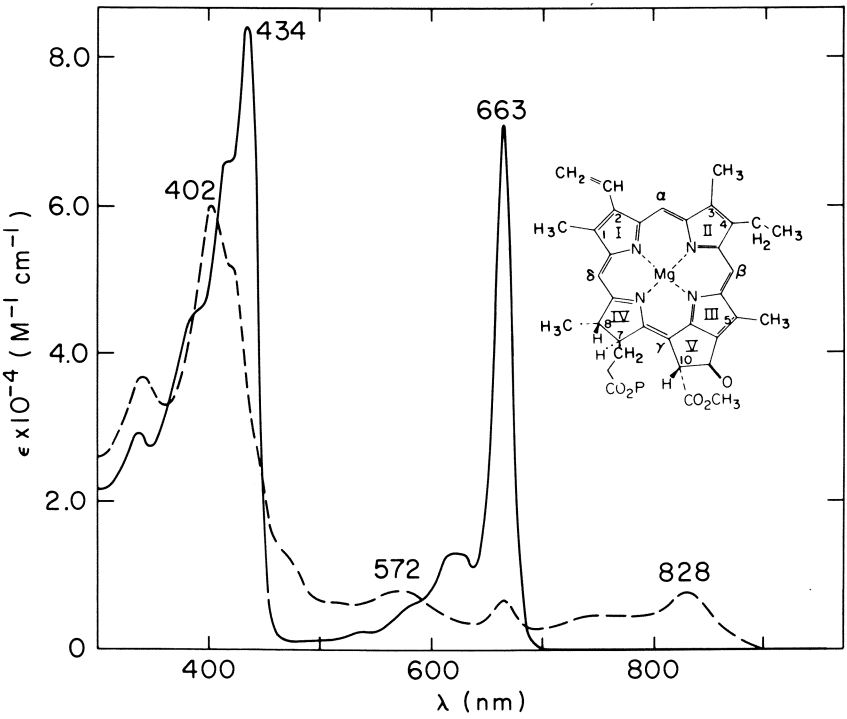

Figure 4. Optical spectra of Chl (—) and $Chl^+ClO_4^-$ (---) at 25°C in 3:1 CH_2Cl_2–THF.

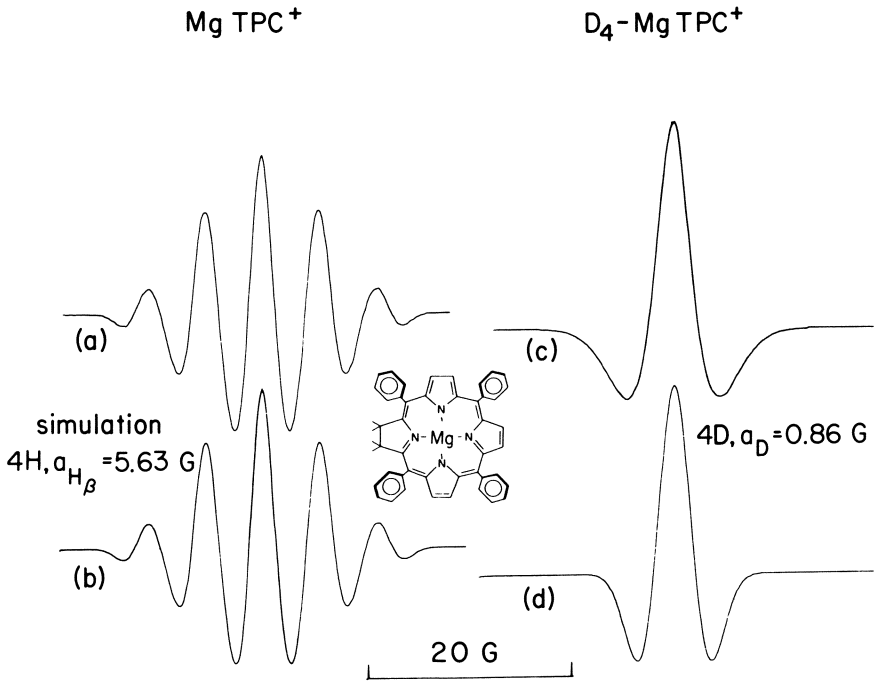

Figure 5. Second derivative ESR spectra, in CH_2Cl_2 at 20°C, of $MgTPC^+ClO_4^-$ (a) and $MgTPC^+ClO_4^-$-d_4 (c) (deuterated at the reduced ring). The simulations demonstrate that the experimental spectra a and c are, respectively, determined by four equivalent protons (b) and four deuterons (d). g = 2.0026.

of the four protons of that ring by deuterons results in a narrowed ESR spectrum (Figure 5c) attributable to four deuterons with a_D = 0.86 G, as expected because of the differences in gyromagnetic ratios (a_D/a_H = 0.1535) and nuclear spins of hydrogen and deuterium, and as confirmed by simulation (Figure 5d).

Iterative extended Hückel calculations predict that two nearly degenerate ground states, separated by ~1000 cm^{-1}, are possible for oxidized chlorins. The calculated unpaired spin densities for these states are listed in Table I. Similar profiles are obtained by self-consistent field Pariser–Parr–Pople calculations (*38*). The experimentally observed splitting constant of a β-proton is given by $a_H = \rho_c(-9.2 + 96.7\cos^2\theta)$, in which ρ_c is the spin density on the α-carbon of the π-system (C_1 and C_4 in the present case) and θ is the dihedral angle between the $2p_z$ orbital of the α-carbon and the plane defined by C_α, C_β, and H_β (*47*). X-ray diffraction studies of single crystals indicate that θ for the β-protons of the saturated rings ranges from an average of 34° in zinc tetraphenylchlorin (*48*) to 45° in ethyl chlorophyllides (*44*).

Table I. Unpaired Spin Densities for Cation and Anion Radicals of Mg Chlorin[a]

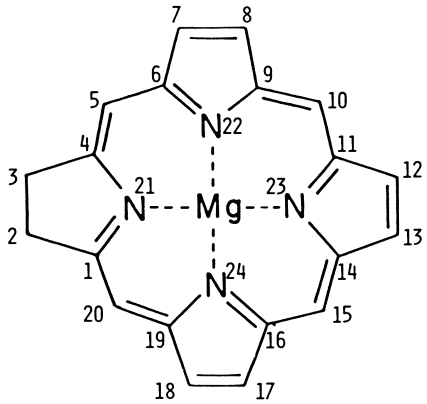

Position	Cation $\rho_\pi(^2A_2)$	Cation $\rho_\pi(^2B_2)$	Anion $\rho_\pi(^2A_2)$
1,4	0.093	0.008	0.021
2,3	0.038	0.001	0.001
5,20	0.051	0.129	0.065
6,19	0.055	0.001	0.045
7,18	0.027	0.008	0.057
8,17	0.024	0.006	0.060
9,16	0.059	0.002	0.041
10,15	0.006	0.124	0.081
11,14	0.053	0.002	0.011
12,13	0.024	0.009	0.006
21(N)	0.000	0.105	0.124
22,24(N)	0.028	0.081	0.000
23(N)	0.000	0.072	0.096
Mg	0.000	0.077	0.000

[a] C_{2v} symmetry with the y-axis along N21–N23.

These values, combined with the predicted spin density of 0.093 for a $^2A_2$ state (Table I), yield splitting constants, a_H, of 5.3 and 3.6 G (for θ = 34° and 45°, respectively) compared with the 5.6 G found experimentally. Thus, the magnitude of the β-proton splittings observed for $MgTPC^+C10_4^-$ is in general accord with the spin densities predicted for the α-carbons of the saturated ring in the $^2A_2$ state.

The electronic configuration of monomeric Chl^+ in methylene chloride or methylene chloride–methanol, in which the radical exhibits a 9-G linewidth, was mapped by ENDOR and selective deuteration

(*38*, *48*, *49*). The results are also consonant with the $^2A_2$ ground state (assuming an approximate C_{2v} symmetry) predicted by PPP calculations (*38*) for a model of Chl^+, and by extended Hückel calculations, which specifically treat the chlorophyll molecule (Table II). In methylene chloride, the β-proton splittings of ring IV are notably smaller in Chl^+ (≈4 G) than in $MgTPC^+C10_4^-$, as expected for the 45° dihedral angle of the β-protons in Chl and the smaller spin densities calculated for the α-carbons (Table II, C-16 and C-19).

However, significant variations in the splitting constants of $MgTPC^+$ can be induced by variations in temperature, solvent, and counterion. At 20°C, a_H = 5.13 G for $MgTPC^+Cl^-$ in methylene chloride; a_H = 5.63 G for $MgTPC^+C10_4^-$ in methylene chloride, 4.40 G in tetrahydrofuran (THF), and 3.99 G in butyronitrile (PrCN) (Figure 6). The difference between methylene chloride and butyronitrile is particularly striking: it is nearly 30%.

A similar effect, reflected in changes of linewidth, is noted with $Chl^+C10_4^-$: ΔH = 9.2 G in CH_2Cl_2, 7.8 G in PrCN, and 7.9 G in THF and CH_2Cl_2–THF at 25°C (*38*). That these changes are not due to dimerization is shown by the optical spectra of Chl in these solvents, which are typical of monomeric Chl (*see* Figure 4), and by comparison of the ENDOR spectra of Chl^+ in frozen solutions of CH_2Cl_2 and CH_2Cl_2–THF (*38*). Although the linewidth of Chl^+ in CH_2Cl_2–THF is 8 G, the methyl proton splittings, ≈1.4 and 2.4 G, are close to those found in pure CH_2Cl_2, 1.0 and 2.6 G. They are clearly not halved as expected for a dimeric radical, and are thus consistent with a monomer configuration. The variations in the large β-proton splittings found in $MgTPC^+$ suggests that the variations in linewidth observed in Chl^+ are also due to changes in β-proton splittings. Computer simulations of the linewidths of Chl^+ in tetrahydrofuran or butyronitrile using the experimentally determined methyl splittings require a decrease in the splittings of the β-protons of ring IV of ~30% to ~2.8 G, in agreement with the changes found in $MgTPC^+$ in the same solvents.

The significant interaction of the chlorins with their environment, as reflected by their ESR spectra, is further illustrated by the wide range of oxidation potentials induced by simple changes in solvent and counterion (Table III). Again, tetrahydrofuran and butyronitrile, which most profoundly affect the electronic configuration, cause the largest changes in redox potential in the presence of a noncomplexing counterion such as $C10_4^-$. Complexation by chloride ion, on the other hand, stabilizes the charge of the cation and thus lowers the oxidation potential.

The ESR and redox changes observed for Chl^+ and $MgTPC^+$ [similar results were also obtained with $ZnTPC^+$ (*47*, *48*)] may reflect mixing of the two nearly degenerate ground states predicted theoretically (Tables I and II). The $^2B_2$ excited state shows significantly

Table II. Unpaired Spin Densities for Cations of Chlorophyll and Anions of Chlorophyll and Pheophytin[a]

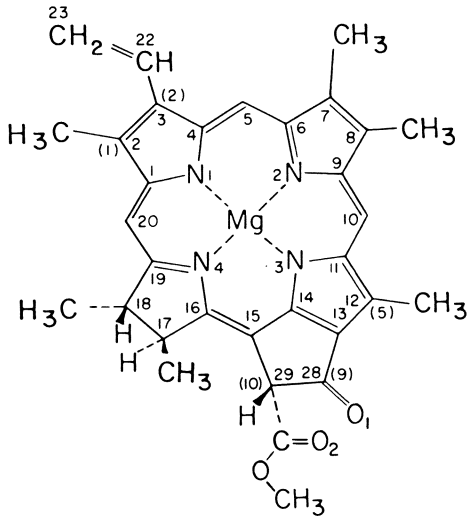

	Chl Cations			*Anions*	
Position[b]	$^2A_2$[c]	$^2B_2$[c]	$^2B_2$[d]	*Chl*[c]	*Pheo*[e]
N1	0.055	0.073	0.120	0.001	0.001
N2	0.022	0.039	0.104	0.090	0.092
N3	0.012	0.037	0.090	0.001	0.002
N4	0.006	0.097	0.119	0.091	0.079
C1	0.042	0.000	0.001	0.050	0.048
C2(1)	0.017	0.014	0.001	0.045	0.045
C3(2)	0.009	0.006	0.001	0.037	0.035
C4	0.059	0.007	0.000	0.041	0.040
C5	0.027	0.094	0.089	0.050	0.052
C6	0.050	0.000	0.001	0.025	0.022
C7	0.026	0.020	0.002	0.001	0.002
C8	0.006	0.008	0.002	0.017	0.018
C9	0.066	0.008	0.001	0.001	0.002
C10	0.008	0.073	0.070	0.097	0.096
C11	0.063	0.001	0.000	0.017	0.018
C12(5)	0.042	0.016	0.001	0.097	0.092
C13	0.014	0.001	0.000	0.022	0.028
C14	0.061	0.014	0.001	0.009	0.010
C15	0.006	0.067	0.080	0.036	0.041
C16	0.065	0.002	0.008	0.003	0.006

Continued on next page.

Table II. *Continued.*

C17	0.019	0.000	0.001	0.000	0.000
C18	0.026	0.002	0.001	0.002	0.002
C19	0.079	0.009	0.001	0.030	0.032
C20	0.063	0.114	0.099	0.049	0.046
01	0.029	0.029	0.019	0.111	0.114
02	0.008	0.140	0.093	0.002	0.003
C28(9)	0.000	0.000	0.000	0.025	0.026
C29(10)	0.000	0.021	0.014	0.000	0.000
C22	0.001	0.001	0.000	0.000	0.001
C23	0.008	0.003	0.000	0.018	0.018
Mg	0.006	0.052	0.007	0.005	—

[a] For an assumed C_{2v} symmetry with the y-axis defined along N2 and N4.
[b] The numbering system corresponds to the structure shown. The numbers in parentheses follow the traditional notation used for the peripheral carbons.
[c] Based on the crystal coordinates of ethyl chlorophyllide-*a* with the vinyl group 31° out of the porphyrin plane, and without an axial ligand.
[d] Crystal coordinates with H_2O as axial ligand.
[e] Based on the crystal coordinates of methyl pheophorbide-*a* with the vinyl group 15° out of plane.

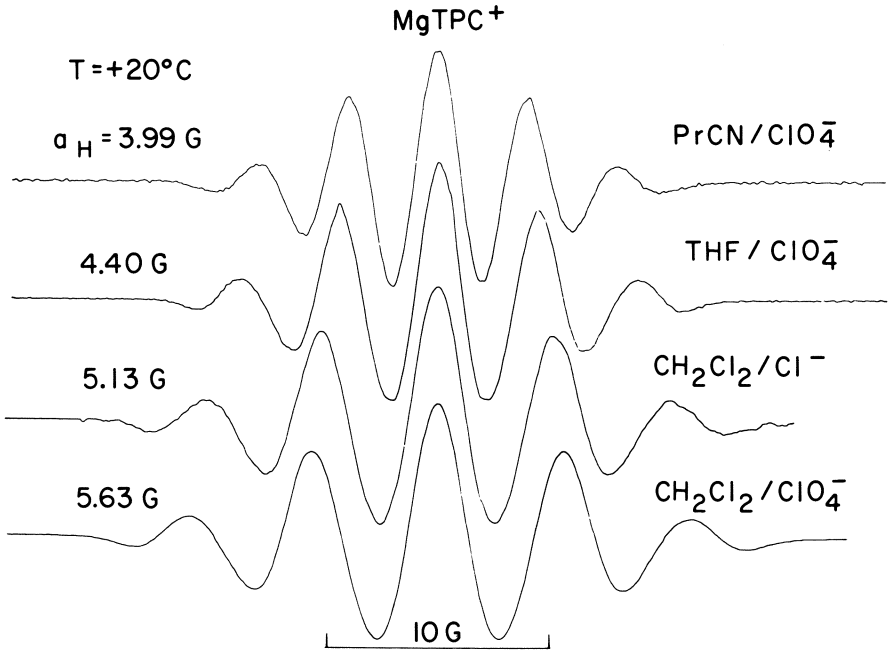

Figure 6. Second derivative ESR spectra, and β-proton coupling constants, of $MgTPC^+$ as a function of solvent and counterion at 20°C.

Table III. Half-wave Oxidation Potentials, $E_{1/2}$ (in V Against Normal Hydrogen Electrode)[a]

Solvent	*Counterion*	*MgTPC*	*Chl-a*
CH_2Cl_2	ClO_4^-	0.66	0.80
	Cl^-	0.60	0.74
PrCN	ClO_4^-	0.73	0.82
	Cl^-	0.65	0.75
THF	ClO_4^-	0.82	0.93

[a] The half-wave potentials are not corrected for junction potentials due to changes in solvent. These effects can be estimated by comparison of the ferrocene–ferricinium couple in the same solvents. $E_{1/2}$ for this oxidation is ≈40 mV larger in THF and ≈30 mV smaller in PrCN than in CH_2Cl_2 (38).

smaller spin densities at the α-carbons of the saturated ring than the $^2A_2$ state. If the solvent or counterion induces a sufficient perturbation to mix in some character of the second state, then the splitting constants of the β-protons would result in lower values than expected for a pure $^2A_2$. Extended Hückel calculations further support this interpretation and actually predict that ligands such as H_2O, CH_3OH, CH_3SH, CH_3CN, and THF would suppress the $^2B_2$ state below the $^2A_2$ in chlorins and Chl. Although this result is not observed experimentally, Hückel and PPP calculations (38) clearly suggest that interactions between the two states are energetically accessible. Changes in the coordination sphere of the chlorins provide a likely mechanism for this mixing. Indeed, resonance Raman and optical spectra indicate that Chl is hexacoordinated in THF and in methyl THF at low temperatures (50–52).

Extension of these results to P-680 leads to the following conclusions:

1. The ESR linewidth of ligated Chl^+ does not differ significantly from that of P-680$^+$.
2. Comparison of the optical difference spectrum ascribed to oxidation of P-680 with that reported here for the oxidation of monomeric Chl in CH_2Cl_2–THF shows reasonable agreement (Figure 7), if the shift from 670 to 680 nm is attributed to coordination of the Chl of P-680, possibly involving nearby protein residues.
3. The oxidation potentials found in vitro for monomeric Chl in coordinating solvents (as high as 0.9 V) approach the limits required for the function of P-680 in oxygen evolution. The optical, magnetic, and redox properties of ligated, monomeric Chl are thus not inconsistent with those attributed to P-680. We propose therefore that P-680 is a monomeric Chl whose physical and chemical

characteristics, and whose function as the phototrap of photosystem II, are determined by its (protein?) environment.

Additional support for this premise derives from resonance Raman and x-ray data for antenna Chl (*53*) and bacterio Chl (*54*), which provide evidence of protein residue–chromophore interactions. Furthermore, the *D* and *E* parameters of the Chl triplet in complexing solvents (*55*) are similar to those of the spin polarized triplet of P-680, obtained from the recombination of P-680$^+$ and its primary acceptor, I^-: P-680$^+$ + I^- → ^{3}P-680 + *I* (*56*).

Anion Radicals and the Primary Acceptors of Photosystems I and II. Unpaired spin densities for the anion of magnesium chlorin are listed in Table I. In contrast to the $^2A_2$ state of the cation radical, the spin densities of the anion are more evenly distributed around the periphery of the molecule, with significantly smaller densities at the reduced ring and larger ones on two of the nitrogens. The ESR spectra of MgTPC$^-$ shown in Figure 8 support the predicted profile. Substitu-

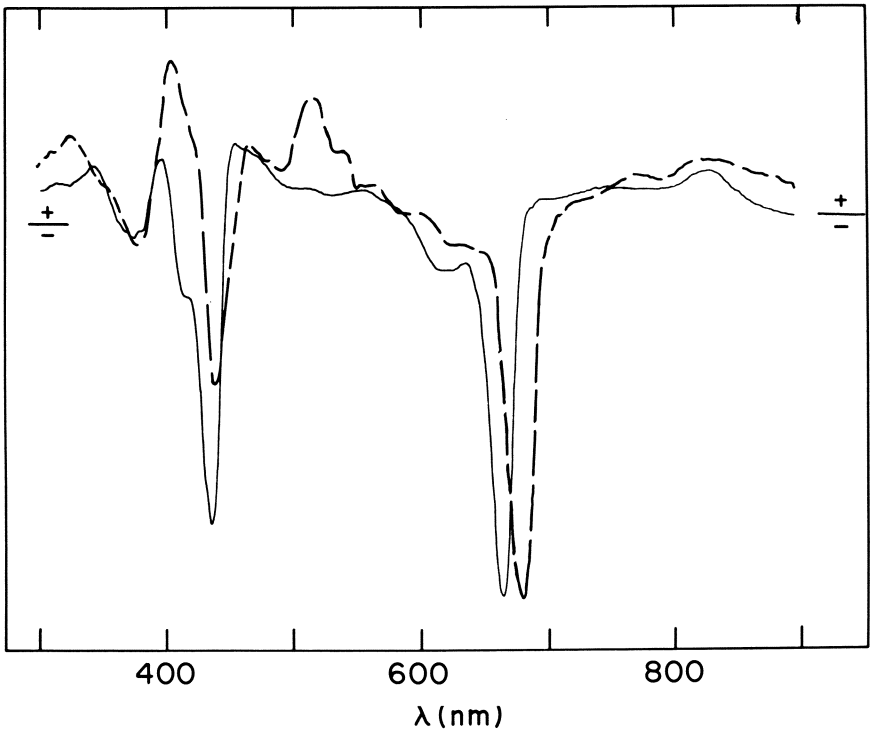

Figure 7. Comparison of the optical changes induced by light in particles enriched in PS II as reported (64) (ΔP-680, ---) and of the difference spectrum caused by the oxidation of Chl in 3:1 CH_2Cl_2–THF (ΔChl, —). The spectra were normalized at ~680 nm.

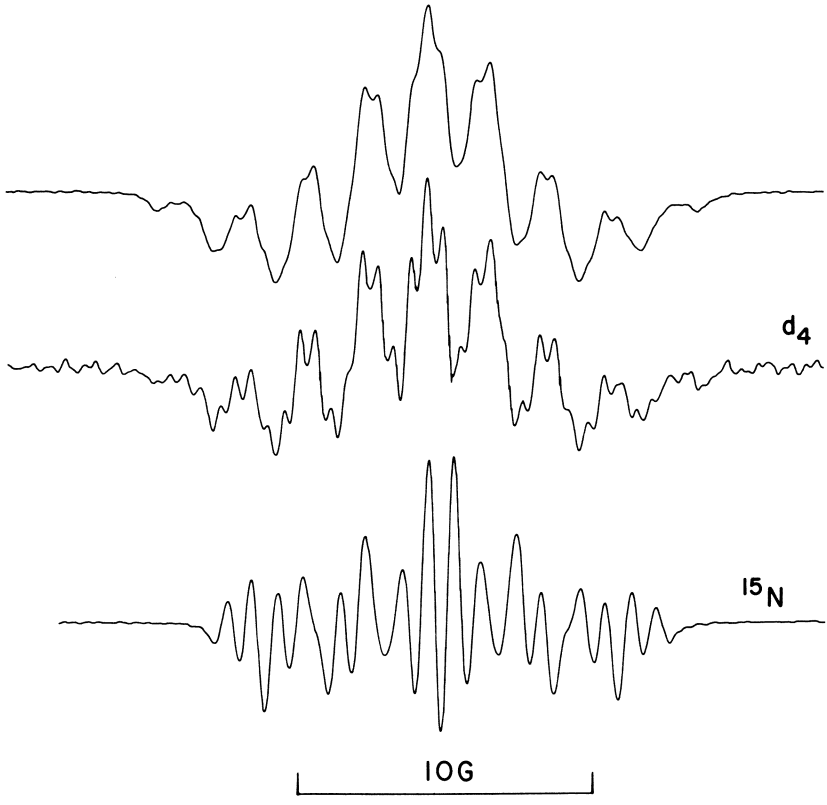

Figure 8. Second derivative ESR spectra of $MgTPC^-$, $MgTPC^-$-d_4 and ^{15}N-$MgTPC^-$ in deuterated DMF at 25°C. The counterion is Bu_4N^+. g = 2.0025

tion of deuterons for the protons of the reduced ring yields only a small improvement in resolution without changing the spectral pattern, indicating that those nuclei do not have large coupling constants. On the other hand, substitution of ^{15}N ($I = \frac{1}{2}$) for ^{14}N ($I = 1$, $a_{^{15}N}/a_{^{14}N} = 1.40$) results in a large spectral rearrangement that reflects the substantial unpaired spin densities predicted theoretically for two of the nitrogens. [A detailed analysis of the spectra will be presented elsewhere (57).]

The unpaired spin densities of Chl^- and $Pheo^-$ (Table II) parallel those of the chlorin anion. ^{14}N ENDOR reveals nitrogen splittings of ~2 G in $Pheo^-$ and Chl^-, in general agreement with the calculations (39). Because methyl groups are easily detected in frozen solutions by ENDOR, the 1- and 5-methyl groups can be used to probe the unpaired spin densities of rings I and III experimentally. Figure 9 illus-

trates two large proton coupling constants in the ENDOR spectra of Chl^- and $Pheo^-$. The M.O. calculations predict that the 1- and 5-methyl groups should display coupling constants in a ratio of ~1:2, and that the 5-methyl group of $Pheo^-$ should be ~5% smaller than that of Chl^-. These were indeed observed. The assignment of the larger splitting to the 5-methyl group is further verified with selectively deuterated methyl pyropheophorbide, in which partial deuteration of the 5-methyl group decreases the height of the ENDOR resonance at 3.7 G, and complete deuteration of the group eliminates that peak completely (Figure 9). The combination of M.O. calculations and

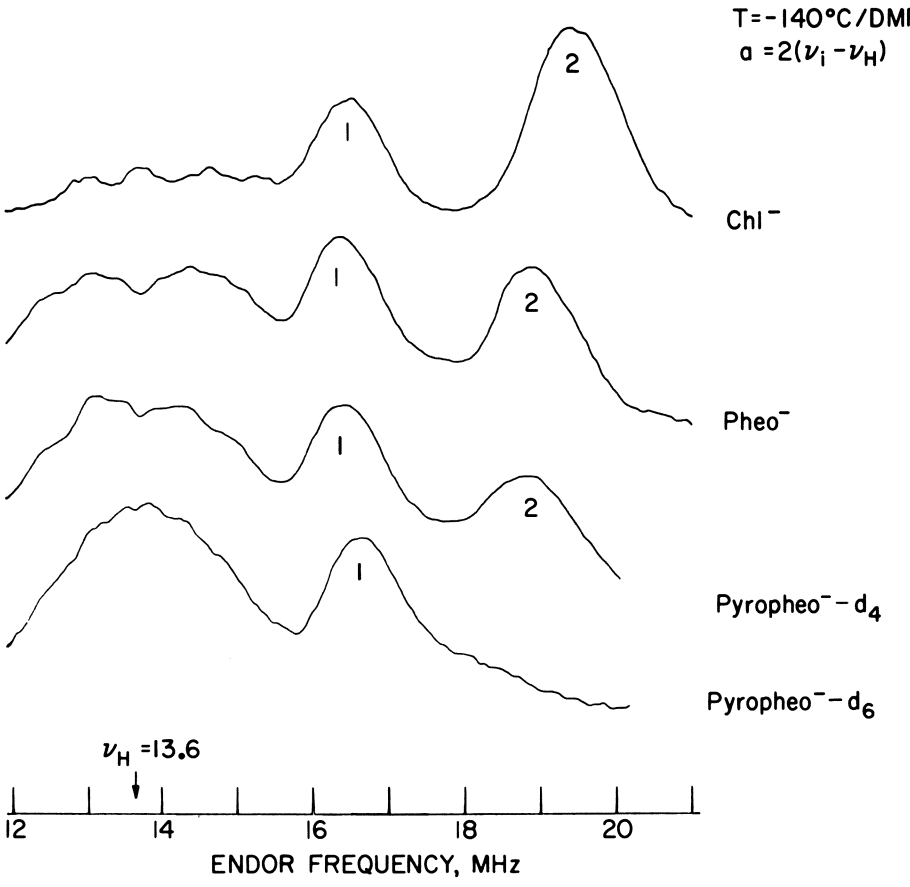

Figure 9. ^1H ENDOR spectra at 130 K of Chl^-, $pheo^-$, and $pyropheo^-$-d_4 in deuterated DMF. The bottom spectrum, run in normal DMF, shows that in $pyropheo^-$-d_6, in which the 5-methyl group is deuterated, peak 2 disappears whereas in $pyropheo^-$-d_4, in which only one proton of the 5-methyl group has been replaced by deuterium, peak 2 is still detected.

deuteration experiments thus strongly suggests that the two ENDOR transitions of ~2 and 4 G can be assigned to the 1- and 5-methyl groups, respectively.

As further characterizations of the spectral signatures of Chl^- and $Pheo^-$, the optical spectra (*17*) of the anion radicals in DMF are presented in Figure 10.

The identities of the primary acceptors of PS I and II are now considered in light of the in vitro results. The primary acceptor of PS II, I^-, can be trapped in two configurations (*18*): one in which I and A_2 are reduced (prep a, I^-, A_2^-) and one in which I is reduced and A_2 is doubly reduced (prep b, I^-, A_2^{2-}). The two preparations yield

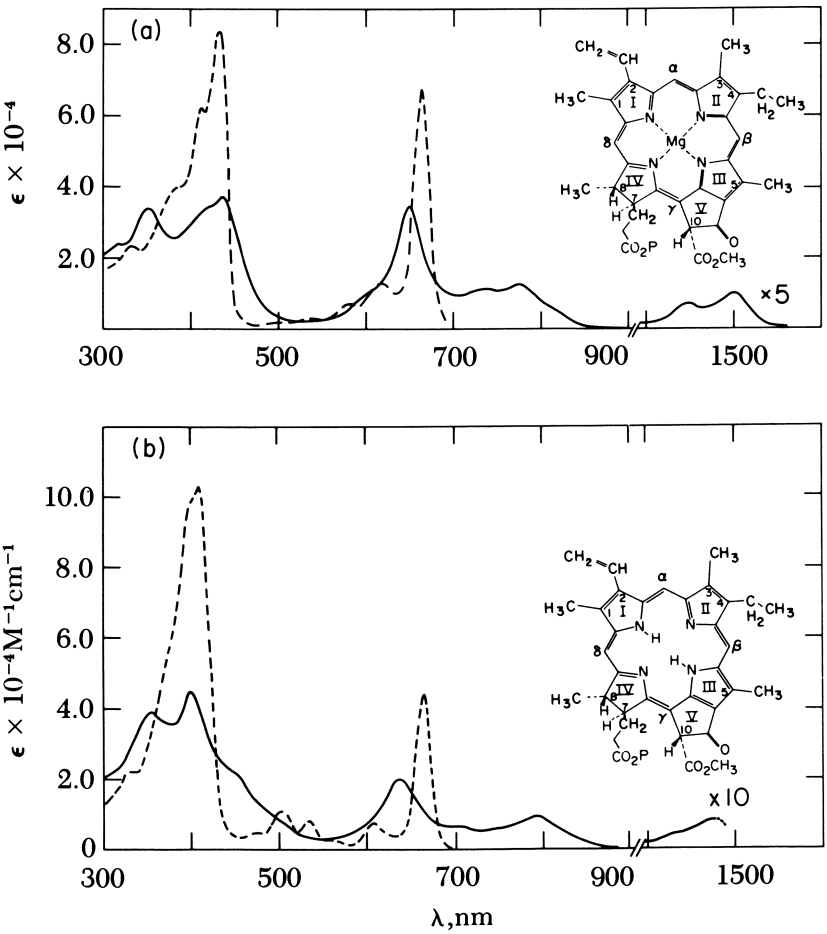

Figure 10. Optical spectra of the anion radicals (—) and of their parent compounds (---) in DMF at 25°C. Key: a, chlorophyll; and b, pheophytin.

(*18*) singlet ESR signals with *g*-values of 2.0033 (±0.0002). The signals saturate easily (ΔH = 13 and 14 G at 0.01 and 1 mW, respectively) and display proton ENDOR resonances at 1.64 and 4.46 G for preparation *a* and 1.64 and 4.36 for *b*. Comparison of these parameters with those of the anion radicals of chlorophyll and pheophytin in vitro (Table IV) indicates that the *g*-values, linewidths, saturation behavior, and ENDOR responses of I^- are clearly similar, but not identical, to those of monomeric anion radicals of Pheo or Chl. Because electron sharing on the ESR time scale between two or more molecules such as $(Chl)_2^-$ or $(Chl–Pheo)^-$ would reduce the ESR linewidth and the hyperfine splittings observed by ENDOR, I^- must therefore be $Pheo^-$ or Chl^- (or possibly a heterogeneous array of the two) but not a dimeric complex.

Comparison of the optical difference spectra obtained on reduction of Pheo and Chl in vitro with those observed on reduction of *I* in PS II fragments in chloroplasts (Figure 11) indicates that many of the optical changes observed in vivo mirror those found upon reduction of

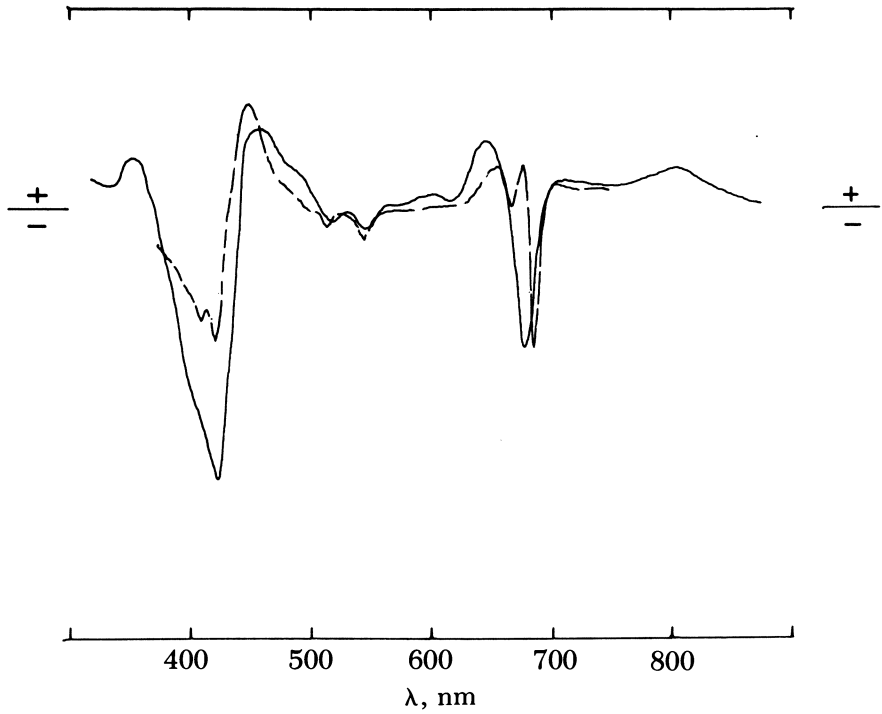

Figure 11. Comparison of the optical changes caused (20, 24) *by the reduction of* I (*ΔPS II*, ---) *and of the difference spectrum obtained* (17) *on electrochemical reduction of Pheo to* $Pheo^-$ *in DMF* (*ΔPheo*, —). *The spectra were normalized at ~680 nm and the Pheo spectrum was red-shifted by ~20 nm* (18).

Published on June 1, 1982 on http://pubs.acs.org | doi: 10.1021/ba-1982-0201.ch021

Table IV. Comparison of the Properties of I^-, Pheo$^-$, A_1^-, and Chl$^-$

Property	I^-, *PS II*	*Pheo*$^{-a}$	*Chl*$^{-a}$	A_1^-, *PS I*
g-value	2.0033(±0.0002)	2.0030(±0.0001)	2.0029(±0.0001)	2.0033(±0.0002)
ΔH, 130K[b]	13.2–13.9G	12.2–13.1	12.1–13.5	13.2–13.9
ENDOR, a_H, G, 130K	prep a: 1.64, 4.46 prep b: 1.64, 4.36	1.95, 3.75	1.95, 4.05	1.7, ~5
Reduction potential, V vs NHE	−0.61(*24*)	−0.64	−0.88	>−0.73(*10*)
Optical spectra	similar to Pheo$^-$ red-shifted ~20 nm(*18, 20, 24*)			similar to Chl$^-$, red-shifted ~20 nm(*13, 14, 23*)

[a] In dimethylformamide (*17*).
[b] Minimum and maximum peak to peak linewidths of the first derivative ESR spectra obtained in the range of 0.01 to 1 mW of microwave power.

Pheo in vitro, but are red-shifted by ~20 nm (*18*). In addition, the midpoint potential estimated for the reduction of *I*, $E_m = -0.61$ V (*24*), is nearly identical to the halfwave potential found (*17*) for the reduction of Pheo in dimethylformamide, −0.64 V, whereas reduction of Chl in the same solvent occurs (*17*) at −0.88 V. The combination of ESR, ENDOR, optical, and redox data thus leads to the conclusion that I^- in PS II exhibits many of the properties of a monomeric anion radical of Pheo.

Although the Pheo anion observed could conceivably be an artifact of the preparation, the following observations render this possibility unlikely. The reducing conditions used in preparation *a* result in the trapping of I^- and A_2^-, the subsequent acceptor in the electron transport chain. This latter species recently was shown (*25*) to comprise an iron–plastoquinone complex (Fe–Q) analogous to the iron–quinone acceptors found in photosynthetic bacteria (*58*). At 10K, in preparation *a*, interactions between the $Pheo^-$ and $(Fe–Q)^-$ radicals give rise to a doublet ESR signal (*18*), which is difficult to saturate and exhibits no ENDOR response. This signal disappears (*25*) if the integrity of the $(Fe–Q)^-$ complex is destroyed by extraction of Q or Fe, or by reduction at room temperature, presumably to $(Fe–Q)^{2-}$ (preparation *b*). These results indicate therefore that the Pheo anion observed is in close proximity to the quinone and is an integral part of the reaction center. A similar doublet signal was detected under comparable conditions in photosynthetic bacteria and was attributed to an analogous interaction between a bacteriopheophytin anion and a reduced iron–menaquinone complex (*58, 59*). Therefore, the initial sequence of electron acceptors in PS II seems to mirror that found in purple bacteria (*48, 58, 59*):

$$\begin{aligned}(B)Chl_n + (B)Pheo + FeQ &\xrightarrow{h\nu} \\ (B)Chl_n^+ + (B)Pheo^- + FeQ &\rightarrow (B)Chl_n^+ + (B)Pheo + FeQ^-\end{aligned} \quad (1)$$

where B = bacterio and Q = plastoquinone in PS II and menaquinone or ubiquinone in bacteria. [An additional BChl precursor to BPheo has been invoked (*60*) in bacteria.]

ESR and ENDOR experiments performed (*18, 39*) on the primary acceptor of PS I trapped in subchloroplast fragments enriched in PS I yield a *g*-value of 2.0033, ΔH = 13–14 G, and ENDOR resonances of 1.7 and ~5 G at 130 K (Table IV). Comparison of recent flash photolysis optical spectra of A_1^- (*13, 14, 23*) with those of Chl^- in vitro show reasonable agreement, but again, the in vivo spectra are red-shifted by ~20 nm. The midpoint potential of A_1 is estimated to be > -0.7 V (*10*) vs. an $E_{1/2}$ value of −0.88 V for Chl^- in DMF. The results suggest

that a monomeric Chl acts as the primary acceptor in PS I. The primary events in PS I can thus be described as follows:

$$P700 + Chl + [Fe\text{–}S] \xrightarrow{h\nu} P700^+ + Chl^- + [Fe\text{–}S] \rightarrow P700^+ + Chl + [Fe\text{–}S]^-$$

As noted, the optical spectra of A_1^- in PS I and I^- in PS II are red-shifted relative to those of Chl^- and $Pheo^-$ in DMF. In addition, the ENDOR coupling constants in the subchloroplast fragments are about 16% lower and 20% larger than the corresponding values of the 1- and 5-methyl groups in DMF. These apparent inconsistencies are now addressed.

The unpaired spin densities listed in Table II for anion radicals of Chl and Pheo used the known crystal coordinates of the corresponding ethyl chlorophyllide (*44*) and methyl pheophorbide (*45*). However, calculations for Chl^- indicate that if the 2-vinyl group is rotated to be perpendicular to the plane of the Chl, the unpaired spin densities decrease by 23% at the 1-carbon and increase by 6% at the 5-carbon, compared to the densities computed using the crystal coordinates of ethyl chlorophyllide-*a*, where the 2-vinyl group makes a torsional angle of 31° to the Chl plane (Table V). These results combined with the in vivo ENDOR data suggest that, as in heme proteins (*61*), neighboring molecules or protein residues impose specific orientations on the substituent groups of the Chl and Pheo within the reaction center. If, in addition to rotating the 2-vinyl group, the protein is assumed to hydrogen bond to the 9-keto group, the calculated unpaired spin density at C-5 (Table V) increases by 15% relative to the "canonical" x-ray configuration. [The calculation simply hydrogen bonds a water molecule to the 9-keto group, as is found in crystalline ethyl chlorophyllide dihydrate (*44*), as a model for hydrogen bonding to a protein residue.] Several other variations, such as ligation of the magnesium atom, an enol form, or transfer of the C-10 proton to the carbomethoxy group do not cause the desired increase in spin density at C-5 (*39a*).

The calculations further indicate that hydrogen bonding and rotation of the substituent groups would cause small shifts in the π- and π^*-orbitals of the molecules, which may account for the small red shifts of the optical spectra observed in vivo relative to those in vitro.

The calculations and model studies presented provide a reasonable explanation for the spectral features of the donors and acceptors observed in vivo in terms of interactions and spatial orientations imposed on the chromophores by the protein environment. In retrospect, this finding is perhaps not surprising in view of the well-documented influence of proteins on heme properties (*62*, *63*). The proposed hydrogen bonding of the protein to the primary acceptors may also repre-

Table V. Unpaired Spin Densities for Pheo⁻ and Chl⁻ with Peripheral Modifications

Chromophore	*Position*	*Crystal Structure Coordinates*[a]	*Vinyl Perp.*[b]	*Hydrogen Bonded*[c]
Chl^-	(1)	0.045	0.035	0.034
	(5)	0.097	0.102	0.112
$Pheo^-$	(1)	0.045	0.034	0.033
	(5)	0.092	0.099	0.107

[a] Vinyl group 31° out of the Chl plane and 15° out of the Pheo plane.
[b] Vinyl group perpendicular to the macrocycle plane.
[c] Vinyl group at 90° and water hydrogen bonded to O_1.

sent a mechanism for converting part of the energy generated by the primary charge separation into protein conformational changes that facilitate subsequent ion transport.

Acknowledgments

This work was supported by the Division of Chemical Sciences, U.S. Department of Energy, Washington, D.C., under Contract No. DE-AC02-76CH00016 at BNL, and by National Science Foundation Grant CHE-78-25557 at U.C.

The authors thank B. Ke for providing the subchloroplast particles.

Literature Cited

1. Govindjee, E., Ed. "Integrated Approach to Plant and Bacterial Photosynthesis;" Academic: New York, in press.
2. "Primary Processes of Photosynthesis;" Barber, J., Ed. Elsevier: Amsterdam, 1977.
3. "Bioenergetics of Photosynthesis;" Govindjee, E., Ed. Academic: New York, 1975.
4. Knaff, D. B. *Photochem. Photobiol.* **1977,** *26,* 327.
5. Bearden, A. J.; Malkin, R. *Q. Rev. Biophysics* **1977,** *7,* 131.
6. Katz, J. J.; Norris, J. R.; Shipman, L. L.; Thurnauer, M. C.; Wasielewski, M. R. *Ann. Rev. Biophys. Bioeng.* **1978,** *7,* 393.
7. Sauer, K. *Ann. Rev. Phys. Chem.* **1979,** *30,* 155.
8. Witt, H. T. *Biochim. Biophys. Acta* **1979,** *505,* 355.
9. Knaff, D. B.; Malkin, R. *Curr. Top. Bioenerg.* **1978,** *7,* 139.
10. Ke, B. *Curr. Top. Bioenerg.* **1978,** *7,* 76.
11. Sauer, K.; Mathis, P.; Acker, S.; Van Best, J. A. *Biochim. Biophys. Acta* **1978,** *503,* 120; *Biochim. Biophys. Acta* **1979,** *545,* 466.
12. Mathis, P.; Sauer, K.; Remy, R. *FEBS Lett.* **1978,** *88,* 275.
13. Shuvalov, V. A.; Dolan, E.; Ke, B. *Proc. Nat. Acad. Sci. USA* **1979,** *76,* 770.
14. Shuvalov, V. A.; Ke, B.; Dolan, E. *FEBS Lett.* **1979,** *100,* 5.
15. Fenton, J. M.; Pellin, M. J.; Govindjee, E.; Kaufmann, K. *FEBS Lett.* **1979,** *100,* 1.
16. Shuvalov, V. A.; Klevanik, A. V.; Sharkov, A. V.; Kryukov, P. G.; Ke, B. *FEBS Lett.* **1979,** *107,* 313.
17. Fujita, I.; Davis, M. S.; Fajer, J. *J. Am. Chem. Soc.* **1978,** *100,* 6280.

18. Fajer, J.; Davis, M. S.; Forman, A.; Klimov, V. V.; Dolan, E.; Ke, B. *J. Am. Chem. Soc.* **1980,** *102,* 7143.
19. Klimov, V. V.; Klevanik, A. V.; Shuvalov, V. A.; Krasnovsky, A. A. *FEBS Lett.* **1977,** *82,* 183.
20. Klimov, V. V.; Dolan, E.; Ke, B. *FEBS Lett.* **1980,** *112,* 97.
21. Friesner, R.; Dismukes, G. C.; Sauer, K. *Biophys. J.* **1979,** *25,* 277.
22. Heathcote, P.; Evans, M. C. W. *FEBS Lett.* **1980,** *111,* 381.
23. Baltimore, B. G.; Malkin, R. *FEBS Lett.* **1980,** *110,* 50.
24. Klimov, V. V.; Allakhverdiev, S. I.; Demeter, S.; Krasnovsky, A. A. *Dokl. Akad. Nauk. SSSR* **1980,** *249,* 227.
25. Klimov, V. V.; Dolan, E.; Shaw, E. R.; Ke, B. *Proc. Nat. Acad. Sci. USA* **1980,** *77,* 7227.
26. Ke, B.; Klimov, V. V.; Dolan, E.; Shaw, E. R.; Shuvalov, V. A.; Parson, W. W.; Fajer, J.; Davis, M. S.; Forman, A. *Proc. Intern. Congress on Photosynthesis,* 5th, 1980, Halkidiki, Greece.
27. Evans, M. C. W.; Sihra, C. K.; Bolton, J. R.; Cammack, R. *Nature* **1975,** *256,* 668.
28. Norris, J. R.; Scheer, H.; Druyan, M. E.; Katz, J. J. *Proc. Nat'l. Acad. Sci. USA* **1974,** *71,* 4897.
29. Feher, G.; Hoff, A. J.; Isaacson, R. A.; Ackerson, L. C. *Ann. N.Y. Acad. Sci.* **1975,** *244,* 239.
30. Phillipson, K. D., Sato, V. L.; Sauer, K. *Biochemistry* **1972,** *11,* 4591.
31. Wasielewski, M. R.; Norris, J. R.; Shipman, L. L.; Lin, C. P.; Svec, W. A. *Proc. Nat. Acad. Sci. USA* **1981,** *78,* 2957.
32. Malkin, R.; Bearden, A. J. *Biochim. Biophys. Acta* **1975,** *396,* 250.
33. Goldfield, M. G.; Halilov, R. I.; Hangulov, S. V.; Kononenko, A. A.; Knox, P. P. *Biochem. Biophys. Res. Commun.* **1978,** *85,* 1199.
34. Van Gorkum, H. J.; Tamminga, J. J.; Haveman, J. *Biochim. Biophys. Acta* **1974,** *347,* 417.
35. Van Gorkum, H. J.; Pulles, M. P. J.; Wessel, J. S. C. *Biochim. Biophys. Acta* **1975,** *408,* 331.
36. Visser, J. W. M.; Rijersberg, C. P.; Gast, P. *Biochim. Biophys. Acta* **1977,** *460,* 36.
37. Visser, J. W. M. Dissertation, State Univ. Leiden, The Netherlands, 1975.
38. Davis, M. S.; Forman, A.; Fajer, J. *Proc. Nat. Acad. Sci. USA* **1979,** *76,* 4170.
39a. Forman, A.; Davis, M. S.; Fujita, I.; Hanson, L. K.; Smith, K. M.; Fajer, J. *Isr. J. Chem.* **1981,** *21,* 265.
39b. Hoff, A. J.; Lendzian, F.; Möbius, K.; Lubitz, W. *Chem. Phys. Lett.* **1982,** *85,* 3.
40. Borg, D. C.; Forman, A.; Fajer, J. *J. Am. Chem. Soc.* **1976,** *98,* 6889.
41. Hanson, L. K.; Chang, C. K.; Davis, M. S.; Fajer, J. *J. Am. Chem. Soc.* **1981,** *103,* 663.
42. Davis, M. S.; Forman, A.; Hanson, L. K.; Thornber, J. P.; Fajer, J. *J. Phys. Chem.* **1979,** *83,* 3325.
43. Chang, C. K.; Hanson, L. K.; Richardson, P. F.; Young, R.; Fajer, J. *Proc. Nat. Acad. Sci. USA* **1981,** *78,* 2652.
44. Chow, H. C.; Serlin, R.; Strouse, C. E. *J. Am. Chem. Soc.* **1975,** *97,* 7230.
45. Fischer, M. S.; Templeton, D. H.; Zalkin, A.; Calvin, M. *J. Am. Chem. Soc.* **1972,** *94,* 3613.
46. Fuhrhop, J. H. *Z. Naturforsch.* **1970,** *325,* 255.
47. Fajer, J.; Davis, M. S. In "The Porphyrins," Dolphin, D., Ed.; Academic Press: New York, 1979; Vol. 4, 197.
48. Fajer, J.; Davis, M. S.; Brune, D. C.; Spaulding, L. D.; Borg, D. C.; Forman, A. *Brookhaven Symp. Biol.* **1976,** *28,* 74.
49. Scheer, H.; Katz, J. J.; Norris, J. R. *J. Am. Chem. Soc.* **1977,** *99,* 1372.
50. Cotton, T. M.; Loach, P. A.; Katz, J. J.; Ballschmitter, K. *Photochem. Photobiol.* **1978,** *28,* 735.

51. Hägele, W.; Schmid, D.; Drissler, F.; Nans, J.; Wolf, H. C. Z. *Naturforsch.* **1978,** *33a,* 1197.
52. Lutz, M., personal communication.
53. Lutz, M. *Biochim. Biophys. Acta,* **1977,** *460,* 408.
54. Matthews, B. W.; Fenna, R. E. *Acc. Chem. Res.* **1980,** *13,* 309.
55. Thurnauer, M. C.; Norris, J. R. *Chem. Phys. Lett.* **1977,** *47,* 100.
56. Rutherford, A. W.; Mullet, J. E. *Biochim. Biophys. Acta* **1981,** *635,* 225.
57. Davis, M. S.; Forman, A.; Fujita, I.; Hanson, L. K.; Fajer, J., submitted for publication.
58. Okamura, M. Y.; Isaacson, R. A.; Feher, G. *Biochim. Biophys. Acta* **1979,** *546,* 394.
59. Dutton, P. L.; Prince, R. C.; Tiede, D. M.; Petty, K. M.; Kaufmann, K. J.; Netzel, T. L.; Rentzepis, P. M. *Brookhaven Symp. Biol.* **1976,** *28,* 213.
60. Shuvalov, V. A.; Parson, W. W. *Proc. Nat'l. Acad. Sci. USA* **1981,** *78,* 957.
61. Takano, T. *J. Mol. Biol.* **1977,** *110,* 569.
62. Lemberg, R.; Barrett, J. "Cytochromes;" Academic: New York, 1973.
63. Ibers, J. A.; Holm, R. H. *Science* **1980,** *209,* 223.
64. Pulles, M. P. J.; Van Gorkum, H. J.; Verschoor, G. M. *Biochim. Biophys. Acta* **1976,** *440,* 98.

RECEIVED for review June 2, 1981. ACCEPTED August 3, 1981.

Model Systems for the Primary Photochemical Events of Photosynthesis and Electron Transfer in Bioenergetic Membranes

PAUL A. LOACH, JENNIFER A. RUNQUIST, JOSEPHINE L. Y. KONG, THOMAS J. DANNHAUSER, and KENNETH G. SPEARS

Northwestern University, Department of Biochemistry and Molecular Biology and Department of Chemistry, Evanston, IL 60201

This chapter describes two model systems that, when coupled together, are designed to effectively reproduce the primary photochemical event of bacterial photosynthesis and subsequent secondary electron transport. In the first model, covalently linked porphyrin–quinone complexes were synthesized and exhibited photochemical charge separation from the excited singlet state. This effect was demonstrated by quenching of fluorescence and formation of a porphyrin (or zinc porphyrin) cation radical and a quinone anion radical in homogeneous solution at room temperature, at 77 K, and in phosphatidylcholine liposomes. The quantum yield was estimated to be near 0.1 for the complex incorporated into liposomes with a radical half-life of 1.5 min. In the second model, for secondary electron transport, metalloporphyrins such as hemin dimethyl ester catalyze electron transport across a phosphatidylcholine lipid bilayer at very high rates, comparable to in vivo electron transport. Catalysis was shown to proceed by an electroneutral diffusion mechanism. These results are discussed from the point of view of future model work and suggest that in vivo electron transport through cytochrome b heme centers may occur in an electroneutral fashion (i.e., by coupled electron and hydrogen ion flow).

0065-2393/82/0201-0515$12.75/0

We developed two model systems that at first may not seem closely related. However, they are each part of an eventually more complicated system. In the more complicated model, the first system is expected eventually to provide charge separation across a lipid bilayer as a result of light absorption. The second system will be catalytic in subsequent secondary electron transport. Thus, we can effectively model the primary photochemical event and coupled secondary electron flow of bacterial photosynthesis, which will provide insights to understanding a variety of in vivo systems. Structurally similar porphyrin complexes were synthesized for the two model systems.

Characteristics of the Primary Photochemical Events in Bacterial Photosynthesis

The best understood of the primary photochemical events in photosynthetic systems are those in photosynthetic bacteria like *Rhodospirillum rubrum* and *Rhodopseudomonas sphaeroides* (*1–5*). Major properties of this system are the following. The primary electron donor consists of two or more protein-bound bacteriochlorophyll molecules (*6–17*), which accept with high efficiency excited singlet state energy from the antenna complex(es) (*6*, *18*, *19*). An electron is donated by this complex from its excited singlet state to another molecule within a time period that is less than 10 ps (*20–22*). The electron comes to rest for about 100 μs on an ubiquinone molecule, which serves as the first stable electron acceptor (*23–27*). The quantum yield for this initial charge separation indicates a very high efficiency [$\geq$0.95; (*28–31*)]. The approximate redox potential span accomplished by the time the electron has reached the first stable electron acceptor ubiquinone is about 0.5 to 0.9 V (*2*, *32*). A cytochrome, such as cytochrome c_2 in *R. rubrum* and *Rps. sphaeroides*, serves as the secondary electron donor to the oxidized bacteriochlorophyll donor unit (*28*, *33*) with an electron transfer rate that varies from about 0.5 μs to a few milliseconds depending on the bacteria. This cytochrome is very tightly coupled and also oxidized with a very high quantum yield (*28*, *31*). Four bacteriochlorophyll molecules, two bacteriopheophytin molecules, and one to three ubiquinone$_{10}$ molecules (probably one, but depends on definition) are tightly bound by one or two polypeptide components as the reaction center or phototrap complex (*5*). This integral complex is mostly contained within the photosynthetic membrane (*5*, *34–37*).

Charge separation to the first stable ubiquinone molecule appears to be electrogenically disposed substantially across the photosynthetic membrane with the bacteriochlorophyll donor unit being near the outer surface of the membrane in the intact cell and the first stable ubiquinone near the inner surface (*38*, *39*). An iron atom is found near

the first stable ubiquinone (Q_A) and the second ubiquinone (Q_B), but is apparently not coordinated to either of them, at least at low temperatures (*5*, *15*, *40*, *41*). This iron is not in a typical iron sulfur center, although cysteine residues may play some role in its binding (*5*, *42*, *43*). If the electron does not participate in normal secondary electron transfer, it may return directly to the primary electron donor unit, presumably by tunneling (*44*, *45*). Secondary electron flow from the first stable ubiquinone molecule (Q_A) to a second ubiquinone molecule (Q_B) occurs in about 100 μs (*27*). *o*-Phenanthroline blocks this latter electron transfer step, which also does not occur at low temperatures.

Recent picosecond spectroscopy measurements suggest that several short-lived intermediate electron acceptors may be identified. One or more of the bacteriochlorophyll molecules responsible for the 800-nm absorbance in the reaction center may serve as an intermediate electron acceptor that directly receives the electron from the bacteriochlorophyll of the donor unit in less than a few ps (*46–48*). This electron is then thought to be passed on to a single bacteriopheophytin molecule in about 5 ps and from there to Q_A in about 200 ps. If electron flow to Q_A is blocked by prior reduction, the electron may return from reduced bacteriopheophytin to the oxidized donor unit and form a complex in its excited triplet state (*49*, *50*). Much of the foregoing information is summarized in Scheme I.

Model System I

On the basis of the preceding description of the in vivo reaction center, the following properties should be an inherent part of a good model system: (1) photochemistry should originate from the metalloporphyrin (or more exactly, magnesium(II) bacteriochlorin) excited singlet state, (2) the quantum yield for charge separation to stable products should be near 1.0, (3) the metalloporphyrin should be the electron donor and a benzoquinone should be the first stable (lifetime longer than 1 μs) electron acceptor, and (4) the charge-separated products should be stable for at least 100 ms at room temperature.

The versatile photochemical activity of porphyrins in general, and chlorophyll in particular, has long been known (*51–53*). Photochemical reaction between chlorophyll and benzoquinones in homogeneous solution has established that high concentrations of benzoquinone (e.g., 0.1 *M*) quench the excited singlet state without producing detectable quantities of oxidized and reduced species (*54*, *55*), although lower concentrations of benzoquinone (e.g., 1 m*M*) can result in charge separation out of the triplet state with reasonably stable oxidized and reduced species (*56*, *57*). Similar photochemical activity

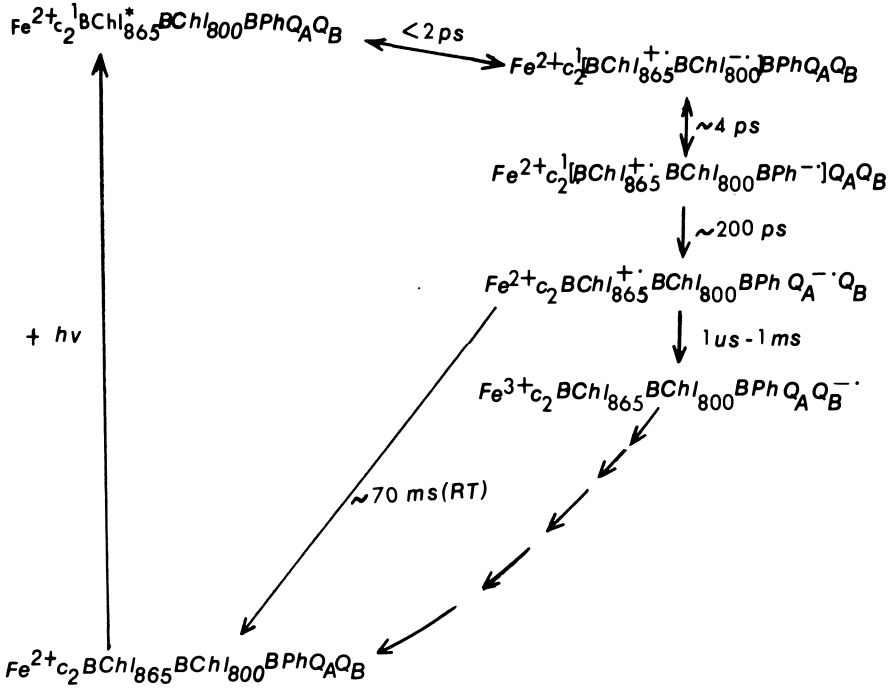

Scheme I. Simple linear scheme for the primary photochemical events in photosynthetic bacteria as observed in R. rubrum *and* Rps. sphaeroides. *$BChl_{865}$ represents the primary electron donor bacteriochlorophyll complex absorbing at 865 nm, $BChl_{800}$ is an additional molecule of bacteriochlorophyll that absorbs at 800 nm and is believed to be a transitory electron acceptor, BPh is a bacteriopheophytin molecule believed to also play a role as an intermediate electron acceptor, Q_A represents the first stable electron acceptor that is a tightly bound ubiquinone molecule, Q_B is a secondary electron acceptor also thought to be a ubiquinone molecule, and Fe^{2+} c_2 represents the ferrous oxidation state of cytochrome c_2.*

was also demonstrated in frozen systems as well as in heterogeneous systems [e.g., films and liposomes (58, 59)].

Because selectively controlling the reaction path in this type of system is difficult, we began a project of synthesizing covalently linked porphyrin dimers and trimers and covalently linked porphyrin–quinone complexes. The covalently linked porphyrin dimer system was useful for studying the transfer of excited singlet state energy from one porphyrin center to another (*60*). Many covalently linked porphyrin species have been synthesized (*60–81*). Recently, we synthesized (*82–86*) a series of covalently linked porphyrin–quinone complexes, which appear to be exceedingly promising complexes for systematically probing photochemical charge separation. With these

model complexes we are imposing a condition which was not possible with the simple models. For example, in the covalently linked porphyrin–quinone complexes, 1 : 1 quinone to porphyrin systems can be studied in a "good" solvent system as well as in limited protic or limited charge environments. Thus, it should be possible to approach much more specifically conditions that were probably selected for the protein binding site of the reaction center of photosynthetic systems over millions of years of evolution.

Experimental for Model System I

The synthesis of covalently linked porphyrin–quinone complexes was previously reported (*82*, *83*). The compounds studied are shown in Structure **I.**

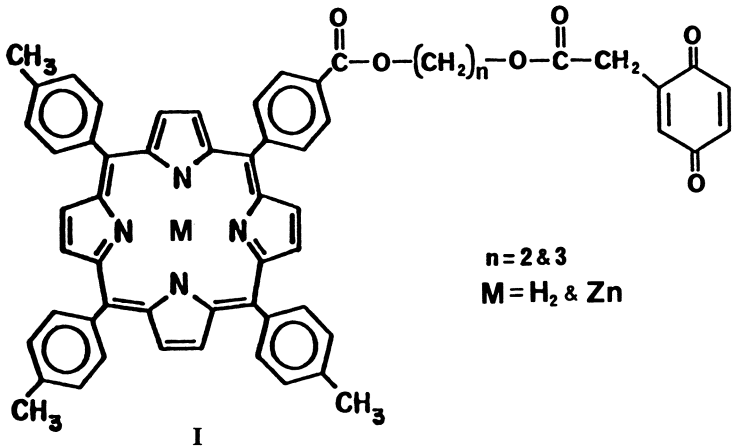

I

M represents a metal such as zinc or two protons for the free base porphyrins. Although the oxidized form of the quinone is shown, the complexes were also prepared with the quinone reduced to a hydroquinone. When M = Zn and n = 3, the compound is referred to as ZnP–3–Q. If the porphyrin is a free base porphyrin and does not contain a metal, the compound is referred to as P–3–Q. If the benzoquinone is reduced to the hydroquinone, then the corresponding abbreviations are ZnP–3–QH_2 and P–3–QH_2.

Solvents used were all of spectroscopic grade. Fluorescence measurements with continuous light were made with a Perkin-Elmer MPF-44A fluorescence spectrometer. Excitation was usually at the wavelength maximum of the Soret band, which was adjusted to an absorbance of 0.30 ± 0.02 nm. The emission spectra were recorded with an excitation bandwidth of 3 nm and an emission bandwidth of 5 nm. Occasionally, excitation at 590 nm was used for P–3–Q. All measurements were at room temperature in air.

The fluorescence lifetimes were measured by time-correlated photon counting techniques with excitation by a mode-locked dye laser pumped by a mode-locked argon ion laser. The dye laser pulses were of ~2 ps full width at half maximum (FWHM) as measured by autocorrelation methods and the

pulse spacing was 10.0 ns. The optics and methods for time-correlated photon counting with lasers were previously described (*87–89*). The excitation conditions for these experiments were $\lambda = 600$ nm, 1–10 mJ of average energy incident on the sample in ~1-mm collimated beam. The fluorescence collection optics were ~12 with an intermediate focus to select the middle 3–4 mm of the 10-mm cuvette. Neutral density and color filters and an aperture were used to adjust the fluorescence intensity. Corning 2-58 and 2-59 filters, which when coupled with the limited red response of an Amperex XP2020 photomultiplier tube, effectively gave fluorescence isolation near ~650 nm.

Electrochemical measurements were taken using cyclic voltammetry. The solvents used in these studies had to be pure and dry. Distilled in glass acetonitrile from Burdick and Jackson was used as received and was stored under nitrogen at all times. Dichloromethane (Distilled in glass, Burdick and Jackson) was dried by shaking with activated molecular sieves for 24 h on a shaker. The supporting electrolyte, tetra-*n*-butylammonium perchlorate (TBAP) (Southwestern Analytical Chemicals) was dried under vacuum at 100°C for 48 h and stored in a vacuum desiccator over phosphorus pentoxide. All data were obtained at room temperature utilizing methods and apparatus previously described (*90, 91*).

Cyclic voltammetry of ZnP–3–QH_2 was performed with an "adder" type operational amplifier potentiostat described previously (*92*). The current flowing between the working and auxiliary electrode was recorded as a function of the reference signal voltage with a Hewlett Packard Model 7001 A *X–Y* recorder.

EPR signals were recorded with a Varian E-3 spectrometer (Varian Associates). Illumination of the sample was provided by the output of a 1000-watt tungsten projection bulb (GE Model DFD). The exciting light passed through a 5-cm thick water filter and two Corning color filters (3-67, 4-94) before being focused onto the window of the EPR sample cavity. All samples were anaerobic utilizing procedures previously described (*25, 32*).

Results and Discussion for Model System I

The absorbance spectra of ZnP–3–Q and ZnP–3–QH_2 are shown in Figure 1. The visible region of the spectra reflects only the spectral properties of the Zn porphyrin part of the molecule, but bands in the UV region are due to both the quinone group and the Zn porphyrin group. The spectra above 350 nm are identical with that of 5-(4-carbomethoxyphenyl)-10,15,20-tritolylporphyrinatozinc in the same solvent. A difference spectrum of the UV region is plotted to show the quinone group more clearly and this spectrum is compared with a similar difference spectrum for 1,4-benzoquinonylethanoic acid. These data show that in this solvent system the quinone group does not perturb the Zn porphyrin absorbance spectrum or vice versa. Therefore, there is no evidence of complex formation and the spectral properties appear to be merely the sum of the two parts of the molecule.

Previously reported NMR data (*83*) also indicated that in chloroform there was no evidence for significant interaction between

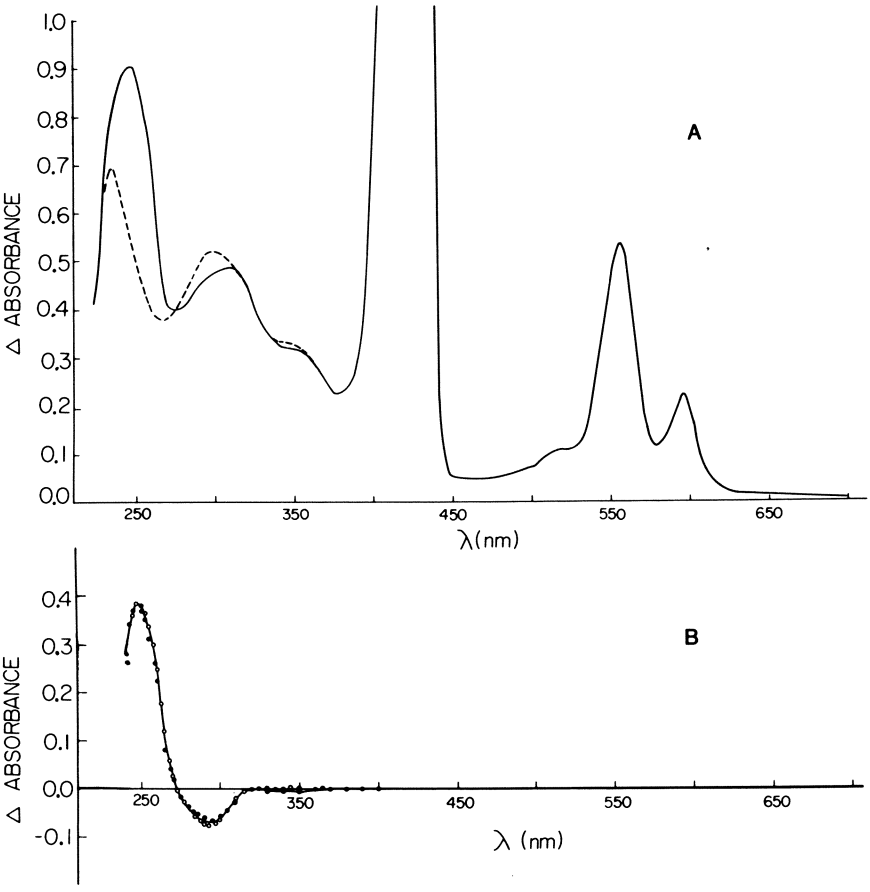

Figure 1. A: Absorbance spectra of ZnP–3–Q (solid line) and ZnP–3–QH_2 (dashed line) in dichloromethane containing 2% ethanol. Potassium borohydride was added to obtain the reduced form. The concentration was 2.5×10^{-5} M, 1-cm cuvettes, room temperature. (Reproduced, with permission, from Ref. 83. Copyright 1980, J. Heterocycl. Chem.)

B: The difference spectrum of ZnP–3–Q minus ZnP–3–QH_2 (●) from part A compared with that for the oxidized minus reduced difference spectrum of homogentisic acid (○) in the same solvent system. Concentrations were 2.5×10^{-5} M in each case. (Reproduced, with permission, from Ref. 83. Copyright 1980, J. Heterocycl. Chem.)

the two parts of the molecule because the peak locations and intensities were identical with appropriate solutions of the unlinked quinone and unlinked Zn porphyrin.

Therefore, the electrochemical behavior of the molecule was expected primarily to reflect properties very similar to those of free or unlinked quinone and Zn porphyrin molecules. Figure 2 shows that

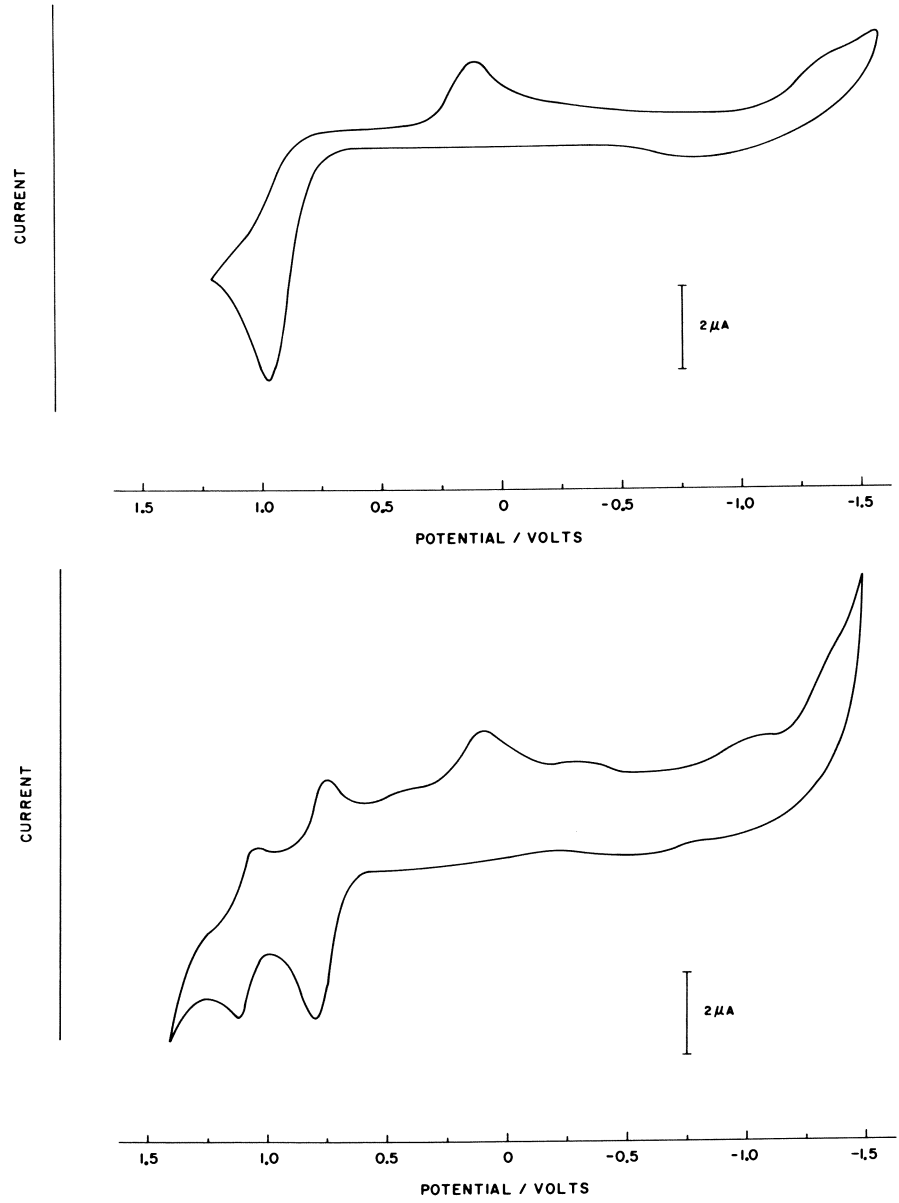

Figure 2. Cyclic voltammograms of 3-benzoyloxypropyl 2,5-dihydroxyphenylacetate (top) and ZnP–3–QH_2 (bottom) in acetonitrile. The supporting electrolyte was tetrabutylammonium perchlorate. Voltages are vs. SCE. The scan rate was 10 mV/s. For the top trace, the scan began at −1.60 V and the initial direction was positive. For the bottom trace, the scan began at +1.50 V and the initial direction was negative.

for ZnP–3–QH_2 this expectation is observed. The cyclic voltammogram very well approximates the sum of that for 3-benzoyloxypropyl 2,5-dihydroxyphenylacetate, used as a representative molecule for the quinone end, and *meso*-tetraphenylporphyrinatozinc [ZnTPP;(93, 94)] as a representative of the Zn porphyrin end. Thus, an irreversible two-electron oxidation of the reduced quinone is observed at 0.79 V vs. SCE and the two waves with $E_{1/2}$ values of 0.80 and 1.14 V vs. SCE reflect the formation of $ZnP^{+\cdot}$ and ZnP^{2+}, respectively.

When the cyclic voltammogram of ZnP–3–Q was measured (*see* Figure 3), the two reversible waves for formation of $ZnP^{+\cdot}$ and ZnP^{2+} were again easily observed, but no reversible waves for formation of Q^{-} and Q^{2-} were observed. A similar behavior was also seen when the benzoquinone form of homogentisic acid was measured by cyclic voltammetry (not shown). Apparently, the methylene group, which is adjacent to the benzoquinone ring as well as to a carboxyl group (or ester in the linked complex), provides a proton that negates the two reversible and well-separated one-electron reductions normally observed in aprotic solvents. Again, the $E_{1/2}$ values for formation of $ZnP^{+\cdot}$ (0.80 V vs. SCE) and ZnP^{2+} (1.14 V vs. SCE) were unaffected by the quinone oxidation state.

Fluorescence Properties. The fluorescence emission and excitation spectra of ZnP–3–QH_2 were measured in several solvents. In dilute solutions, the intensity and wavelength dependence of the fluorescence spectra for ZnP–3–QH_2 were identical to those of the unlinked ZnP molecule. Therefore, a property of the ZnP group, in this case its excited singlet state, was unaffected by the covalently linked hydroquinone group. However, if the quinone was in the benzoquinone oxidation state, significant quenching was observed in every solvent examined (*see* Table I). The extent of quenching was solvent dependent. In general, less quenching was observed in more viscous solvents such as ethylene glycol or 1-hexanol. However, very different effects were observed in some solvents of nearly equal and low viscosity. For example, compare the results for P–3–Q in dichloromethane and dimethylformamide. Because P–3–Q was quenched to about the same extent as ZnP–3–Q in each solvent system for which we have comparable data, zinc contributed no unique effect. Also, because pyridine (a coordinating ligand) was without effect on the ZnP–3–Q fluorescence yield, coordination of the quinone to the zinc does not play a role in the quenching mechanism. Such intramolecular coordination would be most difficult to achieve because of steric restraints. If free benzoquinone were added to a solution of the free zinc porphyrin or free porphyrin at the concentrations employed in the experiments with ZnP–3–Q and P–3–Q, the benzo-

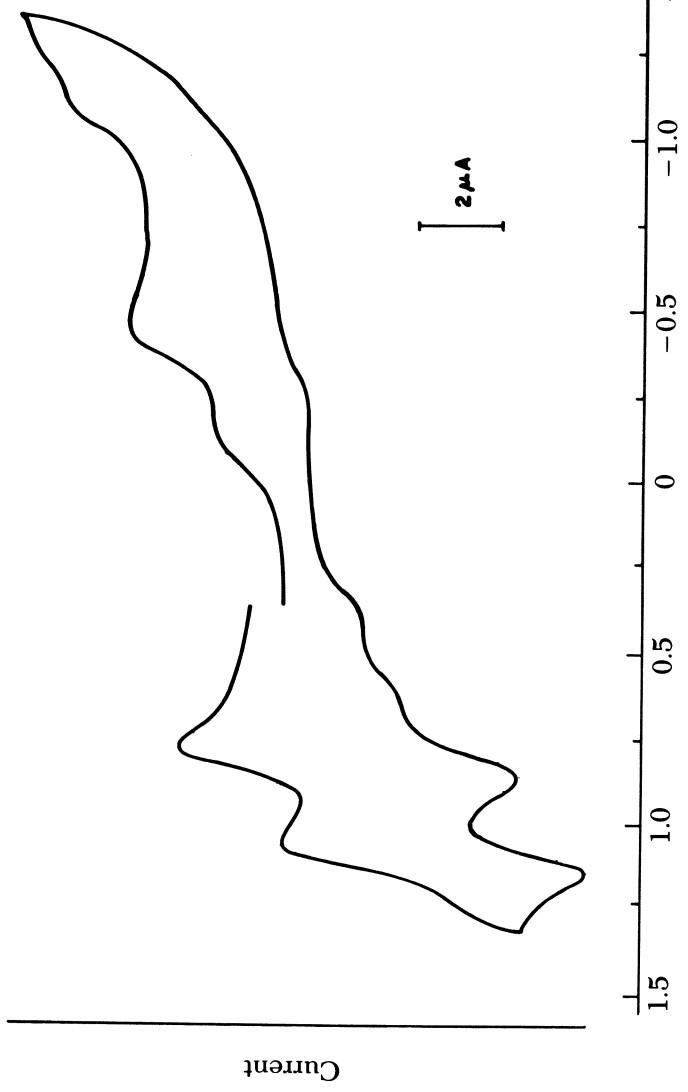

Figure 3. Cyclic voltammogram of 1×10^{-3} M ZnP–3–Q in dichloromethane. The supporting electrolyte was tetrabutylammonium perchlorate. The voltages are vs. SCE. The initial potential was 0.32 V and the initial scan direction was negative.

quinone concentration would need to be increased by a factor of 10^4 or greater before comparable quenching would be observed.

Fluorescence lifetimes were measured in several solvent systems. Dramatic singlet state quenching was observed for both porphyrin–quinone linked systems in acetonitrile or dichloromethane as shown in Table II. The presence of the electrolyte tetrabutylammonium per-

Table I. Relative Fluorescence Yield

Solvent	*Viscosity (Rel)*	*ZnP–3–Q*	*P–3–Q*
Ethylene glycol	1335	—	0.82
1-Hexanol	387	0.59	—
Dimethylformamide	75	—	0.80
Propylene carbonate	—	—	0.45
Dioxane	109	0.51	0.43
Ethanol	100	0.35	—
Acetonitrile	33	0.42	—
Acetonitrile + TBAP	—	0.50	0.51
Dichloromethane	39	0.35	0.22
Dichloromethane + 1% pyridine	—	0.33	—
Petroleum ether	20–28	0.13	—
Pentane	—	—	0.66

Note: Concentration of ZnP–3–Q and P–3–Q was about 5×10^{-7} *M*. All O.D. at wavelength of excitation (Soret band) were 0.30. Room temperature. The fluorescence of the free ZnP or free P was assigned a relative fluorescence yield of 1.0 in each solvent system. These measurements were made in air and the absorbance spectrum of each sample was taken before and after measurement of its fluorescence. In general, no degradation of the sample was observed during this time.

Table II. Fluorescence Lifetimes

	Solvent[a]			
Compound	*ACN*	*DCM*	*DMF*	*PN*
TPP[b]	9.0	8.2	10.6	11.1
P–3–QH_2	8.0	6.5	9.0	7.9
P–3–Q	~1.6[c]	~1.8[c]	8.9	8.2
Zn–TPP	1.8	—	1.8	~1.6[d]
ZnP–3–QH_2	1.8	—	1.7	~1.0[d]
ZnP–3–Q	~0.7[c]	—	1.7	~0.5[d]

[a] Solvents are acetonitrile (ACN), dichloromethane (DCM), dimethylformamide (DMF), and pentane (PN).
[b] TPP is 5,10,15,20-tetraphenylporphyrin.
[c] The decays are very nonexponential and at short times are approximately given by these estimates.
[d] These decays are only estimates because a large component of long-lived decay, probably due to photoproduced metal free porphyrin, reduces the accuracy.

chlorate (TBAP) had no effect on the measurement. The quantum yields showed that the intrinsic radiative decay is constant so that the shortened lifetime is a true quenching process. A comparison of the data in Table II with the fluorescent yields measured with continuous light (Table I) shows a very good overall correlation. Most likely the quenching process involves loss of an electron from the excited singlet state of the porphyrin or Zn porphyrin to the quinone, which results in a charge-separated state. The lifetime data may be expected to be nonexponential (as observed in several systems) for a diffusion-controlled process such as electron transfer. Other mechanisms that might be considered seem unlikely. For example, the quinone has electronic states sufficiently high that an enhancement of singlet–triplet coupling or direct singlet state quenching is a very unlikely process, especially when solvents such as dimethylformamide and acetonitrile behave so differently.

Photochemical Activity. When anaerobic solutions of ZnP–3–Q or P–3–Q were illuminated at room temperature in dichloromethane or acetonitrile containing TBAP, radical species were observable by ESR measurements. A typical result for ZnP–3–Q in acetonitrile is shown in Figure 4 (top). The ESR signal observed is asymmetric. For control experiments, the complex 5-(4-carbomethoxyphenyl)-10,15,20-tritolylporphyrinatozinc was electrochemically oxidized in dichloromethane by controlled potential coulometry and its ESR signal was recorded [*see* Figure 4 (bottom)]. In a similar manner we electrochemically reduced methyl-*p*-benzoquinone to its anion radical and recorded its ESR signal [also Figure 4 (bottom)]. By adding equal concentrations of these two ESR signals together [Figure 4 (bottom)], the resulting asymmetric signal was nearly indistinguishable from the photochemical product with ZnP–3–Q. No such ESR signals were observable when equimolar amounts of free ZnP and free quinone were added together at these concentrations. Thus, the charge-separated state $ZnP^{+\cdot}$–3–$Q^{-\cdot}$ was identified as the photochemical product. The decay of these radicals was too fast (less than 1 ms) to measure with the instrumentation used. The quantum yield for formation of the charge-separated state was estimated to be at least 0.01, perhaps much higher. β-Carotene and oxygen were without effect on the yield of charge-separated products; these molecules greatly quench the excited triplet states (*95*, *96*). Much smaller steady state yields (less than 10%) of photochemical products were found in the absence of TBAP.

Very long-lived radical species also could be observed at low temperature (77 K). The ESR signal of these species was also quite asymmetric and was once again accounted for by the sum of equal concentrations of 5-(4-carbomethoxyphenyl)-10,15,20-tritolylporphyrinatozinc cation and methyl-*p*-benzoquinone anion radical generated

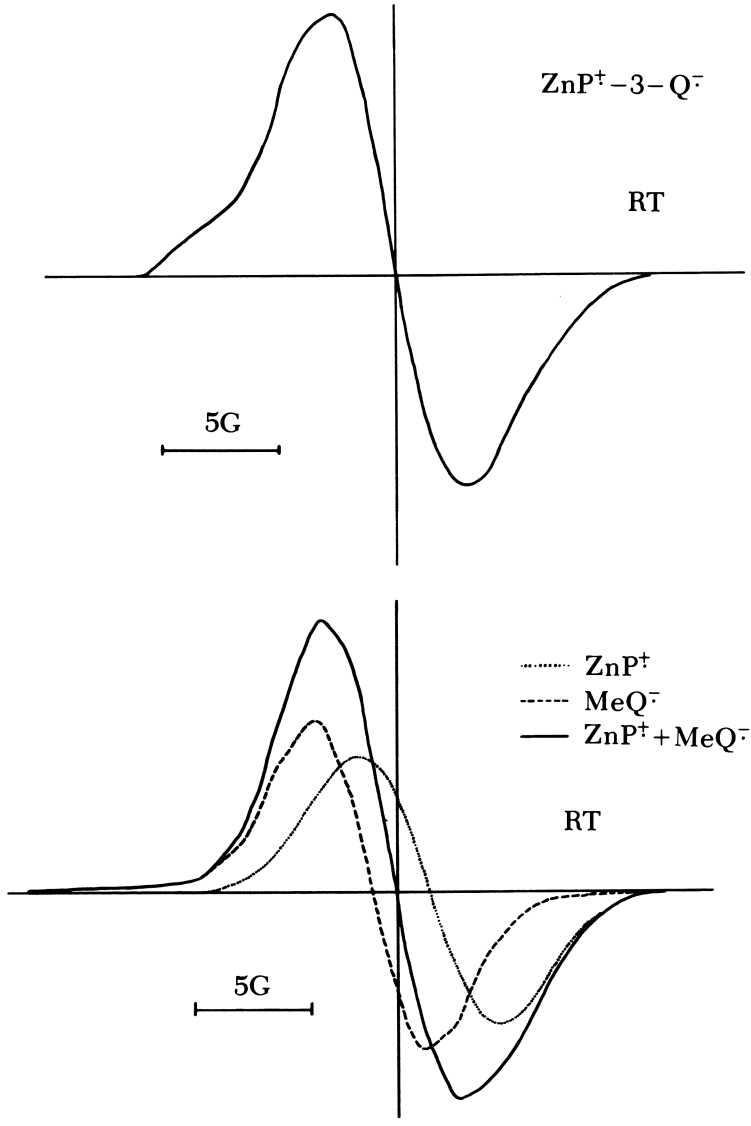

Figure 4. Top: EPR signals produced by excitation of 5×10^{-4} M ZnP–3–Q in acetonitrile (with 0.1 M tetrabutylammonium perchlorate) with light between 555 and 595 nm.

Bottom: EPR signal of the cation radical of approximately 10^{-3} M 5-(4-carbomethoxyphenyl)-10,15,20-tritolylporphyrinatozinc and the anion radical of 3-benzoyloxypropyl 2,5-dihydroxyphenylacetate produced electrolytically in acetonitrile (with 0.1 M tetrabutylammonium perchlorate). The solid line represents the sum of equal spin densities of each radical.

electrochemically and measured by ESR at 77 K. The decay rate for the radicals generated was very slow and up to approximately 5% of the total population of ZnP–3–Q present could be converted to the charge-separated product. The quantum yield determined for formation of the charge-separated state at 77 K was quite low, 2×10^{-5}. In the absence of TBAP the yield of charge-separated products was again only about 10% of those found in its presence.

Perhaps the most interesting matrix in which to test the ZnP–3–Q and P–3–Q complexes for activity is that of a phospholipid bilayer. Following the preparatory procedure described under "Experimental for Model System II," ZnP–3–Q was incorporated into egg yolk phosphatidylcholine vesicles at a ratio of 1 ZnP–3–Q per 250 phospholipid molecules. The absorbance spectrum of the liposomal system was very similar to that shown in Figure 1 with no evidence of degraded products absorbing in the visible region of the spectrum. This system was highly photoactive (*see* Figure 5) and exhibited a very slow decay at room temperature (half-time approximately 1.5 min). The signal was somewhat asymmetric but has not yet been analyzed in detail. Up to about 10% of the ZnP–3–Q present could easily be converted to charge-separated products with 575-nm light. From quantitative measurement of the initial rate of radical formation and the rate of absorbed light at 555–595 nm, a quantum yield of 0.1 was obtained.

Conclusions for Model System I

The measurements of fluorescence quenching and fluorescence lifetimes clearly support the conclusion that the formation of $ZnP^{+\cdot}$–3–$Q^{-\cdot}$ or $P^{+\cdot}$–3–$Q^{-\cdot}$ by photochemical charge separation occurs out of the excited singlet state with a quantum yield as high as 0.8 (on the basis of quenching 80% of fluorescence). At room temperature in homogeneous solution, some of these charge-separated species have a long enough lifetime to be detected easily by ESR with relatively low intensity continuous illumination and were not sensitive to β-carotene or oxygen. In organic solvents, the presence of the TBAP electrolyte stabilized the charge-separated state approximately tenfold. In comparable studies with free chlorophylls, quenching of the excited singlet state by high benzoquinone concentrations results in products that back reacted within a few picoseconds. At low temperature (77 K) in acetonitrile with TBAP present, a substantial portion of ZnP–3–Q could be photochemically converted to $ZnP^{+\cdot}$–3–$Q^{-\cdot}$, which required days to decay in the dark. A similar reactivity at low temperatures was confirmed by Ho et al. (97), who utilized our methods to synthesize the P–3–Q complex.

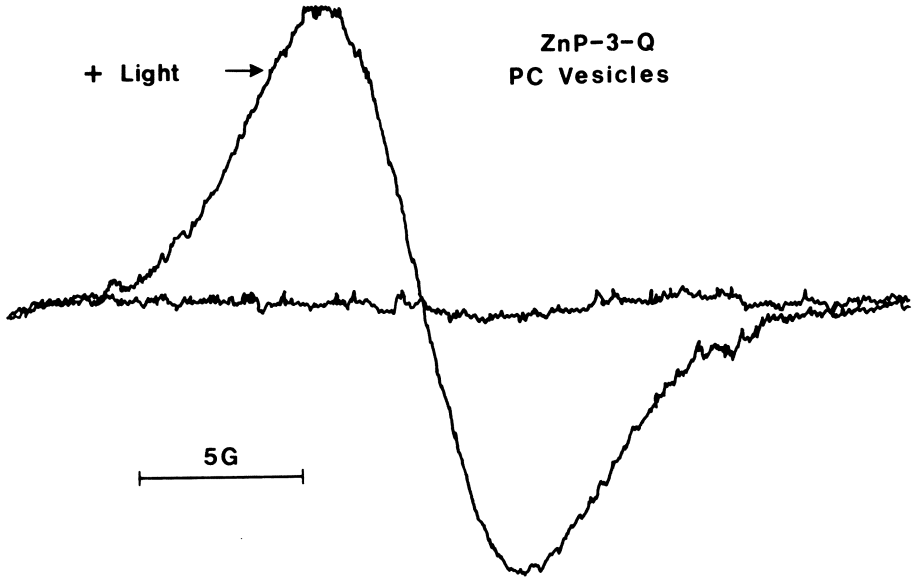

Figure 5. Light-induced EPR signal of ZnP–3–Q in egg yolk phosphatidylcholine vesicles. The trace obtained upon illumination with light of 575 ± 20 nm at 1.65 × 10^5 ergs/cm²/s is marked. The other trace is the dark signal before illumination. Concentration of ZnP–3–Q in the sample was 1 × 10^{-4} M. The ratio of ZnP–3–Q to lipid was 250. The quantity of free radical produced in this experiment was 8 × 10^{-6} M, as determined by direct comparison with a sample containing a known spin density [chromatophores from R. rubrum *(29)]. Nearly the same signal in shape and magnitude was obtained in the presence or absence of air. (Reproduced, with permission, from Ref. 89. Copyright 1982, Pergamon Press, Ltd.)*

The photochemical activity of ZnP–3–Q in egg yolk phosphatidylcholine vesicles at room temperature is especially interesting because of the high quantum yield (0.1) and slow decay ($t_{1/2}$ = 1.5 min) of the charge-separated species. Although this covalently linked complex could be approximately 30 Å from one end to the other in a fully extended conformation, it seems unlikely that it actually spans the bilayer. However, future modifications of this system certainly offer the likelihood of achieving such transbilayer charge separation. Photochemical activity of monomeric chlorophyll incorporated into liposomes reacting with free quinones has been reported (*59*), as has photochemical activity of monomeric or free Mg octaethylporphyrin incorporated into black lipid membranes (BLMs) (*98–100*). The photochemistry in the chlorophyll system was shown to be from the excited triplet state, and the reaction path was not determined in the Mg octaethylporphyrin system. The properties of the charged double

layer at the bilayer water interfaces are obviously of importance in stabilization of these charge-separated systems.

A calculation of the energy available in the excited singlet state and excited triplet state in comparison to that required to create the photochemical products observed (*see* Table III) demonstrates that the photochemistry is not likely to be derived from the excited triplet state in the case of P–3–Q in acetonitrile or dichloromethane when it is excited with low intensity continuous irradiation. Under these conditions, one would expect that some 30% of the energy available per quantum would need to be sacrificed to ensure stable products (*101–104*). Because of the parallel results observed for ZnP–3–Q and P–3–Q in the solvent dependencies of fluorescence quenching and photochemical product formation, one would expect the same mechanism of quenching to be operative in both. Thus, we would suggest that the covalently linked porphyrin–quinone model systems we synthesized provide an efficient electron acceptor at a close enough distance to the porphyrin that charge separation can occur out of the excited singlet state of the porphyrin without the need for complex formation between the ZnP and Q ends of the molecule, making it possible to obtain stable charge-separated products. We are currently involved in an examination of the spectral changes in the time domain of picoseconds, nanoseconds, and microseconds to evaluate better the reaction path and to determine how the model system might be modified to approximate even more closely the in vivo system.

These covalently linked porphyrin–quinone complexes fulfill the first three criteria suggested for a good model system. That is, photo-

Table III. Energy Considerations

			$E_{1/2}$	
Species	E_s	E_t	*DMF*	*DCM*
ZnP	2.06	1.59	0.86	0.71
P	1.93	1.46	1.11	0.95
Q	—	—	−0.59	−0.59
			$\Delta E_{1/2}$	
			DMF	*DCM*
ZnP–3–Q			1.45	1.30
P–3–Q			1.70	1.54

Note: E_s and E_t are calculated energies of excited singlet and triplet states (*142*), respectively, $E_{1/2}$ is the measured polarographic half-wave potential vs. SCE (*143*), and $\Delta E_{1/2}$ is the difference between the $E_{1/2}$ values for formation of the cation radical of the porphyrin species and that for formation of the anion radical of the quinone in the specified solvent.

chemical charge separation probably occurs out of the excited singlet state, a porphyrin or Zn porphyrin cation radical and a quinone anion radical result, and the quantum yield may be as high as 0.8 in some solvent systems. However, although the charge-separated products were stabilized sufficiently to observe them at room temperature in a well-defined homogeneous solvent system, their lifetime is approximately 10^3 times shorter than a good model should exhibit. On the other hand, in the phosphatidylcholine liposome system the radicals produced have quite long lifetimes (1.5 min). In this case, however, the quantum yield is not as high as desirable (0.1 vs. 1.0) and the percent yield (for low light intensities) of charge-separated species is limited to about 10% of the material present. We will continue our work on this particular liposome system to achieve charge separation across the bilayer. A much more detailed characterization of this system will be required to demonstrate the location of the species produced.

Model System II

Electron transport in photosynthetic, bacterial, and mitochondrial systems involves a sequence of oxidation–reduction reactions that occur in intimate association with membranes. A pictorial view of such a system as envisioned for mitochondria is shown in Figure 6. Although good evidence exists for much of the asymmetric electron and proton flow depicted in the scheme, the exact details for any specific part of the sequence are not yet available.

According to the chemiosmotic hypothesis (*106*, *107*), three electron and hydrogen atom loops should exist in the chain to provide the driving force for subsequent phosphorylation. A schematic example of what is accomplished in such a loop is shown in Figure 7. For the electrogenic or "electron wire" part of these loops, many reasonable candidates were assumed to exist, such as a chain of iron sulfur clusters for NADH dehydrogenase, a series of cytochrome b components for the b–c_1 complex, and cytochrome a and a_3 (each with a heme a and a copper center) in cytochrome oxidase. However, experimental proof of the existence of such loops to explain the electroneutral portion (that is, the coupled electron and proton flow) is difficult to obtain. Ubiquinone has long been suggested to provide one path for coupled electron and proton flow because the molecule is uncharged in both the quinone and hydroquinone oxidation states and is considered to be lipophilic enough to diffuse readily across the membrane. However, model liposome studies have raised questions about the efficacy of a UQ_{10} molecule diffusing across a lipid bilayer sufficiently fast to play such a role in in vivo electron transport (*108–110*). Recently, some-

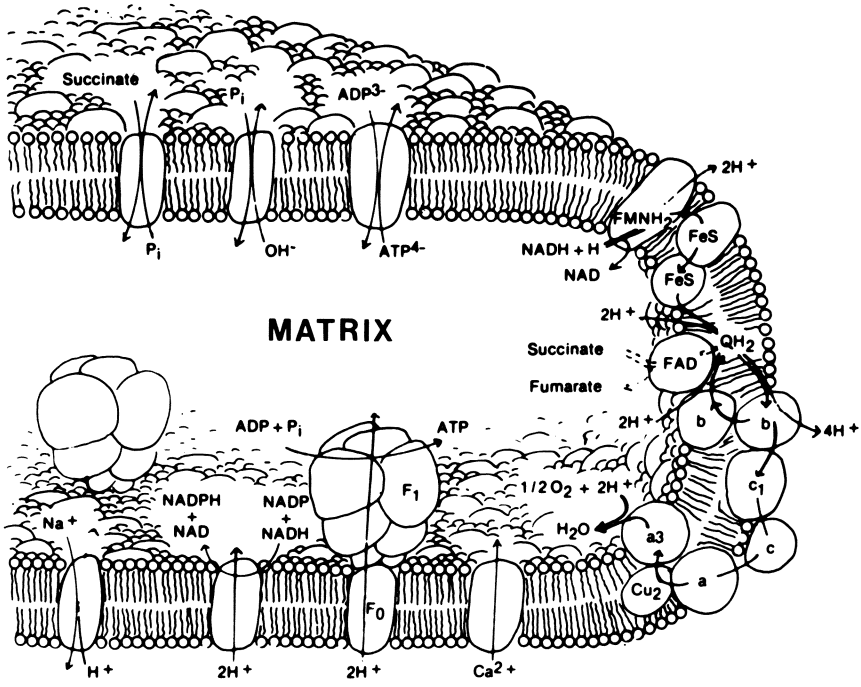

Figure 6. Scheme for electron transport and coupled oxidative phosphorylation in mitochondria. Most abbreviations used are standard for biochemical molecules. Other abbreviations are FeS, an iron sulfur protein of NADH dehydrogenase; and QH_2, ubihydroquinone; b, c_1, c, a, and a_3 are cytochrome components. (Reproduced, with permission, from Ref. 105. Copyright 1978, Harvard University Press.)

what contorted "*Q*-loops" were proposed in an effort to utilize ubiquinone molecules for electroneutral electron and proton transfer (*111–113*). From research with photosynthetic bacteria (*2*, *23–26*, *114–119*), several ubiquinone protein complexes were characterized, some of which may play a role in electron-only electron transport. Similar ubiquinone protein complexes were also recently discovered in mitochondrial systems (*120*). Thus, apparently many protein-bound quinones play an important role in one-electron transport. Whether a proton accompanies the electron in these reactions is unclear.

Our reflections on the kind of redox centers present in electron transport systems led us to consider a series of heme groups, such as those in the cytochrome b complexes presumed to span the bilayer, that would be just as likely to be involved in electroneutral electron transport as in electron-only electron transport. To learn more about electron transport and its coupling to proton and other ion transport in

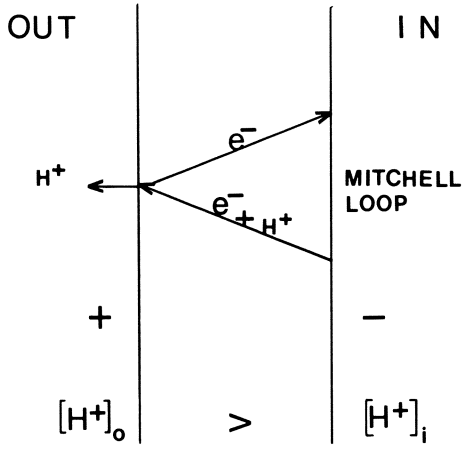

Figure 7. Conceptualization of a Mitchell loop (106, 107). *For a mitochondrion, the IN would be the matrix, and OUT would be the space between the inner and outer membranes. With electron flow through the loop, a charge develops across the bilayer, and the hydrogen ion concentration outside increases relative to that inside.*

membrane systems, we initiated a series of studies of model systems utilizing lipid bilayers (*121–124*). Building on a model liposome system introduced by Hinkle (*125*, *126*), we set out to examine many aspects of intramembrane electron transport as catalyzed by metalloporphyrins. In this liposome system, a highly charged aqueous oxidant-like potassium ferricyanide is trapped within the vesicles and a charged reductant-like sodium dithionite is utilized outside. Because these ions are not permeant, the rate of electron flow across the bilayer is quite slow without a catalyst. The solubility properties of iron porphyrins suggested that a molecule such as hemin dimethyl ester would be as compatible with the hydrocarbon portion of a lipid bilayer as many lipids or ionophores, and as such, it might be free to diffuse from one side of a bilayer to the other in either the ferric or ferrous oxidation state. We therefore tested hemin dimethyl ester for catalysis of electron transfer in a liposome system (as indicated schematically in Figure 8) and it was highly catalytic. The characteristics of such metalloporphyrin catalysis will be described.

Experimental for Model System II

The experimental details for the methodology and materials utilized were recently reported (*124*). Liposomes containing a selected metalloporphyrin were prepared by evaporating onto the glass surface of a 100-mL round-bottom flask a chloroform solution containing 100 mg of egg yolk phosphatidylcholine

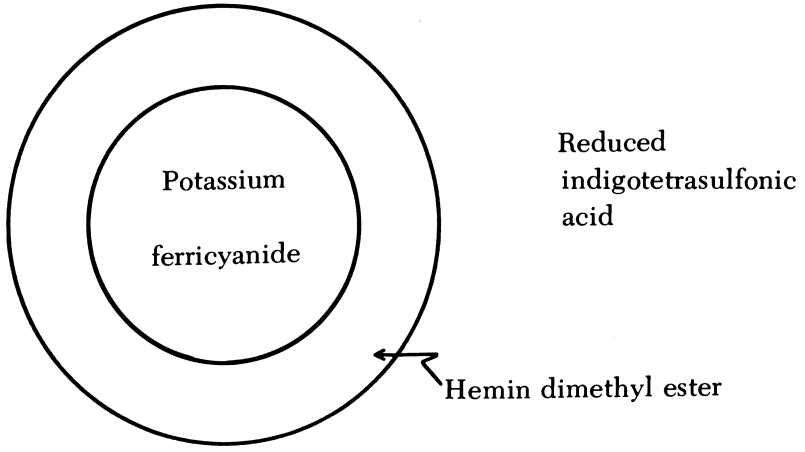

Figure 8. Schematic diagram of the liposome system used in our model electron transport studies. The phospholipid used was usually egg yolk phosphatidylcholine although mixtures of this with cholesterol, cardiolipin, and phosphatidylethanolamine were also examined.

(type III-E, Sigma Chemical Co.), and between 0.05 and 1.0 mg of a chosen metalloporphyrin. The lipids containing the metalloporphyrin were removed from the glass surface by suspending them in aqueous buffer typically containing 0.1 *M* potassium ferricyanide. After sonication and centrifugation to remove larger vesicles, the liposomes were passed through a gel filtration column containing Sephadex G-25 (Sigma Chemical Co.) to remove potassium ferricyanide external to the vesicles. Typical incorporation of metalloporphyrin complexes was between 50 and 85%. Two buffer systems were employed, 0.4 *M* imidazole in which both the ferrous and ferric oxidation states of hemin dimethyl ester were octahedral complexes and low spin (*124*), and 0.2 *M* potassium phosphate in which the ferrous and ferric oxidation states of hemin dimethyl ester were pentacoordinate and high spin (*124*). In some experiments, where noted, a lower concentration of phosphate buffer was employed.

The electron transfer assay was conducted anaerobically in a cuvette containing reduced indigotetrasulfonic acid (or reduced indigodisulfonic acid or horseradish peroxidase) into which the anaerobic vesicle preparation was injected. The absorbance at an appropriate wavelength (600 nm for indigotetrasulfonic acid) was monitored continuously with an Acta CIII spectrophotometer (Beckman Instruments, Inc.).

Results and Discussion for Model System II

Figure 9A shows that hemin dimethyl ester catalyzed electron transport across an egg yolk phosphatidylcholine bilayer at rapid rates. The catalysis showed a first-order dependence on the concentration of reduced indigotetrasulfonic acid (Figure 9B) and hemin dimethyl

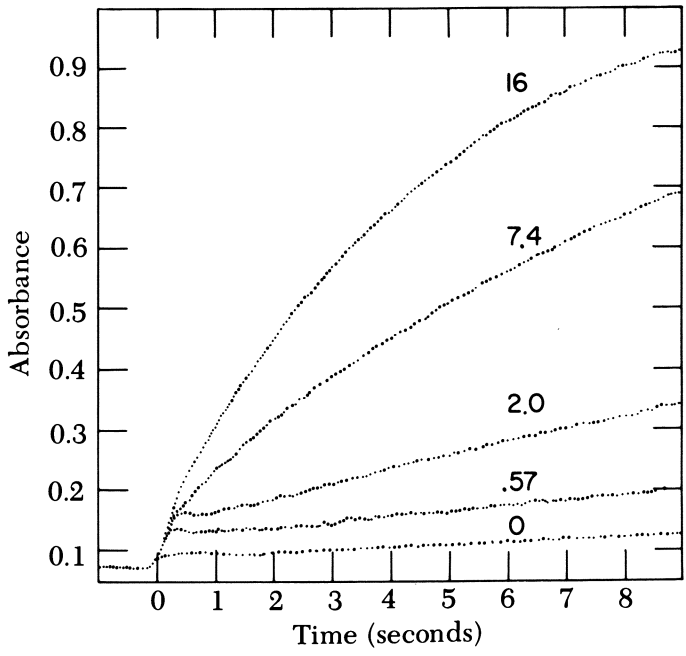

Figure 9A. Absorbance increase at 600 nm observed upon addition of liposomes containing 310 nmol of potassium ferricyanide to an anaerobic solution containing reduced indigotetrasulfonic acid. The quantity (nanomols) of hemin dimethyl ester incorporated into the liposomes during preparation is indicated by the numbers above each curve. Each sample contained 10 mg of egg yolk phosphatidylcholine in 2.85 mL of 0.4 M imidazole buffer, pH 7.0, which contained 0.175 M NaCl, 0.025 M KCl, and 285 m equivalents (5×10^{-5} M; O.D. = 1.0 when oxidized) of reduced indigotetrasulfonic acid.

ester (Figure 9C). Thus, the rate-limiting step under these conditions was the bimolecular reaction beween ferric hemin dimethyl ester and reduced indigotetrasulfonic acid at the exterior surface of the vesicle. The rate-limiting step could be shifted to a process that depended upon the diffusion of the hemin dimethyl ester across the bilayer by arbitrarily choosing conditions of high concentrations of reduced indigotetrasulfonic acid and potassium ferricyanide and low concentration of hemin dimethyl ester. In experiments conducted at the low end of the hemin dimethyl ester to phospholipid ratio, only one hemin dimethyl ester molecule was probably present per vesicle. An almost identical rate of catalyzed electron transport was observed by hemin dimethyl ester in a 0.2 *M* phosphate buffer system. Therefore, the rate of electron transfer was not dependent on whether the iron porphyrin complex was in a high or low spin state.

Dependency on Metalloporphyrin Structure. Changing the structure of the metalloporphyrin generally gave predictable results in catalysis (Table IV). The free base porphyrin, protoporphyrin IX, Ni(II) tetraphenylporphyrin, and Co(II) tetraphenylporphyrin were not catalytic as expected. These three lack a redox transition in the range between +0.5 and −0.1 V, which would appear to be required because of the $E^{\circ\prime}$ values of the aqueous redox materials employed [Fe^{3+}/Fe^{2+} cyanide has an $E^{\circ\prime}$ value near 0.45 V (*127–129*) and that of indigotetrasulfonic acid is near −0.05 V (*127, 129*)]. In addition to the likelihood that the cobalt complex has its redox transition out of the appropriate range for catalysis, it also may be expected to undergo initial redox changes much more sluggishly than the corresponding iron complex (*130, 131*).

A metalloporphyrin complex of special interest is that of hemin, which has two free carboxyl groups. This iron porphyrin complex was not expected to be very catalytic, if at all, at pH 7 because of its

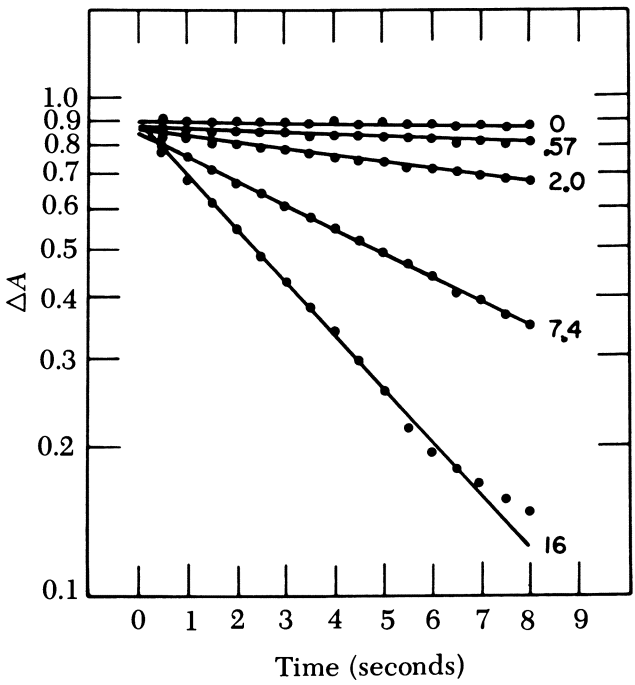

Figure 9B. Log plot of the absorbance difference at 600 nm for the data shown in the top figure. In this plot the Y-axis is proportional to the reduced indigotetrasulfonic acid concentration, which was determined from the absorbance for the fully oxidized indigotetrasulfonic acid minus the absorbance measured at any time after mixing.

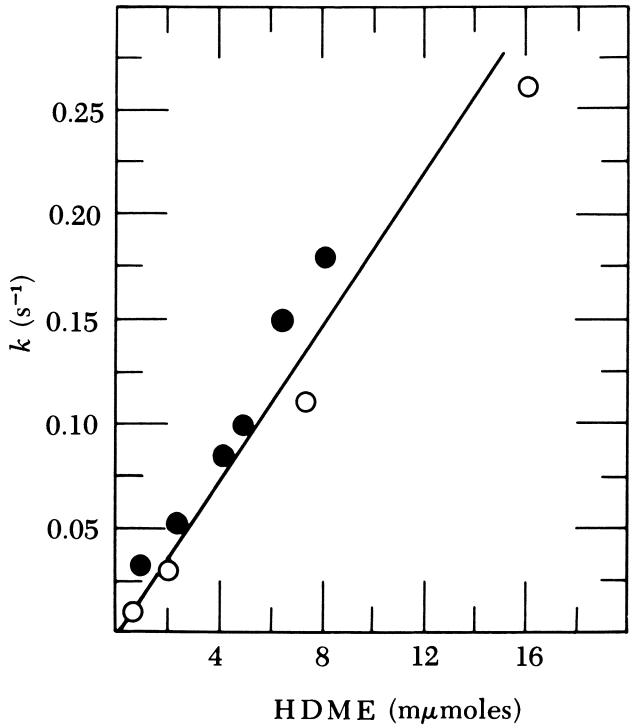

Figure 9C. Dependency of the rate of oxidation of reduced indigotetrasulfonic acid on the hemin dimethyl ester concentration. The open circles represent the data from the experiments indicated in Figures 9A and 9B and the solid circles are data from another similar set of experiments.

carrying one or two negative charges. Such charges were expected to be solvated at the aqueous interface of the bilayer and therefore would not readily allow complete penetration of the heme into the hydrocarbon region. Hemin was, in fact, not catalytic at pH 5, 7, or 10. Thus, the extra polarity afforded by the carboxyl groups appears to prevent across-bilayer diffusion, even when the carboxyls are protonated. Even though the hemin is expected to be partially inserted into the bilayer on each side, no evidence indicates that an electron can traverse the distance between such heme groups. Presumably this distance is of the order of 20–30 Å, which is much larger than an assumed electron jump distance of perhaps 5–10 Å (*132–135*). If an electron was able to hop or tunnel from a heme on one side of the bilayer to a heme on the other, a charge would soon develop across the bilayer (negative inside, positive outside), which would impede further net electron flow. To test for this possibility we added valinomycin (in the presence of potassium) and found it to be without effect in the hemin-containing system.

Published on June 1, 1982 on http://pubs.acs.org | doi: 10.1021/ba-1982-0201.ch022

Table IV. Rate of Catalysis of Electron Transport Across Liposomes by Porphyrin Complexes

Compound	*Buffer*	*Lipid System*	*Internal Redox Component*	*External Redox Component*	*Rate*[a]
Hemin dimethyl ester	Im	EPC	FeCy	$ITSAH_2$	240
Hemin dimethyl ester	P_i	EPC	FeCy	$ITSAH_2$	240
Hemin	Im	EPC	FeCy	$ITSAH_2$	0
Hemin	P_i	EPC	FeCy	$ITSAH_2$	0
PPIX	Im	EPC	FeCy	$ITSAH_2$	0
NiTPP	Im	EPC	FeCy	$ITSAH_2$	0
CoTPP	Im	EPC	FeCy	$ITSAH_2$	0
FeTPP	Im	EPC	FeCy	$ITSAH_2$	0
FeTPP	Im	EPC	FeCy	$ITSAH_2$	430
MnTPP	Im	EPC	FeCy	HRP	900
MnTPP	Im	EPC	FeCy	$ITSAH_2$	200
MnP–MnP	Im	EPC	FeCy	HRP	900
Hemin dimethyl ester	Im	EPC + CL (4 : 1)	FeCy	$ITSAH_2$	192
Hemin dimethyl ester	Im	EPC + PE (1 : 1)	FeCy	$ITSAH_2$	500
Hemin dimethyl ester	Im	DPPC	FeCy	$ITSAH_2$	50
Hemin dimethyl ester	Im	EPC	FeCy	$ITSAH_2$	1250[b]
Hemin dimethyl ester	P_i	EPC	asc	cyt c	600[b]
					1.5

Note: Abbreviations used are PPIX, protoporphyrin IX; TPP, tetraphenylporphyrin; MnP–MnP, covalently linked manganese porphyrin dimer: 5-*p*-benzoyloxypropyl-10,15,20-tri(*p*-tolyl)porphyrinatomanganese-5-*p*-benzoyloxy-10,15,20-tris(4-carbomethoxyphenyl)porphyrinatomanganese (*62*); Im, 0.4 *M* imidazole; P_i, 0.2 *M* potassium phosphate, pH 7.0; EPC, egg yolk phosphatidylcholine; CL, cardiolipin; PE, phosphatidylethanolamine; DPPC, dipalmitylphosphatidylcholine; FeCy, potassium ferricyanide; $ITSAH_2$, reduced indigotetrasulfonic acid; HRP, reduced horseradish peroxidase; asc, ascorbate; cyt c, ferric horse heart cytochrome c.

[a] All rates are in number of electrons transported per molecule of porphyrin per minute at room temperature. Each experiment was conducted as described in the example given in Figure 9.

[b] Temperature for these experiments was 41°C.

Iron tetraphenylporphyrin consistently was about twice as effective as hemin dimethyl ester in the catalytic reaction. The periphery of iron tetraphenylporphyrin is clearly more hydrophobic than that of hemin dimethyl ester and perhaps this feature is important. However, the two porphyrin structures also differ substantially in that the tetraphenylporphyrin has a phenyl group at each methine bridge carbon, whereas the natural porphyrin has a hydrogen atom. Future experiments will further evaluate this difference by testing iron octaethylporphyrin.

Results with manganese tetraphenylporphyrin (MnTPP) were compared with those from iron tetraphenylporphyrin (FeTPP). Although the manganese derivative is catalytic, it is only about one-half as effective as the iron derivative. To evaluate whether this rate difference could be explained by an $E^{\circ\prime}$ value for the MnTPP, which was below that of the indigotetrasulfonic acid, the electrochemical behavior of this complex and others was measured by cyclic voltammetry in dichloromethane. An example of such a measurement on FeTPP is shown in Figure 10. In addition, potentiometric titrations were performed to determine $E^{\circ\prime}$ values of the metalloporphyrins while they are contained in the aqueous liposome suspensions (*see* Figure 11 for such a titration). The results of all these experiments are summarized in Table V. The data for the iron porphyrins appear to be in agreement with expectations. The $E_{1/2}$ value for hemin in dichloromethane is more positive than the $E^{\circ\prime}$ value reported in water. The value of $E^{\circ\prime}$ for hemin in the liposome is also much higher than in water, which may be taken as evidence that the iron porphyrin molecule resides substantially inserted into the hydrocarbon portion of the bilayer. Hemin, hemin dimethyl ester, and FeTPP also follow a trend in which the porphyrins with lower polarity would be more likely to be further embedded in the hydrocarbon region of the bilayer and thus exhibit higher $E^{\circ\prime}$ values when incorporated into the vesicle system. As a result of these determinations, the $E^{\circ\prime}$ value for MnTPP in the vesicles was nearly the same as for FeTPP. Therefore, its effective $E^{\circ\prime}$ value cannot be used to explain its lower rate of catalysis. A more likely explanation, then, is that its rate of reaction with reduced indigotetrasulfonic acid (known to be the rate-limiting step in this system) is slower than that of FeTPP. Consistent with this latter conclusion is the observation of Kadish and Davis (*130*) that manganese octaethylporphyrin hydroxide has a heterogeneous electron transfer rate constant on platinum that is one-fourth to one-fifth of the corresponding Fe porphyrin. Our cyclic voltammograms also showed a substantial slowing of the electron transfer rate of MnTPP on platinum as compared to FeTPP.

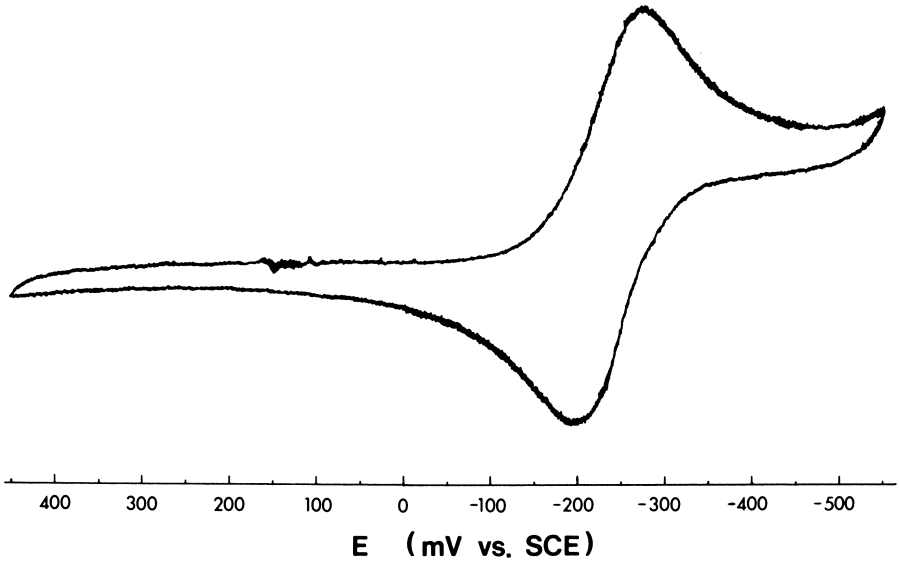

Figure 10. Cyclic voltammogram of 5.4 × 10^{-4} M iron tetraphenylporphyrin in approximately 5 mL of dichloromethane with 0.4 M imidazole and 0.1 M tetrabutylammonium perchlorate present. A platinum electrode was used with a SCE reference cell. Scan rate was 10 mV/s. Sample was prepared in a dry N_2 atmosphere and transferred to the measuring vessel using a syringe. In the measuring cell the sample was degassed further for 30 min with high purity argon that had passed through molecular sieves, copper filings at 400°C, molecular sieves, and dichloromethane before entering the measuring vessel. The initial voltage was 150 mV and the initial scan was negative.

Variation of Aqueous Redox Materials. The aqueous reductant outside the vesicles may easily be changed. We tested the electron transport catalysis with three different external reductants (Figure 12). In the MnTPP-containing liposomes, the catalytic rate more closely approached that of FeTPP when reduced indigodisulfonic acid [$E^{0\prime}$ value at pH 7 = −125 mV (*127*)] was used as the reductant compared with reduced indigotetrasulfonic acid [$E^{\circ\prime}$ value at pH 7 = −46 mV (*127*)]. With reduced horseradish peroxidase [$E^{\circ\prime}$ value = −271 mV (*129*)], the two rates were quite fast and indistinguishable. Most likely, at these increased rates of reaction with the external reductant, another step of the overall catalysis has become rate limiting (e.g., diffusion across the bilayer). The overall rate of catalysis of the horseradish peroxidase system compares very favorably with that of in vivo electron transport (*136*).

Very few aqueous redox materials can be prepared at high enough concentrations in water to be used within the vesicles. One successful system utilizes ascorbic acid inside as reductant and ferric horse heart cytochrome c externally as the oxidant. Measuring the rate of forma-

tion of the reduced α-band of ferrous cytochrome c demonstrated that electron transport occurs with a rate that is about 200 times slower than with the ferricyanide-reduced dye systems (Figure 13). In the latter system hemin dimethyl ester is capable of transbilayer diffusion at a much faster rate than the overall rates of electron transport in the ascorbate–ferric cytochrome c system. Thus, the rate-limiting step in the ferricyanide–reduced dye system must be the electron transport reaction at one of the bilayer interfaces. In future work this system may be used to model electron transport involving cytochrome c and another heme center at a membrane interface.

Evidence for an Electroneutral Mechanism. As was shown in Figure 9, the electron transfer reaction catalyzed by hemin dimethyl

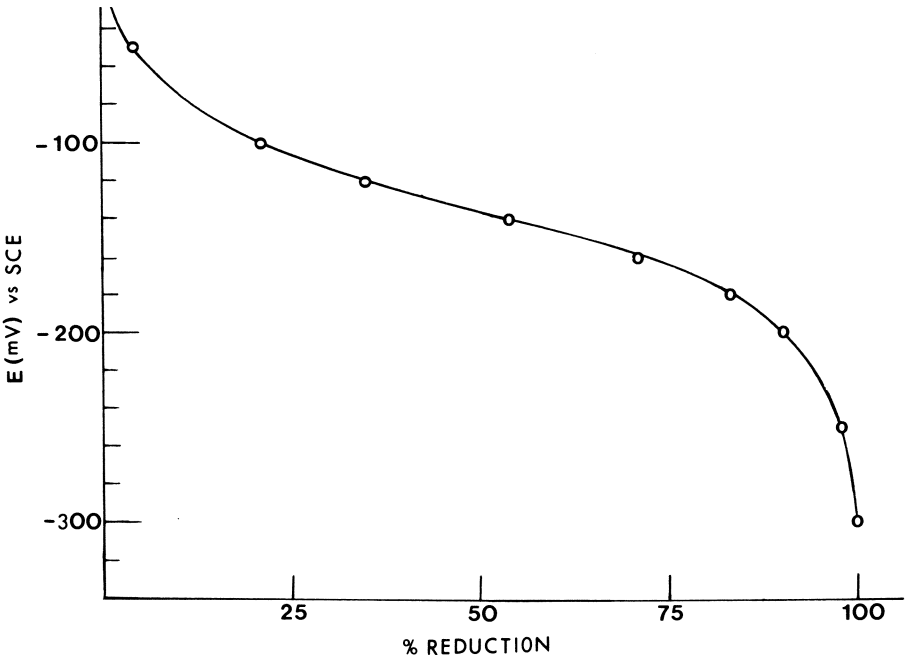

Figure 11. Potentiometric titration of FeTPP incorporated into egg yolk phosphatidylcholine vesicles. A 2.8-nmol sample of FeTPP and 200 mg of phospholipid were present in 25 mL of solution. The sample was degassed for 60 min with argon purified as described in the experiment of Figure 12. The reductant used was a solution of $Na_2S_2O_4$. The potentials were measured after each addition with a platinum grid electrode. About 15 min was required to reach a steady potential after each addition of reductant. Phenazine methosulfate (PMS) (6.4×10^{-5} M) was present as a mediator. The complete absorbance spectrum was recorded at each experimental point indicated and the percent reduction was calculated from this information along with the fully oxidized and fully reduced spectra. The solid curve represents the theoretical behavior for a one-electron titration with a midpoint of −135 mV.

ester rapidly continued to completion, that is, until all the reduced indigotetrasulfonic acid was oxidized (the potassium ferricyanide was in slight excess). This result could only have been observed if the mechanism of catalysis was electroneutral. If the mechanism were electrogenic and created a charge across the bilayer, as suggested for the ferrocene system, then either the reaction would have proceeded to only a few percent of its observed extent (because of buildup of a transbilayer potential) or the bilayer of the liposomes would have broken because of the large charge differential ($\Delta\Psi$) created across it. In control experiments on bilayer stability we demonstrated that ^{14}C-labeled sucrose captured in the internal aqueous space during vesicle formation remained inside during catalyzed electron transport. Thus, the liposomes are quite stable throughout electron transport.

As a further verification that the catalytic process proceeded in an electroneutral manner, we tested for an effect by valinomycin (in the presence of potassium) and an uncoupler, carbonylcyanide-*p*-

Table V. Electrochemical Potentials of M^{3+}/M^{2+} Porphyrin Systems

	Solvent Systems			
Compound[a]	*H_2O*	*PC Vesicles*	*CH_2Cl_2*	*Other*
FeTPP · Im		+97	−3	
FePPIXDME		0	−99	
FePPIX	−160 (pH 7)[b]	−96	−139	
MnTPP · Im		+96	−119	
MnPPIX				−110 (CH_3CN)[c]
MnHPIXDME	−268 (pH 7)[b]			
CoTPP			+990[d]	
NiTPP				+1240 (benzonitrile)[e]
H_2TPP				+1330 (benzonitrile)[e]

Note: The values given are relative to the Standard Hydrogen Electrode (SHE). For simplicity, data obtained vs. SCE were adjusted by adding 245 mV. This is strictly correct, of course, only for aqueous solutions. For aqueous solutions, the value corresponds to the midpoint potential, $E^{0'}$ or E_m. For nonaqueous solution, the numbers represent $E_{1/2}$ values. The $E^{0'}$ values for the aqueous materials are +440 mV for Fe^{3+}/Fe^{2+} cyanide, and −46 mV for indigotetrasulfonic acid. Each experiment in water was conducted in a manner similar to that for which data are given in Figure 11. The data reported in acetonitrile were obtained by conducting cyclic voltammetry in a manner similar to that described in Figure 10.

[a] For abbreviations used see Table IV.
[b] From Ref. *127*.
[c] From Ref. *146*.
[d] From Ref. *128*.
[e] From Ref. *145*.

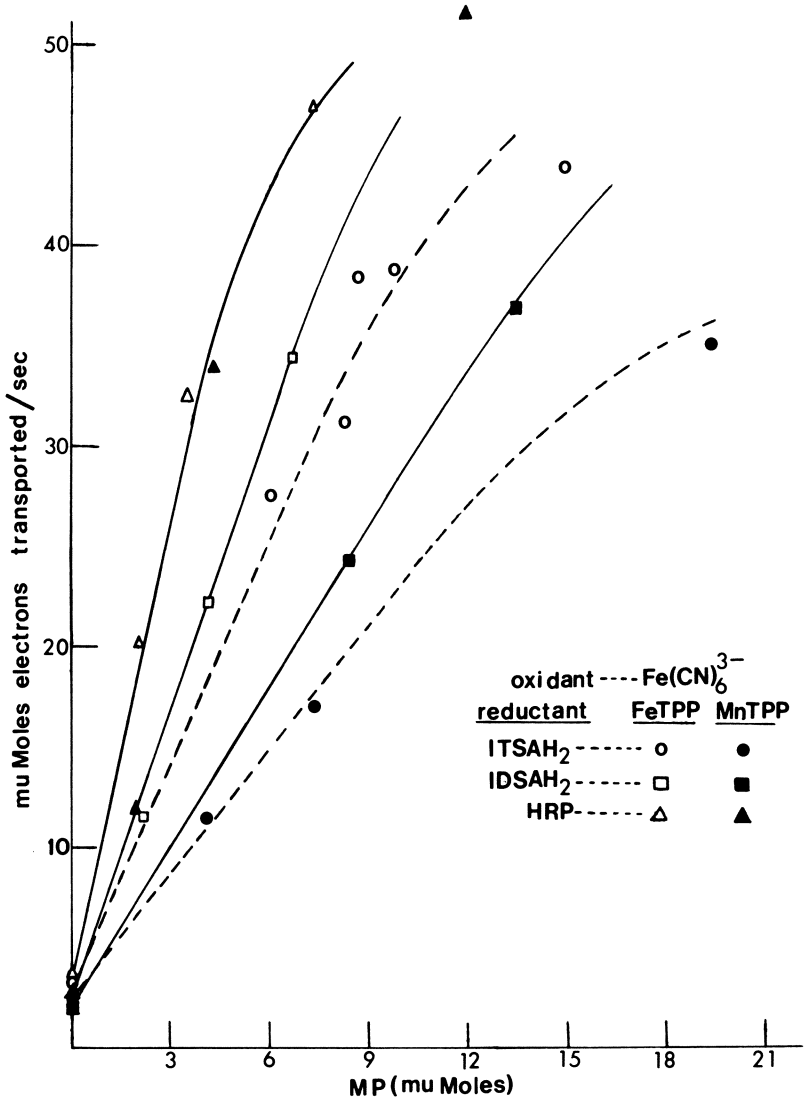

Figure 12. Dependence of the rate of catalysis of electron transport by FeTPP and MnTPP with different reductants. $ITSAH_2$ is reduced indigotetrasulfonic acid, $IDSAH_2$ is reduced indigodisulfonic acid, and HRP is ferrous horseradish peroxidase. The X-axis is the quantity of the metalloporphyrin (MP) present in 8 mg of egg yolk phosphatidylcholine vesicles. The reductants were 7×10^{-5} M $ITSAH_2$ (210 nmol), 6.5×10^{-5} M $IDSAH_2$ (195 nmol) and 4.5×10^{-5} M HRP (135 nmol); 420 nmol of potassium ferricyanide was trapped inside the vesicles; 0.4 M imidazole, pH 7.0, 0.175 M NaCl, and 0.025 M KCl were present in a sample volume of 3.0 mL; anaerobic conditions.

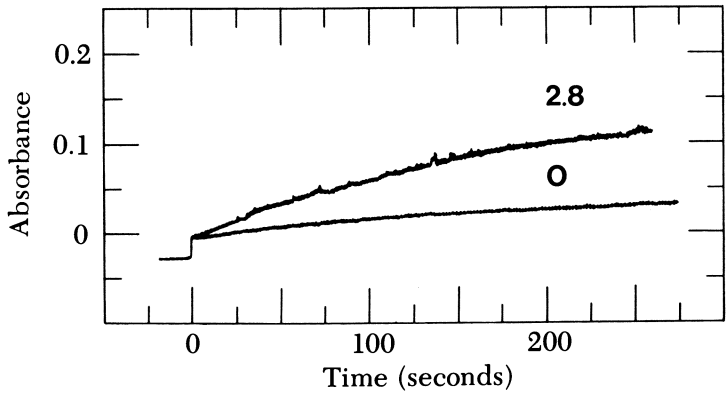

Figure 13. Liposomal electron transport system in which the electron flow was from ascorbic acid (inside) to ferric cytochrome c (outside), catalyzed by hemin dimethyl ester. The absorbance increase followed is that of the 550-nm band of ferrous cytochrome c. The amount (nanomols) of hemin dimethyl ester present in 8 mg of egg yolk phosphatidylcholine is indicated. The ascorbic acid which was captured inside the vesicles was 0.15 M along with 0.2 M $K_2HPO_4 \cdot 3H_2O$, pH 6.8 during vesicle formation. The cytochrome c was 2×10^{-5} M in 2.55 mL of anaerobic buffer containing 0.4 M imidazole, pH 7.0; 0.25 mL of anaerobic vesicles was injected at time zero.

trifluoromethoxyphenylhydrazone (FCCP). These reagents were without significant effect (*124*).

Examination of Anion Movement. For hemin dimethyl ester catalysis of electron transport in the phosphate buffer system one might expect that a hydroxide ion is transported when the ferric form diffuses from the inside to the outside of the vesicle, because hydroxide is likely to be coordinated to the ferric hemin in aqueous systems at pH 7. Evidence for hydroxide coordination comes from measurement of the pH dependency of $E^{\circ\prime}$ values (*127*). It was nevertheless important to test whether any of the other anions present were being transported as participants in the electroneutral process. By utilizing ^{33}P-labeled phosphate, we found that no significant phosphate (less than 0.05 equivalent) was transported out of the vesicles during catalyzed electron transport (*124*). We also tested for the possibility of cyanide transport using a silver cyanide precipitation assay and found no evidence (less than 0.05 equivalent) for transport of this ion (*124*).

Evidence supporting the idea of hydroxide transport was provided by measuring the pH external to the liposomes during electron transport in a weakly buffered system. When reduced indigotetrasulfonic acid was simply titrated by potassium ferricyanide in solution, the pH

decreased due to the release of protons from reduced indigotetrasulfonic acid as it was oxidized. Such a change in pH is indeed noted in Figure 14A. However, if 1 equivalent of hydroxide is transported out with each equivalent of ferric hemin dimethyl ester as electron transport is catalyzed in the model liposomal system, no such pH change would be observed outside the liposomes. Indeed, no significant pH change was found during electron transport (Figure 14B). The slow decrease in pH observed with time after the electron transport reaction is completed probably represents the rate of proton leakage from the vesicles. This observed rate is in good agreement with recently reported values (*137*).

As an independent measure of the ability of ferric hemin dimethyl ester to transport an anion-like hydroxide across an apolar phase, we

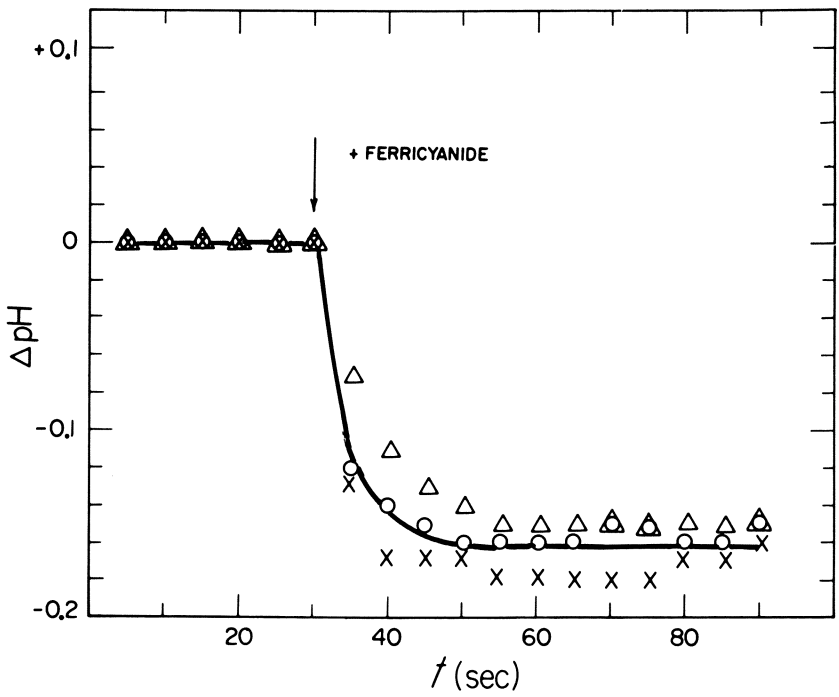

Figure 14A. The pH change in 2 × 10⁻⁴ M phosphate buffer during hemin dimethyl ester catalyzed electron transport in liposomes. Control in which $K_3Fe(CN)_6$ was added directly to reduced indigotetrasulfonic acid. The results of three separate experiments are plotted, each with an initial pH near 7.00. (Reproduced, with permission, from Ref. 124. Copyright 1981, Elsevier/North-Holland Biomedical Press.)

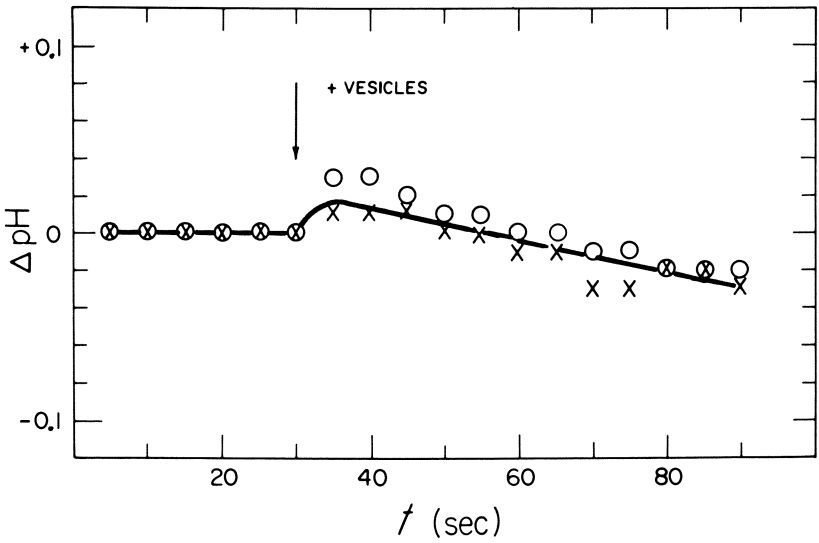

Figure 14B. Complete system. The results of two separate experiments are plotted, each with an initial pH near 7.00. (Reproduced, with permission, from Ref. 124. Copyright 1981, Elsevier/North-Holland Biomedical Press.)

conducted a bulk phase transfer experiment using $S^{14}CN^-$. This radioactive anion was added to one side of this U-tube system involving two aqueous phases separated by chloroform and the rate of appearance of $S^{14}CN^-$ on the other side was monitored. Such bulk phase transport was clearly demonstrated and depended directly on the hemin dimethyl ester concentration (*124*). The rate of transport observed was compatible with a similar carrier role for hemin dimethyl ester in hydroxide transport in the liposomal systems.

Conclusions for Model System II

The experimental data clearly indicate that hemin dimethyl ester functions in catalysis by an electroneutral diffusion mechanism. A summary scheme consistent with the results is shown in Figure 15. In the scheme, a hydroxide ion is coordinated to ferric hemin dimethyl ester as it is formed by reaction with potassium ferricyanide on the inside surface. This electrically neutral complex then diffuses to the outside surface where an electron and a proton are received from reduced indigotetrasulfonic acid. The pentacoordinate ferrous complex diffuses back to the inside surface carrying a water molecule as its fifth ligand. The overall effect of the cycle is to transport an electron and a proton in an electroneutral fashion from the reductant outside to the

oxidant inside. In this sense, the system behaves like the quinone-catalyzed electron and proton transporting systems studied previously (*108*, *109*, *125*, *126*). Valinomycin plus potassium and FCCP were also without effects on those systems.

For hemin dimethyl ester catalysis in imidazole buffer, the anion transported by coordination to the ferric form probably is imidazolate. The pK_a' for ferric porphyrin coordinated imidazole to lose a proton, thus forming coordinated imidazolate, is about 11 in water (*138*, *139*). It would be much lower than this if the imidazolate is additionally stabilizing a positive charge on the ferric porphyrin in the less polar regions of a lipid bilayer. After diffusing across the bilayer, the presumed ferric hemin dimethyl ester–imidazolate complex would be expected to receive both an electron and a proton at the outer surface and then diffuse back to the inner surface as a normal diimidazole hemochrome system. Again, this overall process could also be viewed

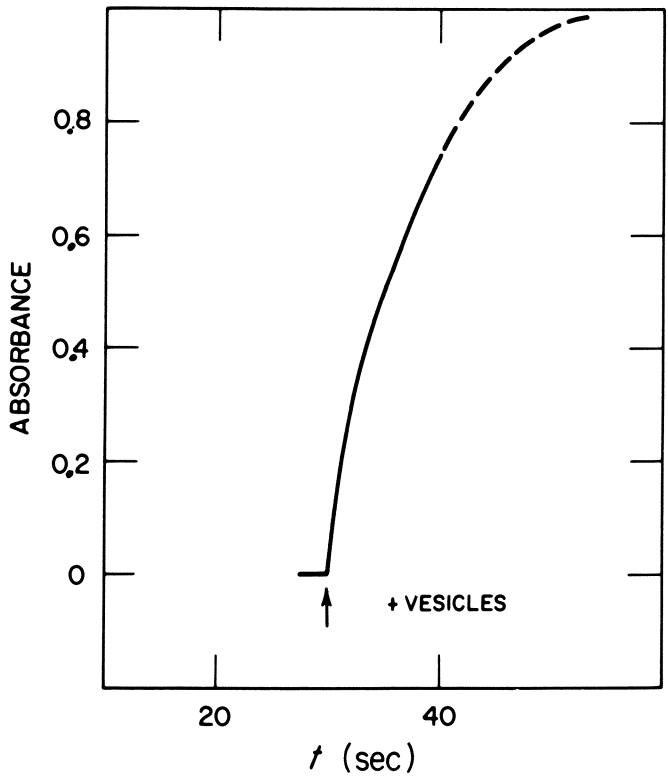

Figure 14C. Rate of electron transfer of the complete system under the conditions of the experiments reported in Figure 14B. (Reproduced, with permission, from Ref. 124. Copyright 1981, Elsevier/North-Holland Biomedical Press.)

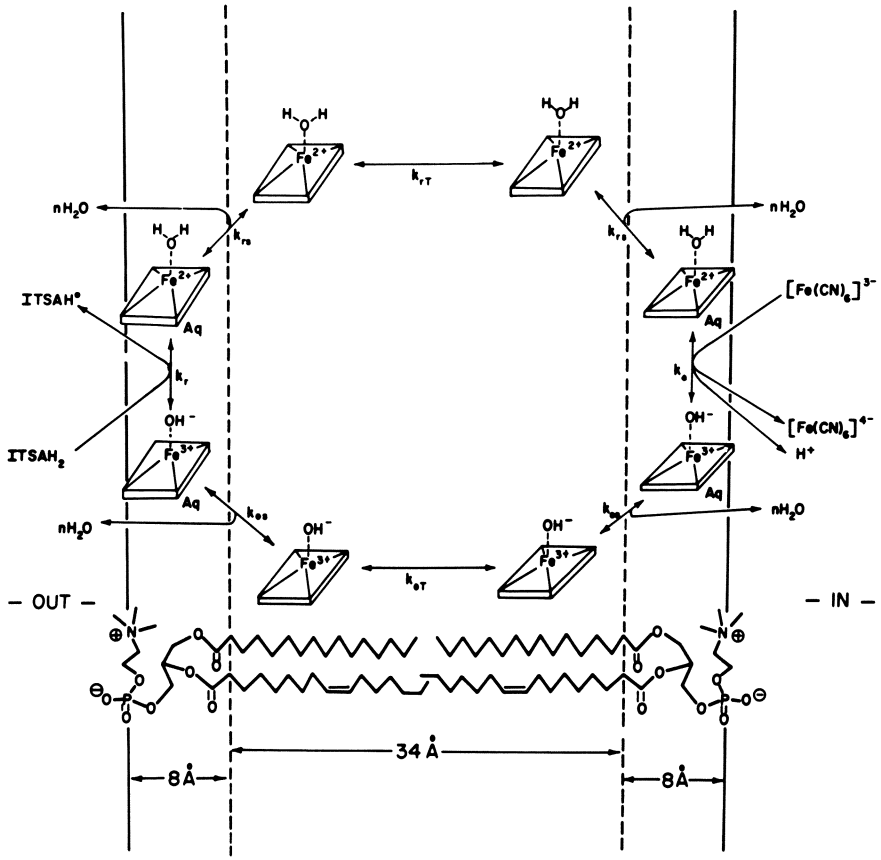

Figure 15. Schematic representation of hemin dimethyl ester catalyzed electron transport in liposomes in phosphate buffer. The rhombi drawn to represent the heme group are approximately the correct size for the conjugated π-system relative to the phospholipid bilayer. Aq represents the fully hydrated porphyrin complex. Although the liposomes have substantial packing differences between the outer and inner halves of the bilayer, these are ignored here. The k *values are used to represent the rate constants for each step:* k_r, *electron transfer rate at outer interface with reduced indigotetrasulfonic acid (*$ITSAH_2$*);* k_o, *electron transfer rate at inner interface with ferricyanide;* k_{rs}, *dehydration rate for reduced hemin dimethyl ester; and* k_{os}, *hydration rate for oxidized hemin dimethyl ester. (Reproduced, with permission, from Ref. 124. Copyright 1981, Elsevier/North-Holland Biomedical Press.)*

as the transport of an electron and a proton from the outer aqueous environment to the inner aqueous space in an electroneutral fashion.

After viewing the results of this model system, it is of interest to again consider in vivo electron transport. Figure 16 (top) schematically portrays the presumed functioning of heme groups in an "electron wire" or electrogenic fashion. In the in vivo complexes the heme centers are presumed not to change position significantly, and for electron transport to occur the heme edges should be within about 5 to 10 Å of each other (*132–135*). Although three such centers are drawn in this scheme, one or two could have been used if their placement within the bilayer were where protein structure provided a narrowed area or if other carriers were also involved. Thus, the only difference between this imagined in vivo system and our model would be the role of diffusion in the model instead of electron hopping between fixed multiple heme centers in vivo. But what would prevent the proton from migrating as well in the in vivo system? All the ligands coordinated to heme and copper in the electron transport pathways of bioenergetic membranes are not known with certainty, but most are acid–base groups and the imidazole group of histidine is almost always one of the ligands involved. Moreover, a ligand-like imidazole will have other groups hydrogen-bonded to it, thus facilitating proton movement (*140, 141*). An electroneutral electron and proton transport through multiple heme centers [e.g., *see* Figure 16 (bottom)] thus deserves serious consideration.

A more detailed view of how this parallel movement of an electron and a proton might occur in an electroneutral fashion through multiple heme centers in vivo is shown in Figures 17A–F. A fundamental requirement for this system to work is that a gated hydrogen bond path across the bilayer is needed to ensure directionality of coupled proton and electron flow, but at the same time prevent proton leakage. It is proposed that minihydrogen-bonding chains (*140, 141*) are connected to ligands that are coordinated to iron and that the small conformational changes that accompany reduction break one minihydrogen-bonding chain and form a new one. Two such gates were used in this example. Other coordinated ligands besides imidazole–imidazolate could have been used, for example, a thiol–thiolate or a carboxyl–carboxylate. The electron donor to the system is arbitrarily suggested to be a protein-bound ubisemiquinone anion radical. It could well be an integral membrane complex near the inside surface rather than a peripheral protein complex that exists in the aqueous region as arbitrarily shown. In photosynthetic bacteria, this scheme could represent passage of an electron from the second protein-bound ubiquinone (Q_B) through perhaps a pair of cytochrome b molecules.

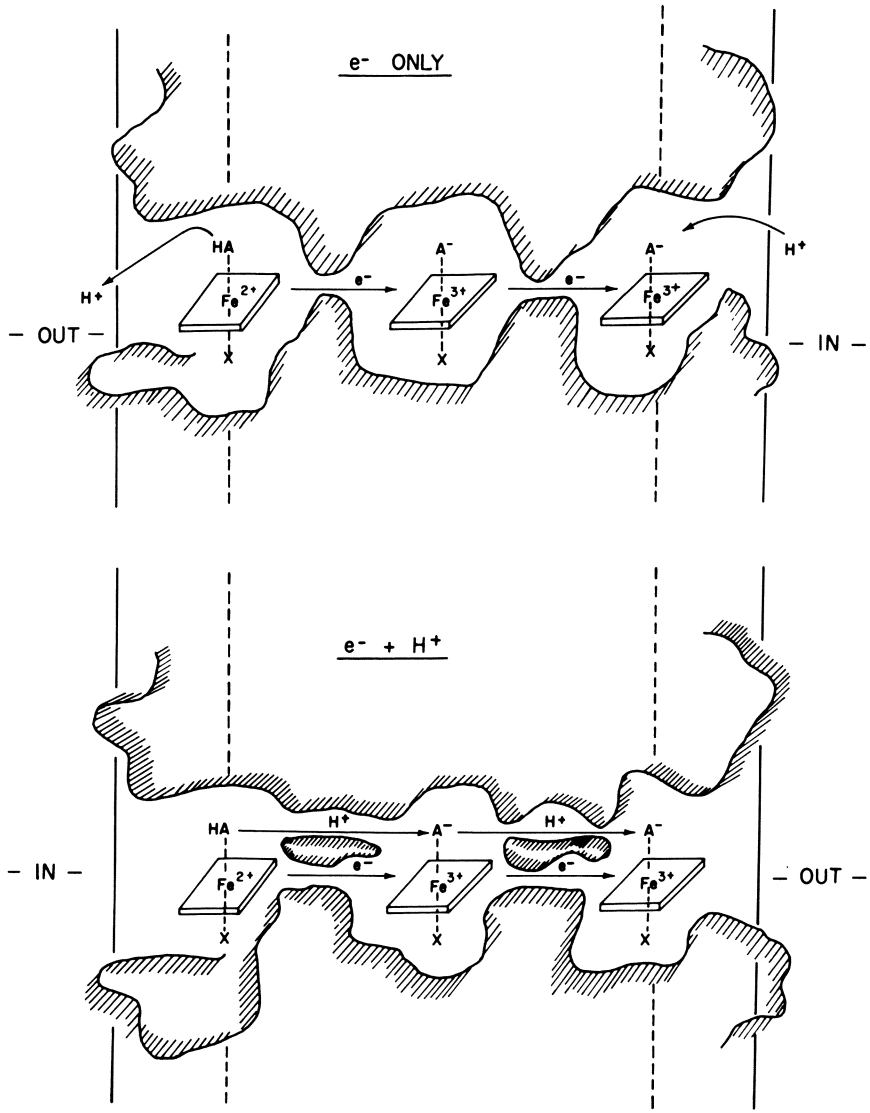

Figure 16. Schematic representation of hypothetical in vivo iron porphyrin electron transport systems. The shaded areas represent part of the protein(s) that binds the iron porphyrin. The porphyrin complex is drawn as an octahedral low-spin structure (six coordinated ligands). The symbol A *could be an imidazole side chain of histidine. The arrows merely indicate the direction of electron and proton flow and should not be construed as indicating equilibria. (Reproduced, with permission, from Ref.* 124. *Copyright 1981, Elsevier/North-Holland Biomedical Press.)*

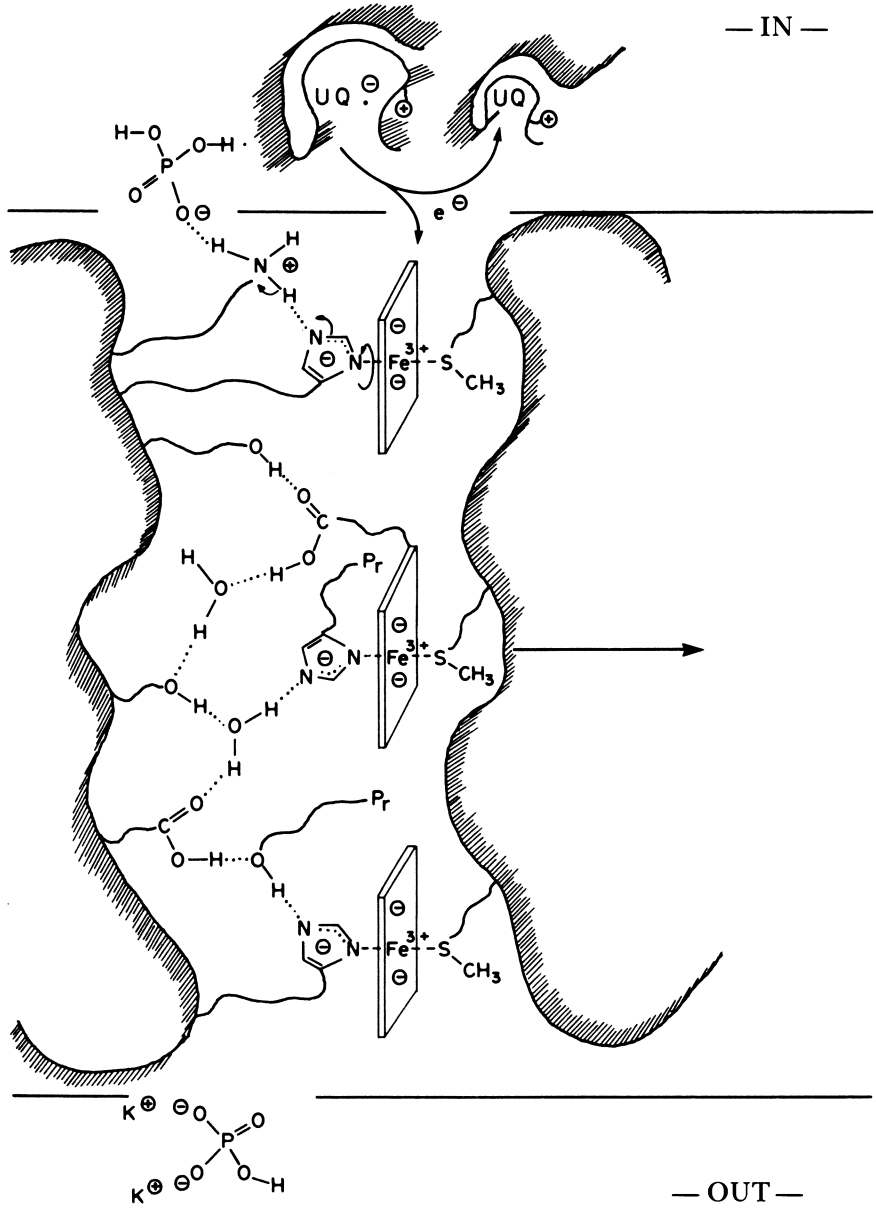

Figure 17. Schematic representation of how in vivo electron transport through cytochromes could be an electroneutral process. Important aspects include a gated hydrogen-bonding network that responds to the oxidation state of the various heme centers. A: above. B–F: continued on next page.

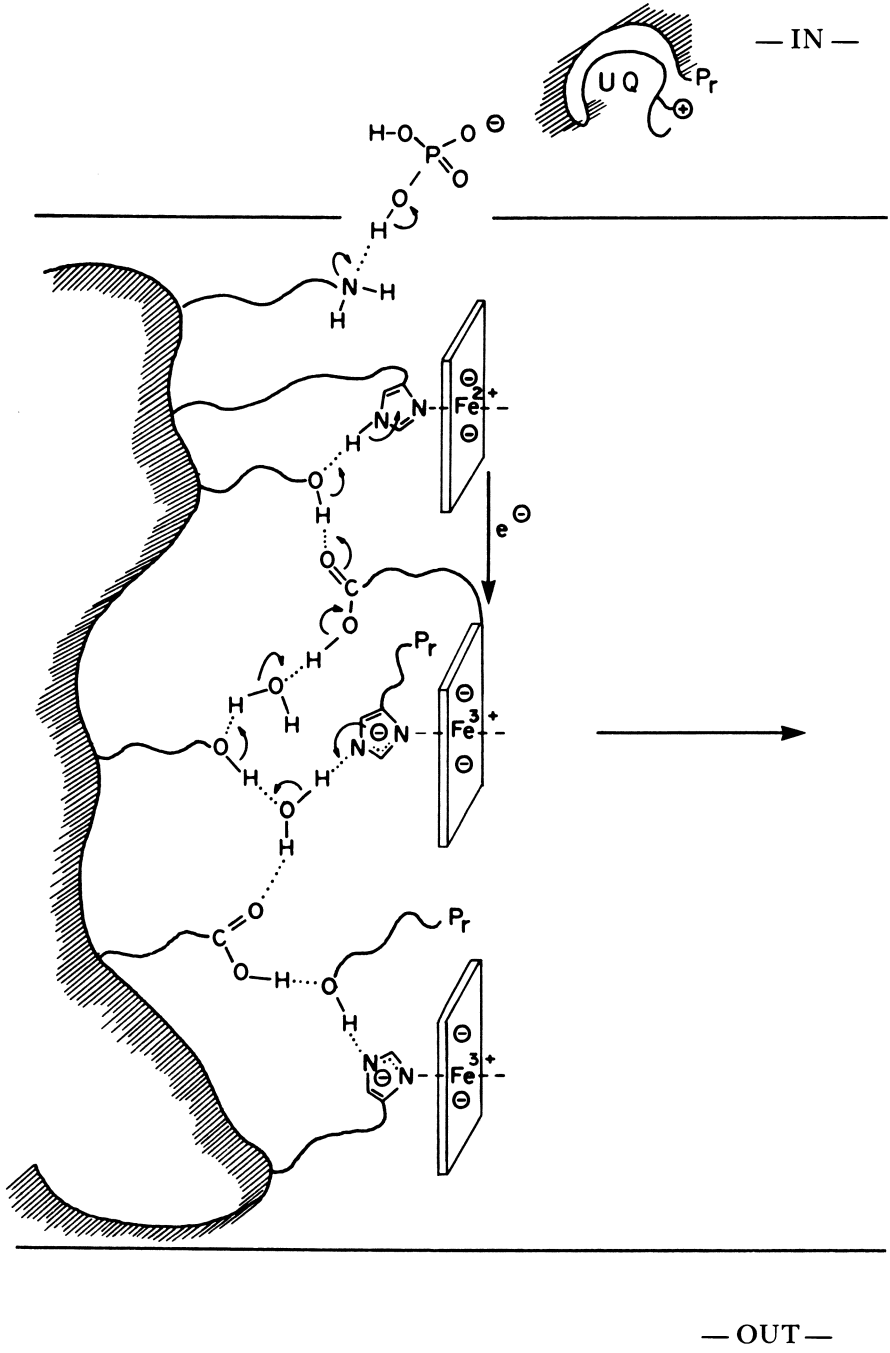

Figure 17B.

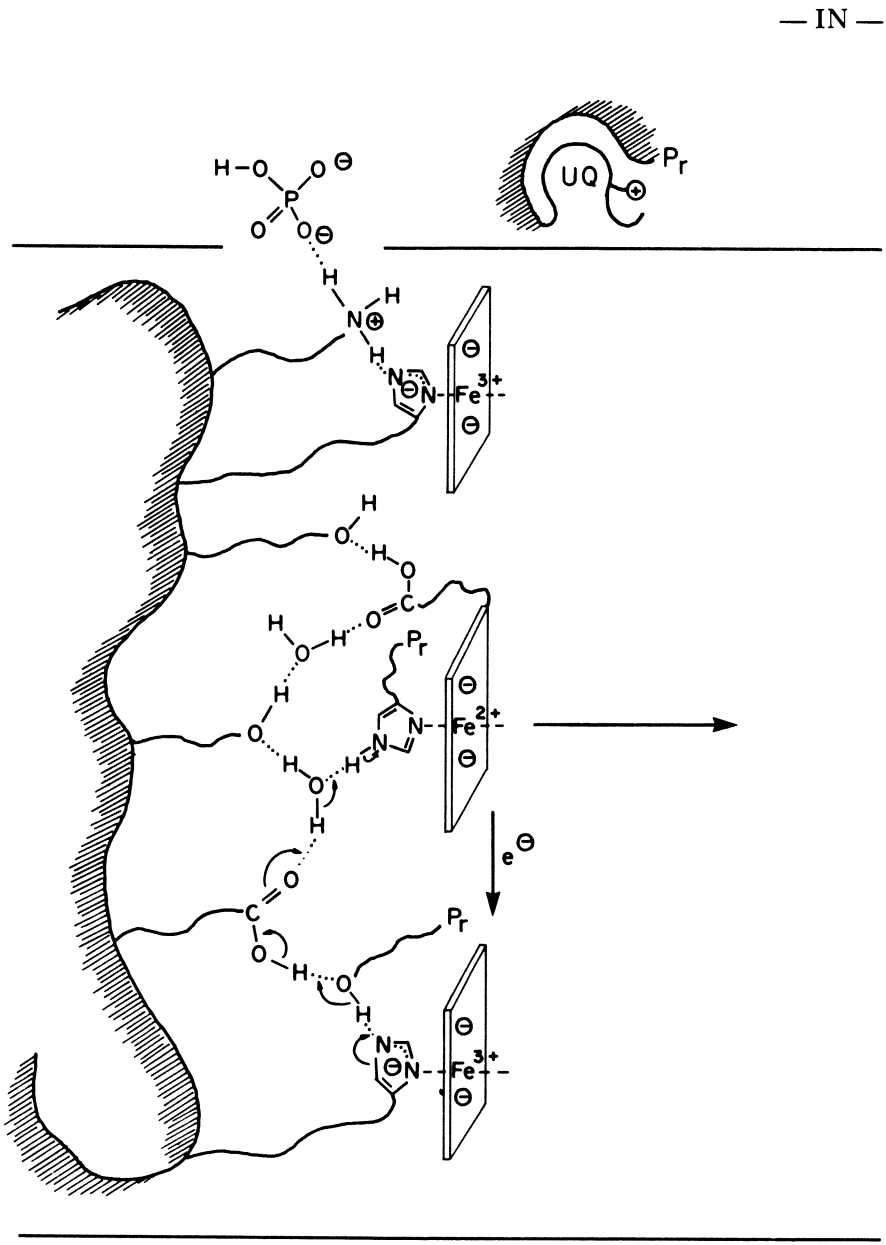

Figure 17C.

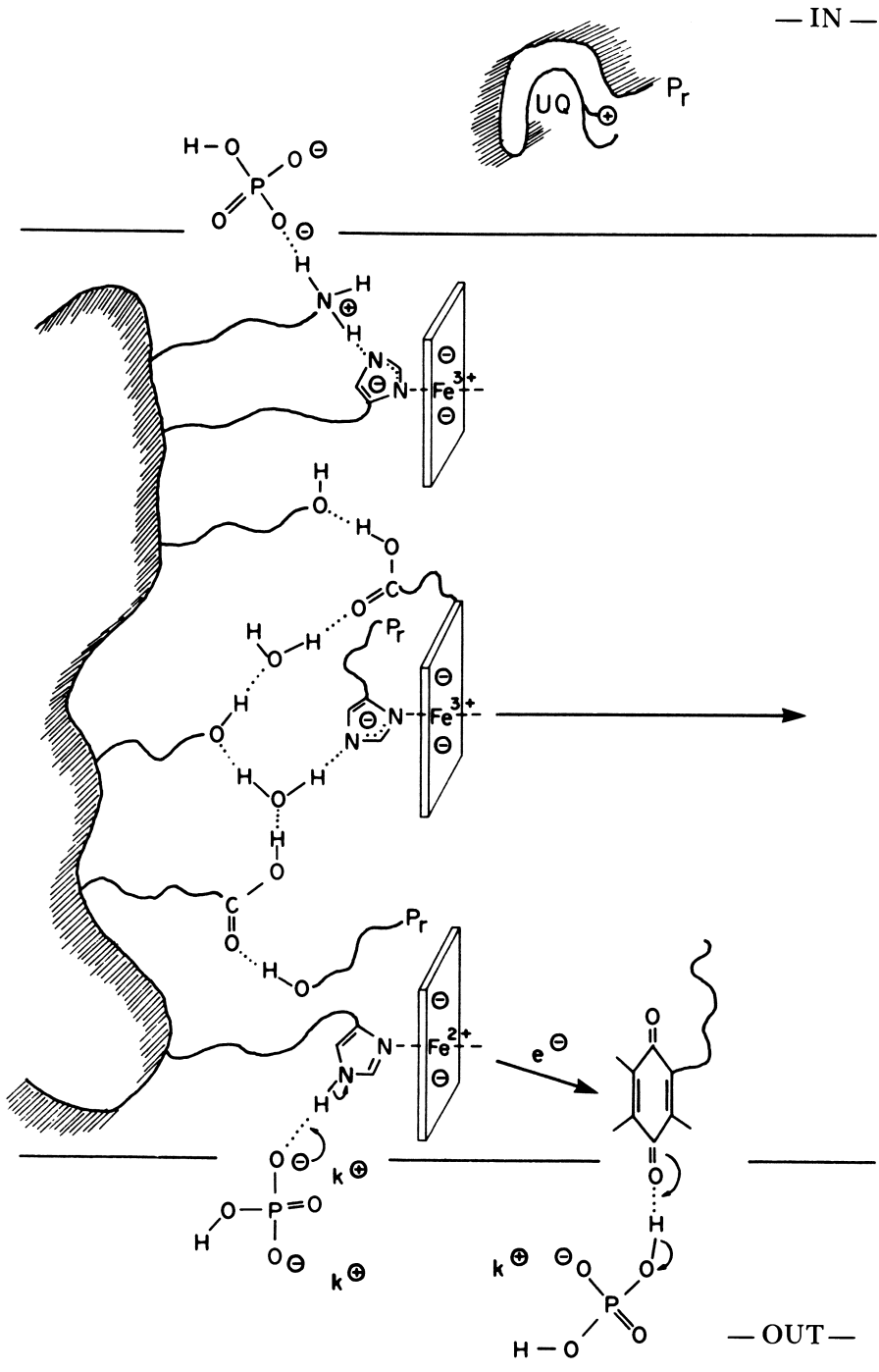

Figure 17D.

In summary, because of the ligation of acid–base groups to heme groups within a membrane protein, one would expect the existence of hydrogen-bonding chains to the groups ligated. Because electron transfer between such heme centers must be over a limited distance of approximately 5 to 10 Å (edge to edge), the minihydrcgen-bonded chains of adjacent heme groups cannot be very far apart and might be expected to communicate easily—purposeful communication may have evolved. Thus, it seems totally unnecessary to limit to ubiquinone all redox steps envisioned to carry both an electron and a proton. It is, in fact, just as natural to think of cytochromes as participants in this function.

— IN —

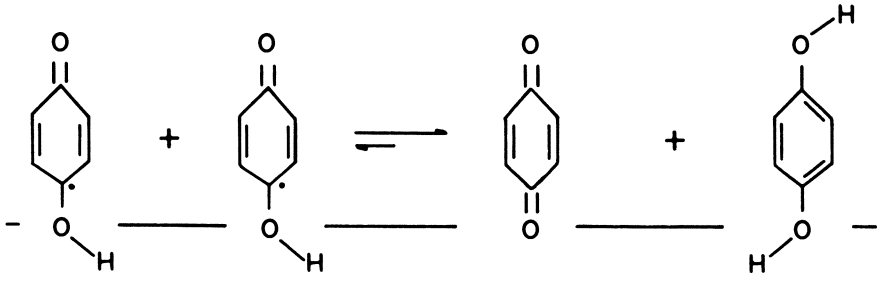

— OUT —

Figure 17E.

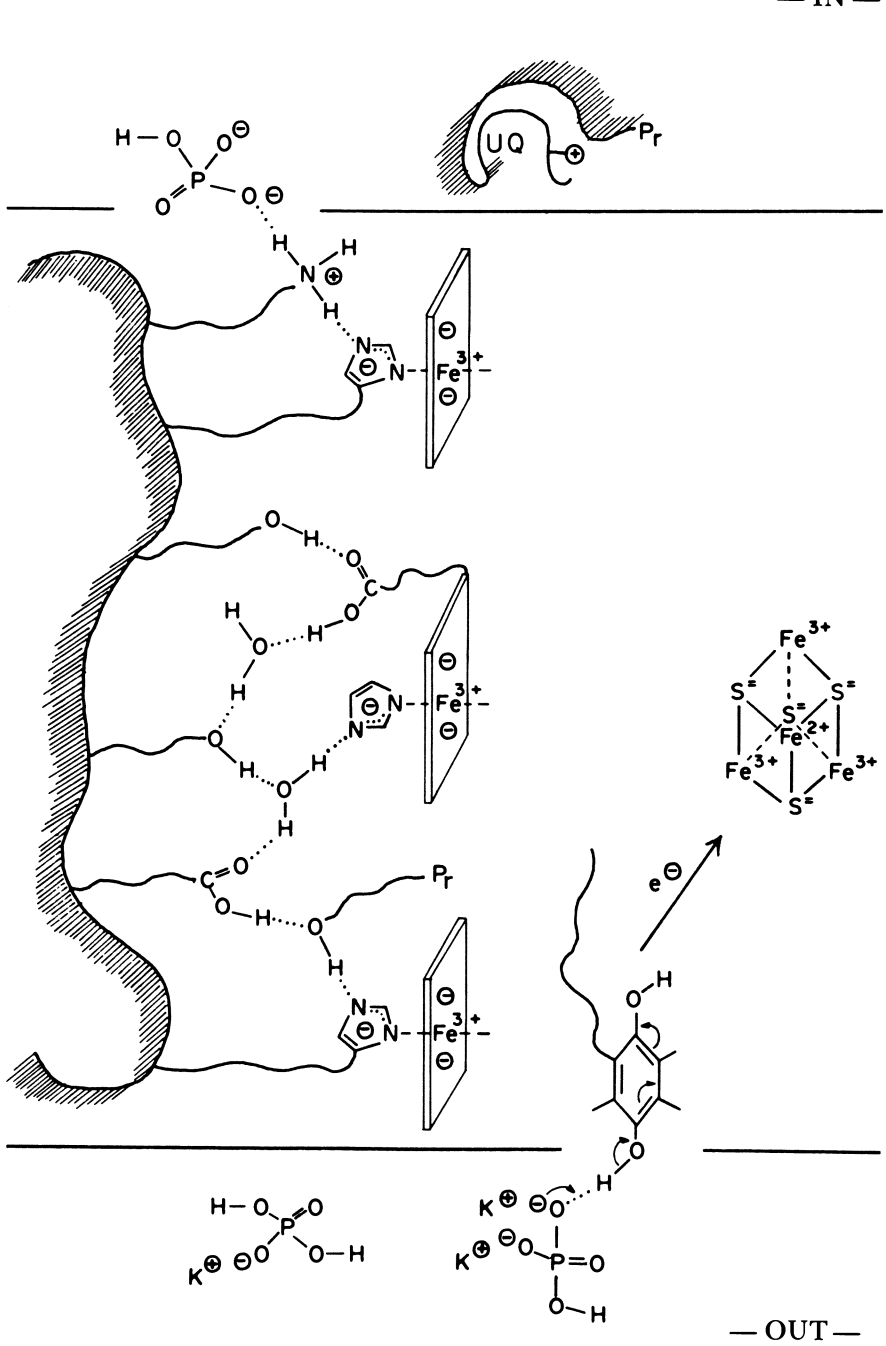

Figure 17F.

Future Directions

A closer approach of the electron transport model to in vivo systems will utilize multiple covalently linked redox centers, which we have synthesized. Furthermore, by combination of the photochemical reaction center model and the electron transport model, we expect to develop and systematically probe a liposome system where charge separation across the bilayer can be achieved by an initial photochemical reaction and the products subsequently coupled through the electron transport model system to achieve cyclic electron flow. The net result of this coupled system would be to create both a $\Delta\Psi$ and a proton gradient without the requirement for aqueous redox materials. This sequence of events, of course, would closely resemble the major processes occurring in photosynthetic bacteria as a result of light absorption and secondary electron flow. These model systems should make it possible to ask systematically many interesting mechanistic questions.

Acknowledgments

The authors thank Therese Cotton for her assistance in the preparation of samples and some cyclic voltammetry measurements, Richard Van Duyne for use of his equipment in some of the cyclic voltammetry measurements, and Frederick Lewis for use of his Perkin Elmer MPF-44A fluorescence spectrometer.

This research was supported by research grants from the National Science Foundation (PCM-7816669) and the National Institutes of Health (GM 26098).

The authors would like to dedicate this paper to Professor David Shemin in honor of his 70th birthday.

Literature Cited

1. Parson, W. W.; Cogdell, R. J. *Biochim. Biophys. Acta* **1975,** *416,* 105.
2. Loach, P. A. In "Progress in Bioorganic Chemistry"; Kaiser, E.T.; Kezdy, F., Eds.; Wiley: New York, 1976; Vol. 4, pp. 89–192.
3. Loach, P. A. *Photochem. Photobiol.* **1977,** *26,* 87.
4. Blankenship, R. E.; Parson, W. W. *Annu. Rev. Biochem.* **1978,** *47,* 635.
5. Feher, G.; Okamura, M. In "The Photosynthetic Bacteria"; Clayton, R. K.; Sistrom, W. R., Eds.; Plenum: New York, 1978; pp. 349–386.
6. Duysens, L. N. M., Ph.D. Thesis, Utrecht, 1952.
7. Clayton, R. K. *Photochem. Photobiol.* **1962,** *1,* 201.
8. Kuntz, Jr., I. D.; Loach, P. A.; Calvin, M. *Biophys. J.* **1964,** *4,* 227.
9. Loach, P. A.; Androes, G. M.; Maksim, A. F.; Calvin, M. *Photochem. Photobiol.* **1963,** *2,* 443.
10. Clayton, R. K. *Photochem. Photobiol.* **1966,** *5,* 669.
11. Loach, P. A.; Sekura, D. L. *Photochem. Photobiol.* **1967,** *6,* 381.
12. Sauer, K.; Dratz, E. A.; Coyne, L. *Proc. Natl. Acad. Sci. U.S.A.* **1968,** *61,* 17.

13. Fuhrhop, J. H.; Mauzerall, D. *J. Am. Chem. Soc.* **1968,** *90,* 3875.
14. Reed, D. W.; Clayton, R. K. *Biochem. Biophys. Res. Commun.* **1968,** *30,* 471.
15. Feher, G. *Photochem. Photobiol.* **1971,** *14,* 373.
16. Norris, J. R.; Uphaus, R. A.; Crespi, H. L.; Katz, J. J. *Proc. Natl. Acad. Sci. U.S.A.* **1971,** *68,* 625.
17. Straley, S. C.; Parson, W. W.; Mauzerall, D. C.; Clayton, R. K. *Biochim. Biophys. Acta* **1973,** *305,* 597.
18. Amesz, J.; Vredenberg, W. J. *Biochim. Biophys. Acta* **1966,** *126,* 254.
19. Clayton, R. K.; Sistrom, W. R. *Photochem. Photobiol.* **1966,** *5,* 661.
20. Zankel, K. L.; Reed, D. W.; Clayton, R. K. *Proc. Natl. Acad. Sci. U.S.A.* **1968,** *61,* 1243.
21. Dutton, P. L.; Kaufmann, K. J.; Chance, B.; Rentzepis, P. M. *FEBS Lett.* **1975,** *60,* 275.
22. Rockley, M. G.; Windsor, M. W.; Cogdell, R. J.; Parson, W. W. *Proc. Natl. Acad. Sci. U.S.A.* **1975,** *72,* 2251.
23. Loach, P. A.; Hall, R. L. *Proc. Natl. Acad. Sci. U.S.A.* **1972,** *69,* 786.
24. Feher, G.; Okamura, M. Y.; McElroy, J. D. *Biochim. Biophys. Acta* **1972,** *267,* 222.
25. Morrison, L.; Runquist, J.; Loach, P. A. *Photochem. Photobiol.* **1977,** *25,* 73.
26. Okamura, M. Y.; Isaacson, R. A.; Feher, G. *Proc. Natl. Acad. Sci. U.S.A.* **1975,** *72,* 3491.
27. Parson, W. W. *Biochim. Biophys. Acta* **1969,** *189,* 384.
28. Loach, P. A.; Sekura, D. L. *Biochemistry* **1968,** *7,* 2642.
29. Loach, P. A.; Walsh, K. *Biochemistry* **1969,** *8,* 1908.
30. Bolton, J. R.; Clayton, R. K.; Reed, D. W. *Photochem. Photobiol.* **1969,** *9,* 209.
31. Wraight, C. A.; Clayton, R. K. *Biochim. Biophys. Acta* **1974,** *333,* 246.
32. Loach, P. A. *Biochemistry* **1966,** *5,* 592.
33. Parson, W. W. *Biochim. Biophys. Acta* **1968,** *153,* 248.
34. Reed, D. W.; Raveed, D.; Reporter, M. *Biochim. Biophys. Acta* **1975,** *387,* 368.
35. Zurrer, H.; Snozzi, M.; Hanselmann, K.; Bachofen, R. *Biochim. Biophys. Acta* **1977,** *460,* 273.
36. Hall, R.; Doorley, P.; Niederman, R. A. *Photochem. Photobiol.* **1978,** *28,* 273.
37. Odermatt, E.; Snozzi, M.; Bachofen, R. *Biochim. Biophys. Acta* **1980,** *591,* 372.
38. Prince, R. C.; Baccarini-Melandri, A.; Hauska, G. A.; Melandri, B. A.; Crofts, A. R. *Biochim. Biophys. Acta* **1975,** *387,* 212.
39. Jackson, J. B.; Crofts, A. R. *Eur. J. Biochem.* **1971,** *18,* 120.
40. Feher, G.; Isaacson, R. A.; McElroy, J. D.; Ackerson, L. C.; Okamura, M. Y. *Biochim. Biophys. Acta* **1974,** *368,* 135.
41. Butler, W. F.; Johnston, D. C.; Shore, H. B.; Fredkin, D. R.; Okamura, M. Y.; Feher, G. *Biophys. J.* **1980,** *32,* 967.
42. Okamura, M. Y.; Steiner, L. A.; Feher, G. *Biochemistry* **1974,** *13,* 1394.
43. Steiner, L. A.; Okamura, M. Y.; Lopes, A. D.; Moskowitz, E.; Feher, G. *Biochemistry* **1974,** *13,* 1403.
44. Devault, D.; Chance, B. *Biophys. J.* **1966,** *6,* 825.
45. McElroy, J. D.; Mauzerall, D. C.; Feher, G. *Biochim. Biophys. Acta* **1974,** *333,* 261.
46. Shuvalov, V. A.; Klevanik, A. V.; Sharkov, A. V.; Matreetz, Ju. A.; Krukov, P. G. *FEBS Lett.* **1978,** *91,* 135.
47. Akhamov, S. A.; Borisov, A. Yu.; Danielius, R. V.; Gadonas, R. A.; Kozlowski, V. S.; Piskarskas, A. S.; Razjivin, A. P.; Shuvalov, V. A. *FEBS Lett.* **1980,** *114,* 149.
48. Parson, W. W.; Shuvalov, V. A. *Proc. 5th Int. Congr. Photosyn.,* in press.

49. Dutton, P. L.; Leigh, J. S.; Seibert, M. *Biochem. Biophys. Res. Commun.* **1972,** *46,* 406.
50. Leigh, J. S.; Dutton, P. L. *Biochem. Biophys. Res. Commun.* **1972,** *46,* 414.
51. Krasnovskii, A. A. *C. R. Acad. Sci. USSR* **1948,** *60,* 421.
52. Rabinowitch, E. I. In "Photosynthesis"; Wiley: New York, 1956; *Vol.* 2, Part 2, p. 1487.
53. Seely, G. R. In "The Chlorophylls"; Vernon, L. P.; Seely, G. R., Eds.; Academic: New York, 1966; p. 523.
54. Gouterman, M.; Holton, D. *Photochem. Photobiol.* **1977,** *25,* 85.
55. Huppert, D.; Rentzepis, P. M.; Tollin, G. *Biochim. Biophys. Acta* **1976,** *440,* 356.
56. Harbour, J. R.; Tollin, G. *Photochem. Photobiol.* **1974,** *19,* 147.
57. Tollin, G. *J. Phys. Chem.* **1976,** *80,* 2274.
58. Cheddar, G.; Castelli, F.; Tollin, G. *Photochem. Photobiol.* **1980,** *32,* 71.
59. Hurley, J. K.; Castelli, F.; Tollin, G. *Photochem. Photobiol.* **1980,** *32,* 79.
60. Anton, J. A.; Loach, P. A.; Govindjee, E. *Photochem. Photobiol.* **1978,** *28,* 235.
61. Schwarz, F. P.; Gouterman, M.; Muljiani, Z.; Dolphin, D. H. *Bioinorg. Chem.* **1972,** *2,* 1.
62. Anton, J. A.; Kwong, J.; Loach, P. A. *J. Heterocycl. Chem.* **1976,** *13,* 717.
63. Boxer, S. G.; Closs, G. L. *J. Am. Chem. Soc.* **1976,** *98,* 5406.
64. Wasielewski, M. R.; Studier, M. H.; Katz, J. J. *Proc. Natl. Acad. Sci. U.S.A.* **1976,** *73,* 4282.
65. Wasielewski, M. R.; Smith, V. H.; Cope, B. T.; Katz, J. J. *J. Am. Chem. Soc.* **1977,** *99,* 4172.
66. Wasielewski, M. R.; Svec, W. A.; Cope, B. T. *J. Am. Chem. Soc.* **1978,** *100,* 1961.
67. Ogoshi, H.; Sugimoto, H.; Yoshida, Z. *Tetrahedron Lett.* **1977,** *2,* 169.
68. Collman, J. P.; Elliot, C. M.; Halbert, T. R.; Tourog, B. S. *Proc. Natl. Acad. Sci. U.S.A.* **1977,** *74,* 18.
69. Kagan, N. E.; Mauzerall, D.; Merrifield, R. B. *J. Am. Chem. Soc.* **1977,** *99,* 5484.
70. Ichimura, K. *Chem. Lett.* **1977,** 641.
71. Chang, C. K.; Kuo, M. S.; Wang, C. B. *J. Heterocycl. Chem.* **1977,** *14,* 943.
72. Chang, C. K. *J. Heterocycl. Chem.* **1977,** *14,* 1285.
73. Chang, C. K. *J. Chem. Soc., Chem. Commun.* **1977,** 800.
74. Chang, C. K. In "Inorganic Compounds with Unusual Properties-II," King, B. R., Ed.; ACS ADVANCES IN CHEMISTRY SERIES, No. 173, ACS: Washington, D.C., 1979; pp. 162–177.
75. Collman, J. P.; Denisevich, P.; Konai, Y.; Marrocco, M.; Koval, C.; Anson, F. C. *J. Am. Chem. Soc.* **1980,** *102,* 6027.
76. Collman, J. P.; Anson, F. C.; Bencosme, S.; Chong, A.; Collins, T.; Denisevich, P.; Evitt, E.; Geiger, T.; Ibers, J. A.; Jameson, G.; Konai, Y.; Koval, C.; Meier, K.; Oakley, R.; Pettman, R.; Schmittou, E.; Sessler, J. *Pure and Appl. Chem.,* in press.
77. Netzel, T. L.; Kroger, P.; Chang, C. K.; Fujita, I.; Fajer, J. *Chem. Phys. Lett.* **1979,** *67,* 223.
78. Paine, III, J. B.; Dolphin, D.; Gouterman, M. *Can. J. Chem.* **1978,** *56,* 1712.
79. Pellin, M. J.; Kaufmann, K. J.; Wasielewski, M. R. *Nature* **1979,** *278,* 54.
80. Pellin, M. J.; Wasielewski, M. R.; Kaufmann, K. J. *J. Am. Chem. Soc.* **1980,** *102,* 1868.
81. Boxer, S. G.; Bucks, R. R. *J. Am. Chem. Soc.* **1979,** *101,* 1883.
82. Kong, J.; Loach, P. In "Frontiers of Biological Energetics: From Electrons to Tissues"; Dutton, P. L.; Leigh, J. S.; Scarpa, A., Eds.; Academic: New York, 1978; Vol. 1, p. 73.
83. Kong, J. L. Y.; Loach, P. A. *J. Heterocycl. Chem.* **1980,** *17,* 737.

84. Kong, J. L. Y., Ph.D. Thesis, Northwestern University, Evanston, IL, 1979.
85. Kong, J. L. Y.; Loach, P. A. 7th Annu. Meet. Am. Soc. Photobiol., Pacific Grove, CA, June 24-28, 1979; Abstr. THPM-A12.
86. Kong, J. L. Y.; Loach, P. A. 3rd Int. Conf. Photochem. Convers. Stor. of Solar Energy, Boulder, CO., August 3-8, 1980; Abstr. I-3, pp. 9–11.
87. Spears, K. G.; Cramer, L. E.; Hoffland, L. D. *Rev. Sci. Instrum.* **1978,** *49,* 255.
88. Spears, K. G.; Steinmetz-Bauer, K. M.; Gray, T. H. In "Picosecond Phenomena II"; Hochstrasser, R.; Kaiser, W.; Shank, C. V., Eds.; Springer: New York, 1980; p. 106.
89. Kong, J. L. Y.; Spears, K. G.; Loach, P. A. *Photochem. Photobiol.* **1982,** *35,* 545.
90. Jeanmaire, D. L.; Suchanski, M. R.; Van Duyne, R. P. *J. Am. Chem. Soc.* **1975,** *97,* 1699.
91. Drake, K. F.; Van Duyne, R. P.; Bond, A. M. *J. Electroanal. Chem.* **1978,** *89,* 231.
92. Morrison, L. E., Ph.D. Thesis, Northwestern University, Evanston, IL, 1978.
93. Fajer, J.; Borg, D. C.; Forman, A.; Dolphin, D.; Felton, R. H. *J. Am. Chem. Soc.* **1970,** *92,* 3451.
94. Wolberg, A.; Manassen, J. *J. Am. Chem. Soc.* **1970,** *92,* 2982.
95. Wasser, R. K. W.; Fuhrhop, J. H. *Ann. N.Y. Acad. Sci.* **1973,** *206,* 533.
96. Zemel, H.; Hoffman, B. M. *J. Am. Chem. Soc.* **1981,** *103,* 1192.
97. Ho, T. F.; McIntosh, A. R.; Bolton, J. R. *Nature* **1980,** *286,* 254.
98. Masters, B.; Mauzerall, D. *J. Membr. Biol.* **1978,** *41,* 377.
99. Ilani, A.; Mauzerall, D. *Biophys. J.* **1981,** *35,* 79.
100. Krakover, T.; Ilani, A.; Mauzerall, D. *Biophys. J.* **1981,** *35,* 93.
101. Ross, R. T.; Calvin, M. *Biophys. J.* **1967,** *7,* 595.
102. Knox, R. S. *Biophys. J.* **1969,** *9,* 1351.
103. Knox, R. S. In "Primary Processes of Photosynthesis"; Barber, J., Ed.; Elsevier: Amsterdam C, Neth., 1977; pp. 55–97.
104. Parson, W. W. *Photochem. Photobiol.* **1978,** *28,* 389.
105. Hinkle, P. C. In "Molecular Specialization and Symmetry in Membrane Function"; Solomon, A. K.; Karnovsky, M., Eds.; Harvard Univer. Press, 1978; pp. 222–228.
106. Mitchell, P. *Eur. J. Biochem.* **1978,** *95,* 1.
107. Mitchell, P. *Science* **1979,** *206,* 1148.
108. Hauska, G. *FEBS Lett.* **1977,** *79,* 345.
109. Futami, A.; Hurt, E.; Hauska, G. *Biochim. Biophys. Acta* **1979,** *547,* 583.
110. Hauska, G. In "Function of Quinones in Energy Conserving Systems"; Trumpower, B., Ed.; Academic: New York, 1981.
111. Mitchell, P. *FEBS Lett.* **1975,** *56,* 1.
112. Mitchell, P. *FEBS Lett.* **1975,** *59,* 137.
113. Prince, R. C.; Dutton, P. L. *Biochim. Biophys. Acta* **1975,** *387,* 609.
114. Vermeglio, A. *Biochim. Biophys. Acta* **1977,** *459,* 516.
115. Wraight, C. A. *Biochim. Biophys. Acta* **1977,** *459,* 525.
116. Wraight, C. A. *Biochim. Biophys. Acta* **1979,** *548,* 309.
117. Vermeglio, A.; Martinet, T.; Clayton, R. K. *Proc. Natl. Acad. Sci. U.S.A.* **1980,** *77,* 1809.
118. Dutton, P. L.; Prince, R. C. *FEBS Lett.* **1978,** *91,* 15.
119. Crofts, A. R.; Bowyer, J. R. *Ann. N.Y. Acad. Sci.* **1980,** *341,* 12.
120. Trumpower, B. L. *J. Bioenerg. Biomembr.* **1981,** *13,* 1.
121. Runquist, J. A.; Loach, P. A. *Biophys. J.* **1979,** *25,* 273a.
122. Runquist, J. A.; Dannhauser, T. J.; Loach, P. A. *Fed. Proc.* **1980,** *39,* 2147.
123. Runquist, J. A.; Dannhauser, T. J.; Loach, P. A. *Biophys. J.* **1981,** *33,* 77a.
124. Runquist, J. A.; Loach, P. A. *Biochim. Biophys. Acta* **1981,** *637,* 231.
125. Hinkle, P. *Biochem. Biophys. Res. Commun.* **1970,** *41,* 1375.
126. Hinkle, P. C. *Fed. Proc.* **1973,** *32,* 1988.

127. Clark, W. M. "Oxidation-Reduction Potentials of Organic Systems"; Krieger, 1960.
128. Truxillo, L. A.; Davis, D. G. *Anal. Chem.* **1975,** *47,* 2260.
129. Loach, P. A. In "Handbook of Biochemistry", 2nd ed.; Sober, H. A., Ed.; Chemical Rubber Co.: Cleveland, OH, 1970; p. J–33.
130. Kadish, K. M.; Davis, D. G. *Ann. N.Y. Acad. Sci.* **1973,** *206,* 495.
131. Fuhrhop, J.-H.; Kadish, K. M.; Davis, D. G. *J. Am. Chem. Soc.* **1973,** *95,* 5140.
132. Mauzerall, D. In "The Porphyrins"; Dolphin, D., Ed.; Academic: New York, 1978; Vol. 5, Part C, pp. 29–52.
133. Van Duyne, R. P.; Fischer, S. F. *Chem. Phys.* **1974,** *5,* 183.
134. Hopfield, J. *Proc. Natl. Acad. Sci. U.S.A.* **1974,** *71,* 3640.
135. Ballard, S. G.; Mauzerall, D. *J. Chem. Phys.* **1980,** *72,* 933.
136. Chappell, J. B. *Biochem. J.* **1964,** *90,* 225.
137. Biegel, C. M.; Gould, J. M. *Biophys. J.* **1981,** *33,* 102a.
138. Harbury, H. A.; Loach, P. A. *J. Biol. Chem.* **1960,** *235,* 3640.
139. Harbury, H. A.; Loach, P. A. *J. Biol. Chem.* **1960,** *235,* 3646.
140. Nagle, J. F.; Horowitz, H. J. *Proc. Natl. Acad. Sci. U.S.A.* **1978,** *75,* 298.
141. Nagle, J. F.; Mille, M.; Horowitz, H. J. *Phys. Chem.* **1980,** *72,* 3959.
142. Gouterman, M. In "The Porphyrins"; Dolphin, D., Ed.; Academic: New York, 1978; Vol. 3, pp. 1–165.
143. Felton, R. H. In "The Porphyrins"; Dolphin, D., Ed.; Academic: New York, 1978; Vol. 5, pp. 53–125.
144. Kadish, K. M.; Thompson, L. K.; Beroiz, D.; Bottomley, L. A. In "Electrochemical Studies of Biological Systems," Sawyer, D. J., Ed.; ACS SYMPOSIUM SERIES, No. 38, ACS: Washington, D.C., 1977; p. 55.
145. Wolberg, A.; Manassen, J. *J. Am. Chem. Soc.* **1970,** *92,* 2982.
146. Davis, D. G. In "The Porphyrins"; Dolphin, D., Ed.; Academic: New York, 1978; Vol. 5, p. 139.

RECEIVED for review June 2, 1981. ACCEPTED August 18, 1981.

Enzymatic and Electrochemical Reduction of Dioxygen

DAVID DOLPHIN, BRIAN R. JAMES,
and H. CURTIS WELBORN[1]

University of British Columbia, Department of Chemistry, Vancouver, British Columbia, Canada V6T 1Y6

Heme proteins utilizing O_2 and H_2O_2 are considered with special emphasis on the mechanisms of oxidation of inactivated carbon–hydrogen bonds by P-450 cytochrome systems. Titration and chemical and spectral studies on a P-450 camphor enzyme reveal that an axially coordinated cysteinyl thiolate ligand present in the Fe(II) [and Fe(III)] state of the enzyme remains bound and deprotonated when O_2 or CO binds at the Fe(II) center. The catalytically active species in the enzyme results after addition of one electron at about −0.2 V (vs. Ag/AgCl) to the Fe(II)O_2 system. Such isoelectronic species within model systems are generated by (1) reaction of Fe(I) porphyrins with O_2, (2) reaction of Fe(II) porphyrins with O_2^-, and (3) an electrochemical one-electron reduction of the Fe(II)(O_2) porphyrin system at −0.24 V. All three model species are identical and appear to be a high spin Fe(III) η^2-peroxide; such a species could function in the enzymatic pathway via an oxene intermediate that inserts directly into the CH bond of the substrate or generates free radicals by abstraction of hydrogen from the substrate. Spectral similarities are noted between the Fe(III) η^2-peroxide and Fe(III)–iodosylbenzene systems, the latter effecting oxidations that closely mimic some carried out by P-450.

Heme proteins play varied roles in the transport, storage, and activation of dioxygen and removal of its reduction products. Scheme 1 shows the many known and postulated intermediates in the chemis-

[1] Current address: Exxon Chemical Company, Baytown, TX, 77520

0065-2393/82/0201-0563$06.25/0

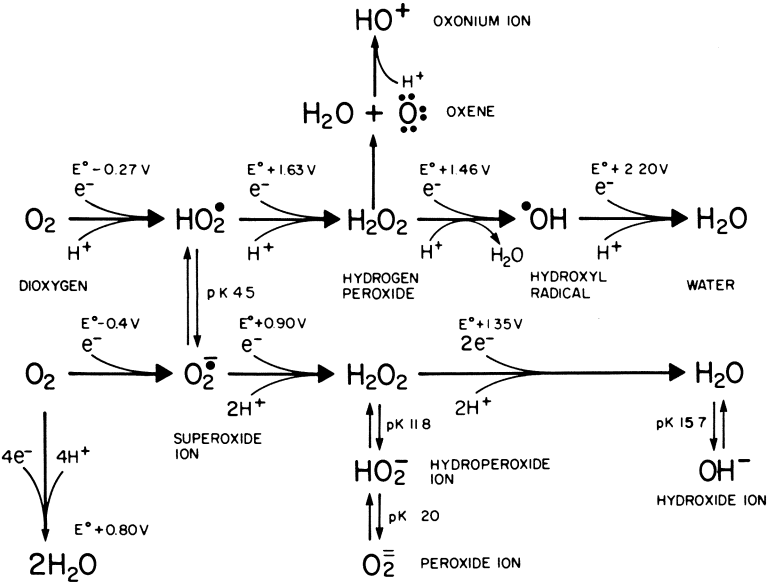

Scheme 1. Redox chemistry of dioxygen (reduction potentials in aqueous solutions at pH 7, vs. SHE)

try of dioxygen reduction. In nature, the four-electron reduction to water is catalyzed by cytochrome oxidase, which contains two heme and two copper centers (*1*, *2*). The characterization of intermediates during the reduction is far from complete, and definitive evidence for either superoxide or peroxide has yet to be found. At the oxidation level of peroxide, heme enzymes both remove this powerful and indiscriminate oxidizing agent and use its oxidizing power in more specific and controlled ways. Thus, myeloperoxidase and chloroperoxidase, both of which are ferric heme proteins in the resting enzyme, undergo two-electron oxidations by hydrogen peroxide to give high oxidation states of the enzymes, which then oxidize chloride to give Cl^+. In chloroperoxidase (*3*), subsequent controlled oxidations of organic substrates occur, but in myeloperoxidase, which is a constituent of the mammalian polymorphonuclear leukocyte (*4*), the chlorine generated in this fashion is but one of several small but powerful inorganic agents including superoxide, singlet oxygen, and hydroxyl radicals that destroy invading organisms and xenobiotic materials (*5*).

Two other closely related heme proteins that interact with hydrogen peroxide are catalase and the horseradish peroxidases, which also are ferric heme proteins in the resting enzymes. In the presence of hydrogen peroxide both are oxidized to their primary complexes (CAT

I and HRP I) (*6*). Oxidized catalase then oxidizes a second molecule of hydrogen peroxide to oxygen with regeneration of the resting enzyme.

$$\text{Cat[Fe(III)porphyrin]}^{+} + H_2O_2 \rightarrow \text{Cat[Fe(IV)porphyrin]}^{3+\cdot} + 2OH^{-}$$

$$\downarrow \quad H_2O_2$$

$$\text{Cat[Fe(III)porphyrin]}^{+} + O_2 + 2H^{+}$$

The chemical or electrochemical reduction of peroxide can generate hydroxyl radicals. Catalase generates no such oxygen radical intermediates; apparently nature devised catalase to bring about the two-electron transfers between peroxides without the intervention of free (and reactive) oxygen radicals (*7*).

Both homolytic and heterolytic cleavage of peroxide can be envisaged, with hydroxyl ($H\dot{\ddot{O}}\cdot$) radical and oxene ($:\ddot{O}:$), respectively, generated. The chemistry of hydroxyl radicals is well-explored and as expected, the radical proves to be a powerful and rather indiscriminate oxidizing agent. The chemistry of oxenes is hardly explored as yet, although triplet oxygen atoms oxidize alkanes (*8*).

Although nature is unlikely to use free hydroxyl radicals or oxene moieties, such species, stabilized by coordination to a metal, make attractive candidates as enzymatic oxidizing agents. The oxidation of unactivated CH bonds is one of the principal modes of action of P-450 cytochromes. These enzymes are widely distributed in both eucaryotes and procaryotes (*9*), and although the specificity of the enzymes may vary widely, the overall reactions that they catalyze are similar (*10, 11*). Initially, the resting ferrihemoprotein is reduced to the ferrous state, which binds dioxygen; a further one-electron reduction initiates the oxidation, which results in one of the oxygen atoms being incorporated into substrate while the other oxygen ends up as water (Scheme 2). A typical example of such an oxidation is that catalyzed by P-450_{cam}, isolated from *Pseudomonas putida* (*12*). This microorganism will grow with *d*-camphor as the only carbon source in a reaction where the hydroxylation of camphor (Scheme 2) is the first step in the conversion of camphor to acetyl CoA. Another recently identified system, heme oxygenase (*13*), converts iron protoporphyrin to bile pigments (*14*). The initial steps in this reaction, which appear to parallel those of cytochromes P-450, are the generation of *meso*-hydroxyhemin (Scheme 2). Our present understanding of the catalytic cycle of P-450 is summarized in Scheme 3, and a considerable body of knowledge concerning the mode of action and the nature of the intermediates has evolved since the discovery of these enzymes.

In fact, cytochromes P-450 have been known for only two decades (*15*), and were named for the intense absorption, at 450 nm, of the ferrous–CO complex. This absorption spectrum can be mimicked

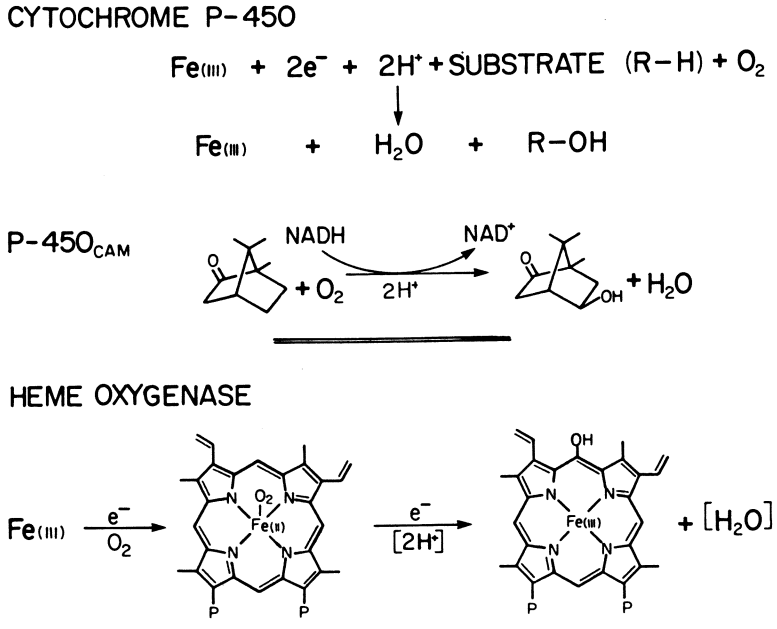

Scheme 2. Activation of dioxygen by heme proteins

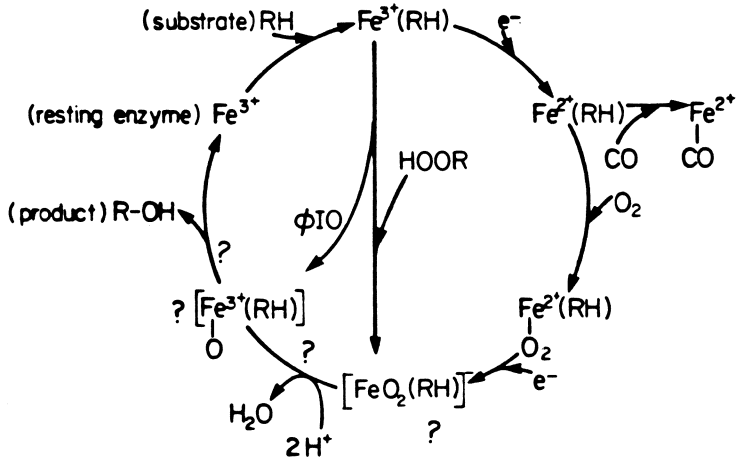

Scheme 3. Cytochrome P-450 enzymatic cycle

when a ferrous–CO complex is coordinated by thiolate ion as the sixth axial ligand (*16*, *17*). However, in the model systems the absorption at ~450 nm was accompanied by an equally intense absorption at higher energy. This same phenomenon was then reported with P-450 itself (*18*). Such an optical spectrum where the "normal" Soret band at ~410 nm is split into a high- and low- (~450 nm) energy component was termed a hyper spectrum by Hanson et al. (*18*), who showed that interaction between the normal π–π^* (Soret) transition and a sulfur $p \rightarrow \pi^*$ charge transfer transition gives rise to the hyper spectrum (*19*).

During the normal enzymatic cycle, oxygen, rather than CO, binds to the ferrous hemoprotein to give the oxygenated complex that appears optically similar to oxymyoglobin. Thus both oxy-P-450$_{cam}$ and oxymyoglobin (whale) absorb at 418 nm. Because we attributed the differences in the optical spectra of P-450 and myoglobin CO-complexes (450 vs. 423 nm) to differences in the sixth axial ligand (RS^- vs. imidazole), the question arises as to how can the oxygenated complexes exhibit similar spectra if the axial ligand is different? One possibility is that upon oxygen binding to P-450 the thiolate is protonated, or displaced by another axial ligand (such as imidazole).

If either of these hypotheses concerning change in axial ligation between the CO and O_2 complexes is correct, then one proton per heme should be involved in the process (Scheme 4).

The measurements of proton balance by direct titration in buffers of low capacity were used to measure the Bohr effect upon oxygenation of hemoglobin (*20*). The same information concerning proton release can be gained by means of optically determining $p_{1/2}$ values [$p_{1/2}$ is the partial pressure of a gas required such that half of the iron(II) center is coordinated by the gas]. Here the change in proton balance (ΔH^+) is given by the relationship $\Delta H^+ = \delta \log p_{1/2}/\delta pH$. We have used both techniques with cytochrome P-450$_{cam}$ (*21*), which being

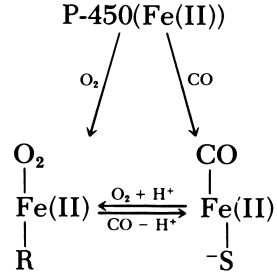

[R = −SH or histidine]

Scheme 4.

monomeric suffers no complications from cooperative effects. Figure 1 shows the data for the binding of CO and O_2 and for their exchange, where only minimal changes in acid dissociation constants occur upon binding of the gaseous ligands. Only about 5% H^+/P-450 is liberated during the carbonylation. Similarly, the O_2/CO replacements reactions show essentially no change in the proton balance.

These results show that the thiolate ion is coordinated to the ferrous heme in the absence of CO and O_2, and it also remains as thiolate when either of these ligands binds to the ferrous iron. Thus, there remains the problem of the lack of a hyper spectrum for the oxygenated P-450 structure [$(RS^-)Fe(II)(O_2)$], particularly because molecular orbital calculations have shown that such thiolate oxygen complexes should give hyper spectra (22). The answer to this dilemma is easily resolved when the optical spectra of oxy-P-450 are examined more closely. Thus, although oxy-P-450 and oxymyoglobin appear superfi-

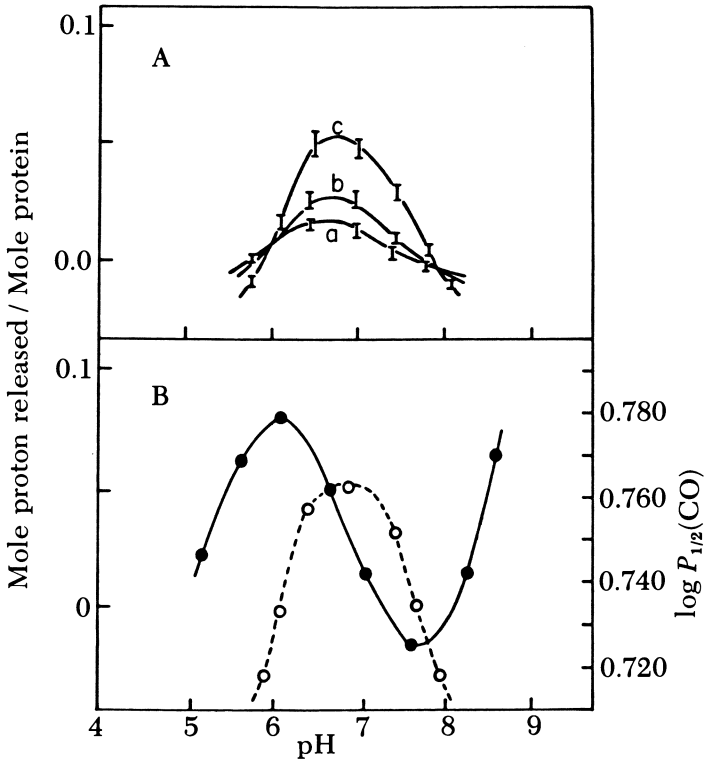

Figure 1. A: Direct titration data at 0°C for O_2-binding (a), replacement of O_2 by CO (b), and CO-binding with ferrous P-450$_{cam}$ (c). B: Spectrophotometric determination of $p_{1/2}$ for CO-binding as a function of pH at 23°C (●); first derivative curve (○).

cially similar with Soret absorptions at 418 nm, oxy-P-450 does indeed show a hyper spectrum (Figure 2) with the low energy transition at 418 nm and the high energy component at 350 nm (*23*). This split (hyper spectrum) is also observed with the enzyme reconstituted with a variety of different hemins (Table I).

Furthermore, the spectra of all of the oxygenated species show only a broad absorption in the visible region, which is also characteristic of hyper spectra. This diffuse absorption in the visible region is paralleled by the P-450–CO complexes, and is in turn quite different from the O_2 and CO complexes of myoglobin, which show two well-resolved absorptions in the visible region. Clearly then the optical spectra of oxygenated P-450 also support the coordination of a thiolate ligand.

The chemistry of oxy-P-450 further supports the suggestion that a thiolate ion is coordinated, and the difference in the sixth axial ligand between oxy-P-450 and oxymyoglobin and hemoglobin (histidine) is reflected in their differing reactivities. Oxyhemoglobin and myoglobin are designed to transport, store, and release dioxygen as required. Thus, these oxygenated complexes, even in vitro, are reasonably stable. Such is not the case with oxy-P-450, which autoxidizes quite rapidly to the ferric enzyme and superoxide (*23*). The rate law for this reaction $k[O_2 \cdot \text{P-450}][H^+]$ differs for that observed with hemoglobin where an overall third-order rate law $k[HbO_2][H^+][X^-]$ is observed (*24*) (X^- being an added nucleophile such as cyanide or halide). This observation is consistent with the loss of superoxide from hemoglobin

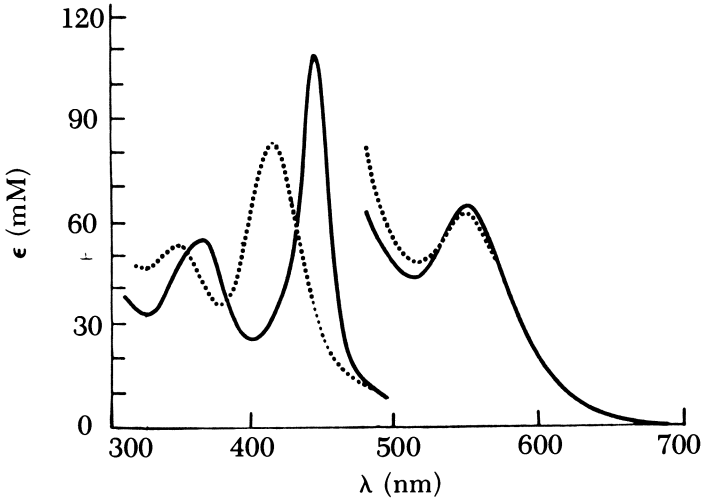

Figure 2. Optical spectra of the carbonylated (—) and oxygenated (· · · ·) ferrous P-450$_{cam}$.

Table I. Hyper Spectra of Reconstituted P-450 Ferrous Oxygen Complexes (23)

Hemin	*High-energy band*	*Low-energy band (nm)*
Meso	344	409
Deutero	335	407
Proto	350	418
Diacetyldeutero	350	438
Dibromodeutero	343	413

requiring formation of a hexacoordinated ferric species containing X^-. In oxy-P-450, the already coordinated thiolate ligand presumably aids the loss of superoxide. Figure 3 shows the spectral changes observed during the autoxidation of oxygenated P-450 and the first-order rate plot for this decomposition in the presence of camphor substrate. In the absence of substrate the autoxidation rates are about 100 times faster, but it is unclear how substrate stabilizes the oxygenated species. Nevertheless, the oxygenated species must be sufficiently stable for the rate-limiting step in the enzymatic reaction, which is the addition of a further electron to this species (Scheme 3).

When dioxygen binds to a ferrous heme protein, charge transfer from iron to oxygen of the ferrous dioxygen complex will generate some ferric superoxide character (I ↔ II, Scheme 5). The degree of charge transfer in hemoglobin and myoglobin is still a matter of some contention, although clearly these proteins exhibit some ferric superoxide character (25). The coordination of a thiolate ion *trans* to dioxygen can be expected to increase the ferric superoxide nature of oxygenated P-450. As already noted (Scheme 3) the next step in the enzymatic cycle is the further one-electron reduction. Formally this could be envisaged as a reduction of the ferrous dioxygen complex to the Fe(I) dioxygen complex (I → III, Scheme 5). Similarly, addition of the electron to the oxygen of I would give the ferrous superoxide complex (I → IV, Scheme 5), whereas addition of the electron to the oxygen moiety of II would give a ferric peroxide complex (II → V). The question arises as to whether III, IV, and V merely represent resonance structures of the same species (and if they do what is the principal contributing form) or are they separate distinct species?

To consider these problems and to mimic the enzymatic reduction of oxygenated P-450, we examined the Reactions a–d outlined in Scheme 5 using model iron porphyrin complexes. The two-electron electrochemical reduction of chloro(tetraphenylporphinato)iron(III) [Fe(III)Cl(TPP)] at −0.9 V vs. Ag/AgCl[2] in acetonitrile–methylene

[2] All potentials reported in this chapter are quoted vs. the Ag/AgCl electrode.

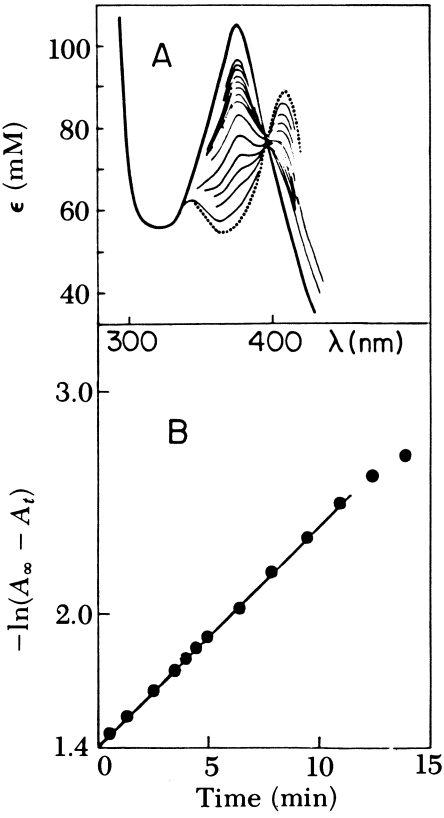

Figure 3. Spectral changes (A) and first-order plot of absorbance at 378 nm (B), during the autoxidation of mesoporphyrin-reconstituted ferrous P-450$_{cam}$ (· · · ·). In the presence of camphor substrate, pH 7.0, 0°C, $t_{1/2}$ = 7.0 min. The product is high spin Fe(III) (—).

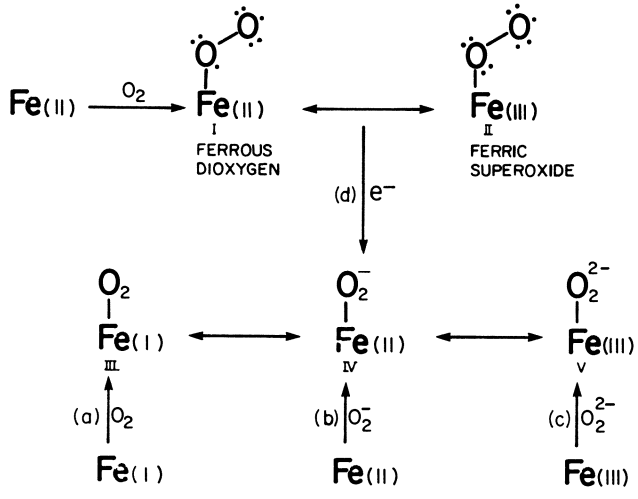

Scheme 5.

dichloride or tetrahydrofuran [containing tetra-*n*-butylammonium hexafluorophosphate $N(n\text{-}Bu)_4PF_6$] generates the corresponding iron(I) complex, $[Fe(I)TPP]^-$ (*26*), which on treatment with dioxygen at −50°C generates a new species (**1**) (λ_{max}[THF] 433, 564, 607, Figure 4). Reaction of **1**, $[Fe(O_2)TPP]^-$, with CO generates [Fe(II)TPP(CO)(THF)], readily identified by its optical spectrum, and presumably superoxide. Compound **1** is identical to that derived from the reaction of oxygen with $Na[Fe(TPP)(THF)_2]$, prepared from [Fe(III)Cl(TPP)], sodium naphthalenide, and crown ether in tetrahydrofuran (*27*). Solutions containing Compound **1** prepared by either route (path a, Scheme 5), exhibit ESR signals at $g = 4.3$ and 2.0 at 77K. Furthermore, the same complex was prepared from Fe(II)TPP and superoxide (path b, Scheme 5) (*28*).

We examined the interaction of chloro(octaethylporphinato)-iron(III) [Fe(III)Cl(OEP)] with the crown ether complex of potassium superoxide in dimethyl sulfoxide. The first equivalent of superoxide acts as a reductant and generates the pink species (λ_{max} 412, 515, 546) Fe(II)OEP (Figure 5). The addition of a second equivalent of superoxide generates **2**, which is orange (λ_{max} 423, 545, 572, Figure 5), and gives rise to an ESR spectrum with signals at $g = 4.2$ and 2.0, similar to that of **1**. Indeed **1** and **2** appear to differ only in the nature of the porphyrin ligand such that **2** can be designated as $[Fe(O_2)OEP]^-$. Complex **2** appears identical to the complex previously prepared in the same way (*28*).

The coordination of peroxide to a ferric porphyrin (route c, Scheme 5) was unsuccessful. Our failure derives from the second pK_a

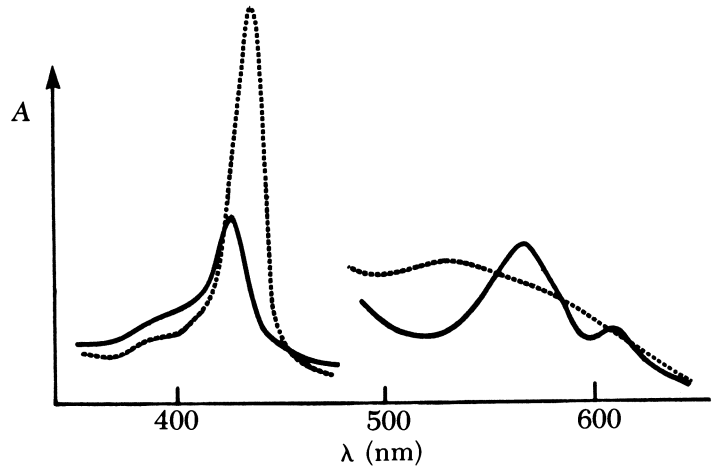

Figure 4. Optical spectrum of $[Fe(I)(TPP)]^-$(· · · ·) prepared by the electrochemical reduction of [Fe(III)Cl(TPP)] in THF–(n-Bu)$_4PF_6$ at −0.9 V, and its reaction with O_2 at −50°C to give 1 (—).

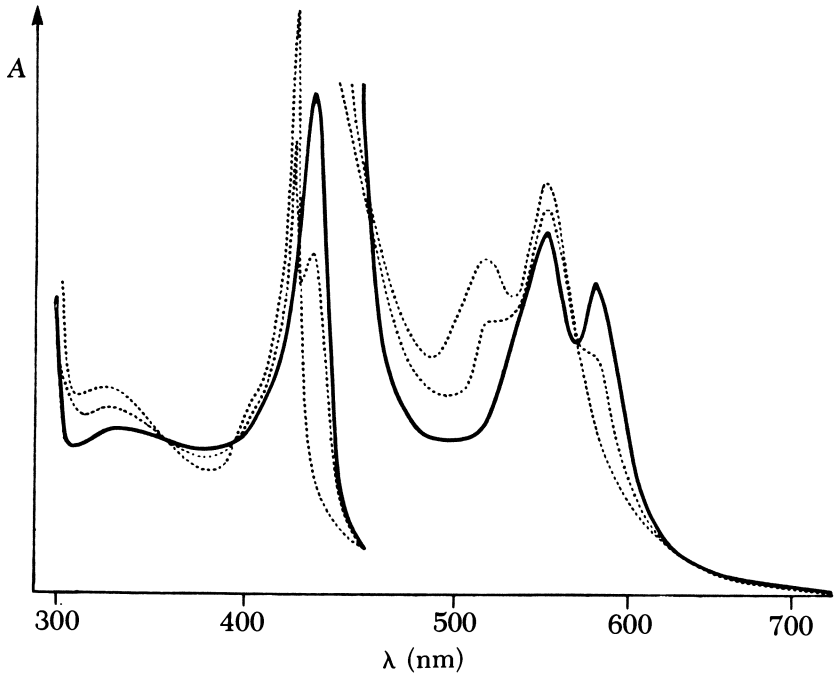

Figure 5. Reaction of Fe(II)(OEP)(· · · ·) in DMSO with crown KO_2 to give **2** *(—).*

value of hydrogen peroxide, which is about 20. The strongly basic properties of the peroxide ion coupled with the solvents, which stabilize Compounds **1** and **2** (principally DMSO), result in acid–base chemistry with O_2^{2-}, rather than coordination to iron.

Hydrogen peroxide, alkyl hydroperoxides, and peracids can shunt the enzymatic cycle of P-450 and replace the oxygen plus the two-electron reductions (Scheme 3). As outlined in Scheme 5, route b or d can give rise to Complex IV. Route d is that used by P-450 whereby the ferrous dioxygen complex is reduced by one electron. We mimicked this reaction (*29*) by examining the direct one-electron reduction of the dioxygen complex of ferrous octaethylporphyrin [Fe(II)(OEP)$L(O_2)$], **3** (L = solvent). The complex assumed to be **3** was prepared by treating Fe(II)OEP at −25°C with dioxygen until there was no further spectral change; the final spectrum (Figure 6) closely resembles those of other hexacoordinated ferrous porphyrin dioxygen species (*28*). Argon was then passed through the solution to remove excess oxygen. Cyclic voltammetry of **3** then showed a reversible (both thermodynamic and electrochemical) couple at −0.24 V (vs. Ag/AgCl) (Figure 7). Bulk electrolysis of **3** was carried out in a 1-mm cuvette lined with a thin platinum gauze electrode, which was transparent to the monitoring

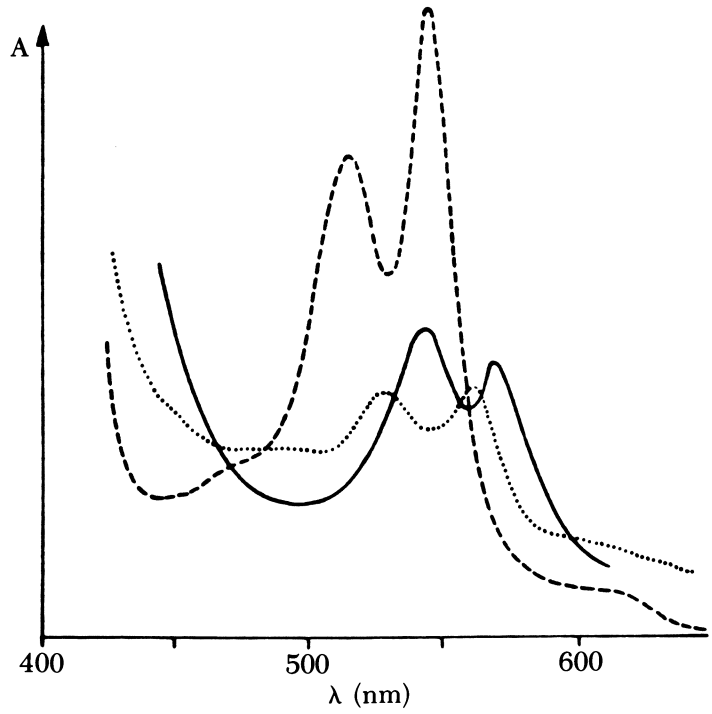

Figure 6. Optical spectra of Fe(II)(OEP) in DMSO–CH_3CH at −25°C (---) and $[Fe(O_2)OEP]^-$(2) (—) prepared by the one-electron electrochemical reduction of Fe(OEP)L(O_2) (3) (· · · ·) at −0.5 V.

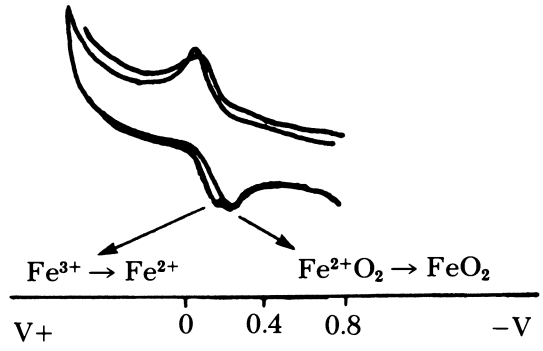

Figure 7. Cyclic voltammogram of Fe(II)(OEP) and Fe(II)(OEP)L(O_2) in DMSO–CH_3CN/(n-Bu)$_4NPF_6$ at −25°C.

beam. Since diffusion is slow at −25°C, the anode was simply placed away from the cathode but not separated by a divider. Reduction at −0.5 V brought about the change in spectrum shown in Figure 6. The one-electron reduction product is identical to the complexes prepared from Fe(I)OEP and O_2, or Fe(II)OEP and superoxide. Thus, no matter which route is pursued (a, b, or d, Scheme 5), these isoelectronic reactions proceed to give the same product. The problem then remains to determine the best description of the electronic structure of this species (III, IV, or V, Scheme 5).

On the basis of EPR and IR measurements (*28*), a high spin ferric η^2-peroxide complex is suggested as the structure for the species prepared by route a, b, or d, and apparently upon reduction the end-on η^1-dioxygen complex is converted to the ferric η^2-peroxide complex **4** (Scheme 6). Whether **4** contains a further axial coordinated solvent ligand *L* is unclear.

As is often observed with the heme protein oxygen system, the electronic configuration suggested by one physical measurement may be somewhat modified by that indicated by other measurements. The classic example is the degree of charge transfer in oxyhemoglobin toward the ferric superoxide configuration, where physical measurements and theoretical studies were discussed in terms of low spin Fe(II)–O_2 and spin-coupled, low spin Fe(III)–O_2(−I) interactions, predominantly in terms of the latter; at least the oxygen is now known to be monohapto bonded (*30*). For Species **4**, although the magnetic moment shows it to be high spin (S = 5/2) iron(III) and the ESR and IR measurements are consistent with the η^2-peroxide formulation, the optical spectra more closely resemble a hexacoordinated ferrous porphyrin complexed to a strong π-acceptor.

No definitive evidence indicates that the ferric η^2-peroxide observed in the electrochemical reduction of oxygenated ferrous OEP (*29*) has the same electronic configuration as the one-electron reduction product of oxy-P-450. Nevertheless, the similarity between the two systems including the similarities in the potentials at which the iron–oxygen complex is reduced (−0.24 vs. −0.20 V) (*31*) (Scheme 7), coupled with the observation that microsomes generate peroxide (*32*) make the peroxide **4** an attractive intermediate for the enzymatic pathway.

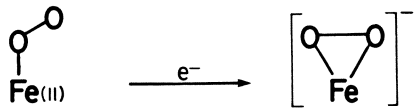

4

Scheme 6.

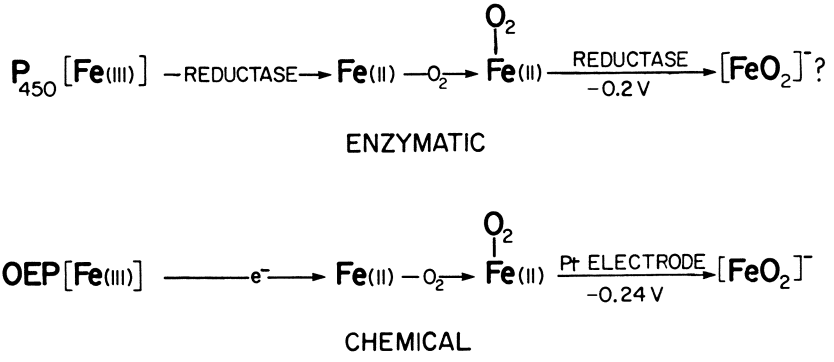

Scheme 7. Comparison between enzymatic and electrochemical reduction of ferrous porphyrin dioxygen complexes

The oxidizing ability of **4** has not been shown (for example, even towards the epoxidation of styrene). If **4** does represent an enzymatic intermediate, how is it activated for oxidation, and at what stage in the reaction is the O–O bond broken? If the thiolate is still axially ligated at this stage, the additional electron density provided would be expected to increase the charge density on the peroxide moiety, making it more susceptible both to electrophilic attack and to bond cleavage. In the net enzymatic reaction two protons are consumed. A direct protonation of **4** followed by loss of water (b, Scheme 8) would lead to the oxene (**5**) (vide infra). However, the active site of the enzyme, above the face of the porphyrin *trans* to the thiolate ligand, is hydrophobic and the transport or accumulation of charge density is likely to be unfavorable. A single turnover of P-450$_{cam}$ showed (*33*) the existence of an intermediate peracid [generated presumably from the nucleophilic attack of the coordinated peroxide of **4** onto a carboxylic acid (a, Scheme 8)]. Heterolytic cleavage of the peracid (or of a hydroperoxide, which the enzyme can use as well) could generate the oxene **5**. As yet no definitive evidence exists for the intermediacy of an oxene during the P-450 enzymatic cycle. However, the oxidant iodosylbenzene can also be utilized by P-450 and the oxygen of the iodosyl group is successfully incorporated into the hydroxylated substrate (*34*).

Extensive work has shown that a simple ferric porphyrin [such as Fe(III)TPP] and iodosylbenzene generates an oxidant that closely mimics the regioselectivity of P-450 (*35*). Iodosylbenzene does not however, readily transfer an oxygen atom to iron(III) porphyrins, although in a corresponding chromium(III) system, oxygen atom transfer readily occurs to give the chromyl porphyrin—Cr(V)(=O)— (Scheme 9) (*36*). This difference in reactivity between the iron and

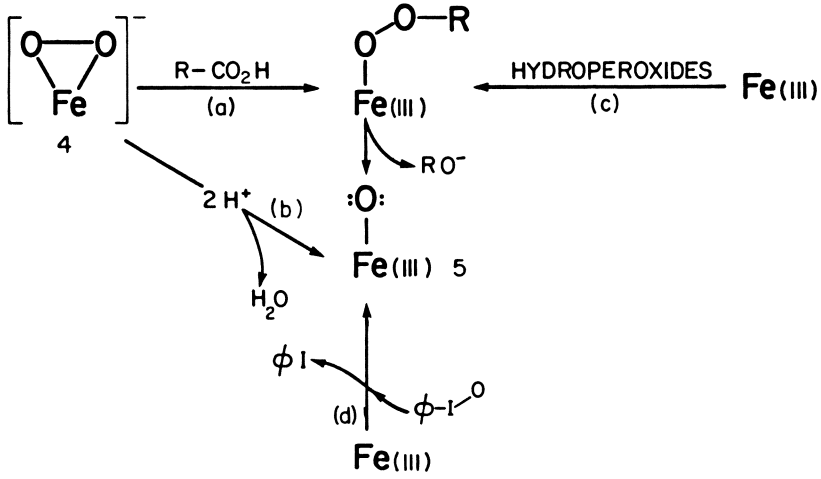

Scheme 8. P-450 active oxidizing agent

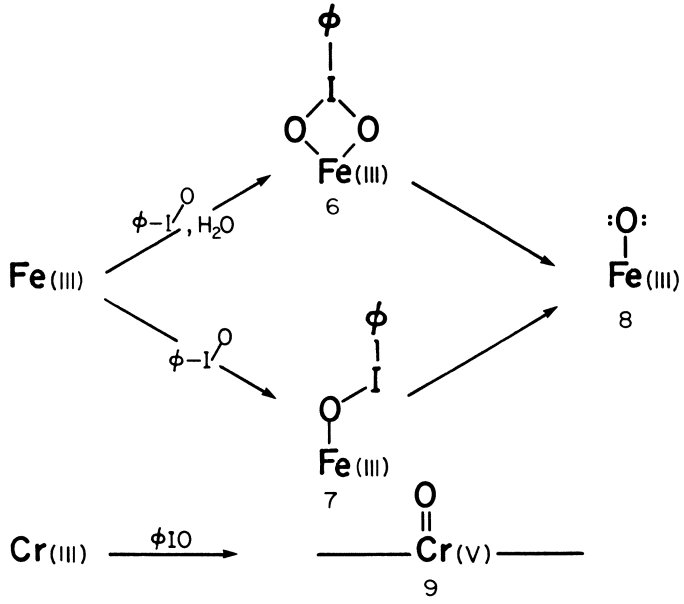

Scheme 9.

chromium systems is readily demonstrated. The iodination and oxidation of polystyrene generates iodosylbenzene covalently bound to an insoluble support. Passing a solution of [Cr(III)Cl(TPP)] over this support at low temperature generates the corresponding chromium(V)–oxo complex, which is eluted from the support. However, when the same experiment is repeated with [Fe(III)Cl(TPP)], the resultant complex is retained on the support, suggesting that a complex between the iodosylbenzene and iron porphyrin is formed. Indeed, when [Fe(III)Cl(TPP)] is treated with iodosylbenzene in acetonitrile at −45°C such a complex is formed (Figure 8). This species will carry out the range of oxidations previously reported (35) and, certainly in the epoxidation of *cis*- and *trans*-stilbene [where only the *cis*diastereomer is oxidized (*34*)], the difference in reactivity can be attributed to the bulk of the still coordinated iodobenzene moiety. The optical spectrum of the ferric iodosylbenzene complex is remarkably similar to that of the ferric η^2-peroxide complex **4** (Figure 9), which suggests a similarity in structure. Free iodosylbenzene readily hydrates and coordination of the hydrated form would give a complex (**6**, Scheme 9) having the same charge as, and a similar structure to, the ferric peroxide complex. The iodosylbenzene may, of course, coordinate as in **7** (Scheme 9) and the similarity in spectra may be merely coincidental. In either case, loss of iodobenzene, either during or before oxidation of substrate, would generate the oxene complex **8**, analogous to the chromyl complex **9** (Scheme 9). The ferric oxene complex and the Cr(V) oxo complex are formally similar since the oxene complex can be written as the ferryl [Fe(V)(=O)] complex (Scheme 10).

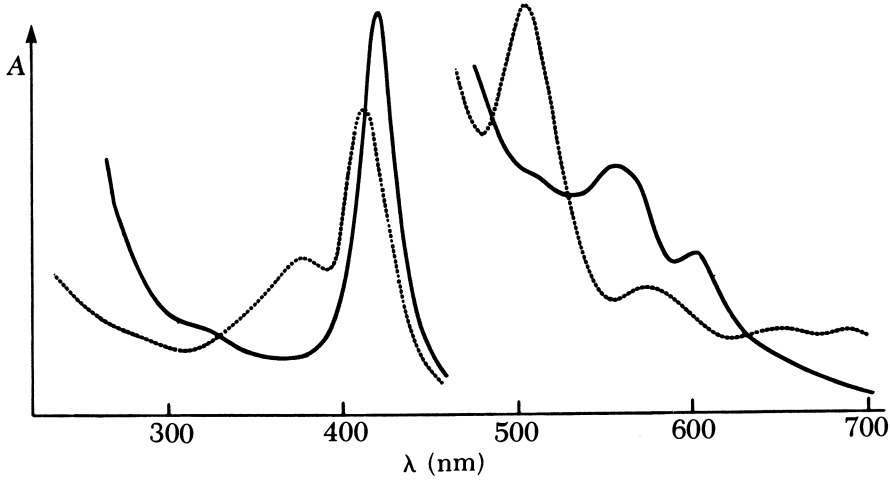

Figure 8. Optical spectra of [Fe(III)Cl(TPP)] (· · · ·) in CH_3CN at −45°C and the product from its reaction with iodosylbenzene (—).

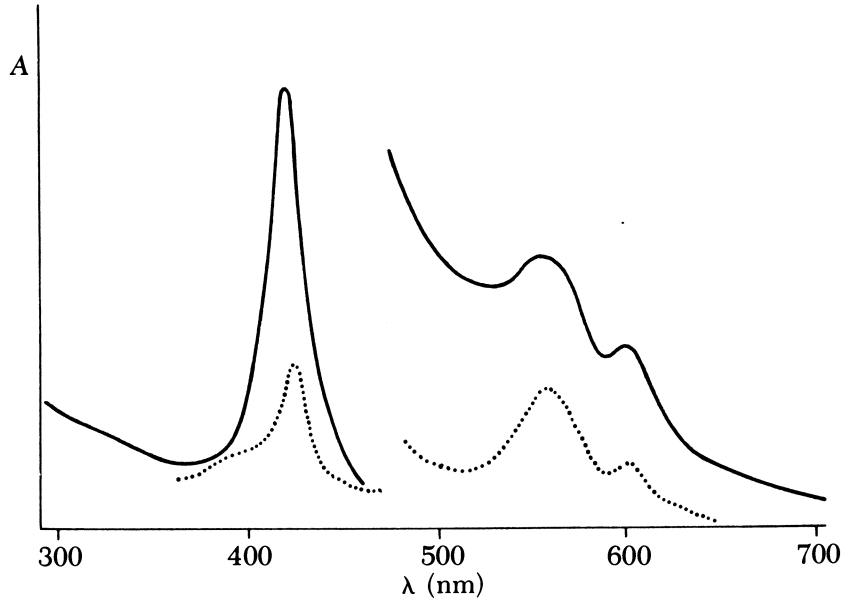

Figure 9. Optical spectra of [Fe(III)(TPP)]. Iodosylbenzene adduct (—) and [Fe(TPP)O_2]$^-$ (1) (· · · ·).

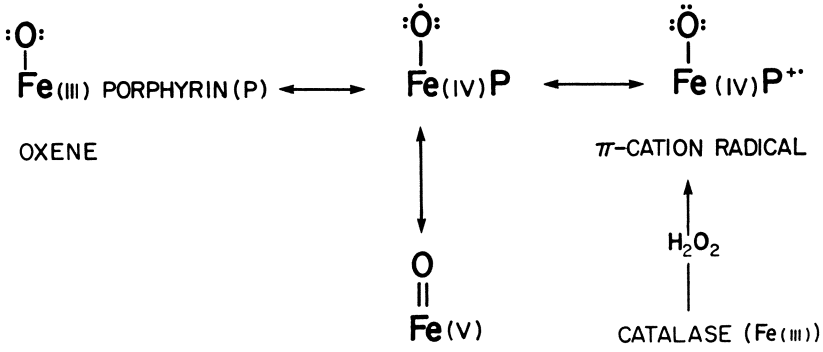

Scheme 10.

Furthermore, additional resonance structures can be written for this system, which include, after protonation, the Fe(IV) porphyrin with a hydroxyl radical and the Fe(IV) porphyrin π-cation radical coordinated by hydroxide (Scheme 10). This step brings us full circle because the two-electron oxidation product of ferric catalase by hydrogen peroxide is indeed the Fe(IV) porphyrin π-cation radical (37). In addition, this oxidation product contains oxygen derived from hydrogen peroxide (38).

These extreme electronic configurations of the ferric oxene and the Fe(IV) π-cation radical allow for speculations on the mode of oxidation of unactivated CH bonds by P-450. By analogy with carbene or nitrene chemistry, direct insertion of oxene into a CH bond would occur with retention of stereochemistry. This result does not necessarily occur with P-450, where hydroxylation can in some cases proceed via substrate intermediates. The best example of this is hydroxylation of tetradeuteronorbornane, where the hydroxylated product retains deuterium (39) (Figure 10). Because the active site of the P-450 enzymes must be hydrophobic, the generation of ionic intermediates seems unlikely. In addition, the similarity between some P-450 catalyzed hydroxylations and those known to proceed via radical intermediates suggests that P-450 itself may function via the generation of substrate radicals (35). Such a process can be facilitated by the ability of the iron porphyrin system to stabilize radical intermediates by storing unpaired electrons either on the metal or macrocyclic ring. Initial abstraction of a hydrogen atom from the substrate (RH, Scheme 11) to generate substrate radical and the equivalent of a hydroxyl radical coordinated to ferric iron could lead to product by subsequent transfer of the hydroxyl radical to substrate radical (Scheme 11). Such a

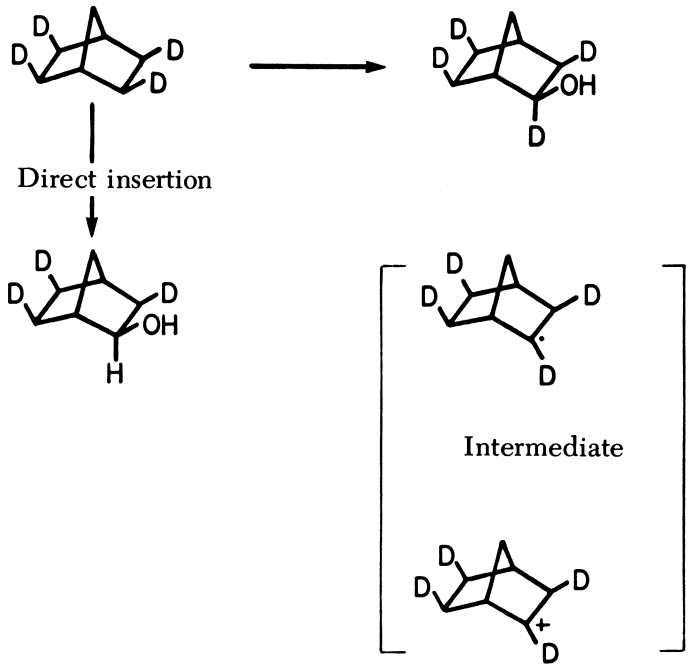

Figure 10. Hydroxylation of tetradeuteronorbornane via direct insertion or through an intermediate.

process was termed an oxygen rebound reaction (*35*), and the P-450-mediated metabolism of the insecticide dieldrin (**10**), by liver microsomes, to the ketone (**11**) can be most readily explained by the intermediacy of a substrate radical followed by reaction with a hydroxyl radical (Scheme 12).

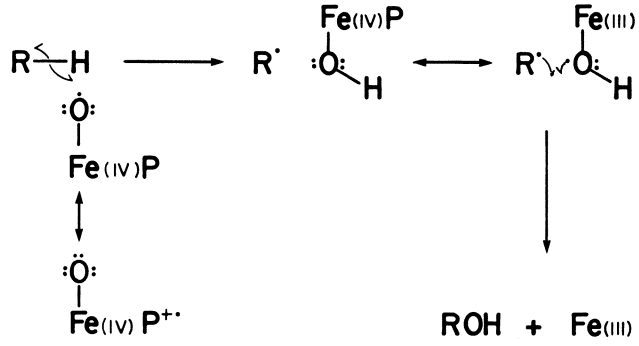

Scheme 11.

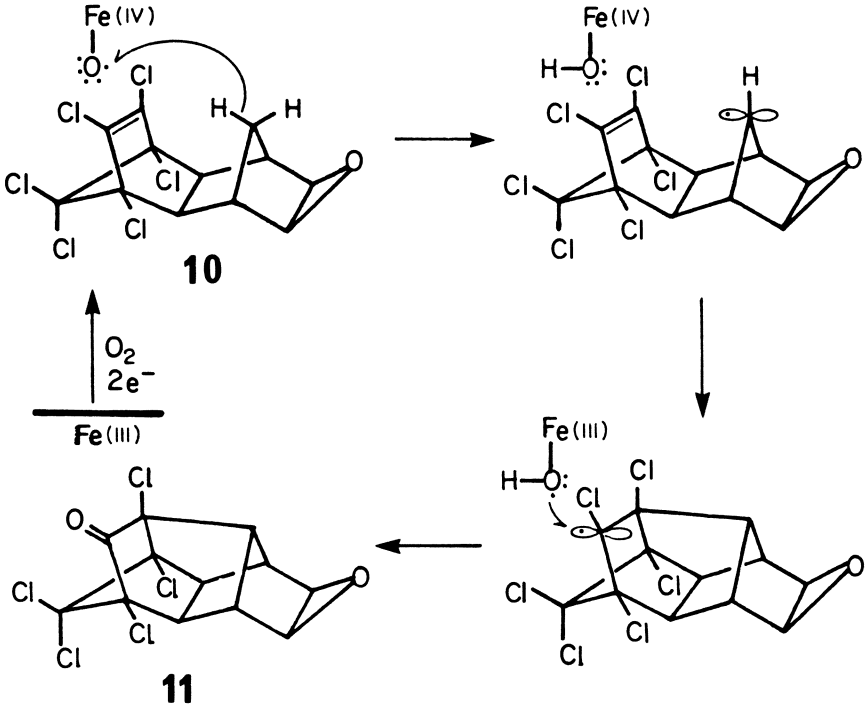

Scheme 12. Proposed mechanism for P-450-mediated metabolism of dieldrin.

Acknowledgments

This is a contribution from the Bioinorganic Chemistry Group, which was supported by grants from the Canadian Natural Sciences and Engineering Research Council and the United States National Institutes of Health (AM 17989).

Literature Cited

1. Wilson, D. F.; Ericinska, M. In "The Porphyrins"; Dolphin, D., Ed.; Academic: New York, 1979; Vol. 7, p. 1.
2. Malström, B. G. In "Metal Ion Activation of Dioxygen"; Spiro, T. G., Ed.; Wiley: New York, 1980; p. 181.
3. Hewson, W. D.; Hager, L. P. In "The Porphyrins"; Dolphin, D., Ed.; Academic: New York, 1979; Vol. 7, p. 295.
4. Harrison, J. E.; Schultz, J. *J. Biol. Chem.* **1976,** *251,* 1371.
5. Babior, B. *New England J. Med.* **1978,** *298,* 721.
6. Dolphin, D.; Felton, R. *Acc. Chem. Res.* **1974,** *7,* 26.
7. Schonbaum, G. R.; Chance, B. In "The Enzymes"; Boyer, P. D., Ed.; Academic: New York, 1976; Vol. 13, p. 363.
8. Hori, A.; Takamuku, S.; Sakurai, H. *J. Org. Chem.* **1977,** *42,* 2318.
9. Griffin, B. W.; Peterson, J. A.; Estabrook, R. W. In "The Porphyrins"; Dolphin, D., Ed.; Academic: New York, 1979; Vol. 7, p. 333.
10. Chang, C. K.; Dolphin, D. In "Bioorganic Chemistry"; van Tamelen, E. E., Ed.; Academic: New York, 1978; Vol. 4, p. 37.
11. Coon, M. J.; White, R. E. In "Metal Ion Activation of Dioxygen"; Spiro, T. G., Ed.; Wiley: New York, 1980; p. 73.
12. Katagiri, M.; Ganguli, B. N.; Gunsalus, I. C. *J. Biol. Chem.* **1968,** *243,* 3543.
13. Kikuchi, G.; Yoshida, T. "Trends in Biochemical Sciences;" Elsevier: Amsterdam, 1980; p. 3.
14. Schmid, R.; McDonagh, A. F. In "The Porphyrins"; Dolphin, D., Ed.; Academic: New York, 1979; Vol. 6, p. 257.
15. Omura, T.; Sato, R. *J. Biol. Chem.* **1962,** *237,* 1375.
16. Chang, C. K.; Dolphin, D. *J. Am. Chem. Soc.* **1975,** *97,* 5948.
17. Collman, J. P.; Sorrell, T. N. *J. Am. Chem. Soc.* **1975,** *97,* 4133.
18. Hanson, L. K.; Eaton, W. A.; Sligar, S. G.; Gunsalus, I. C.; Gouterman, M.; Connell, C. R. *J. Am. Chem. Soc.* **1976,** *98,* 2672.
19. Gouterman, M. In "The Porphyrins"; Dolphin, D., Ed.; Academic: New York, 1979; Vol. 3, p. 1.
20. Antonini, E.; Brunori, M. "Hemoglobin and Myoglobin in their Reactions with Ligands;" North-Holland: Amsterdam, 1964.
21. Dolphin, D.; James, B. R.; Welborn, H. C. *Biochem. Biophys. Res. Commun.* **1979,** *88,* 415.
22. Loew, G. H.; Rohmer, M.-M. *J. Am. Chem. Soc.* **1980,** *102,* 3655.
23. Dolphin, D.; James, B. R.; Welborn, H. C. *J. Mol. Cat.* **1980,** *7,* 201.
24. Wallace, W. J.; Maswell, J. C.; Caughey, W. S. *Biochem. Biophys. Res. Commun.* **1974,** *57,* 1104.
25. Makinen, M. W. In "Biochemical and Clinical Aspects of Oxygen"; Caughey, W. S., Ed.; Academic: New York, 1974; p. 143.
26. Lexa, D.; Momenteau, M., Mispelter, J. *Biochim. Biophys. Acta* **1974,** *338,* 151.
27. Reed, C. A.; Mashiko, T.; Scheidt, W. R.; Haller, R., presented at the *1st Int. Symp. on Oxygen Activation and Selective Oxidations Catalyzed by Transition Metals,* Bendor 1979, Poster Abstract. See also Reed, C. A., Chapter 15 in this book.

28. McCandlish, E.; Miksztal, A. R.; Nappa, M.; Sprenger, A. Q.; Valentine, J. S.; Stong, J. D.; Spiro, T. G. *J. Am. Chem. Soc.* **1980,** *102,* 4268.
29. Welborn, H. C.; Dolphin, D.; James, B. R. *J. Am. Chem. Soc.* **1981,** *103,* 2869.
30. James, B. R. In "The Porphyrins"; Dolphin, D., Ed.; Academic: New York, 1978; Vol. 5, p. 205.
31. Gunsalus, I. C.; Meeks, J. R.; Lipscomb, J. D.; Debrunner, P.; Münck, E. In "Molecular Mechanisms of Oxygen Activation"; Hayaishi, O., Ed.; Academic: New York, 1974; p. 559.
32. Nordblom, G. D.; Coon, M. J. *Arch. Biochem. Biophys.* **1977,** *180,* 343.
33. Sligar, S. G.; Kennedy, K. A.; Pearson, D. C. *Proc. Natl. Acad. Sci. U.S.A.* **1980,** *77,* 1240.
34. Lichtenberger, F.; Nastainczyk, W.; Ullrich, W. *Biochem. Biophys. Res. Commun.* **1976,** *70,* 939.
35. Groves, J. T. In "Metal Ion Activation of Dioxygen"; Spiro, T. G., Ed.; Wiley: New York, 1980, p. 125.
36. Groves, J. T.; Kraper, W. J., Jr. *J. Am. Chem. Soc.* **1979,** *101,* 7613.
37. Dolphin, D. *Isr. J. Chem.* **1981,** *21,* 67.
38. Hager, L. P.; Doubek, D. L.; Silverstein, R. M.; Hargis, J. H.; Martin, J. C. *J. Am. Chem. Soc.* **1972,** *94,* 4364.
39. Groves, J. T.; McClusky, G. A.; White, R. E.; Coon, M. J. *Biochem. Biophys. Res. Commun.* **1978,** *81,* 154.

RECEIVED for review June 2, 1981. ACCEPTED October 15, 1981.

The Reaction Chemistry of Superoxide Ion in Aprotic Media

DONALD T. SAWYER, EDWARD J. NANNI, JR., and JULIAN L. ROBERTS, JR.

University of California, Department of Chemistry, Riverside, CA 92521

Superoxide ion (O_2^-) is a strong Brönsted base, an effective nucleophile, and a moderate one-electron reducing agent. In the presence of O_2^-, polychloro hydrocarbons, are rapidly degraded via a primary nucleophilic displacement of chloride ion; the relative S_N2 second-order rate constants for the chloromethanes are $CCl_4 > CHCl_3 > CH_3Cl > CH_2Cl_2$, with an approximate value of 1300 $M^{-1}s^{-1}$ for CCl_4 in DMF at 25°C. Combination of O_2^- with basic substrates such as hydrophenazines, reduced flavins, and hydroxylamine yields substrate oxidation products via direct transfer of one, two, or three hydrogen atoms to O_2^- from the reduced substrate. Superoxide ion reacts with the cation radical of methyl viologen (MV^+) via a primary radical–radical coupling process to yield a diamagnetic adduct. The latter decomposes, apparently via a peroxide intermediate, to products that may represent the biological toxins of methyl viologen. A similar radical coupling reaction occurs between a neutral flavin radical and O_2^- to yield a flavoperoxide anion. The latter is an effective reaction mimic for flavooxygenases. When O_2^- and reduced transition metal ions are combined, an overall redox process occurs via either direct electron transfer or a series of disproportionation steps. The kinetics and mechanisms of these processes have been studied in relation to those for the superoxide dismutases.

The electron transfer reduction of dioxygen yields superoxide ion (O_2^-) as a primary product in biological (*1*) as well as chemical systems (*2*). This redox process has been characterized by electrochemical studies in aprotic solvents such as dimethylformamide

0065-2393/82/0201-0585$06.00

(DMF) (3) and by pulse radiolysis studies in water (4) (for unit molality as the standard state for O_2 and $O_2^{\cdot-}$)

$$O_2 + e^- \rightleftarrows O_2^{\cdot-} \qquad \left.\begin{array}{l} E^{\circ\prime}_{DMF} = -0.60 \text{ V vs. NHE} \\ E^{\circ\prime}_{H_2O} = -0.17 \text{ V} \end{array}\right\} \quad (1)$$

Figure 1 is a summary of the reduction potentials for dioxygen and its reduction products in aqueous media for acidic, neutral, and basic conditions. These data represent a best estimate from the consideration of pulse radiolysis, electrochemical, spectrophotometric, and calorimetric measurements (4–9), and are based on pK_a values of 4.69 for $HO_2\cdot$ (4) and 11.9 for H_2O_2 (8).

The limited lifetime of superoxide ion in aqueous solutions, because of rapid hydrolysis and disproportionation [(4) and Figure 1],

$$H^+ + O_2^{\cdot-} \rightleftarrows HO_2\cdot \qquad pK_a = 4.69 \quad (2)$$

$$O_2^{\cdot-} + HO_2\cdot \rightarrow O_2 + HO_2^- \qquad k_3 = 1.0 \times 10^8\ M^{-1}s^{-1} \quad (3)$$

$$HO_2\cdot + HO_2\cdot \rightarrow O_2 + H_2O_2 \qquad k_4 = 8.6 \times 10^5\ M^{-1}s^{-1} \quad (4)$$

$$2O_2^- + 2H^+ \rightleftarrows H_2O_2 + O_2 \qquad K_{pH\ 7} = 4 \times 10^{20} \quad (5)$$

prompted numerous investigations of its reaction chemistry in aprotic solvents. In such solvents (and in the absence of protic substrates and trace levels of metal ions) superoxide ion is stable, with a half-life of more than 8 h at millimolar concentrations.

The difference in the reduction potentials for dioxygen in neutral [−0.60 V vs. the normal hydrogen electrode (NHE)] and acidified (+0.12 V vs. NHE) DMF provides an approximate measure of the acidity of $HO_2\cdot$ in aprotic media ($pK_a \approx 13$). Hence, superoxide ion is a stronger base in DMF than in aqueous media because of the much weaker solvation of anions by aprotic solvents. For the same reason, the proton-driven disproportionation of superoxide ion (Equation 5) is even more complete in aprotic solvents and causes superoxide ion to have uniquely strong Brönsted basicity [e.g., 1-butanol ($pK_a = 33$) is deprotonated by superoxide ion in DMF] (10).

This chapter summarizes the primary reaction chemistry of superoxide ion in aprotic solvents. The reactivity of superoxide ion in aqueous media is expected to be similar, but moderated by the leveling effects of water and the competitive proton-induced disproportionation reactions. The latter process yields substrate anions, dioxygen, and hydrogen peroxide. This process, plus similar reactions of acidic substrates in aprotic solvents, leads to oxidations by oxygen and hydrogen peroxide of substrate anions that were erroneously attributed to direct electron transfer to superoxide ion (3).

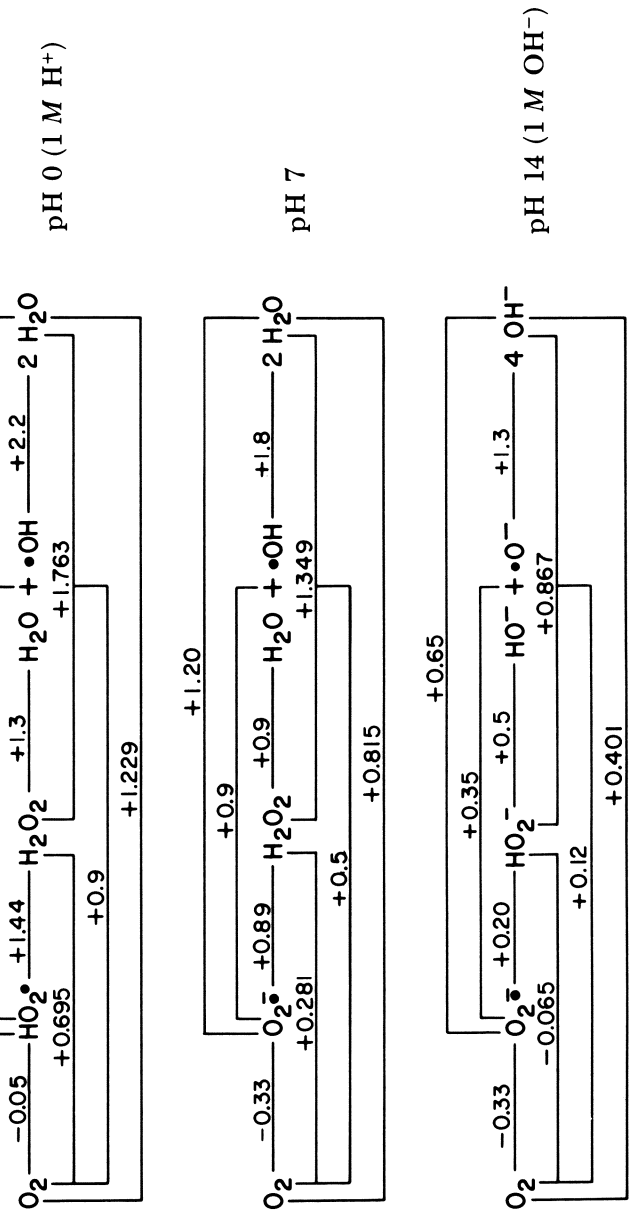

Figure 1. Potentials for oxygen redox couples in aqueous media at 25°C; values represent standard reduction potentials vs. the NHE. The standard state for O_2 is 1 atm.; a standard state of unit molality shifts the one-electron process by +0.17 V; the two-electron process by +0.085 V; the three-electron process by +0.06 V; and the four-electron process by +0.04 V.

Oxidation–Reduction Reactions

One-Electron Reductant. The redox potential for the O_2/O_2^- couple in dimethylformamide (Equation 1) is sufficiently negative to make superoxide a moderate reducing agent. For example, dissolved sulfur dioxide is reduced by superoxide ion (*11*).

$$O_2^- + SO_2 \rightleftarrows O_2 + SO_2^- \qquad K_6 = 5 \tag{6}$$

The process, which is driven to the right by the dimerization of SO_2^- to dithionite ($K_{dimer} = 5 \times 10^3$), indicates that superoxide ion is a more effective one-electron reducing agent than dithionite in DMF.

Other examples of reductions by superoxide ion include 3,5-di-*t*-butyl-*o*-quinone (DTBQ) in DMF

$$O_2^- + DTBQ \rightleftarrows DTBQ^- + O_2 \qquad K_7 = 0.8 \times 10^6 \tag{7}$$

and numerous transition metal complexes in aprotic solvents; Cu(II)(9,10-phenanthroline) (*12*), Cu(II)salicylate (*13*), Mn(III)(TPP)Cl (TPP is tetraphenylporphinato) (*14*), and Fe(III)(TPP)Cl (*15*). In aqueous media, superoxide ion (generated by pulse radiolysis) reduces Fe(III)(EDTA) (*16*) and ferricytochrome *c* (*17*).

$$\text{cyt c}(Fe^{3+}) + O_2^- \rightleftarrows \text{cyt c}(Fe^{2+}) + O_2 \qquad K_8 = 4 \times 10^4 \tag{8}$$

Recent studies (*18*) confirm that substantial amounts of singlet oxygen ($^1O_2$) result from the oxidation of superoxide ion by coordinately saturated transition metal oxidants (with $E^{0\prime}$-values greater than +0.34 V) in DMF. Measurements of singlet oxygen by photon counting indicate a significant yield when ferricenium perchlorate is the oxidant, but a negligible amount from superoxide ion oxidation by $Fe(III)(ClO_4)_3$. This result can be rationalized on the basis that the coordinately saturated ferricenium ion forms a singlet transition-state complex with superoxide ion, $[(Cp)_2Fe:O_2:]_{tr}$. Other oxidants that convert superoxide ion to singlet oxygen include $Mn(III)(O_3terpy)_2^{3+}$ (O_3terpy is 2,2′,2″-terpyridine 1,1′,1″-trioxide) and $[Mn(IV)(o\text{-phen})_2O]_2^{4+}$ (*o*-phen is 1,10-phenanthroline).

Oxidant via Hydrogen-Atom Transfer. The results of a recent investigation (*19*) demonstrate that superoxide is an effective oxidant of basic reducing substrates with readily transferable hydrogen atoms. When superoxide ion is combined (1:1 mol ratio) with either dihydrophenazine or *N*-methylhydrophenazine (both models for reduced flavins) in dimethylformamide, a stoichiometric yield of phenazine or *N*-methylphenazine radical, respectively, results from a two-hydrogen atom or a one-hydrogen atom transfer

$$\text{phenH}_2 + O_2^{\cdot-} + \text{Hsol} \xrightarrow{\text{Hsol}} \text{phen} + \frac{1}{n}(\cdot\text{sol})_n + H_2O + OH^- \quad (9)$$

$$CH_3N\ \text{phenH} + O_2^{\cdot-} \rightarrow CH_3N\ \text{phen}\cdot + HO_2^- \quad (10)$$

Similar reactions are observed for reduced flavins, hydroxylamine, and hydrazine. The stoichiometry of the reactions is controlled by the number of reducing hydrogen atoms per substrate molecule. Conversion of such hydrogen atoms to protons provides stabilization of the reduction products of superoxide ion (O_2^{2-}, $\cdot O^-$, and O^{2-}).

Most of the reported oxidations of protic substrates by superoxide actually represent an initial proton abstraction to give substrate anion and disproportionation species, HO_2^- and O_2 (3). The latter oxidize the substrate anion for catechols and α-tocopherol. Although the same process was suggested for the oxidation of ascorbic acid (3), the total absence of any intermediate O_2 (from the proton-induced disproportionation of $O_2^{\cdot-}$) and a 1:1 initial reaction stoichiometry for the $O_2^{\cdot-}$–acorbic acid reaction to give primarily ascorbate radical anion require an alternative mechanism. These factors and the rapid bimolecular kinetics (k_2, $2.8 \times 10^4\ M^{-1}s^{-1}$) indicate that a concerted hydrogen-atom transfer and proton transfer to superoxide ion from ascorbic acid occurs (*10*)

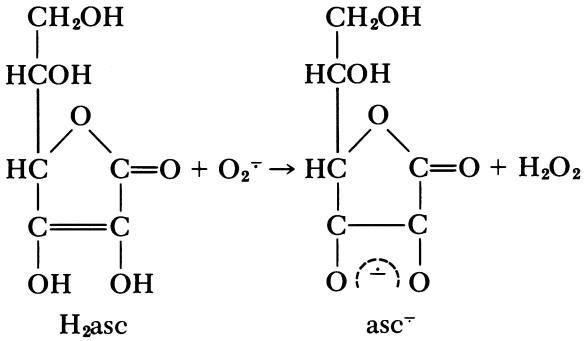

(11)

followed by a proton-induced disproportionation of the ascorbate radical anion ($asc^{\cdot-}$) to dehydroascorbic acid (dehyd) and ascorbate anion ($Hasc^-$)

$$H_2asc + 2\ asc^{\cdot-} \rightarrow dehyd + 2\ Hasc^- \quad (12)$$

Both H_2asc and $asc^{\cdot-}$ appear to be unreactive with hydrogen peroxide in DMF and there is no evidence for a concerted two-hydrogen atom transfer from H_2asc to superoxide ion. The facile oxidation of ascorbate ion in aqueous media at pH 9.9 by superoxide ion [generated by pulse radiolysis (*20*)] probably occurs via a similar hydrogen-atom transfer

mechanism, as suggested previously (*21*). Hence, ascorbic acid appears to be unique among acidic substrates in its ability to reduce superoxide ion directly to hydrogen peroxide without significant concomitant proton-induced disproportionation.

Radical–Radical Coupling

Combination of superoxide ion with the cation radical (MV^+) of methyl viologen (1,1′-dimethyl-4,4′-bipyridinium ion, paraquat) in DMF and DMSO results in a primary radical–radical coupling reaction to yield a diamagnetic product (Figure 2). This conclusion is based on electrochemical, spectroscopic, NMR, electron paramagnetic resonance (EPR), thin-layer chromatography (TLC), high performance liquid chromatography (HPLC), and mass spectrometric measurements (22). Characterization of reaction intermediates and products provides the basis for proposing a self-consistent mechanistic scheme. This is the first definitive example of a radical reaction for superoxide ion.

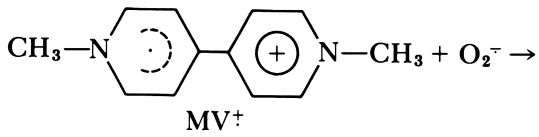

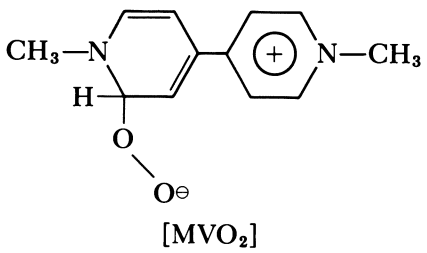

(13)

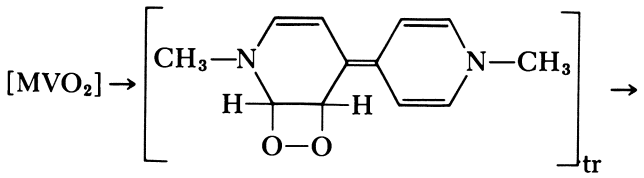

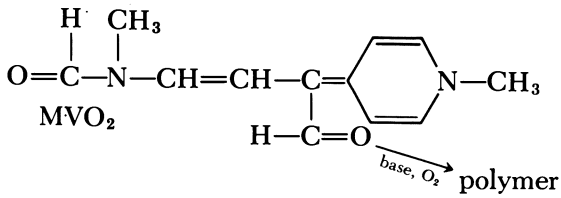

(14)

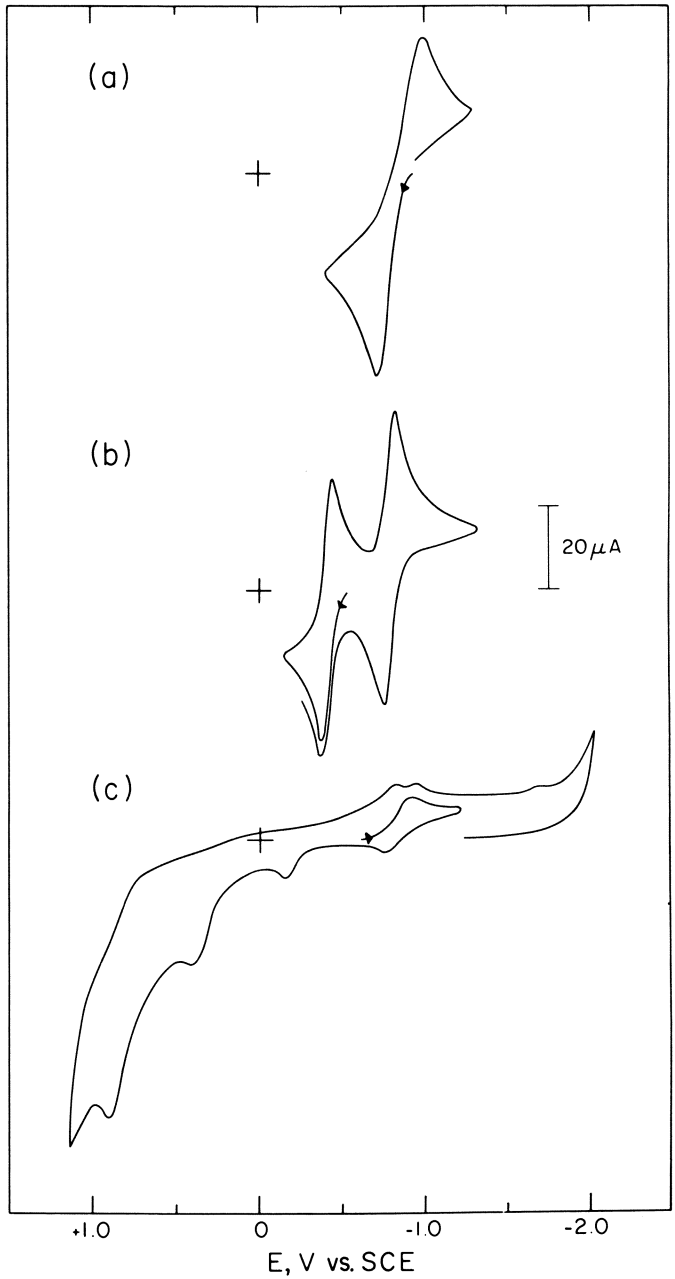

Figure 2. Cyclic voltammograms in DMF (0.1 M tetraethylammonium perchlorate) of a, 1 mM O_2^-; b, 1 mM methyl viologen cation radical (MV^+); and c, 0.5 mM O_2^- plus 0.5 mM MV^+ within 5 min after mixing. Controlled-potential coulometry was used to prepare O_2^- from O_2 and MV^+ from $MVCl_2$. Measurements were made with a Pt electrode (area, 0.23 cm²) at a scan rate of 0.1 V/s (22).

Resonance stabilization apparently precludes significant radical coupling at the C-4 position. Such a process would lead to a symmetrical dioxetane intermediate and dissociation to two 4-*N*-methylpyridone molecules; only trace levels are detected in the product solution.

In the presence of DMSO or other substrates subject to oxygenation by peroxides, [MVO_2] undergoes such reactions before it can form the dioxetane intermediate and products of Equation 14.

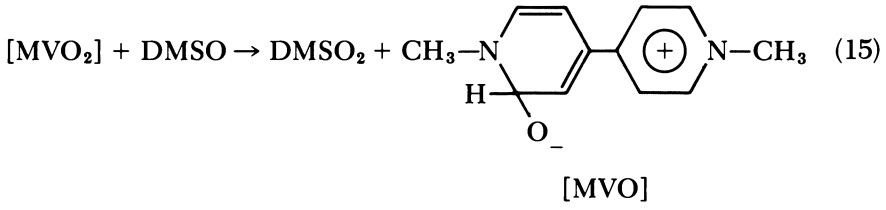

The [MVO] species can rearrange to a lactam, hydrolyze via an epoxide to a glycol, and react with dioxygen to give a pyridone (MVO^+)

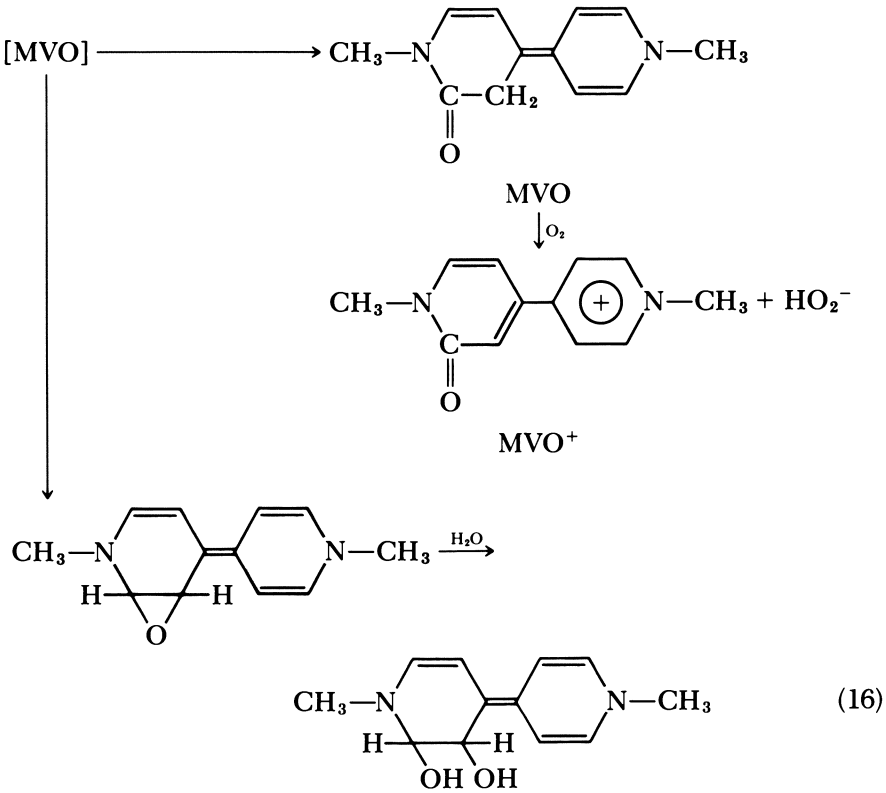

The glycol probably is subject to oxygenation by either [MVO_2] or oxygen to give an α-keto-lactam and other oxygenation products. An apparent monooxygenation by the [MVO_2] peroxide of the MVO lactam (Equation 16) appears to form trace quantities of the dilactam,

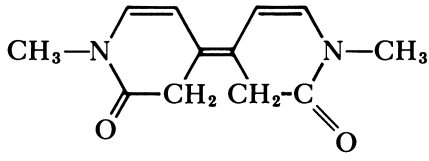

For those situations where excess reduced methyl viologen is combined with limiting amounts of oxygen, the initial formation of superoxide ion

$$MV^{+} + O_2 \rightarrow O_2^{-} + MV^{2+} \qquad (17)$$

should be followed by formation of [MVO_2] (Equation 13). The latter compound represents a significantly greater biological hazard than free superoxide ion. Furthermore, the formation of [MVO_2] means that methyl viologen specifically is involved in toxic reactions rather than acting solely as a reducing agent for the production of superoxide ion (Equation 17).

A similar reactive peroxide ion, N^5-ethyl-4a-peroxy-3-methyllumiflavin (4a-FlEtOO$^-$), results from the combination of superoxide ion and N^5-ethyl-3-methyllumiflavin radical (FlEt·) in aprotic media (*see* Figure 3) (*23*)

$$FlEt^{\cdot} + O_2^{-} \rightarrow FlEtOO^{-} \qquad (18)$$

This reaction represents a second example of superoxide ion acting as a coupling reagent with stable radicals. The neutral radical (FlEt·) can be produced from the one-to-one combination of $FlEt^+$ and O_2^-, or by electrochemical reduction of $FlEt^+$. The 4a-FlEtOO$^-$ species, an effective reaction mimic for flavomonooxygenases (*24*), readily oxygenates dimethyl sulfoxide (DMSO) and other substrates subject to oxygen-atom addition from peroxide ions. The resulting pseudo base, 4a-FlEtO$^-$, reverts to $FlEt^+$ and H_2O upon addition of protons, or is oxidized by any residual oxygen.

In spite of vigorous and persistent research effort (*3*, *25–27*), superoxide ion has not been found to act as an initiator of radical chain reactions. Radical–radical coupling only is observed for those forcing conditions (MV^+ or FlEt· plus superoxide ion) where alternative reactins of superoxide ion are not favored.

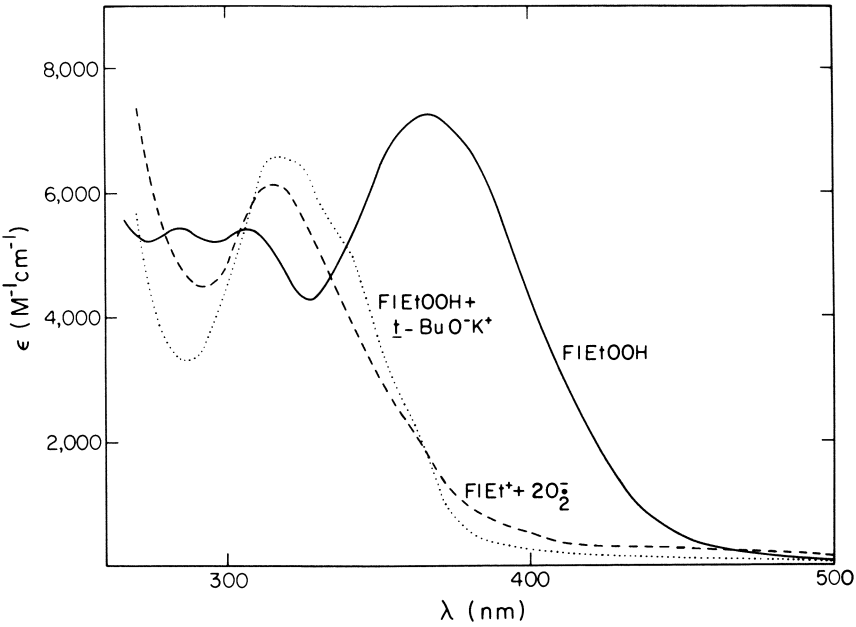

Figure 3. Absorption spectra in DMF (0.1 M tetraethylammonium perchlorate) of a, 0.5 mM N⁵-ethyl-4a-hydroperoxy-3-methyllumiflavin (FlEtOOH); b, 0.52 mM FlEtOOH plus 0.52 mM t-BuO⁻K⁺; and c, 0.49 mM FlEt⁺ plus 1.15 mM O_2^- (23).

Nucleophilicity and Monooxygenase Reactivity by Peroxide Intermediates

Alkyl Halides. Under aprotic conditions, superoxide ion attacks alkyl halides via nucleophilic substitution (*28*). Kinetic studies (*29–32*) confirm that the reaction is first order in substrate and first order in superoxide ion, that the rates follow the order 1° > 2° ≫ 3° and I > Br > Cl, and that the attack by superoxide ion results in inversion of configuration. In aprotic solvents, primary and secondary alkyl halides yield dialkyl peroxides when combined with excess superoxide ion (*31–33*), which is consistent with a multistep mechanism

$$RX + O_2^- \rightarrow RO_2^{\cdot} + X^- \quad (19)$$

$$RO_2^{\cdot} + O_2^- \rightarrow RO_2^- + O_2 \quad (20)$$

$$RO_2^- + RX \rightarrow ROOR + X^- \quad (21)$$

The primary step occurs via an S_N2 displacenent of halide from the carbon. The resulting peroxy radical is reduced by a second super-

oxide ion to give the alkyl peroxide ion, which acts as a nucleophile for attack of a second substrate molecule.

In DMSO (or in the presence of other reactive substrates) Reaction 20 is followed by attack of the solvent by RO_2^- to give dimethylsulfone and alcohols (*30, 34, 35*)

$$RO_2^- + DMSO \rightarrow DMSO_2 + RO^- \quad (22)$$

A recent investigation (*36*) has demonstrated that polychloro hydrocarbons (CCl_4, $CHCl_3$, CH_2Cl_2, and *p,p'*-DDT) are rapidly degraded by superoxide ion in aprotic media (DMF and DMSO). The primary step appears to be a nucleophilic or concerted reductive displacement of chloride ion. Kinetic studies confirm that the initial step is rate limiting and first order with respect to superoxide ion and substrate. The overall reactant and product stoichiometries for the degradation of the polychloromethanes and *p,p'*-DDT in DMF are summarized in Table I. In addition, the second-order rate constants for the primary process are tabulated; the value of 1300 $M^{-1}s^{-1}$ for CCl_4 is the fastest displacement yet observed for superoxide.

Combination of CCl_4 with six equivalents of oxygen in DMSO yields a product solution that, after dilution with water, can be titrated with aqueous HCl. The resulting titration curve is consistent with that for an authentic sample of carbonate ion in the same medium. Because peroxides oxygenate DMSO to its sulfone (*37*), a reasonable conclusion

Table I. Stoichiometries and Kinetics for the Reaction of O_2^- with Polychloromethanes and *p,p'*-DDT in DMF (0.1 *M* Tetraethylammonium Perchlorate) at 25°C

*Substrate (S), 0.1–5 m*M	O_2^- *per S*	Cl^- *released per S*	k_2, $M^{-1}s^{-1}$
CH_3Cl	1	1	80
CH_2Cl_2	2	2	9
$CHCl_3$	4	3	460
CCl_4	6	4	1300
p,p'-DDT	3	2	130

Overall Reactions:

(a) $CH_3Cl + O_2^- \rightarrow \frac{1}{2}CH_3OOCH_3 + Cl^- + \frac{1}{2}O_2$
(b) $CH_2Cl_2 + 2O_2^- \rightarrow CH_2O + 2Cl^- + \frac{3}{2}O_2$
(c) $CHCl_3 + 4O_2^- \rightarrow HC(O)OO^- + 3Cl^- + \frac{5}{2}O_2$
(d) $CCl_4 + 6O_2^- \rightarrow CO_4^{2-} \rightarrow 4Cl^- + 4O_2$
(e) *p,p'*-DDT + $3O_2^-$ → products + $2Cl^- + \frac{3}{2}O_2$

is that the overall product from the reaction of CCl_4 with excess superoxide ion is CO_4^{2-} and that it reacts with this solvent to yield CO_3^{2-}.

When $CHCl_3$ is combined with four equivalents of superoxide ion in DMF, a basic product solution is obtained that has the characteristics of peroxyformate ion (the acidified product solution oxidizes I^- to I_2).

On the basis of these experiments and the reaction stoichiometries, overall reactions are proposed for the degradation of the polychloro substrates (*see* Table I). A self-consistent set of reactions for the superoxide–carbon tetrachloride system illustrates the general mechanistic processes for this class of substrates.

$$CCl_4 + O_2^- \rightarrow [CCl_4(O_2^-)]_{tr} \rightarrow CCl_3O_2^{\cdot} + Cl^- \quad (23)$$

$$CCl_3O_2^{\cdot} + O_2^- \rightarrow CCl_3O_2^- + O_2 \quad (24)$$

$$CCl_3O_2^- + CCl_4 \rightarrow CCl_3OOCCl_3 + Cl^- \quad (25)$$

$$CCl_3OOCCl_3 + 2\ O_2^- \rightarrow 2\ O_2 + 2\ CCl_3O^- \rightarrow 2\ CCl_2O + 2\ Cl^- \quad (26)$$

$$CCl_2O + O_2^- \rightarrow CCl(O)O_2^{\cdot} + Cl^- \quad (27)$$
$$\text{(with } O_2^- \rightarrow CCl(O)O_2^- + O_2\text{)}$$

$$CCl(O)O_2^- + CCl_2O \rightarrow CCl(O)OOCCl(O) + Cl^- \quad (28)$$

$$CCl(O)OOCCl(O) + 2\ O_2^- \rightarrow 2\ CCl(O)O^- + 2\ O_2 \rightarrow 2\ CO_2 + 2\ Cl^- \quad (29)$$

$$CO_2 + 2\ O_2^- \rightarrow CO_4^{2-} + O_2 \quad (30)$$

The peroxide intermediates of Reactions 24, 27, and 30 can participate in monooxygenase reactions in the presence of substrates such as DMSO.

Esters. Another dimension of the nucleophilicity of superoxide ion is its ability to attack the carbonyl carbon of esters to yield carboxylic acid anions and alcohols (*38–40*), and to attack the carbonyl carbon of acyl halides to yield diacyl peroxides (*41*). The ester hydrolysis occurs via acyl oxygen scission on the basis of complete retention of configuration in the alcohol moiety from an optically active ester (*38*).

For the reaction of superoxide ion with ethyl acetate and phenyl acetate in pyridine, the second-order rate constants are 0.011 $M^{-1}s^{-1}$ and 160 $M^{-1}s^{-1}$, respectively (*40*). This ratio of rate constants (10^4) is consistent with other data for the reactions of phenyl and ethyl esters with effective nucleophiles (*42, 43*), and with an S_N2 mechanism. The

primary reaction appears to be a nucleophilic addition that is followed by elimination at the carbonyl carbon (*40*)

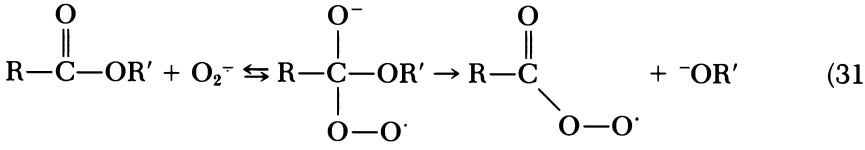

(31)

with subsequent steps to give an overall ester hydrolysis reaction.

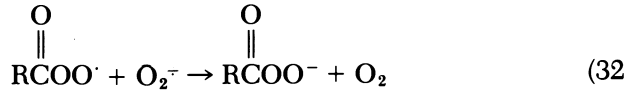

(32)

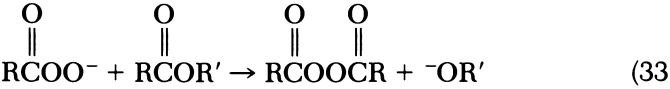

(33)

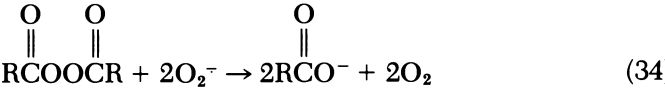

(34)

Addition of superoxide ion to α-keto-, α-hydroxy-, and α-halocarbonyl compounds results in a nucleophilic adduct of the carbonyl carbon, which undergoes an oxidative cleavage to give the carboxylic acid that is derived from the α-position (*44*). Again, the peroxy acid anion intermediates (Equation 32) represent effective monooxygenases for substrates such as DMSO.

A general characteristic of the nucleophilic attack of alkyl halides and esters by superoxide ion is that a peroxy radical is the initial product. This peroxy radical is rapidly reduced by a second superoxide ion to a peroxide anion, which can oxygenate susceptible substrates. Hence, the nucleophilicity of superoxide ion provides a means to activate the reduction product of dioxygen to organoperoxy radicals and organoperoxide ions. This ability may represent a significant hazard in biochemical systems.

Metal-Catalyzed Disproportionation

Metal cations can act as Lewis acids and through charge neutralization can bring about the disproportionation of superoxide ion to dioxygen and a metal peroxide (*45*). Combination of superoxide ion with $Zn(ClO_4)_2$, $Cd(ClO_4)_2$, and $Fe(ClO_4)_2$ results in such a process. For $Mn(ClO_4)_2$ and $Co(ClO_4)$ the resultant metal peroxides are unstable and undergo further disproportionation. A plausible mechanism is out-

lined for manganese(II) to illustrate the rich variety of reactive intermediates

$$Mn^{2+} + O_2^{-} \rightarrow Mn(II)(O_2^{-})^{+} \quad (35)$$

$$Mn(II)(O_2^{-})^{+} + O_2^{-} \rightarrow [\cdot O_2 : Mn(II) : O_2 \cdot] \rightarrow O_2 + Mn(II)(O_2^{2-}) \quad (36)$$

$$Mn(II)(O_2^{2-}) + Mn(II)(O_2^{2-}) \rightarrow 2\ Mn(II)O + O_2 \quad (37)$$

$$Mn(II) + O_2 \rightarrow Mn(III)(O_2^{-})^{2+} \quad (38)$$

$$Mn(III)(O_2^{-})^{2+} + Mn(II) \rightarrow [Mn(III)-O-O-Mn(III)]^{4+} \quad (39)$$

$$[Mn(III)-O-O-Mn(III)]^{4+} + Mn(II) \rightarrow [Mn(III)-O-Mn(III)]^{4+} + [Mn(III)O\cdot]^{2+} \quad (40)$$

$$[Mn(III)O\cdot]^{2+} + Mn(II) \rightarrow [Mn(III)-O-Mn(III)]^{4+} \quad (41)$$

Clearly, many of these intermediates can oxidize and oxygenate various organic functional groups. The chemistry of Equations 35–41 represents a likely mechanism for transition-metal activation of dioxygen, especially with respect to rancidification of fats and oils.

As mentioned, superoxide ion is an effective one-electron reductant for transition-metal ions. Under limited conditions, superoxide ion also can act as an oxidant of reduced transition-metal ions. The process must be augmented through the formation of a stable metal–peroxide intermediate. Examples include Fe(II)ethylenediaminetetraacetic acid (EDTA) in aqueous media (*46*) and iron(II) tetraphenylporphyrin in aprotic media (*15*). Such reactions are an essential part of the favored mechanisms for the superoxide dismutase (SOD) enzymes (*47*). The Fe(III)EDTA system (*48*) represents an effective model for SOD in aqueous media; the proposed mechanism is

$$Fe(III)EDTA + O_2^{-} \rightarrow Fe(II)EDTA + O_2 \quad (42)$$

$$Fe(II)EDTA + O_2^{-} \xrightarrow{H^{+}} Fe(III)EDTA + H_2O_2 \quad (43)$$

The bis(8-quinolinato)manganese(II) complex $[Mn(II)(8\text{-}Q)_2(H_2O)_2]$ also is an effective catalyst for the disproportionation of superoxide ion in aprotic media (*49*), and has been suggested as an effective model for the manganese SOD enzymes (*50*). A reasonable mechanism for the $Mn(II)(8\text{-}Q)(H_2O)_2$ catalyzed disproportionation of superoxide ion involves a Mn(III)–peroxide intermediate, which should be an effective oxidant for superoxide ion.

$$Mn(II)(8\text{-}Q)_2(H_2O)_2 + O_2^{-} \rightarrow Mn(III)(8\text{-}Q)_2(O_2H)(H_2O) + OH^{-} \quad (44)$$

$$Mn(III)(8\text{-}Q)_2(O_2H)(H_2O) + O_2^{-} \xrightarrow{H_2O} Mn(II)(8\text{-}Q)_2(H_2O)_2 + O_2 + HO_2^{-} \quad (45)$$

This mechanism is a realistic model for the manganese–SOD, iron–SOD, and copper–zinc–SOD enzymes.

Summary

Superoxide is a versatile reactant, but its most dominant characteristic is as an effective Brönsted base. It readily removes protons from water and weakly acidic substrates such as 1-butanol, and in so doing it disproportionates to yield peroxide and dioxygen. Under aprotic conditions, its strong basicity causes superoxide ion to act as a powerful nucleophile (probably second only to fluoride ion). Superoxide ion also is a moderate, but facile, one-electron reductant (about as effective as dithionite). Strong one-electron oxidants with closed coordination spheres (e.g., ferricenium ion) oxidize superoxide ion to singlet oxygen. Reduced transition-metal ions are oxidized by superoxide ion when their oxidized state forms stable peroxide adducts. Basic reductants such as dihydrophenazine, dihydroflavins, hydroxylamine, and hydrazine are oxidized by a hydrogen-atom transfer mechanism. The only example of any radical character for superoxide ion is the formation of a diamagnetic adduct with reduced methyl viologen cation radical via a radical–radical coupling mechanism.

Acknowledgment

This work was supported by the National Science Foundation under Grant No. CHE79–22040.

Literature Cited

1. McCord, J. M.; Fridovich, I. *J. Biol. Chem.* **1969,** *244,* 604.
2. Wilshire, J. P.; Sawyer, D. T. *Acc. Chem. Res.* **1979,** *12,* 105.
3. Nanni, E. J., Jr.; Stallings, M. D.; Sawyer, D. T. *J. Am. Chem. Soc.* **1980,** *102,* 4481.
4. Bielski, B. H. J. *Photochem. Photobiol.* **1978,** *28,* 645.
5. Fee, J. A.; Valentine, J. S. In "Superoxide and Superoxide Dismutase"; Michelsen, A. M.; McCord, J. M.; Fridovich, I., Eds.; Academic: New York, 1977; pp. 19–20.
6. Latimer, W. M. "Oxidation Potentials," 2nd ed.; Prentice–Hall: New York, 1952.
7. George, P. In "Oxidases and Related Redox Systems"; King, T. E.; Mason, M. E.; Morrison, M., Eds.; Wiley: New York, 1965; pp. 3–36.
8. Hoare, J. P. In "Oxidation-Reduction Potentials of Aqueous Solutions: A Selective and Critical Source Book"; Bard, A. J.; Parsons, R.; Jordan, Jr., Eds.; Int. Union Pure Appl. Chem., 1981; Chap. 4, in press.
9. Koppenol, W. H. *Nature* **1976,** *262,* 420.
10. Chin, D.-H.; Chiericato, G., Jr.; Nanni, E. J., Jr.; Sawyer, D. T., *J. Am. Chem. Soc.* **1982,** *104,* 1296.
11. Stallings, M. D.; Sawyer, D. T. *J. Chem. Soc., Chem. Comm.* **1979,** 340.
12. Valentine, J. S.; Curtis, A. B. *J. Am. Chem. Soc.* **1975,** *97,* 224.
13. O'Young, C.-L.; Lippard, S. J. *J. Am. Chem. Soc.* **1980,** *102,* 4920.
14. Valentine, J. S.; Quinn, A. E. *Inorg. Chem.* **1976,** *15,* 1997.
15. McCandlish, E.; Miksztal, A. R.; Nappa, M.; Spenger, A. Q.; Valentine, J. S.; Strong, J. D.; Spiro, T. G. *J. Am. Chem. Soc.* **1980,** *102,* 4268.

16. Ilan, Y. A.; Czapski, G. *Biochim. Biophys. Acta* **1977,** *498,* 386.
17. Rao, R. S.; Hazon, E. *J. Phys. Chem.* **1975,** *79,* 397.
18. Nanni, E. J., Jr.; Birge, R. R.; Hubbard, L. M.; Morrison, M. M.; Sawyer, D. T. *Inorg. Chem.* **1981,** *20,* 737.
19. Nanni, E. J., Jr.; Sawyer, D. T. *J. Am. Chem. Soc.* **1980,** *102,* 7591.
20. Bielski, B. H. J.; Richter, H. W. *J. Am. Chem. Soc.* **1977,** *99,* 3019.
21. Afanasev, I. B.; Polozova, H. E. *Zh. Org. Khim.* **1978,** *14,* 1013.
22. Sawyer, D. T.; Nanni, E. J., Jr.; Angelis, C. T.; Dickson, J. *J. Am. Chem. Soc.* **1981,** *103,* 4268.
23. Nanni, E. J., Jr.; Sawyer, D. T.; Ball, S. S.; Bruice, T. C. *J. Am. Chem. Soc.* **1981,** *103,* 2797.
24. Ball, S. S.; Bruice, T. C. *J. Am. Chem. Soc.* **1980,** *102,* 6498.
25. Czapski, G. *Annu. Rev. Phys. Chem.* **1971,** *22,* 171.
26. Ilan, Y. A.; Meisel, D.; Czapski, G. *Isr. J. Chem.* **1974,** *12,* 891.
27. Behar, D.; Czapski, G.; Rabini, J.; Dorfman, L. M.; Schwartz, H. A. *J. Phys. Chem.* **1970,** *74,* 3209.
28. Sawyer, D. T.; Gibian, M. J. *Tetrahedron* **1979,** *35,* 1471.
29. Magno, F.; Seeber, R.; Valcher, S. *J. Electroanal. Chem.* **1977,** *83,* 131.
30. San Fillipo, J., Jr.; Chern, C.-I.; Valentine, J. S. *J. Org. Chem.* **1975,** *40,* 1678.
31. Johnson, R. A.; Nidy, E. G. *J. Org. Chem.* **1975,** *40,* 1680.
32. Gibian, M. J.; Tangpoonpholvivat, R.; Ungermann, T.; Morrison, M. M.; Sawyer, D. T., unpublished data.
33. Dietz, K.; Forno, A. E. J.; Carcombe, B. E.; Peover, M. E. *J. Chem. Soc. B* **1970,** 816.
34. Merritt, M. V.; Sawyer, D. T. *J. Org. Chem.* **1970,** *35,* 2157.
35. Gibian, M. J.; Ungermann, T. *J. Org. Chem.* **1976,** *41,* 2500.
36. Roberts, J. L., Jr.; Sawyer, D. T. *J. Am. Chem. Soc.* **1981,** *103,* 712.
37. Goolsby, A. D.; Sawyer, D. T. *Anal. Chem.* **1968,** *40,* 83.
38. San Fillipo, J., Jr.; Romano, L. J.; Chern, C.-I.; Valentine, J. S. *J. Org. Chem.* **1976,** *41,* 586.
39. Magno, F.; Bontempelli, G. *J. Electroanal. Chem.* **1976,** *68,* 337.
40. Gibian, M. J.; Sawyer, D. T.; Ungermann, T.; Tangpoonpholvivat, R.; Morrison, M. M. *J. Am. Chem. Soc.* **1979,** *101,* 640.
41. Johnson, R. A. *Tetrahedron Lett.* **1977,** 331.
42. Jencks, W. P. "Catalysis in Chemistry and Enzymology"; McGraw–Hill: New York, 1969; pp. 480–487.
43. Bender, M. L. "Mechanisms of Homogeneous Catalysis for Protons to Proteins"; Wiley: New York, 1971; pp. 176–179.
44. San Fillipo, J., Jr.; Chern, C.-I.; Valentine, J. S. *J. Org. Chem.* **1976,** *41,* 1077.
45. Nanni, E. J., Jr., Ph.D. Dissertation, University of California, Riverside, CA, 1980.
46. McClune, G. J.; Fee, J. A.; McCluskey, G. A.; Groves, J. T. *J. Am. Chem. Soc.* **1977,** *99,* 5220.
47. Pick, M.; Rabani, J.; Yost, F.; Fridovich, I. *J. Am. Chem. Soc.* **1974,** *96,* 7329.
48. Stein, J.; Fackler, J. P.; McClune, G. J.; Fee, J. A.; Chan, L. T. *Inorg. Chem.* **1979,** *18,* 3511.
49. Howie, J. K.; Sawyer, D. T. *J. Am. Chem. Soc.* **1976,** *98,* 6698.
50. Howie, J. K.; Morrison, M. M.; Sawyer, D. T. "Electrochemical Studies of Biological Systems"; Sawyer, D. T., Ed.; *ACS Symposium Series, No. 38,* ACS: Washington, D.C., 1977, 97.

RECEIVED for review June 2, 1981. ACCEPTED November 16, 1981.

Electrocatalytic Reduction of Molecular Oxygen Using Water-Soluble and Immobilized Iron and Cobalt Porphyrins

PAUL A. FORSHEY and THEODORE KUWANA

Ohio State University, Department of Chemistry, Columbus, OH 43210

NAGAO KOBAYASHI and TETSUO OSA

Tohoku University, Pharmaceutical Institute, Sendai, Japan 980

The electrocatalytic reduction of molecular oxygen using water-soluble metal macrocyclic compounds was studied, with emphasis on the water-soluble iron and cobalt porphyrins. An electrochemical (EC) catalytic regenerative mechanism appears to be valid for these compounds, with the redox potential of the porphyrin and the heterogeneous electron transfer rate primarily governing the electrode potential for the catalytic reduction of oxygen. Hydrogen peroxide was the initial product for both the iron and cobalt porphyrins; however, the iron porphyrins catalyzed the reduction or dismutation of hydrogen peroxide to water, whereas the cobalt porphyrins showed little reactivity toward hydrogen peroxide. Computer simulation of cyclic voltammetric current–potential curves for these reactions was used to support conclusions based on electrochemical results.

The mechanism of oxygen electrocatalysis using metal macrocyclic complexes such as the iron and cobalt porphyrins has interested us since the mid-1970's. Our approach has involved studying the solution phase catalysis by the electrogenerated reduced state of the water-soluble metal porphyrins and then comparing these results with those obtained with porphyrins that were immobilized on surfaces of carbon electrodes. A major assumption has been that the reaction sequence could be described by an electrochemical (EC) catalytic regeneration

0065-2393/82/0201-0601$07.00/0

mechanism at which the potential of the catalysis was governed by the redox potential of the metal porphyrin. This chapter summarizes the status of our present understanding of the electrocatalytic mechanism for O_2 reduction and presents the salient features, some of which have been published previously (*1–8*), of the study of the water-soluble porphyrins.

The use of metal macrocyclic compounds for the electrocatalytic reduction of molecular oxygen first was introduced by Jasinski (*9*), who reported the electrocatalysis of O_2 with cobalt phthalocyanine adsorbed on carbon and nickel structures (*10*). Shortly thereafter, polymeric metal phthalocyanines were examined (*11*, *12*) and adsorbed iron and cobalt phthalocyanines on pyrolytic graphite electrodes were studied extensively (*13*, *14*). Since then, many publications have described the catalytic activity of such metal macrocycles (*15–20*), including the recent case of the face-to-face cobalt porphyrin (*21*, *22*) that, when adsorbed onto a glassy carbon electrode, apparently reduces O_2 to water in acidic solutions at potentials more positive than the reversible oxygen–hydrogen peroxide potential.

The mechanism of the catalysis using metal macrocyclic compounds has not been well understood probably because of the use of water-insoluble metal macrocycles. Of course, the electrochemist preferred to use insoluble macrocycles so that the catalyst would remain on the surface when the electrode was immersed in aqueous solutions. Often the catalyst was imbedded in the electrode matrix. Unfortunately, the elucidation of the heterogeneous mechanism has been difficult, and a complete description of oxygen reduction has remained elusive.

Our work has centered around the water-soluble iron and cobalt tetrakis(*N*-methyl-4-pyridyl)porphyrin (FeTMPyP and CoTMPyP) and the structure of FeTMPyP is as shown:

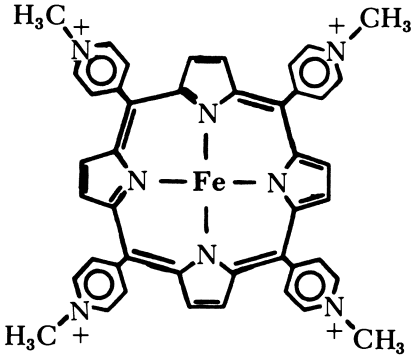

These metal macrocycles are rendered soluble via the cationic methylpyridyl groups on each of the *meso*-positions of the porphyrin ring. The Fe(III)TMPyP first was synthesized by Fleischer and Hambright (*23*) and also has been described by Pasternack and Spiro (*24*).

Our early attempts to use the Fe(III)TMPyP for the catalyzed reduction of O_2 resulted in poorly defined cyclic voltammetric (CV) current–potential (i–E) curves. When the experiments were repeated using highly polished Tokai glassy carbon instead of unpolished pyrolytic graphite, well-defined i–E curves resulted. In Figure 1, Curve a (*1*) is the i–E curve for an uncatalyzed O_2 reduction at a highly polished Tokai glassy carbon electrode in 0.05 M H_2SO_4. Curve b is the i–E wave for the reduction of 2.5×10^{-4} M Fe(III)TMPyP under anaerobic conditions. If this experiment is repeated after the solution is air-saturated, Curve c results. The overpotential for O_2 reduction is reduced by nearly 0.5 V and the peak current, i_p, is increased by ca. eight times over the FeTMPyP wave. Because the potential for O_2

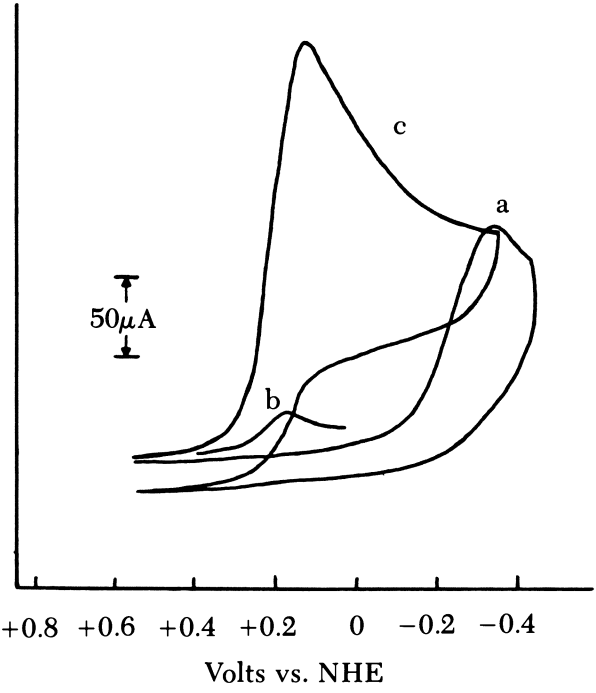

Figure 1. Cyclic voltammograms for the reduction of a, O_2 on a glassy carbon electrode; b, Fe(III)TMPyP in the absence of O_2 and c, O_2 with Fe(II)TMPyP acting as catalyst. O_2 concentration, 2.4×10^{-4} M; Fe(III)TMPyP concentration, 2.5×10^{-4} M. (Curve a taken from Ref. 1.)

reduction appeared to be governed by the redox potential of FeTMPyP, the mechanism for the O_2 catalysis was assumed to be an EC catalytic regeneration mechanism:

$$\text{E step:} \quad \text{Fe(III)TMPyP} + e^- = \text{Fe(II)TMPyP} \tag{1}$$

$$\text{C step:} \quad 2\text{Fe(II)TMPyP} + \text{O}_2 + 2\text{H}^+ = 2\text{Fe(III)TMPyP} + \text{H}_2\text{O}_2 \tag{2}$$

where the product of the reduction was deduced to be hydrogen peroxide from the magnitude of the peak current, $(i_p)_{cat}$, of Curve c. That is, the $(i_p)_{cat}$ was about eight times greater than that of Curve b, which was explained by assigning $n = 2$ for the O_2 to H_2O_2 conversion, and by about a ten times difference in the diffusion coefficients of 2×10^{-6} and 2.1×10^{-5} cm²/s for Fe(III)TMPyP and O_2, respectively. This analysis assumed that the peak currents were diffusion controlled in Fe(III)TMPyP (Curve b) and O_2 (Curve c).

The stoichiometry of Reaction 2 was confirmed (*2*) using rotating-ring-disk studies of air-saturated solutions of 10^{-4} *M* Fe(III)TMPyP at pH 9.0 in 0.1 *M* KCl, and H_2O_2 was produced as the initial product in 95% yield. The catalyst was transferred to the electrode surface by immobilizing Fe(III)tetrakis(*o*-aminophenyl)porphyrin and Fe(III)tetrakis[*N*-(2-hydroxyethyl)-4-pyridyl]porphyrin in a methylacryloylchloride polymer and spin-coating the polymer onto a glassy carbon electrode (*4*). The loading level of these compounds in the polymer governed the extent of O_2 reduction; that is, loadings of 10^{-11} and 10^{-9} mol/cm² produced predominantly H_2O_2 and H_2O, respectively. Results of thin-layer cell coulometric experiments also indicated that O_2 could be reduced to water in the presence of FeTMPyP (*8*).

The differences observed in the extent of O_2 reduction, depending on the experimental conditions and electrochemical method, signified a need for more detailed electrochemical and optically coupled electrochemical studies of FeTMPyP and O_2. We sought to answer the following questions:

1. Was the EC catalytic mechanism valid and could the homogeneous catalysis be transferred to the surface via immobilization?
2. What were the experimental conditions controlling the production of hydrogen peroxide or water in the catalytic reduction?
3. Were metal oxygen complexes involved as precursors or intermediates during O_2 reduction and were such oxygen species as superoxide ion or hydroxyl radicals produced?

4. Could the CV i–E curves be quantitatively described and related to an EC mechanism with associated rate constants?

Characterization of FeTMPyP in the Absence of Oxygen

The electrochemical, acid–base, and dimerization properties of FeTMPyP are summarized in Table I. The monomer, which is the dominant species in acidic solutions, undergoes a well-defined, one-electron, quasi-reversible ($k_s = 5.8 \times 10^{-3}$ cm/s) electron transfer reaction with a $E_{0.85}$ of +0.18 V vs. normal hydrogen electrode (NHE). Thin-layer coulometry confirmed the n-value as 1.02 (±0.02) per iron for the reduction of Fe(III)TMPyP in the absence of O_2 from pH 1 to 13. Both oxidized and reduced states of FeTMPyP were stable, as evidenced by the reproducibility of the optical spectrum of the respective states on redox cycling in a gold minigrid optically transparent thin-layer electrochemical cell (OTTLE).

Table I. Electrochemical, Acid–Base, and Dimerization Properties of FeTMPyP

Property	*Method of Analysis*[a]	*Comments*[b]
Stoichiometry: n = 1.02(±0.02) per iron	thin-layer coulometry	pH 1–13
$E_{0.85}$ = +0.18 V vs. NHE, scan rate = 0.1 V/s	cyclic voltammetry	0.05 M H_2SO_4
$D = 2.5(\pm 0.1) \times 10^{-6}$ cm²/s	chronoamperometry	0.05 M H_2SO_4
Heterogeneous rate constant, k_s = $5.8(\pm 0.9) \times 10^{-3}$ cm/s	cyclic voltammetry	pH 1–9
pK_a of Fe(III)TMPyP: 4.7 and 6.5	$E_{0.85}$ and E_p vs. pH, and spectral data	
pK_a of Fe(II)TMPyP: ca. 7	coulometric titration	
Fe(III)TMPyP dimerization; K_D = $2.2(\pm 0.5) \times 10^3\ M^{-1}$	cyclic voltammetry	dimer important at pH greater than about 6

[a] CV taken at highly polished glassy carbon electrode (Tokai, grade GC10 or 20); Au minigrid electrode used for thin-layer electrochemistry.
[b] Summary of data from Ref. 6.

Controlled potential chronocoulometric experiments were conducted to determine the extent of adsorption, if any, of the FeTMPyP on the surface of the highly polished Tokai glassy carbon. Plots of the charge, Q, vs. square root of time, $t^{1/2}$, were linear; and the slopes of these lines increased with Fe(III)TMPyP concentration in accordance with a diffusion-controlled electrode reaction. More importantly, the extrapolated Q vs. $t^{1/2}$ curves, after correction for background charge, intercepted the Q axis at or slightly below the origin. Because an adsorbed species would produce a positive Q intercept, adsorption of FeTMPyP was negligible.

A number of acid–base studies have been reported. pK_a values of ca. 4.7 and 6.5 for Fe(III)TMPyP (*25*, *26*) were determined by monitoring the optical spectra as a function of pH. Goff and Morgan (*27*), after following the magnetic moment during pH titrations, reported that this compound underwent a high to low spin transition at about pH 5. Reaction 3 in Table II represents the first pK_a and the spin transition as the iron changes coordination from five to six. The product of this reaction, the monohydroxyl species, was reported (*26*) to undergo further deprotonation with a pK_a of 6.5, consistent with Reaction 4 (Table II).

Electrode Reactions 7 through 10 in Table II were proposed to account for the observed CV i–E curves between pH 1 and 13. These reactions reflect conclusions based on the E vs. pH plots of the observed i–E waves, pK_a values of Fe(III)TMPyP and Fe(II)TMPyP, optically coupled electrochemical results (particularly of the dimer), and magnetic circular dichroism (MCD) spectroscopy of the Fe(II)TMPyP. Because much of the data were discussed previously (*6*, *8*), we briefly shall elaborate on only heretofore unpublished data. The pK_a of Fe(II)TMPyP was determined by coulometric titration with electrogenerated hydroxyl ion at a small platinum electrode. The Fe(II)TMPyP was generated in situ by reducing Fe(III)TMPyP at a large platinum electrode in a thoroughly degassed solution. A pK_a of ca. 6.6 was determined from the titration curve for Reaction 5. This pK_a value was confirmed by monitoring at various pH values the optical spectra of Fe(II)TMPyP, obtained with the use of an OTTLE, and by plotting the absorbance at 560 nm as a function of pH.

The MCD spectra (Figure 2) were obtained to study the coordination and spin state of the iron in Fe(II)TMPyP. Associated with the 445-nm absorbance maximum of Fe(II)TMPyP, the MCD spectra showed an intense peak at 450 nm and a trough at 404 nm with $[\theta]\mu$ of 18.0 and −2.6 (units: degree cm^2 dmol^{-1} gauss), respectively. The MCD spectra in the visible region, associated with the 567-nm absorbance maximum, showed two peaks at 542 and 597 nm and a trough at 568 nm with $[\theta]\mu$ of 1.7, 1.8, and −1.5, respectively. The shape, sign,

Table II. Acid–Base, Dimerization, and Redox Reactions of Fe(III)TMPyP and Fe(II)TMPyP

Acid–Base:

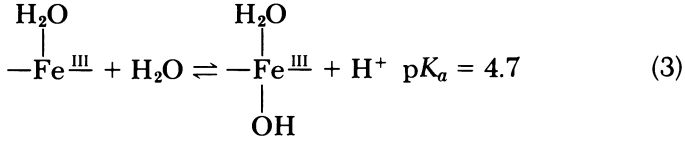

$$-Fe^{III}(H_2O) + H_2O \rightleftharpoons -Fe^{III}(OH) + H^+ \quad pK_a = 4.7 \tag{3}$$

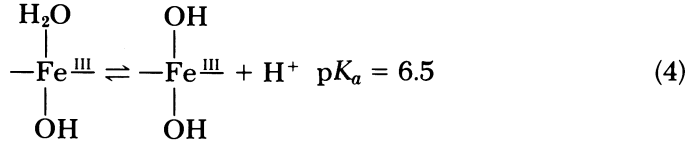

$$-Fe^{III}(H_2O)(OH) \rightleftharpoons -Fe^{III}(OH)_2 + H^+ \quad pK_a = 6.5 \tag{4}$$

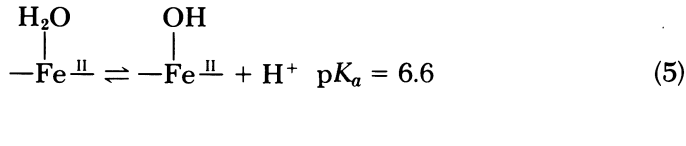

$$-Fe^{II}(H_2O) \rightleftharpoons -Fe^{II}(OH) + H^+ \quad pK_a = 6.6 \tag{5}$$

Dimerization:

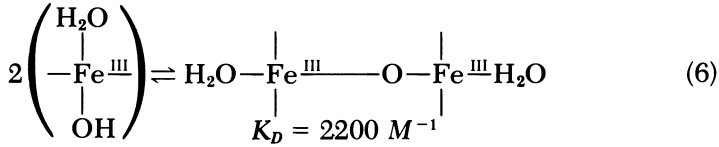

$$2(-Fe^{III}(H_2O)(OH)) \rightleftharpoons H_2O-Fe^{III}-O-Fe^{III}-H_2O \quad K_D = 2200\ M^{-1} \tag{6}$$

Redox:

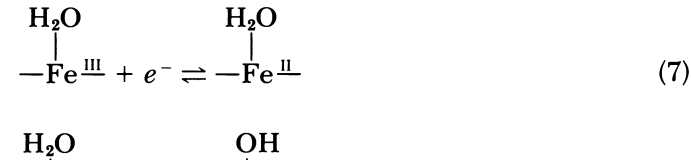

$$-Fe^{III}(H_2O) + e^- \rightleftharpoons -Fe^{II}(H_2O) \tag{7}$$

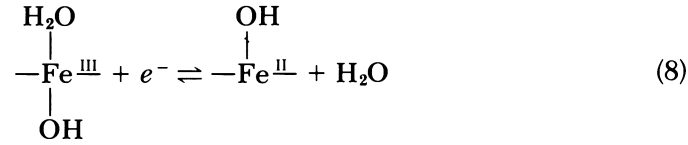

$$-Fe^{III}(H_2O)(OH) + e^- \rightleftharpoons -Fe^{II}(OH) + H_2O \tag{8}$$

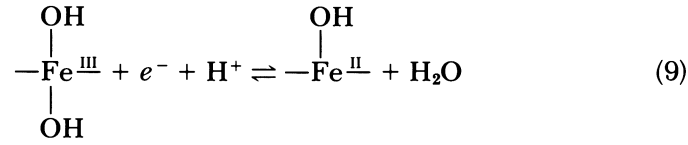

$$-Fe^{III}(OH)_2 + e^- + H^+ \rightleftharpoons -Fe^{II}(OH) + H_2O \tag{9}$$

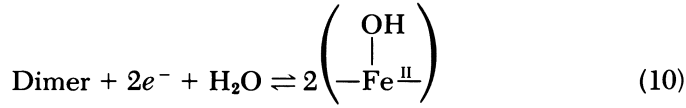

$$\text{Dimer} + 2e^- + H_2O \rightleftharpoons 2(-Fe^{II}(OH)) \tag{10}$$

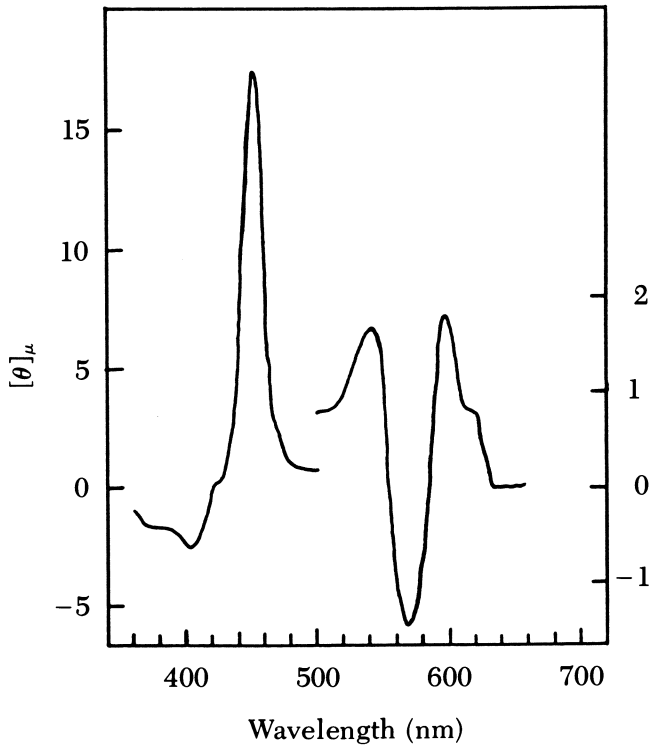

Figure 2. Magnetic circular dichroism spectrum of Fe(II)TMPyP in pH 4.7 acetate buffer. $[\theta]_\mu$ in degree · cm² · dmol⁻¹ · gauss.

and magnitude of the MCD spectra, specifically in the 445-nm region, are quite similar to those reported for ferrous hemoproteins, such as deoxymyoglobin and the reduced form of peroxidase. These compounds were reported to be in a pentacoordinated, high spin form with the iron out of the porphyrin plane (*28*, *29*). This observation suggests that the Fe(II)TMPyP is also a pentacoordinated, high spin state complex. Thus, Reactions 7–9 are written in consideration of these results.

As we previously noted, the cyclic voltammograms for Fe(III)-TMPyP in solutions of pH 7–13 are characterized by two cathodic waves and one anodic wave on reverse scan. The more negative, pH-independent wave at −0.3 V, is due to the reduction of the dimer (Reaction 10, Table II). The anodic wave is pH dependent and is coupled to the reduction wave for the dihydroxyl monomer, Reaction 9. Thus, the dimer rapidly dissociates to the monomeric ferrous species on reduction.

Characteristics of FeTMPyP Reaction with Oxygen

The pH dependence of the O_2 reduction reaction is shown in Figure 3, which shows that the potential for catalysis via Fe(II)TMPyP occurs independently of pH at acidic pH values, as expected. Above about pH 5, the potential varies at a rate of 60 mV/pH unit. At a scan rate of 0.1 V/s, the E_p values of the i–E waves, with and without O_2, virtually coincide over the pH range of 1–13. This correspondence of E_p values with pH leaves little doubt that the potential governing the

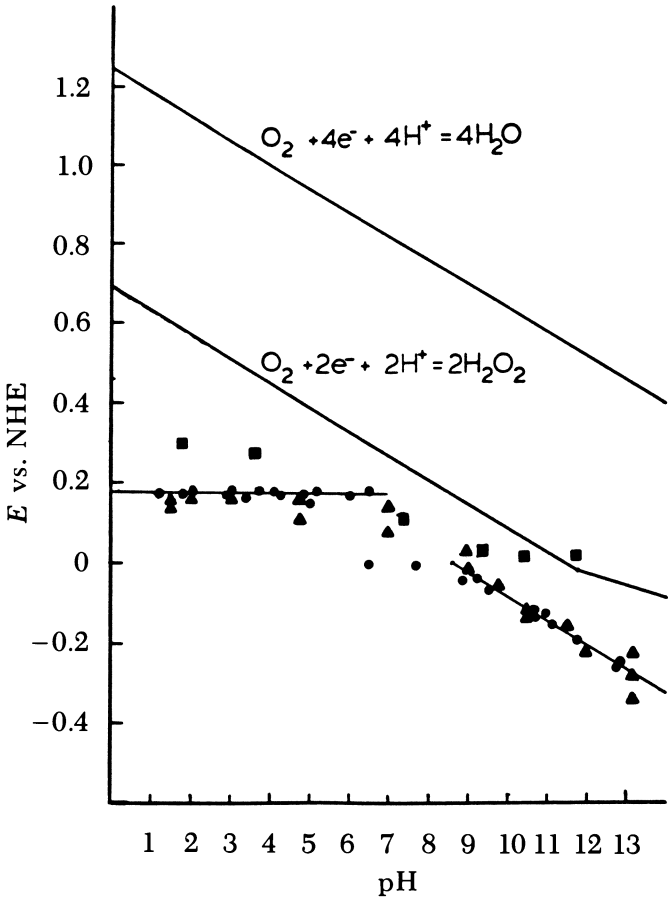

Figure 3. Potential vs. pH for the various reduction processes. Key: ▲, the reduction of O_2 in the presence of Fe(II)TMPyP; ●, the reduction of Fe(III)TMPyP; ■, the reduction of O_2 in the presence of Co(III)TMPyP; and —, E_p value for Fe(III)TMPyP in O_2-free solutions.

O_2 reduction is the redox potential of the Fe(III)TMPyP couple, consistent with the proposed EC mechanism.

To investigate the effect of the FeTMPyP concentration on the extent of O_2 reduction, CV i–E curves were obtained in air-saturated acidic solution as the Fe(III)TMPyP concentration was varied from 10^{-5} to 10^{-3} M. Traces a, b, and c in Figure 4 show typical i–E curves for concentration ratios of Fe(III)TMPyP : O_2 of 0.08 : 1, 1 : 1, and 4 : 1, respectively. Not only does the $(i_p)_{cat}$ readily increase with an increasing Fe(III)TMPyP : O_2 ratio, but the $(E_p)_{cat}$ also shifts to more positive potentials with increasing Fe(III)TMPyP concentration. The computer simulated i–E curves in this figure will be discussed later.

The dependence of $(i_p)_{cat}$ on the Fe(III)TMPyP concentration is shown in Figure 5, Curve a. The current is plotted as a normalized current, $(i_p)_N$, which is the $(i_p)_{cat}$ divided by the current, $(i_p)_{n=1}$, which is expected if O_2 were reduced reversibly via an one-electron reduction

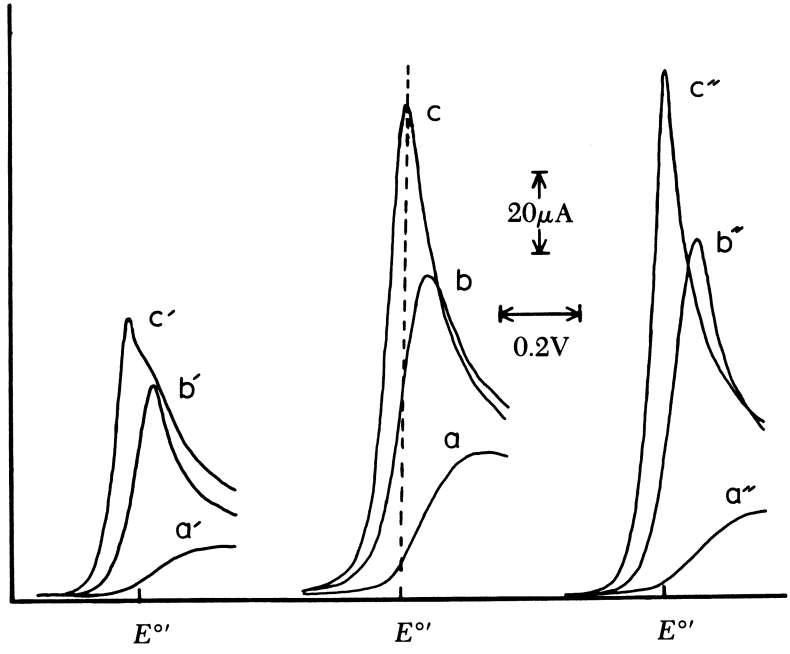

Figure 4. Cyclic voltammograms for the reduction of O_2 with Fe(II)-TMPyP as catalyst. O_2 concentration, 2.4 × 10^{-4} M. Fe(III)TMPyP concentration: a, 2.2 × 10^{-5} M; b, 2.5 × 10^{-4} M; and c, 9.8 × 10^{-4} M; a', b', c', a'', b'', and c'' are the computer-simulated cyclic voltammograms for O_2 reduction under identical conditions as a, b, and c, respectively, but with n = 2 *(a', b', c') or* n = 4 *(a'', b'', c''); scan rate, 0.05 V/s; electrode area, 0.388 cm^2.*

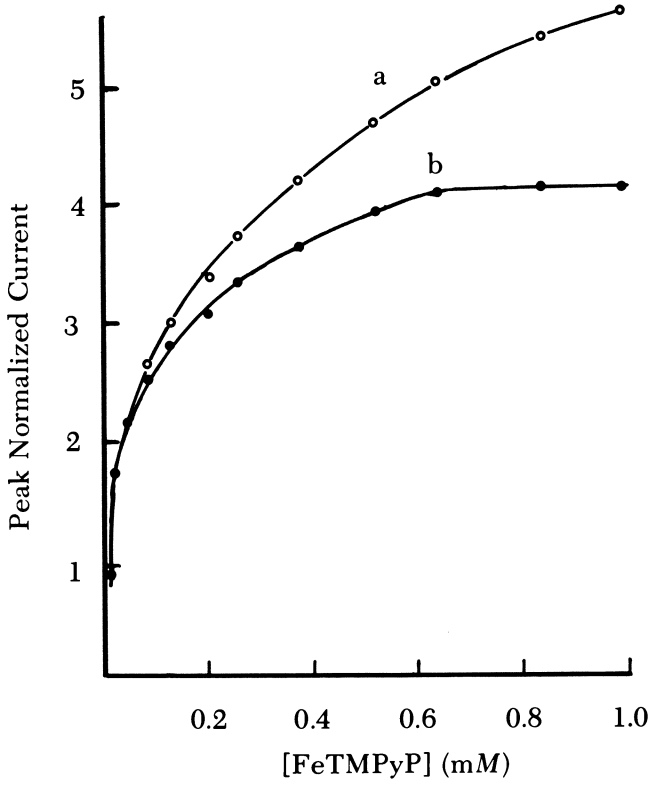

Figure 5. Plot of the peak normalized current vs. Fe(III)TMPyP concentration. Curve a, $(i_p)_N$ vs. [Fe(III)TMPyP]; Curve b, $(i_p)_{N,corr}$ vs. [Fe(III)TMPyP]. O_2 concentration, 2.4 × 10^{-4} M; scan rate, 0.05 V/s; $(i_p)_{n=1}$ calculated for the one-electron reduction of O_2 using the Randles–Sevcik equation and the concentration and diffusion coefficient of O_2.

to superoxide ion at the working electrode. The Randles–Sevcik equation (*30, 31*) was used to calculate this $(i_p)_{n=1}$, with an electrode area of 0.388 cm^2 and a scan rate of 0.05 V/s. The diffusion coefficient and concentration of O_2 were 2.1 × 10^{-5} cm^2/s and 2.4 × 10^{-4} *M*, respectively. As seen in the figure, the $(i_p)_N$ increases rapidly with the Fe(III)TMPyP concentration up to a concentration of ~ 5 × 10^{-4} *M*. No anodic current peak was observed on CV scan reversal until this concentration was reached. Curve b of Figure 5 is the corrected normalized current, $(i_p)_{N,corr}$, which is calculated by subtracting from the $(i_p)_{cat}$ the current that would be obtained from the reduction of Fe(III)TMPyP under anaerobic conditions before calculating the normalized current. The $(i_p)_{N,corr}$ yields a limiting value of $n = 4$, which is

much larger than the value expected for the reduction of O_2 to H_2O_2, and is indicative of the reduction of O_2 to water.

Not surprisingly, we previously interpreted the catalyzed reduction of O_2 as producing mainly H_2O_2 (Figure 1). In these early experiments, the Fe(III)TMPyP : O_2 ratio was ~ 1 : 1 (*see* Curve b of Figure 5) and hence, the calculated n-value from the experimental i_p would be approximately two.

Characteristics of FeTMPyP Reactions with Hydrogen Peroxide

Assuming that the O_2 to water conversion proceeds through H_2O_2 as the initial product, the pathway(s) whereby H_2O_2 may be converted to water must be considered. Initially, the kinetics of the dismutation of H_2O_2 with Fe(III)TMPyP acting as the catalyst were determined by monitoring the H_2O_2 concentration in a stirred solution with a gold microelectrode. The plots of log [H_2O_2] vs. time were linear, and the slopes of these plots increased linearly with the Fe(III)TMPyP concentration. The rate-limiting step for the dismutation was first order in both H_2O_2 and Fe(III)TMPyP. Similar experiments were conducted at pH values ranging from 5.6 to 13. Rate constants determined for the dismutation increased with pH from 5 M^{-1} s^{-1} at pH 5.6 to 1.2 × 10^4 M^{-1} s^{-1} at pH 13. Although a more careful pH study needs to be conducted to understand fully the pH dependence, Reaction 12 (Table III) fulfills the pH and the first-order concentration dependence on H_2O_2 and Fe(II)TMPyP. The iron–peroxide intermediate formed in this reaction proceeds to react with another peroxide to form the products shown in Reaction 13 (Table III). These reactions (12 and 13) are similar to those proposed for catalase activity of other metal macrocyclic compounds (*32*, *33*).

Table III. Reactions of Hydrogen Peroxide with Fe(III)TMPyP and Fe(II)TMPyP

Ferric porphyrin:

$$\text{Fe(III)TMPyP} + H_2O_2 \xrightarrow{k} \text{Fe(III)TMPyP} \cdot O_2H^- + H^+ \quad (12)$$

$$\text{Fe(III)TMPyP} \cdot O_2H^- + H_2O_2 \rightarrow \text{Fe(III)TMPyP} + O_2 + H_2O + OH^- \quad (13)$$

Ferrous porphyrin:

$$\text{Fe(II)TMPyP} + H_2O_2 \rightarrow \text{Fe(II)TMPyP} \cdot O_2H^- + H^+ \quad (14)$$

$$\text{Fe(II)TMPyP} \cdot O_2H^- + \text{Fe(II)TMPyP} + H^+ \rightarrow 2\text{Fe(III)TMPyP} + 2OH^- \quad (15)$$

$$\text{Fe(II)TMPyP} \cdot O_2H^- + e^- + H^+ \rightarrow \text{Fe(III)TMPyP} + 2OH^- \quad (16)$$

Pasternack and Halliwell (*34*) reported that Fe(III)TMPyP underwent decomposition via H_2O_2 during a dismutase reaction with superoxide. To determine the importance of this type of reaction, the rate constant for the decomposition of Fe(III)TMPyP by H_2O_2 was evaluated using the stopped-flow method where the concentration of Fe(III)TMPyP was monitored at 400 nm. Pseudo-first-order conditions were maintained by using at least a 100-fold excess of H_2O_2 to Fe(III)TMPyP. Plots of the ln[Fe(III)TMPyP] vs. time were linear and fitted the rate law:

$$d[\text{Fe(III)TMPyP}]/dt = k[\text{Fe(III)TMPyP}]\,[H_2O_2] \qquad (11)$$

The rate constant, k, for this reaction was calculated to be 5.3 M^{-1} s^{-1} in 0.05 M H_2SO_4. The products of the reaction were assumed to be similar to the bile products formed by the oxidative decomposition of hemes in biological systems (*35*).

Because the rate of H_2O_2 dismutation by Fe(III)TMPyP and the rate of Fe(III)TMPyP decomposition by H_2O_2 were slow in acidic solutions, we realized that oxygen-free (by usual degassing procedure) solutions of Fe(III)TMPyP in the presence of H_2O_2 could be prepared. This finding made it possible to study the reaction(s) between H_2O_2 and electrogenerated Fe(II)TMPyP.

The CV i–E wave for the reduction of Fe(III)TMPyP in the presence of H_2O_2 is shown in Figure 6, Curve e. It is surprisingly similar to Curve d, the catalysis of O_2, which is shown for comparison purposes. Because the reduction of Fe(III)TMPyP contributes to the i_p of both Curves d and e; and because the concentrations and diffusion coefficients of oxygen and peroxide are different, the O_2 to H_2O_2 catalytic peak currents are not in a ratio of 2 : 1. However, similar to the O_2 case, a normalized peak current can be calculated. That is, the $(i_p)_{cat}$ can be corrected for the current due to Fe(III)TMPyP reduction (Trace a, Figure 6), and then this corrected value is normalized by the peak current that would have resulted if H_2O_2 underwent only a one-electron reduction. This latter peak current was calculated using the Randles–Sevcik equation (*30, 31*), where the value of the diffusion coefficient for H_2O_2 was 6.8×10^{-6} cm^2/s (*36*). The corrected normalized current attains a value of 2.0 (+0.2), which would be expected for the reduction of H_2O_2 to H_2O by an EC catalytic mechanism. Also, as in the reduction of O_2, the potential for H_2O_2 catalysis is governed by the FeTMPyP redox couple, again consistent with an EC mechanism.

The proposed reaction steps for the reduction of H_2O_2 invoke an iron–peroxide intermediate (Reaction 14, Table III) that can be reduced further via reaction with another Fe(II)TMPyP or with the elec-

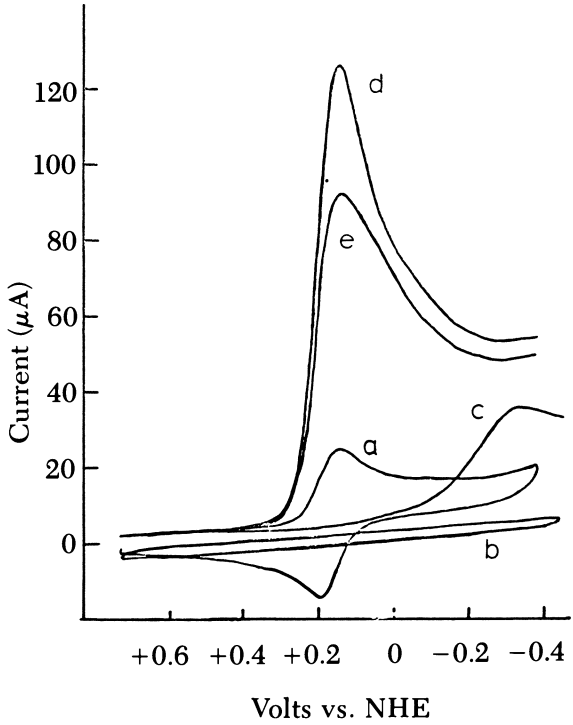

Figure 6. Cyclic voltammograms for the reduction of a, nitrogen-saturated 4.3 × 10⁻⁴ M Fe(III)TMPyP; b, nitrogen-saturated 2.9 × 10⁻⁴ M H_2O_2 on a bare glassy carbon electrode; c, 2.4 × 10⁻⁴ M O_2 on a bare glassy carbon electrode; d, 2.9 × 10⁻⁴ M H_2O_2 and 4.3 × 10⁻⁴ M Fe(III)TMPyP; and e, 2.4 × 10⁻⁴ M O_2 and 4.3 × 10⁻⁴ M Fe(III)TMPyP; 0.05 M H_2SO_4. Scan rate, 0.1 V/s; electrode area, 0.388 cm².

trode (Reactions 15 and 16, respectively). These reactions closely parallel those proposed for the peroxidase enzyme (37). The type of Fe(III)TMPyP species in Reactions 12–16, as well as whether OH^- or H_2O is present in the final products, depends on the solution pH, in accordance with the acid–base equilibria (Reactions 3, 4, and 6 in Table II).

Characteristics of CoTMPyP in the Absence and Presence of Oxygen

Although there are many similarities between the electrochemical, acid–base, and spectral properties of CoTMPyP and FeTMPyP, there are two major differences. The first is that water-soluble Co(III)TMPyP strongly adsorbs onto the surface of the highly polished glassy carbon electrode. The second difference is that H_2O_2 can be

produced quantitatively when O_2 is reduced catalytically by electrogenerated Co(II)TMPyP. These differences also appear when water-soluble Co(III)tetrakis(*N*-pyridylium)porphyrin [Co(III)TPyP] is in acidic solutions where the pyridyl groups are protonated. With these two differences in mind, the properties of CoTMPyP are summarized in Table IV.

In an O_2 saturated 0.05 *M* H_2SO_4 solution of Co(III)TMPyP, in which the CoTMPyP and O_2 concentrations were approximately equal at 1.3×10^{-3} *M* (saturated with pure O_2), the CV $(i_p)_{cat}$ was about five times larger than in oxygen-free solutions. No anodic current was observed on the reverse scan. Plots of $(i_p)_{cat}$ vs. square-root of scan rate were linear, and appeared to be limited by the rate of O_2 diffusion. Analysis of the $(i_p)_{cat}$ indicated that O_2 was reduced to H_2O_2 by a two-electron process. Hydrogen peroxide was confirmed as the product of the reduction by controlled potential coulometric experiments in which the H_2O_2 was identified qualitatively by reaction with $Ti(SO_4)_2$ (38) and quantitated by titration with acidic $KMnO_4$ (38). Hydrogen peroxide was produced with a 90% current efficiency[1].

The potential at which O_2 was reduced catalytically corresponded closely to the redox potential of the cobalt porphyrin. The mechanism is undoubtedly identical to Reactions 1 and 2 written for FeTMPyP; that is, the EC catalytic regeneration mechanism. In contrast to the iron porphyrin, the reduced form of the cobalt porphyrin reacts much more slowly with H_2O_2. This decreased reactivity was demonstrated most clearly by the ability of solution Co(II)TMPyP to generate bulk concentrations of H_2O_2 via the catalytic reduction of O_2. Also, the redox potential for the cobalt porphyrin is some 200 mV more positive than the iron porphyrin. Hence, the catalysis occurred quite near to the reversible redox potential of O_2/H_2O_2.

Because CoTMPyP and CoTPyP adsorbed strongly on the glassy carbon surface, O_2 catalysis could be attained with an electrode pretreated by immersion into a cobalt porphyrin solution prior to using the electrode for O_2 catalysis in a solution free of the cobalt porphyrin. The long-term activity of the adsorbed cobalt porphyrin electrode was limited by deactivation. The deactivation of the porphyrin by peroxide attack was believed to result from the slow decomposition of the porphyrin, rather than from desorptive losses.

Oxygen Electrocatalysis by Other Water-Soluble Iron or Cobalt Porphyrins

The redox potentials (reported as E_p or $E_{0.85}$ from CV data) for several iron and cobalt water-soluble porphyrins, including the cobalt

[1] Calculated by comparing the results of the $KMnO_4$ titration with the charge consumed by O_2 reduction.

Published on June 1, 1982 on http://pubs.acs.org | doi: 10.1021/ba-1982-0201.ch025

Table IV. Electrochemical, Acid–Base, and Spectral Properties of CoTMPyP

Property	*Method and Analysis*	*Comments*	*References*
Stoichiometry; n = 1 per cobalt	CV and coulometry	pH 1–13	*52*
$E_{0.85}$ = +0.42 V vs. NHE scan rate = 0.1 V/s	CV, thin-layer potentiometry	0.05 *M* H_2SO_4	*52, 53*
D = 2.3 (±0.1) × 10^{-6} cm^2/s	chronoamperometry	0.05 *M* H_2SO_4	*53*
Heterogeneous rate constant, k_s	CV	complicated by surface adsorption and variable with electrode pretreatment	
pK_a of Co:III:TMPyP: 6.0 and 10.2	$E_{0.85}$ vs. pH and spectral data		*54*
pK_a of Co(II)TMPyP: est. 9.7	$E_{0.85}$ vs. pH and spectral data		*53*
No dimerization of Co(III)TMPyP	spectral data		*54*
Co(III)TMPyP and Co(III)TPyP strongly adsorbed on glassy carbon surface	CV, differential pulse polarography, raman spectroscopy, and x-ray photoelectron spectroscopy		*53*

Note: CV data taken using a highly polished glassy carbon electrode (Tokai, grade GC 10 or 20).

and iron tetrasulfonated phthalocyanines (CoTSPc and FeTSPc) reported by Zagel et al. (*17*) in the absence and presence of O_2, are listed in Table V. With the exception of these two compounds, CoTSPc and FeTSPc, a close correspondence exists between the redox potential of the compound and the potential for O_2 catalysis. The +3 to +2 reduction of CoTSPc was assigned (*17*) to the CV i–E wave with E_p of +0.80 V vs. SCE and the wave at −0.12 V vs. SCE was assigned to FeTSPc. However, the potential of the rotating ring-disk electrode (RRDE) limiting current for the reduction of O_2 was not attained until a potential of about −0.6 V, which is at or near the potential for the reduction of O_2 on a bare glassy carbon electrode. On the other hand, the limiting current increased by fourfold to fivefold with adsorbed FeTSPc over the uncatalyzed O_2 reduction. The mechanism proposed for the O_2 reduction was

$$\text{M(III)Pc} + e^- = \text{M(II)Pc} \quad (17)$$

$$\text{M(II)Pc} + O_2 = \text{M(III)Pc} \cdot O_2^- \quad (18)$$

$$\text{M(III)Pc} \cdot O_2^- + e^- = \text{intermediates} \quad (19)$$

in which Reaction 18 or 19 was cited as the rate-limiting step dependent on pH. Even though only small yields of H_2O_2 were observed, as determined by monitoring H_2O_2 on the ring electrode, no mechanism for the reduction of H_2O_2 to H_2O was proposed (*17*).

Many researchers reported on the electrocatalytic reduction of O_2 using metallophthalocyanines. Van Veen (*19*) proposed a mechanism for O_2 catalysis, which agreed with that of Zagel et al. (*17*). Van Veen found that the magnitude of the O_2 reduction current correlated directly with the rate of the decomposition of H_2O_2 by the metallophthalocyanine. Although Van Veen (*19*) argued against the relationship between the reduction potential of the catalyst and its electrochemical activity for O_2 reduction, his proposed mechanism has, as its first step, the reduction of the metal macrocyclic catalyst.

Discussion of Mechanism

Several aspects of the detailed mechanism still lack definitive experimental evidence to prove their validity, yet a growing consensus of experimental observations and modeling studies fits a general mechanistic scheme. At present, this scheme indicates that a common intermediate is involved in the redox reactions of oxygen with iron porphyrins, and that both dioxygen and hydrogen peroxide can be reduced by iron porphyrins.

Unlike the adsorbed catalysts on the electrode surface that apparently can transfer successive electrons from the electrode to a solution

Published on June 1, 1982 on http://pubs.acs.org | doi: 10.1021/ba-1982-0201.ch025

Table V. Reduction Potentials for Iron and Cobalt Macrocyclic Compounds

	E_p or $E_{0.85}$[a]					
Compound	*no O_2*	*with O_2*	*Electrode*	*Conditions*	*Comments*	*References*
FeTPyP and FeTMPyP	+0.15	+0.15	highly polished glassy carbon (GC)	0.05 *M* H_2SO_4		*6, 8*
CoTPyP and CoTMPyP	+0.46	+0.30	GC	0.05 *M* H_2SO_4	adsorbs	*3, 4*
FeTHOEPP	+0.14	+0.10	GC	0.05 *M* H_2SO_4		*7*
CoTHOEPP	+0.22	+0.18	GC	0.05 *M* H_2SO_4		*7*
FeTAPP	+0.14	+0.14	GC	0.05 *M* H_2SO_4		*5*
FeTSPc	+0.12, −0.31	−0.17[b]	stress-annealed pyrolytic graphite (SAPG)	0.1 *M* KOH	adsorbs	*17*
CoTSPc	+1.02	−0.10[b]	SAPG	0.1 *M* KOH	adsorbs	*17*
Carbon Electrode		−0.35			no pH dependence	*1*

[a] CV data, potential vs. NHE; scan rate, 0.1 V/s.
[b] $E_{1/2}$ of RRDE data.

substrate, the water soluble ferrous porphyrins are one-electron reducing agents. However, the net stoichiometry for the reduction of O_2 to H_2O_2 or the reduction of H_2O_2 to H_2O requires two electrons in each case. Although the production of the one-electron intermediate, the superoxide ion ($O_2^{\cdot-}$), by Fe(II)TMPyP is thermodynamically unfavorable (by 0.5 V), the superoxide ion has been intimated as a key intermediate in several iron-catalyzed oxygen reactions. A study (*34*) of the superoxide dismutase activity of Fe(III)TMPyP showed that superoxide was reduced at a rate of $3 \times 10^7\ M^{-1}\ s^{-1}$ at pH 10. This rate is nearly identical to the rate of $4 \times 10^7\ M^{-1}\ s^{-1}$ at pH 9 for the reaction of Fe(II)TMPyP with O_2 to form H_2O_2 as measured by RRDE (*2*). The similarities between these rate constants, along with the thermodynamic data, suggest that these reactions proceed through a common intermediate such as a coordination complex between molecular oxygen and the iron porphyrin in which a partial charge was transferred. Complexes such as these were suggested (*39–42*) as intermediates in the reactions of iron hemes with O_2 and $O_2^{\cdot-}$, and were confirmed at low temperatures in nonaqueous solvents (*43*). A reaction scheme consistent with the observations just mentioned involved Reaction 1 and Reactions 20–22:

$$\text{Fe(II)TMPyP} + O_2 = \text{Fe(III)TMPyP} \cdot O_2^{\cdot-} \quad (20)$$

$$\text{Fe(III)TMPyP} \cdot O_2^{\cdot-} + 2H^+ + \text{Fe(II)TMPyP} = 2\text{Fe(III)TMPyP} + H_2O_2 \quad (21)$$

$$\text{or Fe(III)TMPyP} \cdot O_2^{\cdot-} + 2H^+ + e^- = \text{Fe(III)TMPyP} + H_2O_2 \quad (22)$$

where the intermediate is reduced further by another Fe(II)TMPyP or by an electron from the electrode. The formalism used to denote the intermediate suggests electron transfer from the iron porphyrin to the oxygen adduct. However, the extent of charge transfer for intermediates of this type ranges from an experimentally determined value of ca. 80% (*44*) to a theoretical value of near zero (*45*). Based on thermodynamic arguments, the charge transferred from the ferrous iron to the oxygen on the complex must be less than unity. The electron transfer must be driven by another reaction. For Reaction 21 or 22 to occur, the reduction potential of the intermediate must be equivalent to, or more positive than, the reduction potential of Fe(III/II)TMPyP. The reduction potential of the intermediate reasonably may be assumed to be more positive than 0.18 V (the reduction potential of FeTMPyP) when the standard potential of 1.42 V (*46*) for $HO_2 \cdot / H_2O_2$ is considered; for example, the interaction of superoxide with Fe(III)TMPyP may shift the reduction potential of superoxide in the same way that protonation does. The proposed reaction scheme further is supported by pulse radiolysis results (*47*), which suggested the presence of the

same intermediate and indicated that the reaction was first order in O_2 and second order in Fe(II)TMPyP.

The contention that oxygen can be reduced catalytically to H_2O_2 or to H_2O through a pathway involving H_2O_2 was explored through the comparison of digitally simulated CV i–E curves with their experimental counterparts. In the computer calculations of the CV i–E curves (*see* Curves a′, b′, c′, and a″, b″, c″ in Figure 4), the simulations of the EC catalytic sequence included either Reaction 1′ or 23:

$$\text{Fe(III)TMPyP} + e^- \xrightarrow{k_s} \text{Fe(II)TMPyP} \qquad (1')$$

$$2\text{Fe(II)TMPyP} + O_2 + 2H^+ \xrightarrow{k_f} 2\text{Fe(III)TMPyP} + H_2O_2 \qquad (23)$$

or Reactions 1′ and 24:

$$4\text{Fe(II)TMPyP} + O_2 + 4H^+ \xrightarrow{k_f} 2\text{Fe(III)TMPyP} + 2H_2O \qquad (24)$$

where the reactant stoichiometry of the FeTMPyP to oxygen was fixed at 2 : 1 or 4 : 1, corresponding to the reduction of oxygen to hydrogen peroxide (Reaction 23) or water (Reaction 24), respectively. The computer simulations were programmed to include the heterogeneous rate constant, k_s, or Reaction 1′ and a homogeneous bimolecular rate constant, k_f, assuming that a single rate-determining step limited the homogeneous reaction, irrespective of the 2 : 1 or 4 : 1 reactant stoichiometry. The CV i–E profiles were simulated for a wide range of experimental conditions, including the effect of scan rate, the reactant stoichiometry, the concentration ratio, and the k_s and k_f values. Although details of these simulations will be published elsewhere (*48*), interesting features are that (1) the potential of the catalytic oxygen i–E wave is governed primarily by the redox potential of the FeTMPyP and the value of k_s; and (2) the magnitude of the peak catalytic current is determined by the reactant stoichiometry, the concentration of FeTMPyP and O_2, and the value of k_f.

Examples of simulated i–E curves are shown in Figure 4. These curves are calculated using O_2 concentration and diffusion coefficient values of 2.4×10^{-4} M and 2.1×10^{-5} cm²/s, respectively[2]. The left-hand set of the three i–E curves (a′, b′, c′) is simulated for Reaction sequence 1′ and 23. The right-hand set is for Reaction sequence 1′ and 24. The center set is the experimental i–E curves. In all three sets, the

[2] There is considerable uncertainty in the values of the diffusion coefficient, D_{O_2}, and concentration of O_2 for the computer calculations. And hence, uncertainty in the value of $(i_p)_c$. Values of D_{O_2} and C_{O_2} range from minimum of 1.67×10^{-5} cm/s (Ref. *17*) and 2.2×10^{-4} M (Ref. *49*) and maximum of 2.5×10^{-5} cm/s (Ref. *1*) and 2.6×10^{-4} M (Ref. *50*), respectively. Average values were used in the computation for the i–E simulations shown in Figure 4.

i–E curves for the a, b, and c series correspond to ratios of 0.08 : 1, 1 : 1, and 4 : 1, respectively, for the FeTMPyP to O_2 concentration. Note that in all three sets the E_p shifts to more positive values as the FeTMPyP to O_2 concentration ratio increases. Also, the curves are closely related to the $E^{0'}$ of FeTMPyP redox couples in accordance with the EC catalytic mechanism. Particularly, Curves c and c″ are nearly identical with the $(E_p)_{cat}$ values within ±5 mV of each other. This close agreement lends credence to the correctness of the k_s value used in the simulation because the $(E_p)_{cat}$ value changes 120 mV per decade change in k_s. The next item to be noted is the magnitude of the catalytic peak currents between the two simulated sets and the experimental one. Inspection of the curves shows a closer agreement at all FeTMPyP to O_2 concentration ratios when the reactant stoichiometry is 4 : 1 than when it is 2 : 1. Without question, the catalytic peak current (and hence the extent of O_2 reduction) increases as the concentration of FeTMPyP to O_2 increases. For curves calculated for the 4 : 1 reactant stoichiometry (Reaction sequence 1′ and 24), the experimental $(i_p)_{cat}$ values for the 1 : 1 and 4 : 1 concentration ratios are 89 and 94%, respectively, of the corresponding calculated values (compare Curve b and b″ and c with c″ in Figure 4).

The computer simulated i–E curves of the EC catalytic mechanism support the validity of the $(i_p)_{N,corr}$ calculations for the reduction of oxygen and hydrogen peroxide. The simulated curves indicated that the corrected i_p (the total i_p minus the i_p due to the catalyst alone) was the product of the stoichiometric ratio multiplied by the peak current that would be observed if the reactant was reduced only via a one-electron process. This result is in contrast to the current that would result if the reactant was reduced reversibly at an electrode surface by a two- or four-electron process where the n-value is raised to the $^3/_2$ power as in the Randles–Sevcik equation (*30*, *31*). However, the stoichiometric ratio more appropriately may be thought of as a multiplier of the substrate concentration instead of the n-value because, for the EC catalytic mechanism, the substrate replenishes the concentration of the electroactive species (the oxidized catalyst) via the homogeneous reaction.

In these simulations, the stoichiometry does not differentiate between an intermediate species being reduced via the ferrous species or by the electrode. Also, the value of k_f used in these simulations was limited to an upper value of ca. 10^6 M^{-1} s^{-1} because of computer time and stability considerations. Use of the experimentally determined value in the low 10^{-7} M^{-1} s^{-1} range may increase the simulated $(i_p)_{cat}$ by about 15% (calculated by extrapolation). Further details of our computer simulation will be published elsewhere (*48*).

Contrary to the iron porphyrins, the cobalt porphyrins tended to produce H_2O_2 as the end product in the reduction of O_2 at all experimentally accessible concentration ratios. This finding is in contrast to the reports (*21, 22*) in which a cofacial cobalt porphyrin appeared to be able to reduce oxygen to water.

In the present case, the difference presumably is related to the ability of the lower valent form of the metal to bind axially with the peroxide anion. However, the situation is unclear and further studies are necessary to understand the differences in the degree of hydrogen peroxide reduction by these metal porphyrins.

The ultimate goal is to transform the homogeneous EC mode of catalysis into a heterogeneous one by immobilizing the catalyst, in this case a metal porphyrin, on the electrode surface. Successful immobilizations have been demonstrated (*4, 51*). The correspondence between the potential for O_2 catalysis and the redox potential of the metal porphyrin indicated that the EC sequence was maintained.

When the metal macrocycles were incorporated into carbon or graphitic matrices, considerable variation was apparent in the potential for oxygen catalysis compared to the redox potential of the catalyst (if it can be determined), particularly when such electrodes were heat treated (*19*). The environment of the metal complex, particularly with respect to the axial ligation, is undoubtedly very critical to the ability of the metal macrocycle to form the O_2 and H_2O_2 complexes and hence, to their ability to activate these species for reduction. In this context, an axial position is "open" for reaction with O_2 in the postulated pentacoordinated, high spin ferrous FeTMPyP. Such an open position would offer a minimal barrier for O_2 to interact with the metal, and thus would favor fast kinetics.

Acknowledgments

We are pleased to acknowledge the support of this work by grants from the U.S. Air Force Office of Scientific Research and the Koppers Co. The research reported is also part of the cooperative program conducted under National Science Foundation/Japan Society for Promotion of Science. Helpful discussions with H. N. Blount, R. Chan, D. DiMarco, Sue Weng, and D. Karweik are hereby acknowledged.

Literature Cited

1. Kuwana, T.; Fujihira, M.; Sunakawa, K.; Osa, T. *J. Electroanal. Chem.* **1978,** *88,* 299.
2. Kuwana, T.; Bettelheim, A. *Anal. Chem.* **1979,** *51,* 2257.
3. Kuwana, T.; Chan, R. J.; Bettelheim, A. *J. Electroanal. Chem.* **1979,** *99,* 391.

4. Kuwana, T.; Chan, R. J.; Bettelheim, A. *J. Electroanal. Chem.* **1980,** *110,* 93.
5. Kobayashi, N.; Fujihira, M.; Matsue, T.; Osa, T. *J. Electroanal. Chem.* **1979,** *103,* 427.
6. Kuwana, T.; Forshey, P. A. *Inorg. Chem.* **1981,** *20,* 693.
7. Kobayashi, N.; Fujihira, M.; Osa, T.; Kuwana, T. *Bull. Chem. Soc. Jpn.* **1980,** *53,* 2195.
8. Kuwana, T.; Forshey, P. A., unpublished data; Forshey, P. A.; Ph.D. Thesis, Ohio State University, March 1982.
9. Jasinski, R. *J. Electrochem. Soc.* **1965,** *112,* 526.
10. Jasinski, R. *Nature* **1964,** *201,* 1212.
11. Jahneke, H.; Schonborn, M.; Zimmerman, G. *Katal. Phthalocyanine Symp.* **1972,** 71–89.
12. Jahneke, H.; Schonborn, M.; Zimmerman, G. *Top. Curr. Chem.* **1976,** *61,* 133.
13. Kozawa, A.: Zilinois, V. E.; Brodd, R. J. *J. Electrochem. Soc.* **1970,** *117,* 1474.
14. Kozawa, A.; Zilinois, V. E.; Brodd, R. J. *J. Electrochem. Soc.* **1971,** *118,* 1705.
15. Bogdanovshaya, V. A.; Tarasevich, M. R. *Elektrokhimiya* **1975,** *11,* 914.
16. Yeager, E. "Electrocatalysis on Non-Metallic Surfaces," *NBS Spec. Publ.* **1976,** No. 455.
17. Zagal, J.; Bindra, P.; Yeager, E. *J. Electrochem. Soc.* **1980,** *127,* 1506.
18. Behret, H.; Binder, H.; Stanstede, G.; Sherer, G. G. *J. Electroanal. Chem.* **1981,** *117,* 29.
19. Van Veen, J. A. R.; Visser, C. *Electrochim. Acta* **1979,** *24,* 921.
20. Ulstrup, J. *J. Electroanal. Chem.* **1977,** *79,* 191.
21. Collman, J. P.; Marrocco, M.; Denisevich, P.; Koval, C.; Anson, F. C. *J. Electroanal. Chem.* **1979,** *101,* 117.
22. Collman, J. P.; Denisevich, P.; Konai, Y.; Marrocco, M., Koval, C.; Anson, F. C. *J. Am. Chem. Soc.* **1980,** *120,* 6027.
23. Fleisher, E. B.; Hambright, F. *Inorg. Chem.* **1970,** *9,* 1757.
24. Pasternack, R. F.; Spiro, E. G. *J. Am. Chem. Soc.* **1978,** *100,* 968.
25. Wilson, G. S.; Neri, B. P. *Ann. N.Y. Acad. Sci.* **1973,** *206,* 568.
26. Pasternack, R. F.; Malek, P.; Spencer, C. *J. Inorg. Nucl. Chem.* **1977,** *39,* 1865.
27. Goff, H.; Morgan, L. O. *Inorg. Chem.* **1976,** *15,* 12.
28. Vickery, L. E.; Nozawa, T.; Sauer, K. *J. Am. Chem. Soc.* **1976,** *98,* 343.
29. Nozawa, T.; Kobayashi, N.; Hatano, M. *Biochim. Biophys. Acta* **1976,** *427,* 652.
30. Randles, J. E. B. *Trans. Faraday Soc.* **1948,** *44,* 327.
31. Sevcik, A. *Collect. Czech. Chem. Commun.* **1948,** *13,* 349.
32. Waldmeier, P.; Sigel, H. *Inorg. Chem.* **1972,** *11,* 2174.
33. Waldmeier, P.; Sigel, H., *Inorg. Chim. Acta* **1971,** *5,* 659.
34. Pasternack, R. F.; Halliwell, B. *J. Amer. Chem. Soc.* **1979,** *101,* 1026.
35. Boyer, P. D.; Lardy, H.; Myrback, K. "The Enzymes," 2nd ed.; Academic: New York, 1963; Vol. 8, p. 257.
36. Littauer, E. L.; Tsai, K. C., *Electrochim. Acta* **1979,** *24,* 351.
37. Boyer, P. D.; Lardy, H.; Myrback, K. "The Enzymes," 2nd ed.; Academic: New York, 1963; Vol. 8, p. 246.
38. Schumb, W. C.; Satterfield, C. N.; Wentworth, R. L. "Hydrogen Peroxide"; ACS MONOGRAPH SERIES No. 128, Reinholt: New York, 1955.
39. Collman, J. P.; Gagne, R. R.; Reed, C. A.; Halbert, T. R.; Lang, G.; Robinson, W. T. *J. Am. Chem. Soc.* **1975,** *97,* 1427.
40. Basolo, F.; Hoffman, B. M.; Ibers, J. A. *Acc. Chem. Res.* **1975,** *8,* 384.
41. Drago, R. S.; Beugelsdijk, T.; Breese, J. A.; Canady, J. P. *J. Am. Chem. Soc.* **1978,** *100,* 5374.

42. Summerville, D. A.; Jones, R. D.; Hoffman, B. M.; Basolo, F. *J. Chem. Educ.* **1979,** *56,* 157.
43. McCandlish, E. M.; Miksztal, A. R.; Nappa, M.; Spencer, A. Q.; Valentine, J. S.; Strong, J. D.; Spiro, T. G. *J. Am. Chem. Soc.* **1980,** *102,*4268.
44. Drago, R. S.; Corden, B. D. *Acc. Chem. Res.* **1980,** *13,* 353.
45. Goddard III, W. A.; Olafson, B. D. In "Biochemical and Clinical Aspects of Oxygen"; Caughley, W.; Caughley, H., Eds.; Academic: New York; 1979, pp. 87–123.
46. Sawyer, D. T.; Seo, E. T. *Inorg. Chem.* **1977,** *16,* 499.
47. Farragi, M.; Bettelheim, A., Nuclear Research Center-Negev, Beer-sheva, Israel, personal communication.
48. DiMarco, D. M.; Forshey, P. A.; Kuwana, T. In "Chemical Modification of Surfaces," ACS SYMPOSIUM SERIES, No. 192, ACS: Washington, D.C., 1982, p. 71.
49. Gubbins, K.; Walker, R. *J. Electrochem. Soc.* **1965,** *112,* 469.
50. Seidell, A. "Solubilities of Inorganic and Metal Organic Compounds", 3rd ed.; Van Nostrand-Reinhold: New York, 1940; Vol. 1, p. 1352.
51. Rocklin, R. D.; Murray, R. W. *J. Electroanal. Chem.* **1979,** *100,* 271.
52. Rohrbach, D. F.; Deutsch, E.; Heineman, W. R.; Pasternack, R. F. *Inorg. Chem.* **1977,** *16,* 2650.
53. Chan, R. J.; Kuwana, T., unpublished data.
54. Pasternack, R. F.; Cobb, M. S. *J. Inorg. Nucl. Chem.* **1973,** *35,* 4327.
55. Van Veen, J. A. Robert, Ph.D. Thesis, University of Leyden, Holland, 1981.

RECEIVED for review August 10, 1981. ACCEPTED November 30, 1981.

Modern Approaches to the Study of Cytochrome Oxidase

Resonance Raman and Magnetic Circular Dichroism Characterization of the Enzyme and Its Derivatives

WILLIAM H. WOODRUFF[1], ROBERT J. KESSLER, NANCY S. FERRIS, and RICHARD F. DALLINGER

University of Texas, Department of Chemistry, Austin, TX 78712

KEVIN R. CARTER, TONI M. ANTALIS, and GRAHAM PALMER[1]

Rice University, Department of Biochemistry, Houston, TX 77005

Resonance Raman (RR) and magnetic circular dichroism (MCD) spectroscopies are applied to problems involving the structures of stable and transient forms of cytochrome oxidase and its derivatives. Results suggest that resting cytochrome oxidase contains its cytochrome a_3 *heme component as hexacoordinated high spin iron(III). The metastable oxygenated cytochrome oxidase derivatives Compound C, pulsed oxidase, and the hydrogen peroxide adduct of the resting enzyme were studied using low temperature solution techniques. Combined RR and MCD results indicate that cytochrome* a_3 *in these intermediates contains iron(III) in its intermediate spin state* ($S = \frac{3}{2}$). *The low-frequency RR spectrum of resting cytochrome oxidase excited within the cytochrome* a_3 *Soret transition reveals features that apparently are not due to the heme, and that bear a striking resemblance to the RR spectra of azurin, laccase, and plastocyanin, suggesting that electron paramagnetic resonance undetectable copper in cytochrome oxidase may have a structure related to type 1 copper. Fundamental features of the*

[1] To whom correspondence should be addressed.

0065-2393/82/0201-0625$09.75/0

molecular and electronic structure of heme a *are discussed in light of their effect on* $\pi \rightarrow \pi^*$ *electronic, RR, and MCD spectroscopies of heme* a *compared to hemes having effective fourfold symmetry. The effect of these considerations on spectroscopic studies of cytochrome oxidase is predicted.*

Cytochrome oxidase (cytochrome c:O_2 oxidoreductase, EC 1.9.3.1) is the terminal oxidase of cellular respiration in all animals, plants, yeasts, fungi, and some bacteria (*1*). The metal sites of the enzyme comprise two heme irons (heme a) and two copper ions per minimum functional unit having a molecular weight of approximately 140,000 Daltons. Commonly employed terminology concerning cytochrome oxidase defines "cytochrome a" as the heme protein subunit or domain in which the heme is apparently low spin under all conditions and inaccessible to ligation by exogenous (nonprotein) ligands, and "cytochrome a_3" as the heme protein component that is reactive with endogenous ligands including the physiological oxidant O_2; this heme site can assume multiple spin states. One of the copper ions, termed Cu_A, is electron paramagnetic resonance (EPR) detectable in the cupric state and generally oxidizes and reduces in concert with cytochrome a. (One of the many controversies associated with this enzyme is the nature of Cu_A: the two most prominent points of view identify Cu_A as either a highly distorted copper(II) site, or as a Cu^+–$\dot{S}R$ structure with a growing suspicion that some compromise structure is the reality. As our results do not address the structure of this center, identification of Cu_A as a nominal copper center is purely for convenience.) The other copper ion, Cu_U, is EPR undetectable in resting (oxidized) cytochrome oxidase, due to antiferromagnetic coupling to cytochrome a_3 (*2*).

The Cu_A site shares some spectroscopic characteristics with type 1 or blue copper proteins, including electronic absorption near 830 nm and a very small copper hyperfine coupling constant. Much less is known spectroscopically about Cu_U, although the absence of evident transitions in the electronic spectrum often is taken to indicate the Cu_U resembles type 2 copper of multi-copper oxidases; however, some very recent EPR data suggest that some structural distortion is present in the Cu_U site.

The many possible combinations of: (1) accessible oxidation states of the four metal centers of cytochrome oxidase and, additionally, of oxygen, (2) multiple spin states, (3) coordination numbers and ligand identities available to cytochrome a_3, and (4) the possible presence and identity of the bridging ligand(s) between cytochrome a_3 and Cu_U present a rich and complex range of mechanistic options in the function of this enzyme. We have found that the combined techniques of reso-

nance Raman spectroscopy (RRS) and magnetic circular dichroism (MCD) represent an exceptionally informative source of structural information on these metal centers, allowing us to choose among the just mentioned possibilities in several stable and transient cytochrome oxidase derivatives. In particular, RRS can distinguish between vibrational modes of cytochrome a and cytochrome a_3 by selective resonance Raman (RR) enhancement in oxidase derivatives where the electronic spectra of the two cytochromes differ. Systems examined include resting (oxidized) and fully reduced cytochrome oxidase, the cyanide and formate inhibitor complexes of the resting enzyme, the carbon monoxide complex of the reduced enzyme, partially reduced cyanide and carbon monoxide derivatives, and the metastable oxygenated intermediates Compound C, pulsed oxidase, and the hydrogen peroxide adduct of resting enzyme. Appropriate heme a model complexes also were examined.

Experimental

Solubilized beef heart cytochrome oxidase was prepared as described elsewhere (*3*). The final precipitate was dissolved in 0.05 *M* Hepes, pH 7.4, containing either of the three detergents: 0.5% Tween-20, 0.5% Brij-35, or 1% dodecyl maltoside; the latter two detergents are nonfluorescent, which facilitates RR measurement. Buffer identity (Brij-35 or dodecyl maltoside) affected certain spectral features. The preparations were frozen and stored at liquid nitrogen temperature until just prior to dilution for RRS study. Total heme concentration in RR samples was approximately 100 μM. Reduced cytochrome oxidase was prepared from the oxidized preparation by the addition of a slight excess of solid sodium dithionite under a nitrogen atmosphere. The oxidation state of the hemes in the RR samples was confirmed by periodically scanning the RR oxidation state marker peak in the 1350–1380-cm^{-1} region. Cyanide and formate derivatives were prepared by previously reported methods (*4*).

Heme a was isolated from outdated cytochrome oxidase preparations by the method of Takemori and King (*5*, *6*). Hemin a chloride (high spin, pentacoordinated) was converted to the desired spin state by metathesis with $AgClO_4$ or $AgBF_4$ in dichloromethane to produce pentacoordinated, intermediate spin ferriheme a. When desired, dimethyl sulfoxide (DMSO) was added to this solution to produce high-spin, hexacoordinated ferriheme a · 2-DMSO. Alternatively, this complex could be produced by direct metathesis in DMSO solution. RR intensities appeared inordinately low in DMSO solution. In some cases, benzene or propylene carbonate was used as solvent in the just mentioned procedures to minimize interference by solvent Raman peaks. Low spin, hexacoordinated ferriheme a derivatives were prepared by addition of appropriate axial ligands (e.g., substituted imidazoles) to the metathesized solutions or by dissolution of the appropriate heme a derivative in pyridine. Reduced heme a derivatives were prepared using a crown ether derivative of dithionite in methanol (*5*, *6*).

For the low temperature (−20°C) experiments, the stock enzyme was diluted with 35% ethylene glycol, 15 m*M* potassium phosphate, pH 7.2 (at −20°C). The MCD and the optical absorption spectra of resting cytochrome oxidase and the mixed-valence carbon monoxide compound were unaffected

by the presence of 35% ethylene glycol. The mixed-valence carbon monoxide compound (*7*) was prepared by incubating the enzyme anaerobically (≤1 ppm O_2) under carbon monoxide, overnight, in the dark, at 19°C. The preparation was cooled to −20°C and the appropriate spectrum recorded. Compound C was then prepared by admitting oxygen and subjecting the enzyme solution to several brief flashes of intense visible light. The material immediately was converted to Compound C as judged by the changes in the optical spectrum in the Soret and visible regions. No changes occurred in the spectrum prior to exposure to the light.

Pulsed enzyme (*8*) was prepared by reduction of the enzyme with 1 m*M* ascorbate in the presence of catalytic amounts of cytochrome c under a nitrogen atmosphere that subsequently was replaced by carbon monoxide. The sample was cooled to −20° and treated as described previously.

The hydrogen peroxide adduct (*9*) was prepared by the addition of a twentyfold excess of hydrogen peroxide to the enzyme at 10°C. This addition led to a shift of the Soret maximum to 428 nm; the α-band moved to 603 nm but was not as intense as the α-band of Compound C. The MCD spectrum was recorded in the absence of ethylene glycol; resonance Raman spectra recorded in the absence and presence of ethylene glycol were identical.

No significant changes in the absorption of any of the intermediates occurred for at least 30 min; typically, the time required to record the MCD and RR spectra was 15 and 30 min, respectively. RR spectra recorded at longer times showed gradual conversion of each intermediate to resting enzyme.

MCD spectra were recorded on a JASCO J500C spectropolarimeter using a magnetic field of 1.2 Tesla. The sample was maintained at −20°C by passing cold nitrogen gas through a jacketed cell holder. Data were recorded using a 2-nm bandwidth, a scan speed of 50 nm/min, and a time constant of 1 s. Each sample was scanned twice with the magnetic field first parallel (H^+), then antiparallel (H^-) to the optical axis and the spectrum calculated as 0.5 ($H^+ - H^-$). Data were transmitted to the laboratory data system for analysis and plotting.

RR spectra were obtained using a SPEX Ramalog EU spectrometer with a cooled RCA C31034A photomultiplier and an ORTEC 9300 photon counting system; excitation at 413.1 nm was provided by a Spectra Physics 171–01 Krypton laser. Samples for RR study were contained in a 2-mm pathlength spectrophotometer cuvette thermostatted as previously stated. The identical sample and cuvette were used to monitor the UV–visible absorption spectra before and after RR spectra were obtained. Raman scattering was observed in 135° backscattering geometry in a plane perpendicular to the polarization of the laser beam. Optical spectra were recorded using either a Cary 210 or Cary 17 spectrophotometer.

Results and Discussion

Heme a Model Complexes. Symmetric metalloporphyrins have the ordering of porphyrin π-orbital energies shown in Figure 1a, where the lowest unoccupied molecular orbital (LUMO) is a degenerate E_g set, the highest occupied molecular orbital (HOMO) has A_{2u} symmetry, and the next lower orbital is A_{1u} (labels assume D_{4h} symmetry). The two members of the E_g set are identical orbitals comprising an 18-atom π-system, which includes the β-carbon atoms of oppo-

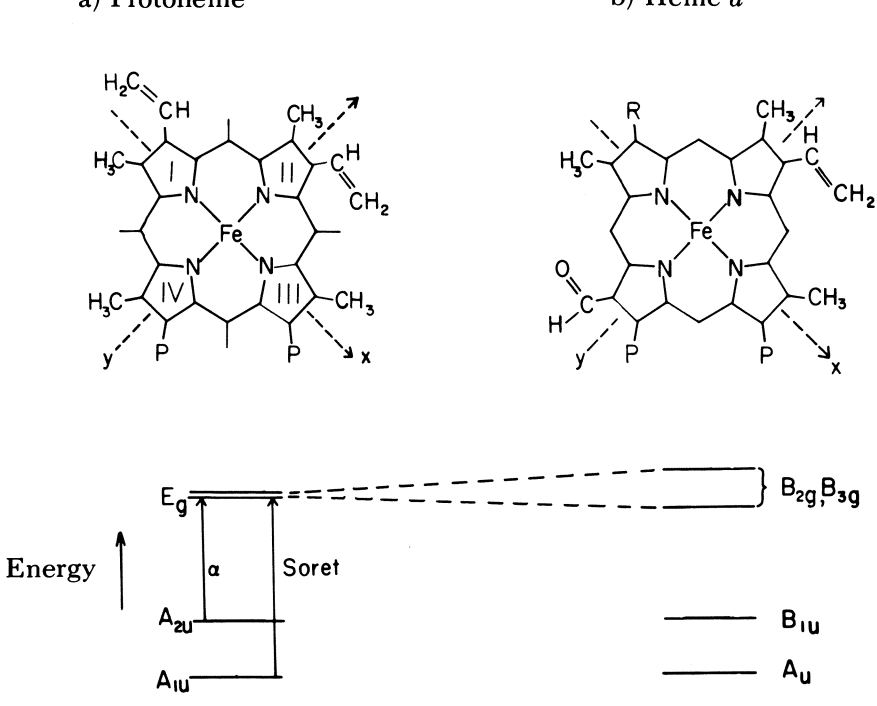

*Figure 1. Molecular and electronic structure (π-orbital energy levels) of symmetric hemes (a, protoheme illustrated) and unsymmetric hemes (b, heme a illustrated) (*See *text). Symmetry labels assume (a) D_{4h} and (b) D_{2h} effective symmetry. Side chain labels: P, propionic acid; and R, a large α-hydroxyl alkyl group the nature of which is discussed elsewhere (*1*).*

site pyrrole rings. Thus, degeneracy of the LUMO does not require full fourfold symmetry of metalloporphyrin substituents, but merely that perturbing groups be distributed symmetrically with respect to the two in-plane Cartesian axes that pass through the porphyrin center and the pyrrole nitrogens (*see* Figure 1). Such is the case with many naturally occurring porphyrins that are substituted on adjacent pyrroles, for example, protoporphyrin IX (Figure 1), mesoporphyrin IX, deuteroporphyrin IX, and others. To a good approximation, all pyrrole substituents where the carbon atom adjacent to the pyrrole is saturated have an identical effect on the porphyrin π-system, regardless of the nature of more distant groups. However, unsaturated substituents that place their own π-systems next to the pyrrole, such as vinyl or formyl

groups, may interact with and perturb the energy of the porphyrin π-system. As noted already, if such a substitution occurs on adjacent pyrroles, the energies of the two members of the E_g set will be perturbed equally and degeneracy of the LUMO will be maintained (as in protoheme, Figure 1a). If, on the other hand, π-active substituents are placed on a single pyrrole or on opposite pyrroles, the energy of the porphyrin π-system along one axis will differ from that along the other, and the degeneracy of the (previously) E_g LUMO will be lifted. Such is the case with heme a (Figure 1b), where all carbon atoms adjacent to the porphyrin are saturated except for the vinyl and formyl groups located on pyrroles II and IV, respectively.

The spectroscopic consequences of degeneracy or nondegeneracy of the heme LUMO are profound. In most hemes (with an E_g LUMO) two purely electronic ($0 \rightarrow 0$) $\pi \rightarrow \pi^*$ transitions are observed, the α-band and the Soret band. Generally a vibronic $0 \rightarrow 1$ sideband on the α-band, denoted the β-band, also is observed. The two $0 \rightarrow 0$ transitions have E_u symmetry and are strongly vibronically coupled, the active coupling vibrations being contained in the product $E_u \times E_u = A_{1g} + A_{2g} + B_{1g} + B_{2g}$ in effective D_{4h} symmetry (*10*). In the RR spectra of symmetric or adjacently substituted metalloporphyrins, vibrational modes having all of these symmetries are resonance enhanced when laser excitation in the region of the α- or β-band is chosen, due to a vibronic coupling, Herzberg–Teller, or "B-term" resonance mechanism (*10, 11*). On the other hand, when laser excitation near the Soret band is chosen, the dominant resonance mechanism is Franck–Condon or "A-term" and only A_{1g} modes are enhanced.

A remarkable consequence of the vibronic coupling RR mechanism in metalloporphyrins is the observation of RR modes with asymmetric or antisymmetric scattering tensors. This effect, first observed by Strekas and Spiro (*12*), is strictly forbidden in normal, nonresonance Raman of solutions because in this nonresonance case the Raman tensor is the classical polarizability tensor, which must be symmetric. In D_{4h} metalloporphyrins, antisymmetric scattering, which is characterized by Raman depolarization ratios ranging from three fourths to infinity, is characteristic of A_{2g} vibrational modes. Thus, these modes are identified easily by the polarization ratio of their scattering. One such mode, denoted "Band IV" (*13*), now is well-established in having its Raman frequency linearly related to metalloporphyrin center-to-nitrogen (Ct–N) distance (core size) (i.e., the distance from the pyrrole nitrogen to the projection of the central metal ion onto the mean plane defined by the four pyrrole nitrogen atoms) for every system so far examined (*see* Figure 2). This correlation is insensitive to other structural features of the molecule (e.g., identity of metal ion, number and identity of axial ligands, etc.) (*13, 14*). Because

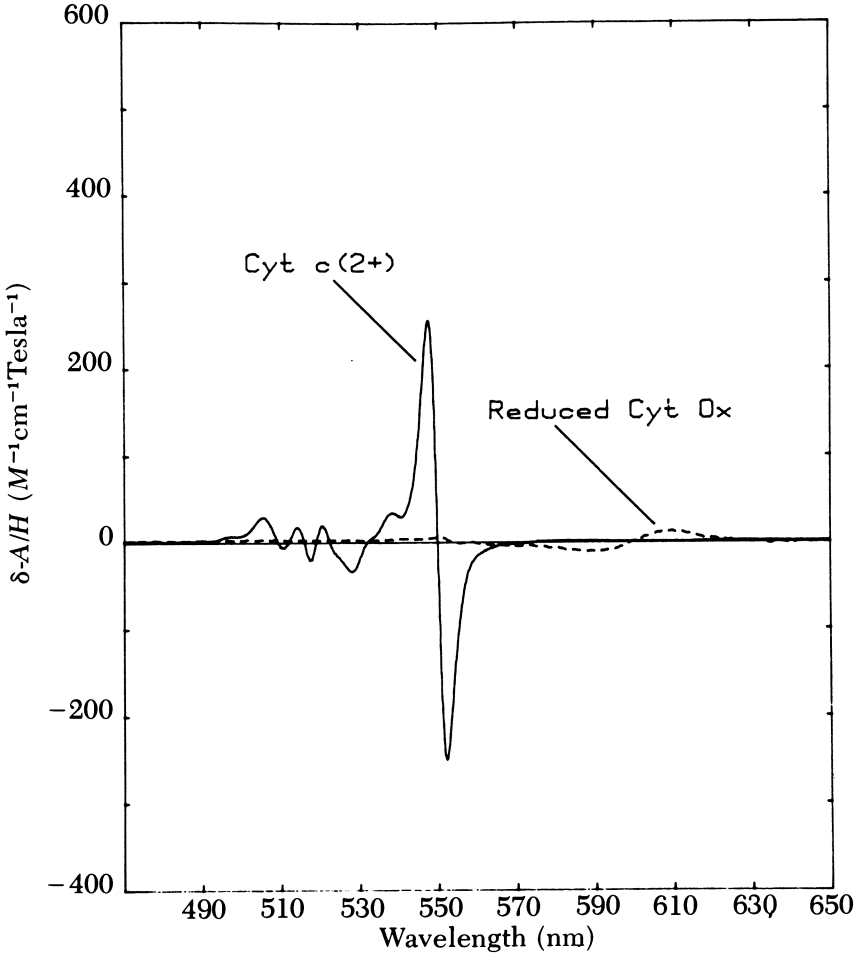

Figure 2. Comparison of the MCD spectra of reduced cytochrome c with that of reduced cytochrome oxidase, illustrating the intense, narrow A-term MCD signal indicating effective fourfold symmetry of the heme of cytochrome c vs. the absence of such a signal, indicating symmetry less than threefold, in cytochrome oxidase.

in iron porphyrins, core size is systematically dependent on spin state of the metal and number of axial ligands, Band IV can be used as a reliable indicator of spin state and coordination number in heme proteins containing symmetrically or adjacently substituted hemes.

The spectroscopic situation differs considerably for hemes such as heme a, which have π-active substituents on opposite pyrroles, or for those hemes substituted on a single pyrrole. Figure 1b shows how the LUMO may be split by such substitution into two nondegenerate, unoccupied orbitals. The representations of these orbitals, assuming

effective D_{2h} symmetry, are B_{3g} and B_{2g}, and their energy ordering is immaterial for the present purposes. In this situation, four $0 \rightarrow 0$ $\pi \rightarrow \pi^*$ electronic transitions are possible, two each of B_{3u} and B_{1u} symmetry. In the RR spectra, only A_{1g} vibrations are enhanced by A-term resonance. Only A_{1g} vibrations are enhanced by B-term resonance involving these nondegenerate transitions, unless the vibronically coupled transitions have dissimilar symmetry. In the latter case, the enhanced vibrations are contained in the product $B_{3u} \times B_{1u} = B_{1g}$. There is no A_{2g} representation in D_{2h} symmetry; A_{2g} in D_{4h} symmetry correlates with B_{1g} in D_{2h} symmetry; therefore, the anomalously polarized (A_{2g}) modes in symmetrically or adjacently substituted metalloporphyrins appear as B_{1g} in D_{2h}. However, B_{1g} in D_{2h} also correlates with B_{1g} and B_{2g} in D_{4h}, and modes having these symmetries (which exhibit depolarized scattering in the more symmetric point group) are free to mix with the formerly A_{2g} modes in D_{2h}. Because of this mixing, two effects are expected. [Both of these effects were noted by others (*15*, *16*), but we first suggested the interpretation of these effects in the context of substituent effects on electronic degeneracy (*17*), and the following elaborates that suggestion.] First, anomalous polarization should be weaker in D_{2h} metalloporphyrins such as heme a than in those with effective D_{4h} symmetry; second, structural correlations such as that of core size with Band IV frequency for D_{4h} metalloporphyrins may be similar superficially, but different quantitatively in the D_{2h} case. The former effect clearly is evident in model studies of heme a using α,β-excitation, where few nonsymmetric vibrations are observed and anomalous polarization, when it occurs, is weak to barely detectable ($0.75 <$ depolarization ratio < 1.0) (*15*, *18*). In particular, Band IV in protoheme derivatives has a depolarization ratio approaching infinity, whereas in heme a the corresponding RR peak has a maximum depolarization ratio of 0.92. Although the second of the just mentioned predictions has not been tested thoroughly using α,β-excitation, existing results (*15*, *18*) support the prediction and results obtained with Soret excitation (*16*, vide infra) confirm the effect for the symmetric vibration corresponding to Band IV.

In addition to rationalizing RR observations, the electronic energy level scheme in Figure 1b accounts for several features of the electronic spectrum of heme a. First, if these energy levels are realistic there should be four $0 \rightarrow 0$ $\pi \rightarrow \pi^*$ transitions rather than the two observed in the D_{4h} hemes. Although this prediction cannot be confirmed in detail because of the present insufficiency of spectroscopic information on heme a, the data that exist (*15*, *16*, *19*) clearly show that the electronic spectra of heme a derivatives are more complex than those of corresponding protoheme and mesoheme derivatives. This finding is the case even for the ferrous hemes where complications of

the spectra due to charge transfer transitions should be minimized. Furthermore, the model (Figure 1b) suggests that the lowest energy $0 \rightarrow 0$ transition should occur at lower energy in D_{2h} hemes (i.e., heme a) than in D_{4h} hemes, because the energies of the occupied molecular orbitals (which involve primarily the inner 16-membered porphyrin ring) will be relatively unaffected by pyrrole substitution, while the more stable member of the split LUMO pair should be lowered considerably in energy compared to the E_g LUMO in the D_{4h} case. This behavior is, of course, quite consistent with the observation of the heme a α-band at ca. 600 nm, which is shifted 40–50 nm to the red compared to symmetric hemes. Finally, the model predicts that the $\pi \rightarrow \pi^*$ transitions will have selective directivity along the in-plane x or y axis (Figure 1) of the porphyrin, because the two nondegenerate unoccupied orbitals involved in $\pi \rightarrow \pi^*$ excitation comprise orthogonal 18-atom π-systems, including opposite pyrrole carbons along the Cartesian axes. One may then expect that RR spectra obtained by exciting a $\pi \rightarrow \pi^*$ transition along one axis will enhance selectively vibrations of the pyrrole rings containing that axis, while excitation of the orthogonal transition will cause enhancement of the vibrations of the other pair of pyrroles. Because the two orthogonal pyrrole pairs are substituted differently, the two sets of RR frequencies need not be the same.

Evidence that this enhancement indeed occurs can be found in the spectra of bis(imidazole) iron(II) (heme a), comparing the results of Babcock et al. (*15*) who used 592-nm excitation with those of Kitagawa et al. (*18*) who used 514.5-nm excitation (the α–β region of the electronic spectrum (*16*) of this heme complex exhibits peaks at 594 nm, $\epsilon = 22$ mM^{-1}cm^{-1}; 540 nm, $\epsilon = 7.1$ mM^{-1}cm^{-1}; and 511 nm, $\epsilon = 7.6$ mM^{-1}cm^{-1}). Table I compares the porphyrin frequencies in the range 1200–1700 cm^{-1} observed in these two studies. Although certain frequencies appear with both excitation conditions (notably the polarized peaks at 1546, 1360, and 1228 cm^{-1}), other modes change between 592 and 514.5 nm (viz., the polarized peak at 1612–1624 cm^{-1} and the anomalously polarized peak at 1581–1592 cm^{-1}). We note the probable consequences of this effect in the study of cytochrome oxidase RRS using α,β-excitation: one must be concerned not only with selective RR enhancement of *either* cytochrome a *or* cytochrome a_3 vibrations as laser wavelength is varied, but also with the possibility of selective enhancement of orthogonal pyrrole modes *within* the heme of a given cytochrome. This complication apparently does not arise when Soret excitation is used, because splitting of the $\pi \rightarrow \pi^*$ transitions is not evident in the Soret region. For the proposed model to be valid, then, the intensity of one of the split $0 \rightarrow 0$ components of the Soret must be much weaker than the other. This condition is reasonable in view of the relative intensities of the α-band and the remaining

Table I. RR Frequencies and Depolarization Ratios ($\rho = I_\perp / I_\parallel$) of Bis(imidazole)Fe(II) (Heme a) in H_2O Using α,β-Excitation Wavelengths (λ_0)

Reference 15[a] $\lambda_0 = 592$ *nm* $\Delta\nu$, cm^{-1} (ρ)	Δ, cm^{-1}	*Reference 18*[b] $\lambda_0 = 514.5$ *nm* $\Delta\nu$, cm^{-1} (ρ)
1612 (0.58)	+12	1624 (p)
1581 (0.92)	+11	1592 (~0.9)
1563, sh	+10	1573, sh
1546 (0.53)	0	1546 (p)
1507 (0.28)	+2	1509 (p)
1468, w	—	—
—	—	1396 (~2)
1391 (0.43)	—	—
1360 (0.42)	0	1360 (~0.4)
1329	+12	1341
1307 (0.95)	+4	1311 (~0.8)
—	—	1245, w
1228 (0.33)	0	1228 (p)

[a] Frequencies are for detergent-dispersed (SDS) heme a (λ_{Soret} = 438 nm).
[b] Frequencies are for aggregated heme a (λ_{Soret} = 453 nm). Aggregation appears not to affect RR frequencies, although intensities are affected (*20*).

structure in the α–β region of ferroheme a. Indeed, there is evidence of a weak feature on the short wavelength side of the Soret peak both in the electronic absorption spectra of heme a derivatives (*15*) and in the MCD spectra of reduced cytochrome oxidase (*21*).

A second striking manifestation of the lowering of the porphyrin symmetry in heme a can be found in a comparison of the MCD spectra of reduced cytochrome c (D_{4h}) and reduced cytochrome a (D_{2h}). The MCD spectrum of c^{2+} exhibits a very intense, characteristically narrow, S-shaped curve (Figure 2), which is known to arise via an MCD A-term (*22a*). The existence of this A-term requires that the LUMO be degenerate as is the case in D_{4h} symmetry (symmetry threefold or higher is required to meet this condition). In cytochrome oxidase, the visible MCD is so weak as almost to be undetectable when presented alongside cytochrome c, a convincing demonstration of the absence of an A-term in either of the two heme a centers. It follows that the heme symmetry is less than threefold, presumably twofold, as we have just stressed. In addition, the change in sign of the MCD dispersion curve between c^{2+} and reduced cytochrome oxidase suggests that the splitting of the LUMO in heme a is greater than the energy difference between the A_u and B_{1u} HOMO's (*22b*).

The RR results of cytochrome oxidase discussed in this chapter are primarily those using direct Soret excitation. Under this condition the Franck–Condon mechanism dominates RR scattering and all observed RR modes are polarized ($\rho \sim 0.33$). The vibrations in the 1000–1700-cm^{-1} region represent primarily C–C and C–N stretching motions of the hemes. Extensive RR studies of heme proteins and model hemes established correlations between these frequencies and structural or electronic parameters of the hemes (*12–14* and ref. therein). These relationships are drawn for D_{4h} hemes just described, generally for α–β-enhanced vibrations; the present case concerns Soret excitation of a D_{2h} heme. Nevertheless, parallels have been established between the RRS of symmetric hemes and heme a/cytochrome oxidase (*16, 17, 23*).

The following discussion concentrates on two primary RR indicator bands of cytochrome oxidase (Figure 3). The first is Band I, the symmetric vibration in the 1350–1390-cm^{-1} region, the frequency of which is sensitive to electron density in porphyrin π^*-orbitals. In practice, Band I is sensitive to two effects: the oxidation state of the metal

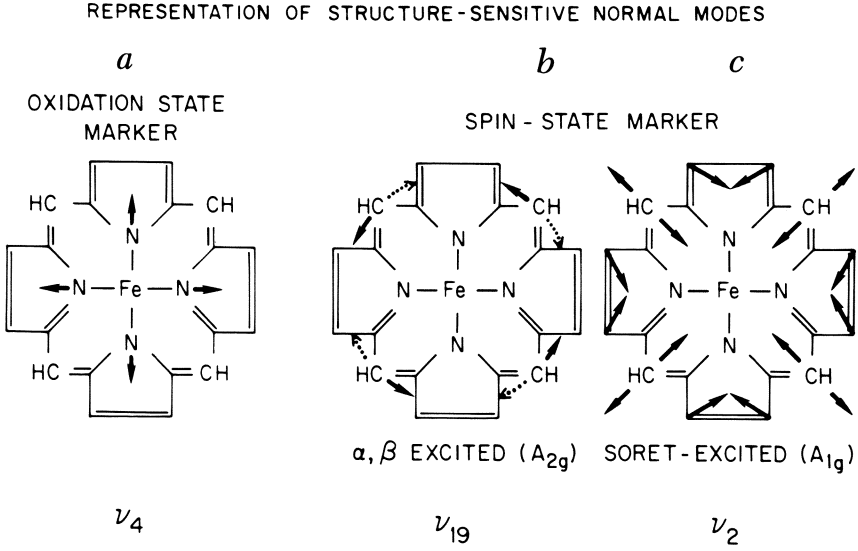

Figure 3. Principal molecular motions contributing to the observed normal vibrational modes of the RR indicator bands: (a) Band I, the polarized oxidation state marker, predominantly symmetric C–N stretch; (b) Band IV, the anomalously polarized core size marker of symmetric metalloporphyrins, predominantly antisymmetric (A_{2g}) stretch of the α-methine carbon bonds resulting in pseudorotation of the methine carbon atoms; and (c) the polarized analog of Band IV in heme a, the symmetric α-methine stretch mixed with the symmetric stretching motion of the pyrrole β–β carbon bonds.

ion, and the presence of axial ligands that have π–acid character and thus may withdraw porphyrin π^*-electron density via the metal (*13*). Figure 4 illustrates typical frequencies of Band I for various iron oxidation states in hemes. Band I is polarized, was assigned as primarily the symmetric C–N stretch (*24*, *25*), and appears in Soret excitation (with residual intensity in the α,β-region) in all hemes including heme a. Its

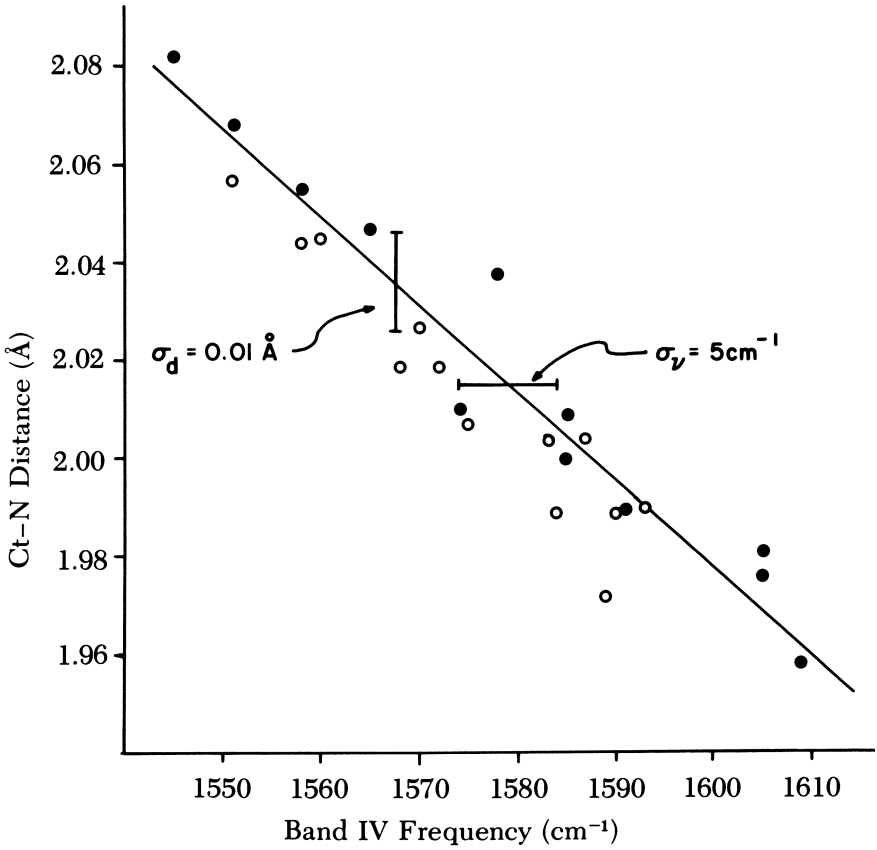

Figure 4. Correlation of the frequency of the anomalously polarized Band IV (see text) of symmetric metalloporphyrins with center-to-nitrogen distance of the porphyrin illustrating the insensitivity of this frequency to structural parameters other than Ct–N. Metals include VO^{2+}, Mn, Fe, Co, Ni, Cu, Rh, Ag, and Sn; axial ligation states include none, one, and two ligands; identity of axial ligands includes F^-, Cl^-, O^{2-}, saturated amines, imidazole, pyridine, phosphites, phosphines, cyanide, and carbon monoxide. Key: ○, iron porphyrins; and ●, non-iron metalloporphyrins.

relationship to oxidation state is the same for heme a as for symmetric hemes in all cases so far tested (*16*).

The second RR indicator band of primary interest here is Band IV, whose relationship to metalloporphyrin Ct–N distance was just discussed and is illustrated in Figure 4. In symmetric hemes, Band IV is anomalously polarized, appears only in α,β-excitation, and is assigned as primarily the antisymmetric stretch of the bonds between the α- and methine carbons (Figure 3). Of course, there is also a symmetric motion involving the α–methine stretch, and the frequency of this mode may be expected to respond similarly to the Ct–N distance as does the true Band IV. Such a relationship has been noted in the Soret excited RR spectra of protoheme-containing proteins (*26*). However, this mode is free to mix with any other symmetric motion of the heme, notably the stretch of the pyrrole bond between the β-carbon atoms (*23*), which cannot contribute to the A_{2g} Band IV in symmetric hemes. Thus, the symmetric Band IV analog may be expected to be: (1) less sensitive to the Ct–N distance because of mixing with peripheral pyrrole motions, and (2) have the slope of its linear dependence on the Ct–N distance (e.g., Figure 3) depend on the identity of pyrrole substituents. From Raman measurements on heme a compounds of known spin state and coordination number, others established (*16, 26*), and we confirmed, that the polarized Band IV analog qualitatively behaves as a reliable core size indicator; however, the dependence of its frequency on the Ct–N distance must be established independently for each set of heme pyrrole substituents from precise x-ray data. This result is illustrated in Figure 5 as a comparison of the dependence of the antisymmetric Band IV on the Ct–N distance vs. that of the polarized Band IV analog of heme a.

Heme a also has an anomalously polarized (B_{1g}) Band IV analog observed in α–β-resonance (*see* Table I) which, because of the nondegeneracy of the electronic transitions just discussed and its ability to mix with other B_{1g} motions, is expected to have its relationship to Ct–N distance affected both by pyrrole substitution and by Raman excitation frequency. Because of insufficient RR studies of heme a using α,β-excitation, this B_{1g} mode cannot be regarded as a useful core size indicator at present.

Magnetic circular dichroism (MCD) also is an extraordinarily selective technique for distinguishing spin states and oxidation states of iron in hemes (*19*). We shall limit the present consideration to MCD of ferric hemes a in the Soret region because this area is related directly to problems concerning cytochrome oxidase discussed later. Figure 6 shows the MCD spectrum of bis(1-methylimidazole) iron(III) (heme a), where the ferric iron is low spin ($S = \frac{1}{2}$). The large amplitude of the MCD signal ($\Delta\epsilon \sim 40\ M^{-1}\text{cm}^{-1}\text{Tesla}^{-1}$) may be noted. The

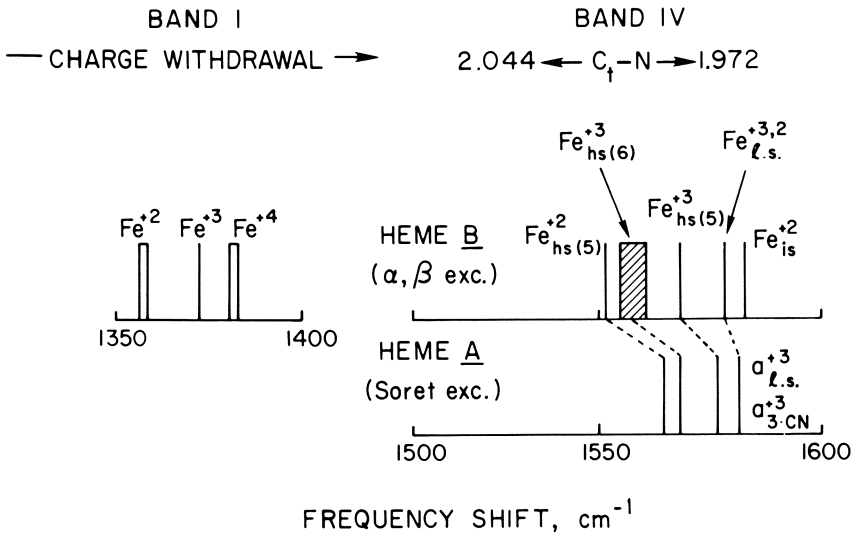

Figure 5. Schematic representation of the frequencies of Band I and Band IV in the RR spectra of symmetric (heme b) and nonsymmetric (heme a) hemes. The Band I frequencies are the same for both classes of hemes.

MCD spectrum of resting (oxidized) cytochrome oxidase is included for comparison. The magnitude of the MCD signal in resting oxidase, per mole of enzyme, is similar to that of low spin ferriheme a despite the fact that the enzyme contains 2 hemes/mol. However, only the heme of cytochrome a is low spin, thus the MCD signal of cytochrome a dominates that of cytochrome a_3 and is the primary contributor to the resting enzyme spectrum. The shift in the MCD spectrum of low spin heme a compared to cytochrome oxidase is consistent with the shift in electronic absorption maximum between the heme a model complex (422 nm) and cytochrome a (427 nm) (*15*, *27*).

The MCD spectra of high spin ($S = \frac{5}{2}$) and intermediate spin ($S = \frac{3}{2}$) ferric heme a model complexes are shown in Figure 7. The pentacoordinated intermediate spin complex, (ferriheme a) · BF_4^-, has essentially no MCD signal in the Soret region. The same is true of the related perchlorate derivative. Two high spin ($S = \frac{5}{2}$) ferriheme a complexes are shown: hemin a chloride, pentacoordinated; and bis(dimethyl sulfoxide) iron(III) (heme a), hexacoordinated. The two spectra are easily distinguishable from one another, but two points must be noted with regard to cytochrome oxidase studies. First, the magnitudes of the MCD signals for the high spin hemes are only ca. 10 M^{-1}

$cm^{-1}Tesla^{-1}$, and therefore the enzyme spectrum is, as noted, dominated by low spin cytochrome a. Second, the high spin MCD signals occur at shorter wavelength than that of the low spin heme a complex, and exhibit a dispersion lineshape opposite in sign to that of the low spin derivative.

We may summarize the complementary nature of the RR and MCD data on heme a model complexes, as they apply to cytochrome oxidase, in the following manner. The RR technique can distinguish between the likely oxidation states of iron. For the ferric oxidation state, RR can distinguish between high spin and low or intermediate spin (Figure 5) and can distinguish between pentacoordination and hexacoordination in the high spin state. The MCD technique also can distinguish oxidation states, and in the ferric state can distinguish unambiguously between low spin and high or intermediate spin. The

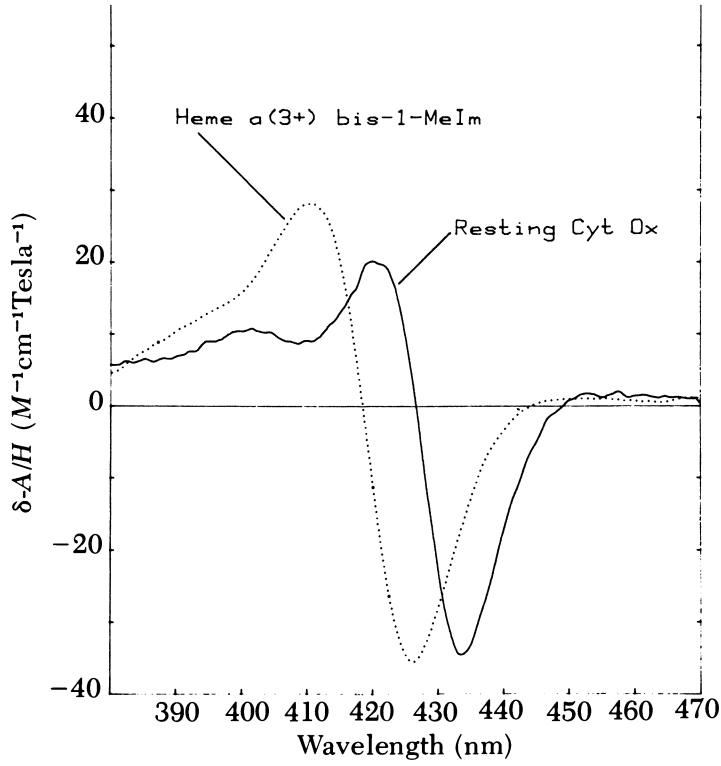

Figure 6. The MCD spectrum in the Soret region of a typical low spin Fe^{3+} heme a model complex, with the MCD spectrum of resting cytochrome oxidase included for comparison. Key: . . . , heme a (3+) bis-1-MeIm; and —, resting cyt ox.

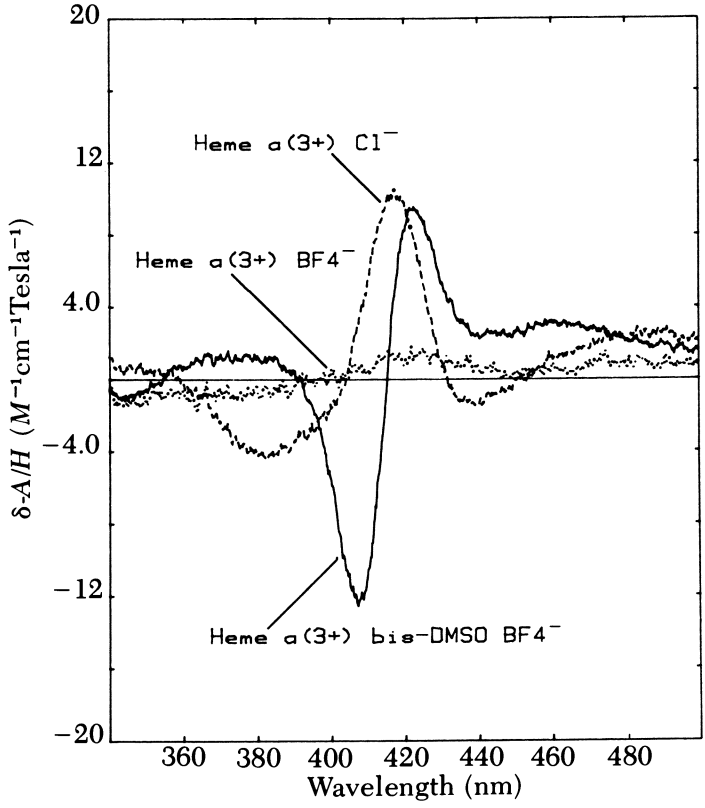

Figure 7. The MCD spectra in the Soret region of heme a model complexes in intermediate spin and high spin states. Both the penta-coordinated and hexacoordinated high spin cases are shown.

intensity of the ubiquitous low spin cytochrome a MCD signal in oxidized forms of the enzyme prevents complete discrimination of spin states by MCD alone. The combination of MCD and RR, however, can make this distinction.

In reduced protein, MCD gives characteristic spectra for high spin ($S = 2$) pentacoordinated heme derivatives (e.g., deoxymyoglobin), and for hexacoordinated low spin hemochromes (e.g., cytochromes a, b, and c). However, complexes with π–acid ligands and cyanide exhibit very weak MCD. The Raman spectra of reduced hemes yield information on the oxidation state; information on the sensitivity of spin state markers to coordination number remains to be established for cytochrome oxidase and heme a derivatives.

Cytochrome Oxidase Resonance Raman. Figure 8 shows the spectra of oxidized and reduced cytochrome oxidase obtained with laser excitation at 413.1 nm. This wavelength is virtually the same as

that assigned to the cytochrome a_3 Soret maximum of oxidized oxidase (414 nm) and near the Soret maximum of oxidized cytochrome a (427 nm) (*21*, *23*, *27*). For reduced oxidase, the position of the Soret maximum is more remote (443 nm), although a weak MCD feature associated with reduced cytochrome a appears at 413.5 nm (*21*, *22a*). Despite the positions of the oxidized and reduced Soret transitions relative to the 413.1-nm laser line, the experimentally observed RR intensities of correlatable high frequency (>1000 cm^{-1}) heme modes essentially are the same in the oxidized and reduced enzyme (*see* Figure 8). This outcome is surprising at first glance, and indeed cannot be accounted for by a simple single state resonance enhancement expression. This point is discussed elsewhere (*17*). The resonance expression:

$$\text{intensity} \propto \frac{\nu_r^4 \epsilon^2}{[(\nu_e - \nu_0)(\nu_e - \nu_r) + \Gamma^2]^2 + (\Gamma \Delta\nu)^2} \quad (1)$$

where ν_e is the electronic transition energy, ν_0 is the laser frequency, ν_r

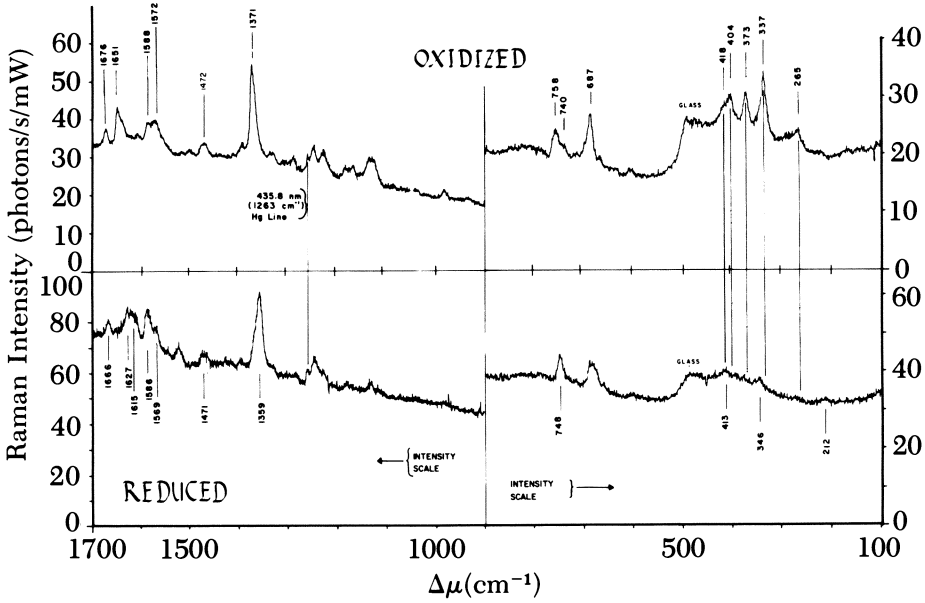

Figure 8. RR spectra of oxidized (unliganded) and reduced cytochrome oxidase obtained by using 413.1-nm excitation. The intensity scales are normalized correctly for laser power and photon-count interval, and the zero of each intensity scale is the true zero of the signal. The spectral region below 900 cm^{-1} was recorded by using a 3-s photon-count interval as opposed to 2 s for the region above 900 cm^{-1}. The adventitious mercury emission line at 1263 cm^{-1} is the 435.8-nm line of the fluorescent room lighting, providing a positive frequency reference.

is the Raman frequency, and $\Delta\nu$ is the Raman shift, correctly predicts the present observation that the Raman scattering intensities of oxidized and reduced cytochrome oxidase are nearly equal when 413.1-nm excitation is employed. (When ν_0 and ν_r are spaced equally on either side of the electronic transition frequency by an amount equal to Γ, the damped resonance term in the denominator vanishes and the quotient is saved from becoming infinite by the "fraternity term" $\Gamma\Delta\nu$.)

The resting enzyme spectrum (Figure 8) differs from that reported in our previous study in that the detergent employed in the present case is dodecyl-β-maltoside rather than Brij-35, which was used in the earlier work. In the previously reported spectra (*17*), features appear at ~1620 and 1518 cm^{-1} which are absent in the present spectra. It has been suggested (*23*) that these features are associated with partial photoreduction of cytochrome oxidase preparations. However, in the spectra obtained in Brij-35 no evidence of photoreduction was apparent, as judged by the absence of any vestige of the ferrous oxidation state indicator at 1358 cm^{-1}. Apparently the 1620 and 1518 cm^{-1} features are sensitive to detergent-related effects as well as photoreduction. A possible explanation is aggregation of the enzyme, which is known to be more extensive in Brij-35 than in dodecyl-β-maltoside (*28*). Studies are underway that will clarify this question (*29*). In any event, the spectrum of resting enzyme (Figure 8) agrees in detail with those obtained under quite different conditions of concentration, detergent, laser power, and sample handling (*15*, *23*).

The low frequency region of the oxidized enzyme shows several prominent peaks below 500 cm^{-1}, yet this region in the reduced protein shows only weak features. Equation 1, which correctly predicts the relative intensities of high frequency heme modes in oxidized and reduced cytochrome oxidase, fails to account for the virtual disappearance of low frequency peaks in the (413.1 nm excited) reduced spectrum. For example, Equation 1 predicts that a 300-cm^{-1} mode of heme a or a_3 should be approximately one-third as intense in reduced oxidase as the analogous mode in oxidized enzyme. The observed intensity difference is at least a factor of ten for the most intense low frequency modes in the oxidized and reduced spectra. This unusual low frequency spectrum is discussed in a subsequent section.

Because of the different Soret absorption wavelengths for cytochrome a and cytochrome a_3 in resting oxidase as well as certain other derivatives, the contributions of the two cytochromes to the oxidase RR spectra can be distinguished by selective RR enhancement using various laser excitation wavelengths (*17*, *23*). Specifically, it was shown (*17*, *23*) that the peak at 1588 cm^{-1} in the resting enzyme spectrum is the low spin core size indicator of cytochrome a and the 1572-cm^{-1} peak is the high spin core size indicator of cytochrome a_3. In addition,

the peak at 1676 cm^{-1} in resting oxidase appears to be a cytochrome a_3 mode exclusively, and was assigned (*20*) as the formyl C=O stretch. This mode functions as a second oxidation state marker, in addition to Band I, shifting to 1666 cm^{-1} in reduced enzyme and specifying the oxidation state of cytochrome a_3. The frequency of this peak, denoted Band VI, only appears to be sensitive to the oxidation state of the iron atom and not to π–acid ligand effects as is Band I (*17*).

The heme a model complex studies (*16*), which we confirmed recently, reveal typical frequencies of the polarized Band IV analog shown in Figure 5 and summarized as follows: low spin iron(III), 1588–1590 cm^{-1}; high spin, pentacoordinated iron(III), 1580–1581 cm^{-1}; and high spin, hexacoordinated iron(III), 1572 cm^{-1}. From measurements on the enzyme, it is found that high spin, presumably pentacoordinated iron(II) has its core size marker at 1568 cm^{-1}. By these criteria, the heme of cytochrome a_3 in resting oxidase must be regarded as high spin, hexacoordinated iron(III). In the reduced enzyme, where cytochrome a_3 is pentacoordinated, EPR spectra of the nitrosyl derivative of reduced enzyme (*30*) and of derivatives of ^{14}N- and ^{15}N-histidine-substituted yeast submitochondrial particles establish clearly that histidine is the proximal axial ligand in reduced cytochrome a_3.

We reported the RR spectra of the formate and cyanide inhibitor complexes of resting cytochrome oxidase (*17*). Except for minor changes in some RR intensities, the spectrum of the formate complex is indistinguishable from that of the resting enzyme. Thus, cytochrome a_3 in the formate adduct still is hexacoordinated, high spin, and formate, if it binds to iron, must replace one of the endogenous ligands. The ligand replaced could be the histidine residue presumed to be present in the resting (as in the reduced) enzyme. Alternatively, the amino acid or other moiety responsible for propagating the antiferromagnetic coupling between Fe_{a3}^{3+} and Cu_U^{2+} might be replaced with formate, maintaining the antiferromagnetic coupling required by the EPR silence of Cu_U^{2+}. A third possibility is that formate does not bind to the heme iron at all, but instead binds to Cu_U^{2+}. It was established recently (*31*) that, in the reduced enzyme, Cu_U^{+} has a coordination site available and binds exogenous carbon monoxide.

The cyanide adduct of resting cytochrome oxidase exhibits the changes expected in the RR spectrum on the transition of cytochrome a_3 to low spin ferric heme a (*17*). The 1572-cm^{-1} peak vanishes, and the 1588-cm^{-1} peak becomes relatively more intense. Other small frequency shifts occur in the high frequency region (>1000 cm^{-1}). In the low frequency region, the prominent peaks below 500 cm^{-1} in resting enzyme still are visible in the cyanide adduct, but are reduced in intensity by approximately a factor of five. Accordingly, the 346-cm^{-1}

heme a mode (vide infra) becomes visible alongside of the 337-cm^{-1} peak, which is the most intense low frequency feature in the resting oxidase spectrum.

Finally, the Band I position in resting cytochrome oxidase (1371 cm^{-1}), when viewed in comparison with Band I frequencies of heme protein systems thought to contain iron(IV) (~1380 cm^{-1}, *see* Figure 5) (*32*), appears inconsistent with the formulation of a_3 in resting cytochrome oxidase as iron(IV), Cu_D^{2+} (*33*). Further details of the relationships of the cytochrome oxidase RR features to those of other heme proteins are discussed elsewhere (*16, 17, 23*).

Metastable Oxygenated Cytochrome Oxidase Derivatives. One approach to the elucidation of the mechanism of oxygen reduction by cytochrome oxidase, developed by Chance et al. (*34, 35*), employed low temperature trapping techniques to stabilize putative intermediates in the overall reoxidation process. Using these methods, a number of spectral intermediates were observed during the reoxidation of four-electron, fully reduced and two-electron, partially reduced (mixed-valence) cytochrome oxidase, viz:

$$\begin{array}{lccccc} \text{fully reduced} \rightarrow & & \text{I} & \rightarrow \text{II} \rightarrow & \text{III} & \dashrightarrow \\ \text{enzyme} + \text{O}_2 & & (\text{A}_1) & & (\text{B}) & \\ \text{mixed-valence} \rightarrow & & \text{I}_\text{M} & \rightarrow \text{II}_\text{M} \rightarrow & \text{III}_\text{M} & \dashrightarrow \\ \text{enzyme} + \text{O}_2 & & (\text{A}_2) & & (\text{C}) & \end{array}$$

The intermediates are designated as suggested by Clore et al. (*36*) with the nomenclature employed by Chance et al. (*34*) shown in parentheses. The broken arrows lead to the fully oxidized enzyme, as judged by the restoration of the EPR signals of cytochrome a^{3+} and Cu_D and the 655-nm absorbance band (*37*). However, this oxidized form of the enzyme, which can be formed within 6 ms at room temperature, differs from the resting enzyme in that it exhibits an unusual EPR spectrum (*37*) and appears to be related to, if not identical with, the pulsed oxidase (*38*).

Most of these low temperature studies exploit absorption spectrophotometry as the primary analytical tool. Unfortunately, this technique, in general, has a relatively low content of structural information, and, as a consequence, conclusions as to the chemical nature of the observed intermediates have been speculative and tenuous.

In an attempt to overcome this limitation, we combined the low temperature trapping procedure with MCD and RR measurements, which potentially can yield much more reliable, structurally relevant data. The results lead to important constraints on the valence and spin states of several oxidized derivatives: (1) Compound C, the oxidation product of two-electron reduced enzyme; (2) the pulsed oxidase, the

product of oxidation of four-electron reduced enzyme; and (3) the recently reported hydrogen peroxide adduct of cytochrome oxidase (9).

The MCD spectrum of resting cytochrome oxidase in the Soret region (Figure 6) is typical of a low spin ferrihemoprotein, and was assigned to cytochrome a^{3+} on the basis of inhibitor studies and from correlations with the optical spectra of the two hemes (*27, 39*). Conversion to the mixed-valence carbon monoxide compound (Figure 9) leads to small increases in MCD at all wavelengths, although there was no gross change in spectral shape. The same spectrum was obtained with spectral bandwidths ranging from 0.5 to 2.0 nm, suggesting little or no photodecomposition of the sample under the experimental conditions. The difference spectrum between these two species represents the difference $a_3^{2+} \cdot CO - a_3^{3+}$ and makes only a small contribution to the total MCD spectrum, as reported previously (*39*). Photolysis in the presence of oxygen leads immediately to the quantitative production of Compound C, as judged by the optical spectrum in the Soret and 600-nm regions. The MCD of this species (Figure 9) is not different significantly from that of the resting enzyme and is clearly smaller

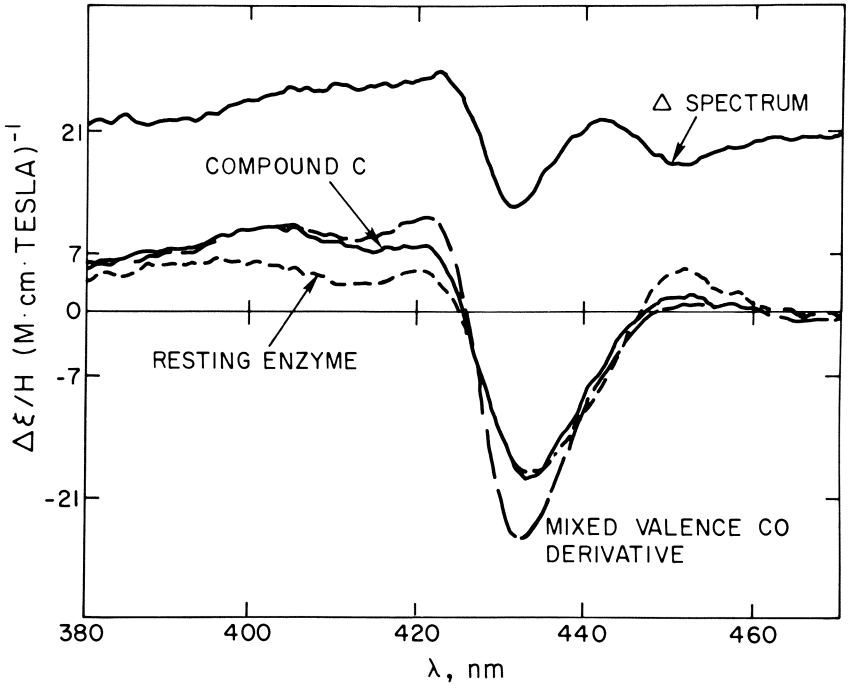

Figure 9. The MCD spectrum of Compound C (see text). The MCD spectra of resting cytochrome oxidase and the starting material for Compound C, the partially reduced mixed-valence carbon monoxide derivative of cytochrome oxidase, are included for comparison.

than that of the partially reduced carbon monoxide derivative used in its formation, although Compound C does appear to have additional small MCD intensity between 400 and 420 nm.

Similar small changes in the MCD spectrum were observed in the visible region. Furthermore, no significant differences were observed between 700 and 1000 nm, but as the quality of the data was relatively poor, we only can state that no major changes occurred in this spectral region. The MCD spectra of pulsed oxidase and the oxidase hydrogen peroxide adduct also almost were indistinguishable from resting enzyme. As both low spin ferric heme a and high spin ferrous heme a exhibit substantial MCD ($\Delta\epsilon$/Tesla = 20–80) (*39*), we conclude that in all three derivatives the spin state of cytochrome a_3 must be different from either of these two possibilities.

The RR spectra of cytochrome oxidase and some of these derivatives are shown in Figure 10; some Raman frequencies are summarized in Table II. Attention now is focused on two regions of the spectrum. With 413.1-nm excitation, the contribution of cytochrome a_3 to the RR spectrum is accentuated because of the relative positions of the Soret maxima of a_3 (414 nm) and a (427 nm) (*23*, *27*). The core expansion region in the RR spectrum of the resting oxidase shows two bands at 1572 cm^{-1} (high spin a_3^{3+}) and 1588 cm^{-1} (low spin a^{3+}) (*40*). The oxidation state marker is at 1372 cm^{-1}, establishing that the hemes are ferric.

In the derivatives characterized in this study, both hemes exhibit their Soret maximum at 428 nm. We therefore anticipate that they will contribute comparable intensities to the RR spectrum regardless of spin state, as is observed in the fully reduced enzyme (*23*), where both

Table II. Selected Raman Frequencies ($\Delta\nu$, cm^{-1}) for Cytochrome Oxidase and Some of Its Derivatives

Resting	*Pulsed*	*Compound C*	*H_2O_2 Adduct*
1372	1372	1374	1374
1470[a]	1470	1470	1470
—	—	1504	—
1572	—	sh	sh
1588	1591	1593	1592
—	1642	1644	1644 (sh)
1651	1651	1651	1652
1676	1676	1676	1676

[a] The peak at ~1470 cm^{-1} is a combination of an oxidase peak and an ethylene glycol peak in the low temperature spectra (pulsed and Compound C).

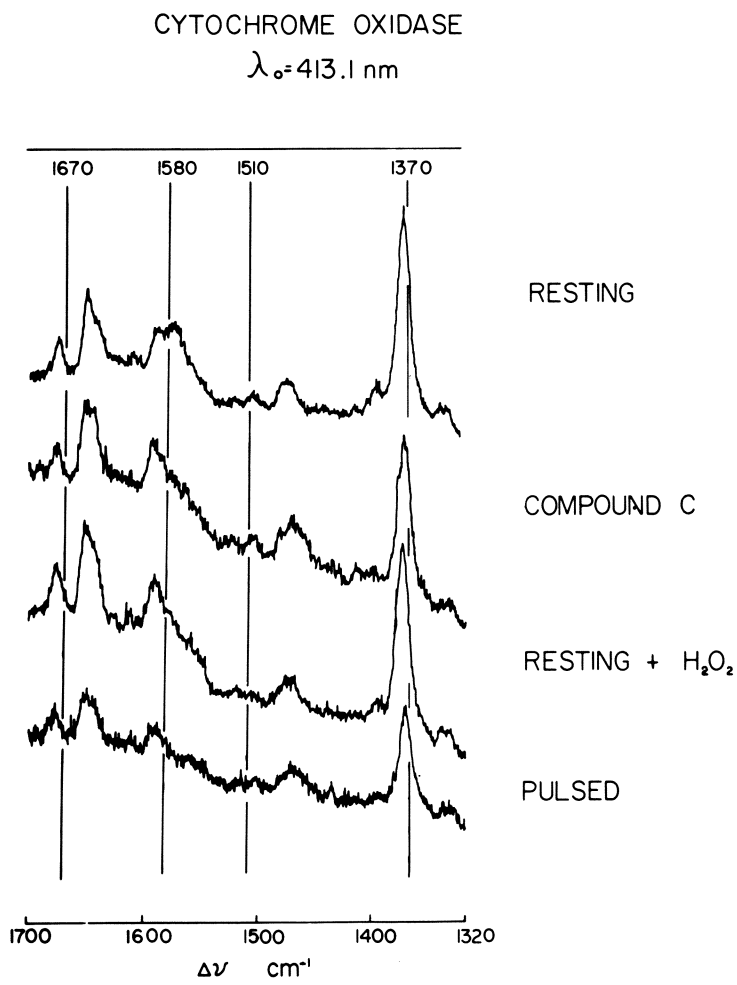

Figure 10. RR spectra in the 1300–1700-cm^{-1} region of resting cytochrome oxidase, Compound C, the H_2O_2 adduct of resting oxidase, and pulsed oxidase.

hemes have their Soret maximum at 443 nm. Consequently, our interpretation only depends on well-established correlations.

On conversion to Compound C, the oxidation state marker clearly lies at 1374 cm^{-1}, thus a_3 is oxidized. This conclusion is confirmed with the high frequency oxidation marker, which appears at 1676 cm^{-1}. The spin state marker lies at 1590–1592 cm^{-1}. The gradual slope on the low frequency side of the 1592-cm^{-1} peak in the spectrum of Compound C and the hydrogen peroxide adduct is an incipient shoulder due to the slow reappearance of the 1572-cm^{-1} line (a_3^{3+}, high spin) of resting

oxidase (*see* "Experimental" section). Thus, in this derivative a_3 cannot be high spin iron(III) or high spin iron(II), which have RR frequencies at 1572 and 1568 cm^{-1}, respectively. Rather, the core expansion marker implies that the Ct–N distance is small, consistent with the following alternatives for a_3:iron(II) (l.s.), iron(III) (l.s., i.s.), iron (IV) (l.s., h.s.), where l.s., i.s., and h.s. refer to low, intermediate, and high spin, respectively.

No obvious differences could be observed between the RR spectra of Compound C, pulsed oxidase, and the hydrogen peroxide adduct (Figure 10, Table II), despite the clear difference in chemical heritage of the three derivatives.

Together, the MCD and Raman data indicate that cytochrome a_3^{3+} cannot be high spin iron(III) (Raman), isolated low spin iron(III) (MCD) or high spin iron(II) (MCD, Raman). The high value for the core expansion marker implies that electron occupation of the in-plane, *d*-electron, σ-antibonding orbitals is minimal, and thus we conclude that cytochrome a_3 is iron(II) (l.s.), iron(III) (i.s.), iron(IV) (l.s. or h.s.), or iron(III) (l.s.) in a special environment.

Combining these conclusions, we are led to the following four alternatives for the states of cytochrome a_3 and Cu_U:

	Cytochrome a_3		Cu_U	Total *S*
1.	$Fe^{2+} \cdot O_2$		Cu^{1+}	0
2.	Fe^{4+} (S = 1,2)		Cu^{1+}	1 or 2
3.	Fe^{3+} ($S = \frac{1}{2}$)	$\leftrightarrow$	Cu^{2+}	0 or 1
4.	Fe^{3+} ($S = \frac{3}{2}$)	$\leftrightarrow$	Cu^{2+}	1 or 2

All other combinations would seem to be excluded by the spectroscopic results. No unequivocal discrimination between these four alternatives can be made with the available data. However, as the derivatives studied appear to be terminal species in the overall reoxidation process, the first alternative, which is formally the initial Michaelis complex of enzyme and oxygen, would seem implausible.

This conclusion is confirmed in the behavior of the Raman peaks in the 1666–1676-cm^{-1} region, which recently were established as a reliable oxidation state marker for cytochrome a_3, independent of π-ligand withdrawal effects (*23*). The derivatives of interest exhibit their peaks at 1676 cm^{-1}, consistent with a_3 being in the iron(III) state. Moreover, significant differences were observed (*34*) in the absorption spectra of the putative oxidase–oxygen Michaelis complex (Compound A_2) and Compound C.

The second alternative that involves the iron(IV) redox state seems unlikely in view of the location of the oxidation state marker at 1372 cm^{-1}, a value typical of iron(III), rather than 1380–1382 cm^{-1} as

was suggested for iron(IV) (*32*). However, a final decision on this conclusion must await Raman measurements on authentic high spin iron(IV) model heme compounds.

The two remaining possibilities invoke magnetic coupling between the two centers, and hence imply a close geometric relationship. In Structure 3, Compound C is represented as a binuclear complex of low spin iron(III) with Cu_U^{2+}. This alternative is not eliminated immediately by MCD, which only reliably detects paramagnetic low spin ferric hemes, and in Structure 3 the heme is diamagnetic in the ground state. However, the absence of any measurable MCD implies that the antiferromagnetic exchange interaction must be extremely large as the excited state also should yield strong MCD, as evidenced by the substantial intensity associated with the cytochrome oxidase · cyanide derivative (*21*, *22a*).

These considerations provide a rationale for removing Structure 3 from further consideration, and thus we are left with Structure 4 as the most plausible alternative. In this structure, cytochrome a_3 is in the intermediate ($S = \frac{3}{2}$) ferric spin state and must be coupled magnetically with Cu_U, either ferromagnetically to yield a total spin of 2, or antiferromagnetically to yield a spin of 1. We previously pointed to the numerous examples of antiferromagnetic systems in metalloproteins and the absence of any bonafide examples of ferromagnetism (*2*).

The structure is supported by the value of the oxidation state marker, which requires that the iron be iron(III); it will lead to a small Ct–N distance for the a_3 heme, and hence a high value for the Raman spin state marker, and it is consistent with the MCD results. Consequently, it would seem that Structure 4 provides the best interpretation of the available spectroscopic data.

This conclusion naturally leads to the nature of the transition involved in the conversion of the active pulsed enzyme to the resting species viz:

$$\underset{\text{(pulsed)}}{a_3^{3+}\ (S = \tfrac{3}{2}) \cdot Cu_U^{2+}} \rightarrow \underset{\text{(resting)}}{a_3^{3+}\ (S = \tfrac{5}{2}) \cdot Cu_U^{2+}}$$

Thus, relaxation to the resting enzyme might well be a consequence of a structural perturbation at the heme, which leads to a change in spin state of the iron from intermediate to high spin with an associated loss in reactivity and the well-known spectroscopic changes.

The structural nature of the proposed intermediate spin, oxygenated species is, at present, an open question. However, recent studies report (*41*, *42*) the formation of oxygenated model heme complexes on formal addition of oxygen to an iron(I) porphyrin, by one-electron reduction of a iron(II) porphyrin–O_2 adduct, or by addition of O_2^- to a iron(II) porphyrin. An equivalent process in terms of total redox

equivalents would be the addition of peroxide to a iron(III) porphyrin, which was not accomplished in the model systems. Each of the three species reported was characterized as a high spin, pentacoordinated iron(III) porphyrin peroxide adduct where the O_2^{2-} is bound to the iron in a symmetric bihapto manner with the O–O axis parallel to the heme plane (*41*, *42*). Compound C and the hydrogen peroxide adduct of resting oxidase are equivalent to these model peroxide adducts in terms of total redox stoichiometry, if Compound C is viewed as the one-electron reduction (by Cu_B^+) product of the initial (ferrous cytochrome a_3) · O_2 Michaelis complex. The model complexes are high spin, but they lack a ligand *trans* to the peroxide. The presence of such a *trans* ligand, which must be at least potentially present in cytochrome a_3, might result in the proposed intermediate spin oxygenated cytochrome oxidase species. However, the similarity of the MCD and RR spectra of pulsed oxidase to those of Compound C and the hydrogen peroxide adduct must be regarded as a serious drawback to any presumed similarity of the oxygenated enzyme species to the model complexes just described, because pulsed oxidase is a total of two electrons more reduced than either Compound C or the hydrogen peroxide adduct.

The Low Frequency Resonance Raman Spectrum of Cytochrome Oxidase and the Nature of EPR Undetectable Copper. The 100–1000-cm^{-1} region of the RR spectrum of resting oxidase contains an impressive number of strong features (Figure 8). The 758- and 687-cm^{-1} peaks are observed at similar frequencies in all metalloporphyrin spectra. The lower frequency region (<500 cm^{-1}) sits atop a broad baseline excursion that is due to the Suprasil cell window material of the observation cuvettes. With the exception of the peak at 265 cm^{-1}, none of the features below 500 cm^{-1} was observed in previously published data using either 600.0- (*43*) or 441.6-nm (*44*) excitation. The enhancement of these modes therefore is unique for the present excitation condition. From this result, and the observation that the low frequency RR spectrum essentially disappears on selective reduction of cytochrome a_3, it may be concluded that the modes below 500 cm^{-1} are vibrations of, or are coupled to, the cytochrome a_3 chromophore.

In contrast to their intensity in resting oxidase, the low frequency peaks essentially disappear in reduced oxidase and have sharply reduced intensity in the cyanide adduct. In principle, this effect might be rationalized with respect to the resting → cyanide transition by presuming that the peaks in question represent out-of-plane normal modes that have appreciable Raman intensity in nonplanar, high spin heme a, but are weak or Raman inactive in the planar, low spin case. However, this does not explain the behavior on reduction because the a_3 heme is high spin and nonplanar in reduced oxidase (as evidenced

by Band IV positions). Moreover, calculations based on Equation 1 predict reduction in intensity of low frequency cytochrome a_3 modes from oxidized to reduced oxidase, but only by a factor of three rather than the observed factor of ten or more. As predicted by Equation 1, high frequency heme modes are equally intense in both oxidized and reduced oxidase. It is quite unexpected that the intensity of heme modes in the high frequency range follow Equation 1, while heme modes at a lower frequency do not. One possible explanation is that the low frequency modes in resting oxidase are not due to heme explicitly, but instead are associated with an axial group(s) ligated to the iron. If this explanation is correct, the observed modes may be due to the bridge between the a_3 heme and Cu_U^{2+}, or even the Cu_U^{2+} structure itself (*33*, *45*). The low intensity of the low frequency modes of the cyanide adduct and their disappearance on reduction may then be related to the weaker axial electronic interactions (which are reflected in the small antiferromagnetic coupling constant for the a_3^{3+}–Cu_U^{2+} interaction) in low spin cytochrome a_3 (*2*), and the absence of such interactions in the reduced enzyme.

To test whether or not the low frequency cytochrome a_3 RR spectrum may be due to axial nonheme structures, the low frequency RR spectra of several heme a model complexes that have spin and ligation states that may occur in resting oxidase were examined. A typical spectrum, that of bis(DMSO)Fe^{2+} (heme a) [which contains high spin, hexacoordinated Fe(III)] is shown in Figure 11 (bottom trace). The spectra of high spin, pentacoordinated and low spin, hexacoordinated ferric heme a are similar. Only two RR modes of significant intensity are observed, at 346 and 265 cm^{-1}, with approximately equal intensity. The 265-cm^{-1} mode corresponds to the weak feature of similar frequency observed in cytochrome oxidase (Figure 11). The 346-cm^{-1} mode does not correspond to the peak at 337 cm^{-1} observed in cytochrome oxidase with 413.1-nm excitation. This can be seen by comparing the relative intensities of the 265- and 346-cm^{-1} peaks in the spectrum of the model heme with the relative intensities at 265 and 337 cm^{-1} in cytochrome oxidase.

There is a cytochrome oxidase mode that corresponds to the 346-cm^{-1} heme a peak. It is the 346-cm^{-1} mode that is observed in both oxidized and reduced oxidase when 600- or 441.6-nm excitation is employed. The 346-cm^{-1} peak only can be observed using 413.1-nm excitation if the 337-cm^{-1} intensity is attenuated by the addition of cyanide. The 337-cm^{-1} peak and the remaining features that are observed in cytochrome oxidase but absent in heme a (373, 404, and 418 cm^{-1}) must (unless the protein has an unprecedented and highly selective effect on heme RR intensities) be due to vibrations of nonheme structures other than the porphyrin macrocycle.

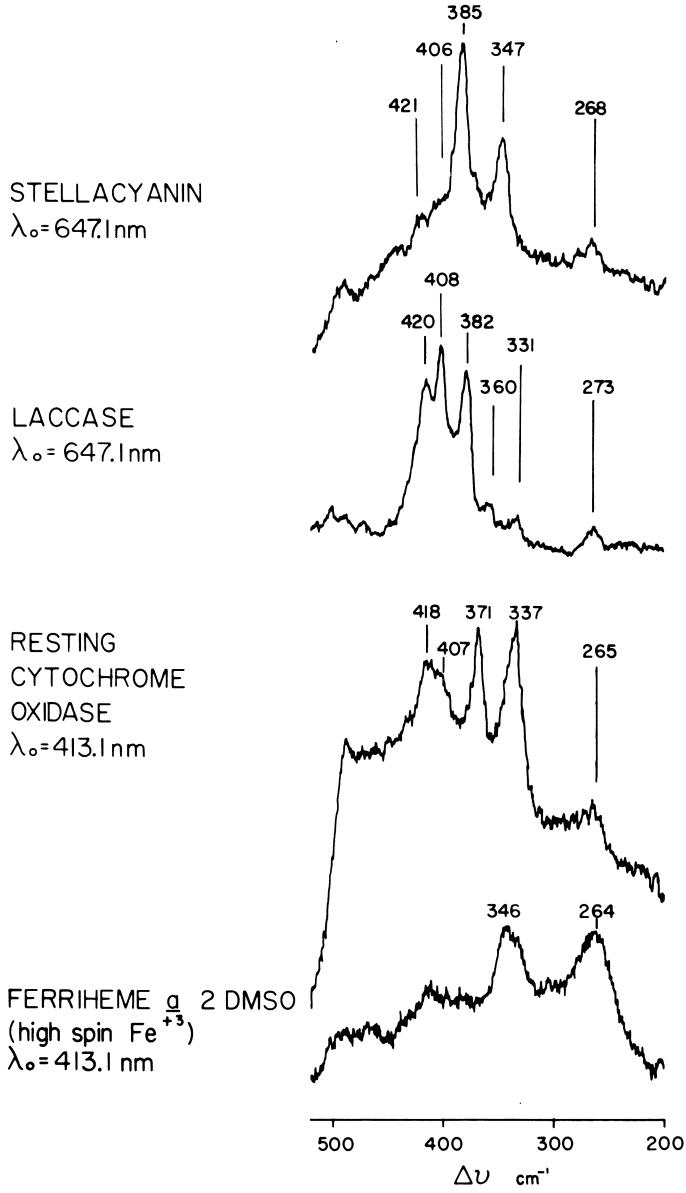

Figure 11. The low frequency (200–500 cm^{-1}) RR spectrum of resting cytochrome oxidase using direct cytochrome a_3 Soret resonance (413.1 nm) compared to the hexacoordinated, high spin heme a model complex, and the blue copper centers (S → Cu LMCT resonance, 647.1 nm) of laccase and stellacyanin.

One or two of these low frequency modes might be associated with the stretching vibrations of iron–(axial ligand) bonds. One of these ligands is probably histidine imidazole (*30, 46*). However, it is unlikely that any of the modes observed in resting oxidase are due to the Fe^{3+}–N (Im) stretch. In deoxymyoglobin, this mode appears at 221 cm^{-1}; in ferri-HRP it appears at 274 cm^{-1}; and in bis(imidazole)Fe (OEP) it appears at 290 cm^{-1} (*47–49*). By analogy to other ferriheme–imidazole systems, therefore, the 373-cm^{-1} and higher frequencies are unlikely to be an Fe^{3+}—N(Im) stretch in resting enzyme (*47–49*). The peak observed at 212 cm^{-1} in reduced oxidase is a reasonable candidate for the vibration of Fe(II)–N(Im) bond.

The frequency range of the observed peaks, 337–418 cm^{-1}, might be consistent with an axial oxide ion bridging Fe^{3+} and Cu_C^{2+}, but our isotope studies argue against such an assignment (*23*). Dissolution of a pelleted resting oxidase preparation in 90% $H_2{}^{18}O$, followed by a 16-h incubation at 0°C, produced no detectable changes in RR spectrum. (The $H_2{}^{18}O$ and $H_2{}^{16}O$ spectra were compared by digital subtraction of the spectra using a microprocessor-controlled recorder.) This result is consistent with (but does not prove) the absence of a a_3^{3+}–O^{2-}–Cu_C^{2+} bridge; it does, however, make it unlikely that an oxide bridge is responsible for any of the observed low frequency modes. Other possible candidates for the bridging group include imidazolate (his), phenolate (tyr), and thiolate (cys). Bridging imidazolate is not expected to have Fe–N frequencies very different from imidazole. Tyrosinate might have Fe–O frequencies near 400 cm^{-1}, but the Fe–O stretch in transferrin is not observed (*50*) and thus, such an axial mode also might be weak in the present case. However, there is good precedent for assigning one of the observed cytochrome oxidase peaks as an Fe^{3+}–$^-$SR stretch. The RR spectrum of cytochrome P-450 (cam) shows an intense peak at 351 cm^{-1} that was assigned (*51*) as an Fe–N(Im) stretch. However, in light of the heme–imidazole data (*47–49*) noted already, and more recent extended x-ray absorption fine structure (EXAFS) studies of P-450 (cam) (*58*), this mode is almost certainly an Fe–S (cys) stretch. In addition, the Fe^{3+}–S (cys) frequencies in adrenodoxin and HIPIP (*52*) are 350 cm^{-1} and 358 cm^{-1}, respectively; axial ferriheme ligands similar to RS^-, viz., Cl^- and Br^-, have Fe–X frequencies of 364 cm^{-1} and 279 cm^{-1}, respectively (*47–49*). Thus, the RR data are consistent with the identity of the bridging ligand in resting oxidase as being thiolate (cys), and the 337-cm^{-1} mode is a reasonable candidate for axial Fe–S stretch.

Figure 11 includes a comparison of the resting cytochrome oxidase RR spectrum with the RR spectra of the type 1 copper centers in laccase and stellacyanin. There is a striking similarity between the spectrum of the resting oxidase, minus the 337-cm^{-1} peak, and the

laccase type 1 spectrum. If the iron–(bridging ligand) vibration in oxidase is assigned to one of the higher frequency (>400 cm^{-1}) modes, the remaining spectrum resembles stellacyanin in the 300–400-cm^{-1} region. This resemblance was noted previously (*17, 45*). Thus, the RR data suggest that Cu_U resembles a type 1 or blue copper center. This observation is remarkable because the excitation wavelength, 413.1 nm, is in resonance with the heme Soret absorption, and not with the characteristic blue copper transition, which is centered at 600 nm (note the excitation wavelength, 647.1 nm, for the laccase and stellacyanin spectra). One of two mechanisms might provide enhancement of copper-associated modes under this resonance condition. First, strong electronic interactions between the heme and copper, promoted by antiferromagnetic coupling, might allow the copper-associated vibrations to be coupled to the heme Soret transition. Second, the copper center itself might have an electronic transition near 400 nm that is buried beneath the heme Soret but that is strong enough to provide significant enhancement of copper–ligand modes. Concerning the latter possibility, it should be noted (1) that blue copper proteins customarily have a relatively weak ($\epsilon \sim 1000\ M^{-1}cm^{-1}$) electronic transition near 400 nm, and (2) all simple copper–thioether complexes have an intense ($\epsilon \sim 8000\ M^{-1}cm^{-1}$) $S(\sigma) \rightarrow Cu^{2+}$ LMCT transition near 400 nm that results in strong enhancement of copper–ligand modes (*53, 54*). There is evidence (*55*) that bridging thiol ligands appear somewhat "thioether-like" to copper(II), exhibiting broad electronic transitions in the 450–500-nm region. We cannot, at this time, reject the possibility that there is a copper transition centered in the near UV; a Raman excitation profile should establish whether or not resonance enhancement is promoted by the a_3 heme uniquely.

X-ray edge absorption data on cytochrome oxidase have been cited as evidence that Cu_U resembles stellacyanin (*56*). Prior to our RR studies (*17, 45*) this evidence was the only datum that suggested any blue copper-like properties for Cu_U. Quite recently (*57*), a preliminary report from the same laboratory of the EXAFS determination of the metal coordination shells in cytochrome oxidase has appeared. The interpretation presented is that the cytochrome a_3 heme is coordinated axially by a nitrogen ligand at 2.14 Å and a cysteine sulfur at 2.60 Å. The sulfur is said to bridge the Fe^{3+} and Cu_U^{2+} in resting oxidase with a Cu–S distance of 2.17 Å and a Fe–Cu distance of 3.75 Å, whence the Fe–S—Cu angle is 103°. The Cu_U^{2+} environment is reiterated to be stellacyanin-like. It may be asked reasonably whether such a coordination environment can result in cytochrome a_3 being high spin as is observed in the resting enzyme. By comparison, cytochrome P-450 (LM2) contains a hexacoordinated heme with axial ligands that currently are believed to be cysteine thiolate and water (*58*). Although

one of these ligands is classically weak, the iron(III) in P-450 (LM2) is low spin. Thus, the combination of imidazole and cysteine probably would render cytochrome a_3 low spin, in contrast to the observed high spin configuration deduced from susceptibility MCD and Raman measurements. However, the axial Fe–S distance in P-450 (LM2) is 2.19 Å (*58*) compared to 2.60 Å reported for cytochrome a_3. Such a bond length change conceivably could reduce the axial ligand field sufficiently to allow for the observed high spin state of cytochrome a_3. However, by Badger's Rule, the bond length change also should reduce the 351-cm^{-1} Fe–S stretch observed in P-450 (cam) to 211 cm^{-1} in cytochrome oxidase. No vibration near 211 cm^{-1} is observed in resting oxidase.

An interesting consequence of the proposed cytochrome a_3 structure (*57*) is that sulfur uniquely, among all proposed bridging ligands, may be capable of bridging Fe(a_3) and Cu_U in the reduced as well as the oxidized states. Sulfur is a perfectly reasonable ligand for Fe(II) and Cu(I) as well as Fe(III) and Cu(II). In fully reduced oxidase such a bridge clearly does not exist; nevertheless, a Fe^{2+}–S–Cu^{+} bridge remains a mechanistic possibility in the turnover dynamics of cytochrome a_3.

The only major inconsistency between the present RR results and the cytochrome a_3 structure proposed on the basis of the EXAFS results (*57*) is noted already, viz., the long Fe–S bond distance compared to the observed vibrational frequencies. A minor difference lies in the apparent nature of the Cu_U structure. Both techniques suggest a blue copper-like environment for Cu_U. However, the x-ray edge data are interpreted in terms of Cu_U virtually being identical with stellacyanin; the RR data suggest closer similarity to azurin–laccase–plastocyanin. Recent EPR data on a partially oxidized cytochrome oxidase (*59, 60*) and on partially reduced enzyme at high pH (*60*), where Cu_U becomes EPR detectable, show $A_{\parallel}$ for Cu_U to be intermediate between typical values for blue copper proteins and normal tetragonal copper (*59, 60*). The EPR results may suggest a disposition of ligands in Cu_U that is less tetrahedral, more flattened, than is typical for blue copper. This arrangement is a possible consequence of the hypothetical elimination of the bridging ligand from the heme, breaking the antiferromagnetism and rendering Cu_U detectable by EPR. The apparent absence of a S → Cu(II) LMCT transition near 600 nm due to Cu_U also suggests *d*-orbital energy levels of Cu_U different from those of blue copper, if a Cu–S bond is present in Cu_U.

Conclusions

The $\pi \rightarrow \pi^*$ electronic spectroscopy, the MCD, and the RRS of heme a can be understood in terms of a model in which the substitu-

tion of opposite pyrroles by vinyl and formyl substituents causes lifting of the degeneracy of the E_g LUMO that exists in other hemes. Nevertheless, the RR oxidation state or π^* electron density indicator peak, Band I, scales for heme a precisely as it does for other hemes. However the RR core size indicators do not, and new calibrations of Band IV frequency vs. heme Ct–N distance must be drawn for heme a. Multiple "Bands IV" apparently exist when α,β-excitation is employed, due to dissimilarity of the pyrroles along the x and y in-plane axes. However, Soret excitation results in a polarized Band IV analog, which allows core size information to be determined and therefore the spin state and coordination number of heme a to be inferred.

Application of the heme a model complex data to cytochrome oxidase shows that cytochrome a_3 contains high spin, hexacoordinated iron(III) in the resting enzyme. The RR data do not support an iron(IV) formulation of resting oxidase. Cytochrome a_3 is high spin iron(II) in the fully reduced enzyme. Combined studies of metastable oxygenated derivatives of cytochrome oxidase by RR and MCD suggest that Compound C, pulsed oxidase, and the hydrogen peroxide adduct of the resting enzyme all contain the cytochrome a_3 heme as intermediate spin iron(III). The redox configuration of cytochrome a_3 in Compound C and the hydrogen peroxide adduct is similar to recently characterized model hemes where peroxide appears to be bound to iron(III) in a symmetric bihapto manner parallel to the heme plane.

The low frequency RRS of cytochrome a_3 in resting cytochrome oxidase exhibits peaks due to axial nonheme structures. The observed peaks are at higher frequencies than expected for Fe^{3+}–N (imidazole) stretch, although such a mode may be observed in reduced enzyme. No Fe^{3+}–O mode due to bridging oxide is revealed by ^{18}O isotope experiments. One of the observed peaks is assignable to Fe^{3+}–O (tyrosine phenolate) or Fe^{3+}–S (cysteine thiolate), with the latter assignment favored on the basis of intensity arguments and by comparison to cytochrome P-450 (cam) RR results. The remaining low frequency peaks markedly are similar to the blue copper protein RR spectra, particularly those of azurin, laccase, and plastocyanin. Taken together, the RR evidence is consistent with a cytochrome a_3 structure in which the heme is hexacoordinated, high spin iron(III), the axial ligands are histidine imidazole and cysteine thiolate, the sulfur forms the bridge to Cu_U^{2+}, and the environment of Cu_U^{2+} is similar to copper in azurin and plastocyanin. Other spectroscopic data suggest a more flattened geometry for Cu_U^{2+} than for the metal sites of plastocyanin and azurin.

Effects of detergent on the RR spectra of cytochrome oxidase are noted, distinct from, and in addition to, the previously observed photoreduction of the resting enzyme. Investigation of the nature of these

effects, further RR study of electron transfer intermediates, study of copper depleted oxidase preparations, and application of novel spectroscopic probes such as time-resolved resonance Raman are now in progress.

Acknowledgments

This work was supported by grants from the NIH, GM 21337 (GP) and AM 21333 (WW); NSF grant CHE78–09338 (WW), and the Welch Foundation C–636 (GP) and F–733 (WW).

Literature Cited

1. Lemberg, R.; Barrett, J. "The Cytochromes"; Academic: New York, 1973.
2. Tweedle, M.; Wilson, L. J.; Garcia-Iniquez, L.; Babcock, G. T.; Palmer, G. *J. Biol. Chem.* **1978,** *153,* 8065–71.
3. Hartzell, R.; Beinert, H. *Biochem. Biophys. Acta* **1974,** *368,* 318–38.
4. Babcock, G. T.; Vickery, L. E.; Palmer, G. *J. Biol. Chem.* **1976,** *251,* 7970–19.
5. Takemori, S.; King, T. E. *J. Biol. Chem.* **1965,** *240,* 504–13.
6. Mincey, T.; Traylor, T. G. *Bioinorg. Chem.* **1978,** *9,* 409–20.
7. Greenwood, C.; Wilson, M. T.; Brunori, M. *Biochem. J.,* **1974,** *137,* 205–15.
8. Antonini, E.; Brunori, M.; Colisimo, A.; Greenwood, C.; Wilson, M. T. *Proc. Natl. Acad. Sci. U.S.A.* **1977,** *74,* 3128–32.
9. Bickar, D.; Bonaventura, C.; Bonaventura, J. *Fed. Proc.* **1980,** *39,* 2061.
10. Spiro, T. G.; Strekas, T. C. *J. Am. Chem. Soc.* **1974,** *96,* 338–43.
11. Albrecht, A. C.; Hutley, M. C. *J. Chem. Phys.* **1971,** *52,* 4137–43.
12. Strekas, T. C.; Spiro, T. G. *Biochem. Biophys. Acta* **1972,** *278,* 188–92.
13. Spiro, T. G.; Burke, J. M. *J. Am. Chem. Soc.* **1976,** *98,* 5482–89.
14. Spaulding, C. D.; Chang, C. C.; Yu, N. T.; Felton, R. H. *J. Am. Chem. Soc.* **1975,** *97,* 2517–20.
15. Babcock, G. T.; Ondrias, M. R.; Gobeli, D. A.; Vansteelandt, J.; Leroi, G., *FEBS Lett.* **1979,** *108,* 147–51.
16. Callahan, P. M.; Babcock, G. T. *Biochem.* **1981,** *20,* 952–58.
17. Woodruff, W. H.; Dallinger, R. F.; Antalis, T. M.; Palmer, G. *Biochem.* **1981,** *20,* 133–38.
18. Kitagawa, T.; Kyogoku, Y.; Orii, Y. *Arch. Biochem. Biophys.* **1977,** *181,* 228–35.
19. Carter, K. R.; Palmer, G., unpublished data.
20. Salmeen, I., Rimai, L.; Babcock, G. T. *Biochem.* **1978,** *17,* 800–06.
21. Babcock, G. T.; Vickery, L. E.; Palmer, G. *J. Biol. Chem.* **1976,** *251,* 7907–19.
22a. Sutherland, J. C.; Klein, M. P. *J. Chem. Phys.* **1972,** *57,* 76–86.
22b. Michl, J. *J. Am. Chem. Soc.* **1979,** *100,* 6812.
23. Babcock, G. T.; Callahan, P. M.; McMahon, J. J.; Ondrias, M. R.; Salmeen, I. *Biochem.* **1981,** *20,* 909–66.
24. Kitagawa, T.; Abe, M.; Ogoshi, H. *J. Chem. Phys.* **1978,** *69,* 4516–25.
25. Stein, P.; Burke, J. M.; Spiro, T. G. *J. Am. Chem. Soc.* **1975,** *97,* 2309–10.
26. Yamamoto, T.; Palmer, G.; Gill, D.; Salmeen, I.; Rimai, L. *J. Biol. Chem.* **1973,** *248,* 5211–13.
27. Vanneste, W. *Biochem.* **1966,** *5,* 838–48.
28. Ferguson-Miller, S.; Van Aken, T.; Rosenear, P. "Abstracts of Papers," *Symposium on Interactions Between Iron and Proteins in Oxygen and Electron Transport;* Airlie, Virginia, 1980.

29. Woodruff, W. H.; Babcock, G. T.; Palmer, G., unpublished data.
30. Palmer, G.; Antalis, T.; Babcock, G. T.; Garcia-Iniquez, L.; Tweedle, M.; Wilson, L. J.; Vickery, L. E. "Mechanisms of Oxidizing Enzymes"; Singer, T. P.; Ondarza, R. N., Eds.; Elsevier: New York, 1978.
31. Alben, J. O.; Altschold, R. A.; Fiamingo, F.; Moh, P. "Abstracts of Papers," *Symposium on Interactions Between Iron and Proteins in Oxygen and Electron Transport;* Airlie, Virginia, 1980.
32. Sievers, D.; Osterlund, K.; Ellfolk, N. *Biochem. Biophys. Acta* **1978,** *581,* 1–14.
33. Seiter, C. H. A.; Angelos, S. G. *Proc. Natl. Acad. Sci. U.S.A.* **1980,** *77,* 1806–08.
34. Chance, B.; Saronio, C.; Leigh, J. S. *J. Biol. Chem.* **1975,** *250,* 9226–37.
35. Chance, B.; Graham, N.; Legallais, V. *Anal. Biochem.* **1975,** *67,* 522–79.
36. Clore, G. M.; Andreasson, L. E.; Karlsson, B.; Aasa, R.; Malmstrom, B. G. *Biochem. J.* **1980,** *185,* 139–54; 155–67.
37. Shaw, R. W.; Hansen, R. E.; Beinert, H. *J. Biol. Chem.* **1978,** *253,* 6637–40.
38. Antonini, E.; Brunior, M.; Colisimo, A.; Greenwood, C.; Wilson, M. T. *Proc. Natl. Acad. Sci. U.S.A.* **1977,** *74,* 3128–32.
39. Babcock, G. T.; Vickery, L. E.; Palmer, G. *J. Biol. Chem.* **1976,** *251,* 7907–19.
40. Greenwood, C.; Wilson, M. T.; Brunori, M. *Biochem. J.* **1974,** *137,* 205–15.
41. Reed, C. A.; Mashiko, T.; Simonneaux, G.; Scholz, W.; Marchon, J-C.; Haller, K. J.; Schcidt, W. R.; Lang, G. "Abstracts of Papers," *181st Nat. Meet., ACS, March–April, 1981; Analytical, 110.*
42. Becker, J. K.; Dolphin, D.; Domazetis, G.; James, B. R.; Pickett, S. "Abstracts of Papers," *181st Nat. Meet., ACS, March–April, 1981; Analytical, 163.*
43. Bocian, D. F.; Lemley, A. T.; Petersen, N. O.; Brudvig, G. W.; Chan, S. I. *Biochem.* **1979,** *18,* 4396.
44. Babcock, G. T.; Salmeen, I. *Biochem.* **1979,** *18,* 2493–98.
45. Woodruff, W. H.; Dallinger, R. F.; Antalis, T. M.; Palmer, G. "Interactions between Iron and Proteins in Oxygen and Electron Transport"; Ho, C., Ed.; Elsevier: New York; in press.
46. Stevens, T. H.; Chan, S. I. *J. Biol. Chem.* **1981,** *256,* 1069–71.
47. Kitagawa, T.; Nagai, K.; Tsubaki, M. *FEBS Lett.* **1979,** *104,* 376–78.
48. Nagai, K.; Kitagawa, T.; Morimoto, H. *J. Mol. Biol.* **1980,** *136,* 271–89.
49. Kitagawa, T.; Abe, M.; Kyogoku, Y.; Ogoshi, H.; Watanabe, E.; Yoshida, Z. *J. Phys. Chem.* **1976,** *80,* 1181–90.
50. Gaber, B. P.; Miskowski, V.; Spiro, T. G. *J. Am. Chem. Soc.* **1974,** *96,* 6868–73.
51. Champion, P. M.; Gunsalus, I. C. *J. Am. Chem. Soc.* **1977,** *99,* 2000–03.
52. Tang, S-P. W.; Spiro, T. G.; Mukai, K.; Kimura, T. *Biochem. Biophys. Res. Commun.* **1973,** *53,* 869–74.
53. Ferris, N. S.; Woodruff, W. H. submitted for publication in *J. Am. Chem. Soc.*
54. Ferris, N. S.; Woodruff, W. H.; Rorabacher, D. B.; Jones, T. E.; Ochrynowycz, L. A. *J. Am. Chem. Soc.* **1978,** *100,* 5939–42.
55. Schugar, H. J.; Ou, C.; Thich, J. A.; Potenza, J. A. *J. Am. Chem. Soc.* **1976,** *98,* 3047–48.
56. Powers, L.; Blumberg, W. E.; Chance, B.; Barlow, C. H.; Leigh, J. S.; Smith, J.; Yonetani, T.; Vik, S.; Peisach, J. *Biochem. Biophys. Acta* **1979,** *546,* 520–38.
57. Powers, L.; Chance, B.; Ching, Y.; Angiolillo, P. *Biophys. J.* **1981,** *33,* 95a.
58. Cramer, S. P.; Dawson, J. H.; Hodgson, K. O.; Hager, L. P. *J. Am. Chem. Soc.* **1978,** *100,* 7282–90.
59. Malmstrom, B. G.; Karlsson, B.; Aasa, R.; Andreasson, L-E.; Clore, G. M.; Vanngard, T. "Abstracts of Papers," *Symposium on Interactions Between Iron and Proteins in Oxygen and Electron Transport;* Airlie, Virginia, 1980.

60. Carithers, R.; Palmer, G., *J. Biol. Chem.*, **1981**, submitted.
61. Spiro, T. G.; Loehr, T. M. In "Advances in Infrared and Raman Spectroscopy"; Clark, R. J. H.; Hester, R. E., Eds.; Heyden & Sons: London, 1975; Vol. 1, pp. 98–142.

RECEIVED for review June 2, 1981. ACCEPTED November 16, 1981.

Utility of Proton Hyperfine Shifts in Elucidating the Electronic Structure of Horseradish Peroxidase Compounds I and II and Their Model Compounds

L. LATOS-GRAZYNSKI, ALAN L. BALCH, and GERD N. LA MAR

University of California, Department of Chemistry, Davis, CA 95616

This chapter reviews proton NMR spectroscopic studies of the electronic and molecular structure of horseradish peroxidase (HRP) in its reactive forms. The resting state is characterized by a rigid heme pocket with the iron bound to an axial imidazole with intact N_1–H and a quantum mechanical admixture S = $\frac{3}{2}$, $\frac{5}{2}$ spin state for the metal. HRP Compound II is characterized by very small hyperfine shifts in its proton NMR spectrum, and a complete assignment of the spectrum awaits further developments. The proton NMR spectrum of HRP Compound I is unlike that of any previously characterized iron porphyrin, and supports the $(FeO)^{2+}$/porphyrin π cation radical model. The heme environment of HRP Compound I is rigid, with evidence that the heme vinyl groups are locked in two in-plane positions. The spectra of various states of HRP are compared with those of relevant model compounds. Data obtained with carbene complexes of iron porphyrins suggest that the oxidizing equivalents in an iron–oxo complex may be stored by inserting an (formal) oxygen atom into an iron–nitrogen bond. Models for $(FeO)^{2+}$ porphyrin complexes are available through the reaction of N*-methylimidazole with peroxo-bridged iron porphyrin dimers.*

The reduction of dioxygen to water constitutes the terminal step in the respiratory electron transport chain. However, dioxygen metabolism at other stages can also result in the formation of the partially

0065-2393/82/0201-0661$06.00/0

reduced species, hydrogen peroxide and superoxide. These species have potential toxic effects. The catalases and superoxide dismutases are existing enzymes that are capable of destroying these species. Another group of enzymes, the peroxidases, couple the destruction of hydrogen peroxide with the oxidation of organic substrates.

Horseradish peroxidase (HRP), a heme enzyme, is a readily available representative of this group of peroxidases and has received considerable study (*1*, *2*). A number of different oxidation states of the prosthetic group have been detected. These oxidation states are shown in Scheme I, along with the reaction pathways that interconnect them (*1*, *2*). The productive catalytic cycle involves: the resting enzyme, which contains iron(III); the green Compound I (HRP I); and the red Compound II (HRP II). The physiological significance of the other oxidation states shown in Scheme I is less clear. Many details of the molecular and electronic structure of the HRP states remain unresolved, despite extensive studies using a wide variety of physicochemical techniques. Some of these points include the location of the oxidizing equivalents in HRP I and II, and the role of axial imidazole deprotonation in stabilizing these forms.

NMR Spectroscopy of Heme and Hemoproteins

Proton NMR hyperfine shifts can provide, in principle, a wealth of electronic and structural information about the paramagnetic center in hemoproteins in various oxidation and spin states (*3*, *4*). The unpaired spin of the hemin perturbs the proton resonances of the prosthetic group, coordinated ligands, and some of the amino acids in the neighborhood of the heme iron. This perturbation permits the resolution of many peaks that are shifted away from the generally poorly resolved diamagnetic envelope [the region 0–10 ppm from sodium 3-(trimethylsilyl)-1-propanesulfonate (DSS)] (*3*, *5*). These hyperfine shifted resonances are extremely sensitive to the oxidation, ligation, and spin states of the system, and are influenced by the heme–apoprotein interaction that can affect the orientation of porphyrin-bound substituents (particularly vinyl groups) and the plane of the axial imidazole ligands (*3–23*).

Each previously characterized spin, ligation, and oxidation state ("state") of iron porphyrins has a characteristic spectral pattern. In most cases, the hyperfine shift patterns can be rationalized on the basis of interaction of available, spin-containing *d*-orbitals of iron and the appropriate porphyrin and axial ligand orbitals. An extensive review describes the various delocalization pathways (*4*). We used characteristic average shift values (Table I) for well-characterized states of iron porphyrins to assess the likelihood that hyperfine shift patterns account for the properties of the reactive forms of HRP.

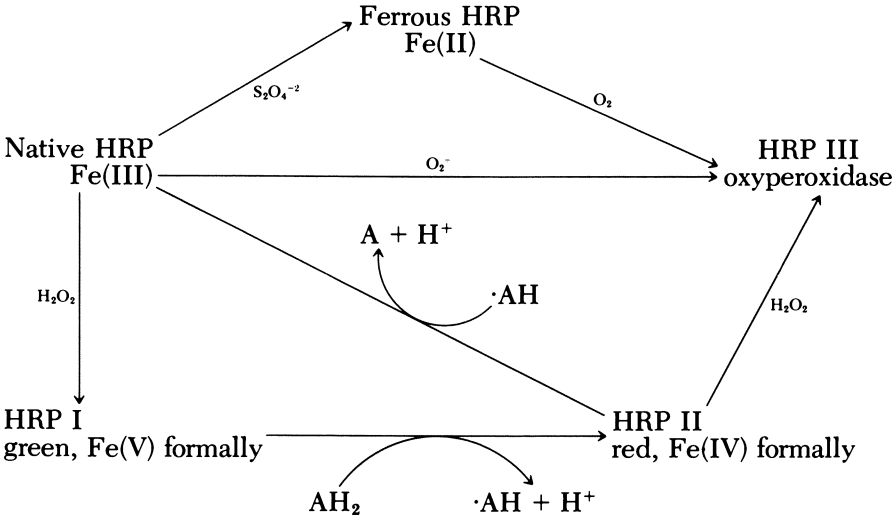

Scheme I. The productive catalytic cycle involves Native HRP, HRP I, and HRP II. The overall reaction catalyzed is $H_2O_2 + H_2A \rightarrow 2H_2O + A$.

Two important factors relevant to our interpretations have emerged from our previous studies on both models and more readily characterized hemoproteins (i.e., myoglobin, and insect hemoglobin). First, the relative hyperfine shift of both pyrrole-bound protons and methyl groups of the heme core must be observed to characterize the heme state. This restriction requires observations to be made on isostructural systems containing protoporphyrin (**A**, R = vinyl) and deuteroporphyrin (**A**, R = hydrogen). Unambiguous assignment of resonances to particular protons necessitates the use of stereospecifically deuterated porphyrins. Second, for a given state, models and proteins have essentially the same average hyperfine shift for a particular functional group (*4*). However, protein-bound heme invariably exhibits a large, in-plane anisotropy that is manifested by a large spread of hyperfine shifts in a particular functional group. Most importantly, in the low spin iron(III) state the pattern of the methyl hyperfine shifts can be used to uniquely determine the orientation of the axial histidyl imidazole.

Another spectral property of interest for these paramagnetic hemoproteins is the linewidth, whose relative values reflect an inverse, sixth dependence on the distance of the proton involved from the paramagnetic center (*7*). Analysis of linewidths becomes particularly important in cases where two paramagnetic centers have been proposed to exist.

The spectroscopic probe found most useful in characterizing the axial histidine and the iron–imidazole bonding is the resonance of the

exchangeable imidazole N_1–H (**B**). Again, the resonance position of this N_1–H signal falls in the same spectral window for identical states of models and proteins. Hence, the detection of this proton resonance eliminates the presence of a deprotonated imidazole. However, shift differences between models and proteins may allow for an interpretation of the extent of imidazolate character imposed on the axial ligand by hydrogen bonding to a protein-acceptor residue.

Proton NMR Studies of HRP

Resting State. The resting state contains iron(III) with one axial imidazole ligand (*23–34*). Although proton NMR spectroscopy has not resolved the question (*31–34*) of what ligand, if any, occupies the remaining axial site, it has contributed valuable information about other significant properties. These properties include the spin state of the iron, the rigidity of the heme crevice, and the state of imidazole deprotonation. As shown later, the question of imidazole N_1–H protonation/deprotonation is significant for all forms of HRP. The spectrum of resting HRP, along with resonance assignments, is shown in Figure 1. The reduced magnetic susceptibility of resting state HRP, along with its electron spin resonance (ESR) spectrum, led to the suggestion that the iron was present in an unusual quantum mechanical admixed spin state with $\frac{5}{2}$ and $\frac{3}{2}$ character (*36–40*). Comparison of the proton NMR spectra of native and deuteroheme reconstituted HRP confirms the mixed spin state because the observed shift pattern is most similar to the shift patterns of model compounds that also have the admixed $\frac{5}{2}$–$\frac{3}{2}$ state (*11*).

The temperature dependence of the resonances of the side chains reflects a rigid heme pocket. This finding contrasts with observations made on myoglobin (*10, 41*). The highly buried nature of the heme environment is demonstrated further by the extremely slow rate of exchange of the N_1–H of the proximal histidine. Detection of a broad, but exchangeable, proton at +100 ppm, which is essentially the same location as found in myoglobin, ensures that the axial imidazole ligand is present with the N_1–H intact. Moreover, the insensitivity of the N_1–H resonance position to substrate bonding disproves the previous contention (*42*) that stabilization of the substrate/protein binding involves hydrogen bonding to the proximal histidine N_1–H.

Addition of sodium cyanide to resting HRP gives a hexacoordinated form, which, although physiologically irrelevant, is particularly useful for spectroscopic structure determination. The Curie behavior of the resonances of the heme peripheral substituents and the observation of a N_1–H signal are similar to those features in metcyanomyoglobin. This result offers further confirmation of the rigid nature of the

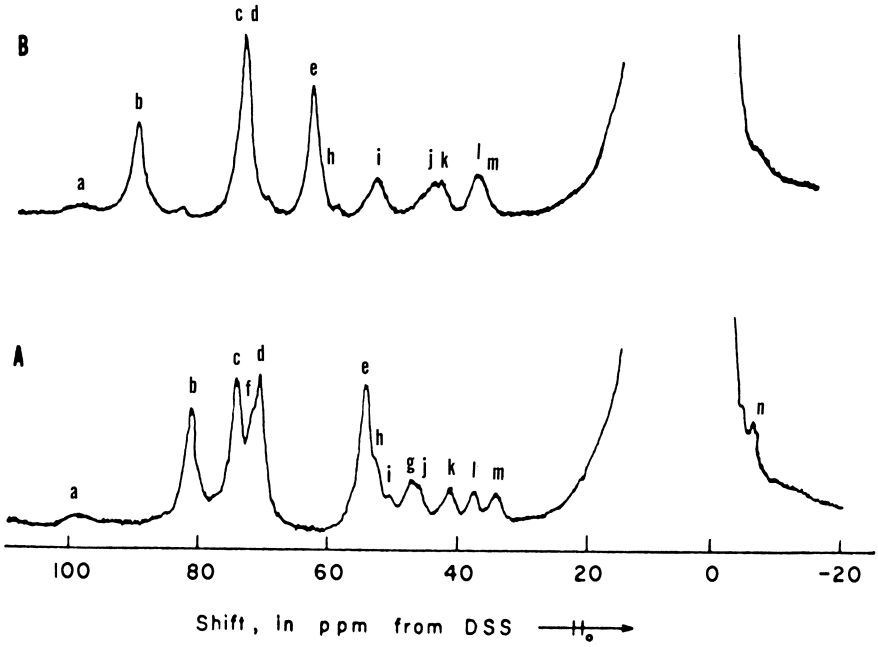

Figure 1. Proton NMR spectra (360 MHz) of: A, native HRP; and B, deutero HRP in ^2H_2O, pH 7, 25°C. Assignments [11] A: a, N_1H; b, 8-CH_3; c, 5-CH_3; d, 3-CH_3; e, 1-CH_3; f, vinyl; g–l, vinyl, propionic acid $H_{\alpha's}$(?), proximal histidyl $H_{\beta's}$(?); and m,n, vinyl H_β. B: a, N_1H; b, 5-CH_3; c, 1-CH_3; d, 8-CH_3; e, 3-CH_3; and h–m, propionic acid $H_{\alpha's}$(?), proximal histidyl $H_{\beta's}$. Spectra from Ref. 35.

heme pocket and the presence of an essentially neutral axial imidazole. Deuterium labeling studies establish that the axial imidazole's plane is oriented along the N–Fe–N axis of Pyrroles 1 and 3. Significantly, deuteroheme reconstitution of HRP reveals a 180° rotation of the porphyrin (heme disorder), which may account for the differential stabilities of Compound I formed from differently substituted porphyrins (vida infra).

HRP Compound II. HRP II contains an $(FeO)^{2+}$ unit with a triplet ground state and an axial histidyl imidazole (*37, 38, 43–47*). The proton NMR spectrum of this form obtained from d_6-diacetyldeuteroheme (**A**, R = H, $COCD_3$ groups in the 6- and 7-positions in place of the propionic acid side chains) reconstituted HRP is shown in Figure 2. Similar spectra were recorded for native HRP and for ferryl myoglobin, the green species obtained by treating metmyoglobin with excess hydrogen peroxide (*49–51*). In all cases, the paramagnetic shifts are among the lowest recorded for any heme protein. The peaks in the 17–14-ppm region tentatively have been as-

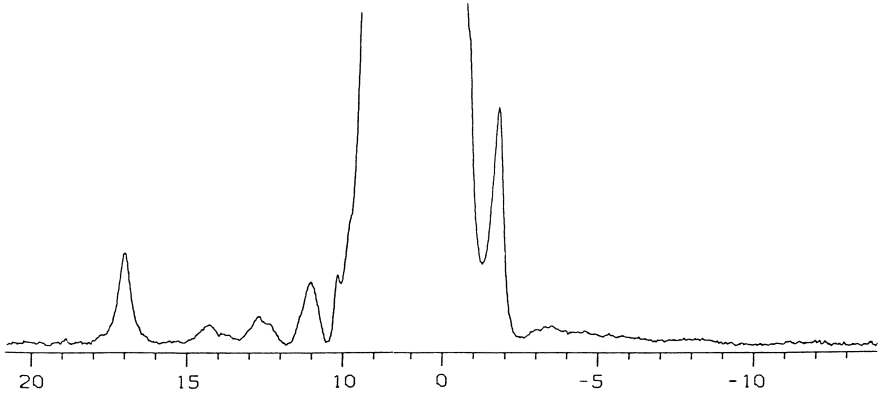

Figure 2. Proton NMR spectrum (360 MHz) of d_6*-diacetyl deutero HRP Compound II (15°C). Spectrum taken from Reference* 48.

signed to heme methyl groups (*49–55*). However, the actual assignment only can be made when suitable deuterium labeling studies, now in progress, are completed. The low stability of the HRP II form has hampered this work.

Model compounds, *N*-MeImPFeO (*N*-MeIm is *N*-methylimidazole, P is a synthetic porphyrin dianion) recently were obtained. Their properties are discussed in a later section.

HRP Compound I. The electronic and molecular structures of HRP I have been the subjects of extensive investigation. Numerous different electronic structures have been proposed for this highly oxidized species. These structures include: simple iron(V), *meso*-porphyrin attacked iron(IV), and iron(IV) with a free radical that may be based on an amino acid side chain or on the porphyrin (porphyrin π-cation radical). Magnetic susceptibility studies (*38*) indicate that HRP I has three unpaired electrons, although data from Mossbauer spectroscopy (*43, 44, 52*) indicate that the iron environments in HRP I and HRP II are very similar. The ESR, ENDOR (*52–54*), and electronic spectra (*55, 56*) of HRP I all are consistent with the presence of a porphyrin cation radical. However, in the related species, Compound I of cytochrome c peroxidase, the presence of an amino acid-based radical was detected by ESR spectroscopy (*57, 58*).

Initial proton NMR studies (*49–51*) indicated that high spin Fe(IV) was present in HRP I. This interpretation was based on the apparent similarities of the heme methyl shifts in resting HRP and HRP I, and hence the presence of an amino acid-based free radical was required. The use of isotope labeling and deuteroheme substitution later revealed (*19, 35*) that the hyperfine shift pattern for HRP I (whose proton NMR spectrum is shown in Figure 3) is inconsistent with the presence of high spin iron(IV), but likewise did not correspond to any

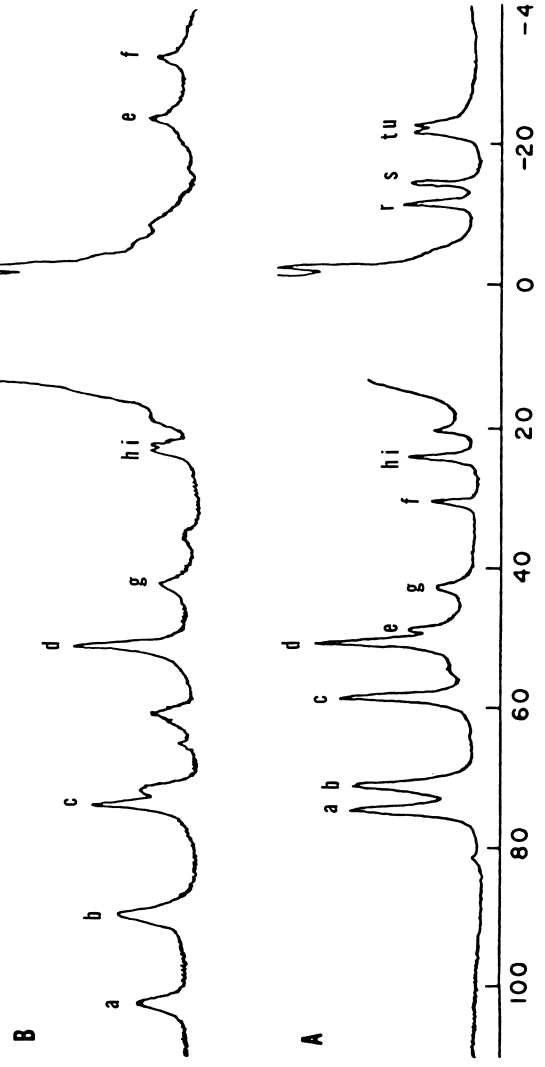

Figure 3. Proton NMR spectra (360 MHz) of: A, HRP Compound I; and B, deutero hemin HRP Compound I in 0.2 M NaCl/^2H_2O, 25°C. Assignment [19] A: a, 8-CH_3; b, 3-CH_3; c, 5-CH_3; d, 1-CH_3; e, 4-CH_α(?); f, 2-CH_α(?); g–j, 6,7α-CH_2 (?); 4,s, 2,4-H (cis); and t,v, 2,4-H (trans). B: a, 3-CH_3; b, 1-CH_3; c, 5-CH_3; d, 8-CH_3; e,f, 2,4-pyrrole; and g,j, 6,7α-CH_2. Spectra from Reference 35.

of the previously characterized iron porphyrin states given in Table I. Moreover, quantitative analysis of the linewidths of the individually assigned peripheral groups eliminated a nearby amino acid-based free radical, and supported the cation radical formulation for the second oxidizing equivalent. In contrast to optical spectroscopy at low temperature, the heme methyl linewidths in the proton NMR spectra support identical orbital ground states for HRP I and deutero HRP I. The NMR shifts have not enabled identification of the orbital ground state. Theoretical calculations for the proposed a_{1u} state indicate that the spin density is localized at the pyrrole nitrogen and *meso*-carbons (*59*). The inability to detect *meso*-proton resonances is indirect support for the a_{1u} state. Planned experiments to search for the *meso*-resonance by ^{2}H-NMR spectroscopy with *meso*-deuterated HRP may provide direct support.

The proton NMR spectrum of HRP I provides conformation of the steric constraints imposed on the motion of the heme peripheral substituents by the protein. Thus, the resonances identified as the vinyl α-protons, in fact, represent two environments that interconvert slowly on the NMR time scale and have been interpreted as representing in-plane vinyl groups that differ by 180° in rotational position. A rationalization of the unusual conformation involves a potential role for the vinyl groups in extending the conjugated π-system of the porphyrin, thereby stabilizing the highly oxidized species. Native HRP I is more stable than deuteroporphyrin reconstituted HRP I. This differential stability may be attributed to the role of the vinyl groups and their orientation in stabilizing this oxidized state.

Table I. Typical Porphyrin Hyperfine Shifts of Iron Complexes and Hemoproteins (25°C, ppm)

		Porphyrin Functional Group				
Oxidation State	*Spin*	CH_3[a]	H[a]	H_α[b]	H_β[b]	*Reference*
Fe(II)	1	45	−3	32	0–3	*15*
	2	8	42	5	2–3	*9, 16*
Fe(III)	1/2	13	−20	4	−8	*6, 8, 14*
	3/2	60	0			*11, 12*
	5/2[c]	45	65	35	−4	*10, 13*
Fe(IV)	5/2[d]	65	55	38	−9	
	1		−5			*18*
	2		70	60		*17*

[a] $-CH_3$, H attached to peripheral pyrrole carbons.
[b] H_α, H_β vinyl protons.
[c] Pentacoordinated.
[d] Hexacoordinated.

Ferrous [Fe(II)] HRP. The proton NMR spectrum of the Fe(II) form of HRP resembles that of deoxymyoglobin (*59*). In particular, the N_1–H proton is resolved, and falls in a region similar to that of deoxymyoglobin. A protein conformational change modulated by another titratable residue induces a significant change in the N_1–H paramagnetic shift. In conjunction with resonance Raman studies, these results show that the state of hydrogen bonding of the N_1–H proton is involved in this process (*59*, *60*).

Models of Oxidizing Enzymes

Carbene Complexes of Iron Porphyrins. The vinylidene carbene [VC=:C=C(p-$C_6H_4Cl)_2$] complexes of iron porphyrins, PFe(VC), and their oxidation products, P(VC)FeCl, possibly may serve as models for HRP II and HRP I (*61*, *62*). This claim was based on similarities in the optical spectra of the model compounds and the enzyme intermediates, as well as the magnetic susceptibility of P(VC)FeCl, which indicates an $S = \frac{3}{2}$ spin state.

Proton NMR spectra of PFe(VC) alone and in the presence of pyridine or *N*-methylimidazole indicate that this molecule is diamagnetic ($S = 0$), and hence is inadequate as a model for HRP II. These proton NMR spectra are, however, fully consistent with the existence of a complex containing a normal iron porphyrin unit and a carbene ligand axially bound to iron.

The proton NMR spectra of P(VC)FeCl exhibited remarkable features (*63*). Characteristic spectral patterns are presented in Figure 4. The peak assignments were verified by selective deuteration. The observation of four pyrrole proton resonances, three with hyperfine shifts of −30 to −50 ppm and a fourth with a shift of 12 ppm, is particularly striking. This observation, coupled with the analysis of the spectra of the analogous complex obtained from deuterohemin (which clearly shows 16 porphyrin methyl resonances) indicates that the porphyrin no longer retains its fourfold symmetry. Indeed, the carbene has inserted into an iron–nitrogen bond on oxidation, and the reversible process interconverting PFe(VC) and P(VC)FeCl is shown in Equation 1. Thus, four unique products are analogous to Structure **2** for deuterohemin and hence, the 16 methyl resonances. The structure of TPP(VC)FeCl was determined by x-ray crystallography (*64*).

These observations raise new possibilities for the structure of the reactive forms of oxidizing heme enzymes. Because the end-carbon of the carbene is isoelectronic with an oxygen atom, complexes containing the FeO^{2+} and FeO^{3+} units may choose to store their oxidizing equivalents by inserting an oxygen atom into an iron–nitrogen bond. Consequently, Structure **3** possibly may be involved in the chemical

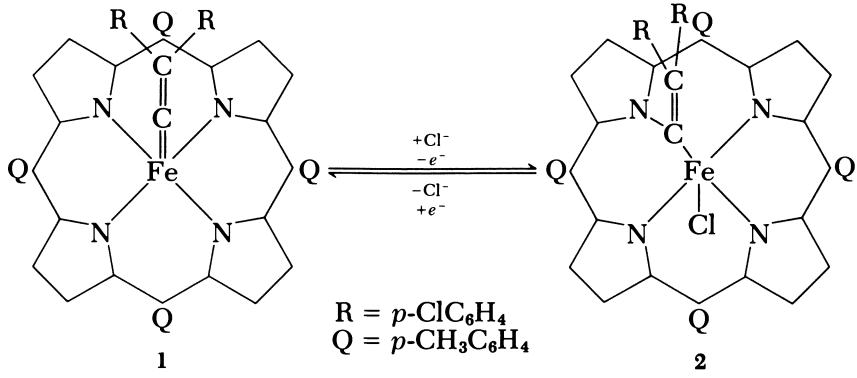

1 2

Equation 1

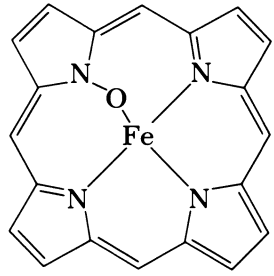

3

transformations of oxo–iron complexes. Such a structure for the active hydroxylating form of cytochrome P-450 would appear to be an intriguing possibility.

Ferryl $(FeO)^{2+}$ Complexes of Iron Porphyrins. Two groups of iron(IV) porphyrin complexes were examined. Electrochemical oxidation of iron(III) complexes PFeX and PFeOFeP produce the iron(IV) species $PFeX^+$ and $PFeOFeP^{2+}$, and the mixed valence species $PFeOFeP^+$ (*17*, *55*, *56*). Only $PFeX^+$ is relevant as a model for a monomeric heme enzyme.

Another group of iron(IV) porphyrins is available via Equation 2 (*18*), where B may be pyridine or *N*-methylimidazole. These complexes are

$$2PFe(II) + O_2 \rightarrow PFe(III)OOFe(III)P \xrightarrow{B} 2BPFe(IV)O \qquad (2)$$

stable in solution at low temperature (−80° to ~ −20°C) and were characterized by their proton NMR and electronic spectra. Their magnetic susceptibilities and the Curie behavior of the hyperfine shifts indicate that the complexes have a triplet ground state. The

ability of BPFeO to transfer its oxygen atom quantitatively to triphenylphosphine and form triphenylphosphine oxide verifies the existence of the FeO^{2+} unit in this reactive intermediate (*65*). Further work comparing the chemical shifts of identical functional groups in these model compounds with those observed for HRP II are necessary. Preliminary studies on (B)OEPFeO (OEP is the dianion of octaethylporphyrin) indicate that the *meso*-proton resonance appears at 14 ppm downfield (extrapolated to 25°C) from tetramethylsilane (TMS). This assignment suggests that the downfield hyperfine shifted resonances of HRP II actually may be *meso*-protons rather than the heme methyls, as originally assigned (*49–51*). Further studies of this problem are in progress.

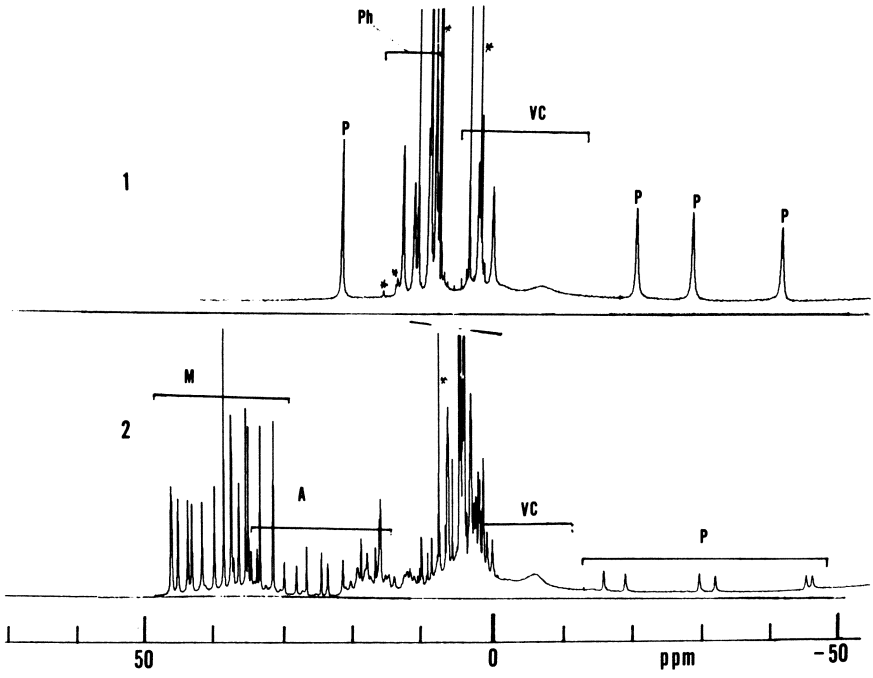

Figure 4. Proton NMR spectra (360 MHz) of: 1, TPP(VC)FeCl and 2, DPDME(VC)FeCl in $CDCl_3$/25°C (VC, vinylidene; Ph, phenyl; p, pyrrole; and m, methyl, propionic acid $H_{a's}$). Spectra taken from Reference 63.

Acknowledgments

We thank our collaborators K. M. Smith, J. deRopp, D. H. Chin, and R. J. Cheng for their assistance, and the National Institutes of Health (HL–16087, GM–26226), and the UCD NMR Facility for support.

Literature Cited

1. Dunford, H. B.; Stillman, J. S. *Coord. Chem. Rev.* **1976,** *19,* 182–251.
2. Hewson, W. D.; Mayer, L. P. In "The Porphyrins"; Dolphin, D., Ed.; Academic: New York, 1979; Vol. 7, pp. 295–332.
3. La Mar, G. N. In "Biological Application of Magnetic Resonance"; Shulman, R. G., Ed.; Academic: New York, 1979; pp. 61–157.
4. La Mar, G. N.; Walker, F. A. In "The Porphyrins"; Dolphin, D., Ed.; Academic: New York, 1979; pp. 61–157.
5. Morrow, J. S.; Gurd, F. R. N.; Crit. C. R. C. *Rev. Biochem.* **1975,** *3,* 221–287.
6. Mayer, A.; Ugame, S.; Shulman, R. G.; Uamane, T.; Cavaleiro, J. A. S.; Rocha-Gonsalves, A. M. d'A.; Venner, G. W.; Smith, K. M.; *J. Mol. Biol.* **1974,** *86,* 749–756.
7. Swift, T. J. In "NMR of Paramagnetic Molecules"; La Mar, G. N.; Horrocks, Jr., W. D.; Holm, R. H., Eds.; Academic: New York, 1973, pp. 53–83.
8. La Mar, G. N.; Budd, D. L.; Viscio, D. B.; Smith, K. M.; Langry, K. C. *Proc. Natl. Acad. Sci. U.S.A.* **1978,** *75,* 5755–5759.
9. La Mar, G. N.; Budd, D. L.; Sick, H.; Gersonde, K., *Biochim. Biophys. Acta* **1978,** *537,* 270–283.
10. La Mar, G. N.; Budd, D. L.; Smith, K. M.; Langry, K. C. *J. Am. Chem. Soc.* **1980,** *102,* 1822–1827.
11. La Mar, G. N.; deRopp, J. S.; Smith, K. M.; Langry, K. C. *J. Biol. Chem.* **1980,** *255,* 6646–6652.
12. Goff, H.; Shimomura, E. *J. Am. Chem. Soc.* **1980,** *102,* 31–37.
13. Budd, D. L.; La Mar, G. N.; Smith, K. M.; Nayyir-Mazhir, R. *J. Am. Chem. Soc.* **1979,** *101,* 6091–6096.
14. La Mar, G. N.; Viscio, D. B.; Smith, K. M.; Caughey, W. S.; Smith, M. L. *J. Am. Chem. Soc.* **1978,** *100,* 8085–8092.
15. Goff, H.; La Mar, G. N.; Reed, C. A. *J. Am. Chem. Soc.* **1977,** *99,* 3641–3646.
16. Goff, H.; La Mar, G. N. *J. Am. Chem. Soc.* **1977,** *99,* 6599–6606.
17. Phillipi, M. A.; Goff, H. *J. Am. Chem. Soc.* **1979,** *101,* 7641–7643.
18. D.-H. Chin; Blach, A. L.; La Mar, G. N. *J. Am. Chem. Soc.* **1980,** *102,* 1446–1448.
19. La Mar, G. N.; de Ropp, J. S.; Smith, K. M.; Langry, K. C. *J. Biol. Chem.* **1981,** *256,* 237–243.
20. Williams, R. J. P.; Wright, P. E.; Mazza, G.; Ricard, J. R. *Biochim. Biophys. Acta* **1975,** *412,* 127–147.
21. Morishima, I.; Ogawa, S. *J. Biol. Chem.* **1979,** *254,* 2814–2820.
22. Izuha, T.; Ogawa, S.; Inubushi, T.; Yonezawa, T.; Morishima, I. *FEBS Lett.* **1976,** *64,* 156–158.
23. Morishima, I.; Ogawa, S.; Inubushi, T.; Yonezawa, T.; Izuha, T. *Biochemistry* **1977,** *16,* 5109–5115.
24. George, P.; Lyster, R. L. *Proc. Nat. Acad. Sci. U.S.A.* **1974,** *44.*
25. Yamada, H.; Yamazaki, I. *Arch. Biochem. Biophys. Acta* **1974,** *165,* 728–738.
26. Richard, J.; Marne, G.; Williams, R. J. P. *Eur. J. Chem. Biochem.* **1972,** *28,* 566–578.

27. Morrison, R.; Schonbaum, G. R. *Annu. Rev. Biochem.* **1976,** *45,* 867–888.
28. Phelps, C.; Forlani, L.; Antonini, E. *Biochem. J.* **1971,** *124,* 605–614.
29. Yonetani, T.; Yamamoto, H.; Erman, J. E.; Leigh, Jr., J. S.; Reed, G. H. *J. Biol. Chem.* **1972,** *247,* 2447–2455.
30. La Mar, G. N.; de Ropp, J. S. *Biochem. Biophys. Res. Commun.* **1979,** *90,* 36–41.
31. Lanir, A.; Schejter, A. *Biochem. Biophys. Res. Commun.* **1975,** *62,* 199–203.
32. Vak-Pavlovic, S.; Siterer, Y. *Biochem. Biophys. Res. Commun.* **1977,** *79,* 885–891.
33. Spiro, T. G.; Strong, J. D.; Stein, P. *J. Am. Chem. Soc.* **1979,** *101,* 2648–2655.
34. Rakshit, G.; Spiro, T. G. *Biochemistry* **1974,** *13,* 5317–5323.
35. La Mar, G. N.; deRopp, J. S. *J. Am. Chem. Soc.* **1980,** *102,* 395–397.
36. Leigh, J. S.; Maltempo, M. M.; Ohlsson, P. I.; Paul, K. G. *FEBS Lett.* **1975,** *51,* 304–308.
37. Maltempo, M. M.; Ohlsson, P. I.; Paul, K. G.; Petersson, L.; Ehrenberg, A. *Biochemistry* **1979,** *18,* 2935–2941.
38. Theorell, H.; Ehrenberg, A. *Arch. Biochem. Biophys.* **1952,** *41,* 442–461.
39. Schonbaum, G. R. *J. Biol. Chem.* **1973,** *248,* 502–511.
40. Tamura, M. *Biochim. Biophys. Acta* **1971,** *243,* 249–258.
41. La Mar, G. N.; Viscio, D. B.; Gersonde, K.; Sick, H. *Biochemistry* **1978,** *17,* 361–367.
42. Schejter, A.; Lanir, A.; Epstein, N. *Arch. Biochem. Biophys.* **1976,** *174,* 36–44.
43. Maeda, Y.; Morita, Y. *Biochem. Biophys. Res. Commun.* **1967,** *29,* 680–685.
44. Moss, T. -H.; Ehrenberg, A.; Bearden, A. J. *Biochemistry* **1969,** *8,* 4159–4162.
45. Mauk, M. R.; Girotti, A. W. *Biochemistry* **1974,** *13,* 1757–1763.
46. Mayer, L. P.; Doubek, D. L.; Silverstein, R. M.; Margis, J. H.; Martin, J. C. *J. Am. Chem. Soc.* **1972,** *94,* 4364–4366.
47. Loew, G. H.; Kert, C. H.; Jhelmeland, L. M.; Kirchner, R. F. *J. Am. Chem. Soc.* **1977,** *99,* 3534–3536.
48. deRopp, J. S. Ph.D. Thesis, University of California, Davis, 1981.
49. Morishima, I.; Ogawa, S. *J. Am. Chem. Soc.* **1978,** *100,* 7125–7127.
50. Morishima, I.; Ogawa, S. *Biochem. Biophys. Res. Commun.* **1978,** *83,* 946–953.
51. Morishima, I.; Ogawa, S. *Biochemistry* **1978,** *17,* 4384–4388.
52. Schulz, C. E.; Devaney, P. W.; Winkler, H.; Debrunner, P. G.; Doan, N.; Chiang, R.; Rutter, R.; Hager, L. P. *FEBS Lett.* **1979,** *103,* 102–105.
53. Aasa, R.; Vanngard, T.; Dunford, H. B. *Biochim. Biophys. Acta* **1975,** *391,* 259–264.
54. Roberts, J. E.; Hoffman, B. H.; Rutter, R.; Hager, L. P. *J. Biol. Chem.* **1980,** *256,* 2118–2121.
55. Dolphin, D.; Felton, R. H.; Borg, D. C.; Fajer, J. *J. Am. Chem. Soc.* **1970,** *92,* 743–745.
56. Dolphin, D.; Forman, A.; Borg, D. C.; Fajer, J.; Felton, R. H. *Proc. Natl. Acad. Sci. U.S.A.* **1971,** *68,* 614–618.
57. Yonetani, T.; Schleyer, M.; Ehrenberg, A. *J. Biol. Chem.* **1966,** *241,* 3240–3247.
58. Hottman, B. M.; Roberts, J. G.; Brown, T. G.; Kang, C. H.; Margoliash, E. *Proc. Natl. Acad. Sci. U.S.A.* **1978,** *76,* 6132–6136.
59. La Mar, G. N.; deRopp, J. S. *J. Am. Chem. Soc.* in press.
60. Teroka, J.; Kitagawa, T. *Biochem. Biophys. Res. Comm.* **1980,** *93,* 694–700.
61. Mansuy, D.; Longe, M.; Chottard, J. C. *J. Am. Chem. Soc.* **1979,** *101,* 6437–6438.
62. Mansuy, D.; *Pure Appl. Chem.* **1980,** *52,* 681–690.

63. Latos-Grazynski, L.; Cheng, R.-J.; La Mar, G. N.; Blach, A. L. *J. Am. Chem. Soc.* **1981,** *102,* 4270–4272.
64. Cheng, R.-J; Olmstead, M. M.; Balch, A. L., unpublished data.
65. Chin, D.-H.; La Mar, G. N.; Balch, A. L. *J. Am. Chem. Soc.* **1980,** *102,* 5945–5947.
66. Tamura, M.; Hori, H. *Biochim. Biophys. Acta* **1972,** *289,* 20–29.
67. Hanson, L. K.; Chang, G. K.; Davis, M. S.; Fajer, J. *J. Am. Chem. Soc.* **1981,** *103,* 663–670.

RECEIVED for review June 12, 1981. ACCEPTED December 7, 1981.

Redox Chemistry of the 3,5-Di-*tert*-butylcatecholato and *o*-Semiquinonato Complexes of Transition Metal Ions in Aprotic Media

DER-HANG CHIN, STEPHEN E. JONES, LUIS E. LEON, PAULA BOSSERMAN, MARTIN D. STALLINGS, and DONALD T. SAWYER

University of California, Department of Chemistry, Riverside, CA 92521

The redox chemistry of several substituted catechols, o-semiquinones, and o-quinones in four aprotic solvents (dimethyl sulfoxide, dimethylformamide, acetonitrile, and dichloromethane) has been characterized by electrochemical and spectroscopic methods. This characterization has served as a reference base for a detailed study of the redox reactions for the catecholato and o-semiquinonato complexes of manganese(IV), manganese(III), manganese(II), iron(III), iron(II), molybdenum(VI), molybdenum(V), molybdenum(IV), and vanadium(V), vanadium(IV), vanadium(III) ions. The results confirm that these systems prefer a hard acid–hard base interaction, for example $MN(IV)(cat)_3^{2-}$ *rather than* $Mn(II)(cat)(SQ)_2^{2-}$ *(where cat represents catechol and SQ represents semiquinone), and that the highest oxidation state of the metal is stabilized by catechol ligands for coordinately saturated conditions.*

The catechols are effective bidentate ligands that form a variety of stable complexes with metal ions. This special quality is utilized in numerous biological systems for metal-ion transport and storage, and has prompted renewed interest in the transition-metal ion coordination chemistry with catechol ligands. Catechol complexes of chromium (III), copper (II), zinc (II), cobalt (II), and nickel (II) were

0065-2393/82/0201-0675$09.25

observed in the 1920s (*1*, *2*). Later studies were directed to the rare earth– (*3*), alkaline earth– (*4*, *5*), rhenium– (*6*), and iron– (*7*) catechol complexes. More recently, stability constants and associated thermodynamic quantities were determined for copper(II)–catechol complexes by polarographic and potentiometric methods (*8*, *9*), and for copper(II)–, zinc(II)–, nickel(II)–, cobalt(II)–, manganese(II)–, cadmium(II)–, and magnesium(II)–catechol complexes by the Calvin–Bjerrum pH-titration and related methods (*10–12*). Metal-catalyzed oxidations of catechols were studied for the manganese(II) and cobalt(II) ions in bicarbonate buffer (*13*); a mechanism involving a bound dioxygen intermediate was proposed (*14*).

During the past decade the importance of metal–catechol complexes in biology has become evident. For example, enterobactin was shown to be an essential sequestering agent for iron(III) transport in *Salmonella typhimurium* and *Escherichia coli* (*15*); it represents the most stable iron(III) complex yet observed ($K > 10^{52}$) (*16*). This siderophore molecule contains three catechol chelating groups that bind iron(III) through the vicinal dioxo function (*17*, *18*). Kinetic studies showed that enterobactin is capable of removing iron from transferrin in the blood serum (*19*). It also has been considered as a drug for treatment of certain genetic diseases related to abnormally high concentrations of iron in the blood (*20*).

Quinones are intermediates in the biosynthesis of tetracyclines (*21*), aflatoxins (*22*), and other secondary metabolites (*23*). However, their most important reaction in biology is reversible electron transfer reduction to the corresponding semiquinone and hydroquinone or catechol. Quinones are essential components in the electron transport chain associated with the formate dehydrogenases (*24*), which are widely distributed in plants and microorganisms. Although metals may not be vital cofactors, molybdenum, tungsten, selenium, and iron have been detected in these enzymes (*25–27*).

Quinones also are involved in the primary electron transfer processes of photosynthesis (*28*), and their reduced forms may interact with the manganese cofactor that catalyzes the oxygen-evolution process of photosystem II (*29*); a transient radical species has been detected in oxygen-evolving spinach chloroplasts (*30*). The magnetic behavior and electron paramagnetic resonance (EPR) line-shape of this transient radical indicate that it probably is a quinoidal species in close proximity to a paramagnetic ion, probably manganese. A model for the manganese cofactor of photosystem II has been designed (*31*) in which the manganese–catechol–semiquinone–OH chelate system provides a template to promote formation of the O–O bond during the water oxidizing process.

The addition of catechol or catecholamine reverses the inhibition of Na–K-ATPase (where ATPase represents adenosine triphosphatase)

(*32*), dynein ATPase (*33*), and LAD-1 (where LAD represents lactic acid dehydrogenase) (*33*) by vanadate. A study of the reaction of a catecholamine, norepinephrine, with vanadium(V) indicates that the metal is complexed before it is reduced by the ligand (*34*).

Beyond biological systems, the catechol dianion has proved to be an effective hard-base ligand for the ions of manganese (*35*, *36*), molybdenum (*35–41*), and vanadium (*42*, *43*). In addition, there have been several investigations of *o*-semiquinone (SQ) complexes of metal ions (*44*, *45*). These complexes were formed by the combination of *o*-semiquinolates of alkaline metals with the halides of the transition metals in tetrahydrofuran (THF) in an inert atmosphere. The metal $(SQ)_3$ complexes of chromium, molybdenum, tungsten, vanadium, titanium, lanthanum, and iron also were obtained in aqueous media by reacting the catechols with the transition-metal salts in the presence of base and air (*46*). Several tris(*o*-semiquinonato) complexes of vanadium(III), chromium(III), and iron(III) were synthesized and structurally characterized (*47*, *48*). For the iron(III)–(9,10-phenanthrene-semiquinone)$_3$ complex (*48*), the three *o*-semiquinone ligands are in a trigonally distorted octahedral coordination geometry. In addition, bis(*o*-semiquinonato) complexes of cobalt(II) and nickel(II) (*49*) and of molybdenum(VI) (*50*) have been discussed. The latter complex, $[Mo(VI)]_2O_5(PSQ)_2$ (PSQ = 9,10-phenanthrene-*o*-semiquinone), is diamagnetic, which implies that the two semiquinone ligands are coupled.

Stable one-to-one *o*-semiquinone complexes are formed with the ions of the group IIB, IIIA, IIIB, and IVB metals (*51–55*). Two additional examples include cobalt(III) (DTBC) (DTBSQ) (bipyridyl) (DTBC = 3,5-di-*tert*-butylcatechol; DTBSQ = 3,5-di-*tert*-butyl-*o*-semiquinone) (*56*) and $Pd(PPh_3)_2(Cl_4SQ)^+$ (Cl_4SQ = 3,4,5,6-tetrachloro-*o*-semiquinone) (*57*). The ESR spectrum of the latter species indicates that the unpaired electron is localized on the semiquinone ligand.

Clearly, the catechol dianion and the semiquinone anion radical form stable complexes with transition metal ions. Because several essential biological systems are dependent on metal–catechol complexes, a fuller understanding of the coordination chemistry and redox reactions for this class of metal chelates is desirable, especially for the aprotic conditions that prevail in biomembranes. This knowledge is particularly important for those circumstances where the metal ion has the propensity to oxidize catechol to its semiquinone and quinone. Until recently, electrochemical characterizations of the redox properties of metal–catechol systems in aprotic media were limited to the chromium(III)–catechol (*58*, *59*) and the cobalt(III)–catechol (*60*) complexes. The redox chemistry of the 3,5-di-*tert*-butylcatecholato (DTBC) and 3,5-di-*tert*-butyl-*o*-semiquinonato (DTBSQ) complexes of

several transition metal ions have been a major interest of our group. An early study described a vanadium–DTBC complex, which appeared to bind oxygen reversibly in methanol solutions (*61*). Unfortunately, we have been unable to duplicate the synthesis and isolation of this purported tetrahedral vanadium(IV) $(DTBC)_2$ complex. Hence, the reported reversible adducts of O_2, CO, and NO with the complex represent spurious results, and the spectral and structural interpretations are believed to be fallacious.

In recent reports, two molybdenum–catechol complexes, bis [bis(3,5-di-*tert*-butylcatecholato)oxomolybdenum(VI)], $[Mo(VI)O(DTBC)_2]_2$, and its monomer, $Mo(VI)O(DTBC)_2$, were characterized (*62–64*). The monomer species can be reduced electrochemically to $Mo(V)O(DTBC)_2^-$, which exhibits an ESR resonance at $g = 1.94$ and undergoes reoxidation to the original species by electron transfer to oxygen molecules to yield superoxide ions. The system has been proposed as a reaction mimic for the xanthine oxidase enzyme.

When base is added to a solution of $[Mo(VI)O(DTBC)_2]_2$, a red–orange binuclear molybdenum(VI) species is obtained, bis(tetra-*n*-butylammonium) - μ - oxobis[(3,5 - di - *tert* - butylcatecholato) dioxomolybdenum(VI)]. Crystallographic investigation (*62*) of the complex revealed a $Mo(VI)_2O_5$ fragment that sits on top of two paired catecholato ligands (Figure 1). This complex, plus the related catecholate dianion, $[Mo(VI)]_2O_5(O_2C_6H_4)_2^{2-}$ (*65*), and the neutral 9,10-phenanthrene-*o*-semiquinone complex, $[Mo(VI)]_2O_5(O_2C_{14}H_8)_2$ (*55*), have similar structures within the inner coordination spheres. All have bridges of catecholato and semiquinone ligands between two metals through one oxygen.

The aqueous chemistry of tris(catecholato) complexes of manganese(II) and manganese(III), as well as the reversible oxidation of $Mn(III)(DTBC)_3^{3-}$ to a unique tris(semiquinonato)manganese(III) complex, was investigated (*66*). The 3,5-di-*tert*-butylcatechol anion complexes of manganese(II), manganese(III), and manganese(IV) were studied in aprotic solvents by electrochemical, spectroscopic, and magnetic methods (*67*, *68*).

This chapter summarizes the results of recent investigations of the redox chemistry of the 3,5-di-*tert*-butylcatecholato (DTBC) and *o*-semiquinonato (DTBSQ) ligands and their complexes of manganese, iron, molybdenum, and vanadium ions in aprotic media.

Results and Discussion

Redox Chemistry of DTBC, DTBQ, and DTBSQ. The cyclic voltammogram of $DTBCH_2$ in dimethylformamide (DMF) exhibits two irreversible reduction peaks at -1.47 and -2.25 V vs. SCE. It also has

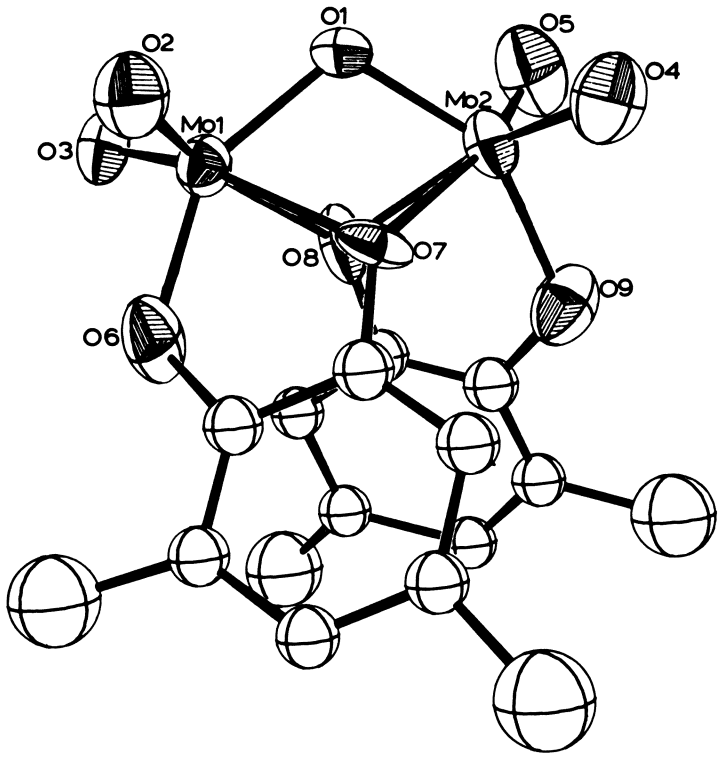

Figure 1. Schematic view of the orange, anionic binuclear molybdenum(VI)–DTBC complex, $[Mo(VI)]_2O_5[O_2C_6H_2(t\text{-}Bu)_2]_2^{2-}$. tert-Butyl methyl carbon atoms have been omitted for clarity.

one irreversible oxidation peak at +0.97 V to give a product that is reduced at −0.32 V (Figure 2). In neutral or acidic solution, controlled potential oxidation of $DTBCH_2$ at +1.25 V removes two electrons per molecule. The oxidized solution exhibits the same absorption spectrum that is observed for DTBQ, and a cyclic voltammogram with three reduction peaks (−0.29 V vs. saturated calomel electrode (SCE), −0.45 V, and −0.54 V). The peak at −0.29 V results from the reduction of the quinone in the presence of protons, that at −0.45 V results from the reduction of free protons (*69*), and that at −0.54 V results from the reduction of DTBQ. Controlled potential reduction of this oxidized DTBC solution at −0.55 V consumes two electrons and yields a solution with the voltammetry and spectroscopy of $DTBCH_2$. The latter

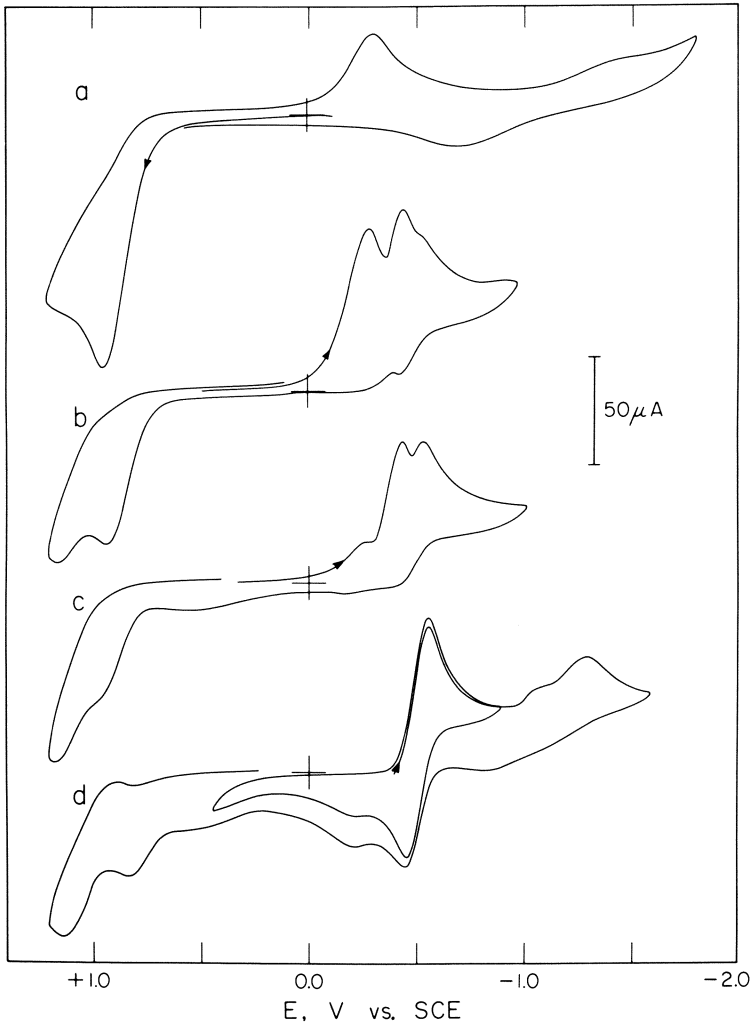

*Figure 2. Cyclic voltammogram for 1.45 m*M *solutions of a, 3,5-di-tert-butylcatechol ($DTBCH_2$); b, solution a after exhaustive oxidation at +1.25 V vs. SCE; c, solution b plus 1.45 m*M *tetraethylammonium hydroxide (TEAOH); and d, solution b plus 2.90 m*M *TEAOH. All in DMF that contains 0.1* M *tetraethylammonium perchlorate (TEAP) at a Pt electrode (surface area 0.23 cm^2). Scan rate, 0.2 V/s.*

species is reduced at −1.60 V by a one-electron process to yield hydrogen gas and a product whose electrochemistry and spectroscopy are identical to that for a one-to-one combination of tetraethylammonium hydroxide (TEAOH) and $DTBCH_2$ (Figure 3).

The electrochemical behavior of DTBQ in aprotic media is illustrated by Figure 2d. The first couple represents reduction to the

semiquinone anion radical, which was confirmed by controlled potential coulometry, ESR, and absorption spectroscopy. The second reduction is a one-electron irreversible process to give the dianion. The ratio of the anodic-to-cathodic peak currents increases to unity as the scan rate is increased, which indicates that there is some enhancement of the cathodic peak current at low scan rates. Addition of water to DTBQ causes an additional decrease in this ratio. A double step chronoamperometric experiment indicated that a proton-induced disproportionation of the semiquinone anion is accelerated by trace quantities of water (*70*).

The semiquinone of DTBQ (DTBSQ) exhibits a single reduction peak at −1.35 V; the reverse scan has a major oxidation peak at −0.46 V due to DTBSQ plus a small peak due to $DTBCH^-$. The DTBSQ

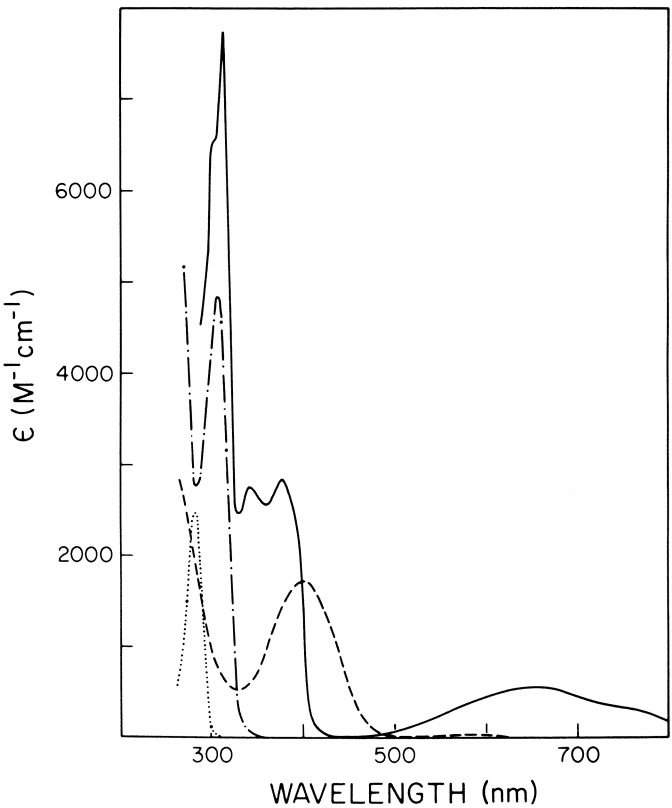

*Figure 3. Absorption spectra of 2.0 m*M *solutions of 3,5-di-*tert*-butylcatechol ($DTBCH_2$), 3,5-di-*tert*-butylcatechol monoanion ($DTBCH^-$), 3,5-di-*tert*-butyl-o-benzoquinone (DTBQ) plus 2.0 m*M *$HClO_4$, and 3,5-di-*tert*-butyl-o-benzosemiquinone ($DTBSQ^-$) plus 2.0 m*M *TEAOH in DMF. Key: —, $DTBQ^- + OH^-$; ----, $DTBQ + H^+$; — · — ·, DTBC + OH^-; and . . . ., DTBC.*

species is stabilized by the addition of base [tetraethylammonium hydroxide (TEAOH)] to a DTBQ solution before it is electrolytically reduced. When DTBSQ is reduced to $DTBC^{2-}$ in the absence of base, a redox reaction occurs such that DTBSQ is the major product observed for the reverse scan. When DTBSQ is reduced in the presence of base, the major product is the catechol monoanion. The ratio of anodic peak currents for DTBSQ and $DTBCH^-$ indicates that $DTBCH^-$ is the predominant species present at slow scan rates.

Table I summarizes the redox reactions and their redox potentials for DTBC, DTBQ, and DTBSQ in four aprotic solvents. Reactions 1 and 2 are equivalent to the addition of base. Reduction of $DTBSQ^-$ to $DTBC^{2-}$ (Equation 4) yields a strong base and an effective reductant of solvent protons. During controlled potential electrolysis of DTBQ, the hydroxide ion that is generated by the hydrolysis of $DTBC^{2-}$ with trace H_2O suppresses the ability of water to act as an oxidant. Hence, only oxidation peaks due to the catechol monoanion and the hydroxide ion are observed for the final product solution.

Manganese Complexes. Figure 4 illustrates the cyclic voltammograms for DMF solutions that contain 1 : 1, 1 : 2, and 1 : 3 mol ratios of $Mn(II)(DMU)_6(ClO_4)_2$(DMU = 1,3-dimethylurea) to DTBQ. Controlled potential electrolysis for the 1 : 1 solution at −0.65 V vs. SCE requires 1.5 electrons per DTBQ and yields a pale green solution. The magnetic moment decreases after electrolysis from 6.1 B.M., for a high spin d^5 manganese(II) ion, to 5.1 B.M., for a high spin d^4 manganese(III) complex. The 1 : 2 manganese(II)- to- DTBQ system exhibits one reduction peak (−0.46 V); controlled potential electrolysis at −0.65 V requires 1.5 electrons per DTBQ and yields a pale green solution with a magnetic moment of 5.0 B.M. (indicative of a high spin d^4 manganese(III) complex). The product species has a single oxidation peak at +0.17 V that is coupled to a peak at −0.46 V for the reverse scan. Controlled potential oxidation of this pale green solution at +0.25 V yields manganese(II) and DTBQ. An initial negative scan of the 1 : 3 manganese(II)-to-DTBQ solution yields two reduction peaks (−0.46 and −0.50 V). Controlled potential electrolysis at −0.65 V requires 1.5 electrons per DTBQ and yields a distinctive dark blue solution, which has a magnetic moment of 3.9 B.M. and is characteristic of $Mn(IV)(DTBC)_3^{2-}$ (*68*). The single-crystal x-ray structure for $Na_2Mn(IV)(DTBC)_3$ was determined to have a symmetric octahedral configuration. In DMF, this complex has an irreversible reduction peak at −1.25 V. Controlled potential electrolysis at −1.40 V requires one electron per manganese and yields a pale green solution that is ESR silent at +77 K and has a magnetic moment of 5.1 B.M. at room temperature. A positive scan of the $Mn(IV)(DTBC)_3^{2-}$ complex exhibits a one-electron process at −0.38 V vs. SCE that is followed by a

Published on June 1, 1982 on http://pubs.acs.org | doi: 10.1021/ba-1982-0201.ch028

Table I. Summary of Redox Reactions and Potentials for the DTBQ–DTBSQ$^-$–DTBCH$_2$ System in Aprotic Media[a]

Reaction	*Redox Potential, V, vs. SCE*[b]			
	AN	*DMF*	*DMA*	*$(CH_3)_2SO$*
(1) $DTBCH_2 + e^- \rightarrow \frac{1}{2}H_2 + DTBCH^-$	−1.22	−1.47	−1.25	−1.84
(2) $DTBCH^- + e^- \rightarrow DTBCH^{2-} \rightarrow \frac{1}{2}H_2 + DTBC^{2-}$	—[c]	−2.25	−2.15	—[c]
(3) $DTBQ + e^- \rightleftarrows DTBSQ^-$	−0.51	−0.49	−0.44	−0.47
(4) $DTBSQ^- + e^- \rightleftarrows DTBC^{2-} \xrightarrow{H_2O} DTBCH^- + OH^-$				
$\xrightarrow{H_2O} \frac{1}{2}H_2 + DTBSQ^- + OH^-$				
(5) $DTBCH^- \rightarrow DTBSQH^{\cdot} + e^- \rightarrow \frac{1}{2}DTBCH_2 + \frac{1}{2}DTBQ$	−0.12	−0.14	−0.14	−0.13
(6) $DTBCH_2 \rightarrow DTBQ + 2H^+ + 2e^-$	+1.19	+0.97	+1.07	+0.96
(7) $DTBQ + 2H^+ + 2e^- \rightarrow DTBCH_2$	+0.40	−0.32	−0.26	−0.19

[a] AN represents acetonitrile; DMF, dimethylformamide, DMA, dimethylacetamide; and $(CH_3)_2SO$, dimethyl sulfoxide.
[b] For reversible processes, the redox potential is the mean of the cathodic and anodic peak potentials; for irreversible processes, it is the peak potential at a scan rate of 0.1 V/s.
[c] Not observed in this solvent.

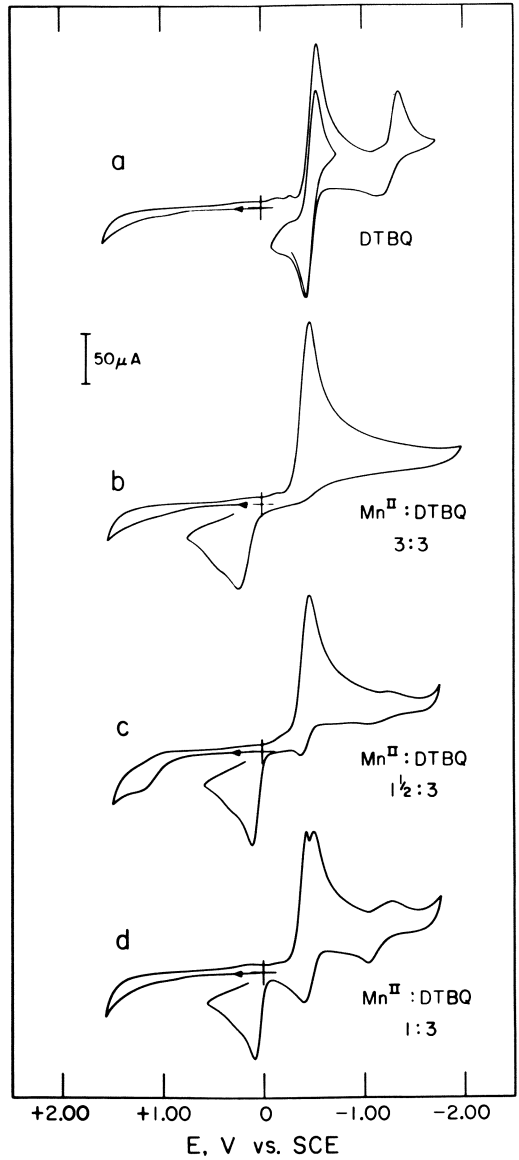

*Figure 4. Cyclic voltammograms in DMF (0.1 M TEAP) of a, 3.0 mM of 3,5-di-*tert*-butyl-o-quinone (DTBQ); b, 3mM DTBQ plus 3 mM [Mn(II)(DMU)$_6$](ClO$_4$)$_2$; c, 3mM DTBQ plus 1.5 mM [Mn(II)(DMU)$_6$](ClO$_4$)$_2$; and c, 3 mM DTBQ plus 1 mM [Mn(II)(DMU)$_6$](ClO$_4$)$_2$. Scan rate, 0.1 V/s; Pt electrode (area, 0.23 cm^2).*

three-electron oxidation at +0.17 V. Controlled potential coulometry at −0.25 V yields manganese(II) and three equivalents of free DTBQ (confirmed by ESR and electronic spectroscopy, respectively).

To determine if the *o*-semiquinone is involved as an intermediate in the manganese–DTBQ redox systems, DTBSQ was synthesized electrochemically and added to manganese(II). Combination of two equivalents of DTBSQ with one equivalent of manganese (II) causes an immediate color change from blue to pale green. On the basis of cyclic voltammetry and absorption spectroscopy, approximately one-half of the DTBSQ is converted to free quinone. The same is true for the 3:1 DTBSQ-to-manganese(II) combination, which has a dark green color. Controlled potential electrolysis at −0.65 V requires one equivalent of electrons and yields a dark blue solution with the same cyclic voltammogram as that for $Mn(IV)(DTBC)_3^{2-}$ (68).

The electrochemistry of manganese(II) with DTBQ (1:3 mol ratio) in CH_3CN is different from that in either DMF or dimethyl sulfoxide (DMSO) (Figure 5). An initial negative scan yields reduction peaks at −0.24 and −0.60 V, both two-electron processes, with three one-electron oxidations at −0.44, −0.15, and +0.14 V and a two-electron oxidation at +0.56 V for the reverse scan. Controlled potential electrolysis at −0.71 V requires 1.5 electrons per DTBQ (as in DMF and DMSO), and yields a dark blue solution. The electrolysis product has a one-electron reduction peak at −1.38 V.

Table II summarizes the redox and formation Reactions 8–16 for the manganese–DTBC–DTBSQ–DTBQ system. Reduction of the various manganese(II)-to-DTBQ systems occurs via Equations 11–13. Reduction of the 1:1 and 1:2 manganese(II)-to-DTBQ systems yields the same product with an absorption maxima at 285 nm, a magnetic susceptibility of 5.0 B.M., and equivalent electrochemistry. All data are consistent with the formation of the $Mn(III)(DTBC)_2^-$ complex.

Reduction of the 1:3 manganese(II)-to-DTBQ system requires four electrons in two steps,

$$Mn(II) + 2DTBQ + 3e^- \xrightarrow{-0.46\ V} Mn(III)(DTBC)_2^- \quad (17)$$

$$Mn(III)(DTBC)_2^- + DTBQ + 1e^- \xrightarrow{-0.51\ V} Mn(IV)(DTBC)_3^{2-} \quad (18)$$

The $Mn(IV)(DTBC)_3^{2-}$ complex is reduced at −1.25 V vs. SCE to form $Mn(III)(DTBC)_3^{3-}$. The lack of a reverse anodic peak implies an electrochemical (EC) mechanism, probably with residual water in the solvent.

$$Mn(III)(DTBC)_3^{3-} + H_2O \rightarrow Mn(III)(DTBC)_2^- + DTBCH^- + OH^- \quad (19)$$

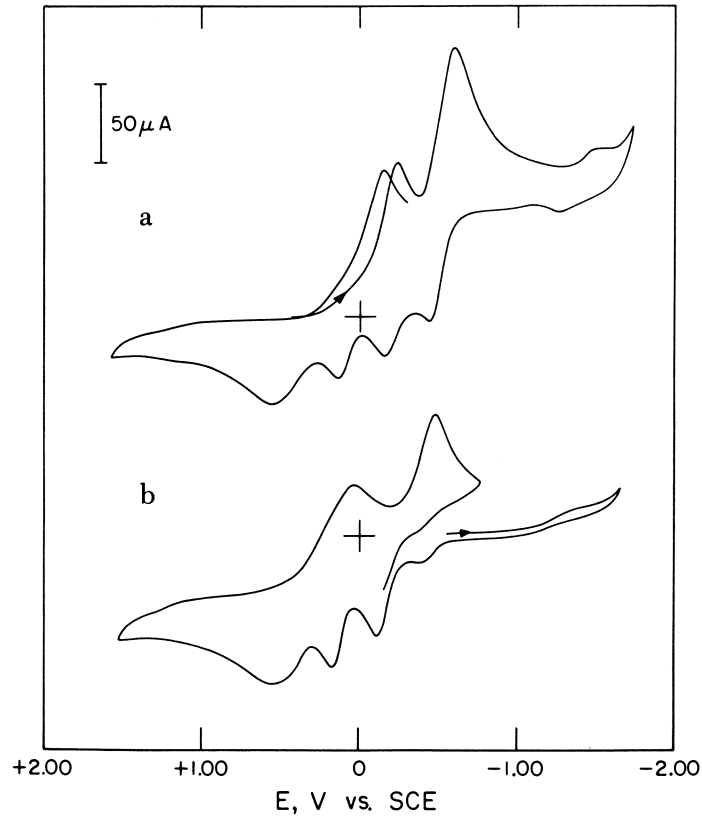

Figure 5. Cyclic voltammogram in CH_3CN (0.1 M TEAP) of a, 3 mM DTBQ plus 1 mM $[Mn(II)(DMU)_6](ClO_4)_2$; and b, cyclic voltammogram after electrolysis of a at −0.72 V vs. SCE. Scan rate, 0.1 V/s; Pt electrode (area, 0.23 cm^2).

This mechanism is confirmed by the presence of an anodic peak at −0.17 V (due to $DTBCH^-$ oxidation) and an absorption band at 285 nm [due to $Mn(III)(DTBC)_2^-$] after controlled potential reduction at −1.40 V.

When three equivalents of DTBSQ are added to one equivalent of manganese(II), the light green $Mn(III)(DTBC)_2^-$ complex is formed, plus one equivalent of free DTBQ. A possible mechanism involves initial semiquinone coordination to manganese followed by electron transfer and disproportionation to bound catechol and free quinone.

In CH_3CN, the individual redox processes can be observed as a cascade of one-electron steps for reduction and reoxidation of the $Mn(IV)(DTBC)_3^{2-}$ complex back to starting materials (Figure 5).

Published on June 1, 1982 on http://pubs.acs.org | doi: 10.1021/ba-1982-0201.ch028

Table II. Redox Reactions for the 3,5-Di-*tert*-butylcatecholato ($DTBC^{2-}$) Complexes of Manganese and for Their Formation from Reduction of 3,5-Di-*tert*-butyl-*o*-quinone (DTBQ)

Reaction	*Redox Potentials, V, vs. SCE*[a]		
	$E^{\circ\prime}$	$E_{p,c}$	$E_{p,a}$
(8) $DTBQ + e^- \rightleftarrows DTBSQ^-$	−0.44	−0.55	
(9) $DTBSQ^- + e^- \rightleftarrows DTBC^{2-}$	−1.17	−1.33	
(10) $Mn(II) + DTBCH_2 + 2\ OH^- \rightarrow Mn(II)DTBC + 2H_2O$			
(11) $2Mn(II) + 2DTBQ + 3e^- \rightarrow Mn(III)(DTBC)_2^- + Mn(II)$		−0.46	
(12) $Mn(II) + 2DTBQ + 3e^- \rightarrow Mn(III)(DTBC)_2^-$		−0.46	
(13) $Mn(II) + 3DTBQ + 4e^- \rightarrow Mn(IV)(DTBC)_3^{2-}$		−0.46, −0.49	
(14) $Mn(IV)(DTBC)_3^{2-} + e^- \rightarrow Mn(III)(DTBC)_3^{3-}$		−1.26	
(15) $Mn(III)(DTBC)_2^- \rightarrow Mn(II) + 2DTBQ + 3e^-$			+0.17
(16) $Mn(IV)(DTBC)_3^{2-} \rightarrow Mn(II) + 3DTBQ + 4e^-$			+0.38, +0.17

Note: All reactions in DMF (0.1 *M* TEAP).

[a] For reversible processes, the redox potential ($E^{0\prime}$) represents the mean of the cathodic ($E_{p,c}$) and anodic ($E_{p,a}$) peak potentials; for irreversible processes, the peak potentials are for a scan rate of 0.1 V/s.

$$\mathrm{Mn(IV)(DTBC)_3^{2-}} \xrightarrow[\mathrm{CH_3CN}]{-0.15\ \mathrm{V}} \mathrm{Mn(IV)(DTBC)_2(DTBSQ)^-} + e^- \quad (20)$$

$$\downarrow$$

$$\mathrm{Mn(III)(DTBC)_2^-} + \mathrm{DTBQ}$$

$$\downarrow +0.14\ \mathrm{V}$$

$$\mathrm{Mn(III)(DTBC)(DTBSQ)} + e^-$$

$$\downarrow$$

$$\mathrm{Mn(II)(DTBC)} + \mathrm{DTBQ}$$

$$\downarrow +0.56\ \mathrm{V}$$

$$\mathrm{Mn(II)} + \mathrm{DTBQ} + 2e^-$$

The broad peak centered at +0.56 V represents a two-electron process because it is coupled to the two-electron reduction peak at +0.03 V.

Iron Complexes. Figure 6 illustrates the cyclic voltammetry for the 1:1, 1:2, and 1:3 $Fe(II)(ClO_4)_2 \cdot 6H_2O$–DTBQ systems in $(CH_3)_2SO$. The couple at $E^{\circ\prime}_{1/2}$ = +0.26 V vs. SCE is due to the reversible Fe(II)/Fe(III) oxidation–reduction reaction. The 1:1 iron(II)-to-DTBQ system in $(CH_3)_2SO$ exhibits a reduction peak at −0.84 V that results from the Fe(II)/Fe(0) couple. This peak increases and shifts in potential when iron(II) is added to the solution (appearance of a sharp peak at −0.56 V for the reverse scan is due to the Fe(0)/Fe(II) reaction). The reduction peak at −0.51 V is characteristic of free DTBQ, with subsequent association of the generated semiquinone anion with the iron ions. The reduction peak for the 1:3 system at −1.46 V is due to the formation of $DTBC^{2-}$ from $DTBSQ^-$. The oxidation peaks at −1.25 and −0.38 V result from free $DTBC^{2-}$ and $DTBSQ^-$, respectively. Reoxidation of the electrosynthesized complexes occurs in distinct one-electron steps that are followed by a two-electron oxidation back to the starting materials. Proton NMR, UV–visible, and cyclic voltammetry measurements confirm that the ligand is not degraded during the electrochemical cycle. Table III summarizes the electrochemical reactions that are observed for the iron(II)–DTBQ system.

Table III. Number of Electrons Transferred per Iron During Controlled Potential Electrolysis of 1 m*M* Fe(II) in the Presence of 0, 1, 2, and 3 m*M* DTBQ, Respectively

	Electrolysis potential, V, vs. SCE		
*[DTBQ], m*M	*+0.45*	*0.00*	*−0.70*
0	+1.0	0	—
1	+0.6	−0.8	−1.4
2	+0.6	−1.0	−3.0
3	+0.7	−1.3	−4.2

Note: A positive sign indicates an oxidation process and a negative sign indicates a reduction process. All reactions in $(CH_3)_2SO$ (0.1 *M* TEAP) at a Pt electrode.

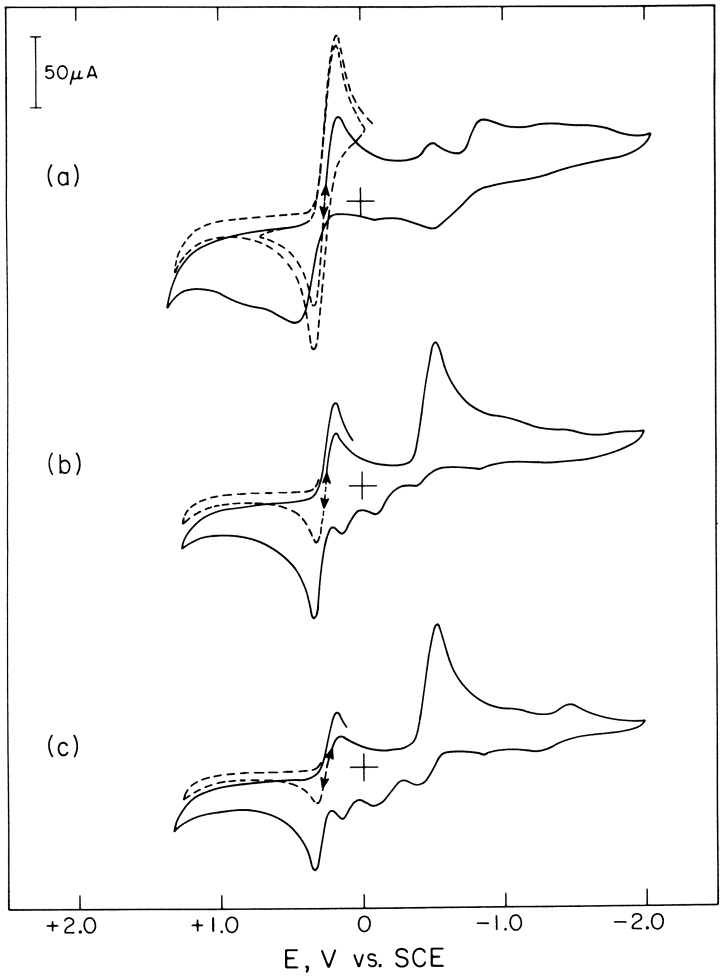

Figure 6. Cyclic voltammograms for solutions that result when iron(II) and DTBQ are combined in the ratio of a, 3 mM:3 mM; b, 1.5:3; and c, 1:3 in $(CH_3)_2SO$ that contains 0.1 M TEAP. Scan rate, 0.1 V/s. All scans originate at the rest potential for the solutions.

The Fe(III)(DTBSQ)$_3$ complex (*71*) is stable in CH_2Cl_2 solution and exhibits a unique cyclic voltammogram. When Fe(III)(DTBSQ)$_3$ is added to $(CH_3)_2SO$, a rapid redox reaction occurs with vivid color changes. An important feature is that the addition of Fe(III)(DTBSQ)$_3$ to $(CH_3)_2SO$ yields a solution that is indistinguishable from the solution from the 1:3 combination of iron(III) and DTBSQ$^-$ (based on electrochemical, spectroscopic, NMR, and magnetic susceptibility measurements). The data indicate the formation of Fe(III)(DTBC)(DTBSQ) plus one equivalent of free quinone.

Electrochemical and spectroscopic measurements for various mole-ratios of $DTBSQ^-$ with iron(II) provide insight into the reaction paths and nature of the products. The cyclic voltammogram for the 1 : 1 $Fe(II)(ClO_4)_2 \cdot 6H_2O$–$DTBSQ^-$ system is similar to that obtained after controlled potential reduction at 0 V of a 1 : 1 iron(II) : DTBQ solution. A 1 : 2 combination of $Fe(II)(ClO_4)_2 \cdot 6H_2O$ and $DTBSQ^-$ yields a solution with voltammetric reduction peaks at −0.17 and −1.47 V. The former peak is coupled to a one-electron oxidation peak at −0.08 V. Controlled potential reduction at −0.30 V requires one electron per iron and yields a solution similar to the reaction product of the 1 : 2 iron(II)–DTBQ system (Figure 6b). Controlled potential reduction of the 1 : 3 $Fe(II)(ClO_4)_2 \cdot 6H_2O$–$DTBSQ^-$ system at −0.65 V results in the transfer of 1.5 electrons per iron to yield a product whose electrochemistry is identical to that of the reduction product (at −0.65 V) of the 1 : 3 iron(II)–DTBQ system (Figure 6c).

When $DTBC^{2-}$ is added to $[Fe(III)(H_2O)_6](ClO_4)_3$, the resulting complexes exhibit substantially different electrochemistry from those that are formed by reduction of DTBQ in the presence of iron(II). Additional peaks appear in the cyclic voltammogram and the observed magnetic moments are smaller. A positive scan yields additional oxidation peaks at −0.25 and +0.84 V; the latter peak is due to OH^- oxidation.

A 1 : 1 combination of $Fe(III)(ClO_4)_3 \cdot 6H_2O$ and $DTBC^{2-}$ exhibits the same electrochemical and spectroscopic properties as a 1 : 1 combination of $Fe(II)(ClO_4)_2 \cdot 6H_2O$ and $DTBSQ^-$ in wet $(CH_3)_2SO$. The differences between the UV–visible spectra for 1 : 2 and 1 : 3 combinations of iron(III) and $DTBC^{2-}$, and for 1 : 2 and 1 : 3 combinations of iron(II) and $DTBSQ^-$ are illustrated in Figure 7. The intense bands at 293 and 305 nm have been assigned to ligand $\pi \rightarrow \pi^*$ transitions in other metal–catechol complexes (*60, 62, 63, 68, 72–75*). The spectra indicate the presence of catecholate and semiquinone ligands, as well as of free DTBQ in both systems (*see* Figure 3 also). These results indicate that the iron(III) complexes are binuclear, probably via a μ-oxo-bridge in alkaline or wet $(CH_3)_2SO$.

On the basis of the experimental results, a self-consistent set of redox and formation reactions for the iron–catechol and iron–semiquinone systems can be formulated. Reduction of the quinone occurs first, followed by coordination of two semiquinones to one iron(II) ion and rapid disproportionation of the bound $DTBSQ^-$ groups. This reaction sequence is analogous to the manganese–catechol system. Ferrous ion contributes one electron to the overall electron stoichiometry in all of the reactions studied.

The spectroscopy and electrochemical results indicate that the initial reaction of the iron(II)–DTBQ system in $(CH_3)_2SO$ is the formation of an iron–semiquinone adduct.

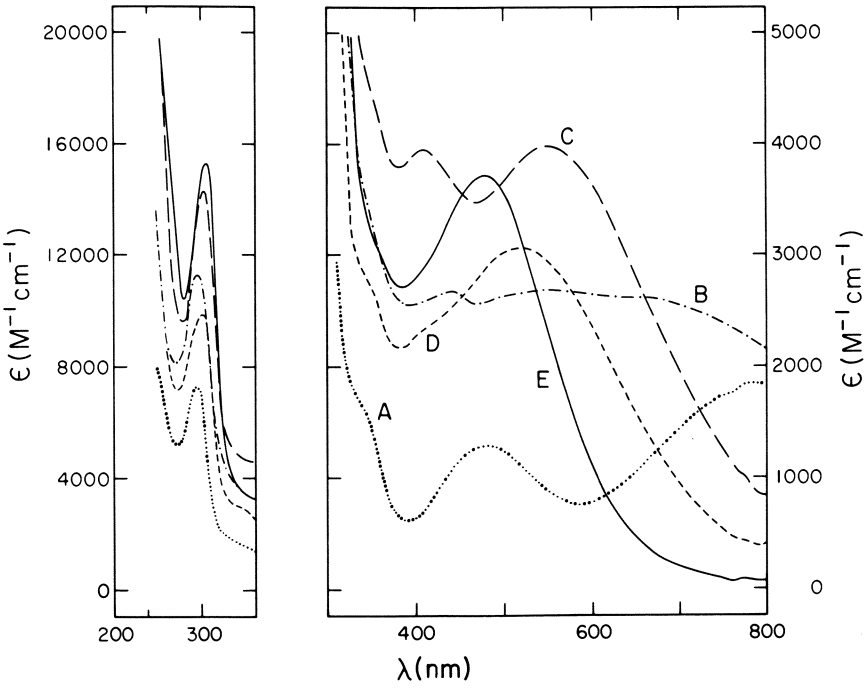

*Figure 7. UV–visible spectra for the solutions that result when iron(II) and 3,5-di-*tert*-butyl-o-semiquinone ($DTBSQ^-$) are combined in the ratio of A, 1:1; B, 1:2; and C, 1:3, and when iron(III) and 3,5-di-*tert*-butylcatechol dianion ($DTBC^{2-}$) are combined in the ratio of D, 1:2; and E, 1:3 in $(CH_3)_2SO$.*

$$Fe(II) + DTBQ \xrightarrow{(CH_3)_2SO} Fe(III)(DTBSQ)^{2+} \quad (21)$$

For the 1:2 and 1:3 iron(II)–DTBQ systems, a single multielectron reduction peak is observed at −0.51 V. The same reaction and pathway results when three equivalents of $DTBSQ^-$ are added to one equivalent of iron(II).

$$Fe(II) + 2DTBQ + 3e^- \xrightarrow{-0.51\ V} Fe(III)(DTBC)_2^- \quad (22)$$

$$Fe(II) + 3DTBQ + 4e^- \xrightarrow{-0.51\ V} Fe(III)(DTBC)_2(DTBSQ)^{2-}$$

$$Fe(III)(DTBC)_2(DTBSQ)^{2-} \xrightarrow{1e^-,\ -1.30\ V} Fe(III)(DTBC)_3^{3-} \quad (23)$$

$$Fe(II) + 3DTBSQ^- \rightarrow Fe(III)(DTBC)_2^- + DTBQ \quad (24)$$

Disproportionation of the $Fe(III)(DTBSQ)_3$ complex in $(CH_3)_2SO$ occurs in a similar fashion. A one-electron reduction at −0.17 V

$$\mathrm{Fe(III)(DTBSQ)_3} \xrightarrow{(CH_3)_2SO} \mathrm{Fe(III)(DTBC)(DTBSQ)} + \mathrm{DTBQ}$$
$$\downarrow 1e^- \quad -0.17\ \mathrm{V} \qquad (25)$$
$$\mathrm{Fe(III)(DTBC)_2^-} + \mathrm{DTBQ}$$

yields a product that is electrochemically and spectroscopically indistinguishable from the product of Equation 24.

Because of the complexity of the mixtures that result from the combination of iron(III) and $DTBC^{2-}$ in wet or alkaline $(CH_3)_2SO$, the reaction pathway and final products cannot be established definitely. However, on the basis of the experimental results, a self-consistent mechanism for the electron-transfer and complexation reactions for the iron(II)–DTBQ systems in such media can be proposed

$$2\mathrm{Fe(II)} + 2\mathrm{DTBQ} + 2e^- \xrightarrow{-0.31\ \mathrm{V}} 2\mathrm{Fe(III)(DTBSQ)^{2+}} \qquad (26)$$
$$\downarrow \mathrm{H_2O}$$
$$[\mathrm{Fe(III)(DTBSQ)-O-Fe(III)(DTBSQ)}]^{2+} + 2\mathrm{H^+}$$
$$\downarrow 2e^- \quad -1.20\ \mathrm{V}$$
$$\mathrm{Fe(III)(DTBC)-O-Fe(III)(DTBC)}$$

In $(CH_3)_2SO$, iron(II) is oxidized by DTBQ to some extent, and the presence of OH^- shifts the reaction further to the right. For a 1:2 iron(II)–DTBQ system a likely reaction sequence is

$$2\mathrm{Fe(II)} + 4\mathrm{DTBQ} + 2e^- \xrightarrow{-0.31\ \mathrm{V}} 2\mathrm{Fe(II)(DTBSQ)_2} \xrightarrow{\mathrm{H_2O}} \qquad (27)$$
$$\mathrm{Fe(III)(DTBSQ)_2-O-Fe(III)(DTBSQ)_2} + 2\mathrm{H^+}$$
$$\downarrow$$
$$2\mathrm{DTBQ} + \mathrm{Fe(III)(DTBC)-O-Fe(III)(DTBC)}$$
$$\downarrow 2e^- \quad -0.54\ \mathrm{V}$$
$$[\mathrm{Fe(III)(DTBC)(DTBSQ)-O-Fe(III)(DTBC)(DTBSQ)}]^{2-}$$
$$\downarrow 2e^-, \mathrm{H_2O} \quad -0.30\ \mathrm{V}$$
$$2\mathrm{Fe(III)(DTBC)_2^-} + \mathrm{OH^-}$$

For the 1:3 iron(II)–DTBQ system a similar scheme probably occurs.

$$2\text{Fe(II)} + 4\text{DTBQ} + \text{H}_2\text{O} + 4e^- \xrightarrow{-0.49\text{ V}} [\text{Fe(III)(DTBC)}_2\text{–O–Fe(III)(DTBC)}_2]^{4-} \quad (28)$$

$$[\text{Fe(III)(DTBC)}_2\text{(DTBSQ)–O–Fe(III)(DTBC)}_2\text{(DTBSQ)}]^{6-}$$

$$2\text{Fe(III)(DTBC)}_3^{3-} + 2\text{OH}^-$$

These reactions are based on the electrochemical, spectroscopic, and magnetic susceptibility measurements (Table IV) for iron(II)–DTBQ combinations in wet $(CH_3)_2SO$. Because the solutions contain a mixture of monomeric and dimeric complexes, the formation of μ-oxo-dimer iron(III) species is conjectural but consistent with known chemistry. In alkaline $(CH_3)_2SO$, the $Fe(III)(DTBC)_3^{3-}$ complex is hydrolyzed rapidly.

$$2\text{Fe(III)(DTBC)}_3^{3-} + \text{H}_2\text{O} \rightarrow [\text{Fe(III)(DTBC)}_2\text{–O–Fe(III)(DTBC)}_2]^{4-} + 2\text{DTBCH}^- \quad (29)$$

The electrochemical shoulder at −0.25 V is characteristic of the μ-oxo species; the oxidation peak at +0.84 V probably is due to OH^-.

These reactions indicate that iron(III) forms stable mixed-ligand complexes with $DTBC^{2-}$ and $DTBSQ^-$ in $(CH_3)_2SO$. The equilibria between these complexes can be shifted by the presence of trace amounts of water, OH^-, and free reagents (DTBQ, $DTBSQ^-$, or $DTBC^{2-}$).

Table IV. Magnetic Moments (μ) for the Iron(II)–$DTBSQ^-$ and Iron(III)–$DTBC^{2-}$ Systems in Dimethyl Sulfoxide Solutions

Iron Species	*Semiquinone/ Catechol Species*	*Fe/DTBSQ⁻ Fe/DTBC²⁻; mole ratio*	*μ, (B.M.)*[a]
Fe(II)	$DTBSQ^-$	1:1	5.4
Fe(II)	$DTBSQ^-$	1:2	5.1
Fe(II)	$DTBSQ^-$	1:3	4.8
Fe(III)	$DTBC^{2-}$	1:1	5.4
Fe(III)	$DTBC^{2-}$	1:2	4.3
Fe(III)	$DTBC^{2-}$	1:3	4.2
$Fe(III)(DTBSQ)_3$	—	—	4.8
$Fe(II)(C10_4)_2 \cdot 6H_2O$	—	—	5.0
$Fe(III)(C10_4)_3 \cdot 6H_2O$	—	—	4.8

[a] For 10 m*M* iron in $(CH_3)_2SO$.

Molybdenum Complexes. Several catechol complexes of molybdenum(VI) have been synthesized and characterized by spectroscopic, electrochemical, and x-ray diffraction measurements (*61–64*). When 3,5-di-*tert*-butylcatechol anion ($DTBC^{2-}$) is the ligand, the results indicate that a purple binuclear complex is formed in apolar solvents (toluene, CH_2Cl_2), $[Mo(VI)O(DTBC)_2]_2$. Addition of donor solvents [$(CH_3)_2SO$ or DMF] or of strong ligands (imidazole or CN^-) causes the dimer to dissociate to a green mononuclear species. These and related redox reactions for the molybdenum–$DTBC^{2-}$ system are summarized in Table V.

Addition of base, in the presence of air, to a DMF solution of $[Mo(VI)O(DTBC)_2]_2$ results in the formation of an orange anionic complex, $Mo(VI)_2O_5(DTBC)_2^{2-}$ (Equation 34, Table V). The cyclic voltammetry for this complex in DMF is limited to anodic peaks for initial scans (Figure 8). Reduction peaks only are observed after an initial

Table V. Summary of Reactions for the Molybdenum–$DTBC^{2-}$ System in Aprotic Media.

(30) $[Mo(VI)O(DTBC)_2]_2 \overset{\text{solvent}}{\rightleftharpoons} 2Mo(VI)O(DTBC)_2(sol)$
Purple; stable in CH_2Cl_2, toluene. Green; stable in DMSO, DMF.

(31) $[Mo(VI)O(DTBC)_2]_2 + 2H_2O \rightarrow 2Mo(VI)O(DTBC)_2(H_2O)$
Green

(32) $Mo(VI)O(DTBC)_2(sol) + \text{imidazole} \rightarrow Mo(VI)O(DTBC)(\text{imidazole}) + \text{sol}$
Purple

(33) $Mo(VI)O(DTBC)_2(sol) + e^- \xrightarrow{(CH_3)_2SO,AN,DMSO} Mo(V)O(DTBC)_2(sol)^-$ $E_{p,c} = -0.5$ V vs. SCE

(34) $[Mo(VI)O(DTBC)_2]_2 + 2OH^- + 2O_2 \rightleftarrows [Mo(VI)O(DTBC)(DTBSQ)(O_2^-)]_2^{2-}, \text{tr} \overset{H_2O}{\rightleftharpoons} [Mo(VI)]_2O_5(DTBC)_2^{2-} + 2O_2 + 2DTBCH_2$
Orange

(35) $Mo(V)O(DTBC)_2(sol)^- + e^- \xrightarrow{(CH_3)_2SO,AN,DMF} [Mo(IV)O(DTBC)_2]_{tr}^{2-} \xrightarrow{(CH_3)_2SO} [Mo(VI)O_2(DTBC)_2]_{tr}^{2-} + (CH_3)_2S \xrightarrow{H_2O} \tfrac{1}{2}[Mo(VI)]_2O_5(DTBC)_2^{2-}$ $E_{p,c} = -1.2$ V

(36) $Mo(IV)O(DTBC)_2^{2-} \xrightarrow[H_2O]{DMF,AN} \tfrac{1}{2}[Mo(VI)]_2O_5(DTBC)_2^{2-} + H_2 + OH^- + DTBCH_2$

(37) $[Mo(VI)]_2O_5(DTBC)_2^{2-} \overset{DMF}{\rightleftharpoons} [Mo(VI)]_2O_5(DTBC)(DTBSQ)^- + e^-$ $E^{\circ\prime} = +0.25$ V

(38) $[Mo(VI)]_2O_5(DTBC)(DTBSQ)^- \xrightarrow{H_2O} [Mo(VI)]_2O_5(DTBC) + \tfrac{1}{2}DTBCH^- + \tfrac{1}{2}DTBQ$

(39) $[Mo(VI)]_2O_5(DTBC)_2^{2-} + 2OH^- \rightarrow [Mo(VI)]_2O_7^{2-} + DTBCH_2 + DTBQ + 2e^-$ $E_{p,a} = -0.05$ V

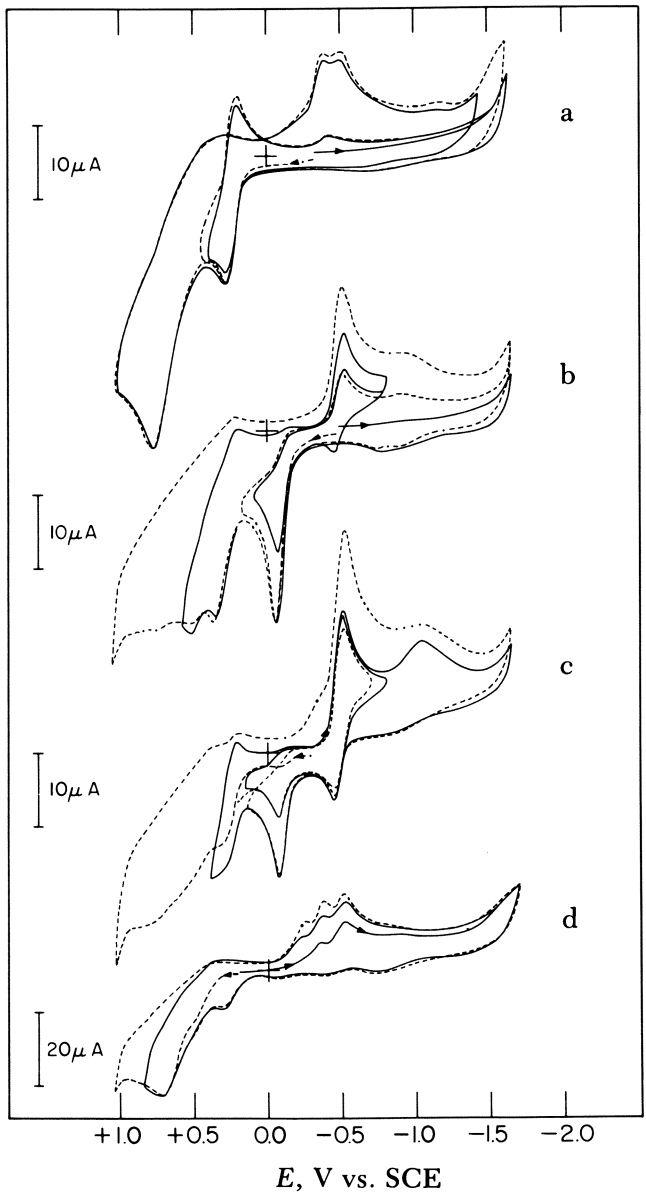

Figure 8. Cyclic voltammograms in DMF (0.1 M TEAP) of a, 1 mM $[Mo(VI)]_2O_5(DTBC)_2^{2-}$; b, 1 mM $[Mo_2(VI)]_2O_5(DTBC)_2^{2-}$ plus one equivalent TEAOH; c, solution b after oxidation at 0.0 V (one electron transferred per Mo); and d, 1 mM $[Mo_2(VI)]_2O_5(DTBC)_2^{2-}$ after electrochemical oxidation at +0.33 V (0.5 electron transferred per Mo).

positive scan to +0.75 V, which is sufficient to oxidize the catecholate ligands to DTBQ. If positive scans are reversed at potentials less than +0.70 V, a reversible oxidation couple occurs at +0.25 V. Controlled potential coulometry at +0.33 V (Figure 8) results in an overall oxidation of one electron per binuclear complex to a light-green solution with a broad absorption shoulder at 335–380 nm (ϵ 2800), a shoulder at 325 nm (ϵ 3200), and a shoulder at 278 nm. This electrolysis converts the original molybdenum(VI) complex to a product with a simple, one-line ESR signal (g = 2.00, a width of 14 G, and a peak-to-peak separation of 2.4 G). Further electrolysis of the oxidized solution at −0.33 V yields the original complex, $[Mo(VI)]_2O_5(DTBC)_2^{2-}$.

The couple at +0.25 V for $[Mo(VI)]_2O_5(DTBC)^{2-}$ corresponds to the reversible oxidation of bound $DTBC^{2-}$ to bound $DTBSQ^-$ (Figure 8a and Equations 37 and 38, Table V). After controlled potential oxidation at +0.33 V, a mixed DTBC–DTBSQ complex results, which is decomposed by H_2O to an inert molybdenum(VI) dimer and DTBQ.

Controlled potential oxidation at 0 V vs. SCE of a solution with two equivalents of OH^- per $[Mo(VI)]_2O_5(DTBC)^{2-}$ (Figure 8b) consumes two electrons per binuclear complex to yield a green solution (Figure 8c) that has absorption maxima at 386 nm (ϵ 6000), 370 nm (ϵ 6000), and a shoulder at 292 nm. It also exhibits a single ESR signal at g = 2.00 with a width of 18 G and a peak-to-peak separation of 2.6 G. The product solution decomposes to give an electrochemically inert molybdenum(VI) species plus DTBQ (Equations 37–39, Table V).

The addition of strong ligands (CN^- or imidazole) causes the solution to become dark red–brown with a new absorption band at 570 nm, which apparently results from ligand-to-metal charge transfer. Similar charge transfer bands also are observed for $[Mo(VI)O(DTBC)_2]_2$ and its monomer, $Mo(VI)O(DTBC)_2$, in the presence of strong electron-donating ligands. If a large excess of a strong-field ligand is added to $[Mo(VI)]_2O_5(DTBC)_2^{2-}$, the solution becomes colorless on standing, and free 3,5-di-*tert*-butylcatechol is formed. Apparently, such ligands displace the catechols from the complex to yield molybdenum(VI).

The IR of $[Mo(VI)]_2O_5(DTBC)_2^{2-}$ is dominated by bands due to the catechol ligands, but additional strong bands are observed at 976, 917, and 885 cm^{-1}. The 976-cm^{-1} band has been assigned to the C–O bonds of the ligands. The other two bands are due to a symmetrical and antisymmetrical metal–oxygen stretching mode for the terminal oxygens of *cis*-dioxomolybdenum(VI) (*76*, *77*).

In the presence of base, dioxygen spontaneously oxidizes catechol, as well as metal–catechol complexes, to yield mixed catechol–semiquinone species (*67*). The superoxide ion that results from catechol oxidation by oxygen in the presence of base should readily affect reduction of molybdenum(VI), as well as of any free DTBQ

that results from displacement of semiquinone by base (followed by disproportionation). Moreover, any such free DTBQ can oxidize the reduced molybdenum back to molybdenum(VI). Thus, the oxygen acts as a simple electron transfer agent for an intramolecular redox process (Equation 34, Table V).

Vanadium Complexes. In aqueous media, vanadium(V) oxidizes catechol to form quinone and vanadium(IV) (*42*, *78*). However, combination of $VOCl_3$ with $DTBCH_2$ in anhydrous CH_2Cl_2 yields a stable 1:2 vanadium(V)–$DTBC^{2-}$ complex.

Because protic species have an effect on the vanadium oxidation state (*79*), disodium 3,5-di-*tert*-butylcatechol (Na_2DTBC) was used with $VOCl_3$ in CH_2Cl_2 to synthesize the dark blue (λ_{max}, 680 nm) complex formulated as $NaV(V)O(DTBC)_2$. However, the product of the combination of $V(IV)O(acac)_2$ (where acac represents acetylacetonate) and catechol plus triethylamine was identified conclusively as $V(cat)_3^{2-}$ (where cat represents catechol) (*80*). When $V(cat)_3^{2-}$ is oxidized by electrolysis, it yields a product with a spectrum that is almost identical to the spectrum for a solution of $NaV(V)O(DTBC)_2$. The small electrochemical diffusion currents for this product in $(CH_3)_2SO$, CH_3CN, and CH_2Cl_2, in addition to proton NMR data, indicate that the material probably is polymeric (Figure 9). The two oxidation peaks that are observed for the complex in $(CH_3)_2SO$ correspond to ligand oxidations. Controlled potential electrolysis at +0.38 V results in a four-electron oxidation to produce two DTBQ molecules per vanadium(V) complex. Controlled potential electrolysis of the reduction peak at −0.45 V requires one electron and results in the appearance of a vanadium(IV) EPR signal. Reversal of an initial cathodic scan after this reduction produces a new oxidation peak at −0.38 V that also is present for an initial anodic scan after the coulometric oxidation of vanadium(IV) to vanadium(V) at −0.55 V.

Addition of HCl to $NaV(V)O(DTBC)_2$ in CH_3OH, in the presence of air, results in a purple solution with the same electronic spectra as the previously alleged oxygen adduct of vanadium(IV)$(DTBC)_2$ (*61*). This same spectrum is obtained on mixing $VOCl_3$ with $DTBSQ^-$ in CH_3OH. However, attempts to isolate a vanadium(V)–semiquinone complex by solvent evaporation result in the disproportionation of $DTBSQ^-$ to DTBQ and a blue vanadium(V)–DTBC complex.

The brown $Na_2V(IV)O(DTBC)_2$ complex can be prepared by the combination of one equivalent of $VO(acac)_2$ and two equivalents of Na_2DTBC in CH_2Cl_2. The spectroscopy of this complex is highly solvent dependent. Magnetic and spectroscopic measurements indicate that $Na_2V(IV)O(DTBC)_2$ is unstable in protic media. Cyclic voltammetry of this complex in CH_2Cl_2 and CH_3CN indicate that the vanadium(IV) is not reduced, but is oxidized at +0.18 V in CH_2Cl_2 and at

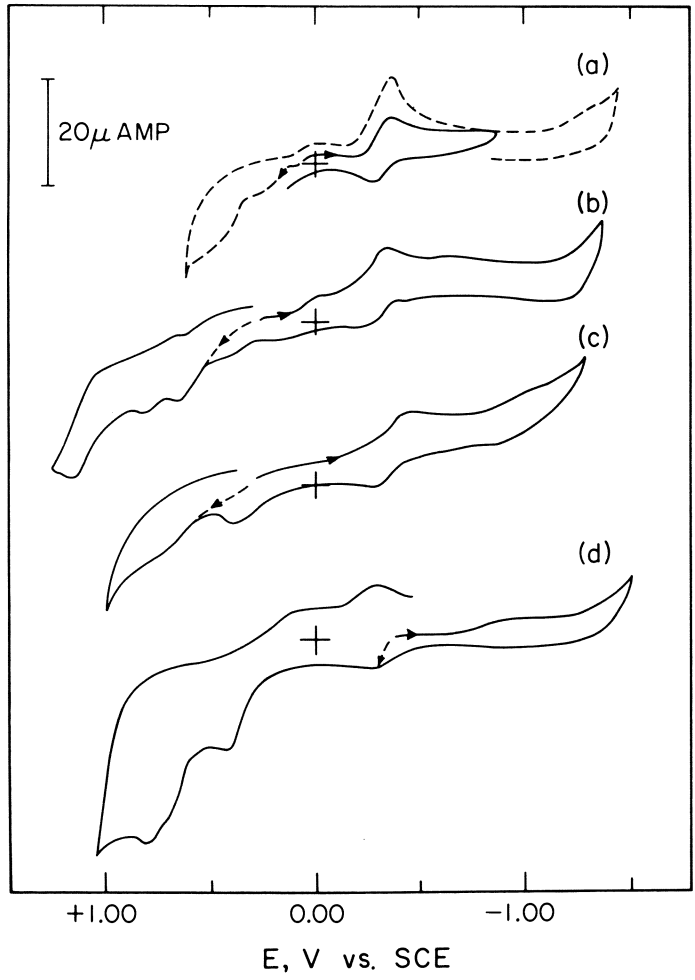

Figure 9. Cyclic voltammograms for 1 mM solutions of the reaction product of $V(V)OCl_3$ and Na_2DTBC in a, $(CH_3)_2SO$; b, CH_3CN; c, CH_2Cl_2; and d, for 1 mM $Na_2V(V)O(OCH_3)(DTBC)_2$ in CH_2Cl_2 (or its decomposition product). Scan rate, 0.01 V/s at a Pt electrode (area, 0.23 cm^{-1}).

−0.13 V in CH_3CN. Reversal of the scan after this peak results in a reduction peak at −0.52 V in CH_2Cl_2 and at −0.40 V in CH_3CN. Controlled potential electrolysis at the first anodic peak potential removes one electron to give a product solution that is ESR silent and free of DTBQ. Hence, this species appears to be the vanadium(V) complex, $NaV(V)O(DTBC)_2$. Electrolysis at the more positive peak potentials removes two electrons to yield DTBQ.

The blue crystalline complex, $Na_2V(IV)Cl_2(DTBC)_2$, was isolated from the direct reaction of $SOCl_2$ with $Na_2V(IV)O(DTBC)_2$ (*81*). A comparison of the IR spectra for $Na_2V(IV)O(DTBC)_2$ and $Na_2V(IV)Cl_2(DTBC)_2$ indicates the presence of a band at 880 cm^{-1} for the vanadium-terminal oxygen stretch. The magnetic moments for $Na_2V(IV)O(DTBC)_2$ and $Na_2V(IV)Cl_2(DTBC)_2$ in CH_2Cl_2 are 1.72 and 1.75 B.M., respectively. This finding confirms that oxidation of the vanadium center has not occurred.

The cyclic voltammetry for $Na_2V(IV)Cl_2(DTBC)_2$ in CH_2Cl_2 is illustrated by Figure 10, and indicates that an initial cathodic scan yields three reversible redox couples. Controlled potential electrolysis confirms that each couple is due to a one-electron process, presumably the metal center because they do not correspond to ligand reductions; that is,

$$V(IV) \underset{+0.13\ V}{\overset{1e^-\ +0.08\ V}{\rightleftharpoons}} V(III) \underset{-0.38\ V}{\overset{1e^-\ -0.44\ V}{\rightleftharpoons}} V(II) \underset{-1.20\ V}{\overset{1e^-\ -1.25\ V}{\rightleftharpoons}} V(I) \qquad (40)$$

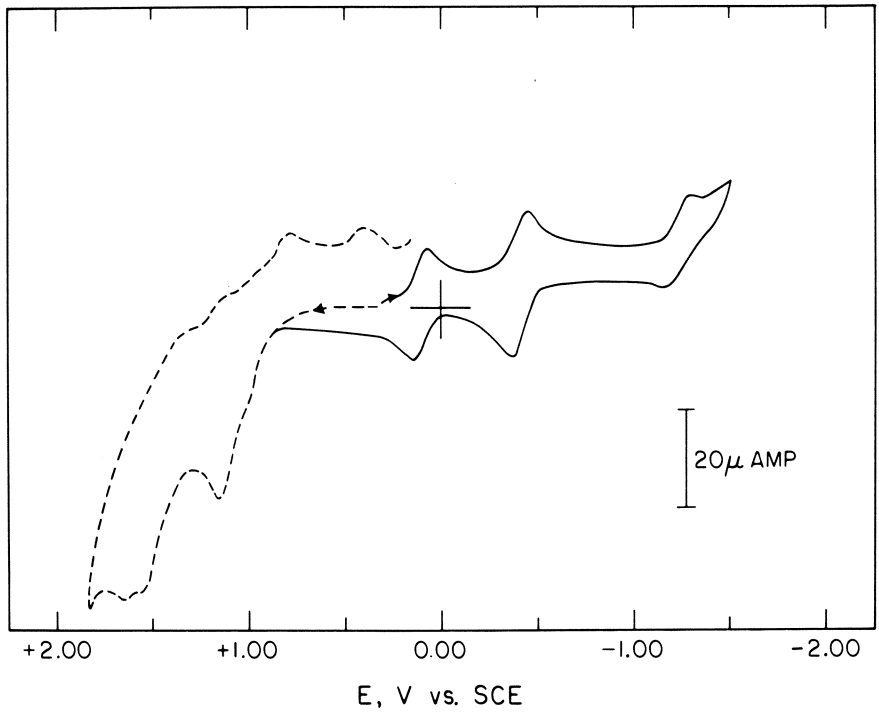

Figure 10. Cyclic voltammetry for a 1 mM solution of $Na_2V(IV)Cl_2(DTBC)_2$ in CH_2Cl_2. Scan rate, 0.10 V/s at a Pt electrode (area, 0.23 cm^{-1}).

The formation of a vanadium(I) complex is unprecedented, and this assignment must be viewed as tentative. The solutions formed during these electrolyses are highly unstable and preclude magnetic susceptibility measurements. Three irreversible oxidation peaks at +1.13, +1.51, and +1.63 V are observed for an initial positive scan of $Na_2V(IV)Cl_2(DTBC)_2$ in CH_2Cl_2. Controlled potential electrolysis at +1.25 V removes two electrons per complex, but does not yield DTBQ or DTBSQ.

The $Na_2V(IV)Cl_2(DTBC)_2$ complex is extremely sensitive to water and oxygen, and is oxidized to vanadium(V) by CH_3OH. The rapid reaction with methanol probably results from the strong affinity of vanadium(IV) for oxygen.

$$Na_2V(IV)Cl_2(DTBC)_2 + CH_3OH \rightarrow V(V)(OCH_3)(DTBC)_2 + \tfrac{1}{2}H_2 + 2NaCl \quad (41)$$

Dark green crystals of $Na_3V(III)(DTBC)_3$ can be obtained from the combination of three equivalents of Na_2DTBC with one equivalent of $V(III)(acac)_3$ in CH_2Cl_2. In the presence of air, either the solid complex or its solution in CH_2Cl_2 irreversibly change color to blue within seconds. The complex is not stable in protic solvents. Although the UV–visible spectrum of $Na_3V(III)(DTBC)_3$ in CH_2Cl_2 is similar to that for $Na_2V(IV)O(DTBC)_2$, its magnetic moment (2.93 B.M.) and the absence of a vanadium–oxygen stretch in its IR spectrum confirm that it is a unique species.

The electrochemistry of $Na_3V(III)(DTBC)_3$ in CH_2Cl_2 exhibits two reversible, one-electron oxidation couples at +0.13 and +0.40 V, plus several irreversible peaks at +1.18 V. The oxidation potential for the first peak is the same as is observed on the reverse scan from reduction of $Na_2V(IV)Cl_2(DTBC)_2$, which has been assigned to the vanadium(III)-to-vanadium(IV) oxidation. Oxidative electrolysis at the potentials for the remaining peaks results in the formation of DTBQ. In contrast to the $Na_2V(IV)Cl_2(DTBC)_2$ complex, the $Na_3V(III)(DTBC)_3$ complex does not exhibit any reduction peaks.

Tables VI and VII summarize the electrochemical and spectroscopic properties of the vanadium–catechol complexes. Several stable complexes can be synthesized without change of oxidation state in aprotic media. Addition of protons in the form of CH_3OH or H_2O results in the conversion of the lower oxidation states of vanadium to vanadium(V), which is stable in protic media. For the vanadium–DTBC system, metal oxidation usually occurs before ligand oxidation. Hence, only a semiquinone complex of vanadium(V) is a viable prospect.

The terminal oxygen of the vanadyl group in the vanadium(IV)–DTBC complexes has a dramatic effect on their electrochemistry. The

Published on June 1, 1982 on http://pubs.acs.org | doi: 10.1021/ba-1982-0201.ch028

Table VI. Redox Reactions for the 3,5-Di-*tert*-butylcatechol ($DTBC^{2-}$) Complexes of Vanadium(V), Vanadium(IV), and Vanadium(III) in Aprotic Media

Reaction	*Solvent*	*Redox Potentials V vs. SCE* [a] $E^{\circ\prime}$	$E_{p,c}$	$E_{p,a}$
(42) $V(V)O(DTBC)_2^- + e^- \rightarrow V(IV)O(DTBC)_2^{2-}$	$(CH_3)_2SO$		−0.45	
(43) $V(V)O(DTBC)_2^- \rightarrow V(V) + 2DTBQ + 4e^-$	$(CH_3)_2SO$			+0.30
(44) $V(V)O(OCH_3)(DTBC)_2^{2-} \rightarrow V(V)O(OCH_3)(DTBC) + DTBQ + 2e^-$ [b]	$(CH_3)_2SO$			+0.43
(45) $V(V)O(OCH_3)(DTBC) \rightarrow V(V) + DTBQ + 2e^-$ [b]	$(CH_3)_2SO$			+0.78
(46) $Na_2V(IV)(DTBC)_2 \rightarrow NaV(V)O(DTBC)_2 + Na^+ + e^-$	CH_2Cl_2			+0.18
	AN			−0.13
(47) $NaV(V)O(DTBC)_2 \rightarrow V(V)O(DTBC)^+ + DTBQ + Na^+ + 2e^-$	CH_2Cl_2			+0.35
	AN			+0.46
(48) $V(V)O(DTBC)^+ \rightarrow V(V) + DTBQ + 2e^-$	CH_2Cl_2			+0.61
	AN			+1.12
(49) $Na_2V(IV)Cl_2(DTBC)_2 + e^- \rightleftarrows NaV(III)(DTBC)_2 + 2Cl^- + Na^+$	CH_2Cl_2	+0.11		
(50) $NaV(III)(DTBC)_2 + Na^+ + e^- \rightleftarrows Na_2V(II)(DTBC)_2$ [b]	CH_2Cl_2	−0.41		
(51) $Na_2V(II)(DTBC)_2 + e^- \rightleftarrows Na_2V(I)(DTBC)_2^-$ [b]	CH_2Cl_2	−1.23		
(52) $Na_3V(III)(DTBC)_3 \rightleftarrows Na_2V(IV)(DTBC)_3 + Na^+ + e^-$	CH_2Cl_2	+0.11		
(53) $Na_2V(IV)(DTBC)_3 \rightleftarrows NaV(V)(DTBC)_3 + Na^+ + e^-$	CH_2Cl_2	+0.37		
(54) $NaV(V)(DTBC)_3 \rightarrow V(V) + 3DTBQ + Na^+ + 6e^-$	CH_2Cl_2			+1.18

[a] For reversible processes, the redox potentials ($E^{\circ\prime}$) represents the mean of the cathodic ($E_{p,c}$) and anodic ($E_{p,a}$) peak potentials; for irreversible processes, the peak potentials are for scan rates of 0.1 V/s.

[b] Tentative.

Published on June 1, 1982 on http://pubs.acs.org | doi: 10.1021/ba-1982-0201.ch028

Table VII. Spectroscopic Properties for the 3,5-Di-*tert*-butylcatechol Complexes of Vanadium(V), Vanadium(IV), and Vanadium(III) in Aprotic Media

Complex	*Solvent*	*UV–Visible* λ_{max}, *nm* (ϵ)	*Vanadium Magnetic Moment (B.M.)*	*DTBC Proton NMR, ppm vs. TMS*	*EPR* g-*Value*	*A(gauss)*
$[NaV(V)O(DTBC)_2]$	$(CH_3)_2SO$	700 (2700)	diamagnetic	1.43, 1.53		
		282 (7350)		1.57, 1.64		
	AN	680 (3550)		1.18, 1.23		
		271 (6550)		1.26, 1.38		
	CH_2Cl_2	680 (3720)		1.40, 1.47		
		274 (7180)		1.61		
$Na_2V(V)O(OCH_3)(DTBC)_2$	$(CH_3)_2SO$	600 (2600)	diamagnetic	1.49, 1.61		
		295 (7570)				
$Na_2V(IV)O(DTBC)_2$	CH_2Cl_2	283 (36300)	1.72		1.96	95
	AN	290 (53300)	1.73		1.96	90
$Na_2V(IV)Cl_2(DTBC)_2$	CH_2Cl_2	690 (5260)	1.75		1.96	100
		287 (6310)				
$Na_3V(III)(DTBC)_3$	CH_2Cl_2	284 (49000)	2.93			

$Na_2V(IV)O(DTBC)_2$ complex cannot be reduced electrochemically; it does undergo a quasi-reversible oxidation process. In contrast, the $Na_2V(IV)Cl_2(DTBC)_2$ complex exhibits three reversible, one-electron reduction couples, but not an oxidation peak for vanadium(IV) to vanadium(V). Most vanadyl compounds are pentacoordinated, which implies that vanadium cannot accept another ligand electron-pair because of the orbital distortion from the terminal oxygen atom. The $Na_3V(III)(DTBC)_3$ complex exhibits the same electrochemical reversibility as $Na_2V(IV)Cl_2(DTBC)_2$ because of the absence of the vanadyl moiety. It cannot be reduced (presumably, due to its high negative density), but it is oxidized by removal of one electron to form the blue $Na_2V(IV)(DTBC)_3$ complex.

Biological Relevance

Because many metalloproteins are bound to biomembranes, their in vivo environment probably is relatively aprotic. Hence, the redox properties of catechols and of metal–catechol complexes in aprotic solvents probably have thermodynamic and mechanistic relevance to biological systems. The current understanding of photosystem II is that manganese acts as a charge accumulator in the oxygen-evolving apparatus, and is an integral part of the enzyme-catalyzed oxidation of H_2O to O_2. For the manganese(II)–(DTBQ) system, its conversion to the $Mn(IV)(DTBC)_3^{2-}$ complex by the addition of four electrons has a striking parallel to the photosystem II process.

The present results confirm that the bonding for the catechol complexes of the higher oxidation state transition metal ions is dominated by hard acid–hard base interactions. The manganese(II) ion is considered to be much softer than the manganese(III) and manganese(IV) ions because of its larger size, smaller charge, and higher polarizability. The hard nature of the vicinal oxo ions of the $DTBC^{2-}$ dianion should make the "hard–hard" interaction between a higher oxidation state transition metal ion and the catechol dianion strong, and stabilize the electropositive metal center (*82*). The stability of the manganese(III) and manganese(IV) catechol complexes illustrates these effects. All of the systems in the present study are consistent in their tendency to achieve a hard acid–hard base interaction; that is, $Mn(IV)(DTBC)_3^{2-}$ rather than $Mn(III)(DTBC)_2(DTBSQ)^{2-}$, and $[Fe(III)(DTBC)_2]_2O^{4-}$ rather than $Fe(II)(DTBC)(DTBSQ)^-$.

Stable DTBC complexes of vanadium(III), vanadium(IV), and vanadium(V) can be prepared in aprotic media, but in protic media only the vanadium(V) complexes are stable. This behavior is in contrast to the reaction of pyrocatechol with vanadium in which vanadium(IV) appears to be the stable oxidation state in CH_3OH (*83*).

Apparently, the inductive effect of the *tert*-butyl groups affects redox properties of the respective pyrocatechol and $DTBCH_2$ complexes. For instance, the reduction of fully protonated pyrocatechol to the monoanion occurs at −1.17 V in CH_3CN, whereas the corresponding reaction with $DTBCH_2$ occurs at −1.22 V. In protic media, combination of vanadium(IV) with $DTBCH_2$ results in the formation of a vanadium(IV) complex that is oxidized by free protons to form vanadium(V).

Because solutions of vanadium(II) and catechol reduce dinitrogen to ammonia at room temperature (*79*), the vanadium–catechol system has been proposed as a model for nitrogenase. The present investigation of the vanadium–DTBC complexes illustrates the dramatic influence that the oxo group of vanadyl ion has on the complexes' electrochemistry. The fact that reversible electron transfer processes only are observed for the deoxygenated species undoubtedly is relevant to the design of small-molecule reaction mimics for vanadium redox proteins. The removal of the terminal oxygen from the vanadyl–DTBC complexes results in highly redox-active species. The lower oxidation states appear to be especially effective reductants for protic substrates.

The similarity of vanadium and molybdenum chemistry implies that the terminal oxygen atoms of the molybdenum–DTBC complexes may affect their redox chemistry. The monomeric $Mo(V)O(DTBC)_2^-$ complex, which has been suggested as a model for the xanthine oxidase enzyme, exhibits three irreversible reduction peaks (*64*); the $[Mo(VI)]_2O_5(DTBC)_2^{2-}$ complex cannot be reduced electrochemically. Both systems confirm that the addition of an electron to the central metal ion is inhibited by the distorted orbitals due to the terminal oxygen atoms.

Acknowledgments

This work was supported by the National Institutes of Health—U.S.P.H.S. under Grant No. GM–22761, the National Science Foundation under Grant No. CHE79–22040, and by the U.S. Department of Agriculture, Forest Service, Forest Products Laboratory, Madison, Wisconsin, under Agreement No. 12–176.

Literature Cited

1. Weinland, R.; Walter, E. Z. *Anorg. Allg. Chem.* **1923,** *126,* 141; *Chem. Abstr.* **1923,** *17,* 2542.
2. Weinland, R.; Sperl, H. Z. *Anorg. Allg. Chem.* **1925,** *150,* 69; *Chem. Abstr.* **1926,** *20,* 717.
3. Fernandes, L. *Gazz. Chim. Ital.* **1926,** *56,* 628; *Chem. Abstr.* **1927,** *21,* 866.
4. Scholder, R.; Wolf, M. Z. *Anorg. Allg. Chem.* **1933,** *210,* 184; *Chem. Abstr.* **1933,** *27,* 2106.

5. Scholder, R.; Schletz, E. Z. *Anorg. Allg. Chem.* **1933,** *211,* 161; *Chem. Abstr.* **1933,** *27,* 2645.
6. Sen, D.; Ray, F.; *J. Indian Chem. Soc.* **1953,** *30,* 253.
7. Babko, A. K.; *J. Gen. Chem. USSR* **1946,** *16,* 968.
8. Freimund, R.; Alan, L. *Inorg. Chem.* **1966,** *5,* 1542.
9. Sillen, L. G.; Martell, A. E. *Chem. Soc. Spec. Publ.* **1964,** *17.*
10. Athavale, V. T.; Prabhu, L. H.; Vartak, D. G. *J. Inorg. Nucl. Chem.* **1966,** *28,* 1237.
11. Murakami, Y.; Kodunaga, M. *Bull. Chem. Soc. Jpn.* **1964,** *37,* 1562.
12. Sandhu, S. S.; Sandhu, R. S.; Kumaria, J. N.; Singh, J.; Sekhon, W. S. *J. Indian Chem. Soc.* **1976,** *L111,* 114.
13. Grinstead, R. R. *Biochem.* **1964,** *3,* 1308.
14. Tyson, C. A.; Martell, A. E. *J. Am. Chem. Soc.* **1972,** *94,* 939.
15. Pollack, J. R.; Neilands, J. B. *Biochem. Biophys. Res. Commun.* **1970,** *38,* 989.
16. Harris, W. R.; Carrano, C. J.; Cooper, S. R.; Sofen, S. R.; Ardeef, A. E.; McArdle, J. M.; Raymond, K. N. *J. Am. Chem. Soc.* **1979,** *101,* 6097.
17. Harris, W. R.; Raymond, K. N. *J. Am. Chem. Soc.* **1979,** *101,* 6534.
18. Cooper, S. R.; McArdle, J. V.; Raymond, K. N. *Proc. Natl. Acad. Sci. U.S.A.* **1978,** *75,* 3551.
19. Carrano, C. J.; Raymond, K. N. *J. Am. Chem. Soc.* **1979,** *101,* 5401.
20. Weitl, F. L.; Harris, W. R.; Raymond, K. N. *J. Med. Chem.* **1979,** *22,* 1281.
21. Biollag, M.; Buchi, G.; Milne, G. *J. Am. Chem. Soc.* **1970,** *92,* 1035.
22. McCormick, J. R. D.; Jensen, E. R. *J. Am. Chem. Soc.* **1968,** *90,* 7126.
23. Curtis, R. F.; Hassall, C. H.; Parry, D. R. *Chem. Comm.* **1970,** 1512.
24. Ljungdahl, L. G. In "Molybdenum and Molybdenum Containing Enzymes," Coughlan, M., Ed.; Pergammon: Oxford, England, 1980; p. 465.
25. Enoch, H. G.; Lester, R. L.; *J. Bacteriol.* **1972,** *110,* 1032.
26. Scheses, P. A.; Thaner, R. K. *Eur. J. Biochem.* **1978,** *85,* 125.
27. Miller, V.; Willnow, P.; Ruschig, P.; Hopner, T. *Eur. J. Biochem.* **1978,** *83,* 485.
28. Knaff, D. B.; Malkin, R.; Myron, J. C.; Stoller, M.; *Biochim. Biophys. Acta* **1977,** *459,* 402.
29. Metzner, H. "Photosynthetic Oxygen Evolution"; Academic: New York, 1978.
30. Warden, J. T.; Blankenship, R. E.; Sauer, K. *Biochim. Biophys. Acta* **1976,** *423,* 426.
31. Lawrence, G. L.; Sawyer, D. T. *Coord. Chem. Rev.* **1978,** *27,* 173.
32. Josephson, L.; Cantley, Jr., L. C. *Biochem.* **1977,** *16,* 4572.
33. Gibbons, I. R.; Cosson, M. P.; Evans, J. A.; Gibbons, B. H.; Houck, B.; Martinson, K. H.; Sale, W. S.; Tang, W. Y. *Proc. Natl. Acad. Sci. U.S.A.* **1978,** *75,* 2220.
34. Cantley, L. C., Jr.; Ferguson, J. H.; Kustin, K. *J. Am. Chem. Soc.* **1978,** *100,* 5210.
35. Mentasti, E.; Pelizetti, E.; Paramaurd, E.; Giarandi, G. *Inorg. Chim. Acta* **1975,** *12,* 61.
36. Schraff, J. P.; Genin, R. *Anal. Chim. Acta* **1975,** *78,* 201.
37. Rukarina, T. G.; Downs, H. H.; Pierpont, C. G. *J. Am. Chem. Soc.* **1974,** *96,* 5573.
38. Downs, H. H.; Pierpont, C. G. *J. Am. Chem. Soc.* **1975,** *97,* 2123.
39. Buchanan, R. M.; Pierpont, C. G. *J. Am. Chem. Soc.* **1975,** *97,* 4912.
40. Lui, S. T.; Kustin, K. *J. Am. Chem. Soc.* **1973,** *95,* 2487.
41. Soni, R. N.; Bartusek, M. *J. Inorg. Nucl. Chem.* **1971,** *33,* 2557.
42. Kustin, K.; Lui, S.; Nicolini, C.; Topper, D. L. *J. Am. Chem. Soc.* **1974,** *97,* 7410.
43. Henry, R. P.; Mitchell, P. C. H.; Pone, J. E. *J. Chem. Soc. A* **1971,** 3392.
44. Muller, E. et al. *Lieb. Ann. Chem.* **1965,** *688,* 134.

45. Abakumov, G. A.; Razuvaev, G. A.; Lobanov, A. V. USSR Patent 527434, 1975; *Byull. Izobr.* **1976,** *33,* 75.
46. Razuvaev, G. A.; Shal'nova, K. G.; Abakumova, L. G.; Abakumov, G. A. *Izv. Akad. Nauk. SSSR Ser. Khim.* **1977,** *7,* 1642.
47. Buchanan, R. M.; Downs, H. H.; Shorthill, W. B.; Pierpont, C. G.; Kessel, S. L.; Hendrickson, D. N. *J. Am. Chem. Soc.* **1978,** *100,* 4318.
48. Buchanan, R. M.; Kesel, S. L.; Downs, H. H.; Pierpont, C. G.; Hendrickson, D. N. *J. Am. Chem. Soc.* **1978,** *100,* 7894.
49. Buchanan, R. M.; Fitzgerald, B. J.; Pierpont, C. G. *Inorg. Chem.* **1979,** *18* (12), 3439.
50. Pierpont, C. G.; Buchanan, R. M. *J. Am. Chem. Soc.* **1975,** *97,* 6450.
51. Razuvaev, G. A.; Abakumov, G. A.; Klimov, E. S. *Dokl. Akad. Nauk. SSSR* **1971,** *201,* 624.
52. Abakumov, G. A.; Klimov, E. S. *Dokl. Akad. Nauk. SSSR* **1972,** *202,* 827.
53. Abakumov, G. A.; Klimov, E. S. *Izv. Akad. Nauk. SSSR Ser. Khim.* **1972,** 1199.
54. Klimov, E. S.; et al. *Dokl. Akad. Nauk. SSSR* **1974,** *218,* 844.
55. Abakumov, G. A.; et al. *J. Organomet. Chem.* **1974,** *64,* 327.
56. Buchanan, R. M.; Pierpont, C. G. *J. Am. Chem. Soc.* **1980,** *102,* 4951.
57. Balch, A. L. *J. Am. Chem. Soc.* **1973,** *95,* 2723.
58. Downs, H. H.; Buchanan, R. M.; Pierpont, C. G. *Inorg. Chem.* **1979,** *18,* 1736.
59. Sofen, S. R.; Ware, D. C.; Cooper, S. R.; Raymond, K. N. *Inorg. Chem.* **1979,** *18,* 234.
60. Wicklund, P. A.; Brown, D. G. *Inorg. Chem.* **1976,** *15,* 396.
61. Wilshire, J. P.; Sawyer, D. T. *J. Am. Chem. Soc.* **1978,** *100,* 3972.
62. Wilshire, J. P.; Leon, L.; Bosserman, P.; Sawyer, D. T.; Buchanan, R. M.; Pierpont, C. G. In "The Chemistry and Uses of Molybdenum"; Barry, H. F.; Mitchell, P. C. H., Eds.; Climax Molybdenum Co., Ann Arbor, Mich., Third Int. Conf.; 1979; p. 264.
63. Wilshire, J. P.; Leon, L.; Bosserman, P.; Sawyer, D. T. *J. Am. Chem. Soc.* **1979,** *101,* 3379.
64. Wilshire, J. P.; Leon, L.; Bosserman, P.; Sawyer, D. T. In "Molybdenum Chemistry of Biological Significance"; Newton, W. E.; Otsuka, S., Eds.; Plenum: New York, 1980; p. 327.
65. Stormyan, L. O.; Tkacher, V. V.; Shirshora, T. G. *Dolk. Akad. Nauk. SSSR* **1972,** *205,* 609.
66. Magers, K. D.; Smith, C. G.; Sawyer, D. T. *Inorg. Chem.* **1978,** *17,* 515.
67. Magers, K. D.; Smith, C. G.; Sawyer, D. T. *J. Am. Chem. Soc.* **1978,** *100,* 989.
68. Magers, K. D.; Smith, C. G.; Sawyer, D. T. *Inorg. Chem.* **1980,** *19,* 492.
69. Eggins, B. R.; Chambers, J. R. *J. Electrochem. Soc.* **1970,** *117,* 186.
70. Mastragostino, M.; Nadjo, L.; Saveant, J. M. *Electrochim. Acta* **1968,** *13,* 721.
71. Kuz'min, V. A.; Khudyakov, I. V.; Popkov, A. V.; Karoli, L. L. *Izv. Akad. Nauk. SSSR Ser. Khim.* **1975,** 2431.
72. Havelkova, L.; Bartusek, M. *Collect. Czech. Chem. Comm.* **1969,** *34,* 2919.
73. Martin, J. L.; Takats, J. *Can. J. Chem.* **1975,** *53,* 572.
74. Tyson, C. A.; Martell, A. E. *J. Am. Chem. Soc.* **1968,** *90,* 3379.
75. Brown, D. G.; Reinprecht, J. T.; Vogel, G. C. *Inorg. Nucl. Chem. Lett.* **1979,** *12,* 399.
76. Wing, R. M.; Callahan, K. P. *Inorg. Chem.* **1969,** *8,* 871.
77. Griffith, W. P. *J. Chem. Soc. A,* **1969,** 211.
78. Pelizzetti, E.; Mentasti, E.; Pramauro, E.; Saini, G. *J. Chem. Soc. D* **1974,** 1940.
79. Shilov, A. E. *Biol. Aspects Inorg. Chem.* **1976,** *197.*
80. Cooper, S. R.; Koh, Y. B.; Raymond, K. N. *J. Am. Chem. Soc.* **1982,** *104,* in press.

81. Pasquali, M.; Marchetti, F.; Floriani, C. *Inorg. Chem.* **1979,** *18,* 2401.
82. Lowry, T. H.; Richardson, K. S. In "Mechanism and Theory in Organic Chemistry"; Harper & Row: New York, 1976; pp. 165–168.
83. Ferguson, J.; Kustin, K. *Inorg. Chem.* **1979,** *18,* 3349.

RECEIVED for review June 2, 1981. ACCEPTED December 5, 1981.

Electrochemistry and Spectroscopy of Catalytically Active Molybdenum–Catechol Complexes

HARRY O. FINKLEA, SUZANNE K. LAHR, and
FRANKLIN A. SCHULTZ

Florida Atlantic University, Department of Chemistry, Boca Raton, FL 33431

Electrochemical reduction of the cis*-dioxo Mo(VI)–catechol complex, $MoO_2(cat)_2^{2-}$, produces stable mononuclear Mo(V), Mo(IV), and Mo(III) complexes in weakly alkaline aqueous solution. Electrochemistry and spectroscopy are used to characterize these species and the conditions promoting their formation. Their catalytic reactions with several oxo anions are studied. Coordination reactions at sites generated by reductive removal of oxo groups stabilize the reduced monomers and also mediate the redox, spectroscopic, and catalytic properties of the molybdenum center. These results help explain the relationship between molecular structure and redox properties of a mononuclear molybdenum site. These findings are discussed in relation to the behavior of the molybdenum-containing enzymes (xanthine oxidase, sulfite oxidase, and nitrate reductase) that carry out oxygen-atom transfer reactions.*

The molybdenum-containing enzymes aldehyde oxidase, sulfite oxidase, xanthine oxidase, and nitrate reductase catalyze reactions in which an oxygen atom is added to or removed from the substrate molecule (*1*, *2*). Isolation of a common low-molecular weight cofactor from the last three of these species (*3*, *4*) plus physicochemical studies of the enzymes themselves (*5–17*) suggest a similar environment for the molybdenum atom in these systems. Important features of the environment include mononuclear structure with respect to Mo, oxomolybdenum bonding, predominantly sulfur ligation in the re-

0065-2393/82/0201-0709$06.25/0

mainder of the coordination sphere, cycling among Mo(VI), Mo(V), and Mo(IV) oxidation states during electron transfer, and Mo(V) EPR signals that are sensitive to the binding of substrates, products, and buffer anions at the metal site. Consistent with well-known structural features of molybdenum complexes (*18*), most likely the Mo(VI), Mo(V), and Mo(IV) states in the enzymes contain two, one, and one terminally bonded oxo groups, respectively, although presence of one terminal sulfido in place of oxo was proposed for the active oxidized form of xanthine oxidase (*15*).

Redox chemistry of oxomolybdenum complexes in both aqueous and nonaqueous media often is complicated by irreversible chemical reactions that occur after electron transfer and lead to poorly characterized products. The well-characterized (*19–21*) *cis*-dioxo Mo(VI)–catechol complex, $MoO_2(cat)_2^{2-}$ (I) (H_2cat = 1,2-dihydroxybenzene), can be reduced to stable Mo(V), Mo(IV), and Mo(III) monomers in

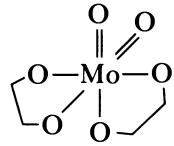

I

aqueous solution. This series of complexes is an effective vehicle for studying the relationship between structural and redox chemistry at a mononuclear molybdenum center. Important components in this relationship include reversible removal of oxo groups upon reduction in oxidation state and subsequent coordination reactions at these sites, which stabilize reduced monomeric species. In addition, the reduced complexes catalyze the reduction of a number of oxo anions. We review here our recent studies (*22–24*) on the electrochemical, spectroscopic, and catalytic properties of aqueous molybdenum–catechol complexes and discuss possible implications for the behavior of molybdenum-containing enzymes that catalyze oxygen-atom transfer reactions.

Experimental

Full details of experimental procedures are provided in References *22–24*. Complex I was formed by adding $Na_2MoO_4 \cdot 2H_2O$ to a 50-fold or greater excess of catechol (*20*). Voltammetric experiments were conducted at a hanging mercury drop electrode of 0.022 cm^2 area. Dc polarographic experiments were conducted with a capillary having characteristics of m = 1.82 mg/s

and t = 4.3 s at −0.8 V in 1 M KCl and 0.15 M H_2cat (pH 9.4). Spectroelectrochemistry was done in a transparent thin-layer cell containing an amalgamated gold minigrid working electrode. The cell design was similar to that of Anderson et al. (25). EPR spectra were recorded at room temperature with a Varian V-4502 instrument. Samples were prepared by controlled potential reduction at a mercury pool cathode and transferred anaerobically to the EPR cell on a Schlenk line. The monomeric Mo(V) content of the solution was established by two means: (1) measurement of the voltammetric peak current for Mo(V) → Mo(VI) oxidation following controlled potential reduction, and (2) double integration of the Mo(V) EPR signal intensity and comparison to that observed for a standard solution of $K_3Mo(CN)_8$. Agreement between the two techniques was ±20%. Unless otherwise noted, potentials are reported vs. the saturated calomel reference electrode (SCE).

Results and Discussion

Aqueous Electrochemistry at pH 3.5–7. The cyclic voltammogram in Figure 1 is representative of the electrochemical behavior of $MoO_2(cat)_2^{2-}$ in weakly acidic solution. Peak current magnitudes, peak potential separations, and controlled-potential coulometric experiments confirm the successive transfer of one and two electrons, in agreement with the initial polarographic study of this complex (*26*). Thus, reduction ensues from Mo(VI) → Mo(V) and Mo(V) → Mo(III). The pH dependences of the voltammetric half-wave potentials indicate the uptake of two protons in each electron transfer step and conversion of an oxo group to a coordinated water molecule:

$$MoO_2(cat)_2^{2-} + 2H^+ + e^- \rightleftarrows MoO(H_2O)(cat)_2^- \quad (E_{1/2})_1 \quad (1)$$

$$MoO(H_2O)(cat)_2^- + 2H^+ + 2e^- \rightleftarrows Mo(H_2O)_2(cat)_2 \quad (E_{1/2})_2 \quad (2)$$

Coordination of additional ligands or buffer components occurs at these aquo sites and is detectable from shifts in $(E_{1/2})_1$ and $(E_{1/2})_2$ with changes in their concentrations. Thus, species such as L = pyridine or imidazole form mono adducts in the Mo(V) state and mono and bis adducts in the Mo(III) state.

$$MoO(H_2O)(cat)_2^- + L \rightleftarrows MoO(L)(cat)_2^- + H_2O \quad \beta_1^V \quad (3)$$

$$Mo(H_2O)_2(cat)_2^- + L \rightleftarrows Mo(H_2O)(L)(cat)_2^- + H_2O \quad \beta_1^{III} \quad (4)$$

$$Mo(H_2O)_2(cat)_2^- + 2L \rightleftarrows Mo(L)_2(cat)_2^- + 2H_2O \quad \beta_2^{III} \quad (5)$$

Scheme I summarizes the combined redox and coordination chemistry of molybdenum–catechol complexes at pH 3.5–7. Table I contains equilibrium constants for formation of several of the Mo(V) and Mo(III) adducts.

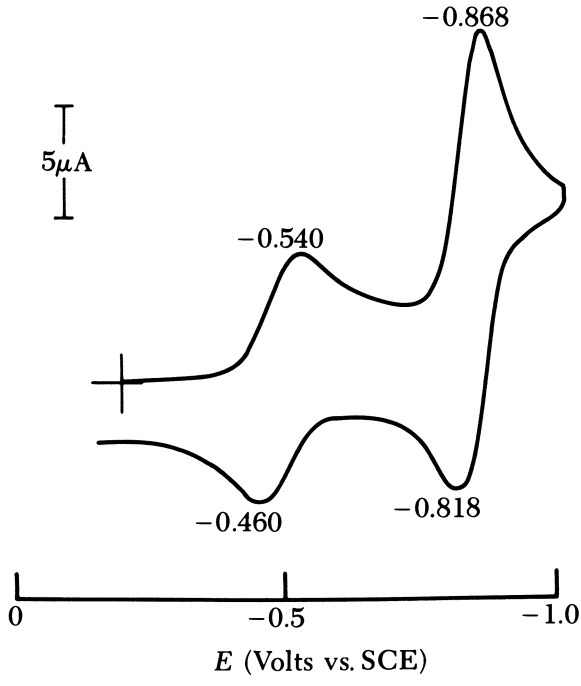

Figure 1. Cyclic voltammogram of $MoO_2(cat)_2^{2-}$ in pH 6.56 pyridine buffer (22). Conditions: 1 mM $MoO_2(cat)_2^{2-}$, 0.02 M pyH^+, 0.18 M py (pH 6.56), 0.1 M H_2cat, and ν = 0.2 V/s.

Because the equilibrium in Reaction 3 is labile and not shifted extensively to the right, the Mo(V) monomer is stable only transiently at pH < 7. After reduction to the Mo(V) state, dimerization ensues to the di-μ-oxo species, $Mo_2O_4(cat)_2(H_2O)_2^{2-}$. This reaction proceeds by dissociation of L and one molecule of catechol from $MoO(L)(cat)_2^-$ leaving an incompletely substituted monomeric center, **II**, which undergoes dimerization by acid-dependent and acid-independent pathways (22).

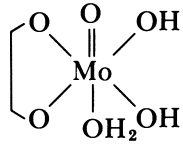

II

Aqueous Electrochemistry at pH 9–10. THE Mo(VI)–Mo(V) COUPLE. Mo(V)–catechol monomer is stabilized more completely against dimerization at pH > 9. One-electron, controlled-potential reduction of $MoO_2(cat)_2^{2-}$ in a solution buffered with excess catechol produces the cyclic voltammogram shown in Figure 2A. The anodic peak at −0.56 V corresponds to oxidation of Mo(V) monomer, present at 80–90% of the total Mo concentration under these conditions, and that at −0.20 V to oxidation of the residual Mo(V), present as dimer.

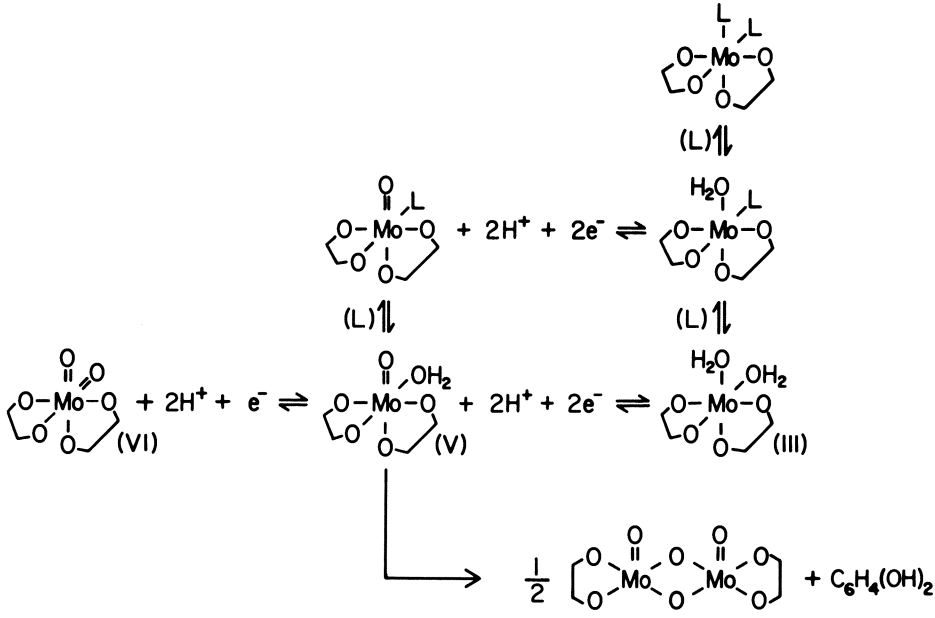

Scheme I. Redox and coordination chemistry of molybdenum–catechol complexes at pH 3.5–7 (22).

Table I. Formation Constants of Mo(V)– and Mo(III)–Catechol Complexes with Monodentate Ligands

Ligand	$\beta_1^{V}(M^{-1})$	$\beta_1^{III}(M^{-1})$	$\beta_2^{III}(M^{-2})$
Pyridine	4×10^1	1×10^4	6×10^5
Imidazole	8×10^2	3×10^4	2×10^6
$Hcat^-$	1.7×10^4		
NH_3	$\sim 5 \times 10^1$[a]	2×10^2	

[a] Estimated from EPR signal intensities.

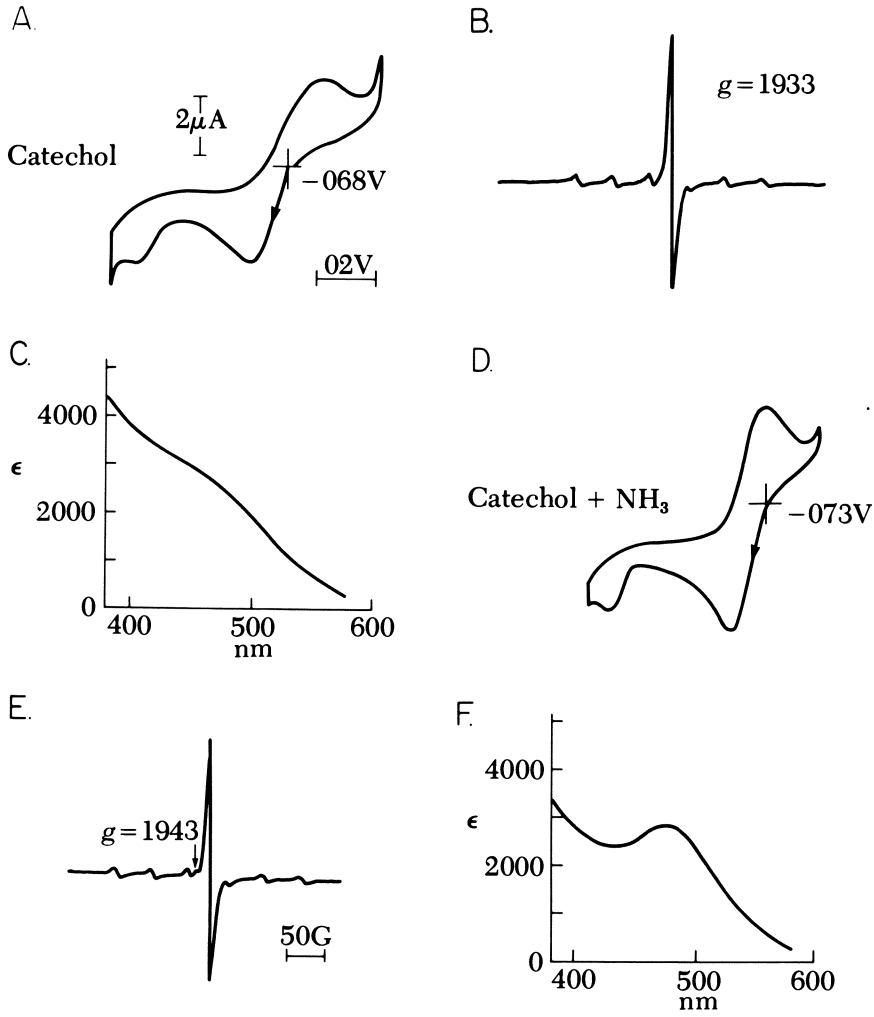

Figure 2. Cyclic voltammograms at 50 mV/s (A,D), EPR spectra (B,E), and visible absorption spectra (C,F) of Mo(V) complexes produced by one-electron controlled-potential reduction of $MoO_2(cat)_2^{2-}$ *at pH >9. Solution conditions (A–C): 2 mM Mo, 0.15 M* H_2cat*, 1 M KCl, pH 9.4; (D–F): 2 mM Mo, 0.1 M* H_2cat*, 1 M* NH_4Cl*, and 1 M* NH_2*, pH 9.6.*

The monomer–dimer distribution is confirmed by quantitative measurement of the intensity of the Mo(V) EPR signal that is observed for the reduced solution (Figure 2B). The pH and catechol dependences of the Mo(VI)–Mo(V) potential under these conditions indicate that the electrode half-reaction is

$$MoO_2(cat)_2^{2-} + H_2cat + H^+ + e^- \rightleftarrows MoO(Hcat)(cat)_2^{2-} + H_2O \qquad (E_{1/2})_1' \qquad (6)$$

Thus, the EPR signal at $g = 1.933$, which has a $^{95,97}Mo$ hyperfine coupling constant of $A = 45 \times 10^{-4}cm^{-1}$, is assigned to the species $MoO(Hcat)(cat)_2^{2-}$. The visible spectrum of this species recorded in a thin-layer spectroelectrochemical cell exhibits a shoulder at ~465 nm (21,500 cm^{-1}) with $\epsilon \cong 2400\ M^{-1}cm^{-1}$ (Figure 2C). An absorption at this energy is characteristic of MoO^{3+} complexes (*18*).

Virtually identical electrochemical behavior and no change in $(E_{1/2})_1'$ is observed in buffers containing NH_3 or amines in addition to catechol (Figure 2E). However, under these conditions, a small new EPR signal appears at $g = 1.943$ (Figure 2D), and the visible absorption band intensifies and becomes better defined with $\lambda_{max} = 470$–475 nm and $\epsilon \cong 2600\ M^{-1}cm^{-1}$ (Figure 2F). These spectroscopic changes are attributed to a small extent of substitution, estimated to be 3–5% from EPR signal intensities, by RNH_2 for $Hcat^-$ on the Mo(V) center.

$$MoO(Hcat)(cat)_2^{2-} + RNH_2 \rightleftarrows MoO(RNH_2)(cat)_2^- + Hcat^- \qquad (7)$$

The redox and coordination behavior of the Mo(VI)–Mo(V) couple at pH > 9 is depicted in Scheme II. Stabilization of monomeric Mo(V) is achieved by firm coordination of monodentate, monoprotonated catechol ($\beta_1^V = 1.7 \times 10^4 M^{-1}$, Table I) at the site generated by removal of one oxo group from $MoO_2(cat)_2^{2-}$. Dissociation of the first proton from H_2cat [$pK_a = 9.23$ (*27*)] assists this coordination. Approximately 10–20% of the Mo(V) exists as a dimer under these conditions. At pH < 7 a small amount of monomeric Mo(V) is detected in equilibrium with $Mo_2O_4(cat)_2(H_2O)_2^{2-}$ (*22*), and this finding suggests a $Mo(V)_2 \rightleftarrows 2Mo(V)$ equilibrium that is shifted largely to the right at high pH and to the left at low pH.

The Mo(VI)–Mo(V)–catechol couple is the first example of reversible electrochemical conversion between MoO_2^{2+} and MoO^{3+} centers yielding stable, characterizable products. If the monodentate ligand L remains at the site of the displaced oxo group *cis* to Mo=O, then $MoO_2(cat)_2^{2-}$ and $MoO(L)(cat)_2^-$ constitute a structurally related redox pair analogous to the compounds $MoO_2(tox)_2$ and $MoOCl(tox)_2$

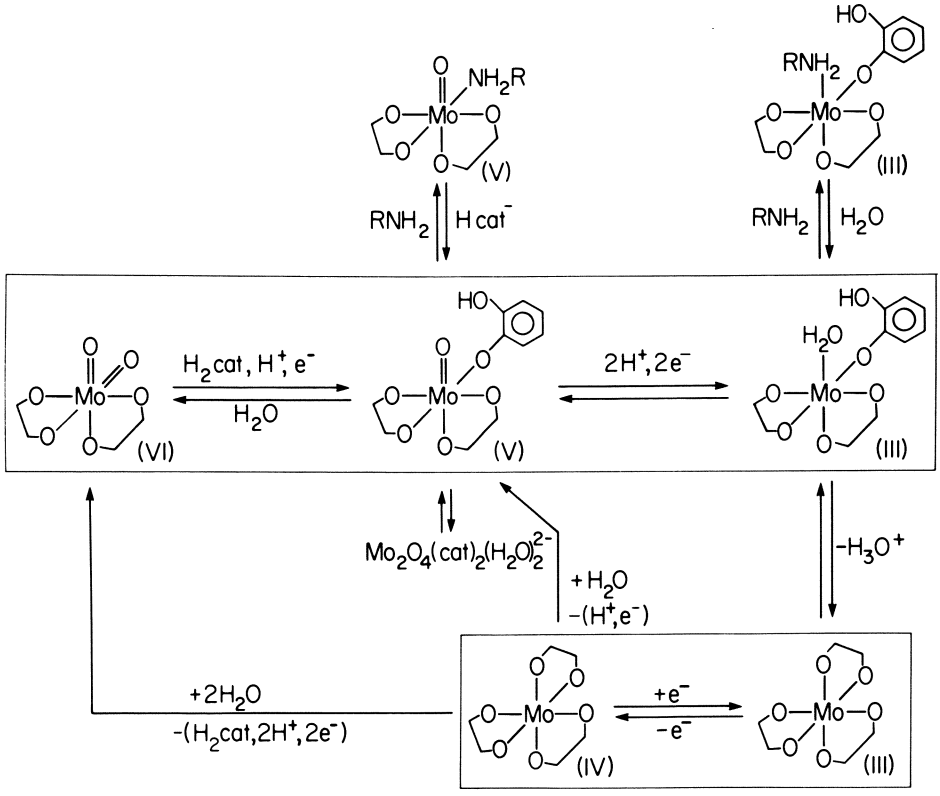

Scheme II. Redox and coordination chemistry of molybdenum–catechol complexes at pH >9 (23).

(Htox = 8-mercaptoquinolinol), recently characterized (*28*). Substitution reactions at this site affect the redox, spectroscopic, and catalytic properties of the Mo(V) center. Therefore, this coordination position is similar in several respects to the anion-binding site of the Mo(V) state of xanthine oxidase, sulfite oxidase, and nitrate reductase (*9*, *10*, *15–17*). Further aspects of this relationship are discussed in the concluding section of this chapter.

GENERATION OF Mo(IV) AND Mo(III) SPECIES. At high pH the character of the second $MoO_2(cat)_2^{2-}$ reduction wave changes from a two-electron Mo(V) → Mo(III) step to one in which an ensuing chemical reaction leads to formation of an intermediate formally in the Mo(IV) oxidation state. This behavior is illustrated in Figure 3 for a pH 7.7 ethylenediamine buffer. The 0.2 V/s experiment shows the expected two-electron reduction of Mo(V) at −0.95 V.

$$MoO(Hcat)(cat)_2^{2-} + 2H^+ + 2e^- \rightleftarrows Mo(H_2O)(Hcat)(cat)_2^{2-} \quad (E_{1/2})'_2 \quad (8)$$

The slower sweep rate experiment allows time for a chemical reaction to transform the reversible two-electron reduction into a net, irreversible one-electron reduction followed by a reversible one-electron reduction. Similar results are observed at pH > 9, but with the Mo(V) → Mo(IV) and Mo(IV) ⇄ Mo(III) waves overlapping one another.

Conditions of pH > 9 are preferred for studying the products of these electrode reactions, because the low-valent species are stable and can be generated quantitatively under these conditions. For example, controlled-potential electrolysis of Mo(VI) at a potential several hundred millivolts more negative than −1.1 V requires 3 faradays/mol of molybdenum and produces a yellow Mo(III) solution. A cyclic voltammogram initiated at −1.4 V in this solution reveals a reversible oxidation wave (*see* 0.01 V/s trace in Figure 3) having a peak current magnitude and peak potential separation consistent with a one-electron transfer and a half-wave potential of $(E_{1/2})_3 = -1.10$ V. Oxidation of the Mo(III) solution at a potential several hundred millivolts more positive than −1.1 V requires 1 faraday/mol of molybdenum and produces a red Mo(IV) solution. A cyclic voltammogram initiated in the negative direction from −0.9 V in this solution reveals a reversible reduction wave with the same parameters as the Mo(III) oxidation wave. Controlled potential oxidation of the Mo(IV) solution at −0.4 V requires 2 faradays/mol of molybdenum and returns the system to the original Mo(VI) state.

Figure 4 shows visible absorption spectra recorded in a thin-layer spectroelectrochemical cell under potentiostatic control during interconversion of the Mo(IV) and Mo(III) species. The Nernst plot of spectrally measured log [Ox]/[Red] vs. applied potential (29) and the quantity of charge transferred in the Ox → Red conversion establish the Mo(IV)–Mo(III) couple as a reversible, one-electron, monomeric redox system. Its spectroscopically measured formal potential, $E^{0\prime} = -1.09$ V, is in good agreement with the pH-independent half-wave potential of −1.10 V measured by cyclic voltammetry.

A mechanism for formation of the Mo(IV) species is offered in Scheme II. Since a third catechol molecule becomes coordinated to molybdenum in Reaction 6, Reaction 8 probably is followed by a chemical reaction in which the monodentate catechol ligand undergoes a chelate ring closure reaction to produce a tris(catecholato) Mo(III) complex:

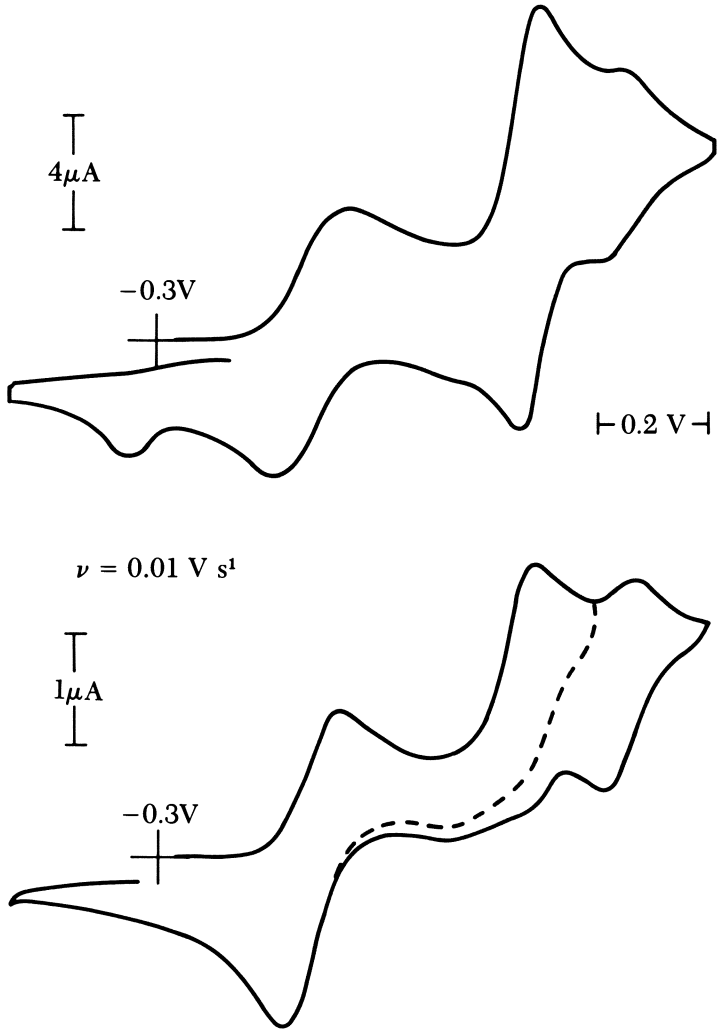

Figure 3. Cyclic voltammograms of $MoO_2(cat)_2^{2-}$ at 200 and 10 mV/s in pH 7.72 ethylenediamine buffer, 1 mM Mo, 0.15 M H_2cat, ionic strength = 0.5 (23).

$$Mo(H_2O)(Hcat)(cat)_2^{2-} \rightarrow Mo(cat)_3^{3-} + H_3O^+ \quad (9)$$

The potential at which this complex is generated is sufficiently positive to cause its one-electron oxidation (either heterogeneously by the electrode or homogeneously by a solution oxidant) to a Mo(IV) complex; thus, a net irreversible one-electron reduction is observed. Con-

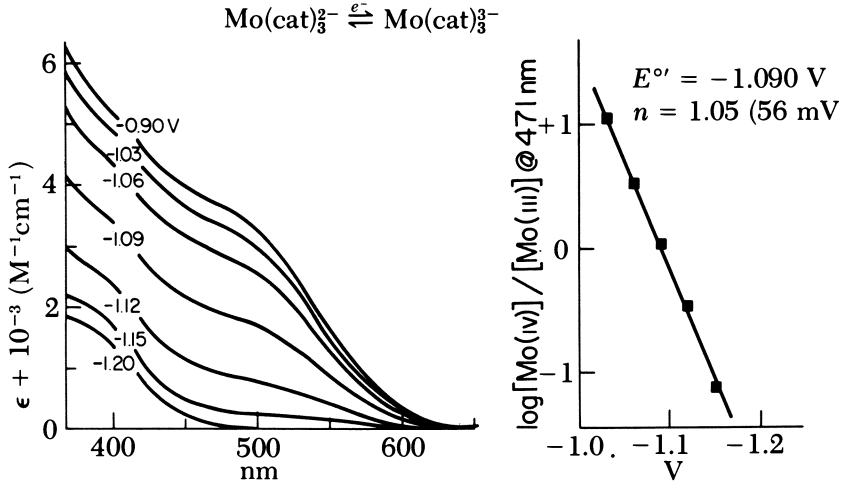

Figure 4. Spectroelectrochemical conversion of Mo(IV)- and Mo(III)-catechol complexes. Solution conditions: 2 m M Mo, 0.15 M H_2cat, 1 M KCl, 1 M NH_4Cl, and 1 M NH_3, pH 9.6 (23).

tinuing the voltammetric sweep to more negative potentials reveals the reversible one-electron reduction:

$$Mo(cat)_3^{2-} + e^- \rightleftarrows Mo(cat)_3^{3-} \qquad (E_{1/2})_3 \qquad (10)$$

Formulation of the Mo(IV) and Mo(III) complexes as triscatecholate species is consistent with coordination of a third catechol ligand in Reaction 6 and observations that a number of metal ion triscatecholate and tetrakiscatecholate complexes undergo reversible one-electron transfers in nonaqueous (*30, 31*) and alkaline aqueous (*32, 33*) media. Reaction 10 also could be considered as a ligand-centered electron transfer, with the Mo(IV) complex represented as a coordinated semiquinone, Mo(III)(cat)$_2$(SQ$^{\cdot-}$)$^{2-}$. The possibility of ligand-centered electron transfer was discussed for closely related Cr(III)–catecholate complexes (*30, 31*), and examples of transition metal complexes with coordinated semiquinone were reported recently (*34, 35*). No information as yet helps resolve this question, and isolation and characterization of the Mo(IV) complex remain to be carried out to accomplish this goal.

Scheme II reflects the extent to which the coordination and redox chemistries of molybdenum–catechol complexes are interrelated at pH > 9. Firm binding of ligands at sites generated by removal of oxo groups stabilizes the reduced monomers against dimerization. The structural changes that ensue when ligands replace oxo groups also

cause successive electron transfers to be accomplished more easily. As a result, the four oxidation states, Mo(VI) through Mo(III), can be generated as stable monomeric species within a range of about 450 mV.

Electrocatalytic Reduction of Oxo Anions. The ability of molybdenum to catalyze chemically (*36–38*) and electrochemically (*39–41*) the reduction of oxo anions led us to examine the reactivity of such species during electrochemical reduction of molybdenum–catechol complexes. Information on the composition and structure of electrode reaction products of these complexes can then serve as a basis for understanding the features that control catalytic reactivity at a mononuclear molybdenum site.

Figure 5 shows dc polarographic and cyclic voltammetric traces of pH 9.4 catechol solutions containing: nitrite ion, Mo(VI), and Mo(VI) plus nitrite ion. Catalytic reduction of nitrite occurs in two regions: (1) at potentials between −0.7 and −1.0 V, where Mo(VI) is reduced to Mo(V), and (2) at potentials in the vicinity of −1.1 V, where Mo(V) is reduced to Mo(IV) by the sequence of Reactions 8 and 9 plus the reverse of Reaction 10. When the potential is swept to more negative values, the current diminishes and defines a maximum. In a cyclic voltammetric experiment (left side of Figure 5C) the current also defines a cathodic maximum when swept in the positive direction from potentials more negative than −1.1 V. These observations are characteristic of a catalytic chemical reaction interposed between sequential charge transfer steps (*42*). Figure 5 demonstrates that both the Mo(V) and Mo(IV) oxidation states are effective in the catalytic reduction of nitrite ion; that Mo(IV) is more reactive than Mo(V); and that the Mo(III) is either inactive or substantially less reactive than Mo(IV) and Mo(V).

Other substrates reduced by the Mo(IV)– and Mo(V)–catechol complexes are chlorate and bromate ion (Table II). In both cases traces similar to Figure 5C are recorded in the presence of these ions, and the sequence of reactivity is Mo(IV) > Mo(V) > Mo(III). Because the potentially more oxidizing nitrate and perchlorate anions are inactive, the feature responsible for catalytic activity appears to be the nucleophilic character of the substrate imparted by the unshared pair of electrons on its central atom.

The kinetics of the Mo(V)–nitrite reaction were studied by cyclic voltammetry and dc polarography. Results conform to the behavior of a catalytic EC mechanism (*43*, *44*), although the complete mechanism probably is more complicated. The rate constants (k_{obs}) reported in Table II should not be considered accurate for this reason, but their relative values are useful in determining qualitative aspects of the mechanism. Under pseudo first-order conditions [nitrite ion and

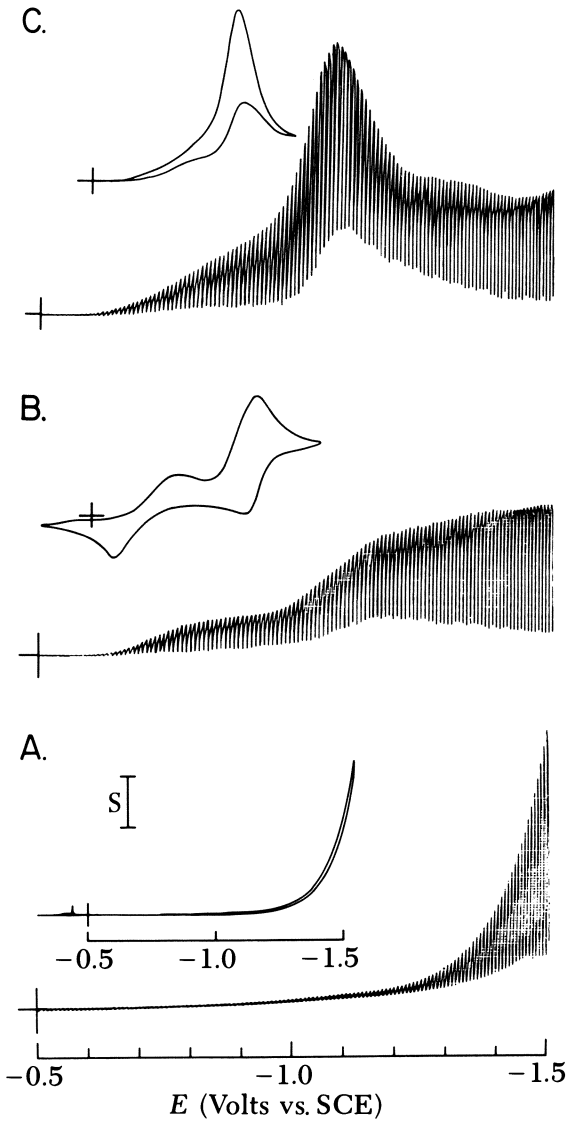

Figure 5. Dc polarographic and 20 mV/s cyclic voltammetric traces of 0.15 M H_2cat, *1* M *KCl, pH 9.4 solutions containing A, 0.2* M KNO_2, S = *1 μA; B, 1 m*M *Mo(VI),* S = *5 μA for dc polarography,* S = *2 μA for cyclic voltammetry; and C, 1 m*M *Mo(VI) + 0.2* M KNO_2, S = *10 μA.*

Table II. Substrates Catalytically Reduced by Mo(V)- and Mo(IV)-Catechol Complexes

	$k_{obs}(M^{-1}s^{-1})$[a]	
Substrate	*Mo(V)*	*Mo(IV)*[b]
NO_2^-	2.5×10^1	4×10^2
ClO_3^-	1.5×10^1	6×10^2
BrO_3^-	2.0×10^3	3×10^6
NO_3^-	No reaction	
ClO_4^-	No reaction	

[a] Observed second-order rate constant in the presence of excess substrate and excess constant catechol concentration, as defined by Equation 15. Determined by cyclic voltammetry from theory for a catalytic reaction following reversible charge transfer (*43*). Values are uncorrected for reaction stoichiometry and subject to limitations of accuracy discussed in the text. 0.15 *M* H_2cat, 1 *M* KCl, pH 9.

[b] Estimated as described in footnote *a* by correcting total current of the maximum near −1.1 V for catalytic and diffusion-limited current owing to Mo(V) and dividing by diffusion-limited current expected for a one-electron transfer.

catechol present in excess over Mo(VI)], the catalytic reaction rate is directly proportional to the molybdenum and nitrite concentrations and inversely proportional to the concentration of monoprotonated catechol ($Hcat^-$). There is no pH dependence other than that attributable to the protonation of $Hcat^-$. When excess NO_2^- is reacted with $MoO(Hcat)(cat)_2^{2-}$, spectroscopic and electrochemical measurements indicate that $MoO_2(cat)_2^{2-}$ is regenerated quantitatively. These findings are consistent with the mechanism given as follows in which nitrite ion first replaces $Hcat^-$ in a rapidly established equilibrium, followed by a rate-determining step and one or more subsequent reactions that produce $MoO_2(cat)_2^{2-}$.

$$MoO_2(cat)_2^{2-} + H_2cat + H^+ + e^- \rightleftarrows MoO(Hcat)(cat)_2^{2-} + H_2O \quad (11)$$

$$MoO(Hcat)(cat)_2^{2-} + NO_2^- \underset{k_{-1}}{\overset{k_1}{\rightleftharpoons}} MoO(NO_2)(cat)_2^{2-} + Hcat^- \quad (12)$$

$$MoO(NO_2)(cat)_2^{2-} \xrightarrow[\text{r.d.s.}]{k_2} MoO(ONO)(cat)_2^{2-} \quad (13)$$

$$MoO(ONO)(cat)_2^{2-} \longrightarrow MoO_2(cat)_2^{2-} + \text{products} \quad (14)$$

Consistent with similar catalytic reactions of Mo(V) in nonaqueous solvents (*36*, *37*), the rate-determining step is presumed to involve rearrangement of coordinated NO_2^- from a nitrogen-bonded to an oxygen-bonded species. If this change is accomplished so that an oxygen atom of NO_2^- becomes located *cis* to the oxo group on Mo(V), then

a favorable situation exists for rapid electron transfer and regeneration of $MoO_2(cat)_2^{2-}$. Because bonding of nitrite initially through nitrogen would occupy the final octahedral coordination site *cis* to Mo=O, a possible means of achieving this rearrangement is through the intermediate structure:

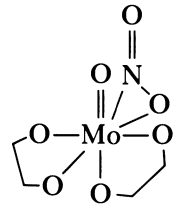

III

A heptacoordinated, pentagonal bipyramidal structure similar to **III** was observed in Mo(VI)–benzohydroxamate complexes containing oxygen and nitrogen-bonded hydroxylamide as an η^2 ligand (*45*).

An appropriate rate law for the mechanism described by Reactions 11–14 is

$$\text{rate} = -\frac{d[\text{Mo(V)}]}{dt} = \frac{k_1k_2[\text{Mo(V)}][\text{substrate}]}{k_{-1}[\text{Hcat}^-] + k_2} \cong \frac{k_1k_2[\text{Mo(V)}][\text{substrate}]}{k_{-1}[\text{Hcat}^-]} = k_{\text{obs}}[\text{Mo(V)}][\text{substrate}] \quad (15)$$

Values of the observed second-order rate constant, $k_{obs} = k_1k_2/k_{-1}[Hcat^-]$, subject to the limitations already discussed, are listed in Table II for the various substrates. Detailed mechanistic studies were not completed for ClO_3^- and BrO_3^-, but these ions are expected to react with Mo(V) in a manner similar to NO_2^-.

The nitrogen-containing product of Reaction 14 is expected to be nitric oxide. However, NO is not detected, and additional redox reactions apparently occur following Reaction 14. Titrations of $MoO(Hcat)(cat)_2^{2-}$ with nitrite indicate a $Mo(V):NO_2^-$ stoichiometry of between 2 and 3 : 1. Thus, nitrous oxide, dinitrogen, or a mixture of these gases may be the ultimate reaction products.

Quantitative study of the catalytic reactions of Mo(IV) is complicated by the fact that these processes are preceded by reactions involving Mo(V). However, the pattern of reactivity obtained from the relative rate constants in Table II indicates that coordination by a nucleophilic substrate also is a requirement for catalysis by molyb-

denum(IV). An important question is whether the greater reactivity of this species results from special features attributable to the d^2 configuration of Mo(IV), if the formalism $Mo(IV)(cat)_3^{2-}$ is correct, or to the occurrence of unpaired electron density on the ligands, if the formalism $Mo(III)(cat)_2(SQ)^{2-}$ is correct. Details of the catalytic reactions of this oxidation state are under investigation to help answer this question.

Implications for Behavior of Oxomolybdenum Enzymes. Although catechol ligand and its oxomolybdenum complexes are remote from direct biological relevance, several features that are apparent from the redox and catalytic behavior of these mononuclear species merit discussion.

The Mo(VI)–Mo(V) couple is an example of reversible redox conversion between MoO_2^{2+} and MoO^{3+} centers, structures that reasonably might be expected to be present in the Mo(VI) and Mo(V) states of the enzymes. Previous electrochemical investigations conducted in nonaqueous solvents have encountered irreversible behavior almost exclusively when reduction of $Mo(VI)O_2$ species or oxidation of Mo(V)O species is attempted (*46–50*). Thus, a protic environment facilitates reversible exchange of one oxo group within the MoO_2^{2+}–MoO^{3+} couple. The aquo coordination site generated by this reduction is the locus of substitution reactions that can alter the redox, spectroscopic, and catalytic properties of the Mo(V) center. These observations parallel the behavior of the Mo(V) states of xanthine oxidase, sulfite oxidase, and nitrate reductase, where binding of substrates, products, or buffer anions at the metal site affects the redox potentials (*10, 51, 52*) and Mo(V) EPR signals (*6, 10, 15–17*) of the enzymes.

For molybdenum–catechol complexes, the Mo(VI)–Mo(V) redox potential is mediated by the effect of coordination Reactions 3 and 6 on electrode Reaction 1. This potential shifts in the positive direction favoring Mo(VI) → Mo(V) reduction when a ligand is bound in place of an oxo group. Similar shifts are noted when products or buffer anions are bound in the Mo(V) states of the enzymes (*51, 52*). Coordination reactions at oxo sites not only favor the attainment of lower oxidation states in molybdenum complexes, but also stabilize monomeric species against dimerization. Consequently, at pH > 9 it is possible to generate monomeric Mo(VI), Mo(V), Mo(IV), and Mo(III) complexes within a range of ca. 450 mV. The structural and compositional changes that occur during electron transfer lead to a compression of redox states, an important feature of molecules that must carry out multielectron reactions.

Spectroscopic properties of $MoO(Hcat)(cat)_2^{2-}$ indicate that the sixth coordination site on this complex has additional features in

common with the Mo(V) anion-binding site of oxomolybdenum enzymes. This condition is exemplified by the appearance of a new EPR signal and intensification of the 21,500-cm^{-1} absorption band when an amine is substituted for $Hcat^-$. Exchange of ligands in the coordination sphere of MoO^{3+} complexes frequently leads to changes in these spectroscopic properties (*18, 53–56*). Because of the reversible character of the Mo(VI)–Mo(V) conversion, this substitution most likely is confined to an equatorial site *cis* to Mo=O in the complexes $MoO(L)(cat)_2^{n-}$ (for L = $Hcat^-$, n = 2; for L = RNH_2, pyridine, imidazole, n = 1). Although rearrangement of L to the site *trans* to Mo=O may occur, no evidence supports this possibility, and the process may be blocked by chelation of catechol at this position.

Binding of a nucleophilic substrate at the exchangeable coordination site on $MoO(Hcat)(cat)_2^{2-}$ appears to be a prerequisite to the catalytic reduction of NO_2^-, ClO_3^-, and BrO_3^- by Mo(V). Failure to reduce nitrate clearly contrasts with the enzymatic behavior, but this discrepancy can be attributed in part to solvent, because nitrite is a moderately strong and nitrate a very weak nucleophile in water (*57*). Reduction of NO_3^- by other Mo(V) complexes was observed in nonaqueous solvents (*36–38*), where coordination of this anion is more favored. The contrasting behavior of NO_3^- and NO_2^- in different solvent media supports a previous suggestion (*36*) that the molybdenum center at the active site of nitrate reductase experiences a predominantly nonaqueous environment.

A final point is a possible explanation of the oxidation-state changes and redox-potential separations observed for the oxomolybdenum enzymes. Table III illustrates that a common feature of nitrate reductase, sulfite oxidase, and xanthine oxidase is closely spaced Mo(VI)–Mo(V) and Mo(V)–Mo(IV) redox steps. Although the molybdenum–catechol complexes provide an example of structural changes that lead to closely spaced redox states, the weight of experimental evidence is that the oxomolybdenum enzymes cycle among Mo(VI), Mo(V) and Mo(IV) rather than Mo(VI) through Mo(III) oxidation states (*2*), and that the lower oxidation states probably retain at least one terminally bonded oxo group (*11, 13, 14*). Thus, the redox sequence in these enzymes probably is best represented by MoO_2^{2+}, MoO^{3+}, and MoO^{2+} centers.

A reaction sequence for linking these three redox states into an electron transfer sequence similar to that expected in the enzymes is proposed in Scheme III. The scheme is constructed by combining the reversible proton-dependent MoO_2^{2+}–MoO^{3+} couple demonstrated for octahedral complexes in this work with recent reports of reversible MoO^{3+}–MoO^{2+} electrochemistry observed under aprotic conditions for square pyramidal complexes containing either a single tetradentate

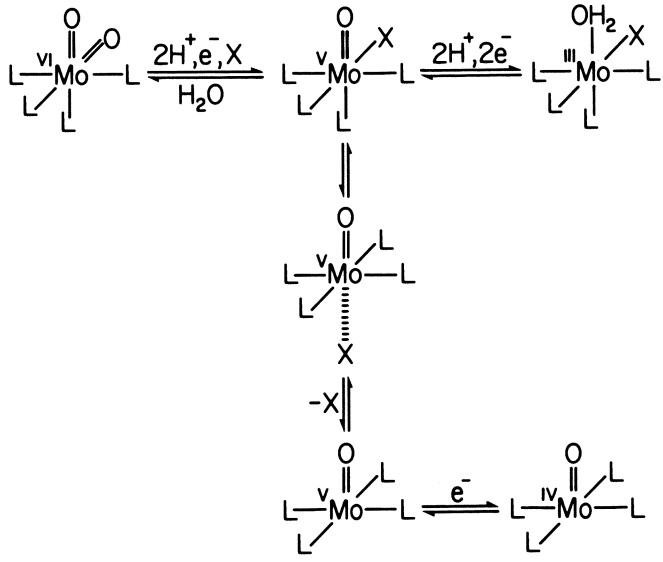

Scheme III. Reaction sequence for linking MoO_2^{2+}–MoO^{3+} and MoO^{3+}–MoO^{2+} redox couples.

Table III. Redox Potentials of Oxomolybdenum Enzymes

	Mo(VI)/*Mo*(V)	*Mo*(V)/*Mo*(IV)	*Ref.*
Nitrate reductase (pH 7)	+220	+180	58
Sulfite oxidase (pH 7)	+38	−163	11
Xanthine oxidase (pH 8) (native)	−355	−355	51
Xanthine oxidase (pH 8) (desulfo)	−440	−480	51
Mo–catechol (pH 8)	−480	—	[a]

Note: Values are in millivolts vs. NHE.
[a] $E_{1/2}$ of Reaction 1 extrapolated to pH 8.

aminothiolate ligand (*59*) or four monodentate thiophenolate ligands (*60*). A change in coordination number is required between the Mo(VI) and Mo(IV) states. This change is achieved by rearrangement of monodentate ligand X to the position *trans* to Mo=O in the Mo(V) state. In this location the Mo–X bond would be weakened or possibly broken by the *trans* influence of the oxo group (*61*, *62*). The presence of one less ligand on the metal would cause the potential of the Mo(V)–Mo(IV) couple to shift in the positive direction and become more nearly equal to the Mo(VI)–Mo(V) potential. In addition, a substrate binding site becomes available in the lower oxidation states. A

crucial undeveloped element in this model is control of proton availability. Protons are required for reversibility of the MoO_2^{2+}–MoO^{3+} conversion, but must be excluded to preserve reversibility of the MoO^{3+}–MoO^{2+} conversion and to prevent reduction to a lower oxidation state. The enzymes may control this feature by means of ligand-bound hydrogen atoms (*63*). In addition, considerable ligand flexibility is required to accommodate the change in coordination number with change in oxidation state. Satisfying these requirements promises to be a challenging aspect in the development of more refined models for the oxomolybdenum enzymes.

Acknowledgments

Support of this research by the National Science Foundation under Grant No. CHE 80-20442 is gratefully acknowledged. The authors also thank J. W. McDonald, W. E. Newton, and G. D. Watt of the Charles F. Kettering Research Laboratory, Yellow Springs, Ohio, for their help in obtaining the EPR results described.

Literature Cited

1. Coughlan, M. P. "Molybdenum and Molybdenum-Containing Enzymes"; Pergamon: Oxford, England, 1980.
2. Bray, R. C. In "The Enzymes"; Boyer, P. D., Ed.; Academic: New York, 1975; Vol. 12, Chapter 6.
3. Johnson, J. L.; Hainline, B. E.; Rajagopalan, K. V. *J. Biol. Chem.* **1980,** *255,* 1783.
4. Johnson, J. L. In "Molybdenum and Molybdenum-Containing Enzymes"; Coughlan, M. P., Ed.; Pergamon: Oxford, England, 1980; pp. 345–383.
5. Bordas, J.; Bray, R. C.; Garner, C. D.; Gutteridge, S.; Hasnain, S. S. *Biochem. J.* **1980,** *191,* 499.
6. Gutteridge, S.; Lamy, M. T.; Bray, R. C. *Biochem. J.* **1980,** *191,* 285.
7. Gutteridge, S.; Bray, R. C. *Biochem. J.* **1980,** *189,* 615.
8. Malthouse, J. P. G.; Gutteridge, S.; Bray, R. C. *Biochem. J.* **1980,** *185,* 767.
9. Lamy, M. T.; Gutteridge, S.; Bray, R. C. *Biochem. J.* **1980,** *185,* 397.
10. Barber, M. J.; Coughlan, M. P.; Kanda, M.; Rajagopalan, K. V. *Arch. Biochem. Biophys.* **1980,** *201,* 468.
11. Cramer, S. P.; Gray, H. B.; Scott, N. S.; Barber, M.; Rajagopalan, K. V. In "Molybdenum Chemistry of Biological Significance"; Newton, W. E.; Otsuka, S., Eds.; Plenum: New York, 1980; pp. 156–68.
12. Cramer, S. P.; Johnson, J. L.; Rajagopalan, K. V.; Sorrell, T. N. *Biochem. Biophys. Res. Commun.* **1979,** *91,* 434.
13. Cramer, S. P.; Gray, H. B.; Rajagopalan, K. V. *J. Am. Chem. Soc.* **1979,** *101,* 2772.
14. Tullius, T. D.; Kurtz, D. M., Jr.; Conradson, S. D.; Hodgson, K. O. *J. Am. Chem. Soc.* **1979,** *101,* 2776.
15. Gutteridge, S.; Tanner, S. J.; Bray, R. C. *Biochem. J.* **1978,** *175,* 887.
16. Gutteridge, S.; Tanner, S. J.; Bray, R. C. *Biochem. J.* **1978,** *175,* 869.
17. Vincent, S. P.; Bray, R. C. *Biochem. J.* **1978,** *171,* 639.
18. Stiefel, E. I. *Prog. Inorg. Chem.* **1977,** *22,* 1.
19. Tkachev, V. V.; Atovmyan, L. O. *Koord. Khim.* **1975,** *1,* 845.
20. Kustin, K.; Liu, S.-T. *J. Am. Chem. Soc.* **1973,** *95,* 2487.

21. Havelkova, L.; Bartusek, M. *Collect. Czech. Chem. Commun.* **1969,** *34,* 2919.
22. Charney, L. M.; Schultz, F. A. *Inorg. Chem.* **1980,** *19,* 1527.
23. Charney, L. M.; Finklea, H. O.; Schultz, F. A. *Inorg. Chem.* **1982,** *21,* 549.
24. Finklea, H. O.; Lahr, S. K.; Schultz, F. A., unpublished data.
25. Anderson, C. W.; Halsall, H. B.; Heineman, W. R. *Anal. Biochem.* **1979,** *93,* 366.
26. Zelinka, J.; Bartusek, M.; Okac, A. *Collect. Czech. Chem. Commun.* **1973,** *38,* 2898.
27. Martell, A. E.; Smith, R. M. "Critical Stability Constants"; Plenum: New York, 1977; Vol. 3, p. 200.
28. Yamanouchi, K.; Enemark, J. H. *Inorg. Chem.* **1979,** *18,* 1626.
29. DeAngelis, T. P.; Heineman, W. R. *J. Chem. Educ.* **1976,** *53,* 594.
30. Sofen, S. R.; Ware, D. C.; Cooper, S. R.; Raymond, K. N. *Inorg. Chem.* **1979,** *18,* 234.
31. Downs, H. H.; Buchanan, R. M.; Pierpont, C. G. *Inorg. Chem.* **1979,** *18,* 1736.
32. Magers, K. D.; Smith, C. G.; Sawyer, D. T. *Inorg. Chem.* **1978,** *17,* 515.
33. Sofen, S. R.; Cooper, S. R.; Raymond, K. N. *Inorg. Chem.* **1979,** *18,* 1611.
34. Kessel, S. L.; Emberson, R. M.; Debrunner, P. G.; Hendrickson, D. N. *Inorg. Chem.* **1980,** *19,* 1170.
35. Buchanan, R. M.; Pierpont, C. G. *J. Am. Chem. Soc.* **1980,** *102,* 4951.
36. Garner, C. D.; Hyde, M. R.; Mabbs, F. E.; Routledge, V. I. *J. Chem. Soc., Dalton Trans.* **1975,** 1180.
37. Hyde, M. R.; Garner, C. D. *J. Chem. Soc., Dalton Trans.* **1975,** 1186.
38. Taylor, R. D.; Todd, P. G.; Chasteen, N. D.; Spence, J. T. *Inorg. Chem.* **1979,** *18,* 44.
39. Haight, G. P., Jr. *Acta Chem. Scand.* **1961,** *15,* 2012.
40. Kolthoff, I. M.; Hodara, I. *J. Electroanal. Chem.* **1963,** *5,* 2.
41. Chikryzova, E. G.; Kiriyak, L. G. *Zh. Anal. Khim.* **1974,** *29,* 2420.
42. Polcyn, D. S.; Shain, I. *Anal. Chem.* **1966,** *38,* 376.
43. Nicholson, R. S.; Shain, I. *Anal. Chem.* **1964,** *36,* 706.
44. Koutecky, J. *Collect. Czech. Chem. Commun.* **1953,** *18,* 311.
45. Wieghardt, K.; Holzbach, W.; Hofer, E.; Weiss, J. *Inorg. Chem.* **1981,** *20,* 343.
46. Isbell, A. F., Jr.; Sawyer, D. T. *Inorg. Chem.* **1971,** *10,* 2449.
47. DeHayes, L. J.; Faulkner, H. C.; Doub, W. H., Jr.; Sawyer, D. T. *Inorg. Chem.* **1975,** *14,* 2110.
48. Taylor, R. D.; Street, J. P.; Minelli, M.; Spence, J. T. *Inorg. Chem.* **1978,** *17,* 3207.
49. Rajan, O. A.; Chakravorty, A. *Inorg. Chim. Acta* **1979,** *37* L503.
50. Cliff, C. A.; Fallon, G. D.; Gatehouse, B. M.; Murray, K. S.; Newman, P. J.; *Inorg. Chem.* **1980,** *19,* 773.
51. Cammack, R.; Barber, M. J.; Bray, R. C. *Biochem. J.* **1976,** *157,* 469.
52. Barber, M. J.; Bray, R. C.; Cammack, R.; Coughlan, M. P. *Biochem. J.* **1977,** *163,* 279.
53. Boorman, P. M.; Garner, C. D.; Mabbs, F. E. *J. Chem. Soc., Dalton Trans.* **1975,** 1299.
54. Dilworth, J. R.; McAuliffe, C. A.; Sayle, B. F. *J. Chem. Soc., Dalton Trans.* **1977,** 849.
55. Chen, G. J.-J.; McDonald, J. W.; Newton, W. E. *Inorg. Chim. Acta* **1979,** *35,* 93.
56. Scullane, M. I.; Taylor, R. D.; Minelli, M.; Spence, J. T.; Yamanouchi, K.; Enemark, J. H.; Chasteen, N. D. *Inorg. Chem.* **1979,** *18,* 3213.
57. Langford, C. H.; Parris, M. In "Comprehensive Chemical Kinetics"; Bamford, C. H.; Tipper, C. F. H., Eds.; Elsevier: London, 1972; Vol. 7, p. 23.
58. Vincent, S. P. *Biochem. J.* **1979,** *177,* 757.

59. Spence, J. T.; Minelli, M.; Kroneck, P. *J. Am. Chem. Soc.* **1980,** *102,* 4538.
60. Bradbury, J. R.; Wedd, A. G.; Bond, A. M. *J. Chem. Soc., Chem. Commun.* **1979,** 1022.
61. Appleton, T. G.; Clark, H. C.; Manzer, L. E. *Coord. Chem. Rev.* **1973,** *10,* 335.
62. Shustorovich, E. M.; Porai-Koshits, M. A.; Buslaev, Yu. A. *Coord. Chem. Rev.* **1975,** *17,* 1.
63. Stiefel, E. I.; Newton, W. E.; Watt, G. D.; Hadfield, K. L.; Bulen, W. A. In "Bioinorganic Chemistry–II," Raymond, K. N., Ed.; ACS ADVANCES IN CHEMISTRY SERIES, No. 162, ACS: Washington, D. C., 1977; p. 353.

RECEIVED for review June 2, 1981. ACCEPTED August 10, 1981.

INDEX

A

B

C

D

E

F

G

H

I

K

L

M

N

O

P

Q

R

S

T

U

V

W

X

Z